

PRINCIPLES OF POLYMER PROCESSING

Second Edition

ZEHEV TADMOR

*The Wolfson Department of Chemical Engineering
Technion-Israel Institute of Technology
Haifa, Israel*

COSTAS G. GOGOS

*Otto H. York Department of Chemical Engineering
Polymer Processing Institute
New Jersey Institute of Technology
Newark, New Jersey*



An SPE Technical Volume

 **WILEY-
INTERSCIENCE**

A John Wiley & Sons, Inc., Publication

PRINCIPLES OF POLYMER PROCESSING

PRINCIPLES OF POLYMER PROCESSING

Second Edition

ZEHEV TADMOR

*The Wolfson Department of Chemical Engineering
Technion-Israel Institute of Technology
Haifa, Israel*

COSTAS G. GOGOS

*Otto H. York Department of Chemical Engineering
Polymer Processing Institute
New Jersey Institute of Technology
Newark, New Jersey*



An SPE Technical Volume

 **WILEY-
INTERSCIENCE**

A John Wiley & Sons, Inc., Publication

Regarding the cover: The five bubbles contain images that represent the five elementary steps of polymer processing. The bottom image is a picture of the Thomas Hancock masticator, the first documented processing machine, developed in 1820. This image was originally published in the book *Thomas Hancock: Personal Narrative of the Origin and Progress of the Caoutchouc or India-Rubber Manufacture in England* (London: Longman, Brown, Green, Longmans, & Roberts, 1857).

Copyright © 2006 by John Wiley & Sons, Inc. All rights reserved

Published by John Wiley & Sons, Inc., Hoboken, New Jersey
Published simultaneously in Canada

No part of this publication may be reproduced, stored in a retrieval system, or transmitted in any form or by any means, electronic, mechanical, photocopying, recording, scanning, or otherwise, except as permitted under Section 107 or 108 of the 1976 United States Copyright Act, without either the prior written permission of the Publisher, or authorization through payment of the appropriate per-copy fee to the Copyright Clearance Center, Inc., 222 Rosewood Drive, Danvers, MA 01923, (978) 750-8400, fax (978) 750-4470, or on the web at www.copyright.com. Requests to the Publisher for permission should be addressed to the Permissions Department, John Wiley & Sons, Inc., 111 River Street, Hoboken, NJ 07030, (201) 748-6011, fax (201) 748-6008, or online at <http://www.wiley.com/go/permission>.

Limit of Liability/Disclaimer of Warranty: While the publisher and author have used their best efforts in preparing this book, they make no representations or warranties with respect to the accuracy or completeness of the contents of this book and specifically disclaim any implied warranties of merchantability or fitness for a particular purpose. No warranty may be created or extended by sales representatives or written sales materials. The advice and strategies contained herein may not be suitable for your situation. You should consult with a professional where appropriate. Neither the publisher nor author shall be liable for any loss of profit or any other commercial damages, including but not limited to special, incidental, consequential, or other damages.

For general information on our other products and services or for technical support, please contact our Customer Care Department within the United States at (800) 762-2974, outside the United States at (317) 572-3993 or fax (317) 572-4002.

Wiley also publishes its books in a variety of electronic formats. Some content that appears in print may not be available in electronic formats. For more information about Wiley products, visit our web site at www.wiley.com.

Library of Congress Cataloging-in-Publication Data:

Tadmor, Zehev, 1937-

Principles of polymer processing / Zehev Tadmor, Costas G. Gogos. – 2nd ed.
p. cm.

Includes index.

ISBN 0-471-38770-3 (cloth)

1. Polymers. 2. Polymerization. I. Gogos, Costas G. II. Title.

TP1087.T32 2006

668.9–dc22

2006009306

Printed in the United States of America

10 9 8 7 6 5 4 3 2 1

Series Preface

The Society of Plastics Engineers is pleased to sponsor and endorse the second edition of *Principles of Polymer Processing* by Zehev Tadmor and Costas Gogos. This volume is an excellent source and reference guide for practicing engineers and scientists as well as students involved in plastics processing and engineering. The authors' writing style and knowledge of the subject matter have resulted in an enjoyable and thoughtful presentation, allowing the reader to gain meaningful insights into the subject.

SPE, through its Technical Volumes Committee, has long sponsored books on various aspects of plastics. Its involvement has ranged from identification of needed volumes and recruitment of authors to peer review and approval of new books. Technical competence pervades all SPE activities, from sponsoring new technical volumes to producing technical conferences and educational seminars. In addition, the Society publishes periodicals, including *Plastics Engineering*, *Polymer Engineering and Science*, and *The Journal of Vinyl and Additive Technology*.

The resourcefulness of some 20,000 practicing engineers, scientists, and technologists has made SPE the largest organization of its type worldwide. Further information is available from the Society of Plastics Engineers, 14 Fairfield Drive, Brookfield, Connecticut 06804 or at www.4spe.org.

Susan E. Oderwald

*Executive Director
Society of Plastics Engineers*

Preface to the Second Edition

Tremendous science and engineering progress has been made in polymer processing since the publication of the First Edition in 1979. Evolution in the field reflects the formidable contributions of both industrial and academic investigators, and the groundbreaking developments in rheology, polymer chemistry, polymer physics, life sciences and nanomaterials, in instrumentation and improved machinery. The emerging disciplines of computational fluid mechanics and molecular modeling, aided by exponentially expanding computing power are also part of this evolution.

As discussed in Chapter 1 of this Second Edition, polymer processing is rapidly evolving into a *multidisciplinary* field. The aim is not only to analyze the complex thermo-mechanical phenomena taking place in polymer processing equipment, *per se*, but to quantitatively account for the *consequences*, on the fabricated polymer products. Thus, the focus of future polymer processing science will shift away from the machine, and more on the product, although the intimate material-machine interactions in the former are needed for the latter.

Consequently, this edition contains not only updated material but also a significant restructuring of the original treatment of polymer processing. First, we deleted Part I which discussed polymer structure and properties, since the subject is thoroughly covered in many classic and other texts. Second, in light of the important technological developments in polymer blends and reactive processing, new chapters on Devolatilization, Compounding and Reactive Processing, and Twin Screw and Twin Rotor-based Processing Equipment are introduced. These processes are widely used because of their unique abilities to affect rapid and efficient solid deformation melting and chaotic mixing.

However, the basic philosophy we advocated in the First Edition, which was to analyze polymer processing operations in terms of *elementary* and *shaping* steps, which are common to all such processing operations, and thereby unifying the field is retained. We have continued our attempt to answer not only “how” the machines and processes work, but also “why” they are best carried out using a specific machine or a particular process. In fact, we believe that this approach has contributed to the fundamental understanding and development of polymer processing in the last quarter-century, and to the change of focus from the machine to the quantitative prediction of product properties.

As with the First Edition, this volume is written both as a textbook for graduate and undergraduate students, as well as resource for practicing engineers and scientists. Normally, a two-semester course is needed to cover the material in the text. However for students who are familiar with fluid mechanics, heat transfer and rheology, it is possible to cover the material in one semester.

To enhance the usefulness of the Second Edition for both students and practitioners of the field, an extensive Appendix of rheological and thermo-mechanical properties of commercial polymers, prepared and assembled by Dr. Victor Tan, and for teachers, a complete problem Solution Manual, prepared by Dr. Dongyun Ren are included. For all it is hoped that this Second Edition, like the First, proves to be a useful professional “companion”.

We would like to acknowledge, with gratitude, the role and help of many: foremost, the invaluable assistance of Dr. Dongyun Ren, who spent almost three years with us at the Technion and NJIT/PPI, assisting with many aspects of the text preparation, as well as the Solution Manual; and Dr. Victor Tan, whose expert and meticulous work in measuring and gathering rheological and thermo-mechanical polymer properties provides the data needed to work out real problems. In addition, we wish to thank our colleagues, and students, who have influenced this book with their advice, criticism, comments, and conversations. Among them are David Todd, Marino Xanthos, Ica Manas-Zloczower, Donald Sebastian, Kun Hyun, Han Meijer, Jean-Francois Agassant, Dan Edie, John Vlachopoulos, Musa Kamal, Phil Coates, Mort Denn, Gerhard Fritz, Chris Macosko, Mike Jaffe, Bob Westover, Tom McLeish, Greg Rutledge, Brian Qian, Myung-Ho Kim, Subir Dey, Jason Guo, Linjie Zhu and Ming Wan Young. Special thanks are due to R. Byron Bird for his advice and whose classic approach to Transport Phenomena, inspired our approach to polymer processing as manifested in this book.

There are others we wish to mention and recall. While they are no longer with us, their work, ideas, and scientific legacy resurface on the pages of this book. Among them: Joe Biesenberger, Luigi Pollara, Peter Hold, Ally Kaufmann, Arthur Lodge, Don Marshall, Imrich Klein, Bruce Maddock, and Lew Erwin.

We wish to thank our editor, Amy Byers, our production editor, Kristen Parrish, the copy editor Trumbull Rogers, and the cover designer Mike Rutkowski. We give special thanks to Abbie Rosner for her excellent editing of our book and to Mariann Pappagallo and Rebecca Best for their administrative support.

Finally, we thank our families, who in many respects paid the price of our lengthy preoccupation with this book at the expense of time that justly belonged to them.

ZEHEV TADMOR
COSTAS G. GOGOS

Haifa, Israel
Newark, New Jersey
May 2006

Preface to the First Edition

This book deals with polymer processing, which is the manufacturing activity of converting raw polymeric materials into finished products of desirable shape and properties.

Our goal is to define and formulate a coherent, comprehensive, and functionally useful engineering analysis of polymer processing, one that examines the field in an integral, not a fragmented fashion. Traditionally, polymer processing has been analysed in terms of specific processing methods such as extrusion, injection molding calendaring, and so on. Our approach is to claim that what is happening to the polymer in a certain type of machine is *not unique*: polymers go through similar experiences in other processing machines, and these experiences can be described by a set of *elementary processing steps* that prepare the polymer for any of the *shaping* methods available to these materials. On the other hand, we emphasize the *unique* features of particular polymer processing methods or machines, which consist of the particular elementary step and shaping *mechanisms* and *geometrical solutions* utilized.

Because with the approach just described we attempt to answer questions not only of “how” a particular machine works but also “why” a particular design solution is the “best” among those conceptually available, we hope that besides being useful for students and practicing polymer engineers and scientists, this book can also serve as a tool in the process of creative design.

The introductory chapter highlights the technological aspects of the important polymer processing methods as well as the essential features of our analysis of the subject. Parts I and II deal with the fundamentals of polymer science and engineering that are necessary for the engineering analysis of polymer processing. Special emphasis is given to the “structuring” effects of processing on polymer morphology and properties, which constitute the “meeting ground” between polymer engineering and polymer science. In all the chapters of these two parts, the presentation is utilitarian; that is, it is limited to what is necessary to understand the material that follows.

Part III deals with the elementary processing steps. These “steps” taken together make up the total thermomechanical experience that a polymer may have in any polymer processing machine prior to shaping. Examining these steps separately, free from any particular processing method, enables us to discuss and understand the range of the mechanisms and geometries (design solutions) that are available. Part III concludes with a chapter on the modeling of the single-screw extruder, demonstrating the *analysis* of a complete processor in terms of the elementary steps. We also deal with a new polymer processing device to demonstrate that *synthesis* (invention) is also facilitated by the elementary-step approach.

We conclude the text with the discussion of the classes of shaping methods available to polymers. Again, each of these shaping methods is essentially treated independently of

any particular processing method. In addition to classifying the shaping methods in a logical fashion, we discuss the “structuring” effects of processing that arise because the macromolecular orientation occurring during shaping is fixed by rapid solidification.

The last chapter, a guide to the reader for the analysis of any of the major processing methods in terms of the elementary steps, is necessary because of the unconventional approach we adopt in this book.

For engineering and polymer science students, the book should be useful as a text in either one-semester or two-semester courses in polymer processing. The selection and sequence of material would of course be very much up to the instructor, but the following syllabi are suggested: *For a one-semester course:* Chapter 1; Sections 5.2, 4, and 5; Chapter 6; Sections 7.1, 2, 7, 9, and 10; Sections 9.1, 2, 3, 7, and 8; Chapter 10; Section 12.1; Sections 13.1, 2, 4, and 5; Section 14.1; Section 15.2; and Chapter 17—students should be asked to review Chapters 2, 3, and 4, and for polymer science students the course content would need to be modified by expanding the discussion on transport phenomena, solving the transport methodology problems, and deleting Sections 7.7, 9, and 10. *For a two-semester course: in the first semester,* Chapters 1, 5, and 6; Sections 7.1, 2, and 7 to 13; Sections 8.1 to 4, and 7 to 13; Chapters 9 and 10; and Sections 11.1 to 4, 6, 8, and 10—students should be asked to review Chapters 2, 3, and 4; and *in the second semester,* Chapters 12 and 13; Section 14.1, and Chapters 15, 16, and 17.

The problems included at the end of Chapters 5 to 16 provide exercises for the material discussed in the text and demonstrate the applicability of the concepts presented in solving problems not discussed in the book.

The symbols used follow the recent recommendations of the Society of Rheology; SI units are used. We follow the stress tensor convention used by Bird et al.,* namely, $\boldsymbol{\pi} = P\boldsymbol{\delta} + \boldsymbol{\tau}$, where $\boldsymbol{\pi}$ is the total stress tensor, P is the pressure, and $\boldsymbol{\tau}$ is that part of the stress tensor that vanishes when no flow occurs; both P and τ_{ii} are positive under compression.

We acknowledge with pleasure the colleagues who helped us in our efforts. Foremost, we thank Professor J. L. White of the University of Tennessee, who reviewed the entire manuscript and provided invaluable help and advice on both the content and the structure of the book. We further acknowledge the constructive discussions and suggestions offered by Professors R. B. Bird and A. S. Lodge (University of Wisconsin), J. Vlachopoulos (McMaster University), A. Rudin (University of Waterloo), W. W. Graessley (Northwestern University), C. W. Macosko (University of Minnesota), R. Shinnar (CUNY), R. D. Andrews and J. A. Biesenberger (Stevens Institute), W. Resnick, A. Nir, A. Ram, and M. Narkis (Technion), Mr. S. J. Jakopin (Werner-Pfleiderer Co.), and Mr. W. L. Krueger (3M Co.). Special thanks go to Dr. P. Hold (Farrel Co.), for the numerous constructive discussions and the many valuable comments and suggestions. We also thank Mr. W. Rahim (Stevens), who measured the rheological and thermophysical properties that appear in Appendix A, and Dr. K. F. Wissbrun (Celanese Co.), who helped us with the rheological data and measured η_0 . Our graduate students of the Technion and Stevens Chemical Engineering Departments deserve special mention, because their response and comments affected the form of the book in many ways.

*R. B. Bird, W. E. Stewart, and E. N. Lightfoot, *Transport Phenomena*, Wiley, New York, 1960; and R. B. Bird, R. C. Armstrong, and O. Hassager, *Dynamics of Polymeric Liquids*, Wiley, New York, 1977.

We express our thanks to Ms. D. Higgins and Ms. L. Sasso (Stevens) and Ms. N. Jacobs (Technion) for typing and retyping the lengthy manuscript, as well as to Ms. R. Prizgintas who prepared many of the figures. We also thanks Brenda B. Griffing for her thorough editing of the manuscript, which contributed greatly to the final quality of the book.

This book would not have been possible without the help and support of Professor J. A. Biesenberger and Provost L. Z. Pollara (Stevens) and Professors W. Resnick, S. Sideman, and A. Ram (Technion).

Finally, we thank our families, whose understanding, support, and patience helped us throughout this work.

ZEHEV TADMOR
COSTAS G. GOGOS

Haifa, Israel
Hoboken, New Jersey
March 1978

Contents

- 1 *History, Structural Formulation of the Field Through Elementary Steps, and Future Perspectives, 1***
 - 1.1 Historical Notes, 1
 - 1.2 Current Polymer Processing Practice, 7
 - 1.3 Analysis of Polymer Processing in Terms of Elementary Steps and Shaping Methods, 14
 - 1.4 Future Perspectives: From Polymer Processing to Macromolecular Engineering, 18

- 2 *The Balance Equations and Newtonian Fluid Dynamics, 25***
 - 2.1 Introduction, 25
 - 2.2 The Balance Equations, 26
 - 2.3 Reynolds Transport Theorem, 26
 - 2.4 The Macroscopic Mass Balance and the Equation of Continuity, 28
 - 2.5 The Macroscopic Linear Momentum Balance and the Equation of Motion, 32
 - 2.6 The Stress Tensor, 37
 - 2.7 The Rate of Strain Tensor, 40
 - 2.8 Newtonian Fluids, 43
 - 2.9 The Macroscopic Energy Balance and the Bernoulli and Thermal Energy Equations, 54
 - 2.10 Mass Transport in Binary Mixtures and the Diffusion Equation, 60
 - 2.11 Mathematical Modeling, Common Boundary Conditions, Common Simplifying Assumptions, and the Lubrication Approximation, 60

- 3 *Polymer Rheology and Non-Newtonian Fluid Mechanics, 79***
 - 3.1 Rheological Behavior, Rheometry, and Rheological Material Functions of Polymer Melts, 80
 - 3.2 Experimental Determination of the Viscosity and Normal Stress Difference Coefficients, 94
 - 3.3 Polymer Melt Constitutive Equations Based on Continuum Mechanics, 100
 - 3.4 Polymer Melt Constitutive Equations Based on Molecular Theories, 122

4 *The Handling and Transporting of Polymer Particulate Solids, 144*

- 4.1 Some Unique Properties of Particulate Solids, 145
- 4.2 Agglomeration, 150
- 4.3 Pressure Distribution in Bins and Hoppers, 150
- 4.4 Flow and Flow Instabilities in Hoppers, 152
- 4.5 Compaction, 154
- 4.6 Flow in Closed Conduits, 157
- 4.7 Mechanical Displacement Flow, 157
- 4.8 Steady Mechanical Displacement Flow Aided by Drag, 159
- 4.9 Steady Drag-induced Flow in Straight Channels, 162
- 4.10 The Discrete Element Method, 165

5 *Melting, 178*

- 5.1 Classification and Discussion of Melting Mechanisms, 179
- 5.2 Geometry, Boundary Conditions, and Physical Properties in Melting, 184
- 5.3 Conduction Melting without Melt Removal, 186
- 5.4 Moving Heat Sources, 193
- 5.5 Sintering, 199
- 5.6 Conduction Melting with Forced Melt Removal, 201
- 5.7 Drag-induced Melt Removal, 202
- 5.8 Pressure-induced Melt Removal, 216
- 5.9 Deformation Melting, 219

6 *Pressurization and Pumping, 235*

- 6.1 Classification of Pressurization Methods, 236
- 6.2 Synthesis of Pumping Machines from Basic Principles, 237
- 6.3 The Single Screw Extruder Pump, 247
- 6.4 Knife and Roll Coating, Calenders, and Roll Mills, 259
- 6.5 The Normal Stress Pump, 272
- 6.6 The Co-rotating Disk Pump, 278
- 6.7 Positive Displacement Pumps, 285
- 6.8 Twin Screw Extruder Pumps, 298

7 *Mixing, 322*

- 7.1 Basic Concepts and Mixing Mechanisms, 322
- 7.2 Mixing Equipment and Operations of Multicomponent and Multiphase Systems, 354
- 7.3 Distribution Functions, 357
- 7.4 Characterization of Mixtures, 378
- 7.5 Computational Analysis, 391

8 *Devolatilization, 409*

- 8.1 Introduction, 409
- 8.2 Devolatilization Equipment, 411
- 8.3 Devolatilization Mechanisms, 413

- 8.4 Thermodynamic Considerations of Devolatilization, 416
 - 8.5 Diffusivity of Low Molecular Weight Components in Molten Polymers, 420
 - 8.6 Boiling Phenomena: Nucleation, 422
 - 8.7 Boiling–Foaming Mechanisms of Polymeric Melts, 424
 - 8.8 Ultrasound-enhanced Devolatilization, 427
 - 8.9 Bubble Growth, 428
 - 8.10 Bubble Dynamics and Mass Transfer in Shear Flow, 430
 - 8.11 Scanning Electron Microscopy Studies of Polymer Melt Devolatilization, 433
- 9 *Single Rotor Machines, 447***
- 9.1 Modeling of Processing Machines Using Elementary Steps, 447
 - 9.2 The Single Screw Melt Extrusion Process, 448
 - 9.3 The Single Screw Plasticating Extrusion Process, 473
 - 9.4 The Co-rotating Disk Plasticating Processor, 506
- 10 *Twin Screw and Twin Rotor Processing Equipment, 523***
- 10.1 Types of Twin Screw and Twin Rotor–based Machines, 525
 - 10.2 Counterrotating Twin Screw and Twin Rotor Machines, 533
 - 10.3 Co-rotating, Fully Intermeshing Twin Screw Extruders, 572
- 11 *Reactive Polymer Processing and Compounding, 603***
- 11.1 Classes of Polymer Chain Modification Reactions, Carried out in Reactive Polymer Processing Equipment, 604
 - 11.2 Reactor Classification, 611
 - 11.3 Mixing Considerations in Multicomponent Miscible Reactive Polymer Processing Systems, 623
 - 11.4 Reactive Processing of Multicomponent Immiscible and Compatibilized Immiscible Polymer Systems, 632
 - 11.5 Polymer Compounding, 635
- 12 *Die Forming, 677***
- 12.1 Capillary Flow, 680
 - 12.2 Elastic Effects in Capillary Flows, 689
 - 12.3 Sheet Forming and Film Casting, 705
 - 12.4 Tube, Blown Film, and Parison Forming, 720
 - 12.5 Wire Coating, 727
 - 12.6 Profile Extrusion, 731
- 13 *Molding, 753***
- 13.1 Injection Molding, 753
 - 13.2 Reactive Injection Molding, 798
 - 13.3 Compression Molding, 811

14 *Stretch Shaping, 824*

14.1 Fiber Spinning, 824

14.2 Film Blowing, 836

14.3 Blow Molding, 841

15 *Calendering, 865*

15.1 The Calendering Process, 865

15.2 Mathematical Modeling of Calendering, 867

15.3 Analysis of Calendering Using FEM, 873

Appendix A *Rheological and Thermophysical Properties of Polymers, 887*

Appendix B *Conversion Tables to the International System of Units (SI), 914*

Appendix C *Notation, 918*

Author Index, 929

Subject Index, 944

1 History, Structural Formulation of the Field Through Elementary Steps, and Future Perspectives

- 1.1 Historical Notes, 1
- 1.2 Current Polymer Processing Practice, 7
- 1.3 Analysis of Polymer Processing in Terms of Elementary Steps and Shaping Methods, 14
- 1.4 Future Perspectives: From Polymer Processing to Macromolecular Engineering, 18

Polymer processing is defined as the “engineering activity concerned with operations carried out on polymeric materials or systems to increase their utility” (1). Primarily, it deals with the conversion of raw polymeric materials into finished products, involving not only shaping but also compounding and chemical reactions leading to macromolecular modifications and morphology stabilization, and thus, “value-added” structures. This chapter briefly reviews the origins of current polymer processing practices and introduces the reader to what we believe to be a rational and unifying framework for analyzing polymer processing methods and processes. The chapter closes with a commentary on the future of the field, which is currently being shaped by the demands of predicting, a priori, the final properties of processed polymers or polymer-based materials via simulation, based on first molecular principles and multiscale examination (2).

1.1 HISTORICAL NOTES

Plastics and Rubber Machinery

Modern polymer processing methods and machines are rooted in the 19th-century rubber industry and the processing of natural rubber. The earliest documented example of a rubber-processing machine is a rubber *masticator* consisting of a toothed rotor turned by a winch inside a toothed cylindrical cavity. Thomas Hancock developed it in 1820 in England, to reclaim scraps of processed natural rubber, and called it the “pickle” to confuse his competitors. A few years later, in 1836, Edwin Chaffee of Roxbury, Massachusetts, developed the *two-roll mill* for mixing additives into rubber and the *four-roll calender* for the continuous coating of cloth and leather by rubber; his inventions are still being used in the rubber and plastics industries. Henry Goodyear, brother of Charles Goodyear, is credited with developing the *steam-heated two-roll mill* (3). Henry Bewley and Richard Brooman apparently developed the first ram extruder in 1845 in England (4), which was used in wire coating. Such a ram extruder produced the first submarine cable,

Principles of Polymer Processing, Second Edition, by Zehev Tadmor and Costas G. Gogos.
Copyright © 2006 John Wiley & Sons, Inc.

laid between Dover and Calais in 1851, as well as the first transatlantic cable, an Anglo-American venture, in 1860.

The need for continuous extrusion, particularly in the wire and cable field, brought about the single most important development in the processing field—the *single screw extruder* (SSE), which quickly replaced the noncontinuous ram extruders. Circumstantial evidence indicates that A. G. DeWolfe, in the United States, may have developed the first screw extruder in the early 1860s (5). The Phoenix Gummiwerke has published a drawing of a screw dated 1873 (6), and William Kiel and John Prior, in the United States, both claimed the development of such a machine in 1876 (7). But the birth of the extruder, which plays such a dominant role in polymer processing, is linked to the 1879 patent of Mathew Gray in England (8), which presents the first clear exposition of this type of machine. The Gray machine also included a pair of heated feeding rolls. Independent of Gray, Francis Shaw, in England, developed a screw extruder in 1879, as did John Royle in the United States in 1880.

John Wesley Hyatt invented the thermoplastics injection-molding machine in 1872 (9), which derives from metal die-casting invented and used earlier. Hyatt was a printer from Boston, who also invented Celluloid (cellulose nitrate), in response to a challenge award of \$10,000 to find a replacement material for ivory used for making billiard balls. He was a pioneering figure, who contributed many additional innovations to processing, including blow molding. His inventions also helped in the quick adoption of phenol-formaldehyde (Bakelite) thermosetting resins developed by Leo Baekeland in 1906 (10). J. F. Chabot and R. A. Malloy (11) give a detailed history of the development of injection molding up to the development and the widespread adoption of the reciprocating injection molding machine in the late 1950s.

Multiple screw extruders surfaced about the same time. Paul Pfeleiderer introduced the *nonintermeshing, counterrotating twin screw extruder* (TSE) in 1881, whereas the *intermeshing* variety of twin screw extruders came much later, with R. W Eastons co-rotating machine in 1916, and A. Olier's positive displacement counterrotating machine in 1921 (12). The former led to the ZSK-type machines invented by Rudolph Erdmenger at Bayer and developed jointly with a Werner and Pfeleiderer Co. team headed by Gustav Fahr and Herbert Ocker. This machine, like most other co-rotating, intermeshing TSEs, enjoys a growing popularity. They all have the advantage that the screws wipe one another, thus enabling the processing of a wide variety of polymeric materials. In addition, they incorporate "kneading blocks" for effective intensive and extensive mixing. They also generally have segmented barrels and screws, which enables the machine design to be matched to the processing needs. There is a broad variety of twin and multiple screw mixers and extruders; some of them are also used in the food industry. Hermann (12) and White (7) give thorough reviews of twin screw and multiple screw extruders and mixers.

The first use of gear pumps for polymeric materials dates from Willoughby Smith, who, in 1887, patented such a machine fed by a pair of rolls (4). Multistage gear pumps were patented by C. Pasquetti (13). Unlike single screw extruders and co-rotating twin screw extruders (Co-TSE), gear pumps are positive-displacement pumps, as are the counter-rotating, fully intermeshing TSEs.

The need for mixing fine carbon black particles and other additives into rubber made rubber mixing on open roll mills rather unpleasant. A number of enclosed "internal" mixers were developed in the late 19th century, but it was Fernley H. Banbury who in 1916 patented an improved design that is being used to this day. The Birmingham Iron Foundry in Derby, Connecticut, which later merged with the Farrel Foundry and Machine of Ansonia, Connecticut, built the machine. This mixer is still the workhorse of rubber

processing, and is called the Banbury mixer after its inventor (14). In 1969, at Farrel, Peter Hold et al. (15) developed a “continuous version” of the Banbury called the Farrel Continuous Mixer (FCM). A precursor of this machine was the nonintermeshing, twin-rotor mixer called the Knetwolf, invented by Ellerman in Germany in 1941 (12). The FCM never met rubber-mixing standards, but fortunately, it was developed at the time when high-density polyethylene and polypropylene, which require postreactor melting, mixing, compounding, and pelletizing, came on the market. The FCM proved to be a very effective machine for these postreactor and other compounding operations.

The Ko-Kneader developed by List in 1945 for Buss AG in Germany, is a single-rotor mixer-compounder that oscillates axially while it rotates. Moreover, the screw-type rotor has interrupted flights enabling kneading pegs to be fixed in the barrel (12).

The ram injection molding machine, which was used intensively until the late 1950s and early 1960s, was quite unsuitable to heat-sensitive polymers and a nonhomogeneous product. The introduction of the “torpedo” into the discharge end of the machine somewhat improved the situation. Later, screw plasticators were used to prepare a uniform mix fed to the ram for injection. However, the invention of the *in-line* or reciprocating-screw injection molding machine, attributed to W. H. Willert in the United States (16), which greatly improved the breadth and quality of injection molding, created the modern injection molding machine.¹

Most of the modern processing machines, with the exception of roll mills and calenders, have at their core a screw or screw-type rotor. Several proposals were published for “screwless” extruders. In 1959, Bryce Maxwell and A. J. Scalora (17) proposed the *normal stress extruder*, which consists of two closely spaced disks in relative rotational motion, with one disk having an opening at the center. The primary normal stress difference that polymeric materials exhibit generates centripetal forces pumping the material inward toward the opening. Robert Westover (18) proposed a *slider pad extruder*, also consisting of two disks in relative motion, whereby one is equipped with step-type pads generating pressure by viscous drag, as screw extruders do. Finally, in 1979, one of the authors (19) patented the *co-rotating disk processor*, which was commercialized by the Farrel Corporation under the trade name Diskpack. Table 1.1. summarizes chronologically the most important inventions and developments since Thomas Hancock’s rubber mixer of 1820. A few selected inventions of key new polymers are included, as well as two major theoretical efforts in formulating the polymer processing discipline.

A Broader Perspective: The Industrial and Scientific Revolutions

The evolution of rubber and plastics processing machinery, which began in the early 19th century, was an integral part of the great Industrial Revolution. This revolution, which transformed the world, was characterized by an abundance of innovations that, as stated by

1. William Willert filed a patent on the “in-line,” now more commonly known as the *reciprocating screw injection molding machine* in 1952. In 1953 Reed Prentice Corp. was the first to use Willert’s invention, building a 600-ton machine. The patent was issued in 1956. By the end of the decade almost all the injection molding machines being built were of the reciprocating screw type.

Albert (Aly) A. Kaufman, one of the early pioneers of extrusion, who established Prodex in New Jersey and later Kaufman S. A. in France, and introduced many innovations into extrusion practice, told one of the authors (Z.T.) that in one of the Annual Technical Conference (ANTEC) meetings long before in-line plasticating units came on board, he told the audience that the only way to get a uniform plasticized product is if the ram is replaced by a rotating and reciprocating screw. Aly never patented his innovative ideas because he believed that it is better to stay ahead of competition than to spend money and time on patents.

TABLE 1.1 The Chronological History of Processing Machines, and Some Other Key and Relevant Developments

Machine	Process	Inventor	Date	Comments
The 'Pickle'	Batch mixing	T. Hancock	1820	Reclaim rubber
Roll mill	Batch mixing	E. Chaffe	1836	Steam-heated rolls
Calender	Coating and sheet forming	E. Chaffe	1836	Coating cloth and leather
<i>Vulcanization of Rubber</i>		<i>Charles Goodyear</i>	<i>1839</i>	
Ram extruder	Extrusion	H. Bewly and R. Brooman	1845	
Screw extruder	Extrusion	A. G. DeWolfe	1860	Attributed to Archimedes for water pumping.
		PhoenixGummiwerke	1873	
		W. Kiel and J. Prior	1876	The most important machine for plastics and rubber
		M. Gray	1879	
		F. Shaw	1879	
		J. Royle	1880	
Injection molding	Injection molding	J. W. Hyatt	1872	Used first for Celluloid
Counterrotating, nonintermeshing twin screw extruder	Extrusion	P. Pfeleiderer	1881	
Gear pump	Extrusion	W. Smith	1887	Pasqueti invented the multistage gear pump.
<i>Bakelite</i>		<i>Leo Baekeland</i>		<i>First purely synthetic plastics</i>
Co-rotating, intermeshing twin screw extruder	Mixing and extrusion	R. W. Easton	1916	
The Banbury	Batch mixing	F. H. Banbury	1916	Developed for rubber mixing.
Counterrotating, intermeshing twin screws	Extrusion	A. Olier	1912	Positive displacement pump

Landes (20) “almost defy compilation and fall under three principles: (a) the substitution of machines—rapid, regular, precise, tireless—for human skill and effort; (b) the substitution of inanimate for animate source of power, in particular, the invention of engines for converting heat into work, thereby opening an almost unlimited supply of energy; and (c) the use of new and far more abundant raw materials, in particular, the substitution of mineral, and eventually artificial materials for vegetable or animal sources.”

Central to this flurry of innovation was James Watt’s invention of the modern steam engine, in 1774. Watt was the chief instrument designer at the University of Glasgow, and he made his great invention when a broken-down Thomas Newcomen steam engine, invented in 1705 and used for research and demonstration, was brought to him. This was a rather inefficient machine, based on atmospheric pressure acting on a piston in a cylinder in which steam condensed by water injection created a vacuum, but it was the first man-made machine that was not wind or falling-water driven. Watt not only fixed the machine, but also invented the modern and vastly more efficient steam engine, with steam pressure acting on the system and the separate condenser.

The great Industrial Revolution expanded in waves with the development of steel, railroads, electricity and electric engines, the internal combustion engine, and the oil and chemical industries. It was driven by the genius of the great inventors, from James Watt (1736–1819) to Eli Whitney (1765–1825), who invented the cotton gin, Samuel Morse (1791–1872), Alexander Graham Bell (1847–1922), Thomas Alva Edison (1847–1931), Guglielmo Marchese Marconi (1874–1937), Nikola Tesla (1856–1943), and many others. These also included, of course, J. W. Hyatt, Leo Baekeland, Charles Goodyear, Thomas Hancock, Edwin Chaffe, Mathew Gray, John Royle, and Paul Pfleiderer who, among many others, through their inventive genius, created the rubber and plastics industry.

The Industrial Revolution, which was natural resource- and cheap labor-dependent, was ignited in the midst of an ongoing scientific revolution, which started over two centuries earlier with Nicolas Copernicus (1473–1543), Galileo Galilei (1564–1642), Johannes Kepler (1571–1630), René Descartes (1596–1650) and many others, all the way to Isaac Newton (1642–1727) and his great *Principia* published in 1687, and beyond—a revolution that continues unabated to these very days.

The two revolutions rolled along separate tracks, with little interaction between them. This is not surprising because technology and science have very different historical origins. Technology derives from the ordinary arts and crafts (both civilian and military). Indeed most of the great inventors were not scientists but smart artisans, technicians, and entrepreneurs. Science derives from philosophical, theological, and speculative inquiries into nature. Technology is as old as mankind and it is best defined² as our accumulated knowledge of making all we know how to make. Science, on the other hand, is defined by dictionaries as “a branch of knowledge or study derived from observation, dealing with a body of facts and truths, systematically arranged and showing the operation of general laws.” But gradually the two revolutions began reinforcing each other, with science opening new doors for technology, and technology providing increasingly sophisticated tools for scientific discovery. During the 20th century, the interaction intensified, in particular during World War II, with the Manhattan Project, the Synthetic Rubber (SBR) Project, the development of radar, and many other innovations that demonstrated the

2. Contrary to the erroneous definitions in most dictionaries as “the science of the practical or industrial arts or applied science.”

power of science when applied to technology. In the last quarter of the century, the interaction between science and technology intensified to such an extent that the two effectively merged into an almost indistinguishable entity, and in doing so ignited a new revolution, the current, ongoing scientific–technological revolution. This revolution is the alma mater of high technology, globalization, the unprecedented growth of wealth in the developed nations over the past half-century, and the modern science and technology–based economies that are driving the world.

The polymer industry and modern polymer processing, which emerged in the second half of the 20th century, are very much the product of the merging of science and technology and the new science–technology revolution, and are, therefore, by definition high-tech, as are electronics, microelectronics, laser technologies, and biotechnology.

1.2 CURRENT POLYMER PROCESSING PRACTICE

The foregoing historical review depicted the most important machines available for polymer processing at the start of the *explosive* period of development of polymers and the plastics industry, which took place after World War II, when, as previously pointed out, science and technology began to merge catalytically. Thus, the Rubber and Plastics Technology century of 1850–1950 in Table 1.2 (2a), characterized by inventive praxis yielding machines and products, which created a new class of materials and a new industry, came to a close. In the half-century that followed, “classical” polymer processing, shown again in Table 1.2, introduced and utilized engineering analysis and process simulation, as well as innovation, and created many improvements and new developments that have led to today’s diverse arsenal of sophisticated polymer processing machines and methods of processing polymers and polymer systems of ever-increasing complexity and variety. As discussed later in this chapter, we are currently in transition into a new and exciting era for polymer processing.

A snapshot of the current status of the plastics industry in the United States, from the economic and manufacturing points of view, as reported by the Society of Plastics Industries (SPI) for 2000 (21), shows that it is positioned in *fourth* place among manufacturing industries after motor vehicles and equipment, electronic components and accessories, and petroleum refining, in terms of shipments. Specifically:

1. The value of polymer-based products produced in the United States by polymer (resin) manufacturers was \$ 90 billion. This industry is characterized by a relatively small number of very large enterprises, which are either chemical companies, for which polymer production is a very sizable activity (e.g., The Dow Chemical Company), or petrochemical companies, for which, in spite of the immense volume of polymers produced, polymer production is a relatively minor activity and part of vertically integrated operations (e.g., ExxonMobil Corporation).
2. The value of finished plastics products shipped by U.S. polymer processors was \$ 330 billion. Polymer processing companies are large in number and of small-to-medium size. They are specialized, have only modest financial and research resources, but are by-and-large innovative, competitive, entrepreneurial, and seemingly in constant forward motion, which is characteristic of the first period of development of the rubber and plastics industry.

TABLE 1.2 The Historical Evolution of Polymer Processing

Time Frame	1850–1950	1950–2000	Transition	Future
	Rubber and Plastics Technology	“Classical” Polymer Processing	Polymer Processing for Structuring	Macromolecular engineering
Focus	Product	Process and machine design (product)	Process and designed products	New products and structures
Scale	Machine invention	Machine	Product microstructuring	“Pushing the Limits”
Activity	Machine Industry Entrepreneurial	Product Corporate labs Academe Industry	Product micro (structure)	Product molecular microstructure
Discipline	Inventive Praxis	Transport phenomena GNF rheology Computational fluid mechanics	Academe Corporate labs Advanced compounders Transport phenomena Full rheology Melt/solids physics Interfacial phenomena Polymer chemistry In-line characterization Thermodynamics CHE, ME, CHEM, PHYS academe/industry Customized structure/properties Value-added materials New application fields	Gov/edu/com collaboration High-tech start-ups New industry Macromolecular physics, chemistry, rheology Multiscale transport and computations Molecular-scale probes Molecular biology Macromolecular engineers/scientists Truly advanced polymer materials New generation or globally applicable polymers
Profession	Technologists Inventors New Class of Materials New Industry	CHE, ME, CHEM industry/academe Ability to process very diverse polymers Large resin and processing industries > \$10 ¹² worldwide		
Benefits				

3. The U.S. labor force employed by resin producers is a quarter of million, and by polymer processors is a million and a half.

A lay-of-the-land presentation, in *flowchart* form, of the *thermomechanical experiences* of polymer systems in *processing equipment* used for important polymer processing manufacturing activities, is presented next. The aim is not only to inform but also to illustrate the *inherent commonality* of the thermomechanical experiences of polymer systems among the various types of equipment and operations used, which will help to *unify* and *structure* the understanding and analysis of polymer processing equipment and operations.

Postreactor Polymer Processing (“Finishing”) Operations

As is depicted in flowchart form in Fig. 1.1, the product of a gas-phase polymerization reactor produced in a typical polymer (resin) manufacturer’s plant at rates up to 40 t/h, is exposed to separation and drying steps to obtain pure polymer in particulate (powder) form. It is then dry mixed with a proprietary package of very low concentration additives—thermal, ultraviolet (UV), and oxidative stabilizers, as well as processing aids. The dry-mixed powder stream is metered into very large (mega) Co-TSEs or continuous melter/mixers (CMs), where the processes of *particulate solids handling* (PSH), *melting*, *mixing/homogenizing*, and *melt conveying* and *pressurization* must take place very rapidly, due to the high production-rate requirements.

This is the *first* thermomechanical experience of the reactor polymer, and it will *not be the last*. The equipment choice of Co-TSE or CM is made on the basis of the unique ability of these devices to cause very rapid melting and laminar mixing. We refer to the four processes just discussed as the *elementary steps of polymer processing*. The melt stream exiting the Co-TSE or the CM, both of which have poor melt pumping capabilities, is fed into very large gear pumps (GPs), which are positive displacement, accurate melt *conveying/pumping* devices. The melt is pumped into an underwater pelletizer with a

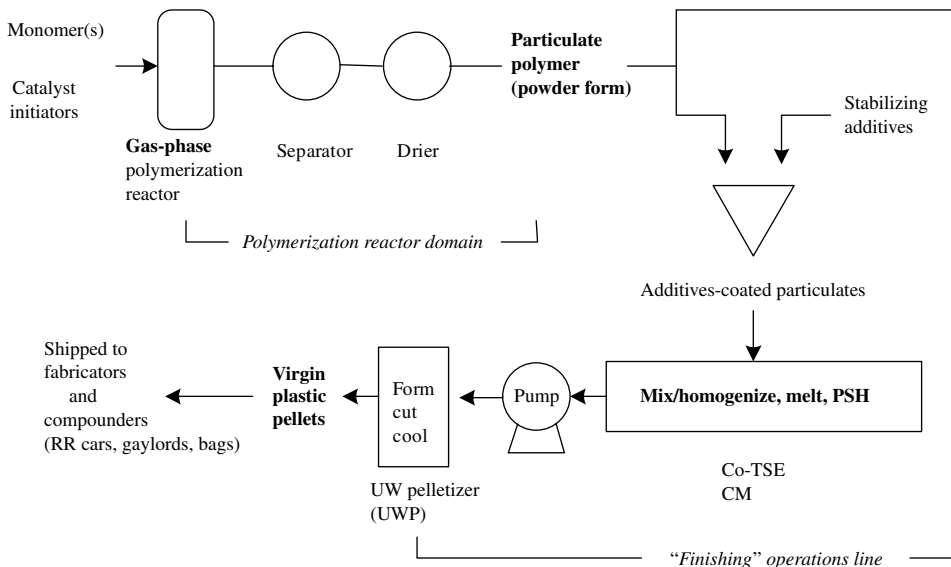


Fig. 1.1 Postreactor polymer processing (“finishing”) operations.

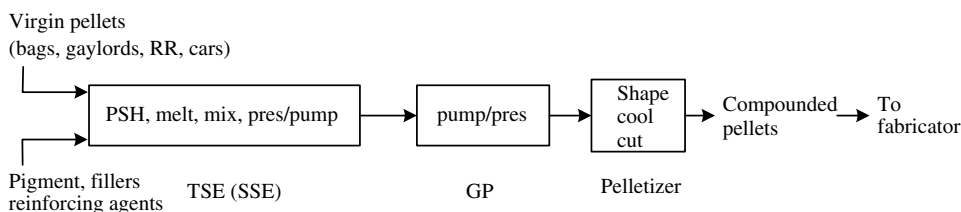


Fig. 1.2 Polymer compounding operations.

multihole die, where the exiting strands are cut into small pellets and cooled by the cold-water stream, which takes them to a water-polymer separator. The wet pellets are then dried and conveyed into silos; they are the “virgin” plastics pellets sold by polymer manufacturers to processing companies, shipped in railroad cars in 1000-lb gaylord containers or 50-lb bags.

Polymer Compounding Operations

The polymer compounding line is shown schematically in Fig. 1.2. Virgin pellets from resin manufacturers are compounded (mixed) with pigments (to form color concentrates), fillers, or reinforcing agents at moderate to high concentrations. The purpose of such operations is to improve the properties of the virgin base polymer, or to give it specialized properties, adding value in every case. The production rates are in the range of 1000–10,000 lb/h. The processing equipment’s critical task is to perform *laminar distributive* and *dispersive* mixing of the additives to the level required to obtain finished product property requirements. Furthermore, other additives, such as chopped glass fibers, are often fed after the compounding equipment has melted the pellets, in order to minimize degrading the attributes of the additives, such as fiber length. Finally, to assist the laminar mixing process, the additives may be surface-treated.

The processing equipment used by polymer compounders is mainly co-rotating and counterrotating TSEs, with occasional single-screw extruders (SSEs) in less demanding compounding lines. As is indicated in Fig. 1.2, the same elementary steps of polymer processing described previously in postreactor processing are performed by compounding equipment. The compounded stream is typically fed into a multihole strand die and the strands are first water cooled and then chopped to form pellets. The compounding operation exposes the reactor polymer to its second thermomechanical processing experience. The compounded product is shipped to fabricators of finished plastic products, commonly known as “processors.”

Reactive Polymer Processing Operations

Reactive polymer processing modifies or functionalizes the macromolecular structure of reactor polymers, via *chemical reactions*, which take place in polymer processing equipment after the polymer is brought to its molten state. The processing equipment then takes on an additional attribute, that of a “reactor,” which is natural since such equipment is uniquely able to rapidly and efficiently melt and distributively mix reactants into the very viscous molten polymers. The operation is shown schematically in Fig. 1.3.

The feed stream can be reactor polymer in powder form, which is then chemically modified (e.g., peroxide molecular weight reduction of polypropylene, known as

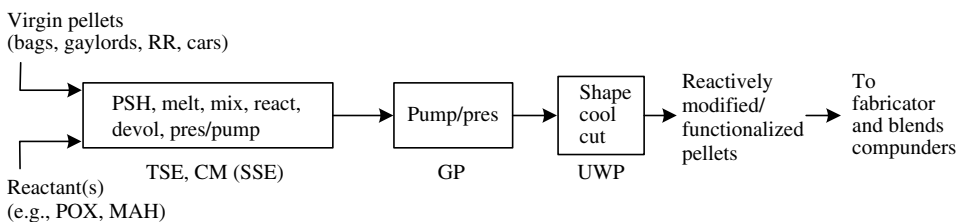


Fig. 1.3 Reactive polymer processing operations.

viscracking). Such reactive processing is usually carried out at high rates by resin manufacturers, and includes, after chemical modification and removal of volatiles, the incorporation of the proprietary additives package. Alternatively, the polymer feed stream is very often composed of virgin pellets, which undergo reactive modification such as functionalization (e.g., the creation of polar groups on polyolefin macromolecules by maleic anhydride).

As seen in Fig.1.3, here again the reactor-processing equipment used affects the same elementary steps of polymer processing as previously given, but now a *devolatilization* process to remove small reaction by-product molecules has been added. Because of the need for rapid and uniform melting and efficient distributive mixing (in order to avoid raising the molten polymer temperature), Co- and counterrotating TSEs as well as CMs are used, all of which can fulfill the reactive processing requirements for these elementary steps. Reactive processing, then, can either be the first or second thermomechanical experience of reactor polymers.

The reactively modified stream is then transformed into pellets, either by underwater or strand pelletizers. The pellets are again dried and shipped to plastic product fabricators, who need such specially modified macromolecular structures to fulfill product property requirements.

Polymer Blending (Compounding) Operations

These polymer processing (compounding) operations are employed for the purpose of creating melt-processed polymer *blends* and *alloys*. After the discovery of the major commodity and engineering polymers during the second to sixth decades of the 20th century, and as the cost of bringing a new polymer to market began to rise dramatically, both the polymer industry and academia focused on developing polymer blends with novel and valuable properties, in order to enlarge the spectrum of available polymers and to satisfy final plastic product property requirements in cost-effective ways. Thus, as is shown in Fig. 1.4, since about 1960, the increase in the number of commercially valuable polymer blends has powerfully driven the growth of the plastics industry and directly led to the rapid introduction of plastics in new and critical product application areas.

Turning to the polymer blending operations shown in Fig. 1.5, the feed stream consists of two or more polymers (virgin or reactively modified pellets) and a compatibilizer in small concentrations, which is necessary to create fine and stable polymer blend morphologies, since polymers are generally incompatible with each other. The processing equipment must quickly melt each polymer (concurrently or sequentially), and then rapidly and efficiently affect distributive and dispersive mixing of the melt components and the compatibilizer. Co- and counterrotating TSEs can satisfy these elementary steps that are important to blending operations.

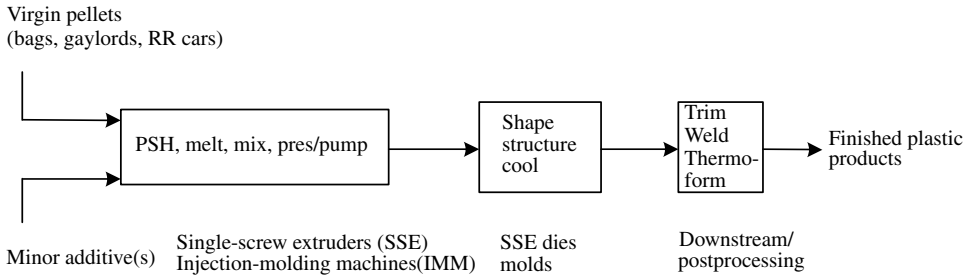


Fig. 1.6 Plastic product fabrication operations.

equipment used are again the same as given previously. In product fabrication operations, though, it is of paramount importance that the *pressurization* capabilities of the equipment be very strong, since we need a *melt pump* to form the shape of a plastic product by forcing the melt through a die or into a mold. Thus the equipment used by product fabricators are SSEs and injection molding machines, which have modest particulate solids handling, melting, and mixing capabilities, but are excellent melt pumps.

The molten stream of polymers flowing through dies or into cold molds is rapidly cooled to form the solid-product shape. As a consequence of the rapid cooling, some macromolecular orientations imparted during flow and near the product surfaces, where cooling first occurs, are retained. The retained orientations in plastic products impart specific anisotropic properties to the product and, in the case of crystalizable polymers, special property-affecting morphologies. The ability to affect the above is called *structuring* (23), which can be designed to impart extraordinarily different and beneficial properties to plastic products.

Structuring is also carried out in postshaping operations, mainly by stretching the solid formed product uni- or biaxially at temperatures appropriate to maximizing the retained orientations without affecting the mechanical integrity of the product.

In-Line Polymer Processing Operations

The polymer product fabrication operations may be either the second or third thermo-mechanical experience of the base polymer. Since polymers are subject to thermal degradation, and since there is a cost associated with each of the melting/cooling cycles, significant efforts are currently being made to develop what are called in the polymer processing industry, *in-line* processing operations. These operations and equipment sequentially conduct and functionally control any of the operations discussed earlier with plastic product fabrication at the end, thus allowing for a smaller degree of macromolecular and additive-properties degradation, and reducing the processing fabrication cost. The practice is relatively new, and has required the functional coupling and control of pieces of processing equipment that have distinctly different elementary step strengths: rapid, uniform, and efficient melting and mixing versus robust pressurization and accurate “metering” of the product stream. In-line polymer processing operations are shown schematically in Fig. 1.7.

From a plastics industry point of view, combining the various compounding, reactive processing and blending operations with the finished product fabrication operation, in a single line and under one roof, holds the potential for the product *fabricator* to become the

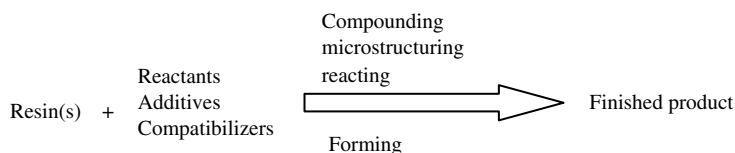


Fig. 1.7 In-line polymer processing operations (in-line compounding).

compounder as well. Furthermore, since fabricators are intimately involved with the properties needed by the finished product, they would be able to “fine-tune” the microstructuring of their polymer system to better meet the property needs of the products they are fabricating. Such capabilities will enable processors to respond to requests for customized polymer systems, that is, to satisfy “mass customization” needs of users of plastic products.

Additionally, there is clear evidence that a small number of resin manufacturers “will become more of enablers, creating new value-added businesses (of micro-structured polymer products) ever closer to the ultimate consumer” (2c). This translates into the planning by these companies for commercial expansion into compounding operations, widening the spectrum of their products, and further contributing to mass customization needs. Such developments and trends characterize the current “transition” phase of the polymer industry and of polymer processing, as depicted in Table 1.2. This period, it is hoped, will mark the gateway to a future where polymer processing will evolve into *macromolecular engineering*. We will briefly discuss this possibility in the last section of this chapter.

1.3 ANALYSIS OF POLYMER PROCESSING IN TERMS OF ELEMENTARY STEPS AND SHAPING METHODS

The field of polymer processing has been traditionally and consistently analyzed (24) in terms of the prevailing processing methods, that is, extrusion, injection molding, blow molding, calendering, mixing and dispersion, rotational molding, and so on. In analogy to chemical engineering,³ these processes have been viewed as the “unit operations” of polymer processing. At the time of the writing of the first edition of this text (24), when polymer processing was maturing into a well-defined and well-studied engineering discipline, we found it necessary to reexamine this classic way of analyzing the field, because the manner in which a field is broken down into its component elements has profound educational implications. A carefully worked out analysis should evolve into an abstract structure of the field that accomplishes the following objectives:

1. Focuses attention on underlying engineering and scientific principles, which are also the basis of the unifying elements to all processes.
2. Helps develop creative engineering thinking, leading to new, improved design.
3. Provides an overall view of the field, facilitating quick and easy assimilation of new information.

3. Systematic engineering analysis of chemical processes led to the definition of a series of “unit operations,” such as distillation, absorption, and filtration, which are common to different chemical processes (e.g., see W. L. McCabe and J. C. Smith, *Unit Operations in Chemical Engineering*, 2nd ed., McGraw-Hill, New York, 1967).

A quarter of a century later, and in retrospect, the analysis that we presented then, and that we discuss later, helped fulfill the previously defined objectives, and moved the field forward.

The Shaping Steps

The first step we take in our analysis of polymer processing is to clearly define its objective(s). In this case, the objective is undoubtedly *shaping polymer products*. The shaping operation can be preceded and followed by many manipulations of the polymer to prepare it for shaping, modify its properties, and improve its appearance. Nevertheless, the essence of polymer processing remains the shaping operation. The selection of the shaping method is dictated by product geometries and sometimes, when alternative shaping methods are available, by economic considerations. Reviewing the various shaping methods practiced in the industry, we can classify them in the following groups:

1. Calendering and coating
2. Die forming
3. Mold coating
4. Molding and casting
5. Stretch shaping

The first shaping method is a steady continuous process. It is among the oldest methods, and is used extensively in the rubber and plastics industries. It includes the classic calendering, as well as various continuous coating operations, such as knife and roll coating.

Die forming, which is perhaps the most important industrial shaping operation, includes all possible shaping operations that consist of forcing a melt through a die. Among these are fiber spinning, film and sheet forming, pipe, tube, and profile forming, and wire and cable coating. This is also a steady continuous process, in contrast to the last three shaping methods, which are cyclic.

The term “mold coating” is assigned to shaping methods such as dip coating, slush molding, powder coating, and rotational molding. All these involve the formation of a relatively thick coating on either the inner or the outer metal surfaces of the molds.

The next shaping method is molding and casting, which comprises all the different ways for stuffing molds with thermoplastics or thermosetting polymers. These include the most widely used shaping operations of injection molding, transfer molding, and compression molding, as well as the ordinary casting of monomers or low molecular weight polymers, and *in situ* polymerization.

Finally, stretch shaping, as implied by the name, involves shaping of preformed polymers by stretching. Thermoforming, blow molding, stretch blow molding, and cold forming can be classified as secondary shaping operations. The first three are very widely used.

The complex rheological properties of polymeric melts play a dominant role in the shaping operations. Thus, the introduction of one of the most striking aspects of non-Newtonian behavior, that of shear-thinning (pseudoplasticity), has been successfully incorporated into the analysis of melt flow inside polymer processing equipment. Similarly, by applying the modern sophisticated tools of numerical methods, the incorporation of the elastic nature of the polymer is being carried out with increasing success, particularly in stretch shaping.

As mentioned earlier, during shaping and postshaping operations, a good deal of structuring, that is, retained macromolecular orientation and specific morphologies, can and is being imparted to the final plastic products. Structuring has long been understood to be of very significant technological importance. The detailed understanding of structuring requires the ability to quantitatively describe the flow of rheologically complex melts, heat transfer, nucleation, and crystallization under stress. Work in this area is now underway, as we discuss in the last section of the chapter.

The Elementary Steps

The polymer is usually supplied to the processors in a particulate form. Shaping of the polymer takes place only subsequent to a series of preparatory operations. The nature of these operations determines to a large extent the shape, size, complexity, choice, and cost of the processing machinery. Hence, the significance of a thorough understanding of these operations cannot be overemphasized. One or more such operations can be found in *all* existing machinery, and we refer to them as *elementary steps* of polymer processing.

There are five clearly identifiable elementary steps:

1. Handling of particulate solids
2. Melting
3. Pressurization and pumping
4. Mixing
5. Devolatilization and stripping

Defining “handling of particulate solids” as an elementary step is justified, considering the unique properties exhibited by particulate solids systems. Subjects such as particle packing, agglomeration, consolidation, gravitational flow, arching, compaction in hoppers, and mechanically induced flow must be well understood to ensure sound engineering design of processing machines and processing plants.

Subsequent to an operation involving solids handling, the polymer must be melted or heat softened prior to shaping. Often this is the slowest, and hence the *rate-determining* step in polymer processing. Severe limitations are imposed on attainable melting rates by the thermal and physical properties of the polymers, in particular, the low thermal conductivity and thermal degradation. The former limits the rate of heat transfer, and the latter places rather low upper bounds on the temperature and time the polymer can be exposed. On the other hand, beneficial to increasing the rate of melting is the very high polymer melt viscosity, which renders dominant the role of the viscous energy dissipation (VED) heat-source term. Plastic energy dissipation (PED) (25,26) arising from the compressive and shear deformation of compacted polymer solid particulates in twin rotor equipment, such as Co-TSEs, is such a powerful heat source that it may result in nearly instant melting. All these factors emphasize the need to find the best geometrical configuration for obtaining the highest possible rates of melting, and for determining the processing equipment needed for rapid and efficient melting.

The molten polymer must be pumped and pressure must be generated to bring about shaping—for example, flow through dies or into molds. This elementary step, called *pressurization and pumping*, is completely dominated by the rheological properties of polymeric melts, and profoundly affects the physical design of processing machinery. Pressurization and melting may be simultaneous, and the two processes do interact with

each other. Moreover, at the same time, the polymer melt is also mixed by the prevailing laminar flow. Mixing the melt distributively to obtain uniform melt temperature or uniform composition (when the feed consists of a mixture rather than a single-component polymer), “working” the polymer for improving properties, and a broad range of mixing operations involving dispersive mixing of incompatible polymers, breakup of agglomerates, and fillers—all these belong to the elementary step of “mixing.”

The last elementary step of devolatilization and stripping is of particular importance to postreactor compounding, blending, and reactive processing operations, although it also occurs in commonly used processes, for example, devolatilizing in vented two-stage SSEs. This elementary step involves mass transfer phenomena, the detailed mechanisms of which have been investigated in some depth since the publication of the first edition of this book, and therefore, unlike in the first edition, here we devote a full chapter to this step. Yet, more research is needed to fully elucidate this complex process.

This theoretical analysis of processing in terms of elementary steps, which considers the basic physical principles and mechanisms involved in each elementary step, has been helpful since its introduction, in gaining better insight into the currently used processing methods, encouraging further work on their mathematical formulations, and perhaps also stimulating creative engineering thinking on improved processing methods. It has helped provide answers not only to “how” a certain product works, but to “why” a product is made a certain way and, foremost, “why” a particular machine configuration is the “best” or the appropriate one to use. The latter question is indeed the essence of engineering. For these reasons we will maintain and add to this approach in this edition.

Structural Breakdown of Polymer Processing

The elementary steps, as well as the shaping operations, are firmly based on the principles of *transport phenomena*, *fluid mechanics* and *heat and mass transfer*, *polymer melt rheology*, *solid mechanics*, and *mixing*. These principles provide the basic tools for quantitatively analyzing polymer processing. Another fundamental input necessary for understanding polymer processing is the physics and chemistry of polymers. As we noted earlier, final product properties can be immensely improved by structuring.

Figure 1.8 schematically summarizes our approach to the breakdown of the study of polymer processing. Raw material is prepared for shaping through the elementary steps. The elementary steps may precede shaping or they may be simultaneous with it. Structuring takes place throughout these processes, and subsequent to them. Finally, postshaping operations for purposes other than structuring (printing, decorating, etc.) may follow.

Clearly, to be able to fully utilize the added degree of freedom for product design provided by structuring, a full understanding and computational handling of polymer chemistry, polymer rheology at a macromolecular level, and the physics of phase changes under stress fields and nonisothermal conditions has to be carried out. With advances in those fields and the exponential growth of available computing power, significant advances are already being made toward achieving specific processed product properties, not through trial and error, but process simulation (2d).

The conceptual breakdown of polymer processing dating back to the first edition of 1979, presented earlier, *remains the same*. Yet the field and the industry, in the current transition period, have been focusing on and growing through what used to be called compounding, and is now expanded from the simple dispersion and distribution of fillers in polymer melts, to encompass microstructure development and stabilization in

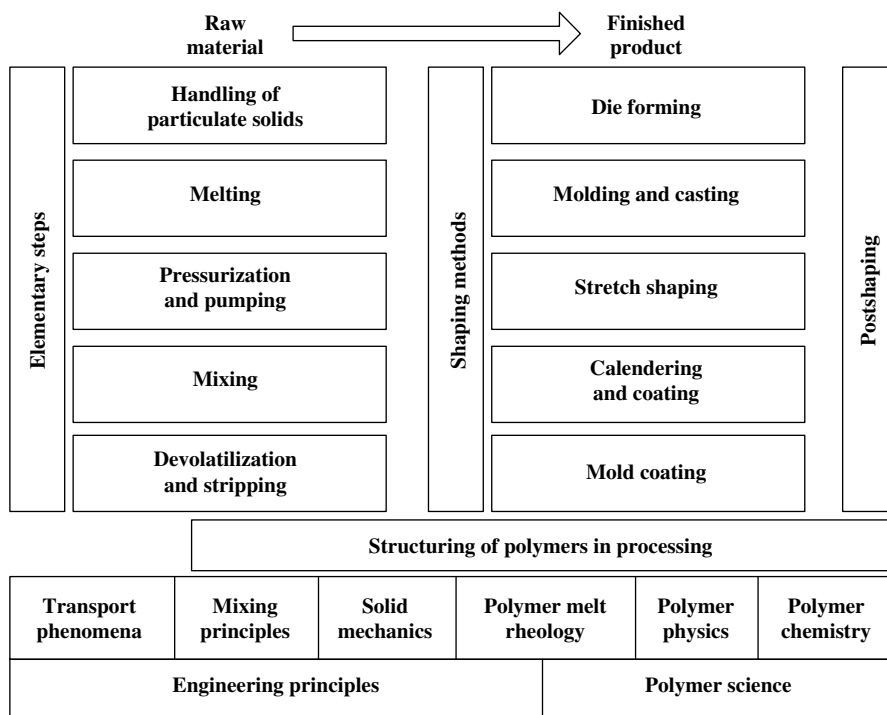


Fig. 1.8 Conceptual structural breakdown of polymer processing product fabrication operations (23).

immiscible, compatibilized, and reactive interphase multicomponent polymer systems of blends and alloys to create “designer pellets.” In this activity, the important elementary steps are rapid melting, affected mostly by PED and VED (that we referred to as dissipative mix-melting (23a, 25, 26)), rapid distributive and dispersive mixing created by extensional time-varying flows, and devolatilization, often occurring in the presence of reactions involving polymer melts. Co- and counterrotating TSEs, not shear-drag flow melting and pumping devices (e.g., SSEs), are the processing equipment used in these endeavors.

The conceptual breakdown in Fig. 1.9 (27) simply indicates the fact that in compounding, blending, and reactive processing, the base polymer(s) undergo two thermomechanical elementary-step experiences, and that the product of the first are value-added and microstructured pellets, while the second is used primarily for fabricating finished products. The important elementary steps for each experience, and the physical mechanisms that affect them, are different, because of the different objectives in each.

1.4 FUTURE PERSPECTIVES: FROM POLYMER PROCESSING TO MACROMOLECULAR ENGINEERING

In May 2002 an International Invited Workshop, attended by leading researchers in polymer processing and polymer engineering science, was convened in order to take stock of the historical evolution of the field of polymer processing, analyze current developments in research, take note of structural changes in the industry, and consider future trends. The underlying rationale, outlined in Appendix A of the final report (2), was

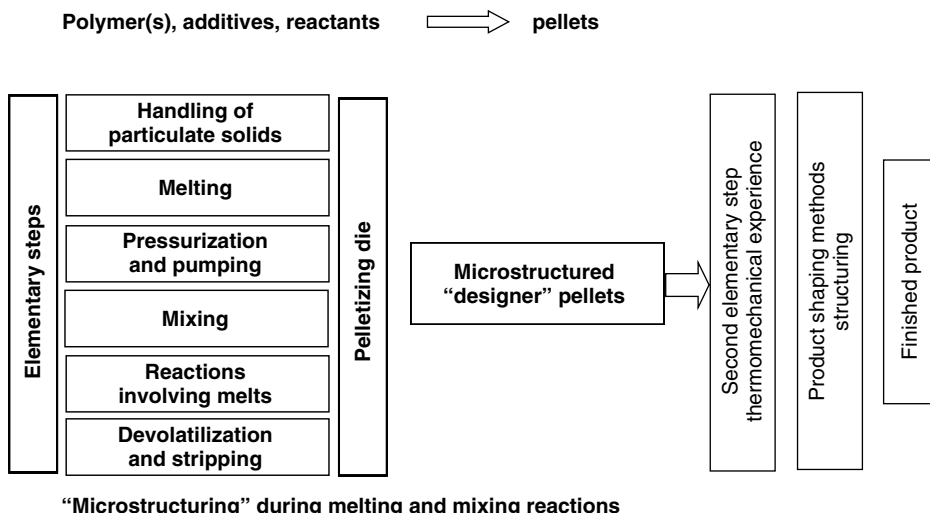


Fig. 1.9 Conceptual breakdown of polymer compounding, blending, and reactive polymer processing (27). Designer pellets are processed in extruders or injection molding machines to form products, with the possibility of further structuring or ‘destructuring’.

the proposition that this new and still evolving engineering discipline, propelled by the revolutionary developments in polymer physics, polymer chemistry, computational fluid mechanics, sophisticated novel instrumentation capabilities, modern catalysis, and developments in molecular biology, is diverging into a broad-based multidisciplinary activity, not unlike biotechnology and nanotechnology. Therefore, it is at a turning point.

Needless to say, for both authors working on this second edition, the workshop held the additional potential of providing a glimpse at the future development of the field. Thus, we present below some of the major topics of deliberation and conclusions of the workshop, drawing liberally from the text of the Final Report.

Central to the deliberations was to first outline in broad brush-strokes the knowledge so far acquired, and identify general areas where future research is needed. The guiding questions were: What do we know? What do we know that we don’t know? What do we need to know? What are the “boundaries” of the field? Which are the relevant disciplines needed for getting ahead in what increasingly appears to be a multidisciplinary field? And how can polymer processing become a strategic element in the “chain of knowledge”?

There was agreement among the participants that much has been accomplished in the past decades by classic polymer processing (Fig. 1.2). During this period, polymer processing focused on analyzing the major polymer processing equipment and processes (SSEs, TSEs, injection molding machines, blow molding machines, vacuum forming machines, calenders and roll mills, rotational molding machines, batch and continuous mixers, etc.). In doing so, the field grew and matured with the realization (as noted in Section 1.3) that there are common phenomena in the thermomechanical experiences of the material in the diverse polymer processing equipment and processes described earlier. This realization led to the elucidation and simulation of the detailed mechanisms and sequence of events that take place in these machines and in the continuous and cyclic shaping processes: flow of particulate solids; principles of melting of plastics in SSEs; principles of distributive, dispersive, and chaotic mixing;

principles and mechanisms of devolatilization; flow of non-Newtonian polymeric melts in complex conduits with moving surfaces using analytical, finite difference and finite element techniques; transient developing flows into cavities; wall stress-free one-, two- and three-dimensional flows as in fiber spinning, bubble formation, and complex blow molding operations, to name a few; degradation reactions in processing equipment, and so forth.

Not everything was elucidated to the same level and, as discussed in the following paragraphs, much remains to be done in classic polymer processing. The knowledge base developed so far was founded on, and rooted in, several disciplines, such as transport phenomena—including fluid mechanics, heat transfer and molecular diffusion of chemical species, non-Newtonian fluid mechanics, rheology (continuum and, to a lesser extent, molecular), resin thermophysical properties and state equations, classic mathematical techniques, and computational fluid mechanics, as well as polymer physics and thermodynamics. The focus of past research, as well as much of the current research, is on the *process* and the *scale of examination* of the *machine*, with the objective of developing optimized processes and improved machines.

During this period, relatively little emphasis was placed on the product and its microscopic and molecular structure, though there was rudimentary and semiquantitative treatment of what was termed *structuring* (2b, 23). Today, in some of the larger research-and-development centers, an important transition is being made, to focus on the product and its properties on the micro and molecular scale.

Areas on the process side identified as needing further research are:

- A better understanding of and advanced mathematical formulation of all the basic mechanisms under realistic machine conditions with a single polymeric feed or a mixture of them, with the goal of simulating the process as a whole;
- A fundamental and multidisciplinary understanding of melting of compacted polymer particulates under high deformation rates;
- A much deeper understanding of the details on how the process affects the structure on micro and molecular levels;
- Materials/machine interactions, three-dimensional viscoelastic behavior and stability of polymeric liquids;
- Transient flow and nonisothermal rheology;
- Nucleation and crystallization under stress;
- Molecular orientation phenomena;
- Reaction and polymerization under flow and deformation;
- Multiphase flows at high rates of strains;
- Heat, momentum, mass, entropy balances at “finite domain structure levels” of solids and liquids, during deformation, melting, and solidification;
- Thermodynamics of interfaces;
- Phase transition;
- Molecular models and modeling;
- Quantitative connection of structures and structure formation at the molecular and micro scale to final properties;
- Measurement techniques, including process in-line measurements, at the molecular and micro-scale levels to verify theories and predictions.

However, even the complete understanding of these areas will not suffice to reap the full benefits embedded in the macromolecular nature of polymeric materials, which are inherent in the naturally occurring and synthetic polymeric building blocks. For that, a priori quantitative prediction of product properties, made of yet nonexistent chains or combinations of chains of different monomeric building blocks from basic principles, requiring information of only the macromolecular structure and processing conditions, is needed.

Interesting comparisons were made to other fields, such as semiconductors, which cannot be produced without thorough knowledge at the quantum mechanics level and fine-tuned processing; multiscale computing in solids mechanics, in which microscopic behavior is being predicted from first principles on atomic scales; drug development with computer simulation screening of new molecules; modern catalysis and biocatalysts; and molecular biology with potential adaptation of self-assembly properties to other fields, such as biological microchips.

It was concluded that modern polymer processing, or rather *future* polymer processing (see Table 1.2), will focus not on the machine, but on the *product*. The long-range goal will be to predict the properties of a product made from a yet nonexistent polymer or polymer-based material, via simulation based on first molecular principles and multiple-scale examination. This approach, using increasingly available computing power and highly sophisticated simulation, might mimic nature by targeting properties via complex molecular architectural design. However, two important and key challenges have to be met successfully in order to achieve this goal: first, highly sophisticated simulations require highly sophisticated molecular models, which do not exist at present; second, a far more detailed understanding of the full and complex thermomechanical history that transpires in the polymer processing machine is needed. Then, such analysis will lead not only to new products, but will also improve existing machines or even lead to radically new machines; nevertheless, the focus will remain on the product. The goal is to engineer new and truly advanced materials with yet unknown combinations of properties, which might open up a new “golden age” for the field, reminiscent of the 1950s, 1960s, and 1970s, when most of the currently used polymers were developed.

Thus, the terms “polymer processing,” “polymer engineering,” or “plastics engineering” have become too narrow and confining, and a more accurate description of the emerging new field ought to be *macromolecular engineering*. As noted earlier, the new field is inherently *multidisciplinary* in nature, and if it is to be developed at a world-class level, requires close collaboration between many disciplines of science and engineering. Hence, the emphasis must shift from the individual researcher to large team efforts, this having profound consequences to academic research, as well as academic departmental boundaries. Real progress will only be possible by pooling substantial resources, and the allocation of these significant resources should be facilitated by vision, planning, and a comprehensive alliance between government, academia, and industry.

Macromolecular engineering is part of a broader scene. On the very fundamental level, its boundaries merge with molecular biology, on the one hand, and the growing field of complex fluids, that grows out of chemistry, physical chemistry, physics, and chemical engineering, on the other hand. The preceding, in turn, has profound educational implications, pointing to the possible creation of an entirely new and unified underlying discipline, and a basic undergraduate curriculum in *molecular, macromolecular and supramolecular engineering*, leading to specialization in *chemical molecular engineering* (currently chemical engineering), *macromolecular engineering* (currently polymer processing and engineering), and *biomacromolecular engineering* (currently

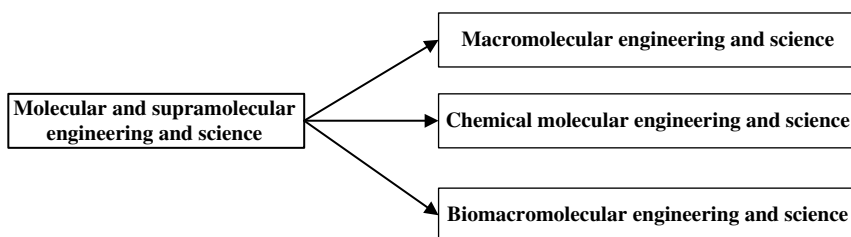


Fig. 1.10 A curricular structure discussed during the Touchstones of Modern Polymer Processing workshop, where a novel discipline called *Molecular and Supramolecular Engineering and Science*, becomes the initial, common core of macromolecular, chemical molecular, and Biomacromolecular engineering.

biochemical engineering or biotechnology). Such a curricular structure is depicted in Fig. 1.10.

Recently, Jos Put, discussed (28) the very enlightening view of J. L. Atwood et al. (29) on the nature of molecular biology and synthetic chemistry, shown in Fig. 1.11. Nature has achieved a tremendous level of complexity and control in living organisms, with a limited number of building blocks; synthetic (polymer) chemistry has used a much more diverse number of building blocks and achieved only limited, controlled structural complexity. Nature is able to do this by supreme control on the molecular level (MW, MWD, sequence, tacticity, etc.), by ordering on the nanolevel, and by perfect macroscopic design. On the other hand, macromolecular synthetic chemistry has made great strides by utilizing chemical species diversity, while achieving very modest controlled structural complexity. Biotechnology has begun to broaden the chemical diversity of bioapplicable systems, and synthetic nano chemistry is achieving remarkable controlled complexity at the nano level, utilizing and offering structurally ordered platforms to macromolecules. Thus, the merging of the boundaries of macromolecular engineering and molecular biology offers formidable potential for new materials and products. This is depicted by the 45° vector direction in Fig. 1.11.

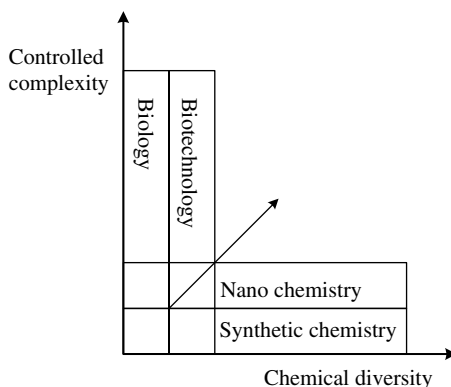


Fig. 1.11 The diagram used by J. L. Atwood et al. (29), to depict the differences between synthetic chemistry and biology in terms of the “building blocks” used and the attained structural controlled complexity.

Macromolecular engineering from the research point of view is clearly a broad-based multidisciplinary field. Consequently, the research scene and practices, in particular in academia, require restructuring. The classic “individual faculty member–graduate student(s)” model is expected to be replaced by the large, multidisciplinary team model, because, as pointed out earlier, only these larger teams can be expected to conduct groundbreaking research. Such teams should consist of several senior faculty members in the needed disciplines, co-advising several graduate students as well as trained professionals who deal with advanced instrumentation, computing, data analysis, and literature searches.

It is perhaps worth adding that such large multidisciplinary groups already exist at leading centers of macromolecular engineering research. In fact, we are witnessing the first promising examples of a priori quantitative predictions of the solid product properties requiring information of only the macromolecular structure and processing conditions from such large multidisciplinary groups. For example, Han E. H. Meijer et al. at the Materials Technology, Dutch Polymer Institute, Eindhoven University of Technology (30,31) proposed such an a priori prediction for the yield stress of polycarbonate (PC) specimens obtained under different molding conditions. Their work is based on defining a novel state parameter that uniquely determines the current state of amorphous solids and utilizes the classic constitutive model representation of such solids as presented by Haward and Thackray (32), who identified two contributions to the total stress: one that accounts for the rate-dependent plastic flow response attributed to intermolecular interactions on a segmental scale (33,34) and represented by a nonlinear Maxwell element (35), and the other that accounts for the strain-hardening contribution that is due to the macromolecular orientation of the entangled network using a neo-Hookean elastic model (36).

REFERENCES

1. E. C. Bernhardt and J. M. McKelvey, “Polymer Processing – New Engineering Specialty”, *Mod. Plast.*, **35**, (July) 154–155, (1958).
2. Final Report of the international invited workshop “*Touchstones of Modern Polymer Processing – From Classic Polymer Processing to Macromolecular Process Science*”, May 10–12, 2002, The Polymer Processing Institute at NJIT, Newark, NJ (a) Table 1, p. 11, (b) Z. Tadmor, Appendix A, p. 21, (c) Industrial Considerations p. 13, (d) Z. Tadmor Appendix A, pp. 24 and 25.
3. C. Goodyear, *Gum Elastic* (private printing), New Haven, CT, 1855.
4. M. Kaufman, “The Birth of the Plastics Extruder,” *Polym. Plast.*, 243–251 (June, 1969).
5. V. M. Hovey, “History of Extrusion Equipment for Rubber and Plastics,” *Wire and Wire Prod.*, **36**, 192 (1961).
6. G. Schenkel, *Plastics Extrusion Technology and Theory*, Iliffe Books, Ltd., London, 1966.
7. J. L. White, “Elastomer Rheology and Processing,” *Rubber Chem. Technol.*, **42**, 256–338 (1969).
8. M. Gray, British Patent 5056 (1879).
9. J. W. Hyatt, *Ind. Eng. Chem.*, **6**, 158 (1914).
10. J. H. Dubois, *Plastics History USA*, Cahners Books, Boston, 1975.
11. J. F. Chabot and R. A. Malloy, “A History of Thermoplastic Injection Molding. Part I – The Birth of an Industry”, *J. Inj. Mold. Technol.*, **1**, 1 (1997).
12. H. Herrmann, *Scheneken Maschinen Inder Versahrenstechnik*, Springer Verlag, Berlin, 1972.

13. C. Pasquetti, British Patent, 638, 364 (1950).
14. D. H. Killeffer, "Banbury the Master Mixer", Palmerton, NY, 1962.
15. E. H. Ahlenfeld, P. Hold, A. J. Baldwin, W. A. Rapetsky, and H. R. Scharer, U.S. Patent 3, **154**, 802 (1969).
16. William H. Willert, "Injection Molding Apparatus," U.S. Patent 2, **734**, 226 (1956).
17. B. Maxwell and A. J. Scalora, *Mod. Plast.*, **37**, 107 (1959).
18. R. F. Westover, "A Hydrodynamic Screwless Extruder," *SPE J.*, **18**, 1473 (1962); also U.S. Patent 3, **123**, 861 (1964).
19. Z. Tadmor, U.S. Patent 4, **142**, 805 (1979); U.S. Patent 4, **194**, 841 (1980).
20. D. Landes, *The Wealth and Poverty of Nations*, W. W. Norton, New York, 1998; Abacus, London, 2001. Chapter 13, "The Nature of Industrial Revolution."
21. Information Presented by the Society of Plastics Industries (SPI), 2002. <plasticsdatasource.org>
22. C. G. Gogos, "From Compounding to Micro-structuring to Reactive Processing," Keynote Lecture, Extrusion Division, *Proc. 55th Soc. Plastics Eng. Ann. Technical Conf.*, Toronto, Canada 1997.
23. Z. Tadmor and C. G. Gogos, *Principles of Polymer Processing*, Wiley-Interscience, New York, 1979, (a) Chapter 9, Section 9.1.
24. E. C. Bernhardt, *Processing of Thermoplastic Materials*, Reinhold, New York, 1959.
25. C. G. Gogos, Z. Tadmor, and M.-H. Kim, "Melting Phenomena and Mechanisms in Polymer Processing Equipment," *Adv. Polym. Techn.*, **17**, 286 (1998).
26. B. Qian and C. G. Gogos, "The Importance of Plastic Energy Dissipation (PED) to the Heating and Melting of Polymer Particulates in Intermeshing Co-rotating Twin Screw Extruders: An Experimental Investigation," *Adv. Polym. Techn.*, **19**, 287 (2000).
27. C. G. Gogos, "Elementary Steps and 'Structuring' of Polymers—Then and Now," Symposium 13 Honoring Z. Tadmor's 60th Birthday, paper 13-I, *Extended Abstracts in the 13th Meeting of the Polymer Processing Society*, Secaucus, NJ, 1997.
28. J. Put, "Business in Polymeric Materials," European Polymer Federation in Collaboration with AIM Magazine, Special Issue, July 2001.
29. J. L. Atwood, J.-M. Lehn, J. E. D. Davies, D. D. Nicol, and F. Vogte, *Comprehensive Supramolecular Chemistry*, Pergamon Press, Amsterdam, 1996.
30. L. E. Govaert, T. A. P. Engels, E. T. J. Klompen, G. W. M. Peters, and H. E. H. Meijer, "Processing-induced Properties in Glassy Polymers," *Int. Polym. Process.*, **20**, 170 (2005).
31. H. E. H. Meijer and L. E. Govaert, "Mechanical Performance of Polymer Systems: The Relation Between Structure and Properties," *Prog. Polym. Sci.*, **30**, 915–938 (2005).
32. R. N. Haward and G. Thackray, "The Use of a Mathematical Model to Describe Isothermal Stress-Strain Curves in Glassy Thermoplastics," *Proc. R. Soc. London, Series A*, **302** (1471), 453 (1967).
33. T. A. Tervoort, E. T. J. Klompen, and L. E. Govaert, "A Multi-mode Approach to Finite, Three-dimensional Nonlinear Viscoelastic Behavior of Polymer Glasses," *J. Rheol.*, **40**, 779 (1996).
34. E. T. J. Klompen, Ph.D Thesis, Eindhoven University of Technology, The Netherlands (2005), Chapter 6.
35. F. P. T. Baaijens, "Calculation of Residual Stresses in Injection Molded Products," *Rheol. Acta*, **30**, 284 (1991).
36. L. E. Govaert, P. H. M. Timmermans, and W. A. M. Brekelmans, "The Influence of Intrinsic Strain Softening on Strain Localization in Polycarbonate: Modeling and Experimental Validation," *J. Eng. Mater. Tech.*, **122**, 27 (2000).

2 The Balance Equations and Newtonian Fluid Dynamics

- 2.1 Introduction, 25
- 2.2 The Balance Equations, 26
- 2.3 Reynolds Transport Theorem, 26
- 2.4 The Macroscopic Mass Balance and the Equation of Continuity, 28
- 2.5 The Macroscopic Linear Momentum Balance and the Equation of Motion, 32
- 2.6 The Stress Tensor, 37
- 2.7 The Rate of Strain Tensor, 40
- 2.8 Newtonian Fluids, 43
- 2.9 The Macroscopic Energy Balance and the Bernoulli and Thermal Energy Equations, 54
- 2.10 Mass Transport in Binary Mixtures and the Diffusion Equation, 60
- 2.11 Mathematical Modeling, Common Boundary Conditions, Common Simplifying Assumptions and the Lubrication Approximation, 60

2.1 INTRODUCTION

The engineering science of “transport phenomena” as formulated by Bird, Stewart, and Lightfoot (1) deals with the transfer of momentum, energy, and mass, and provides the tools for solving problems involving fluid flow, heat transfer, and diffusion. It is founded on the great principles of conservation of *mass*, *momentum* (Newton’s second law), and *energy* (the first law of thermodynamics).¹ These conservation principles can be expressed in mathematical equations in either *macroscopic* form or *microscopic* form.

In this chapter, we derive these equations in some detail using the generalized, coordinate-free formulation of the Reynolds Transport Theorem (2). We believe that it is important for every student or reader to work through these derivations at least once. We then discuss the nature of the stress and rate of deformation tensors, demonstrate the use of the balance equations for problem solving with Newtonian fluids using analytical and numerical techniques, discuss the *lubrication approximation*, which is very useful in modeling of polymer processing operations, and discuss the broad principles of *mathematical modeling* of complex processes.

1. See R. Feynman, *The Character of Physical Law*, MIT Press, Cambridge, MA, 1967, where the profound nature of the conservation laws is discussed.

2.2 THE BALANCE EQUATIONS

Since in “transport processes” mass, momentum, and energy are *transported* from one part of the medium to another, it is essential that proper “bookkeeping” be applied to keep track of these quantities. This can be done using *balance equations*, which are the mathematical statements of the physical laws of conservation. These are very general laws that *always* hold, and they apply to all media: solids or fluids, stationary or flowing. These equations can be formulated over a specified *macroscopic* volume, such as an extruder, or a *microscopic* volume taking the form of a differential (field) equation that holds at every point of the medium. In the former case, the balance holds over the *extensive* quantities of mass, momentum, and energy, whereas in the latter case, it holds over their *intensive* counterparts of density, specific momentum, and specific energy, respectively.

In the formulation of the microscopic balance equations, the molecular nature of matter is ignored and the medium is viewed as a *continuum*. Specifically, the assumption is made that the mathematical points over which the balance field-equations hold are big enough to be characterized by property values that have been averaged over a large number of molecules, so that from point to point there are no discontinuities. Furthermore, *local equilibrium* is assumed. That is, although transport processes may be fast and irreversible (dissipative), from the thermodynamics point of view, the assumption is made that, locally, the molecules establish equilibrium very quickly.

2.3 REYNOLDS TRANSPORT THEOREM

The physical laws of conservation of mass, momentum, and energy are commonly formulated for closed *thermodynamic systems*,² and for our purposes, we need to transfer these to open *control volume*³ formulations. This can be done using the Reynolds Transport Theorem.⁴

Let P represent some extensive property of the system (e.g., mass, momentum, energy, entropy) and let p represent its intensive counterpart (i.e., per unit mass), such that:

$$P = \int_{\mathcal{V}} \rho p \, d\mathcal{V} \quad (2.3-1)$$

where \mathcal{V} is the volume of the system, which can be a function of time, t . The Reynolds Transport Theorem states that the substantial derivative (see Footnote 6) of P is

$$\frac{DP}{Dt} = \int_{\mathcal{V}} \frac{\partial}{\partial t} (\rho p) \, dV + \int_S \rho p \mathbf{v} \cdot \mathbf{n} \, dS \quad (2.3-2)$$

2. A *thermodynamic system* is an arbitrary volume of matter without any transportation of matter across its surface.

3. The *control volume* is an arbitrary, fixed volume in space.

4. We assume the reader is familiar with vector notation, which is covered in many texts (e.g., Ref. 1), and except for brief explanatory comments, no summary of vector operation is presented. However, the tabulated components of the balance equations in various coordinate systems presented in this chapter should enable the reader to apply them without any detailed knowledge of vector operations.

where V is the *control volume* fixed in space, S is the surface area of the control volume, \mathbf{v} is the velocity field, and \mathbf{n} is the unit outward normal vector to the control surface. In physical terms, Eq. 2.3-2 states that the rate of change of P of the *system*, at the instant it coincides with the *control volume*, is the sum of two terms: the rate of change of P within the control volume, and the net rate of flow of P out of the control volume.

Proof of Eq. 2.3-2 First we take the substantial derivative of Eq. 2.3-1

$$\left. \frac{DP}{Dt} \right|_{\text{system}} = \frac{d}{dt} \int_V \rho p \, dV \quad (\text{a})$$

Then by defining $P_s = P_{\text{system}}$ we can express the left-hand side of Eq. (a)

$$\frac{DP_s}{Dt} = \lim_{\Delta t \rightarrow 0} \frac{P_{s,t+\Delta t} - P_{s,t}}{\Delta t} \quad (\text{b})$$

Next we let the arbitrary volume of P_s coincide at time t with the control volume. Since the volume is arbitrary, we can do so without losing generality. But because there is the flow of matter in the space, at time $t + \Delta t$ the volume of P_s will be different, as shown in Fig. 2.1.

Looking at the figure we see that there are three distinct volume regions, A , B , and C . The control volume equals the sum $A + B$, and the system equals $B + C$. Therefore P_s at time $t + \Delta t$ can be expressed as

$$P_{s,t+\Delta t} = P_{B,t+\Delta t} + P_{C,t+\Delta t} = P_{CV,t+\Delta t} - P_{A,t+\Delta t} + P_{C,t+\Delta t} \quad (\text{c})$$

and

$$P_{s,t} = P_{CV,t} \quad (\text{d})$$

where the subscript CV stands for control volume. Substituting Eqs. (c) and (d) into Eq. (b) gives

$$\frac{DP_s}{Dt} = \lim_{\Delta t \rightarrow 0} \frac{P_{CV,t+\Delta t} - P_{CV,t}}{\Delta t} + \lim_{\Delta t \rightarrow 0} \frac{P_{C,t+\Delta t}}{\Delta t} - \lim_{\Delta t \rightarrow 0} \frac{P_{A,t+\Delta t}}{\Delta t} \quad (\text{e})$$

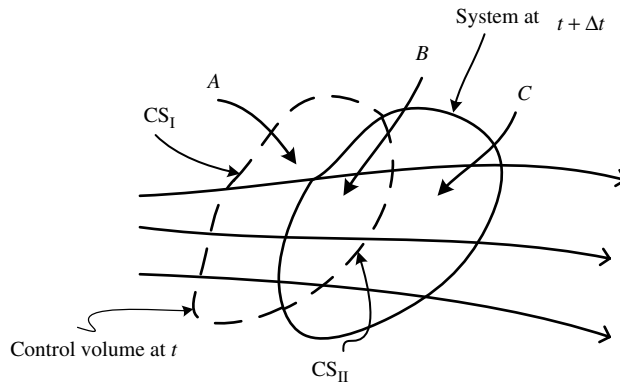


Fig. 2.1 The *control volume* (broken curve) and the *thermodynamic system* (solid curve) at time $t + \Delta t$ in a flowing medium. The *control volume* and the *thermodynamic system* coincide at time, t .

The first expression on the right hand side is the partial differential in time of P_{CV} , $\partial P_{CV}/\partial t$. Now, $P_{C,t+\Delta t}$ is due to flow through surface CS_{II} of the control volume, separating volumes B and C , which can be calculated as follows:

- The local volumetric rate of flow is $\mathbf{v} \cdot \mathbf{n} dS$
- The local rate of flow of the property is $\rho p \mathbf{v} \cdot \mathbf{n} dS$
- The differential quantity of P_C transported over time Δt is $dP_C = \Delta t \rho p \mathbf{v} \cdot \mathbf{n} dS$

Thus, the total amount of P_C transported over surface CS_{II} and time Δt is given by:

$$P_{C,t+\Delta t} = \Delta t \int_{CS_{II}} \rho p \mathbf{v} \cdot \mathbf{n} dS \quad (\text{f})$$

and, therefore,

$$\lim_{\Delta t \rightarrow 0} \frac{P_{C,t+\Delta t}}{\Delta t} = \int_{CS_{II}} \rho p \mathbf{v} \cdot \mathbf{n} dS \quad (\text{g})$$

Similarly we can show that

$$\lim_{\Delta t \rightarrow 0} \frac{P_{A,t+\Delta t}}{\Delta t} = - \int_{CS_I} \rho p \mathbf{v} \cdot \mathbf{n} dS \quad (\text{h})$$

The reason for the negative sign is that $\mathbf{v} \cdot \mathbf{n}$ for flow into the system is negative. Substituting Eqs. g and h into Eq. e yields the following equation:

$$\frac{DP_S}{Dt} = \frac{\partial}{\partial t} \int_V \rho p dV + \int_S \rho p \mathbf{v} \cdot \mathbf{n} dS \quad (\text{i})$$

where S is the total surface ($CS_I + CS_{II}$) of the control volume and V is its volume, which is identical to Eq. 2.3-2. This concludes the proof.

2.4 THE MACROSCOPIC MASS BALANCE AND THE EQUATION OF CONTINUITY

In deriving the balance equations, we use vector notation and the sign convention adopted by R. B. Bird, W. E. Stewart, and E. N. Lightfoot in their classic book *Transport Phenomena* (1).

We begin the derivation of the conservation of mass by simply inserting into Eq. 2.3-2, $P = M$ and $p = 1$, yielding directly the *macroscopic mass balance equation*:

$$\frac{\partial}{\partial t} \int_V \rho dV + \int_S \rho \mathbf{v} \cdot \mathbf{n} dS = 0 \quad (2.4-1)$$

We can convert the surface integral in Eq. 2.4-1 to a volume integral using the *Gauss Divergence Theorem*^{5,6} to yield:

$$\frac{\partial}{\partial t} \int_V \rho dV + \int_V (\nabla \cdot \rho \mathbf{v}) dV = 0 \quad (2.4-2)$$

But by definition, we have selected a fixed control volume, therefore the order of differentiation by time and integration can be reversed to get:

$$\int_V \left(\frac{\partial \rho}{\partial t} + \nabla \cdot \rho \mathbf{v} \right) dV = 0 \quad (2.4-3)$$

For this equation to hold for any arbitrary volume V , the kernel of the integral must vanish, resulting in the *equation of continuity*:

$$\frac{\partial \rho}{\partial t} + \nabla \cdot \rho \mathbf{v} = 0 \quad (2.4-4)$$

Equation 2.4-4 can be rewritten in terms of the substantial derivative as:

$$\frac{D\rho}{Dt} = -\rho(\nabla \cdot \mathbf{v}) \quad (2.4-5)$$

Equation 2.4-4 states the mass conservation principle as measured by a *stationary* observer. The derivative $(\partial/\partial t)$ is evaluated at a *fixed position* in space (this is referred to as the Eulerian point of view); whereas, Eq 2.4-5 states the conservation principle, as

5. The Gauss Divergence Theorem states that if V is a volume bounded by a closed surface S , and \mathbf{A} is a continuous vector field, then $\int_V (\nabla \cdot \mathbf{A}) dV = \int_S (\mathbf{n} \cdot \mathbf{A}) dS$.

6. The recurring vectorial operator ∇ , known as del or nabla, is a differential operator that, in rectangular coordination is defined as:

$$\nabla = \delta_1 + \frac{\partial}{\partial x_1} + \delta_2 + \frac{\partial}{\partial x_2} + \delta_3 + \frac{\partial}{\partial x_3}$$

where δ_i are unit vectors in directions x_1, x_2 and x_3 . For the derivation of ∇ in curvilinear coordinates, see Problem 2.1. The “substantial derivative,” namely, the change in time of some property in a fluid element while being convected (or riding with) the fluid in terms of ∇ , is given by:

$$\frac{D}{Dt} = \frac{\partial}{\partial t} + \mathbf{v} \cdot \nabla$$

Recall that the operation of ∇ on a scalar quantity is the gradient, which is a vector. For example, if ∇ is operated on a scalar pressure field P , then ∇P is the pressure gradient vector field, which can have different values in the three spatial directions. The operation of ∇ on a vector field can either be the divergence or the curl of the vector field. The former is obtained by the dot product (also called the scalar product) as $\nabla \cdot \mathbf{v}$ or $\text{div } \vec{v}$, where the result is a scalar; whereas, the latter is obtained by the cross product (also called the vector product) $\nabla \otimes \mathbf{v}$, or $\text{curl } \mathbf{v}$, and the result is a vector field.

TABLE 2.1 The Equation of Continuity in Several Coordinate Systems

Rectangular Coordinates (x, y, z)

$$\frac{\partial \rho}{\partial t} + \frac{\partial}{\partial x}(\rho v_x) + \frac{\partial}{\partial y}(\rho v_y) + \frac{\partial}{\partial z}(\rho v_z) = 0$$

Cylindrical Coordinates (r, θ, z)

$$\frac{\partial \rho}{\partial t} + \frac{1}{r} \frac{\partial}{\partial r}(\rho r v_r) + \frac{1}{r} \frac{\partial}{\partial \theta}(\rho v_\theta) + \frac{\partial}{\partial z}(\rho v_z) = 0$$

Spherical Coordinates (r, θ, ϕ)

$$\frac{\partial \rho}{\partial t} + \frac{1}{r^2} \frac{\partial}{\partial r}(\rho r^2 v_r) + \frac{1}{r \sin \theta} \frac{\partial}{\partial \theta}(\rho v_\theta \sin \theta) + \frac{1}{r \sin \theta} \frac{\partial}{\partial \phi}(\rho v_\phi) = 0$$

Source: Reprinted with permission from R. B. Bird, W. E. Stewart, and E. N. Lightfoot, *Transport Phenomena*, Wiley, New York, 1960.

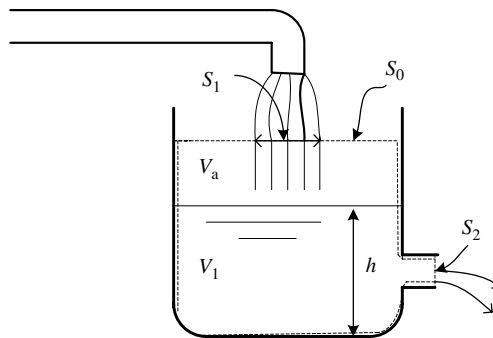
measured (reported) by an observer who is moving with the fluid (this is referred to as the Lagrangian point of view). Table 2.1 gives Eq. 2.4-4 in rectangular, cylindrical, and spherical coordinate systems.

For an incompressible fluid, the density is constant, that is, it does not change in time or spatial position, and therefore Eq. 2.4-5 simplifies to:

$$\nabla \cdot \mathbf{v} = 0 \tag{2.4-6}$$

In fluid dynamics we frequently invoke the incompressibility assumption, even though fluid densities change with pressure and temperature, and these may vary in time and space. If the density change cannot be neglected, then an appropriate *equation of state* of the form $\rho = \rho(T, P)$ must be used in conjunction with the balance equations.

Example 2.1 The Use of the Macroscopic Mass Balance for a Vessel with Salt Solution A liquid-filled vessel shown in the accompanying figure contains a 10% by weight salt solution. At time $t = 0$ we begin feeding a 2% by weight salt solution at 20 kg/h and extracting 10 kg/h solution. Find the amount of solution M and salt S in the vessel as a function of time.



Solution Using the macroscopic mass balance Eq. 2.4-1, we first define the control volume as shown by the dotted line in the figure. Note that we defined the control volume above the liquid surface. Next, we apply Eq. 2.4-1 to the control volume which, taking into account all streams entering and leaving the tank, yields:

$$\frac{\partial}{\partial t} \int_{V_l} \rho_{\text{sol}} dV + \frac{\partial}{\partial t} \int_{V_a} \rho_{\text{air}} dV - \rho_{\text{sol},2\%} v_1 S_1 + \rho_{\text{sol}} v_2 S_2 + \rho_{\text{air}} \frac{dh}{dt} S_0 = 0$$

(change in M in CV) (mass flow in) (air mass flow out)
 (change in air mass in CV) (mass flow out)

Note that \mathbf{n} is normal to the surface and points outward from the control volume, hence, streams entering are negative and leaving are positive. Now the second and last terms cancel each other so they can be dropped to yield:

$$\frac{dM}{dt} - 20 + 10 = 0$$

and integration with the given initial condition gives:

$$M(\text{kg}) = 1000 + 10t(\text{min})$$

We next apply Eq. 2.4-1 to the salt:

$$\frac{\partial}{\partial t} \int_V \left(\frac{S}{M} \right) \rho_{\text{sol}} dV - 20 \times 0.02 + 10 \left(\frac{S}{M} \right) = 0$$

where the first term is $\partial S / \partial t$ and S/M is the instantaneous salt concentration, leading to:

$$\frac{dS}{dt} + \frac{10S}{1000 + 10t} = 0.4$$

which results after integration with initial conditions $S = 100$ at $t = 0$, in

$$S(\text{kg}) = \frac{10000 + 40t + 0.2t^2}{100 + t}$$

where t is in minutes. The ratio of S/M gives the concentration of salt as a function of time. This will show that, as time goes toward infinity, the concentration approaches inlet concentration.

Example 2.2 The Radial Velocity in a Steady, Fully Developed Flow Show that in a steady, fully developed flow of an incompressible liquid in a pipe, the radial velocity component vanishes.

Solution In a pipe flow we have, in principle, three velocity components v_z , v_θ , and v_r . The equation of continuity in cylindrical coordinates is given in Table 2.1. For an incompressible fluid, this equation reduces to

$$\frac{1}{r} \frac{\partial}{\partial r} (r v_r) + \frac{1}{r} \frac{\partial v_\theta}{\partial \theta} + \frac{\partial v_z}{\partial z} = 0$$

However, because of symmetry, v_θ must vanish and, in a fully developed flow $\partial v_z / \partial z = 0$, we therefore obtain

$$\frac{\partial}{\partial r}(rv_r) = 0$$

which, upon integration, yields $rv_r = C$, where C is a constant. However, since there is no flow across the wall, $C = 0$, and hence the radial velocity must vanish everywhere.

2.5 THE MACROSCOPIC LINEAR MOMENTUM BALANCE AND THE EQUATION OF MOTION

Newton's Second Law is a statement of conservation of linear momentum for a system:

$$\frac{D\mathbf{P}_s}{Dt} = \sum_i \mathbf{F}_i \quad (2.5-1)$$

where \mathbf{P}_s is the linear momentum $m\mathbf{v}$ of a body of mass m ; $D\mathbf{P}_s/Dt$ is the substantial derivative of the linear momentum; and $\sum_i \mathbf{F}_i$ are the forces acting on the body. Substituting Eq. 2.5-1 into Eq. 2.3-2 with $p \equiv \mathbf{v}$, we get:

$$\frac{\partial}{\partial t} \int_V \rho \mathbf{v} dV + \int_S \rho \mathbf{v} \mathbf{v} \cdot \mathbf{n} dS = \mathbf{F}_b + \mathbf{F}_s \quad (2.5-2)$$

where \mathbf{F}_b are the body forces (e.g., gravitation), and \mathbf{F}_s the surface forces (e.g., viscous forces) that are acting on the control volume. If there are other forces, such as electric or magnetic forces, acting on the control volume, they should be added to Eq. 2.5-2 and appropriately accounted for. Within this text, however, the only forces that we will consider are gravitational and viscous forces.

Now Eq. 2.5-2 is a vectorial equation that has three components, reflecting the fact that linear momentum is *independently* conserved in the three spatial directions. For a rectangular coordinate system, Eq. 2.5-2 becomes:

$$\frac{\partial}{\partial t} \int_V \rho v_x dV + \int_S v_x \rho \mathbf{v} \cdot \mathbf{n} dS = \mathbf{F}_{bx} + \mathbf{F}_{sx} \quad (2.5-3)$$

$$\frac{\partial}{\partial t} \int_V \rho v_y dV + \int_S v_y \rho \mathbf{v} \cdot \mathbf{n} dS = \mathbf{F}_{by} + \mathbf{F}_{sy} \quad (2.5-4)$$

$$\frac{\partial}{\partial t} \int_V \rho v_z dV + \int_S v_z \rho \mathbf{v} \cdot \mathbf{n} dS = \mathbf{F}_{bz} + \mathbf{F}_{sz} \quad (2.5-5)$$

For deriving the *equation of motion*, which is the microscopic counterpart of the macroscopic momentum balance, we proceed as in the case of the mass balance and first

rewrite Eq. 2.5-2 using the Gauss Divergence Theorem to get:

$$\int_V \left[\frac{\partial}{\partial t} (\rho \mathbf{v}) + \nabla \cdot \mathbf{v} (\rho \mathbf{v}) \right] dV = \mathbf{F}_b + \mathbf{F}_s \quad (2.5-6)$$

Next, we consider the forces that act on the control volume. The body forces are due to gravitation and act on all the mass in the control volume:

$$\mathbf{F}_b = \int_V \rho \mathbf{g} dV \quad (2.5-7)$$

The surface forces that act on the control volume are due to the stress field in the deforming fluid defined by the stress tensor $\boldsymbol{\pi}$. We discuss the nature of the stress tensor further in the next section; at this point, it will suffice to state that $\boldsymbol{\pi}$ is a symmetric second-order tensor, which has nine components. It is convenient to divide the stress tensor into two parts:

$$\boldsymbol{\pi} = P\boldsymbol{\delta} + \boldsymbol{\tau} \quad (2.5-8)$$

where P is a scalar quantity, which is the “pressure,” $\boldsymbol{\delta}$ is the identity tensor defined as:

$$\boldsymbol{\delta} = \begin{pmatrix} 1 & 0 & 0 \\ 0 & 1 & 0 \\ 0 & 0 & 1 \end{pmatrix} \quad (2.5-9)$$

and $\boldsymbol{\tau}$ is the *dynamic* or *deviatoric* component of the stress tensor, which accounts for the viscous stresses created in the fluid as a result of flow.

Thus Eq. 2.5-8 can be written as

$$\begin{pmatrix} \pi_{11} & \pi_{12} & \pi_{13} \\ \pi_{21} & \pi_{22} & \pi_{23} \\ \pi_{31} & \pi_{32} & \pi_{33} \end{pmatrix} = P \begin{pmatrix} 1 & 0 & 0 \\ 0 & 1 & 0 \\ 0 & 0 & 1 \end{pmatrix} + \begin{pmatrix} \tau_{11} & \tau_{12} & \tau_{13} \\ \tau_{21} & \tau_{22} & \tau_{23} \\ \tau_{31} & \tau_{32} & \tau_{33} \end{pmatrix} \quad (2.5-10)$$

which expresses nine separate scalar equations relating the respective components of the tensors: $\pi_{ij} = P\delta_{ij} + \tau_{ij}$, where $\delta_{ij} = 1$ for $i = j$, and $\delta_{ij} = 0$ for $i \neq j$. For convenience, the tensor $\boldsymbol{\pi}$ is called the *total* stress tensor and $\boldsymbol{\tau}$ is simply the stress tensor. Clearly, $\pi_{ij} = \tau_{ij}$ for $i \neq j$ and $\pi_{ii} = P + \tau_{ii}$ for $i = j$. Thus, the total normal stress incorporates the contribution of the “pressure,” P , which is isotropic. In the absence of flow, at equilibrium, the pressure P becomes identical to the thermodynamic pressure, which for pure fluids is related to density and temperature via a state equation.

Two difficulties are associated with P . First, flow implies nonequilibrium conditions, and it is not obvious that P appearing during flow is the same pressure as the one defined in thermodynamics. Second, when the incompressibility assumption is invoked (generally used in solving polymer processing problems) the meaning of P is not clear, and P is regarded as an arbitrary variable. No difficulty, however, arises in solving practical problems, because we only need to know the pressure *gradient*.

Turning back to Eq. 2.5-6, the surface forces F_s can now be expressed in terms of the total stress tensor $\boldsymbol{\pi}$ as follows:

$$\mathbf{F}_s = - \int_S \boldsymbol{\pi} \cdot \mathbf{n} dS \quad (2.5-11)$$

where the minus sign is introduced to account for the forces the surrounding fluid applies on the control volume.

Substituting Eqs. 2.5-11 and 2.5-7 into Eq. 2.5-6, using the Gauss Divergence Theorem, we obtain:

$$\int_V \left[\frac{\partial}{\partial t}(\rho \mathbf{v}) + \nabla \cdot \mathbf{v}(\rho \mathbf{v}) \right] dV = \int_V \rho \mathbf{g} dV - \int_V \nabla \cdot \boldsymbol{\pi} dV \quad (2.5-12)$$

or

$$\int_V \left[\frac{\partial}{\partial t}(\rho \mathbf{v}) + \nabla \cdot \mathbf{v}(\rho \mathbf{v}) + \nabla \cdot \boldsymbol{\pi} - \rho \mathbf{g} \right] dV = 0 \quad (2.5-13)$$

Equation 2.5-13 is valid for any arbitrary control volume. The only way this can hold true is if the kernel of the integral vanishes, that is,

$$\frac{\partial}{\partial t}(\rho \mathbf{v}) + \nabla \cdot \mathbf{v} \rho \mathbf{v} + \nabla \cdot \boldsymbol{\pi} - \rho \mathbf{g} = 0 \quad (2.5-14)$$

which is the *equation of motion*. But, $\nabla \cdot \mathbf{v} \rho \mathbf{v} = \mathbf{v}(\nabla \cdot \rho \mathbf{v}) + \rho \mathbf{v} \cdot \nabla \mathbf{v}$. Thus Eq. 2.5-14 can be written as

$$\rho \frac{\partial \mathbf{v}}{\partial t} + \mathbf{v} \frac{\partial \rho}{\partial t} + \mathbf{v} \nabla \cdot \rho \mathbf{v} + \rho \mathbf{v} \cdot \nabla \mathbf{v} + \nabla \cdot \boldsymbol{\pi} - \rho \mathbf{g} = 0 \quad (2.5-15)$$

Furthermore, the second and third terms express the product of \mathbf{v} with the *equation of continuity*. Thus they equal zero, and Eq. 2.5-15 reduces to

$$\rho \frac{\partial \mathbf{v}}{\partial t} + \rho \mathbf{v} \cdot \nabla \mathbf{v} = -\nabla \cdot \boldsymbol{\pi} + \rho \mathbf{g} \quad (2.5-16)$$

or, in terms of the substantial derivative, we get:

$$\rho \frac{D\mathbf{v}}{Dt} = -\nabla \cdot \boldsymbol{\pi} + \rho \mathbf{g} \quad (2.5-17)$$

which we recognize as Newton's Second Law, which states that the mass (per unit volume) times acceleration⁷ equals the sum of the forces acting on the fluid element.

Next, we substitute Eq. 2.5-8 into Eq. 2.5-16 to yield the common form of the *equation of motion*:

$$\rho \frac{\partial \mathbf{v}}{\partial t} + \rho \mathbf{v} \cdot \nabla \mathbf{v} = -\nabla P - \nabla \cdot \boldsymbol{\tau} + \rho \mathbf{g} \quad (2.5-18)$$

7. Recall that the substantial derivative implies that we "ride" with the fluid element.

where the terms on the left-hand side express accumulation of momentum and the convection of momentum, respectively, and those on the right side express the forces acting on the fluid element by the pressure gradient, the stresses in the flowing fluid, and the gravitational forces. The three components of the equation of motion, in rectangular, cylindrical, and spherical coordinates are given in Table 2.2.

TABLE 2.2 The Equation of Motion in Terms of τ in Several Coordinate Systems

Rectangular Coordinates (x, y, z)

$$\begin{aligned}\rho \left(\frac{\partial v_x}{\partial t} + v_x \frac{\partial v_x}{\partial x} + v_y \frac{\partial v_x}{\partial y} + v_z \frac{\partial v_x}{\partial z} \right) &= -\frac{\partial P}{\partial x} - \left(\frac{\partial \tau_{xx}}{\partial x} + \frac{\partial \tau_{yx}}{\partial y} + \frac{\partial \tau_{zx}}{\partial z} \right) + \rho g_x \\ \rho \left(\frac{\partial v_y}{\partial t} + v_x \frac{\partial v_y}{\partial x} + v_y \frac{\partial v_y}{\partial y} + v_z \frac{\partial v_y}{\partial z} \right) &= -\frac{\partial P}{\partial y} - \left(\frac{\partial \tau_{xy}}{\partial x} + \frac{\partial \tau_{yy}}{\partial y} + \frac{\partial \tau_{zy}}{\partial z} \right) + \rho g_y \\ \rho \left(\frac{\partial v_z}{\partial t} + v_x \frac{\partial v_z}{\partial x} + v_y \frac{\partial v_z}{\partial y} + v_z \frac{\partial v_z}{\partial z} \right) &= -\frac{\partial P}{\partial z} - \left(\frac{\partial \tau_{xz}}{\partial x} + \frac{\partial \tau_{yz}}{\partial y} + \frac{\partial \tau_{zz}}{\partial z} \right) + \rho g_z\end{aligned}$$

Cylindrical Coordinates (r, θ, z)

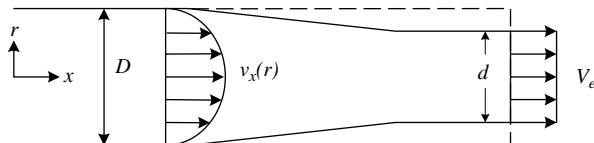
$$\begin{aligned}\rho \left(\frac{\partial v_r}{\partial t} + v_r \frac{\partial v_r}{\partial r} + \frac{v_\theta}{r} \frac{\partial v_r}{\partial \theta} - \frac{v_\theta^2}{r} + v_z \frac{\partial v_r}{\partial z} \right) &= -\frac{\partial P}{\partial r} - \left(\frac{1}{r} \frac{\partial}{\partial r} (r \tau_{rr}) + \frac{1}{r} \frac{\partial \tau_{r\theta}}{\partial \theta} - \frac{\tau_{\theta\theta}}{r} + \frac{\partial \tau_{rz}}{\partial z} \right) + \rho g_r \\ \rho \left(\frac{\partial v_\theta}{\partial t} + v_r \frac{\partial v_\theta}{\partial r} + \frac{v_\theta}{r} \frac{\partial v_\theta}{\partial \theta} + \frac{v_r v_\theta}{r} + v_z \frac{\partial v_\theta}{\partial z} \right) &= -\frac{1}{r} \frac{\partial P}{\partial \theta} - \left(\frac{1}{r^2} \frac{\partial}{\partial r} (r^2 \tau_{r\theta}) + \frac{1}{r} \frac{\partial \tau_{\theta\theta}}{\partial \theta} + \frac{\partial \tau_{\theta z}}{\partial z} \right) + \rho g_\theta \\ \rho \left(\frac{\partial v_z}{\partial t} + v_r \frac{\partial v_z}{\partial r} + \frac{v_\theta}{r} \frac{\partial v_z}{\partial \theta} + v_z \frac{\partial v_z}{\partial z} \right) &= -\frac{\partial P}{\partial z} - \left(\frac{1}{r} \frac{\partial}{\partial r} (r \tau_{rz}) + \frac{1}{r} \frac{\partial \tau_{\theta z}}{\partial \theta} + \frac{\partial \tau_{zz}}{\partial z} \right) + \rho g_z\end{aligned}$$

Spherical Coordinates (r, θ, ϕ)

$$\begin{aligned}\rho \left(\frac{\partial v_r}{\partial t} + v_r \frac{\partial v_r}{\partial r} + \frac{v_\theta}{r} \frac{\partial v_r}{\partial \theta} + \frac{v_\phi}{r \sin \theta} \frac{\partial v_r}{\partial \phi} - \frac{v_\theta^2 + v_\phi^2}{r} \right) &= -\frac{\partial P}{\partial r} - \left(\frac{1}{r^2} \frac{\partial}{\partial r} (r^2 \tau_{rr}) + \frac{1}{r \sin \theta} \frac{\partial}{\partial \theta} (\tau_{r\theta} \sin \theta) + \frac{1}{r \sin \theta} \frac{\partial \tau_{r\phi}}{\partial \phi} - \frac{\tau_{\theta\theta} + \tau_{\phi\phi}}{r} \right) + \rho g_r \\ \rho \left(\frac{\partial v_\theta}{\partial t} + v_r \frac{\partial v_\theta}{\partial r} + \frac{v_\theta}{r} \frac{\partial v_\theta}{\partial \theta} + \frac{v_\phi}{r \sin \theta} \frac{\partial v_\theta}{\partial \phi} + \frac{v_r v_\theta}{r} - \frac{v_\phi^2 \cot \theta}{r} \right) &= -\frac{1}{r} \frac{\partial P}{\partial \theta} - \left(\frac{1}{r^2} \frac{\partial}{\partial r} (r^2 \tau_{r\theta}) + \frac{1}{r \sin \theta} \frac{\partial}{\partial \theta} (\tau_{\theta\theta} \sin \theta) + \frac{1}{r \sin \theta} \frac{\partial \tau_{\theta\phi}}{\partial \phi} + \frac{\tau_{r\theta}}{r} - \frac{\cot \theta}{r} \tau_{\phi\phi} \right) + \rho g_\theta \\ \rho \left(\frac{\partial v_\phi}{\partial t} + v_r \frac{\partial v_\phi}{\partial r} + \frac{v_\theta}{r} \frac{\partial v_\phi}{\partial \theta} + \frac{v_\phi}{r \sin \theta} \frac{\partial v_\phi}{\partial \phi} + \frac{v_\phi v_r}{r} + \frac{v_\theta v_\phi}{r} \cot \theta \right) &= -\frac{1}{r \sin \theta} \frac{\partial P}{\partial \phi} - \left(\frac{1}{r^2} \frac{\partial}{\partial r} (r^2 \tau_{r\phi}) + \frac{1}{r} \frac{\partial \tau_{\theta\phi}}{\partial \theta} + \frac{1}{r \sin \theta} \frac{\partial \tau_{\phi\phi}}{\partial \phi} + \frac{\tau_{r\phi}}{r} + \frac{2 \cot \theta}{r} \tau_{\theta\phi} \right) + \rho g_\phi\end{aligned}$$

Source: Reprinted with permission from R. B. Bird, W. E. Stewart, and E. N. Lightfoot, *Transport Phenomena*, Wiley, New York, 1960.

Example 2.3 The Use of the Macroscopic Momentum Balance to Calculate the Diameter of a Free Jet A free jet of diameter d leaves a horizontal tube of diameter D , as shown in the accompanying figure. Assuming a laminar, fully developed velocity profile at the exit of the tube, and neglecting gravitational forces and the drag of the air on the free jet, prove that $d/D = (0.75)^{0.5}$.



Solution We first select the control volume as shown by the dotted line in the figure, assuming that, at the downstream end of the control volume, the velocity profile in the free jet is flat. Next, we apply the macroscopic momentum balance, Eq. 2.5-3, to the control volume. We need be concerned only with the x component, because this is the only momentum that crosses the control volume boundaries. The flow is steady, and therefore the time-dependent term vanishes, as do the forces, since there are none acting on the control volume. Thus the equation reduces to:

$$\int_S v_x \rho \mathbf{v} \cdot \mathbf{n} \, dS = 0 \quad (\text{E2.3-1})$$

The velocity profile in a laminar flow is given by $v_x = V_0 [1 - (r/R)^2]$, where V_0 is the maximum velocity. At the exit, the velocity is uniform and given by V_e . Substituting these terms into Eq. E2.3-1 gives:

$$-\rho \int_S V_0^2 [1 - (r/R)^2]^2 \, dS + \rho V_e^2 (\pi d^2/4) = 0 \quad (\text{E2.3-2})$$

or

$$-2\pi V_0^2 (D/2)^2 \int_0^1 \xi (1 - \xi^2)^2 \, d\xi + V_e^2 (\pi d^2/4) = 0 \quad (\text{E2.3-3})$$

where $\xi = r/R$, which then yields:

$$\left(\frac{d}{D}\right)^2 = \frac{1}{3} \left(\frac{V_0}{V_e}\right)^2 \quad (\text{E2.3-4})$$

Next we apply the macroscopic mass balance, Eq. 2.4-1, which gives a second relationship between the variables:

$$-\rho \int_S V_0 [1 - (r/R)^2] \, dS + \rho V_e (\pi d^2/4) = 0 \quad (\text{E2.3-5})$$

which results in

$$\frac{V_0}{V_e} = 2 \left(\frac{d}{D} \right)^2 \quad (\text{E2.3-6})$$

Combining Eqs. E2.3-4 and E2.3-6 gives the desired result of $d/D = 0.75^{0.5}$.

2.6 THE STRESS TENSOR

Consider a point P in a continuum on an arbitrary surface element ΔS (defined by the normal \mathbf{n}), as in Fig. 2.2. Let $\Delta \mathbf{f}_i$ be the resultant force exerted by the material on the positive side of the surface on that of the negative side across ΔS .

The average force per unit area is $\Delta \mathbf{f}_i / \Delta S$. This quantity attains a limiting nonzero value as ΔS approaches zero at point P (Cauchy's stress principle). This limiting quantity is called the *stress vector*, or traction vector \mathbf{T}' . But \mathbf{T}' depends on the orientation of the area element, that is, the direction of the surface defined by normal \mathbf{n} . Thus it would appear that there are an infinite number of unrelated ways of expressing the state of stress at point P .

It turns out, however, that the state of stress at P can be completely specified by giving the stress vector components in *any three mutually perpendicular planes* passing through the point. That is, only nine components, three for each vector, are needed to define the stress at point P . Each component can be described by two indices ij , the first denoting the orientation of the surface and the second, the direction of the force. Figure 2.3 gives these components for three Cartesian planes. The nine stress vector components form a second-order Cartesian tensor, the stress tensor⁸ π' .

Furthermore, some argumentation based on the principles of mechanics and experimental observations, as well as molecular theories, leads to the conclusion that the stress tensor is symmetric, that is,

$$\pi'_{ij} = \pi'_{ji} \quad (2.6-1)$$

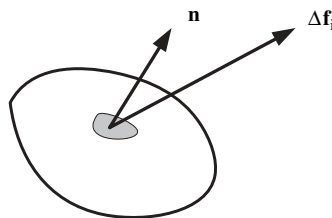


Fig. 2.2 An arbitrary surface element with direction defined by normal \mathbf{n} with resultant force $\Delta \mathbf{f}_i$ acting at point P .

8. Note that we differentiate the stress tensor π' discussed in this section from the previously discussed stress tensor π because they are defined on the basis of different sign conventions, as discussed later in the chapter.

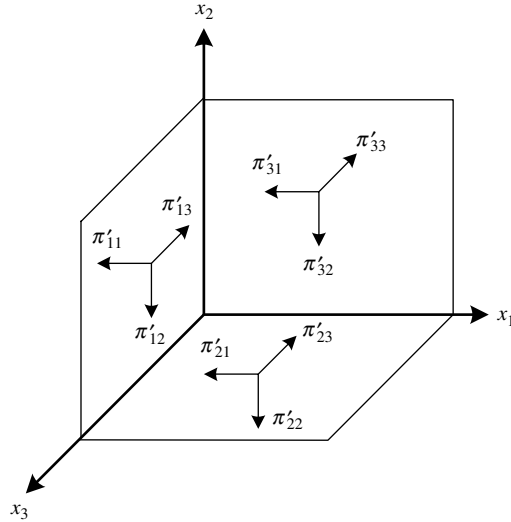


Fig. 2.3 The nine Cartesian components of the stress tensor. In the limit, the cube shrinks to point P .

Hence, only six independent components of the stress tensor are needed to fully define the state of the stress at point P , where π'_{ii} are the normal stress components, and π'_{ij} ($i \neq j$) are the shear-stress components.

By considering the forces that the material on the positive side of the surface (i.e., material on the side of the surface at which the outward normal vector points) exerts on the material on the negative side, a stress component is *positive* when it acts in the positive direction of the coordinate axes and on a plane whose outer normal points in one of the positive coordinate directions (or if both of the previously mentioned directions are negative).

A stress component is negative if any *one* direction is negative. Hence, by this sign convention, generally used in mechanics and mechanical engineering, tensile stresses are positive and compressive stresses are negative. Moreover, according to this sign convention, all the stresses shown in Fig. 2.3 are positive. Unfortunately, this sign convention is *opposite* to that resulting from momentum transport considerations, thus $\pi'^{\dagger} = -\pi$ (where \dagger stands for ‘transpose’). In the latter sign convention, as pointed out by Bird et al. (1), if we consider the stress vector $\pi_n = \mathbf{n} \cdot \boldsymbol{\pi}$ acting on surface $d\mathbf{S}$ of orientation \mathbf{n} , the force $\pi_n d\mathbf{S}$ is that exerted by the material on the negative side onto that on the positive side. (According to Newton’s Third Law, this force is equal and opposite to that exerted by the material of the positive side to the material of the negative side.) It follows, then, that, in this latter convention, tensile stresses are negative. In this book we follow this latter sign convention.

As we pointed out in the introductory remarks, polymer processing is the simultaneous occurrence of momentum, heat, and occasionally, mass transfer in multicomponent systems. This sign convention, as shown in the following paragraphs, leads to consistency among the three transport processes. Nevertheless, it is worth emphasizing that the sign convention used in no way affects the solution of flow problems. Once constitutive equations are inserted into the equation of motion, and stress components are replaced by velocity gradients, the two sign conventions lead to identical expressions.

Generally, from the tensor π or tensor τ , which is related to the former via Eq. 2.5-8, three independent scalar invariant entities can be formed by taking the trace of τ . The three invariants are:

$$I_\tau = \text{tr } \tau = \sum_1^3 \tau_{ii} \tag{2.6-2}$$

$$II_\tau = \text{tr } \tau^2 = \sum_1^3 \sum_1^3 \tau_{ij}\tau_{ji} \tag{2.6-3}$$

$$III_\tau = \text{tr } \tau^3 = \sum_1^3 \sum_1^3 \sum_1^3 \tau_{ij}\tau_{jk}\tau_{ki} \tag{2.6-4}$$

and the magnitude of the stress tensor τ denoted as τ is given by:

$$\tau = |\tau| = \sqrt{\frac{1}{2}(\tau:\tau)} = \sqrt{\frac{1}{2}II_\tau} \tag{2.6-5}$$

Example 2.4 The Similarity Between the Three Transport Phenomena Consider an infinite slab of solid shown in Fig. E2.4(a) with a constant temperature difference over its surfaces.

The temperature gradient for $T(0) > T(b)$ is negative and given by

$$\frac{dT}{dy} = -\frac{T(0) - T(b)}{b}$$

and using Fourier’s law, the heat is given by:

$$q_y = -k \frac{dT}{dy} = \frac{k}{b}[T(0) - T(b)]$$

where k is the thermal conductivity. Clearly, for the case shown, the heat flux is in the positive y direction, and flows from high temperature to low temperature.

Now consider the case of one-dimensional diffusion of component A shown in Fig. E2.4(b). Similarly, the concentration gradient for $C_A(0) > C_A(b)$ is negative and given by:

$$\frac{dC_A}{dy} = -\frac{C_A(0) - C_A(b)}{b}$$

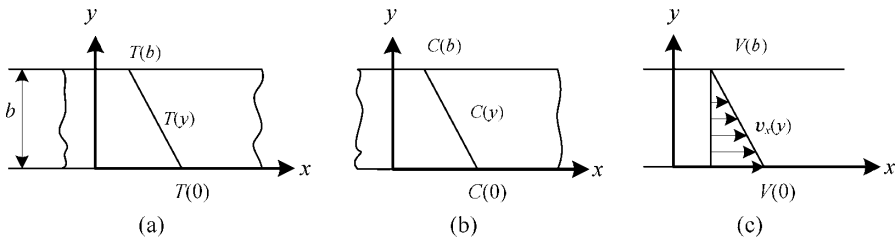


Fig. E2.4 (a) Temperature, (b) concentration, and (c) velocity profile over infinite slabs of material. In (c) the fluid is confined between two parallel plates in relative motion.

Using Fick's law (assuming constant density and low concentration of the diffusing component), the mass flux is positive and is given by

$$J_{Ay} = -\mathcal{D}_{AB} \frac{dC_A}{dy} = \mathcal{D}_{AB}[C_A(0) - C_A(b)]$$

where \mathcal{D}_{AB} is the binary diffusion coefficient. As in the case of heat flux, the flux of the A component is positive, and it flows from high concentration to low concentration.

Finally, let us examine the flow of viscous fluid between two parallel plates in relative motion [Fig. E2.4(c)]. Because of intermolecular forces, the fluid layer next to the bottom plate will start moving. This layer will then transmit, by viscous drag, *momentum* to the layer above it, and so on. The velocity gradient for $v_x(0) > v_x(b)$ is positive and given by

$$\frac{dv_x}{dy} = -\frac{V(0)}{b}$$

Using Newton's law, which holds for an important class of fluids, we get:

$$\tau_{yx} = -\mu \frac{dv_x}{dy} = \frac{\mu}{b} V(0)$$

where μ is the viscosity. Clearly, the flux of x momentum is the shear stress, and it is in the y direction from the lower plate to the upper one; that is, it flows downstream the velocity profile, from high velocity to low velocity, and there is a *positive* momentum flux according to the coordinate system used. This example demonstrates the similarity of the three transport processes, and the reason for defining the fluxes of heat, mass, and momentum in Fourier's, Fick's, and Newton's laws with a negative sign.

2.7 THE RATE OF STRAIN TENSOR

We know from everyday experience that applying a given tensile or shear stress to a solid material results in a given deformation. In the elastic range, Hooke's law predicts a linear deformation with the applied stress. The elastic modulus in Hooke's law specifies the nature of the particular solid. Yet in viscous fluids, the applied stress is not related to the *deformation* of the fluid, but to the *rate* at which the fluid is being deformed, or to the *rate of strain*. As we shall see in this section, in order to define the rate of strain of a fluid at a given point, we need nine (six independent) numbers. Therefore, just like *stress*, the *rate of strain* is a second-order symmetric tensor. It is the nature of the relationship between the *stress* and the *rate of strain* tensors that the *constitution* of the particular fluid being deformed is manifested. The generally empirical equations relating the two, therefore, are called *constitutive equations*.

In an important class of materials, called *Newtonian*, this relationship is linear and one parameter—the viscosity—specifies the constitution of the material. Water, low-viscosity fluids, and gases are Newtonian fluids. However, most polymeric melts are non-Newtonian and require more complex constitutive equations to describe the relationship between the stress and the rate of strain. These are discussed in Chapter 3.

Geometric Considerations of the Rate of Strain Tensor

We first consider a small rectangular element at time t in shear flow, as shown in Fig. 2.4. This element is a vanishingly small differential element, and therefore without loss of generality we can assume that the local velocity field is linear, as shown in the figure.

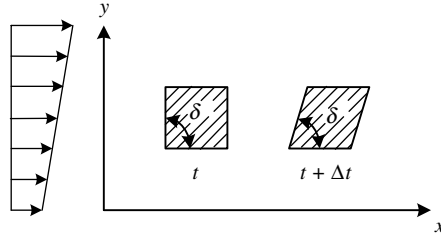


Fig. 2.4 The deformation of a fluid element in unidirectional shear flow.

At time $t + \Delta t$ the rectangular fluid element is translated in the x direction and deformed into a parallelogram. We define the *rate of shear* as $-d\delta/dt$, where δ is the angle shown in the figure.

Out of simple geometrical considerations, we express the rate of shear in terms of velocity gradients as follows:

$$\begin{aligned}
 -\frac{d\delta}{dt} &= \lim_{\Delta t \rightarrow 0} \frac{\delta_{t+\Delta t} - \delta_t}{\Delta t} \\
 &= -\lim_{\Delta t \rightarrow 0} \left\{ \frac{\pi/2 - \arctan \left[\frac{(v_{x,y+\Delta y} - v_{x,y})\Delta t / \Delta y}{\Delta t} \right] - \pi/2}{\Delta t} \right\} \\
 &= \lim_{\Delta y \rightarrow 0} \frac{v_{x,y+\Delta y} - v_{x,y}}{\Delta y} = \frac{dv_x}{dy}
 \end{aligned} \tag{2.7-1}$$

Thus, we find that the rate of shear (or *shear rate*, as it is commonly referred to), or the rate of change of the angle δ , simply equals the velocity gradient.

We can extend this analysis to general flow fields $v(x, y, z, t)$ by considering the deformation of the fluid element in the x, y, z, y , and x, z planes. In such a case, for the x, y plane we get (see Problem 2.6):

$$-\frac{d\delta_{x,y}}{dt} = \frac{\partial v_x}{\partial y} + \frac{\partial v_y}{\partial x} = \dot{\gamma}_{xy} \tag{2.7-2}$$

and for the other two planes we get:

$$-\frac{d\delta_{y,z}}{dt} = \frac{\partial v_y}{\partial z} + \frac{\partial v_z}{\partial y} = \dot{\gamma}_{yz} \tag{2.7-3}$$

$$-\frac{d\delta_{x,z}}{dt} = \frac{\partial v_x}{\partial z} + \frac{\partial v_z}{\partial x} = \dot{\gamma}_{xz} \tag{2.7-4}$$

where we defined the shear components of the rate of deformation tensor $\dot{\gamma}$ in Cartesian (rectangular) coordinates.

Now that we have discussed the geometric interpretation of the rate of strain tensor, we can proceed with a somewhat more formal mathematical presentation. We noted earlier that the (deviatoric) stress tensor τ related to the flow and deformation of the fluid. The kinematic quantity that expresses fluid flow is the velocity gradient. Velocity is a vector and in a general flow field each of its three components can change in any of the three

spatial directions, giving rise to nine velocity gradient components. We can therefore define a *velocity gradient tensor* $\nabla \mathbf{v}$ (i.e., the dyadic product of ∇ with \mathbf{v}), which in Cartesian coordinates can be written as:

$$\nabla \mathbf{v} = \begin{pmatrix} \frac{\partial v_1}{\partial x_1} & \frac{\partial v_1}{\partial x_2} & \frac{\partial v_1}{\partial x_3} \\ \frac{\partial v_2}{\partial x_1} & \frac{\partial v_2}{\partial x_2} & \frac{\partial v_2}{\partial x_3} \\ \frac{\partial v_3}{\partial x_1} & \frac{\partial v_3}{\partial x_2} & \frac{\partial v_3}{\partial x_3} \end{pmatrix} \quad (2.7-5)$$

A fluid in motion may simultaneously deform and rotate. Decomposing the velocity gradient tensor into two parts can separate these motions:

$$\nabla \mathbf{v} = \frac{1}{2}(\dot{\boldsymbol{\gamma}} + \boldsymbol{\omega}) \quad (2.7-6)$$

where $\dot{\boldsymbol{\gamma}}$ and $\boldsymbol{\omega}$ are the *rate of strain* and the *vorticity* tensors, respectively, defined as:

$$\dot{\boldsymbol{\gamma}} = \nabla \mathbf{v} + (\nabla \mathbf{v})^\dagger \quad (2.7-7)$$

and

$$\boldsymbol{\omega} = \nabla \mathbf{v} - (\nabla \mathbf{v})^\dagger \quad (2.7-8)$$

where $(\nabla \mathbf{v})^\dagger$ is the *transpose*⁹ $\nabla \mathbf{v}$. Thus by inserting Eq. 2.7- 5 and its transpose into Eq. 2.7- 7, we get the following expression for the rate of deformation tensor in Cartesian coordinates:

$$\dot{\boldsymbol{\gamma}} = \begin{pmatrix} 2\frac{\partial v_1}{\partial x_1} & \frac{\partial v_2}{\partial x_1} + \frac{\partial v_1}{\partial x_2} & \frac{\partial v_3}{\partial x_1} + \frac{\partial v_1}{\partial x_3} \\ \frac{\partial v_1}{\partial x_2} + \frac{\partial v_2}{\partial x_1} & 2\frac{\partial v_2}{\partial x_2} & \frac{\partial v_3}{\partial x_2} + \frac{\partial v_2}{\partial x_3} \\ \frac{\partial v_1}{\partial x_3} + \frac{\partial v_3}{\partial x_1} & \frac{\partial v_2}{\partial x_3} + \frac{\partial v_3}{\partial x_2} & 2\frac{\partial v_3}{\partial x_3} \end{pmatrix} \quad (2.7-9)$$

For simple shear flow (as between parallel plates in relative motion) Eq. 2.7-9 reduces to:

$$\dot{\boldsymbol{\gamma}} = \begin{pmatrix} 0 & 1 & 0 \\ 1 & 0 & 0 \\ 0 & 0 & 0 \end{pmatrix} \dot{\gamma} \quad (2.7-10)$$

where $\dot{\gamma}$ is the *shear rate*, which is a scalar quantity related to the second invariant of $\dot{\boldsymbol{\gamma}}$ (see Eqs. 2.6-5 and 2.6-3) as follows:

$$\dot{\gamma} = \sqrt{\frac{1}{2}(\dot{\boldsymbol{\gamma}} : \dot{\boldsymbol{\gamma}})} \quad (2.7-11)$$

9. The indices are “transposed”—that is, the rows and columns are interchanged (180° flip on the diagonal).

For simple shear flow we get:

$$\dot{\gamma} = \frac{dv_x}{dy} = \frac{d}{dy} \left(\frac{dx}{dt} \right) = \frac{d}{dt} \left(\frac{dx}{dy} \right) = \frac{d\gamma}{dt} \quad (2.7-12)$$

where γ is the shear strain.

2.8 NEWTONIAN FLUIDS

In the previous section we discussed the nature and some properties of the stress tensor $\boldsymbol{\tau}$ and the rate of strain tensor $\dot{\boldsymbol{\gamma}}$. They are related to each other via a *constitutive equation*, namely, a generally empirical relationship between the two entities, which depends on the nature and *constitution* of the fluid being deformed. Clearly, imposing a given stress field on a body of water, on the one hand, and a body of molasses, on the other hand, will yield different rates of strain. The simplest form that these equations assume, as pointed out earlier, is a linear relationship representing a very important class of fluids called *Newtonian fluids*.

In 1687 Isaac Newton proposed a simple equation relating the shear stress to the velocity gradient in fluids, and defined *viscosity* as the ratio between the two:

$$\mu = - \frac{\tau_{yx}}{\left(\frac{dv_x}{dy} \right)} \quad (2.8-1)$$

This equation is known as ‘Newton’s law’. Of course, it is not really a ‘physical law’, but only an empirical relationship describing a limited, yet very important class of fluids. Newton’s law is generally valid for ordinary fluids with molecular weights below 1000. Gases, water, low molecular weight oils, and so on, behave under most normal conditions according to Newton’s law, namely, they exhibit a linear relationship between the shear stress and the consequent shear rate.

Equation 2.8-1 holds only for simple shearing flow, namely, when there is one velocity component changing in one (normal) spatial direction. The most general Newtonian constitutive equation that we can write for an arbitrary flow field takes the form:

$$\boldsymbol{\tau} = -\mu\dot{\boldsymbol{\gamma}} + (2\mu/3 - \kappa)(\boldsymbol{\nabla} \cdot \mathbf{v})\boldsymbol{\delta} \quad (2.8-2)$$

where κ is the *dilatational* viscosity. For an incompressible fluid (and polymers are generally treated as such), $\boldsymbol{\nabla} \cdot \mathbf{v} = 0$ and Eq. 2.8-2 reduces to:

$$\boldsymbol{\tau} = -\mu\dot{\boldsymbol{\gamma}} \quad (2.8-3)$$

Equations 2.8-2 and 2.8-3 are coordinate-independent compact tensorial forms of the Newtonian constitutive equation. In any particular coordinate system these equations break up into nine (six independent) scalar equations. Table 2.3 lists these equations in rectangular, cylindrical and spherical coordinate systems.

TABLE 2.3 The Components of $\boldsymbol{\tau} = -\mu\dot{\boldsymbol{\gamma}} + (2\mu/3 - \kappa)(\boldsymbol{\nabla} \cdot \mathbf{v})\boldsymbol{\delta}$ in Several Coordinate Systems**Rectangular Coordinates** (x, y, z)

$$\begin{aligned}\tau_{xx} &= -\mu \left[2 \frac{\partial v_x}{\partial x} - \frac{2}{3} (\boldsymbol{\nabla} \cdot \mathbf{v}) \right] \\ \tau_{yy} &= -\mu \left[2 \frac{\partial v_y}{\partial y} - \frac{2}{3} (\boldsymbol{\nabla} \cdot \mathbf{v}) \right] \\ \tau_{zz} &= -\mu \left[2 \frac{\partial v_z}{\partial z} - \frac{2}{3} (\boldsymbol{\nabla} \cdot \mathbf{v}) \right] \\ \tau_{xy} = \tau_{yx} &= -\mu \left[\frac{\partial v_x}{\partial y} + \frac{\partial v_y}{\partial x} \right] \\ \tau_{yz} = \tau_{zy} &= -\mu \left[\frac{\partial v_y}{\partial z} + \frac{\partial v_z}{\partial y} \right] \\ \tau_{zx} = \tau_{xz} &= -\mu \left[\frac{\partial v_z}{\partial x} + \frac{\partial v_x}{\partial z} \right] \\ (\boldsymbol{\nabla} \cdot \mathbf{v}) &= \frac{\partial v_x}{\partial x} + \frac{\partial v_y}{\partial y} + \frac{\partial v_z}{\partial z}\end{aligned}$$

Cylindrical Coordinates (r, θ, z)

$$\begin{aligned}\tau_{rr} &= -\mu \left[2 \frac{\partial v_r}{\partial r} - \frac{2}{3} (\boldsymbol{\nabla} \cdot \mathbf{v}) \right] \\ \tau_{\theta\theta} &= -\mu \left[2 \left(\frac{1}{r} \frac{\partial v_\theta}{\partial \theta} + \frac{v_r}{r} \right) - \frac{2}{3} (\boldsymbol{\nabla} \cdot \mathbf{v}) \right] \\ \tau_{zz} &= -\mu \left[2 \frac{\partial v_z}{\partial z} - \frac{2}{3} (\boldsymbol{\nabla} \cdot \mathbf{v}) \right] \\ \tau_{r\theta} = \tau_{\theta r} &= -\mu \left[r \frac{\partial}{\partial r} \left(\frac{v_\theta}{r} \right) + \frac{1}{r} \frac{\partial v_r}{\partial \theta} \right] \\ \tau_{\theta z} = \tau_{z\theta} &= -\mu \left[\frac{\partial v_\theta}{\partial z} + \frac{1}{r} \frac{\partial v_z}{\partial \theta} \right] \\ \tau_{zr} = \tau_{rz} &= -\mu \left[\frac{\partial v_z}{\partial r} + \frac{\partial v_r}{\partial z} \right] \\ (\boldsymbol{\nabla} \cdot \mathbf{v}) &= \frac{1}{r} \frac{\partial}{\partial r} (rv_\theta) + \frac{1}{r} \frac{\partial v_\theta}{\partial \theta} + \frac{\partial v_z}{\partial z}\end{aligned}$$

Spherical Coordinates (r, θ, ϕ)

$$\begin{aligned}\tau_{rr} &= -\mu \left[2 \frac{\partial v_r}{\partial r} - \frac{2}{3} (\boldsymbol{\nabla} \cdot \mathbf{v}) \right] \\ \tau_{\theta\theta} &= -\mu \left[2 \left(\frac{1}{r} \frac{\partial v_\theta}{\partial \theta} + \frac{v_r}{r} \right) - \frac{2}{3} (\boldsymbol{\nabla} \cdot \mathbf{v}) \right] \\ \tau_{\phi\phi} &= -\mu \left[2 \left(\frac{1}{r \sin \theta} \frac{\partial v_\phi}{\partial \phi} + \frac{v_r}{r} + \frac{v_\theta \cot \theta}{r} \right) - \frac{2}{3} (\boldsymbol{\nabla} \cdot \mathbf{v}) \right] \\ \tau_{r\theta} = \tau_{\theta r} &= -\mu \left[r \frac{\partial}{\partial r} \left(\frac{v_\theta}{r} \right) + \frac{1}{r} \frac{\partial v_r}{\partial \theta} \right] \\ \tau_{\theta\phi} = \tau_{\phi\theta} &= -\mu \left[\frac{\sin \theta}{r} \frac{\partial}{\partial \theta} \left(\frac{v_\phi}{\sin \theta} \right) + \frac{1}{r \sin \theta} \frac{\partial v_\theta}{\partial \phi} \right] \\ \tau_{\phi r} = \tau_{r\phi} &= -\mu \left[\frac{1}{r \sin \theta} \frac{\partial v_r}{\partial \phi} + r \frac{\partial}{\partial r} \left(\frac{v_\phi}{r} \right) \right] \\ (\boldsymbol{\nabla} \cdot \mathbf{v}) &= \frac{1}{r^2} \frac{\partial}{\partial r} (r^2 v_r) + \frac{1}{r \sin \theta} \frac{\partial}{\partial \theta} (v_\theta \sin \theta) + \frac{1}{r \sin \theta} \frac{\partial v_\phi}{\partial \phi}\end{aligned}$$

Source: Reprinted with permission from R. B. Bird, W. E. Stewart, and E. N. Lightfoot, *Transport Phenomena*, Wiley, New York, 1960.

Inserting Eq. 2.8-3 into the equation of motion, 2.5-18, we get¹⁰ the celebrated Navier–Stokes¹¹ equation:

$$\rho \frac{\partial \mathbf{v}}{\partial t} + \rho \mathbf{v} \cdot \nabla \mathbf{v} = -\nabla P + \mu \nabla^2 \mathbf{v} + \rho \mathbf{g} \quad (2.8-4)$$

The symbol defined as ∇^2 is called the *Laplacian*. Table 2.4 lists the components of the Navier–Stokes equation in the various coordinate systems.

We should note that the Navier–Stokes equation holds *only* for Newtonian fluids and incompressible flows. Yet this equation, together with the equation of continuity and with proper initial and boundary conditions, provides *all* the equations needed to solve (analytically or numerically) *any* laminar, isothermal flow problem. Solution of these equations yields the pressure and velocity fields that, in turn, give the stress and rate of strain fields and the flow rate. If the flow is nonisothermal, then simultaneously with the foregoing equations, we must solve the thermal energy equation, which is discussed later in this chapter. In this case, if the temperature differences are significant, we must also account for the temperature dependence of the viscosity, density, and thermal conductivity.

Polymer processing flows are always laminar and generally *creeping* type flows. A creeping flow is one in which viscous forces predominate over forces of inertia and acceleration. Classic examples of such flows include those treated by the hydrodynamic theory of lubrication. For these types of flows, the second term on the left-hand side of Eq. 2.5-18 vanishes, and the Equation of motion reduces to:

$$\rho \frac{\partial \mathbf{v}}{\partial t} = -\nabla P + \mu \nabla^2 \mathbf{v} + \rho \mathbf{g} \quad (2.8-5)$$

and the Navier–Stokes equation for creeping flows reduces to:

$$\rho \frac{\partial \mathbf{v}}{\partial t} = -\nabla P + \mu \nabla^2 \mathbf{v} + \rho \mathbf{g} \quad (2.8-6)$$

On the other extreme of negligible viscosity, which is of little interest to the subject matter of this book, but is added for the sake of comprehensiveness, the equation of motion reduces to

$$\rho \frac{\partial \mathbf{v}}{\partial t} + \rho \mathbf{v} \cdot \nabla \mathbf{v} = -\nabla P + \rho \mathbf{g} \quad (2.8-7)$$

which is the well-known Euler equation, after the Swiss mathematician Leonard Euler, who derived it in 1775.

Finally, for the no-flow situation ($\mathbf{v} = 0$), the equation of motion reduces to

$$\nabla P = \rho \mathbf{g} \quad (2.8-8)$$

which is the basic equation of hydrostatics.

10. Note that: $-\nabla \cdot \boldsymbol{\tau} = \mu \nabla \cdot \dot{\boldsymbol{\gamma}} = \mu \nabla \cdot [\nabla \mathbf{v} + (\nabla \mathbf{v})^t] = \mu [\nabla^2 \mathbf{v} + \nabla(\nabla \cdot \mathbf{v})] = \mu \nabla^2 \mathbf{v}$

11. Claude Louis Navier (1785–1836) was a French scientist who, using molecular arguments, derived the equation in 1828; George Gabriel Stokes (1819–1903) was a British physicist who made many contributions to the theory of viscous flow in the period 1845–1850.

TABLE 2.4 The Navier–Stokes Equation in Several Coordinate Systems**Rectangular Coordinates** (x, y, z)

$$\begin{aligned}\rho \left(\frac{\partial v_x}{\partial t} + v_x \frac{\partial v_x}{\partial x} + v_y \frac{\partial v_x}{\partial y} + v_z \frac{\partial v_x}{\partial z} \right) &= -\frac{\partial P}{\partial x} + \mu \left(\frac{\partial^2 v_x}{\partial x^2} + \frac{\partial^2 v_x}{\partial y^2} + \frac{\partial^2 v_x}{\partial z^2} \right) + \rho g_x \\ \rho \left(\frac{\partial v_y}{\partial t} + v_x \frac{\partial v_y}{\partial x} + v_y \frac{\partial v_y}{\partial y} + v_z \frac{\partial v_y}{\partial z} \right) &= -\frac{\partial P}{\partial y} + \mu \left(\frac{\partial^2 v_y}{\partial x^2} + \frac{\partial^2 v_y}{\partial y^2} + \frac{\partial^2 v_y}{\partial z^2} \right) + \rho g_y \\ \rho \left(\frac{\partial v_z}{\partial t} + v_x \frac{\partial v_z}{\partial x} + v_y \frac{\partial v_z}{\partial y} + v_z \frac{\partial v_z}{\partial z} \right) &= -\frac{\partial P}{\partial z} + \mu \left(\frac{\partial^2 v_z}{\partial x^2} + \frac{\partial^2 v_z}{\partial y^2} + \frac{\partial^2 v_z}{\partial z^2} \right) + \rho g_z\end{aligned}$$

Cylindrical Coordinates (r, θ, z)

$$\begin{aligned}\rho \left(\frac{\partial v_r}{\partial t} + v_r \frac{\partial v_r}{\partial r} + \frac{v_\theta}{r} \frac{\partial v_r}{\partial \theta} - \frac{v_\theta^2}{r} + v_z \frac{\partial v_r}{\partial z} \right) \\ &= -\frac{\partial P}{\partial r} + \mu \left[\frac{\partial}{\partial r} \left(\frac{1}{r} \frac{\partial}{\partial r} (rv_r) \right) + \frac{1}{r^2} \frac{\partial^2 v_r}{\partial \theta^2} - \frac{2}{r^2} \frac{\partial v_\theta}{\partial \theta} + \frac{\partial^2 v_r}{\partial z^2} \right] + \rho g_r \\ \rho \left(\frac{\partial v_\theta}{\partial t} + v_r \frac{\partial v_\theta}{\partial r} + \frac{v_\theta}{r} \frac{\partial v_\theta}{\partial \theta} + \frac{v_r v_\theta}{r} + v_z \frac{\partial v_\theta}{\partial z} \right) \\ &= -\frac{1}{r} \frac{\partial P}{\partial \theta} + \mu \left[\frac{\partial}{\partial r} \left(\frac{1}{r} \frac{\partial}{\partial r} (rv_\theta) \right) + \frac{1}{r^2} \frac{\partial^2 v_\theta}{\partial \theta^2} + \frac{2}{r^2} \frac{\partial v_r}{\partial \theta} + \frac{\partial^2 v_\theta}{\partial z^2} \right] + \rho g_\theta \\ \rho \left(\frac{\partial v_z}{\partial t} + v_r \frac{\partial v_z}{\partial r} + \frac{v_\theta}{r} \frac{\partial v_z}{\partial \theta} + v_z \frac{\partial v_z}{\partial z} \right) \\ &= -\frac{\partial P}{\partial z} + \mu \left[\frac{1}{r} \frac{\partial}{\partial r} \left(r \frac{\partial v_z}{\partial r} \right) + \frac{1}{r^2} \frac{\partial^2 v_z}{\partial \theta^2} + \frac{\partial^2 v_z}{\partial z^2} \right] + \rho g_z\end{aligned}$$

Spherical Coordinates (r, θ, ϕ)

$$\begin{aligned}\rho \left(\frac{\partial v_r}{\partial t} + v_r \frac{\partial v_r}{\partial r} + \frac{v_\theta}{r} \frac{\partial v_r}{\partial \theta} + \frac{v_\phi}{r \sin \theta} \frac{\partial v_r}{\partial \phi} - \frac{v_\theta^2 + v_\phi^2}{r} \right) \\ &= -\frac{\partial P}{\partial r} + \mu \left(\nabla^2 v_r - \frac{2}{r^2} v_r - \frac{2}{r^2} \frac{\partial v_\theta}{\partial \theta} - \frac{2}{r^2} v_\theta \cot \theta - \frac{2}{r^2 \sin \theta} \frac{\partial v_\phi}{\partial \phi} \right) + \rho g_r \\ \rho \left(\frac{\partial v_\theta}{\partial t} + v_r \frac{\partial v_\theta}{\partial r} + \frac{v_\theta}{r} \frac{\partial v_\theta}{\partial \theta} + \frac{v_\phi}{r \sin \theta} \frac{\partial v_\theta}{\partial \phi} + \frac{v_r v_\theta}{r} - \frac{v_\phi^2 \cot \theta}{r} \right) \\ &= -\frac{1}{r} \frac{\partial P}{\partial \theta} + \mu \left(\nabla^2 v_\theta + \frac{2}{r^2} \frac{\partial v_r}{\partial \theta} - \frac{v_\theta}{r^2 \sin^2 \theta} - \frac{2 \cos \theta}{r^2 \sin^2 \theta} \frac{\partial v_\phi}{\partial \phi} \right) + \rho g_\theta \\ \rho \left(\frac{\partial v_\phi}{\partial t} + v_r \frac{\partial v_\phi}{\partial r} + \frac{v_\theta}{r} \frac{\partial v_\phi}{\partial \theta} + \frac{v_\phi}{r \sin \theta} \frac{\partial v_\phi}{\partial \phi} + \frac{v_\phi v_r}{r} + \frac{v_\theta v_\phi}{r} \cot \theta \right) \\ &= -\frac{1}{r \sin \theta} \frac{\partial P}{\partial \phi} + \mu \left(\nabla^2 v_\phi - \frac{v_\phi}{r^2 \sin^2 \theta} + \frac{2}{r^2 \sin \theta} \frac{\partial v_r}{\partial \phi} + \frac{2 \cos \theta}{r^2 \sin^2 \theta} \frac{\partial v_\theta}{\partial \phi} \right) + \rho g_\phi\end{aligned}$$

Source: Reprinted with permission from R. B. Bird, W. E. Stewart, and E. N. Lightfoot, *Transport Phenomena*, Wiley, New York, 1960. In these equations

$$\nabla^2 = \frac{1}{r^2} \frac{\partial}{\partial r} \left(r^2 \frac{\partial}{\partial r} \right) + \frac{1}{r^2 \sin \theta} \frac{\partial}{\partial \theta} \left(\sin \theta \frac{\partial}{\partial \theta} \right) + \frac{1}{r^2 \sin^2 \theta} \left(\frac{\partial^2}{\partial \phi^2} \right)$$

Although polymeric melts are generally non-Newtonian, many problems in polymer processing are initially solved using the Newtonian assumption, because these solutions (a) provide simple results that help gain insight into the nature of the process; (b) provide quick, rough, quantitative estimates; and (c) the rigorous non-Newtonian solution may be too time-consuming for the problem at hand. Yet, for a true appreciation of polymer processing, the non-Newtonian character of the material must be considered. The study of non-Newtonian behavior forms an active branch of the science of rheology, and is discussed in Chapter 3.

In the meantime, we will solve a number of flow problems that are highly relevant to polymer processing problems, which demonstrate the rather straightforward use of the equation of motion and continuity.

Example 2.5 Parallel Plate Flow The methodology for formulating and solving flow problems involves the following well-defined and straightforward steps:

- Step 1. Draw a schematic figure of the flow configuration, visualize the flow on physical grounds, pick the most appropriate coordinate system, and make some sensible assumptions about the velocity components.
- Step 2. Reduce the equation of continuity to the form appropriate for the problem at hand.
- Step 3. Reduce the equation of motion or the Navier–Stokes equation to the form appropriate for the problem at hand. Take advantage of the results of the equation of continuity.
- Step 4. State the boundary and initial conditions, if any.
- Step 5. Solve the differential equations for the velocity profiles, which then lead to the volumetric flow rate expression, shear stress, and rate distribution, power consumption, and so forth.
- Step 6. Sketch out the velocity profiles and velocity gradient profiles and see if they are reasonable for the problem at hand.

In this example, we consider the viscous, isothermal, incompressible flow of a Newtonian fluid between two infinite parallel plates in relative motion, as shown in Fig. E2.5a. As is evident from the figure, we have already chosen the most appropriate coordinate system for the problem at hand, namely, the rectangular coordinate system with spatial variables x , y , z . We placed the coordinate system at the stationary lower plate, with the coordinate y pointing across the flow field, and z pointing in the direction of the flow. The upper plate is moving at constant velocity V_0 and the lower plate is stationary. Derive (a) the velocity profile; (b) the flow rate; (c) the shear stress and shear rate distributions, and (d) the power consumption.

Solution This flow configuration is of great significance in polymer processing and it is important to understand in depth. We therefore discuss it in some detail.

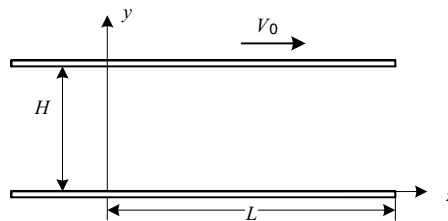


Fig. E2.5a Two parallel plates in relative motion. The upper plate moves at a constant velocity V_0 and the lower plate is stationary.

The *infinite* parallel plates construct may sound theoretical and impractical, but it is not. The flow in screw extruder channels, between the rotor and the wall of an internal mixer or between the rolls of calenders and roll-mills, to mention a few, can be considered to first approximation as taking place locally between parallel plates in relative motion.

We assume a *creeping laminar flow* because, in all practical cases, the very high viscosities of polymeric melts preclude turbulent flow. With increasing Reynolds number prior to reaching turbulence, viscous dissipation heating and degradation will take place. The following table, which illustrates characteristic values of some typical fluids, gives a sense of the magnitude of viscosities of polymeric melts:

Characteristic Viscosities of Some Typical Fluids (Ns/m²)

Fluid	Viscosity	Character	Fluid	Viscosity	Character
Air	10 ⁻⁵	Gas	Polymeric melts	10 ² –10 ⁶	toffee-like
Water	10 ⁻³	Liquid	Pitch	10 ⁹	stiff
Olive oil	10 ⁻¹	Liquid	Glass	10 ²¹	rigid
Glycerin	1	Thick liquid			

We also assume *isothermal flow*. Of course, no viscous flow can be truly isothermal, because the friction between the sliding layers of fluid generates heat, called *viscous dissipation*. But slow viscous flows in narrow channels can be assumed, at first approximation, to be isothermal. This assumption greatly simplifies the solution and provides simple, useful working equations.

We further assume that the flow is *steady in time*. We make this assumption because most machines operate continuously, and even in reciprocating machines such as, for example, injection-molding machines, the flow can be viewed instantaneously as steady state. Finally, we assume that the fluid is *incompressible* and *Newtonian*, that the *flow is fully developed*, that is, $\partial v_z / \partial z = 0$, and that the *gravitational forces are negligible* compared to viscous forces.

(a) Now we begin the actual solution of the problem. We start with the equation of continuity and, turning to Table 2.1, we find that, for an incompressible fluid (constant density), it reduces to

$$\frac{\partial v_x}{\partial x} + \frac{\partial v_y}{\partial y} + \frac{\partial v_z}{\partial z} = 0 \quad (\text{E2.5-1})$$

The third term on the left-hand side vanishes because we assumed fully developed flow, as does the first term because we do not expect any flow in the neutral x direction. Thus we are left with $dv_y/dy = 0$, which upon integration, yields $v_y = C$, where C is a constant. But v_y must equal zero on the plate surfaces and therefore, $v_y = 0$ everywhere.

Now we turn to the Navier–Stokes equation in Table 2.4. We take each component and analyze it term by term, dropping those that equal zero. This simple process leads to the following equations:

$$\frac{\partial P}{\partial x} = 0 \quad (\text{E2.5-2})$$

$$\frac{\partial P}{\partial y} = 0 \quad (\text{E2.5-3})$$

$$\mu \frac{\partial^2 v_z}{\partial y^2} = \frac{\partial P}{\partial z} \quad (\text{E2.5-4})$$

Equations E2.5-2 and E2.5-3 tell us that the pressure P is *not* a function of x or y . Thus P can only be a function of z . Considering Eq. E2.5-4, with partial derivatives replaced by ordinary derivatives, we find that the left-hand side of the equation is a function only of y , the right-hand side of the equation is a function only of z , and the only way this can happen is if they both equal a constant:

$$\mu \frac{d^2 v_z}{dy^2} = \frac{dP}{dz} = C \quad (\text{E2.5-5})$$

This situation has a number of interesting implications. First, it implies that the *pressure gradient* for such flows must be a constant, that is, the pressure changes (drops or rises—we do not yet know which) linearly with distance. We can further conclude that, in principle, a moving plate that drags liquid with it, as in this case, may, in principle, *generate* pressure in the direction of flow and that this pressure will increase linearly with distance, just as pressure drops linearly with distance, in pipe flow, for example.

Equation E2.5-5 can be integrated, but first we define the following dimensionless variables: $u_z = v_z/V$ and $\xi = y/H$. Since the pressure gradient is constant, we can replace it by the pressure drop:

$$\frac{dP}{dz} = \frac{P_L - P_0}{L} \quad (\text{E2.5-6})$$

where P_L and P_0 are the pressure at $z = 0$ and $z = L$, respectively. Clearly, if the pressure at the exit is higher than at the entrance, we know that pressure rises in the direction of flow and the pressure gradient is positive, and vice versa. Rewriting Eq. E2.5.6 in dimensionless form gives:

$$\frac{d^2 u_z}{d\xi^2} = \frac{H^2}{\mu V L_0} (P_L - P_0) \quad (\text{E2.5-7})$$

which can be integrated with the boundary condition $u_z(0) = 0$ and $u_z(1) = 1$, to give:

$$u_z = \xi - \xi(1 - \xi) \frac{H^2}{2\mu V_0} \left(\frac{P_L - P_0}{L} \right) \quad (\text{E2.5-8})$$

Clearly, the first term on the right-hand side expresses a linear velocity profile due to the drag of the moving plate, and the second term is a parabolic profile due to the pressure gradient. We will explore the velocity profile after we derive the flow rate.

(b) We obtain the flow rate by integrating the velocity over the cross section:

$$\begin{aligned} q &= \int_0^H v_z dy = V_0 H \int_0^1 u_z d\xi \\ &= \frac{V_0 H}{2} - \frac{H^3}{12\mu L} (P_L - P_0) \end{aligned} \quad (\text{E2.5-9})$$

where q is the net flow rate per unit width, the first term on the right-hand side is the *drag flow* q_d :

$$q_d = \frac{V_0 H}{2} \quad (\text{E2.5-10})$$

and the second term is the *pressure flow* q_p :

$$q_p = \frac{H^3}{12\mu L}(P_0 - P_L) \quad (\text{E2.5-11})$$

For further insight into the flow rate equation, we can now rewrite Eq. E2.5-9 as follows:

$$\frac{dP}{dz} = \frac{P_L - P_0}{L} = \frac{12\mu}{H^3}(q_d - q) \quad (\text{E2.5-12})$$

This equation now clearly demonstrates that the parallel plate geometry will generate pressure if $q_d > q$, that is, provided that the *moving plate drags more fluid than is actually delivered*. Under these conditions the parallel-plate geometry becomes a *pump*. This requires a *restriction* or die at the discharge end. We can further see that the pressure generation is proportional to the viscosity. Therefore, the high viscosities encountered with polymeric melts increase the device pressurization capability (of course, high viscosities also imply large pressure drops over dies and restrictions). We can further see that, at constant discharge rate q , increasing plate velocity will increase the pressure generation (by increasing q_d).

Plate velocity in actual machines becomes tantamount to speed of rotation and becomes an *operating* variable. Furthermore, we find that pressurization is inversely proportional with the gap size to the cube, which becomes a sensitive *design* variable. The maximum pressure that can be generated is obtained by setting $q = 0$, to get

$$\left(\frac{dP}{dz}\right)_{\max} = \frac{6\mu V_0}{H^2} \quad (\text{E2.5-13})$$

Finally, it can easily be shown (see Problem 2.12) from Eq. E2.5.9 that, for a given *net flow rate* q there is an optimum $H = 3q/V_0$ for a maximum pressure rise of

$$\left(\frac{dP}{dz}\right)_{\max,q} = \frac{6\mu V_0^3}{27q^2} \quad (\text{E2.5-14})$$

Equation E2.5-9 further indicates that, in the absence of a pressure drop, the net flow rate equals the drag flow rate. Note that q_p is positive if $P_0 > P_L$ and pressure flow is in the positive z direction and negative when $P_L > P_0$. The net flow rate is the sum or *linear superposition* of the flow induced by the drag exerted by the moving plate and that caused by the pressure gradient. This is the direct result of the linear Newtonian nature of the fluid, which yields a linear ordinary differential equation. For a non-Newtonian fluid, as we will see in Chapter 3, this will not be the case, because viscosity depends on shear rate and varies from point to point in the flow field.

By dividing Eq. E2.5-11 by Eq. E2.5-10 we get a useful expression for the pressure-to-drag flow ratio:

$$\frac{q_p}{q_d} = \frac{q - q_d}{q_d} = \frac{H^2}{6\mu LV_0}(P_0 - P_L) \quad (\text{E2.5-15})$$

Next we substitute Eq. E2.5-15 into Eq. E2.5-8 to yield:

$$u_z = \zeta + 3\frac{q_p}{q_d}\zeta(1 - \zeta) \quad (\text{E2.5-16})$$

We can plot the dimensionless velocity profile with pressure-to-drag flow ratio as a single parameter. When this ratio is zero we get pure drag flow, when it assumes a value of -1 , the

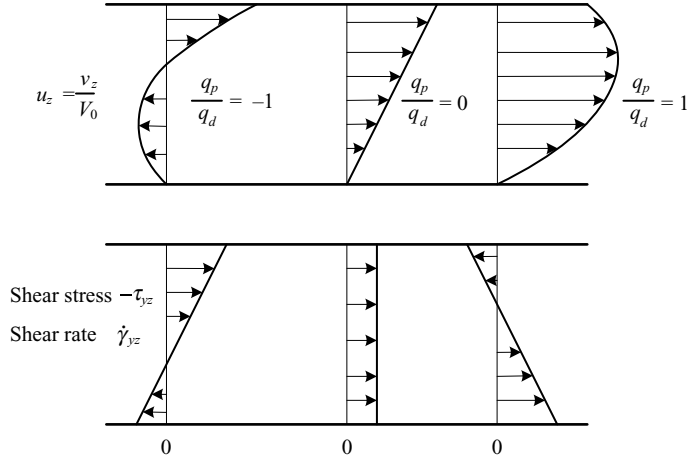


Fig. E2.5b Schematic representation velocity shear rate and shear stress profiles of a Newtonian fluid between parallel plates.

net flow rate is zero, and when the value is $+1$, the net flow rate is twice the drag flow rate. As the value of this ratio increases, the velocity profile approaches a parabolic profile of pure pressure flow between two stationary parallel plates. Figure E2.5b shows the characteristic velocity profiles.

(c) By taking the derivative of the velocity we obtain the shear rate:

$$\dot{\gamma}_{yz} = \frac{dv_z}{dy} = \frac{V_0}{H} \frac{du_z}{d\xi} = \frac{V_0}{H} \left[1 + 3(1 - 2\xi) \frac{q_p}{q_d} \right] \quad (\text{E2.5-17})$$

This equation shows that, when the pressure to drag flow ratio equals $-1/3$, the shear rate at the stationary plate is zero, when it equals $+1/3$, the shear rate at the moving plate is zero, and when it equals zero, the shear is constant and equals V_0/H . In this range the velocity profile exhibits no extremum. In terms of the net flow rate, the condition of no extremum in velocity is:

$$\frac{2q_d}{3} < q < \frac{4q_d}{3} \quad (\text{E2.5-18})$$

With the shear rate at hand, we can calculate the local viscous dissipation per unit volume. From Table 2.3 we note that the only nonvanishing shear-stress component is $\tau_{yz} = \tau_{zy}$ which is given by

$$\tau_{yz} = -\mu \dot{\gamma}_{yz} = -\mu \frac{V_0}{H} \left[1 + 3(1 - 2\xi) \frac{q_p}{q_d} \right] \quad (\text{E2.5-19})$$

and the stress at the moving plate $\tau_{yz}(1)$ becomes

$$\tau_{yz}(1) = -\mu \frac{V_0}{H} \left[1 - 3 \frac{q_p}{q_d} \right] \quad (\text{E2.5-20})$$

Figure E2.5b depicts the shear rate and shear stress profiles normalized by the pure drag flow values for a number of pressure-to-drag flow ratios.

(d) The power input per unit area needed to drag the moving plate is given by

$$P_w = -V_0 \tau_{yz}(1) = \mu \frac{V_0^2}{H} \left[1 - 3 \frac{q_p}{q_d} \right] \quad (\text{E2.5-21})$$

where the minus sign is introduced because, according to the sign convention adopted in this book, the shear stress $\tau_{yz}(1)$ is the stress exerted by the fluid on the plate. The *total power input* into a system of length L and width W is

$$P_w = \mu \frac{V_0^2 L W}{H} \left[1 - 3 \frac{q_p}{q_d} \right] \quad (\text{E2.5-22})$$

For pressure-to-drag flow ratios above 1/3, the P_w becomes negative, implying that power is flowing *out* of the system via the moving plate. In this case, the pressure drop is negative, implying that an outside power source pressurized the liquid and some of that is extracted by the moving (now restraining rather than forward dragging) plate, with the rest of the power dissipated into heat. The *specific power input*, defined as the power input into a unit volume of material leaving the system, is given by

$$\frac{P_w}{qW} = \mu \frac{V_0^2 L}{Hq} \left[1 - 3 \frac{q_p}{q_d} \right] = 2\mu \frac{V_0 L}{H^2} \frac{\left(1 - 3 \frac{q_p}{q_d} \right)}{\left(1 + \frac{q_p}{q_d} \right)} \quad (\text{E2.5-23})$$

Clearly, the power input and the specific power input both vanish at a pressure-to-drag flow ratio of 1/3, when the shear stress at the wall is zero. It is also worth noting that the specific power input is proportional to viscosity and plate velocity, and inversely proportional to the distance squared.

From Eq. E2.5-17 we can calculate the total viscous dissipation between the parallel plates. The second invariant of the rate of strain tensor multiplied by the viscosity gives the viscous dissipation per unit volume. From Table 2.3 we find that, for the case at hand, the second invariant reduces to $\dot{\gamma}_{yz}^2$; therefore, the total viscous energy dissipation (VED) between the plates will be given by

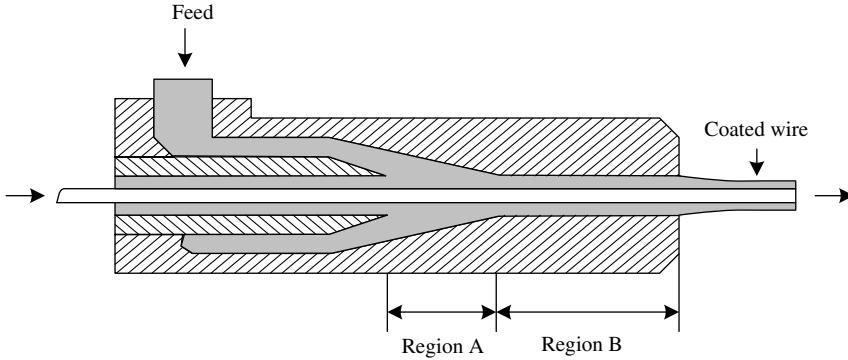
$$\tau : \dot{\boldsymbol{\gamma}} = \mu \dot{\gamma}^2 = LHW \int_0^1 \mu \dot{\gamma}_{yz}^2 d\xi = \frac{\mu V_0^2 L W}{H} \left[1 + 3 \left(\frac{q_p}{q_d} \right)^2 \right] \quad (\text{E2.5-24})$$

Now the difference between the total power input (Eq. E2.5-22) and the total viscous dissipation (Eq. E2.5-24) is the power converted into pressure. Indeed, if we subtract the latter from the former, we get exactly $q(P_L - P_0)$, which is the power input required for raising the pressure. This pressure also will be converted into heat through a die, and therefore the expression given in Eq. E2.5-23 correctly gives the total power input into the exiting fluid.

Example 2.6 Axial Drag and Pressure Flow between Concentric Cylinders The accompanying figure provides a schematic representation of a wire-coating die. We wish to analyze the flow of polymeric melt in the tip region of the die where the flow is confined in an annular space created by an axially moving wire in a constant-diameter die. This section determines the thickness of the coating. Polymer melt is forced into the die by an extruder at high pressure, bringing it in touch with the moving wire. The wire moves at relatively high speeds of up to 1000–2000 m/min. The wire drags with it the melt and the flow is a combined pressure and drag flow. Derive expressions for (a) the velocity profile in the tip region, (b) the

shear rate and stress profile, (c) an expression for the flow rate and (d) an expression for the coating thickness.

In Region A, flow cross-section converges to a constant value in the tip Region A. The wire moves at a constant speed.



Solution

(a) The flow boundaries are best described by a cylindrical coordinate system. We assume an incompressible, Newtonian fluid flowing at steady state in a fully developed isothermal flow. We visualize the flow with one nonvanishing velocity component, $v_z(r)$, which is a function of only r . The θ direction is neutral and we do not expect flow in this direction. Moreover, it is easy to show, along the lines of the previous example, that $v_r = 0$, and, therefore, the components of the Navier–Stokes equation in cylindrical coordinates listed in Table 2.4 reduce to:

$$\frac{\partial P}{\partial r} = 0 \quad (\text{E2.6-1})$$

$$\frac{\partial P}{\partial \theta} = 0 \quad (\text{E2.6-2})$$

$$\frac{\partial P}{\partial z} = \mu \left[\frac{1}{r} \frac{\partial}{\partial r} \left(r \frac{\partial v_z}{\partial r} \right) \right] \quad (\text{E2.6-3})$$

Thus we find that the pressure is a function of only z and, since the right-hand side of Eq. E2.6-3 is a function of only r , $\partial P/\partial z = \text{constant}$. We can therefore rewrite this equation as an ordinary differential equation and integrate it with boundary conditions $v_z(R_i) = V_0$ and $v_z(R_o) = 0$, where R_i and R_o are the inner and outer radii, respectively, to give:

$$v_z = V_0 \left(\frac{\ln(r/R_o)}{\ln \alpha} \right) + \frac{R_o^2}{4\mu} \left(-\frac{dP}{dz} \right) \left[1 - \left(\frac{r}{R_o} \right)^2 - (1 - \alpha^2) \frac{\ln(r/R_o)}{\ln \alpha} \right] \quad (\text{E2.6-4})$$

where $\alpha = R_i/R_o$. Note that the pressure gradient $-(dP/dz) = (P_0 - P_L)/L$, where P_0 and P_L are the pressures at the beginning of the tip region and at the exit, respectively, and L is the length of the tip region, is positive because pressure drops in the direction of motion.

(b) Taking the derivative of Eq. E2.6-4 with respect to r gives:

$$\dot{\gamma}_{rz} = \frac{\partial v_z}{\partial r} = \frac{V_0}{\ln \alpha} \cdot \frac{1}{r} - \frac{(P_0 - P_L)}{4\mu L} \left[2r - \frac{(1 - \alpha^2)}{\ln \alpha} \cdot \frac{R_o^2}{r} \right] \quad (\text{E2.6-5})$$

The shear stress can be obtained with Eq. E2.6-5 as follows:

$$\tau_{rz} = -\mu \dot{\gamma}_{rz} = \frac{(P_0 - P_L)}{4L} \left[2r - \frac{(1 - \alpha^2)}{\ln \alpha} \cdot \frac{R_0^2}{r} \right] - \frac{\mu V_0}{\ln \alpha} \cdot \frac{1}{r} \quad (\text{E2.6-6})$$

(c) The flow rate can be obtained by integrating Eq. E2.6-4 as follows:

$$Q = \frac{\pi R_0^4 (P_0 - P_L) (1 - \alpha^2)}{8\mu L} \left(1 + \alpha^2 + \frac{1 - \alpha^2}{\ln \alpha} \right) - \pi R_0^2 V_0 \left(\alpha^2 + \frac{1 - \alpha^2}{2 \ln \alpha} \right) \quad (\text{E2.6-7})$$

Note that the flow rate increases with the pressure drop and decreases with increasing wire speed at constant die geometry.

(d) We define the polymer coating thickness as δ . The circular cross-section area of the coating lay is given as

$$S = \pi(R_i + \delta)^2 - \pi R_i^2 = \pi \delta(2R_i + \delta) \quad (\text{E2.6-8})$$

In terms of the mass balance in an incompressible fluid, we have

$$Q = V_0 S = \pi V_0 \delta(2R_i + \delta) \quad (\text{E2.6-9})$$

Equation E2.6-9 can be rewritten as

$$\delta^2 + 2R_i \delta - K = 0 \quad (\text{E2.6-10})$$

where

$$K = \frac{Q}{\pi V_0} \quad (\text{E2.6-11})$$

Solving Eq. E2.6-10 according to the limit of $\delta > 0$ gives

$$\delta = R_i \left[\sqrt{1 + \frac{K}{R_i^2}} - 1 \right] \quad (\text{E2.6-12})$$

If an assumption of $K/R_i^2 \gg 1$ is made, the preceding equation can be rewritten by first taking two terms of a binomial expansion for it:

$$\delta = \frac{K}{2R_i} = \frac{Q}{2\pi R_i V_0} \quad (\text{E2.6-13})$$

Inserting Eq. E2.6.7 into the preceding equation results in

$$\delta = \frac{R_0^4 (P_0 - P_L) (1 - \alpha^2)}{16\mu L R_i V_0} \left(1 + \alpha^2 + \frac{1 - \alpha^2}{\ln \alpha} \right) - \frac{R_0^2}{2R_i} \left(\alpha^2 + \frac{1 - \alpha^2}{2 \ln \alpha} \right) \quad (\text{E2.6-14})$$

Note that the thickness of the coating layer is proportional to the pressure drop and inversely proportional to wire speed.

2.9 THE MACROSCOPIC ENERGY BALANCE AND THE BERNOULLI AND THERMAL ENERGY EQUATIONS

Polymer processing operations, by and large, are nonisothermal. Plastics pellets are compacted and heated to the melting point by interparticle friction, solid deformation

beyond the yield point, and conduction. The molten polymer is heated or cooled by temperature-controlled processing machine walls, and the deforming viscous polymer melt constantly undergoes heating by internal viscous dissipation. Therefore, we need to account for nonisothermal effects via appropriate equations.

The starting point is the first law of thermodynamics, which states mathematically the great principle of conservation of energy:

$$dE = \delta Q + \delta W \quad (2.9-1)$$

where E is the total energy of a system, δQ is the heat added *to* the system, and δW is the work done *on* the system. The differential δ signifies that the changes on the right-hand side of the equation are *path* dependent. The rate of change of the energy in the systems is given by:

$$\left. \frac{dE}{dt} \right|_{\text{system}} = \dot{Q} + \dot{W} \quad (2.9-2)$$

where

$$E_{\text{system}} = \int_{\mathcal{V}} e \rho \, dV \quad (2.9-3)$$

and where e is the specific energy or energy per unit mass. Substituting the energy E and specific energy e for P and p , respectively, in the Reynolds Transport Theorem, Eq. 2.3-2 we get the macroscopic total energy balance equation:

$$\frac{dE}{dt} = \frac{\partial}{\partial t} \int_{\mathcal{V}} \rho e \, dV + \int_{\mathcal{S}} \rho e \mathbf{v} \cdot \mathbf{n} \, dS = \dot{Q} + \dot{W} \quad (2.9-4)$$

The total rate of heat added to the control volume through the control surfaces can be expressed in terms of the local heat flux \mathbf{q} as follows:

$$\dot{Q} = - \int_{\mathcal{S}} \mathbf{q} \cdot \mathbf{n} \, dS \quad (2.9-5)$$

where the negative sign was introduced to be consistent with \dot{Q} , which defined heat added to the system as positive (recall that \mathbf{n} is the *outward* unit normal vector). The rate of work done on the control volume through the control surfaces and by gravitation is given by

$$\dot{W} = - \int_{\mathcal{S}} \boldsymbol{\pi} \cdot \mathbf{n} \cdot \mathbf{v} \, dS + \int_{\mathcal{V}} \rho \mathbf{g} \cdot \mathbf{v} \, dV \quad (2.9-6)$$

Substituting Eqs. 2.9-5 and 2.9-6 into Eq. 2.9-4 gives

$$\frac{\partial}{\partial t} \int_{\mathcal{V}} \rho e \, dV + \int_{\mathcal{S}} \rho e \mathbf{v} \cdot \mathbf{n} \, dS + \int_{\mathcal{S}} \mathbf{q} \cdot \mathbf{n} \, dS + \int_{\mathcal{S}} \boldsymbol{\pi} \cdot \mathbf{n} \cdot \mathbf{v} \, dS - \int_{\mathcal{V}} \rho \mathbf{g} \cdot \mathbf{v} \, dV = 0 \quad (2.9-7)$$

and using Gauss' Divergence Theorem, we can rewrite it as

$$\frac{\partial}{\partial t} (\rho e) + \nabla \cdot \mathbf{v} \rho e + \nabla \cdot \mathbf{q} + \nabla \cdot \boldsymbol{\pi} \cdot \mathbf{v} - \rho \mathbf{g} \cdot \mathbf{v} = 0 \quad (2.9-8)$$

Next we break the total specific energy into specific kinetic and internal energies:

$$e = \frac{1}{2}v^2 + u \tag{2.9-9}$$

to give

$$\frac{\partial}{\partial t} \left(\frac{1}{2}\rho v^2 + \rho u \right) + \nabla \cdot \left(\frac{1}{2}\rho v^2 + \rho u \right) \mathbf{v} + \nabla \cdot \mathbf{q} + \nabla \cdot \boldsymbol{\pi} \cdot \mathbf{v} - \rho \mathbf{g} \cdot \mathbf{v} = 0 \tag{2.9-10}$$

Equation 2.9-10 is the total differential energy balance, and it contains both thermal and mechanical energies. It is useful to separate the two. We can do this by taking the dot product of the equation of motion with the velocity vector \mathbf{v} to get the mechanical energy balance equation:

$$\frac{\partial}{\partial t} (\rho v^2) + \nabla \cdot \left(\frac{1}{2}\rho v^2 \right) \mathbf{v} + \mathbf{v} \cdot (\nabla \cdot \boldsymbol{\pi}) - \rho \mathbf{v} \cdot \mathbf{g} = 0 \tag{2.9-11}$$

Integration of Eq. 2.9-11 leads to the *macroscopic mechanical energy balance* equation, the steady-state version of which is the famous *Bernoulli equation*. Next we subtract Eq. 2.9-11 from Eq. 2.9-10 to obtain the differential thermal energy-balance equation:

$$\frac{\partial}{\partial t} (\rho u) + \nabla \cdot (\rho u) \mathbf{v} + \nabla \cdot \mathbf{q} + \boldsymbol{\pi} : \nabla \mathbf{v} = 0 \tag{2.9-12}$$

Substituting $\boldsymbol{\pi} = P\boldsymbol{\delta} + \boldsymbol{\tau}$, we get:

$$\frac{\partial}{\partial t} (\rho u) = -\nabla \cdot (\rho u) \mathbf{v} \quad -\nabla \cdot \mathbf{q} \quad -P(\nabla \cdot \mathbf{v}) \quad -\boldsymbol{\tau} : \nabla \mathbf{v} \tag{2.9-13}$$

rate of increase
in internal energy
per unit volume
net rate of
addition of
internal energy
by convective
transport per
unit volume
rate of internal
energy addition
by conduction
per unit volume
reversible rate
of internal
energy increase
per unit volume
irreversible
rate of internal
energy increase
per unit volume
by viscous dissipation

or

$$\rho \frac{Du}{Dt} = -\nabla \cdot \mathbf{q} - P(\nabla \cdot \mathbf{v}) - \boldsymbol{\tau} : \nabla \mathbf{v} \tag{2.9-14}$$

This equation simply states that the increase in internal energy of a fluid element riding with the stream is due to the heat flux, the reversible increase of internal energy per unit volume by compression, and viscous dissipation or the irreversible conversion of internal friction to heat. Should there be another type of heat source (e.g., chemical reaction), it can be added to the equation.

The heat flux can be expressed in terms of temperature gradient by the Fourier equation:

$$\mathbf{q} = -k\nabla T \tag{2.9-15}$$

and the internal energy in terms of enthalpy $u = h - P/\rho$, which in turn is expressed in terms of specific heat to give¹² the two following expressions for the equation of change of temperature:

$$\begin{aligned}\rho C_v \frac{DT}{Dt} &= \nabla \cdot k \nabla T - T \left(\frac{\partial P}{\partial T} \right)_\rho (\nabla \cdot \mathbf{v}) - \boldsymbol{\tau} : \nabla \mathbf{v} \\ \rho C_p \frac{DT}{Dt} &= \nabla \cdot k \nabla T - \left(\frac{\partial \ln \rho}{\partial \ln T} \right)_p \frac{DP}{Dt} - \boldsymbol{\tau} : \nabla \mathbf{v}\end{aligned}\quad (2.9-16)$$

The first equation is listed in rectangular, cylindrical, and spherical coordinates in Table 2.5. For incompressible Newtonian fluids with constant thermal conductivity, Eq. 2.9-16 reduces to:

$$\rho C_v \frac{DT}{Dt} = k \nabla^2 T + \frac{1}{2} \mu (\dot{\boldsymbol{\gamma}} : \dot{\boldsymbol{\gamma}}) \quad (2.9-17)$$

which is listed in various coordinate systems in Table 2.6.

Clearly, then, the temperature dependence of viscosity, on the one hand, and the viscous dissipation term that depends on the magnitude of the local rate of deformation, on the other hand, couple the energy equation with the equation of motion, and they must be solved simultaneously.

Example 2.7 Nonisothermal Parallel Plate Drag Flow with Constant Thermophysical Properties Consider an incompressible Newtonian fluid between two infinite parallel plates at temperatures $T(0) = T_1$ and $T(H) = T_2$, in relative motion at a steady state, as shown in Fig. E2.7 The upper plate moves at velocity V_0 . (a) Derive the temperature profile between the plates, and (b) determine the heat fluxes at the plates.

Solution

(a) By assuming constant thermophysical properties, the equation of motion and energy are decoupled. The velocity profile between the plates is simple drag flow $v_z = V_0(y/H)$, and all other velocity components equal zero. We now turn to the equation of energy in rectangular coordinates in Table 2.6, which reduces to:

$$k \frac{d^2 T}{dy^2} + \mu \left(\frac{dv_z}{dy} \right)^2 = 0 \quad (E2.7-1)$$

Substituting the linear drag velocity profile $(dv_z/dy) = V_0/H$ into Eq. 2.7-1, and defining $\xi = y/H$ subsequent to integration, yields:

$$\frac{T - T_1}{T_2 - T_1} = \xi + \frac{\text{Br}}{2} \xi(1 - \xi) \quad (E2.7-2)$$

where Br is the dimensionless Brinkman number defined as

$$\text{Br} = \frac{\mu V_0^2}{k(T_2 - T_1)} \quad (E2.7-3)$$

12. For details see R. Byron Bird, Warren E. Stewart and Edwin N. Lightfoot, *Transport Phenomena*, 2nd ed., Wiley, New York, 2002, pp. 336–340.

TABLE 2.5 The Equation of Energy in Terms of Energy and Momentum Fluxes in Several Coordinate Systems**Rectangular Coordinates** (x, y, z)

$$\begin{aligned} & \rho C_v \left(\frac{\partial T}{\partial t} + v_x \frac{\partial T}{\partial x} + v_y \frac{\partial T}{\partial y} + v_z \frac{\partial T}{\partial z} \right) \\ &= - \left[\frac{\partial q_x}{\partial x} + \frac{\partial q_y}{\partial y} + \frac{\partial q_z}{\partial z} \right] - T \left(\frac{\partial P}{\partial T} \right)_\rho \left(\frac{\partial v_x}{\partial x} + \frac{\partial v_y}{\partial y} + \frac{\partial v_z}{\partial z} \right) \\ & \quad - \left\{ \tau_{xx} \frac{\partial v_x}{\partial x} + \tau_{yy} \frac{\partial v_y}{\partial y} + \tau_{zz} \frac{\partial v_z}{\partial z} \right\} \\ & \quad - \left\{ \tau_{xy} \left(\frac{\partial v_x}{\partial y} + \frac{\partial v_y}{\partial x} \right) + \tau_{xz} \left(\frac{\partial v_x}{\partial z} + \frac{\partial v_z}{\partial x} \right) + \tau_{yz} \left(\frac{\partial v_y}{\partial z} + \frac{\partial v_z}{\partial y} \right) \right\} \end{aligned}$$

Cylindrical Coordinates (r, θ, z)

$$\begin{aligned} & \rho C_v \left(\frac{\partial T}{\partial t} + v_r \frac{\partial T}{\partial r} + \frac{v_\theta}{r} \frac{\partial T}{\partial \theta} + v_z \frac{\partial T}{\partial z} \right) \\ &= - \left[\frac{1}{r} \frac{\partial}{\partial r} (r q_r) + \frac{1}{r} \frac{\partial q_\theta}{\partial \theta} + \frac{\partial q_z}{\partial z} \right] - T \left(\frac{\partial P}{\partial T} \right)_\rho \left(\frac{1}{r} \frac{\partial}{\partial r} (r v_r) + \frac{1}{r} \frac{\partial v_\theta}{\partial \theta} + \frac{\partial v_z}{\partial z} \right) \\ & \quad - \left\{ \tau_{rr} \frac{\partial v_r}{\partial r} + \tau_{\theta\theta} \frac{1}{r} \left(\frac{\partial v_\theta}{\partial \theta} + v_r \right) + \tau_{zz} \frac{\partial v_z}{\partial z} \right\} \\ & \quad - \left\{ \tau_{r\theta} \left[r \frac{\partial}{\partial r} \left(\frac{v_\theta}{r} \right) + \frac{1}{r} \frac{\partial v_r}{\partial \theta} \right] + \tau_{rz} \left(\frac{\partial v_z}{\partial r} + \frac{\partial v_r}{\partial z} \right) + \tau_{\theta z} \left(\frac{1}{r} \frac{\partial v_z}{\partial \theta} + \frac{\partial v_\theta}{\partial z} \right) \right\} \end{aligned}$$

Spherical Coordinates (r, θ, ϕ)

$$\begin{aligned} & \rho C_v \left(\frac{\partial T}{\partial t} + v_r \frac{\partial T}{\partial r} + \frac{v_\theta}{r} \frac{\partial T}{\partial \theta} + \frac{v_\phi}{r \sin \theta} \frac{\partial T}{\partial \phi} \right) \\ &= - \left[\frac{1}{r^2} \frac{\partial}{\partial r} (r^2 q_r) + \frac{1}{r \sin \theta} \frac{\partial}{\partial \theta} (q_\theta \sin \theta) + \frac{1}{r \sin \theta} \frac{\partial q_\phi}{\partial \phi} \right] \\ & \quad - T \left(\frac{\partial P}{\partial T} \right)_\rho \left(\frac{1}{r^2} \frac{\partial}{\partial r} (r^2 v_r) + \frac{1}{r \sin \theta} \frac{\partial}{\partial \theta} (v_\theta \sin \theta) + \frac{1}{r \sin \theta} \frac{\partial v_\phi}{\partial \phi} \right) \\ & \quad - \left\{ \tau_{rr} \frac{\partial v_r}{\partial r} + \tau_{\theta\theta} \frac{1}{r} \left(\frac{\partial v_\theta}{\partial \theta} + v_r \right) + \tau_{\phi\phi} \left(\frac{1}{r \sin \theta} \frac{\partial v_\phi}{\partial \phi} + \frac{v_r}{r} + \frac{v_\theta \cot \theta}{r} \right) \right\} \\ & \quad - \left\{ \tau_{r\theta} \left[r \frac{\partial}{\partial r} \left(\frac{v_\theta}{r} \right) + \frac{1}{r} \frac{\partial v_r}{\partial \theta} \right] + \tau_{r\phi} \left[r \frac{\partial}{\partial r} \left(\frac{v_\phi}{r} \right) + \frac{1}{r \sin \theta} \frac{\partial v_r}{\partial \phi} \right] \right. \\ & \quad \left. + \tau_{\theta\phi} \left[\frac{\sin \theta}{r} \frac{\partial}{\partial \theta} \left(\frac{v_\phi}{\sin \theta} \right) + \frac{1}{r \sin \theta} \frac{\partial v_\theta}{\partial \phi} \right] \right\} \end{aligned}$$

Source: Reprinted with permission from R. B. Bird, W. E. Stewart, and E. N. Lightfoot, *Transport Phenomena*, Wiley, New York, 1960.

TABLE 2.6 The Equation of Thermal Energy in Terms of Transport Properties (for Newtonian fluids at constant ρ , μ and k . Note that constant ρ implies that $C_v = C_p$)

Rectangular Coordinates (x, y, z)

$$\begin{aligned} & \rho C_v \left(\frac{\partial T}{\partial t} + v_x \frac{\partial T}{\partial x} + v_y \frac{\partial T}{\partial y} + v_z \frac{\partial T}{\partial z} \right) \\ &= k \left[\frac{\partial^2 T}{\partial x^2} + \frac{\partial^2 T}{\partial y^2} + \frac{\partial^2 T}{\partial z^2} \right] + 2\mu \left\{ \left(\frac{\partial v_x}{\partial x} \right)^2 + \left(\frac{\partial v_y}{\partial y} \right)^2 + \left(\frac{\partial v_z}{\partial z} \right)^2 \right\} \\ &+ \mu \left\{ \left(\frac{\partial v_x}{\partial y} + \frac{\partial v_y}{\partial x} \right)^2 + \left(\frac{\partial v_x}{\partial z} + \frac{\partial v_z}{\partial x} \right)^2 + \left(\frac{\partial v_y}{\partial z} + \frac{\partial v_z}{\partial y} \right)^2 \right\} \end{aligned}$$

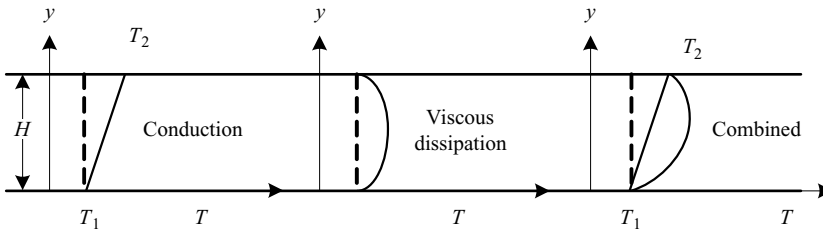
Cylindrical Coordinates (r, θ, z)

$$\begin{aligned} & \rho C_v \left(\frac{\partial T}{\partial t} + v_r \frac{\partial T}{\partial r} + \frac{v_\theta}{r} \frac{\partial T}{\partial \theta} + v_z \frac{\partial T}{\partial z} \right) \\ &= k \left[\frac{1}{r} \frac{\partial}{\partial r} \left(r \frac{\partial T}{\partial r} \right) + \frac{1}{r^2} \frac{\partial^2 T}{\partial \theta^2} + \frac{\partial^2 T}{\partial z^2} \right] + 2\mu \left\{ \left(\frac{\partial v_r}{\partial r} \right)^2 + \left[\frac{1}{r} \left(\frac{\partial v_\theta}{\partial \theta} + v_r \right) \right]^2 + \left(\frac{\partial v_z}{\partial z} \right)^2 \right\} \\ &+ \mu \left\{ \left[r \frac{\partial}{\partial r} \left(\frac{v_\theta}{r} \right) + \frac{1}{r} \frac{\partial v_r}{\partial \theta} \right]^2 + \left(\frac{\partial v_z}{\partial r} + \frac{\partial v_r}{\partial z} \right)^2 + \left(\frac{1}{r} \frac{\partial v_z}{\partial \theta} + \frac{\partial v_\theta}{\partial z} \right)^2 \right\} \end{aligned}$$

Spherical Coordinates (r, θ, ϕ)

$$\begin{aligned} & \rho C_v \left(\frac{\partial T}{\partial t} + v_r \frac{\partial T}{\partial r} + \frac{v_\theta}{r} \frac{\partial T}{\partial \theta} + \frac{v_\phi}{r \sin \theta} \frac{\partial T}{\partial \phi} \right) \\ &= k \left[\frac{1}{r^2} \frac{\partial}{\partial r} \left(r^2 \frac{\partial T}{\partial r} \right) + \frac{1}{r^2 \sin \theta} \frac{\partial}{\partial \theta} \left(\sin \theta \frac{\partial T}{\partial \theta} \right) + \frac{1}{r^2 \sin^2 \theta} \frac{\partial^2 T}{\partial \phi^2} \right] \\ &+ 2\mu \left\{ \left(\frac{\partial v_r}{\partial r} \right)^2 + \left(\frac{1}{r} \frac{\partial v_\theta}{\partial \theta} + \frac{v_r}{r} \right)^2 + \left(\frac{1}{r \sin \theta} \frac{\partial v_\phi}{\partial \phi} + \frac{v_r}{r} + \frac{v_\theta \cot \theta}{r} \right)^2 \right\} \\ &+ \mu \left\{ \left[r \frac{\partial}{\partial r} \left(\frac{v_\theta}{r} \right) + \frac{1}{r} \frac{\partial v_r}{\partial \theta} \right]^2 + \left[r \frac{\partial}{\partial r} \left(\frac{v_\phi}{r} \right) + \frac{1}{r \sin \theta} \frac{\partial v_r}{\partial \phi} \right]^2 \right. \\ &\left. + \left[\frac{\sin \theta}{r} \frac{\partial}{\partial \theta} \left(\frac{v_\phi}{\sin \theta} \right) + \frac{1}{r \sin \theta} \frac{\partial v_\theta}{\partial \phi} \right]^2 \right\} \end{aligned}$$

Source: Reprinted with permission from R. B. Bird, W. E. Stewart, and E. N. Lightfoot, *Transport Phenomena*, Wiley, New York, 1960.


Fig. E2.7 Schematic temperature profiles between the parallel plates in relative motion at different temperatures with temperature-independent physical properties.

which measures the ratio of the rate of thermal heat generation by viscous dissipation to rate of heat conduction. Clearly, in the absence of viscous dissipation, the temperature profile between the plates is linear; whereas, the contribution of viscous dissipation is a parabolic, and the linear combination of the two yields the desired temperature profile as depicted in Fig. E2.7.

(b) The heat fluxes at the two plates are obtained by differentiating Eq. E2.7-2, and substituting it at $y = 0$ and $y = H$ into the Fourier equation to give:

$$q_y(H) = -k \frac{T_2 - T_1}{H} + \frac{\mu V_0^2}{2H} \quad (\text{E2.7-4})$$

$$q_y(0) = -k \frac{T_2 - T_1}{H} - \frac{\mu V_0^2}{2H} \quad (\text{E2.7-5})$$

If $T_2 > T_1$, $q_y(0)$ will always be negative. The flux of heat into the lower plate is the sum of conduction and one half of the rate of heat generated by viscous dissipation. At the upper plate, on the other hand, the flux may be either negative (into the fluid) or positive (into the plate) or zero, depending on the relative values of heat flux due to conduction and viscous dissipation.

2.10 MASS TRANSPORT IN BINARY MIXTURES AND THE DIFFUSION EQUATION

Subsequent to polymer manufacture, it is often necessary to remove dissolved volatiles, such as solvents, untreated monomer, moisture, and impurities from the product. Moreover, volatiles, water, and other components often need to be removed prior to the shaping step. For the dissolved volatiles to be removed, they must diffuse to some melt–vapor interface. This mass-transport operation, called *devolatilization*, constitutes an important elementary step in polymer processing, and is discussed in Chapter 8. For a detailed discussion of diffusion, the reader is referred to the many texts available on the subject; here we will only present the equation of continuity for a binary system of constant density, where a low concentration of a minor component A diffuses through the major component:

$$\frac{DC_A}{Dt} = \mathcal{D}_{AB} \nabla^2 c_A + \dot{R}_A \quad (2.10-1)$$

where the diffusivity \mathcal{D}_{AB} was assumed constant, c_A is the molar concentration of the species A , and \dot{R}_A is the molar rate of production of A per unit volume (e.g., by chemical reaction). The equation, containing the flux and source terms, is identical in form to Eq. 2.9-17, hence, the components of the equation in the various coordinate systems can be easily obtained from Table 2.6.

2.11 MATHEMATICAL MODELING, COMMON BOUNDARY CONDITIONS, COMMON SIMPLIFYING ASSUMPTIONS, AND THE LUBRICATION APPROXIMATION

Mathematical Modeling

Engineering design, analysis, control, optimization, trouble shooting, and any other engineering activity related to specific industrial *processes*, *machines*, or *structures* can best be performed using a *quantitative* study of effect of the parameters as well as of the

design and process variables on the process, machine, or structure. In any of these contexts, this undertaking calls for *mathematical modeling*¹³ of the specific entity. Hence, engineering mathematical modeling, as the name implies, refers to the attempt to mimic (describe) the actual engineering entity through mathematical equations, which will always contain simplifications about the nature of the substances involved, the relative magnitudes of the various physical effects, and the geometry of the space in which the phenomena take place. But “simplification” is not quite the right definition for what is done in modeling. A better description would be *construction of analogs*. These may be physical analogs or mental analogs, which are amenable to mathematical formulation. A successful modeler is someone with a thorough understanding of the physical mechanisms, who is imaginative enough to create the analog in such a way that it captures the essential elements of the process, and is then able to cast it into mathematical equations.

Aris (3) more formally defined a mathematical model thus: “a system of equations, Σ , is said to be a model of prototypical system, S , if it is formulated to express the laws of S and its solution is intended to represent some aspect of the behavior of S .” Seinfeld and Lapidus (4) gave a more specific definition: “Mathematical model is taken to mean the formulation of mathematical relationships, which describe the behavior of actual systems such that the dependent and independent variables and parameters of the model are directly related to physical and chemical quantities in the real system.”

All the mathematical formulations presented in the following chapters are mathematical models of polymer processing subsystems and systems that generally consist of a series of intricate, mostly transport-based, physical phenomena occurring in complex geometrical configurations.

Clearly, then, a mathematical model is always an *approximation* of the real system. The better the model, the closer it will approximate the real system.

It is worth noting at this point that the various scientific theories that quantitatively and mathematically formulate natural phenomena are in fact *mathematical models of nature*. Such, for example, are the kinetic theory of gases and rubber elasticity, Bohr’s atomic model, molecular theories of polymer solutions, and even the equations of transport phenomena cited earlier in this chapter. Not unlike the engineering mathematical models, they contain simplifying assumptions. For example, the transport equations involve the assumption that matter can be viewed as a continuum and that even in fast, irreversible processes, local equilibrium can be achieved. The paramount difference between a mathematical model of a natural process and that of an engineering system is the required level of accuracy and, of course, the generality of the phenomena involved.

An engineering mathematical model may consist of a single algebraic equation, sets of partial differential equations, or any possible combination of various kinds of equations and mathematical operations, often in the form of large computer programs. Indeed, the revolutionary developments in computer technology have immensely increased the modeling possibilities, their visualization and their interpretation, bringing all engineering models much closer to the real process. They have also vastly expanded the practical use of numerical solutions such as finite difference methods and finite elements.

The quantitative study of the *process*, which as we stressed at the outset, is the reason for modeling, is called *simulation*. But modeling and simulation have useful functions

13. The word “model” derives from the Latin word *modus* which means a “measure,” hinting toward a change in scale.

beyond the quantitative study of the process. An attempt to build a model for a complex process requires first of all a clear definition of objectives, which is often both useful and educational. In addition, by repeated simulations, a better understanding of the process is achieved, greatly improving our insight and developing our engineering intuition. Using a model, we can study extrapolation or scale-up problems and the effect of individual variables, and explore sensitivity and stability problems. All of these are often difficult, costly, or even impossible to carry out in the actual processes.

Model building consists of assembling sets of various mathematical equations, originating from engineering fundamentals, such as the balance equations which, together with the appropriately selected boundary conditions, bear the interrelations between variables and parameters corresponding to those in the actual processes. Modeling a complex process, such as a polymer processing operation, is done by breaking it down into clearly defined *subsystems*. These are then assembled into the complete model. The latter is tested for *experimental verification*. A mathematical model, no matter how sophisticated and complicated, is of little use if it does not reflect reality to a satisfactory degree as proved by experimentation.

There are various ways to classify mathematical models (5). First, according to the nature of the process, they can be classified as *deterministic* or *stochastic*. The former refers to a process in which each variable or parameter acquires a certain specific value or sets of values according to the operating conditions. In the latter, an element of uncertainty enters; we cannot specify a certain value to a variable, but only a most probable one. Transport-based models are deterministic; residence time distribution models in well-stirred tanks are stochastic.

Mathematical models can also be classified according to the mathematical foundation the model is built on. Thus we have *transport phenomena*-based models (including most of the models presented in this text), *empirical* models (based on experimental correlations), and *population-based* models, such as the previously mentioned residence time distribution models. Models can be further classified as *steady* or *unsteady*, *lumped parameter* or *distributed parameter* (implying no variation or variation with spatial coordinates, respectively), and *linear* or *nonlinear*.

In polymer processing, the mathematical models are by and large deterministic (as are the processes), generally transport based, either steady (continuous process, except when dynamic models for control purposes are needed) or unsteady (cyclic process), linear generally only to a first approximation, and distributed parameter (although when the process is broken into small, finite elements, locally lumped-parameter models are used).

Common Simplifying Assumptions

In the examples discussed so far, as well as those to be discussed throughout this book, several common simplifying assumptions are introduced without proof or discussion. Their validity for polymeric materials is not always obvious and they merit further discussion.

The No-slip Condition The no-slip condition implies that, at a solid-liquid interface, the velocity of the liquid equals that of the solid surface. This assumption, based on extensive experimentation, is widely accepted in fluid mechanics, though its validity is not necessarily obvious.

The slip of viscoelastic polymeric materials (and flow instabilities) was reviewed in detail by Denn (6). Apparent slip at the wall was observed with highly entangled linear polymers, but not with branched polymers or linear polymers with insufficient numbers of

entanglements per chain. The slip was observed at stresses below the onset of visible extrudate distortions. Yet more advanced experimental tools need to be developed to examine slip and its length scales.

Three theories were proposed to explain wall-slip: (a) adhesive failure at the wall, (b) cohesive failure within the material as a result of disentanglement of chains in the bulk and chains absorbed on the wall, and (c) the creation of a lubricating surface layer at the wall either by a stress-induced transition, or by a lubricating additive. If the polymer contains low molecular weight components or slip-additives, their diffusion to the wall will create a thin lubricating layer at the wall, generating apparent slip.

Slip at the wall is closely related to extrudate instabilities, but in normal flow situations within machines, in virtually all but exceptional cases, the no-slip condition is assumed for solving flow problems.

Liquid–liquid interface At the interface between two immiscible liquids, the boundary conditions that must be satisfied are (a) a continuity of both the tangential and the normal velocities (this implies a no-slip condition at the interface), (b) a continuity of the shear stress, and (c) the balance of the difference in normal stress across the interface by the interfacial (surface) force. Thus the normal stresses are not continuous at the interface, but differ by an amount given in the following expression:

$$P_1 - P_0 = \Gamma \left(\frac{1}{R_1} - \frac{1}{R_2} \right) \quad (2.11-1)$$

where $P_1 - P_0$ is the pressure difference, due to the surface tension Γ , action on a curved surface of radii of curvature of R_1 and R_2 .

The Steady State Assumption A physical process has reached a *steady state* when a stationary observer, located at *any* point of the space where the process is taking place, observes no changes in time. Mathematically, this statement reduces to the condition where, in the field equations describing the process, all the $\partial/\partial t$ terms vanish. In reality, processes are very rarely truly steady. Boundary conditions, forcing functions, system resistance, and composition or constitution of the substances involved change periodically, randomly, or monotonically by small amounts. These changes bring about process response fluctuations. In such cases the process can still be treated as if it were steady using the *pseudo–steady state approximation*.

To illustrate this approximation, let us consider a pressure flow in which the driving-force pressure drop varies with time. We set $\partial\rho/\partial t$ and $\partial\mathbf{v}/\partial t$ in the equations of continuity and motion, respectively, equal to zero and proceed to solve the problem as if it were a steady-state one, that is, we assume ΔP to be constant and not a function of time. The solution is of the form $\mathbf{v} = \mathbf{v}(x_i, \Delta P(t), \text{geometry, etc.})$. Because ΔP was taken to be a constant, \mathbf{v} is also a constant with time. The pseudo–steady-state approximation “pretends” that the foregoing solution holds for any level of ΔP and that the functional dependence of \mathbf{v} on time is $\mathbf{v}(x_i, t) = \mathbf{v}(x_i, \Delta P(t), \text{geometry, etc.})$. The pseudo–steady state approximation is not valid if the values of $\Delta(\rho\mathbf{v})/\Delta t$ (Δt being the characteristic time of fluctuation of ΔP) obtained using this approximation contribute to an appreciable fraction of the mean value of the applied ΔP .

The Constant Thermophysical-Properties Assumption The last commonly used set of assumptions in liquid flow (isothermal, as well as nonisothermal) and in conductive heat

transfer is to treat k , C_p , and ρ as *constant* quantities, independent of T and P . In polymer processing, where both heat transfer and flow take place, typical temperature variations may reach up to 200 °C and pressure variations, 50 MN/m². Under such significant variations, the density of a typical polymer would change by 10 or 20%, depending on whether it is amorphous or crystalline, while k and C_p would undergo variations of 30 to 40%.

Under normal conditions, when solving momentum and energy equations, we can usually assume the polymer melt to be incompressible, but the melt density at the prevailing pressures and temperatures should be carefully evaluated. Assuming constant C_p and k (taken at the average temperature), though it may affect the results of heat transfer or coupled heat transfer and flow in polymer processing, do give very good approximations.

The Lubrication Approximation

In polymer processing, we frequently encounter creeping viscous flow in slowly tapering, relatively narrow, gaps as did the ancient Egyptians so depicted in Fig. 2.5. These flows are usually solved by the well-known *lubrication approximation*, which originates with the famous work by Osborne Reynolds, in which he laid the foundations of hydrodynamic lubrication.¹⁴ The theoretical analysis of lubrication deals with the hydrodynamic behavior of thin films from a fraction of a mil (10^{-3} in) to a few mils thick. High pressures of the



Fig. 2.5 Lubrication of a sledge used to transport the statue of Ti in ancient Egypt, about 2400 B.C. [Reprinted by permission from G. Hähner and N. Spencer, “Rubbing and Scrubbing,” *Physics Today*, September, 22 (1998).]

14. Osborne Reynolds published his monumental paper on lubrication in 1886 (*Phil. Trans. R. Soc.*, **177**, 157–234). The paper was entitled “On the Theory of Lubrication and Its Application to Mr. Beauchamps Tower’s Experiments.” Mr. Tower was an engineer working for the railroads who was trying to understand the mechanism of lubrication of railroad cars. He observed experimentally that a very thin layer of lubricating oil appears to be able to support the huge load of a railroad car. Unable to explain these observations, he turned to Reynolds. Honoring Reynolds’ contribution to the field of lubrication, the commonly used engineering unit for viscosity, lb_s/in², is called a “reyn” (just as the unit “poise” is named after Poiseuille).

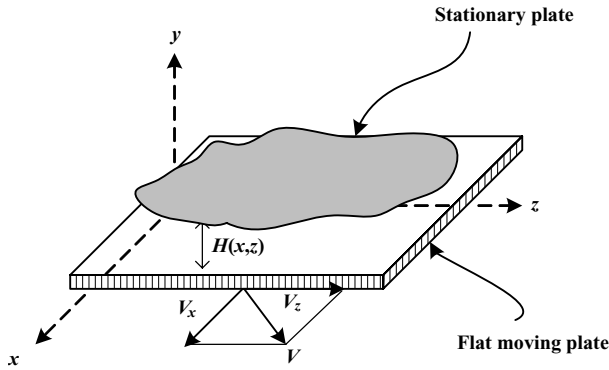


Fig. 2.6 Flow region formed by two closely spaced plates with variable gap $H(x,z)$. The lower plate is flat and moves at velocity V . The upper plate is slowly undulating.

order of thousands of psi (millions of newtons per square meter) may develop in these films as a result of the relative motion of the confining walls. In polymer processing we are generally dealing with films that are several orders of magnitude thicker, but since the viscosity of polymeric melts is also several orders of magnitude higher than the viscosity of lubricating oils, the assumptions leading to the lubrication approximation are valid in polymer processing as well. Next we review the principles of hydrodynamic lubrication.

Consider a narrow two-dimensional gap with slowly varying thickness in the x,z plane with the containing wall in relative motion. Specifically, the characteristic length in the x,z plane is much larger than the characteristic length in the perpendicular direction. Without loss in generality, we can assume that the flow is confined between a flat surface moving in the x,z , plane and a slowly undulating fixed surface at distance $H(x,z)$ from the flat plate, as shown in Fig. 2.6.

According to the lubrication approximation, we can quite accurately assume that *locally* the flow takes place between two parallel plates at $H(x,z)$ apart in relative motion. The assumptions on which the theory of lubrication rests are as follows: (a) the flow is laminar, (b) the flow is steady in time, (c) the flow is isothermal, (d) the fluid is incompressible, (e) the fluid is Newtonian, (f) there is no slip at the wall, (g) the inertial forces due to fluid acceleration are negligible compared to the viscous shear forces, and (h) any motion of fluid in a direction normal to the surfaces can be neglected in comparison with motion parallel to them.

According to these assumptions, the only nonvanishing velocity components are v_x and v_z , and the equations of continuity and motion in the Cartesian coordinate system in Tables 2.1 and 2.4 reduce, respectively, to:

$$\frac{\partial v_x}{\partial x} + \frac{\partial v_z}{\partial z} = 0 \tag{2.11-2}$$

$$\frac{\partial P}{\partial x} = \mu \frac{\partial^2 v_x}{\partial y^2} \tag{2.11-3}$$

$$\frac{\partial P}{\partial y} = 0 \tag{2.11-4}$$

$$\frac{\partial P}{\partial z} = \mu \frac{\partial^2 v_z}{\partial y^2} \tag{2.11-5}$$

Equation 2.11-4 implies that there is no transverse pressure gradient. The boundary conditions for solving the equations are $v_x(H) = v_z(H) = 0$ and $v_x(0) = V_x, v_z(0) = V_z$. Equations 2.11-3 and 2.11-5 can be directly integrated to give the velocity profiles, recalling that P is not a function of y :

$$v_x(y) = V_x \left(1 - \frac{y}{H}\right) + \frac{yH}{2\mu} \left(\frac{\partial P}{\partial x}\right) \left(\frac{y}{H} - 1\right) \quad (2.11-6)$$

$$v_z(y) = V_z \left(1 - \frac{y}{H}\right) + \frac{yH}{2\mu} \left(\frac{\partial P}{\partial z}\right) \left(\frac{y}{H} - 1\right) \quad (2.11-7)$$

which upon integration gives the volumetric flow rates per unit width, q_x and q_z :

$$q_x = \frac{V_x H}{2} + \frac{H^3}{12\mu} \left(-\frac{\partial P}{\partial x}\right) \quad (2.11-8)$$

$$q_z = \frac{V_z H}{2} + \frac{H^3}{12\mu} \left(-\frac{\partial P}{\partial z}\right) \quad (2.11-9)$$

The equation of continuity is next integrated over y :

$$\int_0^H \left(\frac{\partial v_x}{\partial x} + \frac{\partial v_z}{\partial z}\right) dy = 0 \quad (2.11-10)$$

and substituting Eqs. 2.11-6 and 2.11-7 into Eq. 2.11-10 gives

$$\frac{\partial}{\partial x} \left(H^3 \frac{\partial P}{\partial x}\right) + \frac{\partial}{\partial z} \left(H^3 \frac{\partial P}{\partial z}\right) = 6\mu \frac{\partial H}{\partial x} V_x + 6\mu \frac{\partial H}{\partial z} V_z \quad (2.11-11)$$

which is known as the *Reynolds equation* for incompressible fluids. By solving it for any $H(x,z)$ the two-dimensional pressure distribution $P(x,z)$ is obtained, from which the local pressure gradients can be computed and, via Eqs. 2.11-6 to 2.11-9, the local velocity profiles and flow rates obtained.

The lubrication approximation facilitates solutions to flow problems in complex geometries, where analytical solutions either cannot be obtained or are lengthy and difficult. The utility of this approximation can well be appreciated by comparing the almost exact solution of pressure flow in slightly tapered channels to that obtained by the lubrication approximation.

The lubrication approximation as previously derived is valid for purely viscous Newtonian fluids. But polymer melts are viscoelastic and also exhibit normal stresses in shearing flows, as is discussed in Chapter 3; nevertheless, for many engineering calculations in processing machines, the approximation does provide useful models.

Example 2.8 Flow between Two Infinite Nonparallel Plates in Relative Motion

Consider an incompressible Newtonian fluid in isothermal flow between two non-parallel plates in relative motion, as shown in Fig. E2.8, where the upper plate is moving at constant velocity V_0 in the z direction. The gap varies linearly from an initial value of H_0 to H_1 over length L , and the pressure at the entrance is P_0 and at the exit P_1 . Using the lubrication approximation, derive the pressure profile.

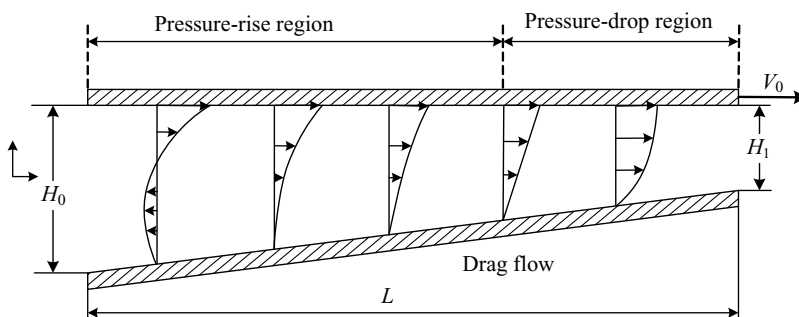


Fig. E2.8 Two non-parallel plates in relative motion, with schematic velocity profiles corresponding to a pressure-rise zone followed by a pressure-drop zone when entrance and exit pressures are equal.

Solution We can gain insight into the nature of the flow if we first consider the special case where the pressure at the entrance P_0 equals the pressure at the exit P_1 . Figure E2.8 shows the schematic velocity profiles at different locations. At a steady state, the net volumetric flow rate of an incompressible fluid must be constant. Since the gap between the plates is wide at the entrance and narrow at the exit, the drag flow decreases linearly from entrance to exit. Hence, in order to maintain a uniform *net* flow rate, pressure must initially rise (with opposing pressure flow reducing drag flow), and drop toward the exit (with the pressure flow augmenting the drag flow). Clearly, the pressure profile must reach a maximum, at which point the pressure gradient is zero and the flow is pure drag flow. Of course, if $P_0 \neq P_1$ the pressure may rise continuously, drop continuously, or go through a maximum, depending on the conditions.

The Reynolds equation (Eq. 2.11-11) for one-dimensional flow, as in the case at hand, reduces to:

$$\frac{d}{dz} \left(H^3 \frac{dP}{dz} \right) = 6\mu V_0 \frac{dH}{dz} \quad (\text{E2.8-1})$$

where z is the flow direction. Equation E2.8-1 can be integrated with respect to z to give

$$H^3 \frac{dP}{dz} = 6\mu V_0 H + C_1 \quad (\text{E2.8-2})$$

where C_1 is an integration constant, which can be conveniently expressed in terms of H^* defined as the separation between the plates where $dP/dz = 0$. If the pressure exhibits a maximum within $0 \leq z \leq L$, then H^* is the separation between the plates at that location; if the pressure profile exhibits no maximum in this range, the mathematical function describing the pressure as a function of z will still have a maximum at $z < 0$ or $z > L$, and H^* will be the “separation” between the virtual plates extended to that point. Thus, Eq. E2.8-2 can be written as

$$\frac{dP}{dz} = 6\mu V_0 \frac{H - H^*}{H^3} \quad (\text{E2.8-3})$$

and integrated to give the pressure profile:

$$P = P_0 + 6\mu V_0 \int_0^z \frac{H - H^*}{H^3} dz \quad (\text{E2.8-4})$$

where $P(0) = P_0$. For a constant taper, the dimensionless gap size as a function of distance is given by:

$$\zeta = \zeta_0 - (\zeta_0 - 1) \frac{z}{L} \quad (\text{E2.8-5})$$

where $\zeta = H/H_1$ and $\zeta_0 = H_0/H_1$. Substituting Eq. E2.8-5 into Eq. E2.8-4 and integrating, the latter gives the desired pressure profile:

$$P = P_0 + \frac{6\mu V_0 L}{H_0 H_1} \left[\frac{\zeta_0 - \zeta}{\zeta(\zeta_0 - 1)} - \frac{q}{V_0 H_0} \frac{\zeta_0^2 - \zeta^2}{\zeta^2(\zeta_0 - 1)} \right] \quad (\text{E2.8-6})$$

where q is the net flow rate per unit width:

$$q = \frac{1}{2} V_0 H^* \quad (\text{E2.8-7})$$

The pressure distribution therefore depends on a number of variables: geometrical (H_0 , H_1 , and L), operational (V_0 and q), and physical properties (μ). The maximum pressure that can be attained is at $\zeta = 1$ ($z = L$), at closed discharge conditions ($q = 0$):

$$P_{\max} = P_0 + \frac{6\mu L V_0}{H_0 H_1} \quad (\text{E2.8-8})$$

If the entrance and discharge pressures are equal, the pressure profile will exhibit a maximum value at $H^* = 2H_0/(1 + \zeta_0)$. This conclusion therefore focuses attention on an important difference between parallel-plate and non-parallel-plate geometries. In the former, equal entrance and discharge pressure implies no pressurization and pure drag flow, whereas, in the latter, it implies the existence of a maximum in the pressure profile. Indeed, this pressurization mechanism forms the foundation of the lubrication, as is shown in the next example, and explains the experimental observation of pressure profiles along SSEs as we discuss in Chapter 6.

Example 2.9 The Journal-Bearing Problem¹⁵ A journal of radius r_1 is rotating in a bearing of radius r_2 at an angular velocity Ω . The length of the journal and bearing in the z direction is L . Viscous Newtonian oil fills the narrow gap between the journal and bearing. The oil lubricates the bearing, that is, it prevents solid-solid frictional contact between the journal and the bearing. This is accomplished, of course, as a result of the pressure field generated within the film. We wish to derive a mathematical model that explains this mechanism and enables us to compute the forces acting on the journal and torque needed to turn the journal.

Solution We assume that the bearing is eccentric to the rotating journal by a displacement of magnitude, a , as shown in Fig. E2.9a.

The concentric gap is $c = r_2 - r_1$, and clearly $a \leq c$. The gap is very small, and locally we can assume flow between parallel plates. Thus we define a rectangular coordinate system X, Y, Z located on the surface of the journal such that X is tangential to the journal, as indicated in Fig. E2.9a. The gap between the journal and bearing is denoted as $B(\theta)$ and is well approximated as a function of angle θ by the following expression:

$$r_1 + B(\theta) \cong r_2 + a \cos \theta \quad (\text{E2.9-1})$$

15. We follow the solution presented in R. B. Bird, R. C. Armstrong, and O. Hassager, *Dynamics of Polymeric Liquids*, Second Edition Vol. 1, *Fluid Mechanics*, Wiley, New York, 1987, p. 48.

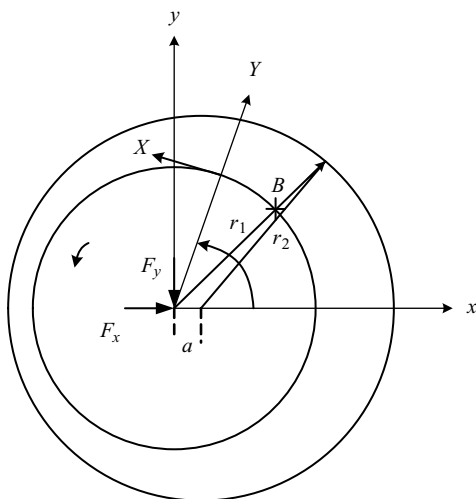


Fig. E2.9a Journal-bearing configuration with centers separated by displacement a . The force acting by the pressure field on the journal is given by component F_y and F_x .

or

$$B(\theta) = c + a \cos \theta \quad (\text{E2.9-2})$$

Invoking the lubrication approximation, the local velocity profile (at a given angle θ) in rectangular coordinates X, Y , with boundary conditions $v_x(0) = \Omega r_1$ and $v_x(B) = 0$ (see Example 2.5) is given by

$$v_x(Y) = \Omega r_1 \left(1 - \frac{Y}{B}\right) - \frac{B^2}{2\mu} \left(\frac{Y}{B}\right) \left(1 - \frac{Y}{B}\right) \frac{dP}{dX} \quad (\text{E2.9-3})$$

Integrating Eq. E2.9-3 gives the flow rate:

$$Q = \frac{1}{2} \Omega r_1 B L - \frac{B^3 L}{12\mu} \frac{dP}{dX} \quad (\text{E2.9-4})$$

In this case, we are not interested in the flow rate, but rather the pressure profile around the journal. Therefore, we express the flow rate, which (at steady state and neglecting leaks on the sides) is constant, in terms of the gap size B_0 at locations where the pressure profile attains maximum or minimum, and where the flow rate equals the local drag flow:

$$Q = \frac{1}{2} \Omega r_1 B_0 L \quad (\text{E2.9-5})$$

There will be two such locations, as schematically indicated in Fig. E2.9b. Substituting Eq. E2.9-5 into Eq. E2.9-4, gives

$$\frac{dP}{dX} = 6\mu \Omega r_1 \left(\frac{1}{B^2} - \frac{B_0}{B^3}\right) \quad (\text{E2.9-6})$$

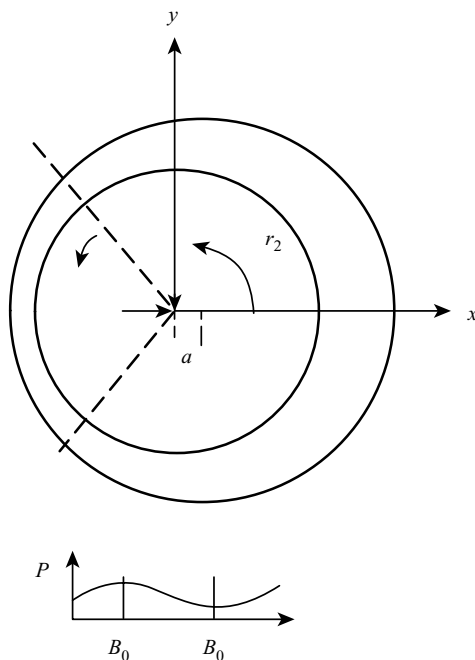


Fig. E2.9b The two broken lines show schematically the locations where the gap size is B_0 and where the pressure profile exhibits a maximum and a minimum.

Next, we obtain an expression for the shear stress by substituting Eq. E2.9-6 into Eq. E2.9-3 subsequent to taking its derivative and multiplying it by viscosity:

$$\tau_{rX}|_{Y=0} = -\mu \frac{dv_X}{dY} = \mu\Omega r_1 \left(\frac{4}{B} - \frac{3B_0}{B^2} \right) \quad (\text{E2.9-7})$$

Next, we substitute Eq. E2.9-2 into Eqs. E2.9-6 and E2.9-7, recalling that $dX = r_1 d\theta$, to get

$$\frac{1}{r_1} \frac{dP}{d\theta} = 6\mu\Omega r_1 \left(\frac{1}{B^2} - \frac{B_0}{B^3} \right) \quad (\text{E2.9-8})$$

$$\tau_{r\theta}|_{r=r_1} = \mu\Omega r_1 \left(\frac{4}{B} - \frac{3B_0}{B^2} \right) \quad (\text{E2.9-9})$$

By integrating Eq. E2.9-8 between $\theta = 0$ and $\theta = 2\pi$, we get an equation that we can solve for B_0 :

$$\int_{P_0}^{P_0} dP = 6\mu\Omega r_1^2 \int_0^{2\pi} \left(\frac{1}{B^2} - \frac{B_0}{B^3} \right) d\theta = \int_0^{2\pi} \left(\frac{1}{B^2} - \frac{B_0}{B^3} \right) d\theta = 0 \quad (\text{E2.9-10})$$

which yields:

$$B_0 = \frac{J_2}{J_3} = c \left(\frac{c^2 - a^2}{c^2 + \frac{1}{2}a^2} \right) \quad (\text{E2.9-11})$$

where J_n is defined as

$$J_n = \int_0^{2\pi} \frac{d\theta}{(c + a \cos \theta)^n}$$

and

$$\begin{aligned} J_1 &= 2\pi(c^2 - a^2)^{-1/2} \\ J_2 &= \frac{dJ_1}{dc} = 2\pi(c^2 - a^2)^{-3/2} \\ J_3 &= -\frac{1}{2} \frac{dJ_2}{dc} = 2\pi \left(c^2 + \frac{1}{2} a^2 \right) (c^2 - a^2)^{-5/2} \end{aligned}$$

Now we can compute the torque given by

$$\mathcal{T} = L \int_0^{2\pi} [-\tau_{r\theta}]_{r=r_1} \Omega r_1^2 d\theta \quad (\text{E2.9-12})$$

by substituting Eq. E2.9-9 into Eq. E.2.9-12 to give

$$\begin{aligned} \mathcal{T} &= -\mu L \Omega r_1^3 (4J_1 - 3B_0 J_2) \\ &= -\frac{2\pi \mu L \Omega r_1^3}{\sqrt{c^2 - a^2}} \frac{c^2 + 2a^2}{c^2 + a^2/2} \end{aligned} \quad (\text{E2.9-13})$$

Next, we calculate the net force the fluid exerts on the journal. The components F_x and F_y of this force, as shown in Fig. E2.9c, are obtained by integrating around the circumference the respective contributions of the pressure and shear stress.

The force in the positive y direction is

$$\begin{aligned} F_y &= L \int_0^{2\pi} (-P \sin \theta - \tau_{r\theta} \cos \theta)_{r=r_1} r_1 d\theta \\ &= L \left\{ [P \cos \theta]_0^{2\pi} + \int_0^{2\pi} - \left[\left(\frac{dP}{d\theta} \right) - \tau_{r\theta} \right] \cos \theta r_1 d\theta \right\} \\ &= L \int_0^{2\pi} - \left[\left(\frac{dP}{d\theta} \right) - \tau_{r\theta} \right] \cos \theta r_1 d\theta \end{aligned} \quad (\text{E2.9-14})$$

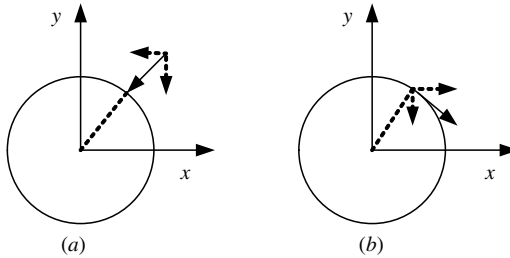


Fig. E2.9c (a) The normal force generated by the pressure and its x and y components. (b) The tangential shear force and its x and y components.

We can simplify this equation by neglecting the $\tau_{r\theta}$ contribution with respect to the $dP/d\theta$ contribution, because the former is of the order r_1/c ; whereas, the latter is of $(r_1/c)^2$. Thus (neglecting higher-order terms from $\tau_{r\theta}$), we obtain for F_y

$$\begin{aligned} F_y &= -Lr_1 \int_0^{2\pi} 6\mu\Omega r_1^2 \left(\frac{1}{B^2} - \frac{B_0}{B^3} \right) d\theta \\ &= -6\mu L r_1^3 \Omega (K_2 - B_0 K_3) \end{aligned} \quad (\text{E2.9-15})$$

where

$$K_n = \int_0^{2\pi} \frac{\cos \theta \, d\theta}{(c + a \cos \theta)^n}$$

and

$$\begin{aligned} K_2 &= \left(\frac{1}{a} \right) (J_1 - cJ_2) \\ K_3 &= \left(\frac{1}{a} \right) (J_2 - cJ_3) \end{aligned}$$

or

$$F_y = - \frac{3\mu(2\pi r_1 L)(\Omega r_1)r_1}{\left(\sqrt{\left(\frac{c}{a} \right)^2 - 1} \right) \left[\left(\frac{c}{a} \right)^2 + \frac{1}{2} \right] a^2} \quad (\text{E2.9-16})$$

The force in the positive x direction, F_x , is

$$F_x = L \int_0^{2\pi} [-P \cos \theta + \tau_{r\theta} \sin \theta]_{r=r_1} d\theta = 0 \quad (\text{E2.9-17})$$

Finally, the pressure distribution is obtained by integrating Eq. E2.9-8 to give

$$P = P_0 + \frac{6\mu\Omega r_1^2 a \sin \theta (c + 0.5a \cos \theta)}{(c^2 + 0.5a^2)(c + a \cos \theta)^2} \quad (\text{E2.9-18})$$

where P_0 is an arbitrary constant pressure.

Thus we see that the net force acts in the negative y direction, and is proportional to viscosity, journal surface area, and tangential speed, and inversely proportional and very sensitive to the displacement a . Indeed, as a approaches zero, the force grows and approaches infinity, so clearly, this force prevents the journal from contacting the barrel with the tight clearance circling the bearing.

REFERENCES

1. R. B. Bird, W. E. Stewart, and E. N. Lightfoot, *Transport Phenomena*, Wiley, New York, 2002.
2. D. Pnueli and H. Gutfinger, *Fluid Mechanics*, Cambridge University Press, Cambridge 1997.
3. R. Aris, *Mathematical Modeling Techniques*, Pitman, San Francisco, 1978.

4. J. H. Seinfeld and L. Lapidus, *Mathematical Methods in Chemical Engineering, Vol. 3, Process Modeling, Estimation and Identification*, Prentice Hall, Englewood Cliffs, NJ, 1974.
5. D. M. Himmelblau and K. B. Bischoff, *Process Analysis and Simulation; Deterministic Systems*, Wiley, New York, 1968.
6. M. M. Denn, "Extrusion Instabilities and Wall Slip," *Ann. Rev. Fluid Mech.*, **33**, 265–287 (2001).

PROBLEMS

2.1 Coordinate Transformation (a) Verify the following relationships for the conversion of any function in rectangular coordinates $\phi(x, y, z)$, into a function in cylindrical coordinates $\psi(r, \theta, z)$

$$\begin{aligned} x &= r \cos \theta, & y &= r \sin \theta, & z &= z \\ r &= \sqrt{x^2 + y^2}, & \theta &= \arctan \frac{y}{x}, & z &= z \end{aligned}$$

(b) Show that the derivatives of any scalar function (including components of vectors and tensors) in rectangular coordinates can be obtained from the derivatives of the scalar function in cylindrical coordinates

$$\begin{aligned} \frac{\partial}{\partial x} &= \cos \theta \frac{\partial}{\partial r} + \left(-\frac{\sin \theta}{r} \right) \frac{\partial}{\partial \theta} \\ \frac{\partial}{\partial y} &= \sin \theta \frac{\partial}{\partial r} + \left(\frac{\cos \theta}{r} \right) \frac{\partial}{\partial \theta} \\ \frac{\partial}{\partial z} &= \frac{\partial}{\partial z} \end{aligned}$$

(Use the Chain Rule of partial differentiation.)

(c) The unit vectors in rectangular coordinates are $\delta_x, \delta_y, \delta_z$, and those in cylindrical coordinates are δ_r, δ_θ , and δ_z . Show that the following relationship between the unit vectors exists

$$\begin{aligned} \delta_r &= \cos \theta \delta_x + \sin \theta \delta_y \\ \delta_\theta &= -\sin \theta \delta_x + \cos \theta \delta_y \\ \delta_z &= \delta_z \end{aligned}$$

and

$$\begin{aligned} \delta_x &= \cos \theta \delta_r - \sin \theta \delta_\theta \\ \delta_y &= \sin \theta \delta_r + \cos \theta \delta_\theta \end{aligned}$$

(d) From the results of (c), prove that

$$\begin{aligned} \frac{\partial}{\partial r} \delta_r &= 0, & \frac{\partial}{\partial r} \delta_\theta &= 0, & \frac{\partial}{\partial r} \delta_z &= 0 \\ \frac{\partial}{\partial \theta} \delta_r &= \delta_\theta, & \frac{\partial}{\partial \theta} \delta_\theta &= -\delta_r, & \frac{\partial}{\partial \theta} \delta_z &= 0 \\ \frac{\partial}{\partial z} \delta_r &= 0, & \frac{\partial}{\partial z} \delta_\theta &= 0, & \frac{\partial}{\partial z} \delta_z &= 0 \end{aligned}$$

(e) The operator ∇ in rectangular coordinates is

$$\nabla = \delta_x \frac{\partial}{\partial x} + \delta_y \frac{\partial}{\partial y} + \delta_z \frac{\partial}{\partial z}$$

Using the results of (b) and (d), derive the expression for ∇ in cylindrical coordinates

(f) Evaluate $\nabla \cdot \mathbf{v}$ in cylindrical coordinates.

2.2 Interpretation of the Equation of Continuity Show that the equation of continuity can be written as

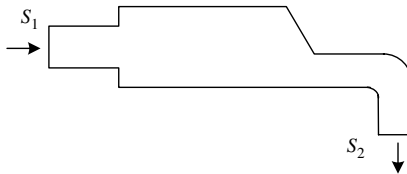
$$\frac{D\rho}{Dt} = -\rho(\nabla \cdot \mathbf{v})$$

where D/Dt is the substantial derivative defined as

$$\frac{D}{Dt} = \frac{\partial}{\partial t} + \mathbf{v} \cdot \nabla$$

2.3 The Equation of Continuity by Differential Mass Balance Derive the equation of continuity in cylindrical coordinates by making a mass balance over the differential volume $\Delta r(r\Delta\theta)\Delta z$.

2.4 Macroscopic Mass Balance in a Steady Continuous System In the flow system shown in the accompanying figure, fluid at velocity V_1 and density ρ_1 enters the system over the inlet surface S_1 , and it leaves at density ρ_2 with velocity V_2 over surface S_2 . The flow is steady state. Derive a mass balance using Eq. 2.4.1.



2.5 The Mean Velocity of Laminar Pipe Flow Use the macroscopic mass-balance equation (Eq. 2.4.1) to calculate the mean velocity in laminar pipe flow of a Newtonian fluid. The velocity profile is the celebrated Poiseuille equation:

$$v_z = v_{max} \left[1 - \left(\frac{r}{R} \right)^2 \right]$$

2.6 The Rate of Strain Tensor Using geometrical considerations, show that in a general flow field

$$\dot{\gamma}_{xy} = \frac{\partial v_x}{\partial y} + \frac{\partial v_y}{\partial x}$$

$$\dot{\gamma}_{yz} = \frac{\partial v_y}{\partial z} + \frac{\partial v_z}{\partial y}$$

$$\dot{\gamma}_{xz} = \frac{\partial v_x}{\partial z} + \frac{\partial v_z}{\partial x}$$

2.7 Spatial Variation of Properties Let $S(\mathbf{r})$ be a scalar field of a property of the continuum (e.g., pressure, temperature, density) at point P defined by radius vector \mathbf{r} .

- (a) Show that for any such scalar field an associated vector field ∇S can be defined such that the dot product of which with unit vector \mathbf{e} expresses the change of property S in direction \mathbf{e} .
- (b) Prove that for a Cartesian coordinate system

$$\nabla S = \delta_x \frac{\partial S}{\partial x} + \delta_y \frac{\partial S}{\partial y} + \delta_z \frac{\partial S}{\partial z}$$

- (c) If $S = xy + z$, find the unit vector of maximum gradient at $P(2,1,0)$
- (d) Prove that for a cylindrical coordinate system

$$\nabla S = \delta_r \frac{\partial S}{\partial r} + \delta_\theta \frac{1}{r} \frac{\partial S}{\partial \theta} + \delta_z \frac{\partial S}{\partial z}$$

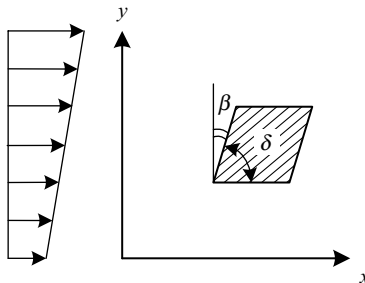
- (e) Prove that for a spherical coordinate system

$$\nabla S = \delta_r \frac{\partial S}{\partial r} + \delta_\theta \frac{1}{r} \frac{\partial S}{\partial \theta} + \delta_\phi \frac{1}{r \sin \theta} \frac{\partial S}{\partial \phi}$$

2.8 Viscous Stresses Acting in a Surface Element Using the expression $\boldsymbol{\pi} \cdot \mathbf{n} ds$, show that the forces acting on a unit surface in plane 2, 3 in a rectangular system is $\boldsymbol{\pi} \cdot \mathbf{n} = \delta_1 \pi_{11} + \delta_2 \pi_{12} + \delta_3 \pi_{13}$.

2.9 Sign Convention of the Stress Tensor $\boldsymbol{\tau}$ Consider a linear shear flow and examine the stress components τ'_{ij}

2.10 The Relationship between Shear Rate and Strain Show that (dv_x/dy) in a simple shear flow is identical to $-(d\gamma/dt)$, where γ is the angle shown in the accompanying figure.



2.11 The Invariants of the Rate of Strain Tensor in Simple Shear and Simple Elongational Flows Calculate the invariants of a simple shear flow and elongational flow.

2.12 Optimum Gap Size in Parallel Plate Flow Show that for the flow situation in Example 2.5, for a given net flow rate the optimum gap size for maximum pressure rise is

$$H = 3q/V_0$$

and the maximum pressure gradient is

$$\left. \frac{dP}{dz} \right|_{max} = \frac{6\mu V_0^2}{27q^2}$$

2.13 Couette Flow Couette flow is the flow in the annular space between two long concentric cylinders of radii R_o and R_i , created by the rotation of one of them. Consider Couette flow with (a) the outer cylinder rotating with angular velocity $\Omega(s^{-1})$; (b) the inner cylinder is rotating with angular velocity $-\Omega(s^{-1})$. (c) Also obtain the result by making a *torque balance* over a thin fluid shell formed by two imaginary fluid cylinders of radii r and $r + \Delta r$ and length $L(R_i < r < R_o)$.

2.14 Axial Drag Flow between Concentric Cylinders Consider the drag flow created in the space formed by two concentric nonrotating cylinders of radii R_o and R_i , with the inner cylinder moving with an axial velocity V . The system is open to the atmosphere at both ends. (a) Derive the velocity profile. (b) Also obtain the result by making a force balance on a thin fluid shell previously discussed.

2.15 Capillary Pressure Flow Solve the problem of flow in a capillary of radius R and length L , where $L \gg R$. The fluid is fed from a reservoir under the influence of an applied pressure P_0 . The exit end of the capillary is at atmospheric pressure. Consider three physical situations: (a) a horizontal capillary; (b) a downward vertical capillary flow; and (c) an upward vertical capillary flow.

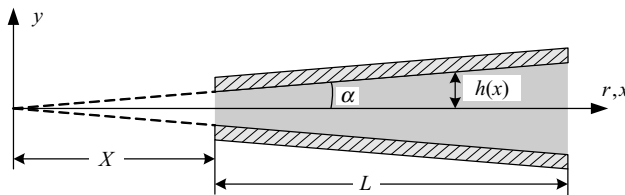
2.16 Axial Pressure Flow between Concentric Cylinders Solve the problem of flow in the horizontal concentric annular space formed by two long cylinders of length L and radii R_i and R_o , caused by an entrance pressure P_0 , which is higher than the exit (atmospheric) pressure. Consider the limit as $(R_o - R_i)/(R_o + R_i)$ approaches zero.

2.17 Helical Flow between Concentric Cylinders Consider the helical flow in an annular space created by a constant pressure drop $(P_0 - P_1)$ and the rotation of the inner cylinder with an angular velocity $\Omega(s^{-1})$.

2.18 Torsional Drag Flow between Parallel Disks Solve the torsional drag flow problem between two parallel disks, one of which is stationary while the other is rotating with an angular velocity $\Omega(s^{-1})$. (Note: $v_\theta/r = \text{constant}$.)

2.19 Radial Pressure Flow between Parallel Disks Solve the problem of radial pressure flow between two parallel disks. The flow is created by a pressure drop $(P|_{r=0} - P|_{r=R})$. Disregard the entrance region, where the fluid enters from a small hole at the center of the top disk.

- 2.20 Flow near a Wall Suddenly Set in Motion** Set up the parallel-plate drag flow problem during its start-up period $t \leq t_{tr}$, when $v_x = f(t)$ in the entire flow region, and show that the resulting velocity profile, after solving the differential equation $v_x/V = 1 - \text{erf}(y/\sqrt{4\mu t/\rho})$, if H is very large.
- 2.21 Heat Conduction across a Flat Solid Slab** Solve the problem of heat transfer across an infinitely large flat plate of thickness H , for the following three physical situations: (a) the two surfaces are kept at T_1 and T_2 , respectively; (b) one surface is kept at T_1 while the other is exposed to a fluid of temperature T_b , which causes a heat flux $q_y|_{y=H} = h_2(T_2 - T_b)$, h_2 being the heat-transfer coefficient ($\text{W/m}^2\cdot\text{K}$); (c) both surfaces are exposed to two different fluids of temperatures T_a and T_b with heat-transfer coefficients h_1 and h_2 , respectively.
- 2.22 Heat Transfer in Pipes** Solve the problem of conductive heat transfer across an infinitely long tube of inside and outside radii of R_i and R_o . Consider the following two physical situations: (a) the surface temperatures at R_i and R_o are maintained at T_i and T_o ; (b) both the inside and outside tube surfaces are exposed to heat transfer fluids of constant temperatures T_a and T_b and heat-transfer coefficients h_i and h_o .
- 2.23 Heat Transfer in Insulated Pipes** Solve case (b) of Problem 2.22 for a composite tube made of material of thermal conductivity k_i for $R_i \leq r \leq R_m$ and of material of thermal conductivity k_o for $R_m \leq r \leq R_o$.
- 2.24 Parallel-Plate Flow with Viscous Dissipation** Consider the nonisothermal flow of a Newtonian fluid whose ρ , C_p and k are constant, while its viscosity varies with temperature as $\mu = Ae^{\Delta E/RT}$. The flow is between two infinite parallel plates, one of which is stationary while the other is moving with a velocity V . The fluid has a considerably high viscosity, so that the energy dissipated ($\frac{1}{2}\mu(\dot{\gamma} : \dot{\gamma})$ in Eq. 2.9 – 17) cannot be neglected. State the equations of continuity, momentum, and energy for the following two physical situations and suggest a solution scheme: (a) $T(0) = T_1$, $T(H) = T_2$ (b) $q_y|_{y=0} = q_y|_{y=H} = 0$.
- 2.25 Flow between Tapered Plates**¹⁶ Consider the steady isothermal pressure flow of a Newtonian and incompressible fluid flowing in a channel formed by two slightly tapered plates of infinite width. Using the cylindrical coordinate system in the accompanying figure and assuming that $v_r(r, \theta), v_\theta = v_z = 0$:



16. W.E. Langlois, *Slow Viscous Flows*, Chapter VIII, Mcmillan, London, 1964.

(a) show that the continuity and momentum equations reduce to

$$\frac{1}{r} \frac{\partial}{\partial r} (rv_r) = 0 \quad \text{or} \quad v_r = \frac{F(\theta)}{r} \quad (\text{a})$$

$$\frac{\partial P}{\partial r} = \frac{\mu}{r^2} \left(\frac{\partial^2 v_r}{\partial \theta^2} \right) \quad (\text{b})$$

$$\frac{\partial P}{\partial \theta} = \frac{2\mu}{r} \left(\frac{\partial v_r}{\partial \theta} \right) \quad (\text{c})$$

Differentiate Eq.(b) with respect to θ and Eq.(c) with respect to r and equate. Solve the resulting equations using the boundary condition

$$v_r(r, \pm\alpha) = 0, \quad Q = \int_{-\alpha}^{\alpha} v_r r \, d\theta$$

to obtain the velocity and pressure fields:

$$v_r(r, \theta) = \frac{Q}{r} \frac{\sin^2 \alpha - \sin^2 \theta}{\sin \alpha \cos \alpha - \alpha + 2\alpha \sin^2 \alpha} \quad (\text{d})$$

$$P(r, \theta) = P_0 + \frac{\mu Q (\sin^2 \alpha - \sin^2 \theta) (X^2/r^2 - 1)}{X^2 \sin \alpha \cos \alpha - \alpha + 2\alpha \sin^2 \alpha} \quad (\text{e})$$

where $P(X, 0) = P_0$.

(b) Show that the two nonvanishing pressure gradients in Cartesian coordinates are

$$\frac{\partial P}{\partial x} = - \frac{2\mu Q (1 + D^2) D^3 h}{E} \frac{h^2 - 3D^2 y^2}{(h^2 + D^2 y^2)^3} \quad (\text{f})$$

$$\frac{\partial P}{\partial y} = - \frac{2\mu Q (1 + D^2) D^4 h}{E} \frac{3h^2 - D^2 y^2}{(h^2 + D^2 y^2)^3} \quad (\text{g})$$

where $D = \tan \alpha$, $h = D(x - X)$ and $E = D - (1 - D^2) \arctan D$.

(c) From the Reynolds equation (Eq. 2.4-11) show that for the tapered channel pressure flow,

$$\frac{\partial P}{\partial x} = - \frac{3Q\mu}{2h^3} \quad (\text{h})$$

Plot the ratio of pressure drops obtained by Eqs. (h) and (f) to show that for $\alpha < 10^\circ$, the error involved using the lubrication approximation is very small.

3 Polymer Rheology and Non-Newtonian Fluid Mechanics

- 3.1 Rheological Behavior, Rheometry, and Rheological Material Functions of Polymer Melts, 80
- 3.2 Experimental Determination of the Viscosity and Normal Stress Difference Coefficients, 94
- 3.3 Polymer Melt Constitutive Equations Based on Continuum Mechanics, 100
- 3.4 Polymer Melt Constitutive Equations Based on Molecular Theories, 122

In Chapter 2 we discussed the engineering science of transport phenomena and Newtonian fluid mechanics. Only *simple fluids* such as gases and small liquid molecules exhibit Newtonian behavior. High molecular weight polymer melts are structurally *complex fluids* in that their macromolecules can assume many *conformations*, which become more *stretched* under flow, while gradually *recovering* into *random* conformations upon removal of the flow stresses. The state of macromolecular conformations profoundly affects intermolecular interactions during flow and, therefore, the viscosity of polymer melts strongly depends on the flow velocity gradients, rendering them non-Newtonian and their viscosity a *rheological material function*, not just a material parameter, as with Newtonian fluids. Furthermore, polymer melts also exhibit, in addition to a viscous nature, an elastic response, since conformations recover from stretched to random. Therefore, melts are *viscoelastic materials*.

A major portion of all the polymer processing shaping operations and elementary steps involves either isothermal or, most often, nonisothermal flow of polymer melts in geometrically complex conduits. Before dealing with the realistic polymer processing flow problems, it is therefore appropriate to examine separately the rheological (flow) behavior of polymer melts in simple flow situations and in the absence of temperature gradients. Our aims are to clarify the physical meaning of terms such as non-Newtonian or viscoelastic behavior, primary normal stress coefficient, and viscosity functions, to discuss briefly, from a primarily physical viewpoint, the constitutive equations that either quantitatively or semiquantitatively describe the observed behavior of polymer melts, and to examine the experimental methods that yield the rheological information needed to characterize polymer melt flow behavior in simple flows.

It is important to note that the rheological material functions obtained experimentally, using *rheometers*, are evaluated in simple flows, which are often called *viscometric* or *rheometric*. A viscometric flow is defined as one in which only one component of the velocity changes in only one spatial direction, $v_x(y)$. Yet these material functions are used to describe the more complex flow situations created by polymer processing equipment. We assume, therefore, that while evaluated in *simple flows*, the *same rheological* properties also apply to complex ones.

The combined effects of flow, geometric channel complexities, and coupled thermo-mechanical phenomena necessitate the use of numerical solutions. In the past 25 years a large number of increasingly powerful numerical simulation packages have been developed commercially taking advantage of the exponential growth in available and affordable computational power to enable solutions of nonisothermal processing flows of non-Newtonian polymer melts. We will describe some of these in the relevant chapters.

3.1 RHEOLOGICAL BEHAVIOR, RHEOMETRY, AND RHEOLOGICAL MATERIAL FUNCTIONS OF POLYMER MELTS

Three kinds of viscometric flows are used by rheologists to obtain rheological polymer melt functions and to study the rheological phenomena that are characteristic of these materials: steady simple shear flows, dynamic (sinusoidally varying) simple shear flows, and extensional, elongational, or shear-free flows.

Steady Simple Shear Flows

This type of flow is obtained either by the relative motion of the rheometer surfaces inducing simple drag flow on the fluid, or by an externally created pressure drop inducing pressure flow on the fluid as shown in Fig. 3.1, parts 1a, 2a, and 3. These flows have the following general flow field: $v_1 = v_1(x_2)$, $v_2 = v_3 = 0$, leading to a single nonzero shear rate component $\dot{\gamma}_{12} \neq 0$. The coordinates x_i for each of the steady shear flows are also shown on Fig. 3.1. The maximum shear rates that are attainable in the simple shear drag flows are very low, below $\dot{\gamma} < 1 \text{ s}^{-1}$, because of secondary flow-induced instabilities generated at the melt sample periphery edges. On the other hand, the operational shear rate range for the externally applied *pressure-induced* capillary flow rheometer is $1 < \dot{\gamma} < 10^4 \text{ s}^{-1}$, covering a range which coincides with most if not all processing flows.

Dynamic (Sinusoidally Varying) Drag Simple Shear Flows

Dynamic (sinusoidally varying) drag simple shear flows are shown in Fig. 3.1, parts 1b and 2b. They are obtained by applying a sinusoidally varying angular displacement $A(\omega, t) = A_0 \sin \omega t$ in the same rheometers that generate steady simple shear flows. Since polymer melts are viscoelastic, the resulting time-varying shear stress has both an in-phase (viscous) and an out-of-phase (elastic) component.

The steady and dynamic drag-induced simple shear-flow rheometers, which are limited to very small shear rates for the steady flow and to very small strains for the dynamic flow, enable us to evaluate rheological properties that can be related to the macromolecular structure of polymer melts. The reason is that very small sinusoidal strains and very low shear rates do not take macromolecular polymer melt conformations far away from their equilibrium condition. Thus, whatever is measured is the result of the response of not just a portion of the macromolecule, but the contribution of the entire macromolecule.

Extensional, Elongational or Shear-free Flows

Extensional, elongational or shear-free flows play a dominant role in the post die-forming step, such as stretching of melt strands in spinning, uniaxial stretching of molten films

Flow	Coordinates x_1 x_2 x_3	Shear Rate	Experimental Results		Rheological Functions Obtained
			Apply	Measure	
1. Cone and plate	$v_1 \neq 0, v_2 = v_3 = 0$ $\dot{\gamma}_{12} \neq 0$ 	$\dot{\gamma}_{12}$ $\dot{\gamma} = \frac{\sin \theta d (v_\phi \sin \theta)}{r}$ $\dot{\gamma} = \frac{\Omega}{\psi_0} = C$	(a). Ω (Steady) $\dot{\gamma} < 1 \text{ s}^{-1}$	<p>Ⓟ Torque $\propto \dot{\gamma}^n$ Normal force on plate</p> <p>Ⓝ Torque $\propto \dot{\gamma}$</p>	<p>Ⓟ $\eta(\dot{\gamma}), \Psi_1(\dot{\gamma}^2), \Psi_2(\dot{\gamma}^2)$</p> <p>Ⓝ $\mu(T)$</p>
			(b). $A = A_0 \sin \omega t$ A_0 : small (Dynamic)	<p>Ⓟ Torque $= f(\omega, t)$ $= C_1 \sin \omega t + C_2 \cos \omega t$ Normal force on plate</p> <p>Ⓝ Torque only $T = T_0 \sin \omega t$</p>	<p>Ⓟ $\eta^*(\omega) = \eta' - i\eta''$; $G' = \eta' \omega$; $G'' = \eta'' \omega$</p> <p>Ⓝ $\mu(T)$</p>
2. Parallel disks (torsional flow)		$\dot{\gamma} = \frac{dv_\theta}{dz}$ $\dot{\gamma} = \frac{\Omega r}{h}$	(a). Ω (Steady) $\dot{\gamma} < 1 \text{ s}^{-1}$	<p>Ⓟ Torque $\propto \dot{\gamma}^n$ Normal force on plate</p> <p>Ⓝ Torque $\propto \dot{\gamma}$</p>	<p>Ⓟ $\eta(\dot{\gamma})$; $(\Psi_1(\dot{\gamma}^2) - \Psi_2(\dot{\gamma}^2))_R$</p> <p>Ⓝ $\mu(T)$</p>
			(b). $A = A_0 \sin \omega t$ A_0 : small (Dynamic)	<p>Torque $= f(\omega, t)$ $= C' \sin \omega t + C'' \cos \omega t$ Normal force on plate</p>	<p>Ⓟ $\eta^*(\omega), G'(\omega), G''(\omega)$</p>
3. Capillary (Poiseuille flow)		$\dot{\gamma} = \frac{dv_z}{dr}$ <p>Ⓟ $\dot{\gamma} = C_1 r^{1/n}$</p> <p>Ⓝ $\dot{\gamma} = C_2 r$</p>	Piston speed (flow rate: Q)	<p>Pressure Drop</p> <p>Ⓟ $\Delta P \propto Q^n$ $n < 1$</p> <p>Ⓝ $\Delta P \propto Q$</p>	<p>Ⓟ $\eta(\dot{\gamma})$;</p> <p>Capillary entrance pressure losses, extrudate swell</p> <p>Ⓝ $\mu(T)$</p>

Fig. 3.1 Examples of simple, viscometric, shear-flow rheometer geometries. 1a, 2a and 3 are *steady* while 1b and 2b are *dynamic* rheological property rheometers. Ⓟ denotes polymer melts, while Ⓝ denotes Newtonian fluids.

exiting a flat film die, or the biaxial stretching of a tubular film exiting a blown film die to form a “bubble.” However, as with shear rheometers, the extensional rheometer flows are simpler than the previously mentioned real flows, because they are spatially uniform, isothermal, and shear-free. The general form of the rate of deformation matrix for incompressible fluids is

$$\dot{\boldsymbol{\gamma}} = \dot{\boldsymbol{\epsilon}} \begin{bmatrix} 1 & 0 & 0 \\ 0 & m & 0 \\ 0 & 0 & -(1+m) \end{bmatrix} \quad (3.1-1)$$

Three uniform, steady extensional flows, which are related to post-die flows and useful to study rheological behavior, and the ability of constitutive equations to predict such behavior, are listed below, and are shown on Fig. 3.2.

Figure 3.2 (Case 1) shows a simple uniaxial extensional flow created by the uniform stretching of a rectangular or a thin filament in the 1 direction. For this flow, $\dot{\epsilon}_{22} = -\dot{\epsilon}_{11}/2$, and because of the incompressibility assumption, $\dot{\epsilon}_{22} = \dot{\epsilon}_{33}$. Thus, in Eq. 3.1-1, $m = -0.5$, giving the following rate of deformation matrix

$$\dot{\boldsymbol{\gamma}} = \begin{bmatrix} \dot{\epsilon} & 0 & 0 \\ 0 & -\dot{\epsilon}/2 & 0 \\ 0 & 0 & -\dot{\epsilon}/2 \end{bmatrix} \quad (3.1-2)$$

For this simple uniaxial extensional flow to be steady, the instantaneous rate of change of the 1 direction length (l) must be constant

$$\frac{1}{l} \frac{dl}{dt} = \dot{\epsilon} = \text{const.} \quad (3.1-3)$$

Defining $a = l/l_0$, we rewrite the preceding equation:

$$\frac{1}{a} \frac{da}{dt} = \dot{\epsilon} \quad (3.1-4)$$

upon integration with l_0 being the length at $t = 0$

$$a(t) = l(t)/l_0 = e^{\dot{\epsilon}t} \quad (3.1-5)$$

Thus, in order to create a steady simple uniaxial extensional flow, the rheometer must cause the thin filament length to increase exponentially in time.

Figure 3.2 shows planar extensional flow generated by the uniform stretching of a thin wide sheet or film in one direction only, while allowing the thickness in the perpendicular direction to decrease. Thus, $\dot{\epsilon}_{11} = -\dot{\epsilon}_{33}$ and $\dot{\epsilon}_{22} = 0$. Therefore, $m = 0$ in Eq. 3.1-1, giving

$$\dot{\boldsymbol{\gamma}} = \dot{\epsilon}_{pl} \begin{bmatrix} 1 & 0 & 0 \\ 0 & 0 & 0 \\ 0 & 0 & -1 \end{bmatrix} \quad (3.1-6)$$

Again, an exponential film length increase is necessary in order to obtain constant $\dot{\epsilon}_{pl}$.

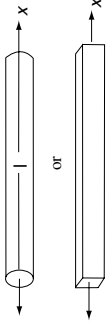
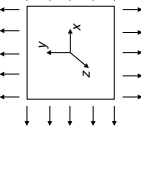
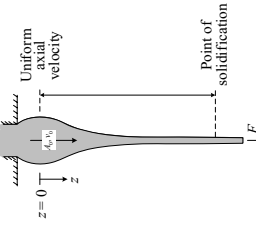
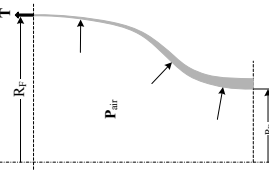
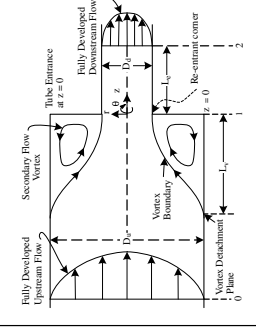
Steady Uniform Extensional Flow		Coordinates x_1 x_2 x_3	Apply	Obtain	Rheological Properties
1. Simple uniaxial extension		x r θ	$l = l_0 e^{\dot{\epsilon} t}$ ($\dot{\epsilon} < 1 s^{-1}$)	$F_1(t), A_1(t)$	<p>Ⓐ $\bar{\eta}(\dot{\epsilon}) = -\frac{F_1}{A_1}$; (steady)</p> <p>$\bar{\eta}^+(\dot{\epsilon}, t) = -\frac{F_1(t)}{A_1(t)}$; (growth)</p> <p>Ⓑ $\bar{\eta}(T) = 3\mu(T)$</p>
	or	x y z			
2. Planar extension		x y z	$l = l_0 e^{\dot{\epsilon}_{pl} t}$ ($\dot{\epsilon}_{pl} < 1 s^{-1}$)	$F_1(t), A_1(t)$	<p>$\bar{\eta}(\dot{\epsilon}_{pl}) = -\frac{F_1}{A_1}$; (steady)</p> <p>$\bar{\eta}^+(\dot{\epsilon}_{pl}, t) = -\frac{F_1(t)}{A_1(t)}$; (growth)</p>
3. Equibiaxial extension		x y z	$l_1(t) = l_2(t) = l_0 e^{\dot{\epsilon}_{bi} t}$ ($\dot{\epsilon}_{bi} < 1 s^{-1}$)	$F(t), A(t)$	<p>$\bar{\eta}(\dot{\epsilon}_{bi}) = -\frac{F}{A}$; (steady)</p> <p>$\bar{\eta}^+(\dot{\epsilon}_{bi}, t) = -\frac{F_1(t)}{A_1(t)}$; (growth)</p>
4. Examples of non-uniform die and post-die forming extensional flows					
					
Fiber spinning (Nonuniform uniaxial extension)	Film blowing (Nonuniform biaxial extension)			Stretch blow molding (Nonuniform biaxial extension)	Die entrance flows (Uniaxial extension and shear flow)

Fig. 3.2 Cases 1, 2, and 3 show steady, uniform extensional flows. Case 4 shows examples of more complex nonuniform stretching flows encountered in polymer processing operations.

In an equibiaxial extensional flow, shown in Fig. 3.2, the film is stretched at a constant rate $\dot{\epsilon}_{bi}$ in two directions, allowing the thickness of the incompressible molten film to decrease. Here $\dot{\epsilon}_{11} = \dot{\epsilon}_{22}$ and $\dot{\epsilon}_{33} = -2\dot{\epsilon}_{11}$. Thus $m = 1$ in Eq. 3.1-1 and

$$\dot{\boldsymbol{\gamma}} = \epsilon_{bi} \begin{bmatrix} 1 & 0 & 0 \\ 0 & 1 & 0 \\ 0 & 0 & -2 \end{bmatrix} \quad (3.1-7)$$

It is quite difficult to experimentally produce the preceding three uniform and isothermal flows, and extensional rheometers are therefore often limited to low attainable $\dot{\epsilon} \sim 1 \text{ s}^{-1}$ and short duration. Nevertheless, polymer processing engineers have to deal with nonuniform, nonisothermal extensional flows with polymer melts which, if they are crystallizable, undergo rapid crystal nucleation and anisotropic growth of the crystalline phase. As mentioned in Chapter 1, these phenomena in actual post-die forming operations cause the formation of unique structures and morphologies, called *structuring*, which greatly affect product properties. For further reading on experimental rheology, the reader is referred to the extensive available literature (e.g., Refs. 1–4).

Let us now turn again to Figs. 3.1 and 3.2 to examine the experimental results obtained with polymer melts in rheometers and the differences between them and those obtained with Newtonian fluids, thus gaining a specific understanding of what *non-Newtonian* behavior means in the response of polymeric melt to deformation.

Rheological Response of Polymer Melts in Steady Simple Shear-Flow Rheometers

Non-Newtonian Viscosity In the *cone-and-plate* and *parallel-disk torsional* flow rheometer shown in Fig. 3.1, parts 1a and 2a, the experimentally obtained torque, and thus the τ_{12} component of the shear stress, are related to the shear rate $\dot{\gamma} = \dot{\gamma}_{12}$ as follows: for Newtonian fluids $\tau_{12} \propto \dot{\gamma}$, implying a *constant* viscosity, and in fact we know from Newton's law that $\tau_{12} = -\mu\dot{\gamma}$. For polymer melts, however, $\tau_{12} \propto \dot{\gamma}^n$, where $n < 1$, which implies a *decreasing* shear viscosity with increasing shear rate. Such materials are called *pseudoplastic*, or more descriptively, *shear thinning*.¹ Defining a non-Newtonian viscosity,² η ,

$$\tau_{12} = \eta(\dot{\gamma})\dot{\gamma} \quad (3.1-8)$$

and assuming that the shear rate dependence of η can be expressed by simple power dependence, which agrees well with experimental measurements of many polymeric melts over a broad shear rate range, we get the following relationship

$$\eta(\dot{\gamma}) = m\dot{\gamma}^{n-1} \quad (3.1-9)$$

1. The term *pseudoplastic* is somewhat outdated because there is nothing "pseudo" in the flow behavior of polymers. In this book we use the term *shear thinning*, which well describes the phenomenon.

2. Non-Newtonian viscosity is sometimes called *apparent viscosity*, presumably because it changes with shear rate. In this book we call it *non-Newtonian viscosity*.

This relationship, as we will see in Section 3.3, is called the Power Law fluid model, and is used extensively in modeling flows in polymer processing.

In conclusion, we thus find that polymer melts are non-Newtonian in that they have a *viscosity that depends on the shear rate* $\dot{\gamma}_{12}$, or the shear stress τ_{12} in steady shear flows. This is the most important non-Newtonian property that we encounter in polymer processing.

Normal Stresses In the steady *cone-and-plate* and *parallel-disk torsional* flow rheometers, again with polymer melts, we observe experimentally a phenomenon that is totally unexpected and unpredictable by Newtonian rheological behavior, namely a *normal force*, F_N , acting on both pairs of plates. For a Newtonian fluid, the only stress component needed to support the single shear rate components $\dot{\gamma} = \dot{\gamma}_{12}$ is shear stress component τ_{12} . This stress component gives rise to the experimentally needed torque, as noted earlier. How can the normal force F_N on the rheometer plates be explained? On the grounds of physical macromolecular behavior, we can reason that the flow in the direction that the velocity points, defined as direction 1, tends to orient the macromolecules in that direction, somewhat like rubber bands stretched around a cylinder. But stretched polymer melt macromolecules want to revert to their equilibrium coiled conformations. This creates *tensile stresses* in the 1 direction, τ_{11} (which act as “strangulation” forces) as well as stresses in the normal direction in which the velocity changes, defined as direction 2, τ_{22} . These normal stresses would be relieved if the rheometer spacing were increased. Thus, in order to maintain the plate spacing constant, we have to impose on the sheared melt a normal force F_N . Because of the difficulties associated with the absolute value of pressure in a flow system (see Chapter 2), we define normal stress differences rather than individual components, such as the *primary* normal stress difference $\tau_{11} - \tau_{22}$. In fact, as we will see later, the measurement of the normal force F_N in the cone and plate rheometer is a direct measure of this normal stress difference.

A graphic example of the consequences of the existence of τ_{11} stress in simple steady shear flows is demonstrated by the well-known Weissenberg *rod-climbing* effect (5). As shown in Fig. 3.3, it involves another simple shear flow, the Couette (6) torsional concentric cylinder flow,³ where $x_1 = \theta$, $x_2 = r$, $x_3 = z$. The flow creates a shear rate $\dot{\gamma}_{12} = \dot{\gamma}$, which in Newtonian fluids generates only one stress component τ_{12} . Polyisobutylene molecules in solution used in Fig. 3.3(b) become oriented in the 1 direction, giving rise to the shear stress component in addition to the normal stress component τ_{11} .

Furthermore, when the cone-and-plate rheometer is outfitted with pressure taps at various radial positions, the experimentally obtained *pressure distribution* is found to be increasing with decreasing radial distance. This, as we will see later, enables us to compute the *secondary* normal stress difference, namely, $\tau_{22} - \tau_{33}$, where direction 3 is the third neutral spatial direction.

Next we define the two normal stress difference functions that arise in simple shear flows

$$\tau_{11} - \tau_{22} = \Psi_1(\dot{\gamma})\dot{\gamma}_{12}^2 \quad (3.1-10)$$

3. The Couette apparatus was developed by Maurice Couette in 1890 as a means for measuring the viscosity of a fluid at small imposed angular velocities of the cylinders.

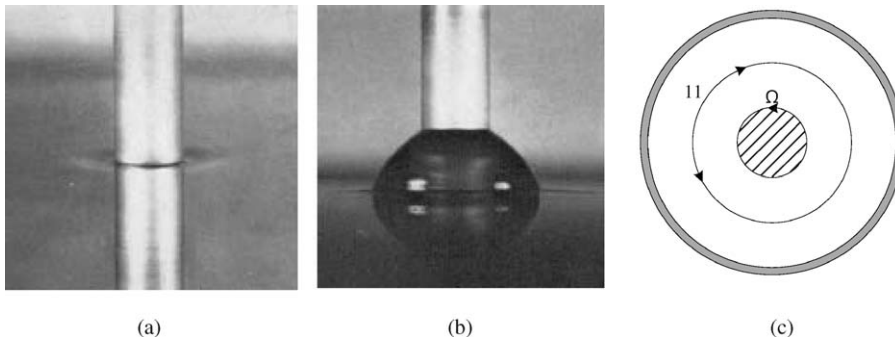


Fig. 3.3 A 9.52-mm D aluminum rod rotating at 10 rps in a wide-diameter cylinder containing (a) Newtonian oil, and (b) polyisobutylene (PIB) solution, which exhibits the rod-climbing Weissenberg effect [from G. S. Beavers and D. D. Joseph, *J. Fluid Mech.*, **69**, 475 (1975)]. (c) Schematic representation of the flow direction flow-induced τ_{11} , causing rod climbing. For Newtonian fluids, $\tau_{11} = 0$, since the small and simple Newtonian fluid molecules are incapable of being “oriented” by the flow.

and

$$\tau_{22} - \tau_{33} = \Psi_2(\dot{\gamma})\dot{\gamma}_{12}^2 \quad (3.1-11)$$

The coefficients Ψ_1 and Ψ_2 , like non-Newtonian viscosity, are also found to be shear rate dependent. The non-Newtonian property of exhibiting normal stresses in shear flows plays an important role in processing under situations in which shear stresses vanish, as in extrudate swell, discussed later in this section.

Capillary Flow Rheometry Next we examine the experimentally obtained results with the capillary flow rheometer shown in Fig. 3.1, which are directly relevant to polymer processing flows, since the attainable shear rate values are in the range encountered in polymer processing. The required pressure drop ΔP does not increase linearly with increases in the volumetric flow rate Q , as is the case with Newtonian fluids. Rather, increasingly smaller increments of ΔP are needed for the same increases in Q . The Newtonian Poiseuille equation, relating flow rate to pressure drop in a tube, is linear and given by

$$\Delta P = \frac{8\mu L}{\pi R^4} Q \quad (3.1-12)$$

On the other hand, for polymer melts, we obtain experimentally a nonlinear relationship

$$\Delta P \propto Q^n \quad (n < 1) \quad (3.1-13)$$

Again, this dependence may reasonably be attributed to a *decreasing* viscosity with *increasing* shear rate. With decreasing viscosity, resistance to flow at higher flow rates decreases as well. It is this decreasing viscosity with increasing shear rates that enables

processing machinery to operate at high rates of production and avoid excessive heat generation that may damage the polymer.

Another important ramification of shear-thinning behavior in capillary or tube flow, relevant to polymer processing, relates to the shape of the *velocity profiles*. Newtonian and shear-thinning fluids are very different, and these differences have profound effects on the processing of polymer melts. The former is parabolic, whereas the latter is flatter and pluglike. The reason for such differences emerges directly from the equation of motion. The only nonvanishing component for steady, incompressible, fully developed, isothermal capillary flow, from Table 2.2, is

$$\frac{1}{r} \frac{d}{dr} (r\tau_{rz}) = -\frac{dP}{dz} \tag{3.1-14}$$

Integrating with the boundary condition $\tau_{rz}(0) = 0$

$$\tau_{zr} = \tau(r) = Cr = -\left(\frac{\Delta P}{2L}\right)r \tag{3.1-15}$$

Equation 3.1-14 holds for all fluids, since it is a physical law. This is shown in Fig. 3.4(a).

But when a rheological model relating $\tau(r)$ versus $\dot{\gamma}(r)$ is substituted into Eq. 3.15, two different shear rate and velocity profiles are obtained. For Newtonian fluids, $\tau(r) = -\mu\dot{\gamma}(r)$, the shear rate profile is

$$\dot{\gamma}(r) = \frac{\Delta P}{2\mu L} r \tag{3.1-16}$$

indicating that the Newtonian shear rate increases linearly with r , as shown in Fig. 3.4(b), whereas for shear-thinning melts, using the Power Law model $\tau(r) = -m\dot{\gamma}(r)^n$, we get

$$\dot{\gamma}(r) = \left(\frac{\Delta P}{2mL}\right)^{1/n} r^{1/n} \tag{3.1-17}$$

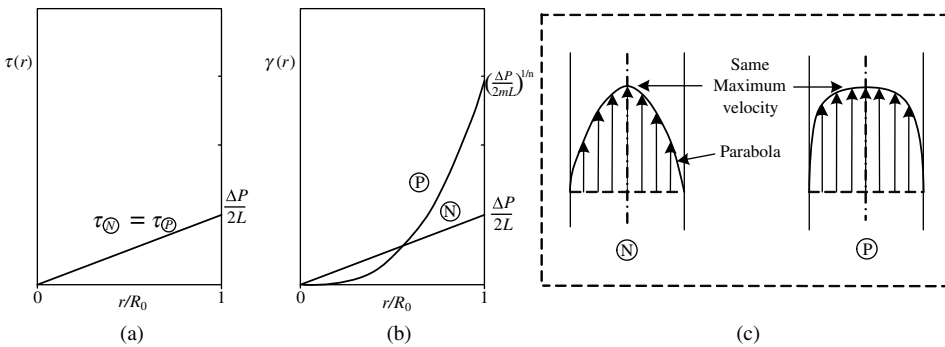


Fig. 3.4 The (a) shear stress, (b) shear rate, and (c) velocity profiles of a Newtonian and a shear-thinning fluid flowing in a capillary of dimensions R is under the influence of the same ΔP , that is, $\tau(r)$.

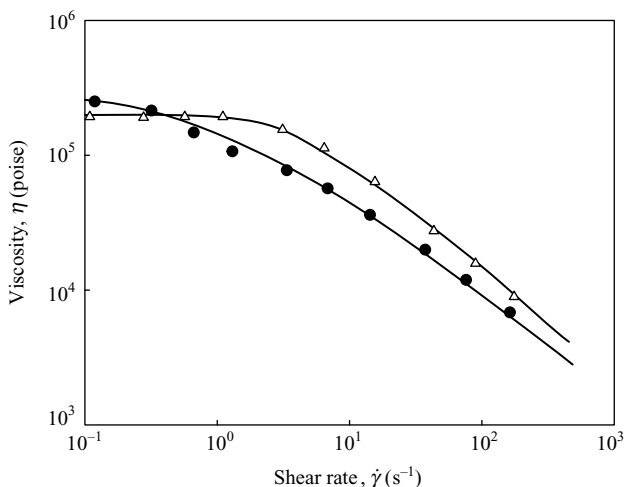


Fig. 3.5 Logarithmic plot of the shear rate-dependent viscosity of a narrow molecular weight distribution $PS(\Delta)$ at $180^\circ C$, showing the Newtonian plateau and the Power Law regions and a broad distribution $PS(\bullet)$. [Reprinted with permission from W. W. Graessley et al., *Trans. Soc. Rheol.*, **14**, 519 (1970).]

Thus for shear-thinning melts, that is, $n < 1$, the shear rate profile, $\dot{\gamma}(r)$, dependence is *stronger than the first power*, as shown again in Fig. 3.4(b). Consequently, as shown in Fig. 3.4(c), shear-thinning polymer melts flow in pressure-induced flows with very high shear rates near the walls, while there is a core of the fluid that is sheared very little. Because of this, and the high polymer melt viscosity, the melt layers next to the wall heat up, while the core flows isothermally. Thus, figuratively speaking, at high shear rates where both shear rate and temperature are high near the capillary wall, the wall polymer melt layer acts almost as a lubricant, while the core flows almost in plug flow. The shear viscosity $\eta(\dot{\gamma})$ of polymer melts typically decreases dramatically with increasing shear rates in the process range of $\dot{\gamma}$ (as shown on Fig. 3.5).

Polymer melts exhibit capillary exit and entrance behavior, which is different than that of Newtonian fluids. Polymer melt extrudates “swell,” that is, increase in diameter, following the capillary exit. This is, again, a ramification of the existence of tensile stresses in the flow direction, encountered earlier. The extrudates in the stress-free boundary region following the exit relieve this axial tension by contracting, and thus expanding radially. Just ahead of the capillary entrance, polymer melts undergo a more complex combined extension and shear flow. The *entrance* pressure drops generated are much higher for melts, because their elongational viscosity is higher than the Newtonian, as we will see later in this section. We will discuss both the preceding phenomena in Chapter 13.

Rheological Response of Polymer Melts to Small, Sinusoidally Varying Shear Deformations, $\gamma(\omega, t) = \gamma_0 \sin \omega t$

The shear rate field that results from such cyclic deformation is

$$\frac{d\gamma}{dt} = \dot{\gamma}(\omega t) = \gamma_0 \omega \cos \omega t = \dot{\gamma}_0 \cos \omega t \quad (3.1-18)$$

The cyclic stress needed to support the imposed strain and flow field is experimentally found to be

$$\tau(\omega, t) = \tau_0' \sin \omega t + \tau_0'' \cos \omega t \quad (3.1-19)$$

The first term of the needed stress is *in phase* with the applied strain; it is, therefore, an *elastic* stress, since elastic materials respond to a stress only by deforming. The second term of Eq. 3.1-19, which is *out of phase* with the applied strain, is in phase with the shear rate, Eq. 3.1-18; it is, therefore, a *viscous* stress, since viscous fluids respond to a stress by flow, where flow is a time-increasing strain and its measure is shear rate (see Section 2.7). The conclusion from the response of polymer melts to small cyclic deformations, then, is that they are *viscoelastic* materials. Their viscous nature is due to the ability of polymer chain segments to *drag* past one another, while their elastic nature is due to the ability of stretched chain segments to *recoil*, thus restoring their coiled configurations, and acting as elastic springs.

An equivalent representation of Eq. 3.1-19, in terms of rheological functions, is

$$\tau(\omega, t) = \dot{\gamma}^0 \eta''(\omega) \sin \omega t + \dot{\gamma}^0 \eta'(\omega) \cos \omega t \quad (3.1-20)$$

where η' and η'' are components of the complex viscosity

$$\eta^*(\omega) = \eta' - i\eta'' \quad (3.1-21)$$

For Newtonian fluids, $\tau(\omega, t) = \mu \cos \omega t$, $\eta' = \mu$, and $\eta'' = 0$.

The viscoelastic response of polymer melts, that is, Eq. 3.1-19 or 3.1-20, become *nonlinear* beyond a level of strain γ_0 , specific to their macromolecular structure and the temperature used. Beyond this strain limit of linear viscoelastic response, η' , η'' , and η^* become functions of the applied strain. In other words, although the applied deformations are cyclic, large amplitudes take the macromolecular, coiled, and entangled structure far away from equilibrium. In the linear viscoelastic range, on the other hand, the frequency (and temperature) dependence of η' , η'' , and η^* is indicative of the specific macromolecular structure, responding to only small perturbations away from equilibrium. Thus, these dynamic rheological properties, as well as the commonly used dynamic moduli

$$G'(\omega) = \omega \eta'' \quad \text{and} \quad G''(\omega) = \omega \eta' \quad (3.1-22)$$

are widely used for the *characterization* of the macromolecular structure by both polymer scientists and engineers (7,8).

The dependence of η' , η'' , G' , and G'' on frequency reflects the ability of macromolecular systems to flow like Newtonian fluids if the experimental time allowed them, $t_{\text{exp}} = 1/\omega$, is very large compared to the time that they require to fully respond macromolecularly. This temperature-dependent, material-characteristic time is commonly called the *relaxation time*, λ , although it is actually a relaxation spectrum (7). Conversely, when t_{exp} is very short, that is, ω is very high compared to λ , the macromolecular system can only respond like an elastic solid, able only to undergo deformation and not flow. In

terms of the dimensionless *Deborah number*,⁴

$$\text{De} = \frac{\lambda}{t_{\text{exp}}} = \lambda\omega \quad (3.1-23)$$

Polymer melts act, qualitatively speaking, as *elastic solids* for $De \gg 1$, as *viscous liquids* for $De \ll 1$, and *viscoelastic materials* in the range in-between. Finally, since both (ω) and $(\dot{\gamma})$ represent rates of change of deformation, it is not surprising that both $\eta^*(\omega)$ and $\eta(\dot{\gamma})$ are rate dependent and shear thinning. As a matter of fact, $\eta^*(\omega)$, which can be evaluated experimentally to very low frequency ranges, as low as 10^{-2} s^{-1} , often forms an extension to $\eta(\dot{\gamma})$ obtained by capillary flow at higher shear rates, as high as 10^4 s^{-1} (9). Thus, the viscosity function can be obtained over six orders of magnitude of frequency/shear rate, yielding information on both molecular structure and processing. Dynamic simple shear-flow rheometers yield information on the first normal stress difference N_1 through the out-of-phase component of the complex viscosity η'' or its equivalent in-phase modulus $G' = \eta''\omega$. The experimentally determined function $2G'(\omega)$ tracks $N_1(\dot{\gamma}^2)$ determined from steady flow cone-and-plate experiments (10,11). Laun (12) suggested another empiricism relating G' and N_1 that fits the data over wider ranges of shear rate and frequencies given by

$$N_1 = \tau_{11} - \tau_{22} = 2G'\eta''(\omega) \left[1 + \left(\frac{\eta''}{\eta'} \right)^2 \right]^{0.7} \Bigg|_{\omega=\dot{\gamma}}$$

In summary, steady and dynamic simple shear rheometric results are complementary: at very low $(\dot{\gamma})$ or (ω) values they both yield useful macromolecular structure characterization. Moreover, $\eta^*(\omega)$ in the range $\omega < 10 \text{ s}^{-1}$ forms an extension of $\eta(\dot{\gamma})$ obtained by capillary rheometry at $\dot{\gamma} > 10 \text{ s}^{-1}$, a range that is relevant to processing.

Rheological Response of Polymer Melts in Steady, Uniform, Extensional Flows

Turning to Fig. 3.2, Case 1, we see that the tensile force F_1 needed to sustain the applied constant extensional rate $\dot{\epsilon}$, either levels off to a constant $F_1(\dot{\epsilon})$ or exhibits strain hardening increasing with time, occasionally in an unbounded fashion; the force is then represented as $F^+(\dot{\epsilon}, t)$. For this uniform extensional flow

$$\frac{F_1}{A} = \tau_{11} + P \quad (3.1-24)$$

where

$$-P = \tau_{22} = \tau_{33} \quad (3.1-25)$$

4. The dimensionless Deborah number was defined and coined by Prof. Marcus Reiner from the Technion–Israel Institute of Technology, and one of the fathers of rheology, in an after-dinner speech at the 4th International Congress on Rheology in Providence, Rhode Island. The Prophetess Deborah, said Marcus, “knew” rheology, because in her song [Judges 5:5] she says “The mountains flowed before the Lord” [הָרִים גָּזְלוּ מִפְּנֵי יְהוָה], so not only did she know that mountains, like everything else, flow but she knew that they flowed before the Lord and not before man for man has a too short lifespan to notice. The ratio of relaxation time to observation time clearly illuminates this point (*Phys. Today*, January 1964).

We define a material function $\bar{\eta}$, commonly called the *elongational* or *extensional viscosity*, through the primary normal stress difference $\tau_{11} - \tau_{22}$; thus, for the case of $F_1(\dot{\epsilon})$, it is given by

$$\bar{\eta}(\dot{\epsilon}) = -\frac{F_1/A}{\dot{\epsilon}} = -\left(\frac{\tau_{11}(\dot{\epsilon}) - \tau_{22}}{\dot{\epsilon}}\right) \quad (3.1-26)$$

and for $F_1^+(\dot{\epsilon}, t)$, the elongational viscosity is given by

$$\bar{\eta}^+(\dot{\epsilon}, t) = -\left(\frac{\tau_{11}(\dot{\epsilon}, t) - \tau_{22}}{\dot{\epsilon}}\right) \quad (3.1-27)$$

Experimentally, in both cases, we have

$$\bar{\eta}(\dot{\epsilon}) = \frac{-F_1(\dot{\epsilon})/A_1}{\dot{\epsilon}} \quad (3.1-28)$$

or

$$\bar{\eta}^+(\dot{\epsilon}, t) = \frac{-F_1(\dot{\epsilon}, t)/A_1}{\dot{\epsilon}} \quad (3.1-29)$$

For a Newtonian fluid in a simple elongational flow, the constitutive equation becomes

$$\boldsymbol{\tau} = -\mu\dot{\boldsymbol{\gamma}} = -\mu \begin{pmatrix} +2\dot{\epsilon} & 0 & 0 \\ 0 & -\dot{\epsilon} & 0 \\ 0 & 0 & -\dot{\epsilon} \end{pmatrix} \quad (3.1-30)$$

thus

$$\tau_{11} - \tau_{22} = -\mu(2\dot{\epsilon} + \dot{\epsilon}) = -3\mu\dot{\epsilon} \quad (3.1-31)$$

Combining Eqs. 3.1-31 and 3.1-26, we obtain the so-called Trouton relation, which defines the *Trouton viscosity* (13).

$$\bar{\eta} = 3\mu \quad (3.1-32)$$

For polymer melts where the low shear rate limiting viscosity value is η_0 , $\bar{\eta} = 3\eta_0$ (14). Examples of extensional viscosity growth, either to a steady $\bar{\eta}(\dot{\epsilon})$ value or to a strain-hardening-like mode, are shown in Fig. 3.6 for the linear nonbranched polystyrene (PS), a high density polyethylene (HDPE) that is only slightly branched with short branches, and a long chain-branched low density polyethylene (LDPE) (15).

We observe that strain-hardening stress and viscosity growth are associated with long chain branching. Long chain branching is a chain structural feature that impedes large macromolecular rearrangements of flow motions because it creates *entanglements*. With this in mind, and the fact that in steady uniform extensional flow, the length is increased *exponentially* to maintain $\dot{\epsilon} = \text{const}$, it is not surprising that even at $\dot{\epsilon} = 10^{-2} \text{ s}^{-1}$, the extensional viscosity still exhibits strain hardening. The Deborah number $\text{De} = \lambda 10^{-2}$ is still larger than unity for LDPE, denoting very long relaxation times $\lambda > 100 \text{ s}$. Similar

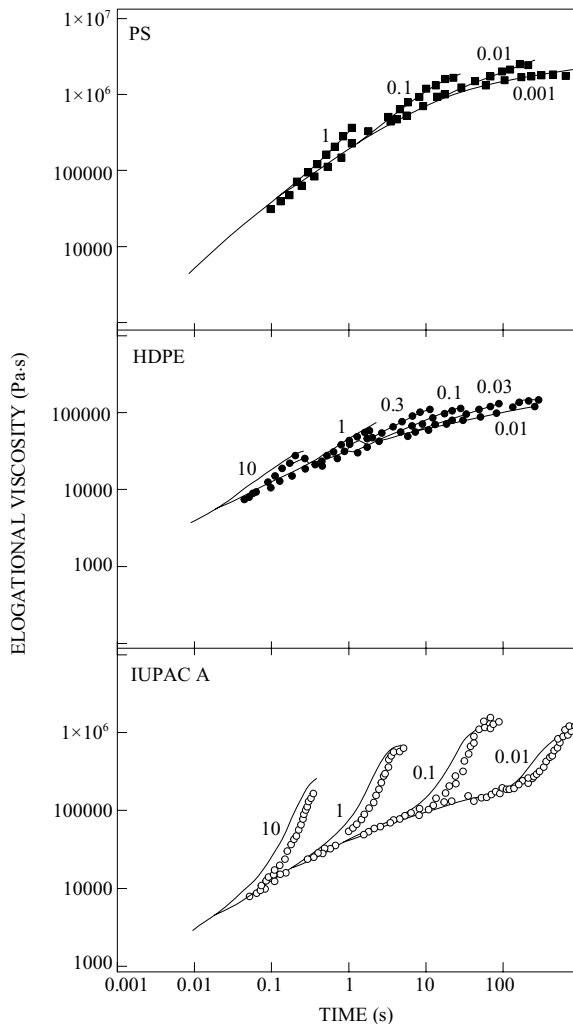


Fig. 3.6 Extensional growth viscosity versus time for polystyrene (top), HDPE, and LDPE. [S. A. Khan, R. K. Prud'homme, and R. G. Larson, *Rheol. Acta*, **26**, 144 (1987).]

results with LDPE are obtained for both the equibiaxial and planar extensional flows, as shown in Fig. 3.7.

Turning to Fig. 3.2, Case 4, we note that the extensional flows encountered by fibers, films, and tubes in *fiber spinning*, *film blowing*, and *stretch blow molding* are not uniform; the strand/film varies in thickness in the stretching direction(s). This extensional flow rheometry once again involves simpler flow, and the rheological results obtained are used to analyze or interpret more complicated, nonuniform, post-die forming flows.

Finally, it is worth discussing briefly the *flow singularity* at the exit corner of pressure-flow dies used for forming fibers and film, which are consequently stretched to orient and structure them. At that location we have to reconcile the fact that the wall melt flow layer must, in nearly zero distance, accelerate from a zero to a finite velocity. Irrespective of the details of this high acceleration, the surface layer undergoes high extensional rate flows,

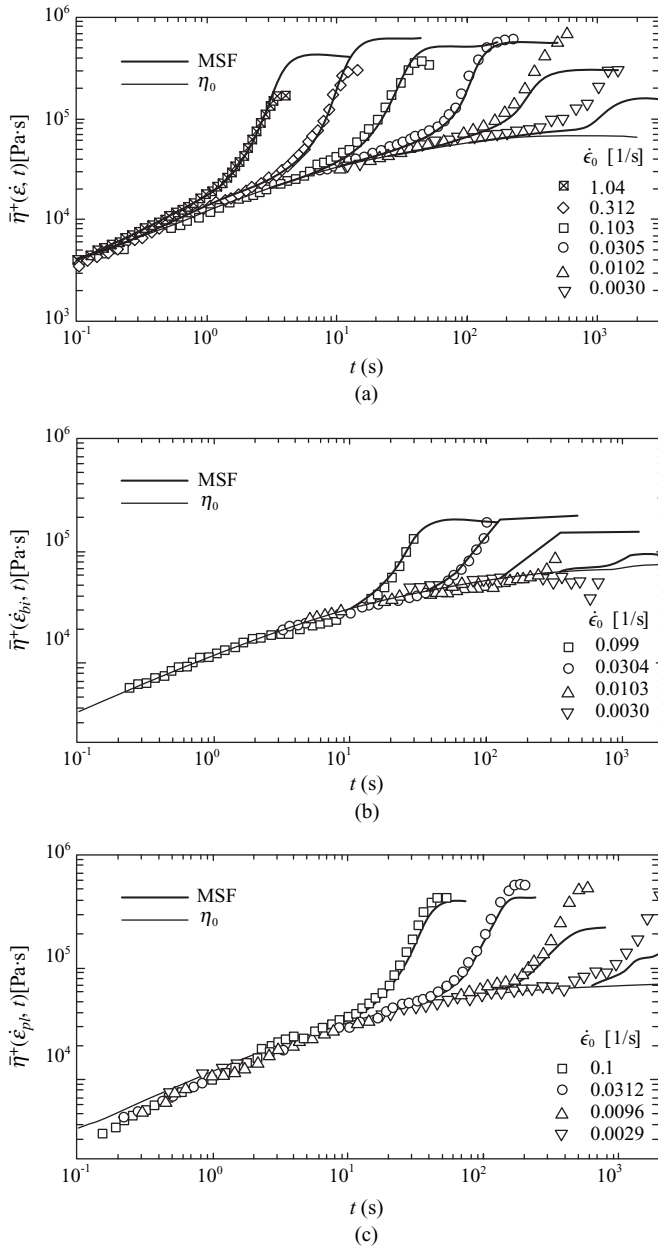


Fig. 3.7 (a) Uniaxial, (b) equibiaxial, and (c) planar extensional viscosities for a LDPE melt. [Data from P. Hachmann, Ph.D. Dissertation, ETH, Zurich (1996).] Solid lines are predictions of the molecular stress function model constitutive equation by Wagner et al. (65,66) to be discussed in Section 3.4.

and consequently, is exposed to potentially very high extensional stresses. Local crack development can occur at critical stresses equal to those needed to rupture the melt, due to its inability to disentangle, thus acting as a fracturing solid. Such phenomena may be the cause of the “shark-skin” (16–19) melt fracture, which is discussed in Chapter 12.

3.2 EXPERIMENTAL DETERMINATION OF THE VISCOSITY AND NORMAL STRESS DIFFERENCE COEFFICIENTS

This section describes two common experimental methods for evaluating η , Ψ_1 , and Ψ_2 as functions of shear rate. The experiments involved are the steady capillary and the cone-and-plate viscometric flows. As noted in the previous section, in the former, only the steady shear viscosity function can be determined for shear rates greater than unity, while in the latter, all three viscometric functions can be determined, but only at very low shear rates. Capillary shear viscosity measurements are much better developed and understood, and certainly much more widely used for the analysis of polymer processing flows, than normal stress difference measurements. It must be emphasized that the results obtained by both viscometric experiments are independent of any constitutive equation. In fact, one reason to conduct viscometric experiments is to test the validity of any given constitutive equation, and clearly the same constitutive equation parameters have to fit the experimental results obtained with *all* viscometric flows.

Example 3.1 Capillary Flow Rheometry The experimental setup used in capillary viscometry is shown schematically in Fig. 3.1, Case 3. Care is taken to have a uniform temperature and to eliminate the piston frictional effects in the reservoir. Either constant pressure or constant flow rate experiments are conducted, depending on the available instrument. At very slow flow rates, with shear rates below 1 s^{-1} , the surface tension of the emerging extrudate, gravity, and the frictional forces between the piston and the reservoir cannot be neglected; thus, the viscosity values obtained in this range are usually too high. A capillary viscometer yields viscosity data up to shear rates, where the phenomenon of melt fracture occurs (see Chapter 12). At high shear rates, the danger of having a high level of viscous dissipation of energy, and thus nonisothermal flow, as pointed out earlier, is very real.

The starting point of our analysis is the z -component momentum equation

$$\frac{dP}{dz} = -\frac{1}{r} \frac{d}{dr}(\tau_{rz}) \quad (\text{E3.1-1})$$

which is valid for all incompressible fluids and is subject to the assumptions of steady and isothermal flow. Integrating Eq. E 3.1-1, we obtain

$$\tau_{rz} = \tau_w \left(\frac{r}{R} \right) \quad (\text{E3.1-2})$$

where τ_w is the shear stress at the “wall” ($r = R$) given by

$$\tau_w = \left(\frac{P_0 - P_L}{2L} \right) R \quad (\text{E3.1-3})$$

The shear stress at the wall τ_w can be experimentally evaluated by measuring R , L , and $P_0 = P_L$.

By assuming only that the polymer melt is viscous and time independent, and that the viscosity is a function of the shear rate, $\eta(\dot{\gamma})$, without the need to specify any specific viscosity function, we can state that for capillary flow at the wall,

$$\tau_w = -\eta \dot{\gamma}_{rz} \Big|_R = \eta \dot{\gamma}_w \quad (\text{E3.1-4})$$

where $\dot{\gamma}_w$ is the shear rate at the wall.

Having the shear stress at the wall from Eq. E3.1-3 as a function of pressure drop, Eq. E3.1-4 suggests that if in some way the shear rate at the wall, $\dot{\gamma}_w$, could be evaluated experimentally from the flow rate at the corresponding pressure drops, the viscosity function could be determined. This is indeed possible because of the volumetric flow rate Q , which can be expressed independently of any constitutive equation as follows

$$Q = 2\pi \int_0^R r v_z(r) dr = 2\pi \left[\left(\frac{r^2 v_z(r)}{2} \right) \Big|_0^R - \int_0^R \frac{r^2}{2} dv_z \right] \quad (\text{E3.1-5})$$

Assuming no slip at the wall of the capillary, we note that the first term on the right-hand side of Eq. E3.1-5 is zero and it becomes

$$Q = -\pi \int_0^R r^2 \left(\frac{dv_z}{dr} \right) dr \quad (\text{E3.1-6})$$

From Eq. E3.1-2, $r = \tau_{yz}R/\tau_w$, a relationship that can be utilized to change the integration variable in Eq. E3.1-6, to obtain the following equation

$$Q = \frac{-\pi R^3}{\tau_w^3} \int_0^{\tau_w} \left(\frac{dv_z}{dr} \right) \tau_{rz}^2 d\tau_{rz} \quad (\text{E3.1-7})$$

Next, Eq. E3.1-7 is differentiated (20) with respect to τ_w using the Leibnitz formula of differentiating an integral⁵ to give

$$\frac{1}{\pi R^3} \left[\tau_w^3 \frac{dQ}{d\tau_w} + 3\tau_w^2 Q \right] = -\tau_w^2 \left(\frac{dv_z}{dr} \right)_{r=R} = \dot{\gamma}_w \tau_w^2 \quad (\text{E3.1-8})$$

Equation E3.1-8 indicates that we can obtain the desired shear rate at the wall if we know the flow rate corresponding to the particular shear stress at the wall and the *change* in flow rate (i.e., the slope of the flow-rate function) at that point. Equation E3.1-8 with Eq. E3.1-3 can be written as

$$\dot{\gamma}_w = -\frac{1}{\pi R^3} \left[3Q + \Delta P \frac{dQ}{d(\Delta P)} \right] \quad (\text{E3.1-9})$$

Finally, we can rewrite Eq. E3.1-9 as

$$\dot{\gamma}_w = \frac{3\Gamma_w}{4} + \frac{\tau_w}{4} \frac{d\Gamma_w}{d\tau_w} \quad (\text{E3.1-10})$$

where Γ is the *Newtonian* shear rate at the wall

$$\Gamma_w = \frac{4Q}{\pi R^3} \quad (\text{E3.1-11})$$

5. The Leibnitz formula:

$$\frac{d}{dx} \int_{a_1(x)}^{a_2(x)} f(s, x) ds = \int_{a_1(x)}^{a_2(x)} \frac{\partial f}{\partial z} ds + \left[f(a_2, x) \frac{da_2}{dx} - f(a_1, x) \frac{da_1}{dx} \right]$$

Either Eq. E3.1-9 or Eq. E3.1-10, known as the “Rabinowitsch” or “Weissenberg–Rabinowitsch” equations, can be used to determine the shear rate at the wall $\dot{\gamma}_w$ by measuring Q and ΔP or τ_w and Γ_w (21). Thus, in Eq. E3.1-4 both τ_w and $\dot{\gamma}_w$ can be experimentally measured for *any* fluid having a shear rate–dependent viscosity as long as it does not slip at the capillary wall. Therefore, the viscosity function can be obtained.

Experimentally, it is found that for polymer melts $\dot{\gamma}_w \geq \Gamma_w$, with the inequality, as noted in Section 3.1, becoming more pronounced at higher shear rates.

Finally, because the results obtained in capillary viscometry, especially for capillaries of small L/R , are influenced by both extensional and shear flow phenomena associated with the fluid spatial accelerations at the capillary entrance, it is necessary to correct the values of τ_w given in Eq. E3.1-3. Chapter 13 covers the nature, magnitude, and significance of these, commonly known as “Bagley” corrections.

The Rabinowitsch equation has been used in the long capillary viscometry data found in Appendix A. Figure E3.1 shows long capillary τ_w vs. Γ_w and τ_w vs. $\dot{\gamma}_w$ results with and without the Rabinowitsch correction.

Example 3.2 Cone-and-Plate Flow Rheometry The cone-and-plate flow apparatus is shown schematically in Fig. E3.2a. The polymer melt flows in the space formed by the rotating cone and stationary plate.

The experimentally measured quantities are:

1. The cone rotational frequency Ω
2. The resulting torque needed to turn the cone \mathcal{T}
3. The total force normal to the fixed plate (thrust) F_N .
4. The pressure distribution on the fixed plate as a function of r :

$$\pi_{\theta\theta}(r)|_{\theta=\pi/2} = P + \tau_{\theta\theta}(r)|_{\theta=\pi/2} \quad (\text{E3.2-1})$$

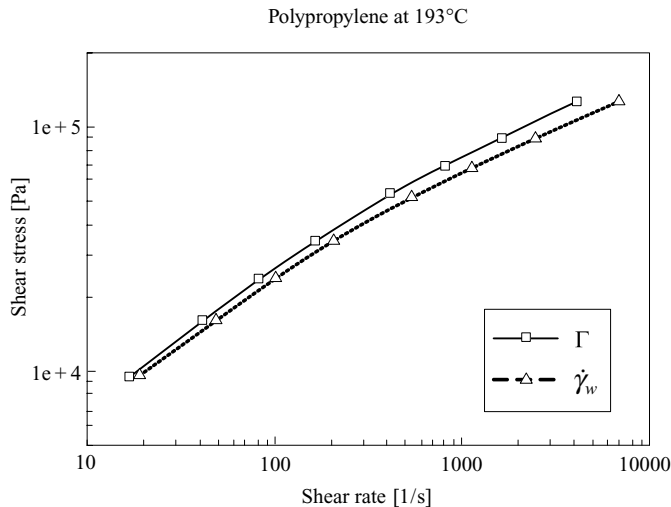


Fig. E3.1 Shear stress vs. shear rate with and without Rabinowitsch correction. [Courtesy of V. Tan, Polymer Processing Institute (PPI), Newark, NJ.]

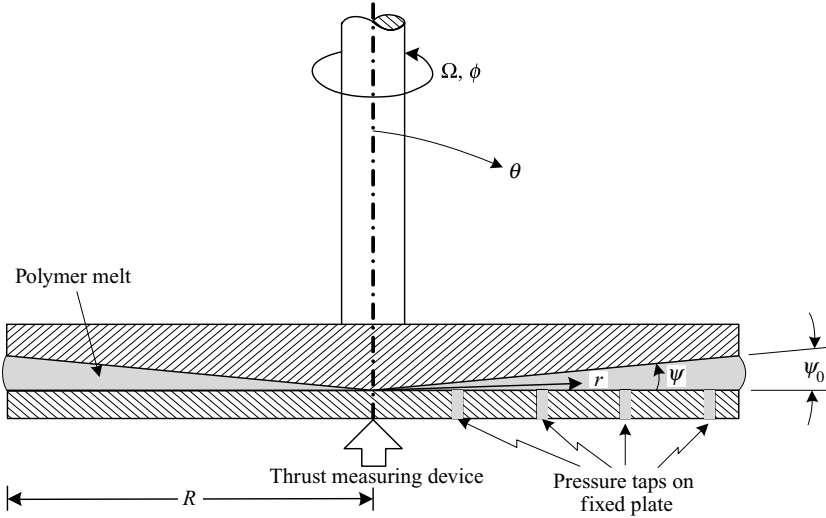


Fig. E3.2a Schematic representation of the cone and plate viscometer.

We note that with the cone-and-plate rheometers, fracture of the polymer melt is observed at shear rates exceeding 10^{-2} or 10^{-1} s^{-1} . Fracture is initiated at the melt-air interface at the perimeter. This has been attributed to the fact that the elastic energy becomes greater than the energy required to fracture the polymer melt at those shear rates (22). Irrespective of the origin of the fracture, it limits the operation of the cone-and-plate instrument to below the previously mentioned shear rates.

The velocity field between the cone and the plate is “visualized” as that of liquid cones described by θ -constant planes, rotating rigidly about the cone axis with an angular velocity that increases from zero at the stationary plate to Ω at the rotating cone surface (23). The resulting flow is a unidirectional shear flow. Moreover, because of the very small ψ_0 (about $1^\circ - 4^\circ$), *locally* (at fixed r) the flow can be considered to be like a torsional flow between parallel plates (i.e., the liquid cones become disks). Thus

$$v_\phi = \Omega r \frac{z}{z_0} \quad (\text{E3.2-2})$$

where z and z_0 can be expressed in terms of the angle $\psi = \pi/2 - \theta$

$$z = r \sin \psi \equiv \psi \quad (\text{E3.2-3})$$

and

$$z_0 = r \sin \psi_0 \equiv r\psi_0 \quad (\text{E3.2-4})$$

Inserting Eqs. E3.2-3 and E3.2-4 into Eq. E3.2-2, the following velocity profile is obtained

$$v_\phi = \Omega r \left(\frac{\psi}{\psi_0} \right) \quad (\text{E3.2-5})$$

Accordingly, the only nonvanishing component of the rate of deformation tensor is $\dot{\gamma}_{\theta\phi} = \dot{\gamma}_{\phi\theta} = (1/r)(\partial v_\phi / \partial \theta)$, and from Eq. E3.2-5 we obtain

$$\dot{\gamma}_{\theta\phi} = -\frac{\Omega}{\psi_0} = \text{constant} \quad (\text{E3.2-6})$$

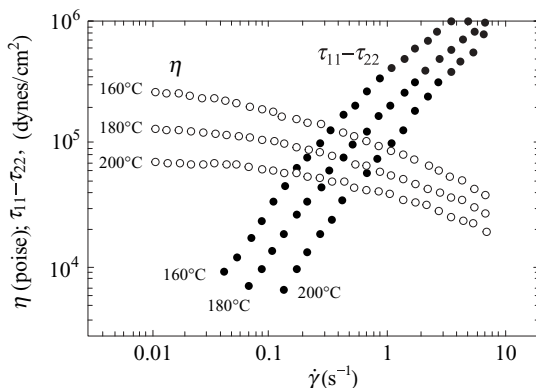


Fig. E3.2b The viscosity η and first (primary) normal stress difference $\tau_{11} - \tau_{22}$ of LDPE evaluated using the Weissenberg rheogoniometer (cone and plate). LDPE is Tenite 800 of density 0.918 g/cm^3 , and $\bar{M}_n = 25,800$. [Reprinted with permission from I. Chen and D. C. Bogue, *Trans. Soc. Rheol.*, **16**, 59 (1972).]

The preceding relationship establishes that the cone-and-plate flow is viscometric, where ϕ is direction 1, that is, the direction of motion, θ is direction 2, that is, the direction in which the velocity changes, and r is direction 3, that is, the neutral direction. Furthermore, the flow field is such that shear rate is constant in the entire flow field, as it is in the flow between parallel plates.

The torque on the shaft of the cone is due to the action of the shear stress $\tau_{\theta\phi}$ on its surface

$$\mathcal{T} = 2\pi \int_0^R (r\tau_{\theta\phi}) r dr \quad (\text{E3.2-7})$$

where $\tau_{\theta\phi}$ is constant, since $\dot{\gamma}_{\theta\phi}$ is constant throughout the flow field. Upon integration, we obtain

$$\tau_{\theta\phi} = \frac{\mathcal{T}}{\left(\frac{2}{3}\pi R^3\right)} \quad (\text{E3.2-8})$$

This expression suffices to determine experimentally the shear stress. Having evaluated both $\tau_{\theta\phi}$ and $\dot{\gamma}_{\theta\phi}$, we can readily obtain the viscosity function $\eta(\dot{\gamma}_{\theta\phi})$. Figure E3.2b gives such data for low-density polyethylene. The data extend beyond the commonly accepted upper limit of shear rate for polymer melts, probably because of the low average molecular weight of the polymer.

To obtain experimental information on normal stresses, we employ and mathematically manipulate the r component of the equation of momentum, which (neglecting centrifugal forces) is

$$-\frac{\partial P}{\partial r} - \frac{1}{r^2} \frac{\partial}{\partial r} (r^2 \tau_{rr}) + \frac{\tau_{\theta\theta} + \tau_{\phi\phi}}{r} = 0 \quad (\text{E3.2-9})$$

Introducing $\pi_{ii} = \tau_{ii} + P$ (no sum)

$$\frac{\pi_{\theta\theta} + \pi_{\phi\phi}}{r} - \frac{1}{r^2} \frac{\partial}{\partial r} (r^2 \pi_{rr}) = 0 \quad (\text{E3.2-10})$$

Upon rearrangement and integration, and taking into account that the negative of the secondary normal stress difference, $\pi_{rr} - \pi_{\theta\theta}$, is a constant (since $\dot{\gamma}_{\theta\phi}$ is constant), and that π_{θ} at $\theta = \pi/2$ (the plate) is a function of the radius, we have

$$[\pi_{\theta\theta}(r) - \pi_{\theta\theta}(R)]_{\theta=\pi/2} = [(\tau_{\phi\phi} - \tau_{\theta\theta}) + 2(\tau_{\theta\theta} - \tau_{rr})] \ln\left(\frac{r}{R}\right) \quad (\text{E3.2-11})$$

The left-hand side of Eq. E3.2-11 can be experimentally evaluated; thus, the quantity in brackets on the right-hand side can be determined.

The normal force on the stationary plate can be expressed as

$$F_N = 2\pi \int_0^R \pi_{\theta\theta} r \, dr - \pi R^2 P_{atm} \quad (\text{E3.2-12})$$

With the help of Eq. E3.2-11 and the relation $P_{atm} = \pi_{rr}(R)$, we obtain, after integration of Eq. E3.2-12, the simple relation for the primary normal stress difference function

$$\tau_{11} - \tau_{22} = \tau_{\phi\phi} - \tau_{\theta\theta} = \frac{-2F_N}{\pi R^2} \quad (\text{E3.2-13})$$

Figure E3.2b shows experimental data for the primary normal stress difference for LDPE.

In summary, and in terms of the viscometric flow notation, we conclude the following about the experimental capabilities of the cone-and-plate viscometric flow:

1. The viscosity function η can be determined with the aid of Eqs. E3.2-6 and E3.2-8.
2. The primary normal stress difference, $\tau_{11} - \tau_{22} = \tau_{\phi\phi} - \tau_{\theta\theta}$, can be calculated through Eq. E3.2-13, and the coefficient Ψ_1 can be calculated from Eq. 3.1-10.
3. The secondary normal stress difference, $\tau_{22} - \tau_{33} = \tau_{\theta\theta} - \tau_{rr}$, can be determined subsequent to the evaluation of $\tau_{11} - \tau_{22}$ using Eq. E3.2-11, and the coefficient Ψ_2 can be calculated from Eq. 3.1-11.

These conditions are subject to the limitation for polymer melts that the applied shear rate $\dot{\gamma} = \Omega/\psi_0$ must be below that which gives rise to fracture in the fluid sample. For solutions of polymers, the upper limit of shear rate (or Ω), however, is one at which the centrifugal forces become important.

Figure E3.2b presents the primary normal stress difference data for LDPE, and Fig. E3.2c presents the primary and secondary normal stress-difference data for a 2.5% polyacrylamide solution, again using a cone-and-plate rheometer.

We note that the primary normal stress coefficient Ψ_1 is positive, whereas the secondary normal stress coefficient Ψ_2 is negative, but with a lot of scatter in the data. It is difficult to measure $(\tau_{22} - \tau_{33})$ and its value is in doubt, but the ratio $-(\tau_{11} - \tau_{22})/(\tau_{22} - \tau_{33})$ appears to be about 0.1.

Bird et al. (24) pointed out a simple method of estimating the primary normal stress difference from viscosity data. The method is approximate, originating with the Goddard-Miller (G-M) (25) constitutive equation (Eq. 3.3-8), and it predicts that

$$\Psi_1(\dot{\gamma}) = \frac{4K}{\pi} \int_0^{\infty} \frac{\eta(\dot{\gamma}) - \eta(\dot{\gamma}')}{(\dot{\gamma}')^2 - \dot{\gamma}^2} d\dot{\gamma}' \quad (\text{3.2-1})$$

where K is an empirical constant. Good fit to data results are obtained, with K equaling about 2 for solutions and 3 for melts.

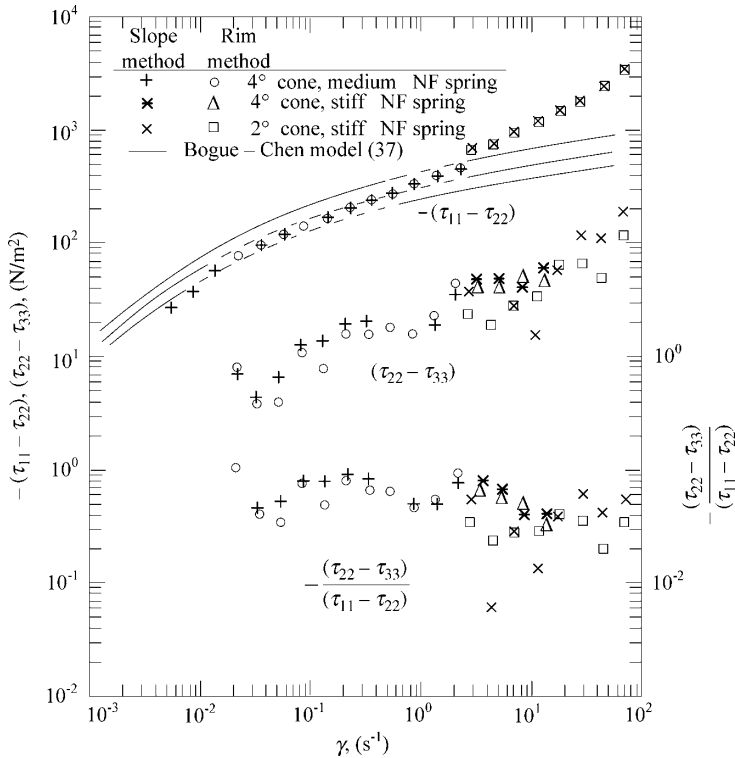


Fig. E3.2c Values for $-(\tau_{11} - \tau_{22})$, $(\tau_{22} - \tau_{33})$ and the ratio $-(\tau_{11} - \tau_{22})/(\tau_{22} - \tau_{33})$ for 2.5% acrylamide solution measured with a cone-and-plate rheometer. [Reprinted with permission from E. B. Christiansen and W. R. Leppard, *Trans. Soc. Rheol.*, **18**, 65 (1974).]

3.3 POLYMER MELT CONSTITUTIVE EQUATIONS BASED ON CONTINUUM MECHANICS

There is a multitude of constitutive equations proposed for polymer melts. However, only a few have been used to solve actual polymer processing problems. Nevertheless, we feel, as we did in the first edition of this book, that it is instructive to trace their origin and to indicate the interrelationship among them. We will do this quantitatively, but without dealing in detail with the mathematical complexities of the subject. The following three families of empirical equations will be discussed:

1. The *generalized Newtonian fluid models* (GNF), which are widely used in polymer processing flow analysis, since they are capable of describing well the very strong shear rate dependence of melts.
2. The *linear viscoelastic models* (LVE), which are widely used to describe the dynamic rheological response of polymer melts below the strain limit of the linear viscoelastic response of polymers. The results obtained are characteristic of and depend on the macromolecular structure. These are widely used as rheology-based structure characterization tools.

3. The *nonlinear viscoelastic models* (VE), which utilize continuum mechanics arguments to cast constitutive equations in coordinate frame-invariant form, thus enabling them to describe all flows: steady and dynamic shear as well as extensional. The objective of the polymer scientists researching these nonlinear VE empirical models is to develop constitutive equations that predict *all* the observed rheological phenomena.

Here we follow the systematic and clear classification and description of the constitutive equations of Bird et al. (14), and we refer the reader who is interested in the detailed development of the subject to that source. There is general agreement that, by and large, the constitutive equations for polymer melts and solutions are special cases of a very general constitutive relation, according to which the stress at any point in a flowing fluid and at any time depends on the entire flow history of the fluid element occupying that point. Because it does not depend on the flow history of adjacent elements, the dependence is “simple,” and the general relation is called the *simple fluid* constitutive equation (26).

One physical restriction, translated into a mathematical requirement, must be satisfied: that is that the simple fluid relation must be “objective,” which means that its predictions should not depend on whether the fluid rotates as a rigid body or deforms. This can be achieved by casting the constitutive equation (expressing its terms) in special frames. One is the *co-rotational* frame, which follows (translates with) each particle and rotates with it. The other is the *co-deformational* frame, which translates, rotates, and deforms with the flowing particles. In either frame, the observer is oblivious to rigid-body rotation. Thus, a constitutive equation cast in either frame is objective or, as it is commonly expressed, “obeys the principle of material objectivity”. Both can be transformed into fixed (laboratory) frame in which the balance equations appear and where experimental results are obtained. The transformations are similar to, but more complex than, those from the substantial frame to the fixed (see Chapter 2). Finally, a co-rotational constitutive equation can be transformed to a co-deformational one.

Goddard (27) expressed the notion of the simple fluid constitutive equation in a co-rotational integral series. The integral series expansion had been used in the co-deformational frame by Green and Rivlin (28) and Coleman and Noll (29). The co-rotational expansion takes the form:

$$\begin{aligned} \tau(x, t) = & - \int_{-\infty}^t G_1(t-t') \dot{\mathbf{\Gamma}}' dt' \\ & - \frac{1}{2} \int_{-\infty}^t \int_{-\infty}^t G_{11}(t-t', t-t'') [\dot{\mathbf{\Gamma}}' \cdot \dot{\mathbf{\Gamma}}'' + \dot{\mathbf{\Gamma}}'' \cdot \dot{\mathbf{\Gamma}}'] dt'' dt' - \dots \end{aligned} \quad (3.3-1)$$

where G_1, G_{11}, \dots are characteristic material functions, $\dot{\mathbf{\Gamma}}$ is the corotating rate of strain (velocity gradient) tensor, t', t'' are integration variables, and t is the present time. Equation 3.3-1 is in an unusable form. There are two alternative routes through which useful constitutive equations can be obtained:

1. Expand $\dot{\Gamma}$ in a Taylor series about $t' = t$

$$\dot{\Gamma}(t, t') = \dot{\gamma}(t) - (t - t') \frac{\mathcal{D}\dot{\gamma}}{\mathcal{D}t} + \dots \quad (3.3-2)$$

where

$$\frac{\mathcal{D}\dot{\gamma}}{\mathcal{D}t} = \frac{\partial\dot{\gamma}}{\partial t} + \{\mathbf{v} \cdot \nabla\dot{\gamma}\} + \frac{1}{2}(\{\boldsymbol{\omega} \cdot \dot{\gamma}\} - \{\dot{\gamma} \cdot \boldsymbol{\omega}\}) \quad (3.3-3)$$

is the co-rotational derivative or *Jaumann* derivative measuring the time rate of change of $\dot{\gamma}$ as measured by an observer who is translating and rotating with the local fluid velocity and vorticity. Keeping only the first two terms of the Taylor series (which means that the flow under consideration is *almost* steady), one can obtain the *second-order fluid* constitutive equation

$$\boldsymbol{\tau} = -\alpha_1 \dot{\gamma} + \alpha_2 \frac{\mathcal{D}\dot{\gamma}}{\mathcal{D}t} - \alpha_{11} \{\dot{\gamma} \cdot \dot{\gamma}\} - \dots \quad (3.3-4)$$

where α_i are constants related to G_1, G_{11}, \dots . For *steady shear flows*, the *Criminale–Ericksen–Filbey* (CEF) constitutive equation can be obtained (30):

$$\boldsymbol{\tau} = -\eta \dot{\gamma} - \left(\frac{1}{2} \Psi_1 + \Psi_2 \right) \{\dot{\gamma} \cdot \dot{\gamma}\} + \frac{1}{2} \Psi_1 \frac{\mathcal{D}\dot{\gamma}}{\mathcal{D}t} \quad (3.3-5)$$

where η, Ψ_1 , and Ψ_2 are the viscosity, first normal stress-difference coefficient, and second normal stress difference coefficient functions, respectively. They are all functions of the magnitude of the rate of strain tensor $\dot{\gamma} = \sqrt{(\dot{\gamma} : \dot{\gamma})}/2$. Because many polymer processing flows are steady shear flows, and because of the physical significance of the material functions η, Ψ_1 , and Ψ_2 , the CEF equation is considered in detail in Example 3.3.

If the normal stress coefficient functions Ψ_1 and Ψ_2 are ignored, the CEF equation reduces to the GNF equation

$$\boldsymbol{\tau} = -\eta \dot{\gamma} \quad (3.3-6)$$

This equation reduces for an incompressible *Newtonian fluid* to Newton's law, which in tensorial form is given by

$$\boldsymbol{\tau} = -\mu \dot{\gamma} \quad (3.3-7)$$

2. If, in Eq. 3.3-1 a single integral term is retained, the *Goddard–Miller* (G–M) constitutive equation is obtained (17, 25):

$$\boldsymbol{\tau} = - \int_{-\infty}^t G(t-t') \dot{\Gamma} dt' \quad (3.3-8)$$

For *small* deformation flows it is evident from Eqs. 3.3-2 and 3.3-3 that $\dot{\Gamma}$ equals $\dot{\gamma}$, thus the G–M equation yields the LVE fluid (14, 28, 29):

$$\boldsymbol{\tau} = - \int_{-\infty}^t G(t-t') \dot{\boldsymbol{\gamma}}(t') dt' \quad (3.3-8a)$$

where $G(t-t')$ is the *relaxation modulus*, which can take specific forms, depending on the LVE “mechanical model” used to simulate the real LVE behavior. For example, if a single Maxwell element, consisting of a “spring” G and a “dashpot” μ in a series is used, the *Maxwell* constitutive equation is obtained

$$\boldsymbol{\tau} + \lambda_0 d\boldsymbol{\tau}/dt = -\eta_0 \dot{\boldsymbol{\gamma}} \quad (3.3-9)$$

where $\lambda_0 = \eta_0/G$. When $\lambda_0 = 0$ ($G \rightarrow \infty$), the Newtonian constitutive equation for an incompressible fluid, Eq. 3.3-7, is obtained.

Including a velocity gradient in the time derivative, we obtain the *Jeffreys model* (31)

$$\boldsymbol{\tau} + \lambda_1 \frac{d}{dt} \boldsymbol{\tau} = -\eta_0 \left(\dot{\boldsymbol{\gamma}} + \lambda_2 \frac{d}{dt} \dot{\boldsymbol{\gamma}} \right) \quad (3.3-10)$$

From the G–M equation, while still in the co-rotational frame, we can choose a specific form of the relaxation modulus. Thus, for a single Maxwell element we can obtain

$$\boldsymbol{\tau} + \lambda_0 \frac{\mathcal{D}\boldsymbol{\tau}}{\mathcal{D}t} = -\eta_0 \dot{\boldsymbol{\gamma}} \quad (3.3-11)$$

This is called the *Zaremba-Fromm-DeWitt* (ZFD) equation.

As stated earlier, the simple fluid concept can be expressed in a series of co-deformational integrals (14, 28, 29)

$$\begin{aligned} \boldsymbol{\tau} = & - \int_{-\infty}^t G_1(t-t') \dot{\boldsymbol{\gamma}}^{[1]'} dt' \\ & - \frac{1}{2} \int_{-\infty}^t \int_{-\infty}^t G_2(t-t', t-t'') \left[\dot{\boldsymbol{\gamma}}^{[1]'} \cdot \dot{\boldsymbol{\gamma}}^{[1]''} + \dot{\boldsymbol{\gamma}}^{[1]''} \cdot \dot{\boldsymbol{\gamma}}^{[1]'} \right] dt'' dt' - \dots \end{aligned} \quad (3.3-12)$$

where G_1, G_2, \dots , are material functions and $\dot{\boldsymbol{\gamma}}^{[1]}$ is the co-deforming rate of strain tensor using covariant differentiation. If contravariant derivatives are used (14)

$$\begin{aligned} \boldsymbol{\tau} = & - \int G^1(t-t') \dot{\boldsymbol{\gamma}}_{[1]}' dt' \\ & - \frac{1}{2} \int_{-\infty}^t \int_{-\infty}^t G^2(t-t', t-t'') \left[\dot{\boldsymbol{\gamma}}_{[1]}' \cdot \dot{\boldsymbol{\gamma}}_{[1]}' + \dot{\boldsymbol{\gamma}}_{[1]}' \cdot \dot{\boldsymbol{\gamma}}_{[1]}' \right] dt'' dt' - \dots \end{aligned} \quad (3.3-13)$$

where G^1, G^2, \dots are material functions and $\dot{\boldsymbol{\gamma}}_{[1]}$ is the co-deforming rate of strain tensor using contravariant differentiation.

As was the case with Eq. 3.3-1, Eqs. 3.3-12 and 3.3-13 are also not usable in their current form. But the same means for making them usable are available (see Ref. 14: Fig. 9.6-1 and Table 9.4-1). Two specific steps to simplify the equation are as follows:

1. For *almost steady flows* one can expand $\dot{\gamma}^{[1]}$ or $\dot{\gamma}_{[1]}$ about $t = t'$ and obtain *second-order* fluid constitution equations in the co-deforming frame. When steady shear flows are considered, the CEF equation is obtained, which, in turn, reduces to the GNF equation for $\Psi_1 = \Psi_2 = 0$ and to a Newtonian equation if, additionally, the viscosity is constant.
2. Setting G_1, G_2, \dots , or G^1, G^2, \dots , equal to zero, Eqs. 3.3-11 and 3.3-12 reduce to G-M-type equations. For example,

$$\boldsymbol{\tau} = - \int_{-\infty}^t G(t-t') \dot{\gamma}_{[1]}' dt' \quad (3.3-14)$$

is the so-called *Oldroyd (32)–Walters (33)–Fredrickson (34)* equation. This equation, when integrated by parts, yields the *Lodge rubber-like liquid* equation (23)

$$\boldsymbol{\tau} = \int_{-\infty}^t M(t-t') \boldsymbol{\gamma}_{[0]}' dt' \quad (3.3-15)$$

where $M(t-t') = dG(t-t')/dt'$ and $\boldsymbol{\gamma}_{[0]}$ is the strain tensor in a co-deforming frame using contravariant differentiation.

For small deformations, Eq. 3.3-14 reduces to the LVE Eqs. 3.3-9 and 3.3-10 ($\dot{\gamma}_{[1]}' = \dot{\gamma}$). On the other hand, for large deformations, while still in the co-deforming frame, one can use a particular linear viscoelastic model to represent $G(t-t')$ in Eq. 3.3-14. If, as before, a single Maxwell element is used, one can obtain the following analog to Eq. 3.3-11

$$\boldsymbol{\tau} + \lambda_0 \boldsymbol{\tau}_{(1)} = -\eta_0 \dot{\boldsymbol{\gamma}} \quad (3.3-16)$$

where $\boldsymbol{\tau}_{(1)}$ is a co-deforming time derivative (14) equal to

$$\boldsymbol{\tau}_{(1)} = \frac{D}{Dt} \boldsymbol{\tau} - \left\{ (\nabla \mathbf{v})^\dagger \cdot \boldsymbol{\tau} + \boldsymbol{\tau} \cdot (\nabla \mathbf{v}) \right\} \quad (3.3-17)$$

Together with Eq. 3.3-17, Eq. 3.3-16 is the *White–Metzner* constitutive equation, which has been used frequently as a nonlinear viscoelastic model. Of course, for small deformations, $\boldsymbol{\tau}_{(1)} = d\boldsymbol{\tau}/dt$, and the single Maxwell fluid equation (Eq. 3.3-9) is obtained.

Finally, a number of commonly used constitutive equations are derived from Eq. 3.3-13 by specifying G^1, G^2, \dots instead of specifying only G^1 and setting G^2, \dots equal to zero. Moreover, in these equations, M_i are allowed to be functions of the invariants of the strain or rate-of-strain tensors, since there is experimental evidence supporting this dependence (35). Examples of such usable integral co-deformational constitutive equations are:

$$\boldsymbol{\tau} = + \int_{-\infty}^t \left[M_1(t-t', I_{\boldsymbol{\gamma}'_{[0]}}, II_{\boldsymbol{\gamma}'_{[0]}}) \boldsymbol{\gamma}_{[0]}' + M_2(t-t', I_{\boldsymbol{\gamma}'_{[0]}}, II_{\boldsymbol{\gamma}'_{[0]}}) \left\{ \boldsymbol{\gamma}_{[0]}' \cdot \boldsymbol{\gamma}_{[0]}' \right\} \right] dt' \quad (3.3-18)$$

which is the *Bernstein–Kearsley–Zappas* (BKZ) (36) constitutive equation, and

$$\boldsymbol{\tau} = + \int_{-\infty}^t M(t-t', II_{\dot{\boldsymbol{\gamma}}}(t)) \left[\left(1 + \frac{\epsilon}{2} \right) \boldsymbol{\gamma}_{[0]}' - \frac{\epsilon}{2} \boldsymbol{\gamma}_{[0]}'^2 \right] dt' \quad (3.3-19)$$

which is the *Bogue* or *Chen-Bogue* (37) and *Bird-Carreau* (38) constitutive equation, depending on the representation of the dependence of M on $II_{\dot{\gamma}}$; ε is a constant.

We have tried to give a quick glimpse of the interrelationships among some commonly used constitutive equations for polymer melts and solutions. None predicts quantitatively the entire spectrum of the rheological behavior of these materials. Some are better than others, becoming more powerful by utilizing more detailed and realistic molecular models. These, however, are more complex to use in connection with the equation of motion. Table 3.1 summarizes the predictive abilities of some of the foregoing, as well as other constitutive equations.

In examples 3.3, 3.4 and 3.5 we discuss three of the models listed above: the LVE, some members of the GNF family and the CEF; the first because it reveals the viscoelastic nature of polymer melts; the second because, in its various specific forms, it is widely used in polymer processing; and the third because of its ability to predict normal stress differences in steady shear flows.

Example 3.3 Small Amplitude Oscillatory Motion of a Linear Viscoelastic Body

We wish to derive the steady state response of a linear viscoelastic body to an externally applied sinusoidal shear strain (dynamic testing) using the constitutive Eq. 3.3-8, which for this viscometric flow reduces to

$$\tau(t) = - \int_{-\infty}^t G(t-t') \frac{d\gamma}{dt'} dt' \quad (\text{E3.3-1})$$

and

$$\frac{d\gamma}{dt'} = \gamma_0 \omega \cos \omega t' \quad (\text{E3.3-2})$$

Let the linear viscoelastic body be represented by a continuous spectrum of relaxation times, that is,

$$G(t-t') = \int_{-\infty}^{+\infty} H(\ln \lambda) e^{-(t-t')/\lambda} d \ln \lambda \quad (\text{E3.3-3})$$

Substituting in the constitutive equation and integrating, we have

$$\begin{aligned} \tau(t) &= - \int_{-\infty}^t \left[\int_{-\infty}^{\infty} H(\ln \lambda) e^{-t/\lambda} e^{+t'/\lambda} d \ln \lambda \right] \gamma_0 \omega \cos \omega t' dt' \\ &= -\omega \gamma_0 \int_{-\infty}^{\infty} H(\ln \lambda) e^{-t/\lambda} \left[\int_{-\infty}^t e^{t'/\lambda} \cos \omega t' dt' \right] d \ln \lambda \\ &= -\gamma_0 \int_{-\infty}^{\infty} \frac{H(\ln \lambda)}{1 + \omega^2 \lambda^2} [\omega \lambda \cos \omega t + \omega^2 \lambda^2 \sin \omega t] d(\ln \lambda) \\ &= -\gamma_0 \left[\int_{-\infty}^{\infty} \frac{H(\ln \lambda) \omega^2 \lambda^2}{1 + \omega^2 \lambda^2} d(\ln \lambda) \right] \sin \omega t \\ &\quad - \gamma_0 \left[\int_{-\infty}^{\infty} \frac{H(\ln \lambda) \omega \lambda}{1 + \omega^2 \lambda^2} d(\ln \lambda) \right] \cos \omega t \end{aligned} \quad (\text{E3.3-4})$$

TABLE 3.1 Selected Constitutive Equations that Have Been Used for Polymer Melts, and Comments on Their Predictive Abilities^a

Equation	$\eta(\dot{\gamma})$	$\Psi_1(\dot{\gamma}), \Psi_2(\dot{\gamma})$	Stress Overshoot	VE Response
Newtonian fluid (3.3-7)	Constant	Zero	No	No
All GNF fluids (Section 3.3)	$\Psi(\dot{\gamma})$ fit depends on model	Zero	No	No
LVE fluids (3.3-8a)	Constant	Zero	No	Predicts small deformation <i>linear</i> response
G-M (3.3-8)	Good fit can be obtained	$\Psi_2 = -0.5\Psi_1; \Psi_i = f(\dot{\gamma})$ (3.2-1)	Yes; followed by spurious oscillations	Predicts nonlinear response in terms of $G(t-t')$ determined from LVE
ZFD (3.3-11)	Abrupt drop for single element; better fit for several λ_{0i}, η_{0i}	$\Psi_2 = -0.5\Psi_1; \Psi_i = f(\dot{\gamma})$	Yes, followed by spurious oscillations	Yes. The pairs $\eta(\dot{\gamma}), \eta'(\omega)$ and $\frac{1}{2}\Psi_1(\dot{\gamma}), \eta''(\omega)$ are identical; semiquantitatively correct
Second-order fluids (3.3-4)	Constant	Ψ_i are constant and related to each other	No	No
CEF fluids (3.3-5)	$\eta(\dot{\gamma})$ unspecified	$\Psi_i(\dot{\gamma})$ unspecified	No	No
Lodge rubberlike liquid (3.3-15)	Constant	$\Psi_1 = \text{constant}; \Psi_2 = 0$	No; predicts elongational stress growth $\eta^+(t, \dot{\epsilon})$	Yes
White-Metzner (3.3-16); (3.3-17)	Constant	$\Psi_1 = \text{constant}; \Psi_2 = 0$	No	Yes
BKZ (3.3-18)	Predicts $\eta(\dot{\gamma})$	$\Psi_1 = f(\dot{\gamma})$ and related to $\eta(\dot{\gamma})$; this relationship tests out semiquantitatively	Yes	Yes
Bogue (Bird-Carreau) (3.3-19)	Good fit; depends on model for M	Good fit; depends on model for M	Yes	Yes

^a For more details on the predictive abilities of the constitutive equations listed, see Ref. 14.

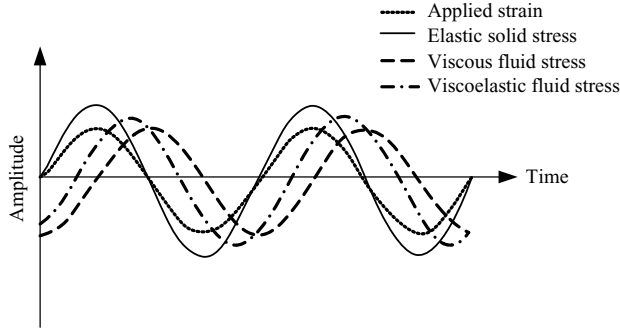


Fig. E3.3 The schematic stress response of elastic, a viscous, and a viscoelastic body to a sinusoidally applied strain.

Thus, according to the result just given, the response of a linear viscoelastic body to a sinusoidal strain (a) lags in time behind the applied strain, and (b) is composed of purely elastic and purely viscous parts. Figure E3.3 illustrates these features.

Furthermore, it is useful to define the following quantities associated with dynamic mechanical testing:

- (a) The in-phase or elastic dynamic modulus

$$G'(\omega) = \int_{-\infty}^{+\infty} \frac{H(\ln \lambda) \omega^2 \lambda^2}{1 + \omega^2 \lambda^2} d(\ln \lambda) \quad (\text{E3.3-5})$$

- (b) The out-of-phase or loss dynamic modulus

$$G''(\omega) = \int_{-\infty}^{+\infty} \frac{H(\ln \lambda) \omega \lambda}{1 + \omega^2 \lambda^2} d(\ln \lambda) \quad (\text{E3.3-6})$$

- (c) The loss tangent or dissipation factor; the ratio of the mechanical energy dissipated to that stored per cycle

$$\tan \delta = \frac{G''}{G'} \quad (\text{E3.3-7})$$

Note that since in this case, the Deborah number, $De = \lambda\omega$, the moduli and the loss tangent, G' , G'' , $\tan \delta$, are *functions of the Deborah number*.

The moduli can be expressed in terms of the *discrete* spectrum of relaxation times given by

$$G(t - t') = \sum_{i=1}^{N_1} G_i e^{-(t-t')/\lambda_i} \quad (\text{E3.3-8})$$

as

$$G' = \sum_{i=1}^{N_1} \frac{G_i \omega \lambda_i^2}{1 + (\omega \lambda_i)^2} \quad (\text{E3.3-9})$$

and

$$G'' = \sum_{i=1}^{N_1} \frac{G_i \omega \lambda_i}{1 + (\omega \lambda_i)^2} \quad (\text{E3.3-10})$$

GNF-based Constitutive Equations

As was pointed out before, the GNF is the generic expression for a whole family of empirical, semiempirical, or molecular model-based equations that were proposed to account for the non-Newtonian, shear-thinning behavior of polymer melts that take the form

$$\boldsymbol{\tau} = -\eta\dot{\boldsymbol{\gamma}} \quad (3.3-20)$$

GNF-based constitutive equations differ in the specific form that the shear rate dependence of the viscosity, $\eta(\dot{\boldsymbol{\gamma}})$, is expressed, but they all share the requirement that the non-Newtonian viscosity $\eta(\dot{\boldsymbol{\gamma}})$ be a function of only the three scalar invariants of the rate of strain tensor. Since polymer melts are essentially incompressible, the first invariant, $I_{\dot{\boldsymbol{\gamma}}} = 0$, and for steady shear flows since $v_1 = f(x_2)$, and $v_2 = v_3 = 0$ the third invariant, $III_{\dot{\boldsymbol{\gamma}}} = 0$, and therefore the non-Newtonian viscosity can only be a function of the second invariant $\eta(\dot{\boldsymbol{\gamma}}) = f(II_{\dot{\boldsymbol{\gamma}}})$. In practice, this functionality is expressed via the *magnitude* of $\dot{\boldsymbol{\gamma}}$, and is given by

$$\dot{\boldsymbol{\gamma}} = \sqrt{\frac{1}{2}II_{\dot{\boldsymbol{\gamma}}}} \quad (3.3-21)$$

For viscometric flows, $II_{\dot{\boldsymbol{\gamma}}} = 2\dot{\gamma}_{12}^2$, and thus the magnitude of $\dot{\boldsymbol{\gamma}}$ is $\dot{\boldsymbol{\gamma}} = |\dot{\gamma}_{12}|$, or the absolute value of the shear rate.

There are numerous fluid models or empirical constitutive equations that comply with the GNF fluid assumptions that were proposed in the literature. They vary in form and in the number of parameters that have to be determined by fitting them to experimental results. Rheological flow curves of non-Newtonian fluids and polymer melts generally exhibit a Newtonian range in the low shear rate range, followed by a broad range of shear-thinning viscosity, and ending in an upper Newtonian range (though the upper range is hardly relevant to polymer melts because of excessive heat generation and the possibility of degradation in this range). These empirical equations have two uses: the primary use is to insert them into the equation of motion to obtain an analytical solution to real processing flow problems. The more complex the empirical model is, the more difficult it is to reach analytical solutions, but even the simplest one converts the equation of motion into a nonlinear set of differential equations as compared to the linear Newtonian equivalent. The second use is to record in a simple way (with the minimum number of required parameters) the experimentally obtained results. This use simply converts a table of results to an algebraic equation. For numerical solutions, such as finite-element methods (FEM), having a more complex empirical equation does not add to the mathematical complexity of the solution. We now review a few of the commonly used empirical equations with an increasing number of parameters.

The Power Law Model

The Power Law model (excluding temperature dependence) is a two-parameter empirical model proposed by Ostwald and de Waele (39). It is based on the experimental observation that by plotting $\ln \eta(\dot{\boldsymbol{\gamma}})$ vs. $\ln(\dot{\boldsymbol{\gamma}})$, a straight line is obtained in the high shear rate region for

many non-Newtonian fluids, including most polymer melts. This suggests the following functional relationship between non-Newtonian viscosity and shear rate

$$\eta(\dot{\gamma}) = m\dot{\gamma}^{n-1} \quad (3.3-22)$$

where $m(\text{Ns}^n/\text{m}^2)$ and the dimensionless n are parameters, commonly called the consistency and Power Law index, respectively. Thus a Power Law constitutive equation can be arrived at:

$$\boldsymbol{\tau} = -m\dot{\gamma}^{n-1} \dot{\boldsymbol{\gamma}} = -m \left[\sqrt{\frac{1}{2}(\dot{\boldsymbol{\gamma}} : \dot{\boldsymbol{\gamma}})} \right]^{n-1} \dot{\boldsymbol{\gamma}} \quad (3.3-23)$$

The parameter m is a sensitive function of temperature, obeying an Arrhenius-type relationship

$$m = m_0 \exp \left[\frac{\Delta E}{R} \left(\frac{1}{T} - \frac{1}{T_0} \right) \right] \quad (3.3-24)$$

where m_0 is the value of m at T_0 , and ΔE is the flow activation energy. For mathematical convenience, a simpler relationship is frequently used

$$m = m_0 e^{-a(T-T_0)} \quad (3.3-25)$$

where a is an empirical parameter. Equation 3.3-25 holds well over relatively narrow temperature ranges.

The following comments can be made about the Power Law equation and the viscosity or “flow curve,” as, for example, that shown in Fig. 3.5:

- The upper limit of the Newtonian plateau is dependent on \overline{M}_w and the melt temperature. Commonly, it is roughly in the region $\dot{\gamma} = 10^{-2}\text{s}^{-1}$. Low viscosity fiber-forming Nylon and polyethylene terephthalate (PET) are important exceptions, as their Newtonian plateau extends to higher shear rates.
- This upper limit decreases with increasing \overline{M}_w , with increasing molecular weight distribution (MWD) at constant \overline{M}_w , and with decreasing melt temperature. On physical grounds, it is considered to terminate roughly where the Deborah number reaches unity.
- If the Power Law equation is used in pressure flows, where $0 \leq \dot{\gamma} \leq \dot{\gamma}_{\max}$, an error is introduced in the very low shear rate Newtonian region. In flow rate computation, however, this is not a very significant (40).
- The transition from the Newtonian plateau to the Power Law region is sharp for monodispersed polymer melts and broad for polydispersed melts (see Fig. 3.5).
- The slope of the viscosity curve in the Power Law region is not exactly constant. The flow index n decreases with increasing shear rate. Thus the Power Law equation holds exactly only for limited ranges of shear rate, for a given value of n .

In conclusion, despite its limitations, the Power Law model is one of the most widely used empirical relations in polymer fluid dynamics, and it gives surprisingly good results, even for nonviscometric and slightly transient flows.

The Ellis Model

The Ellis model (41), is a three-parameter model, in which the non-Newtonian viscosity is a function of the absolute value of the shear stress tensor, τ ,

$$\eta(\tau) = \frac{\eta_0}{1 + (\tau/\tau_{1/2})^{\alpha-1}} \quad (3.3-26)$$

yielding the following constitutive equation

$$\boldsymbol{\tau} = -\eta(\tau)\dot{\boldsymbol{\gamma}} = -\left[\frac{\eta_0}{1 + (\tau/\tau_{1/2})^{\alpha-1}} \right] \dot{\boldsymbol{\gamma}} \quad (3.3-27)$$

where τ is related to the second invariant of the stress tensor as follows

$$\tau = \sqrt{\frac{1}{2} II_{\boldsymbol{\tau}}} \quad (3.3-28)$$

The three parameters are α , which is the slope of the curve $\log(\eta/\eta_0 - 1)$ vs. $\log(\tau/\tau_{1/2})$; $\tau_{1/2}$, which is the shear stress value, where $\eta = \eta_0/2$; and η_0 , which is the zero shear viscosity. Thus the Ellis model matches the low shear Newtonian plateau and the shear-thinning region.

The Cross Model

The Cross and the temperature-dependent Cross-WLF model (42) is an often used GNF-type model accounting for, like the Ellis and Carreau fluids for the viscosity at both low and high shear rates,

$$\eta(\dot{\gamma}, T, P) = \frac{\eta_0(T_1)}{1 + \left[\frac{\eta_0(T)}{\tau^*} \dot{\gamma} \right]^{n-1}} \quad (3.3-29)$$

where n denotes the Power Law index; τ^* the critical stress level at which η transitions from the Newtonian plateau, η_0 , to the Power Law regime; and $\dot{\gamma}$ is the shear rate. If an Arrhenius viscosity temperature dependence is assumed, then a shift factor a_T is defined as

$$\log a_T = \frac{\Delta E}{R} \left(\frac{1}{T_1} - \frac{1}{T_2} \right) \quad (3.3-30)$$

Given the value of the activation energy, ΔE , a master curve $\eta(T, \dot{\gamma})$ can be constructed, and Eq. 3.3-30 becomes

$$\eta = \left[\frac{\eta_0}{1 + \left(\frac{\eta_0}{\tau^*} \frac{\dot{\gamma}}{a_T} \right)^{1-n}} \right] \frac{1}{a_T} \quad (3.3-31)$$

This relation holds well for semicrystalline polymers; for amorphous polymers, it holds for $T > T_g + 100^\circ\text{C}$. Below this region free volume effects predominate necessitating the use of the Arrhenius–WLF equation

$$\log a_T = \frac{\Delta E}{R} \left(\frac{1}{T_1} - \frac{1}{T_2} \right) - b_1 \left(\frac{T_1 - T_2}{b_2 + T_2 - T_1} \right) \quad (3.3-32)$$

The parameters b_1 and b_2 have to be experimentally determined.

The Carreau Model

The Carreau model (43) is a four-parameter model that accounts for the both the low shear rate Newtonian region and the high shear rate upper Newtonian region that is expected (although polymer melts do not reach this region, because of excessive heating and degradation at these high shear rate values):

$$\frac{\eta(\dot{\gamma}) - \eta_\infty}{\eta_0 - \eta_\infty} = \frac{1}{\left[1 + (\lambda\dot{\gamma})^2 \right]^{(1-n)/2}} \quad (3.3-33)$$

where η_0 is the zero shear rate viscosity, η_∞ is the infinite shear-rate viscosity, λ is a parameter with units of (relaxation) time, and n is a dimensionless parameter. Note that the shear-thinning nature of melts is accounted for by the parameter n ($n < 1$), as was the case with the Power Law model. The product $\lambda\dot{\gamma} = \text{De}$ reflects the viscoelastic nature of the melt, which at low De number values $\text{De} \rightarrow 0$ become Newtonian. As De is increased, melts become less viscous and more elastic.

There are numerous other GNF models, such as the Casson model (used in food rheology), the Ellis, the Powell–Eyring model, and the Reiner–Phillippoff model. These are reviewed in the literature. In Appendix A we list the parameters of the Power Law, the Carreau, and the Cross constitutive equations for common polymers evaluated using oscillatory and capillary flow viscometry.

The Bingham Fluid

The Bingham fluid is a two-parameter, somewhat different model from the previous rheological models, in that it has a final yield stress below which there is no flow, whereas above it, the stress is a linear function of the rate of strain

$$\begin{aligned} \eta &= \infty & \tau &\leq \tau_y \\ \eta(\dot{\gamma}) &= \mu_0 + \left(\frac{\tau_y}{\dot{\gamma}} \right) & \tau &> \tau_y \end{aligned} \quad (3.3-34)$$

where τ_y is the yield stress, and μ_0 is the Newtonian viscosity for vanishing yield stress. A typical Bingham plastic fluid is ketchup, but many other fluids have this property, such as “no drip” paints, pastes, and slurries.

Example 3.4 Flow of a Power Law Fluid in Tubes For an isothermal, laminar, fully developed steady pressure flow of an incompressible Power Law model fluid in a horizontal tube without slip, we wish to derive (a) the velocity profile and (b) the flow rate.

(a) For a tubular flow we use the cylindrical coordinate system. Since flow is isothermal and the fluid incompressible, the equation of motion and continuity, together with the

constitutive equation, fully describe the flow. On the basis of symmetry, we assume that there is no θ dependence and that $v_\theta = 0$. Fully developed flow implies that $\partial v_z / \partial z = 0$, and hence the equation of continuity reduces to

$$\frac{\partial}{\partial r}(rv_r) \quad (\text{E3.4-1})$$

which can be integrated to give $rv_r = C$, where C is a constant. Since $v_r = 0$ at the tube radius, we conclude that $C = 0$, and therefore $v_r = 0$. Hence, the only nonvanishing velocity component is v_z , which is a function only of r . Turning to the equation of motion in Table 2.2, the three components of the equation therefore reduce to

$$\begin{aligned} \frac{\partial P}{\partial r} &= 0 \\ \frac{\partial P}{\partial \theta} &= 0 \\ \frac{\partial P}{\partial z} &= -\frac{1}{r} \frac{\partial}{\partial r}(r\tau_{rz}) \end{aligned} \quad (\text{E3.4-2})$$

Clearly, the left-hand side of the equation is a function only of z , since $P \neq f(r, \theta)$, whereas the right-hand side of the last equation is a function only of r ; therefore, they both must equal a constant, indicating that the pressure gradient is constant along the tube and that partial differentials can be replaced by ordinary differentials. Following integration, we get

$$\tau_{rz} = -\left(\frac{r}{2}\right) \frac{dP}{dz} + C_1 \quad (\text{E3.4-3})$$

where C_1 is an integration constant. The constant C_1 is zero, because at $r = 0$, where the velocity has a maximum and the gradient is zero, the shear stress must vanish as well. Thus the shear stress distribution is given by

$$\tau_{rz} = -\left(\frac{r}{2}\right) \frac{dP}{dz} \quad (\text{E3.4-4})$$

indicating that the shear stress increases linearly from a value of zero at the center to a maximum at the wall. The only nonvanishing velocity gradient in this flow is dv_z/dr , and therefore the rate of deformation tensor of Table 2.3 reduces to

$$\dot{\boldsymbol{\gamma}} = \begin{pmatrix} 0 & 0 & \frac{dv_z}{dr} \\ 0 & 0 & 0 \\ \frac{dv_z}{dr} & 0 & 0 \end{pmatrix} \quad (\text{E3.4-5})$$

and the Power Law constitutive equation reduces to

$$\tau_{rz} = -m\dot{\gamma}^{n-1} \frac{dv_z}{dr} \quad (\text{E3.4-6})$$

However, $\dot{\gamma}$ in Eq. E3.4-56 is obtained from Eq. E3.4-5 and given by

$$\dot{\gamma} = \sqrt{\frac{1}{2}(\dot{\boldsymbol{\gamma}} : \dot{\boldsymbol{\gamma}})} = \sqrt{\left(\frac{dv_z}{dr}\right)^2} = \left|\frac{dv_z}{dr}\right| \quad (\text{E3.4-7})$$

where the scalar product of the tensor $\dot{\boldsymbol{\gamma}}$ is $2(dv_z/dr)^2$. By substituting Eq. E3.4-7 into Eq. E3.4-6, we get

$$\tau_{rz} = -m \left| \frac{dv_z}{dr} \right|^{n-1} \frac{dv_z}{dr} \quad (\text{E3.4-8})$$

Note that shear rate $\dot{\gamma}$ is the magnitude of the tensor $\dot{\boldsymbol{\gamma}}$, and therefore it must always be positive. Thus we maintain the absolute-value sign over the term that reflects the shear dependence of the viscosity.

Combining Eq. E3.4-8 with Eq. E3.4-4 yields

$$m \left| \frac{dv_z}{dr} \right|^{n-1} \frac{dv_z}{dr} = \frac{r}{2} \left(\frac{dP}{dz} \right) \quad (\text{E3.4-9})$$

In tubular flow for all r , $dv_z/dr < 0$; therefore

$$\left| \frac{dv_z}{dr} \right| = -\frac{dv_z}{dr} \quad (\text{E3.4-10})$$

and Eq. E3.4-9 can be written as

$$-\frac{dv_z}{dr} = \left(-\frac{r}{2mL} \frac{dP}{dz} \right)^s \quad (\text{E3.4-11})$$

where $s = 1/n$. Note that the pressure gradient in the preceding equation is negative, and therefore the term in parenthesis is positive. This equation can be integrated with boundary condition $v_z(R) = 0$ to give

$$v_z(r) = \left(\frac{R}{s+1} \right) \left[-\frac{R}{2m} \frac{dP}{dz} \right]^s \left[1 - \left(\frac{r}{R} \right)^{s+1} \right] \quad (\text{E3.4-12})$$

For Newtonian fluids with $s = 1$, this equation reduces to the classic parabolic profile.

(b) The volumetric flow rate is obtained by integrating Eq. E3.4-12.

$$\begin{aligned} Q &= \int_0^R 2\pi r v_z dr = \frac{\pi R^3}{s+3} \left[-\frac{R}{2m} \frac{dP}{dz} \right]^s \\ &= \frac{\pi R^3}{s+3} \left[-\frac{R}{2m} \frac{\Delta P}{L} \right]^s \end{aligned} \quad (\text{E3.4-13})$$

where $\Delta P = P_0 - P_L$, P_0 is the pressure at $z = 0$, and P_L at $z = L$. Equation E3.4-13 is the Power Law equivalent to the celebrated Newtonian Hagen–Poiseuille equation, with $s = 1$ and $m = \mu$

$$Q = \frac{\pi R^4}{8\mu L} (P_0 - P_L) \quad (\text{E3.4-14})$$

Example 3.5 The CEF Equation in Steady, Fully Developed Flow in Tubes The viscosity functions in both the Power Law model GNF fluid and the CEF fluid are expected to be

the same. Therefore, assuming that the velocity field of a CEF fluid, in steady viscometric flow, will be the same as that of a purely viscous fluid, we can calculate the stress field needed to maintain such a flow. In this Example, we calculate the stress field needed to maintain the pressure-driven tube flow discussed in Example 3.4.

In Section 3.3 we discussed the origins of the CEF equation

$$\boldsymbol{\tau} = -\eta\dot{\boldsymbol{\gamma}} - \left(\frac{1}{2}\Psi_1 + \Psi_2\right)\{\dot{\boldsymbol{\gamma}} \cdot \dot{\boldsymbol{\gamma}}\} + \frac{1}{2}\Psi_1 \frac{\mathcal{D}\dot{\boldsymbol{\gamma}}}{\mathcal{D}t} \quad (\text{E3.5-1})$$

where the material functions η , Ψ_1 , and Ψ_2 are functions of shear rate, and they hold for steady shear flow and account for the shear-thinning viscosity and for normal stresses.

Our starting point is the rate-of-deformation tensor given in Eq. E3.4-5

$$\dot{\boldsymbol{\gamma}} = \begin{pmatrix} 0 & 0 & \dot{\gamma}_{rz} \\ 0 & 0 & 0 \\ \dot{\gamma}_{rz} & 0 & 0 \end{pmatrix} \quad (\text{E3.5-2})$$

To calculate the stresses generated by the CEF fluid, we need to calculate the quantities $\dot{\boldsymbol{\gamma}} \cdot \dot{\boldsymbol{\gamma}}$ and $\mathcal{D}\dot{\boldsymbol{\gamma}}/\mathcal{D}t$ in Eq. E3.5-1. The first one is a simple matrix multiplication, resulting in

$$\{\dot{\boldsymbol{\gamma}} \cdot \dot{\boldsymbol{\gamma}}\} = \begin{pmatrix} \dot{\gamma}_{rz}^2 & 0 & 0 \\ 0 & 0 & 0 \\ 0 & 0 & \dot{\gamma}_{rz}^2 \end{pmatrix} \quad (\text{E3.5-3})$$

Next we calculate

$$\frac{\mathcal{D}}{\mathcal{D}t}\dot{\boldsymbol{\gamma}} = \frac{\partial}{\partial t}\dot{\boldsymbol{\gamma}} + \{\mathbf{v} \cdot \nabla\}\dot{\boldsymbol{\gamma}} + \frac{1}{2}(\{\boldsymbol{\omega} \cdot \dot{\boldsymbol{\gamma}}\} - \{\dot{\boldsymbol{\gamma}} \cdot \boldsymbol{\omega}\}) \quad (\text{E3.5-4})$$

The first term on the right-hand side is zero because the flow is steady. The components of the second term, $\mathbf{v} \cdot \nabla\dot{\boldsymbol{\gamma}}$, we obtain from Table 3.2

$$\begin{aligned} (\mathbf{v} \cdot \nabla\dot{\boldsymbol{\gamma}})_{rz} &= (\mathbf{v} \cdot \nabla)\dot{\gamma}_{rz} - \frac{v_\theta}{r}\dot{\gamma}_{\theta z} \\ &= \left(v_r \frac{\partial}{\partial r} + \frac{v_\theta}{r} \frac{\partial}{\partial \theta} + v_z \frac{\partial}{\partial z}\right)\dot{\gamma}_{rz} - \frac{v_\theta}{r}\dot{\gamma}_{\theta z} \end{aligned} \quad (\text{E3.5-5})$$

Since $v_r = 0$, $v_\theta = 0$, and $\partial v_z/\partial z = 0$ for a developed flow, the term $(\mathbf{v} \cdot \nabla\dot{\boldsymbol{\gamma}})_{rz} = 0$. Similarly, we evaluate all other components and conclude that $\mathbf{v} \cdot \nabla\dot{\boldsymbol{\gamma}} = 0$. The vorticity tensor $\boldsymbol{\omega}$ can be obtained for this flow from Table 3.3

$$\boldsymbol{\omega} = \nabla\mathbf{v} - (\nabla\mathbf{v})^\dagger = \begin{pmatrix} 0 & 0 & \dot{\gamma}_{rz} \\ 0 & 0 & 0 \\ -\dot{\gamma}_{rz} & 0 & 0 \end{pmatrix} \quad (\text{E3.5-6})$$

Next, with Eqs. E3.5-2 and E3.5-6 we derive

$$\{\boldsymbol{\omega} \cdot \dot{\boldsymbol{\gamma}}\} = \begin{pmatrix} 0 & 0 & \dot{\gamma}_{rz} \\ 0 & 0 & 0 \\ -\dot{\gamma}_{rz} & 0 & 0 \end{pmatrix} \begin{pmatrix} 0 & 0 & \dot{\gamma}_{rz} \\ 0 & 0 & 0 \\ \dot{\gamma}_{rz} & 0 & 0 \end{pmatrix} = \begin{pmatrix} \dot{\gamma}_{rz}^2 & 0 & 0 \\ 0 & 0 & 0 \\ 0 & 0 & -\dot{\gamma}_{rz}^2 \end{pmatrix} \quad (\text{E3.5-7})$$

TABLE 3.2 The Components of $(\mathbf{v} \cdot \nabla \dot{\boldsymbol{\gamma}})$ in Three Coordinate Systems

Rectangular Coordinates^a (x, y, z)

$$\begin{aligned} (\mathbf{v} \cdot \nabla \dot{\boldsymbol{\gamma}})_{xx} &= (\mathbf{v} \cdot \nabla) \dot{\gamma}_{xx} & (\mathbf{v} \cdot \nabla \dot{\boldsymbol{\gamma}})_{xy} &= (\mathbf{v} \cdot \nabla \dot{\boldsymbol{\gamma}})_{yx} = (\mathbf{v} \cdot \nabla) \dot{\gamma}_{xy} \\ (\mathbf{v} \cdot \nabla \dot{\boldsymbol{\gamma}})_{yy} &= (\mathbf{v} \cdot \nabla) \dot{\gamma}_{yy} & (\mathbf{v} \cdot \nabla \dot{\boldsymbol{\gamma}})_{yz} &= (\mathbf{v} \cdot \nabla \dot{\boldsymbol{\gamma}})_{zy} = (\mathbf{v} \cdot \nabla) \dot{\gamma}_{zy} \\ (\mathbf{v} \cdot \nabla \dot{\boldsymbol{\gamma}})_{zz} &= (\mathbf{v} \cdot \nabla) \dot{\gamma}_{zz} & (\mathbf{v} \cdot \nabla \dot{\boldsymbol{\gamma}})_{zx} &= (\mathbf{v} \cdot \nabla \dot{\boldsymbol{\gamma}})_{xz} = (\mathbf{v} \cdot \nabla) \dot{\gamma}_{xz} \end{aligned}$$

Cylindrical Coordinates^b (r, θ, z)

$$\begin{aligned} (\mathbf{v} \cdot \nabla \dot{\boldsymbol{\gamma}})_{rr} &= (\mathbf{v} \cdot \nabla) \dot{\gamma}_{rr} - \frac{v_\theta}{r} (\dot{\gamma}_{r\theta} + \dot{\gamma}_{\theta r}) \\ (\mathbf{v} \cdot \nabla \dot{\boldsymbol{\gamma}})_{\theta\theta} &= (\mathbf{v} \cdot \nabla) \dot{\gamma}_{\theta\theta} + \frac{v_\theta}{r} (\dot{\gamma}_{r\theta} + \dot{\gamma}_{\theta r}) \\ (\mathbf{v} \cdot \nabla \dot{\boldsymbol{\gamma}})_{zz} &= (\mathbf{v} \cdot \nabla) \dot{\gamma}_{zz} \\ (\mathbf{v} \cdot \nabla \dot{\boldsymbol{\gamma}})_{r\theta} &= (\mathbf{v} \cdot \nabla \dot{\boldsymbol{\gamma}})_{\theta r} = (\mathbf{v} \cdot \nabla) \dot{\gamma}_{\theta r} + \frac{v_\theta}{r} (\dot{\gamma}_{rr} - \dot{\gamma}_{\theta\theta}) \\ (\mathbf{v} \cdot \nabla \dot{\boldsymbol{\gamma}})_{\theta z} &= (\mathbf{v} \cdot \nabla \dot{\boldsymbol{\gamma}})_{z\theta} = (\mathbf{v} \cdot \nabla) \dot{\gamma}_{\theta z} + \frac{v_\theta}{r} \dot{\gamma}_{rz} \\ (\mathbf{v} \cdot \nabla \dot{\boldsymbol{\gamma}})_{rz} &= (\mathbf{v} \cdot \nabla \dot{\boldsymbol{\gamma}})_{zr} = (\mathbf{v} \cdot \nabla) \dot{\gamma}_{rz} - \frac{v_\theta}{r} \dot{\gamma}_{\theta z} \end{aligned}$$

Spherical Coordinates^c (r, θ, ϕ)

$$\begin{aligned} (\mathbf{v} \cdot \nabla \dot{\boldsymbol{\gamma}})_{rr} &= (\mathbf{v} \cdot \nabla) \dot{\gamma}_{rr} - \frac{2v_\theta}{r} \dot{\gamma}_{r\theta} - \frac{2v_\phi}{r} \dot{\gamma}_{r\phi} \\ (\mathbf{v} \cdot \nabla \dot{\boldsymbol{\gamma}})_{\theta\theta} &= (\mathbf{v} \cdot \nabla) \dot{\gamma}_{\theta\theta} + \frac{2v_\theta}{r} \dot{\gamma}_{r\theta} - \frac{2v_\phi}{r} \dot{\gamma}_{\theta\phi} \cot \theta \\ (\mathbf{v} \cdot \nabla \dot{\boldsymbol{\gamma}})_{\phi\phi} &= (\mathbf{v} \cdot \nabla) \dot{\gamma}_{\phi\phi} + \frac{2v_\phi}{r} \dot{\gamma}_{r\phi} + \frac{2v_\theta}{r} \dot{\gamma}_{\theta\phi} \cot \theta \\ (\mathbf{v} \cdot \nabla \dot{\boldsymbol{\gamma}})_{r\theta} &= (\mathbf{v} \cdot \nabla \dot{\boldsymbol{\gamma}})_{\theta r} = (\mathbf{v} \cdot \nabla) \dot{\gamma}_{r\theta} + \frac{v_\theta}{r} (\dot{\gamma}_{rr} - \dot{\gamma}_{\theta\theta}) - \frac{v_\phi}{r} (\dot{\gamma}_{\phi\theta} + \dot{\gamma}_{r\phi} \cot \theta) \\ (\mathbf{v} \cdot \nabla \dot{\boldsymbol{\gamma}})_{r\phi} &= (\mathbf{v} \cdot \nabla \dot{\boldsymbol{\gamma}})_{\phi r} = (\mathbf{v} \cdot \nabla) \dot{\gamma}_{r\phi} - \frac{v_\theta}{r} \dot{\gamma}_{\theta\phi} + \frac{v_\phi}{r} [(\dot{\gamma}_{rr} - \dot{\gamma}_{\phi\phi}) + \dot{\gamma}_{r\theta} \cot \theta] \\ (\mathbf{v} \cdot \nabla \dot{\boldsymbol{\gamma}})_{\theta\phi} &= (\mathbf{v} \cdot \nabla \dot{\boldsymbol{\gamma}})_{\phi\theta} = (\mathbf{v} \cdot \nabla) \dot{\gamma}_{\theta\phi} + \frac{v_\theta}{r} \dot{\gamma}_{r\phi} + \frac{v_\phi}{r} [\dot{\gamma}_{\theta r} + (\dot{\gamma}_{\theta\theta} - \dot{\gamma}_{\phi\phi}) \cot \theta] \end{aligned}$$

Source: Reprinted by permission from R. B. Bird, R. C. Armstrong, and O. Hassager, *Dynamics of Polymeric Liquids, 2nd Edition, Vol. I, Fluid Dynamics*, Wiley, New York, 1987.

$$^a(\mathbf{v} \cdot \nabla) = v_x \frac{\partial}{\partial x} + v_y \frac{\partial}{\partial y} + v_z \frac{\partial}{\partial z}$$

$$^b(\mathbf{v} \cdot \nabla) = v_r \frac{\partial}{\partial r} + \frac{v_\theta}{r} \frac{\partial}{\partial \theta} + v_z \frac{\partial}{\partial z}$$

$$^c(\mathbf{v} \cdot \nabla) = v_r \frac{\partial}{\partial r} + \frac{v_\theta}{r} \frac{\partial}{\partial \theta} + \frac{v_\phi}{r \sin \theta} \frac{\partial}{\partial \phi}$$

and

$$\{\dot{\boldsymbol{\gamma}} \cdot \boldsymbol{\omega}\} = \begin{pmatrix} -\dot{\gamma}_{rz}^2 & 0 & 0 \\ 0 & 0 & 0 \\ 0 & 0 & \dot{\gamma}_{rz}^2 \end{pmatrix} \quad (\text{E3.5-8})$$

Thus, Eq. E3.5-4 reduces to

$$\frac{\mathcal{D}}{\mathcal{D}t} \dot{\boldsymbol{\gamma}} = \frac{1}{2} (\{\boldsymbol{\omega} \cdot \dot{\boldsymbol{\gamma}}\} - \{\dot{\boldsymbol{\gamma}} \cdot \boldsymbol{\omega}\}) = \begin{pmatrix} \dot{\gamma}_{rz}^2 & 0 & 0 \\ 0 & 0 & 0 \\ 0 & 0 & -\dot{\gamma}_{rz}^2 \end{pmatrix} \quad (\text{E3.5-9})$$

Table 3.3 Components of the Vorticity Tensor ω in Three Coordinate Systems^a**Rectangular Coordinates** (x, y, z)

$$\omega_{xy} = -\omega_{yx} = \frac{\partial v_y}{\partial x} - \frac{\partial v_x}{\partial y}$$

$$\omega_{yz} = -\omega_{zy} = \frac{\partial v_z}{\partial y} - \frac{\partial v_y}{\partial z}$$

$$\omega_{zx} = -\omega_{xz} = \frac{\partial v_x}{\partial z} - \frac{\partial v_z}{\partial x}$$

Cylindrical Coordinates (r, θ, z)

$$\omega_{r\theta} = -\omega_{\theta r} = \frac{1}{r} \frac{\partial}{\partial r} (rv_\theta) - \frac{1}{r} \frac{\partial v_r}{\partial \theta}$$

$$\omega_{\theta z} = -\omega_{z\theta} = \frac{1}{r} \frac{\partial v_z}{\partial \theta} - \frac{\partial v_\theta}{\partial z}$$

$$\omega_{zr} = -\omega_{rz} = \frac{\partial v_r}{\partial z} - \frac{\partial v_z}{\partial r}$$

Spherical Coordinates (r, θ, ϕ)

$$\omega_{r\theta} = -\omega_{\theta r} = \frac{1}{r} \frac{\partial}{\partial r} (rv_\theta) - \frac{1}{r} \frac{\partial v_r}{\partial \theta}$$

$$\omega_{\theta\phi} = -\omega_{\phi\theta} = \frac{1}{r \sin \theta} \frac{\partial}{\partial \theta} (v_\phi \sin \theta) - \frac{1}{r \sin \theta} \frac{\partial v_\theta}{\partial \phi}$$

$$\omega_{\phi r} = -\omega_{r\phi} = \frac{1}{r \sin \theta} \frac{\partial v_r}{\partial \phi} - \frac{1}{r} \frac{\partial}{\partial r} (rv_\phi)$$

Source: Reprinted with permission from R. B. Bird, R. C. Armstrong, and O. Hassager, *Dynamics of Polymeric Liquids, 2nd Edition, Vol. I, Fluid Dynamics*, Wiley, New York, 1987.

^aAll diagonal components are zero.

Finally, we substitute Eqs. E3.5-2, E3.5-3, and E3.5-9 into Eq. E3.5-1 to obtain the stress field

$$\begin{pmatrix} \tau_{rr} & \tau_{r\theta} & \tau_{rz} \\ \tau_{\theta r} & \tau_{\theta\theta} & \tau_{\theta z} \\ \tau_{zr} & \tau_{z\theta} & \tau_{zz} \end{pmatrix} = -\eta(\dot{\gamma}) \begin{pmatrix} 0 & 0 & \dot{\gamma}_{rz} \\ 0 & 0 & 0 \\ \dot{\gamma}_{rz} & 0 & 0 \end{pmatrix} - \left[\frac{1}{2} \Psi_1(\dot{\gamma}) + \Psi_2(\dot{\gamma}) \right] \begin{pmatrix} \dot{\gamma}_{rz}^2 & 0 & 0 \\ 0 & 0 & 0 \\ 0 & 0 & \dot{\gamma}_{rz}^2 \end{pmatrix} \\ + \frac{1}{2} \Psi_1(\dot{\gamma}) \begin{pmatrix} \dot{\gamma}_{rz}^2 & 0 & 0 \\ 0 & 0 & 0 \\ 0 & 0 & -\dot{\gamma}_{rz}^2 \end{pmatrix} \quad (\text{E3.5-10})$$

From Eq. E3.5-10 we obtain the following nonvanishing stress components:

$$\begin{aligned}\tau_{rz} &= \tau_{zr} = -\eta \dot{\gamma}_{rz} \\ \tau_{rr} &= -\left(\frac{1}{2}\Psi_1 + \Psi_2\right)\dot{\gamma}_{rz}^2 + \frac{1}{2}\Psi_1\dot{\gamma}_{rz}^2 = -\Psi_2\dot{\gamma}_{rz}^2 \\ \tau_{\theta\theta} &= 0 \\ \tau_{zz} &= -\left(\frac{1}{2}\Psi_1 + \Psi_2\right)\dot{\gamma}_{rz}^2 - \frac{1}{2}\Psi_1\dot{\gamma}_{rz}^2 = -(\Psi_1 + \Psi_2)\dot{\gamma}_{rz}^2\end{aligned}\quad (\text{E3.5-11})$$

We therefore observe that unlike in the Power Law model solution with a single shear stress component, τ_{rz} , in the case of a CEF model, we obtain, in addition, two nonvanishing normal stress components. Adopting the sign convention for viscometric flow, where the direction of flow z is denoted as 1, the direction into which the velocity changes r , is denoted as 2, and the neutral direction θ is denoted as direction 3, we get the expressions for the shear stress in terms of the shear rate, the primary, and secondary normal stress differences (see Eqs. 3.1-10 and 3.1-11):

$$\tau_{12} = \tau_{21} = -\eta \dot{\gamma}_{21} \quad (\text{E3.5-12})$$

$$\tau_{11} - \tau_{22} = \tau_{zz} - \tau_{rr} = -\Psi_1 \dot{\gamma}_{21}^2 \quad (\text{E3.5-13})$$

$$\tau_{22} - \tau_{33} = \tau_{rr} - \tau_{\theta\theta} = -\Psi_2 \dot{\gamma}_{21}^2 \quad (\text{E3.5-14})$$

with the three material functions of the CEF equation being identified as follows: $\eta(\dot{\gamma})$ is the viscosity function; $\Psi_1(\dot{\gamma})$ is the first normal stress-difference coefficient; and $\Psi_2(\dot{\gamma})$ is the second normal stress-difference coefficient. Examples of the shear rate dependence of both the viscosity and the coefficient of the first normal stress-difference functions are shown in Fig. E3.5.

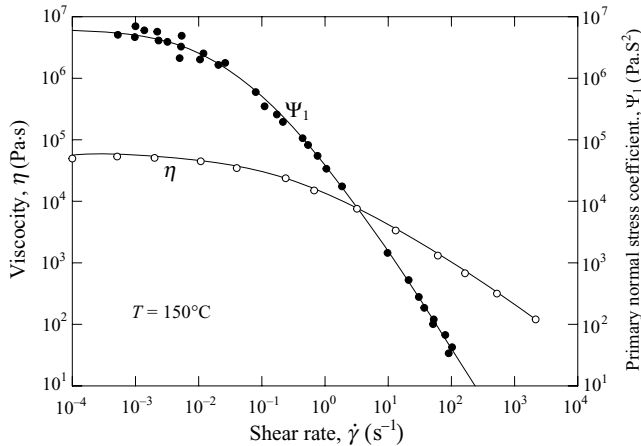


Fig. E3.5 Steady-state shear viscosity η and first normal stress coefficient Ψ_1 , obtained from dynamic measurements versus shear rate for a low-density polyethylene melt, melt I. [H. M. Laun, *Rheol. Acta*, **17**, 1 (1978).]

Example 3.6 Combined Drag and Pressure Flow between Parallel Plates In this example we examine the isothermal, laminar, steady, fully developed combined pressure and drag

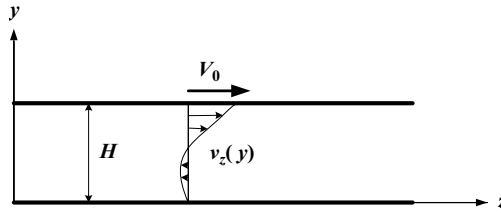


Fig. E3.6a Two parallel plates at a distance H apart with the upper plate moving at constant velocity V_0 . The velocity profile is for a particular flow situation where the pressure is “built up” in the z direction and is sufficiently high to create a “back flow” in the lower part of the channel.

flow of an incompressible Power Law model fluid, between parallel plates in relative motion as shown schematically in Fig. E3.6a. Superimposed on the drag flow there may be a positive or negative pressure gradient. In the figure we show a case where the pressure gradient is positive (i.e., pressure increases in the positive z direction). We present this example for two reasons: first, it is the type of flow that occurs in many types of processing equipment, most notably single-screw extruders, and second, it illustrates the relative complexity introduced in dealing analytically with the *absolute sign* in the Power Law model.

This problem was solved by Hirshberger (44), whose solution we follow. We will derive the velocity profile and the flow rate and demonstrate how to deal with a Power Law model fluid when the flow field where the velocity gradient is negative in one region and positive in the other.

The flow is viscometric because there is only one velocity component, $v_z(y)$, which is changing only in one spatial direction, y . Adopting a rectangular coordinate system, we find in analogy to Example 3.3 that $v_y = v_x = 0$, and therefore the equation of motion reduces to

$$\begin{aligned}\frac{\partial P}{\partial x} &= 0 \\ \frac{\partial P}{\partial y} &= 0 \\ \frac{\partial P}{\partial z} &= -\frac{\partial \tau_{yz}}{\partial y}\end{aligned}\tag{E3.6-1}$$

From the preceding equations we conclude that the pressure is a function of coordinate z only. Consequently, in the last equation the left-hand side is a function of z only, whereas the right-hand side is a function of y only. This is only possible if *both* equal a constant. Thus we conclude that the pressure gradient is constant, that is, pressure rises (or drops) *linearly* with z , and that the shear stress, in the presence of a pressure gradient, is a *linear* function of y , and in the absence of a pressure gradient it is constant across the gap. These observations follow from the momentum balance, and, they are therefore, true for all fluids, Newtonian and non-Newtonian alike.

Following the logic described in Example 3.4, we find that the Power Law model fluid for this viscometric flow reduces to

$$\tau_{yz} = -m \left| \frac{dv_z}{dy} \right|^{n-1} \frac{dv_z}{dy}\tag{E3.6-2}$$

Substituting Eq. E3.6-2 into Eq. E3.6-1 and casting it into dimensionless form, we obtain

$$\frac{d}{d\xi} \left(\left| \frac{dv_z}{dy} \right|^{n-1} \frac{dv_z}{dy} \right) = 6G \quad (\text{E3.6-3})$$

where $u_z = v_z/V_0$, and the dimensionless pressure gradient G is defined as

$$G = \frac{H^{n+1}}{6mV_0^n} \left(\frac{dP}{dz} \right) \quad (\text{E3.6-4})$$

Equation E3.6-3 can be integrated with respect to ξ to give

$$\left| \frac{du_z}{d\xi} \right|^{n-1} \frac{du_z}{d\xi} = 6G(\xi - \lambda) \quad (\text{E3.6-5})$$

where $-6G\lambda$ is an integration constant. The advantage of writing the integration constant this way is that λ acquires a clear physical meaning; it is the location where the shear rate is zero, or the location of the extremum in the velocity profile. We need to know this location in order to rid ourselves of the absolute value in Eq. E3.6-5. Depending on the value of G , there are four velocity profiles that we must consider (Fig. E3.6b). Cases a and b exhibit an extremum in the velocity profile within the flow regime. In the former, the pressure gradient is positive ($dP/dz > 0$); in the latter it is negative ($dP/dz < 0$). Cases c and d exhibit no extremum in the velocity profile within the flow regime, thus, in this case, λ lacks physical meaning, although it still is the location of an extremum value of the mathematical function describing the velocity profile. In Case c, $\lambda < 0$, and in Case d, it is $\lambda > 1$. In Cases c and d, $\dot{\gamma}_{yz} = dv_z/dy$ is positive through the flow regime, whereas in Cases a and b, it changes sign above and below λ .

We note from Eq. E3.6-4 that G may be positive or negative depending on the sign of the pressure gradient. It is, therefore, convenient to introduce at this point a variable accounting for the sign of G

$$\text{sign } G = \frac{G}{|G|} \quad (\text{E3.6-6})$$

We can now rewrite Eq. E3.6-5 as

$$\left| \frac{du_z}{d\xi} \right|^{n-1} \frac{du_z}{d\xi} = 6 \text{ sign } G |G| (\xi - \lambda) \quad (\text{E3.6-7})$$

It can easily be verified that for regions $\xi \geq \lambda$ for both positive and negative pressure gradients (i.e., both Cases a and b), Eq. E3.6-5 can be written as follows:

$$\frac{du_z}{d\xi} = |6G|^s (\xi - \lambda)^s \text{sign } G \quad (\text{E3.6-8})$$

where $s = 1/n$. Similarly, for $\xi \leq \lambda$ we get

$$\frac{du_z}{d\xi} = -|6G|^s (\lambda - \xi)^s \text{sign } G \quad (\text{E3.6-9})$$

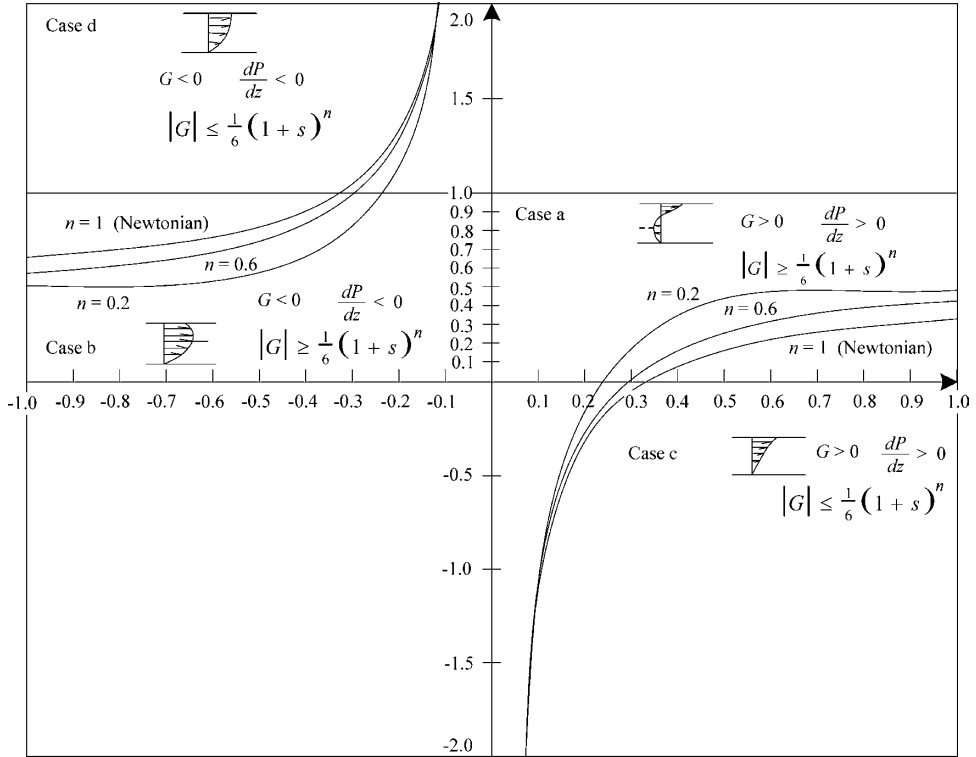


Fig. E3.6b Four regions of the solution of Eq. E3.6-5 corresponding to four types of velocity profiles. In regions (Cases) a and b, the velocity profile exhibits an extremum. In the former the pressure gradient is positive ($dP/dz > 0$); in the latter, it is negative ($dP/dz < 0$). The location of the extremum is at $\xi = \lambda$. In regions c and d, the velocity profile exhibits no extremum in the flow regime. In the former the pressure gradient is positive ($dP/dz > 0$); in the latter, it is negative ($dP/dz < 0$). The curves present solution λ as a function of G from Eq. E3.6-5, for $n = 1$, $n = 0.6$, and $n = 0.2$.

Equations E3.6-8 and E3.6-9 can be integrated subject to boundary conditions $u_z(1) = 1$ and $u_z(0) = 0$, respectively, to give

$$u_z = 1 - \frac{|6G|^s}{(1+s)} \left[(1-\lambda)^{1+s} - (\xi-\lambda)^{1+s} \right] \text{sign } G \quad (\text{E3.6-10})$$

and

$$u_z = \frac{|6G|^s}{(1+s)} \left[(\xi-\lambda)^{1+s} - \lambda^{1+s} \right] \text{sign } G \quad (\text{E3.6-11})$$

Since the velocity is continuous throughout ξ , Eqs. E3.6-10 and E3.6-11 are equal at $\xi = \lambda$, resulting in an equation for the unknown λ as a function of G and $\text{sign } G$

$$\lambda^{1+s} - (1-\lambda)^{1+s} + \frac{1+s}{|6G|^s \text{sign } G} = 0 \quad (\text{E3.6-12})$$

Equation E3.6-12 is a nonlinear algebraic equation that must be solved numerically. However, it provides the limiting values of G for determining a priori whether the flow corresponds to Case a or b. By setting $\lambda = 0$ for $G > 0$, and $\lambda = 1$ for $G < 0$, we obtain the following conditions for the existence of an extremum within the flow region $0 \leq \xi \leq 1$

$$|G| \geq \frac{1}{6}(1+s)^n \quad (\text{E3.6-13})$$

By substituting Eq. E3.6-12 into Eq. E3.6-10, we can rewrite the velocity profile in one equation

$$u_z = \frac{|6G|^s}{(1+s)} \left[|\xi - \lambda|^{1+s} - \lambda^{1+s} \right] \text{sign } G \quad (\text{E3.6-14})$$

subject to the inequality in Eq. E3.6-13.

Turning now to Cases c and d, where no extremum occurs and $du_z/d\xi > 0$, we note that Eq. E3.6-7 can be written for $G > 0$ and $G < 0$, respectively, as

$$\frac{du_z}{d\xi} = (6G)^s (\xi - \lambda)^s \quad G > 0 \quad (\text{E3.6-15})$$

and

$$\frac{du_z}{d\xi} = (-6G)^s (\lambda - \xi)^s \quad G < 0 \quad (\text{E3.6-16})$$

Integration of Eqs. E3.6-15 and E3.6-16 with boundary conditions $u_z(0) = 0$ and $u_z(1) = 1$ results in the following velocity profiles for each of the Cases c and d:

$$u_z = \frac{(6G)^s}{(1+s)} \left[(\xi - \lambda)^{1+s} - (-\lambda)^{1+s} \right] \quad G > 0 \quad (\text{E3.6-17})$$

where λ is obtained from

$$(-\lambda)^{1+s} - (1 - \lambda)^{1+s} + \frac{1+s}{(6G)^s} = 0 \quad G > 0 \quad (\text{E3.6-18})$$

and

$$u_z = \frac{(-6G)^s}{(1+s)} \left[\lambda^{1+s} - (\lambda - \xi)^{1+s} \right] \quad G < 0 \quad (\text{E3.6-19})$$

where λ is obtained from

$$(\lambda)^{1+s} - (\lambda - 1)^{1+s} - \frac{1+s}{(-6G)^s} = 0 \quad G < 0 \quad (\text{E3.6-20})$$

By setting $\lambda = 0$ in Eq. E3.6-18 and $\lambda = 1$ in Eq. E3.6-20, we find the following condition for the flow without an extremum within the flow regime

$$|G| \leq \frac{1}{6}(1+s)^n \quad (\text{E3.6-21})$$

a result that, of course, is predictable from Eq. E3.6-13.

All the velocity profile and the equations for obtaining λ can be collapsed, respectively, into a single equation

$$u_z = \frac{|6G|^s \text{sign } G}{(1+s)} \left(|\xi - \lambda|^{1+s} - |\lambda|^{1+s} \right) = \frac{|\xi - \lambda|^{1+s} - |\lambda|^{1+s}}{|1 - \lambda|^{1+s} - |\lambda|^{1+s}} \quad (\text{E3.6-22})$$

and

$$|\lambda|^{1+s} - |1 - \lambda|^{1+s} + \frac{1+s}{|6G|^s \text{sign } G} = 0 \quad (\text{E3.6-23})$$

In solving for λ in the last equation, we find multiple solutions, but we must recall the following inequalities that help select the right solution

$$\begin{aligned} \text{if } |G| \geq \frac{1}{6}(1+s)^n & \quad \text{then} \quad 0 \leq \lambda \leq 1 \\ \text{if } |G| \leq \frac{1}{6}(1+s)^n & \quad \text{and if } G > 0 \quad \text{then} \quad \lambda \leq 0 \\ \text{if } |G| \leq \frac{1}{6}(1+s)^n & \quad \text{and if } G < 0 \quad \text{then} \quad \lambda \geq 1 \end{aligned}$$

Figure E3.6b, which plots the solution of Eq. E3.6-23 for three n values, also indicates the four solution regions.

Finally, we can integrate the velocity profile to obtain the volumetric flow rate per unit width

$$q = \frac{V_0 H |6G|^s \text{sign } G}{(1+s)(2+s)} \left[(1-\lambda)|1-\lambda|^{1+s} + \lambda|\lambda|^{1+s} - (2+s)|\lambda|^{1+s} \right] \quad (\text{E3.6-24})$$

Figure E3.6c plots the dimensionless flow rate q/q_d , where q_d is the drag flow rate, namely, the flow rate with zero pressure gradient, versus the dimensionless pressure gradient G . The figure shows that, whereas for Newtonian fluids, as expected, there is a linear relationship, non-Newtonian fluids deviate from linearity. The more non-Newtonian the fluid is, the greater is the deviation. Of particular interest is the inflection point indicating, for example, that in screw extruders, even for the isothermal case, increasing die resistance brings about somewhat unexpected changes in flow rate.

3.4 POLYMER MELT CONSTITUTIVE EQUATIONS BASED ON MOLECULAR THEORIES

Molecular theories, utilizing physically reasonable but approximate molecular models, can be used to specify the stress tensor expressions in nonlinear viscoelastic constitutive equations for polymer melts. These theories, called *kinetic theories of polymers*, are, of course, much more complex than, say, the kinetic theory of gases. Nevertheless, like the latter, they simplify the complicated physical realities of the substances involved, and we use approximate “cartoon” representations of macromolecular dynamics to describe the real response of these substances. Because of the relative simplicity of the models, a number of response parameters have to be chosen by trial and error to represent the real response. Unfortunately, such parameters are material specific, and we are unable to predict or specify from them the specific values of the corresponding parameters of other

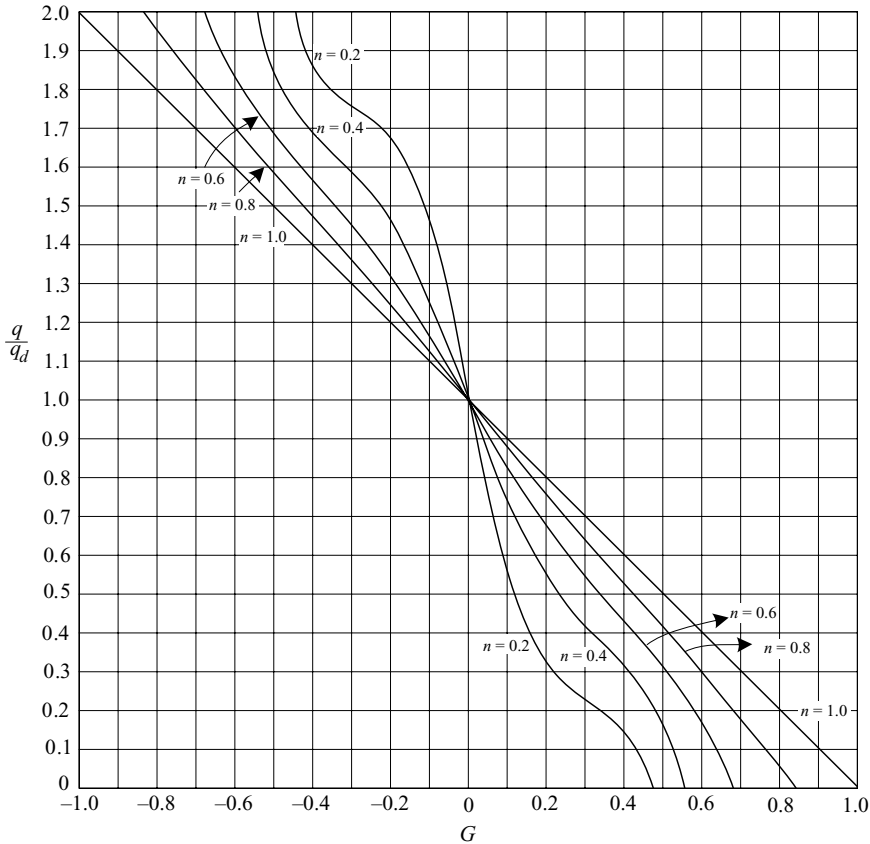


Fig. E3.6c Dimensionless flow rate versus dimensionless pressure gradient, with the Power Law exponent n as a parameter, for parallel-plate flow, as given in Eq. E3.6-24.

substances, even of similar macromolecular structures. In other words, the *kinetic theory* of polymer melts is not *true* molecular theory.

With these comments in mind, we list and briefly discuss the two classes of these theories: the *single molecule* (14) and *entanglement network* theories (23).

Single-molecule Theories

Single-molecule theories originated in early polymer physics work (45) to describe the flow behavior of *very dilute* polymer solutions, which are free of interpolymer chain effects. Most commonly, the macromolecular chain, capable of viscoelastic response, is represented by the well-known *bead-spring* model or “cartoon,” shown in Fig. 3.8(a), which consists of a series of small spheres connected to elastic springs.

Upon flow in the solvent environment, the drag that the solvent exerts on the spheres (representing the viscous nature of the real macromolecule), orients the bead-spring and *stretches* the elastic springs between the beads (which represent the elastic nature of the real macromolecules). The consequent stored energy in the springs is capable of restoring the equilibrium conformations of the bead-springs, but it is resisted by Stokesian drag on

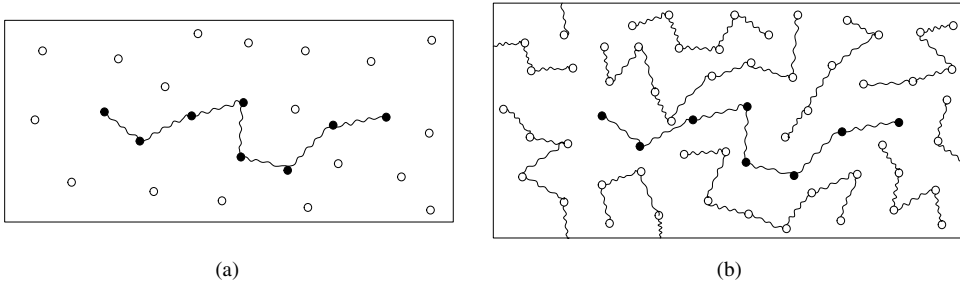


Fig. 3.8 Single-molecule *bead-spring models* for (a) a dilute polymer solution, and (b) an undiluted polymer (a polymer melt with no solvent). In the dilute solution, the polymer molecule can move about in all directions through the solvent. In the undiluted polymer, a typical polymer molecule (black bead) is constrained by the surrounding molecules and tends to execute snakelike motion (“reptation”) by sliding back and forth along its backbone direction (46). [Reprinted by permission from R. B. Bird, W. E. Stewart and E. N. Lightfoot, *Transport Phenomena*, 2nd Edition, Wiley New York (2002).]

the beads, responding with relaxation times that are proportional to the effective solvent drag viscosity and inversely proportional to the elastic spring constant.

Extension of this theory can also be used for treating *concentrated* polymer solution response. In this case, the motion of, and drag on, a single bead is determined by the mean intermolecular force field. In either the dilute or concentrated solution cases, *orientation distribution functions* can be obtained that allow for the specification of the stress tensor field involved. For the concentrated spring-bead model, Bird et al. (46) point out that because of the proximity of the surrounding molecules (i.e., spring-beads), it is easier for the model molecule to move in the *direction of the polymer chain backbone* rather than perpendicular to it. In other words, the polymer finds itself executing a sort of a snake-like motion, called *reptation* (47), as shown in Fig. 3.8(b).

Entanglement Network Theories

Entanglement network theories are based on the following premise: polymer melts are much like cross-linked rubber macromolecular networks, except that their cross-links are due to chain *entanglements* and are *temporary*. Such entanglements are continuously destroyed and formed to establish *network entanglement densities* characteristic of the state of motion of the network, being maximum at equilibrium. Green and Tobolsky (48) extended the rubber elasticity theory (49–52) to liquids with “temporary junctions” with equal probabilities of breaking and reforming. Following Larson (53), the development of the constitutive equation for such liquid with temporary entanglement networks is as follows: Let the probability that a chain breaks loose of a junction point, per unit time, be $1/\lambda$, where λ is of the order of the relaxation time. The probability that the strand does *not* break free in the time interval t' to t (present time), $P_{t',t}$ obeys the differential equation

$$\frac{d}{dt}P_{t',t} = -\frac{1}{\lambda}P_{t',t} \quad (3.4-1)$$

with $P_{t',t} = 1$. Hence

$$P_{t',t} = e^{(t'-t)/\lambda} \quad (3.4-2)$$

When the material is deformed, each strand is stretched affinely until it breaks free from its junction. After it breaks free, it relaxes to a configuration typical of equilibrium. As often as a strand breaks free, another relaxed strand becomes entangled. The probability that a strand breaks free and becomes reentangled in an interval of time between t' and $t' + dt'$ is dt'/λ . The probability that it survives without breaking from time t' to time t is $P_{t',t}$. It obeys the differential equation

$$\frac{d}{dt} P_{t',t} = -\frac{1}{\lambda} P_{t',t} \quad (3.4-3)$$

The contribution $d\tau$ to the stress from those *stretched* strands that meet both of these conditions is, according to Eq. 3.4-1,

$$d\tau = \frac{dt'}{\lambda} P_{t',t} G \gamma_{[1]}(t', t) = G \frac{1}{\lambda} e^{(t'-t)/\lambda} \gamma_{[1]}(t', t) dt' \quad (3.4-3a)$$

with $G = (4/5)vk_B T$, where v is the entanglement density and $\gamma_{[1]}$ is the Finger relative strain tensor between the states of the fluid at t and t' . The total stress produced by strands that became reentangled at all past times, t' , is then

$$\tau = \int_{-\infty}^t m(t-t') \gamma_{[1]}(t', t) dt' \quad (3.4-4)$$

where $m(t-t')$ is the so called *memory function*, which is determined by the linear or the nonlinear viscoelastic spectra, depending on the level of strain. For the former case,

$$m(t-t') = \sum_i \frac{G_i}{\lambda_i} \exp[-(t-t')/\lambda_i] \quad (3.4-5)$$

Equations 3.4-3 and 3.4-4 form the molecular theory origins of the Lodge “rubberlike liquid” constitutive Eq. 3.3-15 (23). For large strains, characteristic of processing flows, the nonlinear relaxation spectrum is used in the memory function, which is the product of the linear spectrum and the *damping function* $h(\gamma)$, obtained from the stress relaxation melt behavior after a series of strains applied in stepwise fashion (53)

In the preceding treatment, the “strands”—entire chains or chain segments—are free to move through any path, for example, relaxing to an equilibrium configuration. But as noted in Fig. 3.9, any given polymer chain is able to move only in a *constrained path*, because of the surrounding chains and, therefore, tends to *move and advance* along its backbone direction by, as pointed out before, in a snakelike, reptation motion.

Pierre-Gilles deGennes (47) utilized this concept and coined the term in his work to explain why the relaxation times of entangled melts have a $\lambda \sim M^{3.4}$ dependence. Earlier, the lateral confinement of melt chains to a *tubelike* region had been postulated by Edwards (54). Since these early days of the reptation theory, a very significant volume of work has been dedicated to incorporating features that are physically reasonable and warranted in

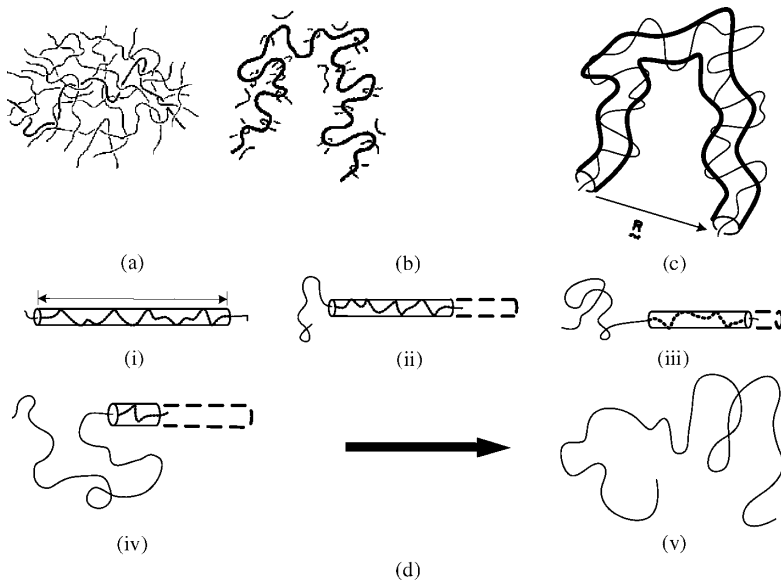


Fig. 3.9. (a) A polymer melt chain entangled in a mesh of other chains. (b) Individual neighboring chain entanglement points that result in (c) the confinement of the given chain to a tubelike region. [(d)(i)–(d)(v)] represents a schematic reptation of the polymer chain out of its (stretched for visualization) tube, requiring a reptation time τ_d . [Reprinted by permission from R. G. Larson, *The Structure and Rheology of Complex Fluids*, Oxford University Press, New York, 1999.]

order to improve the predictions of the corresponding members of the *reptation-based* constitutive equation. But before discussing some of them, it is useful to present a pictorial representation of reptation according to the work of Graessley (55). He considers the polymer chain shown on Fig. 3.9(a), entangled in a mesh of other polymers to be confined by individual chain neighbors in a manner shown in Fig. 3.9(b). As a physical consequence, the polymer chain is confined in a tubelike region shown in Fig. 3.9(c).

Motion within the tube is achieved by a random walk (“primitive path”) of unit steps of the order of the tube diameter, a . When a straight reptation tube is considered, for simplicity, reptation diffusional motion of the chain out of the tube is represented schematically in the steps depicted from Fig. 3.9(d)(i) to Fig. 3.9(d)(v).

Perkins and colleagues (56) have provided graphic and direct evidence of reptation, using a fluorescently stained, very long DNA molecule in an entangled environment of similar unstained DNA molecules. Figure 3.10 shows time-sequence images of such a $60\ \mu\text{m}$ long molecule, which was attached at one end to a small sphere that was pulled through the fluid using a laser-optical trap to form a letter “R.” As seen in the picture sequence, the free end of the DNA undergoes retraction through a tubelike region defined by the surrounding mesh of the invisible neighboring DNA chains.

The retraction follows the path of “R” containing the stretched, strained DNA molecule, strikingly demonstrating reptation. Molecular dynamic computational simulations (a tool of rapidly increasing utility in melt rheology and structuring) also show chain motion that is highly anisotropic, suggesting that diffusion motions of long chains are largely confined in a tube (57), as shown in Fig. 3.11.

The constitutive equations benefiting from the specific representations of reptation theory have the general form of the Lodge rubber-like liquid equation, since they are all

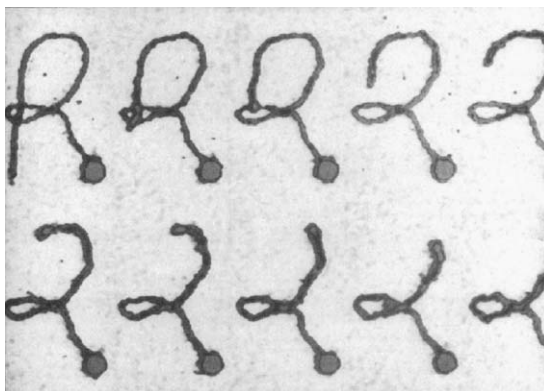


Fig. 3.10. Time sequence of images showing retraction of one end of a fluorescing 60- μm long DNA molecule entangled in a solution of other, nonfluorescing DNA molecules. The fluorescing molecule was attached at one end to a small sphere that was pulled through the solution using a laser-optical trap, to form the letter “R”. The free end then retracts through a tubelike region formed by the surrounding mesh of other, invisible DNA chains. [Reprinted by permission from the cover of *Science*, May 6, 1994 (Copyright 1994, American Association for the Advancement of Science).]

entanglement network theories, treating chain motion, deformations, and entanglements and disentanglements with different degrees of scrutiny and physical assumptions. Thus, the Doi–Edwards equation (58,59) considers the contributors to the stress tensor of the stretched and oriented tube segments due to the flow. This results in the integral form

$$\tau(t) = \int_{-\infty}^t m(t-t') \mathbf{S}_{DE}^{IA}(t') dt' \tag{3.4-6}$$

where \mathbf{S}_{DE}^{IA} , the Doi–Edwards strain measure for tube segments independently aligned

$$\mathbf{S}_{DE}^{IA} = 5 \left\langle \frac{\mathbf{u}' \mathbf{u}'}{(\mathbf{u}')^2} \right\rangle = 5\mathbf{S} \tag{3.4-7}$$

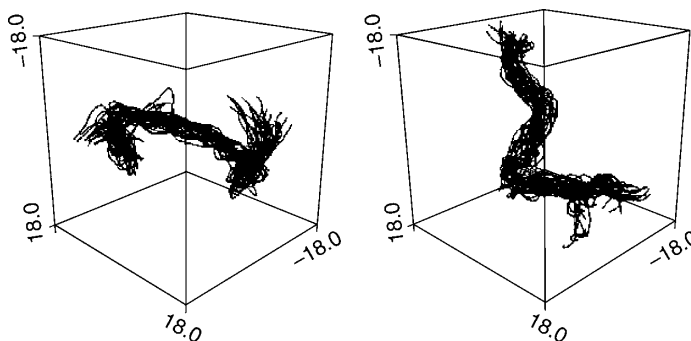


Fig. 3.11. Each of the two images contains superimposed configurations of a chain at many different instants in time in a molecular-dynamics simulation of a melt of such chains in a box. Over the time scale simulated, each chain appears to be confined to a tubelike region of space, except at the chain ends. [Reprinted by permission from K. Kremer and G. S. Grest, *J. Chem. Phys.*, **92**, 5057 (Copyright 1990 American Institute of Physics).]

where \mathbf{S} is the second-order orientation function and \mathbf{u} is the deformation vector. The memory function $m(t - t')$ is expressed as

$$m(t - t') = \frac{G_N^0}{5} \partial F(t - t') / \partial t' \quad (3.4-8)$$

where the plateau modulus is defined from the Treloar theory of rubber elasticity (52):

$$G_n^0 = \frac{3ckTh^2}{a_0^2} \quad (3.4-9)$$

The function $F(t - t')$ is related, as with the temporary network model of Green and Tobolsky (48) discussed earlier, to the survival probability of a tube segment for a time interval $(t - t')$ of the strain history (58,59). Finally, this Doi-Edwards model (Eq. 3.4-5) is for monodispersed polymers, and is capable of moderate predictive success in the non linear viscoelastic range. However, it is not capable of predicting strain hardening in elongational flows (Figs. 3.6 and 3.7).

The *pom-pom polymer reptation model* was developed by McLeish and Larson (60) to represent long chain-branched LDPE chains, which exhibit pronounced strain hardening in elongational flows. This idealized pom-pom molecule has a single backbone confined in a reptation tube, with multiple arms and branches protruding from each tube end, as shown in Fig. 3.12(a). M_b is the molecular weight of the backbone and M_a , that of the arms.

Corresponding dimensionless entanglement lengths are $S_b = M_b/M_e$ for the backbone and $S_a = M_a/M_e$ for the arms, where M_e is the entanglement molecular weight. The dominant contribution to the stress tensor is assumed to arise from the backbone/crossbar segment. Because these branches are entangled with the surrounding molecules, the backbone can readily be stretched in start-up extensional flows, producing strain

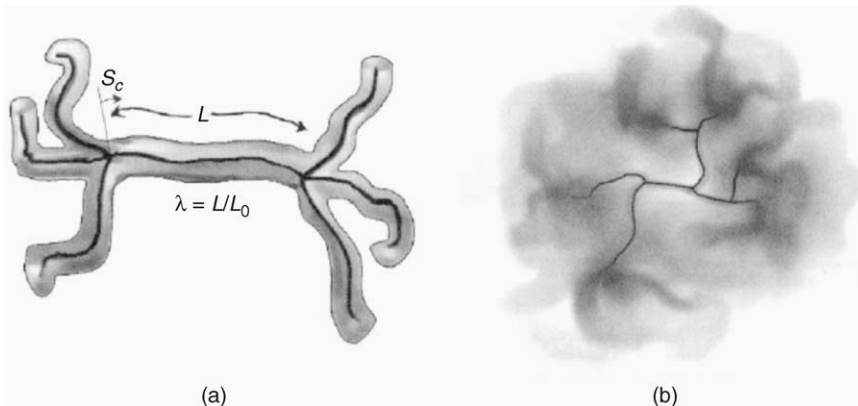


Fig. 3.12 (a) A pom-pom with three arms at each branch point ($q = 3$). At short times the polymer chains are confined to the Doi-Edwards tube. S_c is the dimensionless length of branch point retraction into the tube; λ is the stretch ratio where L is the curvilinear length of the crossbar and L_0 is the curvilinear equilibrium length. (b) Relaxation process of a long-chain-branched molecule such as LDPE. At a given flow rate $\dot{\epsilon}$ the molecule contains an unrelaxed core of relaxation times $\tau > \dot{\epsilon}^{-1}$ connected to an outer “fuzz” of relaxed material of relaxation $\tau < \dot{\epsilon}^{-1}$, behaving as solvent. [Reprinted by permission from N. J. Inkson et al., *J. Rheol.*, **43**(4), 873 (1999).]

hardening when it gets fully stretched and the poms on each end as they “cork” the tube ends. The tension that the poms may be able to sustain and impart on the backbone is qk_B/a , where q is the number of poms and a is the reptation tube diameter. Beyond this, tension in the backbone is sufficient to gradually withdraw the dangling arms into the tube ($S_e > 0$). When this branch point withdrawal is complete, strain-hardening behavior disappears. On the other hand, in start-up of shear flows, the backbone tube stretches only temporarily and eventually goes back to zero as the pom-pom molecule is aligned by the flow, thus producing shear strain softening.

Inkson et al. (61) and McLeish (62) in a recent review have proposed also a *multimode* pom-pom model in an attempt to account for the multiple levels of branching believed to be present in LDPE molecules. Because the precise structure and degree of branching of LDPE molecules are unknown, with no experimental techniques to determine them, the potential exists for these multimode models to “characterize” the LDPE macromolecular structure through fitting with experimental rheological data.

Figure 3.12(b) indicates how a reptating large molecule with multiple branch points relaxes after deformation. The free chain arms relax rapidly, much as the pom-pom arms at the outer branch point. This branch point is able to move one diffusive step after a deep retraction of the chain arms connected to it. This allows the molecular segment in the next (inward) branch point to relax. This, in turn, is repeated until the innermost segment relaxes. The relaxation time of a segment depends hierarchically on the path distance to the nearest free end that can release it from its tube constraint by retraction. The multimode pom-pom models, which utilize a small set of trial-and-error picked modes and utilize experimentally determined discreet relaxation spectra are able to closely account for three rheological functions: $\eta(\dot{\gamma}, t)$, $\bar{\eta}^+(\dot{\epsilon}, t)$, and $\bar{\eta}_{pl}^+(\dot{\epsilon}_{pl}, t)$, simultaneously over four decades of times and rates (61), which is rather remarkable. Still, these models lack the ability to predict the rheological behavior of a structurally slightly different polymer, that is, there is no direct connection to the specific macromolecular characteristics of the polymer melt

Wagner et al. (63–66) have recently developed another family of reptation-based molecular theory constitutive equations, named *molecular stress function* (MSF) models, which are quite successful in closely accounting for all the start-up rheological functions in both shear and extensional flows (see Fig. 3.7). It is noteworthy that the latest MSF model (66) is capable of very good predictions for monodispersed, polydispersed and branched polymers. In their model, the reptation tube diameter is allowed not only to stretch, but also to reduce from its original value. The molecular stress function $f(t)$, which is the ratio of the reduction to the original diameter and the MSF constitutive equation, is related to the Doi–Edwards reptation model integral-form equation as follows:

$$\tau(t) = \int_{-\infty}^t m(t-t') \mathbf{S}_{MSF}(t') dt' = \int_{-\infty}^t m(t-t') f^2 \mathbf{S}_{DE}^{IA}(t') dt' \quad (3.4-10)$$

In the MSF theory, the function, f , in addition to simple reptation, is also related to both the elastic effects of tube diameter reduction, through the Helmholtz free energy, and to dissipative, convective molecular-constraint mechanisms. Wagner et al. arrive at two differential equations for the molecular stress function f : one for linear polymers and one for branched. Both require only two trial-and-error determined parameters.

The constitutive equations discussed previously contain both *linear* and *nonlinear* response parameters. Both have to be evaluated experimentally. The first five to ten terms

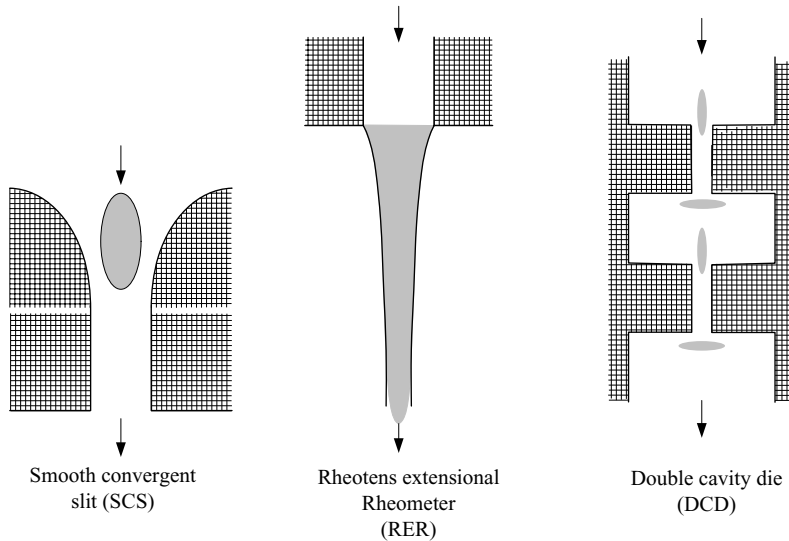


Fig. 3.13 Schematic of three prototype industrial flow (PIF) geometries showing shaded extensional flow regions for each geometry. [Reprinted by permission from J. F. Agassant et al., *Intern. Polym. Proc.*, **17**, 3 (2002).]

of the discrete LVE spectrum constitute a sufficient number of linear response terms. They are derived from small-strain (below the limit of linear viscoelastic response), sinusoidally varying flow experiments, specifically using the experimentally obtained G' , G'' or η^* . Until recently, the nonlinear response parameters have been obtained from flow experiments that are relatively simple (rheometric) and that impose large strains as large step-strain experiments, or extensional flows. Both result in altering the quiescent, entangled macromolecular network of the melts. This practice has left open the question of how relevant the evaluation of all the constitutive equation parameters is, using simple rheometric experiments that do not have the complexity of real processing flows. This question has been the subject of a large-scale investigation by a multidisciplinary network of European polymer researchers, which has been in progress for several years, and is described in by Agassant et al. (67). Two-dimensional, isothermal *prototype industrial flows* (PIF), resembling and closely related to polymer processing practice were used. Three such flows are shown in Fig. 3.13.

The flow birefringence pattern of these flows can be obtained through the use of a pair of flat glass walls. Using image enhancement and the stress-optical law (68),

$$\Delta = C(\tau_{11} - \tau_{22}) \quad (3.4-11)$$

where Δ is the birefringence and C is the stress-optical constant, the principal normal stress difference can be obtained experimentally and enhanced and “skeletalized” by image analysis. This is shown in Fig. 3.14 for the smooth convergent die of the PIFs shown in Fig. 3.13.

Such contours are then compared with numerically derived ones obtained in the following fashion: a nonlinear response constitutive equation is selected (60, 61, 64, 69) to be used with the equation of motion for a given PIF. The numerical solution computational

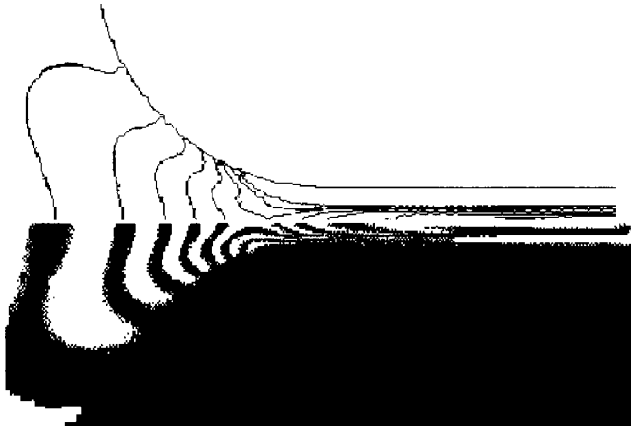


Fig. 3.14 Experimental and matching numerical simulation data for the smooth convergent die geometry of HDPE, Stamyilan HD862 at $T = 190^\circ\text{C}$. [Reprinted by permission from J. F. Agassant et al., *Intern. Polym. Proc.*, **17**, 3 (2002).]

packages required for the solution of the PIFs (as contrasted to the simpler rheometric flows) have to be powerful and the computational demands on both time and computer are daunting. Three different finite-element numerical codes were used: the commercial Fluent Group Polyflow (70), Venus (71), developed at Eindhoven University, and Seve 2 (72), developed at the CEMEF of Ecole des Mines de Paris.

In the example given, the constitutive equation used is a multimode Phan Tien Tanner (PTT). It requires the evaluation of both linear and nonlinear material-response parameters. The linear parameters are a sufficient number of the discrete relaxation spectrum λ_i and η_i pairs, which are evaluated from small-strain dynamic experiments. The values of the two nonlinear material-response parameters are evaluated as follows. Three semiarbitrary initial values of the two nonlinear parameters are chosen and the principal normal stress difference field is calculated for each of them using the equation of motion and the multimode PTT. They are compared at each field point (i, j) to the experimentally obtained normal stress difference and used in the following cost function F

$$F = \left[\sum_{L=1}^n \sum_{j=1}^n \frac{(G_{ij}^{\text{SIM}} - G_{ij}^{\text{exp}})^2}{(G_{ij}^{\text{exp}})^2} \right]^{1/2} \quad (3.4-12)$$

where G_{ij}^{SIM} is the “grey level” of the normalized simulation pattern and G_{ij}^{exp} the corresponding experimental pattern at any (i, j) point. The cost function is then evaluated for each of the three initial nonlinear parameter pairs (69). The simplex optimization method is then employed to arrive at the “optimal” values of the nonlinear parameters, which minimize the value of the cost function. The agreement between the experimentally and numerically obtained birefringence patterns, using the optimal nonlinear parameter pair, is shown in Fig. 3.15; it is very good.

Thus, adequate determination of nonlinear rheological parameters can be obtained, using industrial polymer processing-relevant flows, albeit with very substantial computational efforts, virtually assuring the relevance of the use of the constitutive equation for solving other complex processing flows.

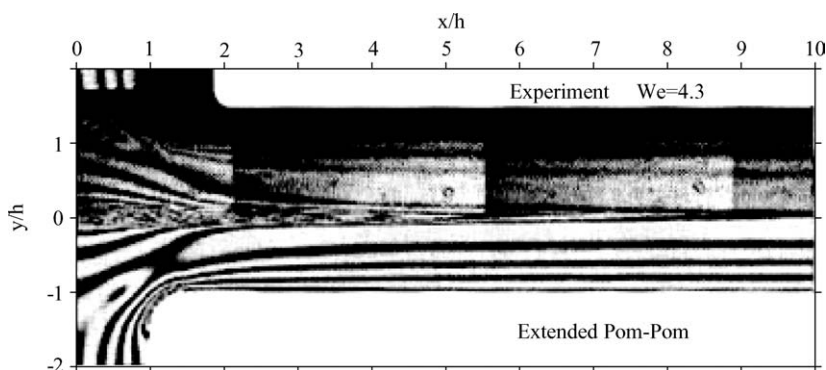


Fig. 3.15 (top) Measured and (bottom) calculated isochromatic fringe patterns for the extended pom-pom model at $We = 4.3$ of LDPE, DSM Stamylan LD 2008 XC43, $T = 150^\circ\text{C}$. [Reprinted by permission from J. F. Agassant et al., *Intern. Polym. Proc.*, **17**, 3 (2002).]

Finally, as we stated at the beginning of this section, all these recent successful molecular theory-based constitutive equations are still not capable of answering the question of what the empirical parameters, chosen by trial and error, will be for a yet-to-be-synthesized polymer, to accurately describe its rheological properties. One expects an answer to this question, if the theory would be based on fundamental molecular properties. The inability to answer this question rests in the fact that molecular theories, such as the previously stated one, are based on physically reasonable, ingeniously conceived and formulated, molecular cartoons. Nevertheless, with available computational power growing exponentially, and the potential synergy between molecular theories and molecular dynamics calculations, predicting the properties of existing macromolecular systems and those yet to come, from “first molecular principles” will not come in the distant future, but sooner.

REFERENCES

1. K. Walters, *Rheometry*, Wiley, New York, 1975.
2. R. I. Tanner, *Engineering Rheology*, Oxford University Press, London, 1985.
3. J. Dealy and K. F. Wissbrun, *Melt Rheology and Its Role in Plastics Processing*, Van Nostrand Reinhold, New York, 1990.
4. C. W. Macosko, Ed., *Rheology: Principles, Measurements and Applications*, Wiley-Interscience, New York, 1994.
5. K. Weissenberg, *Nature*, “A Continuum Theory of Rheological Phenomena,” **159**, 310–311 (1947).
6. M. M. Couette, *Am. Chem. Phys. Ser. VI*, **21**, 433 (1890).
7. J. D. Ferry, *Viscoelastic Properties of Polymers*, Third Edition, Wiley, New York, 1980.
8. H. M. Laun, “Description of the Non-linear Shear Behaviour of a Low Density Polyethylene Melt by Means of an Experimentally Determined Strain Dependent Memory Function,” *Rheol. Acta*, **17**, 1–15 (1978).
9. W. P. Cox and E. H. Mertz, “Correlation of the Complex Viscosity with the Steady Shear Viscosity,” *J. Polymer Sci.*, **28**, 619 (1958).
10. E. B. Christiansen and W. R. Leppard, “Steady-State and Oscillatory Flow Properties of Polymer Solutions,” *Trans. Soc. Rheol.*, **18**, 65–86 (1974).
11. D. G. Baird and D. I. Collias, *Polymer Processing*, Wiley-Interscience, New York, 1998, Chapter 3.

12. H. M. Laun, "Prediction of Elastic Strains of Polymer Melts in Shear and Elongation," *J. Rheol.*, **30**, 459 (1986).
13. F. T. Trouton, *Proc. Roy. Soc.*, **A77**, 426 (1906).
14. R. B. Bird, R. C. Armstrong, and O. Hassager, *Dynamics of Polymeric Fluids*, Second Edition, Vol. I, Wiley, New York, 1987.
15. S. A. Khan, R. K. Prud'homme, and R. G. Larson, "Comparison of the Rheology of Polymer Melts in Shear, and Biaxial and Uniaxial Extensions," *Rheol. Acta*, **26**, 144–151 (1987).
16. F. N. Cogswell, "Stretching Flow Instabilities at the Exits of Extrusion Dies," *J. Non-Newton. Fundam. Mech.*, **2**, 37–47 (1977).
17. J. M. Piau, N. El Kissi, F. Toussaint, and A. Mezghani, "Distortions of Polymer Melt Extrudates and their Elimination Using Slippery Surfaces," *Rheol. Acta*, **34**, 40 (1995).
18. C. Venet and B. Vergnes, "Experimental Characterization of Sharkskin in Polyethylenes," *J. Rheol.*, **41**, 873 (1997).
19. R. P. G. Rutgers and M. R. Mackley, "The Effect of Channel Geometry and Wall Boundary Conditions on the Formation of Extrusion Surface Instabilities for LLDPE," *J. Non-Newton. Fluid Mech.*, **98**, 185 (2001).
20. I. S. Sokolnikoff and R. M. Redhefer, *Mathematics of Physics and Engineering*, McGraw-Hill, New York, 1958, p. 263.
21. K. Weissenberg as cited by B. Rabinowitsch, *Z. Physi-Chem.*, **A145**, 1 (1929).
22. J. F. Hutton, "Fracture of Liquids in Shear," *Nature*, **200**, 646–648 (1963).
23. A. S. Lodge, *Elastic Fluids*, Academic Press, London, 1964.
24. S. I. Abdel-Khalik, O. Hassager, and R. B. Bird, "Prediction of Melt Elasticity From Viscosity Data," *Polym. Eng. Sci.*, **14**, 859 (1974).
25. J. D. Goddard and C. Miller, "An Inverse for the Jaumann Derivative and Some Applications to the Rheology of Viscoelastic Fluids," *Rheol. Acta*, **5**, 177–184 (1966).
26. W. Noll, *Arch. Rat. Mech. Anal.*, **2**, 197 (1958).
27. J. D. Goddard, "A Modified Functional Expansion for Viscoelastic Fluids," *Trans. Soc. Rheol.*, **11**, 380–399 (1967).
28. A. E. Green and R. S. Rivlin, *Arch. Rat. Mech. Anal.*, **1**, 1 (1957).
29. B. D. Coleman and W. Noll, "Foundations of Linear Viscoelasticity," *Rev. Mod. Phys.*, **33**, 239 (1961).
30. W. O. Criminale, Jr., J. L. Ericksen, and G. L. Filbey, Jr., *Arch. Rat. Mech. Anal.*, **1**, 410 (1958).
31. H. Jeffreys, *The Earth*, First Edition, Cambridge University Press, 1924.
32. J. G. Oldroyd, *Proc. R. Soc., London*, **A200**, 45 (1950).
33. K. Walters, *Q. J. Mech. Appl. Math.*, **13**, 444 (1960).
34. A. G. Fredrickson, "On Stress-relaxing Solids – I Flow and Normal Stress Effects," *Chem. Eng. Sci.*, **17**, 155 (1963).
35. J. D. Ferry, M. L. Williams, and D. M. Stern, *J. Chem. Phys.*, **22**, 987 (1954).
36. B. Bernstein, E. A. Kearsley, and L. J. Zappas, "A Study of Stress Relaxation with Finite Strain," *Trans. Soc. Rheol.*, **7**, 391 (1963).
37. D. C. Bogue, "An Explicit Constitutive Equation Based on an Integrated Strain History," *Ind. Eng. Chem. Fundam.*, **5**, 253–259 (1966); also I. Chen and D. C. Bogue, "Time-Dependent Stress in Polymer Melts and Review of Viscoelastic Theory," *Trans. Soc. Rheol.*, **16**, 59–78 (1972).
38. R. B. Bird and P. J. Carreau, "A Nonlinear Viscoelastic Model for Polymer Solutions and Melts–I," *Chem. Eng. Sci.*, **23**, 427 (1968).
39. W. Ostwald, *Kolloid-Z*, **36**, 99 (1925); also A. de Waele, *Oil and Color Chem. Assoc.*, **6**, 23 (1923).
40. Z. Tadmor, "Non-Newtonian Tangential Flow in Cylindrical Annuli," *Polym. Eng. Sci.*, **6**, 203–212 (1966).

41. S. B. Ellis, Thesis, Lafayette College, PA., 1927; cited in R. W. Whorlow *Rheological Techniques*, Halsted Press, New York, 1980.
42. M. M. Cross, "Rheology of Non-Newtonian Fluids: a New Flow Equation for Pseudoplastic Systems," *J. Colloids Sci.*, **20**, 417–437 (1965); also M. M. Cross, "Relation Between Viscoelasticity and Shear-thinning Behaviour in Liquids," *Rheological Acta*, **18**, 609–614 (1979).
43. P. J. Carreau, Ph.D Thesis, Department of Chemical Engineering, University of Wisconsin, Madison (1968).
44. M. Hirshberger, "Flow of Non-Newtonian Fluids in Rectangular Channels," M. S. Thesis, Department of Chemical Engineering, Technion, Israel Institute of Technology, Haifa, 1970.
45. P. E. Rouse, Jr., "A Theory of the Linear viscoelastic Properties of Dilute Solution of Coiling Polymers," *J. Chem. Phys.*, **21**, 1272–1280 (1953).
46. R. B. Bird, W. E. Stewart, and E. N. Lightfoot, *Transport Phenomena*, Second Edition, Wiley, New York, (2002).
47. P. G. deGennes, "Reptation of a Polymer Chain in the Presence of Fixed Obstacles," *J. Chem. Phys.*, **55**, 572–579 (1971).
48. M. S. Green and A. V. Tobolsky, "A New Approach to the Theory of Relaxing Polymeric Media," *J. Chem. Phys.*, **14**, 80–92 (1946).
49. F. T. Wall, "Statistical Thermodynamics of Rubber. II," *J. Chem. Phys.*, **10**, 485–488 (1942).
50. P. J. Flory and J. Rehner, "Statistical Mechanics of Cross-Linked Polymer Networks I. Rubberlike Elasticity," *J. Chem. Phys.*, **11**, 512–520 (1943).
51. H. M. James and E. Guth, "Theory of the Elastic Properties of Rubber," *J. Chem. Phys.*, **11**, 455–481 (1943).
52. L. R. G. Treloar, "The Elasticity of a Network of Long-Chain Molecules—II," *Trans. Faraday Soc.*, **39**, 241–246 (1943).
53. R. G. Larson, *Structure and Rheology of Complex Fluids*, Section 3.4.3, Oxford University Press, New York 1999.
54. S. F. Edwards, "The Statistical Mechanics of Polymerized Material," *Proc. Phys. Soc.*, **92**, 9–16 (1967).
55. W. W. Graessley, *Adv. Polym. Sci.*, **47**, 48 (1982).
56. T. T. Perkins, D. E. Smith, and S. Chu, "Direct Observation of Tube-Like Motion of a Single Polymer Chain," *Science*, **264**, 819–822 (1994).
57. K. Kremer and G. S. Grest, "Dynamics of Entangled Linear Polymer Melts: A Molecular-dynamics Simulation", *J. Chem. Phys.*, **92**, 5057–5086 (1990).
58. M. Doi and S. F. Edwards, *J. Chem. Soc. Faraday Trans. II*, **74**, 1818 (1978).
59. P. G. deGennes, *Scaling Concepts in Polymer Physics*, Cornell University Press, Ithaca, NY, 1979.
60. T. C. B. McLeish and R. G. Larson, "Molecular Constitutive Equations for a Class of Branched Polymers: The Pom-pom Polymer," *J. Rheol.*, **42**, 81 (1998).
61. N. J. Inkson, T. C. B. McLeish, O. G. Harlen, and D. J. Groves, "Predicting Low Density Polyethylene Melt Rheology in Elongational and Shear Flows with 'Pom-pom' Constitutive Equations", *J. Rheol.*, **43**, 873–896 (1999).
62. T. C. B. McLeish, "The Theory of Entangled Polymer Dynamics," *Advances in Physics*, **51**, 1379–1527 (2002).
63. M. H. Wagner and J. Schaeffer, "Constitutive Equations from Gaussian Slip-link Network Theories in Polymer Melt Rheology," *Rheol. Acta*, **31**, 22–31 (1992).
64. M. H. Wagner, H. Bastian, P. Hachmann, J. Meissner, S. Kurtzbeck, H. Münstedt and F. Langouche, "The Strain-hardening Behaviour of Linear and Long-chain-branched Polyolefin Melts in Extensional Flows," *Rheol. Acta*, **39**, 97–109 (2000).

65. M. H. Wagner, P. Ehrecke, P. Hachmann, and J. Meissner, "A Constitutive Analysis of Uniaxial, Equibiaxial and Planar Extension of a Commercial Linear High-density Polyethylene Melt," *J. Rheol.*, **42**, 621–638 (1998).

66. M. H. Wagner, P. Rubio, and H. Bastian, "The Molecular Stress Function Model for Polydisperse Polymer Melts with Dissipative Convective Constraint Release," *J. Rheol.*, **45**, 1387–1412 (2001).

67. J. F. Agassant, F. Baaijens, H. Bastian, A. Bernnat, A. C. B. Bogaerds, T. Coupez, B. Debbaut, A. L. Gavrus, A. Goublomme, M. van Gurp, R. J. Koopmans, H. M. Laun, K. Lee, O. H. Nouatin, M. R. Mackley, G.W. M. Peters, G. Rekers, W. M. H. Verbeeten, B. Vergnes, M. H. Wagner, E. Wassner, and W. F. Zoetelief, "The Matching of Experimental Polymer Processing Flows to Viscoelastic Numerical Simulation," *Int. Polym. Proc.*, **17**, 3–10 (2002).

68. H. Janeschitz-Kriegl, *Polymer Melt Rheology and Flow Birefringence*, Springer-Verlag, Berlin 1983.

69. O. H. Nouatin, Ph.D Thesis, Ecole des Mines de Paris, Sophia Antipolis, France (2000).

70. J. A. Nedler and R. Read, "A Simplex Method for Function Minimization," *Comput J.*, **7**, 308–313 (1965).

71. F. P. T. Baaijens, S. H. A. Selen, H. P. W. Baaijens, G. W. M. Peters, and H. E. H Meijer, "Viscoelastic Flow Past a Confined Cylinder of a Low Density Polyethylene Melt," *J. Non-Newt. Fluid Mech.*, **68**, 173–203 (1997).

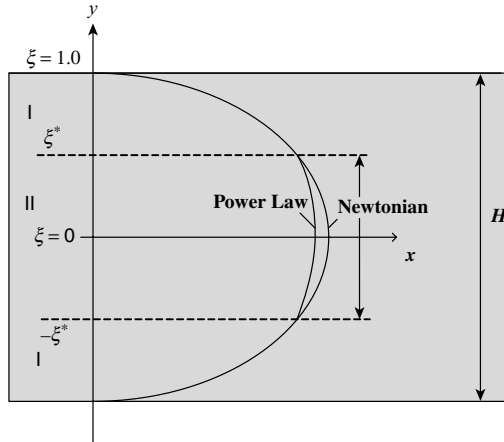
72. C. Braudo, A. Fortin, T. Coupez, Y. Demay, B. Vergnes, and J. F. Agassant, "A Finite Element Method for Computing the Flow of Multi-mode Viscoelastic Fluids: Comparison with Experiments," *J. Non-Newt. Fluid Mech.*, **75**, 1 (1998)

PROBLEMS

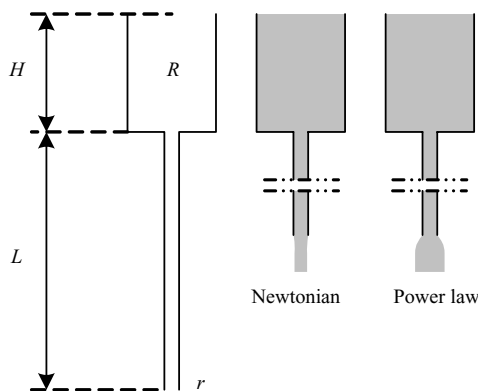
- 3.1 Pressure Flow between Parallel Plates with Various GNF Fluids** Derive expressions for the pressure flow rate of a fully developed, isothermal, steady flow between parallel plates for the following constitutive equations: (a) Power Law model: $\eta = m\dot{\gamma}^{n-1}$, (b) Ellis model: $\eta_0/\eta = 1 + (\tau/\tau_{1/2})^{\alpha-1}$, (c) Bingham Plastic: $\eta = \infty, \tau \leq \tau_0; \eta = \mu_0 + \tau_0/\dot{\gamma}, \tau \geq \tau_0$. (d) Calculate the flow rate per unit width for 2 MI LDPE at 170°C when the pressure gradient is 1.5 MPa/cm and the plate separation is 0.25 cm, using the Power Law model and the Ellis model.
- 3.2 Evaluating the Melt Index (MI) from the Flow Curve** Develop a methodology and computer program logic to evaluate the Melt Index (ASTM Standard D) of a material from its flow curve (non-Newtonian viscosity as a function of shear rate).
- 3.3 Evaluating the Flow Curve from Experimental Data** The flow rate of 3% CMC solution in water was measured in a long capillary as a function of pressure drop. Based on the results given in the following table, compute the non-Newtonian viscosity versus the shear-rate curve.

$4Q/\pi R^3(\text{s}^{-1})$	$\tau_w(\text{N/m}^2)$	$4Q/\pi R^3(\text{s}^{-1})$	$\tau_w(\text{N/m}^2)$
250	220	3500	670
350	255	5000	751
500	298	7000	825
700	341	9000	887
900	382	12500	1000
1250	441	17500	1070
1750	509	25000	1200
2500	584		

3.4 Inherent Errors in Using the Power Law Model in Pressure Flows The shear rate during pressure flow between parallel plates varies from zero at the center to maximum shear rate at the wall, $\dot{\gamma}_w$. Most polymer melts show Newtonian behavior at low shear rates, hence using the Power Law model for calculating flow rate introduces a certain error. How would you estimate the error introduced as a function of ξ^* , where ξ^* is the position below which the fluid is Newtonian? [See Z. Tadmor, *Polym. Eng. Sci.*, **6**, 202 (1966).]



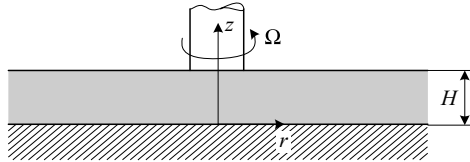
3.5 A Race Between Newtonian and Non-Newtonian Fluids Consider two vertical tubes, side by side, of diameter R and length L , as shown in the following figure, one filled with a Newtonian fluid and the other with a Power Law model fluid. The fluids emerge through a capillary of length l and radius r such that $r \ll R$. As the fluids began to emerge, an interesting phenomenon was observed: first, the level of the non-Newtonian fluids dropped faster than the Newtonian fluid, but then the Newtonian fluid overcame the former. (a) Derive a mathematical model that can explain the observed phenomenon. (b) If, after 10s, the height of both fluids is at $H/2$, what heights will they reach after 20s if the Power Law exponent is 0.5?



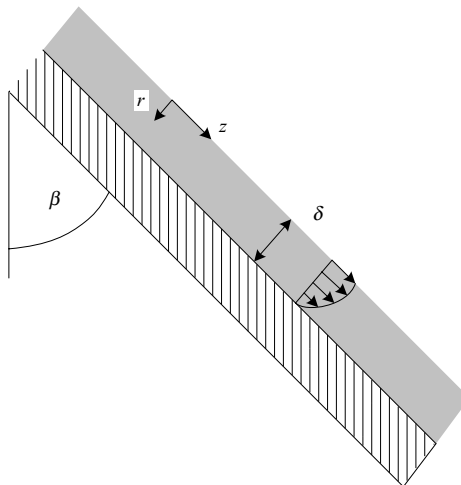
3.6 Stresses Generated by CEF Fluids in Various Viscometric Flows What stresses are necessary to maintain a CEF fluid flowing in the following flows: (a) parallel-plate drag flow; (b) Couette flow with the inner cylinder rotating; and (c) parallel-plate pressure flow. Assume the same type of velocity fields that would be expected

from a GNF or a Newtonian fluid. The three just-named flows are all viscometric. You should obtain the results in Eqs. E3.5-12 to E3.5-14.

- 3.7 Torsional Flow of a CEF Fluid** Two parallel disks rotate relative to each other, as shown in the following figure. (a) Show that the only nonvanishing velocity component is $v_\theta = \Omega r(z/H)$, where Ω is the angular velocity. (b) Derive the stress and rate of deformation tensor components and the primary and secondary normal difference functions. (c) Write the full CEF equation and the primary normal stress difference functions.

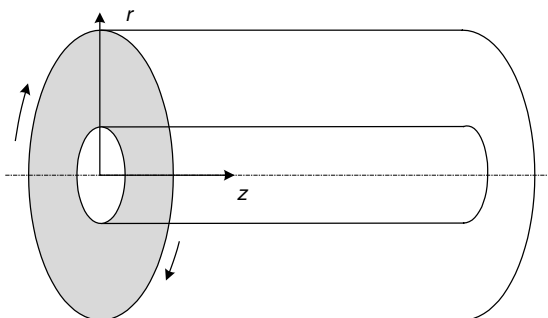


- 3.8 Special Form of the Rabinowitsch Equation** Show that the expression $Q = [\pi R^3/(s + 3)](-R\Delta P/2mL)^s$ is a special form of the Rabinowitsch equation (Eq. E3.1-9) for a Power Law fluid.
- 3.9 The Rabinowitsch Equation for Fluids Exhibiting Slip at the Wall** Derive the Rabinowitsch equation for the case where the fluid has a slip velocity at the wall V_w . [See L. L. Blyler, Jr., and A. C. Hart, *Polym. Eng. Sci.*, **10**, 183 (1970).]
- 3.10 The Flow of Non-Newtonian Fluids in Flows between Almost Parallel Plates** The lubrication approximation was discussed in terms of Newtonian fluids. Considering a nearly parallel plate pressure flow ($H = H_0 - Az$), where A is the “taper,” what additional considerations would have to be made to consider using the lubrication approximation for (a) a shear-thinning fluid flow, and (b) a CEF fluid?
- 3.11 The Flow of a Shear-Thinning Fluid on an Inclined Plate** A shear-thinning viscous liquid defined by $\eta_0/\eta = 1 + (\tau/\tau_{1/2})^{\alpha-1}$ flows at steady state gravitationally on a surface inclined by angle β , as shown in the following figure. (a) Derive an expression for the film thickness δ in terms of the volumetric flow rate. (b) Find its value for $\alpha = 1$.



3.12 Evaluation of GNF Fluid Constants from Viscometric Data Using the flow curve of Chevron/Philips 1409 MI = 50 LDPE in Appendix A, calculate the parameters of the Power Law, Cross and Carreau models.

3.13 Helical Annular Flow Consider the helical annular flow between concentric cylinders with an axial pressure gradient and rotating outer cylinder as shown in the accompanying figure. Specify the equations of continuity and motion (z and θ components) and show that, if a Newtonian fluid is used, the equations can be solved independently, whereas if $\eta = \eta(\dot{\gamma})$, where $\dot{\gamma}$ is the magnitude of $\dot{\gamma}$, the equations are coupled.



3.14 Dimensional Changes in Planar and Biaxial Extensional Flows Determine the rate of dimensional changes that have to be applied on a flat film in order to generate (a) planar extension, and (b) biaxial extension flows.

3.15 Pressure Flow Calculations Using the Equivalent Newtonian Viscosity⁶ Consider fully developed isothermal laminar pressure flow between parallel plates of a shear-thinning liquid with a flow curve fitted to the following polynomial relationship above the shear rate $\dot{\gamma}_0$:

$$\ln \eta = a_0 + a_1 \ln \dot{\gamma} + a_{11} (\ln \dot{\gamma})^2 + a_2 T + a_{22} T^2 + a_{12} T \ln \dot{\gamma} \quad \dot{\gamma} \geq \dot{\gamma}_0,$$

and Newtonian behavior below $\dot{\gamma}_0$:

$$\eta = \eta_0(T), \quad \dot{\gamma} \leq \dot{\gamma}_0$$

The coefficients a_{ij} can be accurately determined from experimental data by standard linear multiple regression methods.

(a) Show that the flow rate per unit width is given by

$$q = -\frac{2h^2}{\tau_w^2} \int_0^{\tau_w} \tau \dot{\gamma} dz$$

where h is half the thickness and τ_w is the shear stress at the wall.

6. E. Broyer, C. Gutfinger, and Z. Tadmor, "Evaluating Flows of Non-Newtonian Fluids," *AIChE J.*, **21**, 198 (1975).

(b) Show that, for a Newtonian fluid, the flow rate can be written as

$$q = \frac{2}{3} \frac{h^2 \tau_w}{\mu}$$

(c) Show that, by defining an equivalent Newtonian viscosity,

$$\bar{\mu} = - \frac{\tau_w^3}{3 \int_0^{\tau_w} \tau \dot{\gamma} d\tau}$$

the flow rate of a non-Newtonian fluid can be calculated with the Newtonian equation in (b) with μ replaced by $\bar{\mu}$.

(d) Show that $\bar{\mu}$ can be expressed uniquely in terms of τ_w and T , for example, by an equation such as

$$\ln \bar{\mu} = b_0 + b_1 \ln \tau_w + b_{11} (\ln \tau_w)^2 + b_2 T + b_{22} T^2 + b_{12} T \ln \tau_w$$

and indicate a procedure for evaluating the coefficients of b_{ij} from a_{ij} .

(e) Using the expression in (d), explain how to calculate the flow rate for a given pressure drop, and the pressure drop for a given flow rate.

3.16 The Secondary Normal Stress Difference as a Stabilizing Force in Wire Coating Dies

Using a CEF equation, it can be shown,⁷ that, if the wire in a wire coating die is off center, a lateral stabilizing force arises proportional to the secondary normal stress-difference function Ψ_2 . Use a bipolar coordinate system ξ, θ, ζ (Fig. P3.16), the components of the equation of continuity, and motion in Table P3.16. Assume that there is no axial pressure gradient and the only nonvanishing velocity component is $v_\zeta(\xi)$, with boundary conditions $v_\zeta(\xi_1, \theta) = V_0$ and $v_\zeta(\xi_2, \theta) = 0$. Further assume the fluid to be incompressible and the flow isothermal.

(a) Show that the velocity profile is given by

$$v_\zeta/V_0 = \frac{\xi - \xi_2}{\xi_1 - \xi_2}$$

(b) Show that the equation of motion reduces to

$$\begin{aligned} \frac{\partial P}{\partial \xi} + X \frac{\partial}{\partial \xi} \left(\frac{1}{X} \tau_{\xi\xi} \right) &= 0 \\ \frac{\partial P}{\partial \theta} - \frac{1}{X} \tau_{\xi\xi} \sin \theta &= 0 \end{aligned}$$

7. Z. Tadmor and R. B. Bird, "Rheological Analysis of Stabilizing Forces in Wire-Coating Dies," *Polym. Eng. Sci.*, **14**, 124 (1974).

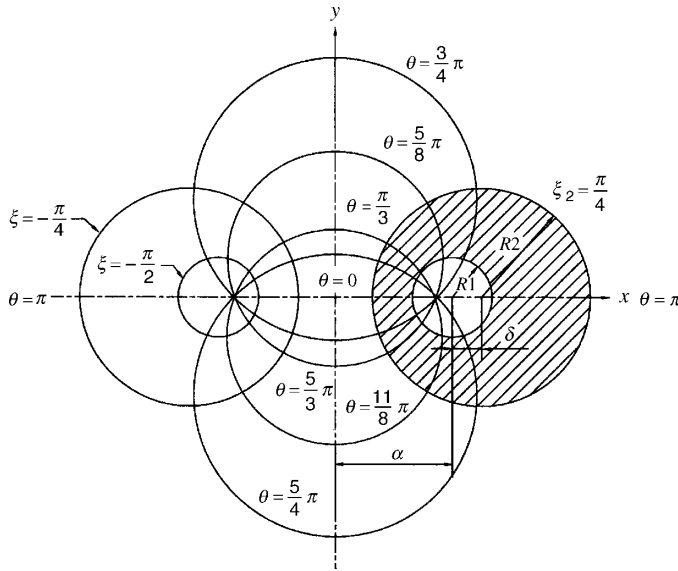


Fig. P3.16 Bipolar coordinate system. The shaded area denotes the cross section of the fluid, and the constant a , the distance of the pole from the origin. [Reprinted by permission from R. Bird, R. Armstrong, and O. Hassager, *Dynamics of Polymeric Liquids, Volume 1, Fluid Mechanics*, Second edition, Wiley, New York, 1987.]

where

$$X = \cosh \xi + \cos \theta$$

(c) Show that the lateral force in the wire per unit length f_x is

$$f_x = -\frac{\Psi_2 \pi V_0^2}{a(\xi_1 - \xi_2)^2}$$

where a is the distance of the poles of the bipolar coordinate system from the origin, which is related to the separation of centers of wire and die δ , via

$$\frac{\delta}{R_2} = \sqrt{1 + \left(\frac{a}{R_2}\right)^2} - \sqrt{\left(\frac{R_1}{R_2}\right)^2 + \left(\frac{a}{R_2}\right)^2}$$

Note that

$$\xi_1 = \sinh^{-1}\left(\frac{a}{R_1}\right) \quad \text{and} \quad \xi_2 = \sinh^{-1}\left(\frac{a}{R_2}\right)$$

3.17 The Single Maxwell Element LVE Constitutive Equation Consider the single Maxwell mechanical element shown in the following figure. The element was at rest for $t < 0$. A shear strain $\gamma_{12}(t)$ is applied at $t = 0$. By stating that the stress is the same in the dashpot and spring, while the total strain is the sum of those

TABLE P3.16 The Equations of Continuity and Motion in Bipolar Coordinates (ξ, θ, ζ)

Continuity

$$\frac{\partial}{\partial t} \rho + \left(\frac{X}{a} \frac{\partial}{\partial \xi} \rho v_\xi + \frac{X}{a} \frac{\partial}{\partial \theta} \rho v_\theta + \frac{\partial}{\partial \zeta} \rho v_\zeta - \frac{1}{a} \sinh \xi \cdot \rho v_\xi + \frac{1}{a} \sin \theta \cdot \rho v_\theta \right) = 0$$

Motion

$$\begin{aligned} & \rho \left[\frac{\partial v_\xi}{\partial t} + v_\xi \left(\frac{X}{a} \frac{\partial}{\partial \xi} v_\xi + \frac{1}{a} v_\theta \sin \theta \right) + v_\theta \left(\frac{X}{a} \frac{\partial}{\partial \theta} v_\xi + \frac{1}{a} v_\theta \sinh \xi \right) + v_\zeta \left(\frac{\partial}{\partial \zeta} v_\xi \right) \right] \\ &= -\frac{X}{a} \frac{\partial P}{\partial \xi} - \left[\frac{X}{a} \frac{\partial}{\partial \xi} \tau_{\xi\xi} + \frac{X}{a} \frac{\partial}{\partial \theta} \tau_{\theta\xi} + \frac{\partial}{\partial \zeta} \tau_{\zeta\xi} + \frac{1}{a} (\tau_{\theta\theta} - \tau_{\xi\xi}) \sinh \xi + \frac{1}{a} (\tau_{\theta\xi} + \tau_{\xi\theta}) \sin \theta \right] + \rho g_\xi \end{aligned}$$

$$\begin{aligned} & \rho \left[\frac{\partial v_\theta}{\partial t} + v_\xi \left(\frac{X}{a} \frac{\partial}{\partial \xi} v_\theta - \frac{1}{a} v_\xi \sin \theta \right) + v_\theta \left(\frac{X}{a} \frac{\partial}{\partial \theta} v_\theta - \frac{1}{a} v_\xi \sinh \xi \right) + v_\zeta \left(\frac{\partial}{\partial \zeta} v_\theta \right) \right] \\ &= -\frac{X}{a} \frac{\partial P}{\partial \theta} - \left[\frac{X}{a} \frac{\partial}{\partial \xi} \tau_{\xi\theta} + \frac{X}{a} \frac{\partial}{\partial \theta} \tau_{\theta\theta} + \frac{\partial}{\partial \zeta} \tau_{\zeta\theta} + \frac{1}{a} (\tau_{\theta\theta} - \tau_{\xi\xi}) \sin \theta - \frac{1}{a} (\tau_{\theta\xi} + \tau_{\xi\theta}) \sinh \xi \right] + \rho g_\theta \end{aligned}$$

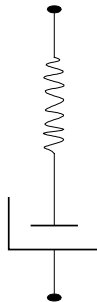
$$\begin{aligned} & \rho \left[\frac{\partial v_\zeta}{\partial t} + v_\xi \left(\frac{X}{a} \frac{\partial}{\partial \xi} v_\zeta \right) + v_\theta \left(\frac{X}{a} \frac{\partial}{\partial \theta} v_\zeta \right) + v_\zeta \left(\frac{\partial}{\partial \zeta} v_\zeta \right) \right] \\ &= -\frac{\partial P}{\partial \zeta} - \left[\frac{X}{a} \frac{\partial}{\partial \xi} \tau_{\xi\zeta} + \frac{X}{a} \frac{\partial}{\partial \theta} \tau_{\theta\zeta} + \frac{\partial}{\partial \zeta} \tau_{\zeta\zeta} - \frac{1}{a} \tau_{\xi\xi} \sinh \xi + \frac{1}{a} \tau_{\theta\theta} \sin \theta \right] + \rho g_\zeta \end{aligned}$$

in which, for Newtonian fluids, $\tau_{ij} = -\mu \{ (\nabla \mathbf{v}) + (\nabla \mathbf{v})^\dagger \}_{ij}$.

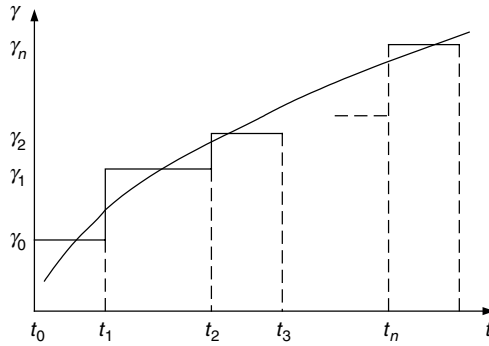
Source: Z. Tadmor and R. B. Bird, "Rheological Analysis of Stabilizing Forces in Wire-Coating Dies," *Polym. Eng. Sci.* **14**, 124 (1974).

Note: For the definition of X and a , see Problem 3.16.

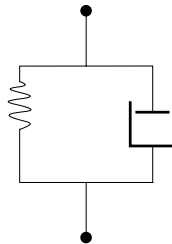
of the spring and the dashpot, obtain Eq. 3.3-9 in shear. Solve the differential equation to obtain $\tau/\gamma_0 = Ge^{-t/\lambda}$ for a stress relaxation experiment, *that is*, $\dot{\gamma}_{12} = \gamma_0$.



3.18 The Boltzmann Superposition Principle Apply the Boltzmann superposition principle to obtain the LVE (Eq. 3.3-8) using $\tau(t) = \gamma_0 Ge^{-t/\lambda}$. Consider the applied strain $\gamma(t)$ as being applied discretely in a series of small steps $\Delta\gamma$, as shown in the following figure:

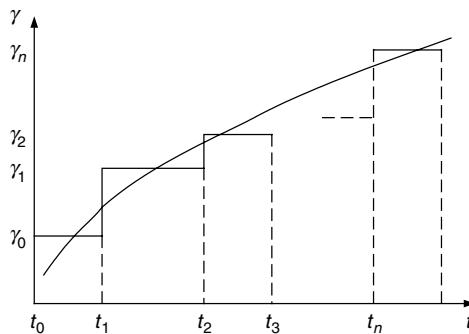


3.19 The Single Voigt Element LVE Constitutive Equation In the Voigt mechanical element shown in the following figure, the total stress is the sum of the stresses on the dashpot and spring. On the other hand, the strain in each component is equal to the total strain. (a) Use these facts to develop the constitutive equation for a single Voigt element. (b) Solve the differential equation for a creep experiment ($\tau = 0, t < 0; \tau = \tau_0, t \geq 0$).



3.20 The Boltzmann Superposition Principle: Alternate form of the LVE Equation

Apply the Boltzmann superposition principle for the case of a continuous stress application on a linear viscoelastic material to obtain the resulting strain $\gamma(t)$ in terms of $J(t - t')$ and $d\tau/dt'$, the stress history. Consider the applied stress in terms of small applied $\Delta\tau_i$, as shown on the accompanying figure.



- 3.21 Creep in Structural Design** A pendulum clock manufacturer wants to replace the metal pendulum arm of the clocks with a polymer rod. Is his idea a good one? Use the answer to Problem 3.20.
- 3.22 Prediction of $\bar{\eta}^+(t)$ by the Rubberlike Liquid Constitutive Equation** Calculate the extensional viscosity as a function of time after the start-up of a steady uniaxial extension of a Lodge rubberlike liquid, Eq. 3.4-3, having a single relaxation time λ_0 and modulus G_0 , Eq. 3.4-4. Before the initiation of the steady extensional flow the sample is and had been at rest, thus the stretch ratio history is: $\lambda(t', t) = \exp[\dot{\epsilon}(t' - t)]$ for $t' > 0$ and $\lambda(t', t) = \exp(\dot{\epsilon}t')$ for $t' \leq 0$ (independent of t')
- 3.23 Prediction of the Steady-State Viscosity in a Simple Shearing Flow by the K-BKZ Constitutive Equation** The K-BKZ (Kaye-Bernstein, Kearsley, and Zappas) constitutive equation [A. Kaye, Note No. 134, College of Aeronautics, Cranford University, U.K. (1962)] has the same integral form as the Green and Tobolsky Lodge rubberlike liquid, but utilizes a strain-dependent modulus $G[(t - t'), \gamma] = m(t - t')h(\gamma) = h(\gamma) \sum_i \frac{G_i}{\tau_i} \exp[(t - t')/\lambda_i]$. Thus, it has the general form $\tau = \int_{-\infty}^t m(t - t')\gamma_{[1]}(t', t) dt'$. Consider a fluid with a single relaxation time, λ_0 , and modulus, G_0 , and with $h(\gamma) = e^{-\gamma}$. Calculate the steady-state shear viscosity function $\eta(\dot{\gamma})$.

4 The Handling and Transporting of Polymer Particulate Solids

- 4.1 Some Unique Properties of Particulate Solids, 145
- 4.2 Agglomeration, 150
- 4.3 Pressure Distribution in Bins and Hoppers, 150
- 4.4 Flow and Flow Instabilities in Hoppers, 152
- 4.5 Compaction, 154
- 4.6 Flow in Closed Conduits, 157
- 4.7 Mechanical Displacement Flow, 157
- 4.8 Steady Mechanical Displacement Flow Aided by Drag, 159
- 4.9 Steady Drag-induced Flow in Straight Channels, 162
- 4.10 The Discrete Element Method, 165

In this chapter we deal with the entire “journey” of polymeric particulate solids, from the polymerization reactor to the shaped and structured finished product. The reader is referred to Chapter 1, which discusses all the processes and elementary steps involved in this journey.

The products of polymerization reactors are most often in particulate form: gas phase and slurry reactors produce porous spherical particulates about 300 μm in diameter; emulsion reactors produce ultrafine 0.1 μm -diameter powder particulates; and suspension reactors produce beads that are 100–1000 μm in diameter. Except for the gas-phase reactor, the particulate product stream has to be dried. The particulate reactor products are then transported in finished form to storage silos. Since they do not contain the necessary “stabilizer package,” and since, fine particulates are in general, more difficult to feed in compounding and final fabrication processing equipment, the following steps are taken. The particulates are transported in fluidized form to conical blenders, where stabilizing additives are spray-mixed onto them. From there, they are metered by weight-in-loss feeders with feed screws into large, twin-rotor melting extruders where melting and intimate mixing of the stabilizers are accomplished. Large, multihole, generally underwater strand dies with fast rotating knife blades in contact with the die-hole ring produce pellets of typical cylindrical dimension, that is, 0.3 cm diameter and 0.3 cm height. The molten pellets are cooled skin-deep by water in turbulent flow in the water box and transported as slurry for further cooling, spin-drying, storage, and shipping into 50-lb bags, 1000 lb gaylords or railroad cars. Typical polymer particulates are shown in Fig. 4.1.

As we pointed out in Chapter 1, the preceding describes the postreactor “finishing” operation. The pellets are then shipped to be compounded, namely, blended with fillers, colorants, or other polymers, where after melting, mixing, and reacting, they form physical

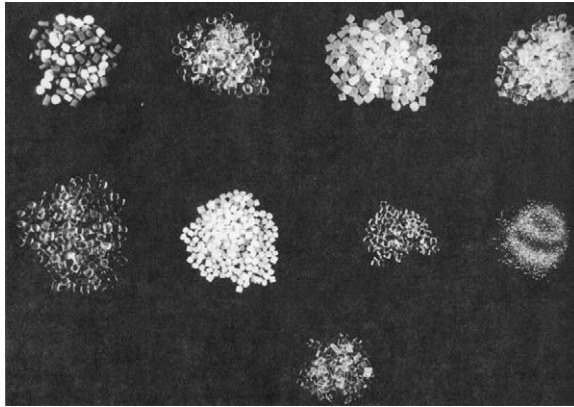


Fig. 4.1 Typical polymer particulates.

or reactive blends, as we shall see in Chapter 11. The pellets are meter-fed into twin rotor compounding equipment and exit again out of multihole dies to be pelletized as hot strands or underwater; in both cases, they are water-cooled and dried, packaged, and shipped to final polymer product fabricators. Finally, pellets are fed into single-rotor shaping processing equipment, such as single screw extruders or injection molding machines. For water-absorbing polymers, such as PET and polyamide (PA), the pellets are dried by hot air for 2 to 4 hours before processing, and transported in airtight conduits in fluidized form, to hoppers sealed from the atmosphere.

All the preceding “particulate handling steps” are affected by the unique properties of all particulates, including polymeric particulates; while they may behave in a fluidlike fashion when they are dry, fluidized and above $100\ \mu\text{m}$, they also exhibit solidlike behavior, because of the solid–solid interparticle and particle–vessel friction coefficients. The simplest and most common example of the hermaphroditic solid/fluidlike nature of particulates is the pouring of particulates out of a container (fluidlike behavior) onto a flat surface, whereupon they assume a stable-mount, solidlike behavior, shown in Fig. 4.2. This particulate mount supports shear stresses without flowing and, thus by definition, it is a solid. The *angle of repose*, shown below, reflects the static equilibrium between unconfined loose particulates.

Solidlike behavior abounds when the surface-to-volume ratio is very high,¹ that is, when the particulates are even mildly compacted, surface-charged, or wet; all contribute to large frictional forces and to nonuniform, often unstable stress fields in both flowing and compacted particulate assemblies, as we discuss later in this chapter. We begin by discussing some of the unique properties of polymer particulates relevant to processing. Comprehensive reviews can be found in the literature (1–4).

4.1 SOME UNIQUE PROPERTIES OF PARTICULATE SOLIDS

Scientific and engineering investigations into the properties and behavior of particulate solids date back to the early work of Coulomb, who in 1776 developed a theory on “soil pressure and resistance,” thus laying sound foundations for important engineering

1. Pellets, compared to fine powders, with low surface-to-volume ratios, are readily flowable, easily fluidized and meter- or hopper-fed. These attributes justify pelletization.

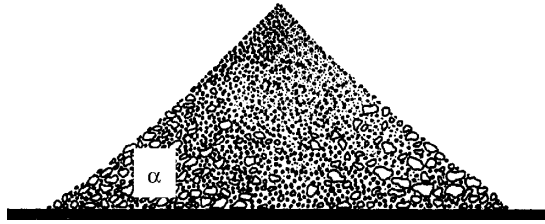


Fig. 4.2 The angle of repose. It should be noted that the angle of repose is generally not a measure of flowability of solids, and as Jenike (22) points out, it is strictly useful only to determine the contour of a pile. Its popularity stems from the ease with which it can be measured.

practices. Later, in 1852, Hagen analyzed the flow of sand in an hourglass, and shortly afterward, Reynolds, in 1885, made his observation on the dilatancy of a deforming mass of sand.² The latter, unique property of particulate solids can be observed while walking on wet sand at the seashore. The sand “whitens” or appears to dry momentarily around the foot because the pressure of the foot dilates the sand.

The analysis of particulate solids systems in analogy to fluids can be divided into statics and dynamics: it is interesting to note that, in spite of the early beginnings of scientific interest in the properties of particulate solids, this field—in particular the dynamics of particulate solids—has not experienced the same intensive scientific development as fluid dynamics. In most engineering curricula, relatively little attention is focused on the analysis of particulate solids. Therefore, as engineers, we are generally ill-equipped to analyze these complex systems and to design equipment for handling them, and we may often be surprised by the behavior of solids, such as, for example, the fact that the drag on the plough is independent of its speed (5).

A closer look at the properties of particulate solids and their response to external forces reveals, as pointed out earlier, that these are a blend of (a) liquidlike behavior, (b) solidlike behavior, and (c) particle-interface-dominated behavior, unique to these systems. Like liquids, particulate systems take the shape of the container they occupy, exert pressure on the container walls, and flow through openings. Yet like solids, they support shearing stresses (hence, they form piles), may possess cohesive strength, and exhibit a nonisotropic stress distribution upon application of a unidirectional load. But unlike liquids, shearing stress is proportional to normal load rather than to rate of deformation, and unlike solids, the magnitude of the shearing stress is generally indeterminate, and all that can be said is that the following inequality holds

$$\tau \leq f' \sigma \quad (4.1-1)$$

where f' is the interparticle static coefficient of friction and σ represents a range of normal forces (“pressures”) that can be applied to the particulate system before a value of shear stress τ is reached that is high enough to start the particles sliding past one another. That is, before particulate solids flow starts, there is a range of equilibrium states and a range of bulk densities allowable. Only at the inception of flow are the frictional forces fully mobilized (4). At this state, the relation takes the form of *Amonton’s law*, discussed in the following subsection, which is the defining equation for the coefficient of static friction.

2. O. Reynolds, “On Dilatancy of Media Composed of Rigid Particles in Contact. With Experimental Illustrations.” *Philos. Mag.*, Ser. 5, 20, 469 (1885).

Solid–Solid (Dry) Friction

Friction is the tangential resistance offered to the sliding of one solid over another, due to dry friction. Friction is an apparently simple phenomenon with very complex mechanisms that take place on a variety of length scales, from atomic to nano and up. The study of friction is part of the engineering–scientific discipline of *tribology*,³ which is the scientific study of friction, wear, and lubrication (6). It was Leonardo da Vinci (1452–1519) who discovered the first two laws of friction, namely, that the area of contact has no effect on friction and that friction is proportional to the load. These two laws were rediscovered later by Guillaume Amontons (1663–1705), and later Charles-Augustin Coulomb (1736–1806), added the third law:

1. The friction force (F_T) is directly proportional to the applied load (F_N); that is, $F_T \propto F_N$, where the proportionality constant for any pair of solid surfaces is called the *coefficient of friction*, f .
2. The force of friction is independent of the apparent area of contact.
3. Kinetic friction is independent of sliding velocity.

Bowden and Tabor (7) suggested a physical explanation for the observed laws of friction. They determined that the true area of contact is but a small fraction of the apparent area of contact, because the surfaces of even the most highly polished material show irregularities appreciably larger than atomic dimensions called in the literature *asperities*, as shown in Fig. 4.3. Thus, with increasing normal load, more asperities come in contact and the average area of contact grows, as shown in Fig. 4.4

Consequently, Bowden and Tabor (7) specify two factors that are responsible for dry friction: the first, and usually the more important factor, is the adhesion that occurs at the

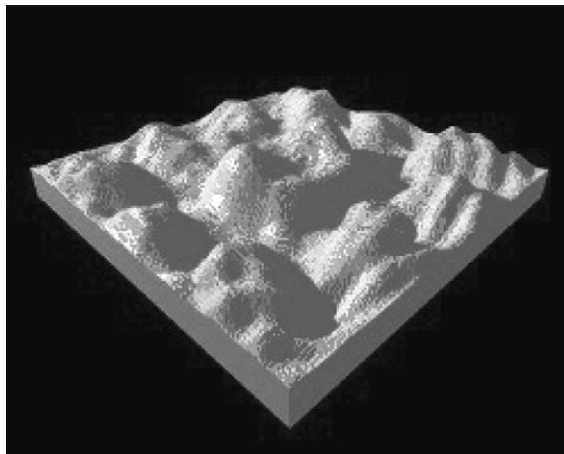


Fig. 4.3 A magnified view of a solid surface showing surface roughness of hills, referred to as asperities, separated by valleys. [Reproduced by permission from I. M. Hutchings, *Tribology: Friction and Wear of Engineering Materials*, Edward Arnold, UK, 1992 (co-published by CRC Press, Boca Raton, FL).]

3. The word “tribology” comes from the Greek word $\tau\rho\iota\beta\omega$, which means “to rub.”

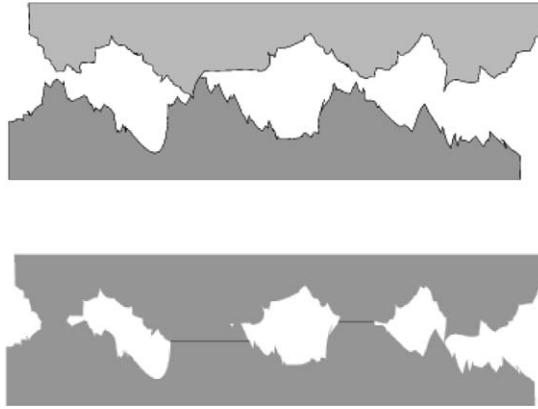


Fig. 4.4 Two surfaces in contact with (a) without normal load, and (b) with normal load.

regions of real contact: these adhesions, welds, or junctions have to be sheared if sliding is to occur; the second factor arises from the plowing and grooving of one surface by the asperities of the other. However, elastic deformation, which precedes the yield point, also plays a role, as does the presence of surface *contaminants*, such as organic compounds or oxides, which tend to decrease adhesion. Disregarding the latter effects, in the case of *static* friction, only adhesion at the contact sites is important, whereas in either sliding or rolling friction, the second factor, plowing, enters the picture. By neglecting the second factor relative to the first, we can approximately explain the first two laws of friction. Because the real contact area is so small, we can assume that, even if the normal load is small, the pressure at the contact points is sufficiently high to reach the value of the yield stress of the softer material σ_y . Assuming that this is indeed the case, that is, that plastic flow occurs, we can argue that the area at a point of contact, A_i is

$$A_i = \frac{F_{N_i}}{\sigma_y} \quad (4.1-2)$$

where F_{N_i} is the load supported by the contact point. An adhering contact point forms a joint that can be broken only when the value of the applied tangential force F_{T_i} reaches the level

$$F_{T_i} = \tau_y A_i \quad (4.1-3)$$

where τ_y is the shear strength of the softer material. If we assume that the total tangential frictional force is simply the sum of all, F_{T_i} , we obtain that

$$F_T = \sum F_{T_i} = \frac{\tau_y}{\sigma_y} \sum F_{N_i} = \left(\frac{\tau_y}{\sigma_y} \right) F_N \quad (4.1-4)$$

Equation 4.1-4 suggests that the *static* coefficient of friction is a material property characteristic of the pair of solid surfaces and, specifically, of the softer solid

$$f' = \frac{\tau_y}{\sigma_y} \quad (4.1-5)$$

By extension, Eqs. 4.1-4 and 4.1-5 are assumed to hold for kinematic friction (f), too, assuming that adhesion predominates. The statement that the kinematic friction coefficient

f is a material property, independent of the geometric nature of the surface and frictional process conditions, is only a rough approximation.

Only recent developments in instrumentation of scanning probe microscopy, such as scanning tunneling microscopy (8) and atomic force microscopy (9), have made it possible to study friction on the nanometer and higher scales. These experiments show that the behavior on the single asperity level is different from that on the macroscopic scale.

One of many complications in the experimental studies, and in developing a theoretical foundation, is the interpretation of the experimental results and the complexity caused by ambient conditions, because real surfaces are always contaminated with airborne molecules, water, hydrocarbons, debris, and the formation of liquid bridges. Moreover, sliding of one solid onto another introduces a new set of circumstances and unknowns. It may lead to high and unknown local temperatures and pressures, generating fresh and chemically different surfaces, and mostly altering the topography of the surface as a result of deformation and wear. For these reasons, the coefficients of static and sliding friction are different. The static coefficient is larger than the sliding (kinematic) coefficient. However, recent findings and techniques lend support to Bowden and Tabor's assumption that the macroscopic, dry frictional behavior is undoubtedly dominated by the physics of individual contacts and interactions of contacting asperities (10,11).

In view of these complexities, it is remarkable that Eq. 4.1-4 represents numerous metal-metal, dry frictional data rather well, for both the static and sliding cases. Polymers, on the other hand, exhibit an even more complex frictional behavior on metal. This is, perhaps, not surprising, since the physical situation involves a relatively soft, viscoelastic, and temperature-dependent material in contact with a hard, elastic, and much less temperature- and rate-dependent material. Empirical evidence of these complexities is the nonlinear relationship between the frictional force and the normal load

$$F_T = CF_N^\alpha \quad (4.1-6)$$

from which a load-dependent coefficient of friction can be deduced

$$f = CF_N^{\alpha-1} \quad (4.1-7)$$

where C is a constant and the exponent α is found to vary between the values of 1 and 0.666. It has been suggested by Lodge and Howell (12) that $\alpha = 2/3$ corresponds to the case of pure elastic deformation at the contact points, whereas $\alpha = 1$, according to Eq. 4.1-4, corresponds to purely plastic (yielding) deformation. Hence, values in between appear to reflect viscoelastic deformation at the contact points. If this is the case, the total contact area would be expected to depend on the normal load, the time of contacts, the temperature, and the speed of sliding. As we shall see later in the chapter, these effects are generally observed. It is worth noting that the expression for the dry coefficient of friction (Eq. 4.1-7) has the same form as that of the viscosity ("internal friction") of a Power Law fluid that describes the non-Newtonian behavior of polymer melts.

From the foregoing it follows that, except for $\alpha = 1$, the coefficient of friction decreases with increasing load, F_N . This observation is a general feature of polymers, namely, that the effective coefficient of friction reduces at higher loads (13,14).

Thus, before we consider the response of particulate systems to externally applied stresses, we must know whether the shear and normal stresses at any point and orientation are above the values specified by the equality of Eq. 4.1-1. Furthermore, since there are two kinds of particulate solids, the noncohesive (free-flowing) and the cohesive, we

comment on the phenomenon of agglomeration, which transforms the former to the latter. Finally, we must remember that, since it is necessary to contain particulate solids, the wall particulate static coefficient of friction and the wall shear and normal forces must be specified. The wall is another location at which flow can be initiated.

4.2 AGGLOMERATION

The term *agglomeration* describes the forming of a cluster of particles from individual particles. Agglomerates form because of the binding of van der Waals forces between individual particles, which require intimate contact to exert any significant attraction. For small particles of sizes up to ultrafine 10 μm , the mass of any one individual particle is so small that it creates a loose-particle agglomeration, and great difficulties in fluidization are encountered. Rotating fluidized beds creating 10–20-g centrifugal fields have recently been used to make the mass of each particulate effectively 10–20 times larger, enabling gas–solid fluidization (15). Presumably, any surface shear stresses imposed on the system have the effect of decreasing the size of agglomerates, either by breakup, or by erosion, or by both (16,17), as is discussed in Chapter 7 in connection with dispersive mixing of solid additives by shear and extensional polymer processing flows. Additionally, solid–solid forces are significantly amplified by increases in pressure exerted on loose particulate assembly regions, leading to “caking.” In the processing of particulate-filled polymers, when the particulates and polymer (powder or pellets) are fed as a solid mixture into either single- or twin-rotor processing equipment, compaction takes place in SSEs, and repeated cycles of compressions in TSEs, often leading to caking before melting. Following melting, such agglomerated “cakes” may be held strongly enough for the shearing stresses in the flowing melt to prevent dispersing them. We discuss such a problem in Chapters 9 and 10.

4.3 PRESSURE DISTRIBUTION IN BINS AND HOPPERS

The static pressure under a *liquid column* is isotropic and is determined by the height of the column above the point of measurement, h , and the density of the liquid ρ

$$P = \rho gH \quad (4.3-1)$$

In a column of particulate solids contained in a vertical bin, the pressure at the base will not be proportional to the height of the column because of the friction between the solids and the wall. Moreover, a complex stress distribution develops in the system, which depends on the properties of the particulate solids as well as the loading method. The latter affects the mobilization of friction, both at the wall and within the powder. Finally, *arching* or *doming* may further complicate matters. Hence, an exact solution to the problem is hard to obtain. In 1895, Janssen (18) derived a simple equation for the pressure at the base of the bin, which is still frequently quoted and used. The assumptions that he made are: the vertical compressive stress is constant over any horizontal plane, the ratio of horizontal and vertical stresses is constant and independent of depth, the bulk density is constant, and the wall friction is *fully mobilized*, that is, the powder is in incipient slip condition at the wall.

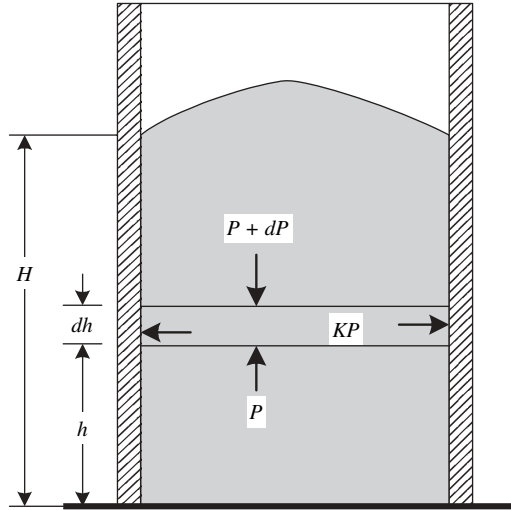


Fig. 4.5 A Vertical bin filled with particulate solids.

A force balance over a differential element (Fig. 4.5) simply using pressure P instead of the compressive stress, with shear stress at the wall $\tau_w = \sigma_w \tan \beta_w + c_w$, where β_w is the angle of internal friction and c_w is the coefficient of cohesion at the wall (14), gives

$$A\rho_b g dh + (P + dP)A = (c_w + f'_w KP)C dh + \frac{PA}{\quad} \quad (4.3-2)$$

[Weight of element]
[Pressure acting downward]
[Frictional forces supporting element]
[Pressure acting upward]

where ρ_b is bulk density, A is the cross-sectional area, C the “wetted” circumference, and K is the ratio of compressive stress in the horizontal direction to compressive stress in the vertical direction. The physical parameter K is discussed by Tadmor and Gogos (19). Integration of Eq. 4.3-2 results in

$$P = P_1 \left[\frac{f'_w CK(h - h_1)}{A} \right] + \frac{(A\rho_b g / C - c_w)}{f'_w K} \left\{ 1 - \exp \left[\frac{f'_w CK(h - h_1)}{A} \right] \right\} \quad (4.3-3)$$

where P_1 is the pressure at height h_1 . For the special case of a cylindrical bin, with $h = H$, where $P_1 = 0$ and $c_w = 0$ (no adhesion between solids and the wall), Eq. 4.3-3 reduces to the more familiar Janssen equation

$$P = \frac{\rho_b g D}{4f'_w K} \left\{ 1 - \exp \left[\frac{4f'_w K(h - H)}{D} \right] \right\} \quad (4.3-4)$$

Clearly the pressure at the base approaches a limiting value as H goes to infinity

$$P_{\max} = \frac{\rho_b g D}{4f'_w K} \quad (4.3-5)$$

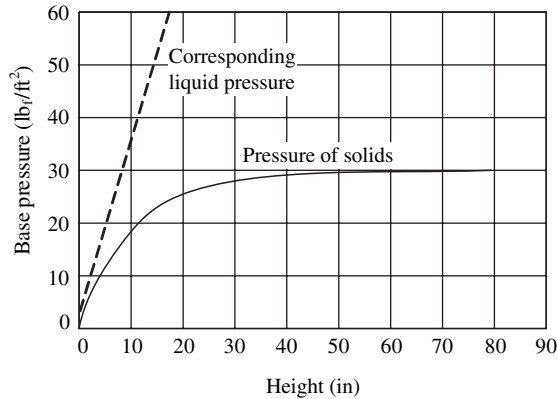


Fig. 4.6 Base pressure in a 10-in-diameter cylindrical hopper filled with 1/8-in PS cubes with $K = 0.521$, $f'_w = 0.523$, and $\rho_b = 39\text{lb}/\text{ft}^3$. [Reprinted by permission from W. L. McCabe and J. C. Smith, *Unit Operations of Chemical Engineering*, McGraw-Hill, New York, 1956.]

Hence, most of the weight is supported frictionally by the walls of the bin. The maximum pressure is proportional to bin diameter and inversely proportional to the coefficient of friction at the wall.

Figure 4.6 plots the pressure measured under a load of PS pellets in a 10-in-diameter cylindrical bin as a function of solids height. The many attempts to verify the Janssen equation have met with varying success, and improved models have been offered (20) (these are discussed in some detail in the first edition of this book), but the *shape* of the curve as predicted by the model is usually observed (4). The underlying reason for the good qualitative agreement is that the particulate assembly in the cylindrical hopper is stripped of its volume-wise particle-to-particle interactions, which are due to interparticle friction. The column of particulates is treated as a *solid plug* with only three properties: density, ρ_b ; the ratio of the compressive stress in the horizontal direction, K ; and the static friction coefficient between the particulates and the hopper wall, f'_w . All these may vary from one location to another, because of neighboring particulate interactions, which include both Newton's second law of motion and a force-deformation constitutive equation for the particulates. The *discrete element method* (DEM), which we discuss in Section 4.10, takes this approach in simulating static and flowing particulate assembly behavior under externally applied and gravity forces.

4.4. FLOW AND FLOW INSTABILITIES IN HOPPERS

In polymer processing practice, we need to ensure that the particulate gravitational mass flow rate of the hopper exceeds, over the complete operating range, the extruder “open discharge” rate (i.e., the rate without any die restriction). That is, hoppers must *not* be the production-rate limiting factor. Second, and more importantly, it is necessary for stable extrusion operations and extruded product quality that the flow be steady and free of *instabilities* of the particulate flow emerging from the hoppers. Finally, as we will see in Chapter 9, we need to know the pressure under the hopper in order to determine the pressure profile in a SSE.

There are generally two types of gravitational flow in bins and hoppers [Fig. 4.7(a), 4.7(c)]: “mass” flow and “funnel” flow. In mass flow, the whole mass of particulate solids

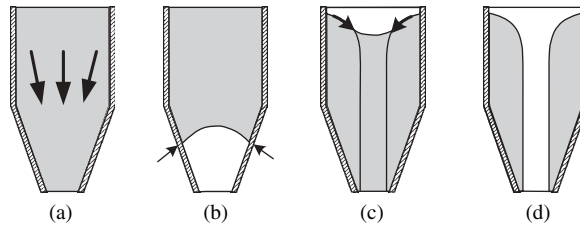


Fig. 4.7 Schematic representation of (a) “mass” flow in hoppers, (b) “arching,” (c) “funnel” flow, and (d) “piping.”

moves toward the exit, and in funnel flow, the particles flow out through a central opening. In the former, the main cause for flow disturbance is doming or arching, where all the weight of the solids is supported by the walls [Fig. 4.7(b)], whereas in the latter flow, disturbances may occur when the solids can sustain the existence of an empty central tube, called ‘*piping*’ [Fig. 4.7(d)]. These and other flow disturbances were discussed by Johanson (21). In both arching and piping, the solids must have consolidated sufficiently to develop the level of strength necessary to sustain the weight of the retained particulate solids. Hence, obstruction to flow is acute in cohesive particulate solids and it depends, in addition to material properties, on hopper geometry, which determines the stress distribution in the system. Jenike (22) and Richmond and Gardner (23), among others, developed design methods and criteria for building obstruction-free hoppers and bins.

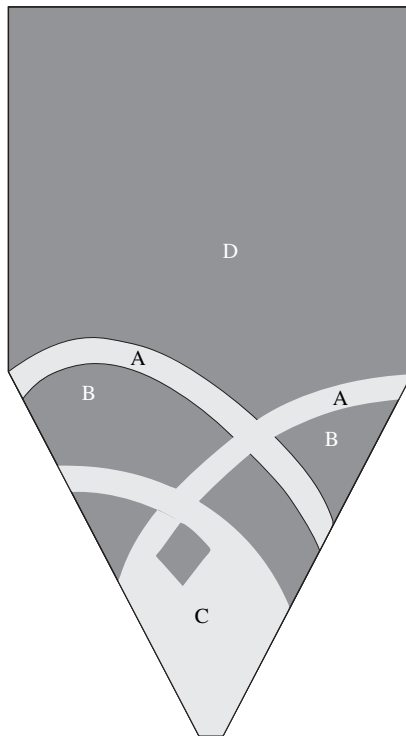


Fig. 4.8 Regions of different flow behavior in two-dimensional hoppers as observed by radiographic techniques. [Reprinted by permission from J. Lee et al., *Trans. Soc. Rheol.*, **18**, 247 (1974).]

The flow pattern in two-dimensional hoppers was studied by Lee et al. (24). They used radiographic techniques to determine simultaneously the flow field and the porosity field. The marks left by tracer particles during discharge permit the evaluation of the local velocity vector, and the intensity of the shade, the porosity. On the basis of both velocity and porosity fields, the authors distinguished between four regions (Fig. 4.8): region D they identified as a “plug-flow zone”; in region B they observed rigid-body behavior; region A appeared to be a “rupture zone,” where intensive deformation occurs, and region C is a free-flow zone. A detailed mapping of the flow kinematics in two-dimensional hoppers using the stereoscopic technique developed by Butterfield et al. (25), was done by Levinson et al. (26). Other noninvasive techniques such as MRI were applied more recently to the study of the flow fields in particulate systems (27,28).

Although a great deal of progress has been made in obtaining flow fields of particulate solids, and design criteria for arch-free flow are available, it is not yet possible to calculate discharge rates from first principles. Hence, empirical equations are used for this purpose. It should be noted, perhaps, that in most polymer processing applications, such as in hopper feeding processing equipment, the maximum, open discharge hopper flow rates are much higher than present processing rates. This was aptly shown in a recent paper by Potente and Pohl (29), where it is shown that hoppers can become limiting (because of flight interference to hopper flows) only at very high screw speeds.

4.5 COMPACTION

The response of particulate solid systems, specifically powders, to forced compaction, is of great interest in a broad range of processes. *Tableting* or *pelleting* of pharmaceutical products, powder pressing in ceramic industries, powder metallurgy, and briquetting of coal can serve as examples. In polymer processing, loose particulate solids are compacted prior to melting inside most processing machinery, and the performance of these machines is greatly influenced by the compaction behavior of the solids.

In polymer processing, compaction is an important and necessary step in order to reduce the interparticle, unoccupied spaces and thus eliminate air. It is essential for melting in both single-screw extruders as well as for twin-rotor processors, as we shall see in Chapters 5 and 10. In twin-rotor devices, such as Co-TSEs, for example, the large and repeated deformation of *compacted* particulates by the “kneading elements,” which induces large *plastic* deformation of particulates, is the dominant melting mechanism.

In other applications, the purpose of compaction is to induce agglomeration. The compaction is obtained by applying an external force. This force is transmitted within the system through the points of contact between the particles. By a process of small elastic and plastic deformation (shear deformation and local failure), the points of contact increase, as do the forces holding the particles together, as discussed in the section dealing with agglomeration. The externally applied force generates an internal stress field, which, in turn, determines the compaction behavior.

It was Wollaston (30) who in 1829 recognized the great pressures needed for compaction of dry powders—an observation that led to his famous toggle press. Since that time, compaction and deformation of powders and particulate systems have been extensively studied (31–35). There are many difficulties in analyzing the compaction process. Troublesome in particular are the facts that the properties of particulate solids vary greatly with consolidation, and that stress fields can be obtained, in principle, only in

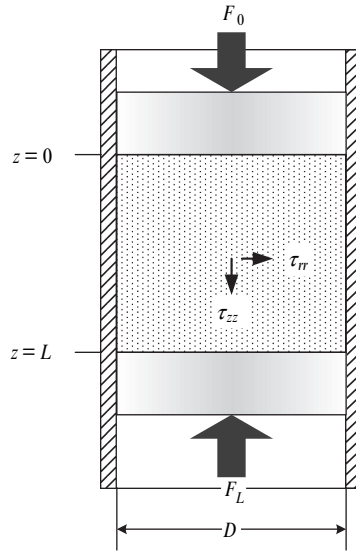


Fig. 4.9 Compaction in a cylindrical channel, between frictionless pistons. F_0 is the applied force, F_L is the resultant force on the lower portion.

the limiting cases of steady flow or in a state of incipient flow when the friction is fully mobilized. In compaction, these conditions are not necessarily fulfilled.

Let us consider an apparently simple situation of compaction of solids in a cylinder (Fig. 4.9). Assuming a uniform stress field, a normal force F_0 applied to the top ram generates within the solids a certain normal stress τ_{zz} , as well as a radial stress τ_{rr} . The frictional shear force due to the latter acts in the opposite direction to the applied force. Hence, the transmitted force to the lower ram, F_L , will be smaller than the applied force. By making a force balance similar to that made in deriving the Janssen equation, and assuming that the wall friction is fully mobilized, that the ratio of axial to radial stresses is a constant throughout, and that the coefficient of friction at the wall is constant, we obtain the following simple exponential relationship between the applied and transmitted force:

$$\frac{F_0}{F_L} = \exp\left(\frac{4f'_w KL}{D}\right) \quad (4.5-1)$$

Experimental data seem to conform to this relationship, yet there are serious doubts about its validity. Both the coefficient of friction and the ratio of normal stresses vary along the compaction (although it appears that their product stays approximately constant, explaining the reasonable agreement with experimental data). Experimental measurement of stresses within the compaction, however, reveal a rather complex stress distribution (31), which depends very much on conditions at the wall and the geometry of the compaction, as shown in Fig. 4.10.

Another question of fundamental importance discussed by Long (33) is the nature of the ratio of axial to radial stresses. Since there is complex stress distribution, the principal axes may not coincide with the axial and radial directions, respectively. Long (33) investigated this relationship by carrying out "radial stress cycles." The cycles are

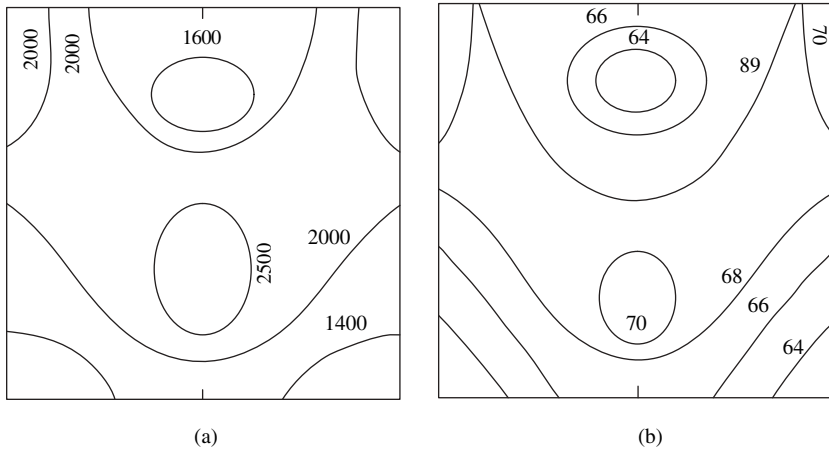


Fig. 4.10 (a) Stress and (b) density distribution in a cylindrical compaction of magnesium carbonate at an applied pressure of 2040 kg/cm^2 . [Reprinted by permission from D. Train, *Trans. Inst. Chem. Eng.*, **35**, 262 (1957).]

obtained by first increasing the axial stress, then decreasing it. A residual radial stress remains after the axial stress has been reduced to zero. This residual stress is responsible for the necessity of forcing the compacted mass out from the die after removal of the axial stress. According to Long, at small axial stresses, before any yield takes place in the powder, the ratio of radial to axial stresses will be given by the Poisson ratio, ν , which is the stress needed to suppress the radial expansion the compact would undergo if it were free to expand. However, once yield takes place, the ratio is determined by some yield criterion such as the Coulomb yield function (19), and a more or less linear increase of radial stress with axial stress is observed.

The response of polymeric particulate solids to compaction was investigated experimentally by Schneider (36) and Goldacker (37). For polyethylene, for example, a constant radial-to-axial stress ratio of 0.4 was observed.

The bulk density of particulate solids increases by compaction. Dilation, mentioned earlier, occurs only in the presence of a free surface, which allows for a loosening of the packing arrangements of the particles. The increase in density, or decrease in porosity, seems to follow an exponential relationship with the applied pressure (38,39)

$$\varepsilon = \varepsilon_0 e^{-\beta' P} \quad (4.5-2)$$

where ε_0 is the porosity at $P = 0$, and β' is a "compressibility coefficient," which, in view of the complex stress distribution in compacts, should depend on properties of the particulate system, on compact geometry, and possibly on the loading history. Therefore, Eq. 4.5-2 can be viewed as an approximate empirical relationship reflecting some average values. The inability to quantitatively describe or predict the internal stresses and deformations of particulate assemblies under static or dynamic loads, and the velocity fields of flowing particulates, has led to the rapidly growing development and use of the numerical method, which is uniquely appropriate for the discreet nature of particulate assemblies.

4.6 FLOW IN CLOSED CONDUITS

In polymer processing, it is usually necessary to force the particulate solids through some sort of closed conduit or channel. In a ram-type injection molding machine, the solids are pushed forward by the advancing ram. They move in a channel that becomes an annular gap upon reaching the torpedo. In a screw extruder, the solids get compacted and *dragged* forward in the helical channel formed between the screw and the barrel. These examples represent the two basic conveying and compaction methods used in polymer processing: external, mechanical, positive displacement conveying and compaction, and drag-induced conveying and compaction by a solid boundary in the direction of flow. In the former, the friction between the solids and the stationary walls reduces the conveying capacity, whereas in the latter, friction between the solids and the moving wall is the *source* of the driving force for conveying. It is perhaps worthwhile to note that the two solids-conveying mechanisms are identical in concept to external mechanical pressurization and drag-induced, viscous pressurization of liquids, discussed in Chapter 6.

Rigorous analysis of the flow of compacted particulate solids in closed conduits is difficult, as we discussed earlier. Discret numerical methods such as DEM, which is discussed in Section 4.10, offer the promise of more rigorous analysis, but these methods are also subject to severe limitations related to small elastic deformations and relatively simple channel geometries. Moreover, the difficulties with using DEM are compounded by the complexities of polymer processing, such as temperature increases as a result of friction and external heating, and the viscoelastic response of polymeric particulate systems under externally applied forces. Thus, despite the very serious doubts as to the validity of the conventional assumptions that compacted particulate systems can be analyzed as a continuum, often referred to as a *solid plug*, which is devoid of internal local assembly rearrangements and deformations, the ‘*solid-plug*’ assumption is widely used in polymer processing modeling. We therefore analyze the following three modes of particulate flows next: mechanical-displacement flow (Section 4.7), steady mechanical-displacement flow aided by frictional drag (Section 4.8), and steady, drag-induced flow in a straight channel (Section 4.9). These are really not flows as we refer to them in fluid mechanics, but rather transport of slightly compressible but otherwise nondeformable plugs.

4.7 MECHANICAL DISPLACEMENT FLOW

We now analyze mechanical-displacement flow in a straight channel of constant cross-sectional area, as shown in Fig. 4.11 (with the upper plate at rest). A column of compacted solids of length L is compressed between two rams. The one on the left exerts a force F_0 on the solids and it is opposed by a smaller force F_L on the right. Thus, friction on the channel walls also opposes the applied resultant force.

A differential force balance with the following assumptions: (a) the compacted solids are either at a steady motion or in a state of incipient slip on the wall (friction at the wall is fully mobilized); (b) axial and radial stresses vary only with the axial distance x ; (c) the ratio of the radial-to-axial stresses is a constant K , independent of location; (d) the coefficient of friction is constant and independent of compaction; and (e) temperature effects in the case of steady motion are negligible, results in

$$F_x - (F_x + dF_x) - C \left(\frac{F_x}{A} \right) K f_i dx = 0 \quad (4.7-1)$$

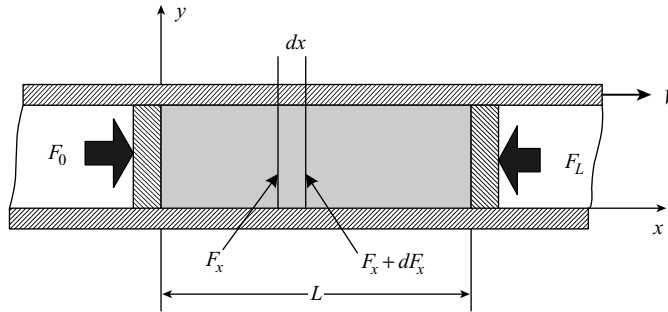


Fig. 4.11 A column of particulate solids compressed between two pistons in a channel with a constant cross section. A force F_0 is applied at $x = 0$, which is balanced by a force F_L at $x = L$. The column is either moving at constant velocity or is stationary. The upper plate is either stationary or is moving with constant velocity.

where f_i is either the static coefficient of friction for the case of incipient motion, or the kinematic coefficient of friction for steady motion; C is the circumference, which for noncircular cross sections is the wetted perimeter; and A is the cross-sectional area.

Integration of Eq. 4.7.1 gives

$$F_x = F_0 e^{-f_i K C x / A} \tag{4.7-2}$$

where F_x is the axial force at location x . The axial stress may be obtained by multiplying the force by the cross-sectional area. The force at the downstream ram F_L is obtained by setting $x = L$ in Eq. 4.7-2.

Hence, in dealing with steady motion of particulate solids, it is evident that the axial stress or “pressure” drops *exponentially*, whereas in the case of liquid flow, it drops *linearly* with distance. This difference stems, of course, from the fact that frictional forces on the wall are proportional to the absolute local value of normal stress or pressure. In liquids, only the pressure gradient and not the absolute value of the pressure affects the flow. Furthermore, Eq. 4.7.2 indicates that the pushing force increases exponentially with the coefficient of friction and with the geometric, dimensionless group CL/A , which for a tubular conduit becomes $4L/D$.

Experimental support on the validity of Eq. 4.7-2 was presented by Spencer et al. (32), who also proposed a theoretical derivation based on considering a discrete number of contact points between solids and containing walls. They assumed isotropic stress distribution ($K = 1$) and obtained an expression identical to Eq. 4.7-2

$$\frac{F_L}{F_0} = e^{-4f_w' L_0 / D} \tag{4.7-3}$$

where L_0 is the initial length of the column. The use of initial length of column, even though the column shortens upon compression, is justified by Spencer et al. on the basis of assuming a constant number of contact points. Experiments were carried out with a stationary column of saran powders and granular polystyrene, and results confirmed the theoretical derivation within experimental error.

Example 4.1 Force Requirements of Ram Injection Molding Machines We consider a ram injection-molding machine consisting of a 2-in-diameter barrel in which a well-fitting

ram reciprocates. We wish to calculate the maximum length of the solid plug the machine can deliver if the downstream pressure during injection is 10,000 psi and the barrel can sustain a radial stress of 25,000 psi. The static coefficient of friction is 0.5, and the radial-to-axial stress ratio is 0.4.

With a 25,000-psi allowed radial stress, the maximum allowable axial stress is $25,000/0.4 = 62,500$ psi. Substituting the appropriate values into Eq. 4.7-3, but not setting $K = 1$, we get

$$\ln(6.25) = (0.5)(0.4)(4)\frac{L}{2}$$

The length L is 4.58 in. Thus with an axial force of about 20,000 lb, we can only press a 4.58-in-long solids column driving the radial stress to its upper limit! Clearly, if it is necessary for injection molding machines of this type to develop such high downstream pressures, appropriate means must be provided to reduce the coefficient of friction on the wall. This can be achieved, for example, by heating the barrel, generating a liquid film on the wall. This will change the drag mechanism to that of a viscous laminar flow, which is independent of the absolute local normal stresses.

4.8 STEADY MECHANICAL DISPLACEMENT FLOW AIDED BY DRAG

Drag-aided, particulate solids flow occurs when at least one of the confining solid walls moves in the direction of flow parallel to its plane. The friction between the moving wall and the solids exerts a forward dragging force on the solids. Figure 4.11 shows a rectangular channel with the upper plate, which forms the top of the channel, moving at a constant velocity in the x direction. Particulate solids are compressed into a column of length L between two rams. We now can differentiate between four possible states of equilibrium:

- a. The solids are stationary with friction on the stationary walls fully mobilized, and with $F_0 > F_L$.
- b. The same as Case 1, but with $F_L > F_0$.
- c. The solids move at constant velocity (less than the velocity of the upper plate) in the positive x direction.
- d. The same as Case 3, but the solids move in the negative x direction.

Force balances on a differential element for these four cases appear in Fig. 4.12. The moving plate exerts a force of $C_1 f_{w1} K(F/A)$ in all cases, where C_1 is the portion of the "wetted" perimeter of the moving plate and f_{w1} is the kinematic coefficient of friction. The stationary channel walls in Cases (a) and (b) exert a force $C_2 f'_{w2} K(F/A)$, where f'_{w2} is the static coefficient of friction and C_2 is the portion of the wetted perimeter of the lower plate and side walls that is stationary. This force points in the direction of increasing force. Thus it points to the left in Case (a) and to the right in Case (b).

Finally in Cases (c) and (d), the stationary walls exert a force $C_2 f_{w2} K(F/A)$, where f_{w2} is the kinematic coefficient of friction. This force acts in the direction opposite to the direction of motion of the plug.

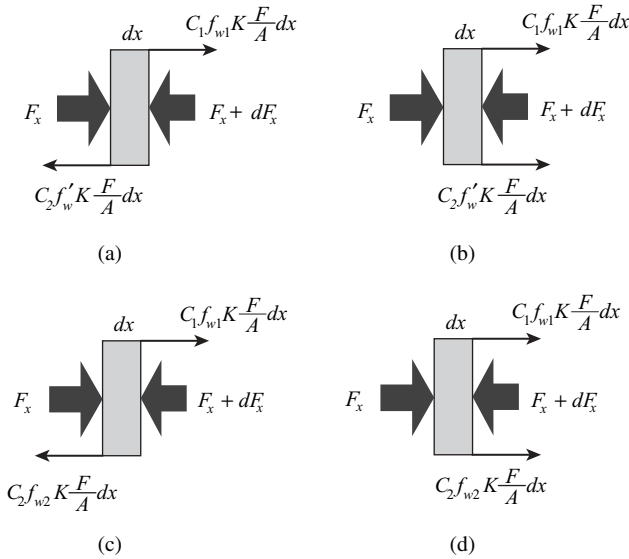


Fig. 4.12 Force balances on a differential element of solids in Fig. 4.11. (a) Stationary solids $F_0 > F_L$; (b) Stationary solids, $F_0 < F_L$; (c) Solids move at constant velocity in the positive x direction. (d) Solids move at constant velocity in the negative x direction.

Force balances such as Eq. 4.7.1, with the further assumption that the channel is flat and the torque induced by couples of forces can be neglected, lead to the following equations.

Case a $F_L < F_0$: Stationary plug; friction mobilized:

$$\frac{F_L}{F_0} = \exp \left[(C_1 f_{w1} - C_2 f'_w) \frac{KL}{A} \right] \tag{4.8-1}$$

Case b $F_L > F_0$: Stationary plug; friction mobilized:

$$\frac{F_L}{F_0} = \exp \left[(C_1 f_{w1} + C_2 f'_w) \frac{KL}{A} \right] \tag{4.8-2}$$

Case c Plug moves in the direction of the upper plate:

$$\frac{F_L}{F_0} = \exp \left[(C_1 f_{w1} - C_2 f_{w2}) \frac{KL}{A} \right] \tag{4.8-3}$$

Case d Plug moves in the direction opposite to the upper plate ($F_L > F_0$):

$$\frac{F_L}{F_0} = \exp \left[(C_1 f_{w1} + C_2 f_{w2}) \frac{KL}{A} \right] \tag{4.8-4}$$

In the foregoing, we have allowed for different kinematic coefficients of friction on the moving plate f_{w1} and the stationary walls f_{w2} .

Analysis of these equations reveals the role of drag on the force and stress distribution. First, we consider the case of a stationary column of solids. Assume that the drag force

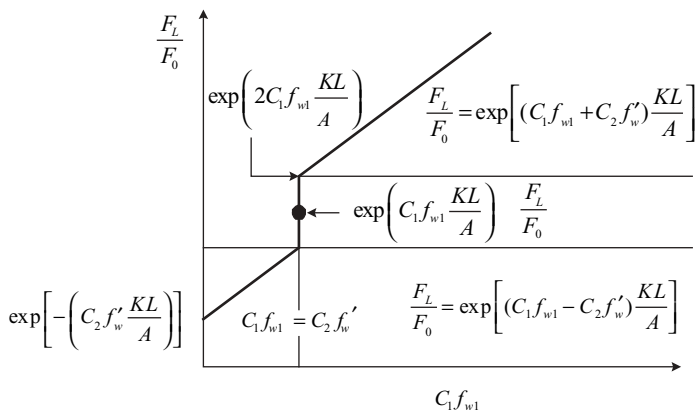


Fig. 4.13 The effect of drag on the ratio F_L/F_0 for a stationary column of solids. (The ordinate is a logarithmic scale.)

exerted by the moving plate can be gradually increased by changing $f_{w1}C_1$, by modifying the surface properties of the plate through coating, roughening, and so on, or increasing C_1 . This is demonstrated graphically in Fig. 4.13.

If $f_{w1}C_1$ is zero, the ratio of the forces is $F_L/F_0 = \exp[-(C_2f'_w)KL/A]$, as given in Eq. 4.7-2. A gradual increase in $f_{w1}C_1$ increases this ratio, implying that, for a given F_L , less and less force has to be exerted on the upstream ram, until this ratio reaches a value of 1 (i.e., $F_L = F_0$) when $C_1f_{w1} = C_2f'_w$. At this point, the forward dragging force exerted by the upper plate exactly compensates the fully mobilized frictional forces on the stationary walls. Now we can slightly increase F_L , thereby demobilizing the friction on the stationary walls. This is indicated by the vertical line in Fig. 4.14. We then reach a point where the frictional forces on the stationary plate are zero and the forward dragging force is fully compensated by the force F_L . Under these conditions

$$\frac{F_L}{F_0} = \exp\left(C_1f_{w1} \frac{KL}{A}\right) \tag{4.8-5}$$

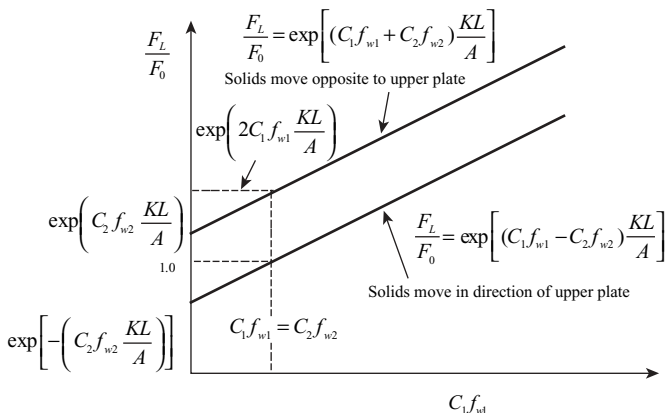


Fig. 4.14 The effect of drag on the ratio F_L/F_0 for a steadily moving column of solids. (The ordinate is a logarithmic scale.)

which is indicated by the heavy dot in Fig. 4.13. The force F_L can gradually be further increased, mobilizing the frictional forces on the stationary walls in the opposite direction until they are fully mobilized, where the ratio of forces is

$$\frac{F_L}{F_0} = \exp\left(2C_1 f_{w1} \frac{KL}{A}\right) \quad (4.8-6)$$

A further increase in $f_{w1}C_1$ will result in an increase in the ratio F_L/F_0 according to Eq. 4.8-2. Analyzing the whole curve, we see that we have a condition indicated by the vertical line in Fig. 4.13, where the force ratio is indeterminate. The condition indicated by the heavy dot on the vertical line can also be interpreted as representing a point where the downstream ram is replaced by a rigid channel block, which responds only to the forces exerted on it by the solids and prevents mobilizing the friction on the stationary walls. This is in agreement with the St. Venant principle, which states that, if statically equivalent and opposing surface tractions are applied on a solid, the differences are negligible at far away locations, that is, on the surface of the stationary walls; hence, this surface plays no role in the force balance.

The same kind of analysis for the case of steadily moving solids leads to similar conclusions, as Fig. 4.14 demonstrates. We should note, though, that in this case, we do not have a continuous transition between the two directions of motion, because within the region between the two curves, the solids must come to rest, thus encountering the two previously discussed cases and leading to possible instabilities.

Both cases, however, vividly demonstrate the profound effect that drag forces, induced by a moving boundary, may have on the force distribution. In positive displacement flow, the addition of a drag permits the reduction of the force F_0 needed to maintain a certain downstream force F_L to any desired level. Moreover, results indicate that drag is capable of generating pressures within the solids above those applied externally. The pressure rise is exponential with distance. The same holds for a moving plug. Hence drag, as we shall see in the next section, is a mechanism by which solids can be compacted as well as conveyed.

4.9 STEADY DRAG-INDUCED FLOW IN STRAIGHT CHANNELS

We have concluded that frictional drag, when applied to a steadily moving column of solids, can generate stresses or pressures above those applied externally. Consider once more the case of a flat rectangular channel with the upper plate moving and the solids moving in the same direction at constant velocity. The force ratio is plotted in the lower curve of Fig. 4.14. Clearly, for any given F_0 (which must be greater than zero, except for the frictionless case), we can get any F_L greater than F_0 , provided $C_1 f_{w1}$ is large enough. This ratio F_L/F_0 seems to be independent of either the plate velocity or the velocity of the solids. All that is required is that these velocities be steady. This result was obtained because we have assumed that the frictional force depends only on normal stress and is independent of velocity, which, as we have seen in this chapter, is a reasonable assumption. Yet the velocity of the solids multiplied by the cross-sectional area gives the flow rate. Thus the previous argument implies that, in this particular setup, flow rate is indeterminate. How, then, can we use the drag-induced flow concept to obtain a geometrical configuration in which flow rate is not only indeterminate but is also predictable? Such a situation would arise if the frictional drag could be made dependent on solids velocity. We can create such a situation by replacing the upper cover

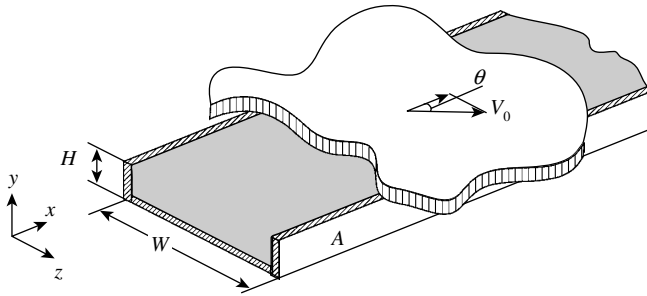


Fig. 4.15 A rectangular channel filled with solids that move in the positive x direction at constant velocity u , covered by an infinite plate moving at constant velocity V_0 at an angle θ to the down-channel direction, z .

plate with an infinite plate, moving not in the down-channel direction, but at an angle, θ , to this direction, as in Fig. 4.15.

The frictional force exerted by the moving plate on the solids remains constant, but the direction of this force will be given by the vectorial difference between the plate velocity and solids velocity (Fig. 4.16). Hence, the velocity component of this force in the down-channel direction, which participates in the force balance, becomes a function of both plate velocity and solids velocity (or flow rate). From the velocity diagram in Fig. 4.16, we obtain the following expression for the angle ϕ , which is the angle between the direction of the force exerted by the moving plate on the solids and the direction of motion of the moving plate (the solids conveying angle) where

$$\tan \phi = \frac{u \sin \theta}{V_0 - u \cos \theta} \tag{4.9-1}$$

where V_0 is the velocity of the upper plate, and u is the velocity of the solids. Note that, for stationary solids, the angle ϕ becomes zero, and it increases with increasing flow rate.

Next we can proceed with the force balance on the differential element shown in Fig. 4.16. We first concentrate on making a down-channel force balance, neglecting the cross-channel component of the forces

$$F_x - (F_x + dF_x) + C_1 f_w K \left(\frac{F_x}{A} \right) \cos(\theta + \phi) dx - C_2 f_w K \left(\frac{F_x}{A} \right) dx = 0 \tag{4.9-2}$$

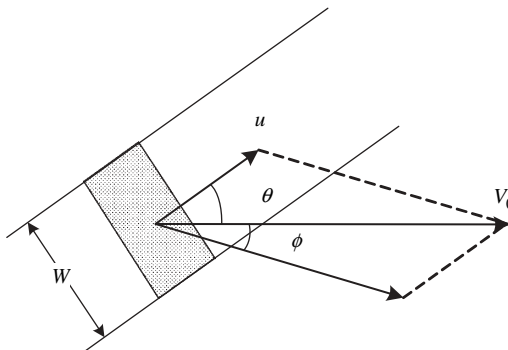


Fig. 4.16 Top view of a differential element of the column of solids in Fig. 4.15.

which upon integration with the initial condition $F(0) = F_0$, gives

$$\frac{P_x}{P_0} = \frac{F_x}{F_0} = \exp \left\{ [C_1 f_{w1} \cos(\theta + \phi) - C_2 f_{w2}] \frac{Kx}{A} \right\} \quad (4.9-3)$$

Hence the ratio of forces, which by dividing by the cross-sectional area also equals the ratio of axial stresses, which we shall refer to as *pressures*, become a function of the flow rate via the angle ϕ determined by Eq. 4.9-1. This implies that, for a given inlet pressure P_0 , a fixed outlet pressure determines the flow rate, or conversely, a given flow rate determines the magnitude of outlet pressure the device can generate. The lower the flow rate, the higher the pressure rise.

The previously described solids conveying mechanism represents, in essence, the conveying of solids in SSEs, although a realistic conveying model for the latter is somewhat more complicated because, as Chapter 9 explains, the channel is curved.

Drag-induced flow in a rectangular channel, as in Fig. 4.15, neglecting cross-channel forces, resulted in Eq. 4.9-3. We now consider the effect of these forces on the conveying mechanism.

At steady flow conditions the moving plate exerts a force on the solids in the $(\theta + \phi)$ direction. This force is separated into two components: one in the down-channel direction, which was used in the force balance, and the other in the cross-channel direction, which was neglected. The latter will have the following effects: it will increase the normal stress on the side wall, A , in Fig. 4.15, and it will alter the stress distribution within the solids. Assume for the sake of simplicity that the St. Venant principle holds, that is, the externally applied force by the plate is completely balanced by the additional force on the side wall A , and within the solids (which will be considered to be located "far" from the places where these tractions act), there will be no effect. In other words, we neglect the changes in the stress distribution within the solids. The cross-channel force component, F^* , is

$$F^* = f_{w1} K \left(\frac{F_x}{HW} \right) (W dx) \sin(\theta + \phi) = \frac{f_{w1} K F_x \sin(\theta + \phi) dx}{H} \quad (4.9-4)$$

where W and H are the width and height of the channels, respectively. Now we can write a down-channel force balance, including the effect of this additional normal force on side wall A on the frictional force along this wall

$$\begin{aligned} F_x - (F_x + dF_x) + f_{w1} K \left(\frac{F_x}{HW} \right) (W dx) \cos(\theta + \phi) - f_{w2} K \left(\frac{F_x}{HW} \right) (W + H) dx \\ - f_{w2} \left[K \left(\frac{F_x}{HW} \right) H dx + F^* \right] = 0 \end{aligned} \quad (4.9-5)$$

which, upon rearrangement and with Eq. 4.9-4, gives

$$\frac{dF_x}{F_x} = \frac{f_{w1} K}{H} \left[\cos(\theta + \phi) - \frac{f_{w2}}{f_{w1}} \left(1 + 2 \frac{H}{W} \right) - f_{w2} \sin(\theta + \phi) \right] dx \quad (4.9-6)$$

Integration of this equation gives

$$\frac{P_x}{P_0} = \frac{F_x}{F_0} = \exp \left\{ \frac{f_{w1} K x [\cos(\theta + \phi) - f_{w2} \sin(\theta + \phi) - f_{w2}/f_{w1} (1 + 2H/W)]}{H} \right\} \quad (4.9-7)$$

Equation 4.9-7 reduces to Eq. 4.9-3 if the second term on the right-hand side vanishes. Clearly the cross-channel force induces additional friction on the side wall, A , which in turn reduces the pressure generation capability for a given flow rate (given angle ϕ), or it reduces the conveying capacity for a given pressure rise.

4.10 THE DISCRETE ELEMENT METHOD

In Sections 4.4 and 4.5, we dealt briefly with particulate flow instabilities in hoppers and the nonhomogeneous stress distributions created under uniaxial loading of a particulate assembly. In this section, we will expand on the *discrete* nature of such assemblies, and refer the reader to the computational and experimental tools that have been developed, and are rapidly advancing, to study such phenomena.

An assembly of particulates is composed of distinct particles that undergo displacements independently from each other, and interact only via *points of contact* between the particles. This *discrete* character of such assemblies results in complex behavior under loading and unloading, as well as under flow, which the available, continuum-based constitutive equations fail to describe. In this section we describe particle dynamics simulations, which are based on the discrete, rather than the continuum nature of particulates, and which offer a better chance to describe the behavior of such systems. Experimentally, it is very difficult to measure internal stresses or flow details in real particulate assemblies. Thus, “model” experimental systems have to be used, which consist of assemblies of geometrically simpler “particles.” For example, DeJosselin de Jong and Verrijt in 1971 (40) used a two-dimensional assembly of photoelastic disks of various sizes under load. Figure 4.17(a), taken from their work, records the “force vector” plots resulting from the two-dimensional loading, and Fig. 4.17(b) shows a simulation by Cundall and Strack (41). The complex stress field is evident where the width of the lines indicates the magnitude of the force.

Relatively simple optical experimental techniques to study *noncohesive* particulate flow have also been developed, such as the polarized light probe system by Allersma (42,43). With this technique, the principal stress distribution and displacement of photoelastic granular material flowing in two-dimensional hoppers, with and without obstructions (distribution bars), can be obtained, as shown in Fig. 4.18.

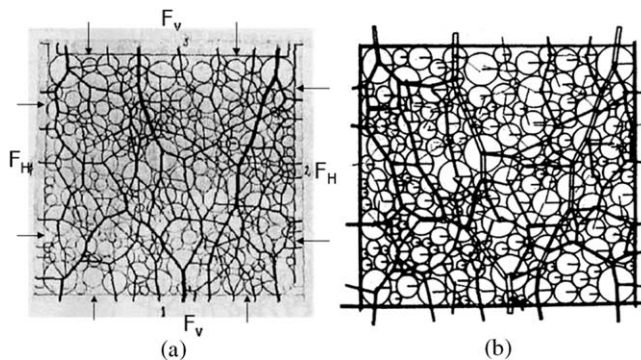


Fig. 4.17 (a) Force vectors obtained in a two-dimensional assembly of photoelastic disks under horizontal and vertical loads, $F_H/F_V = 0.39$. (b) DEM calculations by Cundall and Strack (41) of the force vectors for $F_H/F_V = 0.41$ [Reprinted by permission from P. A. Cundall and O. D. L. Strack, “A Distinct Element Model for Granular Assemblies,” *Géotechnique*, **29**, 47–65 (1979).]

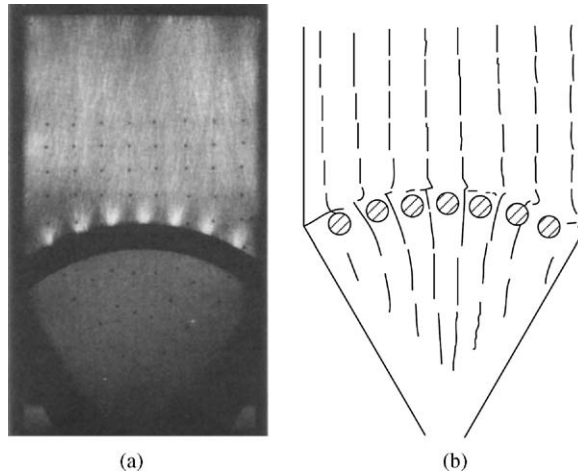


Fig. 4.18 (a) The visualized stress distribution in a hopper with seven distribution bars. (b) The measured particle displacements in the same hopper indicating uniform flow. [Reprinted by permission from H. G. B. Allersma “Optical Analysis of Methods to Influence the Stress Distribution in Hoppers,” in *Mechanics of Deformation and Flow of Particulate Materials*, C. S. Chang et al. Eds., ASCE Publication, New York, 1997.]

Altobelli et al., used a more elaborate three-dimensional MRI technique to study the flow of suspended particles (44) and granular flows (27), also studied by Ng et al. (45) for pellet-sized pills under load, while being sheared in a nonmagnetic “shear box,” similar to the Jenicke cell (22). This technique holds great potential for detecting details of particulate movements and deformations of three-dimensional particulate assemblies, but is currently limited to very low shearing velocities.

In the last decades, the modeling of both compacted particulates and flowing particle assemblies under loads and under flow conditions has been advanced by DEM, first developed by Cundall (46) for two-dimensional compacted-disk assemblies in 1971. The origins of DEM are in the field of molecular dynamics (MD), where the motions of individual molecules are tracked under the influence of an external force (e.g., electrostatic) field (47). Experimental results such as those with model photo-elastic assemblies just discussed have also assisted the development of the DEM simulation models.

In a dynamic particulate assembly, particle–particle interactions dominate. Thus, it is essential for DEM to establish methods for identifying contacts and modeling the contact interactions for all particulates. Most DEM simulations assume that the particles are spheres, to facilitate the identification of the contact location. There are two categories of DEM: the hard-(infinitely rigid) sphere model and the soft-sphere model. The hard-sphere model is appropriate for sparse populations of bodies moving at high speeds, with instantaneous two-body collisions only, which can be modeled as instantaneous exchanges of momentum and energy (48). Haff (49) discusses the physical nature of such binary, collision-dominated systems, resembling gases, but where the collisions are allowed to be *inelastic* in the transfer of momentum and energy. He derives, heuristically, the equation of state and the momentum and energy balances for such systems. This model, however, is not applicable to dense particulate flows and deformation of packed particulates under loads, relevant to polymer particulate solids handling.

On the other hand, in Cundall's soft-sphere model of the DEM, "soft" spheres colliding, or in contact with several neighboring particles, undergo virtual (overlap) deformations, which give rise to reaction (e.g., elastic, springlike) forces normal and tangential to the contact. Thus, each contact can exert both a force and a moment on each particle, the total of which is the resultant of all the contacts and the body forces of gravity and electrostatic fields, if any. The new positions and velocities of each particle are determined by Newton's second law and solving second order differential equations involving the linear and angular acceleration of each particle. The simultaneous solution of the entire assembly differential equations determines the new "state" of the assembly. Figure 4.19 shows the computational flow diagram of the soft-sphere DEM model. It is important to note that this DEM model is equally applicable to static, quasi-static, and dynamic flow conditions.

We follow Cundall and Strack (41) in discussing this DEM model in two-dimensional assemblies of disks under load. The equilibrium contact forces and particle displacements and deformations of a stressed assembly of disks are predicted through a series of calculations tracing the dynamic state of each particle, which is the result of the propagation, through the assembly, of the externally applied wall stresses. Calculations are carried out in sequential, small time increments over which we can assume that the particle velocities and accelerations are constant. The time steps are also small enough so that disk-to-disk interactions (disturbances) have the time to propagate only to immediate "neighbors" and no further. Thus, at all times during the calculations, the resulting forces on any disk are determined only by its interactions with the neighbors it is in contact with. This is the essential computational component that enables DEM to follow nonlinear interactions between very large numbers of district disks, with moderate computer memory requirements.

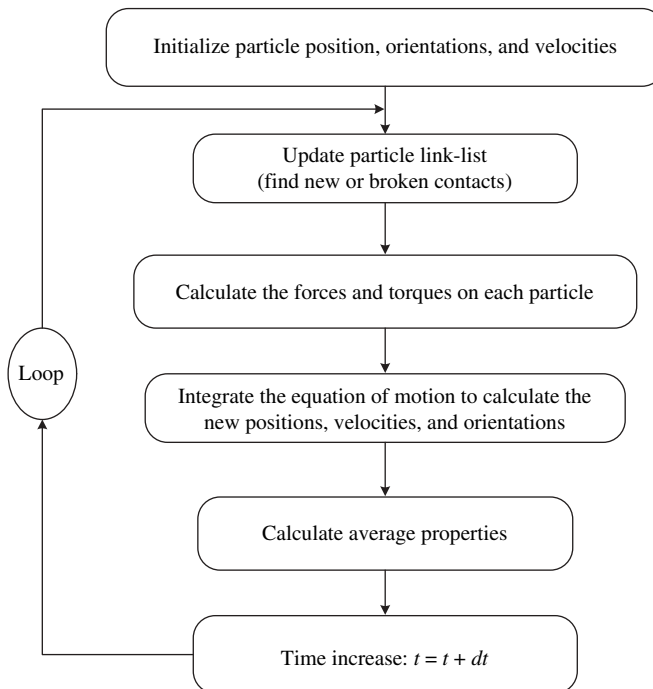


Fig. 4.19 The computational algorithm of the soft-sphere DEM model.

The DEM calculation cycle (as noted in Fig. 4.19) involves the use of Newton's second law, giving the motion of a particle resulting from the forces acting on it, alternating with the use of a force-displacement (particle deformation) constitutive relationship to find contact forces from displacements. The deformations of individual soft particles are "virtual" in the sense that they are used only to calculate reaction forces. The response and deformation of the entire assembly is calculated by the displacements and the rigid-body rotation of all particles. This assumption limits the applicability of the soft-sphere DEM to the description of the dynamic state of packed polymer pellets or powders in processing equipment, such as twin rotor processing equipment, as we will discuss in Section 5.8 and Chapter 10. There, the applied deformations are large and the solid polymer particulates undergo plastic deformations, which cause large temperature increases in the deforming assembly. The following example serves as a simple illustration of the DEM cycling through a force-displacement constitutive response, $F = k \Delta n$, and Newton's second law, which relates the force to acceleration and, thus, particle motion.

Example 4.2 Soft-Sphere Model DEM Treatment of Two Disks Deformed by Two Rigid Walls To demonstrate the basic and simple physical model used in DEM, we turn to a pair of two disks, X and Y , compressed between two rigid walls, as shown in Fig. E4.2.

Initially, at $t = t_0$, the walls and disks touch with no force, $F_N = 0$, Fig. E4.2(a). The walls move toward each other at a constant velocity, v . At time $t = t_0 + \Delta t$ the walls have each moved a distance $v\Delta t$. Since the disturbance cannot travel beyond a single disk as assumed by the model, both disks maintain their initial positions during this time interval. Thus, *overlaps* are created at points A and C , Fig. 4.2(b), given by

$$\Delta n = v\Delta t \quad (\text{E4.2-1})$$

The contact A at time $t + \Delta t$ is defined as the halfway point between A_D and A_w . The relative displacement at A is related to the force resulting from the assumed *linear constitutive response* of the particle (that of a simple "spring" in LVE terms)

$$\Delta F_n = k_n(\Delta n)_{t_1} \quad (\text{E4.2-2})$$

At the two disks at $t_1 = t_0 + \Delta t$

$$F_{X_1} = K_n(\Delta n)_{t_1} \quad F_{Y_1} = -K_n(\Delta n)_{t_1} \quad (\text{E4.2-3})$$

Using Newton's second law of motion to find the accelerations (constant over Δt) of disks X and Y

$$\ddot{X}_1 = \frac{F_{X_1}}{m_X} \quad \ddot{Y}_1 = \frac{F_{Y_1}}{m_Y} \quad (\text{E4.2-4})$$

By integrating \ddot{X}_1 and \ddot{Y}_1 over t_1 to $t_2 = t_0 + 2\Delta t$, the velocities of the two disks at t_2 are determined by

$$(\dot{X}_1)_{t_2} = \left(\frac{F_{X_1}}{m_x}\right)\Delta t \quad (\dot{Y}_1)_{t_2} = \left(\frac{F_{Y_1}}{m_y}\right)\Delta t \quad (\text{E4.2-5})$$

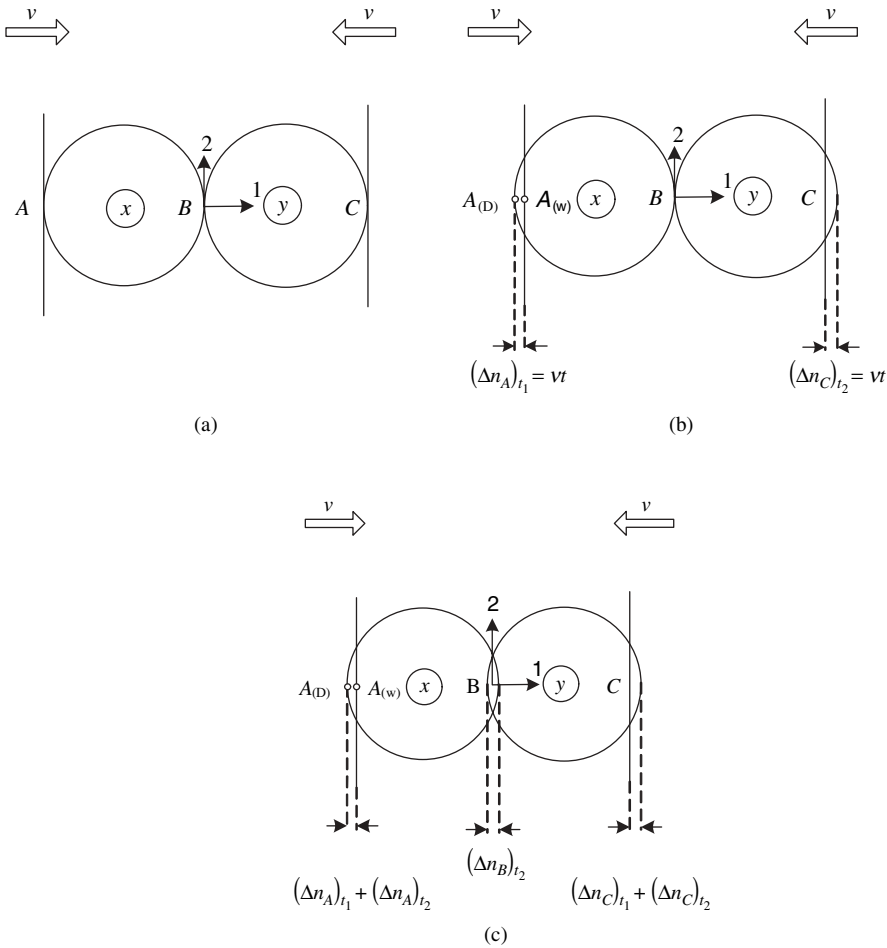


Fig. E4.2 Soft-sphere DEM model for two disks being compressed by two confining walls moving in opposite direction with a velocity v . [Reprinted by permission from P. A. Cundall and O. D. L. Strack, "A Distinct Element Model for Granular Assemblies," *Géotechnique*, **29**, 47–65 (1979).]

Thus the relative displacement at points A , B , and C at t_2 are given by, see Fig. E4.2(a)

$$(\Delta n_A)_{t_2} = \left[v - \left(\frac{F_{X1}}{m_x} \right) \Delta t \right] \Delta t \tag{E4.2-6}$$

$$(\Delta n_B)_{t_2} = \left[\left(\frac{F_{X1}}{m_x} \right) \Delta t - \left(\frac{F_{Y1}}{m_y} \right) \Delta t \right] \Delta t \tag{E4.2-7}$$

$$(\Delta n_C)_{t_2} = \left[\left(\frac{F_{Y1}}{m_y} \right) \Delta t - (-v) \right] \Delta t \tag{E4.2-8}$$

where Δn_i are taken to be positive for compression. This cycle of calculation will be repeated again and again.

In the general case of an assembly with a very large number of disks the calculation cycle is as follows: the $F_i = k\Delta n_i$ is applied at each contact point of any disk and the vectorial sum of the contact forces is calculated to yield the net force acting on the disk. However, for an

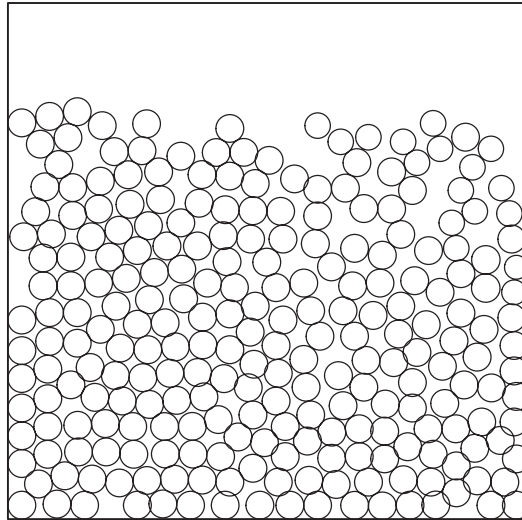


Fig. 4.20 DEM-simulated packing density under gravity for a two-dimensional spherical particulate assembly 50 μm in diameter, with $f' = f'_w = 0.364$ and with van der Waals forces, showing the formation of clusters, which decrease the packing density by more than 10%. [Reprinted by permission from Y. F. Cheng, S. J. Guo, and H. Y. Li, "DEM Simulation of Random Packing of Spherical Particles," *Powder Technol.*, **107**, 123–130 (2000).]

assembly of particles there are both normal and tangential forces, the latter giving rise to moments M_{X_i} and angular acceleration $\ddot{\theta}_{X_i}$, where

$$I_{X_i} \ddot{\theta}_{X_i} = \sum M_{X_i} \quad (\text{E4.2-9})$$

I_{X_i} are the moments of inertia of disks X_i . Interparticle frictional forces are included for both compacted and flowing particulate assemblies

In 1979, Cundall and Strack (41) used the DEM simulation just outlined to compare it with the experiment of de Josselin de Jong (40), and their results are shown in Fig. 4.17(b). The agreement is excellent, qualitatively, and good, quantitatively. What is important is the fact that this experimental verification of the power of soft-sphere DEM simulations established the field and contributed to its rapid growth.

The soft-sphere DEM is also used to model particulate packing under gravity (50), shown in Fig. 4.20, and particulate flows and fluidization (51,52). DEM simulations scarcely have been used to simulate the pellet/powder behavior under flow or compaction. A notable example is the work of Yung, Xu, and Lau (53) in simulating the conveying of polymer pellets in the solids-conveying region of SSEs. The simulated dependence of the conveying rate on the screw speed, barrel, and screw wall friction coefficients is consistent with that observed experimentally.

REFERENCES

1. H. Rumpf, *Particle Technology*, Dordrecht, The Netherlands, Kluwer, 1990.
2. J. P. K. Seville, U. Tüzün, and R. Clift, *Processing of Particulate Solids*, Dordrecht, The Netherlands, Kluwer, 1997.

3. C. Orr, Jr., *Particulate Technology*, Macmillan, New York, 1966.
4. R. L. Brown and J. C. Richards, *Principles of Powder Mechanics*, Pergamon Press, Oxford, 1966.
5. K. Weinghart, "Experiments in Granular Flow," *Annu. Rev. Fluid Mech.*, **7**, 89–114 (1975).
6. D. Dowson, *History of Tribology*, Longman, New York, 1979.
7. R. B. Bowden and D. Tabor, *Friction and Lubrication of Solids*, Oxford Univ. Press, London, 1950.
8. G. Binning, H. Rohrer, Ch. Gerber and E. Weibel, "Surface Studies by Scanning Tunneling Microscopy," *Phys. Rev. Lett.*, **49**, 57–61 (1982).
9. G. Binning, C. F. Quate and Ch. Gerber, "Atomic Force Microscope," *Phys. Rev. Lett.*, **56**, 930–933 (1986).
10. F. Heslot, T. Baumberger, B. Caroli, and C. Caroli, "Creep, Stick-slip and Dry Friction Dynamics: Experiments and a Heuristic Model," *Phys. Rev.*, **E49**, 4973 (1994).
11. A. Tanguy, M. Gounelle and S. Roux, "From Individual to Collective Pinning: Effect of Long-range Elastic Interactions," *Phys. Rev.*, **E58**, 1577 (1998).
12. A. S. Lodge and H. G. Howell, *Proc. Phys. Soc. B Band*, **67**, (1954).
13. K. Schneider, *Kunststoffe*, **59**, 97–102 (1969).
14. B. J. Briskoe, C. M. Pooley, and D. Tabor, in *Advances in Polymer Friction and Wear*, Vol. 5A, L. H. Lee, Eds., Plenum Press, New York, 1975.
15. G. H. Qian, I. Bagyi, I. W. Burdick, R. Pfeffer, H. Shaw, and J. Stevens "Gas-Solid Fluidization in a Centrifugal Field," *AIChE J.*, **47**, 1022–1034 (2001).
16. I. Manas-Zloczower, A. Nir, and Z. Tadmor, *Rubber Chem. Technol.*, **55**, 1250 (1982).
17. K. Allemaskin, I. Manas-Zloczower, and M. Kaufman, "Simultaneous Characterization of Dispersive and Distributive Mixing in a SSE," *Conference Proc., SPE ANTEC*, **61**, 268–272 (2003).
18. H. A. Janssen, "Tests on Grain Pressure Silos," *Z. Vereinsch. Dtsch. Ing.*, **39**, 1045–1049 (1895).
19. Z. Tadmor and C. G. Gogos, *Principles of Polymer Processing*, Section 8.6, Wiley, New York, 1979, Chapter 8.
20. M. Walker "An Approximate Theory for Pressure and Arching in Hoppers," *Chem. Eng. Sci.*, **21**, 975–997 (1966).
21. J. R. Johanson, "Feeding," *Chem. Eng.*, 75–82, (October, 1969).
22. A. W. Jenike, *Gravity Flow of Bulk Solids*, Bulletin #108, Utah Engineering Experimental Station, University of Utah, Salt Lake City, 1961.
23. O. Richmond and G. C. Gardner "Limiting Spans of Arching of Bulk Material in Vertical Channels," *Chem. Eng. Sci.*, **17**, 1071–1078 (1962).
24. J. Lee, S. C. Cowin, and J. S. Templeton "An Experimental Study of the Kinematics of Flow Through Hoppers," *Trans. Soc. Rheol.*, **18**, 247–269 (1974).
25. R. Butterfield, R. M. Harkness, and K. Z. Andrews, "Stereophotogrammetric Methods for Measuring Displacement Fields," *Goetechnique*, **8**, 308 (1970).
26. M. Levinson, B. Smutter, and W. Resnick, "Displacement Velocity Fields in Hoppers," *Powder Technol.*, **16**, 29–43 (1977).
27. M. Nakagawa, S. A. Altobelli, A. Caprihan, E. Fukushima, and E. K. Jeong, "Non-invasive Measurements of Granular Flows by MRI," *Exp. Fluids*, **16**, 54–60 (1993).
28. T. T. Ng, C. Wang, and S. A. Altobelli, "3-D MRI Experiments in Granular Materials," in *Mechanics of Deformation and Flow of Particulate Materials*, C. S. Chang, A. Misra, R. Y. Liang and M. Babic, Eds., ASCE Publication, New York, 1997.
29. H. Potente and T. C. Pohl, "Polymer Pellet Flow out of the Hopper into the First Section of a Single Screw," *Int. Polym. Proc.*, **17**, 11–29 (2002).
30. W. H. Wollaston, *Philos. Trans.*, **119**, 1 (1829).
31. D. Train, "Transmission of Forces Through a Powder Mass During the Process of Pelletizing," *Trans. Inst. Chem. Eng.*, **35**, 262–265 (1957).

32. R. D. Spencer, G. D. Gilmore and R. M. Wiley, "Behavior of Granulated Polymers under Pressure," *J. Appl. Phys.*, **21**, 527–531 (1950).
33. M. Long, "Radial Pressure in Powder Compaction," *Powder Met.*, **6**, 73–86 (1960).
34. H. G. B. Allersma, "Optical Measurements of Stress and Strain in Granular Materials", *Pro. 2nd Int. Conf. Composite Engineering*, New Orleans, LA August 1995, p. 117.
35. C. S. Chang, A. Misra, R. Y. Liang and M. Babic, Eds., *Mechanics of Deformation and Flow of Particulate Materials*, ASCE Publication, New York, 1997.
36. K. Schneider, "Druckausberaitung und Druckverteilung in Schuttgutern," *Chem. Ing. Technol.*, **49** (1969).
37. E. Goldacker, "Untersuchungen zur inneren Reibung von Pulvern, insbesondere im Hinblick auf die Förderung von Extrudern," Dissertation RWTH, Aachen, Germany, 1971.
38. C. Y. Cheng and C. G. Gogos, "Compressibility of Polymer Pellets and Powders," *SPE ANTEC Tech. Papers*, **25**, 156 (1979).
39. K. S. Hyun and M. A. Spalding, "Bulk Density of Solid Polymer Resins as a Function of Temperature and Pressure," *Polym. Eng. Sci.*, **30**, 571 (1990).
40. A. G. de Josselin de Jong and A. Verrijt, *Cah. Grpe fr. Etud. Rheol.*, **2**, 73–86 (1971).
41. P. A. Cundall and O. D. L. Strack, "A Distinct Element Model for Granular Assemblies," *Géotechnique*, **29**, 47–65 (1979).
42. H. G. B. Allersma "Optical Analysis of Stress and Strain in Photoelastic Particle Assemblies," Ph.D. Thesis, Delft University of Technology, Delft, The Netherlands (1987).
43. H. G. B. Allersma "Optical Analysis of Methods to Influence the Stress Distribution in Hoppers" in *Mechanics of Deformation and Flow of Particulate Materials*, C. S. Chang et al., Eds., ASCE Publication, New York, 1997.
44. S. A. Altobelli, R. C. Gilver, and E. Fukushima, "Velocity and Concentration Measurements of Suspensions by MRI," *J. Rheol.*, **35**, 721–734 (1991).
45. T. T. Ng, M. Kelley, and J. Sampson, *Proc. 11th Engineering Mechanics Conf.*, **1**, 572 (1996).
46. P. A. Cundall "A Computer Program for Simulating Progressive Large-scale Movements in Blocky Rock Systems," *Proc. Symp. Int. Soc. Rock. Mech.*, **2**, Nancy, France (1971).
47. D. J. Quensel, D. S. Rimai, and L. P. Demejo, "Molecular Dynamic Modeling of Interfacial Energy," *J. Adhesion Sci. Technol.*, **9**, 1015–1030 (1995).
48. L. Vanel, A. D. Rosato, and R. N. Dave, *Phys. Rev. Lett.*, **17**, 1255 (1997).
49. P. K. Haff, "A Physical Picture of Kinetic Granular Fluids," *J. Rheol.*, **30**, 931–948 (1986).
50. Y. F. Cheng, S. J. Guo, and H. Y. Li, "DEM Simulation of Random Packing of Spherical Particles," *Powder Technol.*, **107**, 123–130 (2000).
51. C. R. Wassgren, C. E. Brennen, and M. L. Hunt, "Vertical Vibration of a Deep Bed of Granular Material in a Container," *J. Appl. Mech.*, **63**, 712–719 (1996).
52. Y. Tsuji, T. Kawaguchi, and T. Tanaka, "Discreet Particle Simulation of Two-dimensional Fluidized Beds," *Powder Tech.*, **77**, 79–87 (1993).
53. K. L. Yung, Y. Xu, and K. H. Lau, "A New Method of Simulating the Conveying of Solid Pellets," *Int. Polym. Proc.*, **17**, 91–94 (2002).

PROBLEMS

- 4.1. **Friction Between Two Surfaces** Answer the following questions or discuss statements: (a) Two clean, highly polished steel surfaces when brought into contact appear to stick as if having very high coefficient of friction. (b) Would the dynamic coefficient of friction between steel and a polymer increase or decrease with increasing surface

roughness. (c) Why would the dynamic coefficient of friction between polymer pellets and a metal increase with time of rubbing one against the other? How would this affect start-up of solid pellet-fed machines? (d) Would you expect the dynamic coefficient of friction to increase or decrease with metal surface temperature? (e) The dynamic coefficient of friction on a clean surface of LDPE is 0.3 and that of HDPE is 0.08. How do you explain the difference?

4.2. Effect of Liquids on Friction (a) Why do cars tend to slip on a wet road? Why is the risk higher with a worn-out tire? (b) Why do certain people lifting something heavy without gloves spit on their palms? (c) Describe in a short essay how it would be to live in a frictionless world.

4.3. Solids Height in an Extruder Hopper An LDPE-fed SSE is equipped with a 10-cm cylindrical hopper. The operation is sensitive to the pressure under the hopper. If the static coefficient of friction is 0.5 and the ratio of compressive stress in the horizontal direction to compressive stress in the vertical direction is 0.5, what should the minimum height of the solids be in the hopper to secure steady operation?

4.4. The Effect of Drag on the Pressure Distribution in Solids Filling a Rectangular Channel A bed of particulate solids is compressed in a rectangular channel between two freely moving rams, with the upper plate of the rectangular channel moving at a constant velocity. The width of the channel is 5 cm and its height is 0.5 cm. The coefficient of friction on the stationary channel walls is 0.5 and the ratio of axial to perpendicular stresses is 0.4 and can be assumed constant throughout the bed. The force on the downstream ram is 1000 N. (a) Calculate the force that has to be applied on the upstream ram at equilibrium conditions as a function of the coefficient of friction on the moving wall that can be varied in the range of 0 to 1.0. (b) What effect will the doubling of the velocity of the moving plate have on the results in part (a)?

4.5. Two-dimensional Pressure Distribution in Solids Filling a Rectangular Channel Consider the rectangular channel geometry shown in Fig. 4.15. Equation 4.9-7 gives the pressure distribution, accounting for the cross-channel force, but neglecting cross-channel pressure distribution. (a) Show that the down-channel pressure distribution that accounts for cross-channel pressure distribution is given by:

$$\ln \frac{\bar{P}(x)}{P(0)} = (R_1 - R_2)x \tag{P4.6-1}$$

where $\bar{P}(x)$ is the mean pressure over the cross-section at location x , the same as before

$$\bar{P}(x) = \frac{P(x, 0)(e^{R_1 W} - 1)}{R_1 W}$$

where $P(x, 0)$ is the axial pressure at $z = 0$ (see Fig. 4.15) and

$$R_1 = f_{w1} \frac{\sin(\theta + \phi)}{H}$$

and

$$R_2 = \frac{f_{w1} \cos(\theta + \phi) - f_{w2}}{H}$$

$$R_3 = \frac{f_{w3} R_1 (e^{R_1 W} + 1)}{e^{R_1 W} - 1}$$

where f_{w1} , f_{w2} , and f_{w3} are the coefficients of friction on the moving plate, channel bottom, and channel sidewalls, respectively. (b) Show that for $R_1 W \rightarrow 0$, Eq. P4.6-1 reduces to Eq. 4.9-7 with $K = 1$.

- 4.6. Flow Rate in a Rectangular Channel** The pressure profile for drag-induced solids conveying in a rectangular channel is given by Eq. 4.9-7. The channel dimensions are $W = 2.5$ in and $H = 0.5$ in. The pressure at a certain upstream position is 10 psig, and 10 in downstream it is 55.7 psig. The coefficient of friction on the moving wall is 0.5 and 0.2 on the stationary walls. The upper wall moves at an angle of 15° to the down-channel direction and at a velocity of 10 in/s. The bulk density is 30 lb/ft^3 and $K = 0.5$. Calculate the mass flow rate of solids.
- 4.7. Experimental Determination of the Storage Friction Coefficient, $4Kf'_w$** Hyun and Spalding⁴ developed a polymer particulate solids compaction cell shown schematically in Fig. P4.7(a) and used it to obtain temperature and pressure-dependent bulk density data, as shown on Fig. P4.7(b₁) and p4.7(b₂).

(a) Comment on the compressibility behavior of the semicrystalline LDPE and amorphous high impact polystyrene (HIPS) (b) the cell was also used to calculate (estimate) the storage friction coefficient $f'_s = 4f'_w K$ in the force balance Eq. 4.5-1. Measuring the top and bottom plunger pressure, they reported the following:

f'_s Values	25°C	50°C	75°C	90°C
LDPE	0.28	0.20	0.18	
HIPS	0.29	0.25	0.24	0.60

Assuming that $P_{\text{avg}} = P = (P_{\text{top}} + P_{\text{bot}})/2$ calculate the ratio of $P_{\text{top}}/P_{\text{bot}}$ for each temperature. Comment on the physical significance of the results. The inner diameter of the cell is $D = 1.4$ cm and H is height of the bulk material in the cell, $D/H = 0.5$.

- 4.8. Calculation of the Particulate Solids Conveying a Screw Feeder** The performance of a feed screw of 1.0-in flight diameter, 0.325-in screw root diameter and 1.2-in lead was experimentally executed for LDPE pellets with a bulk density of 0.45 g/cm^3 by measuring the mass flow rate in the rotational speed range of 10–215 rpm. The results are shown in the table below. Construct a particulates drag-flow model that calculates with results that are in close agreement with the experimental results.

4. K. S. Hyun and M. A. Spalding, *Polym. Eng. Sci.*, **30**, 571 (1990).

Screw Speed (rpm)	Throughput (Exp.) (kg/hr)
10	2.94
20	5.88
50	14.04
100	26.4
150	40.44
200	52.2
215	58.08

4.9. The Discreet-Element Method for an Assembly of Two-dimensional Disks Example 4.2 serves as a simple illustration of the DEM cycling through a *force-displacement constitutive response*, $F_i = k\Delta n_i$ and the *law of motion*, which relates the F_i with \ddot{X}_i and, thus, particle motions. In the general case of an *assembly* with a very large number of disks the calculation cycle is as follows: the $F_i = k\Delta n_i$ is applied at each contact point of any disk and the vectorial sum of the contact forces is calculated to yield the net force acting on the disk. For such an assembly there are both normal and tangential

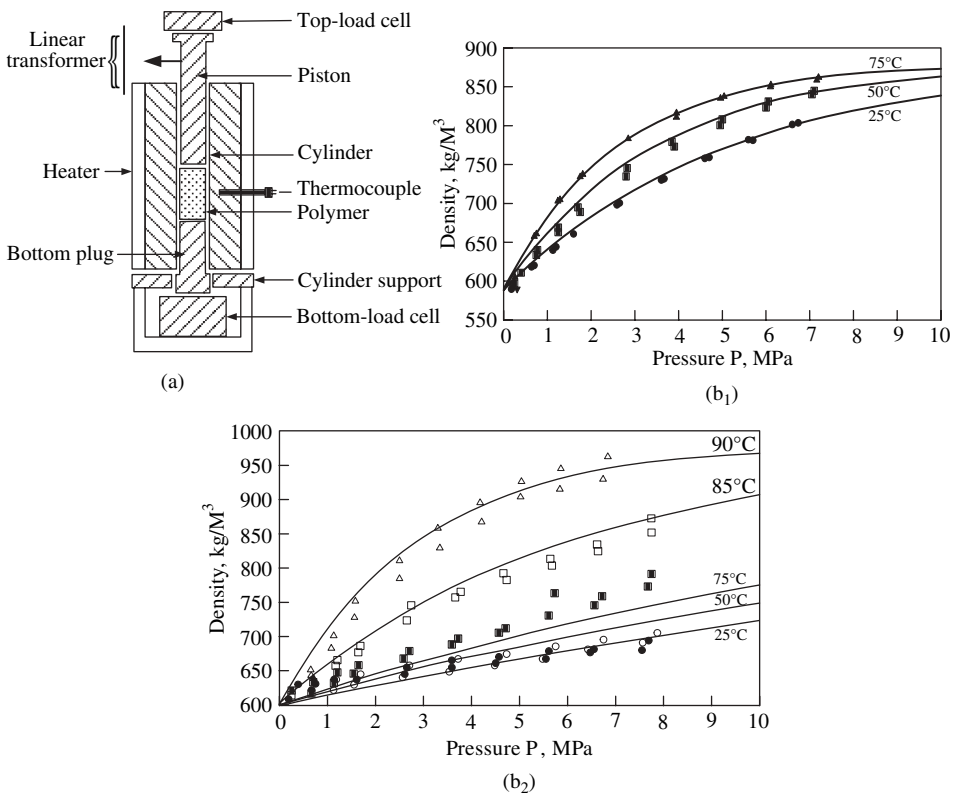


Fig. P4.7 (a) Schematic representation of the compaction cell used by Hyun and Spalding. (b) Experimentally obtained bulk densities of (b₁) LDPE pellets (b₂) HIPS pellets.

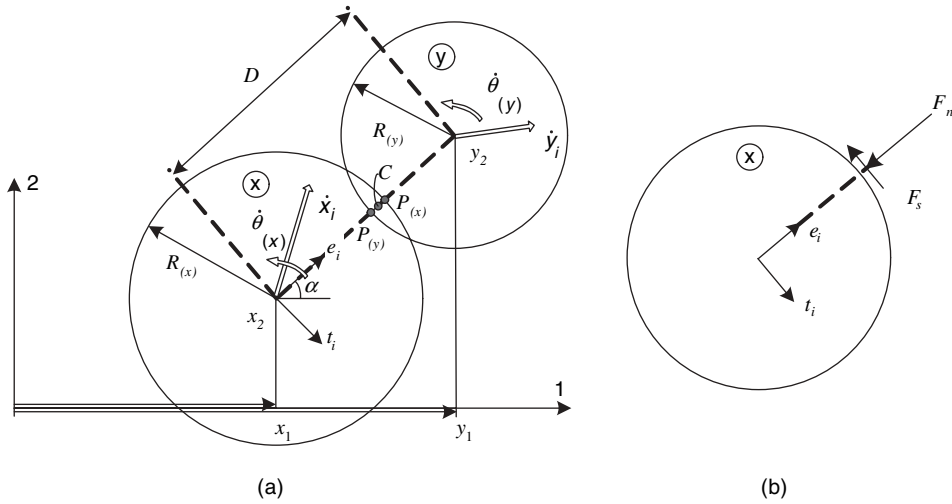


Fig. P4.9 The soft-sphere DEM method for a two-dimensional assembly, demonstrated by the interaction of two disks, x and y . Positive F_n and F_s are as shown.

forces, the latter giving rise to moments M_{X_i} and angular acceleration $\ddot{\theta}_{X_i}$, where

$$I_{X_i} \ddot{\theta}_{X_i} = \sum M_{X_i}$$

where I_{X_i} are the moments of inertia of disks X_i . After the net forces and moments are determined on every disk of the assembly, new accelerations are calculated for Newton's second law for each disk and, from those, their motions.

The more general force-displacement two-dimensional DEM method is shown in Fig. P4.9 for a pair of disks x and y in a dynamic state.

The points $P_{(x)}$ and $P_{(y)}$ are defined as the points of intersection of the line connecting the disk centers with the boundaries of the two disks. Contact takes place if and only if the center-to-center distance D is smaller than the sum of the two disk radii. If this condition is met, the relative (virtual) displacement at the contact C is determined by the integration of the relative velocity, defined as the velocity of point $P_{(x)}$ with respect to $P_{(y)}$. The unit vector $e_i = (\cos \alpha, \sin \alpha) = (y_i - x_i)/D$. The unit vector t_i is obtained by a clockwise 90° rotation of e_i , that is, $t_i = (e_2 - e_1)$. The relative velocity of the point $P_{(x)}$ with respect to $P_{(y)}$ can be expressed as \dot{X}_i

$$\dot{X}_i = (\dot{x}_i - \dot{y}_i) - (\dot{\theta}_{(x)}R_{(x)} + \dot{\theta}_{(y)}R_{(y)})t_i$$

Calculate (a) the relative normal (\dot{n}) and tangential ($\dot{\theta}$) relative velocities and, by integrating the normal and tangential displacements, (b) the increment of the normal ΔF_n and tangential forces ΔF_s using the linear laws $\Delta F_n = k_n \Delta n$ and $\Delta F_s = k_s \Delta s$. (c) Once the normal and shear (tangential) forces are specified for each contact point, the sums $\sum (F_n)_{(x)_i}$ are resolved to the components $\sum (F_n)_{(x)_1}$ and $\sum (F_n)_{(x)_2}$, and the resulting moment on disk x is $\sum M_x = \sum F_s R_{(x)}$; the relations sum the effects of all contacts. From the preceding resultant force and moment on

disk x and Newton's second law on disk x

$$m_{(x)}\ddot{X}_i = \sum (F_n)_{(x)_i}$$

$$I_{(\lambda)}\ddot{\theta}(\lambda) = \sum M(x)$$

Calculate the new velocity and updated position and rotation on each disk.

- 4.10. The Effect of High Single Screw Rotational Speeds in Limiting Operational Mass Throughput Rates** Potente and Pohl⁵ point out that as the single screw rotational speed is increased the actual equipment becomes increasingly smaller than that of the drag throughput rate of the metering section. This is shown on Fig. P4.10. (a) Give the physical reasons for this experimental finding. (b) Given the equipment geometric variables at which rpm value will the throughput rate begin to get affected? $D = 50$ mm, $\theta = 17.4^\circ$, $W = \text{Lead} \times \cos \theta_b - e = D \cos \theta_b - 0.1$ $W = 4.4$ cm and $H = 0.5$ cm; the polymer is LDPE pellets with $\rho_b = 0.45$ g/cc. (c) Is this limitation of practical significance?

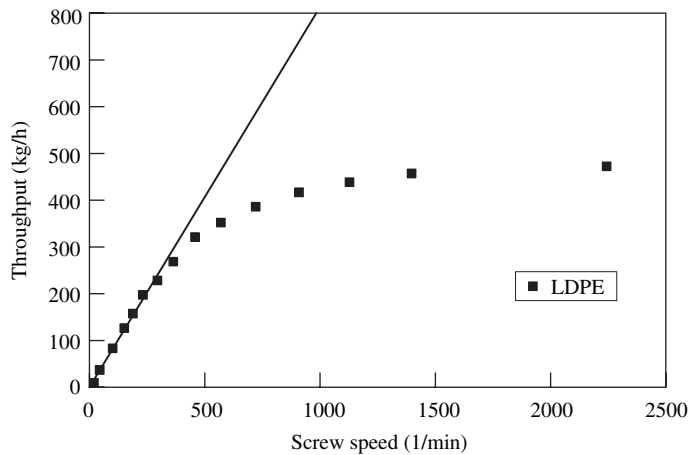


Fig. P4.10 The LDPE throughput rate of a 5 cm square-pitched single screw extruder screw with $e = 0.1$ W and $H = 0.5$ cm.

5. H. Potente and T. C. Pohl, *Int. Polym. Process.*, **17**, 11 (2002).

5 Melting

- 5.1 Classification and Discussion of Melting Mechanisms, 179
- 5.2 Geometry, Boundary Conditions, and Physical Properties in Melting, 184
- 5.3 Conduction Melting without Melt Removal, 186
- 5.4 Moving Heat Sources, 193
- 5.5 Sintering, 199
- 5.6 Conduction Melting with Forced Melt Removal, 201
- 5.7 Drag-induced Melt Removal, 202
- 5.8 Pressure-induced Melt Removal, 216
- 5.9 Deformation Melting, 219

Most shaping operations consist of the flow and deformation of *heat-softened* or *melted* polymers; hence, the preparation of the polymer for the shaping operation generally includes a “heating” or “melting” step. In either case, we define the process of bringing polymers, commonly in particulate form, from the feed temperature to the desired processing temperature range, appreciably above the glass transition temperature, T_g , for amorphous polymers and above the melting point, T_m , for semicrystalline polymers, as the *elementary step of melting*.

The thermal energy requirements to achieve melting can be estimated from the specific enthalpy curves shown in Fig. 5.1. The area under any given curve represents the thermal energy needed to heat or melt one unit mass of that polymer from room to any higher temperature.

We note that semicrystalline polymers, where the “break” points are indicative of T_m , require more energy because they must undergo the phase transition of fusion. For example, about 700 kJ/kg are needed to heat HDPE to 200°C, while for the same processing temperature PS requires about 350 kJ/kg, that is, half the energy.

Melting of particulate solids has received relatively little attention in the classic engineering literature, probably because it is rarely a rate-limiting operation. Nevertheless, Ross (1) in the 1950s did offer a systematic classification of melting methods of fusible solids, though none of them is applicable to polymeric solids. However, melting in polymer processing *is* a very important elementary step, not only because it is often the *rate-controlling* step, which consumes 70–80% of the total processing energy input, but also because it determines to a large extent the product quality related to homogeneity and stability (e.g., injection-molding quality and film-thickness variation, respectively). Additionally, during melting of polymer blends, a major part of the *blend morphology* is being established.

In this chapter we elucidate the physical mechanisms of melting, demonstrate some of the common mathematical tools used in solving them, and demonstrate how these

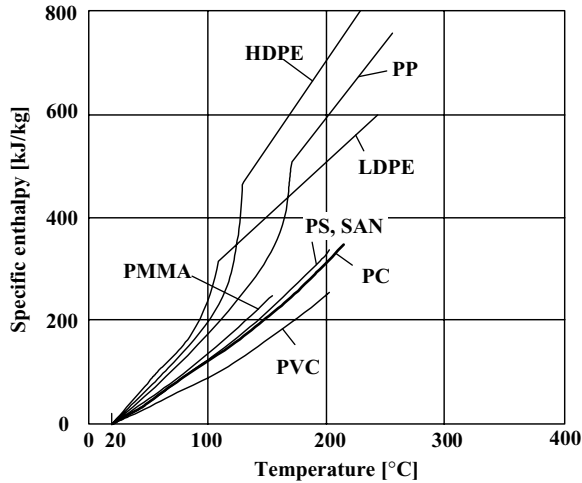


Fig. 5.1 Specific enthalpy curves for some common polymers.

mechanisms, in conjunction with inherent physical properties of polymers, lead to certain geometrical configurations of melting.

After the polymer has been shaped into the desired form, we are faced with the solidification problem (i.e., the inverse of the melting problem). We will find that, some of the solution methods developed in this chapter with regard to melting, are also valid for solidification.

5.1 CLASSIFICATION AND DISCUSSION OF MELTING MECHANISMS

The physical mechanisms that can bring about melting or heating of any substance are included in the terms of the thermal energy balance, Eq. 2.9-14

$$\rho \frac{Du}{Dt} = -\nabla \cdot \mathbf{q} - P(\nabla \cdot \mathbf{v}) - (\boldsymbol{\tau} : \nabla \mathbf{v}) + \dot{S} \quad (5.1-1)$$

In Eq. 5.1-1 we added an additional possible homogeneous energy source \dot{S} (e.g., dielectric heating). Clearly, the equation indicates four alternative sources by which the internal energy of a material can be raised, originating from each one of the terms on the right-hand side of the equation: (a) $(-\nabla \cdot \mathbf{q})$, which is the net rate of internal energy increase per unit volume from an outside source by *heat conduction*; (b) $P(\nabla \cdot \mathbf{v})$, which is the (reversible) rate of internal energy increase per unit volume by *compression*; (c) $[-(\boldsymbol{\tau} : \nabla \mathbf{v})]$, which is the (irreversible) rate of internal energy increase by *flow and deformation*; and (d) \dot{S} , which is a possible external source for *homogeneous internal energy increase* such as dielectric heating. We can also include in such a term exothermic chemical reaction (although this emerges from an appropriately defined internal energy) and ultrasonic heating (although this can also be accounted for by the deformation term).

Let us now discuss, in physical terms, how important each of the previously discussed mechanisms is to the melting of polymers, and the limitations or advantages of each one due to the physical nature of polymers.

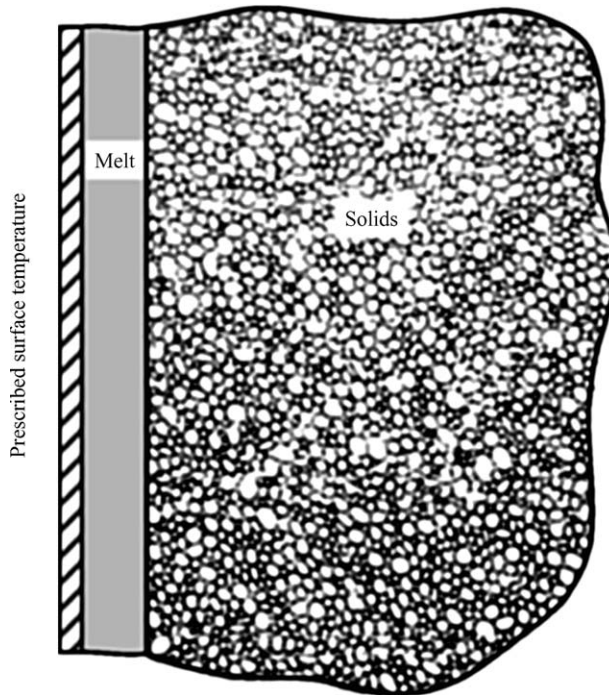


Fig. 5.2 Schematic representation of melting compacted polymeric solids by an outside heat source. A melt layer is formed which grows with time.

Conduction Melting

Conduction melting is the most common mode of raising the temperature of a solid and melting it. The surface temperature of a solid polymer or that of a compacted bed is raised by contact with a hot, solid surface, as shown in Figure 5.2.

As a result of this contact, a molten layer of polymer is formed, which grows with time. The mechanism of this kind of melting can be termed *conduction melting without melt removal*. The rate-controlling factors are the thermal conductivity, the attainable temperature gradients, and the available contact area between the heat source and the melting solid, reflecting material, operational, and configurational constraints, respectively. Thus, the low thermal conductivity of polymers (polymers are thermal insulators) and their temperature sensitivity (which makes them subject to thermal degradation and limits the attainable temperature gradients) place upper limits on the heat fluxes that can be applied.

Example 5.1 Thermal Degradation Characterization Thermal degradation is characterized by two temperature-dependent parameters, the *induction time* $\theta(T)$ for the onset of degradation, as shown in Fig. E5.1(a) for unplasticized Polyvinyl chloride (PVC), and the *rate of degradation*. The latter is shown in Fig. E5.1(b) in terms of the rate of change of the consistency index of the Power Law parameter, as a function of time and temperature, and can be expressed by the following equations:

$$\begin{aligned}
 m(t) &= m_0 & t &\leq \theta(T) \\
 m(t) &= m_0 \exp[Ct \exp^{-\Delta E/RT}] & t &> \theta(T)
 \end{aligned}$$

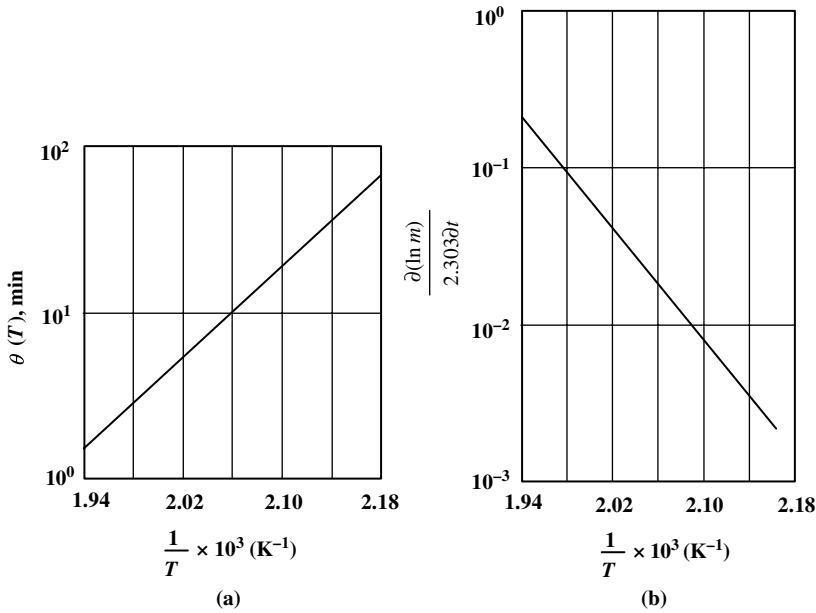


Fig. E5.1 Parameter reflecting thermal degradation of unplasticized PVC, Geon 101 EP-F24, as indicated by the time dependence of the consistency index m of the Power Law fluid model. [Reprinted by permission from E. A. Collins, B. F. Goodrich Chemical Co., Avon Lake, Ohio. Paper presented at the 1965 Society of Plastics Engineers Annual National Technical Conference, March 1966.]

Because of these limitations, and in particular because of the fact that, in such a mechanism, the temperature gradient at the wall that determines the heat flux to the solids drops exponentially with time, this melting mechanism is rather inefficient. However, the latter drawback can be alleviated if some mechanism continuously removes the molten layer. This, as shown in Fig. 5.3, can be accomplished either by applying a force normal to the heated surface, forcing out the melt by pressure flow, or by having the contact surface move parallel to its plane, dragging away the molten layer. These comprise the two

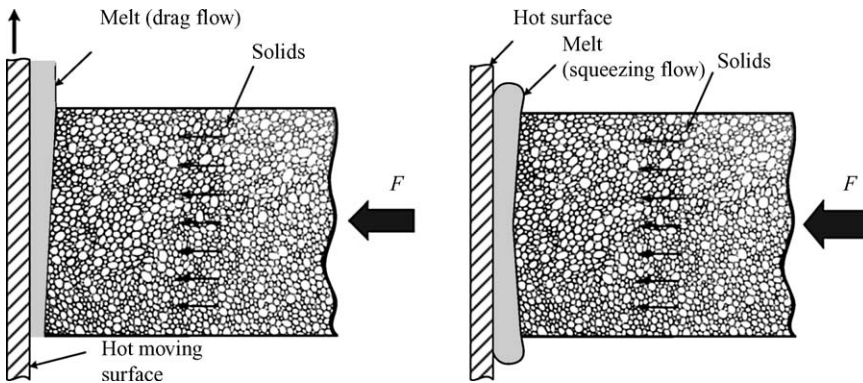


Fig. 5.3 Schematic representation of drag-induced melt removal and pressure-induced melt removal mechanisms.

melting mechanisms of *conduction melting with pressure-induced melt removal* and *drag-induced melt removal*, respectively.

“Grid melters” take advantage of the former mechanism and single screw extruders (SSEs), of the latter. In the elegant drag-removal melting mechanism that takes place in SSEs, significant temperature gradients can be maintained over thin films of melt, which not only quickly removes the freshly molten material from the vicinity of the high temperature zone and reduces the risk of degradation but also generates heat via viscous dissipation, further increasing the efficiency of melting. Moreover, in SSEs, the velocity of the moving solid plane or “wall” is tantamount to screw speed, and it becomes an important operating variable controlling the melting rate. Later in this chapter, we derive mathematical models for all these melting mechanisms.

Compressive Melting

Polymer solids and melts are virtually incompressible, and therefore very high pressures are needed for the term $P(\nabla \cdot \mathbf{v})$ to assume reasonable values. Nevertheless, Menges and Elbe (2) demonstrated the feasibility of an injection molding process based on this mode of melting.

Deformation Melting

For viscous liquids the $[-(\boldsymbol{\tau} : \nabla \mathbf{v})]$ term in Eq. 5.1-1 equals $(\boldsymbol{\tau} : \dot{\boldsymbol{\gamma}})/2$ and expresses the viscous energy dissipation (VED) per unit volume due to friction. The expression of the scalar product of the two tensors is given in the various coordinate systems in Table 2.5. For Newtonian fluids, this term further simplifies to $\mu(\dot{\boldsymbol{\gamma}} : \dot{\boldsymbol{\gamma}})/2$, and is given in the various coordinate systems in Table 2.6. Clearly, this term may be quite significant, because the viscosity of polymeric melts and the shear rates under processing conditions are high. As this term indicates, most polymeric melt flows are nonisothermal. Yet it also represents an important source of heat energy in drag-removal conduction melting, because of the very high shear rates imposed on the thin films in this melting mechanism. In fact, SSEs can be operated adiabatically with all the heat energy for melting originating in viscous dissipation.

As in viscous liquids, solid deformation also leads to irreversible conversion of mechanical energy to heat. In solids, however, deformation must exceed the elastic limit, and the imposed mechanical energy that is not elastically recovered is irreversibly dissipated into heat energy. In the melting step of polymer processing, we deform not a single piece of homogeneous solid polymeric body, but rather *repeated* deformation is imposed on a compacted bed of particulate solids. This generates significant, though nonhomogeneous, *heat energy* throughout the actively deformed bed via two distinct mechanisms: (a) individual polymeric particles undergo repeated deformations, generating heat within the particle, which we define as *plastic energy dissipation* (PED) (3), and (b) mechanical energy is dissipated into heat via interparticle friction, which we define as *frictional energy dissipation* (FED) (3). The compacted bed of solids cannot, of course, be considered a “continuum,” and neither of these heat sources is uniform and homogeneous throughout the bed. Yet, as a *first* approximation for such “active” compacted polymer particulates and assemblies undergoing plastic deformations, we can add two source terms to the equation of thermal energy (Eq. 2.9-16), yielding:

$$\rho_s C_s \frac{DT}{Dt} = -\nabla \cdot \mathbf{q} + \text{PED} + \text{FED} \quad (5.1-2)$$

The PED and FED terms are not easy to describe mathematically since, as pointed out earlier, they are not, strictly speaking, homogeneous sources within the compacted beds or particulate assemblies, which are made up of discrete bodies. Thus, friction takes place between *macroscopic* bodies, and even the deformation field *within* a single particle is nonhomogeneous. Nevertheless, because of their *predominant role* in processing equipment, in particular in co-rotating twin screw extruders (TSEs), these melting sources provide a very effective deformation mix-melting mechanism. When molten polymer regions are formed due to PED and FED, and if the deforming stresses persist, then both PED and VED will act *simultaneously* as heat sources, resulting in a very effective mechanism of deformation mix-melting. We discuss this mechanism in more detail, and formulate it mathematically, in Section 5.8.

Homogeneous Internal Melting

Alternative heating mechanisms to conduction, such as dielectric or ultrasonic energies, have also been attempted. These mechanisms can be dissipated by polymer solids, creating volumewide homogeneous heat sources. With these mechanisms, the governing form of the thermal-energy balance becomes

$$\rho C_s \frac{\partial T}{\partial t} = -\nabla \cdot \mathbf{q} + \dot{S} \quad (5.1-3)$$

Although feasible, as shown by Erwin and Suh (4), using dielectric heating as an energy source is rather limited in polymer processing practice as a *primary* melting mechanism.

In summary, the melting mechanisms that are *effective* in melting polymers at acceptable rates, according to criteria of avoiding thermal degradation and achieving high processing rates, are summarized in Fig. 5.4a as

1. *Conduction melting with forced melt removal*, where both conduction and melt flow-induced VED achieve appreciable melting rates. This is the *primary* melting mechanism in *single rotor* polymer processing equipment. Such equipment, for example, SSEs and injection molding machines, are primarily forming devices, with the large pumping capabilities needed for forming; single-rotor devices allow the compacted polymer particulates to remain *passive*, without participating in the melting process.
2. *Plastic energy dissipation and frictional energy dissipation*, in that order of importance, where compacted polymer particulates are “relentlessly” deformed by *twin rotor devices*, which rapidly raise their temperature and create regions of melts.
3. *Dissipative mix-melting* (DMM), which becomes the operative melting mechanism *after* PED and FED have created a solids-rich melt suspension. In this early two-phase stage, PED may still be dominant. Soon afterwards, as melt-rich suspensions are created, VED becomes the dominant mechanism capable of rapidly eliminating all solids regions. Again *twin rotor co-* and *counterrotating* devices can cause the solid particulate assemblies to deform rapidly and repeatedly, enlisting them in the melting process. This is the reason that such devices are used when uniform and very rapid melting is required, as in postreactor polymer “finishing” operations.

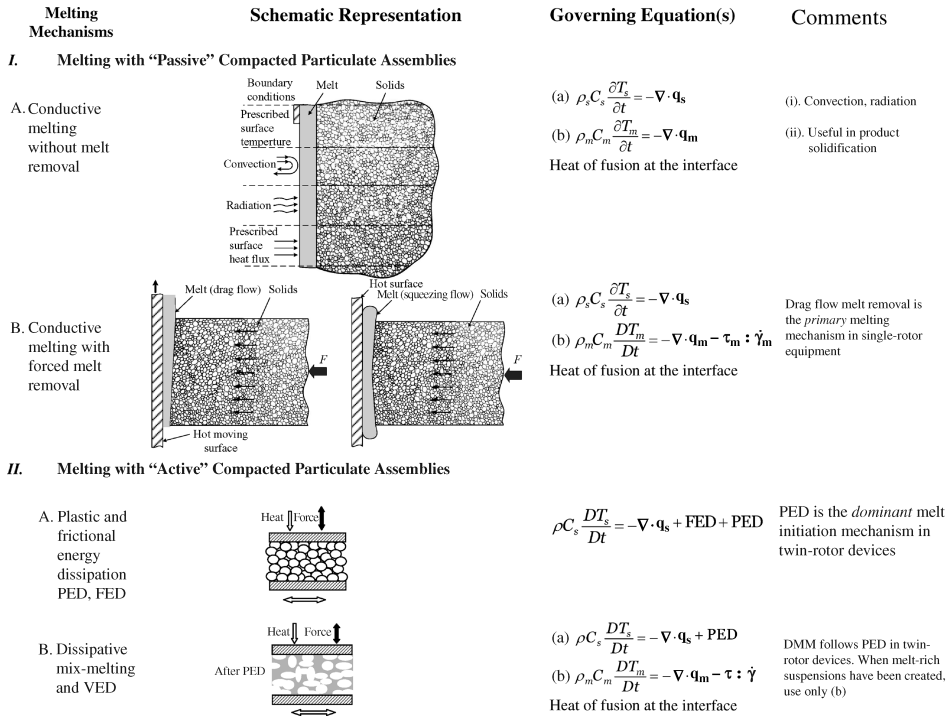


Fig. 5.4 Summary of the main mechanisms of the elementary step of melting. (I) Reprinted from Z. Tadmor and C. G. Gogos, *Principles of Polymer Processing*, Wiley, New York, 1979. (II) Reprinted by permission from C. G. Gogos, Z. Tadmor and M. H. Kim, "Melting Phenomena and Mechanisms in Polymer Processing Equipment," *Adv. Polym. Technology*, **17**, 285–305 (1998).

5.2 GEOMETRY, BOUNDARY CONDITIONS, AND PHYSICAL PROPERTIES IN MELTING

To solve a heat transfer problem in polymer processing, the geometrical boundaries over which heat transfer takes place must be defined, boundary conditions selected, and the nature of the physical properties of the polymer specified.

Although melting in polymer processing may take place in geometrically complex machinery, the rate-determining step can often be modeled in terms of simple geometries, such as semi-infinite bodies, infinite flat slabs, and thin films. Analytical techniques prove to be useful in many of these cases. In solidification, on the other hand, the geometry of the frequently complex finished product coincides with the geometrical boundaries of the heat transfer problem, necessitating the application of *numerical* techniques.

The most important boundary condition in heat transfer problems encountered in polymer processing is the constant surface temperature. This can be generalized to a *prescribed surface temperature* condition, that is, the surface temperature may be an arbitrary function of time $T(0, t)$. Such a boundary condition can be obtained by direct contact with an external temperature-controlled surface, or with a fluid having a large heat transfer coefficient. The former occurs frequently in the heating or melting step in most

processing machinery, whereas the latter may be the case in cooling and solidifying, such as in the water trough solidification of extruded products.

A *prescribed surface convection* condition mathematically is stated as

$$h[T_a(t) - T(0, t)] = -k \frac{\partial}{\partial x} T(0, t) \quad (5.2-1)$$

where $T_a(t)$ is the ambient fluid temperature, and h is the heat transfer coefficient. The exposed surface temperature, $T(0, t)$, is another common boundary condition in heat transfer; in polymer processing, for example, we find it in air cooling of blown films, in oven heating of sheets prior to vacuum forming, in cooling of finished injection molding products, and in many other applications.

Yet another boundary condition encountered in polymer processing is *prescribed heat flux*. Surface-heat generation via solid–solid friction, as in frictional welding and conveying of solids in screw extruders, is an example. Moreover, certain types of intensive radiation or convective heating that are weak functions of surface temperature can also be treated as a prescribed surface heat-flux boundary condition. Finally, we occasionally encounter the highly nonlinear boundary condition of *prescribed surface radiation*. The exposure of the surface of an opaque substance to a radiation source at temperature T_r leads to the following heat flux:

$$\sigma \mathcal{F} [T_r^4 - T^4(0, t)] = -k \frac{\partial}{\partial x} T(0, t) \quad (5.2-2)$$

where $\sigma = 5.6697 \times 10^{-8} \text{ W/m}^2 \text{ K}^4$ [$1.712 \times 10^{-9} \text{ Btu/h ft}^2 \text{ }^\circ\text{R}^4$] is the Stefan–Boltzmann radiation constant, and \mathcal{F} is the combined configuration-emissivity factor. As pointed out earlier, if $T_r \gg T$, the boundary condition Eq. 5.2-2 reduces to a constant-flux condition.

In the melting process, amorphous polymers undergo a second-order transition and change from brittle to rubbery solids at the glass transition temperature, T_g . Although T_g is reported as a single temperature value, the transition actually takes place over a temperature range of the order of 5–10°C. The value of T_g increases with increasing heating rate and applied hydrostatic pressure. Amorphous solids gradually become more deformable as they approach T_g , become “rubberlike” at $T_g < T < T_g + 100^\circ\text{C}$, known as the “rubbery plateau” region, and become fluidlike at $T > T_g + 100^\circ\text{C}$, called the *flow* (terminal) region. The crystalline portion of semicrystalline polymers, on the other hand, undergoes a first-order transition from the solid to the liquid state, with a characteristic heat of fusion λ , at the melting point T_m . Melting of the crystallites occurs over a 10–30°C range, depending on the spectrum of their sizes and perfection level, and on the rate of heating. The reported value of T_m is the temperature value at the *end* of this process; it depends on the polymer structure and, in the case of random copolymers, on the copolymer composition. Block copolymers exhibit the melting temperature characteristic of each of the two homopolymers.

Above T_m , the viscosity of the melt has Arrhenius-type dependence, decreasing (exponentially) with increasing temperature. Therefore a sharp transition is observed in both mechanical and viscous properties of semicrystalline polymers at T_m , resulting in a physical situation that is closer to the classic melting interface of monomeric crystals where, on one side, there is a viscous liquid, and on the other side, an elastic solid.

The physical and thermophysical properties of density, thermal conductivity, and specific heat are temperature dependent. It is a reasonably good approximation to use constant values for both the solid and molten states.

5.3 CONDUCTION MELTING WITHOUT MELT REMOVAL

As pointed out in the previous section, melting can often be modeled in terms of simple geometries. Here we analyze the transient conduction problem in a semi-infinite solid. We compare the solutions of this problem, assuming first (a) constant thermophysical properties, then (b) variable thermophysical properties and finally, and (c) a phase transition with constant thermophysical properties in each phase. These solutions, though useful by themselves, also help demonstrate the profound effect of the material properties on the mathematical complexities of the solution.

The equation of thermal energy (Eq. 2.9-16) for transient conduction in solids without internal heat sources reduces to

$$\rho C_p \frac{\partial T}{\partial t} = \nabla \cdot k \nabla T \quad (5.3-1)$$

If the thermal conductivity k and the product ρC_p are temperature independent, Eq. 5.3-1 reduces for homogeneous and isotropic solids to a linear partial differential equation, greatly simplifying the mathematics of solving the class of heat transfer problems it describes.¹

Example 5.2 Semi-infinite Solid with Constant Thermophysical Properties and a Step Change in Surface Temperature: Exact Solution The semi-infinite solid in Fig. E5.2 is initially at constant temperature T_0 . At time $t = 0$ the surface temperature is raised to T_1 . This is a one-dimensional transient heat-conduction problem. The governing parabolic differential equation

$$\frac{\partial T}{\partial t} = \alpha \frac{\partial^2 T}{\partial x^2} \quad (E5.2-1)$$

where α is the thermal diffusivity, must be solved to satisfy the following initial and boundary conditions $T(x, 0) = T(\infty, t) = T_0$ and $T(0, t) = T_1$. Introducing a new variable² η combines the two independent variables x and t as follows:

$$\eta = Cx t^m \quad (E5.2-2)$$

1. For heat conduction in nonisotropic solids, see Ref. 5.

2. This transformation follows from general similarity solution methods, and is a similarity transformation. The term “similar” implies that profiles of the variable $T = T(x, t)$ (at different coordinates x) differ only by a scale factor. The profiles can be reduced to the same curve by changing the scale along the axis of ordinates. Problems that lack a “characteristic length” are generally amenable to this solution method.

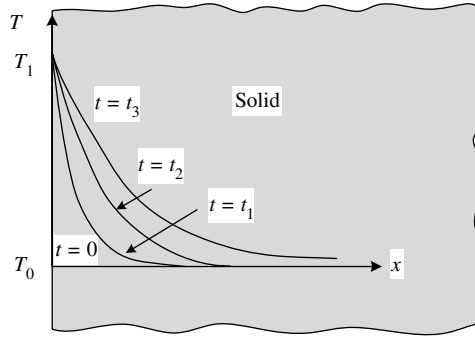


Fig. E5.2 Temperature profiles in a semi-infinite solid with a step change in temperature at the boundary.

where C and M are constants to be determined. Inserting Eq. E5.2-2 into Eq. E5.2-1 results in

$$m\eta \frac{dT}{d\eta} = \alpha C^2 t^{2m+1} \frac{d^2T}{d\eta^2} \quad (\text{E5.2-3})$$

For Eq. E5.2-3 to be independent of t , the following equality must hold: $2m + 1 = 0$ or $m = -1/2$. Thus, the following ordinary differential equation is obtained

$$\frac{d^2T}{d\eta^2} + \frac{1}{2\alpha C^2 \eta} \frac{dT}{d\eta} = 0 \quad (\text{E5.2-4})$$

Next we let $C = 1/\sqrt{4\alpha}$, which further simplifies Eq. E5.2-4 to

$$\frac{d^2T}{d\eta^2} + 2\eta \frac{dT}{d\eta} = 0 \quad (\text{E5.2-5})$$

Equation E5.2-5 can be easily solved by introducing another variable of transformation, $y = dT/d\eta$. The resulting temperature distribution is

$$T = C_1 \frac{\sqrt{\pi}}{2} \text{erf}(\eta) + C_2 \quad (\text{E5.2-6})$$

where

$$\eta = \frac{x}{\sqrt{4\alpha t}} \quad (\text{E5.2-7})$$

and $\text{erf}(z)$ is the well-known “error function” defined as

$$\text{erf}(z) = \frac{2}{\sqrt{\pi}} \int_0^z e^{-s^2} ds \quad (\text{E5.2-8})$$

The constants C_1 and C_2 are obtained from the boundary conditions. Thus, boundary condition $T(0, t) = T_1$ is satisfied if $C_2 = T_1$ whereas both conditions $T(x, 0) = T(\infty, t) = T_0$ imply $T = T_0$ at $\eta \rightarrow \infty$ (which is the direct result of the combination of variables). Thus we get $C_1 = 2(T_0 - T_1)/\pi^{1/2}$. Substituting these values into Eq. E5.2-6 results in

$$\frac{T - T_1}{T_0 - T_1} = \operatorname{erf}(\eta) \quad (\text{E5.2-9})$$

which satisfies both the differential equation and the boundary conditions, and hence is a solution to the problem.

The heat flux into the solid is obtained by differentiating Eq. E5.2-9 with respect to x , and using Fourier's law

$$q_x = -k \left(\frac{\partial T}{\partial x} \right)_{x=0} = -k \left[\frac{T_0 - T_1}{\sqrt{\pi \alpha t}} e^{-\eta^2} \right]_{x=0} = \frac{k}{\sqrt{\pi \alpha t}} (T_1 - T_0) \quad (\text{E5.2-10})$$

The results so far are both interesting and significant. First, we have obtained a particular dimensionless combination of the key variables: distance, time, and thermal diffusivity in Eq. E5.2-7, and the temperature profile becomes a unique function of this single dimensionless variable η .

We shall see later that this combination of the key variables is also characteristic of conduction heating with phase transfer. The heat flux is infinite at $t = 0$, but quickly drops with the inverse of $t^{1/2}$. Thus after 10 s it is only 30% of the flux at 1 s, and after 60 s, it is only 13% of the heat flux at 1 s! The obvious conclusion is that conduction melting without melt removal becomes inefficient for anything but short times.

Example 5.3 The Semi-infinite Solid with Variable Thermophysical Properties and a Step Change in Surface Temperature: Approximate Analytical Solution

We have stated before that the thermophysical properties (k, ρ, C_p) of polymers are generally temperature dependent. Hence, the governing differential equation (Eq. 5.3-1) is nonlinear. Unfortunately, few analytical solutions for nonlinear heat conduction exist (5); therefore, numerical solutions (finite difference and finite element) are frequently applied. There are, however, a number of useful *approximate analytical* methods available, including the integral method reported by Goodman (6). We present the results of Goodman's approximate treatment for the problem posed in Example 5.2, for comparison purposes.

We begin with Eq. 5.3-1 and introduce a variable of transformation for T

$$d\Theta(x, t) = \rho C_p dT \quad (\text{E5.3-1})$$

or in integrated form:

$$\Theta(x, t) = \int_{T_0}^T \rho C_p dT \quad (\text{E5.3-2})$$

where Θ is the heat added per unit volume at location x and time t . Substituting Eq. E5.3-1 into Eq. 5.3-1 gives

$$\frac{\partial \Theta}{\partial t} = \frac{\partial}{\partial x} \alpha(\Theta) \frac{\partial \Theta}{\partial x} \quad (\text{E5.3-3})$$

Next we integrate Eq. E5.3-3 over x from the outer surface ($x = 0$) to a certain, yet unknown depth $\delta(t)$, which is defined as the *thermal penetration depth*

$$\int_0^{\delta} \frac{\partial \Theta}{\partial t} dx = \int_0^{\delta} \left[\frac{\partial}{\partial x} \alpha(\Theta) \frac{\partial \Theta}{\partial x} \right] dx \quad (\text{E5.3-4})$$

The penetration depth reflects the time-dependent distance from the surface to a location where thermal effects become negligible. Using the Leibnitz formula for the left-hand side of Eq. E5.3-4, we get

$$\frac{d}{dt} \int_0^{\delta} \Theta dx - \Theta(\delta, t) \frac{d\delta}{dt}$$

But $\Theta(\delta, t) = 0$, because we defined δ as the distance at which thermal effects fade away; that is we assume that $T(\delta) = T_0$. Thus, the right-hand side of Eq. E5.3-4 simply becomes

$$- \left[\alpha(\Theta) \frac{\partial \Theta}{\partial x} \right]_{x=0}$$

and Eq. 5.3-4 can be rewritten as

$$\frac{d}{dt} \int_0^{\delta} \Theta dx = - \left[\alpha(\Theta) \frac{\partial \Theta}{\partial x} \right]_{x=0} \quad (\text{E5.3-5})$$

The advantage of the Goodman transformation is now apparent: the temperature-dependent thermophysical properties in the integrated differential equation have to be evaluated only at the surface temperature, T_1 . The variation of the properties with the temperature appear in the boundary condition for $\Theta(x, t)$

$$\Theta(x, t) = \Theta_1 = \int_{T_0}^{T_1} \rho C_p dT \quad (\text{E5.3-6})$$

Boundary conditions $T(x, 0) = T(\infty, t) = T_0$ are both taken care of by assuming a time-dependent thermal penetration depth of finite thickness.

Next we assume a temperature profile that a priori satisfies the boundary condition $\Theta(0, t) = \Theta_1$, $\Theta(\delta, 0) = 0$ and $(\partial \Theta / \partial x)_{x=\delta} = 0$, such as

$$\Theta = \Theta_1 \left(1 - \frac{x}{\delta} \right)^3 \quad (\text{E5.3-7})$$

By substituting Eq. E5.3-7 into Eq. E5.3-5, the time dependence of δ is obtained

$$\delta = \sqrt{24\alpha_1 t} \quad (\text{E5.3-8})$$

where α_1 is α evaluated at T_1 . For polymers with typical α values of $1 \times 10^{-7} \text{ m}^2/\text{s}$, the penetration depth is 1 mm after 1 s and 1 cm after 60 s.

From Eq. E5.3-7, we obtain

$$\Theta(x, t) = \Theta_1 \left(1 - \frac{x}{\sqrt{24\alpha_1 t}} \right)^3 \quad (\text{E5.3-9})$$

The temperature profile at any given time is obtained by calculating Θ for various x values ($0 < x < \delta$) and obtaining from Eq. E5.3-7 the corresponding temperatures. The latter, of course, requires knowing the temperature dependences of ρC_p .

For constant thermophysical properties Eq. E5.3-9 reduces to

$$\frac{T - T_0}{T_1 - T_0} = \left(1 - \frac{x}{\sqrt{24\alpha t}}\right)^3 \quad (\text{E5.3-10})$$

The heat flux at $x = 0$ is

$$q_x = \frac{k}{\sqrt{8\alpha t/3}}(T_1 - T_0) \quad (\text{E5.3-11})$$

which can be compared to the exact solution in Eq. E5.2-10, showing a small difference between the two solution methods. This difference depends on the selection of the trial function, and in this case it is 8%.

Example 5.4 Melting of a Semi-infinite Solid with Constant Thermophysical Properties and a Step Change in Surface Temperature: The Stefan–Neumann Problem The previous example investigated the heat conduction problem in a semi-infinite solid with constant and variable thermophysical properties. The present Example analyzes the same conduction problem with a change in phase.

Interest in such problems was first expressed in 1831 in the early work of G. Lamè and B. P. Clapeyron on the freezing of moist soil, and in 1889 by J. Stefan on the thickness of polar ice and similar problems. The exact solution of the phase-transition problem in a semi-infinite medium is due to F. Neumann (who apparently dealt with this kind of problem even before Stefan), and thus, problems of this kind are called Stefan–Neumann problems. The interest in these problems has been growing ever since (7,8).

The presence of a moving boundary between the phases introduces nonlinearity into the boundary conditions. Hence, there are only a few exact solutions, and we must frequently turn to approximate analytical or numerical solutions.

In this example, we consider the classic Stefan–Neumann solution. The solid is initially at a constant temperature T_0 . At time $t = 0$ the surface temperature is raised to T_1 , which is above the melting point, T_m . The physical properties of each phase are different, but they are temperature independent, and the change in phase involves a latent heat of fusion λ . After a certain time t , the thickness of the molten layer is $X_l(t)$; in each phase there is a temperature distribution and the interface is at the melting temperature T_m (Fig. E5.4).

Heat is conducted from the outer surface through the melt to the free interface, where some of the heat is absorbed as heat of fusion, melting some more solid, and the rest is conducted into the solid phase. The densities of melt and solid are usually different. We denote the melt phase with subscript l and the solid with subscript s . The thickness of the molten layer increases because of melting, and there is also a slight increase due to a decrease in density as the solid melts. If there were no decrease in density, the thickness of the molten layer would remain X_s . Thus, the relationship between X_l and X_s is given by

$$\frac{X_l}{X_s} = \frac{\rho_s}{\rho_l} = \beta \quad (\text{E5.4-1})$$

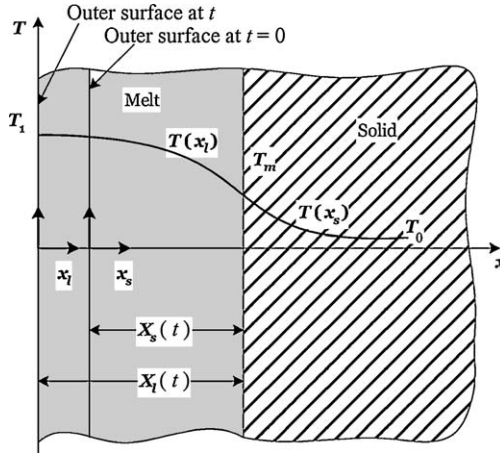


Fig. E5.4 Melting in a semi-infinite solid. $X_l(t)$ is the thickness of the molten layer at time t , $X_s(t)$ is the distance of the interface from the location of external surface at time $t = 0$. The temperature profile in the solid is expressed in coordinate x_s , which is stationary, whereas the temperature profile in the melt is expressed in coordinate x_l , which has its original outer surface of melt, hence, it slowly moves with time if $\rho_s \neq \rho_l$.

The governing differential equation in both phases is Eq. E5.2-1. For the melt phase, it takes the form

$$\frac{\partial^2 T_l}{\partial x_l^2} - \frac{1}{\alpha_l} \frac{\partial T_l}{\partial t} = 0 \quad (\text{E5.4-2})$$

with boundary conditions $T_l(0, t) = T_1$ and $T_l(x_l, t) = T_m$.

It should be noted that the coordinate x_l has its origin at the outer surface of the melt which, if $\rho_s \neq \rho_l$, slowly moves with the melting process. For the solid phase we have

$$\frac{\partial^2 T_s}{\partial x_s^2} - \frac{1}{\alpha_s} \frac{\partial T_s}{\partial t} = 0 \quad (\text{E5.4-3})$$

with the boundary conditions $T_s(\infty, t) = T_0$ and $T_s(x_s, t) = T_m$.

The coordinate x_s has its origin at the external surface when melting started, and it is stationary. In addition to the boundary conditions just given, we can write a heat balance for the interface (this is occasionally referred to as the Stefan condition).

$$k_l \left(\frac{\partial T_l}{\partial x_l} \right)_{x_l=X_l} - k_s \left(\frac{\partial T_s}{\partial x_s} \right)_{x_s=X_s} = \lambda \rho_l \frac{dX_l}{dt} = \lambda \rho_s \frac{dX_s}{dt} \quad (\text{E5.4-4})$$

Heat flux into the interface
Heat flux out from interface
Rate of melting per unit interface

We assume that the temperature profile in each phase has the form of the temperature profile in a semi-infinite solid with a step change in surface temperature as derived in Example 5.2. Thus we get the following temperature profiles for melt and solid phases, respectively,

$$T_l = T_1 + A \operatorname{erf} \left(\frac{x_l}{2\sqrt{\alpha_l t}} \right) \quad (\text{E5.4-5})$$

which automatically satisfies the boundary condition $T_l(0, t) = T_1$, and

$$T_s = T_0 + B \operatorname{erfc}\left(\frac{x_s}{2\sqrt{\alpha_s t}}\right) \quad (\text{E5.4-6})$$

where $\operatorname{erfc}(s) = 1 - \operatorname{erf}(s)$, and which satisfies the boundary condition $T_s(\infty, t) = T_0$. Both equations must satisfy the boundary condition, stating that the temperature at the interface is that of the melting point:

$$T_m = T_1 + A \operatorname{erf}\left(\frac{X_l}{2\sqrt{\alpha_l t}}\right) \quad (\text{E5.4-7})$$

$$T_m = T_0 + B \operatorname{erfc}\left(\frac{X_s}{2\sqrt{\alpha_s t}}\right) \quad (\text{E5.4-8})$$

Now, Eqs. E5.4-7 and E5.4-8 must hold for all times t . This is possible *only* if both X_l and X_s are proportional to the square root of time. We can, therefore, write

$$X_s = K\sqrt{t} \quad (\text{E5.4-9})$$

and with the aid of Eq. E5.4-1 we get

$$X_l = \beta K\sqrt{t} \quad (\text{E5.4-10})$$

where K is an unknown constant. From Eqs. E5.4-9 and E5.4-10 we conclude, without even having the complete solution, that the thickness of the molten layer grows at a rate proportional to the square root of time. It is interesting to note the similarity between the penetration depth, as obtained in the preceding examples, and the location of the interface. This similarity suggests the application of approximate solution methods to phase-transition problems.

The constant K can be evaluated by substituting Eqs. E5.4-5 and E5.4-6 into Eq. E5.4-4. Subsequent to evaluating the constants A and B from the boundary conditions and Eqs. E5.4-9 and E5.4-10

$$\frac{(T_m - T_1)k_l e^{-K^2\beta^2/4\alpha_l}}{\sqrt{\pi\alpha_l}\operatorname{erf}(K\beta/2\sqrt{\alpha_l})} - \frac{(T_0 - T_m)k_s e^{-K^2/4\alpha_s}}{\sqrt{\pi\alpha_s}\operatorname{erfc}(K/2\sqrt{\alpha_s})} = \lambda\rho_l \frac{K\beta}{2} \quad (\text{E5.4.11})$$

The root of this transcendental equation is K , and it is a function of the initial and boundary conditions, as well as the physical properties of the two phases. Tabulated solutions of Eq. E5.4-11 for $\beta = 1$ to four-digit accuracy are given by Churchill and Evans (9). The temperature profiles in the two phases are obtained from Eqs. E5.4-5 and E5.4-6, with the aid of Eqs. E5.4-7 and E5.4-8

$$\frac{T_l - T_m}{T_1 - T_m} = 1 - \frac{\operatorname{erf}(x_l/2\sqrt{\alpha_l t})}{\operatorname{erf}(K\beta/2\sqrt{\alpha_l})} \quad (\text{E5.4-12})$$

and

$$\frac{T_s - T_m}{T_0 - T_m} = 1 - \frac{\operatorname{erfc}(x_s/2\sqrt{\alpha_s t})}{\operatorname{erfc}(K/2\sqrt{\alpha_s})} \quad (\text{E5.4-13})$$

Equations E5.4-12 and E5.4-13 satisfy the differential equation and the boundary and initial conditions. Therefore they form an exact solution to the problem. In the preceding solution we neglected heat convection as a result of the expansion of the melt phase due to the density decrease. The rate of melting per unit area as a function of time can be obtained from Eq. E5.4-10

$$w_A = \rho_l \frac{dX_l}{dt} = \frac{\rho_s K}{2\sqrt{t}} \quad (\text{E5.4-14})$$

Again we note the similarity in the solution of the conduction problem with constant thermophysical properties, to those with variable properties, and with phase transition. Clearly, the rate of melting drops with time as the molten layer, which essentially forms a thermal shield, increases in thickness. This result, once again, directs our attention to the advantage accruing from forced removal of the molten layer from the melting site. The average rate of melting is

$$\bar{w}_A = \frac{1}{t} \int_0^t \frac{\rho_s K}{2\sqrt{t}} dt = \frac{\rho_s K}{\sqrt{t}} \quad (\text{E5.4-15})$$

The preceding examples discuss the heat-conduction problem without melt removal in a semi-infinite solid, using different assumptions in each case regarding the thermophysical properties of the solid. These solutions form useful approximations to problems encountered in everyday engineering practice. A vast collection of analytical solutions on such problems can be found in classic texts on heat transfer in solids (10,11). Table 5.1 lists a few well-known and commonly applied solutions, and Figs. 5.5–5.8 graphically illustrate some of these and other solutions.

Most real cases of polymer melting (and solidification) involve complex geometries and shapes, temperature-dependent properties, and a phase change. The rigorous treatment for such problems involve numerical solutions (12-15) using finite difference (FDM) or FEMs. Figure 5.9 presents calculated temperature profiles using the Crank–Nicolson FDM (16) for the solidification of a HDPE melt inside a flat-sheet injection-mold cavity. The HDPE melt that has filled the cavity is considered to be initially isothermal at 300°F, and the mold wall temperature is 100°F.

5.4 MOVING HEAT SOURCES

Conductive heating with moving heat sources was treated in detail by Rosenthal (17), particularly in relation to metal processing such as welding, machining, grinding, and continuous casting. In polymer processing, we also encounter heat conduction problems with moving heat sources as well as heat sinks. The commonly practiced welding of polyvinyl chloride, the continuous dielectric sealing of polyolefins, the heating of films and thin sheets under intense radiation lamps, and in certain cases, the heating or chilling of continuous films and sheets between rolls are some examples. These processes are usually steady or quasi–steady state, with heat introduced or removed at a point or along a line. We now examine one particular case to demonstrate the solution procedure.

TABLE 5.1 Analytical Solutions to Some Common Heat Transfer Problems (Constant Physical Properties)

Geometry	Initial and Boundary Conditions		Temperature Distribution
Semi-infinite solid	$T(x, 0) = T_0$	$T(0, t) = T_1$	$\frac{T - T_1}{T_0 - T_1} = \text{erf}\left(\frac{x}{\sqrt{4\alpha t}}\right)$
Semi-infinite solid	$T(x, 0) = T_0$	$T(\infty, t) = T_0$	$T - T_0 = \frac{q_0 \sqrt{4\alpha t}}{k} \text{ierfc}\left(\frac{x}{\sqrt{4\alpha t}}\right)$
Flat plate	$T(x, 0) = T_0$	$T(\pm b, t) = T_1$	$\frac{T_1 - T}{T_1 - T_0} = 2 \sum_{n=0}^{\infty} \frac{(-1)^n}{(n + \frac{1}{2})\pi} e^{-(n+\frac{1}{2})^2 \pi^2 (\alpha t/b^2)} \cos\left[\left(n + \frac{1}{2}\right) \pi \frac{x}{b}\right]$
Flat plate	$T(x, 0) = T_0$	$\left. \frac{-\partial T}{\partial x} \right _{x=-b} = \frac{h}{k} [T_1 - T(-b)]$	$\frac{T_1 - T}{T_1 - T_0} = \sum_{n=1}^{\infty} \frac{2 \left(\frac{hb}{k}\right) \cos \beta_n \left(\frac{x}{b}\right)}{\beta_n^2 + \left(\frac{hb}{k}\right)^2} \frac{e^{-\beta_n^2 (\alpha t/b^2)}}{\cos \beta_n}$
Cylinder	$T(r, 0) = T_0$	$T(R, t) = T_1$	$\frac{T_1 - T}{T_1 - T_0} = \frac{2}{R} \sum_{n=1}^{\infty} \frac{J_0(r c_n) e^{-\alpha c_n^2 t}}{c_n J_1(R c_n)} J_0(R c_n) = 0$
Cylinder	$T(r, 0) = T_0$	$\left. k \left(\frac{\partial T}{\partial r}\right) \right _{r=R} = h [T(R) - T_1]$	$\frac{T_1 - T}{T_1 - T_0} = \frac{2}{R} \sum_{n=1}^{\infty} \frac{\exp(-\alpha \beta_n^2 t)}{\left(\frac{h}{k}\right)^2 + \beta_n^2} \left[\frac{h}{k} \frac{J_0(r \beta_n)}{J_0(R \beta_n)} \right]$
Sphere	$T(r, 0) = T_0$	$T(R, t) = T_1$	$\frac{T_1 - T}{T_1 - T_0} = \frac{2R}{\pi r} \sum_{n=1}^{\infty} \frac{(-1)^n}{n} \frac{n \pi r}{R} e^{-\alpha n^2 \pi^2 r^2 / R^2}$
Sphere	$T(r, 0) = T_0$	$\left. k \left(\frac{\partial T}{\partial r}\right) \right _{r=R} = h [T(R) - T_1]$	$\frac{T_1 - T}{T_1 - T_0} = \frac{2 \frac{h}{k} \sum_{n=1}^{\infty} \exp(-\alpha \beta_n^2 t)}{r \beta_n \left[R^2 \beta_n^2 + R \frac{h}{k} \left(R \frac{h}{k} - 1 \right) \right]} \left[\frac{R^2 \beta_n^2 + \left[R \left(\frac{h}{k} \right) - 1 \right]^2}{\beta_n^2} \right]$

$$R \beta_n \cot(R \beta_n) + R \left(\frac{h}{k}\right) - 1 = 0$$

$$\beta_n \tan \beta_n = \frac{hb}{k}$$

$$\beta_n \tan \beta_n = \frac{hb}{k}$$

$$\beta_n J_0(R \beta_n) + \frac{h}{k} J_0(r \beta_n) = 0$$

$$\sin(R \beta_n) \sin(r \beta_n)$$

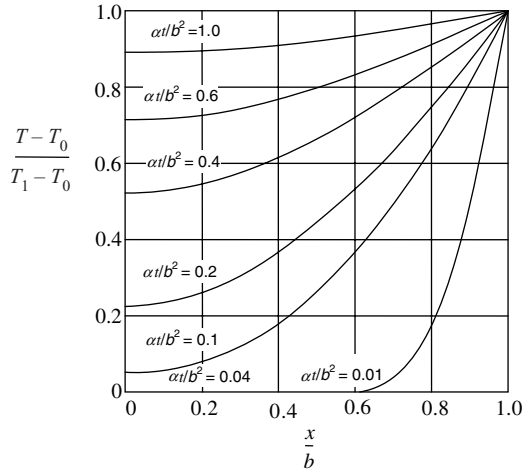


Fig. 5.5 Temperature profiles for unsteady-state heat conduction in finite flat plates: $T(x, 0) = T_0$, $T(\pm b, t) = T_1$. [Reprinted by permission from H. S. Carslaw and J. C. Jaeger, *Conduction of Heat in Solids*, 2nd ed., Oxford University Press, New York, 1973.]

Example 5.5 Continuous Heating of a Thin Sheet Consider a thin polymer sheet infinite in the x direction, moving at constant velocity V_0 in the negative x direction (Fig. E5.5). The sheet exchanges heat with the surroundings, which is at $T = T_0$, by convection. At $x = 0$, there is a plane source of heat of intensity q per unit cross-sectional area. Thus the heat source is moving relative to the sheet. It is more convenient, however, to have the coordinate system located at the source. Our objective is to calculate the axial temperature profile $T(x)$ and the intensity of the heat source to achieve a given maximum temperature. We assume that the sheet is thin, that temperature at any x is uniform, and that the thermophysical properties are constant.

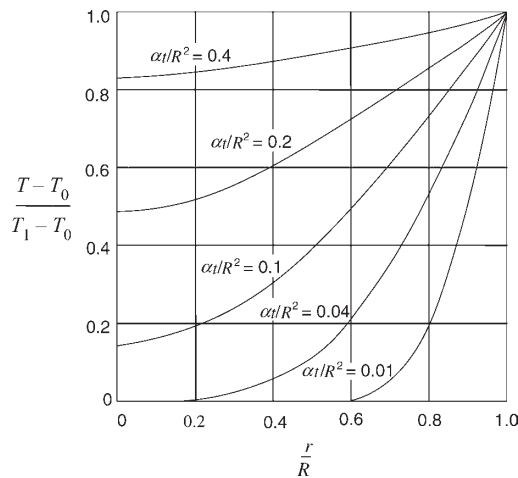


Fig. 5.6 Temperature profiles for unsteady-state heat conduction in infinite cylinders: $T(r, 0) = T_0$, $T(R, t) = T_1$. [Reprinted by permission from H. S. Carslaw and J. C. Jaeger, *Conduction of Heat in Solids*, 2nd ed., Oxford University Press, New York, 1973.]

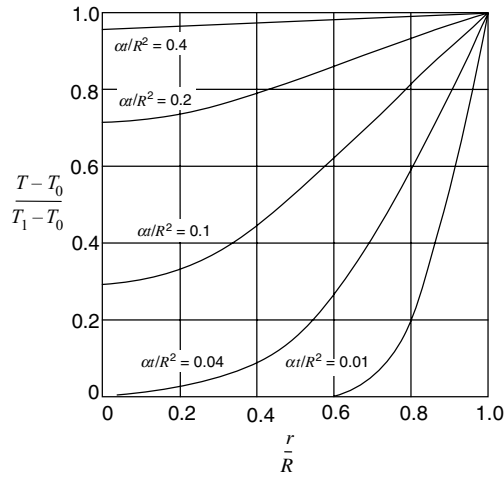


Fig. 5.7 Temperature profiles for unsteady-state heat conduction in spheres: $T(r, 0) = T_0$, $T(R, t) = T_1$. [Reprinted by permission from H. S. Carslaw and J. C. Jaeger, *Conduction of Heat in Solids*, 2nd ed., Oxford University Press, New York, 1973.]

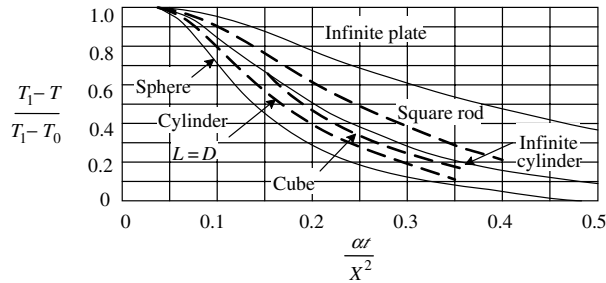


Fig. 5.8 Temperature at the center of different shapes versus time; X is the thickness, side dimension, or diameter; initial temperature is T_0 , then the temperature of the outside surface is raised to T_1 . [Reprinted by permission from H. Gröber and S. Erk, *Die Grundgesetze der Wärmeübertragung*, Springer-Verlag, Berlin, 1933, Fig. 28, p. 58.]

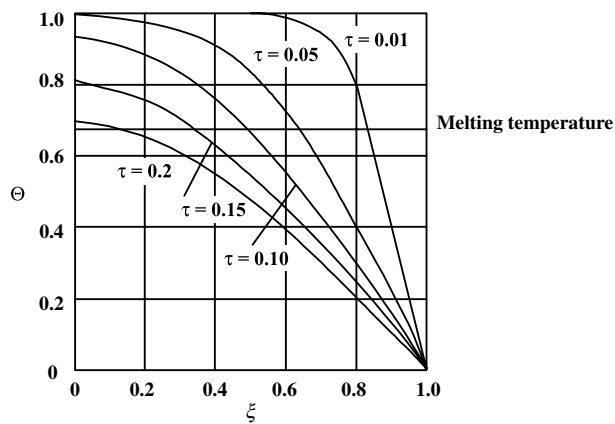


Fig. 5.9 Dimensionless temperature in a thin injection mold during solidification of HDPE. [Reprinted by permission from C. Gutfinger, E. Broyer, and Z. Tadmor, *Polym. Eng. Sci.*, **15**, 515 (1975).]

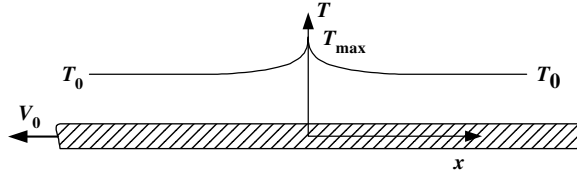


Fig. E5.5 Heating of a moving thin sheet with a plane heat source.

The energy equation for this problem reduces to:

$$\rho C_p V_0 \frac{dT}{dx} = k \frac{d^2 T}{dx^2} - Q_v \quad (\text{E5.5-1})$$

where Q_v is the heat exchanged with the surrounding per unit volume:

$$Q_v = \frac{hc}{A} [T(x) - T_0] \quad (\text{E5.5-2})$$

where c and A are the perimeter and cross-sectional areas, respectively. Substituting Eq. E5.5-2 into Eq. E5.5-1 and using the “excess temperature” $T'(x) = T(x) - T_0$ instead of $T(x)$, we obtain

$$\frac{d^2 T'}{dx^2} - \frac{V_0}{\alpha} \frac{dT'}{dx} - m^2 T' = 0 \quad (\text{E5.5-3})$$

where

$$m = \left(\frac{hc}{kA} \right)^{1/2} \quad (\text{E5.5-4})$$

Equation E5.5-3 is to be solved subject to the boundary conditions $T'(\pm\infty) = 0$. Equation E5.5-3 is a linear second-order differential equation that can be conveniently solved by defining a differential operator $D^n = d^n/dx^n$, yielding

$$\left(D^2 - \frac{V_0}{\alpha} D - m^2 \right) T' = 0 \quad (\text{E5.5-5})$$

in which the differential operator behaves as though it were an algebraic polynomial. Since $T' \neq 0$, the expression in parentheses must equal zero, and solving for D , we get as roots:

$$D = \frac{V_0}{2\alpha} \pm \sqrt{m^2 + \left(\frac{V_0}{2\alpha} \right)^2} \quad (\text{E5.5-6})$$

The temperature profile is then

$$T'(x) = A_1 \exp \left[\left(\frac{V_0}{2\alpha} + \sqrt{m^2 + \left(\frac{V_0}{2\alpha} \right)^2} \right) x \right] + B_1 \exp \left[\left(\frac{V_0}{2\alpha} - \sqrt{m^2 + \left(\frac{V_0}{2\alpha} \right)^2} \right) x \right] \quad (\text{E5.5-7})$$

Since we cannot satisfy both boundary conditions except for the trivial case $T' = 0$, we split our solution into two regions $x \geq 0$ and $x \leq 0$, resulting in the following solutions:

$$T'(x) = B_1 \exp \left[- \left(\sqrt{m^2 + \left(\frac{V_0}{2\alpha} \right)^2} - \frac{V_0}{2\alpha} \right) x \right] \quad x \geq 0 \quad (\text{E5.5-8})$$

and

$$T'(x) = A_1 \exp \left[\left(\sqrt{m^2 + \left(\frac{V_0}{2\alpha} \right)^2} + \frac{V_0}{2\alpha} \right) x \right] \quad x \leq 0 \quad (\text{E5.5-9})$$

Now at $x = 0$ both equations should yield the same, yet unknown maximum temperature T'_{\max} ; thus, we get

$$A_1 = B_1 = T'_{\max} = T'(0) \quad (\text{E5.5-10})$$

The value of T'_{\max} depends on the intensity of the heat source. Heat generated at the plane source is conducted in both the x and $-x$ directions. The fluxes q_1 and q_2 , and in these respective directions are obtained from Eqs. E5.5-8 and E5.5-9:

$$q_1 = kT'_{\max} \left(\sqrt{m^2 + \left(\frac{V_0}{2\alpha} \right)^2} - \frac{V_0}{2\alpha} \right) \quad (\text{E5.5-11})$$

$$q_2 = -kT'_{\max} \left(\sqrt{m^2 + \left(\frac{V_0}{2\alpha} \right)^2} + \frac{V_0}{2\alpha} \right) \quad (\text{E5.5-12})$$

A heat balance at the interface requires

$$q = |q_1| + |q_2| \quad (\text{E5.5-13})$$

Substituting Eqs. E5.5-11 and E5.5-12 into Eq. E5.5-13 and solving for T'_{\max} gives

$$T'_{\max} = \frac{q}{2k \sqrt{m^2 + \left(\frac{V_0}{2\alpha} \right)^2}} \quad (\text{E5.5-14})$$

Thus the maximum excess temperature is proportional to the intensity of the source, and it drops with increasing speed V_0 , and increases in the thermal conductivity and the heat transfer coefficient. From Eqs. E5.5-8 and E5.5-9 we conclude that the temperature drops quickly in the positive x direction as a result of the convection ($V_0 < 0$) of the solid into the plane source, and slowly in the direction of motion. Again, in this chapter we encounter

exponentially dropping temperatures in solids with convection—a frequent situation in melting configurations.

5.5 SINTERING

When solid particles come in contact with each other at elevated temperatures, they tend to coalesce, thereby decreasing the total surface area. This process is called *sintering* (18). It is usually accompanied by a decrease in the total volume of the particulate bed. A decrease in surface area brings about a decrease in (surface) free energy; hence, the surface tension is the driving force for the coalescence process.

The sintering process proceeds in two distinct stages, first by developing interfaces and bridges between adjacent particles with little change in density, followed by a *densification* stage in which the interparticle cavities are eliminated (Fig. 5.10). It should be noted that sintering is a local phenomenon between adjacent particles involving viscous flow. The rate of the process is therefore greatly affected by the local temperature. Hence, along with the sintering process, we usually have to deal with the overall heat transfer problem within the particulate system, where previously discussed solutions are applicable, with the thermophysical properties replaced by “effective” values.

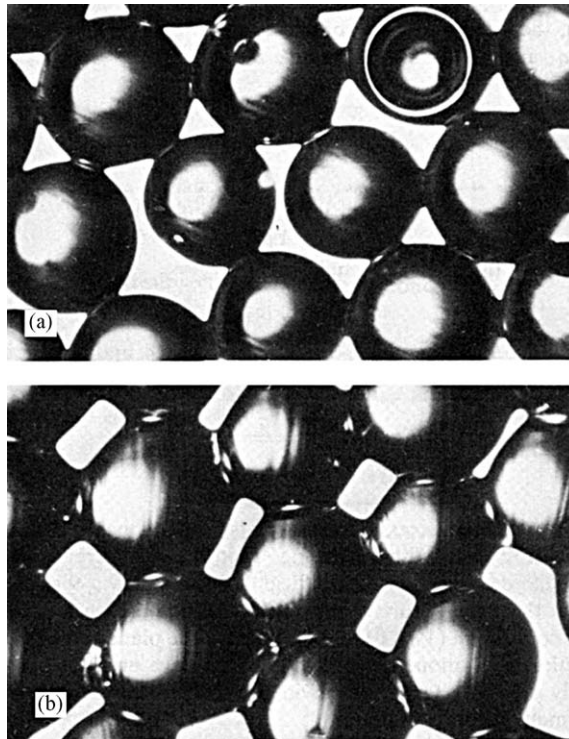


Fig. 5.10 A monolayer of 700 μm . diameter Polymethyl methacrylate (PMMA) beads during a sintering process at 203°C, $\times 50$. (a) After 25 min; (b) after 55 min. [Reprinted by permission from M. Narkis, D. Cohen, and R. Kleinberger, “Sintering Behavior and Characterization of PMMA Particles,” Department of Chemical Engineering, Technion Israel Institute of Technology, Haifa.]

The processing of metallic and ceramic powders by sintering is an old and well-developed technological activity. In polymer processing, melting by a sintering process is practiced in areas such as rotational molding (19,20) and powder coating. Moreover, it provides the only practical way to process polytetrafluoroethylene, whose very high molecular weight precludes other common processing methods (21). Finally, a process of high-pressure compaction, followed by sintering, has been suggested for melting and shaping high-temperature polymers such as polyimides and aromatic polyesters, as well as for physical mixtures of preset composition distribution of more common polymers (22,23).

The model of viscous sintering was developed by Frenkel (24), who derived the following expression for the rate of coalescence of spherical adjacent particles:

$$\frac{x^2}{R} = \frac{2\Gamma}{3\eta}t \quad (5.5-1)$$

subject to $x/R < 0.3$, where x is the neck radius (Fig. 5.11), R is the radius of the particles, Γ is the surface tension, and η is the viscosity. This expression was applied successfully to glass and ceramic materials, but for polymeric materials Kuczynski et al (18), working with polymethyl metacrylate (PMMA), found the experimental data to follow the following type of empirical equation:

$$\left(\frac{x^2}{R^{1.02}}\right)^p = F(T)t \quad (5.5-2)$$

where t is sintering time, and $F(T)$ is a function only of the temperature. For $p = 1$, Eq. 5.5-2 reduces to a Frenkel type of equation. Kuczynski et al. derived this equation theoretically by assuming the melt to be non-Newtonian and to follow the Power Law constitutive equation. The result is

$$\left(\frac{x^2}{R}\right)^{1/n} = \frac{t}{2n} \left(\frac{8n\Gamma}{m}\right)^{1/n} \quad (5.5-3)$$

where n and m are the Power Law model constants. Thus the parameter p in Eq. 5.5-2 acquires rheological meaning. For $n = 1$, Eq. 5.5-3 reduces to the Frenkel equation as corrected by Eshelby (25). Yet the flow field during the coalescence process is probably neither homogeneous nor isothermal; therefore, a complete analysis of the coalescence stage would first require a detailed analysis of the kinematics of the flow field. Thus, the theoretical analysis should preferably be carried out with a viscoelastic

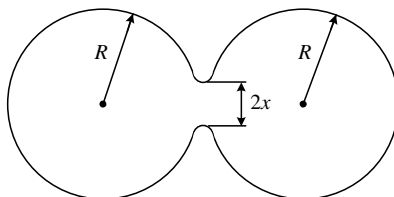


Fig. 5.11 Schematic view of the first stage in the sintering process.

constitutive equation, because viscoelastic effects, as suggested by Lonz (21), may play an important role in sintering of polymeric materials, and accounting for nonisothermal effects.

The coalescence stage is usually considered terminated when x/R reaches a value of 0.5. For the densification stage that follows, Frenkel (24) suggested the following expression:

$$\frac{r}{r_0} = 1 - \frac{\Gamma}{2\eta r_0} t \quad (5.5-4)$$

when r_0 is the initial radius of the approximately spherical cavity formed by the first stage, and r is the radius at time t .

As sintering proceeds and coalescence and densification occur, the overall heat conduction problem does not remain unaffected. Clearly, the effective thermophysical properties change, thereby influencing the overall temperature distribution and the local sintering problem as well.

5.6 CONDUCTION MELTING WITH FORCED MELT REMOVAL

In the preceding sections, we have discussed the physical mechanisms by which thermal energy can be supplied to a solid polymer, and have outlined some of the mathematical tools available for solving these problems. We have dealt with various aspects of “conduction melting without melt removal,” which is generally applicable to melting a semifinished or finished product, as well as to the solidification processes following shaping. We have noticed in most of the problems analyzed that heat fluxes and rates of melting diminish rapidly with time as the molten layer increases in thickness. It follows logically, then, that the rate of melting can be considerably increased by a *continuous removal of the molten layer formed*. This process, as Section 5.1 pointed out, not only leads to high rates of melting, but is the *essential element in creating a continuous steady source of polymer melt*, which in turn is the heart of the most important shaping methods of die forming, molding, calendaring, and coating, as well as for preparing the preshaped forms for the stretch shaping operations.

Removal of the melt, also discussed in Section 5.1, is made possible, in principle, by two mechanisms: drag-induced flow and pressure-induced flow (Fig. 5.4). In both cases, the molten layer must be sheared, leading to viscous dissipation. The latter provides an additional, important source of thermal energy for melting, the rate of which can be controlled externally either by the velocity of the moving boundary in drag-induced melt removal or the external force applied to squeeze the solid onto the hot surface, in pressure-induced melt removal.

In either of these cases we convert external mechanical energy into heat. This source of heat is not negligible; it may even be the dominant or sole source in the melting process, for example, in the case of “autogenous” screw extrusion.³ Having two alternative sources of heat energy provides the processing design engineer with a great deal of flexibility.

3. This term is used for an extrusion operation where the barrel is heated for the start-up, but then heating is discontinued and the only source of heat is viscous dissipation.

Finally, the continuous removal of melt has the added benefit of not exposing polymer melts to high temperature surfaces or regions for long residence times.

From a mathematical point of view, problems of conduction melting with forced melt removal are far more complex than ordinary conduction melting, because they involve the simultaneous solution of the momentum and energy equations. Moreover, boundary conditions are often ill defined.

We will now analyze forced drag melt removal in some detail. This is the dominant melting mechanism in the SSE, and to a very large extent, in the injection molding machine as well. These, of course, are two very important devices for polymer processing forming operations. Chapter 6 discusses the flow in the single screw geometry from first principles, and Chapter 9 analyzes in detail the melting mechanism in single screw-based machines using the melting model presented in Section 5.7.

5.7 DRAG-INDUCED MELT REMOVAL

We consider an infinite slab of isotropic homogenous solid of width W , pressed against a moving hot plate (Fig. 5.12). A highly sheared, thin film of melt is formed between the

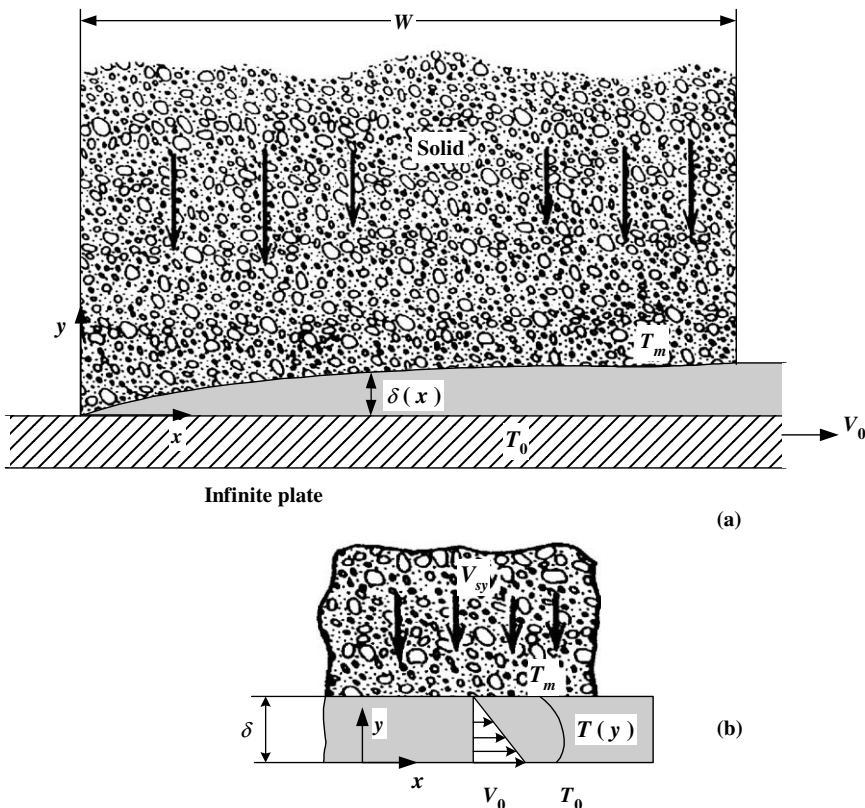


Fig. 5.12 (a) Schematic representation of a slab of polymer melting on a hot moving surface. (b) Enlarged view of a portion of the melt film.

solid and the plate, and this film is continuously removed. After a certain time, steady-state conditions evolve; that is, velocity and temperature profiles become time independent. The problem is two-dimensional, in that the temperature and velocity fields are functions of x and y only. No variations occur in the z direction, which is infinite. The thickness of the melt film is very small at $x = 0$, and it increases in the positive x direction, the shape of the melt film $\delta(x)$ being an a priori unknown function.

Heat is conducted from the hot plate, which is at a constant temperature T_0 , to the solid–melt interface at $T = T_m$, assuming that the polymer is polycrystalline. As discussed in Section 5.1, amorphous polymers at T_g do not change abruptly from brittle solids to viscous liquids. Thus the choice for T_m is not obvious. One can pretend that the transition is sharp and set an arbitrary level of temperature (larger than T_g) at which flow begins to occur. Alternatively, as suggested recently by Sundstrom and Lo (26), the glass transition temperature can be used together with the WLF equation to select an appropriate melting point.

We are seeking a solution for the rate of melting and the temperature distribution of the emerging melt. Clearly, these variables will be functions of the *physical properties* of the solid, the *plate temperature* and velocity, and the *width of the solid slab*.

The drag-removal melting mechanism was discovered and mathematically modeled by Tadmor (27) in connection to melting in SSEs (see Section 9.3). It was further refined, experimentally, verified, and formulated as a self-contained computer package by Tadmor et al. (28–31). Later Vermeulen et al. (32), and Sundstrom and Lo (26) and Sundstrom and Young (33) analyzed the problem both experimentally and theoretically; Mount (34) measured experimental rates of melting, and Pearson (35) analyzed the theoretical problem mathematically in detail, as shown in Fig. 5.12. In this section we follow Pearson's discussion.

In trying to analyze the detailed mechanism of this melting configuration, we must first consider the nature of the solid. For a perfectly rigid, incompressible body moving toward the interface without rotation, the rate of melting at the interface must be independent of the coordinate x , because the bulk velocity of the solid will be uniform across x . Hence, $\delta(x)$ and $P(x)$, and the velocity and temperature fields in the film *must* assume values that will satisfy this requirement, as well as the equations of motion and energy, with the appropriate boundary conditions. But in highly sheared thin films of very viscous polymers formed under a relatively soft deformable bed of particulate solids, a constant pressure assumption in the film is more appropriate. This, in turn, implies that, at steady-state conditions, the *rate of melting* may generally be a *function* of x , although this variation may be small. A *variable* melting rate therefore implies, that the solid either *deforms* or *rotates* or does both.

Solid polymers, in particular, in the form of a bed of compressed pellets or powder as encountered in polymer processing, can be considered deformable. The melt formed at the interface penetrates some of the voids between the particulate solids forming the bed, enabling sliding and rearrangement in the neighborhood of the interface. Through such a mechanism, it is easy to visualize the continuously deforming solid concept. Thus, the physical situation in this case would be one of a slowly deformable solid pressed against the moving hot plate.

The solid interface has a small velocity in the negative y direction that may slowly vary with x . Yet the solid is *rigid enough* to sustain the shear stresses in the film and to prohibit the development of an x -direction interface velocity. We are now in a position to state the

simplifying assumptions to the problem and specify the governing differential equations. The following assumptions are made:

1. Constant thermophysical properties
2. Incompressible fluid
3. No slip at the wall
4. Power Law (or Newtonian) fluid with temperature-dependent viscosity:

$$m = m_0 e^{-a(T-T_m)} \quad (5.7-1)$$

5. Steady state conditions
6. Negligible gravitational forces
7. Laminar flow prevails throughout
8. The film thickness is much smaller than its width $\delta/W \ll 1$

These, together with the small Reynolds number in the film, justifies the use of the lubrication approximation. Moreover, the same considerations lead us to neglect exit effects (at $x = W$), and precise entrance conditions (at $x = 0$) need not be specified.

The equations of continuity and motion, respectively, reduce to

$$\frac{\partial v_x}{\partial x} + \frac{\partial v_y}{\partial y} = 0 \quad (5.7-2)$$

and

$$\frac{\partial P}{\partial x} = \frac{\partial \tau_{yx}}{\partial y} \quad (5.7-3)$$

Since we assume a pure drag flow in the film, Eq. 5.7-3 further reduces to

$$\frac{\partial \tau_{yx}}{\partial y} = 0 \quad (5.7-4)$$

Expressing the shear stress in terms of the local velocity gradient, Eq. 5.7-4 becomes

$$\frac{\partial}{\partial y} \left[e^{-a(T-T_m)} \left(-\frac{\partial v_x}{\partial y} \right)^n \right] = 0 \quad (5.7-5)$$

Equation 5.7-5 can be integrated with respect to y to give

$$-\left(\frac{\partial v_x}{\partial y} \right) = C_1 e^{[a(T-T_m)/n]} \quad (5.7-6)$$

Thereby, if $a = 0$ (i.e., temperature-independent viscosity), the velocity profile is linear for both Newtonian and Power Law fluids. If, however, $a \neq 0$, the local velocity profile

becomes a function of the temperature. Since temperature varies sharply over y , we expect significant nonlinearity of the profile in the y direction. Moreover, because of convection, T is also a (weaker) function of x , introducing a corresponding (weak) x dependence of the velocity profile. Hence, the equations of motion and energy must be solved simultaneously. The latter reduces to

$$\rho_m C_m \left(v_x \frac{\partial T}{\partial x} + v_y \frac{\partial T}{\partial y} \right) = k_m \frac{\partial^2 T}{\partial y^2} - \tau_{xy} \frac{\partial v_x}{\partial y} \quad (5.7-7)$$

where ρ_m , C_m , and k_m are the thermophysical properties of the polymer melt, with heat conduction in the x direction assumed to be much smaller than conduction in the y direction, and further assuming that the only significant contribution to viscous dissipation is that originating from the τ_{yx} component of the stress tensor.

Next we specify the boundary conditions in the film. At the solid boundary we have:

$$T(0) = T_0, \quad v_x(0) = V_0, \quad v_y(0) = 0 \quad (5.7-8)$$

and at the solid–melt interface we have:

$$T(\delta) = T_m, \quad v_x(\delta) = 0 \quad (5.7-9)$$

The velocity $v_y(\delta)$ at any position x is determined by the rate of melting at the interface, to be obtained from the following heat balance:

$$k_m \left(-\frac{\partial T}{\partial y} \right)_{y=\delta} = \rho_m [-v_y(\delta)] \lambda + k_s \left(-\frac{\partial T_s}{\partial y} \right)_{y=\delta} \quad (5.7-10)$$

Rate of heat conducted
into the interface per unit
interface area
Rate of melting at the
interface per unit interface
area times the heat of fusion
Rate of heat conducted
out of the interface per
unit interface area

where λ is the heat of fusion, and k_s and T_s are the thermal conductivity and temperature, respectively, of the solid. The term on the left-hand side is the rate of heat conducted from the hot film into the interface.

For melting to take place, $\partial T / \partial y < 0$. This term is therefore positive and provides the heat source for melting, which as we see on the right-hand side, is used for two purposes: to heat the polymer to the melting point at the interface where $T = T_m$ (second term) and to melt the polymer at the interface (first term).

The last term on the right-hand side can be obtained by solving the temperature profile in the solid bed. Consider a small, x -direction portion of the film and solid [Fig. 5.12(b)]. We assume the solid occupies the region $y > \delta$ (where δ is the local film thickness) and moves into the interface with constant velocity v_{sy} . The problem thus reduces to a one-dimensional steady heat-conduction problem with convection. In the solid, a steady, exponentially dropping temperature profile develops. The problem is similar to that in Section 5.4. The equation of energy reduces to

$$\rho_s C_s v_{sy} \frac{\partial T_s}{\partial y} = k_s \frac{\partial^2 T_s}{\partial y^2} \quad (5.7-11)$$

where ρ_s , C_s , and k_s are the thermophysical properties of the solid polymer. Equation 5.7-11 can be easily solved with the boundary conditions $T_s(\delta) = T_m$ and $T_s(\infty) = T_{s0}$, to give the following temperature profile:

$$T = T_{s0} + (T_m - T_{s0}) \exp \left[\frac{v_{sy}(y - \delta)}{\alpha_s} \right] \quad (5.7-12)$$

The velocity $v_{sy} < 0$, and hence Eq. 5.7-12, satisfies both boundary conditions. The rate of heat conduction out of the interface, noting that $v_{sy}\rho_s = v_y(\delta)\rho_m$, is

$$-k_s \left(\frac{\partial T}{\partial y} \right)_{y=\delta} = -(T_m - T_{s0})v_y(\delta)\rho_m C_s \quad (5.7-13)$$

Thus Eq. 5.7-10 can now be written as

$$k_m \left(\frac{\partial T}{\partial y} \right)_{y=\delta} = \rho_m v_y(\delta) \lambda^* \quad (5.7-14)$$

where

$$\lambda^* = \lambda + C_s(T_m - T_{s0}) \quad (5.7-15)$$

Thus λ^* is the total heat energy required to bring a *solid* from an initial temperature T_{s0} to T_m and to *melt* it at that temperature. Sundstrom and Young (33) solved this set of equations numerically after converting the partial differential equations into ordinary differential equations by similarity techniques. Pearson (35) used the same technique to obtain a number of useful solutions to simplified cases. He also used dimensionless variables, which aid in the physical interpretation of the results, as shown below:

$$\Theta = \frac{T - T_m}{T_0 - T_m} \quad (5.7-16)$$

$$\xi = \frac{x}{W} \quad \text{and} \quad \eta = \frac{y}{\delta} \quad (5.7-17)$$

$$u_x = \frac{v_x}{V_0} \quad \text{and} \quad u_y = \frac{v_y}{V_0(\delta_0/W)} \quad (5.7-18)$$

where the meaning of δ_0 will be clarified below.

We first rewrite the boundary conditions

$$\Theta(0) = 1, \quad u_x(0) = 1, \quad u_y(0) = 0 \quad (5.7-19)$$

$$\Theta(1) = 0, \quad u_x(1) = 0 \quad (5.7-20)$$

The melting condition at the interface (Eq. 5.7-14) reduces to

$$\frac{k_m(T_0 - T_m)W}{\lambda^* \rho_m V_0 \delta_0^2} \left(\frac{\partial \Theta}{\partial \eta} \right)_{\eta=1} = \frac{\delta}{\delta_0} u_y(1) \quad (5.7-21)$$

This relationship provides us with a reasonable choice of δ_0 . Since this boundary condition determines the physical process, the dimensionless group $k_m(T_0 - T_m)W/\lambda^*\rho_m V_0\delta_0^2$ should be of the order of 1. Hence, we can choose δ_0 as

$$\delta_0 = \left(\frac{k_m(T_0 - T_m)W}{\lambda^*\rho_m V_0} \right)^{1/2} \quad (5.7-22)$$

As we shall see later, δ_0 is not merely an arbitrary scaling (normalizing) factor; by the choice we made it turns out to be of the order of the film thickness, provided viscous dissipation or convection are not too significant to the process.

We now can rewrite the transport equation in dimensionless form as follows. The continuity equation is

$$\frac{\partial u_x}{\partial \xi} - \eta \frac{\dot{\delta}}{\delta} \frac{\partial u_x}{\partial \eta} + \frac{\delta_0}{\delta} \frac{\partial u_y}{\partial \eta} = 0 \quad (5.7-23)$$

where $\dot{\delta} = d\delta/d\xi$.

Details of the derivation of Eq. 5.7-23 are as follows. Substituting u_x and u_y from Eq. 5.7-18 into the equation of continuity results in

$$V_0 \frac{\partial u_x}{\partial x} + \frac{V_0 \delta_0}{W} \frac{\partial u_y}{\partial y} = 0$$

Next we rewrite the partial differentials in terms of the new variables η and ξ . We recall that $u_x(\xi, \eta)$, $u_y(\eta)$, $\xi = F_1(x)$, and $\eta = F_2(x, y)$. The x dependence in η is due to $\delta(x)$. Hence, we can write

$$\begin{aligned} \frac{\partial u_x}{\partial x} &= \frac{\partial u_x}{\partial \xi} \frac{\partial \xi}{\partial x} + \frac{\partial u_x}{\partial \eta} \frac{\partial \eta}{\partial x} = \frac{1}{W} \frac{\partial u_x}{\partial \xi} - \frac{y}{\delta^2} \frac{\partial \delta}{\partial x} \frac{\partial u_x}{\partial \eta} \\ &= \frac{1}{W} \frac{\partial u_x}{\partial \xi} - \frac{\eta}{W} \frac{\dot{\delta}}{\delta} \frac{\partial u_x}{\partial \eta} \end{aligned}$$

Similarly, we obtain

$$\frac{\partial u_y}{\partial y} = \frac{\partial u_y}{\partial \xi} \frac{\partial \xi}{\partial y} + \frac{\partial u_y}{\partial \eta} \frac{\partial \eta}{\partial y} = \frac{1}{\delta} \frac{\partial u_y}{\partial \eta}$$

The dimensionless form of the equation of motion is

$$\frac{\partial}{\partial \eta} \left[e^{b\Theta} \left(-\frac{\partial u_x}{\partial \eta} \right)^n \right] = 0 \quad (5.7-24)$$

where

$$b = -a(T_0 - T_m) \quad (5.7-25)$$

Finally the equation of energy using the definition of δ_0 becomes

$$\begin{aligned} M^{-1} & \left[u_x \frac{\partial \Theta}{\partial \xi} - u_x \frac{\dot{\delta}}{\delta} \eta \frac{\partial \Theta}{\partial \eta} + u_y \frac{\delta_0}{\delta} \frac{\partial \Theta}{\partial \eta} \right] \\ & = \left(\frac{\delta_0}{\delta} \right)^2 \frac{\partial^2 \Theta}{\partial \eta^2} + \text{Br} \left(\frac{\delta_0}{\delta} \right)^{n+1} e^{b\Theta} \left(-\frac{\partial u_x}{\partial \eta} \right)^{n+1} \end{aligned} \quad (5.7-26)$$

where

$$M = \frac{\lambda^*}{C_m(T_0 - T_m)} \quad (5.7-27)$$

and

$$\text{Br} = \frac{m_0 V_0^{(3n+1)/2} \rho_m^{(n-1)/2} \lambda^* (n-1)/2}{(T_0 - T_m)^{(n+1)/2} k_m^{(n+1)/2} W^{(n-1)/2}} \quad (5.7-28)$$

In these equations, Br is a modified Brinkman number, which is a measure of the extent to which viscous heating is important, and M measures the ratio of heat energy needed to melt the polymer, as compared to that needed to heat the melt to T_0 . If the latter is small, M will be large and the convection terms in the energy equation can be neglected. The dimensionless parameter b measures the significance of the temperature dependence of the viscosity over the temperature range considered (flow activation energy).

Achieving a complete solution of the set of equations above is difficult, as pointed out earlier. In addition to the numerical solution (33), Pearson (35) proposed a heuristic approach. Insight into the nature of melting with drag-forced removal can be obtained, however, by considering some special cases that lead to analytical, closed-form solutions. These simplified cases per se represent very useful solutions to the modeling of processing methods.

Newtonian Fluid with Temperature-Independent Viscosity and Negligible Convection

For a Newtonian fluid close to isothermal conditions (i.e., $n = 1$ and $b \ll 1$), and with convection neglected (i.e., $M \gg 1$), the equation of motion becomes

$$\frac{\partial^2 u_x}{\partial \eta^2} = 0 \quad (5.7-29)$$

which, for the boundary conditions stated in Eqs. 5.7-19 and 5.7-20 has the solution

$$u_x = 1 - \eta \quad (5.7-30)$$

The equation of energy, which for this case can be solved independently, reduces to

$$\frac{\partial^2 \Theta}{\partial \eta^2} + \text{Br} \left(-\frac{\partial u_x}{\partial \eta} \right)^2 = 0 \quad (5.7-31)$$

Substituting Eq. 5.7-30 into Eq. 5.7-31, followed by integration, yields the temperature profile

$$\Theta = 1 - \eta + \frac{\text{Br}}{2}\eta(1 - \eta) \quad (5.7-32)$$

The mean temperature $\bar{\Theta}$ is obtained from Eq. 5.7-32 as follows:

$$\bar{\Theta} = \frac{\int_0^1 u_x \Theta d\eta}{\int_0^1 u_x d\eta} = \frac{2}{3} + \frac{\text{Br}}{12} \quad (5.7-33)$$

Now we can solve Eq. 5.7-21 for u_y (1) by substituting from Eq. 5.7-32 $(\partial\Theta/\partial\eta)_{\eta=1} = -(1 + \text{Br}/2)$ to obtain

$$u_y(1) = -\frac{\delta_0}{\delta} \left(1 + \frac{\text{Br}}{2}\right) \quad (5.7-34)$$

Finally, we turn to the equation of continuity and integrate it over η , after substituting $\partial u_x/\partial\eta = -1$ from Eq. 5.7-30 and noting that $\partial u_x/\partial\xi = 0$, to obtain

$$u_y(1) = -\frac{1}{2} \frac{\dot{\delta}}{\delta_0} \quad (5.7-35)$$

Combining Eqs. 5.7-34 and 5.7-35 subsequent to integration yields the film profile $\delta(\xi)$

$$\delta = \delta_0 \sqrt{(4 + 2\text{Br})\xi} \quad (5.7-36)$$

We have obtained the important result that, with convection neglected, the film thickness is proportional to the square root of the distance. The rate of melting (per unit width) is now given by

$$w_L(x) = \rho_m V_0 \delta \int_0^1 u_x d\eta = \frac{V_0 \delta}{2} \rho_m \quad (5.7-37)$$

By substituting Eq. 5.7-36 into 5.7-37 with $\xi = 1$ and δ_0 from Eq. 5.7-22, we obtain

$$\begin{aligned} w_L &= \left[V_0^2 \delta_0^2 \rho_m^2 \left(1 + \frac{\text{Br}}{2}\right) \right]^{1/2} = \left[\frac{V_0 \rho_m k_m (T_0 - T_m)}{\lambda^*} \left(1 + \frac{\text{Br}}{2}\right) W \right]^{1/2} \\ &= \left[\frac{V_0 \rho_m [k_m (T_0 - T_m) + \mu V_0^2 / 2] W}{\lambda^*} \right]^{1/2} \end{aligned} \quad (5.7-38)$$

The physical meaning of the various terms now becomes evident. The numerator in the square bracket in the last expression contains the sum of heat conduction and viscous dissipation terms. The denominator is the heat energy needed to heat the solid from T_{s0} to melt at T_m . The rate of melting also increases proportionally with the square root of the

plate velocity and slab width. Yet an increase in plate velocity also increases the viscous dissipation.

In this expression we have neglected convection in the film. Tadmor et al. (28) and Tadmor and Klein (29) made an approximate accounting for convection by replacing λ^* with an expression that includes the heat needed to bring the melt from T_m to the mean melt temperature

$$\lambda^{**} = \lambda + C_s(T_m - T_{s0}) + C_m(T_0 - T_m)\bar{\Theta} \quad (5.7-39)$$

Furthermore, by carrying out the mental exercise of “removing” the newly melted material from the interface, “carrying” it to $\xi = 0$, and allowing it to flow into the film at that point, the film thickness will stay constant and the resulting effect will be a reduction of w_L in Eq. 5.7-38 by a factor of $\sqrt{2}$.

Power Law Model Fluid with Temperature Dependent Viscosity

Both shear thinning and temperature dependence of viscosity strongly affect the melting rate. Their effect on the rate of melting can be estimated by considering a case in which convection is neglected and viscous dissipation is low enough to permit the assumption that the viscosity variation across the film is determined by a linear temperature profile:

$$\Theta = 1 - \eta \quad (5.7-40)$$

The equation of motion (Eq. 5.7-24) reduces to

$$\frac{\partial}{\partial \eta} \left[e^{b(1-\eta)} \left(-\frac{\partial u_x}{\partial \eta} \right)^n \right] = 0 \quad (5.7-41)$$

Equation 5.7-41 can be solved for the local velocity profile $u_x(\eta)$

$$u_x = \frac{e^{b'\eta} - e^{b'}}{1 - e^{b'}} \quad (5.7-42)$$

where

$$b' = \frac{b}{n} = -\frac{a(T_0 - T_m)}{n} \quad (5.7-43)$$

Clearly, b' is a dimensionless number that takes into account both the temperature and shear rate viscosity dependence.

The equation of energy (Eq. 5.7-26), reduces in this case to

$$\frac{\partial^2 \Theta}{\partial \eta^2} + \text{Br} \left(\frac{\delta_0}{\delta} \right)^{n-1} e^{b(1-\eta)} \left(-\frac{\partial u_x}{\partial \eta} \right)^{n+1} = 0 \quad (5.7-44)$$

Substituting Eq. 5.7-42 into Eq. 5.7-44, followed by integration, yields

$$\Theta = (1 - \eta) + \text{Br} \left(\frac{\delta_0}{\delta} \right)^{n-1} \left(\frac{b'}{1 - e^{-b'}} \right)^{n+1} \left(\frac{e^{-b'}}{b'^2} \right) \left[1 - e^{b'\eta} - \eta(1 - e^{b'}) \right] \quad (5.7-45)$$

As in the Newtonian case, we solve Eq. 5.7-21 for $u_y(1)$, after obtaining $(\partial\Theta/\partial\eta)_{\eta=1}$ from Eq. 5.7-45

$$u_y(1) = - \left(\frac{\delta_0}{\delta} \right) \left[1 + \text{Br} \left(\frac{\delta_0}{\delta} \right)^{n-1} \left(\frac{b'}{1 - e^{-b'}} \right)^{n+1} \left(\frac{b' - 1 + e^{-b'}}{b'^2} \right) \right] \quad (5.7-46)$$

Finally, the equation of continuity (Eq. 5.7-23), with $\partial u_x/\partial \xi = 0$ and subsequent to substituting $\partial u_x/\partial \eta$ from Eq. 5.7-42, results in

$$-\eta \left(\frac{\dot{\delta}}{\delta_0} \right) \left(\frac{b'e^{b'\eta}}{1 - e^{b'}} \right) + \frac{\partial u_y}{\partial \eta} = 0 \quad (5.7-47)$$

which is integrated to give

$$u_y(1) = \frac{\dot{\delta}}{\delta_0} \left[\frac{1}{b'(1 - e^{b'})} \right] \left[e^{b'}(b' - 1) + 1 \right] \quad (5.7-48)$$

Combining Eqs. 5.7-46 and 5.7-48 results in a differential equation for δ

$$\delta \frac{d\delta}{d\xi} = \frac{-\delta_0^2 \left[1 + \text{Br} \left(\frac{\delta_0}{\delta} \right)^{n-1} \left(\frac{b'}{1 - e^{-b'}} \right)^{n+1} \left(\frac{b' - 1 + e^{-b'}}{b'^2} \right) \right]}{\frac{e^{b'}(b' - 1) + 1}{b'(1 - e^{b'})}} \quad (5.7-49)$$

An approximate solution of Eq. 5.7-49 can be obtained if a mean δ value is assumed in the term $(\delta_0/\delta)^{n-1}$. This is a weak dependence of the viscous dissipation term on δ . The resulting melt film profile is

$$\delta = \delta_0 \left\{ \frac{4 \left[1 + \text{Br} \left(\frac{\delta_0}{\delta} \right)^{n-1} \left(\frac{b'}{1 - e^{-b'}} \right)^{n+1} \left(\frac{b' - 1 + e^{-b'}}{b'^2} \right) \right] \xi}{U_2} \right\}^{1/2} \quad (5.7-50)$$

where

$$U_2 = 2 \frac{1 - b' - e^{-b'}}{b'(e^{-b'} - 1)} \quad (5.7-51)$$

By substituting the expressions of δ_0 and Br from Eqs. 5.7-22 and 5.7-28, respectively, Eq. 5.7-50 can be written as

$$\delta = \left\{ \frac{2[2k_m(T_0 - T_m) + U_1]x}{U_2 \rho_m V_0 \lambda^*} \right\}^{1/2} \quad (5.7-52)$$

where

$$U_1 = \frac{2m_0 V_0^{n+1}}{(\delta)^{n-1}} \left(\frac{b'}{1 - e^{-b'}} \right)^{n+1} \left(\frac{b' - 1 + e^{-b'}}{b'^2} \right) \quad (5.7-53)$$

The rate of melting (per unit width) is given by

$$w_L(x) = \rho_m V_0 \delta \int_0^1 u_x d\eta = \frac{V_0 \delta \rho_m}{2} U_2 \quad (5.7-54)$$

And substituting δ from Eq. 5.7-52 into Eq. 5.7-54 gives

$$w_L(x) = \left\{ \frac{\rho_m V_0 U_2 [k_m(T_0 - T_m) + U_1/2]x}{\lambda^*} \right\}^{1/2} \quad (5.7-55)$$

Thus the physical significance of U_2 and U_1 becomes evident. The former reflects the reduction ($U_2 < 1$) of the rate of melt removal of the film by drag flow as a result of temperature dependence and shear thinning of the viscosity, whereas $U_1/2$ is the rate of viscous dissipation (per unit width) in the melt film. The relative significance of conduction and dissipation for melting is obtained by comparing the two terms in the square Brackets in Eq. 5.7-55.

If convection is to be accounted for by the same approximate method as described in the previous Newtonian case, then λ^* in Eq. 5.7-55 is replaced by λ^{**} , which is given in Eq. 5.7-39, and $w_L(x)$ given in Eq. 5.7-55 is reduced by a factor of $\sqrt{2}$. Finally, the mean temperature of the film

$$\bar{\Theta} \equiv \frac{\int_0^1 u_x \Theta d\eta}{\int_0^1 u_x d\eta} \quad (5.7-56)$$

is obtained by substituting Eqs. 5.7-40 and 5.7-42 into Eq. 5.7-56

$$\bar{\Theta} = \frac{b'/2 + e^{-b'}(1 + 1/b') - 1/b'}{b' + e^{-b'} - 1} \quad (5.7-57)$$

This is an approximate expression because, for the sake of simplicity, a linear temperature profile was used rather than Eq. 5.7-45. The preceding expressions were applied to the solution of the melting problem in screw extruders (28,29). This is discussed in Chapter 9.

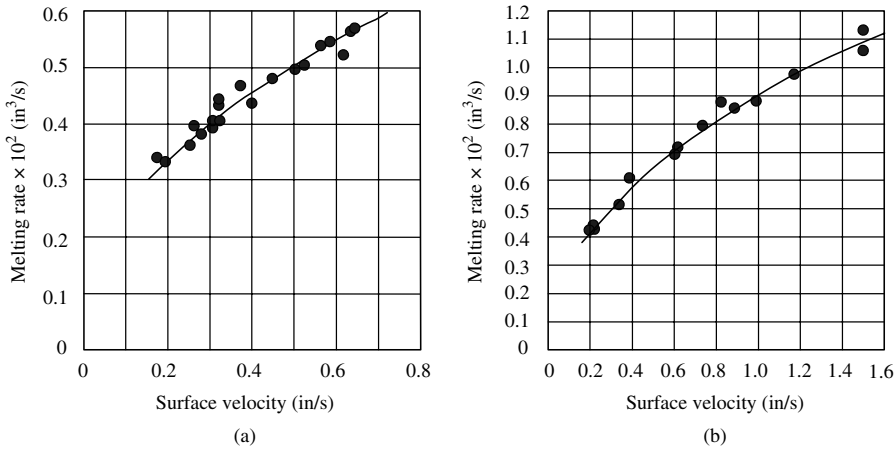


Fig. E5.6 Rate of melting of a 2×2 -in block of HDPE on a hot rotating drum. (a) Drum temperature at 154°C . (b) Drum temperature at 168°C . Rate of melting measured in volume of displaced solid. [Reprinted by permission from D. H. Sundstrom and C. Young, “Melting Rates of Crystalline Polymers under Shear Conditions,” *Polym. Eng. Sci.*, **12**, 59 (1972).]

Example 5.6 Drag-induced Melt Removal Melting The rate of melting of a 2×2 in. block of solid HDPE at room temperature of 25°C on a hot rotating drum was measured by Sundstrom and Young (33). Their results appear in Fig. E5.6. (a) Analyze the effects of drum speed and temperature in light of the previously derived theoretical models. (b) Calculate the rate of melting at a drum speed of 1 in/s on a 168°C drum, using a Newtonian model and compare it to the experimental value. (c) Repeat step (b) with a Power Law model with a linear temperature profile in the melt film.

The rheological properties of the HDPE used in the experiments follow a Power Law model (33)

$$\eta = 4.0334 \times 10^3 e^{-0.010872(T-127)} \dot{\gamma}^{-0.547}$$

where η is the non-Newtonian viscosity ($\text{N}\cdot\text{s}/\text{m}^2$), T is the temperature ($^\circ\text{C}$), and $\dot{\gamma}$ is the shear rate s^{-1} . The Power Law exponent is $n = 0.453$. The melting point (33) is 127°C . The heat of fusion is $218 \text{ kJ}/\text{kg}$. The specific heat of the solid polymer is $2.3 \text{ kJ}/\text{kg}\cdot^\circ\text{C}$, and that of the melt (28) is $2.512 \text{ kJ}/\text{kg}\cdot^\circ\text{C}$. The thermal conductivity of HDPE melt is a function of temperature (36)

$$k = 0.0573 + 0.0010467T$$

where k is in $\text{W}/\text{m}\cdot^\circ\text{C}$ and T is the temperature ($^\circ\text{C}$). Finally, the density of the solid polymer is $955 \text{ kg}/\text{m}^3$ and that of the melt (28) is $776 \text{ kg}/\text{m}^3$.

Solution

(a) The first step is to evaluate the relative significance of heat conduction and viscous dissipation. This is provided by the Brinkman number in Eq. 5.7-28, which for a Newtonian liquid, reduces to

$$\text{Br} = \frac{\mu V_0^2}{k_m(T_0 - T_m)}$$

An estimate of the melt viscosity can be obtained from the Power Law expression given earlier, assuming a shear rate of 50 s^{-1} and taking a mean temperature of $(168 + 127)/2 = 147.5^\circ\text{C}$. (We will check later whether these assumptions are acceptable.) This yields

$$\begin{aligned}\mu &= (4.0334 \times 10^3) e^{-0.010872(147.5-127)} (50)^{-0.547} \\ &= 379.8 \text{ N} \cdot \text{s/m}^2\end{aligned}$$

The tangential velocity of the drum selected is 1 in/s, or $V_0 = 0.0254 \text{ m/s}$, and the thermal conductivity at the mean temperature is $0.212 \text{ W/m}^\circ\text{C}$. Thus

$$\text{Br} = \frac{(379.8)(0.0254)^2}{(0.212)(168 - 127)} = 0.0282$$

Clearly, viscous dissipation is not significant in the experimental range given for the 168°C drum temperature experiments. Neither is it significant for the lower drum temperature experiments, which were conducted at lower drum speeds. It follows from the theoretical models (Eqs. 5.7-38 and 5.7-55) that the rate of melting in this case is proportional to the square root of drum speed and the temperature difference ($T_0 - T_m$)

$$w_L \propto \sqrt{V_0(T_0 - T_m)}$$

It is easy to verify that the curves in Fig. E5.6 follow quite well the predicted increase in rate of melting with drum speed. For example, the predicted rate of melting at 1.6 in/s from the corresponding value at 0.2 in/s is $0.4\sqrt{1.6/0.2} = 1.13 \text{ in}^3/\text{s}$, which is very close to the measured value. Similarly, selecting a fixed drum speed of 0.5 in/s, the measured rate of melting at 154°C is $0.5 \text{ in}^3/\text{s}$. The predicted value at 168°C is $0.5\sqrt{(168 - 127)/(154 - 127)} = 0.616 \text{ in}^3/\text{s}$, which once again is very close to the measured value.

(b) The rate of melting is evaluated from Eq. 5.7-38. First, however, the viscosity calculation is reexamined. This is done by calculating the film thickness from Eqs. 5.7-22 and 5.7-36. The former gives δ_0 with $W = 0.0508 \text{ m}$ and with λ^* calculated from Eq. 5.7-15

$$\lambda^* = 218 \times 10^3 + 2.3 \times 10^3(127 - 25) = 452.6 \times 10^3 \text{ J/kg}$$

Thus

$$\delta_0 = \left[\frac{(0.212)(168 - 127)(0.0508)}{(452.6 \times 10^3)(776)(0.0254)} \right]^{1/2} = 2.225 \times 10^{-4} \text{ m}$$

and the maximum film thickness at $\xi = 1$ from Eq. 5.7-36 is

$$\delta_{\max} = 2.225 \times 10^{-4} \sqrt{(4) + (2)(0.0282)} = 4.481 \times 10^{-4} \text{ m}$$

The mean film thickness is $3.353 \times 10^{-4} \text{ m}$, and the mean shear rate is $0.0254/3.353 \times 10^{-4} = 76 \text{ s}^{-1}$. The mean temperature is obtained from Eq. 5.7-33

$$\bar{\Theta} = \frac{2}{3} + \frac{0.0282}{12} = 0.669$$

Hence, $\bar{T} = 0.669(168 - 127) + 127 = 154.4$. Repeating the calculations with the viscosity evaluated at 76 s^{-1} and 154°C temperature, and with thermal conductivity of $0.218 \text{ W/m}\cdot^\circ\text{C}$, results in a viscosity of $281 \text{ N}\cdot\text{s/m}^2$, $\text{Br} = 0.0203$, $\delta_0 = 2.256 \times 10^{-4} \text{ m}$, a mean film thickness of $3.495 \times 10^{-4} \text{ m}$, a mean shear rate of 73 s^{-1} , and a mean temperature of 154°C .

Using these values, the rate of melting is calculated from Eq. 5.7-38

$$\begin{aligned} w_L &= \left[(0.0254)^2 (2.256 \times 10^{-4})^2 (776)^2 (1 + 0.0203/2) \right]^{1/2} \\ &= 4.469 \times 10^{-3} \text{ kg/m}\cdot\text{s} \end{aligned}$$

The rate of melting for the whole block is $(4.469 \times 10^{-3})(0.0508) = 2.27 \times 10^{-4} \text{ kg/s}$, which is equivalent to $0.0145 \text{ in}^3/\text{s}$ (note that the volume measured by Sundstrom and Young (33) is the displaced solid). Comparing this result with the measured value of $0.009 \text{ in}^3/\text{s}$ indicates that the Newtonian model overestimates the rate of melting by about 60%. In the model used, the effect of convection in the film was neglected. By accounting for convection as discussed earlier, the rate of melting is given by

$$\begin{aligned} w_L &= \left[\frac{V_0 \rho_m [k_m (T_0 - T_m) + \mu V_0^2 / 2] W}{2 [\lambda^* + C_m (T_0 - T_m) \Theta]} \right] \\ &= \left\{ \frac{(0.0154)(776) [(0.218)(168 - 127) + (281)(0.0254)^2 / 2] (0.0508)}{2 [(452.6 \times 10^3) + (2.512 \times 10^3)(168 - 127)(0.669)]} \right\}^{1/2} \\ &= 2.945 \times 10^{-3} \text{ Kg/m}\cdot\text{s} \end{aligned}$$

which results in a total rate of melting of $0.00956 \text{ in}^3/\text{s}$. This is only 6% above the measured value.

(c) To calculate the rate of melting from Eq. 5.7-55 we first calculate b' , U_1 , and U_2 as follows:

$$b' = - \frac{(0.010872)(168 - 127)}{(0.453)} = -0.984$$

From Eq. 5.7.51, U_2 is obtained

$$U_2 = (2) \frac{(-0.984) - (1) + e^{0.984}}{(-0.984)(1 - e^{0.984})} = 0.839$$

which indicates that the reduction in drag removal due to temperature dependence of viscosity is 16%. Finally, U_1 is obtained from Eq. 5.7-53 using the previously estimated mean film thickness

$$\begin{aligned} U_1 &= \frac{(2)(4.0334 \times 10^3)(0.0254)^{1.453}}{(3.495 \times 10^{-4})^{-0.547}} \left(\frac{0.984}{e^{0.984} - 1} \right)^{1.453} \left(\frac{(-0.984) - 1 + e^{0.984}}{(-0.984)^2} \right) \\ &= 0.1644 \text{ J/s}\cdot\text{m} \end{aligned}$$

Substituting these values into Eq. 5.7-55, with λ^* replaced by λ^{**} and a factor of 2 in the denominator to account for convection, and with Θ from Eq. 5.7-57, gives

$$\begin{aligned} w_L &= \left\{ \frac{(0.0254)(776)(0.839) [(0.218)(168 - 127) + (0.1644)/(2)] (0.0508)}{(2) [(452.6 \times 10^3) + (2.512 \times 10^3)(168 - 127)(0.695)]} \right\}^{1/2} \\ &= 2.6885 \times 10^{-3} \text{ kg/m}\cdot\text{s} \end{aligned}$$

which is equivalent to a total rate of melting of $0.00872 \text{ in}^3/\text{s}$, or only about 3% below the measured value.

The close agreement between the predictions and the measured rates of melting is to some degree fortuitous because all the thermophysical properties were selected from the literature rather than measured on the particular grade of HDPE used in the experiments. Thermophysical property data can vary for the same polymer over a relatively broad range. In addition, no doubt, experimental errors were also involved in the measured data, and one cannot expect perfect agreement. Nevertheless, it is reasonable to conclude that the *theoretical models* discussed in this section *predict correctly* the change in melting rate with changing experimental conditions, and that they provide *reasonable estimates* of the rate of melting.

Incorporating both the effect of convection in the film and the temperature dependence of the viscosity into the model improves the agreement between predictions and experimental measurements. It should be noted, however, that experimental conditions were such that viscous dissipation was insignificant and the temperature drop across the film was relatively small. Consequently, non-Newtonian effects, and effects due to the temperature dependence of viscosity, were less significant than were convection effects. This may not be the case in many practical situations, in particular with polymers, whose viscosity is more temperature sensitive than that of HDPE.

5.8 PRESSURE-INDUCED MELT REMOVAL

In the pressure-induced process, the melt is removed by the squeezing action of the solid on the melt; hence, the *force* by which the solids are pushed against the hot surface becomes the dominant rate-controlling variable. This melting process is less important in polymer processing than the drag removal process. Nevertheless, as Stammers and Beek (37) point out, in manufacturing certain synthetic fibers (e.g., polyester yarns) the polymer is melted on a melting grid; the melting process on such a melting grid is that of pressure removal of the melt. Stammers and Beek developed the following approximate theoretical model for the melting process.

Consider a polymer bar of radius R pressed by force F_N against a hot metal bar at constant temperature T_b of the same radius, as in Fig. 5.13. A film of melt is formed that is being squeezed out by radial flow.

The following simplifying assumptions are made:

1. The solid is rigid and moves with constant velocity toward the hot bar.
2. The film between the polymer and the hot bar has a constant thickness, δ .
3. Flow in the film is laminar.
4. The fluid is Newtonian.
5. Viscosity is temperature independent.
6. Thermophysical properties are constant.
7. Steady state.
8. Gravitational forces are negligible.
9. Convection and viscous dissipation on the film are negligible.

Some of these assumptions may be questionable, for example, the assumptions that the solid is rigid and the film thickness constant. In reality, as the preceding section

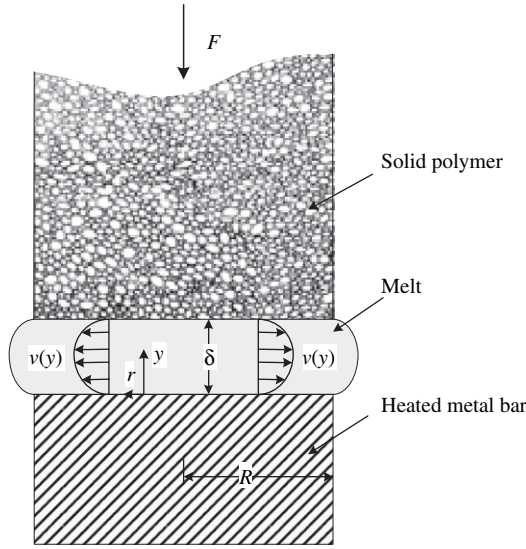


Fig. 5.13 Schematic representation of a solid polymer melting on a hot metal bar.

demonstrated, allowing the solid to deform and using an a priori unknown $\delta(r)$ would be more plausible. Nevertheless the foregoing assumptions do allow the “construction” of a simple model for the process, providing insight into its nature. Moreover, the model did show reasonably good agreement with experiments carried out with polyethylene and polyoxymethylene.

With the rigid polymer assumption, the total rate of melting can immediately be written as

$$w_T = \pi(-v_{sy})\rho_s R^2 \tag{5.8-1}$$

where $v_{sy} < 0$ is the velocity of the solid polymer. Our objective is to find a relationship between the velocity v_{sy} , the operating conditions (the pushing force F_N , the hot plate, and solid temperatures), and the polymer physical properties.

By pressing the bar against the plate, a radial velocity profile will be induced in the melt film, thus removing the newly melted polymer from the location of melting, and draining it. The mean radial velocity at any location r , v_r can be expressed in terms of (the yet unknown) velocity v_{sy} by a simple mass balance

$$\rho_s \pi r^2 (-v_{sy}) = 2\pi r \delta \bar{v}_r \rho_m \tag{5.8-2}$$

where δ is the local separation between the interface and plate. Thus from Eq. 5.8-2 the mean radial velocity with $\beta = \rho_s/\rho_m$ is

$$\bar{v}_r = \frac{r(-v_{sy})\beta}{2\delta} = \frac{1}{\delta} \int_0^\delta v_r dy \tag{5.8-3}$$

The radial component of the equation of motion reduces to

$$\frac{dP}{dr} = \mu \frac{d^2 v_r}{dy^2} \quad (5.8-4)$$

We have substituted ordinary differentials for the partial differentials in the equation of motion because the left-hand side is only a function of r , whereas we assume the right-hand side is only a function of y (lubrication approximation). Therefore, they simply equal a constant. Equation 5.8-4 can now be integrated over y , with boundary conditions $v_r(0) = 0$ and $v_r(\delta) = 0$, to give

$$v_r = \frac{1}{2\mu} \frac{dP}{dr} (y - \delta)y \quad (5.8-5)$$

An expression for the pressure gradient dP/dr versus r can be obtained by substituting Eq. 5.8-5 into Eq. 5.8-3

$$-\left(\frac{dP}{dr}\right) = \frac{6\mu(-v_{sy})r\beta}{\delta^3} \quad (5.8-6)$$

Integration of Eq. 5.8-6 with the boundary condition $P(R) = P_0$, where P_0 can be the atmospheric pressure, leads to the following pressure profile:

$$P(r) - P_0 = \frac{3\mu(-v_{sy})\beta}{\delta^3} (R^2 - r^2) \quad (5.8-7)$$

The total force F_N can be calculated from the pressure profile:

$$F_N = \int_0^R 2\pi r P(r) dr = \pi R^2 P_0 + \left(\frac{3\mu\pi(-v_{sy})R^4\beta}{2\delta^3} \right) \quad (5.8-8)$$

Equation 5.8-8 is, in effect, the relationship we are looking for, and by rearranging it we get a relationship of the velocity v_{sy} in terms of the external total force F_N and a number of other variables

$$(-v_{sy}) = \frac{2\delta^3(F_N - \pi P_0 R^2)}{3\pi\mu R^4\beta} \quad (5.8-9)$$

We cannot, however, calculate the melting rate of this geometrical configuration from Eq. 5.8-9 because we do not yet know the value of δ . This value is determined by the rate of heat conducted into the solid–melt interface. If we make use of one more of the simplifying assumptions just given, namely, that viscous dissipation is negligible, the following simple heat balance can be made on the interface (see Eq. 5.7-14)

$$k_m \left(\frac{T_b - T_m}{\delta} \right) = \rho_s (-v_{sy}) [\lambda + C_s (T_m - T_b)] \quad (5.8-10)$$

where T_0 is the initial temperature of the solid. Substituting Eq. 5.8-9 into Eq. 5.8-10 results in the final expression, which is the process-design equation

$$(-v_{\text{sy}}) = \frac{0.6787}{R} \left(\frac{F_N - \pi P_0 R^2}{\mu \beta} \right)^{1/4} \left[\frac{k_m (T_b - T_m)}{\rho_s [\lambda + C_s (T_m - T_0)]} \right]^{3/4} \quad (5.8-11)$$

The melting capacity of this geometrical configuration can easily be calculated from Eqs. 5.8-11 and 5.8-1.

The results are very revealing and instructive. The rate of melting increases with the total force F_N , but only to the one fourth power. The physical explanation for this is that with increasing force, the film thickness is reduced, thus increasing the rate of melting. However, the thinner the film, the larger the pressure drops that are needed to squeeze out the melt. The dependence on the plate temperature is almost linear. The inverse proportionality with R is perhaps the most important result from a design point of view. If viscous dissipation were included, some of these results would have to be modified.

Stammers and Beek (37) have performed a number of experiments to verify the theoretical model just described, using polyethylene and polyoxymethylene. The linear relationship between $v_{\text{sy}}/(F_N)^{1/4}$ and $[(T_b - T_m)^{3/4}/\mu^{1/4}]$, as predicted by Eq. 5.8-11, was clearly established, and the slope calculated from this equation agreed well with the experimental data.

5.9 DEFORMATION MELTING

It is evident from the foregoing discussion that considerable effort has been invested in elucidating the mechanism of conduction melting, and in particular that of conduction melting with forced drag flow melt removal, the latter because it is the operative melting mechanism in single-rotor processing equipment such as SSEs and injection-molding machines. We will discuss in detail the utilization of this melting mechanism in the modeling of single-rotor melting in Chapter 9, a task that proves to be rather straightforward, due to the ordered segregation of the two polymer phases involved: the flowing molten polymer, and the "passive," gradually melting, compacted particulate "bed."

On the other hand, we discussed and presented in physical terms the very powerful melting mechanisms resulting from repeated, large deformations, forced on compacted particulate assemblies by twin co- or counterrotating devices. These mechanisms, which we refer to in Section 5.1, are *frictional energy dissipation* (FED), *plastic energy dissipation* (PED), and *dissipative mix-melting* (DMM).

At the time of the writing of the first edition of this text (38), we wrote the following about mechanical energy dissipation in repeatedly deforming "active" compacted particulates and the evolution of their melting:

... the dominant source of energy for melting (in twin rotor devices) is mechanical energy introduced through the shafts of the rotors and converted into thermal energy by continuous gross deformation of the particulate charge of polymer... by a number of mechanisms: individual particle deformations [now known as PED (3)], inter-particle friction [now known as

FED (3)] and viscous dissipation in the molten regions. As melting progresses the latter mechanism becomes dominant. Mixing disperses the newly formed melt into the mass [creating a solids-rich suspension]; the melt that comes in intimate contact with solid particles cools down and at the same time heats up the surface layer of the particles; the particulate solid charge is eventually converted into a richer, thermally inhomogeneous suspension and ultimately into a homogeneous one. . . . Nevertheless, the advantages of this melting method dictate that more theoretical [and experimental] analysis be devoted to it in the near future.

Indeed, over the last decade, the area of melting of active compacted particulate assemblies in twin-rotor equipment has received a good deal of experimental attention. This body of experimental work utilizes both glass windows on sections of the barrel for on-line observations (39–43) and, more often, extracted solidified “carcasses” of the processed stream, which are sectioned along the downstream direction in the melting region (3,44–50). This body of work has confirmed the existence, and elucidated the natures of PED, FED, and DMM and, most importantly, has confirmed the evolution of melting in twin-rotor devices mentioned earlier. Such evolution, based on extensive “carcass” analyses for both polypropylene (PP) pellets and powder feeds in Co-TSEs, is shown in Fig. 5.14 (3,51).

As seen in the figure, the successive downstream states of the PP pellets as they are conveyed, consolidated, and melted, result from PED, VED, and DMM taking place throughout the volume of the processed stream. The small size of the 30-mm-diameter

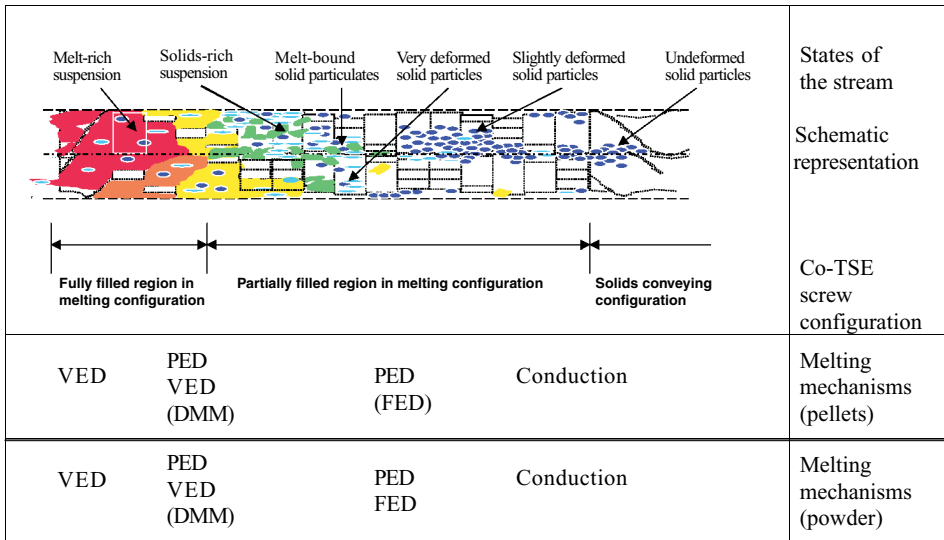


Fig. 5.14 Schematic representation of the evolution of melting of polypropylene (PP) pellets in a 30-mm-diameter co-TSE. The figure represents rendition of the analyses of many experimental carcasses. Shown are: the physical states of the pellets stream being melted; a schematic of the carcass “morphology”; the screw conveying/kneading element sequence; and the melting mechanisms responsible for affecting melting of the pellets stream. Shown in the bottom row are the melting mechanisms responsible for advancing melting of a polypropylene powder feed. [Reprinted by permission from M. H. Kim, Ph.D Dissertation Department of Chemical Engineering, Stevens Institute of Technology, Hoboken, NJ., (1999).]

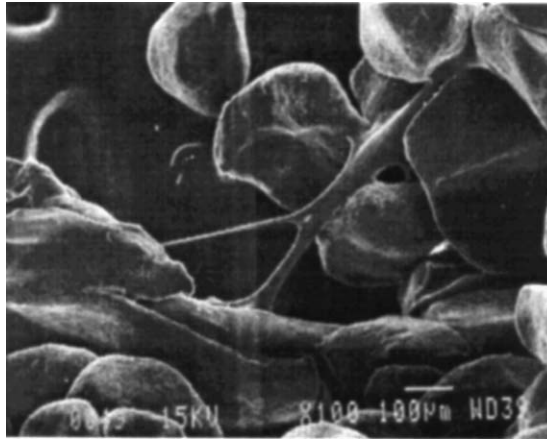


Fig. 5.15 Evidence of melting of fine particulates of PP powder melted in a 30-mm Co-TSE, taking place in the partially filled kneading section. Such molten fines are capable of creating, as glue points, particulate clusters. [Reprinted by permission from M. Esseghir, D. W. Yu, C. G. Gogos, and D. B. Todd, *SPE ANTEC Tech Papers*, **43**, 3684 (1997).]

split-barrel extruder with a maximum channel depth of 4 mm causes pellets to be deformed, that is, undergo PED, even in partially filled sections upstream of the consolidated particulates melting zone.

Carcasses of PP powder feed (not shown in Fig. 5.14) do show clear evidence of the melting of single particulates by FED, becoming local “glue points” and creating clusters of powder particulates, as shown in Fig. 5.15. Further evidence of FED was provided by Shih et al. (39) working with a glass end-plate Brabender Plasticorder melting powder charges. Gogos et al. (51) investigated the melting behavior of three PP powder systems using Shih’s experimental device. The three powder systems differed in concentration of fine particulates. The fines-rich system exhibited very early and fast evidence of cluster formation: the power generated by neighboring particulates moving at different speeds (Δv) while under a normal force F_N is

$$p_w = fF_N \Delta v \quad (5.9-1)$$

where f is the interparticle coefficient of friction. Small particulates wedged between larger ones in the “nip” compressing region between the rotors will melt first by FED, because of their large surface-to-volume ratio.

We now turn our attention to PED. As mentioned earlier, individual pellets become grossly deformed while in compacted assemblies, for example, in kneading sections of the Co-TSE. These volumewise particulate deformations make the particulate assemblies active participants in the process of melting through the mechanism of PED. Two questions must be addressed: (a) how powerful a heat source term is PED? and (b) how can the complex reality of compacted particulate assemblies undergoing large and repeated deformations be described and simulated mathematically?

We know from our discussion of deforming particulate “beds” in Chapter 4 that the answer to the second question, that is, the quantification of PED in deforming assemblies,

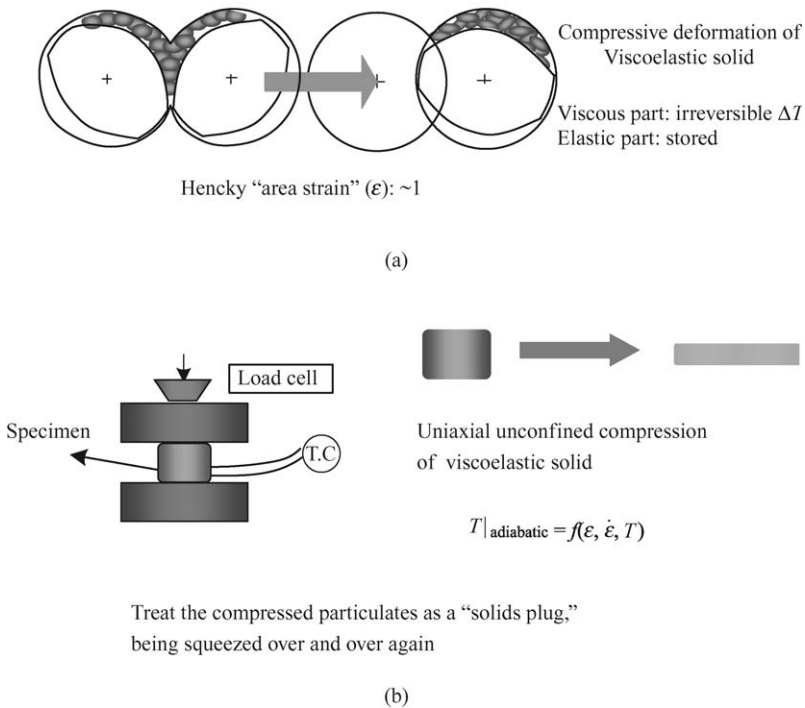


Fig. 5.16 Schematic representation of (a) a compacted pellet assembly undergoing kneading (squeezing) deformations as the pair of kneading paddles co-rotates, reducing the available volume, forcing them to move into connecting spaces of neighboring down- and upstream kneading element pairs; (b) a single molded disk undergoing unconfined compressive deformation, used by Gogos et. al. (3) to represent the "complex" physical reality shown in (a) and estimate the resulting actual PED. [Reprinted by permission from M. H. Kim, Ph.D Dissertation, Department of Chemical Engineering, Stevens Institute of Technology, Hoboken, NJ, (1999).]

is not available to date because of the complexity of the physical phenomena involved. For this reason, Kim (52) and Gogos et al. (3) decided to probe and elucidate the physical nature and magnitude of PED by measuring or estimating the adiabatic temperature rise in single molded-polymer disks undergoing rapid, unconfined compressive deformations. The complexity of deforming particulate assemblies by kneading Co-TSE elements are shown side by side with the simplicity of the experiments conducted by Kim and Gogos in Fig. 5.16 (52).

Typical results obtained during unconfined compressive deformation experiments using direct thermocouple measurements—a difficult experimental task—are shown in Fig. 5.17. A number of the results are important: the magnitude of the increases in the observed specimen temperature is significant; temperature increases are negligible in the initial elastic deformation region, as expected; and the magnitude of the measured "adiabatic" temperature rise ΔT_a increases with the strength of the polymer because of the higher deformation stresses. Thus, for strong amorphous polymers below T_g , such as PS, the observed ΔT_a values are almost one order of magnitude larger than those obtained with semicrystalline polymers at temperatures between T_g and T_m . It was found experimentally that the measured ΔT_a values can be closely approximated by relating the

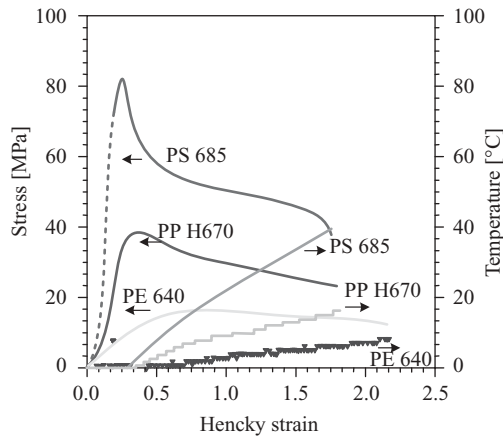


Fig. 5.17 Unconfined compression stress–strain curves and experimentally measured temperature increase ΔT_a as a function of strain for PS (Dow 685), LDPE (Dow 640), and PP (LG H670). The initial test specimen was at 26°C and the crosshead speed of the compressing bar with the load cell was 25.4 mm/min. The specimen dimensions were: 101 mm diameter and 71 mm height. [Reprinted by permission from M. H. Kim, Ph.D Thesis, Department of Chemical Engineering, Stevens Institute of Technology, Hoboken, NJ (1999).]

“area” under the stress–strain curve with the adiabatic specific enthalpy increase during compression

$$\text{PED} = \int_{\varepsilon_e}^{\varepsilon} \sigma d\varepsilon = \rho C_p \Delta T_a \quad (5.9-2)$$

or

$$\Delta T_a = \frac{\int_{\varepsilon_e}^{\varepsilon} \sigma d\varepsilon}{\rho C_p} \quad (5.9-3)$$

Note that, since the stress–strain curves are dependent on the applied strain rate and the specimen temperature, both PED and ΔT_a are functions of the strain, strain rate, and temperature.

Kim (52) conducted a large number of compressive deformation experiments using specimens at increasingly higher initial temperatures at the highest experimental strain rate available to the universal testing machine used. With these data he constructed iso-PED curves in the Hencky strain–initial specimen temperature space, shown in Fig. 5.18(a). Excellent estimates of the PED generated on PS disks of any initial temperature above room temperature undergoing deformation to any strain $\varepsilon < 1.6$ at 25.4 cm/s can thus be obtained. Furthermore, using Eq. 5.9-2 the iso-PED results can be transformed to the so ΔT_a curves shown in Fig. 5.18(b). Using this figure, one can get a good estimate of how much the initial temperature of a PS will increase after successive $\varepsilon_{\text{Hencky}} = 1$ deformations, as indicated in Fig. 5.19.

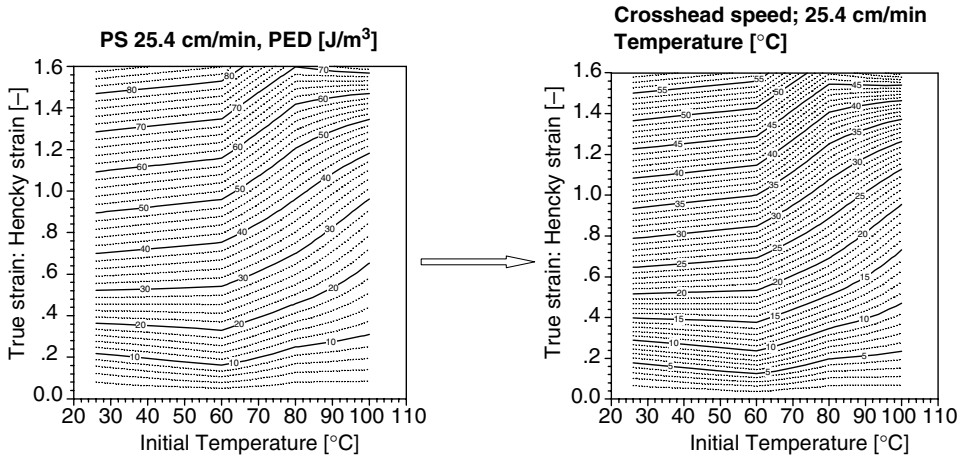


Fig. 5.18 (a) Iso-PED (J/m^2) curves obtained from unconfined compressive deformation experiments of Dow PS 685 cylindrical specimens compressed at 25.4 cm/min. Many experiments were conducted for a number of initial specimen temperatures (T_i) and with a number of applied strains at each T_i . (b) iso ΔT_a ($^{\circ}C$) for PS 685 derived from curves in part (a) employing the relation $\Delta T|_{\epsilon_0, T_i} = PED/\rho\bar{C}_p$. [Reprinted by permission from M. H. Kim, Ph.D. Thesis, Department of Chemical Engineering, Stevens Institute of Technology, Hoboken, NJ (1999).]

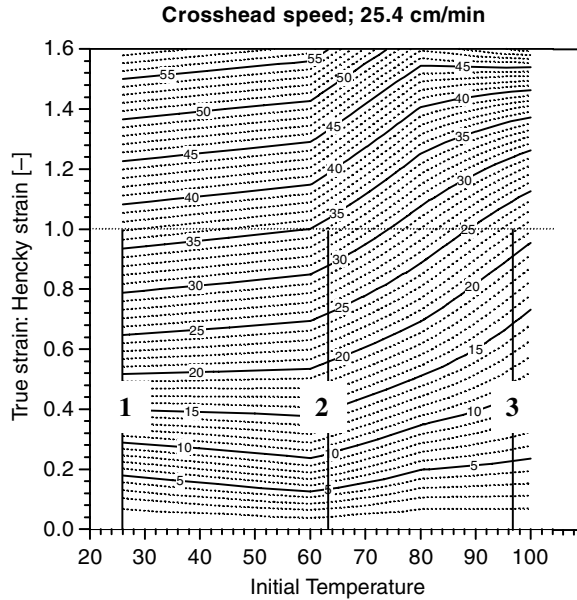


Fig. 5.19 The effect of consecutive unconfined compressive deformations on the temperature increase of a PS cylinder initially at 26 $^{\circ}C$. The first $\epsilon = 1$ deformation increases for sample temperature by 37 $^{\circ}C$; the second starting from 26 + 37 = 63 $^{\circ}C$, increases it to 97 $^{\circ}C$, close to T_g . [Reprinted by permission from M.H. Kim, Ph.D. Thesis, Department of Chemical Engineering, Stevens Institute of Technology, Hoboken, NJ (1999).]

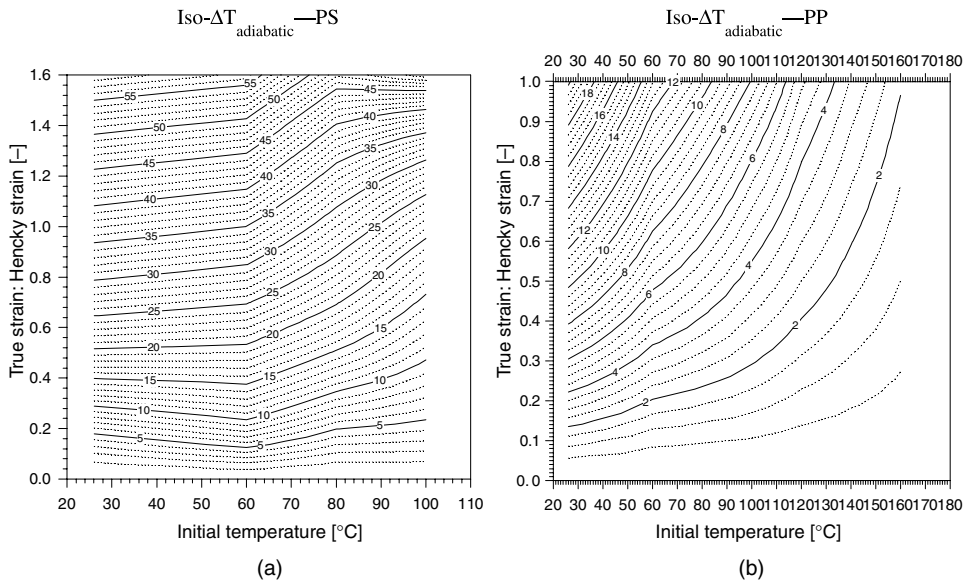


Fig. 5.20 The PED for PP is apparently smaller in magnitude than that for PS; it is also more temperature dependent, decreasing with increasing initial temperature. Semicrystalline plastics are weaker and their amorphous phase in the region $T > T_g$ becomes more mobile, rapidly lowering the needed deformation stresses. [Reprinted by permission from M.H. Kim, Ph.D. Thesis, Department of Chemical Engineering, Stevens Institute of Technology, Hoboken, NJ (1999).]

After the first $\varepsilon = 1$ deformation, the initial sample temperature (26°C) will increase by 37°C to $(26^\circ + 37^\circ) = 63^\circ\text{C}$. After the second deformation, the new sample temperature will be $63^\circ + 34^\circ = 97^\circ\text{C}$. It is striking that only two successive compressive $\varepsilon = 1$ deformations are capable of raising the PS sample temperature very close to T_g . The conclusion from such experimental findings, which we will discuss further in connection with twin rotor devices in Chapter 10, is that PED is a very powerful melting mechanism for PS.

Similar experiments were conducted to evaluate the magnitude of PED in semicrystalline polymers in the region $T_{room} < T < T_m$. Iso-PED and iso- ΔT_a curves for Dow LDPE 640 are shown in Fig. 5.20(a) and 5.20(b). These curves show dramatic differences when compared to those for PS: not only the *magnitude* of the PED and, consequently, the ΔT_a values are *smaller*, for example, for PS at an initial temperature of 26°C after $\varepsilon = 1$, $\Delta T_a = 37^\circ\text{C}$, while for LDPE it is only 10°C , but the *temperature sensitivity* of PED is much stronger for LDPE, so much so that at an initial temperature of 80°C for PS, it is 27°C , while for LDPE, it is only 4°C .

The physical origin for this difference is indicated in Fig. 5.21: amorphous polymers below T_g exhibit a constant modulus, since they are single-phase, rigid-chain structures, while semicrystalline, two-phase structures in the range $T_g < T < T_m$ become weaker with increasing temperature, due to the increased mobility of the amorphous chains.

The theoretical models that have been proposed to quantify and simulate the melting phenomena taking place in “active” compacted particulates are still rudimentary, not for lack of effort and interest, but because of the physical complexities involved, as noted

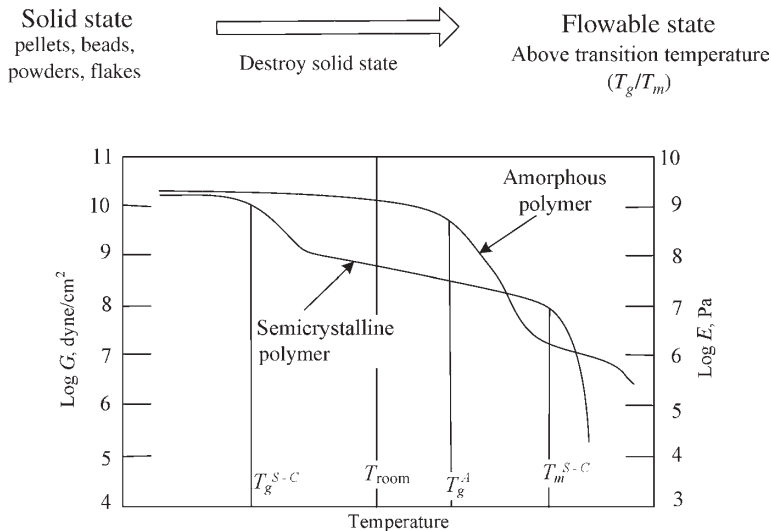


Fig. 5.21 Polymer feed temperatures are at or near T_{room} . For common amorphous plastics, $T_{\text{room}} < T_g$, and for semicrystalline $T_g < T_{\text{room}} < T_m$. As discussed in the text, PED, through large solid-state irreversible deformations, makes the solid an “active participant” in the melting process, rapidly creating a molten state. The modulus of amorphous polymer is higher and less temperature dependent in the region $T > T_{\text{room}}$. Consequently, the magnitude of amorphous PED is larger and less temperature dependent when compared to semicrystalline PED.

earlier. Vergnes et al. (53) concur with the foregoing analysis and suggest that “Gogos et al. (3) showed the important roles of pellets plastic deformation and interparticle friction, which modify (i.e., should be included in) the thermal energy balance.” These phenomena, they continue, “should probably be taken into account in heat generation for melting. However, it remains difficult to quantify properly these terms, and the lack of physical data makes it difficult to introduce them in a model.”

Potente and Melish (49), Vergnes et al. (53), Bawiskar and White (54), and Zhu et al. (55) have proposed simulation models to describe melting in the Co-TSEs. These models are all based on the assumption that melting occurs mainly by VED during the flow of suspensions of solid polymer particulates in melts, with the evolution of melting involving the decrease in the size of the particulates. In Chapter 10 we will review the model of Vergnes et al., the PED-based model of Gogos et al. (56) and Kim and Gogos (57), and one by Jung and White (58). The latter two consider the PED contributions to melting in full Co-TSE kneading elements.

REFERENCES

1. T. K. Ross, “Heat Transfer to Fusible Solids,” *Chem. Eng. Sci.*, **1**, 212–215 (1952).
2. G. Menges and W. Elbe, “Untersuchungen des Einzugsand Plastifizierhaltens von Schnecken-spritzgiessmaschinen,” Beitrag zum 5. Kunststofftechnischen Kolloquium des Institut für Kunststoffverarbeitung, Aachen, Germany, 1970.
3. C. G. Gogos, Z. Tadmor, and M. H. Kim, “Melting Phenomena and Mechanisms in Polymer Processing Equipment,” *Adv. Polym. Technol.*, **17**, 285–305 (1998).

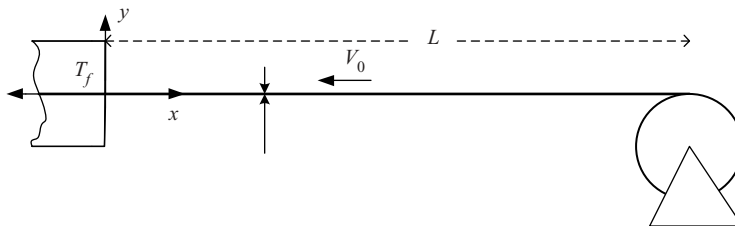
4. L. Erwin and N. P. Suh, "A Method for the Rapid Processing of Thermoplastic Articles," *Polym. Eng. Sci.*, **16**, 841–846 (1976).
5. E. R. G. Eckert and R. M. Drake, Jr., *Analysis of Heat Transfer*, McGraw-Hill, New York, 1972: (a) p. 219; (b) p. 157; (c) p. 12.
6. T. R. Goodman, "Application of Integral Methods for Transient Nonlinear Heat Transfer," in *Advances in Heat Transfer*, Vol. I, T. F. Irvine, Jr., and J. P. Hartnett, Eds., Academic Press, New York, 1964, pp. 51–122.
7. S. G. Bankoff, "Heat Conduction or Diffusion with Change in Phase," in *Advances in Chemical Engineering*, Academic Press, New York, 1964, pp. 75–100.
8. L. I. Rubinstein, "The Stefan Problem," in *Translation of Mathematical Monographs*, Vol. 27, American Mathematical Society, Providence, RI, p. 5, 1971.
9. S. W. Churchill and L. B. Evans, "Coefficients for Calculation of Freezing in a Semi-infinite Region," *Trans. Am. Soc. Mech. Eng., J. Heat Transfer*, **93**, 234–236 (1971).
10. H. S. Carslaw and J. C. Jaeger, *Conduction of Heat in Solids*, Second Edition, Oxford University Press, New York, 1959.
11. W. M. Rosenhow and J. P. Hartnett, *Handbook of Heat Transfer*, McGraw-Hill, New York, 1973.
12. J. Eisenberg and G. deVahl Davis, "FDM Methods in Heat Transfer," in *Topics in Transport Phenomena*, C. Gutfinger, Ed., Wiley, New York, 1975.
13. G. E. Myers, *Analytical Methods in Conduction Heat Transfer*, McGraw-Hill, New York, 1971, Chapter 8.
14. A. M. Clausing, "Numerical Methods in Heat Transfer," in *Advanced Heat Transfer*, B. T. Chao, Ed., University of Illinois Press, Urbana, 1969, pp. 157–216.
15. G. M. Dusinberre, *Heat Transfer Calculations by Finite Differences*, Second Edition, International Textbook, Scranton, PA., 1961.
16. J. Crank and P. Nicolson, "A Practical Method for Numerical Evaluation of Solutions of Partial Differential Equations of the Heat-conducting Type," *Proc. Cambridge. Philos. Soc.*, **43**, 50–67 (1947).
17. D. Rosenthal, "A Theory of Moving Sources of Heat and its Application to Metal Treatment," *Trans. Am. Soc. Mech. Eng.*, **68**, 849–866 (1946).
18. G. C. Kuczynski, B. Neuville, and H. P. Toner, "Study of Sintering of Poly(Methyl Methacrylate)," *J. Appl. Polym. Sci.*, **14**, 2069–2077 (1970).
19. M. A. Rao and J. L. Throne, "Principles of Rotational Molding," *Polym. Eng. Sci.*, **12**, 237–250 (1972).
20. J. L. Throne, "Rotational Molding Heat Transfer – an Update," *Polym. Eng. Sci.*, **16**, 257–264 (1976).
21. J. F. Lonz, "Sintering of Polymer Materials," in *Fundamental Phenomena in the Material Sciences*, Vol. 1, *Sintering and Plastic Deformation*, L. J. Bonis and H. H. Hausner, Eds., Plenum Press, New York, 1964.
22. D. M. Bigg, "High Pressure Molding of Polymeric Powders," Proc. of the Society of Plastics Engineers 33rd Annu. Tech. Conf., Atlanta, May 1975, pp. 472–476.
23. G. S. Jayaraman, J. F. Wallace, P. H. Geil, and E. Baer, "Cold Compaction Molding and Sintering of Polystyrene," *Polym. Eng. Sci.*, **16**, 529–536 (1976).
24. J. Frenkel, *J. Phys. (U.S.S.R)*, **9**, 385 (1945).
25. J. D. Eshelby, *Trans. Am. Inst. Mech. Eng.*, **185**, 806 (1949).
26. D. H. Sundstrom and J. R. Lo, "Softening Rates for Polystyrene under Shear Conditions," *Polym. Eng. Sci.*, **18**, 422 (1978).

27. Z. Tadmor, "Fundamentals of Plasticating Extrusion. I. A Theoretical Model for Melting," *Polym. Eng. Sci.*, **6**, 185–190 (1966). First presented at the Society of Plastics Engineers Annual Technical Conference, Montreal Canada, April 1966.
28. Z. Tadmor, I. J. Duvdevani, and I. Klein, "Melting in Plasticating Extruders Theory and Experiments," *Polym. Eng. Sci.*, **7**, 198–217 (1967).
29. Z. Tadmor and I. Klein, *Engineering Principles of Plasticating Screw Extrusion*, Van Nostrand Reinhold, New York, 1970.
30. Z. Tadmor and I. Klein, "Melting in Plasticating Extruders" in I. Klein and D. I. Marshall, Eds., *Computer Programs for Plastics Engineers*, Reinhold, New York, 1968, Chapter 6.
31. Z. Tadmor, "Machine Invention, Innovation, and Elementary Steps," *Adv. Polym. Technol.*, **21**, 87–97 (2002).
32. J. R. Vermeulen, P. M. Gerson, and W. J. Beek, "The Melting of a Bed of Polymer Granules on a Hot Moving Surface," *Chem. Eng. Sci.*, **26**, 1455 (1971).
33. D. H. Sundstrom and Chi-Chang Young, "Melting Rates of Crystalline Polymers under Shear Conditions," *Polym. Eng. Sci.*, **12**, 59–63 (1972).
34. E. M. Mount, III, "The Melting of High Density Polyethylene on a Heated, Moving Metal Surface—A Comparison of Experimental and Theoretical Results," M.S. thesis, Rensselaer Polytechnic Institute, Troy, NY, (1976).
35. J. R. A. Pearson, "On the Melting of Solids near a Hot Moving Interface, With Particular Reference to Beds of Granular Polymers," *Int. J. Heat Mass Transfer*, **19**, 405–411 (1976).
36. T. R. Fuller and A. L. Fricke, "Thermal Conductivity of Polymer Melts," *J. Appl. Polym. Sci.*, **15**, 1729–1736 (1971).
37. E. Stammers and W. J. Beek, "The Melting of a Polymer on a Hot Surface," *Polym. Eng. Sci.*, **9**, 49–55 (1969).
38. Z. Tadmor and C. G. Gogos, *Principle of Polymer Processing*, Wiley, New York, 1979, Chapter 9.
39. C. K. Shih, D. G. Tynan, and D. A. Denelsbek, "Rheological Properties of Multicomponent Polymer Systems Undergoing Melting or Softening during Compounding," *Polym. Eng. Sci.*, **31**, 1670 (1991).
40. N. Hashimoto, J. Kakizaki, *JPS Tech. Rev.*, **16**, 48 (1994).
41. T. Sakai, "The Development of On-line Techniques and Novel Processing Systems for the Monitoring and Handling of the Evolution of Microstructure in Nonreactive and Reactive Polymer Systems," *Adv. Polym. Technol.*, **14**, 277 (1995).
42. A. C. Y. Wong, F. Zhu, and T. Liu, "Qualitative Study on Intermeshing Co-rotating Twin Screw Extrusion Using Novel Visual Technique," *Plast. Rubber Comps. Proc. Appl.*, **26**, 271 (1997).
43. L. Zhu and X. Geng, "Visual Research of Melting Mechanism of Polymer Pellets in Intermeshing Co-rotating Twin-screw Extrusion," *SPE ANTEC Tech. Papers*, **55**, 3684 (1997).
44. D. B. Todd, "Melting of Plastics in Kneading Blocks," *Int. Polym. Proc.* **8**, 113 (1993).
45. J. Curry, "Melting Mechanisms in ZSK Extruders," *SPE ANTEC Tech. Papers*, **41**, 92 (1995).
46. H. T. Chan and D. A. DuFresne, "Kneading Block Melting Study," *SPE ANTEC Tech. Papers*, **53**, 302 (1995).
47. F. Busby, T. W. McCullough, K. R. Hugues, and R. O. Kirk, "Melting of Homopolymers in Co-rotating, Intermeshing Twin-screw Extruders," *SPE ANTEC Tech. Papers*, **54**, 3571 (1996).
48. M. Esseghir, D. W. Yu, C. G. Gogos, and D. B. Todd, "Melting Mechanisms of Single-component Polymers in Co-rotating Twin-Screw Kneading Blocks Through Visual and Microscopic Analysis," *SPE ANTEC Tech. Papers*, **43**, 3684 (1997).

49. H. Potente and U. Melish, "Theoretical and Experimental Investigations of the Melting of Pellets in Co-rotating Twin-screw Extruders," *Int. Polym. Proc.*, **11**, 101 (1996).
50. S. Bawiskar and J. L. White, "A Composite Model for Solid Conveying, Melting, Pressure and Fill Factor Profiles in Modular Co-rotating Twin Screw Extruders," *Int. Polym. Proc.*, **12**, 1331 (1997).
51. C. G. Gogos, M. Esseghir, D. W. Yu, D. B. Todd and J. Curry, "The Twin-screw Mixing Element Evaluator: On-line Performance Evaluation of Modular Twin-screw Mixing Elements," *SPE ANTEC Tech. Papers*, **40**, 270 (1994).
52. M. H. Kim, Ph.D. Dissertation, Department of Chemical Engineering, Stevens Institute of Technology, Hoboken, NJ, (1999).
53. B. Vergnes, G. Souveton, M. L. Delacour, and A. Ainsler, "Experimental and Theoretical Study of Polymer Melting in a Co-rotating Twin Screw Extruder," *Int. Polym. Process.*, **16**, 351–362 (2001).
54. S. Bawiskar and J. L. White, "Melting Model for Modular Self Wiping Co-rotating Twin Screw Extruders," *Polym. Eng. Sci.*, **38**, 727 (1998).
55. L. Zhu, K. A. Narh, and X. Geng, "Modeling of Particle-dispersed Melting Mechanism and its Application in Corotating Twin-screw Extrusion," Paper presented at the 17th Polymer Processing Society Meeting, Montreal, Canada (2001).
56. G. Gogos, B. Qian, D. B. Todd, and M. H. Kim, "A Predictive Melting Model for Polymer Particulates in Co-TSE's," *SPE ANTEC Tech. Papers*, **47**, 134 (2001).
57. M. H. Kim and C. G. Gogos, "Melting Phenomena and Mechanisms in Co-TSEs," *SPE ANTEC Tech. Papers*, **47**, 145 (2001).
58. H. Jung and J. L. White, "Investigations of melting Phenomena in Modular Co-rotating Twin Screw Extrusion," *Int. Polym. Process.*, **18**, 127 (2003).

PROBLEMS

5.1 Feeding a Metal Strip into a Hot Oven A thin metal strip of thickness δ and width W is fed at a constant speed V_0 into a hot furnace at temperature T_f , as shown in the figure. Find the minimum distance L where the feeding roll can be placed, such that the strip temperature should not exceed T_1 , while the room temperature is T_0 and $T_1 > T_0$. Assume that the strip temperature at $x = 0$ equals the furnace temperature, and that heat transfer is uniaxial in the x direction (no heat losses).



5.2 Here Are the Answers. What Were the Questions? (a) Different operators got different readings because they immersed the thermometer for different periods of time. (b) After immersing the bulb for time $t = MC_p/hA$, the dimensionless

temperature $\theta = (T_f - T)/(T_f - T_i)$ reached $1/e$, and after twice that time $1/e^2$, where T_f is the fluid temperature, T_i the initial temperature, M is the mass of the bulb, and h is the heat-transfer coefficient.

- 5.3 Solution of Heat Transfer Problems by Combination of Variables** Show that the partial differential equation

$$\frac{\partial T}{\partial t} = \alpha \frac{\partial^2 T}{\partial x^2}$$

is reduced to the ordinary differential equation E5.2-3 by defining a new variable $\eta = Cxt^m$, where C and m are constants. Note that we combine the variables in such a way that $T = f(\eta)$, where $\eta = F(x, t)$. Use the Chain Rule to obtain expressions for $\partial T/\partial t$, $\partial T/\partial x$, and $\partial^2 T/\partial x^2$, then substitute for $\partial\eta/\partial t$, $\partial\eta/\partial x$, and $\partial^2\eta/\partial x^2$.

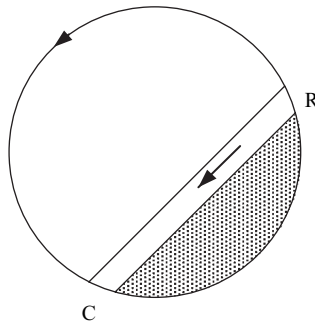
- 5.4 Time-dependent Temperature Boundary Conditions** (a) Consider the heat-transfer problem involved inside a semi-infinite solid of constant properties with a varying surface temperature:

$$T(0, t) = T_0 + A \cos(\omega t)$$

(b) Show that, with time, the relative amplitude of temperature $A_r = A(x)/A(0)$ is given by $A_r = \exp(-x\sqrt{\pi}/x_0)$ where $x_0 = \sqrt{2\pi\alpha/\omega}$. If the heat-transfer period equals the fluctuation period $2\pi/\omega$, then x_0 is a good estimate of the penetration thickness.

(c) Find the penetration thickness for a period of 100 s for LDPE, which has thermal diffusivity of $\alpha = 7 \times 10^{-8} \text{ m}^2/\text{s}$.

- 5.5 Rotational Molding** Throne et al.⁴ investigated heat-transfer problems in rotational molding of polymeric powders. One of the simulation models for heat transfer they have considered is depicted in the accompanying figure. The lower



4. See M. Anandha Rao and J. L. Throne, "Principles of Rotational Molding," *Polym. Eng. Sci.*, **12**, 237 (1972).

(shaded) area represents a stagnant pool of polymer powder that undergoes rigid-body rotation with the rotating mold. When it reaches point R , it releases and falls back to C , where it is again heated by the hot mold wall. For each cycle, the time of contact is the time it takes for the mold to rotate from C to R . During the flowing stage, the powder is considered to be mixed thermally.

By following their work, using the Goodman method (6) and a temperature profile

$$T(x, t) = T_s \left(1 - \frac{x}{\delta(t)} \right)^3$$

where $T_s = T(0, t) = T_\infty(1 - e^{-\beta t}) + T^*$, with T_∞ the oven setpoint temperature, β the experimentally determined characteristic time of heating of the mold, and T^* the initial offset temperature, show that the penetration thickness $\delta(t)$ is given by

$$\delta(t) = \frac{2\sqrt{6\alpha_s}}{T_\infty(1 - e^{-\beta t_2}) + T^*} \left\{ t_c [T_\infty^2 + 2T_\infty T^* + T^{*2}] + \left[\frac{2T_\infty^2}{\beta} + \frac{2T_\infty T^*}{\beta} \right] (e^{-\beta t_2} - e^{-\beta t_1}) - \frac{T_\infty^2}{2\beta} (e^{-2\beta t_2} - e^{-2\beta t_1}) \right\}^{1/2}$$

where $t_c = t_2 - t_1$ is the time of contact, $\alpha_s = \alpha$ at $x = 0$.

5.6 Dielectric Heating In dielectric heating, the rate of heat generated per unit volume for a field strength \mathcal{F} of frequency f is

$$G = 13.3 \times 10^{-14} f \mathcal{F}^2 k' \tan \delta$$

where G is in $\text{cal/cm}^3\text{s}$, k' is the dielectric constant, and δ is the loss tangent. Derive the one-dimensional temperature profile $T(x)$ in a slab of width b and constant thermophysical properties with dielectric heating of intensity G . The slab is initially at a uniform temperature T_0 and $T(b) = T(-b) = T_0$.

Answer:

$$T - T_0 = \frac{G}{2k} \left\{ (b^2 - x^2) - \frac{32b^2}{\pi^3} \sum_{n=0}^{\infty} \frac{1}{(2n+1)^2} \exp \frac{-\alpha(2n+1)^2 \pi^2 t^2}{4b^2} \times \sin \left[\frac{(2n+1)\pi}{2} \left(1 + \frac{x}{b} \right) \right] \right\}$$

5.7 Frictional Welding Two pieces of PMMA are to be welded frictionally. Estimate the normal pressure that has to be applied in order to raise the interface temperature from 25°C to 120°C in 1 s. The relative velocity between the sheets is 10 cm/s. The thermal conductivity of PMMA is $4.8 \times 10^{-4} \text{ cal/cm} \cdot \text{s}$, the thermal diffusivity is $9 \times 10^{-4} \text{ cm}^2/\text{s}$, and the coefficient of friction is 0.5.

5.8 Fluidized-bed Coating of an Article A rectangular metal article with dimensions of $0.5 \times 5.0 \times 10.0$ cm is to be coated with PVC powder to a uniform coat thickness of 0.01 cm, using the fluidized-bed coating process. The fluidized-bed temperature is 20°C and the initial metal temperature is 150°C . (a) Assuming no convective losses to the fluidized bed, what would the metal temperature decrease need to be to form the desired coat thickness? (b) Estimate the effect of convective heat losses on the temperature decrease of the metal.

5.9 Parallel-Plate, Nonisothermal Newtonian Drag Flow with Constant Viscosity (a) Show that the temperature profile in steady drag flow of an incompressible Newtonian fluid between parallel plates at distance H apart, in relative motion V_0 and different constant temperatures, T_1 and T_2 , assuming constant thermophysical properties and temperature independent viscosity, is given by

$$\frac{T - T_1}{T_2 - T_1} = \xi + \text{Br}\xi(1-\xi)$$

where $\xi = y/H$ and Br is the Brinkman number defined as

$$\text{Br} = \frac{\mu V_0^2}{k(T_2 - T_1)}$$

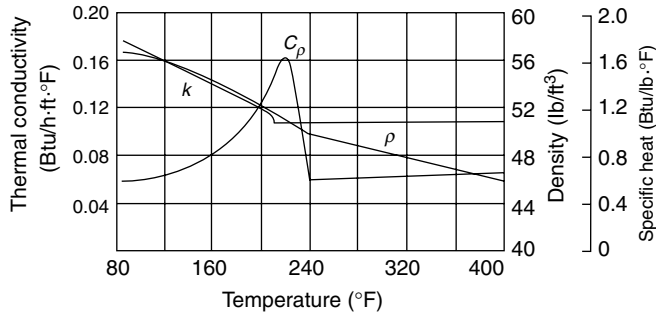
(b) Calculate the heat fluxes at the two plates.

5.10 Parallel-Plate, Nonisothermal Newtonian Drag Flow with Temperature-dependent Viscosity (a) Review the approximate linear perturbation solution given in Example 1.2-2 in R. B. Bird, R. C. Armstrong, and O. Hassager, *Dynamics of Polymeric Fluids*, Vol. 1, Wiley, New York, 1977. (b) Review an exact analytical solution in B. Martin, *Int. J. Non-Newtonian Mech.*, **2**, 285–301 (1967).

5.11 Formation of Thick Polymer Sheets Forming thick sheets of unplasticized amorphous polymers (e.g., PVC) is difficult because of the frequency of void formation during cooling. For this reason such products are sometimes made by pressing together a number of thin extruded sheets between hot plates in hydraulic presses. (a) Using Fig. 5.8 estimate the time required to fuse together twenty sheets of PVC, each 0.05 cm thick, initially at 20°C , by pressing them between two hot plates kept at a constant temperature of 150°C . Use the thermo-physical data in Appendix A. (b) Discuss the problem of thermal degradation.

5.12 Cooling of Extruded PE Wire⁵ Consider a copper conductor, 0.16 in in diameter, coated by extrusion to a 0.62-in insulated wire (first transatlantic cable core wire). The conductor is preheated to the extrusion temperature 412°F , and

5. R. D. Biggs and R. P. Guenther, *Mod. Plast.*, **1963**, 126 (May 1963).



exits into a water trough maintained at 80°F at 42 ft/min. Assuming a flat temperature distribution in the copper, since its conductivity is about 2000 times that of PE, solve the heat transfer problem of cooling the insulated wire in terms of a heat-transfer coefficient of 500 (Btu/ft²·hr·°F) and the thermophysical properties for PE shown in accompanying figure.

- 5.13 Adiabatic Compression Heating** Melting of polymers by adiabatic compression has been shown to be feasible for processes such as injection molding (2). Discuss this method, in principle, in terms of an order-of-magnitude analysis of the terms of the thermal energy balance for an amorphous (PS) and a semicrystalline polymer (LDPE). Use the data in Appendix A.
- 5.14 Melting Efficiency with Melt Removal in Conductive Melting** There are four reasons for melt removal (from the heat-transfer region) in conductive melting. The first is efficiency of melting; the second is avoidance of thermal degradation by shortening the residence time of the melt in regions near high-temperature surfaces; the third is the further generation of heat in the entire volume of the melt by viscous dissipation of mechanical energy; and the fourth is that melt removal induces laminar mixing and thermal homogenization. In this Problem, we wish to compare the melting efficiency and polymer melt stability for the “melting” of PVC with and without melt removal. A slab of PVC 8 × 8 × 2 cm at 20°C is to be melted by a hot metal surface at 200°C. Melt removal is accomplished by moving the hot surface at a speed of 1 cm/s. Use data in Fig. 5.3 and Appendix A. Assume an average value for ρ , k , and C_p below and above T_g .
- 5.15 Sintering of PS “Pearls”** Calculate the rate of coalescence of PS “pearls” made from suspension polymerization, which are 0.2 cm in diameter. The temperature of the sintering process is 180°C. Use the Power Law constants of the unmodified PS in Appendix A. The surface tension of the melt can be taken to be 32.4 dyne/cm.⁶

6. H. Schonhorn, “Theory of Adhesive Joints,” in *Adhesion and Bonding*, N. M. Bikales, Ed., Wiley, New York, 1971.

- 5.16 *Flow and Heat Transfer in the Molten Film during Melt Removal*** Formulate equations of the coupled heat transfer and flow problems involved during the melt removal (by a simple shearing flow) in the conductive heating of a polymer sheet. If x is the direction of the melt removal and y the direction of the main temperature gradient, allow both v_x and v_y to be nonzero (because $\delta = \delta(x)$); also, allow for a convective heat flux in the x direction. Assume that the polymer is crystalline, with constant “average” values for ρ , k , and C_p .
- 5.17 *Heat Transfer in Blow Molding*** Estimate the cooling time of a 15 cm long, 4 cm in O.D., and 0.3 cm thick HDPE parison at 200°C, which is inflated onto a 10-cm-diameter and 15-cm-long cylindrical bottle mold at 15°C by 5°C cold air. Solve the heat-transfer problem involved. Use the ρ , k , and C_p data given in Appendix A. Assume that the inner surface of the bottle is at 15°C.
- 5.18 *Heat Transfer in Underwater Pelletizing*** In underwater pelletizing, the melt strands are extruded directly in a water bath and “chopped” by a rotating, high-speed knife into short-length cylinders called *pellets*. Consider an LDPE extrudate at 200°C, chopped into pellets of $L = D = 0.4$ cm in a bath kept at 10°C. (a) Formulate the complete heat-transfer problem. (b) Estimate the time required to cool the center of the pellet to 70°C by assuming that pellet surface temperature equals the temperature of the water.

6 Pressurization and Pumping

- 6.1 Classification of Pressurization Methods, 236
- 6.2 Synthesis of Pumping Machines from Basic Principles, 237
- 6.3 The Single Screw Extruder Pump, 247
- 6.4 Knife and Roll Coating, Calenders, and Roll Mills, 259
- 6.5 The Normal Stress Pump, 272
- 6.6 The Co-rotating Disk Pump, 278
- 6.7 Positive Displacement Pumps, 285
- 6.8 Twin Screw Extruder Pumps, 298

The polymeric melt generated by the melting step must be conveyed and *pressurized* or *pumped* by the processing machine to force it *through* dies, or *into* molds, to assume useful shapes. This is the subject matter of this chapter.

We shall analyze pressurization, starting with its basic principles. First, by analyzing the various terms in the equation of motion, we deduce the possible mechanisms for pumping and pressurizing a fluid. This exercise maps out the theoretical envelope of pressurization mechanisms. Then, via a set of logical deductions, we uncover the simplest and most fundamental geometrical elements of *all* pumps, which through a sequence of systematic steps will lead us to a rich arsenal of machine configurations, among them, not surprisingly, most common pumps. In fact, this latter step serves as a formal means to *synthesize* or *invent* novel machine configurations. Finally, we examine in some detail the mathematical modeling of the most important, common machine configurations, deriving practical *design* equations.

Pumping or pressurization is perhaps the most characteristic polymer processing step, because it shows how dominant an effect the very high viscosity of polymeric melts has on processing machine configurations. High viscosity mandates very high pressures to force the melt through restrictions at the desired processing rate. Extrusion pressures up to 50 MN/m^2 (500 atm) and injection pressures up to 100 MN/m^2 (1000 atm) are not uncommon in practice. We shall see that most machines have *narrow gap* configurations, which not only enable the generation of high pressures, but also provide for good temperature control of the melt and lead to relatively short residence times. Furthermore, we shall also see that the common, practical processing machines have not only relatively short residence times but also narrow *residence time distributions*, enabling them to process temperature-sensitive polymeric materials.

6.1 CLASSIFICATION OF PRESSURIZATION METHODS

The response of a fluid to external forces is governed by the equation of motion. Therefore, by carefully analyzing the various terms of the equation of motion

$$\rho \frac{D\mathbf{v}}{Dt} = -\nabla P - \nabla \cdot \boldsymbol{\tau} + \rho \mathbf{g} \quad (6.1-1)$$

we can discover *all* the possible and fundamentally different pressurization mechanisms.

We first note that the equation of motion provides information only on pressure *gradients* in the liquid, and provides no information regarding the *absolute* value of the pressure. The latter is determined by *external* conditions imposed on the system. For example, the pressure in a liquid contained in a cylinder equipped with a plunger is determined by the *force* exerted by the plunger on the liquid, plus the hydrostatic head. We classify this pressurization method as *static pressurization*, because the pressure can be maintained without flow and without motion of the containing walls. The level of pressure that we can generate by this method is independent of the *rheological* properties of the fluid. Furthermore, the flow that results from this pressurization method, if we provide an exit for the liquid, is called *positive-displacement flow*. We already encountered this type of flow in Chapter 4 in solids conveying. The outstanding characteristic of this type of flow is an external surface moving *normal* to its plane and thus *displacing* part of the fluid. This pressurization method is used quite extensively in polymer processing, for example, in injection molding, compression molding, counterrotating fully intermeshing twin screw extrusion, and gear pump extrusion.

An alternative means for generating pressure in a fluid is by inducing an internal *pressure gradient*. To achieve this, a positive gradient in the direction of flow is needed for generating pressure. The equation of motion indicates that a nonzero pressure gradient can, in principle, be generated if any of the remaining three terms ($\rho D\mathbf{v}/Dt$, $\nabla \cdot \boldsymbol{\tau}$, and $\rho \mathbf{g}$) has a nonzero value. The first term may acquire a nonzero value only if the fluid is in motion and there is acceleration (or rather deceleration). The second term will acquire a nonzero value only if the fluid is under deformation. Hence, these are defined as *dynamic pressurization mechanisms*. The third term, which is the gravitational term, creates a hydrostatic pressure gradient and is utilized, for example, in casting.

Since polymeric melts are characterized by having high viscosity, the dominant pressurization mechanism stems from $\nabla \cdot \boldsymbol{\tau}$ (which is proportional to viscosity). Clearly, the higher the viscosity, the larger this term becomes, and potentially larger pressure gradients can be generated. Thus, the high viscosity of the polymeric melts becomes an asset in this pressurization mechanism.

The purpose of pressurization is to *generate* pressure as pumps do (as opposed to lose pressure, as in pipe flow). This can only be achieved by a moving external surface that “drags” the melt, leading to *drag-induced flows*. Indeed, the outstanding characteristic feature of *viscous dynamic pressurization* is a surface moving *parallel* to its plane. This, unlike a surface moving *normal* to its plane, will not displace the liquid, but *drag* it along. The high viscosity implies high momentum transport rates normal to the moving surface. Single screw extruders (SSEs), co-rotating intermeshing twin screw extruders (TSEs), calenders and roll mills, and co-rotating disk processors generate the pressure needed to shape, form, and mix the material by this mechanism.

Viscous dynamic pressurization is not the only pressurization mechanism that stems from the $\nabla \cdot \boldsymbol{\tau}$ term of the equation of motion. As discussed in Chapter 3, polymeric melts exhibit

normal stress differences, and these stresses may also yield a nonzero value to this term. Indeed, the normal stress extruder utilizes this mechanism of pressurization.

The $\rho D\mathbf{v}/Dt$ term in the equation of motion accounts for acceleration. In polymer processing this is not a very important source of pressurization. Yet centrifugal casting takes advantage of angular acceleration as a mechanism for generating pressure, and linear deceleration to generate “impact molding.”

Finally we note that, in principle, a reduction in density can generate pressure in a closed system. Low-pressure structural molding and certain reaction injection molding processes involving foaming during the molding operation generate sufficient pressure to force the melt to fill the mold.

Although the equation of motion provides information on the *possible* sources of pressurization, the actual multitude of *realistic* geometric configurations that can make efficient use of these mechanisms is a matter of creative engineering design. In the next section, we propose a methodology for *synthesizing* or *inventing* such geometrical configurations in a rational and systematic way (1,2). This process will also help elucidate the pressurization mechanism of the machines and the underlying reasons for their particular shape.

6.2 SYNTHESIS OF PUMPING MACHINES FROM BASIC PRINCIPLES

Machine *invention* is clearly an act of *synthesis*, as is engineering design. In synthesis we *construct*, *assemble*, and *put together* ideas, elements, concepts, or combinations of these in order to create an artifact that hopefully does something useful. We combine elements into a whole, into a new entity.

In contrast to invention and engineering design, in science we mostly *analyze*. We *decompose* the whole into its constituent elements. We deconstruct. And, of course, this process of *deconstruction* helps us discover the laws of nature. Similarly, when the tools of analysis and the fundamentals of science are applied to technology, to an engineering discipline, or an industrial process, they are also decomposed into their fundamental building blocks and elements. These are then systematically arranged and generalized in order to create a formal structure. Then by *recombining* the elements and building blocks in novel ways into a *new* whole, inventions and innovations can be made. Thus, through *analysis*, the fundamental building blocks and elements of processes and machines can be uncovered, and after they are uncovered, they can be *reassembled* in a rather formal way in a myriad of different ways to create new inventions and innovations.

The historical origins of this approach, often referred to as the *morphological* approach, go back to Frantz Reuleaux (3), who was seeking an “elementary structure of the machine simple enough to be general and exhaustive enough to provide designs for special constructions,” and was later generalized by Simon (4), Hubka (5), and others. In this section, we apply this methodology to polymer processing.

In the previous section, by exploring alternative mechanisms for pressurizing a liquid, we arrived at two basic geometrical *machine elements*, namely, a plate moving normal to its plane and a plate moving parallel to its plane. These are shown in Fig. 6.1.

Next we take these two elements and combine them with a second *stationary* or *moving* plate to create the basic *building blocks* for machine design. A building block is the simplest geometrical configuration that captures the most fundamental element of the



Fig. 6.1 The two basic machine elements: a plane moving normal to its plane and a plane moving parallel to its plane.

pressurization mechanism. For example, we already demonstrated in Example 2.5 that two parallel plates in relative motion capture the mechanism of single screw extrusion pumping, and therefore this is the building block of the SSE.

There are 14 distinguishable building blocks that can be constructed from the two machine elements and a second plate placed parallel or at an angle to the machine elements, as shown in Fig. 6.2. Not all of them have the same practical significance, not all of them may lead to useful design solutions, but they are all clear, distinguishable machine building blocks.

Next we construct machine configurations using the building blocks. In order to do this we must first find a practical solution for creating a constantly moving “infinite” plate. This can, of course, be accomplished by employing rotational motion. In the case of the plate moving parallel to itself, Fig. 6.3 shows several possible alternatives for achieving such motion: an infinite moving belt, the outside of a solid cylinder, the inside of hollow cylinder, and the face of a disk. Many other geometrical shapes can create moving surfaces, but they will not differ fundamentally from the ones in Fig. 6.3.

In the case of a plate moving normal to itself there are two options: (a) via simple reciprocating action, as in reciprocating plunger pumps and injection and compression molding machines, which can also take the form of rolling cylinders, as in intermeshing counterrotating twin screws; and (b) by placing planes on a rotary element, as is the case with gear pumps. These are shown schematically in Fig. 6.4.

Now we proceed with the formal invention process by pairing building blocks with the foregoing design solution to the moving surfaces. A number of the examples that follow will clarify the process.

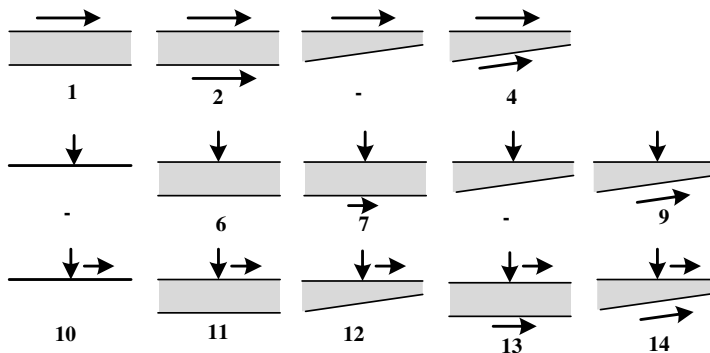


Fig. 6.2 Fourteen different building blocks created from the two machine elements and stationary plates. Note that motion of the second plane in the opposite direction will not create new building blocks because only the relative motion between the planes matters.

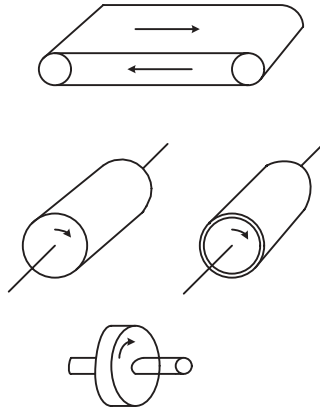


Fig. 6.3 Some design solutions for creating infinite surfaces moving parallel to their plane.

Example 6.1 The Synthesis of the Roll Pump Consider building block 1 in conjunction with an infinite surface created by a rotating solid cylinder, as shown in Fig. E6.1a(a) and Fig. E6.1a(b). The curvature of the cylinder does not change the concept and mechanism of drag flow. Next, the stationary surface must be created. The simplest solution is to place the solid cylinder inside a stationary barrel, as in Fig. E6.1a(c) and Fig. E6.1a(d), where in addition we created entrance and exit ports through the barrel separated by a solid obstruction.

Thus, we have invented a new geometrical configuration for a viscous pump. We can now easily construct a mathematical model and design such a pump for a desired pressure and flow rates. The pressurization capability of such a pump, at a given frequency of rotation and geometry, is proportional to the length of the flow channel. In our case, this will be one circumference. We can relax this constraint by assembling several rolls in sequence, as shown in Fig. E6.1b. This leads to an apparently infinite number of possible solutions, because in principle we can add as many rolls as we wish. Of course, most of these will not be practical solutions. Single roll extruders can be designed not only as pumps, but as complete processors

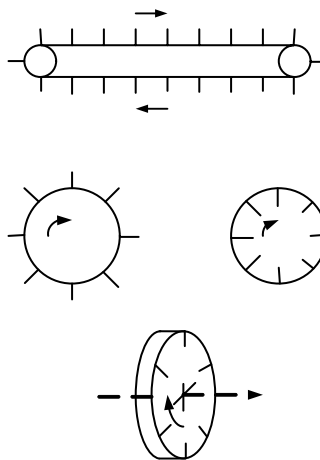


Fig. 6.4 Some possible design solutions for creating periodic continuous motion of a surface normal to its plane.

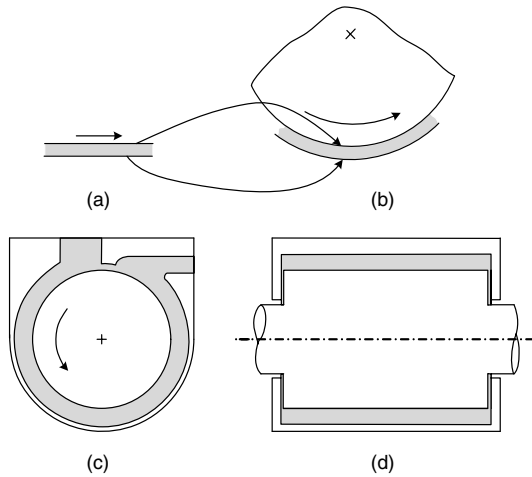


Fig. E6.1a The synthesis of a roll pump from building block 1. (a) The building block; (b) a rotating solid cylinder forms the moving surface; (c) the inner surface of a hollow cylinder forms the stationary surface. The two surfaces create a curved shallow pumping channel. Entrance and exit ports are formed by openings in the outer cylinder, and they are separated by a “channel block”; (d) side view of the roll pump.

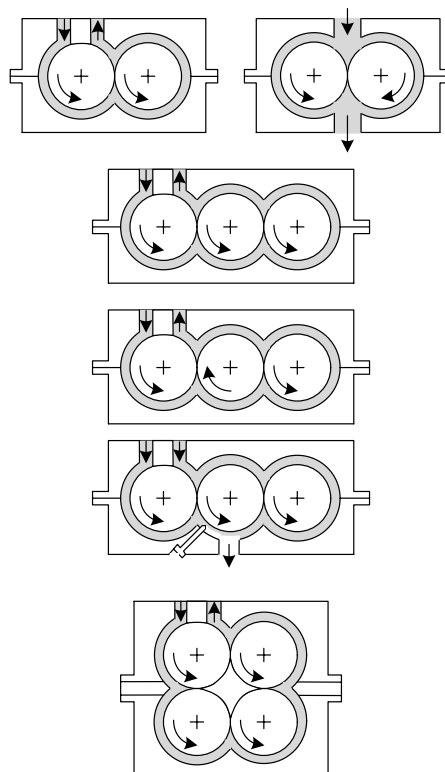


Fig. E6.1b Alternative design solution of a roll pump from building block 1. On the top we see two two-roll pumps: one co-rotating and the other counterrotating. The latter is a toothless gear pump; where the pumping mechanism is viscous drag rather than positive displacement. In the middle we have three three-roll configurations, and at the bottom a four-roll pump.

(1), and, in fact, such machines have been suggested and built (6,7). However, in practice they have too many disadvantages as compared to the screw-type processors, and are rarely, if ever, used.

Example 6.2 The Synthesis of the Inverse Single Screw Pump There is, however, another, more elegant way to relax the channel-length constraint, as shown in Fig. E6.2. After one circumference, a flow channel formed by the moving and stationary planes of a given width can be twisted helically by an amount equal to the width of the channel to create a much longer *helical* channel on the same roll or shaft. The channel itself can be simply machined onto the inner surface of the stationary cylinder or barrel.

By mathematical modeling, it can be shown that the twisting of the channel does not alter the mechanism of pressurization, but only slightly reduces the pumping efficiency. The motion of the moving surface, which now is at a certain angle to the direction of flow, reduces drag or pumping by a factor given by the cosine of this angle. But on the other hand, the twisting of the channel into a helical one brings about important gains. A cross-channel drag flow is induced, leading to better mixing and reduced residence time distribution. It enables the drag-removal melting mechanism to take place, and it also enables the operation of a partially filled channel for venting, devolatilization, and smooth

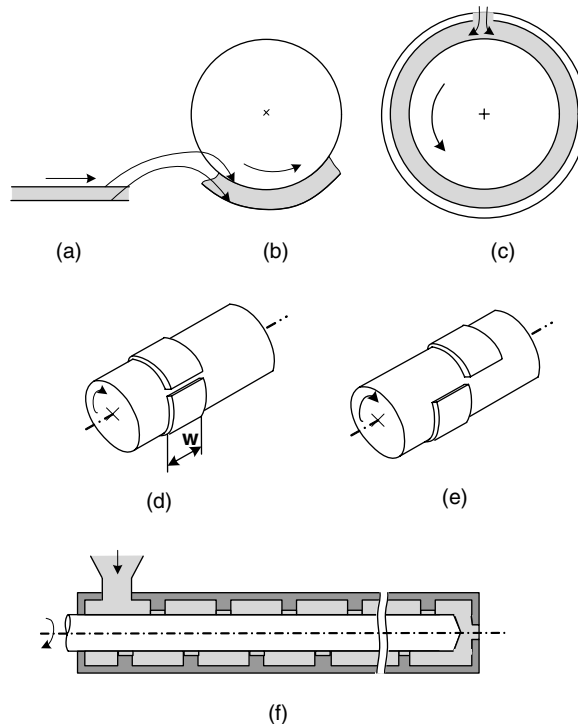


Fig. E6.2 The synthesis of an inverse screw extruder from building block 1. (a) The building block; (b) a rotating solid cylinder forms the moving surface; (c) the inner surface of a hollow cylinder forms the stationary surface. The result is a single roll processor without the channel block; (d) the shallow channel is wrapped around the rotating shaft; (e) the shallow channel relaxes the length constraint; (f) cross section of an inverse screw processor.

conveying of particulate solids. Finally, from a mechanical design point of view, the helical geometrical configuration makes it easy to feed the machine through an opening in the stationary barrel and discharge it by terminating the shaft, as shown in Fig. E6.2. The resulting machine is, in fact, an inverse screw extruder, where the screw channel is machined into the inside of the barrel and a smooth shaft rotates in it.¹

Example 6.3 The Synthesis of the Hollow Cylinder Pump We take building block 1 and use the inner surface of a hollow cylinder as the moving surface. The procedure follows the same conceptual lines of design as outlined in the previous examples and it is clearly demonstrated in Fig. E6.3a. A small variation is to have the entrance and exit ports at different ends of the shaft, as shown in Fig. E.6.3b.

Example 6.4 The Synthesis of the Single Screw Extruder The SSE is the most common, important, and extensively used processing machine. It was invented and patented by Mathew Gray in 1879, although it is generally attributed to Archimedes (it is still called the “Archimedes screw”) and the ancient Egyptians supposedly had the device long before that (8). Continuing in this distinguished tradition, this important machine configuration can

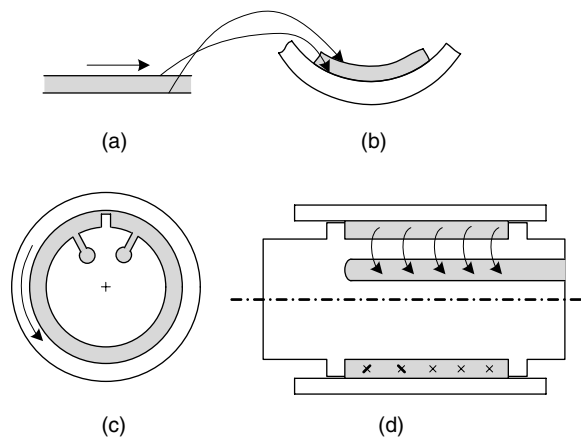


Fig. E6.3a The synthesis of a hollow cylinder pump. (a) The building block; (b) a rotating hollow cylinder forms the moving plane; (c) the stationary plane is formed by the outer surface of a solid stationary shaft. A channel block separates inlet and outlet. Feeding and discharge are carried out through slits in the shaft leading to axial holes drilled in the shaft; (d) the two surfaces that form a shallow curved channel are bounded by a sidewall or “flight” running along the circumference of the shaft.

1. Using this concept, a helical barrel rheometer (HBR) was developed. It is a single screw pump with a straight shaft and a helically wound channel machined into the barrel, with the clearance being the difference between the barrel and shaft diameters. At closed discharge the pressure drop across one flight can be directly related to the melt viscosity, given the geometry and frequency of rotation. With this design the pressure trace is steady with time and not a saw-tooth as in an SSE screw pump, eliminating the need for pressure transducer time response analysis. It is pressure generating and can thus be used as an online rheometer, since it can pump the sample stream back to the processing equipment. Additionally, since it can pressurize the melt during viscosity measurements, it is capable of measuring the effect of foaming agent diluents on the melt viscosity. [D. B. Todd, C. G. Gogos, and D. N. Charalambopoulos, U.S. Patent 5,708,197 (1998); D. B. Todd, C. G. Gogos, M. Esseghir, and D. W. Yu, “Monitoring Process Viscosities with a New On-line Rheometer,” *Plastics Eng.*, **53**, 107 (1997); S. K. Dey, D. B. Todd, and C. Wan, “Viscosity of Blowing Agent-laden Polymers,” *SPE ANTEC Tech. Papers*, **50**, 3122 (2004).]

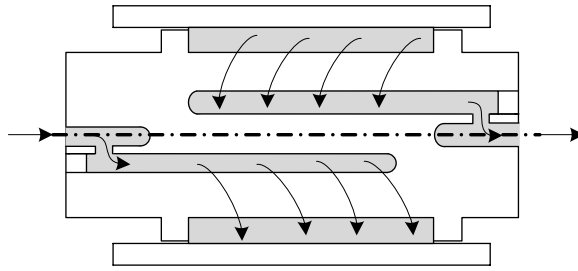


Fig. E6.3b Side view of a hollow cylinder pump with feed port at one end of the shaft and discharge at the other end.

easily be “invented” in a systematic way by pairing building block 1 with the inner surface of a rotating hollow cylinder, as shown in Fig. E6.4.

As in the inverse screw pump, we relax the channel length constraint to one circumference by twisting it and making it helical [Fig. E6.4(d)]. We create the helical channel by machining it onto a solid shaft, resulting in a screw. We now have a single

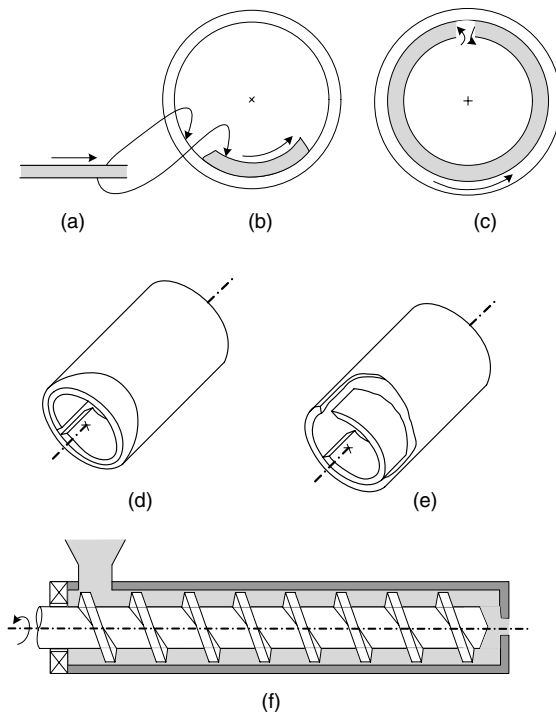


Fig. E6.4 The synthesis of the SSE for building block 1. (a) The building block; (b) a rotary hollow cylinder forms the moving plane; (c) the shallow channel of certain width spread over one circumference of the cylinder; (d) a twisted helical channel relaxes the length constraint; (e) the channel machined onto a solid shaft, the rotation of the cylinder interchanged with that of the shaft, and feeding and discharge ports fixed on the cylinder or barrel, resulting in an SSE.

screw placed inside a rotating hollow barrel. Next, we set the rotation of the barrel and that of the screw in opposite directions,² and then by creating an entry port in the barrel and terminating the screw for discharge, we obtain the SSE configuration, as shown in Fig. E6.4(e).

Example 6.5 The Synthesis of the Disk Processor In this example, we once again take building block 1 and pair it with the flat face of a rotating disk to obtain a disk processor, as shown in Fig. E6.5a. As was the case in the roll pump, the inlet and outlet ports are cut into the

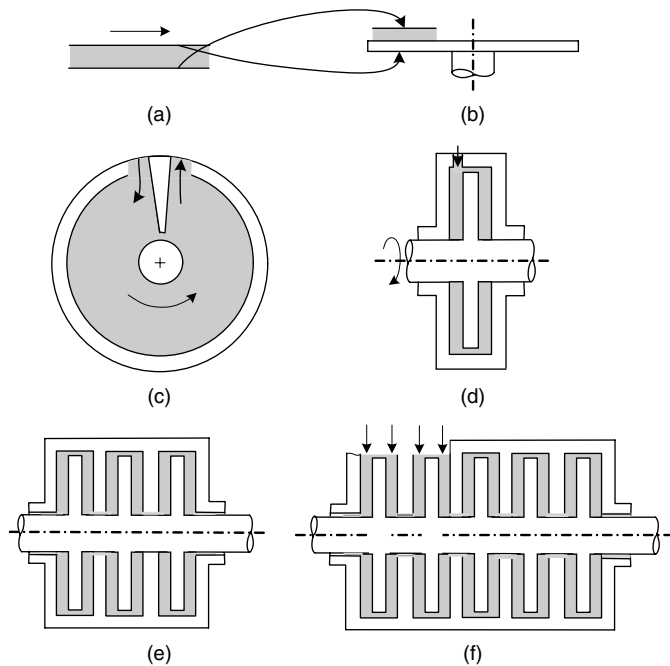


Fig. E6.5a The synthesis of a disk pump from building block 1. (a) The building block; (b) a rotating disk forms the moving plane; (c) front view of the pump in a closure with inlet and outlet ports separated by a channel block; (d) side view of the pump having two pumping chambers on either side of the rotating disk; (e) multichamber-multistage setup with material moving from stage to stage via “transfer channels” (not shown) machined in the closure connecting discharge port of the downstream chamber with the inlet port of the upstream one; (f) parallel-in series combination of chambers.

2. If centrifugal forces play no role in the mechanisms taking place in the machine, as is the case for viscous polymeric materials at common screw speeds, then from a fluid mechanics point of view, it makes no difference whatsoever if the barrel rotates or if the screw rotates in the opposite direction. A fluid particle in the screw channel is oblivious to what moves. It only senses the relative motion generating the shearing forces. However, it is far more convenient to place the coordinate system on the screw, because then the boundary conditions become far simpler, with stationary channel walls and a single surface (that of the barrel), moving relative to them. Moreover, we are interested in the motion of the melt relative to the stationary screw channel due to drag exerted by the barrel surface, and not relative to a stationary barrel on which rigid rotation is superimposed. Just consider a slippery barrel surface, which leaves the melt rotating in unison with the screw with zero output. Clearly, for a fluid particle, the screw will appear stationary. Therefore, in analyzing SSEs theoretically, we assume that the screw is stationary and that the barrel rotates in the opposite direction.

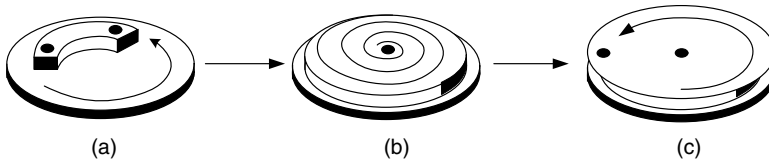


Fig. E6.5b The synthesis of a flat spiral pump from building block 1. (a) A section of the curved channel formed by a stationary plane and the rotating disk plane; (b) the extension of the channel into a flat spiral; (c) outside view of the flat spiral pump, with the spiral channel machined into the surface of one disk and another closely spaced rotating disk covering it.

barrel and separated by a “channel block.” Clearly, both surfaces of the disk can be utilized as shown in Fig. E6.5a(d). Moreover, like the roll pump, we can relax the length restriction by using a multichamber–multistage arrangement as in Fig. E6.5a(e), or by creating a spiral channel on the surface of the flat disk, as shown in Fig. E6.5b.

Example 6.6 The Synthesis of the Rotating Cup Pump We now take building block 2 and pair it with both a rotating solid cylinder and a hollow cylinder to create two moving planes, as shown in Fig. E6.6a. The separation between the axial inlet and outlet ports machined into the cover plate [Fig. E6.6a] is a bit cumbersome and has to be created by an axial channel block attached to the cover plate and extending into the cup. Apparently, no such machine actually exists and it may not be too useful, but the point is that this

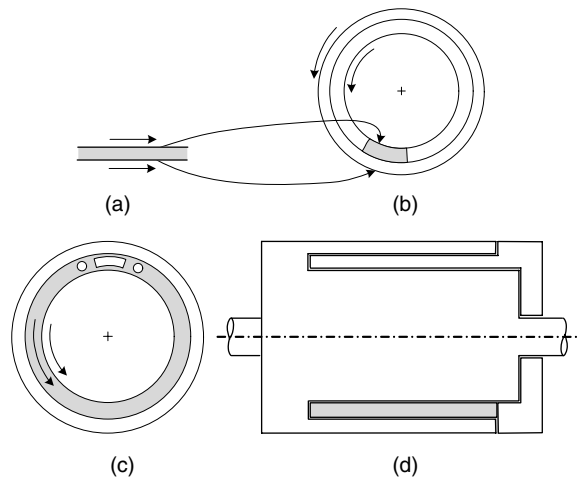


Fig. E6.6a The synthesis of the rotating cup pump from building block 2. (a) The building block; (b) a rotating solid cylinder and a rotating hollow cylinder for the moving planes; (c) the rotating elements are separated by a channel block with feeding and discharge ports shown on either side; (d) side view of the processor where the rotating elements are combined into a rotating cup and a stationary cover plate closure holds the channel block.

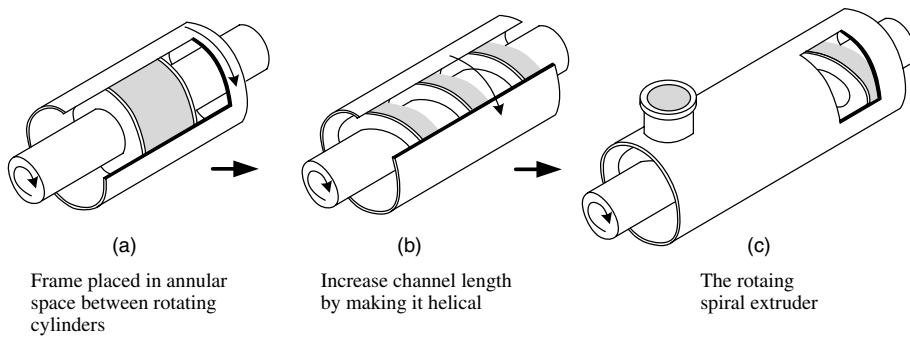


Fig. E6.6b The synthesis of the free rotating flight pump from building block 2. (a) an annular channel is created between the rotating shaft and hollow cylinder; (b) the channel is twisted and extended into a helical spiraling channel; (c) the channel is formed by a spiral that rotates between a stationary shaft and stationary barrel, with a feed port and exit port machined into the barrel.

novel configuration, which would surely work, emerged systematically from our “invention” procedure.

As in the previous examples, we can relax the channel length limitation either by adding a second stage using an axially rotating cup pump or alternatively, by creating a spiral channel between a rotating shaft and hollow cylinder, as shown in Fig. E6.6b. This leads to a rotating spiral pump which, when optimized, generates eightfold more pressure at the same frequency of rotation (for a Newtonian fluid) as the single screw pump. Building such a pump for viscous liquids and high pressure is mechanically rather challenging, but it is a common configuration for short solids feeders.

Example 6.7 The Synthesis of the Co-rotating Disk Processor The last example in synthesizing new machine configurations from building blocks is the co-rotating disk processor. Here we pair building block 2 with the moving planes of two rotating disks, as shown in Fig. E6.7. The disks are attached to a rotating shaft enclosed within a stationary barrel with inlet and outlet ports, separated by a channel block. The space thus created forms a processing chamber.

Processing chambers can be connected in parallel or in series. In the latter case, material can be conveniently transferred from one chamber to the next via transfer channels machined into the barrel. Heating and cooling of the disks can be accomplished by temperature-controlled liquids fed through rotary joints into the shaft and the disks. Theoretical analysis shows that this geometrical configuration is most effective not only for pumping but for all the other elementary steps as well. This configuration was invented by one of the authors (9) and the concept was commercialized by the Farrel Company in Ansonia, CT (10–16), which manufactured and sold a whole series of such machines, trademarked Diskpack (See Section 9.4).

The preceding examples have shown the potential of the methodology using only two building blocks. Some additional examples are given in the problems listed in Section 6.5 and at the end of this chapter. The others are left as a challenge to the readers. Uncovering a novel design solution hidden among the multitude of alternatives offers a worthy experience in what can be termed “the joy of design.”

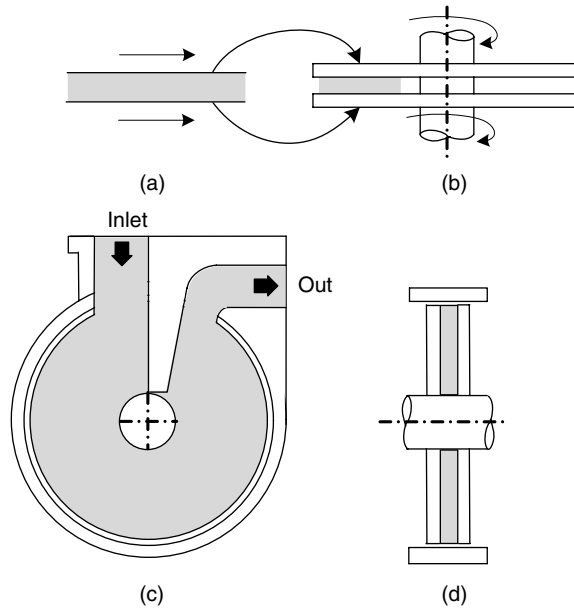


Fig. E6.7 The synthesis of the co-rotating-disk pump. (a) The building block; (b) two co-rotating disks form the moving planes; (c) front view of the processor showing the inlet and outlet ports separated by the channel block; (d) side view of the pump.

6.3 THE SINGLE SCREW EXTRUDER PUMP

In this section we derive a simple mathematical model for the single screw pump. In such a model, we seek relationships between performance and operating variables with the geometrical variables as parameters.

The single screw configuration has held its ground for over 125 years as the simplest and most useful geometrical configuration for processing plastics. In fact, the bulk of plastics are processed using an SSE, shown schematically in Fig. 6.5, at least once in their journey from raw material to finished product. A detailed treatment of single screw extrusion is given by Tadmor and Klein (17).

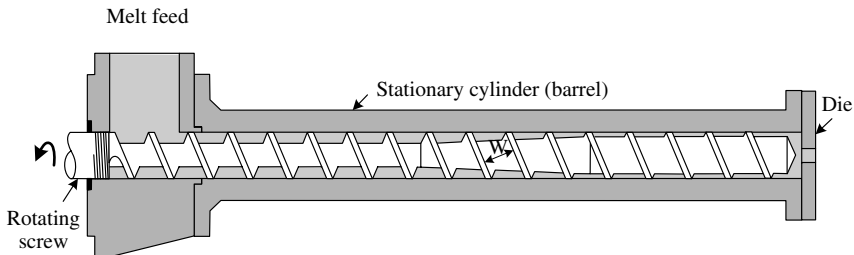


Fig. 6.5 Schematic view of an SSE. Its main components are a rotating screw within a stationary barrel. Polymer is fed through an inlet port and leaves the machine through a closure equipped with a die at the discharge end. Not shown in the figure are the electric motor drive and gear reducer for adjusting the rotational speed.

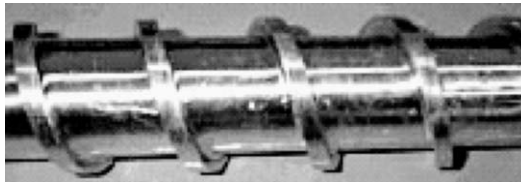


Fig. 6.6 A single-flighted square-pitched screw.

Not only is the single screw a very efficient pump but, as we saw in Chapter 4, it also conveys particulate solids well, and by virtue of its geometry it triggers and maintains the elegant *drag-removal melting mechanism* (see Section 5.7). It operates smoothly and conveniently with partially filled screws for venting (see Problem 6.9) and having a narrow residence time distribution, it enables processing of temperature-sensitive materials. It is a good extensive distributive mixer, though of course being close to plug flow, it lacks back mixing,³ and contrary to common wisdom, it can also be designed for dispersive mixing (2).

The single screw as shown in Figs. 6.6 and 6.7 is a relatively simple geometrical configuration that is easy to manufacture, and therefore relatively inexpensive. Thus multiple screws can be retained with a single machine for different applications.

Geometry

Single screw extruders range in size from as small as 2 cm to as large as 75 cm in diameter, with axial length L to diameter D (taken at the tip of flight) ratios of 24 to 26, although occasionally we find extruders with L/D ratios as high as 40 or as low as 8. The latter are generally either rubber extruders or early⁴ thermoplastic extruders. Between the tip of the

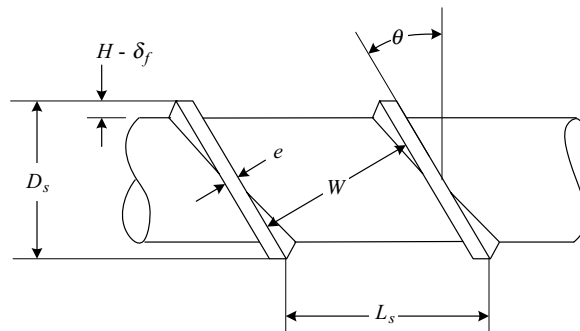


Fig. 6.7 Geometry of a square-pitched single-flighted screw.

3. Albert Aly Kaufman, one of the pioneers of extrusion, who established the celebrated Prodex Extruder Manufacturing Company, used to say "What goes in comes out. Don't expect the screw to even-out non-uniform feeding of additives. It can't."

4. The extruders used for rubber do not require the length of those used for plastics, because they do not need as long a melting section as plastics do. When the plastics industry adopted the rubber machinery, it imitated the rubber extruder design, but as demands for output and quality mounted, the length-to-diameter ratio of the extruder grew over time, until it leveled off at current values.

flight of the screw and the inner surface of the barrel D_b , there is a small radial clearance δ_f of the order of 0.1–0.3% of D_b . Polymer melt fills this gap and acts as a lubricant, preventing metal-to-metal contact. The diameter of the screw at the tip of the flights is $D_s = D_b - 2\delta_f$. The axial distance of one full turn of the flight is called the *lead* L_s .

Most screws of SSEs are single flighted, with $L_s = D_s$, referred to as *square-pitched screws*. The radial distance between the root of the screw and the barrel surface is the *channel depth*, H . The main design variable of screws is the *channel depth profile* that is $H(z)$, where z is the helical, down-channel direction, namely, the direction of net flow of the material. The angle formed between the flight and the plane normal to the axis is called the *helix angle*, θ , which, as is evident from Fig. 6.8, is related to lead and diameter

$$\tan \theta = \frac{L_s}{\pi D} \quad (6.3-1)$$

The value of the helix angle is therefore a function of the diameter. At the tip of the flight it is smaller than at the root of the screw. A square-pitched screw, neglecting the flight clearance, has a helix angle of 17.65° ($\tan \theta = 1/\pi$) at the flight tip.

The width of the channel W is the perpendicular distance between the flights, and as shown in Fig. 6.8, is

$$W = L_s \cos \theta - e \quad (6.3-2)$$

where e is the flight width. Clearly, since θ is a function of radial distance, so is W . Finally, the helical distance along the channel z is related to the axial distance l

$$z = \frac{l}{\sin \theta} \quad (6.3-3)$$

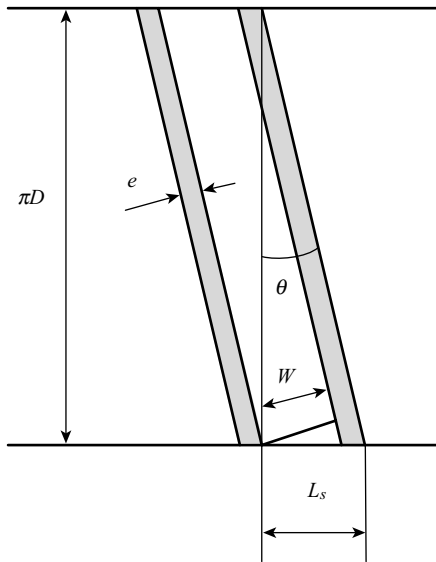


Fig. 6.8 The geometry of an unwound channel. This geometry is obtained by “painting” with ink the tips of the flights and rolling them one full turn on a sheet of paper. The track left by the flights is shown in the figure.

The Isothermal Newtonian “Standard” Mathematical Pumping Model

The mathematical model of isothermal flow of a Newtonian fluid in shallow-screw channels results in a simple design equation, which gives excellent insight into the flow mechanism and is very useful for first-order calculations. This model serves as the classic *pumping model* for single screw extrusion.

We commence its development by reversing the conceptual synthesis process. The space between a tightly fitting screw and the barrel is a helical channel. We unwind the channel from the screw and lay it on a flat surface. The result is a shallow rectangular straight channel, as in Fig 6.9.

The barrel surface becomes a flat plate covering the channel and moving at constant velocity of V_b at an angle θ_b to the down channel direction

$$V_b = \pi ND_b \quad (6.3-4)$$

where N is the frequency of rotation. The surface velocity of the barrel can be decomposed into down-channel and cross-channel components, given, respectively, by

$$V_{bz} = V_b \cos \theta_b \quad (6.3-5)$$

and

$$V_{bx} = V_b \sin \theta_b \quad (6.3-6)$$

The former drags the polymer melt toward the exit, whereas the latter induces cross-channel mixing.

Comparing the present flow configuration to that in Example 2.5 of flow between two infinite parallel plates in relative motion, we note two important differences. First, the flow in the down-channel z direction is two-dimensional due to the stationary side walls created by the flight [i.e., $v_z(x, y)$], and the barrel surface has a velocity component in the x direction that results in a circulatory flow in the cross-channel direction.

The simplifying assumptions for solving this flow problem are the same as those used in Example 2.5 for parallel plate flow, namely, we assume the flow to be an incompressible,

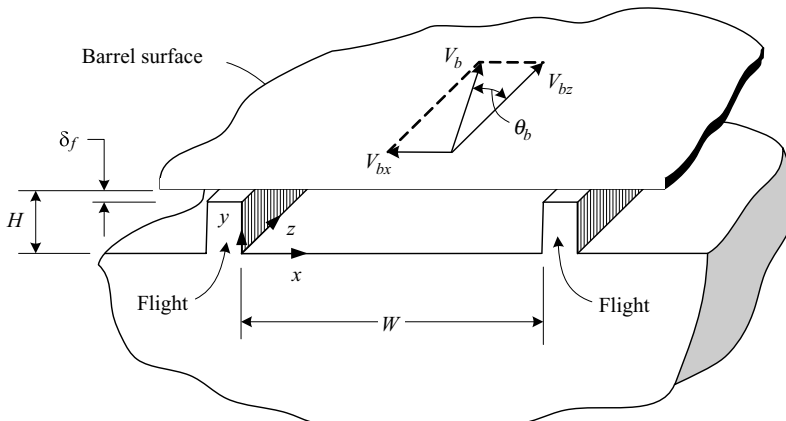


Fig. 6.9 Geometry of the unwound rectangular channel.

steady, isothermal, fully developed flow of a Newtonian fluid. The three components of the Navier–Stokes equation in rectangular coordinates defined in Fig. 6.9 reduce to

$$\rho \left(v_x \frac{\partial v_x}{\partial x} + v_y \frac{\partial v_x}{\partial y} \right) = - \frac{\partial P}{\partial x} + \mu \left(\frac{\partial^2 v_x}{\partial x^2} + \frac{\partial^2 v_x}{\partial y^2} \right) \quad (6.3-7)$$

$$\rho \left(v_x \frac{\partial v_y}{\partial x} + v_y \frac{\partial v_y}{\partial y} \right) = - \frac{\partial P}{\partial y} + \mu \left(\frac{\partial^2 v_y}{\partial x^2} + \frac{\partial^2 v_y}{\partial y^2} \right) \quad (6.3-8)$$

$$\rho \left(v_x \frac{\partial v_z}{\partial x} + v_y \frac{\partial v_z}{\partial y} \right) = - \frac{\partial P}{\partial z} + \mu \left(\frac{\partial^2 v_z}{\partial x^2} + \frac{\partial^2 v_z}{\partial y^2} \right) \quad (6.3-9)$$

where ρ is the density of the melt. In these equations the velocity components are not functions of z , since the flow is fully developed. It is further assumed that the flow in the cross-channel direction is also fully developed. This is a good approximation for shallow channels, except in the close neighborhood of the flights. Therefore, $\partial v_x/\partial x$, $\partial v_y/\partial x$, and $\partial v_z/\partial x$ vanish, and with these assumptions we obtain from the equation of continuity that $\partial v_y/\partial y = 0$, and consequently that $v_y = 0$. Equation 6.3-8 thus reduces to $\partial P/\partial y = 0$, implying that the pressure is a function of only x and z . Therefore, Eq. 6.3-7 reduces to

$$\frac{\partial P}{\partial x} = \mu \frac{\partial^2 v_x}{\partial y^2} \quad (6.3-10)$$

In Eq. 6.3-9 the left-hand side represents acceleration terms, which in the case of slow motion of a viscous fluid, will be much smaller than the terms representing the viscous forces on the right-hand side. In a typical flow situation in extruders, the ratio of the inertia to viscous forces is of the order of 10^{-5} (17a). Thus Eq. 6.3-9 reduces to

$$\frac{\partial P}{\partial z} = \mu \left(\frac{\partial^2 v_z}{\partial x^2} + \frac{\partial^2 v_z}{\partial y^2} \right) \quad (6.3-11)$$

Returning to Eq. 6.3-10, it is clear that the right-hand side is a function of y only, whereas, the left-hand side is a function only of x and z . Since neither side is dependent on the variable of the other, both must equal a constant, and Eq. 6.3-10 can be integrated to give

$$v_x = \frac{y^2}{2\mu} \left(\frac{\partial P}{\partial x} \right) + C_1 y + C_2 \quad (6.3-12)$$

The integration of constants C_1 and C_2 is evaluated from the boundary conditions $v_x(0) = 0$ and $v_x(H) = -V_{bx}$. Substituting these boundary conditions into Eq. 6.3-12 yields the cross-channel velocity profile

$$u_x = -\xi + \xi(\xi - 1) \left(\frac{H^2}{2\mu V_{bx}} \frac{\partial P}{\partial x} \right) \quad (6.3-13)$$

where $u_x = v_x/V_{bx}$ and $\xi = y/H$. This equation correctly indicates that the cross-channel velocity profile depends on the cross-channel pressure gradient. But neglecting leakage flow, the net cross-channel flow rate is zero

$$\int_0^1 u_x d\xi = 0 \quad (6.3-14)$$

which, subsequent to substituting Eq. 6.3-13 and integration, enables us to express the pressure gradient in terms of the other variables as follows

$$\frac{\partial P}{\partial x} = -6\mu \frac{V_{bx}}{H^2} = -6\mu \frac{\pi ND_b \sin \theta_b}{H^2} \quad (6.3-15)$$

Thus we observe that the cross-channel gradient is proportional to screw speed and barrel diameter, and inversely proportional to the square of the channel depth. By substituting Eq. 6.3-15 into Eq. 6.3-13, we obtain the cross-channel velocity profile

$$u_x = \xi(2 - 3\xi) \quad (6.3-16)$$

shown in Fig. 6.10.

We note that the melt circulates around a plane located at exactly two-thirds of the channel height. A fluid particle in the upper one-third of the channel will move in the negative x direction at the velocity determined by its y position. Then, as the particle approaches the flight, it turns around and will move in the positive x direction at location y^* . The relationship between y and y^* can be obtained by a simple mass balance. We shall return to this subject and its implication in Chapter 7 when discussing extensive mixing in screw extruders.

The velocity profile just derived has been repeatedly verified experimentally (17b). Deviation from it occurs only in the close neighborhood of the flights [at $x < H/2$ or $x > (W - H/2)$], where the fluid acquires $v_y(x, y)$ components.

A full analytical solution of the cross channel flow $v_x(x, y)$ and $v_y(x, y)$, for an incompressible, isothermal Newtonian fluid, was presented recently by Kaufman (18), in his study of Renyi entropies (Section 7.4) for characterizing advection and mixing in screw channels. The velocity profiles are expressed in terms of infinite series similar in form to Eq. 6.3-17 below. The resulting vector field for a channel with an aspect ratio of 5 is shown

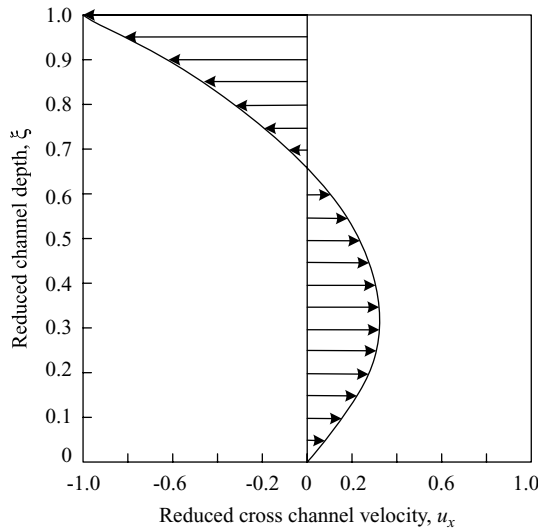


Fig. 6.10 Cross-channel velocity profile from Eq. 6.3-16. Note that melt circulates around a plane located at exactly two-thirds of the height.

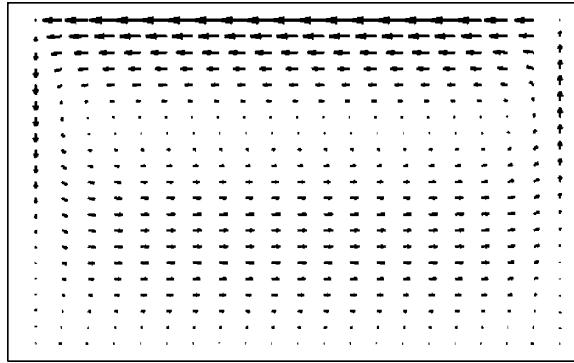


Fig. 6.11 Vector field of the cross-channel flow of an incompressible isothermal Newtonian fluid in a channel with an aspect ratio of 5. [Reprinted by the permission from M. Kaufman, “Advection and Mixing in Single Screw Extruder—An Analytic Model,” *The AIChE Annu. Tech. Conf. Meeting Proc.*, San Francisco (2003).]

in Fig. 6.11. We note the stagnant region in the lower corners and at two-thirds of the height. The side wall effects are evident up to a distance of about $H/2$.

In the down-channel direction, the velocity profile is obtained by solving the partial differential equation (Eq. 6.3-11). It can be shown (17a) that the pressure gradient $\partial P/\partial z$ is constant (although P is a function of both x and z), which makes the solution, where the boundary conditions are $v_z(x, 0) = 0$, $v_z(x, H) = V_{bz}$, $v_z(0, y)$, and $v_z(W, y) = 0$, rather straightforward.

Pure pressure flow was first formulated and solved by Joseph Boussinesq in 1868, and combined pressure and drag flow in 1922 by Rowell and Finlayson (19) in the first mathematical model of screw-type viscous pumps. The detailed solution by the method of separation of variables is given elsewhere (17c), and the resulting velocity profile is given by

$$u_z = \frac{4}{\pi} \sum_{i=1,3,5}^{\infty} \frac{\sinh(i\pi h \zeta)}{i \sinh(i\pi h)} \sin(i\pi \chi) + \left(\frac{H^2}{2\mu V_{bz}} \frac{\partial P}{\partial z} \right) \times \left[\zeta^2 - \zeta + \frac{8}{\pi^3} \sum_{i=1,3,5}^{\infty} \frac{\cosh[i\pi(\chi - 0.5)/h]}{i^3 \cosh(i\pi/2h)} \sin(i\pi \zeta) \right] \quad (6.3-17)$$

where $u_z = v_z/V_{bz}$, $\chi = x/W$, and $h = H/W$.

Figure 6.12 depicts the velocity distribution of pure drag flow ($\partial P/\partial z = 0$) as constant velocity curves at different H/W ratios. We note the increasing significance of the restraining effect of the flight with increasing H/W ratios.

The flow rate through the extruder, the pressure profile along the screw, and the power consumption are the main quantities of interest for design, and these are calculated next from the velocity profile. The net volumetric flow rate Q is obtained by integrating Eq. 6.3-17 across the channel

$$Q = WHV_{bz} \int_0^1 \int_0^1 u_z d\zeta d\chi \quad (6.3-18)$$

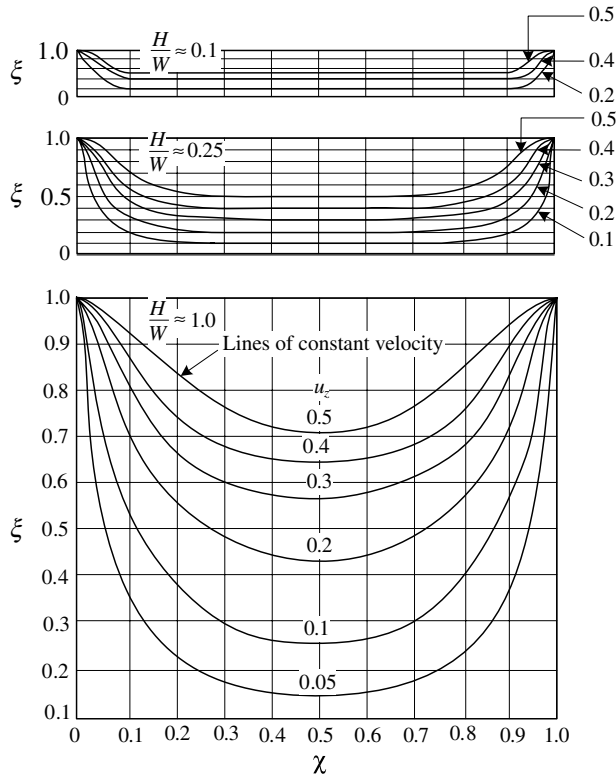


Fig. 6.12 Down-channel velocity distribution for pure drag flow from Eq. 6.3.17 for various H/W ratios. [Reprinted by permission from E. C. Bernhardt, Ed., *Processing of Thermoplastic Materials*, Reinhold, New York, p. 290 (1959).]

The integration of the infinite series in Eq. 6.3-17 is permissible termwise, because the series is uniformly converging. The results are given by

$$Q = \frac{V_{bz}WH}{2} F_d + \frac{WH^3}{12\mu} \left(-\frac{\partial P}{\partial z} \right) F_p \tag{6.3-19}$$

where F_d and F_p are “shape factors” for drag and pressure flow, respectively. They assume values that are smaller than 1 and represent the restricting effect of the flight on flow between infinite parallel plates. They are given by

$$F_d = \frac{16W}{\pi^3 H} \sum_{i=1,3,5}^{\infty} \frac{1}{i^3} \tanh\left(\frac{i\pi H}{2W}\right) \tag{6.3-20}$$

$$F_p = 1 - \frac{192H}{\pi^5 W} \sum_{i=1,3,5}^{\infty} \frac{1}{i^5} \tanh\left(\frac{i\pi W}{H}\right) \tag{6.3-21}$$

Note that the shape factors plotted in Fig. 6.13 are a function of only the H/W ratio. The effect of the flight on the pressure flow is stronger than that on drag flow. When the ratio H/W diminishes, both approach unity. In this case, Eq. 6.3-19 reduces to the simplest possible model for pumping in screw extruders, that is, isothermal flow of a Newtonian fluid between two parallel plates.

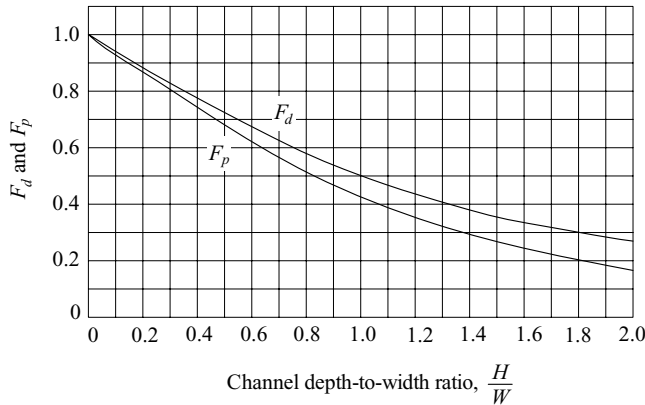


Fig. 6.13 Shape factors for drag and pressure flows from Eqs. 6.3-20 and 6.3-21.

Equations 6.3-19 is the well-known isothermal Newtonian extrusion theory. Since it was obtained by the solution of a linear differential equation, it is composed of two *independent* terms, the first representing the contribution of drag flow Q_d , and the second, the pressure flow, Q_p . The net flow rate is the linear superposition of the two.

$$Q = Q_d + Q_p \quad (6.3-22)$$

We note that if the pressure gradient is positive (pressure rises in the direction of flow), the pressure-flow term is negative and $Q < Q_d$, whereas if pressure drops in the direction of flow, $Q > Q_d$. The ratio of pressure to drag flow is obtained from Eq. 6.3-19

$$\frac{Q_p}{Q_d} = -\frac{H^2}{6\mu V_{bz}} \left(\frac{\partial P}{\partial z} \right) \frac{F_p}{F_d} \quad (6.3-23)$$

A negative pressure flow for the positive pressure gradient led to the term *back flow*, namely, that the pressure drives the fluid opposite to the direction of the net flow. This term led to the erroneous concept that actual flow toward the feed end occurs in some part of the channel. However, it is important to note that *under no condition* does the melt flow backward along the screw axis.⁵ Fluid particles may move backward along the z direction, but not along the axial direction, l . Once a fluid particle passes a given axial location, it cannot cross this plane backward. This is evident from the velocity profile in the axial direction:

$$v_l = v_x \cos \theta + v_z \sin \theta \quad (6.3-24)$$

Substituting Eqs. 6.3-16 and 6.3-17 (which for very shallow channels simplify to the velocity profile between infinite parallel plates given in Eq. E2.5-8 with $V_0 = V_{bz}$, and $(P_L - P_0)/L = \partial P/\partial z$ into Eq. 6.3-24, using Eq. 6.3-23, and assuming that $\theta_b \cong \theta$, we get

$$u_l = 3\xi(1 - \xi) \left(1 + \frac{Q_p}{Q_d} \right) \sin \theta \cos \theta \quad (6.3-25)$$

5. Except if a head pressure higher than the pressure generated by the screw is imposed at the discharge end (e.g., by another extruder in head-on configuration).

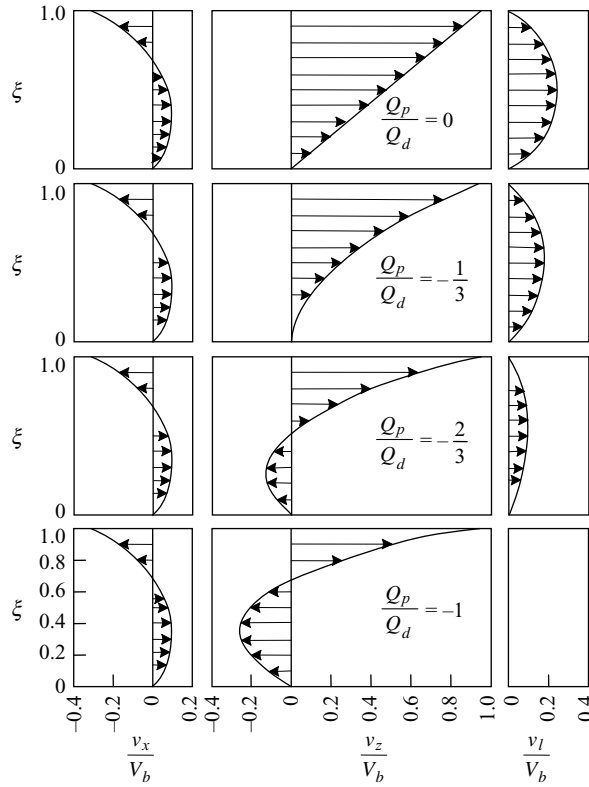


Fig. 6.14 Cross-channel, down-channel, and axial velocity profiles for various Q_p/Q_d values, in shallow square-pitched screws [Reproduced by permission from J. M. McKelvey, *Polymer Processing*, Wiley, New York, 1962.]

where $u_l = v_l/V_b$. We observe that this equation implies that for helix angles between 0 and $\pi/2$, u_l is always positive. In other words, in the axial direction there cannot be any backflow. Moreover, the shape of the velocity profile is parabolic with the maximum velocity at midplane $\xi = 0.5$. The value at the maximum is determined by the pressure to drag flow ratio. For closed discharge ($Q_d + Q_p = 0$), u_l vanishes everywhere. The maximum velocity increases with reduction in pressure flow until it reaches a maximum value for pure drag flow

$$u_{l,max} = \frac{3}{4} \sin \theta \cos \theta \tag{6.3-26}$$

The velocity at any ξ as indicated by Eq. 6.3-25 is a function of the helix angle θ and attains a maximum value at $\theta = \pi/4$. Hence this is also the optimum helix angle for maximum flow rate.⁶ Figure 6.14 shows cross- and down-channel and axial velocity profiles for various pressure-to-drag flow ratios. From the velocity profiles, we can deduce the path of the fluid particles in the channel, as depicted in Fig. 6.15.

6. In spite of this, screws are normally square pitched with a 17.6° helix angle. The reason is that the optimum is rather flat and the gain in flow rate not that significant. Moreover, a 45° helix will yield a more sensitive screw to fluctuating head pressure, and finally, the other elementary steps are not necessarily optimal at 45° .

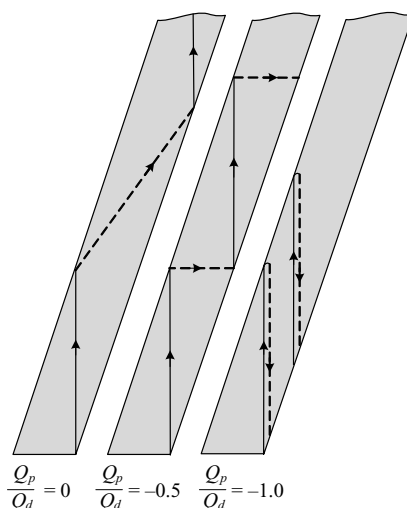


Fig. 6.15 The path of a fluid particle in the screw channel for $Q_p/Q_d = 0$, $Q_p/Q_d = -0.5$, $Q_p/Q_d = -1.0$. Solid lines show the path of the fluid in the upper portion of the channel at a selected value of $\xi = 0.9$, and the broken lines show the path of the same fluid particle in the lower portion of the channel at the corresponding $\xi^* = 0.35$.

At closed discharge conditions when the net flow rate or throughput is zero ($Q_p/Q_d = -1$), the fluid particle circulates at a fixed axial plane by advancing and retreating in the z and x directions. As the particles come close to the flight, they acquire velocity in the y direction (neglected in this model) and turn around. Under closed discharge conditions we also note that fluid particles at $\xi = 2/3$ are stationary. As the throughput increases, the loops open and the fluid particles travel along a flattened helical path. The closer the flow is to pure drag flow, the more open the loops of the helix are. Thus polymer particles travel in a path that is a flat helix within a helical channel.

So far we have neglected the effect of the flight clearance. As small as the clearance is, polymer melt is being dragged across the clearance by the barrel surface and the pressure drop may pump melt across the flight width. This creates a continuous leakage flow from downstream locations to (one turn back) upstream locations, reducing net flow rate.

It is very difficult to accurately evaluate the effect of leakage flow across the flight in a real situation with significant non-Newtonian and nonisothermal effects included. At the very high shear rates prevailing in the clearance, these might be quite significant, and even tax sophisticated finite element methods (FEMs). But for the isothermal Newtonian model, a useful approximate solution has been derived (17d). The analysis leads to a modified design equation (Eq. 6.3-19):

$$Q = \frac{V_{bz}W(H - \delta_f)}{2} F_d + \frac{WH^3}{12\mu} \left(-\frac{\partial P}{\partial z} \right) F_p(1 + f_L) \quad (6.3-27)$$

where δ_f is the radial flight clearance and f_L is given by

$$f_L = \left(\frac{\delta_f}{H} \right)^3 \frac{e}{W} \frac{\mu}{\mu_f} + \frac{\left(1 + \frac{e}{W} \right) \left[\frac{1 + e/W}{\tan^2 \theta} + \frac{6\mu V_{bz}(H - \delta_f)}{H^3(\partial P/\partial z)} \right]}{1 + \frac{\mu}{\mu_f} \left(\frac{H}{\delta_f} \right)^3 \frac{e}{W}} \quad (6.3-28)$$

where μ_f is the viscosity in the flight clearance and μ is the viscosity in the channel. This is an attempt to approximately account for non-Newtonian effects by evaluating the viscosity at the prevailing shear rates in the clearance. For Newtonian fluids the two are equal.

Equation 6.3-28 suggests that drag flow is always reduced by the flight clearance by a factor of $1 - \delta/H$. The effect of pressure flow is more complicated. In the special case of pure drag flow ($\partial P/\partial z = 0$), the cross-channel pressure gradient creates higher pressure at the pushing flight than one turn back at the trailing flight, causing pressure leakage back-flow across the flight. This leakage flow increases if pressure rises in the down-channel direction, and decreases if pressure drops in the down-channel direction over that one turn segment.

We have seen how the screw extruder pump is *synthesized* from a simple building block of two parallel plates in relative motion. We have also seen how the *analysis* of the screw extruder leads in first approximation back to the shallow channel parallel plate model. We carried out the analysis for isothermal flow of a Newtonian fluid, reaching a model (Eq. 6.3-27) that is satisfactory for gaining a deeper insight into the pressurization and flow mechanisms in the screw extruder, and also for first-order approximations of the pumping performance of screw extruders.

The screw extruder is equipped with a die, and the flow rate of the extruder as well as the pressure rise at a given screw speed are dependent on both, as shown in Fig. 6.16. The screw characteristic line at a given screw speed is a straight line (for isothermal Newtonian fluids). This line crosses the abscissa at open discharge (drag flow rate) value and the ordinate at closed discharge condition. The die characteristic is linearly proportional to the pressure drop across the die. The operating point, that is, the flow rate and pressure value at which the system will operate, is the cross-point between the two characteristic lines, when the pressure rise over the screw equals the pressure drop over the die.

The classic extrusion model gives insight into the screw extrusion mechanism and first-order estimates. For more accurate design equations, it is necessary to eliminate a long series of simplifying assumptions. These, in the order of significance are (a) the shear rate-dependent non-Newtonian viscosity; (b) nonisothermal effects from both conduction and viscous dissipation; and (c) geometrical factors such as curvature effects. Each of these

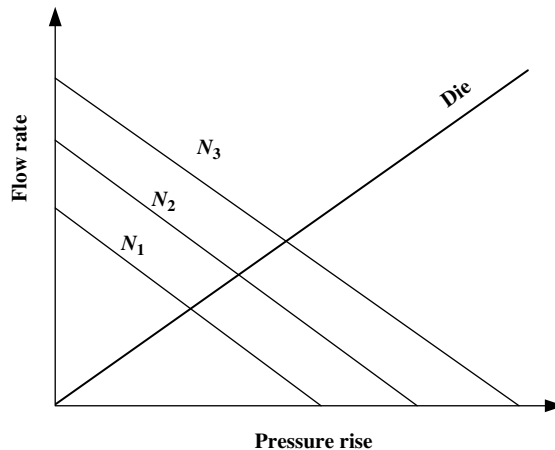


Fig. 6.16 Screw characteristic lines at three screw speeds $N_1 < N_2 < N_3$ and die characteristic line.

introduces significant mathematical complications. Thus, whereas it is possible to derive analytical parallel-plate extrusion models for an isothermal non-Newtonian fluid (e.g., using Power Law or Ellis fluid models), it is impossible to have an analytical solution for channel flows and certainly for nonisothermal flows.

Even the parallel plate non-Newtonian isothermal model is no longer a linear superposition of drag and pressure flow, but a more complex combination of the variables. Nonisothermal flows by and large require numerical solutions. The ultimate model would be a model for nonisothermal flow of a non-Newtonian fluid in the actual helical channel, including leakage flow and accounting for boundary conditions (e.g., barrel temperature and screw temperature profiles,⁷ and possible slip on solid surfaces). Recent advances in computerized fluid mechanics (CFM) using FEMs indeed enable such solutions. However, they may be time-consuming and expensive and also exhibit numerical difficulties with real melts that are not only shear thinning but also viscoelastic fluids, in situations of sudden changes in geometry, such as, for example, at the entrance and exit to flight clearance, and with circulating flows as those occurring in the screw channel.

Historically, before CFM or even FEMs were available, two complementary approaches were used to tackle this problem. On the one hand, there was a continuing effort to solve increasingly more realistic flow situations analytically or numerically. This approach was taken by Griffith (20), Colwell and Nicholls (21), Pearson (22) Zamodits (23), Booy (24), Choo et al. (25), Nebrensky et al. (26), Hami and Pittman (27), Pearson (28), Pittman and Rashid (29), Bruker et al. (30), and others. On the other hand, “approximate correction factors” were derived using simple models, which could improve accuracy by accounting at least for the bulk part of the complexity. The “shape factors” in Eq. 6.3-27 can be viewed as correction factors accounting for the wall effect on the parallel-plate model. Thus, by comparing Couette and annular pressure flow with straight corresponding straight-channel flows, a “curvature correction” factor can be derived separately for drag and pressure flows (17e). Some nonisothermal correction factors and non-Newtonian correction factors can be similarly evaluated. These lumped-parameter stepwise models, discussed in Section 9.1, surprisingly agree reasonably well with experiments using minimal computational effort.

6.4 KNIFE AND ROLL COATING, CALENDERS, AND ROLL MILLS

Knife coating is shown schematically in Fig. 6.17, and roll coating, roll mills, and calenders are shown schematically in Fig. 6.18. These are devices that generate pressure on the basis of Building Blocks 3 and 4, namely, two nonparallel plates in relative or joint motion. The processing function of each device is made possible by the fact that these geometrical configurations can generate pressure. Thus they are not pumps per se, although two rolls can act as a continuous pump, as shown in Fig 6.18(d).

7. The correct barrel temperature to be used is the inner surface temperature. This is generally not known and a heat transfer problem in the barrel must be solved in conjunction with the flow model of the melt in the screw channel. Screw temperature is generally not controlled and it can be assumed to be roughly equal to the average melt temperature.

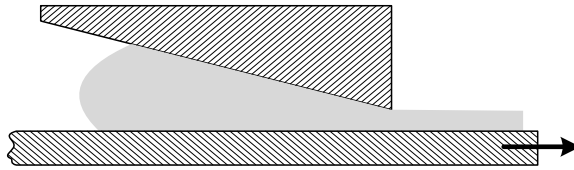


Fig. 6.17 Schematic representation of knife coating, based on building block 3.

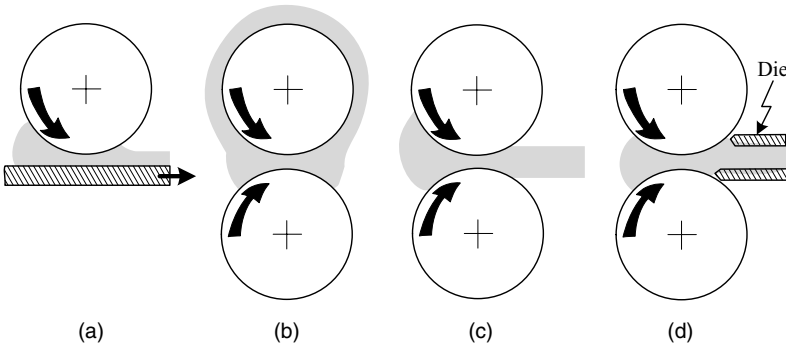


Fig. 6.18 Schematic representation of pressure generating devices based on building blocks 4: (a) roll coating; (b) roll mill; (c) calender; (d) twin roll extruder.

Non-parallel Plate Drag Flow

The flow configuration of building block 3, of two non-parallel plates in relative motion, shown in Fig. 6.19, was analyzed in detail in Example 2.8 using the lubrication approximation and the Reynolds equation. This flow configuration is not only relevant to knife coating and calendering, but to SSEs as well, because the screw channel normally has constant-tapered sections. As shown in Fig. 6.19, the gap between the plates of length L is H_0 and H_1 at the entrance and exit, respectively, and the upper plate moves at constant velocity V_0 .

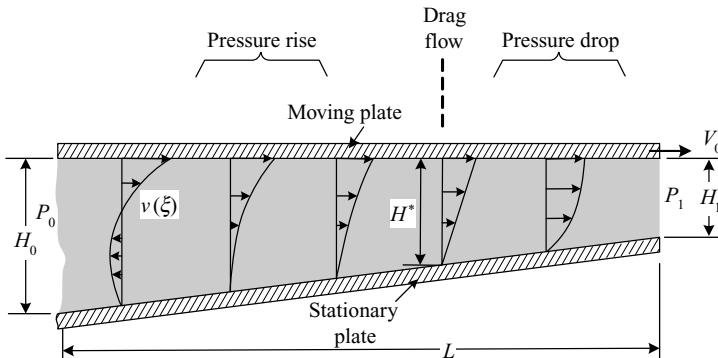


Fig. 6.19 Two non-parallel plates in relative motion, with schematic velocity profiles for a condition with equal entrance and exit pressure, in which case the pressure profile exhibits a maximum in the flow range.

As shown in Example 2.8, the pressure profile along the plates is given by

$$P = P_0 + \frac{6\mu LV_0}{H_0 H_1} \left[\frac{\zeta_0 - \zeta}{\zeta(\zeta_0 - 1)} - \left(\frac{q}{V_0 H_0} \right) \frac{\zeta_0^2 - \zeta^2}{\zeta^2(\zeta_0 - \zeta)} \right] \tag{6.4-1}$$

where P_0 is pressure at the entrance, $\zeta_0 = H/H_1$, $\zeta = H_0/H_1$, and q is the volumetric flow rate per unit width, which can be expressed in terms of the channel gap where pressure exhibits a maximum value, H^*

$$q = \frac{1}{2} V_0 H^* \tag{6.4-2}$$

The pressure profile thus depends on a number of variables: geometrical (H_0 , H_1 , and L), operational (q , V_0), and physical property variables, and the viscosity μ . The maximum pressure that can be attained is $\zeta = 1$ ($z = L$) at closed discharge condition ($q = 0$)

$$P_{\max} = P_0 + \frac{6\mu V_0 L}{H_0 H_1} \tag{6.4-3}$$

By examining Eq. 6.4-1, as pointed out in Example 2.8, we see that at equal entrance and discharge pressures, the pressure profile exhibits a maximum at $H^* = 2H_0/(1 + \zeta_0)$, or at $z/L = \zeta_0/(1 + \zeta_0)$, which for $\zeta_0 = 2$ is two-third of the way down the channel. This result focuses attention on the important difference between parallel plate and non-parallel plate geometries. In the former, equal inlet and outlet pressures imply no pressurization and pure drag flow; in the latter it implies the existence of a maximum in pressure profile. Indeed, as we saw in Section 2.11, Example 2.9, this pressurization mechanism forms the foundation of hydrodynamic lubrication.

The gap between the plates does not have to change gradually; it can be an abrupt change, as shown in Fig. 6.20, with a pressure profile rising linearly and then dropping linearly, with the maximum value at the step decrease in height. Slider pads are used for hydrodynamic lubrication because they have good loading capacity. Westover (31) converted this pressurization method into a continuous rotary slider pad pump, as shown in Fig. 6.21.

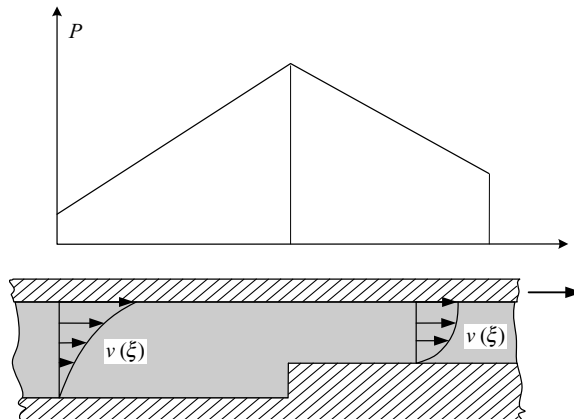


Fig. 6.20 Schematic representation of a slider pad.

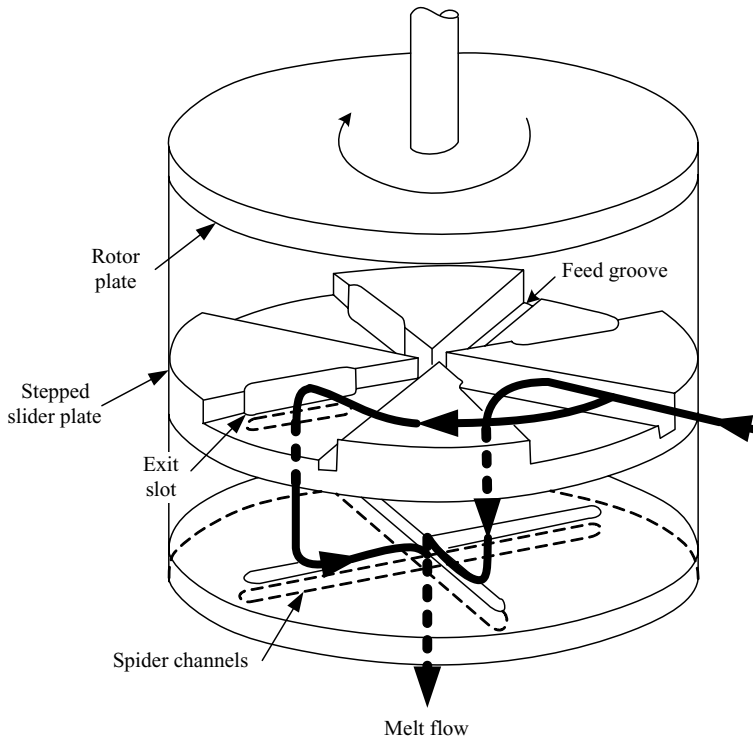


Fig. 6.21 A rotary-sector slider pad extruder. [Reprinted by permission from R. F. Westover, “A Hydrodynamic Screwless Extruder” *Soc. Plastics Eng. J.*, 1473 (1962).]

Finally, as pointed out earlier, extruder screws have tapered channel sections. The various shaped pressure profiles that can be obtained in simple non-parallel plate geometry explain the experimentally observed pressure profiles in screw extruders. For example, in a common metering screw (with a constant channel depth feed section, followed by a tapered section and a constant channel depth metering section), under normal conditions the pressure profile exhibits a maximum in the tapered section with the pressure dropping in the metering section to the die pressure.

From Eq. 6.4-1, with $\zeta = 1$ we can obtain an expression for the flow rate in terms of the pressure drop over the tapered section given by

$$q = \frac{V_0 H_0}{2} \left(\frac{2}{1 + \zeta_0} \right) + \frac{H_0^3}{12\mu} \left(\frac{P_0 - P_1}{L} \right) \left(\frac{2}{\zeta_0(1 + \zeta_0)} \right) \quad (6.4-4)$$

For parallel plates, $\zeta_0 = 1$, this equation reduces to Eq. 6.3-19 with pressure *drop* replacing pressure *gradient*. Hence, the terms containing ζ_0 can be viewed as “correction factors” of the parallel plate model for tapered geometries.

Example 6.8 Knife Coating Consider a knife at angle to a substrate, which moves at velocity V_0 and being covered by a thin film coating of a viscous Newtonian liquid of thickness δ , as shown schematically in Fig. E6.8. Derive an expression for the film thickness δ .

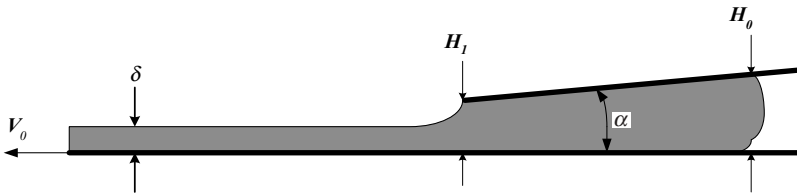


Fig. E6.8 An infinitely long substrate coated by a knife coater at angle α to it.

Solution We assume that Eq. 6.4-4 holds with $P_0 = P_1$ and $q = V_0\delta$, and it reduces to

$$\delta = \frac{H_0}{1 + \zeta_0} = \frac{H_1}{1 + 1/\zeta_0}$$

where $\zeta_0 = H_0/H_1$. Clearly, for a knife placed parallel to the substrate, the thickness of the coating is one half of the gap, and the higher the taper the closer the thickness comes to the gap size at the exit point, which will be reached with a sharp-edge coating, with the knife perpendicular to the substrate.

Two Rotating Rolls: Roll Mills and Calenders

The two rotating roll geometry of roll-mills and calenders is an important application of the non-parallel plate pressurization concept with both plates moving, stemming from building block 4 in Figure 6.2. There are, however, some differences between the two cases. In roll mills the operation is generally a batch operation with the polymer forming a continuous blanket around one of the rolls and the two rolls generally rotating at different frequencies. In calenders, on the other hand, there is one pass between any set of two rolls, which occasionally are of different radii, and operate at different speeds. The purpose of the former is to melt and mix the polymer, whereas the aim of the latter is to shape a product. Hence, we discuss roll mills in more detail in Chapter 7, which deals with mixing, and in Chapter 15, which covers calendering. Nevertheless the nip flow in both cases is based on the same principle of pressurization, and thus it is addressed in this chapter.

Figure 6.22 depicts schematically the flow configuration. Two identical rolls of radii R rotate in opposite directions with frequency of rotation N . The minimum gap between the rolls is $2H_0$. We assume that the polymer is uniformly distributed laterally over the roll width W . At a certain axial (upstream) location $x = X_2$ ($X_2 < 0$), the rolls come into contact with the polymeric melt, and start “biting” onto it. At a certain axial (downstream) location $x = X_1$, the polymeric melt detaches itself from one of the rolls. Pressure, which is assumed to be atmospheric at X_2 , rises with x and reaches a maximum upstream of the minimum gap location (recall the foregoing discussion on the pressure profile between non-parallel plates), then drops back to atmospheric pressure at X_1 . The pressure thus generated between the rolls creates significant separating forces on the rolls. The location of points X_1 and X_2 depends on roll radius, gap clearance, and the total volume of polymer on the rolls in roll mills or the volumetric flow rate in calenders.

First we derive the simple Newtonian model following Gaskell’s (32) and McKelvey’s (33) models. The following assumptions are made: the flow is steady, laminar, and isothermal; the fluid is incompressible and Newtonian; there is no slip at the walls; the

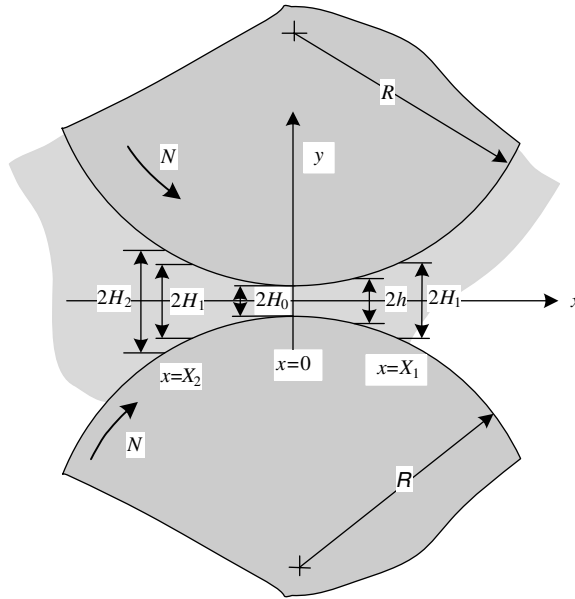


Fig. 6.22 The nip region of the two-roll geometry, with radii R . A rectangular coordinate system is placed at the midplane in the gap between the rolls connecting the two roll centers.

clearance-to-radius ratio is $h/R \ll 1$ throughout the region; in other words, we assume narrow gap flow with slowly varying gap separation, which enables us to invoke the lubrication approximation (which implies that the velocity profile at any location x with local gap separation $2h$ equals the velocity profile between two infinite parallel plates at a distance $2h$ apart, with pressure gradient and plate velocities equal to the local values between the rolls); finally, gravity forces are neglected and there is only one nonvanishing component $v(y)$. Hence, the equation of continuity and motion, respectively, reduce to

$$\frac{dv_x}{dx} = 0 \tag{6.4-5}$$

and

$$\frac{dP}{dx} = -\frac{\partial\tau_{yx}}{\partial y} = \mu\frac{\partial^2v_x}{\partial y^2} \tag{6.4-6}$$

Equation 6.4-6 can be integrated twice without difficulty, because the pressure P is a function of x only. The boundary conditions are $v_x(\pm h) = U$, where U is the tangential velocity of the roll surface

$$U = 2\pi NR \tag{6.4-7}$$

The resulting velocity profile is

$$v_x = U + \frac{y^2 - h^2}{2\mu} \left(\frac{dP}{dx} \right) \tag{6.4-8}$$

Note that Eq. 6.4-8 indicates that for a positive pressure gradient (i.e., pressure rises in the positive x direction), $v_x(0) < U$, and for a negative pressure gradient, $v_x(0) > U$.

The flow rate per unit width q is obtained by integrating Eq. 6.4-8 to give

$$q = 2 \int_0^h v_x dy = 2h \left(U - \frac{h^2}{3\mu} \frac{dP}{dx} \right) \quad (6.4-9)$$

At steady state, q is constant and dependent on position x . To solve for the pressure profile, we require that the velocity be uniform at the exit $v_x(y) = U$. This requirement implies that $\tau_{yx} = 0$, and from Eq. 6.4-6 we conclude that the pressure gradient also vanishes at this point. Hence, the flow rate in Eq. 6.4-9 can be expressed in terms H_1 and U as

$$q = 2H_1U \quad (6.4-10)$$

Substituting Eq. 6.4-10 into Eq. 6.4-9, subsequent to some rearrangement, gives

$$\frac{dP}{dx} = \frac{3\mu}{H_1^2} \left(1 - \frac{H_1}{h} \right) \left(\frac{H_1}{h} \right)^2 \quad (6.4-11)$$

Equation 6.4-11 implies that the pressure gradient is zero not only at $x = X_1$ but also at $x = -X_1$, where h also equals H_1 , and where, as we shall see later, the pressure profile exhibits maximum. The pressure profile is obtained by integrating Eq. 6.4-11 with the boundary condition $P(X_1) = 0$. First, however, we must find a functional relationship between h and x . From plane geometry we get the following relationship

$$h = H_0 + R - \sqrt{R^2 - x^2} \quad (6.4-12)$$

which can be simplified by expanding the $\sqrt{R^2 - x^2}$ using the binomial series and retaining only the first two terms. This results in

$$\frac{h}{H_0} = 1 + \rho^2 \quad (6.4-13)$$

where

$$\rho^2 = \frac{x^2}{2RH_0} \quad (6.4-14)$$

Integration of Eq. 6.4-11, subsequent to substituting Eqs. 6.4-13 and 6.4-14, gives the pressure profile

$$P = \frac{3\mu U}{4H_0} \sqrt{\frac{R}{2H_0}} \left\{ \left[\frac{\rho^2 - 1 - 5\lambda^2 - 3\lambda^2\rho^2}{(1 + \rho^2)^2} \right] \rho + (1 - 3\lambda^2) \tan^{-1} \rho + C(\lambda) \right\} \quad (6.4-15)$$

where

$$\lambda^2 = \frac{X_1^2}{2RH_0} \quad (6.4-16)$$

and the constant of integration $C(\lambda)$ is obtained by setting $P = 0$ at $\rho = \lambda$

$$C(\lambda) = \frac{(1 + 3\lambda^2)}{(1 + \lambda^2)}\lambda - (1 - 3\lambda^2)\tan^{-1}\lambda \quad (6.4-17)$$

McKelvey suggested the following approximation for $C(\lambda)$

$$C(\lambda) \cong 5\lambda^3 \quad (6.4-18)$$

The maximum pressure is obtained by substituting $\rho = -\lambda$ into Eq. 6.4-15

$$P_{\max} = \frac{3\mu U}{4H_0} \sqrt{\frac{R}{2H_0}} [2C(\lambda)] \cong \frac{15\mu U \lambda^3}{2H_0} \sqrt{\frac{R}{2H_0}} \quad (6.4-19)$$

Note that the maximum pressure is very sensitive to λ . An increase in λ brings about both a broadening of the pressure profile as well as an increase in the maximum value. This is demonstrated in Fig. 6.23 where $P/P_{\max, \lambda=1}$ is plotted versus ρ with λ as a parameter.

Results indicate that for any given λ , there is a particular upstream position at which the pressure drops to zero, which is denoted as X_2 . This unique relationship between λ and X_2 , obtained by setting $P = 0$ in Eq. 6.4-15, is plotted in Fig. 6.24 in terms of $\rho_2 = X_2 \sqrt{2RH_0}$. Note that both ρ_2 and X_2 are negative. Finally, another property of the pressure profile is that at $x = 0$, the pressure equals exactly $P_{\max}/2$.

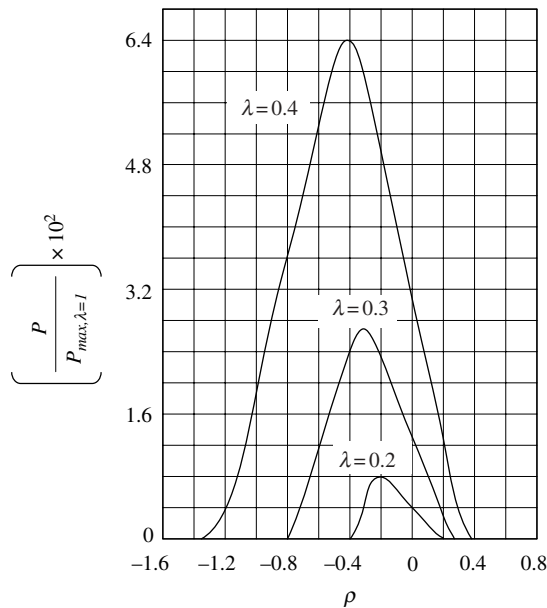


Fig. 6.23 Pressure profiles between rolls with λ as a parameter. [Reprinted by permission from J. M. McKelvey, *Polymer Processing*, Wiley, New York, 1962.]

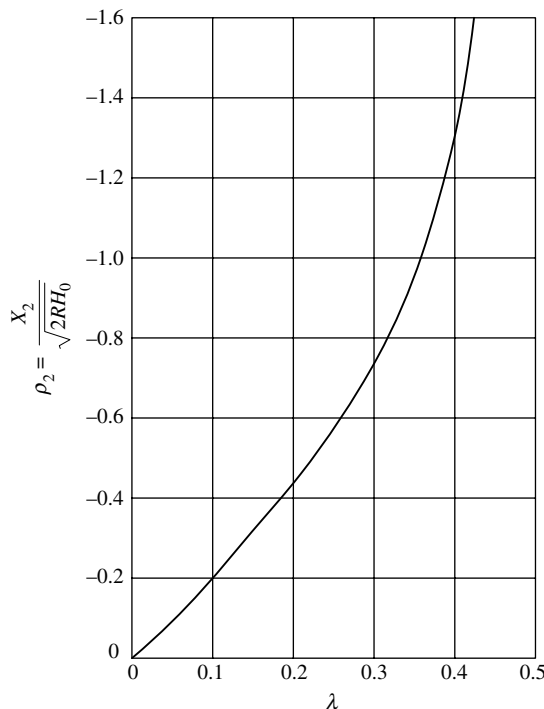


Fig. 6.24 Relationship between ρ_2 , where the rolls “bite” onto the polymer (equivalent to X_2) and λ where the polymer detaches (equivalent to X_1). [Curve based on computation from G. Ehrmann and J. Vlachopoulos, *Rheol. Acta*, **14**, 761 (1975).]

The velocity profile is obtained by substituting Eq. 6.4-11 into Eq. 6.4-8, with the aid of Eqs. 6.4-13, 6.4-14, and 6.4-16

$$u_x = 1 + \frac{3(1 - \xi^2)(\lambda^2 - \rho^2)}{2(1 + \rho^2)} \quad (6.4-20)$$

where $u_x = v_x/U$ and $\xi = y/H$. Figure 6.25 shows velocity profiles for $\lambda^2 = 0.1$.

Equation 6.4-20 indicates that at a certain axial location ρ^* at $\xi = 0$, a stagnation point may occur ($v_x(0) = 0$)

$$\rho^* = -\sqrt{2 + 3\lambda^2} \quad (6.4-21)$$

For $\lambda = 0.425$, the stagnation point is at the contact point; hence, for $\lambda > 0.425$ a circulatory flow develops in the entrance region.

The rate of strain and stress distributions can now be obtained from the velocity profile, which together with Eq. 6.4-13, gives:

$$\dot{\gamma}_{yx}(\xi) = \frac{3U(\rho^2 - \lambda^2)}{H_0(1 + \rho^2)^2} \xi \quad (6.4-22)$$

and

$$\tau_{yx}(\xi) = \frac{3\mu U(\lambda^2 - \rho^2)}{H_0(1 + \rho^2)^2} \xi \quad (6.4-23)$$

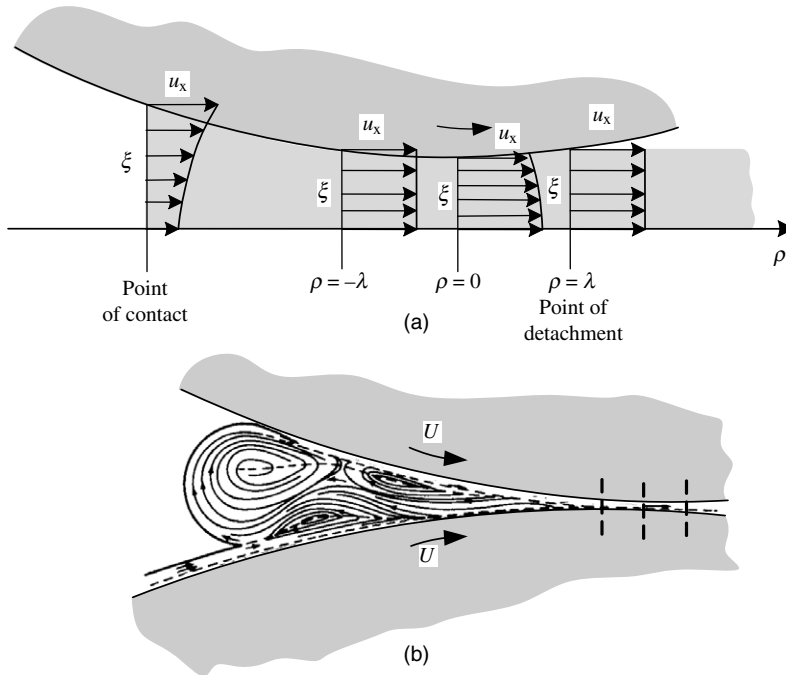


Fig. 6.25 (a) Velocity profiles between rolls for $\lambda^2 = 0.1$ from Eq. 6.4-25. At $\rho = \pm\lambda$ velocity profiles are flat (plug type flow) because pressure gradients vanish at these locations. At $\rho = -2.46\lambda$ the melt comes in contact with the rolls and the velocity profile indicates a pressure rise in the direction of flow. (b) Schematic view of flow patterns obtained by W. Unkrüer using color tracers. His results indicate circulation patterns not predicted by the Gaskell model. [W. Unkrüer, “Beitrag zur Ermittlung des Druckverlaufes und der Fließvorgänge im Walzspalt bei der Kalanderverarbeitung von PVC Hart zu Folien,” Doctoral Dissertation, Technische Hochschule Aachen, Aachen, Germany, 1970. See also, W. Unkrüer, *Kunststoffe*, **62**, 7 (1972).]

An extremum in shear rate $\dot{\gamma} = |\dot{\gamma}_{yx}|$ and stress occur at the roll surface at $\rho = 0$, where the gap is at minimum

$$\dot{\gamma}_{\text{ext}} = \frac{3U\lambda^2}{H_0} \tag{6.4-24}$$

and

$$\tau_{\text{ext}} = \frac{3\mu U\lambda^2}{H_0} \tag{6.4-25}$$

but the overall maximum value of the shear stress and shear rate occur at $\rho = \rho_2$ if $\rho_2 > -\sqrt{1 + 2\lambda^2}$, and at $\rho = -\sqrt{1 + 2\lambda^2}$ if $\rho_2 < -\sqrt{1 + 2\lambda^2}$. The total power input into both rolls can now be calculated by integrating the product of roll velocity and the shear stress at the surface, which is obtained by setting $\xi = 1$ in Eq. 6.4-23

$$P_w = 2UW\sqrt{2RH_0} \int_{\rho_2}^{\lambda} \tau_{yx}(1) d\rho \tag{6.4-26}$$

where W is the width of the rolls, resulting in

$$P_w = 3\mu WU^2 \sqrt{\frac{2R}{H_0}} f(\lambda) \quad (6.4-27)$$

where

$$f(\lambda) = (1 - \lambda^2) [\tan^{-1} \lambda - \tan^{-1} \rho_2] - \left[\frac{(\lambda - \rho_2)(1 - \rho_2 \lambda)}{(1 + \rho_2^2)} \right] \quad (6.4-28)$$

Figure 6.26(a) plots the function $f(\lambda)$.

Finally, the force separating the two rolls is obtained by integrating the pressure given in Eq. 6.4-15 over the area of the rolls this pressure acts upon

$$F_N = W \sqrt{2RH_0} \int_{\rho_2}^{\lambda} P d\rho \quad (6.4-29)$$

resulting in

$$F_N = \frac{3\mu URW}{4H_0} g(\lambda) \quad (6.4-30)$$

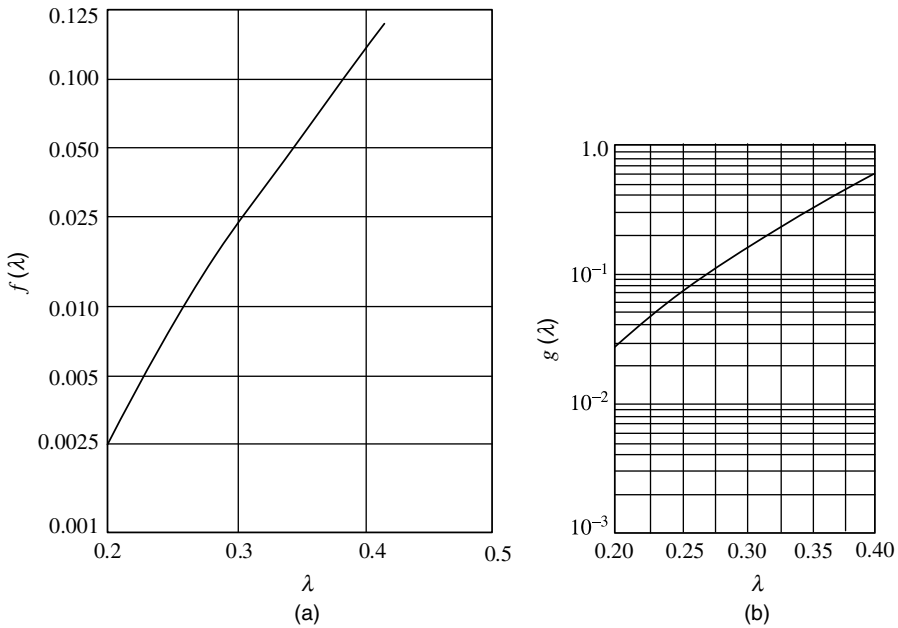


Fig. 6.26 (a) Relation between $f(\lambda)$ and λ from Eq. 6.4-28 [Reprinted by permission from G. Ehrmann and J. Vlachopoulos, *Rheol. Acta.*, **14**, 761-764 (1975).] (b) $g(\lambda)$ and λ from Eq. 6.4-31. [Reprinted by permission from J. M. McKelvey, *Polymer Processing*, Wiley, New York 1962.)]

where

$$g(\lambda) = \left(\frac{\lambda - \rho_2}{1 + \rho_2^2} \right) [-\rho_2 - \lambda - 5\lambda^3(1 + \rho_2^2)] + (1 - 3\lambda^2)[\lambda \tan^{-1} \lambda - \rho_2 \tan^{-1} \rho_2] \quad (6.4-31)$$

The function $g(\lambda)$ is given in Fig. 6.26(b). Note that in calculating the separating force, we have neglected the roll curvature, which is consistent with the simplifying assumption on which the model is based, namely, that $h/R \ll 1$. The treatment of non-Newtonian fluids was outlined by Gaskell (32) in his original publication for Bingham Fluids. Later, McKelvey (33) reported a detailed solution for Power Law model fluids.

As shown in Fig. 6.25(a) $\dot{\gamma}_{yx}(\xi) \geq 0$ for $\rho < -\lambda$, and $\dot{\gamma}_{yx} \leq (\xi) \leq 0$ for $\rho > -\lambda$, where $-\lambda$ is a yet unknown location, and where the pressure profile exhibits a maximum value (or $dP/dx = 0$). Moreover, because of symmetry, we have the convenient boundary condition $\tau_{yx} = \dot{\gamma}_{yx} = 0$ at $y = 0$ or $\xi = 0$. Making the same simplifying assumptions as the Newtonian analysis, the following results are obtained for the velocity profile and flow rate:

$$v_x = U + \frac{\text{sign}(\dot{P})}{(1+s)} \left[\frac{\text{sign}(\dot{P})}{m} \frac{dP}{dx} \right] (y^{1+s} - h^{1+s}) \quad (6.4-32)$$

where $\text{sign}(\dot{P})$ is defined as

$$\text{sign}(\dot{P}) = \frac{dP/dx}{|dp/dx|} = \begin{pmatrix} +1 & \rho < -\lambda \\ -1 & \rho > -\lambda \end{pmatrix} \quad (6.4-33)$$

and

$$q = 2h \left\{ U - \text{sign}(\dot{P}) \left(\frac{h}{2+s} \right) \left[\text{sign}(\dot{P}) \frac{h}{m} \frac{dP}{dx} \right]^s \right\} \quad (6.4-34)$$

By expressing the flow rate in terms of the clearance at the point of detachment, the following expression is obtained for the pressure gradient:

$$\frac{dP}{dx} = K \frac{[\text{sign}(\dot{P})(\rho^2 - \lambda^2)]^n}{(1 + \rho^2)^{2n+1}} \quad (6.4-35)$$

where

$$K = \text{sign}(\dot{P}) m \sqrt{\frac{2R}{H_0}} \left[\frac{(2+s)}{2H_0} \right]^n \quad (6.4-36)$$

The pressure profile is obtained by numerical integration of Eq. 6.4-35, where λ is given by Eq. 6.4-16 and is determined by the flow rate.

Experimental measurements of pressure profiles in calenders were conducted by Bergen and Scott (34). A strain gauge transducer was embedded in the surface of one of the 10-in-diameter rolls, and traces were recorded at various conditions corresponding to both calendaring and roll milling.

Figure 6.27 compares the experimental pressure profiles using plasticized thermo-plastic resin (unfortunately, the rheological flow curve was not provided) with

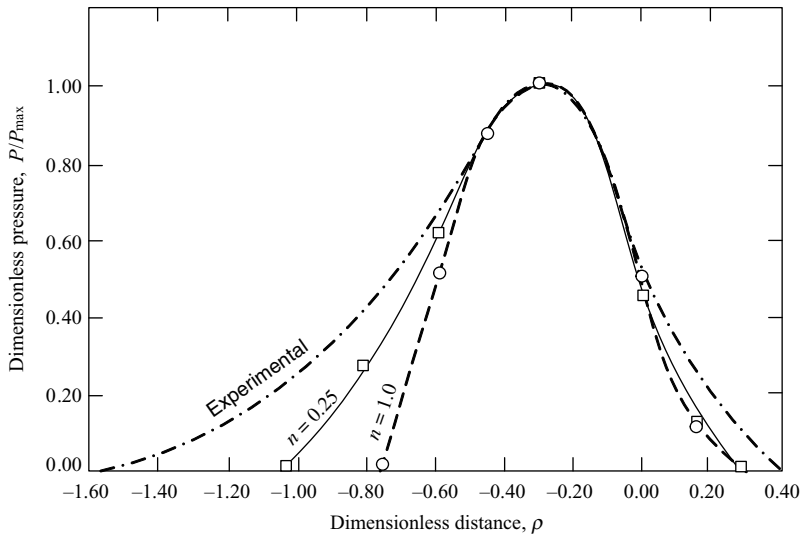


Fig. 6.27 Comparison between experimental pressure profile for plasticized thermoplastic resin (34) and theoretical pressure profiles for $n = 1$ and $n = 0.25$ calculated by Kiparissides and Vlachopoulos (35). The theoretical curves were calculated both by finite element method and analytically by way of Gaskell type models, as discussed in this section, giving virtually identical results. [Reprinted by permission from C. Kiparissides and J. Vlachopoulos, "Finite Element Analysis of Calendering," *Polym. Eng. Sci.*, **16**, 712–719 (1976).]

theoretically calculated profiles by Kiparissides and Vlachopoulos (35) using Newtonian and Power Law model fluid models. The maximum pressure was forced to coincide by appropriate selection of λ . With a Newtonian fluid, a good agreement between experiment and theory is observed in the region $\rho > -\lambda$; whereas, in the region $\rho < -\lambda$, the theoretical prediction falls well below the experimental measurements. The same conclusion is reached when the comparison is made by selecting a viscosity that forces the experimental and theoretical curves to coincide at $\rho = 0$, and matching the location of maximum pressures, as done originally by Bergen and Scott (34). This effective viscosity was lower by three orders of magnitude than the measured viscosity. The latter, however, was measured at much lower shear rates than those prevailing in the nip region.

This disagreement between theory and practice must therefore partly be due to the non-Newtonian shear-thinning viscosity. This conclusion is supported by the work of Kiparissides and Vlachopoulos (35), who showed that for a Power Law model fluid, lower n values reduce the disagreement between theory and experiments, as illustrated in Fig. 6.27. They used the FEM for computing the pressure profile, which eliminates the geometrical approximations needed in the Gaskell model.

Alternatively the two-roll geometry can be conveniently represented by bipolar coordinates, as suggested by Finston (36). This approach, as well as the FEM, enables the analyses of both equal and unequal roll diameters and frequency of rotation, termed asymmetrical calendering. However, the FEM method provides the most flexibility in dealing with both Newtonian and non-Newtonian fluids and asymmetrical calendering. Chapter 15 covers this method in some detail.

In addition to the shear thinning effect, other non-Newtonian properties bring about additional complexities in the flow pattern, as demonstrated by Unkrüer (37), such as cross-machine flow superimposed on the main machine-direction flow in the inlet region.

By using color tracers, he also revealed a much more complex flow and several circulating regions, as shown in Fig. 6.25. The results indicate that the incoming stream of melt elastic normal-stress properties and possibly roll deflection may all affect the flow pattern. All these effects are neglected in the Gaskell model; therefore, it is not surprising that the predication of the model is at variance with the experimental findings. Yet, the model does explain the basic elements of the process; it gives an insight into its nature and can serve well for first-order approximations. Further discussion on calendering is given in Chapter 15.

6.5 THE NORMAL STRESS PUMP

In Section 6.1 we noted that the term $\nabla \cdot \tau$ in the equation of motion is an important source of pressurization. We have further pointed out that this source may be related either to viscosity or to the normal stress difference coefficient. We discuss the latter case in this section.

Consider a two-disk geometry of radii R with one of the disks rotating at frequency Ω and a non-Newtonian polymeric melt filling the space between them, as shown in Fig. 6.28. This geometrical arrangement is a schematic representation of a centripetal⁸ normal stress extruder suggested by Maxwell and Scalora (38) and analyzed by a number of investigators, both theoretically and experimentally (39–41).

When a Newtonian fluid is placed between the disks, the centrifugal forces created by the rotational motion “sucks” the fluid in through the die and expels it at the circumference, much as a centrifugal pump would do. If a non-Newtonian fluid exhibiting normal stresses is placed between the disks, however, an opposite effect is observed, namely, an inward radial flow *into* the die. We have seen in Example 3.2, Eq. E3.2-13, that for the cone-and-plate flow, which is similar to flow between parallel disks, the total thrust on the plate is given by that product of the plate area and one-half the primary normal stress difference. Furthermore, we saw that the experimentally measured radial pressure distribution increases logarithmically with *decreasing* radius, the relationship containing both the primary and secondary normal stress differences.

In the normal stress extruder we first want to evaluate the pressure at the center as a function of disk outer radius, frequency of rotation, and rheological properties. We do this in the absence of radial flow (i.e., for a closed discharge condition), which will give us the

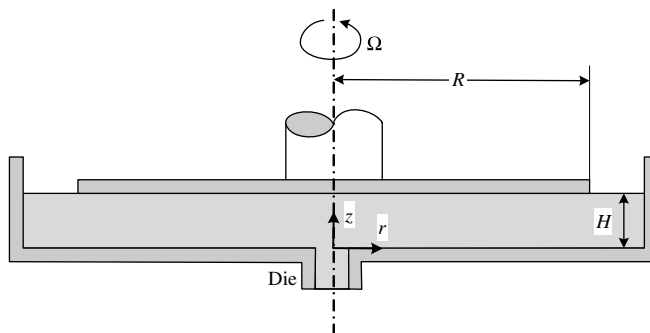


Fig. 6.28 Schematic view of the normal stress extruder. Polymer melt is placed between the disks. The upper disk is attached to a rotating shaft at frequency of rotation Ω . A pressure profile of increasing pressure toward the center develops, and the melt is extruded through the die.

8. The first centripetal pump resulting from non-Newtonian properties of liquids was suggested by Marcus Reiner in the 1950s.

maximum attainable pressure for the set conditions, and we neglect any possible secondary flows as well ($v_r = v_z = 0$), although such flows (“cigar rolling”) have been observed (30). These flows impose practical limits on the pressurization capability of the normal stress extruder by forcing upper limits on Ω and R . Yet even under these rather severe simplifying assumptions, unlike the flow in the cone and plate configuration, the flow between the disks is nonviscometric, because the nonvanishing velocity component v_θ is a function of both r and z , $v_\theta(r, z)$. Nevertheless, we use the Criminale–Ericksen–Filbey (CEF) equation (Eq. 3.3-5), which, as pointed out in Chapter 3, is applicable to moderately nonviscometric flows with reasonable accuracy. Finally, steady isothermal flow with no-slip at the walls is assumed.

To determine what stresses are generated in the torsional disk flow of a CEF fluid, we assume that its flow field is that of a pure viscous fluid; then we calculate the tensor quantities $\nabla \mathbf{v}$, $\dot{\boldsymbol{\gamma}}$, $\boldsymbol{\omega}$, $\{\dot{\boldsymbol{\gamma}} \cdot \dot{\boldsymbol{\gamma}}\}$, $\{\boldsymbol{\omega} \cdot \dot{\boldsymbol{\gamma}}\}$, and $\{\mathbf{v} \cdot \nabla \dot{\boldsymbol{\gamma}}\}$ that appear in the CEF equation. Obtaining these quantities, we substitute them in the constitutive equation to find out which are the nonzero stress components.

Assuming that the flow kinematics of CEF and Newtonian fluids are identical, the velocity profile in steady torsional disk flow is

$$v = \Omega r \frac{z}{H} \quad (6.5-1)$$

where H is the separation between the disks. Thus from Table 2.3 and Table 3.3, we obtain

$$\dot{\boldsymbol{\gamma}} = \begin{pmatrix} 0 & 0 & 0 \\ 0 & 0 & \frac{\Omega r}{H} \\ 0 & \frac{\Omega r}{H} & 0 \end{pmatrix} \quad (6.5-2)$$

$$\boldsymbol{\omega} = \begin{pmatrix} 0 & 2\frac{\Omega r}{H} & 0 \\ -2\frac{\Omega r}{H} & 0 & -\frac{\Omega r}{H} \\ 0 & \frac{\Omega r}{H} & 0 \end{pmatrix} \quad (6.5-3)$$

The following expressions are obtained from Eqs. 6.5-2 and 6.5-3:

$$\{\dot{\boldsymbol{\gamma}} \cdot \dot{\boldsymbol{\gamma}}\} = \begin{pmatrix} 0 & 0 & 0 \\ 0 & \left(\frac{\Omega r}{H}\right)^2 & 0 \\ 0 & 0 & \left(\frac{\Omega r}{H}\right)^2 \end{pmatrix} \quad (6.5-4)$$

$$\{\boldsymbol{\omega} \cdot \dot{\boldsymbol{\gamma}}\} = \begin{pmatrix} 0 & 0 & \frac{2\Omega^2 rz}{H^2} \\ 0 & -\left(\frac{\Omega r}{H}\right)^2 & 0 \\ 0 & 0 & \left(\frac{\Omega r}{H}\right)^2 \end{pmatrix} \quad (6.5-5)$$

and

$$\{\dot{\boldsymbol{\gamma}} \cdot \boldsymbol{\omega}\} = \begin{pmatrix} 0 & 0 & 0 \\ 0 & \left(\frac{\Omega r}{H}\right)^2 & 0 \\ -\frac{2\Omega^2 r z}{H^2} & 0 & -\left(\frac{\Omega r}{H}\right)^2 \end{pmatrix} \quad (6.5-6)$$

Finally, using Table 3.2 we obtain

$$\{\mathbf{v} \cdot \nabla \dot{\boldsymbol{\gamma}}\} = \begin{pmatrix} 0 & 0 & -\frac{\Omega^2 r z}{H^2} \\ 0 & 0 & 0 \\ -\frac{\Omega^2 r z}{H^2} & 0 & 0 \end{pmatrix} \quad (6.5-7)$$

Substituting the preceding equation into the CEF equation (Eq. 3.3-5) gives

$$\begin{pmatrix} \tau_{rr} & \tau_{r\theta} & \tau_{rz} \\ \tau_{\theta r} & \tau_{\theta\theta} & \tau_{\theta z} \\ \tau_{zr} & \tau_{z\theta} & \tau_{zz} \end{pmatrix} = -\eta \begin{pmatrix} 0 & 0 & 0 \\ 0 & 0 & \frac{\Omega r}{H} \\ 0 & \frac{\Omega r}{H} & 0 \end{pmatrix} - \frac{1}{2}(\Psi_1 + 2\Psi_2) \begin{pmatrix} 0 & 0 & 0 \\ 0 & \left(\frac{\Omega r}{H}\right)^2 & 0 \\ 0 & 0 & \left(\frac{\Omega r}{H}\right)^2 \end{pmatrix} \\ + \frac{\Psi_1}{2} \begin{pmatrix} 0 & 0 & 0 \\ 0 & -\left(\frac{\Omega r}{H}\right)^2 & 0 \\ 0 & 0 & \left(\frac{\Omega r}{H}\right)^2 \end{pmatrix} \quad (6.5-8)$$

Thus, the stress components for the assumed flow kinematics and for $\dot{\boldsymbol{\gamma}} = \dot{\boldsymbol{\gamma}}_{\theta z}(r) = (\Omega r/H)$:

$$\begin{aligned} \tau_{rr} &= 0 \\ \tau_{\theta\theta} &= -(\Psi_1 + \Psi_2) \left(\frac{\Omega r}{H}\right)^2 = -(\Psi_1 + \Psi_2) \dot{\boldsymbol{\gamma}}^2 \\ \tau_{zz} &= -\Psi_2 \left(\frac{\Omega r}{H}\right)^2 \\ \tau_{\theta z} = \tau_{z\theta} &= -\eta \left(\frac{\Omega r}{H}\right) = -\eta \dot{\boldsymbol{\gamma}} \\ \tau_{r\theta} = \tau_{\theta r} = \tau_{rz} = \tau_{zr} &= 0 \end{aligned} \quad (6.5-9)$$

Hence the normal stress difference functions, keeping in mind the direction convention as discussed in Section 3.1, and noting that in this case θ is direction 1, z is direction 2, and r is direction 3, are

$$\tau_{11} - \tau_{22} = -\Psi_1 \left(\frac{\Omega r}{H}\right)^2 = -\Psi_1 \dot{\boldsymbol{\gamma}}^2 \quad (6.5-10)$$

and

$$\tau_{22} - \tau_{33} = -\Psi_2 \left(\frac{\Omega r}{H} \right)^2 = -\Psi_2 \dot{\gamma}^2 \quad (6.5-11)$$

Having all the stress tensor components, we can proceed with the equation of motion, whose components reduce to (41)

$$-\rho \frac{v_\theta^2}{r} = -\frac{\partial P}{\partial r} + \frac{\tau_{\theta\theta}}{r} \quad (6.5-12)$$

$$\frac{\partial P}{\partial \theta} = 0 \quad (6.5-13)$$

and

$$\frac{\partial P}{\partial z} = 0 \quad (6.5-14)$$

Hence, we find that the pressure is a function of only the coordinate r . Substituting $\tau_{\theta\theta}$ from Eq. 6.5-9 and Eq. 6.5-1 into Eq. 6.5-12, we obtain

$$\frac{dP}{dr} = \rho \Omega^2 r \left(\frac{z}{H} \right)^2 - (\Psi_1 + \Psi_2) \left(\frac{\Omega}{H} \right)^2 r \quad (6.5-15)$$

The first term on the right-hand side is due to centrifugal forces and contributes to *increasing* the pressure with r , as expected; whereas, the second term is due to normal stress differences and contributes to *decreasing* pressure with r , because as pointed out in Chapter 3, experimental evidence for the shear-rate range of interest indicates that Ψ_1 is positive and Ψ_2 is negative and smaller by an order of magnitude (namely, $-\Psi_2/\Psi_1 \sim 0.1$). Furthermore, we note a certain inconsistency between the assumptions and the results. For the *assumed* velocity profile, we obtained from the equation of motion that $P \neq f(z)$; yet Eq. 6.5-15 indicates a z dependence. In reality, we should obtain a circulatory flow due to circulatory motion resulting in nonvanishing $\partial P/\partial z$, v_z , and v_r terms. Our solution is, therefore, valid only for negligible circulatory flow. Indeed, we are interested in the particular case of negligible centrifugal forces as compared to normal stress forces. Next, we average the pressure over z to obtain

$$\frac{d\bar{P}}{dr} = \rho \frac{\Omega^2 r}{3} - (\Psi_1 + \Psi_2) \left(\frac{\Omega}{H} \right)^2 r \quad (6.5-16)$$

Equation 6.5-16 can be integrated to give the pressure at $r = 0$:

$$\begin{aligned} \bar{P}(0) &= \bar{P}(R) + \left(\frac{\Omega}{H} \right)^2 \int_0^R (\Psi_1 + \Psi_2) r dr - \rho \frac{\Omega^2 R^2}{6} \\ &= \bar{P}(R) + \int_0^{\Omega R/H} (\Psi_1 + \Psi_2) \dot{\gamma} d\dot{\gamma} - \rho \frac{\Omega^2 R^2}{6} \end{aligned} \quad (6.5-17)$$

Assuming that Ψ_1 and Ψ_2 are shear rate independent, we obtain the following expression for the pressure at $r = 0$:

$$\bar{P}(0) = \bar{P}(R) + \frac{1}{2} \left(\frac{\Omega R}{H} \right)^2 (\Psi_1 + \Psi_2) - \rho \frac{\Omega^2 R^2}{6} \quad (6.5-18)$$

which is the design equation for the normal stress pump.

We find the maximum pressure rise at the center of the disk to be proportional to the square of $\Omega R/H$, which is the shear rate at $r = R$. Moreover, by comparing Eq. 6.5-18 to Eqs. 6.5-10 and 6.5-11, we find that this pressure rise is the sum of the primary and secondary normal stress-difference functions $\{ -[(\tau_{11} - \tau_{22}) + (\tau_{22} - \tau_{33})] \}$ at $r = R$, less centrifugal forces. Since Ψ_2 is probably negative, it opposes pressurization; hence, the source of the pressurization in the normal stress extruder is the *primary* normal stress difference function Ψ_1 .

Example 6.9 The Maximum Pressure in the Normal-Stress Extruder Calculate the maximum pressure (at closed discharge) in a normal stress extruder of two 25-cm radius disks at 0.5 cm apart, shearing Low Density Polyethylene (LDPE) at 60 rpm and 200°C.

Solution We do not have good data on Ψ_2 , but we know that it is an order of magnitude smaller than Ψ_1 , therefore, we shall assume the former to be negligible compared to the latter. The shear rate ranges from zero at the center to a maximum value at R , $\dot{\gamma}(R) = \Omega R/H = 314.2 \text{ s}^{-1}$. Figure 3.26 shows experimental data on Ψ_1 for LDPE. At 200°C we can calculate the following shear rate dependence

$$\Psi_1(\dot{\gamma}) \cong 9 \times 10^4 \dot{\gamma}^{-0.92}$$

Furthermore, we assume that this relationship holds for shear rates greater than 10 s^{-1} . Then, substituting this relationship into Eq. 6.5-17 followed by integration and taking $P(R) = 0$ and melt density 0.75 g/cm^3 , we obtain

$$\bar{P}(0) = \frac{(9 \times 10^4)}{(1.08)} (314.2^{1.08}) - \frac{(0.75)(25^2)}{(6)} = 4.17 \times 10^6 \text{ N/m}^2 \text{ (605 psi)}$$

Two facts are worth noting. First, the normal stress pressurization is indeed much greater (10^5 times) than that brought about by centrifugal forces. Second, the level of the maximum pressure generated even at closed discharge is significant but inadequate for most processing applications. One could suggest increasing the disk speed, but we must remember that secondary flows (e.g., cigar rolling) will place rather tight upper bounds.

So far we have neglected radial flow, but in a normal stress extruder the objective is to extrude the polymer melt through a die. Such flow, however, implies a pressure loss in the inward radial direction, consequently reducing the maximum pressure at the die entrance. The die resistance determines the ensuing flow rate; at steady flow conditions, the pressure rise in the radial direction equals the pressure drop across the die.

Rigorous analytical solution of this flow problem is difficult. Good et al. (40) proposed the following approximate analytical approach, which resulted in good agreement with their experiments: they assumed that the pressure rise due to normal stresses (ΔP_{NS}) in a closed discharge condition, the pressure loss between the disks due to radial flow (ΔP_{RF}), and entrance losses into the die (ΔP_{DE}) are related to the available pressure drop for pumping across the die as follows:

$$\Delta P_T = \Delta P_{NS} - \Delta P_{RF} - \Delta P_{DE} \quad (6.5-19)$$

Figure 6.29 compares predicted pressures with an experimentally measured pressure using a polyacrylamide solution. There is an optimum separation between the disks for

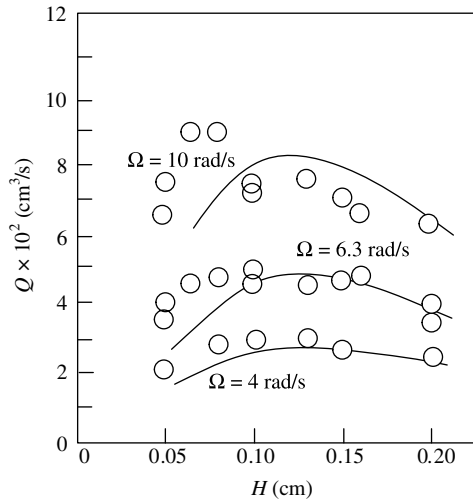


Fig. 6.29 Flow rate versus disk gap separation in normal stress pump. The polymer used was polyacrylamide solution at 28°C. Smooth curves indicate calculated values. The die was 0.482 cm long and had a diameter of 0.244 cm. [Data replotted from P. A. Good, A. J. Swartz, and C. W. Macosko, *AIChE J.*, **20**, 67(1974).]

maximum pressurization due to the different H dependence of pressure rise due to normal stress and pressure drop due to viscous radial flow.

The normal stress extruder can also be used for melting, as shown in Fig. 6.30. However, because of the limited pressurization capability, various modifications have

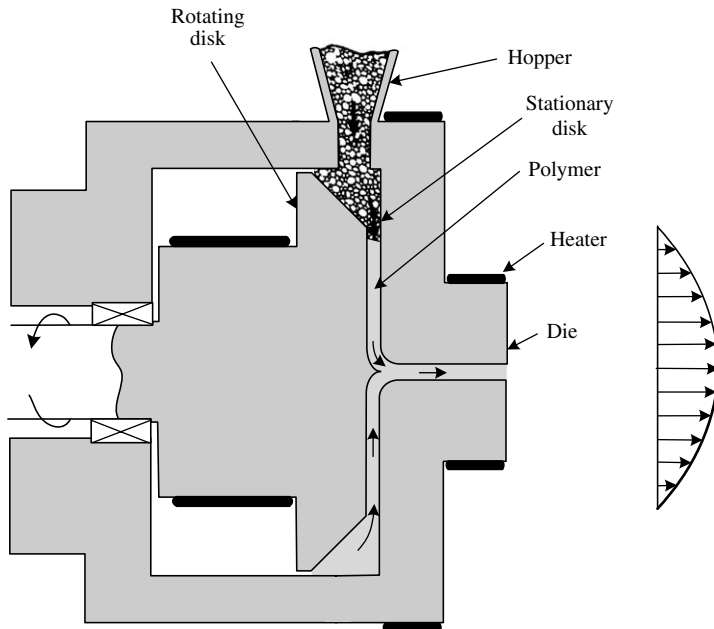


Fig. 6.30 Schematic representation of a plasticating normal stress extruder.

been suggested, one of these being a combination with a screw. Yet in spite of the modification, it has found only limited use as an extrusion system, although it appears that a later modification (42) has certain advantages in processing hard-to-mix materials.

6.6 THE CO-ROTATING DISK PUMP

In Example 6.7 we described the synthesis of a co-rotating disk processor (CDP) from building block 2 consisting of two jointly moving plates. In this section we wish to derive a mathematical model to relate flow rate and pressure rise with geometrical and operational variables. We begin by first making a comparison between a jointly moving plate configuration (JMP) pump and a single moving plate configuration (SMP) pump (43).

Example 6.10 A Comparison between an SMP- and a JMP-based Pump Figure E6.10 shows the two configurations with plates at distance H apart and constant plate velocities of V_0 . For steady, fully developed isothermal flow of a Newtonian fluid, we have shown in Example 2.5 that the flow rate is given by

$$q = \frac{V_0 H}{2} - \frac{H^3}{12\mu} \left(\frac{\Delta P}{L} \right) \quad (\text{E6.10-1})$$

where H is the separation between the plates, L is the length of the plates, ΔP is the pressure rise ($P_{\text{discharge}} - P_{\text{inlet}}$), and μ is the viscosity. This equation can be rearranged as

$$\Delta P = \frac{12\mu}{H^3} \left(\frac{V_0 H}{2} - q \right) \quad (\text{E6.10-2})$$

For the JMP configuration, it is easy to show that the corresponding equations are

$$q = V_0 H - \frac{H^3}{12\mu} \left(\frac{\Delta P}{L} \right) \quad (\text{E6.10-3})$$

and

$$\Delta P = \frac{12\mu}{H^3} (V_0 H - q) \quad (\text{E6.10-4})$$

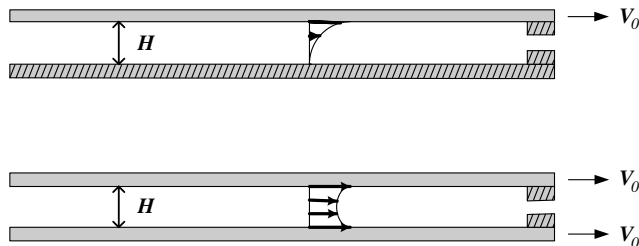


Fig. E6.10 Jointly moving plate (JMP) and single moving plate (SMP) configurations with schematic velocity profiles.

The increase in the drag-flow rate has a profound effect on performance. For a given flow rate q , the optimum gap size in SMP and JMP configurations can be obtained by differentiating Eqs. E6.10-2 and E6.10-4, respectively, with respect to H to give $H_{\text{opt}} = 3q/V_0$ and $H_{\text{opt}} = 3q/2V_0$. Next we substitute these values in Eqs. E6.10-2 and E6.10-4 and find that the ratio of pressure rises is

$$\frac{(\Delta P_{\text{max}})_{\text{JMP}}}{(\Delta P_{\text{max}})_{\text{SMP}}} = 8 \quad (\text{E6.10-5})$$

Similarly, we find that the maximum flow-rate ratio for a given pressure rise is

$$\frac{(q_{\text{max}})_{\text{JMP}}}{(q_{\text{max}})_{\text{SMP}}} = \sqrt{8} \quad (\text{E6.10-6})$$

For non-Newtonian Power Law model fluids, these ratios are

$$\frac{(\Delta P_{\text{max}})_{\text{JMP}}}{(\Delta P_{\text{max}})_{\text{SMP}}} = (1 + s)2^{(1+n)} \quad (\text{E6.10-7})$$

and

$$\frac{(q_{\text{max}})_{\text{JMP}}}{(q_{\text{max}})_{\text{SMP}}} = 2(1 + s)^{1/(1+n)} \quad (\text{E6.10-8})$$

where n is the power law exponent, and $s = 1/n$.

Thus, for Newtonian fluids, the pressurization capability of the optimized JMP is eight times that of the SMP, and for non-Newtonian fluids, the ratio exhibits a minimum at $n = 0.801$ and rises to 11.59 at $n = 0.25$; whereas, the flow rate at fixed pressure rise for Newtonian fluids is $8^{1/2} = 2.83$ times in JMP as compared to SMP, and for non-Newtonian fluids with $n = 0.25$ it rises to 7.25. Clearly, the JMP configuration is about an order of magnitude more efficient than the SMP one. Moreover, the specific power input in a JMP configuration for Newtonian fluids is one-half that of the SMP, and for $n = 0.25$, it is one-fifth; the corresponding ratios for specific power dissipated into heat are, one-quarter and $1/25$, respectively.

The geometrical configuration of the CDP is shown in Fig. 6.31. The space between the disks can be parallel or wedged, with the latter being the optimum configuration. Tadmor et al (44) derived the mathematical model for the CDP assuming steady, fully developed⁹ laminar, isothermal flow of an incompressible non-Newtonian Power Law model liquid. We begin with the parallel-disk configuration, with disk outer and inner radii R_d and R_s , respectively, at a distance H apart and rotating at frequency N . We select a cylindrical coordinate system located at the center of the shaft between the disks. As the disks rotate, they drag the fluid from the inlet to the outlet, and when there is a resistance at the outlet (i.e., a die), pressure is built up toward the outlet. We assume steady isothermal and laminar fully developed flow of an incompressible non-Newtonian Power Law model fluid, and further assume that the effect of the root of the screw and barrel are negligible.¹⁰

9. This assumption is valid only far from the inlet and exit regions, but as we shall see later, the distance between the disks is relatively small, and therefore this assumption is quite reasonable.

10. This implies that $H \ll R_d - R_s$, an assumption equivalent to neglecting flight effects in an SSE. Later we will show how to account for these "wall" effects.

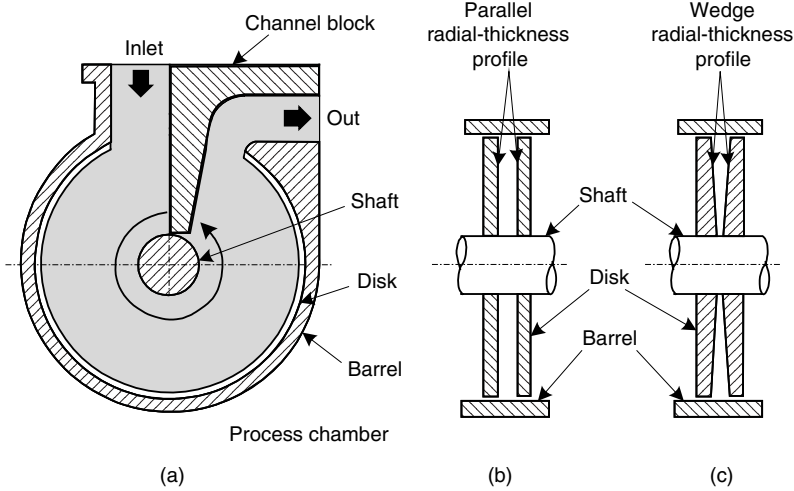


Fig. 6.31 Schematic view of a co-rotating-disk pump. (a) The disks are attached to a rotating shaft and placed within a barrel having an inlet and an outlet port, separated by a channel block attached to the stationary barrel. The space between inlet and outlet ports, the disks, and the channel block form the processing chamber, (b) parallel arrangements of the disks; (c) wedge-shaped disks.

The only nonvanishing velocity component is v_θ and it is a function only of the angular coordinates r and z . The other two velocity components v_z and v_r vanish, as implied from the equation of continuity for fully developed flow. The flow kinematics also imply that $\tau_{rr} = \tau_{zz} = \tau_{\theta\theta} = \tau_{rz} = 0$ and the only nonvanishing stress components are $\tau_{\theta z}$ and $\tau_{r\theta}$. Consequently the equation of motion reduces to

$$\frac{\partial P}{\partial r} = 0 \tag{6.6-1}$$

$$-\frac{1}{r} \frac{\partial P}{\partial \theta} = \frac{1}{r^2} \frac{\partial}{\partial r} (r^2 \tau_{r\theta}) + \frac{\partial \tau_{\theta z}}{\partial z} \tag{6.6-2}$$

$$\frac{\partial P}{\partial z} = 0 \tag{6.6-3}$$

Equations 6.6-1 and 6.6-3 indicate that P is only a function of θ . Furthermore, since the right-hand side of Eq. 6.6-2 is not a function of θ , we conclude that $\partial P / \partial \theta$ is a constant, that is, the angular pressure gradient is constant or the pressure rises linearly with θ . The stress components $\tau_{\theta z}$ and $\tau_{r\theta}$, consistent to our assumption, reduce to

$$\tau_{r\theta} = -\eta \left[r \frac{\partial}{\partial r} \left(\frac{v_\theta}{r} \right) \right] \tag{6.6-4}$$

$$\tau_{\theta z} = -\eta \frac{\partial v_\theta}{\partial z} \tag{6.6-5}$$

The relative significance of these stress components can be estimated by the following order-of-magnitude calculations

$$\frac{|\tau_{r\theta}|}{|\tau_{\theta z}|} = \frac{\left| r \frac{\partial}{\partial r} \left(\frac{v_\theta}{r} \right) \right|}{\left| \frac{\partial v_\theta}{\partial z} \right|} \cong \frac{r \left(\frac{1}{R_d - R_s} \right) \left(\frac{\Omega r}{r} \right)}{\left(\frac{\Omega r}{H} \right)} \cong \frac{H}{R_d - R_s} \tag{6.6-6}$$

where Ω is the angular velocity. Clearly, in the geometry considered here, $H/(R_d - R_s) \ll 1$ and therefore $\tau_{r\theta} \ll \tau_{\theta z}$. The stress component $\tau_{r\theta}$ vanishes at the disk surfaces and increases toward the center. In a wedge-shaped gap ($H/r = \text{constant}$) the angular velocity v_θ/r is not a function of r and $\tau_{r\theta}$ vanishes everywhere. In either case, Eq. 6.6-2 reduces to

$$-\frac{1}{r} \frac{\partial P}{\partial \theta} = \frac{\partial \tau_{\theta z}}{\partial z} \quad (6.6-7)$$

which can be integrated to give

$$\tau_{\theta z} = -\left(\frac{1}{r} \frac{dP}{d\theta}\right)z + C \quad (6.6-8)$$

where C is an integration constant. Due to symmetry, $\tau_{\theta z} = 0$ at $z = 0$, and therefore, $C = 0$. Expressing this stress component in terms of the velocity gradients using the Power Law model gives

$$m \left| \frac{\partial v_\theta}{\partial z} \right|^{n-1} \frac{\partial v_\theta}{\partial z} = \left(\frac{1}{r} \frac{dP}{d\theta}\right)z \quad (6.6-9)$$

where m and n are the Power Law parameters. The velocity gradient is positive for $z > 0$, and Eq. 6.6-9 can be written as

$$\frac{\partial v_\theta}{\partial z} = \left[\frac{1}{mr} \left(\frac{dP}{d\theta}\right) \right]^s z^s \quad (6.6-10)$$

where $s = 1/n$. The velocity component v_θ is a function of z and r , but from the previous conclusion that $\tau_{r\theta} \approx 0$, it follows that $\partial(v_\theta/r)/\partial r \approx 0$, and therefore $v_\theta/r = f(z)$, where $f(z)$ is yet an unknown function of z , or

$$v_\theta = rf(z) \quad (6.6-11)$$

Substituting Eq. 6.6-11 into Eq. 6.6-10 gives

$$rf'(z) = \left[\frac{1}{mr} \left(\frac{dP}{d\theta}\right) \right]^s z^s \quad (6.6-12)$$

which subsequent to integration yields

$$f(z) = \left[\frac{1}{mr} \frac{dP}{d\theta} \right]^s \frac{z^{s+1}}{s+1} + C_0(r) \quad (6.6-13)$$

where $C_0(r)$ is an integration constant that may be a function of r . Substituting Eq. 6.6-13 into Eq. 6.6-11 gives

$$v_\theta = \left[\frac{1}{mr} \frac{dP}{d\theta} \right]^s \frac{z^{s+1}}{s+1} + C_1(r) \quad (6.6-14)$$

where $C_1(r) = rC_0(r)$ is evaluated from the boundary conditions $v_\theta = (H/2) = 2\pi Nr$ to give the required velocity profile:

$$v_\theta = 2\pi Nr - \frac{1}{s+1} \left[\frac{1}{mr} \left(\frac{dP}{d\theta} \right) \right]^s \left[\left(\frac{H}{2} \right)^{s+1} - z^{s+1} \right] \quad (6.6-15)$$

The flow rate is obtained by integrating the velocity profile over the cross section

$$Q = 2 \int_{R_s}^{R_d} \int_0^{H/2} v_\theta dz dr = \pi NHR_d^2(1 - \alpha^2) - \frac{H^{2+s}}{2^{1+s}} \frac{R_d^{1-s}}{(2+s)m^s} \frac{(1 - \alpha^{1-s})}{(1-s)} \left(\frac{dP}{d\theta} \right)^s \quad (6.6-16)$$

where $\alpha = R_s/R_d$. Now the pressure gradient can be expressed in terms of pressure drop (or rise) as follows:

$$\frac{dP}{d\theta} = \frac{P_{\text{out}} - P_{\text{in}}}{2\pi\varepsilon} = \frac{\Delta P}{2\pi\varepsilon} \quad (6.6-17)$$

where P_{in} and P_{out} are the inlet and outlet pressures, respectively, and $\varepsilon < 1$ is the fraction of circumference in which pressurization is taking place.

In Eq. 6.6-16 the first term on the right-hand side is the drag flow and the second term is the pressure flow. The net flow rate is their linear superposition, as in the case of the Newtonian model in single screw extrusion. The reason that in this case this is valid for non-Newtonian flow as well is because the drag flow is simply plug flow.

The shear rate distribution is obtained by differentiating the velocity profile Eq. 6.6-15 to give

$$\dot{\gamma}_{\theta z} = \left(\frac{z}{mr} \frac{dP}{d\theta} \right)^s \quad (6.6-18)$$

The power consumption is obtained by the product of the shear stress at the wall and the local disk velocity integrated over the disk surface

$$P_w = 2 \int_{R_s}^{R_d} \int_0^{2\pi\varepsilon} 2\pi Nr \tau_w r dr d\theta \quad (6.6-19)$$

The shear stress at the wall is

$$\tau_w = -m\dot{\gamma}_w^n = \frac{H}{2r} \frac{dP}{d\theta} \quad (6.6-20)$$

Substituting Eq. 6.6-20 into Eq. 6.6-19 subsequent to integration yields

$$P_w = \pi NHR_d^2(1 - \alpha^2)\Delta P = Q_d\Delta P \quad (6.6-21)$$

where Q_d is the drag flow.

It is easy to show that the maximum flow rate for a given pressure rise, or the maximum pressure rise for a given flow rate, are obtained for such a gap size H that satisfies the following relationship:

$$\frac{Q}{Q_d} = \frac{s+1}{s+2} \quad (6.6-22)$$

For a wedge-shaped gap such that

$$\frac{H}{r} = \frac{H_d}{R_d} \quad (6.6-23)$$

where H_d is the gap size at $r = R_d$ the velocity profile is

$$\frac{v_\theta}{r} = 2\pi N - \frac{1}{s+1} \left[\frac{1}{m} \left(\frac{dP}{d\theta} \right) \right]^s \left(\frac{H_d}{R_d} \right)^{s+1} \left[1 - \left(\frac{2z}{H} \right)^{s+1} \right] \quad (6.6-24)$$

We note that the angular velocity profile v_θ/r in this geometry is independent of radial position.

The flow rate is obtained by integrating the velocity profile over the cross section of the channel to give

$$Q = \frac{2}{3} \pi N H_d R_d^2 (1 - \alpha^3) - \frac{H_d^{s+2} R_d^{1-s} (1 - \alpha^3)}{6(s+2)2^s m^s} \left(\frac{dP}{d\theta} \right)^s \quad (6.6-25)$$

Example 6.11 Drag Flow Rate in a CDP Pump Consider a 20-cm-diameter disk CDP with $\alpha = 0.5$ and $H = 1$ cm rotating at 240 rpm. Calculate the volumetric flow rate.

Solution From Eq. 6.6-24 we get

$$Q_d = \pi \times 4(\text{s}^{-1}) \times 10^{-2}(\text{m}) \times (10^{-1})^2(\text{m}^2) \times (1 - 0.5^2) = 9.427 \times 10^{-4} \text{ m}^3/\text{s}$$

or 56.52 l/min. By attaching 11 disks to the same shaft we will increase the flow rate tenfold to 565.2 l/min, or 3.39 tons/h if the density is 1 g/cm³. This is a very substantial flow rate for viscous liquids in laminar flow. In the next Example we examine the pressurization capability of the CDP.

Example 6.12 Flow Rate of LDPE in a CDP with Fixed Head Pressure Calculate the flow rate of a 2MI LDPE ($m = 4.31 \times 10^3 \text{ N} \cdot \text{s}^n/\text{m}^2$, $n = 0.5$) in a 7.5-in-diameter CDP, with $\alpha = 0.5$ and wedged channel with $H_d = 0.25$ in, rotating at 75 rpm with a discharge pressure of 1200 psi. Assume that entrance and exit parts occupy 90° of the circumference.

Solution First we express the angular pressure gradient in terms of the pressure rise

$$\frac{dP}{d\theta} = \frac{\Delta P}{2\pi\epsilon}$$

where the $\varepsilon = 0.75$ is the fraction of the circumference in which pressurization is taking place. Next, we insert the given data into Eq. 6.6-33 to obtain the flow rate:

$$\begin{aligned} Q &= \frac{2}{3}\pi(1.25)(0.635 \times 10^{-2})(9.525 \times 10^{-2})^2(1 - 0.5^3) \\ &\quad - \frac{(0.635 \times 10^{-2})^{2+2}}{6(2+2)(9.525 \times 10^{-2})} \left(\frac{8.2728 \times 10^6}{4\pi(0.75)(4.31 \times 10^3)} \right)^2 (1 - 0.5^3) \\ &= 1.3197 \times 10^{-4} - 0.2581 \times 10^{-4} \text{ [m}^3/\text{s]} \\ &= 1.0616 \times 10^{-4} \text{ [m}^3/\text{s]} = 0.382 \text{ [m}^3/\text{h]} \end{aligned}$$

or using a density of 0.9 g/cm^3 results in 343.8 kg/h .

The barrel surface exerts a retarding effect on flow rate, just as the flights in a screw extruder do. Edelist and Tadmor (45) derived the shape correction factors for Newtonian fluids, which are plotted for parallel disks as a function of $H/(R_d - R_s)$ in Fig. 6.32 and for wedge-shaped disks in Fig. 6.33.

Table 6.1 provides all the design equations including power, specific power, temperature rise and mean residence time for both types of pumps. This theoretical model was verified experimentally by Tadmor et al. (43) by pumping molten polystyrene (PS) in a 7.5-in-diameter single-stage single-chamber experimental Diskpack¹¹ equipped with several pressure transducers at various angular positions, as shown in Fig. 6.34. The pressure profiles are shown in Fig. 6.35.

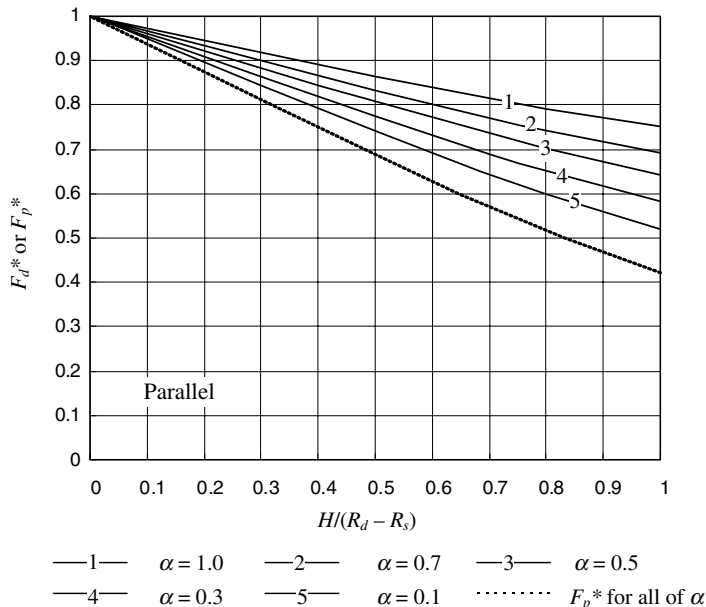


Fig. 6.32 Shape-correction factors for parallel-shaped chambers. [Reproduced by permission from Y. Edelist and Z. Tadmor, "Velocity Profiles in a Co-rotating Disk Processor" *Polym. Process Eng.*, **1**,1 (1983).]

11. The CDP was commercially developed into a processing machine by the Farrel Corporation of Ansonia, CT, USA, under the brand name Diskpack.

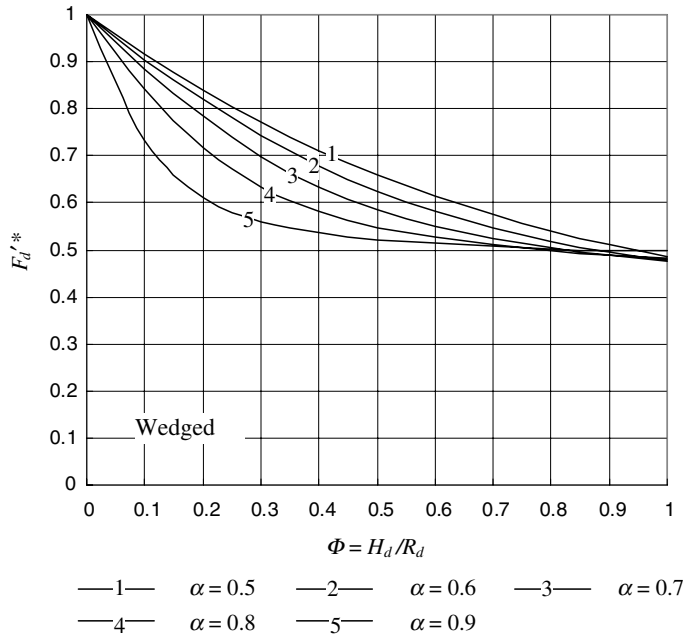


Fig. 6.33 Shape-correction factors for wedge-shaped chambers. [Reproduced by permission from Y. Edelist and Z. Tadmor, “Velocity Profiles in a Co-rotating Disk Processor” *Polym. Process Eng.*, **1**, 1 (1983).]

The experiments were conducted at a constant disk speed of 70 rpm and started with open discharge, after which a discharge valve was gradually closed. Notice that, as the valve is closed, the chamber begins filling up and the discharge pressure increases. The profiles are linear as predicated by the model. As closed discharge conditions are approached, viscous dissipation begins increasing the temperature and reducing the viscosity, with a consequent drop in discharge pressure.

Figure 6.36 compares theoretical to experimental pressure gradient measured in the foregoing experimental machine and in a 350-mm-diameter machine for three different polymeric melts. Results indicate that the experimentally measured pressure gradients are up to 20% higher than the theoretical ones. Some possible reasons that have been suggested are either the increased drag due to cooler disks as compared to melt temperature, or stress overshoot (higher transient viscosities than used in the calculation).

Finally, Edelist and Tadmor (45) used a photogrammetric technique to experimentally verify the calculated velocity profiles, adding credibility to the theoretical model.

6.7 POSITIVE DISPLACEMENT PUMPS

Positive displacement pumps are based on a surface moving normal to its plane (building block 5 in Fig. 6.2) pressurizing the melt by an externally imposed (mechanical) force, and creating a positive displacement-type flow. There are a number of advantages to positive-displacement pumps as compared to drag-induced pumps. The latter are sensitive to the conditions at the moving surface such as, for example, wall temperature and slip at the wall, whereas, the former are generally insensitive to these problems. Moreover, flow rate

TABLE 6.1 Design Equations for Co-rotating Disk Pumps.

	Parallel Chamber	Wedge Chamber
Volumetric flow rate	$Q = Q_d - Q_p$	$Q = Q'_d - Q'_p$
Drag flow rate	$Q_d = \pi N H R_d^2 (1 - \alpha^2) F_d$	$Q'_d = \frac{2}{3} \pi N H_d R_d^2 (1 - \alpha^3) F'_d$
Pressure flow rate	$Q_p = \frac{H^2 R_d}{2(s+2)} \left(\frac{1 - \alpha^{1-s}}{1-s} \right) \left[\frac{H}{2mR_d} \left(\frac{dP}{d\theta} \right) \right]^s F_p$	$Q'_p = \frac{H_d^2 R_d (1 - \alpha^2)}{6(2+s)} \left(\frac{H_d}{2mR_d} \frac{dP}{d\theta} \right)^s F'_p$
Pressure flow for Newtonian fluids	$Q_{pN} = \frac{H^3 \ln \alpha}{12\mu} \left(\frac{dP}{d\theta} \right) F_p$	$Q_{pN} = \frac{H_d^3 (1 - \alpha^3)}{36\mu} \left(\frac{dP}{d\theta} \right) F'_p$
Angular pressure gradient	$\frac{dP}{d\theta} = \frac{P_{\text{out}} - P_{\text{in}}}{2\pi\epsilon} \frac{\Delta P}{\Delta P}$	
Pressure rise	$\Delta P = 4\pi m \epsilon \frac{R_d^{1-n}}{H_d^{1+2n}} \left[\frac{2(2+s)(1+s)}{F_p'(1-\alpha^{1-s})} \right]^n (Q_d - Q)^n$	$\Delta P = 4\pi m \epsilon \frac{R_d^{1-n}}{H_d^{1+2n}} \left[\frac{6(2+s)}{F_p'(1-\alpha^3)} \right]^n (Q'_d - Q)^n$
Pressure to drag flow ratio	$\frac{Q_p}{Q_d} = \frac{H}{2\pi N R_d} \left[\frac{1 - \alpha^{1-s}}{(1-s)(1-\alpha^2)} \right] \left[\frac{H}{2mR_d} \left(\frac{dP}{d\theta} \right) \right]^s \frac{1}{(2+s)} \frac{F_p}{F_d}$	$\frac{Q'_p}{Q'_d} = \frac{H_d}{4\pi N R_d} \left[\frac{H_d}{2mR_d} \left(\frac{dP}{d\theta} \right) \right]^s \frac{1}{(2+s)} \frac{F'_p}{F'_d}$
Shaft power	$P_w = Q_d \Delta P$	$P_w = Q'_d \Delta P$
Specific energy	$P_w = \left(\frac{Q_d}{Q} \right) \Delta P$	$P_w = \left(\frac{Q'_d}{Q} \right) \Delta P$
Torque	$T = H_d R_d^2 (1 - \alpha^2) \frac{\Delta P}{2}$	$T = H_d R_d^2 (1 - \alpha^3) \frac{\Delta P}{3}$
Total rate of viscous heat dissipation	$E_v = Q_p \Delta P$	$E_v = Q'_p \Delta P$

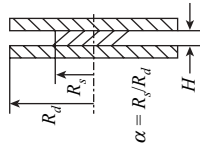
Adiabatic temperature rise

$$\Delta T_a = \left(\frac{1}{\rho C_p} \right) \left(\frac{Q_p}{Q} \right) \Delta P$$

Mean residence time

$$\bar{t} = \frac{Q_d \varepsilon}{NQ} \quad (F_d = 1)$$

Geometry

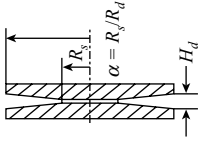


Fluid model

$\tau = \eta \dot{\gamma}$ where η is the non-Newtonian viscosity, which is a function of $\dot{\gamma}$, the magnitude of the tensor $\dot{\gamma}$ [$\dot{\gamma} = (\frac{1}{2} \dot{\gamma} : \dot{\gamma})^{1/2}$], $\eta = m \dot{\gamma}^{n-1}$, where m and n are the Power Law model parameters and $s = 1/n$. For simple shear flow, $\dot{\gamma}$ is the shear rate. For Newtonian fluids, $n = 1$ and $\eta = m = \mu$.

$$\Delta T_a = \left(\frac{1}{\rho C_p} \right) \left(\frac{Q_p}{Q} \right) \Delta P$$

$$\bar{t} = \frac{Q_d \varepsilon}{NQ} \quad (F_d' = 1)$$



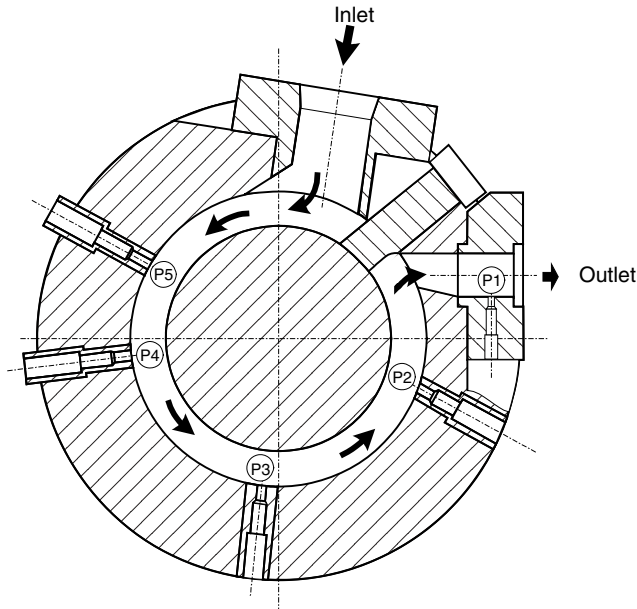


Fig. 6.34 A 7.5-in-diameter co-rotating disk pump. (Courtesy of Farrel Corporation.)

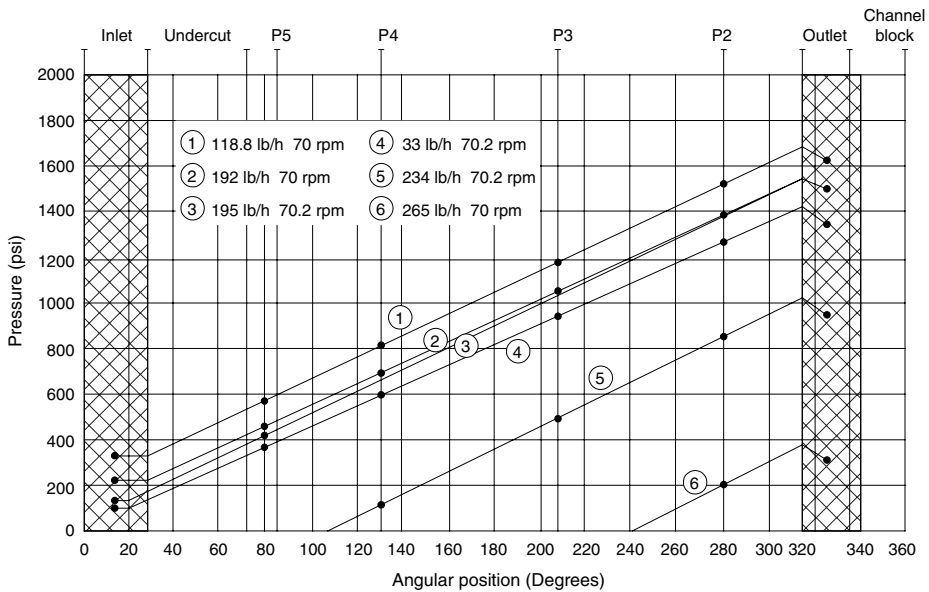


Fig. 6.35 Characteristic linear pressure profiles for molten PS in a 7.5-in-diameter pump at various discharge pressures. [Reproduced by permission from Z. Tadmor, P.S. Mehta, L.N. Valsamis and J. Yang “Co-rotating Disk Pumps for Viscous Liquids,” *Ind. Eng. Chem. Process. Res. Devel.*, **24**, 311–320 (1985).]

control (metering) is generally better and pressure sensitivity lower in positive displacement pumps as compared to drag-induced flow.

First we want to gain some insight into the nature and mechanism of positive displacement flow. In the next two examples we examine the plunger–cylinder

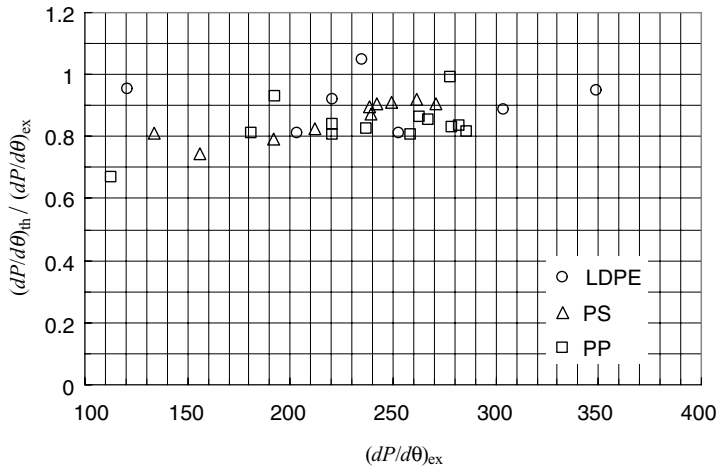


Fig. 6.36 Predicted versus measured pressure gradients for LDPE, PS, and PP. [Reproduced by permission from Z. Tadmor, P.S. Mehta, L.N. Valsamis and J. Yang “Co-rotating Disk Pumps for Viscous Liquids,”. *Ind. Eng. Chem. Process. Res. Devel.*, **24**, 311–320 (1985).]

pump and axially moving disk configurations shown schematically in Fig. 6.37(a) and Fig. 6.37(b).

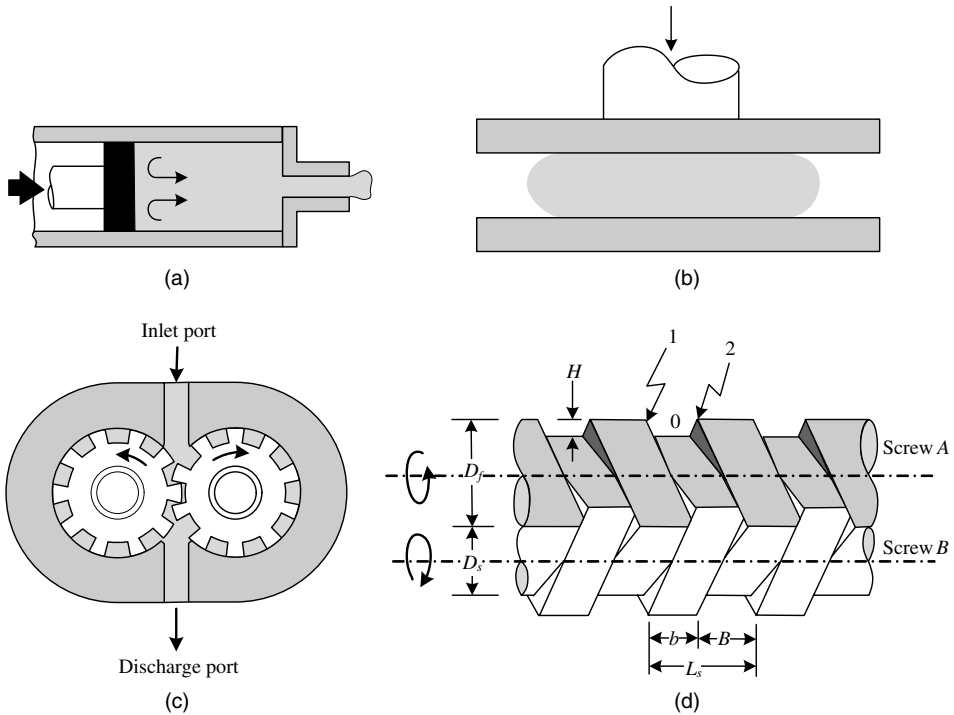


Fig. 6.37 Schematic representation of four geometrical configurations utilizing external mechanical pressurization giving rise to positive displacement flow. (a) Axially moving plunger in a cylinder. (b) Squeezing disks. (c) Intermeshing gear pump. (d) Counterrotating intermeshing twin screws.

Example 6.13 Plunger–Cylinder Pump The first recorded application of the plunger-cylinder pump in the field of polymer processing appears to have occurred in 1845 in England, for the extrusion of guttapercha. The main disadvantage of this pump for extrusion is its non-continuous operation.¹² This is, of course, irrelevant to injection molding, where the polymeric melt is pumped into the die by an axially moving cylinder. Now we discuss the flow field in front of the cylinder.

It is easier to visualize the flow field in front of the plunger in a coordinate system located on the moving surface of the plunger (*Lagrangian* point of view), as shown in Fig. E6.13. In this coordinate system, if the cylinder moves at a velocity V_0 , the cylinder has a $-V_0$ velocity. By its axial motion, the cylinder drags the adjacent liquid toward the plunger. As a fluid particle approaches the plunger surface, it must acquire an inward radial velocity component while gradually decelerating the axial velocity component to zero. Then it begins to acquire a positive axial velocity component. Hence, the resulting flow pattern is one that has a “skin” layer of liquid moving toward the plunger, and a core layer moving axially away from the plunger. Such a flow pattern was termed by Rose (46)¹³ as “a reverse fountain flow.”

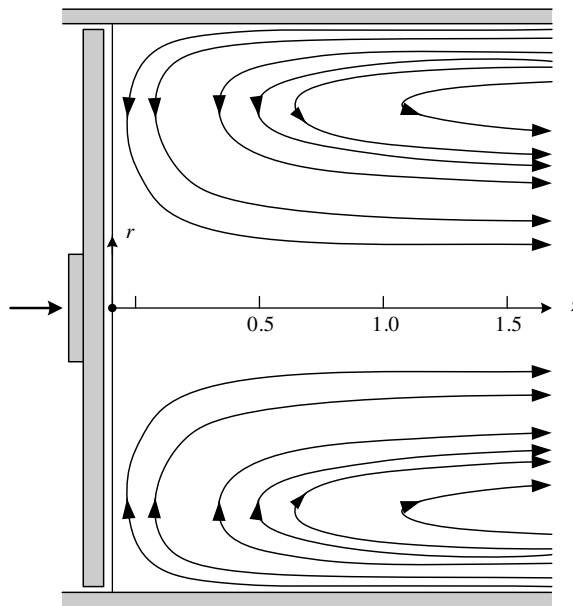


Fig. E6.13 Computed streamlines in front of the plunger, assuming isothermal flow, Newtonian fluid, and a frictionless plunger surface.

12. In an attempt to eliminate this disadvantage, Bob Westover designed a continuous plunger-type extruder using four sets of plunger cylinders, two for melting and two for pumping. [See R. F. Westover, “Continuous Flow Ram Type Extruder,” *Mod. Plast.* (1963).] He also designed a viscometer with two plunger cylinders connected head-on with a capillary tube between them to evaluate the effect of hydrostatic pressure on viscosity.

13. Rose examined the flow pattern in a capillary tube where one immiscible liquid displaces another one. In the front end of the displacing liquid the flow pattern is one he termed “fountain flow,” and in the other “reverse fountain flow.” In polymer processing the significance of the former was demonstrated in the advancing melt front in mold filling (see Chapter 13).

Bhattacharji and Savic (47) derived the following approximate velocity profiles:

$$v_z = V_0 \left(1 - \frac{2r^2}{R^2} \right) \left(1 - e^{-z\sqrt{6/R}} \right) \quad (\text{E6.13-1})$$

and

$$v_r = -\frac{V_0\sqrt{6}r}{R^3} (R^2 - r^2) e^{-z\sqrt{6/R}} \quad (\text{E6.13-2})$$

We note that if V_0 is added to v_z , the “laboratory” frame of reference is restored (i.e., stationary cylinder and moving plunger), and that at large z values the velocity profile converges to the familiar Poiseuille-type parabolic profile. We also observe that at an axial distance of one radius from the plunger, 91% of the fully developed velocity profile is obtained and at one diameter from the plunger, 99% is obtained. Finally, we note that at $r = R/\sqrt{2}$ the axial velocity component vanishes (equals the velocity of the plunger), at $r > R/\sqrt{2}$ the fluid moves toward the plunger, and at $r < R/\sqrt{2}$ it moves away from the plunger.

Example 6.14 Squeezing Flow between Two Parallel Disks This flow characterizes compression molding; it is used in certain hydrodynamic lubricating systems and in rheological testing of asphalt, rubber, and other very viscous liquids.¹⁴ We solve the flow problem for a Power Law model fluid as suggested by Scott (48) and presented by Leider and Bird (49). We assume a quasi-steady-state “slow” flow¹⁵ and invoke the lubrication approximation. We use a cylindrical coordinate system placed at the center and midway between the plates as shown in Fig. E6.14a.

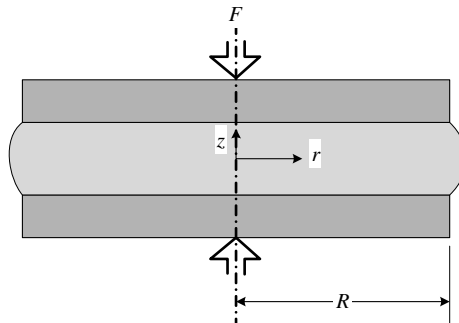


Fig. E6.14a Schematic representation of squeezing flow with a cylindrical coordinate system placed midway between the disks.

14. The Williams Plastometer, which is based on this geometry, has been used in the rubber industry for many years. [I. Williams, “Plasticity and its Measurement,” *Ind. Eng. Chem.*, **16**, 362–364 (1931).] More recently, Leider and Bird (49) pointed out the advantage of this simple geometry for transient nonviscometric rheological testing of polymeric melts.

15. For “fast” squeezing flow we would need a constitutive equation that accounts for the stress overshoot phenomenon.

In light of these assumptions, the Power Law model reduces to:

$$\tau_{rz} = m \left(-\frac{dv_r}{dz} \right)^n \quad (\text{E6.14-1})$$

and the equation of continuity reduces to

$$\frac{1}{r} \frac{\partial}{\partial r} (rv_r) + \frac{\partial v_z}{\partial z} = 0 \quad (\text{E6.14-2})$$

which can be integrated to give

$$-\dot{h}\pi r^2 = 2\pi r \int_0^h v_r dz \quad (\text{E6.14-3})$$

where $\dot{h} = dh/dt$ is the instantaneous disk velocity. The r component of the equation of motion with inertial terms and normal-stress terms omitted, reduces to

$$\frac{\partial \tau_{rz}}{\partial z} = -\frac{\partial P}{\partial r} \quad (\text{E6.14-4})$$

The time dependence of v_r is introduced through the boundary condition at $h(t)$ as given by Eq. E6.14-3, where

$$v_r(h) = 0 \quad (\text{E6.14-5})$$

Furthermore, requirements of symmetry dictate that $\partial v_r / \partial z = 0$ or $\tau_{rz} = 0$ at $z = 0$. It follows from the simplifying assumptions that the other two components of the equation of motion reduce to $\partial P / \partial \theta = 0$ and $\partial P / \partial z = 0$, hence the pressure P is a function of r only, and Eq. E6.14-3 can be integrated with respect to z , to give:

$$\tau_{rz} = \left(-\frac{\partial P}{\partial r} \right) z \quad (\text{E6.14-6})$$

Substituting Eq. E6.14-6 into Eq. E6.14-1 and integrating over z we obtain the velocity profile:

$$v_r = \frac{h^{1+s}}{1+s} \left(-\frac{1}{m} \frac{dP}{dr} \right)^s \left[1 - \left(\frac{z}{h} \right)^{1+s} \right] \quad (\text{E6.14-7})$$

where $s = 1/n$. Note that this velocity profile is identical to that of a Power Law model fluid in fully developed flow between parallel plates with the local pressure gradient and instantaneous disk separation. By substituting the velocity v_r from Eq. E6.14-7 into Eq. E6.14-3, followed by integration, a differential equation for the pressure gradient is obtained in terms of the instantaneous disk velocity:

$$\frac{dP}{dr} = -m \left(\frac{2+s}{2h^{s+2}} \right)^n (-\dot{h})^n r^n \quad (\text{E6.14-8})$$

which can be integrated to obtain the pressure profile

$$P = P_a + m \frac{(2+s)^n}{(n+1)} \frac{(-\dot{h})^n R^{1+n}}{2^n h^{1+2n}} \left[1 - \left(\frac{r}{R} \right)^{1+n} \right] \quad (\text{E6.14-9})$$

where P_a is the atmospheric pressure. The maximum pressure, as expected, is at the center of the disk. The total instantaneous force that must be applied to the disk to maintain the velocity \dot{h} is obtained from Eq. E6.14-9 by integrating the product of the pressure and the differential surface area to give:

$$F_N = m\pi \frac{(2+s)^n}{(3+n)} \frac{(-\dot{h})^n R^{3+n}}{2^n h^{1+2n}} \quad (\text{E6.14-10})$$

which is the Scott equation. Note that, for a Newtonian fluid, the force is proportional to the fourth power of the radius, and inversely proportional to the third power of the separation gap.

Normally we would apply a *constant* force and measure the gap separation profile. This is obtained from Eq. E6.14-10

$$\frac{h(t)}{h_0} = \left[1 + \frac{2(1+s)(3+n)^s}{2+s} \left(\frac{F_N}{\pi m R^2} \right)^s \left(\frac{h_0}{R} \right)^{1+s} t \right]^{(-n)/(1+n)} \quad (\text{E6.14-11})$$

where $h_0 = h(0)$. Finally, the preceding equation yields the value of the “half time,” that is, the time needed to reduce the gap size to half its initial value:

$$\frac{t_{1/2}}{n} = K_n \left(\frac{\pi m R^2}{F_N} \right)^s \left(\frac{R}{h_0} \right)^{1+s} \quad (\text{E6.14-12})$$

where

$$K_n = \left(\frac{2^{1+s} - 1}{2n} \right) \left(\frac{2+s}{1+s} \right) \left(\frac{1}{1+s} \right)^s \quad (\text{E6.14-13})$$

According to the Scott equation, plotting $\ln(t_{1/2})$ versus $\ln(1/F_N)$ should give a straight line. This is what Leider (50) observed with a series of fluids in the Scott equation range. However, Leider and Bird (49) extended the analysis to include stress overshoot phenomena by using a semiempirical expression for the shear stress:

$$\tau_{rz} = m \left(-\frac{dv_r}{dz} \right)^n [1 + (b\dot{\gamma}t - 1)e^{-t/(\lambda a n)}] \quad (\text{E6.14-14})$$

where λ is a time constant and $\dot{\gamma}$ is the shear rate, which modifies Eq. E6.14-10 to

$$F_N = m\pi \frac{(2+s)^n}{(3+n)} \frac{(-\dot{h})^n R^{3+n}}{2^n h^{1+2n}} \left\{ 1 + \left[\frac{(2+s)}{2^{1+s}} \left(\frac{-\dot{h} h_0^s}{h^{2+s}} \right) b t - 1 \right] e^{-t/(\lambda a n)} \right\} \quad (\text{E6.14-15})$$

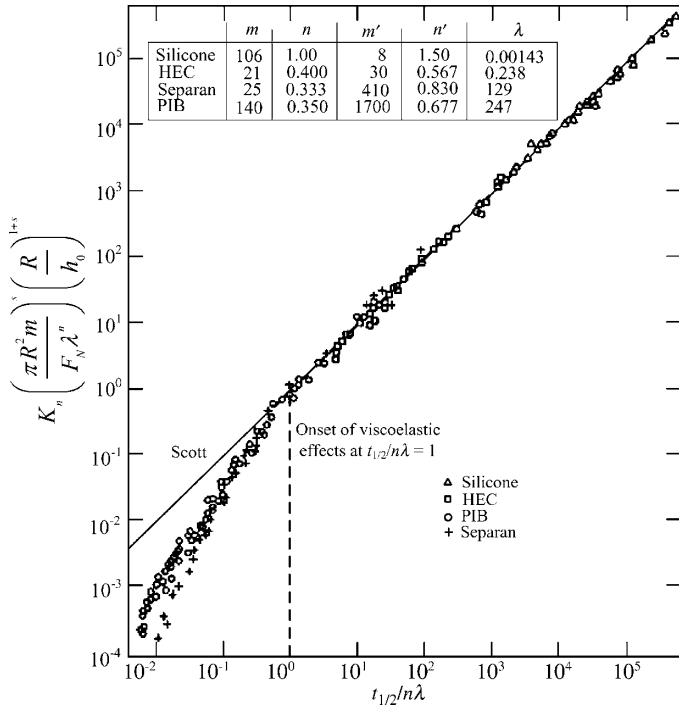


Fig. E6.14b Dimensionless plot of squeezing flow data by Leider (50) representing 181 runs for four fluids: silicone oil, 1% solution of hydroxyethyl cellulose (HEC), 0.5% solution of Separan (polyacrylamide) in glycerin, and polyisobutylene solution. [Reprinted by permission from P. J. Leider, “Squeezing Flow between Parallel Disks, II, Experimental Results,” *Ind. Eng. Chem. Fundam.*, **13**, 342–346 (1974).]

Their experimental results are shown in Fig. E6.14b, which plots dimensionless half-time versus dimensionless reciprocal force. Clearly, the Scott equations describe the experimental results given earlier as $t_{1/2}/n\lambda = 1$. They recommend that the choice of the parameter λ be made on the basis of the Power Law parameters m and n and a similar Power Law relationship of the primary normal stress difference function $\Psi_1(\dot{\gamma}) = m_1 \dot{\gamma}^{1/(m-n)}$ as follows:

$$\lambda = \left(\frac{m_1}{2m}\right)^{1/(n_1-n)} \tag{E6.14-16}$$

They also recommend the selection of parameters a and b so as to give the best fit for the stress overshoot data obtained for a constant shear-rate experiment. By following this procedure, good agreement between experiments and theory was obtained, as demonstrated in Fig. E6.14b.

Next we examine two important *continuous* positive-displacement pumps: the gear pump and the co-rotating fully intermeshing twin-screw pumps. First we show in the following Example how to convert building block 5 into a continuous intermeshing twin-screw pump.

Example 6.15 Conversion of Building Block 5 in Figure 6.2 Consisting of a Plate Moving Normal to its Plane into a Fully Intermeshing Counterrotating Twin-screw Pump

The conceptual process is a bit tortuous, but as shown in Fig. E6.15a, it is not unreasonable. In step one we wish to convert axial motion into rotary motion. This can be achieved by using by a rolling cylinder over a flat plate. Next we have the rolling cylinder move around a second solid cylinder. Then the rolling cylinder is sliced into segments and the second cylinder converted into a screw such that the rolling segments roll in the screw channel. Finally, the rolling cylinders in the screw channel can be replaced by a second intermeshing screw rotating in the opposite direction to the first screw, which will push the material forward in the same fashion, leading to a fully intermeshing twin-screw pump. Note that a 90° angle twin screw converts (conceptually) into a gear pump.

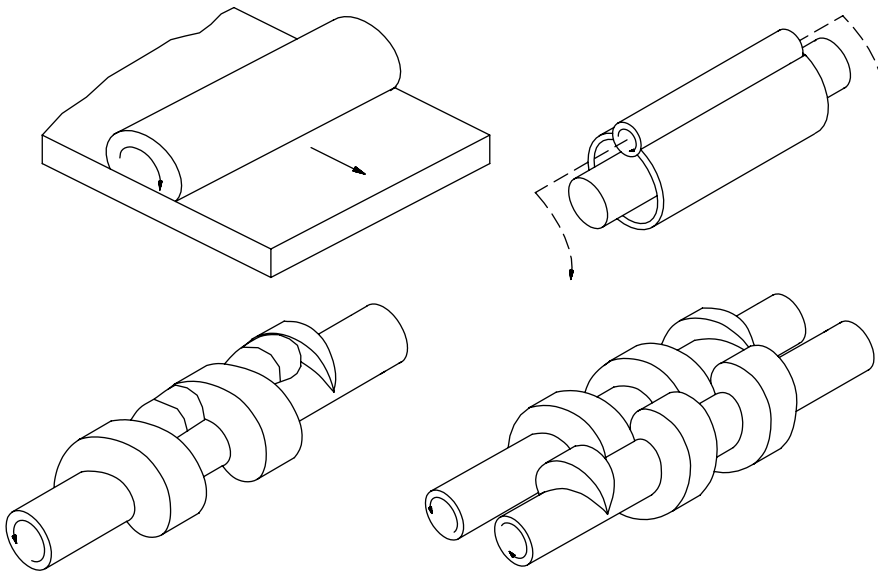


Fig. E6.15a The synthesis of the intermeshing counterrotating TSE, the gear pumps, and paddle pump from building block 5.

The gear pump [Fig. 6.37(c)] permits accurate flow-rate metering, coupled with high discharge pressure for both low and high viscosity liquids. In polymer processing, gear pumps were applied in pumping low molecular weight (low viscosity) polymers such as nylons for high-rate pelletizing after reactors of polyolefines, and as “booster” pumps attached to the discharge end of plasticating extruders for both raising pressure and for accurately controlling flow rate (e.g., in fiber spinning).

The principle of operation of gear pumps is simple: The melt is fed between the exposed adjacent gear teeth, and transported by the rotating gears from inlet port to the discharge port. During this time the liquid is enclosed in a small space created by the adjacent teeth, the root of the gear and the housing. The latter moves relative to the gear generating drag-induced rotational flow within the space, similar to the cross-channel circulatory flow in SSEs. There is also a small leakage flow in the clearance over the teeth.

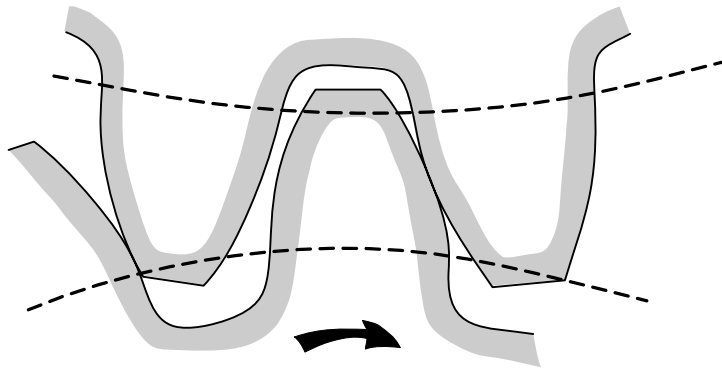


Fig. 6.38 Tooth configuration of gear pumps.

The inlet and outlet ports are sealed from each other by meshed gears. The meshing action squeezes the melt out of the discharge space. The flow is continuous, but every instant that a new set of gear teeth is exposed to the discharge space, both the pressure and flow rate are affected, and thus both oscillate slightly at a frequency proportional to gear speed times the number of teeth.

The shape of the gear is generally of the involute¹⁶ type (Fig. 6.38). With straight-teeth gears, liquid can be trapped between the intermeshing teeth, resulting in “backlash” with its excessive noise and wear. With low-viscosity liquid, this problem can be relieved by positioning strategically located relief ports. Since this is not possible for polymeric melts, double helical gears are normally used, as shown in Fig. 6.39. Upon intermeshing, this geometry of teeth results in a squeezing-out action of the melt, from the center outward.

Example 6.16 The Flow Rate of a Gear Pump Ideally the displaced volume determines the flow rate of a gear pump, and it is independent of rheological properties. If the volume of

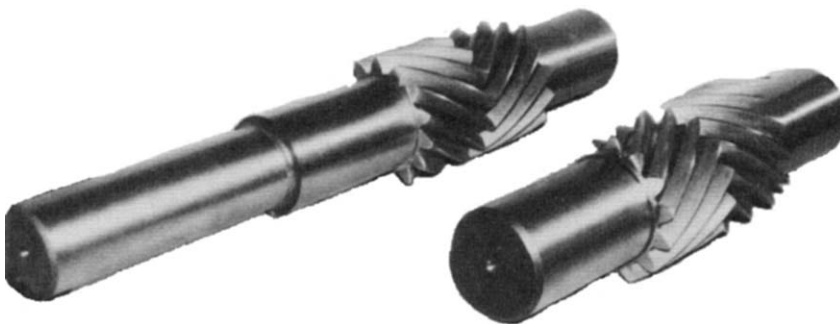


Fig. 6.39 Double helical gears. [Photograph courtesy of Farrel Corp., Ansonia, CT.]

16. Such a shape is derived from the curve obtained by the end of a string wrapped around the circumference of a stationary cylinder and being unwrapped under tension.

the space between the teeth is given by V_n , the number of teeth n , and the speed of rotation N , the volumetric flow rate Q will be given by

$$Q = V_n n N \quad (\text{E6.16-1})$$

The die resistance at the discharge port determines the discharge pressure.

In reality, however, some leakage does occur between the teeth and the housing, and between the intermeshing gears, somewhat reducing pumping efficiency. The leakage flow is sensitive, of course, to viscosity. A full hydrodynamic analysis of gear pumps would require the evaluation of the leakage flows (51), the circulatory flow within the space between the teeth, and the squeezing flow between the meshing teeth, where the stresses on the gear teeth are affected by both the viscosity as well as non-Newtonian elastic properties of the liquid such as stress overshoot. Moreover, nonisothermal conditions should be accounted for. Yet as shown in Fig. E6.16, the theoretical flow rate is reasonably close to experimental results for very good first-order estimations.

Gear pumps are characterized by relatively high flow rates at low frequencies of rotation with low specific power consumption, but they also have a number of disadvantages. In gravitational feeding, there is an upper limit of viscosity beyond which the polymer will not fill the gears, resulting in what is called *starving*. When used downstream, low pressure-generating processing equipment, such as co-rotating intermeshing TSEs in postreactor finishing operations, the processing equipment must operate under conditions that deliver the melt to the gear-pump melt intake at a set minimum

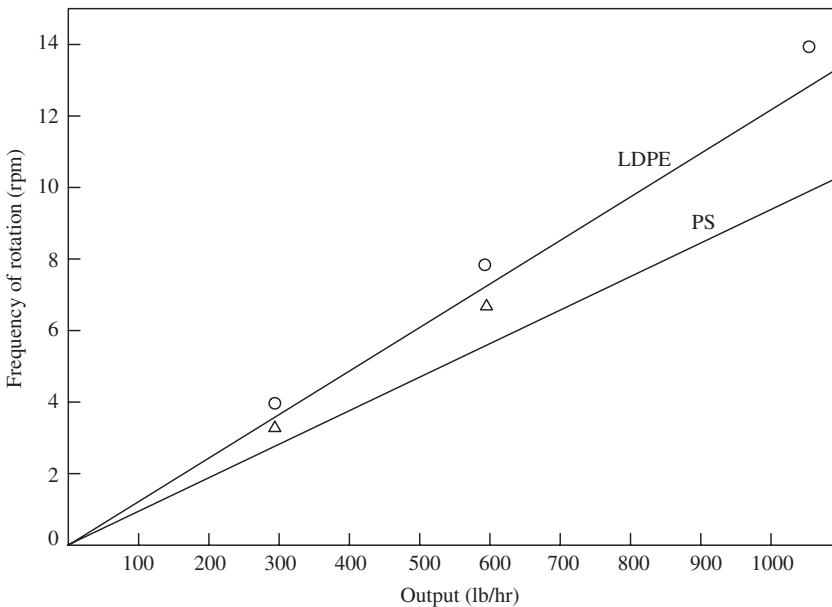


Fig. E6.16 Output versus gear frequency of rotation for a 5.6-in-diameter 4.5 in wide, double (30°) helical, 14-teeth 0.67-in-deep gear pump, and with LDPE (circles) and PS (triangles). Smooth curves are the theoretical ones at the respective densities. [Reprinted with permission from C. Y. Cheng, Farrel Corp., Ansonia, CT, private communication, 1972.]

value of the order of 100–200 psi. The other limitation is the large forces that can develop in the meshing region, which tend to separate the gears and create wear. Finally, gear pumps may not be used for thermally and shear sensitive polymers because of the numerous dead spots present.

6.8 TWIN SCREW EXTRUDER PUMPS

By placing two screws side by side to create a TSE (52–54), the number of geometrical design variables, compared to a SSE, is greatly enriched. Indeed, TSEs come in a large variety of configurations and arrangements with a wealth of patent literature. The three principal variants are shown in Fig. 6.40, and they are (a) the direction of rotation, (b) the level of intermeshing, and (c) the level of engagement. The resulting types of flow channels are shown in Fig. 6.41.

The screws can *co-rotate*, in which case the screws have helix angles in the same direction (either right-handed or left-handed), or *counterrotate*, in which case, the screws have opposite helix angles. The screws can be nonintermeshing or intermeshing, that is, the flight of one screw penetrates into the channel of the other. In the latter case, the screws can be fully or partially engaged. When fully engaged, the flight of one screw completely fills the channel of the other and the screws are “self-wiping.” Depending on the geometry of the screw of a corotating fully intermeshing twin screw, as shown in Fig. 6.41, the channel may be continuous, with a smooth transition from the channel of one screw to that

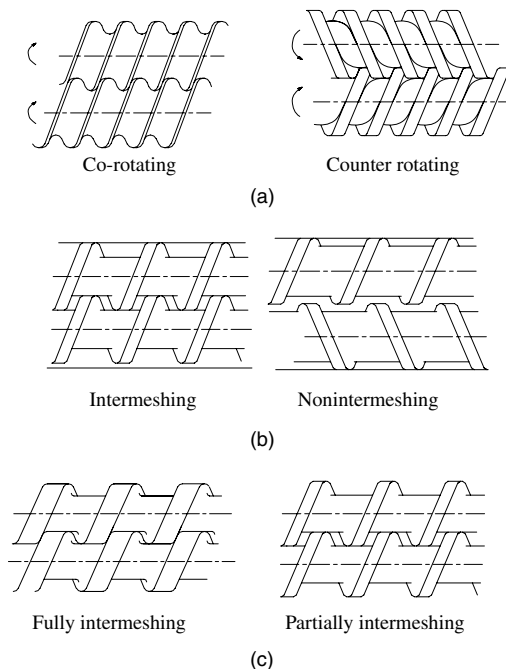


Fig. 6.40 Classification of TSEs systems. [Reproduced by permission from J. F. Agassant, P. Avenas, J.-Ph. Sergent, B. Vergnes, and M. Vincent, *La Mise en Forme Des Matières Plastiques, Technique et Documentation*, Third Edition, Technique & Documentation, Paris, 1996].

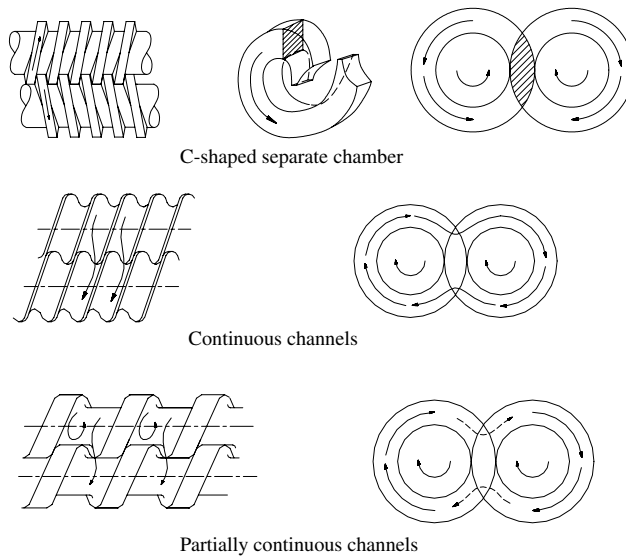


Fig. 6.41 Different types of TSE flow channels. [Reproduced by permission from J. F. Agassant, P. Avenas, J.-Ph. Sergent, B. Vergnes, and M. Vincent, *La Mise en Forme Des Matières Plastiques, Technique et Documentation*, Third Edition, Technique & Documentation, Paris, 1996].

of the other, or partially continuous, with the flight width partially blocking the passage from the channel of one screw to that of the other.

The fully intermeshing Co-TSEs are used extensively in all applications where mild to intensive compounding must be done. These machines are constructed with multiple-section screws,¹⁷ each having different geometrical designs, and with self-wiping kneading blocks. In the case of counterrotating fully intermeshing TSEs, the channel of one screw is completely blocked by the other, creating isolated channel segments. This positive displacement type of TSE, which has good plasticating capability at low specific energy consumption, sometimes uses conical screws to reduce the size of the isolated chamber space as it moves from entrance to exit. In addition, screws can be single or multiflighted. Screws do not have to be of equal size (in which case, for intermeshing screws they rotate at different speeds), though in all practical cases they are. Finally, there may be more than two screws, but these will be not discussed here. Clearly, the number of available geometrical design variables greatly exceeds those of most other processing machines.

This rich variety of design solutions, with their complex geometrical features, implies the need for a complementary, rich arsenal of theoretical analyses. Such a resource has never been created and only the most prevalent types of machines have been analyzed in reasonable detail. Among these are the co-rotating fully intermeshing TSEs, the counterrotating fully intermeshing TSEs, and the tangential nonintermeshing TSEs.

Pumping and pressurization in these three configurations are analyzed next.

17. The screw segments (elements) are assembled on keyed shafts.

The Co-rotating Intermeshing Screw Pump

The pumping mechanism of the co-rotating intermeshing twin screw is drag-induced flow, much like that of the SSE based on building block 1 in Fig. 6.2. Its main advantage is its self-wiping surfaces, including the flights and root of the screw, which eliminate dead spots, while its disadvantages include higher machining costs due to the tight clearances, and some limitation on power inputs due to the proximity of the axes of the two screws.

First, we discuss the geometry of the co-rotating intermeshing twin screw, which was studied in detail by Booy (56), who derived the relevant geometrical relationships. Consider a section perpendicular to the axes of the screws as shown in Fig. 6.42 for single-, double-, and triple-flighted screws, with the detailed geometrical variables of double-flighted screws shown in Fig. 6.43.

The cross section, fulfilling the requirement of self-wiping, has a *unique shape* determined by only three variables: the diameter, $2R_s$, the centerline distance, C_L , and the number of tips or parallel flights, n . The whole screw can be viewed as the axial assembly of an infinite number of infinitely thin slices of screws slightly rotated relative to each other, with each pair fully wiping each other. Hence, for the geometrical definitions of any screw section, it is sufficient to study the geometry of a single pair.

The angle ψ bounding the interpenetrating region, as shown in Fig. 6.43, is given by

$$\cos \psi = \frac{C_L/2}{R_s} = \rho_c/2 \tag{6.8-1}$$

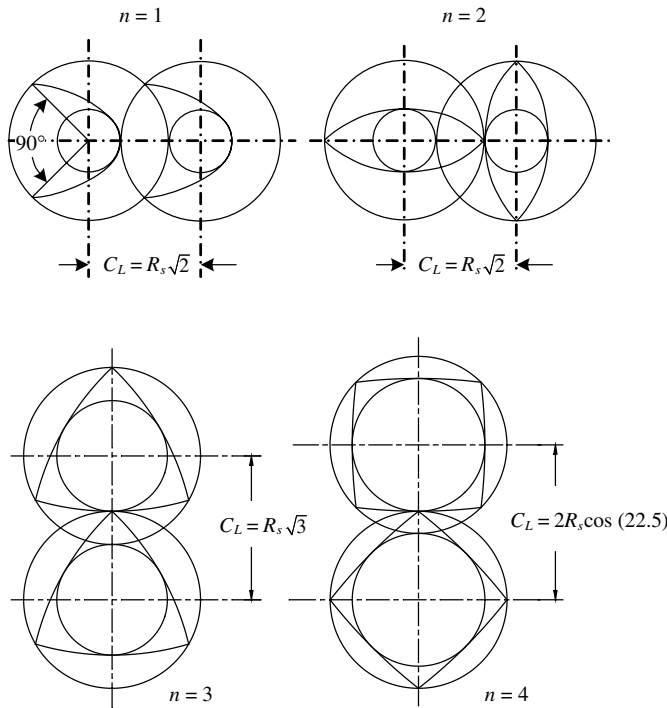


Fig. 6.42 Schematic cross sections of co-rotating fully intermeshing twin screws for single-, double-, triple-, and quadruple-flighted screws. [Reprinted by permission from M. L. Booy, “Geometry of Fully Wiped Twin-Screw Equipment” *Polym. Eng. Sci.*, **18**, 973 (1978).]

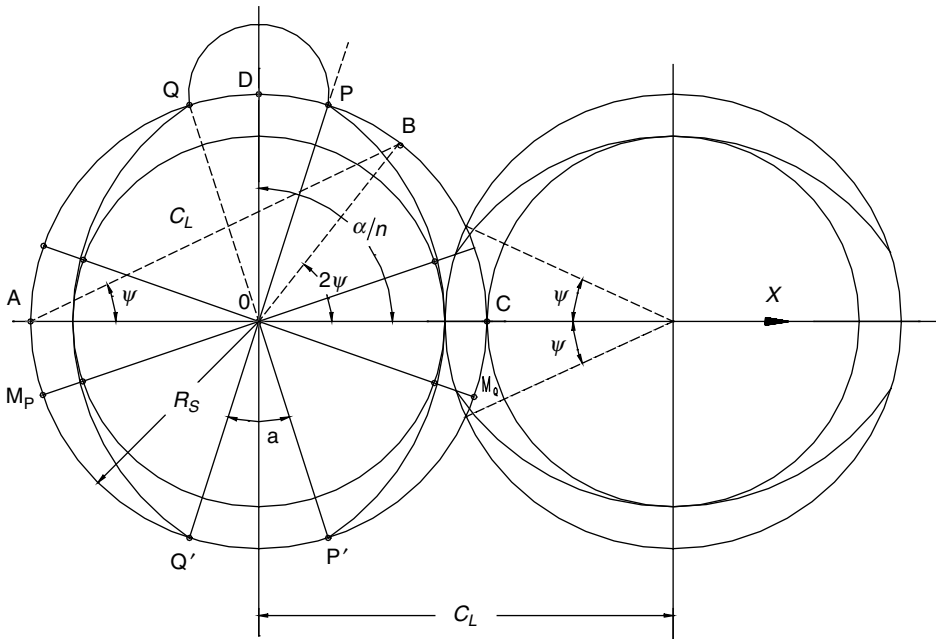


Fig. 6.43 Geometrical parameters of a co-rotating fully intermeshing double-flighted twin screw. [Reprinted by permission from M. L. Booy, “Geometry of Fully Wiped Twin-Screw Equipment” *Polym. Eng. Sci.*, **18**, 973 (1978).]

where the dimensionless parameter ρ_c is the ratio of centerline distance to the barrel radius. The angle defining the width of the flight tip α is related to angle ψ by the following relationship

$$\alpha = \frac{\pi}{n} - 2\psi \tag{6.8-2}$$

Thus for double-channel screws, $n = 2$, Eq. 6.8-2 shows that a ψ value of $\pi/4$ yields a zero tip angle, $\alpha = 0$, and from Eq. 6.8-1 $\rho_c = \sqrt{2}$. Similarly, for a triple flighted screw $\alpha = 0$ and $\rho_c = \sqrt{3}$ at $\psi = \pi/6$. Smaller ψ angles or larger ρ_c lead to larger tip angles α .

The channel-depth profile is shown in Fig. 6.44. Between points B_1 and B_2 over an angle equaling the tip of flight α , the channel depth is constant and has a maximum value of $H = 2R_s - C_L$; between points A and P, namely, over the tip of the flight, the channel depth is zero (i.e., equals the radial clearance that is neglected in this analysis). Between points B and A the channel depth varies with the angle γ as follows:

$$H(\gamma) = R_s(1 + \cos \gamma) - \sqrt{C_L^2 - R_s^2 \sin^2 \gamma} \tag{6.8-3}$$

We note that the channel depth at any angle γ remains constant in the down-channel direction.

The area of the barrel cross section A_{bc} and the area of the screw cross section A_s , are, respectively,

$$A_{bc} = 2(\pi - \psi)R_s^2 + C_LR_s \sin \psi \tag{6.8-4}$$

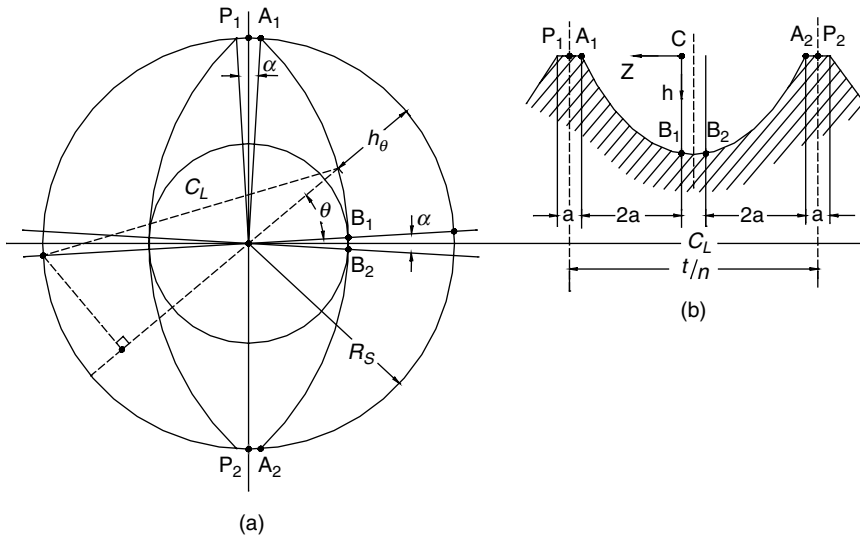


Fig. 6.44 The channel-depth profile (a) in a cross section normal to the axis, and (b) an axial cross section. [Reprinted by permission from M. L. Booy, “Geometry of Fully Wiped Twin Screw Equipment” *Polym. Eng. Sci.*, **18**, 973 (1978).]

and

$$A_s = n(\psi C_L^2 - C_L R_s \sin \psi) = \frac{1}{2} n \alpha [R_s^2 - (C_L - R_s)^2] \tag{6.8-5}$$

The free cross-sectional area, A_f , between screws and barrel is

$$A_f = A_{bc} - A_s \tag{6.8-6}$$

and the free volume between screws and barrel V_f is

$$V_f = A_f L \tag{6.8-7}$$

where L is the axial length of the extruder. The mean residence time is obtained by dividing free volume by the volumetric flow rate.

As in single screw geometry, the helix θ , is given by

$$\tan \theta = \frac{B}{2\pi r} \tag{6.8-8}$$

where r is the radial position, and B is the lead. The channel width is given by

$$W = \frac{B \cos \theta}{n} - e \tag{6.8-9}$$

where e is the flight width perpendicular to the down-channel direction; it is given by

$$e = \alpha R_s \sin \theta \tag{6.8-10}$$

In SSEs the number of parallel channels equals the number of parallel flights. In a TSE the number of parallel channels is larger than the number of flights. For example, as

indicated in Fig. 6.42, for double-flighted screws we obtain three parallel channels. In general the number of parallel channels, m , is given by

$$m = 2n - 1 + \frac{\alpha n}{\pi} \quad (6.8-11)$$

but since α is small, the number of parallel channels can be well approximated by $m = 2n - 1$.

Figures 6.45(a) and 6.45(b) show schematically the cross section of a double-flighted screw configuration with the three parallel channels, and the flattened unwound screws showing the markings of the flight tips, with corresponding points T and A marked on both. At the particular cross section shown, Channel 1 is confined to Screw 1, Channel 3 is partly in Screw 1 and partly in Screw 2, and Channel 2 is confined to Screw 2. Figure 6.45(b) also shows the passage of the material from the channels of Screw 1 to those of Screw 2 and back again. Thus, the streakline described by a fluid particle is a spiral within the helical channel of Screw 1, passing to similar spiral motion in the helical channel of Screw 2. At closed discharge, at the axial location shown in the figure, in Channels 1 and 2 fluid particles will be circulating in the C-shaped planes of each screw, and in Channel 3 they will be circulating between the two screws in the plane shown.

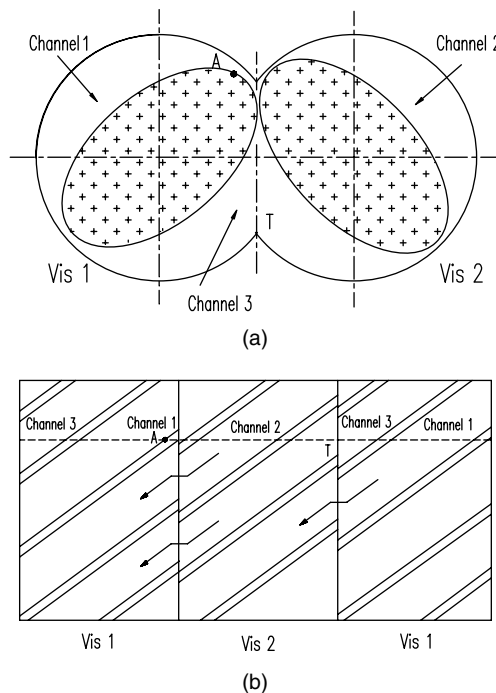


Fig. 6.45 (a) Schematic view of a double-flighted screw identifying the three parallel channels; (b) a section of the flattened unwound screws with the markings of the flight tips. The figure shows a short section of Screw 1 connecting to Screw 2 and back to Screw 1. [Reproduced by permission from J. F. Agassant, P. Avenas, J. Ph. Sergent, B. Vergnes, and M. Vincent, *La Mise en Forme Des Matières Plastiques, Technique et Documentation*, Third Edition, Technique & Documentation, Paris, 1996.]

We also notice in Fig. 6.45(b) that for small values, the transition from one screw to the next is smooth, creating an almost continuous flow; whereas for larger α values, the flight of the “other” screw creates an obstruction to flow.

Newtonian flow models for fully filled elements were developed by several authors (57–61). Here we derive the simplest isothermal Newtonian model for calculating the flow rate in a channel, which is identical to that of SSEs, as discussed in detail in Section 6.3. The volumetric flow rate in each channel is $Q_{ch} = Q/m$, where Q is the total volumetric flow rate.

Thus, considering a channel of length L_c , width W , and height H , the flow rate Q_{ch} is given by

$$Q_{ch} = \frac{1}{2} V_{bz} WH - \frac{WH^3}{12\mu} \frac{\Delta P_c}{L_c} \quad (6.8-12)$$

where ΔP_c is the pressure rise over length L_c , and V_{bz} is the down-channel velocity of the barrel surface relative to the screw:

$$V_{bz} = V_b \cos \theta = 2\pi NR_s \cos \theta \quad (6.8-13)$$

Now it is clear that the drag- and pressure-flow components need to be multiplied by appropriate shape factors.¹⁸ The total pressure rise, ΔP_t , depends on its length L_t :

$$\Delta P_t = \Delta P_c \frac{L}{L_c} \left(1 - \frac{\psi}{\pi} \right) \quad (6.8-14)$$

where the factor $1 - \psi/\pi$ was introduced to account for the fact that, in the transition space between the screws, drag flow vanishes because of the opposing motion of the other screw.

The Counterrotating Intermeshing Screw Pump

An excellent historical review and applications of this type of extruder were produced by White (53), and the flow was modeled by Janssen et al. (62) and Wyman (63), whose derivation we follow. The easiest way to visualize the conveying mechanism of a counterrotating intermeshing TSE is to place a robot “viewer” into the screw channel at point 0 in Fig. 6.37(d) and let it report its observations. We first stop the rotation of the screws and tell our viewer to explore the space around it. It will report that the space is entirely confined by steel walls: the barrel surface from above, the flights of screw *A* at either side, and the intermeshing flight of screw *B* both up-channel and down-channel. The space is a helically distorted C-shaped channel that can be shown schematically, as in Fig. 6.46, or by molding silicone rubber into the space in Fig. 6.47. Clearly, by fully

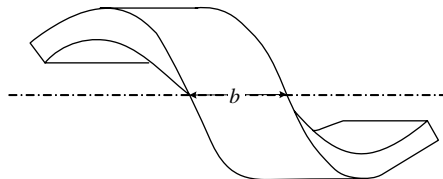


Fig. 6.46 The three-dimensional schematic view of the channel segments formed by two counterrotating intermeshing twin screws.

¹⁸ See Table 10.8.

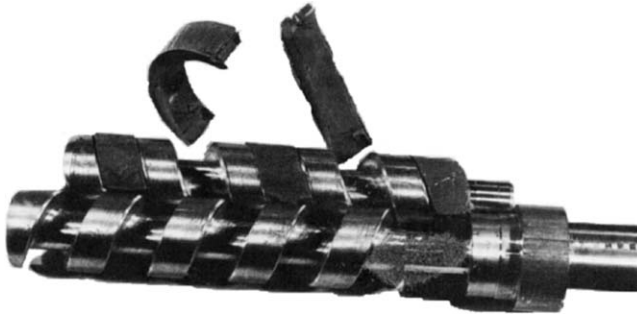


Fig. 6.47 Two intermeshing screws with the channel segments of one of the screws filled with silicone rubber, reproducing the shape of the channel segments. Two segments are pulled out, one retaining the original curved shape and the other flattened out into a trapezoidal channel.

meshing two mirror-image screws, both screw channels are subdivided into short helical segments. We next derive simple mathematical models for the flow rate and velocity profiles within the chambers.

Unlike in drag-induced flows, where we compute the flow rate from the velocity profiles, in this case, because of the positive displacement nature of the flow, we could easily relate flow rate to the axial motion of the closed chambers. But in order to understand the nature of the flow inside the chamber, for mixing and power consumption we do need to derive the detailed velocity profiles.

What happens when the screws start to rotate? The robot viewer will report that all the walls of the confined space began moving, but if it moves axially with velocity:

$$V_l = L_s N \quad (6.8-15)$$

where L_s is the lead shown in Fig. 6.37(d), and N is the frequency of screw rotation, the walls are moving parallel to their surface and it can maintain a fixed position relative to the wall. Thus, the whole compartment is transported at constant axial velocity toward the die. From this *Lagrangian* point of view, the barrel surface will be moving with velocity V_l in the opposite direction, and the root of the screw in the *up-channel helical direction* with velocity,

$$V_s = NZ_s \quad (6.8-16)$$

where Z_s is the helical length of one full turn on the root of the screw, given by

$$Z_s = \frac{L_s}{\sin \theta_s} \quad (6.8-17)$$

where θ_s is the helix angle on the root of the screw. From these equation we get

$$V_s = \frac{V_l}{\sin \theta_s} \quad (6.8-18)$$

The flights are, of course, also moving in the same direction as the root of the screw.

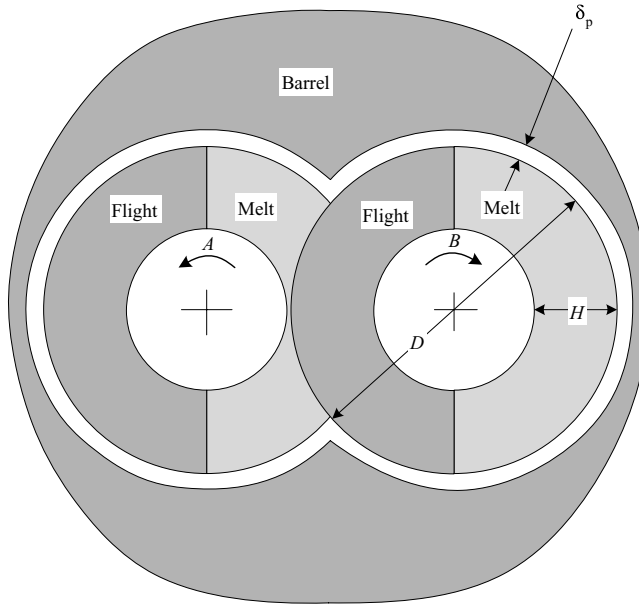


Fig. 6.48 Schematic view of the cross section of an intermeshing counterrotating TSE.

Now that the physical configuration has been clarified, we can consider in detail the mathematical model for the process. First, we find a relationship between the flow rate and the geometrical and operational variables. Neglecting leakage flow between the screws, as well as that between the screws and the barrel, this is simply given by multiplying the velocity V_l with the cross-sectional area of the melt-filled channel, A_m , as shown in Fig. 6.48

$$Q = V_l A_m \tag{6.8-19}$$

For single-flighted screws, A_m (indicated in Fig. 6.48 by the dotted area) equals the full cross-sectional area of the annular space between the root of one screw $\pi(D_f - H)H$ less the area corresponding to the overlap of the flanks of the flights. Thus neglecting flight clearance, we get

$$A_m = \pi(D_f - H)H - \frac{D_f^2}{2} \cos^{-1} \left(1 - \frac{H}{D_f} \right) + \frac{D_f - H}{2} \sqrt{H(2D_f - H)} \tag{6.8-20}$$

The volumetric flow rate (both screws) is given by

$$Q = \pi N \bar{D} L_s H \left[1 - \frac{1}{2\pi} \left(\frac{D_f}{\bar{D}} \right) \left(\frac{D_f}{H} \right) \cos^{-1} \left(1 - \frac{H}{D_f} \right) + \frac{1}{2\pi} \left(\frac{D_f}{\bar{D}} \right) \left(1 - \frac{H}{D_f} \right) \sqrt{\frac{2D_f}{H} - 1} \right] \tag{6.8-21}$$

where $\bar{D} = D_f - H$ is the mean diameter. The actual flow rate is less than the theoretical value because of leakage flows between chambers. Specifically, there are leakage flows

between the screw flights and the barrel, between the tips of flights of one screw and the root of the second screw, and between the flanks of the flights. These leakage flows were calculated by Janssen et al. (62,64–67), who also carried out experiments with Newtonian fluids, confirming their theoretical model, and by Klenk (68–70) and Doboczky (71,72). Power consumption in twin-screw geometry is given by Schenkel (6), who also analyzes the various twin screws and compares their action to single-screw pumps.

We now develop a simple model, termed the *plate-and-frame* model, which approximates the flow patterns inside the chamber. Since the chambers move at constant axial velocity given by Eq. 6.8-15, from a *Lagrangian* point of view, that is, from the point of view of an observer moving axially at this velocity, the channel walls appear at fixed position and the velocity profile within the chamber can be assumed as being at steady state. Assuming relatively shallow channels, we unwind the channel and flatten it out, as shown in Fig. 6.49. We note the surface of the barrel, which moves at velocity V_l in the direction opposite to the forward axial direction, and the root of the screw, which moves at velocity V_s in the upstream helical direction. The flights, of course, move together with the root of the screw. The blocking screw rotates with a tangential velocity πND_s . The end result of the simplified model is as follows: The flights and the cylinders (screw *B*) form a parallelepiped frame. The “frame” is placed within two infinite plates: the surface of the barrel and the root of the screw. Figure 6.50 depicts top and side views of this plate-and-frame model. Each retaining surface moves parallel to its plane, as pointed out earlier and shown in the figure.

The velocity of the barrel surface can be broken down into two components: down-channel $V_l \sin \theta_b$ and cross-channel $V_l \cos \theta_b$ toward the “pushing” flight. The screw velocity is the vectorial sum of two components: the tangential velocity of the root of the screw πND_s and the velocity of the barrel or the viewer V_l . Finally, Fig. 6.50(b) gives the first hint of the nature of the flow pattern in the chamber. We note that both the screw and the barrel drag melt toward the pushing screw. Neglecting end effects and assuming that the net flow rate is zero (no leakage), the shape of the velocity profile in the down-channel direction (v_z) must assume a shape as indicated in Fig. 6.50(b). This also implies a pressure buildup against the pushing screw.

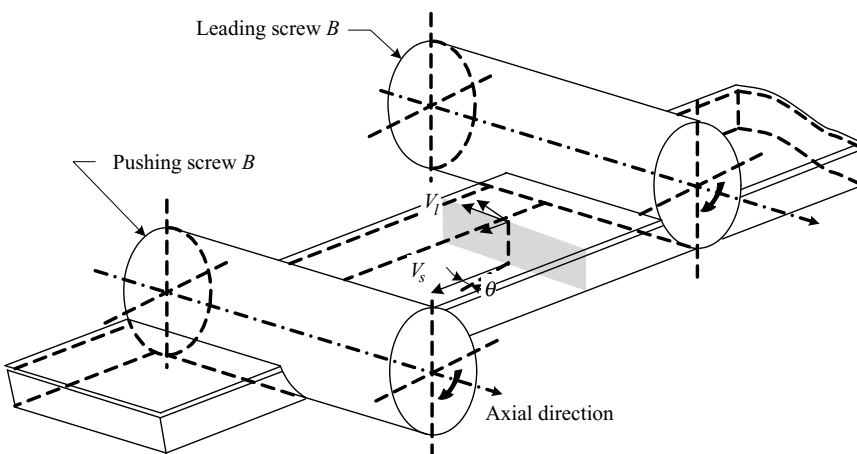


Fig. 6.49 The unwound helical channel segment forming a single chamber of the counterrotating twin screw.

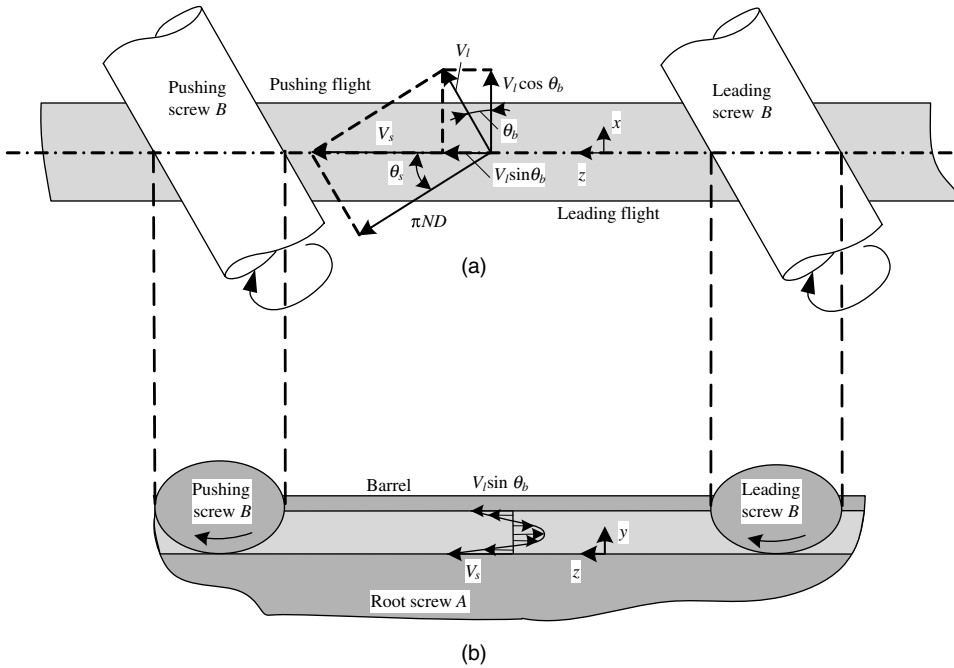


Fig. 6.50 (a) Top, and (b) side views of the unwound channel shown in Fig. 6.49.

We next derive the exact velocity profile, assuming steady, laminar, isothermal, and fully developed flow without slip at the walls, of an incompressible Newtonian fluid. The equation of continuity reduces to

$$\frac{\partial v_y}{\partial y} = 0 \tag{6.8-22}$$

which upon integration yields $v_y = \text{constant}$; but since v_y vanishes at either plate, it must vanish everywhere. Thus, we find that $v_y = 0$. The velocity components that are left in the equation of motion are $v_z(y)$ and $v_x(y)$. The equation of motion reduces to

$$\frac{\partial P}{\partial x} = \mu \frac{\partial^2 v_x}{\partial y^2} \tag{6.8-23}$$

and

$$\frac{\partial P}{\partial z} = \frac{\partial^2 v_z}{\partial y^2} \tag{6.8-24}$$

with boundary conditions

$$v_x(0) = 0 \tag{6.8-25}$$

$$v_x(H) = V_l \cos \theta_b \tag{6.8-26}$$

$$v_z(0) = V_s \tag{6.8-27}$$

$$v_z(H) = V_l \sin \theta_b \tag{6.8-28}$$

The y component of the equation of motion indicates that $P \neq f(y)$; thus, Eqs. 6.8-23 and 6.8-24, with the preceding boundary conditions, can be integrated to give the required velocity profiles

$$v_x = V_l \cos \theta_b \xi + \xi(\xi - 1) \left(\frac{H^2}{2\mu} \frac{\partial P}{\partial x} \right) \quad (6.8-29)$$

and

$$v_z = (V_l \sin \theta_b - V_s) \xi + \xi(\xi - 1) \left(\frac{H^2}{2\mu} \frac{\partial P}{\partial z} \right) + V_s \quad (6.8-30)$$

where H is the channel depth. By assuming zero net flow rate in both directions (no leakage), we integrate the velocity profiles to obtain the following expression for the pressure gradients:

$$\frac{\partial P}{\partial x} = \frac{6\mu V_l \cos \theta_b}{H^2} \quad (6.8-31)$$

and

$$\frac{\partial P}{\partial z} = \frac{6\mu(V_l \sin \theta_b + V_s)}{H^2} \quad (6.8-32)$$

Thus, as in SSEs, the pressure rises linearly in the directions of the pushing flight and pushing screw, reaching a maximum at the corner between them. However, the absolute pressure cannot be determined from the model unless the chamber is partially empty, where the pressure can be assumed atmospheric. Otherwise, the leakage flow must be considered and the pressure profile along the screw determined.

By substituting Eqs. 6.8-31 and 6.8-32 into Eqs. 6.8-29 and 6.8-30, respectively, we obtain

$$\frac{v_x}{V_l \cos \theta_b} = \xi(3\xi - 2) \quad (6.8-33)$$

and

$$\frac{v_z}{V_l \sin \theta_b} = \xi(3\xi - 2) + \frac{V_s}{V_l \sin \theta_b} (1 - 4\xi + \xi^2) \quad (6.8-34)$$

Figure 6.51 shows the velocity profiles for square pitched screws ($\theta = 17.65^\circ$), with $V_l \sin \theta_b = 1$. The velocity profiles reveal intense internal circulation, whereby melt is dragged by the root of the screw toward the pushing screw in the lower portion of the channel, while it flows in the opposite direction (opposing the motion of the barrel surface) in the upper portion of the channel. At the same time, there is also circulatory flow in the channel width direction where in the upper part of the channel, the melt is dragged by the barrel surface toward the pushing flights and flows back in the lower portion of the channel. The interaction of the two velocity profiles eliminates the possibility of any stagnant layers.

The paths described by the fluid particles will depend on their initial location and will be quite complex. In principle, these paths can be calculated from the velocity profiles and

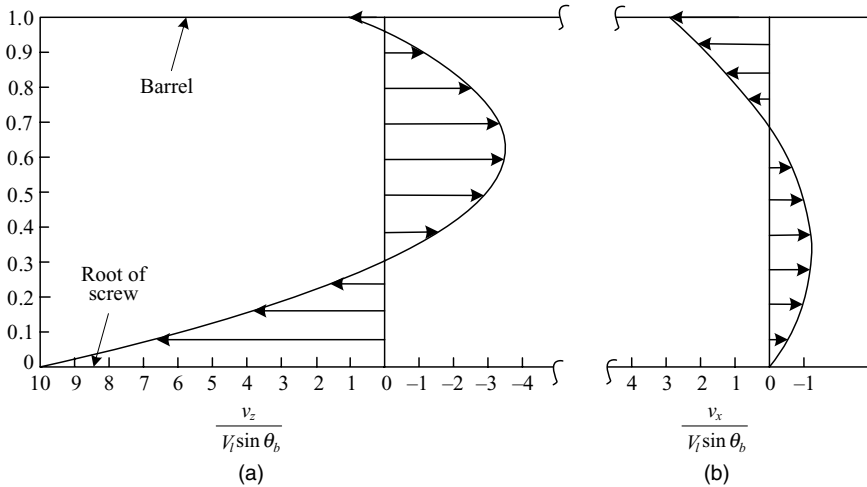


Fig. 6.51 Velocity profiles in the (a) down-channel and (b) cross-channel directions, assuming a square pitched screw. Basis: $V_l \sin \theta_b = 1$, $V_s / (V_l \sin \theta_b) = 1 / \sin \theta_s \sin \theta_b \cong 10$, $v_x(1) / V_l \sin \theta_b = v_x(1) / (V_l \cos \theta_b) (\cos \theta_b / \sin \theta_b) \cong v_x(1) / (V_l \cos \theta_b) \cong 3.13$.

they are expected to have the shape of open-loop helices. The situation is somewhat more complicated in the neighborhood of the nips (Fig. 6.52). Near the pushing flight, both the pushing screw and the root of the screw A drag melt toward the nip. This results in intensive mixing with both high rates and high stresses. The opposite effect occurs at the trailing screw. We discuss the nip regions in Chapter 10.

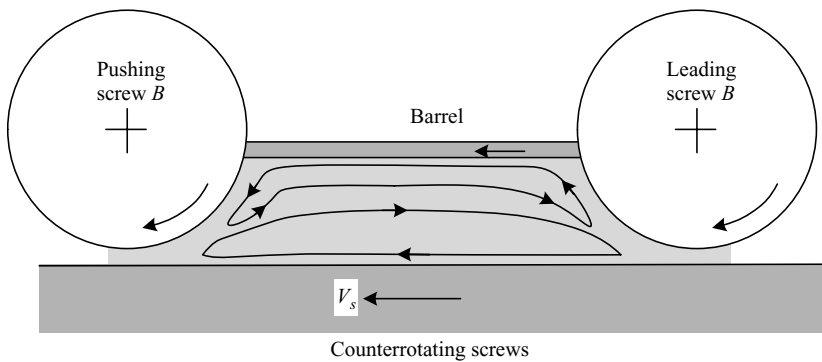


Fig. 6.52 Schematic representation of the streamlines in the neighborhood of the “nips.”

The Tangential Nonintermeshing Twin-screw Pump

This TSE consists of two parallel counterrotating screws, as shown in Fig. 6.53. The distance between the screw centers is $L < D_b$, where D_b is the barrel diameter; thus, there is an open axial slit along the barrel. This type of extruder has advantages for the feeding of particulate solids (e.g., powder), venting, and devolatilization of the molten polymer.

Kaplan and Tadmor (74) proposed a mathematical model for isothermal pumping in this extruder for Newtonian fluids, which they termed “the three plate model.” We follow that

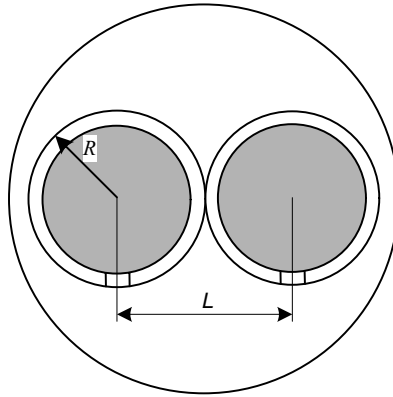


Fig. 6.53 Cross-sectional view of the twin-screw extruder. L is the distance between the centers of the screws and $D_b = 2R$ is the barrel diameter.

model and assume that the screws have identical frequencies of rotation and are positioned such that their respective flights oppose each other. The flow conditions in the channels of both screws are identical, and therefore, solving for one provides a complete solution.

As in single screw analysis, we assume that one screw is stationary while the barrel (with the other screw) is rotating in the opposite direction at the same frequency of rotation. A viewer “riding” on a fluid particle in the stationary screw channel will observe the root of the screw below and the screw flights on either side or the barrel above. The barrel surface, however, is not a smooth continuous surface like it is in a single screw pump, but at every turn of the barrel a slit passes by. Through the slit, the observer will see the other rotating screw. For shallow channels, we unwind the screw channel and place it on a rectangular coordinate system with the slitted barrel, as shown in Fig. 6.54.

A cross section perpendicular to the root of the screw and parallel to the flights is shown in Fig. 6.55, where the other screw across the slit is shown. Clearly, the two screws move at the same velocity in the same direction; therefore, they will appear to each other as stationary. Thus, neglecting curvature and flight effects, the model simplifies to a three-parallel plate model, as shown in Fig. 6.56, with the lower and upper plates representing

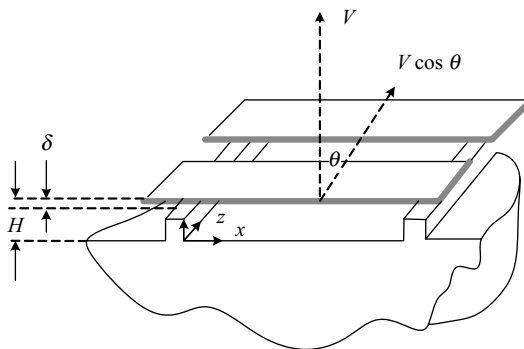


Fig. 6.54 The geometry of the unwound channel with the slitted barrel moving at velocity V_b and V_{bz} in the down-channel direction.

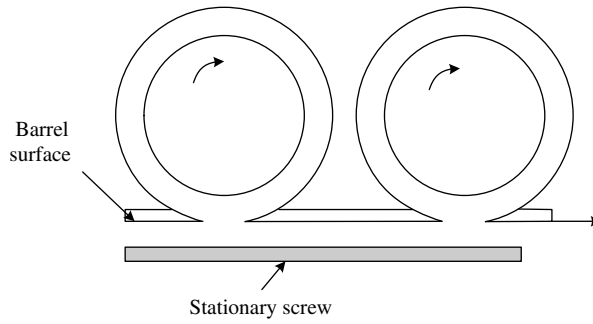


Fig. 6.55 A down-channel cross-sectional view of the unwound channel.

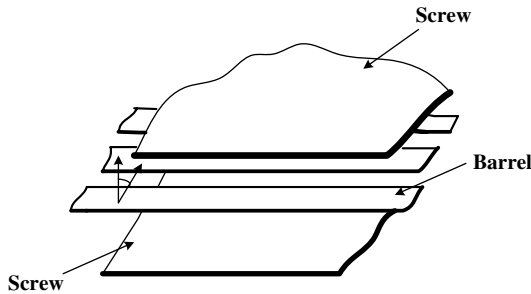


Fig. 6.56 The three-parallel plate model. The upper and lower stationary plates represent the screws, and the slitted midplate is the barrel surface.

the two screws, which are stationary, and the moving central slitted plate representing for both screws the barrel surface. The velocity of the slitted barrel is $V_b = \pi ND_b$ at an angle θ (the helix angle) to the down-channel direction, z . The slits in the barrel are perpendicular to the direction of movement.

Now, for convenience, we assume that the barrel surface is stationary and that the upper and lower plates representing the screws move in the opposite direction, as shown in Fig. 6.57, but for flow rate calculations, it is the material retained on the barrel rather than that dragged by the screw that leaves the extruder. We assume laminar, isothermal, steady, fully developed flow without slip on the walls of an incompressible Newtonian fluid. We distinguish two flow regions marked in Fig. 6.57 as Zone I and Zone II. In the former, the flow is between two parallel plates with one plate moving at constant velocity relative to

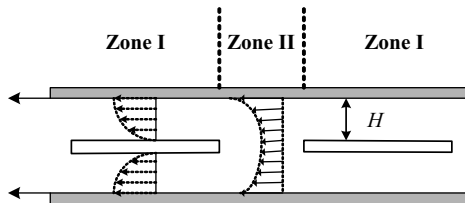


Fig. 6.57 Schematic representation of the velocity profiles in Zones II and I. Note that in Zone I pressure is built up due to drag flow between screw and barrel, whereas, in Zone II pressure is lost due to the pure pressure flow.

the other, and pressure can be generated as in single-screw extrusion. In Zone II, the flow is pressure-driven between two parallel plates and pressure drops.

The velocity profile in Zone I, with the boundary conditions $v_z(0) = 0$ and $v_z(H) = -V_{bz}$ is

$$v_z = \frac{1}{2\mu} \left(\frac{\partial P}{\partial z} \right) y^2 - \left[\frac{1}{2\mu} \left(\frac{\partial P}{\partial z} \right) H + \frac{V_{bz}}{H} \right] y \quad (6.8-35)$$

where H is the channel depth in Zone I. The velocity profile in this zone relative to a stationary screw is

$$v'_z = v_z + V_{bz} \quad (6.8-36)$$

and the flow rate Q delivered by one of the screws is obtained by integrating Eq. 6.8-36, subsequent to inserting Eq. 6.8-35 into Eq. 6.8-36

$$Q = \frac{1}{2} V_{bz} HW - \frac{H^3 W}{12\mu} \left(\frac{\partial P}{\partial z} \right) \quad (6.8-37)$$

Equation 6.8-37 expresses the flow rate in Zone I as a function of the pressure gradient in this zone, and is identical to the single-screw theory.

The pressure rise (or drop) in this Zone ΔP_1 is obtained from Eq. 6.8-37

$$\Delta P_1 = \frac{12\mu}{WH^3} \left(\frac{1}{2} V_{bz} WH - Q \right) \Delta z_1 \quad (6.8-38)$$

where Δz_1 is the helical length of the channel screw from the end of the slit in the barrel to the beginning of the next one. Clearly, if the drag flow rate is higher than the net flow rate, pressure will rise in the down-channel direction.

In Zone II, the velocity profile with boundary conditions $v_z(H) = -V_{bz}$ and $(\partial v_z / \partial y)_{y=0} = 0$ is

$$v_z = \frac{y^2 - H^2}{2\mu} \left(\frac{\partial P}{\partial z} \right) - V_{bz} \quad (6.8-39)$$

The velocity profile relative to stationary screws is given by Eq. 6.8-36 and, integrating it subsequent to substituting Eq. 6.8-39, gives the flow rate *per screw* as

$$Q = -\frac{wH^3}{3\mu} \left(\frac{\partial P}{\partial z} \right) \quad (6.8-40)$$

Clearly, positive flow rate requires a negative pressure gradient, that is, a pressure drop or pressure loss. The pressure drop is given by

$$\Delta P_2 = -\frac{3\mu Q}{WH^3} \Delta z_2 \quad (6.8-41)$$

where Δz_2 is the helical length of the screw channel in the slitted zone.

The total pressure change along one full turn is the sum of Eqs. 6.8-38 and 6.8-41

$$\Delta P_t = \frac{6\mu}{H^2} V_{bz} \Delta z_1 - \frac{3\mu Q}{WH^3} (4\Delta z_1 - \Delta z_2) \quad (6.8-42)$$

which can be written in terms of the fraction of the down-channel length without a slit on the barrel $f = \Delta z_1 / \Delta z_t$ to give

$$\frac{\Delta P_t}{\Delta z_t} = \frac{6\mu V_{bz}}{H^2} f - \frac{3\mu Q}{WH^3} (1 + 3f) \quad (6.8-43)$$

Finally, from Eq. 6.8-44 the flow rate per screw, Q , can be expressed as

$$Q = \frac{1}{2} WHV_{bz} F_{DTW} - \frac{WH^3}{12\mu} \left(\frac{\Delta P_t}{\Delta z_t} \right) F_{PTW} \quad (6.8-44)$$

where

$$F_{DTW} = \frac{4f}{1 + 3f} \quad (6.8-45)$$

$$F_{PTW} = \frac{4}{1 + 3f} \quad (6.8-46)$$

which is the single screw model with appropriate correction factors for the effect of the slit. Since $f < 1$, the drag-flow term is reduced because of the loss in drag in the slitted area, and the pressure-flow term is increased because of the larger gap in the slitted section. For $f = 1$, Eq. 6.8-46 converges, as it should to the single-screw parallel-plate model.

Kaplan and Tadmor (73) expanded the model to include leakage flow effects, considered non-Newtonian fluids, and verified the model experimentally with a polyisobutylene. We discuss the flow further in a tangential, nonintermeshing TSE in Chapter 10.

REFERENCES

1. Z. Tadmor, "The Synthesis of Polymer Processing Machines," *Int. Polym. Process.*, **5**, 1–14 (1990).
2. Z. Tadmor, "Machine Invention, Innovation and Elementary Steps," *Adv. Polym. Technol.*, **21**, 87–97 (2002).
3. F. Reuleaux, *Cinématique*, "Principales d'une Théorie Générale des Machines," Librairie F. Savy, Paris, 1877.
4. H. A. Simon, *The Science of the Artificial*, MIT Press, Cambridge, MA, 1969.
5. V. Hubka, *Principles of Engineering Design*, Butterworth, Boston, 1982.
6. G. Schenkel, *Plastics Extrusion Technology and Theory*, Illife Books, London, 1966.
7. G. Schenkel, "Trends and Highlights in Polymer Processing 1938–1988," *Int. Polym. Process.*, **3**, 3 (1988).

8. I. Asimov, *Asimov's Biographical Encyclopedia of Science and Technology*, Avon Books, New York, 1976.
9. Z. Tadmor, "Method for Processing Polymeric Materials," U.S. Patent 4,142,805, and "Method and Apparatus for Processing Polymeric Materials," U.S. Patent 4,194,841.
10. Z. Tadmor, P. Hold, and L. N. Valsamis, "A Novel Polymer Processing Machine. Theory and Experimental Results," *Proc. 37th Annu. Techn. Conf. of the Society of Plastics Engineers*, New Orleans, (November 1979), pp. 193–204.
11. P. Hold, Z. Tadmor, and L. V. Valsamis, "Applications and Design of a Novel Polymer Processing Machine," *Proc. 37th Annu. Techn. Conf. of the Society of Plastics Engineers*, New Orleans, (November 1979), 205–211.
12. Z. Tadmor, L. N. Valsamis, P. S. Mehta, and Y. C. Yang, "Corotating Disk Pumps for Viscous Liquids," *IEC Process Design Devel.*, **24**, 311–320 (1985).
13. P. S. Mehta, L. N. Valsamis, and Z. Tadmor, "Foam Devolatilization in Multi-Channel Corotating Disk Processors," *Polym. Process Eng*, **2**, 103–128 (1984).
14. Z. Tadmor, "Corotating Disk Scraped Surface Heat Exchangers," *Food Techn.*, Dec 1985 pp. 66–74.
15. I. Edelist and Z. Tadmor, "Velocity Profiles in Corotating Disk Processors," *Polym. Process Eng*, **1**, 1 (1983).
16. B. David and Z. Tadmor, "Extensive Mixing in Corotating Processors," *Int. Polym. Processing*, **3**, 28–47 (1988).
17. Z. Tadmor and I. Klein, *Engineering Principles of Plasticating Extrusion*, Van Nostrand-Reinhold, New York, 1970. (a) p. 190, (b) p. 202, (c) p. 194–199, (d) p. 397, (e) Chapters 6 and 8.
18. M. Kaufman, "Advection and Mixing in Single Screw Extruder—An Analytic Model," *The AIChE Annual. Techn. Conf. Meeting Proc.*, San Francisco (2003).
19. R. S. Rowell and D. Finlayson, "Screw Viscosity Pumps," *Engineering*, **114**, 606 (1922); *ibid.*, **126**, 249 (1928).
20. R. M. Griffith, "Fully Developed Flow in Screw Extruders," *Ind. Eng. Chem. Fundam.*, **1**, 180–187 (1962).
21. R. E. Colwell and K. R. Nicholls, "The Screw Extruder," *Ind. Eng. Chem.*, **51**, 841–843 (1959).
22. J. R. A. Pearson, *Mechanical Principles of Polymer Melt Processing*, Oxford Pergamon Press, Oxford, 1966.
23. H. Zamodits, *Extrusion of Thermoplastics*, Ph.D. Thesis, University of Cambridge, 1964; also H. Zamodits and J. R. A. Pearson, "Flow of Melt in Polymer Extruders, Part 1. The Effect of Transverse Flow on a Superimposed Temperature Profile," *Trans. Soc. Rheol.*, **13**, 357 (1969).
24. M. L. Booy, "The Influence of Non-Newtonian Flow on Effective Viscosity and Channel Efficiency in Screw Pumps," *Polym. Eng. Sci.*, **21**, 93 (1981).
25. K. P. Choo, M. L. Hami, and J. F. T. Pittman, "Deep Channel Operating Characteristics of a Single Screw Extruder: Finite Element Predictions and Experimental Results for Isothermal Non-Newtonian Flow," *Polym. Eng. Sci.*, **21**, 100 (1981).
26. J. Nebrensky, J. F. T. Pittman, and J. M. Smith, "Flow and Heat Transfer in Screw Extruder, I. A Variational Analysis Applied in Helical Coordinates," *Polym. Eng. Sci.*, **13**, 209 (1973).
27. M. L. Hami and J. F. T. Pittman, "Finite Element Solutions for Flow in a Single-Screw Extruder, Including Curvature Effects", *Polym. Eng. Sci.*, **20**, 339 (1980).
28. J. R. A. Pearson, *Mechanics of Polymer Processing*, Elsevier, London, 1985.
29. J. F. T. Pittman and K. Rashid, "Heat Transfer in Recirculating Extruder Channel Flow," *J. Polym. Eng.*, **5**, 1 (1985).
30. I. Bruker, C. Miaw, A. Hasson, and G. Balch, "Numerical Analysis of the Temperature Profile in the Melt Conveying Section of a Single Screw Extruder: Comparison with Experimental Data," *Polym. Eng. Sci.*, **27**, 504 (1987).

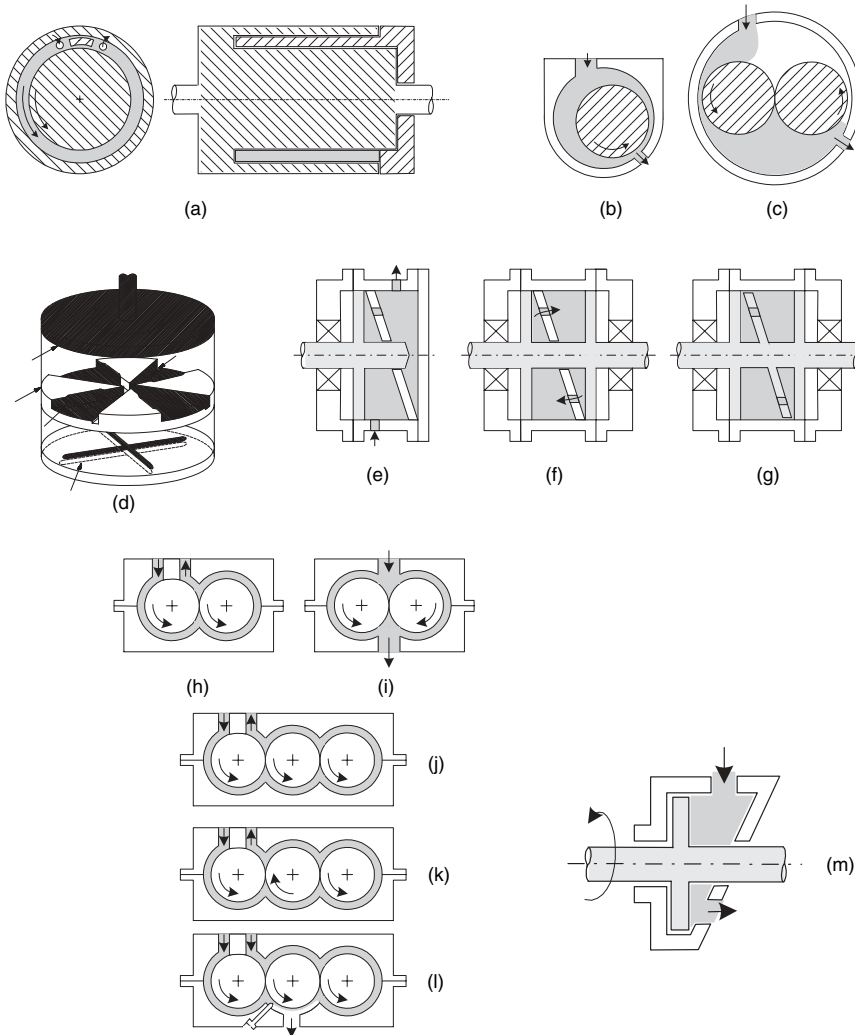
31. R. F. Westover, "A Hydrodynamic Screwless Extruder" *Soc Plastics Eng. J.*, **18**, 1473–1480 (1962).
32. R. E. Gaskell, "The Calendering of Plastics," *J. Appl. Mech.*, **17**, 334–336 (1950); also see D. I. Marshall and E. C. Bernhardt, in "Calendering," *Processing of Thermoplastic Materials*, Krieger, Huntington, New York, 1959, Chapter 6.
33. J. M. McKelvey, *Polymer Processing*, Wiley, New York, 1962.
34. J. T. Bergen and G. W. Scott, Jr., "Pressure Distribution in the Calendering of Plastic Materials," *J. Appl. Mech.*, **18**, 101–106 (1951).
35. C. Kiparissides and J. Vlachopoulos, "Finite Element Analysis of Calendering," *Polym. Eng. Sci.*, **16**, 712–719 (1976).
36. M. Finston, "Thermal Effects in the Calendering of Plastics Materials," *J. Appl. Mech.*, **18**, 12 (1951).
37. W. Unkrüer, "Beitrag zur Ermittlung des Druckverlaufes und der Fliessvorgänge im Walzspalt bei der Kalanderverarbeitung von PVC Hart zu Folien," Doctoral Dissertation, Technische Hochschule Aachen, Aachen, Germany, 1970; see also W. Unkrüer, *Kunststoffe*, **62**, 7 (1972).
38. B. Maxwell and A. J. Scalora, "The Elastic Melt Extruder Works Without Screw," *Mod. Plast.*, **37**(2), 107 (1959).
39. V. L. Kocherov, Yu. L. Lukach, E. A. Sporyagin, and G. V. Vinogradov, "Flow of Melts in Disk-type Extruder," *Polym. Eng. Sci.*, **13**, 194–201 (1973).
40. P. A. Good, A. J. Schwartz, and C. W. Macosko, "Analysis of the Normal Stress Extruder," *AIChE. J.*, **20**, 67–73 (1974).
41. R. B. Bird, R. C. Armstrong, and O. Hassager, *Dynamics of Polymeric Fluids*, Vol. 1, *Fluid Mechanics*, JWiley 1977, p.397.
42. B. Maxwell, "A New Method of Solving the Feeding and Melting Zone Problems in the Normal Stress Extruder," Presented at the 31st Annu. Tech. Conf. of the Society Plastics Engineers, Montreal Canada (1975).
43. Z. Tadmor, P. S. Mehta, L. N. Valsamis and J. Yang, "Corotating Disk Pumps for Viscous Liquids," *Ind. Eng. Chem. Process Des. Devel.*, **24**, 311–320 (1985).
44. Z. Tadmor, P. Hold, and L. Valsamis, "A Novel Polymer Processing Machine" Proc. 37th Annu. Tech. Conf. of the Society of Plastics Engineers, New Orleans, 1979; also A. Tadmor, P. Hold, and L. Valsamis, *Plast. Eng.*, Part I, 1979, pp. 193–204, Part II, 1979, pp. 34–37.
45. I. Edelist and Z. Tadmor, "Velocity Profiles in a Corotating Disk Processor," *Polym. Process Eng.*, **1**, 1 (1983).
46. W. Rose, "Fluid-Fluid Interface in Steady Motion," *Nature*, **191**, 242–243 (1961).
47. S. Bhattacharji and P. Savic, "Real and Apparent Non Newtonian Behavior in Viscous Pipe flow of Suspensions Driven by a Fluid Piston," *Proc. Heat and Mass Transfer Fluid Mechanics Institute*, **15**, 248 (1965).
48. J. R. Scott, *IRI Trans.*, **7**, 169 (1931).
49. P. J. Leider and R. B. Bird "Squeezing Flow Between Parallel Discs I. Theoretical Analysis," *Ind. Eng. Chem. Fundam.*, **13**, 336–341 (1974).
50. P. J. Leider, "Squeezing Flow between Parallel Discs II Experimental Results," *Ind. Eng. Chem. Fundam.*, **13**, 342–346 (1974).
51. A. Ishibashi, "Studies of Volumetric Efficiency and Theoretical Delivery of Gear Pumps," *Bull. Jp. Soc. Mech. Eng.*, **13**, 688–696 (1970).
52. J. F. Agassant, P. Avenas, J.-Ph. Sergent, B. Vergnes, and M. Vincent, *La Mise en Forme des Matières Plastiques, Technique et Documentation*, Paris, 1996.
53. J. L. White, *Twin Screw Extrusion Technology and Principles*, Hanser, Munich, 1990.
54. J. L. White, A. Y. Coran and A. Moet, *Polymer Mixing Technology and Engineering*, Hanser, Munich, 2001.

55. H. Herrmann, U. Burkhardt, and S. Jacopin, "A Comprehensive Analysis of Multiscrew Extruder Mechanisms," *Proc. 35th Annu. Techn. Conf., Society of Plastics Engineers*, Montreal, Quebec, Canada (1977).
56. M. L. Booy, "Geometry of Fully Wiped Twin-Screw Equipment," *Polym. Eng. Sci.*, **18**, 973 (1978).
57. M. L. Booy, "A Noniterative Numerical Solutions of Poisson's and Laplace's Equations with Applications to Slow Viscous Flow", *Trans. ASME Series D*, **88**, 725–733 (1966); also, "Isothermal Flow of Viscous Liquids in Corotaing Twin Screw Devices," *Polym. Eng. Sci.*, **20**, 1220 (1980).
58. C. D. Denson and B. K. Hwang, "The Influence of the Axial Pressure Gradient on Flow Rate for Newtonian Liquids in a Self Wiping, Corotating Twin Screw Extruder," *Polym. Eng. Sci.*, **20**, 965 (1980).
59. W. Szydowski and J. L. White, "An Improved Theory of Metering in an Intermeshing Corotating twin-screw extruder," *Adv. Polym. Technol.*, **7**, 177 (1987).
60. J. Tayeb, B. Vergnes, and G. J. Della Valle, *J. Food Sci.*, **53**, 616 (1988).
61. D. Goffart, D. J. vander Wal, E. M. Klomp, H. W. Hoogstraten, L. P. B. M Janssen, L. Bregse, and Y. Trolez, "Three-dimensional Flow Modeling of a Self-wiping Corotating Twin-screw Extruder. Part I: The Transporting Section," *Polym. Eng. Sci.*, **36**, 901 (1996).
62. L. P. B. M. Janssen, L. P. H. R. M. Mulders, and J. M. Smith, "A Model for the Output from the Pump Zone of the Double-screw Processor or Extruder," *Plast. Polym.*, **43**, 93 (1975).
63. C. E. Wyman, "Theoretical Model for Intermeshing Twin Screw Extruders: Axial Velocity Profile in Shallow Channels," *Polym. Eng. Sci.*, **15**, 606–611 (1975).
64. L. P. B. M. Janssen, *Twin Screw Extrusion*, Elsevier, Amsterdam, 1978.
65. L. P. B. M. Janssen, J. J. Pelgrom, and J. M. Smith, *Kunststoffe*, **66**, 724 (1976).
66. L. P. B. M. Janssen, and J. M. Smith, *Plast. Rubber Process.*, **44**, 90 (1976).
67. J. A. Speur, H. Mavridis, J. Vlachopoulos, and L. P. B. M. Janssen, "Flow patterns in the calender gap of a counterrotating twin screw extruder," *Adv. Polym. Technol.*, **7**, 39 (1987).
68. K. P. Klenk, "Property-based technology for processing rigid PVC power on single- and twin screw extruders, (Beitrag zur werkstoffgerechten Verarbeitung von PVC hary-Pulver auf Ein- und ZweiSchnecken- Extruder)," *Plastverarbeiter*, **22**, 33–38 (1971).
69. K. P. Klenk, "Processing rigid PVC power on single- screw and twin- screw extruders in consistency with material properties, (Beitrag zurwerkstoffgerechten Verarbeitung von PVC hart- Pulver auf Einund Zwei- Schnecken- Extrudern)," *Plastverarbeiter*, **22**, 105–109 (1971).
70. K. P. Klenk, *Plastverarbeiter*, **22**, 189 (1971).
71. Z. Doboczky, *Plastverarbeiter*, **16**, 58 (1965).
72. Z. Doboczky, *Plastverarbeiter*, **16**, 395 (1965).
73. A. Kaplan and Z. Tadmor, "Theoretical Model for Non-Intermeshing Twin Screw Extruders," *Polym. Eng. Sci.*, **14**, 58–66 (1974).

PROBLEMS

6.1 Pressurization Methods The equation of motion indicates the possible alternative sources of pressurization. Indicate the source of the following pressurization methods: human heart, centrifugal pump, gear pump, blow molding, volcanoes, single screw extruder, ram extruder, injection molding, compression molding, centripetal pump, and fully intermeshing co- and counterrotating screw extruder.

6.2 Novel Pumping Configurations The accompanying figure shows a series of pump configurations. Identify the building block the pump is based upon and its operation.



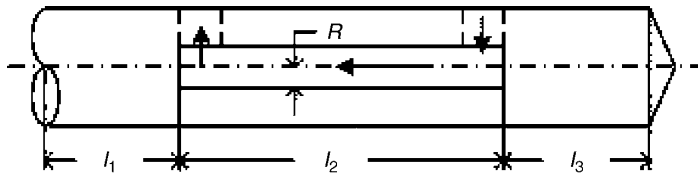
6.3 The Roll Pump Derive a mathematical model for the roll-pump [depicted in Fig. E6.1a(c)] having a barrel inner diameter, D_b , and a roll diameter, D_s , relating the flow rate, Q , pressure rise, $P_{out} - P_{in}$, and roll speed, N , to the relevant geometrical variables. Neglect back flow over the channel blade clearance.

6.4 Parallel-Plate Flow of Newtonian Fluids A Newtonian polymeric melt with viscosity $0.2 \text{ lb}_f/\text{in}^2$ and density $48 \text{ lb}/\text{ft}^3$, is pumped in a parallel-plate pump at steady state and isothermal conditions. The plates are 2 in wide, 20 in long, and 0.2 in apart. It is required to maintain a flow rate of 50 lb/h. (a) Calculate the velocity of the moving plate for a total pressure rise of 100 psi. (b) Calculate the optimum gap size for the maximum pressure rise. (c) Evaluate the power input for the parts (a) and (b). (d) What can you say about the isothermal assumption?

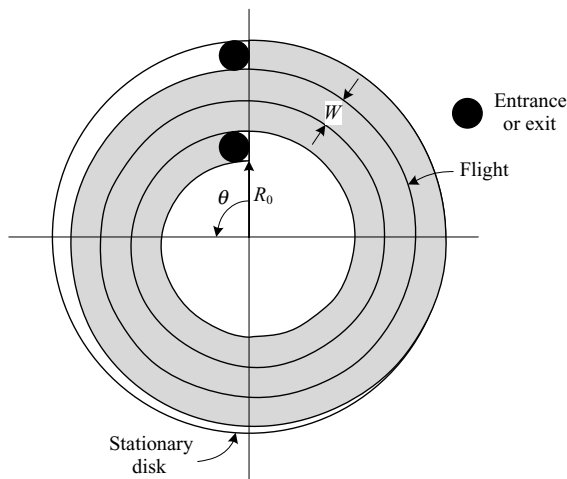
6.5 Screw Extruders for Pumping Water It is claimed that the Greek mathematician Archimedes (born in Sicily about 287 B.C. and died about 212 B.C.) invented the device called the screw of Archimedes for pumping water, though the Egyptians are supposed to have had the device long before for pumping water from the Nile. Discuss the use of extruders for water pumping. What are the limitations and advantages?

6.6 The Freely Rotating Spiral Extruder Pump A free-standing spiral flight, fitted with a small clearance between a stationary barrel of diameter D_b and stationary solid cylinder of diameter D_s rotates at a constant frequency of rotation N . (a) Which building block among those listed in Fig. 6.2 is this pumping device built on? (b) Assuming a shallow-channel configuration, derive a mathematical model relating the flow rate, Q , pressure rise, $P_{out} - P_{in}$, and N , to the geometrical variables as the parameters.

6.7 Single-screw Pump with Inner Recycle A constant channel-depth single-screw pump with a linearly rising pressure has a hollow shaft, as shown in the accompanying figure, connected to the channel such that part of the flow is recycled. Assuming isothermal Newtonian flow (a) derive an expression for the flow rate of the extruder, and (b) for the recycle rate.

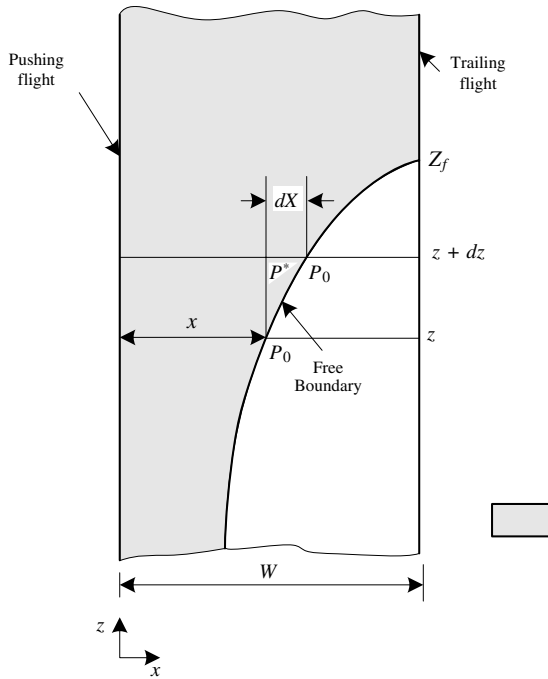


6.8 Flat Spiral Pump A spiral flight of height H is welded to a stationary disk creating a spiral channel of constant width W , as shown in the accompanying figure. By placing a second disk over the channel, a flat spiral pump is created. Clockwise rotation of the upper disk pumps liquid from the outer inlet port to the inner exit port. Derive an expression for the flow rate of an incompressible Newtonian fluid in isothermal flow.

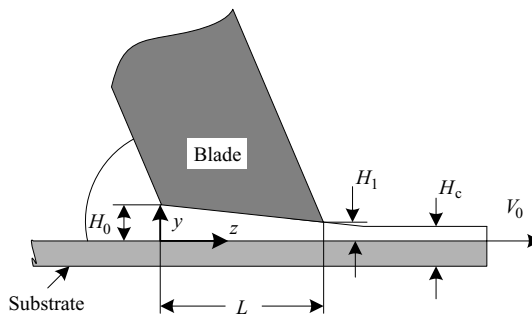


6.9 Partially Filled Screw Channel The accompanying figure below shows a partially filled screw channel. Using the single-screw Newtonian parallel plate model show that the free boundary profile is given by¹⁹

$$\left(1 - \frac{X}{W}\right) + \frac{X_0}{W} \ln \left[\frac{1 - \frac{X_0}{W}}{\frac{X}{W} - \frac{X_0}{W}} \right] = \frac{z_f - z}{W \tan \theta_b}$$



6.10 Blade Coating A schematic view of a blade-coating operation is shown in the accompanying figure. (a) Show that the coating thickness is $H_c = H_0 / (1 + \zeta_0)$



19. A. Berlis, E. Broyer, C. Mund, and Z. Tadmor, "Flow Patterns in Aprtially Filled Extruder Screw," *Plastics Polym.*, **41**, 145–148 (June 1973).

where $\zeta_0 = H_0/H_1$. (b) Show that the normal force on the blade F_N is given by²⁰

$$F_N = \left(\frac{6\mu L^2 W V_0}{H_0 H_1} \right) \left(\frac{1 - \zeta_0(1 - \ln \zeta_0)}{(\zeta_0 - 1)^2} \right)$$

- 6.11 Nonsymmetric Calendering²¹** Derive the pressure distribution of a Newtonian fluid in a calender (a) with different size rolls but equal peripheral speed; (b) with different speeds but equal-size rolls. Make the same simplifying assumptions that were made in the Gaskell model in Section 6.4.
- 6.12 Non-Newtonian Flow between Jointly Moving Parallel Plates (JMP) Configuration** Derive the velocity profile for isothermal Power Law model fluid in JMP configuration.
- 6.13 Relative Efficiency of the JMP and Single Moving Plate (SMP) Configurations²²** (a) Derive and prove Eqs. 6.6-7 and 6.6-8; (b) Show that the specific power input, and the power dissipated into heat, of the optimized JMP and SMP models are given by $(p_w)_{\text{JMP}}/(p_w)_{\text{SMP}} = 1/(1 + s)$ and $(p_w^*)_{\text{JMP}}/(p_w^*)_{\text{SMP}} = 1/(1 + s)$.
- 6.14 Design of Co-rotating-disk Coal-slurry Pump** Moderately viscous suspensions of 50–70% finely pulverized coal in oil and water can be used as a substitute for liquid fuel. The suspension is a non-Newtonian Power Law model fluid with $m = 16 \text{ N s}^n/\text{m}^2$, $n = 0.82$ at 60°C , with density $100 \text{ lb}/\text{ft}^3$, and a specific heat of $1 \text{ Btu}/\text{lb}^\circ\text{F}$. Design a 100-gpm co-rotating-disk pump with 10 parallel wedge-shaped chambers and $\alpha = 0.5$, generating 100 psi head pressure. The inlet and outlet and the channel block occupies 25% of the circumference.

20. Y. Greener and S. Middleman, "Blade Coating of Viscoelastic Fluids," *Polym. Eng. Sci.*, **14**, 791–796 (1974).

21. R. E. Gaskell, "The Calendering of Plastic Materials," *J. App. Mech.*, **17**, 334–336 (1950).

22. Z. Tadmor, P. S. Mehta, L. N. Valsamis, and J. C. Yang, "Corotating Disk Pumps for Viscous Liquids," *Ind. Eng. Chem. Process Des. Devel.*, **24**, 311–320 (1985).

7 Mixing

- 7.1 Basic Concepts and Mixing Mechanisms, 322
- 7.2 Mixing Equipment and Operations of Multicomponent and Multiphase Systems, 354
- 7.3 Distribution Functions, 357
- 7.4 Characterization of Mixtures, 378
- 7.5 Computational Analysis, 391

In this chapter we discuss the elementary step of mixing. We will not deal with mixing of low- or medium-viscosity liquids, but only with mixing of highly viscous polymeric melts. *Mixing* is not only a very important step in the processing of polymeric materials for achieving the required mechanical, physical and chemical properties and the desired appearance of the product in processing machines. Compounding—that is, *mixing together* a variety of components such as different polymeric materials, solid, and liquid additives, sometimes accompanied by a chemical reaction—is often used to produce a plastic material with new and improved properties. In fact, compounding actually offers a far less expensive and more practical route for creating a wide variety of new, improved products than the development of chemically new polymers.

Mixing principles are relevant to many disciplines: what makes mixing polymeric materials unique is their exceptionally high viscosity. There are numerous texts (1–5) that are entirely devoted to the complex problem of mixing of polymers and plastics, and we refer the reader to them for further reading.

In this chapter we will discuss the mixing operations and machines, present an overview of the principles of mixing mechanisms, review characterization tools of mixtures, and outline mathematical tools and models for analyzing mixing processes.

7.1 BASIC CONCEPTS AND MIXING MECHANISMS

Definitions of Mixtures and Mixing Mechanisms

We start our discussion with two fundamental concepts: *mixture* and *mixing*. The former defines the nature of the state of the materials we are concerned with, while the latter, concerns the mechanism by which we manipulate a property of the former. *Mixture* is defined (4) as “the state formed by a complex of two or more ingredients which do not bear a fixed proportion to one another and which, however commingled, are conceived as retaining a separate existence.”

Mixing is an operation that is intended to reduce the nonuniformity of the mixture. This can be accomplished only by inducing physical motion of the ingredients. In general, three

basic types of motion are involved in mixing; *molecular diffusion*, *eddy motion*, and *bulk flow*, or advection (5). Molecular diffusion is driven by a concentration (chemical potential) gradient and occurs spontaneously. It is the dominant mechanism of mixing in gases and low-viscosity liquids. In turbulent mixing, molecular diffusion is superimposed on the gross random eddy motion, which in turn can occur within a larger scale convective or bulk flow, also known as *advection*.¹

In polymer processing, because of the very high viscosities of polymeric melts, the flow is laminar and eddy motion due to turbulence is absent; therefore, it cannot contribute to mixing. Similarly, molecular diffusion does not contribute much to mixing because it occurs extremely slowly. We are therefore left with convection as the dominant mixing mechanism.²

Convection involves movement of fluid particles, blobs of fluid, or clumps of solid in a system from one spatial location to another. Convection results in mixing either if the *interfacial area*, between the minor and the major component, *increases* (6), or if the minor component is distributed throughout the major component without necessarily increasing interfacial area (7). The former criterion is relevant primarily to liquid–liquid mixing, and the latter to solid–liquid and solid–solid mixing. Convective mixing can be achieved by a simple bulk rearrangement of the material that involves a plug-type flow and requires no continuous deformation of the material. Therefore it can be termed *bulk-convective mixing*, *plug-convective mixing*, or simply, *distributive mixing*. Spencer and Wiley (6) have referred to this kind of mixing as *repetitive mixing*, and McKelvey (8) has used the term *simple mixing*.

This kind of mixing through repeated rearrangement of the minor component can, in principle, reduce composition nonuniformity to the molecular level. The repeated rearrangement in *distributive mixing* can be either *random* or *ordered*. The former is the process that takes place, for example, in V-blenders and many other solid–solid mixers, as shown schematically in Fig. 7.1. However, convective mixing in polymer processing is achieved mainly by imposing laminar shear, elongation (stretching), and squeezing (kneading) deformation on the mixture, resulting in an *increase of the interfacial area* (IA) separating the components. Hence, we term this kind of convective mixing, *laminar-convective mixing*. Others refer to it as *streamline mixing* (6) or simply *laminar mixing* (8).

We can generally state that if a liquid–liquid system is to be mixed by a laminar mixing mechanism, permanent deformation or strain must be imposed on the system (6). The term

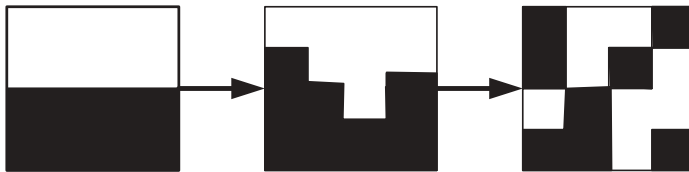


Fig. 7.1 Schematic representation of random distributive mixing (e.g., a process that takes place in a V-blender).

1. *Advection* is derived from the Latin words *ad* and *vehere*, meaning “to carry to.” *Convection*, used in the chemical engineering literature, derives from the Latin words *con* and *vehere*, meaning to “bring together.” In chaotic mixing, as indicated later in the chapter, the former appears to be the more appropriate term.

2. We should note at this point, however, that if one of the components is a low molecular weight material (e.g., certain antioxidants, foaming agents, dyes used for fibers, or slip additives), molecular diffusion may be a significant factor in the mixing process.

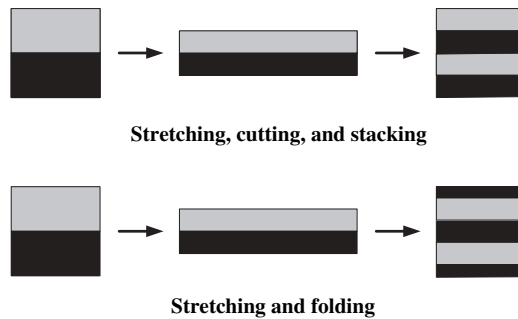


Fig. 7.2 The top figure indicates a mixing protocol of mixing by stretching–cutting–stacking, yielding 2^{n+1} layers after n steps, in this case, $n = 1$. The bottom figure shows a stretching–folding bakers’ transformation yielding $1 + 2^n$ layers, in this case, $n = 2$.

“strain” in the context of laminar mixing excludes elastic or delayed elastic strains and certainly not rigid body rotation and translation. Furthermore, for the interfacial surface to increase, *both* phases must deform. Hence the rheological properties of both phases may play an important role.

We can impose strain on a mixture by either stretching or shearing it. Figure 7.2 depicts two stretching mixing protocols. In the first one we stretch the mixture of rheologically identical grey and black fluids, cut it, and stack it. The interfacial area increases and the two components are distributed throughout the volume. A more practical mixing protocol, which actually takes place in mixers, is the “bakers’ transformation,” consisting of repeated stretching and folding. Continuing this process will very effectively reduce nonuniformity to any required level. In fact, this mixing protocol, if repeated in time, generates exponential rather than linear mixing as in the case of shear flow, and in some 20 repetitions nanodimensions can be reached. Static mixers, such as Kenics, Ross and Sultzler mixers, are based on this mechanism, as well as mixing protocols conducive to chaotic advection.

Laminar mixing by shear flow is depicted in Fig. 7.3 in the case of pressure flow in a tube. The tube is filled with grey viscous liquid with a string of spherical black minor component. Imposing a pressure drop on the fluid will set it into motion and will induce shear deformation. The deformation after a given time t_1 is zero at the centerline, where shear rate vanishes, and maximum at the wall. The black spherical fluid deforms into spheroids with a consequent increase in interfacial area which, as we will see, is a quantitative measure of laminar mixing. Clearly, in laminar mixing, be it stretching or shearing, the decisive variable is *strain*, whereas the *rate of application* of strain or *stresses* play no role. This is indeed the case for compatible (miscible) viscous systems with negligible *cohesive forces*. In these cases, shear stresses are irrelevant to the mixing mechanism.

However, when we have a component that does exhibit cohesive strength, the local stresses do play a very decisive role in the mixing operation. Examples of such components are solid agglomerates (e.g., carbon black), viscoelastic polymer blobs or droplets, and gas bubbles. Moreover, with viscoelastic systems, in particular, the rate of stress buildup or local stress histories may also be important. This kind of mixing is referred to as *dispersive mixing* (8) for solid–liquid mixtures and *homogenization* for liquid–liquid mixtures. These are *intensive* mixing operations in contrast to laminar mixing discussed earlier, which is also termed *extensive* mixing.

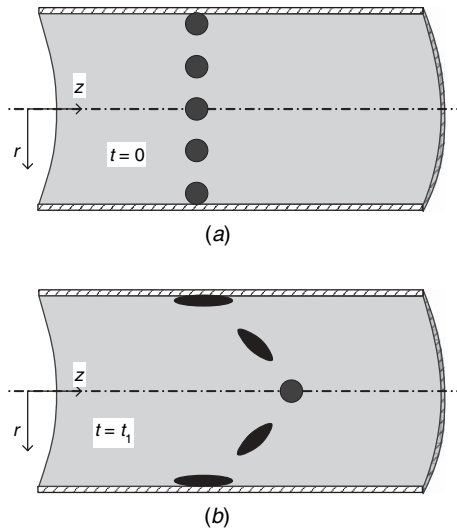


Fig. 7.3 Laminar mixing in laminar pipe flow. Dark areas are occupied by a tracer consisting of the bulk liquid and a small amount of a dye.

In summary, there are basically two mixing mechanisms. The first is *dispersive* or *intensive mixing*, which involves the reduction of the size of a component having *cohesive character*, within a continuous liquid phase. The component may be solid agglomerate, a noncompatible liquid phase or a gas bubble. The cohesive character of agglomerates is due to van der Waals forces between the particles of the agglomerate, to surface tension and elastic properties of liquid droplets, and to surface tension of gaseous bubbles. The second is *distributive, laminar, or extensive* mixing of components, which stretches the interfacial area elements between the components lacking a cohesive character and distributes them throughout the volume. This classification is depicted in Fig. 7.4, which indicates that in distributive mixing, we not only need to stretch the interfacial area, but also, as we will see

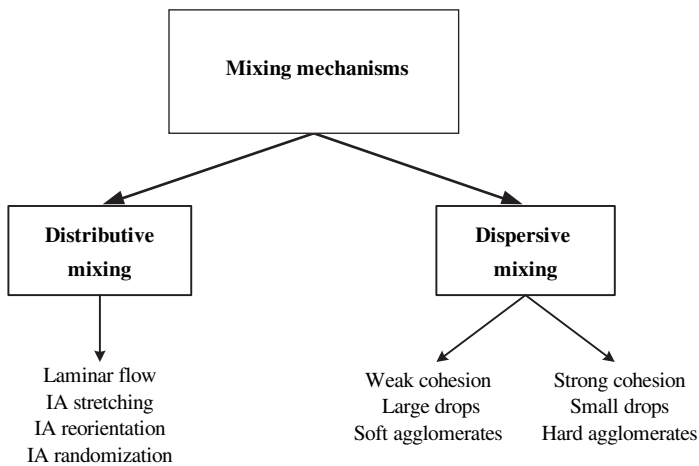


Fig. 7.4 Classification of mixing mechanisms.

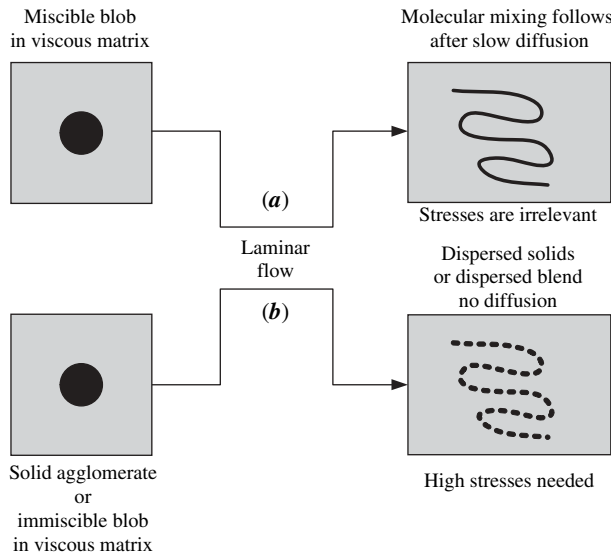


Fig. 7.5 Schematic representation of (a) laminar distributive mixing where the blob is stretched and deformed and distributed throughout the volume; (b) shows the same process as (a) but with an immiscible liquid or a soft agglomerate where the stretching leads to a breakup process.

later, to reorient it for effective mixing, as well as to randomize the interfacial elements throughout the volume.

Chaotic mixing, to be discussed later, may be very effective in stretching, folding, and randomizing interfacial area elements. In dispersive mixing we distinguish between weak and strong cohesive forces. In large droplets, the capillary number defined as $Ca = \tau a / \Gamma$, where τ is the shear stress in the continuous phase, Γ is the surface tension, and a is the characteristic size, is large, and therefore shear forces dominate over cohesive forces, and the droplet deforms in an affine manner into filaments, which at some point break up into smaller droplets. These smaller droplets deform and in a given shear stress of the continuous phase reach an equilibrium deformation. With increasing shear stress they break when the capillary number reaches a certain critical value. Clearly, the smaller the droplet the higher the shear stress needs to be to break it. In the case of agglomerates, if they are large and soft, not unlike large liquid droplets, they deform with the liquid phase and the mechanism is more like extensive mixing. In the case of strong agglomerates, a *critical threshold shear stress* is needed to overcome the cohesive forces and break them. As we will discuss later, unlike liquid droplets, the breakup of strong agglomerates is size independent.

The mechanisms of mixing of miscible and immiscible liquids and soft agglomerates are depicted in Fig. 7.5, and that of hard solid agglomerates in Fig. 7.6. In the former, elongational and shear stretching is the dominant mechanism, whereas, the latter is shear stress dominated.

Laminar Mixing of Homogeneous Liquids

In the following two examples we show the quantitative relationship between shear strain and interfacial area and the effect of orientation in laminar mixing.

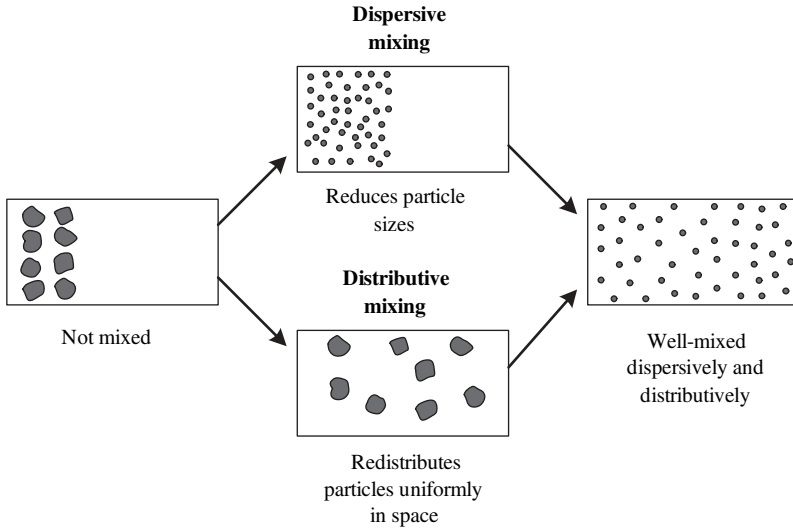


Fig. 7.6 Dispersive mixing of hard solid agglomerates and immiscible liquid droplets that, after breakup, are distributed throughout the volume.

Example 7.1 The Relationship between Interfacial Area and Shear Strain When two viscous liquids are mixed, the interfacial area between them increases. The use of interfacial area increases, as a quantitative measure for laminar mixing was first suggested by Brothman et al. (9) and later by Spencer and Wiley (6). This section relates the change of an interfacial area element to the total strain imposed on the viscous fluid.

Consider an arbitrarily oriented surface element in a homogeneous *simple shear* flow field $v_x = \dot{\gamma}_{yx}y$ [Fig. 7.1a]. The surface element at time t_0 is confined between two position vectors ρ_1 and ρ_2 . The area of the surface element is

$$A_0 = \frac{1}{2}|\mathbf{c}| = \frac{1}{2}|\rho_1 \times \rho_2| \quad (\text{E7.1-1})$$

The vector \mathbf{c} is normal to the surface, and its orientation in space is specified by two of the three directional cosines; $\cos \alpha_x$, $\cos \alpha_y$, and $\cos \alpha_z$, which satisfy the following equation:

$$\cos^2 \alpha_x + \cos^2 \alpha_y + \cos^2 \alpha_z = 1 \quad (\text{E7.1-2})$$

The angles α_x , α_y , and α_z [Fig. E7.1a(a)] are expressed in terms of the components of the vector \mathbf{c} as follows:

$$\cos \alpha_x = \frac{c_x}{|\mathbf{c}|} \quad \cos \alpha_y = \frac{c_y}{|\mathbf{c}|} \quad \cos \alpha_z = \frac{c_z}{|\mathbf{c}|} \quad (\text{E7.1-3})$$

The position vectors ρ_1 and ρ_2 can be expressed in terms of their components as

$$\rho_1 = x_1 \delta_x + y_1 \delta_y + z_1 \delta_z \quad (\text{E7.1-4})$$

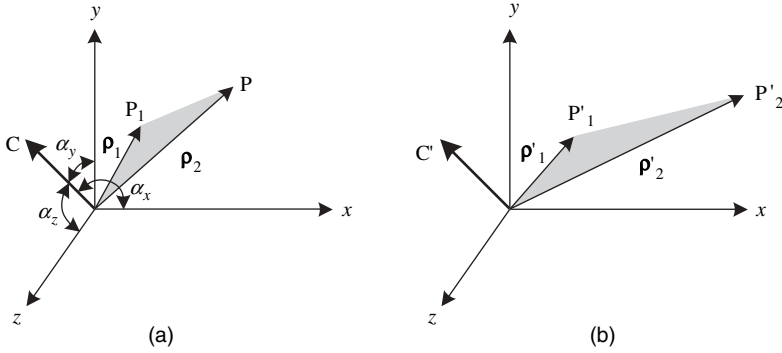


Fig. E7.1a Surface element confined between position vectors ρ_1 and ρ_2 in a simple shear flow $v_x = \dot{\gamma}_{xy}y$. (a) At time t_0 . (b) At a later time t' .

and

$$\rho_2 = x_2\delta_x + y_2\delta_y + z_2\delta_z \tag{E7.1-5}$$

where x_1, y_1 and z_1 and x_2, y_2 , and z_2 are the coordinates of points P_1 and P_2 in Fig. E7.1a(a). Substituting Eqs. E7.1-4 and E7.1-5 into Eq. E7.1-1, we obtain

$$\begin{aligned} \mathbf{c} &= \rho_1 \times \rho_2 \\ &= \begin{vmatrix} \delta_x & \delta_y & \delta_z \\ x_1 & y_1 & z_1 \\ x_2 & y_2 & z_2 \end{vmatrix} \\ &= (y_1z_2 - z_1y_2)\delta_x + (z_1x_2 - x_1z_2)\delta_y \\ &= (x_1y_2 - x_2y_1)\delta_z \\ &= c_x\delta_x + c_y\delta_y + c_z\delta_z \end{aligned} \tag{E7.1-6}$$

Thus the initial area at t_0 is

$$A_0 = \frac{1}{2}|\mathbf{c}| = \frac{1}{2}(c_x^2 + c_y^2 + c_z^2)^{1/2} \tag{E7.1-7}$$

After a certain elapsed time, Δt , the new interfacial area is confined between the position vectors ρ'_1 and ρ'_2 as shown in Fig. E7.1a(b), such that

$$\rho' = \rho + \mathbf{v}\Delta t \tag{E7.1-8}$$

where the velocity vector \mathbf{v} for simple shear flow is

$$\mathbf{v} = \dot{\gamma}y\delta_x + (0)\delta_y + (0)\delta_z \tag{E7.1-9}$$

or

$$\mathbf{v}\Delta t = \gamma y\delta_x + (0)\delta_y + (0)\delta_z \tag{E7.1-10}$$

where γ is the total strain. By substituting Eq. E7.1-10 into Eq. E7.1-8, the new position vectors, in terms of their components, become

$$\boldsymbol{\rho}'_1 = (x_1 + \gamma y_1)\boldsymbol{\delta}_x + y_1\boldsymbol{\delta}_y + z_1\boldsymbol{\delta}_z \quad (\text{E7.1-11})$$

and

$$\boldsymbol{\rho}'_2 = (x_2 + \gamma y_2)\boldsymbol{\delta}_x + y_2\boldsymbol{\delta}_y + z_2\boldsymbol{\delta}_z \quad (\text{E7.1-12})$$

The cross product of the two position vectors becomes

$$\mathbf{c}' = \boldsymbol{\rho}'_1 \times \boldsymbol{\rho}'_2 = \begin{vmatrix} \boldsymbol{\delta}_x & \boldsymbol{\delta}_y & \boldsymbol{\delta}_z \\ x_1 + \gamma y_1 & y_1 & z_1 \\ x_2 + \gamma y_2 & y_2 & z_2 \end{vmatrix} = c_x\boldsymbol{\delta}_x + (c_y - \gamma c_x)\boldsymbol{\delta}_y + c_z\boldsymbol{\delta}_z \quad (\text{E7.1-13})$$

where c_x , c_y , and c_z are the components of vector \mathbf{c} defined in Eq. E7.1-6. The new interfacial area A is therefore,

$$A = \frac{1}{2}|\mathbf{c}'| = \frac{1}{2}\left(c_x^2 + c_y^2 + c_z^2 - 2c_x c_y \gamma + c_x^2 \gamma^2\right)^{1/2} \quad (\text{E7.1-14})$$

The ratio of the two areas at $t_0 + \Delta t$ and t_0 is obtained by dividing Eq. E7.1-14 by Eq. E7.1-7, and making use of the definition of directional cosines in Eq. E7.1-3

$$\frac{A}{A_0} = \left(1 - 2\cos\alpha_x \cos\alpha_y \gamma + \cos^2\alpha_x \gamma^2\right)^{1/2} \quad (\text{E7.1-15})$$

This expression, derived by Spencer and Wiley (6), indicates that the increase in interfacial area is a function of initial orientation and total strain. For large deformations, Eq. E7.1-15 reduces to

$$\frac{A}{A_0} = |\cos\alpha_x| \gamma \quad (\text{E7.1-16})$$

We, therefore, obtain the important conclusion that the increase in interfacial area is *directly proportional to total strain*. Hence, total strain becomes the critical variable for the quantitative characterization of the mixing process. We further conclude from Eq. E7.1-15 that at low strains, depending on the initial orientation, the interfacial area may increase or decrease with imposed strain. This implies clearly that strain may demix as well as mix two components. Indeed if the fluid is sheared in one direction a certain number of shear units, an equal and opposite shear will take the fluid back to its original state (no diffusion).

The role of initial orientation is evident from Eq. E7.1-15. The increase in the interfacial area attains a maximum when the initial orientation of the interfacial area is the yz plane ($\cos\alpha_x = 1, \cos\alpha_y = 0$). The interfacial area remains unchanged if $\cos\alpha_x = 0$ or $c_x = 0$. From Eq. E7.1-6 we note that this occurs if $y_1 = y_2 = 0$ or $z_1 = z_2 = 0$, implying,

respectively, that the surface A_0 is either in the xz or the xy plane. In the former case the plane is translated undeformed, whereas in the latter it is deformed, yet retains the same area.³

In practice we are dealing with interfacial area elements oriented in all directions, as would be the case, for example, of a random distribution of minor-component cubical particles in a major component. Consider a collection of surface area elements of initial size A_0 , randomly orientated in space. The fraction of area elements, or the probability of a single area element pointing in that direction, is given by infinitesimal surface area of a sphere pointing in that direction

$$f(\theta, \varphi) d\theta d\varphi = \frac{1}{4\pi} \sin \theta d\theta d\varphi \quad (\text{E7.1-17})$$

where θ and φ are spherical coordinates, as shown in Fig. E7.1b. Therefore $f(\theta, \varphi) d\theta d\varphi$ is the probability of finding a surface area, with orientation defined by a unit normal vector, between θ and $\theta + d\theta$ and φ and $\varphi + d\varphi$. The angle θ in the spherical coordinate system is identical to the angle α_y , whereas the angle φ relates to angles α_x and α_z as follows:

$$\cos \alpha_x = \sin \alpha_y \sin \varphi \quad (\text{E7.1-18})$$

Equation E7.1-16 can now be written as

$$\frac{A}{A_0} = |\sin \theta \cos \varphi| \gamma \quad (\text{E7.1-19})$$

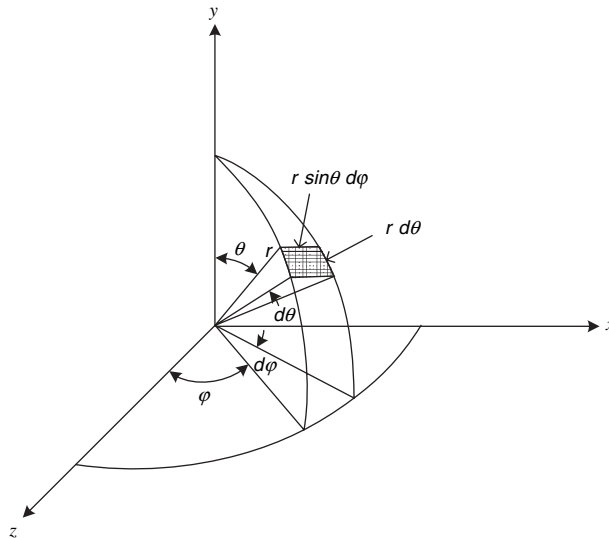


Fig. E7.1b Spherical coordinates r, θ, φ .

3. Considering the latter case, it would appear that mixing does occur despite the constant surface area. Indeed, if we consider two dimensional mixing over a plane, mixing would occur, but in such a case the criterion for mixing would be the perimeter rather than the area.

and the mean change in interfacial areas with random orientation becomes

$$\frac{A}{A_0} = \int_{\varphi=0}^{\varphi=2\pi} \int_{\theta=0}^{\theta=\pi} |\sin \theta \cos \varphi| \gamma \frac{1}{4\pi} \sin \theta d\theta d\varphi = \frac{\gamma}{2} \quad (\text{E7.1-20})$$

that is, one-half of the total imposed shear strain.

The average *striation thickness* r , defined in as total volume divided by one-half of the total interfacial area, can be written as

$$r = \frac{2}{(A/A_0)(A_0/V)} \quad (\text{E7.1-21})$$

Substituting Eq. E7.1-20 into Eq. E7.1-21 and expressing the ratio of initial surface area to volume in terms of the volume fraction of the minor component x_v and minor cube side L , ($A_0/V = 6x_v/L$) results in

$$r = \frac{2}{3} \frac{L}{x_v \gamma} = \frac{2r_0}{\gamma} \quad (\text{E7.1-22})$$

where r_0 is the initial striation thickness given by $L/3x_v$.

The foregoing clearly indicates that striation thickness is inversely proportional to total strain. We also note that the initial striation thickness is proportional to the size of the cube and inversely proportional to the volume fraction of the minor component. Hence, for any required final striation thickness, the larger the particles and the smaller the volume fraction of the minor component the more total strain is required. Therefore it is more difficult to mix a small amount of minor components into a major, than to make a 50–50 mixture, and the larger the individual particles of the minor, the more difficult it is to mix. By using Eq. E7.1-22, we can estimate the strain needed to reduce the striation thickness to a level where molecular diffusion or Brownian motion will randomize the mixture for a given strain rate and within the time (residence time) allotted for mixing.

A good rule of thumb for an adequate mixing in processing equipment is a total strain of the order 10,000–25,000 shear units. This implies a four orders of magnitude reduction in striation thickness.

An expression for the increase in interfacial area in tensile elongational flow was derived by Mohr et al. (10). Erwin (11) derived an expression for general homogeneous flow fields

$$\frac{A}{A_0} = \left[\frac{\cos^2 \alpha'}{\lambda_x^2} + \frac{\cos^2 \beta'}{\lambda_y^2} + \frac{\cos^2 \gamma'}{\lambda_z^2} \right]^{1/2} \quad (\text{E7.1-23})$$

where $\cos \alpha'$, $\cos \beta'$, and $\cos \gamma'$ are directional cosines with respect to the *principal axes* of the strain tensor in the initial state, and λ_x , λ_y , and λ_z are the principal elongational ratios.

Example 7.2 The Effect of Orientation We want to find the optimal orientation of an interfacial area element for maximum stretching of the area. By taking the derivative

of Equation E7.1-15 with respect to γ , we get the instantaneous stretching of the area

$$\frac{dA}{d\gamma} = A_0 \left[\frac{-\cos \alpha_x \cos \alpha_y + \gamma \cos^2 \alpha_x}{(1 - 2\gamma \cos \alpha \cos \alpha_y + \gamma^2 \cos^2 \alpha_x)^{1/2}} \right] \quad (\text{E7.2-1})$$

which at $\gamma = 0$, when $A = A_0$, becomes

$$\frac{dA}{d\gamma} = -A \cos \alpha_x \cos \alpha_y \quad (\text{E7.2-2})$$

Thus the instantaneous stretching depends only on the orientation of the interfacial area element. It may *increase* or *decrease*, depending on orientation. The maximum stretching is obtained when $\alpha_x = 135^\circ$, $\alpha_y = 45^\circ$, and $\cos \alpha_z = 0$, which maximizes the product $\cos \alpha_x \cos \alpha_y$. This implies that the interfacial area element, along the z axis, is perpendicular to the direction of shear, and in the x, y plane is at 45° to it. This gives

$$\frac{dA}{d\gamma} = \frac{A}{2} \quad (\text{E7.2-3})$$

which upon integration yields

$$A = A_0 e^{\gamma/2} \quad (\text{E7.2-4})$$

This important result indicates that if an interfacial area element is maintained at all times at 45° to the direction of the shear, stretching becomes exponential with shear. In fact, this situation is identical to pure shear or elongational deformation.

Figure E7.2 compares a stepwise increase in interfacial area in simple shear flow with optimal initial orientation, and simple shear flow where, at the beginning of each step, the interfacial area element is placed 45° to the direction of shear. The figure shows that, whereas in the former case the area ratio after four shear units is 4.1, in the latter case the ratio is 6.1, with a theoretical value of 7.3 when the 45° between the plane and direction of shear is maintained at all times. We note, however, that it is quite difficult to generate steady extensional flows for times sufficiently long to attain the required total elongational strain. This is why a mixing protocol of stepwise stretching and folding (bakers' transformation) is so efficient. Not only does it impose elongational stretching, but it also distributes the surface area elements over the volume.

With unidirectional shear, the efficiency of mixing, as expressed by instantaneous stretching starts with zero; when the interfacial area element is perpendicular to the direction of shear, it reaches a maximum value at 45° , and from that point on it begins to diminish, making the mixing less and less efficient. Frequent reorientation is therefore desirable, as is the case with random chaotic mixing, which occurs in typical internal mixers and some continuous mixers.

Chaotic Laminar Mixing of Homogeneous Liquids

Anyone who has looked into a real batch mixer and observed the complexity of the distribution of, say, a colored blob of liquid in a white matrix must have concluded that the

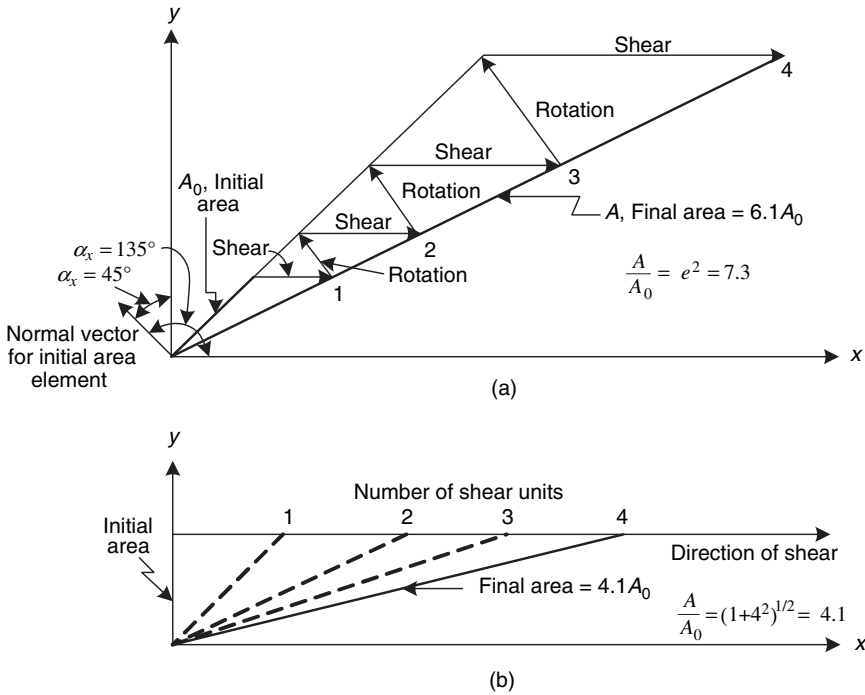


Fig. E7.2 Schematic representation of interfacial area increase in simple shear flow. (a) With initial orientation of 45° to the direction of shear, and after each shear unit, the plane is rotated back to 45° orientation. (b) With optimal initial orientation and no rotation.

flow appears not only complex but quite chaotic. In fact, as it turns out, under proper circumstances it *is* chaotic. This is a very surprising finding considering that there is no turbulence and that the flow is *deterministic*. In other words, in principle, we could calculate the path of every fluid particle from the velocity fields, which in turn follow from the basic equations, the rheological properties and the boundary conditions. Mathematically, in a Lagrangian representation, this takes the form of the following set of differential equations:

$$\begin{aligned} \dot{x} &= v_x(x, y, z, t) \\ \dot{y} &= v_y(x, y, z, t) \\ \dot{z} &= v_z(x, y, z, t) \end{aligned} \tag{7.1-1}$$

By integrating these equations over time, the position of any fluid particle with a given initial condition can be predicted at any time t . This approach is different from the common approach in fluid mechanics where flow is described in terms of velocity fields. However, by following the motion of the fluid we obtain a physically more profound understanding of mixing.

If the flow is steady in time, we speak about the x,y,z space as the *phase space* and the integral curves as *trajectories*, or in this case, the *pathlines*. If the fluid is also

incompressible, pathlines coincide with *streamlines*,⁴ and if the flow is two-dimensional and steady in time, then

$$\dot{x} = -\frac{\partial\psi}{\partial y} \quad \dot{y} = \frac{\partial\psi}{\partial x} \quad (7.1-2)$$

where ψ is the *stream function*. Equations 7.1-2 are integrable and fully define the streamlines. Now it is sufficient to let v_x and v_y be functions of time in such a way that a discontinuity of the slope of the pathline is introduced. This would make the equation nonintegrable, which may lead the system to become chaotic, as would be the case, for example, in time-periodic flows or time-periodic mixing protocols. In such cases, the fluid particle switches from one pathline to another, and thus can lead to pathline or streamline crossing.

Aref (12, 13) was the first to investigate such systems. He analyzed an idealized system consisting of an incompressible, inviscid, two-point alternating vortex flow, as shown in Fig. 7.7. The flow field is assumed to be steady whenever a vortex is activated. The fluid particle moves along one streamline and when the vortex is switched, it embarks on another one.

Results demonstrate that when agitators are switched the slope of the pathline becomes discontinuous. We will see later in this chapter how this mechanism may produce an essentially stochastic response in the Lagrangian sense. Aref termed this *chaotic advection*, which he suggested to be a new intermediate regime between turbulent and laminar advection. The chaos has a kinematic origin, it is temporal—that is, along trajectories associated with the motion of individual fluid particles. Chaos is used in the sense of sensitivity of the motion to the *initial position* of the particle, and *exponential divergence* of adjacent trajectories.

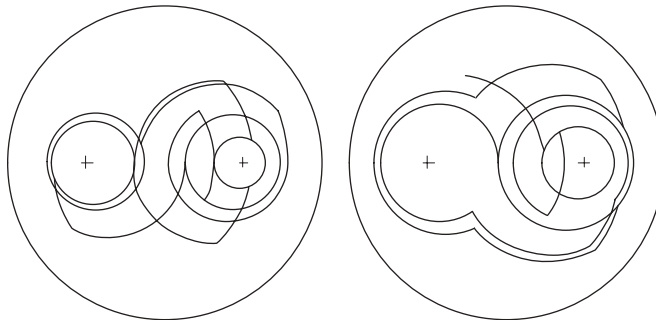


Fig. 7.7 Sample particle trajectories in a twin vortex flow. The agitator location is set by the amplitude, which is 0.5 (i.e., it is at midpoint between the center and the perimeter) and marked by the crosses. The dimensionless period for each vortex is 0.5. The mixing protocol is to activate one agitator for a period of time and then switch to the other agitator. [Reprinted by permission from H. Aref, “Stirring Chaotic Advection,” *J. Fluid Mech.*, **143**, 1–21 (1984).]

4. *Pathline* is the trajectory a fluid particle describes in the phase space; *streamline* is a line that is tangent to the direction of flow at any point; mathematically, streamlines are calculated via $dx/dt = \partial\psi/\partial y$, $dy/dt = -\partial\psi/\partial x$, where ψ is the *stream function*; *streakline* is a line that connects all fluid particles that passed a given point in space; *timeline* is a line that crosses a given fixed set of fluid particles and follows them in time. For steady flows, *streamlines*, *streaklines*, and *pathlines* coincide.

A computationally simple and relatively inexpensive diagnostic tool to identify chaotic flow is the Poincaré section or map. In periodic modulation, where the flow plane coincides with the phase plane, as is the case with the “blinking vortex” flow, the Poincaré section consists of a set of stroboscopic images spaced by a period of modulation. It is calculated as follows: A set of virtual fluid particles is placed in the flow at time $t = 0$. The positions of the particles are displayed at $t = nT$, where n is an integer and T is the time period, such that $\mathbf{v}(\mathbf{x}, t) = \mathbf{v}(\mathbf{x}, t + T)$. This procedure is a point transformation, namely, each particle is *mapped* to its new position. The Poincaré section detects *integrability* by placing stroboscopic images of a given particle at different times on a *smooth curve*. It signals *nonintegrability* or chaos by *smearing* the set of stroboscopic images of a given point over a region of finite extent.

Figure 7.8 shows Aref’s computation of the twin vortex flow of given amplitude and various time periods. Initially nine marker points were placed along the y axis and six along the x axis. Clearly, for very small periods (the switching between the two vortexes is very fast), we essentially get steady state flow and the marker particles fall along the

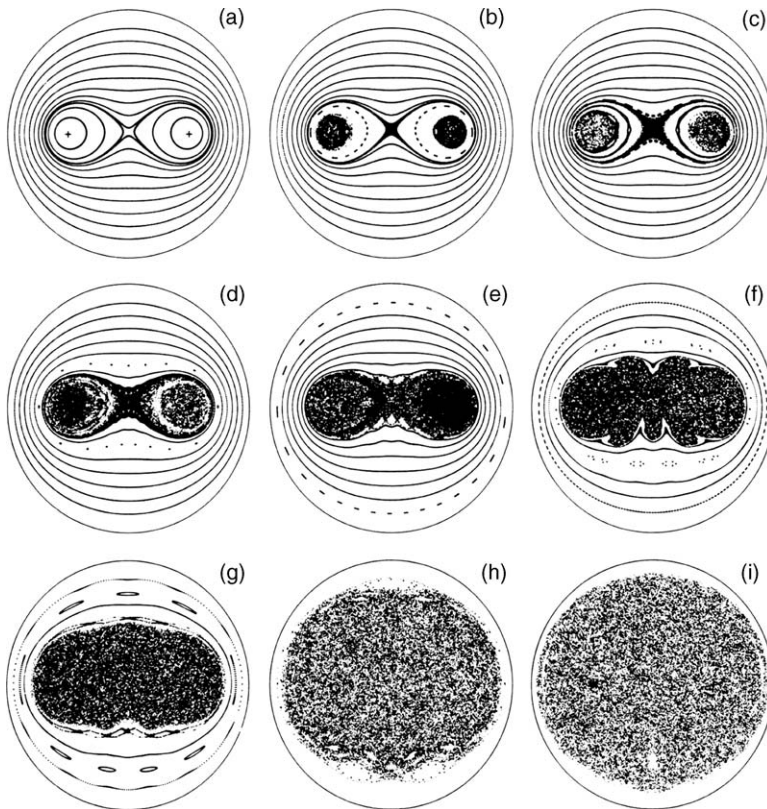


Fig. 7.8 Poincaré sections after 2000 cycles. Initially nine marker points were placed along the y axis and six along the x axis. The dimensionless amplitude was 0.5, as in Fig. 7.7. The parameter was the dimensionless period: (a) 0.05; (b) 0.10; (c) 0.125; (d) 0.15; (e) 0.20; (f) 0.35; (g) 0.50; (h) 1.0; (i) 1.5. For the smallest values of the time period we see that the virtual marker points fall on smooth curves. The general shape of these curves would be the streamlines of two fixed continuously operating agitators. As the time period increases the virtual marker particles fall erratically and the regions indicate chaotic flow. With increasing time periods larger and larger areas become chaotic. [Reprinted by permission from H. Aref, “Stirring Chaotic Advection,” *J. Fluid Mech.*, **143**, 1–21 (1984).]

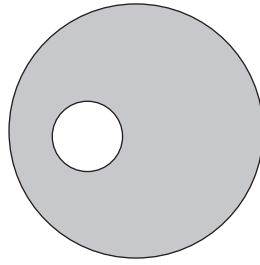


Fig. 7.9 Eccentric coaxial cylinders or journal bearing configuration. In the mixing protocol, the cylinders rotate alternately in the clockwise and counterclockwise directions.

streamlines. But, as the time period increases, we observe increasing areas of smeared marker points or chaotic regions, until almost all of the area is chaotic. Physically this means that no matter where the marker's place was originally, it may end up anywhere over the flow region. Rather than selecting just a few particles spread over the cross section, we could use a much larger number to create a small blob or patch, and follow how they are smeared over the cross section. In this case, of course, the initial location will be important.

Inviscid blinking twin vortex flow is highly idealized and the chaos observed in this type of flow may not be indicative of realistic viscous flow behavior. Yet, Aref and Balachandar (14), as well as Chaiken et al. (15,16), who used the term *Lagrangian turbulence*, showed that the former results also hold for periodic viscous creeping flows in a Couette-type flow with on-off, rotating, eccentric coaxial cylinders, as shown in Fig. 7.9 Figure 7.10 shows a typical Poincaré section, which reveals a rich mixture of regular and chaotic particle motion. Chaiken et al. (15) were the first to verify theoretical predictions with experimental studies using an eccentric cylinder setup with glycerin, and placing drops of dye at strategic points on the surface of the fluid and running the experiments for hundreds of periods. Figure 7.11 shows a comparison after 134 periods, after which time the dye had spread fairly uniformly over most of the fluid. However, the dye did not



Fig. 7.10 Poincaré sections of viscous Newtonian flow in alternately turning eccentric cylinders. The inner cylinder turned counterclockwise for a given time, and then the outer cylinder was turned clockwise for 800 periods. There were 11 initial particles. [Reprinted by permission from J. Chaiken, R. Chevray, M. Tabor, and Q. M. Tan, "Experimental Study of Lagrangian Turbulence in Stokes Flow," *Proc. R. Soc. London A*, **408**, 165–174 (1986).]

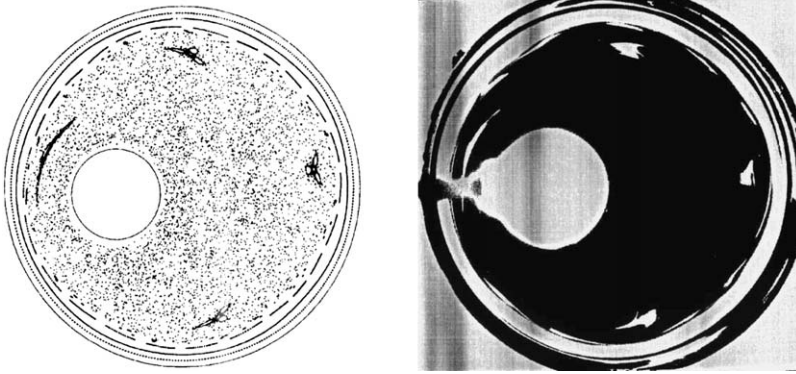


Fig. 7.11 Comparison of computed Poincaré section with experimental observation. The experiment was run for 134 periods, after which time the dye had spread fairly uniformly over most of the fluid. However, the dye did not penetrate the four small elliptic islands embedded in the chaotic sea, and their shape is in qualitative agreement with that observed numerically. Note that in the experimental results, the colors were reversed. [Reprinted by permission from J. Chaiken, R. Chevray, M. Tabor, and Q. M. Tan, “Experimental Study of Lagrangian Turbulence in Stokes Flow,” *Proc. R. Soc. London A*, **408**, 165–174 (1986).]

penetrate the four small elliptic islands embedded in the chaotic sea, and their location and shape is in qualitative agreement with that observed numerically, lending experimental support to the computational predictions.

At the same time Chien, Rising, and Ottino (17) studied chaotic flow in two-dimensional cavity flows with a periodic moving wall, which is relevant to mixing of viscous polymeric melts. All two-dimensional flows, as pointed out by Ottino (18), consist of the same building blocks: hyperbolic points and elliptic points. A fluid particle moves toward a hyperbolic point in one direction and away from it in another direction, whereas the fluid circulates around parabolic points, as shown in Fig. 7.12.

Time-dependent, periodic, two-dimensional flows can result in streamlines that in one flow pattern cross the streamlines in another pattern, and this may lead to the stretching-and-folding mechanism that we discussed earlier, which results in very efficient mixing. In such flow situations, the outflow associated with a hyperbolic point can cross the region of inflow of the same or another hyperbolic point, leading, respectively, to homoclinic or heteroclinic intersections; these are the fingerprints of chaos.

Such systems can produce horseshoe maps. Figure 7.13 shows the flow patterns in a glycerin-filled rectangular cavity with the top and bottom plate moving in a sinusoidal fashion. It is instructive to compare the complexity of the pattern arising from time-dependent motion with a steady motion that leads to simple closed streamlines and therefore to rather poor mixing. Figure 7.14 shows the elliptic and hyperbolic points in Fig. 7.13. A detailed review of the field of chaotic advection can be found in Ottino (19) and Wiggins and Ottino (20).

The scale in chaotic laminar mixing goes down from the machine scale to a scale where the continuum hypothesis breaks down and phenomena are dominated by physical effects, due to intermolecular forces, such as van der Waals. Danescu and Zumbrennen (21) and Zumbrennen and Chibber (22) took advantage of this and devised an ingenious device to create “controlled” three-dimensional chaotic flows, with which they were able to tailor the morphology and properties of blend films and composites.

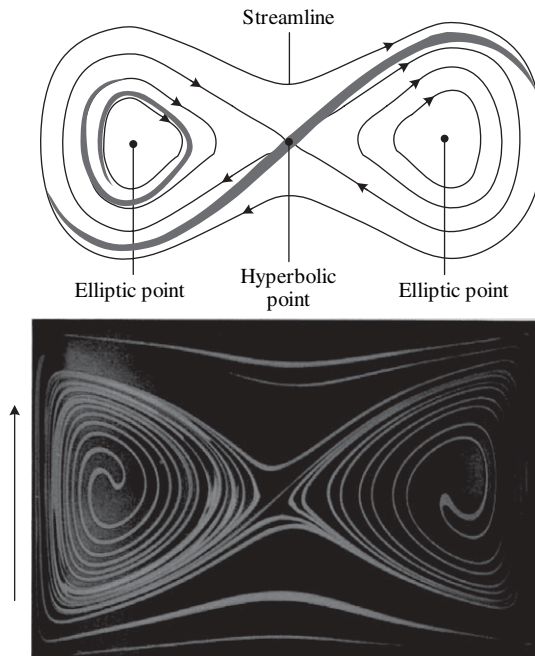


Fig. 7.12 The flow pattern (bottom) is generated in a cavity filled with glycerin with the walls moving continuously in opposite directions. The flow pattern (top) has two elliptic and one hyperbolic point. [Reprinted by permission from J. M. Ottino, “The Mixing of Fluids,” *Sci. Am.*, **20**, 56–67, 1989.]

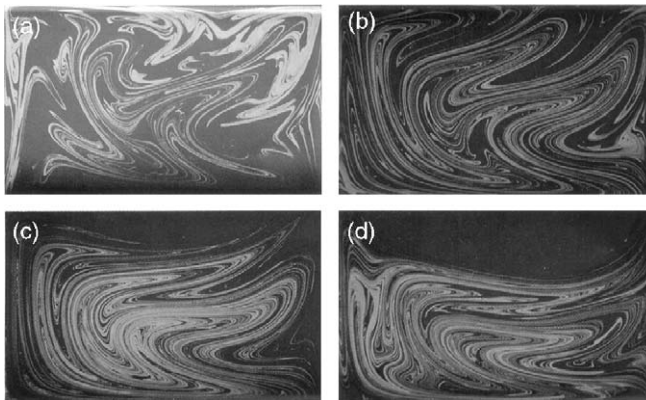


Fig. 7.13 Evolution of a blob of colored fluid placed at location $x = 2.2$ cm and $y = 3.1$ cm in a glycerin-filled, 10.3-cm by 6.2-cm rectangular cavity. The top and bottom move according to $v_{\text{top}} = U_{\text{top}} \sin^2(\pi t/T)$ and $v_{\text{bot}} = U_{\text{bot}} \sin^2(\pi t/T + \pi/2)$, where $U = 2.69$ cm/s. The photographs correspond to different time periods: (a) $T = 15$ s; (b) $T = 20$ s; (c) $T = 25$ s; (d) $T = 30$ s; and displacements (a) 1612 cm; (b) 752 cm; (c) 951 cm; (d) 1452 cm. From a mixing point of view, at 20 s there seems to be an optimum. Beyond that, a large regular region appears to be growing. [Reprinted by permission from J. M. Ottino, C. W. Leong, H. Rising, and P. D. Swanson, “Morphological Structures Produced by Mixing in Chaotic Flows,” *Nature*, **333**, 419–425 (1988).]

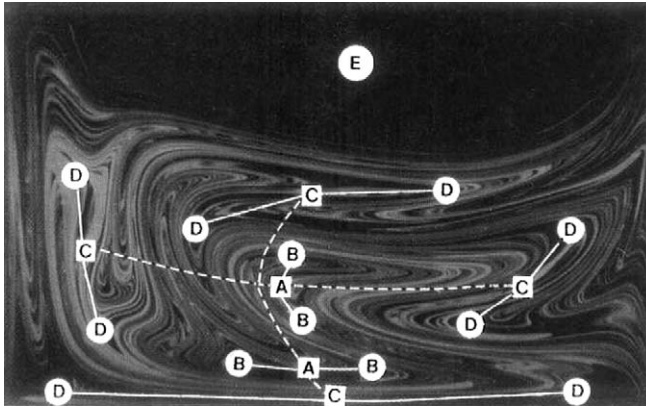


Fig. 7.14 Elliptic and hyperbolic points in Fig. 7.13(d). Circles represent elliptic points, and squares, hyperbolic points. [Reprinted by permission from J. M. Ottino, C. W. Leong, H. Rising, and P. D. Swanson, “Morphological Structures Produced by Mixing in Chaotic Flows,” *Nature*, **333**, 419–425 (1988).]

Mixing of Nonhomogeneous Liquids

Laminar mixing frequently involves systems containing components that have significantly different rheological properties, such as mixing of different grades of the same polymer, mixing of two components of the same polymer, one of which contains various additives, mixing different polymers, and thermally nonhomogeneous systems. The main question we address in this section is the effect of the difference in rheological properties on the mixing process. Upon initial approximation, this difference is reflected in the viscosity ratio.

It is generally accepted in the field of mixing that it is more difficult to mix a high-viscosity minor component into a low viscosity major component than vice versa. This is in agreement with the previously mentioned requirement that to achieve laminar mixing, both components must be deformed and, of course, it is harder to deform a high viscosity minor component placed in an easily deforming low viscosity major component than the other way around. This point can be further amplified by the following example (8a).

Example 7.3 Effect of Viscosity Ratio on Shear Strain in Parallel-Plate Geometry Consider a two-parallel plate flow in which a minor component of viscosity μ_2 is sandwiched between two layers of major component of viscosities μ_1 and μ_3 (Fig. E7.3). We assume that the liquids are incompressible, Newtonian, and immiscible. The equation of motion for steady state, using the common simplifying assumption of negligible interfacial tension, indicates a constant shear stress throughout the system. Thus, we have

$$\mu_1 \dot{\gamma}_1 = \mu_2 \dot{\gamma}_2 = \mu_3 \dot{\gamma}_3 \quad (\text{E7.3-1})$$

By expressing the shear rates in terms of velocity drop, it is easy to show that

$$\dot{\gamma}_2 = \frac{V}{H} \left[\frac{1}{(1 - \Phi)(\mu_2/\mu_1) + \Phi} \right] \quad (\text{E7.3-2})$$

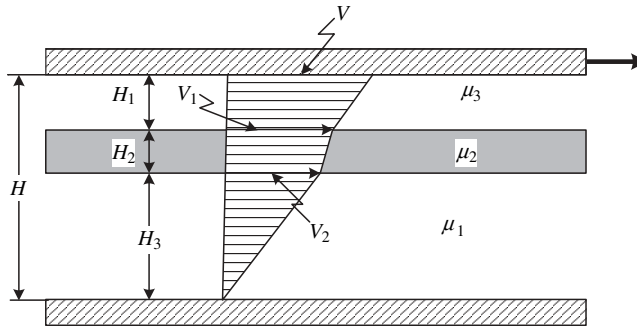


Fig. E7.3 Velocity profile for drag flow between parallel plates of layers of immiscible Newtonian liquids.

where V is the velocity of the upper plate, H is the gap between the plates, and $H_2/H = \Phi$ is the fraction of the gap occupied by the minor component. Clearly, the shear rate attainable in the minor component is a function of the viscosity ratio μ_2/μ_1 and Φ . If $\Phi \ll 1$, $\dot{\gamma}_2 \approx (V/H)\mu_1/\mu_2$ indicating little deformation for high-viscosity ratios μ_2/μ_1 . Furthermore, the shear rate in the minor component is more sensitive to the viscosity ratio at low Φ values. The relevance of these conclusions to mixing, however, must be treated very cautiously, since the Example reflects an idealized setup. Moreover, in actual mixing, a very low-viscosity component may tend to migrate to high shear-rate zones, and in other cases one of the phases may break down into a noncontinuous phase.

However, predictions from simple flows, such as those described in Example 7.3 above, cannot be generalized to more realistic systems. Bigg and Middleman (23) analyzed a somewhat more realistic system of flow in a rectangular channel, shown in Fig. 7.15. The motion of the upper surface induces partial mixing of the fluids, and the interfacial area, which was calculated as a function of time, is used as a quantitative measure of the laminar mixing. The “marker and cell” calculation method, developed by Harlow and Welch (24), was used to solve the flow field and calculate the position of the interface. The evolution of the interface of two fluids of equal viscosities and densities in a channel with an aspect ratio of 0.52, and a

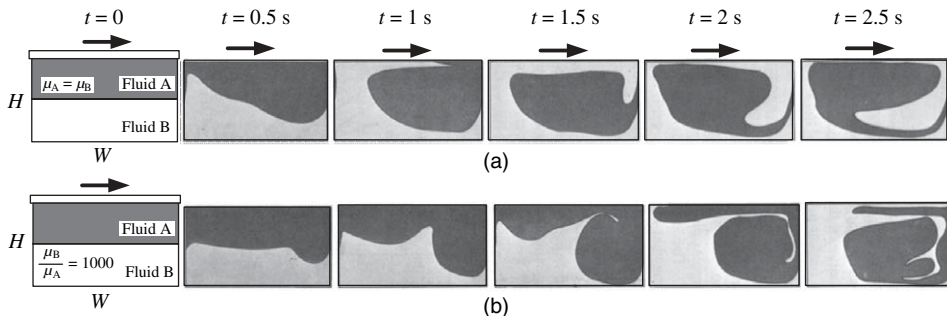


Fig. 7.15 The evolution of interface between the two fluids initially stratified. (a) $\mu_A = \mu_B$, $H/W = 0.52$, $Re = 38.7$. (b) $\mu_B/\mu_A = 1000$, $H/W = 0.52$, $Re_{upper} = 1000$, $Re_{lower} = 1$. [Reprinted by permission from D. M. Bigg and S. Middleman, “Laminar Mixing of a Pair of Fluids in a Rectangular Cavity,” *Ind. Eng. Chem. Fundam.*, **13**, 184 (1974).]

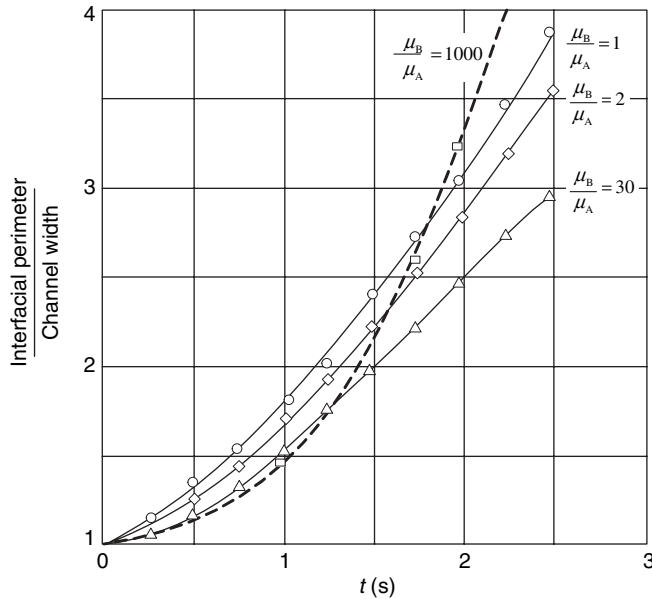


Fig. 7.16 The evolution of interfacial area as a function of time for the rectangular channel circulatory flow shown in Fig. 7.15, at various viscosity ratios. [Reprinted by permission from D. M. Bigg and S. Middleman, "Laminar Mixing of a Pair of Fluids in a Rectangular Cavity," *Ind. Eng. Chem. Fundam.*, **13**, 184 (1974).]

modified Reynolds number defined as $V_0 W \rho / \mu$, where V_0 is the velocity of the plate, W the width of the channel, of 38.7 is shown in Fig. 7.15(a). Note that after 2.5 s, distinct striations between the two fluids have been formed.

Next, the effect of the viscosity ratio was investigated on interface evolution. Figure 7.16 shows that for viscosity ratios up to 30, the evolution of the interfacial area was reduced. In these simulations the Reynolds number in the upper layer was maintained at the previous level. If, however, the viscosity ratio was increased to 1000, together with an increase in Reynolds number of the upper layer, a more complex picture evolved, as indicated in Fig. 7.15(b) and the broken curve in Fig. 7.16. The high Reynolds number in the upper region with vortex formation may be somewhat misleading, yet it draws attention to the fact that with variation in viscosity, the Reynolds number also changes and flow conditions may be altered. Bigg and Middleman (23) have also presented experimental verification to their theoretical calculations.

One could perhaps then conclude that for good mixing, the viscosities of the two components should be similar, at least when equal proportions are mixed. This conclusion seems to be supported by Irving and Saxton (4), who observed a general trend of *reduction* in mixing quality with *increasing* viscosity ratio in a laboratory BR Banbury mixer. A polyethylene superconcentrate (50% carbon black) was diluted with unfilled polymer to polyethylene concentrate (25% carbon black). The viscosity of the superconcentrate was varied by changing the carrier resin. The fraction of black above 100 mesh/g was measured as a function of the viscosity ratio. Results plotted in Fig. 7.17 clearly indicate that a high viscosity ratio leads to an increasing number of unmixed black or poor mixing.

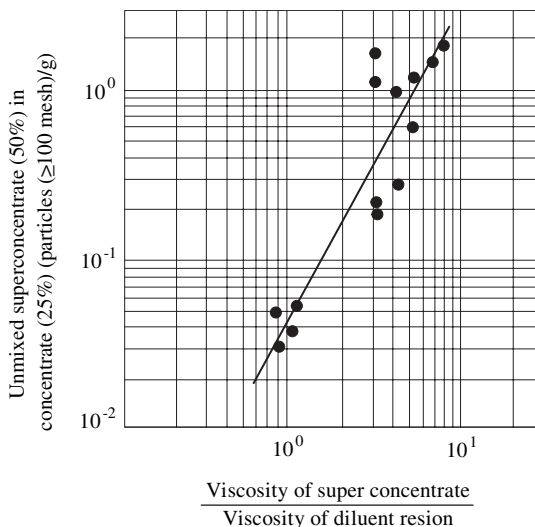


Fig. 7.17 Unmixed polyethylene superconcentrate (50% carbon black) in a mixture of superconcentrate and unfilled polyethylene as a function of viscosity ratio. [Reprinted by permission from V. W. Uhl and J. B. Gray, *Mixing Theory and Practice*, Vol. II, Academic Press, New York, 1967.]

Mixing of Immiscible Liquids, and Filament and Droplet Breakup

Mixing immiscible liquid polymeric components leads to the very important class of materials that comprises blends and alloys. Figure 7.18 shows some typical morphologies of polystyrene and high density polyethylene blends. This is an immiscible system, and we can observe spherical dispersed structures, fibers, co-continuous structures, and lamellar structures of the minor component. The morphology affects the properties of the blend, and therefore, for these materials, processing is an effective way to structure the product with desirable properties. We discuss blends and alloys and their processing in Chapters 10 and 11. In this section, we review some of the relevant principles and the basic mechanisms of such a mixing process.

First, we note that miscibility and compatibility mean the same thing. The former refers generally to liquid systems, whereas, the latter usually designates solid systems. There are two aspects of the question of miscibility: Will the two liquids mix (thermodynamics), and how long would this process take (kinetics)? The second aspect is important in polymer–polymer and polymer–monomer systems, because of the low diffusivities involved. Thermodynamically, the mixture will be stable if, at temperature T ,

$$\Delta G = \Delta H - T\Delta S \leq 0 \quad (7.1-3)$$

where ΔG , ΔH , and ΔS are the Gibbs free energy, heat, and entropy of mixing. Increasing temperature tends to favor the thermodynamic conditions for mixing, since ΔS is almost always positive. Naturally, the rate of mixing (if $\Delta G < 0$) also increases with temperature because of increased diffusivities. To predict when mixing is possible, one must be able to calculate ΔH and ΔS . The heat of mixing can be estimated using either the solubility

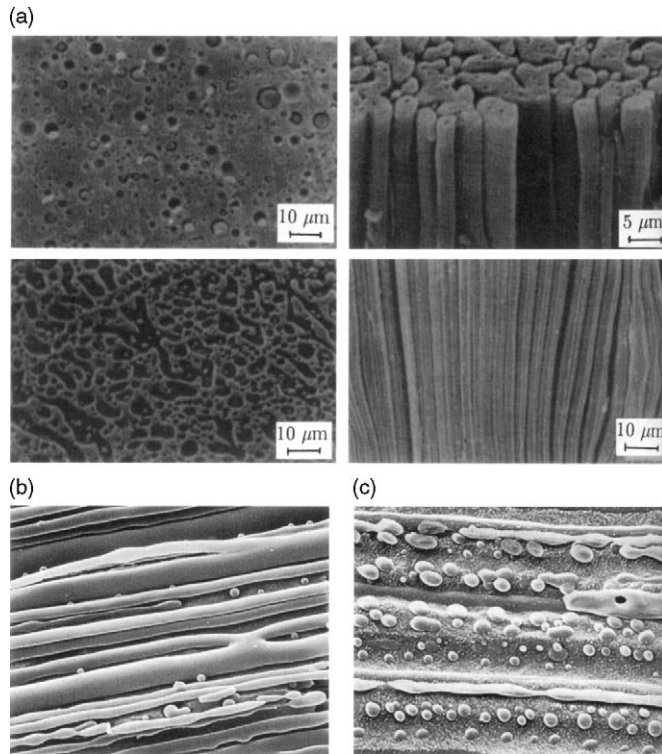


Fig. 7.18 (a) Characteristic morphologies of an incompatible blend of high density polyethylene and polystyrene; (b) extruded fiberlike structure of the blend; (c) same as (b), but with a larger air gap between the die and the quench bath giving enough time for the fibers to break into droplets. [Reprinted by permission from H. E. H. Meijer, "Processing for Properties," in *Material Science and Technology*, R. W. Cahn, P. Haasen, E. J. Kramer, Eds., Wiley-VCH, Weinheim, 1997.]

parameter δ (cohesive energy density) of the liquids (25,26) or the parameter χ_1 , which represents the interaction energy per solvent molecule divided by kT

$$\Delta\tilde{H} = v_1 v_2 (\delta_1 - \delta_2)^2 \quad (7.1-4)$$

where $\Delta\tilde{H}$ is the heat of mixing per unit volume, and

$$\Delta H = \chi_1 k T N_1 v_2 \quad (7.1-5)$$

where v_1 and v_2 are the volume fractions of the solvent and solute, N_1 is the number of solvent moles, and k is the Boltzmann constant. In a polymer–polymer system, it is not clear which is the solvent and which the solute.

The entropy of mixing can be evaluated approximately from statistical mechanics, by applying the Flory–Huggins theory (27,28)

$$\Delta S = -k(N_1 \ln v_1 + N_2 \ln v_2) \quad (7.1-6)$$

Using these expressions, which hold for flexible monodispersed, polymer–solvent systems of normal heat of mixing, we can obtain the critical conditions for phase separation. Such

predictions indicate that miscibility over the entire composition range occurs between solvents and polymers when $|\delta_1 - \delta_2| < 1.7$, and between polymer melts when $|\delta_1 - \delta_2| < 0.1$, for $M \approx 10^5$. The more restrictive requirement for polymer–polymer systems stems from the relatively small entropy increase of such systems upon mixing.

We now consider the deformation of a droplet the size of a pellet, which is a realistic upper bound of the dispersed phase in practice (29). The order of magnitude of the capillary number (Ca), assuming a viscosity of 100 Pa/s, a shear rate of 100 s^{-1} , a surface tension of a 10^{-2} N/m , and a drop radius of 10^{-3} m , is 10^3 , which is much larger than the $\text{Ca}_{\text{crit}} \approx 1$. Thus, shear forces overcome cohesive forces. The drop will not reach an equilibrium deformation, but will deform affinely with the matrix into elongated filaments that may break up into small droplets or stay and lead to lamellar-type morphologies. The small droplets, in turn, depending on the capillary number, may break into yet smaller entities. Thus, in immiscible systems, mixing commences with a distributive mixing mechanism and may gradually proceed toward a mechanism of liquid breakdown.

Next we examine the breakup mechanism of immiscible droplets in a continuous phase and that of liquid filaments (30).

Figures 7.18(b) and 7.18(c) show the breakup into droplets of an extended filament of high density polyethylene in a polystyrene matrix. In Fig. 7.18(b) the distance between the extruder die and the quenching bath is short and the fiber freezes before breaking up, whereas in Fig. 7.18(c) the distance was increased, giving the filaments sufficient time for breakup. As the filament extends, its diameter is reduced until shear forces no longer dominate the surface tension cohesive forces and the filaments breaks into droplets, just like a stream of water from a faucet breaks up into droplets.

Lord Rayleigh (31) was the first to investigate the stability of an infinitely long, liquid cylinder embedded in an immiscible liquid matrix driven by surface tension, taking into account inertia. Weber (32) considered stresses in the thread, and Tomotika (33) included the viscosity of the matrix as well. The analysis follows the evolution in time of small Rayleigh sinusoidal disturbance in diameter (Fig. 7.19):

$$R(z) = \bar{R} + \alpha \sin(2\pi z/\lambda) \quad (7.1-7)$$

where \bar{R} is the average radius ($< R_0$), α is the amplitude, and λ is the wavelength of the disturbance. Initially, the small amplitudes of all wavelengths exist, but dependent on the viscosity ratio of the two phases, one particular wavelength, λ_m , becomes dominant and grows the fastest, bringing about the breakdown. The disturbance amplitude grows exponentially in time

$$\alpha = \alpha_0 e^{\beta t} \quad (7.1-8)$$

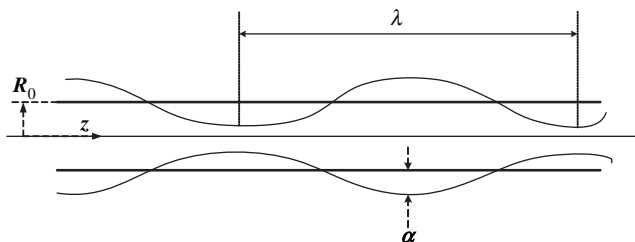


Fig. 7.19 A liquid thread of radius R_0 with a Rayleigh sinusoidal disturbance.

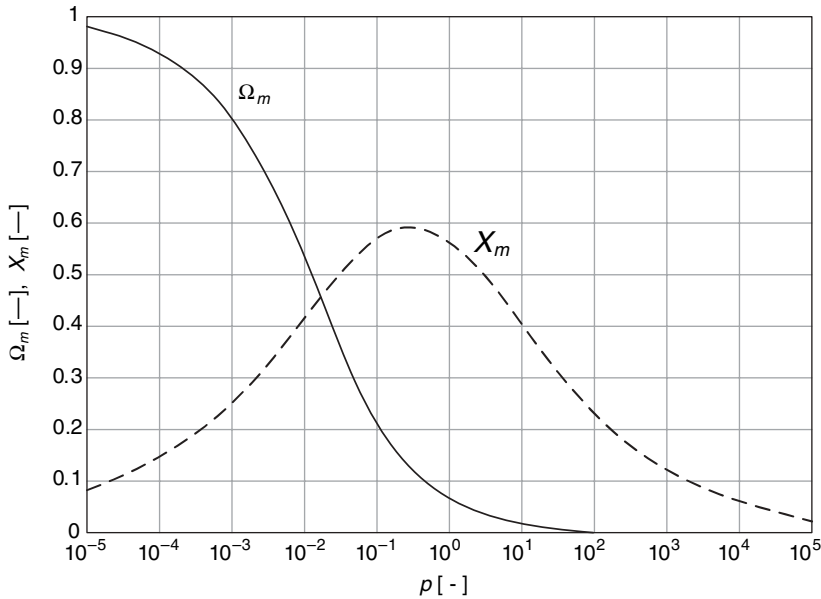


Fig. 7.20 The dimensionless factor Ω_m and the dominant wave number $X_m = 2\pi R_0/\lambda_m$ versus the viscosity ratio $p = \mu_d/\mu_c$. [Reprinted by permission from H. H. Meijer and J. M. H. Janssen, "Mixing of Immiscible Liquids," in *Mixing and Compounding of Polymers*, I. Manas-Zloczower and Z. Tadmor, Eds., Hanser, Munich 1994.]

where β is given by

$$\beta = \frac{\Gamma\Omega(\mu_d/\mu_m)}{2\mu_d R_0} \quad (7.1-9)$$

where Γ is the surface tension, Ω is a dimensionless factor that is a function of the viscosity ratio of the dispersed to matrix phases given in Fig. 7.20, and α_0 is the initial amplitude that is estimated from Brownian motion:⁵

$$\alpha_0 = \left(\frac{21kT}{8\pi^{3/2}\Gamma} \right)^{1/2} \quad (7.1-10)$$

For a given viscosity ratio there is a predominant wavelength that grows fastest and brings about the breakdown of the liquid fiber into droplets. The size of the droplets formed is evaluated from a mass balance

$$\frac{4}{3}\pi R_{\text{drop}}^3 = \pi R_0^2 \lambda_m \quad (7.1-11)$$

5. W. Kuhn, *Kolloid, Z.*, **132**, 84 (1953).

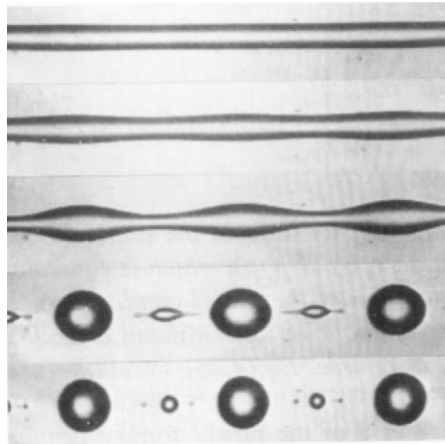


Fig. 7.21 The photograph shows the breakup of a 0.35-mm-diameter castor oil thread with viscosity 0.7 Pa·s, in a quiescent silicone oil of viscosity 0.9 Pa·s. Both phases are Newtonian, and the interfacial surface tension is 0.004 N/m. The experiment was carried out at room temperature and the time between successive photographs was 1 s. [Reprinted by permission from H. H. Meijer and J. M. H. Janssen, “Mixing of Immiscible Liquids,” in *Mixing and Compounding of Polymers*, I. Manas-Zloczower and Z. Tadmor, Eds., Hanser, Munich (1994).]

resulting in

$$R_{\text{drop}} = R_0 \left(\frac{3\pi}{2X_m} \right)^{1/3} \quad (7.1-12)$$

The time to breakup can be calculated from Eq. 7.1-8 as the time needed for the disturbance amplitude to reach the breakup amplitude α_b . This happens when α_b reaches the average radius of the thread $\bar{R} = (2/3)^{0.5} R_0$. Thus,

$$t_b = \frac{1}{\beta} \ln(\alpha_b/\alpha_0) \quad (7.1-13)$$

Figure 7.21 shows the breakup of a 0.35-mm-diameter castor oil thread in quiescent silicone oil. Both phases are Newtonian. We notice between two main droplets a second generation of droplets formed from the instability of the extended “neck,” and there is also a hint of a third generation of droplets as well.

Although the dominant mixing mechanism of an immiscible liquid polymeric system appears to be stretching the dispersed phase into filament and then form droplets by filament breakup, individual small droplet may also break up at $Ca \gg Ca_{\text{crit}}$. A detailed review of this mechanism is given by Janssen (34). The deformation of a spherical liquid droplet in a homogeneous flow field of another liquid was studied in the classic work of G. I. Taylor (35), who showed that for simple shear flow, a case in which interfacial tension dominates, the drop would deform into a spheroid with its major axis at an angle of 45° to the flow, whereas for the viscosity-dominated case, it would deform into a spheroid with its major axis approaching the direction of flow (36). Taylor expressed the deformation D as follows

$$D = \frac{L - B}{L + B} \quad (7.1-14)$$

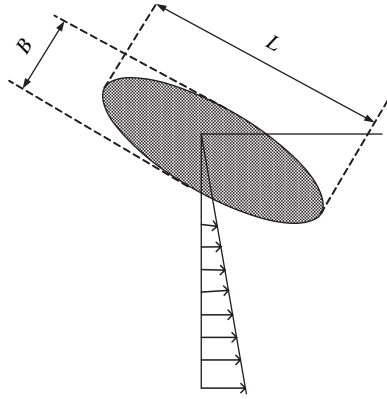


Fig. 7.22 A single droplet of liquid deformed into a spheroid in a homogeneous shear flow field.

where L and B are the major and minor axes of the spheroid (Fig. 7.22). At equilibrium, a steady flow field ensues in the droplet, and for small deformations, the deformation D is given by

$$D = \frac{\mu_0 \dot{\gamma} r}{\Gamma} \frac{19p + 16}{16(p + 1)} \quad (7.1-15)$$

where μ_0 is the viscosity of the continuous phase, $\dot{\gamma}$ the shear rate, r the initial droplet radius, Γ the interfacial tension, and $p = \mu_d/\mu_m$ the ratio of viscosities of the dispersed and continuous phases, respectively. With $\dot{\gamma}$ replaced by $2\dot{\epsilon}$, where $\dot{\epsilon}$ is the rate of elongation, Eq. 7.1-15 also holds for two-dimensional steady planar elongational flow, $v_x = \dot{\epsilon}_p l x$, $v_y = -\dot{\epsilon}_p l y$, $v_z = 0$. Taylor also showed that for high p values, the final deformation becomes a function of p only

$$D = \left(\frac{5}{4}\right) p^{-1} \quad (7.1-16)$$

The problem of droplet breakup was also investigated by Taylor (36), Rumscheidt and Mason (37), Grace (38), and others. Following the suggestion of Taylor, Rumscheidt and Mason assumed that a droplet will burst when the pressure drop generated across the interface exceeds the surface tension force, which tends to hold it together. This condition can be shown to occur at a critical deformation of $D = 1/2$ for shear and planar extension flows. Experimental evidence has revealed a complex bursting behavior, but the critical deformation at burst agreed reasonably well with the theoretical predictions up to a viscosity ratio of about 4. Above this value, no droplet bursting was observed. This is evident from experimental droplet breakup studies done by Grace (38) and shown in Fig. 7.23 where the Ca_{crit} is plotted versus the viscosity ratio for simple shear and planar flows of Newtonian fluids.

Above the critical value, the viscous shear stresses overrule the interfacial stresses, no stable equilibrium exists, and the drop breaks into fragments. For $p > 4$, it is not possible to break up the droplet in simple shear flow, due to the rotational character of the flow. Figure 7.23 also indicates that in shear flow, the easiest breakup takes place when the

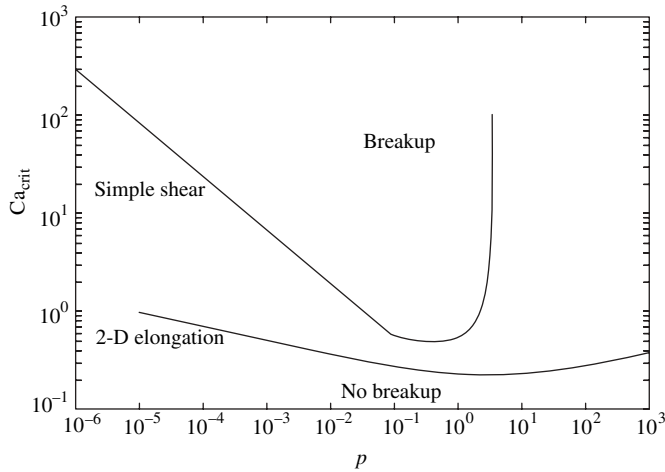


Fig. 7.23 Critical capillary number for droplet breakup as a function of viscosity ratio p in simple shear and planar elongational flow. [Reprinted by permission from H. P. Grace, *Chem. Eng. Commun.*, **14**, 2225 (1971).]

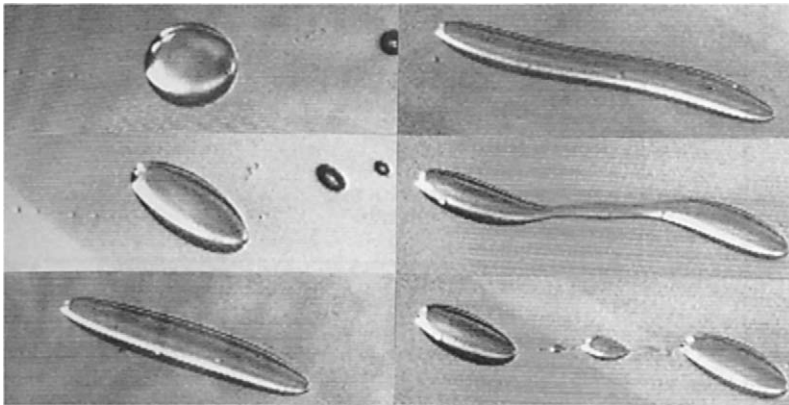


Fig. 7.24 Breakup of a droplet of ~ 1 mm diameter in simple shear flow of Newtonian fluids with viscosity ratio of 0.14, just above the critical capillary number. [Reprinted by permission from H. E.H. Meijer and J. M. H. Janssen, "Mixing of Immiscible Fluids," in *Mixing and Compounding of Polymers*, I. Manas-Zloczower and Z. Tadmor, Eds., Hanser, Munich (1994).]

viscosity ratio is in the range 0.1 to 1.0. In Fig. 7.24 a sequence of photographs shows the deformation of a Newtonian droplet into a spheroid, the appearance of a necking process, and the breakup of the deformed droplet into two large droplets and a sequence of smaller ones.

Dispersion of Solid Agglomerates

The dispersion of carbon black into rubber is the classic example of dispersion of solid agglomerates. The mechanical and physical properties of the rubber (e.g., in tires) depend

to a large extent on the quality of the dispersion of these agglomerates. In the case of carbon black, the agglomerates, which may range from 10 μm to 100 μm and above, are made up of smaller aggregates of the order of 0.1 μm , which in turn are made up of fused-together primary carbon black particles of the order of 0.02 μm . It is the size of the primary particle that determines the surface area of the black, whereas the “strength” of the agglomerate is dependent on the size and “structure” of the aggregate, which are held together by cohesive London–van der Waals forces. A detailed description of carbon black structure and reinforcement was given by Gessler, Hess, and Medalia in a sequence of three classic papers (39). Other solid fillers and additives, such as calcium carbonates, silicates, clays, and organic pigments, form their own particular agglomerates.

In dispersive mixing the clusters of particles held together by cohesive forces (agglomerates) are successively broken apart by hydrodynamic stresses imposed on the external surfaces of the deforming liquid matrix, which in turn generate internal stresses within the cluster (40). A detailed review of dispersive mixing was given by Manas-Zloczower (41), and in this section we will follow her discussion.

It is generally agreed that, at least for the carbon black–rubber system, the dispersion process undergoes a number of stages: (a) incorporation of the powder; (b) “wetting” the powder (i.e., the penetration of the liquid into the agglomerate); (c) deagglomeration (i.e., the breaking up the agglomerate into aggregate or the smallest constituent element); and (d) randomization of the particles throughout the volume. Among these, deagglomeration is generally the rate-controlling step.

Both elongational and shear flow fields, as shown below, can generate the internal stretching stresses needed to break up an agglomerate. Elongational flow is more efficient than shear flow, yet it is more difficult to reach the critical rates of elongation needed for breakup. Because of power and heat removal constraints, it is not possible to impose on the whole mass of the mixture the shear stresses needed to bring about breakup, therefore all mixers are designed with regions of narrow gaps and high shear zones (e.g., the small clearances between the moving blades and the cool wall in an internal mixer) with the rest of the mixer designed to bring about randomization of the mixture. This leads to the concept of the *two-zone model*, consisting of a recirculating stream between a high shear zone and a well-mixed zone containing the bulk of the material. Normally, the entrance to the high shear zone is wedged, creating elongational flow patterns. In this region soft agglomerates are stretched and separated into smaller entities, and closely spaced hard agglomerates or fragments of agglomerates are separated from each other. Moreover, the wedged entrance also builds hydrodynamically the pressure level needed to avoid slip in the high shear zones.

Agglomerate Structure and Cohesiveness

Most models treat the agglomerate as an assembly of small spheres and relate its tensile strength to the cohesive forces between spheres. Manas-Zloczower, Nir, and Tadmor (42), in modeling dispersive mixing in internal mixers, adopted the model proposed by Rumpf (43) for calculating the strength of the agglomerates. According to the Rumpf model, the theoretical tensile strength σ is given by

$$\sigma = \frac{9}{8} \left(\frac{1 - \varepsilon}{\varepsilon} \right) \frac{F}{d^2} \quad (7.1-17)$$

where ε is the volume void fraction, which can be estimated from the mean coordination number

$$k_c \varepsilon \simeq 3.1 \simeq \pi \quad (7.1-18)$$

where d is the diameter of the spherical particles, and F is the force of a single bond given by

$$F = \frac{Ar}{12z^2} \quad (7.1-19)$$

where A is the Hamaker (44) constant for interaction of two bodies of like materials—of the order of $5 \times 10^{-20} - 5 \times 10^{-19}$ J, and z is the physical adsorption separation distance (for adhering spheres, z is typically 0.4 nm). For carbon black particles in rubber, F (in Newtons) was estimated to be (42)

$$F = C_0 d \quad (7.1-20)$$

where C_0 is in the range 4.06×10^{-11} to 4.78×10^{-11} N/nm, and d is the diameter in nanometers.

Substituting Eq. 7.1-20 into Eq. 7.1-17 and multiplying it by the cross-sectional area S of the agglomerate gives the cohesive force of the agglomerate

$$F_c = \frac{9}{8} \left(\frac{1 - \varepsilon}{\varepsilon} \right) \frac{C_0}{d} S \quad (7.1-21)$$

where S is the cross-sectional area at the rupture plane. In a sphere or axisymmetric body this will be given by πc^2 .

Example 7.4 The Strength of Carbon Black Agglomerates Calculate the tensile strength of two carbon black agglomerates made, respectively, of 150-nm and 500-nm spherical aggregates, assuming an ideal coordination of 12.

Solution The force between two aggregates, with an average C_0 value of 4.5×10^{-11} N/nm, will be 6.75×10^{-9} N and 22.5×10^{-9} N, for the aggregates of 150 nm and 500 nm, respectively. The porosity from Eq. 7.1-18 is 0.258. Next, the tensile strength is calculated from Eq. 7.1-21 to give 9.7×10^5 N/m² (140.7 psi) and 2.91×10^5 N/m² (42.2 psi), respectively. Clearly, smaller aggregates form much stronger agglomerates.

Hydrodynamic Forces in Shear Flow

Consider a single, freely suspended axisymmetric particle in a homogeneous shear flow field of an incompressible Newtonian liquid. The free suspension condition implies that the *net* instantaneous force and torque on the particle vanish. There is, however, a finite net force along the axis that one half of the particle exerts on the other, as shown schematically in Fig. 7.25.

Nir and Acrivos (45) showed that this force is given by

$$F_h = \chi \pi \mu \dot{\gamma} c^2 \sin^2 \theta \sin \phi \cos \phi \quad (7.1-22)$$

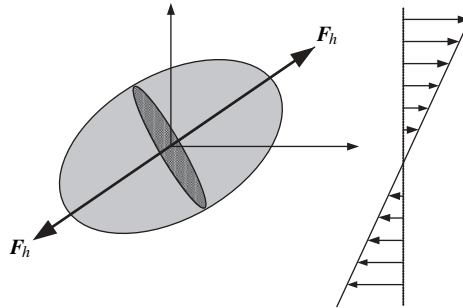


Fig. 7.25 An axisymmetric particle freely rotating in a simple shear field. The force F_h exerted by one half of the particle on the other is zero when the main axis is perpendicular to the flow direction; it reaches a maximum tensile strength at 45° and it drops to zero at 90° . Then at 135° it will reach maximum compression and return to zero at 180° . If the ellipsoid is at a certain angle to the direction of shear, the same phenomenon takes place, except that the tensile and compressive forces will be smaller and the particle will rotate and wobble. If the agglomerate is spherical it will smoothly rotate and a maximum tensile strength will be generated along an axis at 45° to the direction of shear.

where χ is a numerical constant⁶ that depends on the shape of the particle, μ is the viscosity of the liquid, $\dot{\gamma}$ is the local shear rate, c is a dimension characterizing the size of the particle, and θ and ϕ are instantaneous orientation Euler angles defined in Fig. 7.26.

Equation 7.2-22 indicates that the separating force is proportional to the local shear stress ($\mu\dot{\gamma}$) in the liquid, it is a sensitive function of the Euler angles of orientation, and is proportional to the projection of the cross-sectional area ($S = \pi c^2$). The angular velocities of rotation of the freely suspended spheroid particle were given by Zia, Cox, and Mason (46)

$$\begin{aligned} \frac{d\theta}{dt} &= b\dot{\gamma} \sin \theta \cos \theta \sin \phi \cos \phi \\ \frac{d\phi}{dt} &= \dot{\gamma} \frac{r_e \cos^2 \phi + \sin^2 \phi}{r_e^2 + 1} \end{aligned} \tag{7.1-23}$$

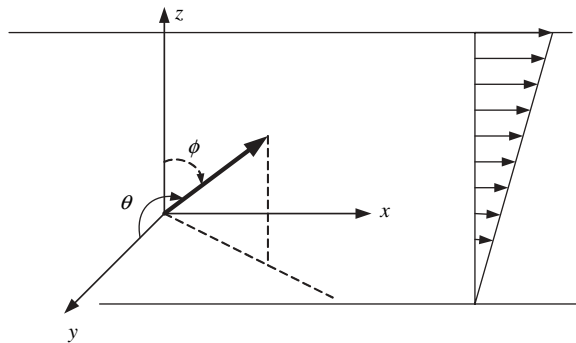


Fig. 7.26 Euler angles of orientation.

6. Nir and Acrivos (45) computed the value of χ for a doublet of touching equal spheres to be 12.23.

where r_e is the large-to-small axes ratio. Equation 7.2-23 can be integrated to give $\theta(t)$ and $\phi(t)$ in terms of initial orientations, and these indicate that the period of rotation τ is given by

$$\tau = \frac{2\pi}{\dot{\gamma}} \left(\frac{r_e^2 + 1}{r_e^2} \right) \quad (7.1-24)$$

implying that the hydrodynamic separating force also varies periodically with time within the same period, and oscillates between tension and compression. The maximum separating force is obtained from Eq. 7.2-22 with $\theta = 90^\circ$ and $\phi = 45^\circ$

$$F_{h,\max} = \pi \frac{\lambda}{2} \mu \dot{\gamma} c^2 \quad (7.1-25)$$

Agglomerates will rupture when the hydrodynamic separating forces exceed the cohesive forces (i.e., $F_h/F_c > 1$). The ratio is obtained by dividing Eq. 7.1-22 by Eq. 7.1-21

$$\frac{F_h}{F_c} = Z \sin^2 \theta \sin \phi \cos \phi \quad (7.1-26)$$

where

$$Z = \frac{8}{9} \lambda \mu \dot{\gamma} \left(\frac{\varepsilon}{1 - \varepsilon} \right) \frac{d}{C_0} \quad (7.1-27)$$

These equations indicate that according to this model: (a) agglomerate rupture is *independent* of size (the physical reason is that both the hydrodynamic separating force and the cohesive forces are proportional to the cross-section area at the rupture plane); (b) that the ratio F_h/F_c is proportional to d , thus the smaller the aggregate in the agglomerate, the higher the shear stress in the liquid must be to reach the breakup condition $F_h/F_c > 1$; and (c) the less optimal the orientation of the main axis of an axisymmetric agglomerate is, the more difficult it is to break it up. This means that axisymmetric agglomerates in preferred orientation will break in the high shear region and those that are not will pass the region unbroken. In other words, only a fraction of the agglomerates will break in one passage through the high shear zone. For those oriented in the most favorable direction ($\theta = 90^\circ$ and $\phi = 45^\circ$) or spherical particles, breakup requires $Z > 2$.

Manas-Zloczower and Feke (47a) extended the model to other linear flows and found that in the pure elongation and biaxial extension, the breakup criterion is $Z > 1$, and in uniaxial extension, $Z > 0.5$.

Direct experimental observation of the rupture of agglomerates in uncured styrene-butadiene rubber (SBR) in simple shear flow was obtained by Collin and Peuvrel-Disdier (48), supporting the previously discussed mechanism. It is shown on Fig. 7.27. The shear rate was 6 s^{-1} , yielding a shear stress of 130,000 Pa-s. The agglomerate is broken into two large, about equal-sized pieces with some debris, and separated.

Scurati et al. also proposed an alternative model (47b), whereby the agglomerate rather than breaking undergo a process of erosion in shear flow, with the rate proportional to the difference between the hydrodynamic force acting on the agglomerate and the cohesive force holding it together

$$-\frac{dD}{dt} = K \dot{\gamma} (F_h - F_c) \quad (7.1-28)$$

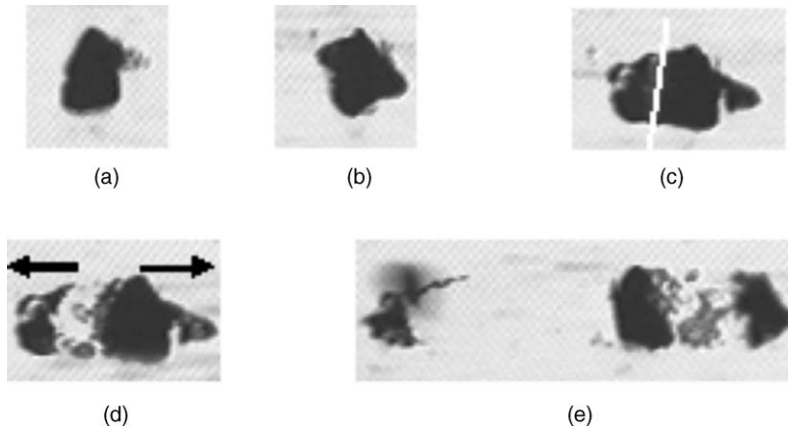


Fig. 7.27 Rupture time sequence of a carbon black agglomerate ($R_0 = 30\ \mu\text{m}$) in a styrene-co-butadiene rubber (SBR) in simple shear flow. The shear rate was $13.5\ \text{s}^{-1}$ resulting in a shear stress of 130,000 Pa. [Reprinted by permission from V. Collin, “Etude Rhéo-optique des Mécanismes de Dispersion du Noir de Carbone dans des Elastomères,” Doctoral Dissertation, Ecole des Mines de Paris, Sophia, Antipolis, France (2004).]

where D is the agglomerate diameter. In erosion, small fragments from the outer surface of the agglomerate are detached. When the debonding is significant, this mechanism is referred to as “ribbon peeling” or “onion peeling.” These two mechanisms, occurring separately or simultaneously were also experimentally observed by Astruc, as shown on Figs. 7.28 (a), (b), and (c).

It would be reasonable to assume that all these mechanisms operate in real dispersion. Hard agglomerates, which are most damaging to the product, would most likely break by the rupture mechanism, while softer agglomerates may erode.

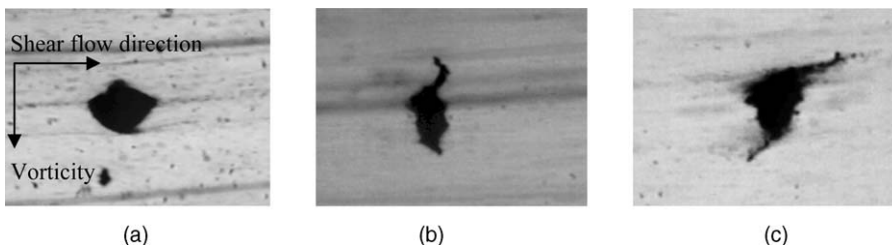


Fig. 7.28 Erosive dispersion of a carbon black agglomerate in butadiene rubber (BR) in simple shear flow, showing (a) the “onion peeling” mechanism, (b) a “ribbon peeling” mechanism and (c) both mechanisms. [Reprinted by permission from M. Astruc, “Etude Rheo-optique des Mécanismes de Dispersion de Mélanges sous Cisaillement Simple: 1. Mélanges concentrés de polymères immiscibles, 2. Mélanges polymères-charges poreuses,” Doctoral Dissertation, Sophia Antipolis, Ecole des Mines de Paris, France (2001).]

Example 7.5 The Shear Stresses Needed to Break 100 μm Diameter Spherical Carbon Black Agglomerates having Tensile Strengths given in Example 7.4.

Solution The cross-sectional area of the agglomerate is $(\pi/4)(10^{-4})^2 = 0.785 \times 10^{-8} \text{ m}^2$. Therefore, the cohesive forces of the agglomerates are $7.62 \times 10^{-3} \text{ N}$ and $2.28 \times 10^{-3} \text{ N}$, for the smaller and larger aggregates, respectively. The maximum hydrodynamic separating force from Eq. 7.1-25 is $(0.785 \times 10^{-8})(12.23/2)(\mu\dot{\gamma}) = 4.80 \times 10^{-8}(\mu\dot{\gamma}) \text{ N}$. The shear stresses needed to break the agglomerate will be $(7.62 \times 10^{-3})/(4.80 \times 10^{-8}) = 1.5875 \times 10^5 \text{ N/m}^2$ and $(2.28 \times 10^{-3})/(4.80 \times 10^{-8}) = 0.475 \times 10^5 \text{ N/m}^2$, respectively. These correspond to 23.0 psi and 6.89 psi. The order of magnitude of the mean shear rate under the blade of an internal mixer is in the range of 200s^{-1} to 500s^{-1} . Assuming a relatively low viscosity of $0.1 \text{ lb}_f\text{s/in}^2$, the shear stress range is 20 psi to 50 psi, namely, in the range needed to break the agglomerate.

7.2 MIXING EQUIPMENT AND OPERATIONS OF MULTICOMPONENT AND MULTIPHASE SYSTEMS

In the previous section we reviewed the rich variety of *mixing mechanisms* encountered in the processing of polymers. In this section we review the kind of machinery used for carrying out these mechanisms. There is a considerable arsenal of machinery; some are specifically designed for a particular mixing operation, while others are “ordinary” pieces of processing equipment designed for other elementary steps as well as for mixing. In attempting to classify mixers, we first distinguish between (a) *batch* and (b) *continuous mixers*. We review their design and analysis or simulation of their functions in Chapters 9 and 10.

Batch Mixers

Batch mixer are the oldest type of mixer developed for rubber processing, and they are still widely used. Batch mixers are very versatile because operating conditions can be varied during the cycle, additives can be added at an optimal time sequence, and good temperature control can be maintained; furthermore, they are available in a very broad range of sizes and, if need be, can be incorporated in continuous lines.

There are no standard engineering classification methods for mixing equipment, and often, quite different types of mixers can fulfill the same mixing task. Nevertheless, we can subdivide mixers used in processing into three broad categories: particulate solids mixers, laminar distributive mixers, and laminar dispersive mixers. This classification, on the basis of application, is supported by the nature of the primary mixing mechanism taking place in them.

Particulate solids mixers, also referred to as *blenders*, generally involve a random distributive mixing mechanism. On the basis of their operation, they can be further subdivided into “tumbling” type, “agitating ribbon” type, and “fluidized bed” type mixers. The tumbling-type mixers are the simplest and least expensive, but they cannot handle difficult mixtures. There is a tendency for segregation; stickiness is a problem, and a considerable electrostatic charge may be created during interparticle and wall-particle rubbing. The latter property may be advantageous, however, as in the dry blending of pigments with nonpolar polymers, or during the mixing of two components with opposite electric charges, when charging can greatly improve the mixing.

Ribbon blenders consist of some moving elements, such as a spiral element, that induce convective motion. They are good for cohesive particulate mixtures, but they require more power than tumbling blenders and are more difficult to clean. In ribbon-type blenders, as well as some other types, PVC dry blend can be prepared by slowly spraying small amounts of liquid additives into the mixture. Such additives may sometimes generate the formation of small, soft balls, which should be avoided if a free-flowing dry blend is desired. Ribbon blenders generate considerable static electricity.

Finally, fluidized-bed mixers are rapid mixers, but cannot, of course, deal with cohesive powders or a very wide distribution of particulate sizes; neither are they suitable for powder mixtures with pronounced size, density, and shape variations because of segregation problems. They generate small static electric charges.

Liquid mixers can be subdivided on a practical basis of mixture viscosity. On one end we have the low viscosity mixers, such as the impeller type, and on the other, high-speed dispersion mixers. In this viscosity range, turbulent mixing may still play a significant role. In the medium range, we have the various double-blade units such as the sigma blade mixer. This design consists of a rectangular trough curved at the bottom to form two half-cylinders. The two blades revolve toward each other at different frequencies of rotation. Usually, a ratio of 2:1 is used. Mixing is induced by imparting both axial and tangential motion. The clearance between the blades and shell is small, about 1 mm, to eliminate stagnant regions. These mixers handle liquids in the viscosity range of 0.5–500 N·s/m². Another group of double-blade mixers consists of the overlapping-blade type, in which the blades rotate at the same frequency of rotation. Double-blade mixers are widely used in the preparation of reinforced plastics, as well as for mixing and kneading a large variety of viscous liquids and pastes.

At the high viscosity end of this classification, which is our primary interest, we find, among others, the high intensity internal mixers such as the Banbury-type mixer⁷ and the roll-mill, both extensively used in the rubber and plastics industries. These mixers, in addition to imparting laminar distributive mixing, are characterized by forcing the mixture to pass, repeatedly, through high shear-stress zones where dispersive mixing takes place. We note here that laminar batch mixers most often require *efficient melting capabilities*, since operations start with mixtures with at least one polymer component in the solid state. We will return to these mixers for a more detailed analysis later.

Continuous Mixers

All single and twin rotor polymer continuous mixers must be capable of efficiently affecting the elementary steps of particulate solids handling and melting, before carrying out laminar distributive and dispersive mixing. It is noteworthy, as we discuss in Chapters 10 and 11, that laminar mixing occurs *simultaneously* with melting. To enhance the laminar mixing process leading to both compositional and temperature uniformity, single-rotor continuous mixers are equipped with special rotors or screws. To enhance dispersive mixing, twin-rotor mixers have special dispersive *mixing elements*. These are positioned “strategically” along the length of the screw(s), always, of course, after most of the feed stream has been melted. The prime example of a continuous dispersive mixer is the co-rotating intermeshing twin screw extruder with kneading elements. The screw and the kneading elements are segmented; thus, by sliding them on a keyed shaft in a certain order, the rotor design can be matched to the mixing needs. We discuss these mixing elements in Chapters 9 and 10. Another method of

7. See D. H. Killeffer, *Banbury, the Master Mixer*, Palmerton, NY (1962).

improving mixing in continuous laminar mixers is with the incorporation of *static* or *motionless* pressure flow mixers placed downstream of the screw(s).

The name “motionless” mixer is derived from the fact that these devices achieve mixing without any moving parts. Instead, through ingenious construction, they rearrange the flow field and reshuffle the fluid streams in such a way that the interfacial area increases appreciably and predictably, in an ordered fashion as the fluid mixture flows through each one of the repetitive mixing elements making up the motionless mixers. Although the exact mixing pattern is specific to the particular type of motionless mixer used, it is generally true that the interfacial area between the major and minor components is increased in two ways: by shear or extensional flow and by splitting and recombining fluid streams. Both involve pressure losses. Thus there is a practical limit to the number of motionless mixer elements that can be used, and hence the quality of mixing that can be achieved by these devices. In Section 7.5, which deals with computational analysis, we present computer-simulated flow patterns in a Kenics motionless mixer. Here we briefly describe the Ross ISG (Interfacial Surface Generator).

Schott et al. (49) have reviewed these motionless mixers commonly used in the polymer processing industry. The Ross ISG is shown in Fig. 7.29(a). In each element, the four

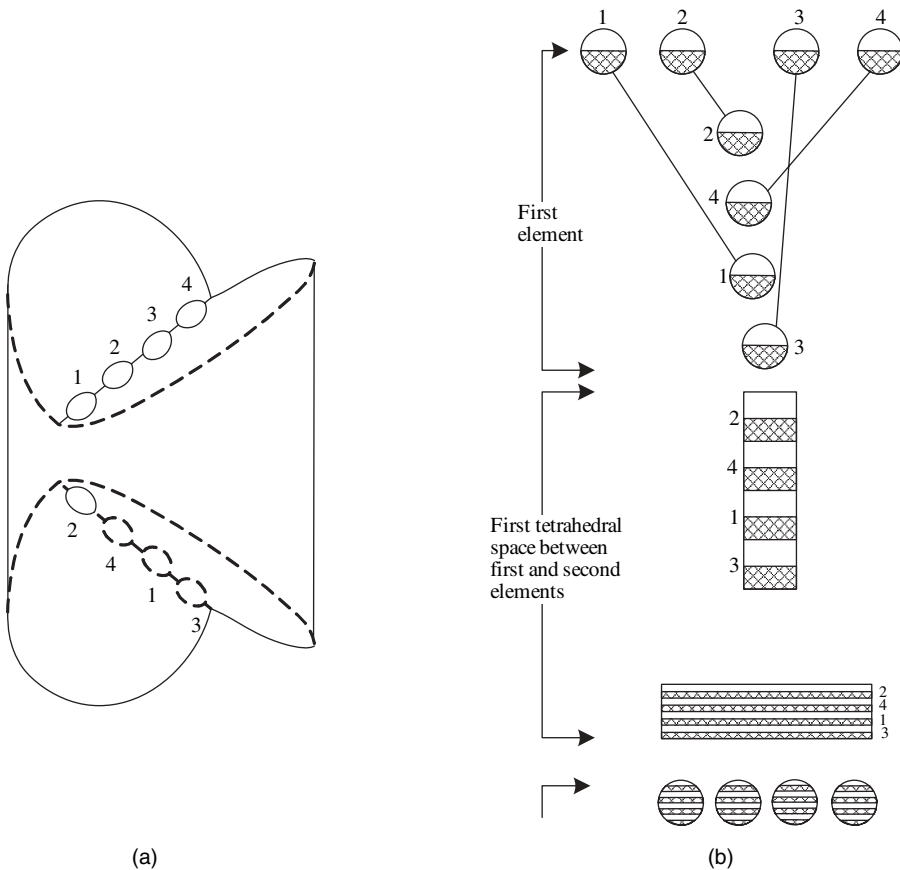


Fig. 7.29 Schematic representation of (a) the Ross ISG mixing element, and (b) its ordered distributive mixing action.

circular entrance holes form a line perpendicular to that formed by the exit holes. This is achieved by drilling the holes obliquely with respect to the axis of the element and in such a way that an outside entrance has an inside exit, thus achieving radial mixing. This is shown in Fig. 7.29(b). It is evident that the flow inside each mixing element undergoes practically no mixing, except for the radial redistribution of the four streams. On the other hand, by construction, a tetrahedral space is formed between two consecutive elements. The four streams from the first element join together in this space, creating new interfaces (*striations*), as shown in the last part of Fig. 7.29(b). The flow that occurs in the tetrahedral spaces is divergent–convergent in nature and results in an effective stretching of the interfacial area-elements. In this stretched state the fluid is divided into four streams by the holes of the second element where radial redistribution will occur again. The net result of the fluid stream combination and flow is the fourfold increase of the number of striations, N_s . Following the fluid through consecutive elements, one can easily show that the relation between N_s and the number of elements E is

$$N_s = 4^E \quad (7.2-1)$$

Other common continuous mixers involve substantial modification of single and twin screw extruders, aimed at improving distributive mixing capability in particular, and leading to the development of continuous mixers such as the Transfermix (50) and the Buss Ko-Kneader (51). Another approach in continuous mixer development is to transform batch mixers into continuous ones. Thus, the roll-mill can be converted into a continuous mixer by feeding raw material on one side and continuously stripping product on the other side. In addition, the Banbury mixer was imaginatively transformed into the Farrel Continuous Mixer (FCM) by Ahlefeld et al. (52), and, later, two similar continuous mixers were developed by Okada et al. (53) at Japan Steel Works and by Inoue et al. (54) at Kobe Steel.

Continuous mixing has the advantages of large output, uninterrupted operation, greater product uniformity, easier quality control, and reduced manpower. It has the disadvantages of generating lower dispersive mixing quality and smaller possessing flexibility in switching to new mixtures. The feed must be maintained uniformly with time, and the mixing “protocol,” the order of introducing the components into the mixture, may be difficult to change. The design of a continuous mixer is aimed toward a uniform outlet composition across the exiting stream, as well as composition uniformity in time. The former is achieved by imparting to all fluid particles leaving the mixer similar total deformation (i.e., narrow strain-distribution function) as well as exposure to stresses, and by feeding the mixer with a grossly uniform mixture; ample shuffling and rearrangement throughout the mixer also must be ensured. Uniformity in time can be obtained by careful metering of the inlet rate of the ingredients.

7.3 DISTRIBUTION FUNCTIONS

By *distribution functions* we mean mathematical functions that account for the fact that a certain variable describing a property or process cannot be fully defined by a single number, but rather a whole range of numbers is needed.

The most common distribution function that we encounter with polymers is the *molecular weight distribution* (MWD). Clearly, most polymerizations do not yield macromolecules identical in length, but rather a range of lengths or weights. Thus we need to define MWD functions.

Similarly, in continuous operations the residence times that exiting fluid elements experienced in the system are not necessarily uniform, but there is a distribution of residence times that we must take into account, and we must define *residence time distribution (RTD) functions*.

As pointed out above, there are certain process characteristics in mixing that define the mixing process, such as the total strain imposed on the fluid element. However, strain is given by the product of time and rate of deformation, and these may assume a range of values even in a batch mixer, let alone a continuous one. Thus, we need to deal with *strain distribution (SDF) functions*. Finally, as discussed in the previous section, dispersion of solid particles in a viscous polymeric melt depends on stress levels. These levels are achieved only in specific regions of a batch or continuous mixer, and fluid particles need to pass *repeatedly* through these regions to be reduced to acceptable sizes. But different fluid particles experience a different number of passages, thus, we need to define *number of passage distribution (NPD) functions*.

We now briefly define and discuss these various distribution functions. We begin with MWD functions, which are familiar to most readers, in order to introduce the other distribution functions.

Molecular Weight Distribution Functions

We begin by defining M_x as the concentration (e.g., mole/l) of molecules having a length of x repeating units or mers.⁸ Clearly, then, $\sum M_x$, where the summation is over all the lengths, is the total number of macromolecules in moles per liter; $\sum xM_x$ is the total number of mers in moles per liter. From these definitions, we obtain the following expressions for the mole fraction and weight fraction of macromolecules of length x , respectively:

$$Y_x = \frac{M_x}{\sum M_x} \quad (7.3-1)$$

and

$$W_x = \frac{xM_x}{\sum xM_x} \quad (7.3-2)$$

Now, we define the moment r of the distribution, μ_r :

$$\mu_r = \sum x^r M_x \quad (7.3-3)$$

8. M_x is a distribution function that can be computed if the kinetics of the polymerization mechanism and the type and condition of polymerization reactor (e.g., batch or continuous, homogeneous or segregated, isothermal or nonisothermal, etc.) are known. [See, for example, Z. Tadmor and J. A. Biesenberger, "The Influence of Chain Initiation Rate on Molecular Weight Dispersion in Free Radical Polymerization," *J. Polym. Sci.*, **B3**, 753–759 (1965); J. A. Biesenberger and Z. Tadmor, "Molecular Weight Distribution in Continuous Linear Addition Polymerization," *J. Appl. Polym. Sci.*, **9**, 3409–3516 (1965); Z. Tadmor and J. A. Biesenberger, "Influence of Segregation on Molecular Weight Distribution in Continuous Linear Polymerization," *Ind. Eng. Chem. Fundam.*, **5**, 336–343 (1966); J. A. Biesenberger and Z. Tadmor, "Residence Time Dependence of Molecular Weight Distributions in Continuous Polymerizations," *Polym. Eng. Sci.*, **6**, 299–305 (1966)]. Otherwise, M_x can be measured experimentally and an empirical function fitted to the measured values. In addition molecular weight averages can be independently measured.

Thus the zero moment $\mu_0 = \sum M_x$, the first moment $\mu_1 = \sum xM_x$, $Y_x = M_x/\mu_0$, and $W_x = xM_x/\mu_1$.

We can now define the various averages using the moments of the distribution:

$$\bar{x}_N = \frac{\mu_1}{\mu_0} = \frac{\sum xM_x}{\sum M_x} = \sum x \frac{M_x}{\sum M_x} = \sum xY_x \quad (7.3-4)$$

$$\bar{x}_W = \frac{\mu_2}{\mu_1} = \frac{\sum x^2M_x}{\sum xM_x} = \sum x \frac{xM_x}{\sum xM_x} = \sum xW_x \quad (7.3-5)$$

$$\bar{x}_z = \frac{\mu_3}{\mu_2} \quad \bar{x}_{z+1} = \frac{\mu_4}{\mu_3}, \quad \text{etc.} \quad (7.3-6)$$

where \bar{x}_N is the number average length, \bar{x}_W is the weight average length, and \bar{x}_z and \bar{x}_{z+1} are the z and the $z + 1$ averages. These averages can be measured experimentally by different techniques (e.g., osmotic pressure, light scattering, and centrifugal separation, respectively). Of course, higher averages can be defined, but if they cannot be measured experimentally, they are of little utility.

Using the moments of distribution, we can easily express weight fraction in terms of mole fraction as follows:

$$W_x = \frac{xM_x}{\sum xM_x} = \frac{xM_x}{\mu_1} = \frac{xM}{\mu_0} \frac{\mu_0}{\mu_1} = \frac{xY_x}{\bar{x}_N} \quad (7.3-7)$$

Next we derive the variance of the distribution:

$$\begin{aligned} \sigma_N^2 &= \sum (x - \bar{x}_N)^2 Y_x \\ &= \sum (x^2 Y_x - 2x\bar{x}_N Y_x + \bar{x}_N^2 Y_x) \\ &= \sum \frac{x^2 M_x}{\mu_0} - 2\bar{x}_N \sum xY_x + \bar{x}_N^2 \\ &= \frac{\mu_2}{\mu_0} - 2\bar{x}_N + \bar{x}_N^2 = \frac{\mu_2 \mu_1}{\mu_1 \mu_0} - \bar{x}_N^2 \\ &= (\bar{x}_W - \bar{x}_N) \bar{x}_N \end{aligned} \quad (7.3-8)$$

The variance measures the *absolute* breadth of the distribution, but properties that depend on the width of the distribution would depend on the width *relative* to the average. For this reason the *dispersion index* is defined as the ratio of the weight to the number average molecular weight, which is related to the variance as follows:

$$D_N = \frac{\bar{x}_W}{\bar{x}_N} = 1 - \frac{\sigma_N^2}{\bar{x}_N} \quad (7.3-9)$$

Further properties of the distribution can be obtained from the averages. One such measure is g_N , which measures the skewness of the distribution. A positive skewness indicates a tilt toward higher x values and a negative value toward the smaller values of x :

$$g_N = \frac{\sum (x - \bar{x}_N)^3}{\sigma_N^3} = \frac{\bar{x}_N (\bar{x}_z \bar{x}_W - 3\bar{x}_W \bar{x}_N + 2\bar{x}_N^2)}{\sigma_N^3} \quad (7.3-10)$$

Residence Time Distribution Functions

Polymers are temperature-sensitive materials, and prolonged exposure to high temperatures may result in thermal degradation. The degree of degradation depends on the time-temperature history of the polymer. Often polymer systems are processed with temperature-activated reacting additives (foaming agents, cross-linking agents), or the system as a whole is reactive, as is the case in reaction injection molding and reactive extrusion. In these systems, the extent of chemical reaction in the processing equipment depends, of course, on the time-temperature history. Extrudates of many polymers (e.g., nylon 66) contain varying amounts of “gels,” which may be a result of excessive residence time of a small fraction in processing vessels.

In all the just-mentioned examples, quantitative prediction and design require the detailed knowledge of the residence time distribution functions. Moreover, in normal operation, the time needed to purge a system, or to switch materials, is also determined by the nature of this function. Therefore the calculation and measurement of RTD functions in processing equipment have an important role in design and operation.

The definition of RTD functions is credited to Danckwerts (55). We first differentiate between the internal RTD function $g(t) dt$ and the external RTD function $f(t) dt$. The former is *defined* as the fraction of fluid volume *in* the system with a residence time between t and $t + dt$, and the latter is defined as the fraction of *exiting* flow rate with a residence time between t and $t + dt$. From these definitions we can define the cumulative functions $G(t)$ and $F(t)$, respectively, as follows:

$$G(t) = \int_{t_0}^t g(t) dt \quad (7.3-11)$$

and

$$F(t) = \int_{t_0}^t f(t) dt \quad (7.3-12)$$

where t_0 is the shortest residence time. It follows from the definition that

$$G(\infty) = F(\infty) = 1 \quad (7.3-13)$$

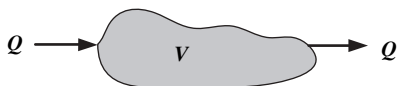
The mean residence time is given by

$$\bar{t} = \int_{t_0}^{\infty} tf(t) dt \quad (7.3-14)$$

and at steady state it equals the volume of the system divided by the volumetric flow rate.

The Relationships among the RTD Functions

Consider a steady continuous flow system of volume V characterized by a certain external RTD $F(t)$ or $f(t) dt$, in which a “white” fluid flows at a constant volumetric flow rate of Q .



Suppose that at time $t = 0$, we switch to a “red” fluid having otherwise identical properties, without altering the flow rate. Following the switch, after any time t we can make, with the aid of the definitions of the RTD functions, the following material balance of red fluid:

$$\begin{array}{rcccl}
 Q & - & QF(t) & = & \frac{d}{dt}[VG(t)] \\
 \text{Rate of flow of red in} & & \text{Rate of flow of red out} & & \text{Rate of change of red in} \\
 & & & & \text{the system}
 \end{array} \tag{7.3-15}$$

Recalling that the mean residence time is given by

$$\bar{t} = \frac{V}{Q} \tag{7.3-16}$$

Eq. 7.3-15 with Eq. 7.3-11 can be written as

$$g(t) = \frac{1 - F(t)}{\bar{t}} \tag{7.3-17}$$

Using Eq. 7.3.16, it is possible to derive all the interrelationships of the RTD functions, which are listed in Table 7.1. The two extreme flow systems with respect to RTD are the *plug flow* system, which exhibits no distribution of residence times, and the *continuous stirred tank* (CST), which exhibits perfect back-mixing and has the following RTD function:

$$F(t) = 1 - e^{-t/\bar{t}} \tag{7.3-18}$$

In this case, because perfect back mixing exists, the internal and external RTD functions are identical. This can be easily verified from Table 7.1, recalling that the minimum residence time in this case is zero. This is generally not the case in laminar flow systems where, in principle, the RTD functions can be calculated from the velocity profiles. It should be noted that in complex systems, a precise description of the path the fluid follows between subsystems is also needed to calculate the RTD.

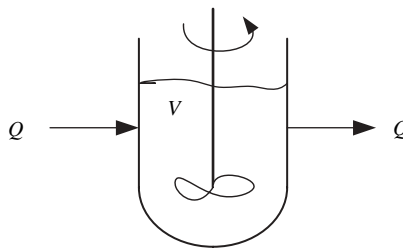
TABLE 7.1 Relationships among the Various RTD Functions

Given	Calculate			
	$f(t)$	$F(t)$	$g(t)$	$G(t)$
$f(t)$	$f(t)$	$\int_{t_0}^t f(t') dt'$	$\frac{1}{\bar{t}} - \frac{1}{\bar{t}} \int_{t_0}^t f(t') dt' \quad t \geq t_0$	$\frac{1}{\bar{t}} - \frac{1}{\bar{t}} \int_{t_0}^t \int_{t_0}^{t'} f(t'') dt'' dt' \quad t \geq t_0$
$F(t)$	$\frac{dF(t)}{dt}$	$F(t)$	$\frac{1 - F(t)}{\bar{t}} \quad t \geq t_0$	$\frac{1}{\bar{t}} - \frac{1}{\bar{t}} \int_{t_0}^t F(t') dt' \quad t \geq t_0$
$g(t)$	$-\bar{t} \frac{dg(t)}{dt} \quad t \geq t_0$	$1 - \bar{t}g(t) \quad t \geq t_0$	$g(t)$	$\int_{t_0}^t g(t') dt'$
$G(t)$	$-\bar{t} \frac{d^2G(t)}{dt^2} \quad t \geq t_0$	$1 - \bar{t} \frac{dG(t)}{dt} \quad t \geq t_0$	$\frac{dG(t)}{dt}$	$G(t)$

For many cases in which the RTD cannot be calculated theoretically, experimental techniques have been developed to measure it. Such techniques are used by introducing a tracer material into the system and recording its concentration at the exit.⁹ These methods are discussed in great detail in the literature. In general, a step change in tracer concentration results directly in the $F(t)$ function, and an impulse type of tracer injection results directly in the $f(t)$ function.

Example 7.6 Residence Time Distribution in a CST: Kinetic Derivation Consider a CST of volume V and volumetric flow rate Q (depicted in the figure below). At time $t = 0$ we increase the inlet concentration, in volume fraction, from zero to $X(0)$. Unlike in the previous Example, in a CST the concentration of the exiting stream at time t is identical to that in the tank and equals $X(t)$. A simple mass balance gives

$$Q - QX(t) = \frac{d}{dt}[VX(t)] \quad (\text{E7.6-1})$$



The solution of Eq. E7.6-1 with the initial condition $X(t) = 0$ is

$$X(t) = 1 - e^{-t/\bar{t}} \quad (\text{E7.6-2})$$

But, by definition $F(t) = X(t)$, because $X(t)$ is the fraction of volume consisting of the liquid that entered the tank at $t = 0$, and therefore it must have a residence time of t or less,

$$F(t) = 1 - e^{-t/\bar{t}} \quad (\text{E7.6-3})$$

From Table 7.1

$$f(t) dt = g(t) dt = \frac{1}{\bar{t}} e^{-t/\bar{t}} dt \quad (\text{E7.6-4})$$

and $G(t) = F(t)$. As expected, in a well-stirred tank, external and internal RTD functions are identical.

Example 7.7 Residence Time Distribution in a CST: Stochastic Derivation¹⁰ A better insight into the nature of RTD functions can be obtained by deriving the RTD in CST

9. It should be noted, however, that most of these techniques assume a plug-type inlet flow into the system. If this is not the case, special care must be taken in introducing the tracer material (e.g., in an impulse signal, the amount of tracer must be proportional to the local velocity, otherwise complex corrections may be required).

10. J. A. Biesenberger, private communication.

stochastically. Imagine that we divide the continuous feed into discrete steps, whereby at each step, we inject into the well-stirred tank an infinitesimally small volume $\delta V = Q\delta t$, and at the same time we randomly withdraw a sample of the same size. At exactly time $t = 0$ we inject a “red” sample δV , and we ask what is the probability for it to be withdrawn exactly at time t . The probability that the first sample withdrawn will *not* be the marked sample is $(1 - \delta V/V)$. The probability that after n withdrawals the marked sample will *not* be withdrawn is $(1 - \delta V/V)^n$. The probability P that the marked sample *will* be withdrawn on the $n + 1$ drawing is

$$P = \left(1 - \frac{\delta V}{V}\right)^n \frac{\delta V}{V} \quad (\text{E7.7-1})$$

Next we take the log of Eq. E7.7-1 to get

$$\ln P = n \ln \left(1 - \frac{\delta V}{V}\right) + \ln \left(\frac{\delta V}{V}\right) \quad (\text{E7.7-2})$$

but $\delta V/V$ is infinitesimally small, and we can rewrite Eq. E7.7-2 as

$$\ln P = -n \frac{\delta V}{V} + \ln \frac{\delta V}{V} \quad (\text{E7.7-3})$$

or

$$P = e^{-n\delta V} \frac{\delta V}{V} \quad (\text{E7.7-4})$$

But, $\delta V = Q\delta t = \delta t/\bar{t}$, and we get

$$P = f(t) dt = e^{-t/\bar{t}} dt \quad (\text{E7.7-5})$$

Clearly, the probability of a fluid particle that enters at $t = 0$ leaving at after time t equals exactly the fraction of flow rate leaving the vessel between time t and $t + dt$.

In a similar way we can derive the RTD in a series of CSTs.

Example 7.8 Residence Time Distribution Functions in Fully Developed Laminar Flow of a Newtonian Fluid in a Pipe The velocity distribution

$$v_z = C(R^2 - r^2) \quad (\text{E7.8-1})$$

where $C = \Delta P/4L\mu$. The residence time of a fluid particle depends on its radial position

$$t = \frac{L}{v_z} = \frac{L}{C(R^2 - r^2)} \quad (\text{E7.8-2})$$

where L is the length of the pipe. The minimum residence time $t_0 = L/CR^2$ is at the center of the pipe where the velocity is at maximum. Thus the residence time ranges from t_0 to infinity at the wall. We can now rewrite Eq. E7.8-2 as

$$\frac{t}{t_0} = \frac{1}{1 - (r/R)^2} \quad (\text{E7.8-3})$$

The residence distribution function $f(t) dt$, which was defined as the fraction of exiting flow rate with a residence time between t and $t + dt$, is *exactly* the fraction of flow rate between r and $r + dr$. Thus

$$f(t) dt = \frac{dQ}{Q} = \frac{2\pi r v_z dr}{\int_0^R 2\pi r v_z dr} = \frac{2r v_z dr}{R^2 L / 2t_0} \quad (\text{E7.8-4})$$

and by using Eqs. E7.8-1 and E7.8-2, we express r and v_z in terms of t , to obtain

$$\begin{aligned} f(t) dt &= \frac{2t_0^2}{t^3} dt & t \geq t_0 \\ f(t) dt &= 0 & t < t_0 \end{aligned} \quad (\text{E7.8-5})$$

and the mean residence time

$$\bar{t} = \int_{t_0}^{\infty} t f(t) dt = 2t_0 \quad (\text{E7.8-6})$$

The other RTD functions can be easily obtained from the relationships in Table 7.1. These are

$$\begin{aligned} F(t) &= 1 - \left(\frac{t_0}{t}\right)^2 & t \geq t_0; & & F(t) = 0 & t < t_0 \\ g(t) dt &= \frac{t_0}{2t^2} dt & t \geq t_0; & & g(t) dt = \frac{1}{2t_0} dt & t < t_0 \\ G(t) &= 1 - \frac{t_0}{2t} & t \geq t_0; & & G(t) = \frac{1}{2t_0} & t < t_0 \end{aligned} \quad (\text{E7.8-7})$$

Strain Distribution Functions

If we accept the premise that the total strain is a key variable in the quality of laminar mixing, we are immediately faced with the problem that in most industrial mixers, and in processing equipment in general, different fluid particles experience different strains. This is true for both batch and continuous mixers. In the former, the different strain histories are due to the different paths the fluid particles follow in the mixer, whereas in a continuous mixer, superimposed on the different paths there is also a different residence time for every fluid particle in the mixer. To quantitatively describe the various strain histories, *strain distribution functions* (SDF) were defined (56), which are similar in concept to the residence time distribution functions discussed earlier.

In the following discussion, the meaning of strain is restricted to shear strain, and specifically to the magnitude of the shear $\gamma = \int_0^t \dot{\gamma}_{yx}(t') dt'$

Batch Mixers In a batch mixer the shear rates throughout the volume are not uniform, and neither are the residence times of various fluid particles in the various shear-rate regions. Consequently, after a given time of mixing, different fluid particles experience different strain histories and accumulate different shear strains γ . The SDF, $g(\gamma) d\gamma$, is defined as the fraction of the fluid in the mixer that has experienced a shear strain from γ to $\gamma + d\gamma$. Alternatively, it is the probability of a fluid particle fed to the mixer to accumulating a shear strain of γ in time t . By integrating $g(\gamma) d\gamma$, we get:

$$G(\gamma) = \int_0^{\gamma} g(\gamma) d\gamma \quad (7.3-19)$$

where $G(\gamma)$ is the fraction of liquid that experienced a strain of less than γ . The mean strain is

$$\bar{\gamma} = \int_0^{\gamma_{\max}} \gamma g(\gamma) d\gamma \quad (7.3-20)$$

The function SDF depends on mixer geometry operating conditions and the rheological properties of the fluid. Next, we derive the SDF for some simple idealized mixers.

Example 7.9 Strain Distribution Function in Drag (Couette) Flow between Concentric Cylinders Consider a Power Law model fluid placed between two long concentric cylinders of radii R_i and R_0 . At a certain time the inner cylinder is set in motion at constant angular velocity Ω rads/s. Assuming steady isothermal laminar flow without slip at the walls, neglecting gravitational and centrifugal forces, the velocity profile is

$$\frac{v_{\theta}}{\Omega R_i \rho} = \frac{\beta^{2s} - \rho^{2s}}{\rho^{2s}(\beta^{2s} - 1)} \quad (E7.9-1)$$

where v_{θ} is the tangential velocity, $\rho = r/R_i$, $\beta = R_0/R_i$, and $s = 1/n$, with n being the Power Law fluid exponent. Taking the derivative of Eq. E7.9-1, we obtain the shear rate

$$\dot{\gamma}_{r\theta} = \rho \frac{d}{dr} \left(\frac{v_{\theta}}{R_i \rho} \right) = \frac{2s\Omega\beta^{2s}}{\rho^{2s}(\beta^{2s} - 1)} \quad (E7.9-2)$$

Clearly, the shear rate is maximum at the inner cylinder and minimum at the outer cylinder. The difference between their respective values increases with curvature (increasing β) and with departure from Newtonian behavior (increasing s). The total strain is obtained by simply multiplying the shear rate by time

$$\gamma = \dot{\gamma}_{r\theta} t = \frac{2s\Omega\beta^{2s}t}{\rho^{2s}(\beta^{2s} - 1)} \quad (E7.9-3)$$

Note that Ωt divided by 2π is simply the total number of revolutions. The ratio of maximum to minimum strain across the gap is

$$\frac{\gamma_{\max}}{\gamma_{\min}} = \beta^{2s} \quad (\text{E7.9-4})$$

The striation thickness is inversely proportional to total strain, and therefore the ratio of the striation thickness at the outer and inner radii is

$$\frac{r_o}{r_i} = \frac{\gamma_{\max}}{\gamma_{\min}} = \beta^{2s} \quad (\text{E7.9-5})$$

This effect is evident in the experimental work of Bergen et al. (7), who investigated the mixing of black-and-white linoleum composition in a concentric cylinder mixer. Figure E7.9a presents the initial condition and mixing resulting after 1 and 20 revolutions. Results indicate that after 20 revolutions, a “band” of “uniform” gray mixture is created at the moving inner cylinder, yet a lack of mixing is very evident at the region close to the outer cylinder. The authors relate the nonuniformity to a Bingham fluid response. Although this may partly be the reason, one would expect a mixing nonuniformity even with a Newtonian fluid, and certainly with a Power Law model fluid, as indicated by Fig. E7.9b.

In this particular case, the outer and inner radii are 0.75 and 0.5 in, respectively; hence, the curvature $\beta = 1.5$. It follows from Eq. E7.9-5 that the ratio of the striation thickness for a Newtonian fluid is 2.25; for a power law fluid with $n = 0.5$, it is 5.06, and for a power law fluid with $n = 0.25$, it is 25.6 (!). A better insight into the nature of this problem can be

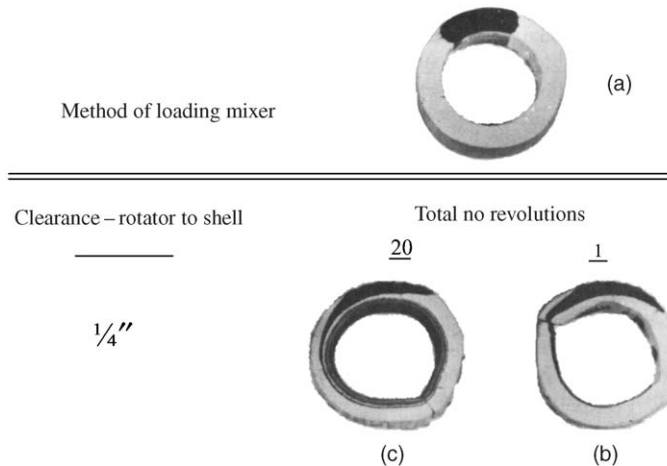


Fig. E7.9a Mixing of unmatured linoleum compound between concentric cylinder mixers. (a) Method of loading—initial condition. (b) After one revolution. (c) After 20 revolutions. Diameter of inner cylinder, 1 in; radial clearance, 0.25 in. [Reprinted by permission from J. T. Bergen et al., “Criteria for Mixing and the Mixing Process,” paper presented at the 14th National Technical Conference, Society of Plastics Engineers, Detroit, 1958.]

obtained by calculating the SDF $G(\gamma)$. The fraction of material that experiences a total strain of γ or less is equivalent to the fraction of material found between ρ and β

$$G(\gamma) = \frac{\pi(R_o^2 - R^2)L}{\pi(R_o^2 - R_i^2)L} = \frac{\beta^2 - \rho^2}{\beta^2 - 1} \tag{E7.9-6}$$

where L is the length of the “mixer.” Substituting Eq. E7.9-3 into Eq. E7.9-6, we get

$$G(\gamma) = \frac{\beta^2}{\beta^2 - 1} \left[1 - \left(\frac{\gamma_{\min}}{\gamma} \right)^n \right] \tag{E7.9-7}$$

where γ_{\min} is the minimum strain (at the outer radius) given by

$$\gamma_{\min} = \frac{2s\Omega t}{\beta^{2s} - 1} \tag{E7.9-8}$$

The SDF function, $g(\gamma) d\gamma$, is obtained by differentiating Eq. E7.9-7

$$g(\gamma) d\gamma = n \left(\frac{\beta^2}{\beta^2 - 1} \right) \left(\frac{\gamma_{\min}^n}{\gamma^{n+1}} \right) d\gamma \tag{E7.9-9}$$

Finally, the mean strain $\bar{\gamma}$ is

$$\bar{\gamma} = \int_{\gamma_{\min}}^{\gamma_{\max}} \gamma g(\gamma) d\gamma = \gamma_{\max} \left[\frac{1 - \beta^{2(1-s)}}{(\beta^2 - 1)(s - 1)} \right] \tag{E7.9-10}$$

Figure E7.9b shows the SDFs for the particular case (c) in Fig. E7.9a, with n as a parameter. We note that even for a Newtonian fluid, 56% of the material experiences a strain

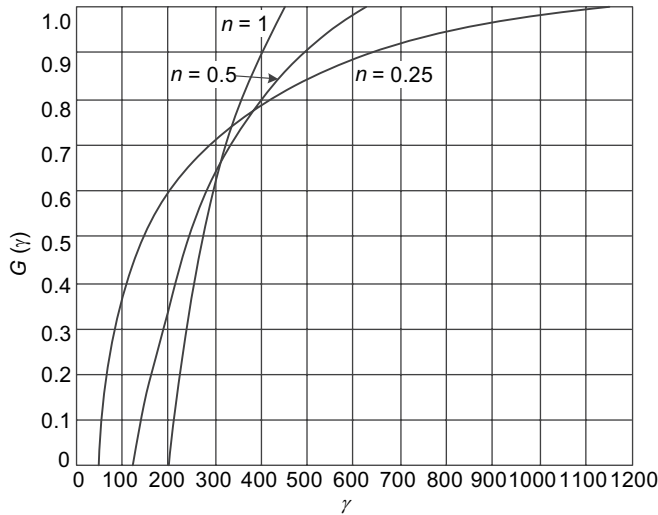


Fig. E7.9b Strain distribution function in $G(\gamma)$ of a power law model fluid in Couette flow between concentric cylinders for the case (c) of Fig. E7.9a

less than the mean, with the distribution spreading over a range of 200–450 shear units. It is important to note that the 56% falling below the mean is in a narrower strain range (about 100) than the remaining 44% (which fall in a strain range of about 150 shear units). The nonuniformity substantially increases with decreasing n . As the mean strain drops, the distribution broadens, and becomes distorted such that higher fractions of material below the mean experience strains in relatively narrower ranges than the smaller fractions above the mean. Thus for $n = 0.25$, 66% of the material falls below the mean in a strain range of about 200 shear units, whereas the remaining 34% experience strain above the mean in a range of about 800 shear units.

The rheological properties of the polymer used in the experiment of Bergen et al. (7) were not reported. If the polymer behaved like a Bingham plastic, one would certainly expect the nonuniformity as proposed by the authors, but as indicated by the foregoing calculations, one would expect nonuniform mixing even with Newtonian fluids, because of the mixer curvature. Furthermore, as seen in Fig. 7.35, the nonuniformity in mixing is considerably amplified by shear thinning, providing an alternative plausible explanation for the experimental observation without the need to assume a Bingham plastic type of flow.

Clearly, then, a mixer characterized by a broad SDF, in spite of favorable initial conditions, leads to a nonuniform mixture. To reduce the nonuniformity to acceptable levels, part of the material must be overmixed. Hence, a narrow SDF is preferable for good mixing.

Continuous Mixers In continuous mixers, exiting fluid particles experience both different shear rate histories and residence times; therefore they have acquired different strains. Following the considerations outlined previously and parallel to the definition of residence-time distribution function, the SDF for a continuous mixer $f(\gamma) d\gamma$ is defined as the fraction of exiting flow rate that experienced a strain between γ and $\gamma + d\gamma$, or it is the probability of an entering fluid particle to acquire strain γ . The cumulative SDF, $F(\gamma)$, defined by

$$F(\gamma) = \int_{\gamma_0}^{\gamma} f(\gamma) d\gamma \quad (7.3-21)$$

is the fraction of exiting flow rate with strain less than or equal to γ , where γ_0 is the *minimum* strain. The mean strain of the exiting stream is

$$\bar{\gamma} = \int_{\gamma_0}^{\infty} \gamma f(\gamma) d\gamma \quad (7.3-22)$$

The SDF, like the RTD functions, can be calculated from the velocity distribution in the system; that is, a certain flow pattern determines both functions. The reverse, however, does not necessarily apply. The calculation of the SDF requires a complete description of the flow pattern, whereas RTD functions often can be calculated from a less than complete flow pattern. For example, the RTD of axial annular flow between two rotating concentric cylinders (helical flow) of a Newtonian fluid depends only on the axial velocity, whereas the SDF depends on both the axial and the tangential velocity

distributions. Clearly, SDFs cannot be calculated from experimentally measured RTD functions.

The following example examines the SDF in drag flow between parallel plates. In this particular flow geometry, although the shear rate is constant throughout the “mixer,” a rather broad SDF results because of the existence of a broad residence time distribution. Consequently, a minor component, even if distributed at the inlet over all the entering streamlines and placed in an optimal orientation, will not be uniformly mixed in the outlet stream.

Example 7.10 The Strain Distribution Function in Parallel Plate Drag Flow Two parallel plates in relative motion with each other can be viewed as an idealized continuous mixer. A given plane perpendicular to the plates marks the entrance to the “mixer,” and another plane at a distance L downstream, the exit from the mixer, Fig. E7.10a. We assume that a fluid entering the gap between the plates had no previous strain history and that a fully developed pure drag flow exists between the plates. Clearly, although the shear rate is uniform throughout the system, the closer we get to the upper plate, the shorter the residence time will be; hence, the fluid particles will experience lower total strains. Moreover, because the velocities are higher in this region, a larger fraction of the existing flow rate will experience the lower strains.

The velocity distribution for a fully developed, isothermal drag flow between parallel plates separated by a distance of H and with the upper plate moving at constant velocity, V_0 , in a rectangular coordinate system located at the stationary plate, is $v_x = yV_0/H$, and the flow rate is $q = V_0H/2$. The fraction of exiting flow rate between y and $y + dy$ is given by

$$f(y) dy = \frac{dq}{q} = \frac{2y dy}{H^2} \quad (\text{E7.10-1})$$

We can now compute the fraction of exiting flow rate in the region greater than y (which equals the fraction of flow rate below time t , where t corresponds to the time of residence of the fluid at location y) as

$$F(y) = \int_y^H f(y) dy = 1 - \frac{y^2}{H^2} \quad (\text{E7.10-2})$$

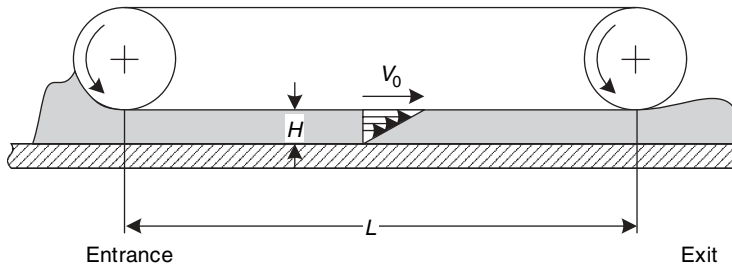


Fig. E7.10a Schematic representation of a continuous parallel plate mixer.

The uniform shear rate is $\dot{\gamma} = V_0/H$ and the residence time at location y is

$$t = \frac{L}{v_x} = \frac{HL}{V_0 y} \quad (\text{E7.10-3})$$

The shear strain is the product of the shear rate and the residence time

$$\gamma = \dot{\gamma}t = \frac{L}{y} \quad (\text{E7.10-4})$$

The minimum strain at the moving plate is L/H . By substituting y in terms of γ from Eq. E7.10-4 into Eq. E7.10-2, we get the SDF

$$F(\gamma) = 1 - \left(\frac{L}{H\gamma}\right)^2 \quad (\text{E7.10-5})$$

and

$$f(\gamma) d\gamma = \frac{2L^2}{H^2\gamma^3} d\gamma \quad (\text{E7.10-6})$$

The mean strain, using Eqs. 7.3-22 and E7.10-6, is

$$\bar{\gamma} = \int_{\gamma_0}^{\infty} \gamma f(\gamma) d\gamma = \int_0^H \gamma f(y) dy = 2\frac{L}{H} \quad (\text{E7.10-7})$$

Thus Eq. E7.10-5 can be written as

$$F(\gamma) = 1 - \left(\frac{\bar{\gamma}}{2\gamma}\right)^2 \quad (\text{E7.10-8})$$

Figure E7.10b shows the SDF and compares it to that of circular tube flow of a Newtonian fluid. The SDF is broad with about 75% of the flow rate experiencing a strain below the mean strain. A better insight into the meaning of the SDF is obtained by following simultaneously the reduction of the striation thickness and the flow rates contributed by the various locations between the plates (Fig. E7.10c). The distance between the plates is divided into 10 layers. We assume for the schematic representation of the SDF that the strain is uniform within each layer. Let us consider in each alternate layer two cubical minor particles separated by a certain distance, such that the initial striation thickness is r_0 . By following the deformation of the particles with time, we note that although the shear rate is uniform, since the residence time is different, the total strain experienced by the particle is minimal at the moving plate and increases as we approach the stationary plate. But the quality of the “product” of such a mixer will not be completely determined by the *range* of strains or striations across the flow field; the flow rate of the various layers also plays a role, as Fig. E7.10c indicates. A sample collected at the exit will consist, for example, of 17% of a poorly mixed layer *B* and only 1%

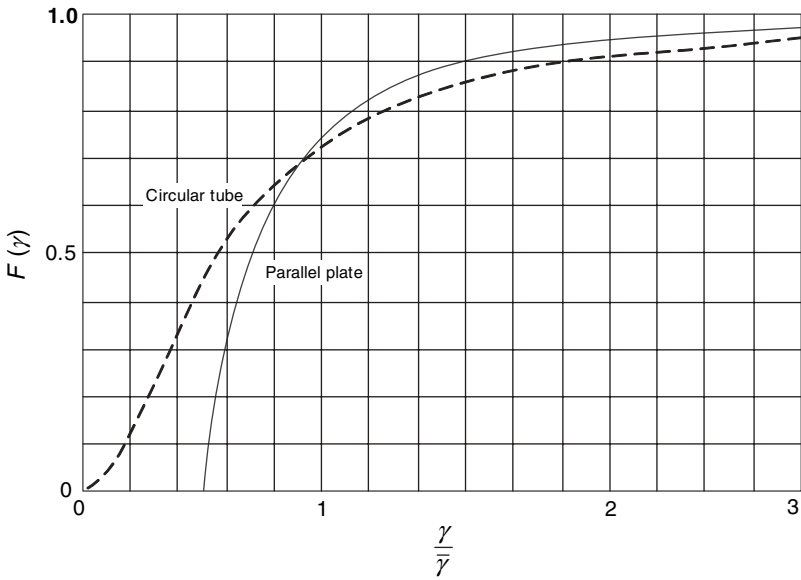


Fig. E7.10b SDFs for drag flow in parallel plate mixer and Newtonian laminar tube flow.

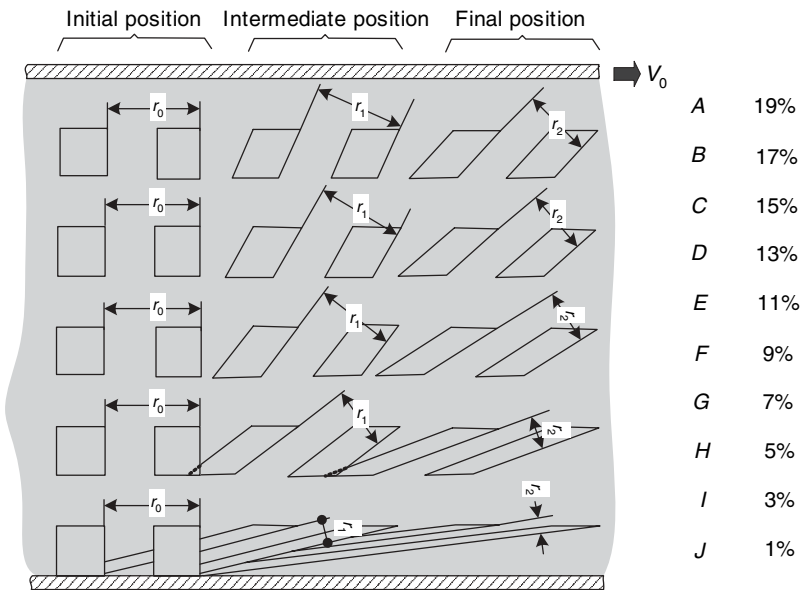


Fig. E7.10c Schematic representation of the striation thickness at various locations in a parallel plate mixer with drag flow. The striation thickness at the entrance to the mixer is r_0 , somewhere at the middle r_1 , and at the exit it is r_2 . Note that r_2 is large for particles close to the moving upper plate (because of the short residence time) and small for particles close to the stationary lower plate. The fraction of flow rate at the exit of layers at different heights is shown at the right.

of well-mixed layer J . The SDF reflects the combined effect of accumulated strain and local flow rate.

Finally, we would expect that existence of axial pressure gradients, which greatly affect the velocity profile, would also significantly affect the SDF, hence the mixing performance.

Example 7.11 The Strain Distribution Function in Parallel Plate Combined Pressure and Drag Flow The parallel plate geometry, as we observed in the preceding chapters, plays a rather dominant role in polymer processing. It is therefore worthwhile to examine an idealized continuous “parallel plate mixer” under more realistic flow conditions, where a pressure gradient is superimposed on the drag flow. The pressure gradient can be considered to be an “operating variable” that can be manipulated during the process to improve mixing performance. The SDFs for a combined pressure (q_p) and drag flow (q_d) between parallel plates and pure pressure flow were first derived by Lidor and Tadmor (56). Table 7.2 tabulates the results and also lists the corresponding velocity profiles, minimum strain, and mean strain expressions. In addition, the SDFs for pressure flow in a circular pipe are listed for comparison. In the case of combined pressure and drag flow, the SDF cannot be explicitly expressed in terms of γ , but only in terms of the dimensionless height $\xi = y/H$, which in turn is uniquely related to γ . The analysis was made for fully developed, isothermal, steady laminar flow of an incompressible Newtonian fluid. The derivation follows the lines of the derivation presented in Example 7.5 for pure drag flow.

Results reveal a strong effect of the pressure gradient on the SDF, as well as on the mean strain. A positive pressure gradient (pressure rise in the direction of flow, $q_p/q_d < 0$) will not only increase the mean strain, it will also reduce the breadth of the distribution, as shown in Fig. E7.11, whereas a negative pressure gradient has the opposite effect. This conclusion is directly relevant to single-screw extrusion, because the parallel-plate flow forms a simple model of melt extrusion, and it lends theoretical support to the experimental observation that an increase in back pressure (i.e., increase in positive-pressure gradient) in the extruder improves mixing. The mean strain, as Table 7.2 indicates, is proportional to L/H , which is a design variable. Thus, long and shallow conduits favor good mixing. But it does not affect the SDF. Finally, pure pressure flows, as shown in Fig. E7.11, are characterized by broad SDF and a minimum strain of zero. Obviously, pressure flow devices are poor laminar mixers.

Number of Passage Distribution Functions.

The NPD functions for characterizing dispersive mixing in internal batch mixers were developed by Manas-Zloczower et al. (57–60) and for SSEs by Manas-Zloczower and Tadmor (61). They were formalized and generalized by Tadmor (62,63).

Batch and continuous dispersive mixers are designed such that in certain region(s) in the mixer there are narrow passages, imparting to the fluid high shear stresses. In typical batch mixers, examples would be the region between the tips of the rotor and the vessel wall (Fig. 7.30), and in continuous mixers between the screw or rotor flight and the barrel, as well as between two rotors (Fig. 7.31). In the case of a batch mixer, the fluid in the mixer of volume V is assumed to be well-mixed, and from it a recirculating stream at a rate q passes through the high-shear zone. The recirculating flow is mixed with the rest of the fluid. Thus, at any given time there will be fluid elements in the mixer that never passed through the high-shear region and others that passed through this region once, twice, or k times. Therefore, we can characterize the state of the mixer by the *number of passage distribution functions*, $g_k(t)$, defined as the fraction of material volume in a circulating-batch system that has experienced exactly k passages in a volume region of interest. In our

TABLE 7.2 The Strain Distributions Function for Some Simple Flow Geometries with Newtonian Fluids

Flow between Parallel Plates ^a				
Type of Flow	Drag Flow	Pressure Flow	Combined Pressure and Drag Flow	Flow through Tubes
Velocity profiles	$v_z = \xi V_0$	$v_z = 4\xi(1 - \xi)V_{\max}$	$v_z = \left[\xi + 3\xi \frac{q_p}{q_d} (1 - \xi) \right] V_0$	$v_z = \left(1 - \frac{r^2}{R^2} \right) V_{\max}$
$F(\gamma)$	$1 - \left(\frac{\bar{\gamma}}{2\gamma} \right)^2$	$\frac{C}{1 + \sqrt{1 + C^2}} \left(1 + \frac{1}{1 + \sqrt{1 + C^2}} \right)$	$F(\xi) = 1 - \frac{\xi^2}{1 + q_p/q_d} \left[1 + \frac{q_p}{q_d} (3 - 2\xi) \right]$	$1 - \frac{2}{1 + C^2/2 + \sqrt{1 + C^2}}$
Mean strain, $\bar{\gamma}$	$\frac{2L}{H}$	$C = \frac{3\gamma}{2\bar{\gamma}}$	$\gamma(\xi) = \frac{1 + 3(q_p/q_d)(1 - 2\xi)}{\xi \left[1 + 3(q_p/q_d)(1 - \xi) \right]} \left(\frac{1 + q_p/q_d}{2} \right) \bar{\gamma}$	$C = \frac{8\gamma}{3\bar{\gamma}}$
Minimum strain, γ_0	$\frac{L}{H}$	$\frac{3L}{H}$	$2 \frac{L}{H(1 + q_p/q_d)}$ for $-\frac{1}{3} \leq \frac{q_p}{q_d} \leq \frac{1}{3}$	$\frac{8L}{3R}$
		0	Varies with $\frac{q_p}{q_d}$	0

^a In these equations $\xi = y/H$, where H is the separation between the plates, $V_0 = v_z(1)$, V_{\max} is the maximum velocity, and $q_p/q_d = (H^2/6\mu_0 V_0)(-dP/dz)$.

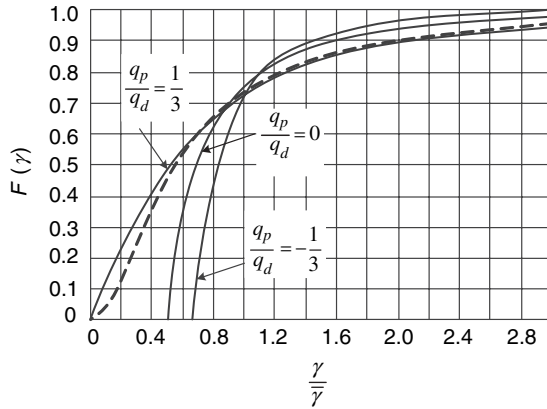


Fig. E7.11 SDFs for fully developed Newtonian, isothermal, steady flows in parallel-plate (solid curves) and tubular (dashed curve) geometries. The dimensionless constant q_p/q_d denotes the pressure gradient. When $q_p/q_d = -1/3$, pressure increases in the direction of flow and shear rate is zero at the stationary plate; $q_p/q_d = 0$ is drag flow; when $q_p/q_d = 1/3$, pressure drops in the direction of flow and the shear rate is zero at the moving plate. The SDF for the latter case is identical to pressure flow between stationary plates. (Note that in this case the location of the moving plate at $\zeta = 1$ is at the midplane of a pure pressure flow with a gap separation of $H' = 2H$.)

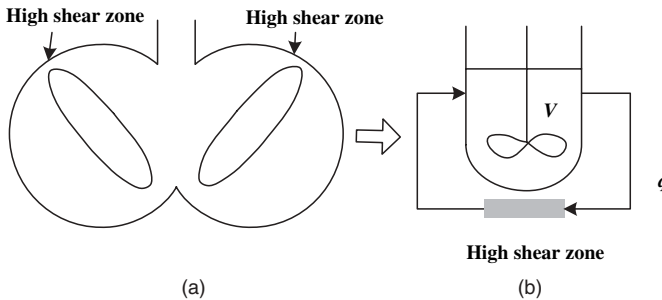


Fig. 7.30 (a) Cross section of batch mixers indicating the high-shear regions between the tip of the rotors and the wall. (b) Schematic view of a well-mixed mixer of volume V and a recirculating flow rate q .

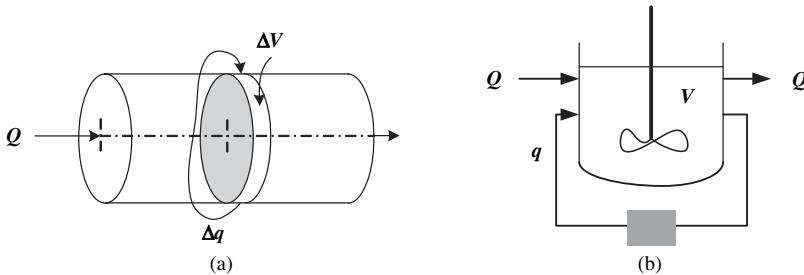


Fig. 7.31 (a) Schematic view of a plug-type flow continuous mixer with a recirculating stream Δq from a differential volume ΔV , which moves axially with the bulk of the pluglike axial flow. The recirculating stream passes through a high-shear zone (e.g., flight tip, or kneading element tip). (b) Schematic view of a continuous mixer of volume V with back mixing, flow rate Q , and a recirculating flow (can be inside the vessel or outside, it makes no difference) rate q over a high-shear zone.

case, this is the high-shear region. The function is discrete in k and continuous in t . The cumulative NPD function, $G_k(t)$, follows from the definition of $g_k(t)$

$$G_k(t) = \sum_{j=0}^k g_j(t) \quad (7.3-23)$$

and its physical interpretation is the fraction of material volume in the system that has experienced no more than k passages in the volume of interest. Clearly, $G_\infty(t) = 1$. Of special interest is the mean number of passages $\bar{k}(t)$, given by

$$\bar{k}(t) = \sum_{j=0}^{\infty} jk_j(t) \quad (7.3-24)$$

and associated with the fraction of material volume characterized by a passage number less than or equal to the mean $G_{\bar{k}}$, and that characterized by $G_{\bar{k}}^*$ ($k > \bar{k}_1$), where $G_{\bar{k}}^* = 1 - G_{\bar{k}}$. The variance of $g_k(t)$ is

$$\sigma^2(t) = \sum_{j=0}^{\infty} (j - \bar{k})^2 g_j(t) \quad (7.3-25)$$

The moments of the distribution are defined as

$$\mu_r = \sum_{j=0}^{\infty} j^r g_j(t) \quad (7.3-26)$$

and in terms of the moments, we can express the average and variance $\bar{k} = \mu_1$ and $\sigma^2 = \mu_2 - \mu_1^2$, respectively. Higher moments of the distribution are useful in characterizing other features of the distribution such as skewness and kurtosis. The former describes the distortion from a symmetrical distribution and the latter the degree of peakedness of the distribution.

We can conveniently generate the moments of the distribution by a generating function defined as

$$g(Z) = \sum_{j=0}^{\infty} g_j Z^{-j} \quad (7.3-27)$$

where Z is the transform variable, by using the following moment generating equation

$$\mu_r = \lim_{Z \rightarrow 1} (-1)^r \left[\left(Z \frac{\partial}{\partial Z} \right)^r g(Z) \right] \quad (7.3-28)$$

In the case of the continuous mixer shown in Fig. 7.31(a), we can assume that the differential volume element is, in effect, a small batch mixer similar to the one described

earlier, that slides from entrance to exit. Thus, at the exit we will find that different fluid particles have experienced a different number of passages. The same is true with the schematic, continuous, well-mixed mixer shown in Fig. 7.31(b).

Next, we define a parallel set of NPD function in continuous flow recirculating systems. We restrict our discussion to steady flow systems. Here, as in the case of RTD, we distinguish between external and internal NPD functions. We define f_k and i_k as the fraction of exiting volumetric flow rate and the fraction of material volume, respectively, that have experienced exactly k passages in the specified region of the system. The respective cumulative distribution functions, F_k and I_k , the means of the distributions, the variances, and the moments of distributions, parallel the definitions given for the batch system.

For steady, constant density flow systems, the internal and external NPDs, in a parallel fashion to RTD, can be shown to be related as follows:

$$i_k = \frac{Q}{q}(1 - F_k) \quad (7.3-29)$$

where Q and q are the volumetric flow rate of the system and the recirculation rate, respectively.

Before presenting an example of NPD in model systems, we briefly review the Theory of Recirculating Systems.

Theory of Recirculating Systems Consider physical systems, such as mixers and reactors, that contain recirculating fluid streams. Within these systems some physical or chemical changes takes place in one or a number of well-defined regions of the system. To characterize such systems, we may wish to know the cycle or passage time, the number of cycles or passages, and the time spent in these regions by any given fluid element in the system.

Passage times and distribution of passage times in recirculating systems were first considered by Shinnar et al. (64) in their analysis of RTD in closed-loop systems. The most important such system is that of blood circulation, but the analysis cited is also relevant to engineering systems such as fluidized-bed reactors. The main objective of this work was the analysis of tracer experiments in recirculating systems. The renewal theory discussed by Cox (65) served as the theoretical framework for their analysis. Both Shinnar et al. (64), and later Mann and Crosby (66) and Mann et al. (67) have shown that the NPD functions can be evaluated from the passage *time* distribution function, which in turn can be obtained from the *renewal theory*.

Following Shinnar et al., consider a fluid element at time $t = 0$, at site A in the recirculating fluid. The passage time of the fluid element from site A to site B is a continuous random variable, with probability density function $f_{AB}(t)$. Site B for our purpose is the region where the physical or chemical change takes place. This site need not be a single point, nor a single fixed region, but any fixed fraction of volume of the system. Next we assign the probability density function $f_{BB}(t)$ for the fluid element at site B to return to site B. The two passage times are independent, and therefore the probability density function of moving from site A (at $t = 0$) to site B in one cycle is the convolution of the two densities $f_{AB}(t) \cdot f_{BB}(t)$. In a similar way we can deduce the density function of k cycles as $f_{AB}(t) \cdot f_{BB}(t)^{*k}$. By making the assumption that $f_{AB}(t) = f_{BB}(t) = f(t)$, the density function becomes $f(t)^{*(k+1)}$, that is, the $(k + 1)$ th-order convolution operator of $f(t)$. Next, in terms of probabilities we can state that the probability of a single fluid

particle, of k cycles, going through site B in a time period between t and $t + \Delta t$ is $f(t)^{* (k+1)} \Delta t$. The total volume of fluid particles (with k cycles) to go through site B is $f(t)^{* (k+1)} V \Delta t$, where V is the material volume in the system. If we let q be the total volumetric flow rate through site B, then the total volume going through site B in the period from t to $t + \Delta t$ is $q \Delta t$. We now can define the NPD, $g_k(t)$, as the fraction of volume in the system that has experienced k passages in time t :

$$g_k(t) = \frac{f(t)^{* (k+1)} V \Delta t}{q \Delta t} = \theta f(t)^{* (k+1)} \tag{7.3-30}$$

where θ is the mean passage time between successive passages. The NPD function $g_k(t)$ is, of course, also the probability of any fluid particle in the system having k passages. In terms of the renewal theory, $g_k(t)$ is the probability of k renewals of the same fluid element in time interval t . If all fluid elements are identical, this is also the fraction of material volume in the system that has experienced k passages.

It is convenient to take the Laplace transformation of Eq. 7.3-30 to give

$$g_k(t) = L \left[\theta f(t)^{* (k+1)} \right] = \theta f(s)^{(k+1)} \tag{7.3-31}$$

and thus, $g_k(t)$ is the inverse of $g_k(s)$

$$g_k(t) = L^{-1} \left[\theta f(s)^{(k+1)} \right] \tag{7.3-32}$$

Consider a simple density function $f(t) = \rho e^{-\rho t}$, describing a Poisson process with a constant age-specific passage rate of $1/\rho = \theta$. This implies that the probability of an additional passage is constant, and independent of either location or passage history; that is, in physical terms, perfect mixing is involved. The Laplace transformation of this density function is $\rho/(\rho + s)$, and by Eq. 7.3-32, $g_k(t)$ becomes

$$g_k(t) = \frac{\lambda^k}{k!} e^{-\lambda} \tag{7.3-33}$$

where λ is the dimensionless time t/θ .

Example 7.12 Number of Passage Distribution Functions in a Batch Mixer with Recirculation We consider the batch mixer in Fig. 7.30(b). We begin by making a mass balance on the change in time of the fraction of volume that never passed through the high-shear zone at time t , $g_0(t)$ as follows

$$V \frac{dg_0(t)}{dt} = -q g_0(t)$$

Rate of change of volume with zero passages
Exit flow rate with zero passages

Integration results in

$$g_0(t) = e^{-t/\theta}$$

TABLE 7.3 NPD Functions, Means, Variances, and Moment of Some Model Batch and Flow Systems with Recirculation

	Well-stirred Batch Vessel	Plug-flow System	Well-stirred Flow System
NPD	$g_k = \frac{\lambda^k}{k!} e^{-\lambda}$	$f_k = \frac{\lambda^k}{k!} e^{-\lambda}$	$f_k = (1 - \alpha)\alpha^k$
Cumulative NPD	$G_k = \Gamma(1 + k, \lambda)/k!$	$F_k = \Gamma(1 + k, \lambda)/k!$	$F_k = \alpha(1 - \alpha^k) + (1 + \alpha)$
Mean number of passages	$\bar{k} = \lambda = t/\theta$	$\bar{k} = \lambda = \frac{q}{Q}$	$\bar{k} = \frac{\alpha}{1 - \alpha} = \frac{q}{Q}$
Generating function	$g(z) = e^{-\lambda} e^{\lambda/z}$		$f(z) = (1 - \alpha) \left(\frac{z}{z - \alpha} \right)$
First moment	$\mu_1 = \lambda$		$\mu_1 = \alpha/(1 - \alpha)$
Second moment	$\mu_2 = \lambda + \lambda^2$		$\mu_1 = \alpha(1 + \alpha)/(1 - \alpha)^2$
Variance	$\sigma^2 = \mu_2 - \mu_1^2 = \lambda$		$\sigma^2 = \mu_2 - \mu_1^2 = \alpha/(1 - \alpha)^2$
Coefficient of variation	$\frac{\sigma^2}{\mu_1^2} = \frac{1}{\lambda}$		$\frac{\sigma^2}{\mu_1^2} = \frac{1}{\alpha} = 1 + \frac{1}{\bar{k}}$

Note: t = mixing time; Q = volumetric flow rate; V = volume of system; $\theta = V/q$ mean circulation time; q = volumetric recirculation rate; $\Gamma(a, b)$ = incomplete beta function.

where $\theta = V/q$ is the mean circulation time. Next we make a balance on $g_k(t)$. In this case, we must take into account that, as in the case of zero passages, the exiting flow rate takes away fluid elements with k passages, but the fluid elements with $k - 1$ passages return to the vessel as fluid elements of k passages:

$$V \frac{dg_k(t)}{dt} = -qg_k(t) + qg_{k-1}(t) \quad k \geq 1$$

Solving this differential equation iteratively for $k = 1, 2, \text{etc.}$, we get the solution given in Eq. 7.3-33.

Table 7.3 lists the various NPD for the well-stirred batch mixer, the plug-flow system with recirculation, and the well-stirred flow system. Figures E7.12a and E7.12b plot the distribution in the batch mixer and the continuous batch mixer. Note that in batch mixers the distribution widens considerably with increasing mean number of passages, and the distribution is much skewed toward low numbers of passages in the flow batch system. Therefore, two mixers with the same mean passages may have very different distributions.

7.4 CHARACTERIZATION OF MIXTURES

A complete characterization of the state of a mixture would require the specification of the size, shape, orientation, and spatial location of every particle, clump, or blob of the minor component. A somewhat less than complete characterization could be provided by a three-dimensional concentration distribution function, as suggested by Bergen et al. (7).

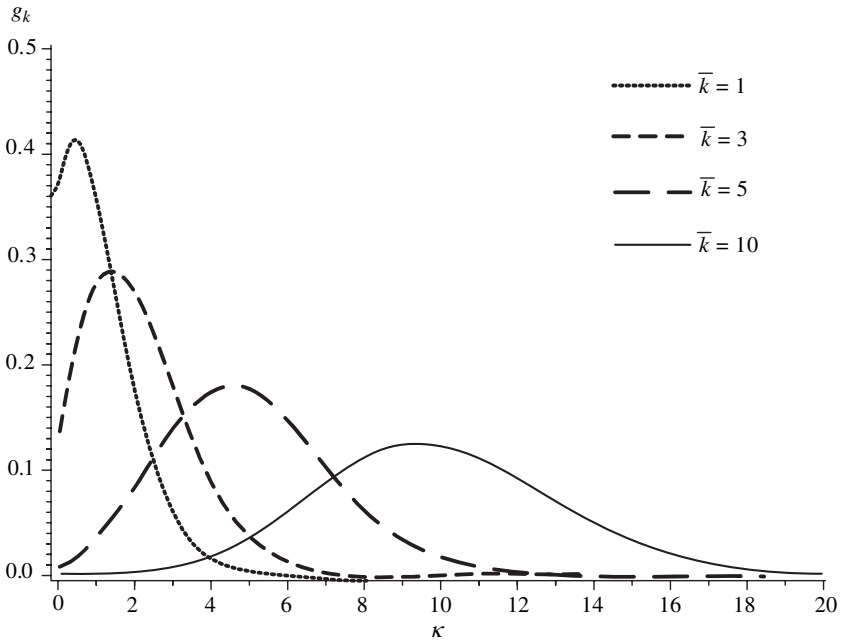


Fig. E7.12a NPD in a batch mixer with the mean number of passages as a parameter.

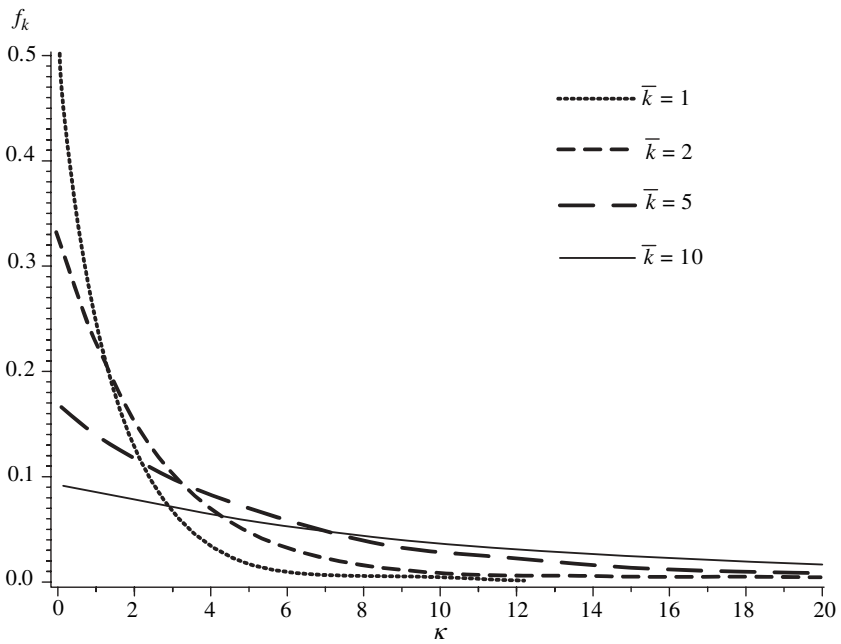


Fig. E7.12b NPD in a well-stirred flow mixer with the mean number of passages as a parameter.

However, for many applications we do not need such a complete characterization of the state of the mixture; in practice, simple methods often suffice. Commonly used methods, for example, are color comparison to a standard for qualitative visual homogeneity, or the measurement of some representative physical property. Between the two extremes of complete characterization and qualitative or semiquantitative practical evaluation, there is room for sound quantitative methods of characterization. We must keep in mind, however, that the “goodness of mixing” is not absolute, but dependent on the required needs.

Generally, in dealing with a mixture, we first examine *overall* or *gross composition uniformity*. By *gross uniformity* we mean some quantitative measure that characterizes the goodness of distribution of the minor component throughout the object or system analyzed. As an example, consider an extrusion line producing blue shopping bags. We might take bags from such a roll and examine them for color uniformity. We may find that they contain virtually the same amount of blue pigment; that is, there is a *perfect gross uniformity* throughout the film.

However, looking closely at a single bag, we may find that, although the overall concentration of pigment is virtually the same in each bag, they display nonuniformity in the form of patches, stripes, streaks, and so on; that is, the bags exhibit a certain *texture*.

Alternatively, the analysis may reveal both widely varying pigment concentrations among bags as well as different textures in each one.

Composition uniformity, however, cannot always be evaluated by visual examination. For example, if the additive is colorless, or if we want *quantitative* answers on blue pigment distribution in the roll of film, we must take *testing samples*, measure the concentration of the minor component at various points in the film, and analyze these for uniformity.

In the preceding discussion we intuitively introduced two concepts that need further clarification. One is the *scale* on which we examine for composition nonuniformity; the second is the *size* of the testing samples.

In this example we are examining the composition uniformity of a *whole* roll of film; this, then, becomes the scale for measuring the composition uniformity. We can, therefore, define a new concept; the *scale of examination*, which is the scale or size of the overall sample we are analyzing for composition uniformity.

We have noted before that by *texture*, we mean composition nonuniformity reflected in patches, stripes, and streaks. Thus, by texture, we mean composition nonuniformity that has some unique *pattern* that can be recognized by visual perception. Thus, a “blind” random sampling of concentration at various points, though it may reveal the existence of compositional nonuniformity and may even suggest the *intensity* of this nonuniformity, will reveal nothing about the character of the texture.

Texture is important in polymer processing because (a) laminar and even chaotic distributive mixing inevitably lead to it, (b) many products are visually examined for lack of texture or for a certain desired texture, and (c) mechanical properties of blends depend on the texture of the mixture.

The Relationship between Texture and Visual Perception

Since texture has a great deal to do with visual perception, it is interesting to discuss some work done on *texture recognition*. The first question we want to focus on is what makes two samples with identical overall concentration exhibit different textures? Perfect gross uniformity implies identical concentration in all samples. Julesz (68), in an interesting

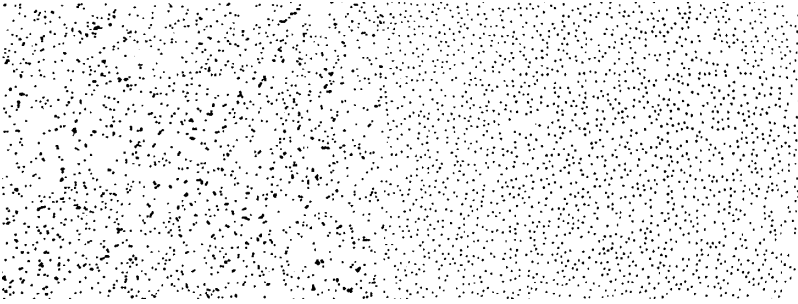


Fig. 7.32 The two textures (left field and right field) have the same first-order statistics (the same number of black dots), but they differ in second-order statistics. In the left field the dots fall at random, whereas in the right field there are at least 10 dot diameters between dots. [Reprinted by permission from B. Julesz, “Experiments in the Visual Perception of Texture” *Sci. Am.*, **232**, 34 (1975).]

paper on visual perception of texture, refers to two samples with the same concentration of a minor component as two samples with the same *first-order statistics*. When dealing with visual perception, first-order statistics has to do with brightness, or rather, luminance. Samples taken from a system with the same first-order statistics may exhibit different *granularity*. Figure 7.32 gives a simple example of two samples sharing the same first-order statistics, but having different granularity or different second-order statistics.

For measuring second-order statistics, Julesz (68) suggests dropping a *dipole* (e.g., a needle) on the two textures and observing the frequency with which both ends of the dipole land on black dots. Identical frequencies imply identical second-order statistics. His experiments indicate that our visual system can discriminate patterns solely by the perceptual process only if they differ in second-order statistics. He made a similar observation with musical “textures,” and found that random melodies could be perceived as being different only if they possessed different second-order statistics.

Figure 7.33 presents a somewhat more complex texture; black, dark gray, light gray, and white squares are mixed such that their respective fractions are equal in the left and right fields. The two textures can be discriminated because there is a difference in

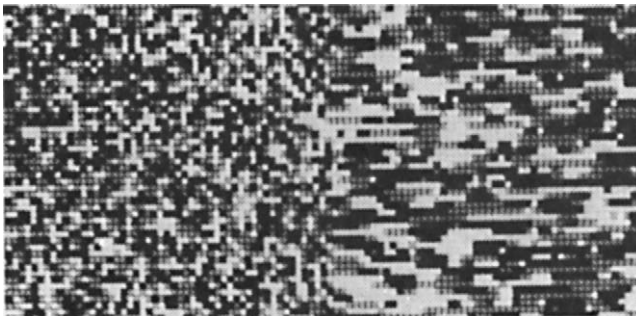


Fig. 7.33 The two textures (left field and right field) made of black, dark gray, light gray, and white squares have the same first-order statistics, but different second-order statistics, which appear as a difference in granularity. [Reprinted by permission from B. Julesz, “Experiments in the Visual Perception of Texture” *Sci. Am.*, **232**, 34 (1975).]

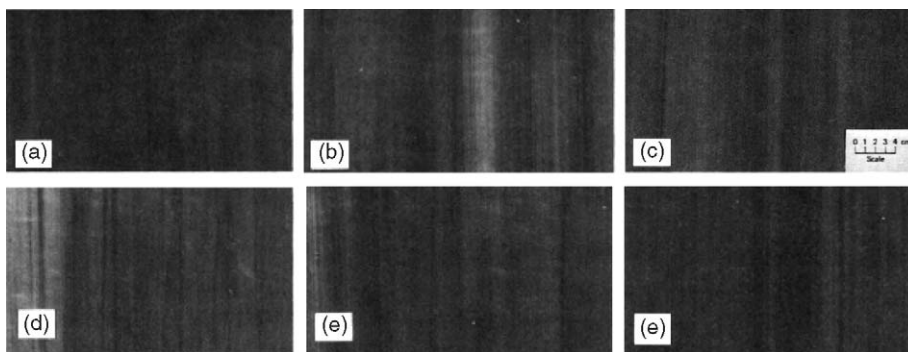


Fig. 7.34 Photographs of extruded LDPE films with carbon black concentrate extruded at various conditions. The barrel temperature ($^{\circ}\text{C}$) and screw speed (rpm) are as follows: (a) $160^{\circ}, 40$; (b) $160^{\circ}, 60$; (c) $160^{\circ}, 80$; (d) $180^{\circ}, 40$; (e) $180^{\circ}, 60$; (f) $180^{\circ}, 80$. [Reprinted by permission from N. Nadav and Z. Tadmor “Quantitative Characterization of Extruded Film Texture,” *Chem. Eng. Sci.*, **28**, 2115 (1973).]

second-order statistics. Third-order differences between the texture could no longer be discriminated by perception, but require a cognitive process of scrutiny. Neither, of course, can such differences be detected by a “dipole throwing process,” but would require a “tripod or triangle throwing process.”

Figure 7.34 shows a number of film samples extruded under different conditions. They have approximately the same carbon black concentration and are grossly uniform or have the same first-order statistics, but clearly exhibit different texture, and thus have different second-order statistics.

Next, we ask what the scale of examination is when we analyze texture. In dealing with gross uniformity, the scale of examination was clearly defined, and equaled the system as a whole. In dealing with texture, the situation is more complex. By perception we can discriminate textures differing in second-order statistics. These may be due to fine and coarse granularity. The human eye, through a hierarchy of feature extractors of increasing complexity, can simultaneously analyze texture on a *range* of scales of examination. This range varies according to the distance from which we view the object. Moreover, if in addition to pure perception we start examining and scrutinizing the texture, we commence a cognitive process activating “hypercomplex feature extractors” in our visual system, leading to more detailed and complex texture and pattern recognition (68), which would require a higher than second-order statistics evaluation process. Similarly, to the human visual system, in attempting to quantitatively characterize the texture of a sample, the scale of examination *should be varied over a range*, determined by the requirements.

Returning to the example of blue shopping bags, we can decide that the upper limit of the scale on which we shall examine texture is the size of a bag, and the lower limit is the resolution capability of the naked eye or the minimum size of nonuniform regions. This range will suffice if the analysis is carried out for evaluating the appearance of a bag. If, however, we are dealing with a blend of two polymers, the mechanical properties of the mixture are affected by the uniformity and texture down to a microscopic scale throughout the volume of the sample.

At the lower limit of the scale of examination, at the level of ultimate particles, we also must characterize the *local structure*. When dealing with dispersion of carbon black particles on this scale of examination, for example, we shall determine whether the

particles are agglomerated in clumps or individually dispersed. This fact may significantly affect the chemical properties (e.g., resistance to weathering of PE containing carbon black) and the mechanical properties of polymers.

In conclusion, mixtures are characterized by *gross uniformity*, *texture*, and *local structure*. Having discussed composition uniformity qualitatively, we now proceed to deal with the quantitative aspects of characterization of mixtures.

Gross Uniformity

A perfect gross uniformity is obtained when there is a uniform concentration of the minor component in all testing samples taken from a system. In the example of shopping bags made from a blown roll of film, this implies the same amount of blue pigment in every bag, provided we have chosen a bag as a sample. In most practical cases, however, complete gross uniformity is not achieved. The *maximum* attainable uniformity is controlled by the mixing method, and the *actual* gross uniformity is determined by the conditions and time of mixing. In *random* mixing processes, the maximum attainable uniformity is given by the binomial distribution (69).

Consider a system of a mixture of a minor component of uniform size in a major component, which can be solid or liquid. In either case, we shall measure the amount of major component in a withdrawn sample as the number of hypothetical particles, each having the same volume as a minor-component particle. If the volume fraction of minor component is p and we withdraw samples containing n particles, the fraction of samples containing k minor particles is given by

$$b(k; n, p) = \frac{n!}{k!(n-k)!} p^k (1-p)^{n-k} \quad (7.4-1)$$

Equation 7.4-1 shows that the distribution of the minor component in the samples depends both on the average concentration of the minor component, p , and on the size of the sample, n . This point becomes more evident by considering the variance of the binomial distribution

$$\sigma^2 = \frac{p(1-p)}{n} \quad (7.4-2)$$

The more particles the samples contain, the narrower the distribution. In samples taken from true solutions, where the ultimate particles are molecules, the number of molecules in the smallest practical withdrawn sample is enormous, the variance will approach a value of zero, and the distribution will be virtually uniform. Figure 7.35 demonstrates the effect of the sample size on the shape of the binomial distribution.

To determine experimentally the closeness of a mixture to random distribution, we must "sample" the mixture, measure the concentration of the minor component in the withdrawn samples, calculate its volume fractions x_i , and compare the resulting distribution to the appropriate binomial distribution. The average volume fraction of the minor in the samples, which is given by

$$\bar{x} = \frac{1}{N} \sum_{i=1}^N x_i \quad (7.4-3)$$

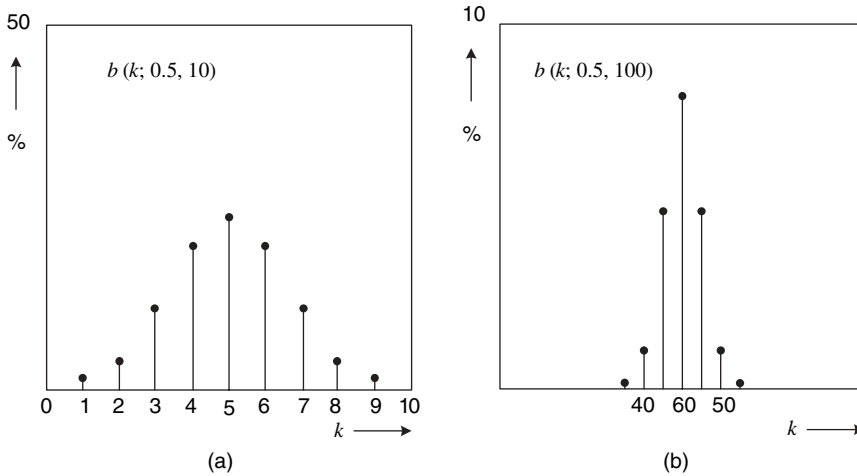


Fig. 7.35 The binomial distribution with $p = 0.5$ and two sample sizes. (a) $n = 10$. (b) $n = 100$.

where N is the number of withdrawn samples, should not be significantly different from the fraction of the minor component in the mixture p . A significant deviation of their values would indicate a faulty testing procedure (70). We can test for the statistical significance of this difference by a t -test or z -test, for sample numbers below and above 30, respectively. In either case, the statistic t (or z) is calculated from the following equation:

$$t(\text{or } z) = \frac{(\bar{x} - p)}{S/\sqrt{N}} \quad (7.4-4)$$

where S^2 is the observed variance (see Eq. 7.4-6) and compared to standard table values. In addition to comparing the means, we also have statistical tests for determining whether the experimentally observed distribution differs significantly from the expected (binomial) distribution, or the difference is only due to chance. The statistic used for this comparison is χ^2 .

In practice, simpler though less reliable tests are used for evaluating the state of mixing. One of these involves calculating certain *mixing indices* that relate representative statistical parameters of the samples, such as the variance and mean, to the corresponding parameters of the binomial distribution. One such index is defined as follows:

$$M = \frac{S^2}{\sigma^2} \quad (7.4-5)$$

where σ^2 is the variance of the binomial distribution, and S^2 is the variance of the samples defined as

$$S^2 = \frac{1}{N-1} \sum_{i=1}^N (x_i - \bar{x})^2 \quad (7.4-6)$$

where x_i is the volume fraction of the minor component in test sample i . Clearly, for a random mixture $M = 1$. For an unmixed state that is a completely segregated system (where samples contain either major or minor components only), the variance from

TABLE 7.4 Mixing Indices Comparing Concentration Distribution in the Samples to a Perfectly Random Mixed State

Mixing Index	Limiting Values	
	Perfectly Mixed	Perfectly Segregated
$\frac{S^2}{\sigma^2}$	1	n
$\frac{\sigma_0^2 - S^2}{\sigma_0^2 - \sigma^2}$	1	0
$\frac{\ln \sigma_0^2 - \ln S^2}{\ln \sigma_0^2 - \ln \sigma^2}$	1	0
$\frac{S^2 - \sigma^2}{p}$	0	$(1-p)\left(1 - \frac{1}{n}\right)$

Eq. 7.4-2 is $\sigma_0^2 = p(1 - p)$ and $M = n$. Some other suggested indices reviewed by Bourne (71) and analyzed by Fan and Wang (72), are listed in Table 7.4

Texture

We now deal with the quantitative characterization of *texture*. Consider a simple, geometrically ordered, checkered texture of dark-gray and light-gray squares. This texture can be easily and fully characterized by measuring the length of a square and the concentrations of the grays. The former characterizes the *scale* of the granularity or segregation, and the latter, the *intensity* of segregation. These two concepts, developed by Danckwerts (55,73) for characterizing the state of mixing in chemical reactors, were also suggested by him for texture characterization (73). Their statistical definition and physical meaning are discussed later in this section. Clearly, the texture will vanish by either reducing the scale of segregation or by reducing the intensity of segregation. These processes are depicted in Fig. 7.36. The goodness of mixing, as far as the texture is concerned, depends on some combination of both scale of segregation and intensity of segregation. If the scale of segregation is small, a large intensity of segregation might be tolerated, and vice versa. Most textures, however, are not as simple as the preceding example. Their granularity and the intensity of segregation may spread over broad ranges, and some meaningful statistical averaging would be useful to quantitatively characterize them.

The Scale of Segregation

The *coefficient of correlation*, $R(r)$, measures the degree of correlation between the concentrations at two points separated by distance r . It is obtained by randomly “throwing” a dipole of length r , and is defined as follows:

$$R(r) = \frac{\sum_{i=1}^N (x'_i - \bar{x})(x''_i - \bar{x})}{NS^2} \tag{7.4-7}$$

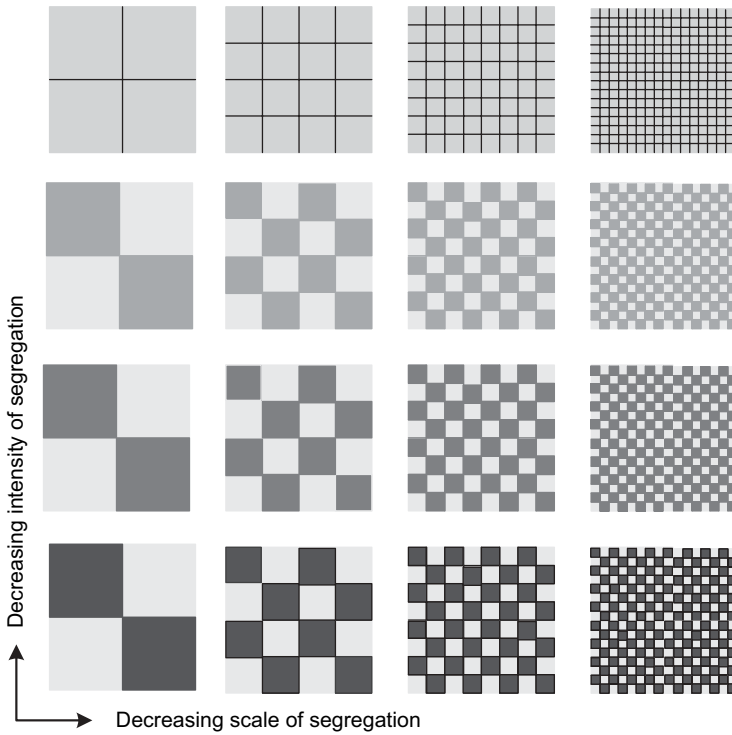


Fig. 7.36 Schematic representation of scale and intensity of segregation.

where x' and x'' are concentrations at the two points, \bar{x} is the mean concentration, N is the total number of couples of concentrations, and S^2 is the variance given by

$$S^2 = \frac{\sum_{i=1}^{2N} (x_i - \bar{x})^2}{2N - 1} \tag{7.4-8}$$

The coefficient of correlation ranges from 1 to -1 , denoting, respectively, perfect positive (both points in each couple have the same concentration) and perfect negative (one point is pure minor, the other is pure major) correlations. Figure 7.37 gives some typical correlograms.

The *scale of segregation* is the integral of the coefficient of correlation from distance zero, where $R(0) = 1$, to distance ζ at which there is no correlation [$R(\zeta) = 0$]

$$s = \int_0^{\zeta} R(r) dr \tag{7.4-9}$$

and it can be calculated along a line, over a surface, or within a volume, depending on how the concentration points are chosen. In all cases, a linear measure of the scale of segregation is obtained.

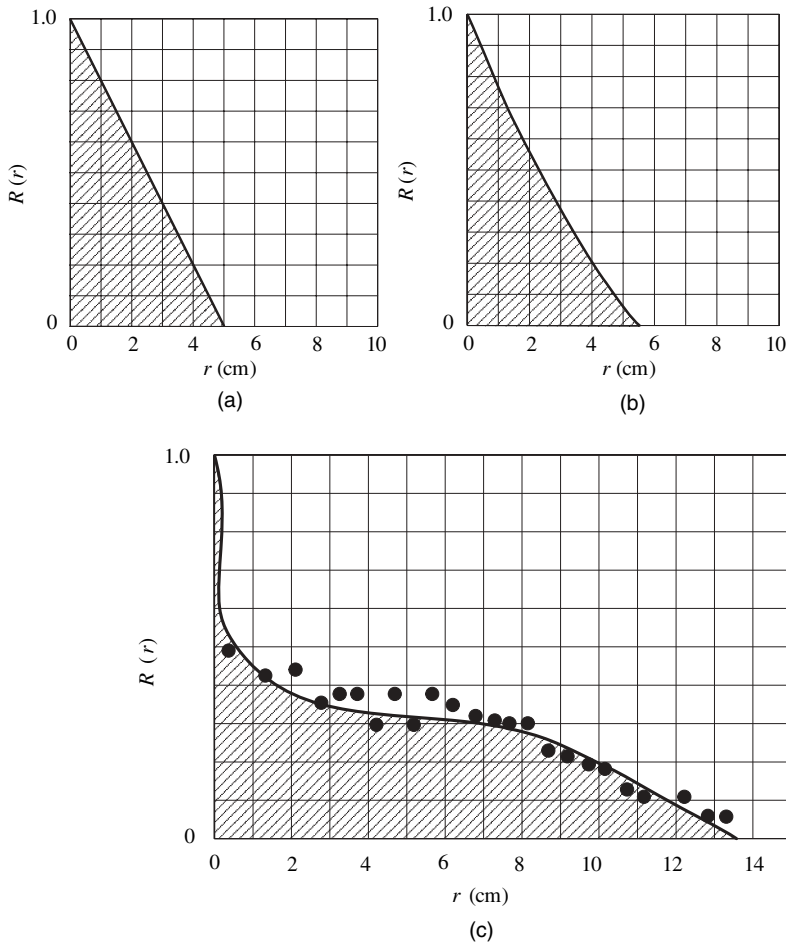


Fig. 7.37 Typical correlograms. (a) Along a line perpendicular to an equally spaced striped texture. (b) Over an area of a checkered board texture. (c) Along a line of an extruded film, as shown in Fig. 7.34, perpendicular to the extrusion direction.

Scale of Segregation Profile

For a complete description of complex texture, the scale of examination must be varied over a range determined by the uniformity requirements and the texture itself. It is not surprising, therefore, to find that the scale of segregation may be a function of the scale of examination, and that by varying the latter over the range of interest and by calculating a *scale of segregation profile*, we obtain a better characterization of texture. Figure 7.38 shows the concentration trace of blown film of LDPE with a carbon black concentrate taken along a line transverse to the “machine” direction (74), and Fig. 7.39 gives the scale of segregation profile that was calculated by varying the scale of examination or the size of the representative sample examined. The actual film samples appear in Fig. 7.34.

In this particular example it should be noted that there are two clearly visible characteristic scales of segregation values, about 6 cm and 0.5 cm. These represent

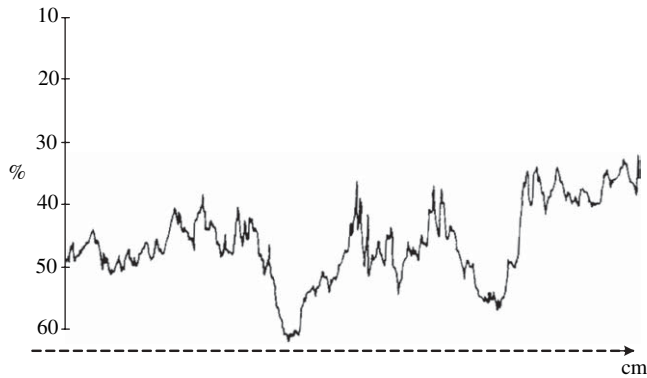


Fig. 7.38 Concentration trace (in relative units of light transmittance) of a PE film sample shown in Fig. 7.34(c), taken perpendicular to the extrusion direction. The linear scale is shown in Fig 7.34(c). [Reprinted by permission from N. Nadav and Z. Tadmor, “Quantitative Characterization of Extruded Film Textures” *Chem. Eng. Sci.*, **28**, 2115 (1973).]

low and medium frequency concentration variations, outstanding in Fig. 7.38, and a less definite lower value that should reflect the high frequency intense texture visible on the samples in Fig. 7.34. The accurate evaluation of the latter was not possible with the experimental method used. Nadav and Tadmor (74) suggested that a relationship may exist between certain mixing modes in extruders and the characteristic scale of segregation values.

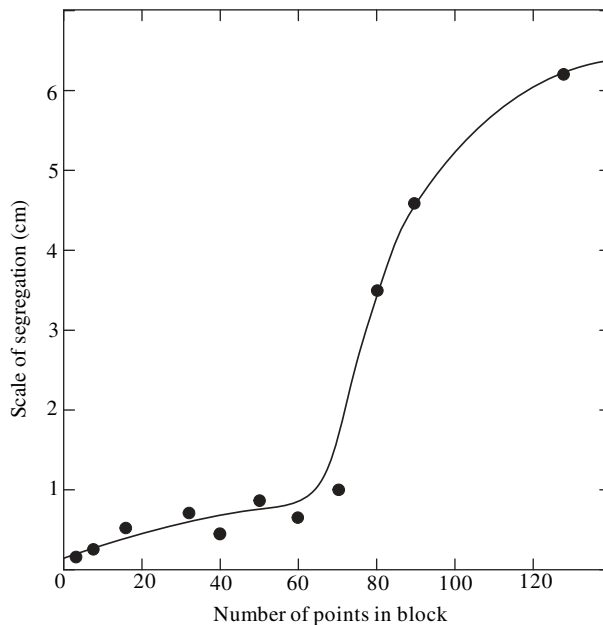


Fig. 7.39 The scale of segregation profile for the PE film in Fig. 7.32(c). [Reprinted by permission from N. Nadav and Z. Tadmor, “Quantitative Characterization of Extruded Film Textures” *Chem. Eng. Sci.*, **28**, 2175 (1973).]

The Intensity of Segregation

The intensity of segregation defined as follows

$$I = \frac{S^2}{\sigma_0^2} \quad (7.4-10)$$

expresses the ratio of the measured variance divided by the variance of a completely segregated system. Concentrations are taken as volume fractions of the minor component in the samples. Hence, for the completely segregated case, the concentration is either 1 or 0. Thus defined, I has a value of 1 when segregation is complete (i.e., the concentration of any point is either pure minor or pure major) and a value of 0 when the concentration is uniform ($S^2 = 0$). The intensity of segregation therefore reflects the departure of the concentration in the various regions from the mean, but not the size of the regions.

The intensity of segregation, as defined in Eq. 7.4-10, reflects to some extent “gross uniformity” on a scale of examination reduced to the scale on which texture is being examined. Referring to the example of blue shopping bags, if we define one bag as the “whole system,” the intensity of segregation, as measured by Eq. 7.4-10, will be a measure of the intensity of blue shade variations and also will reflect the gross composition uniformity of blue pigment within a single bag. Thus, I can be viewed as a particular mixing index.

The Striation Thickness

Another relatively simple measure for characterizing texture that is suggested in the polymer processing literature is the striation thickness, which is defined as the total volume divided by one-half the total interfacial surface (10)

$$r = \frac{V}{(A/2)} \quad (7.4-11)$$

Clearly, the larger the interfacial area is, the smaller the striation thickness. The striation thickness is meaningful in repetitive patterns where it can be measured, such as that shown in Figure 7.2, obtained in practice by “motionless” mixers. Here r equals the linear distance between repetitive units, and completely describes the quality of the mixture. It is worth recalling that for a simple, uniform striped pattern, the scale of segregation was shown to equal one-quarter the thickness of one layer, therefore $s = r/8$. However, in complex textures where a range of striation thickness values are needed to define the texture, this measure becomes inefficient because of the lack of a systematic way to measure it and its imprecise definition. The scale of segregation and the scale of segregation profile, on the other hand, are precisely defined and do provide a more systemic measure for texture.

Entropic Characterization of Distributive Mixing

In Section 7.1 we discussed the thermodynamic condition for a stable mixture given in the Flory–Huggins equation (Eq. 7.1-6), where ΔS denotes the *increase* of entropy due to mixing. This equation is based on Boltzmann’s principle stating that the entropy of a

system can be defined as

$$S = k \ln(\Omega) \quad (7.4-12)$$

where Ω is the number of microstates that are consistent with given macrostate. Since Ω is a natural number (1,2,3, ...), the entropy is positive, and it can be viewed as a measure of the disorder in the system. The greater the disorder, the greater the entropy is.¹¹ Clearly, then, when a system moves from lesser disorder to greater disorder the entropy of the system increases. In distributive mixing, of course, we increase the level of disorder, but this increase is not necessarily directly related to any thermodynamic property. If we mix two components, one black and one white, having exactly the same properties, thermodynamically the system would be stable at any mixing level. However, recently Wang et al. (75,76) introduced entropy as a direct measure of distributive mixing in polymer processing, not from a thermodynamic point of view, but from an *informational* point of view. In information theory the concept of entropy measures the *amount* of randomness of a signal; this concept can be translated to processing where we wish to measure the amount of randomness in a mixture as a measure of the degree of mixing. They start with Shannon's (77) formulation of information entropy, whereby the entropy S of a particular experimental condition with a set of M possible outcomes is given by

$$S = - \sum_{j=1}^M p_j \ln(p_j) \quad (7.4-13)$$

where p_j is the probability (relative frequency) of outcome j . The equation satisfies the following required and useful conditions: (a) that the lowest entropy is $S = 0$, and it corresponds to a condition that one of the probabilities is one and all the rest are zero; (b) that the largest value corresponds to a condition that all probabilities are equal (total disorder). In this case, $p_i = p_0 = \text{const.}$, and

$$S = -p_0 M \ln(p_0) \quad (7.4-14)$$

But, since $Mp_0 = 1$, Eq. 7.4-14 reduces to

$$S = \ln(M) \quad (7.4-15)$$

(c) That S is additive over partitions.¹²

In mixing, where we wish to assess the particle distribution of a minor component into a major component, M is the number of subdomains or "bins" (which can be two-dimensional for analyzing a cross section of the mixture, or three-dimensional for

11. Consider a set of 10 coins that forms the "system." The most ordered macroscopic states are 10 heads up or 10 tails up. In either case, there is one possible configuration, and hence the entropy according to Eq. 7.4-13 is zero. The most disordered state consists of 5 heads up and 5 tails up, which allows for 252 different configurations. This would be the case if we reflip each coin sequentially for a long time. What we have done is mix the system.

12. There are relationships between thermodynamic and informational entropy. For example, the well-known Maxwell's "demon," which reverses thermodynamic entropy with information, but getting that information exactly balances out the thermodynamic gain the demon would otherwise achieve.

volumetric study), into which the whole mixing domain is divided. Varying M implies varying the scale at which we measure the quality of mixing.

Renyi (78) generalized the concept of information entropy to measure different aspects of system homogeneity, and Alemanskin et al. (79), and Alemanskin and Manas-Zloczower (80) adopted the Renyi entropy for measuring mixing. Considering only statistically independent partition, Renyi determined that the information entropy can be replaced with the following single-variable function

$$S = -\frac{\ln \sum_{j=1}^M p_j^\beta}{\beta - 1} \quad (7.4-16)$$

where β is a positive parameter. In the limit as $\beta \rightarrow 1$, Eq. 7.4-16 reduces to the Shanon equation (Eq.7.1-13). For equal probabilities we once again obtain that the maximum entropy is $\ln(M)$, and therefore we can write the following inequality

$$0 \leq S(\beta) \leq \ln(M) \quad (7.4-17)$$

and the ratio of the two can be defined as an index of mixture homogeneity that Shanon called relative entropy

$$I_{en}(\beta) = \frac{S(\beta)}{\ln(M)} \quad (7.4-18)$$

Where $I_{en}(0)$ becomes the ratio of the logarithm of particle-containing bins (Eq. 7.4-16) to the logarithm of the total number of bins. With increasing β values, one would increasingly weigh the subdomains (bins) with higher minor concentration. Figure 7.40 shows the computed $I_{en}(0)$ values with β as a parameter along the length of a (SSE) melting zone with an initial of ten clusters of 577 tracer particles and 2880 bins equally-divided over the cross section. The analysis was made over 16 cross sections, one turn apart, downstream of the initial point where that the tracers were injected. The computed homogeneity indices tend to quickly level off with apparently little improvement in distributive mixing (over the whole cross section). The higher β values seem to indicate that with downstream distance the likelihood of unmixed islands may be more pronounced.

Alemanskin et al. (79) extended the use of the entropic measure of mixing to both dispersive and distributive mixing using essentially modified Shannon entropy for systems with multiple species. These authors have also employed entropy to assess color homogeneity in extruded samples by means of computer image analysis and using standard direct red–blue–red (RGB) correlations (80,81).

7.5 COMPUTATIONAL ANALYSIS

One of the fastest growing fields of activity in polymer processing, or, in the broader context discussed in Chapter 1 of macromolecular engineering and science, is numerical

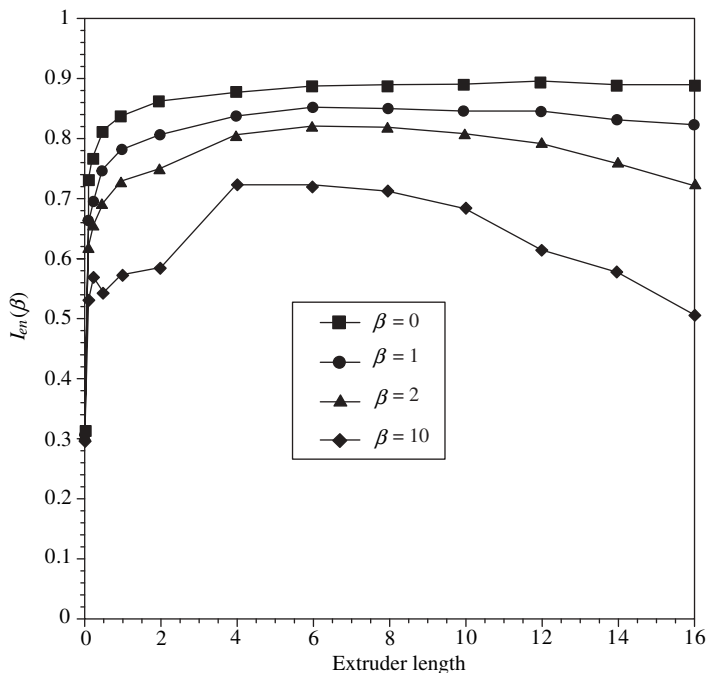


Fig. 7.40 Evolution of I_{en} with β as a parameter along the axial length of a single-screw melt extruder with 10 clusters of 577 tracer particle each and 2880 equal-sized cross-sectional bins. [Reprinted by permission from W. Wang, I. Manas-Zloczower, and M. Kaufman “Entropic Characterization of Distributive Mixing in Polymer Processing Equipment”, *Am. Chem. Eng. J.*, **49**, 1637 (2003).]

computational analysis of flows in processing equipment and shaping steps. This development has special significance in mixing, because this is the only method that can provide quantitative insight into the mixing process. Moreover, it also provides, in principle, the methodology to follow fluid elements in their journey through the processing equipment and thus attempt to predict the degree to which they have changed chemically, if they are reactive, their structuring and final properties.

We do not review the fast-growing field of computational analysis in this book, but in the following paragraphs, we only discuss a special example of mixing. There is a wealth of literature that can be consulted for this purpose. It suffices here to say that there are two basic elements to the computation: first, the velocity fields must be obtained by finite difference or finite element methods, and then particles and surfaces must be tracked. Regarding the former, the mixing process can be viewed as a transformation from one state to the next. The mixing process then can be broken down into a number of steps, each analyzed separately and then combined. This mapping method, originally proposed by Spencer and Wiley (82), is based on tracking of small flow domains, and it follows an initial subdomain grid from an initial grid to an end grid with results stored in a mapping matrix. This method may, in principle, convert a complex problem into a tractable one with reasonable computational effort, and enables alternative mixing protocols to

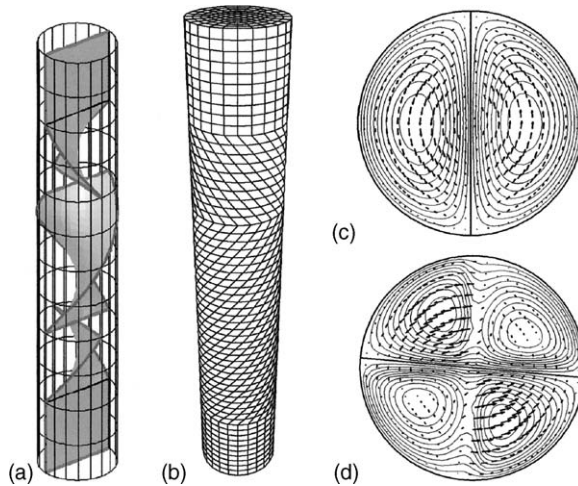


Fig. 7.41 Computation of the velocity pattern in the Kenics mixer. (a) the flow domain; (b) the finite-element grid; (c) the velocities at the cross section in the middle of an element; (d) the same just after the transition. The contours in (c) and (d) are isolines of axial velocity, and the arrows show the lateral velocity. [Reprinted by permission from O. S. Galaktionov, P. D. Anderson, G. W. M. Peters, and H. E. H. Meijer, “Analysis and Optimization of Kenics Mixers,” *Int. Polym. Process.*, **18**,138–150, (2003).]

be analyzed (83–85). This is a simple method that provides information on the spread of the particles in the flow space, but it gives no indication of the spatial distribution of the bulk of the fluid.

An alternative and complementary method is to follow the deformation of the material by following the boundaries of a fluid domain, by either the *front capturing* or *front tracking* technique. In the former, marker particles are distributed over the fluid domain volume and tracked over time, with the surface of the domain being restored by interpolation techniques; in the latter, a separate moving mesh is used to describe the interface between the subdomain and the rest of the volume (86–89).

A good example of the foregoing techniques is the computational analysis of the Kenics mixer, shown in Fig. 7.41(a), carried out by Galaktionov et al. (90,91). The mixer consists of helically twisted, solid separating plates, each dividing the channel into two helical semicircular elements. A number of these are stacked, such that the leading edge of one is perpendicular to the trailing edge of the next one. The pressure-driven melt generates a three dimensional flow that, by repeated stretching, cutting and stacking, leads to chaotic mixing. Since there are no moving elements, the Kenics is a “static mixer.” The velocity profile, using a grid containing 1.6×10^5 elements (400×400 resolutions), was calculated assuming an isothermal flow of a Newtonian fluid with no slip at the walls and in absence of interfacial surface tension, and is shown in Fig. 7.41(c) and 7.41(d).

Having the velocity profile, the evolution of mixing can be studied by computing the concentration distribution of a side-by-side fed black-and-white fluid, with concentrations ($c = 1$) and ($c = 0$) respectively, along the mixer, as shown in Fig. 7.42.

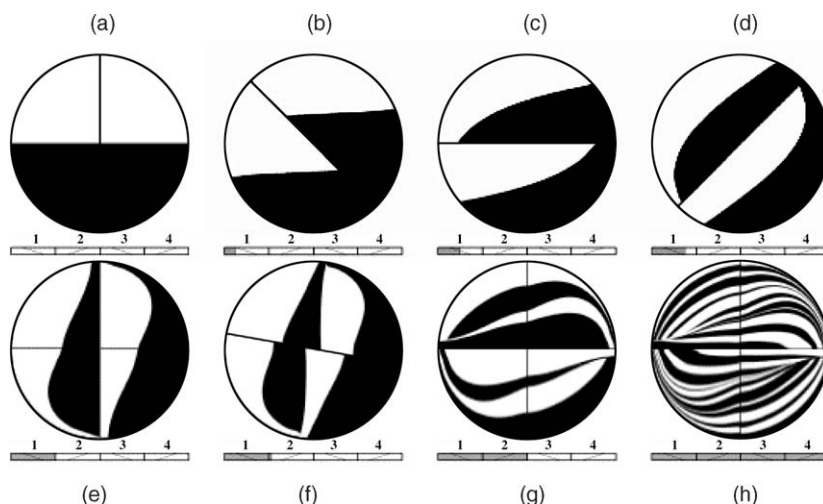


Fig. 7.42 The concentration distribution of a black ($c = 1$) and white ($c = 0$) feed. (a) to (e) The concentration distribution along the first element; (f) 10° into the subsequent element; (g) at the end of the second element; and (h) at the end of the third element. The plates are twisted a total of 180° and with alternate left and right twisting. [Reprinted by permission from O. S. Galaktionov, P. D. Anderson, G. W. M. Peters, and H. E. H. Meijer, “Analysis and Optimization of Kenics Mixers,” *Int. Polym. Process.*, **18**, 138–150 (2003).]

The first image, (a), in the figure shows the initial concentration distribution and the leading edge of the first element. The vertical line denotes the direction of the separating plate. Images (b) to (e) show the evolution of the concentration distribution along the first element. The dotted line in image (e) shows the orientation of the plate in the next element. Clearly, the number of layers (striations) is doubled. Image (f) shows the distribution just 10° into the second, oppositely twisted plate. The striations are cut and dislocated and at the end of the second element, image (g), the number of layers is doubled again, as they are after yet another element in image (h), where 16 striations are observed.

Figure 7.43 shows the concentration distribution along 20 elements with alternately left and right twisting plates at 140° reducing the striation thickness to below

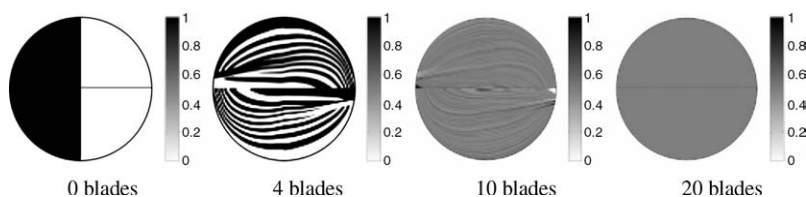


Fig. 7.43 The evolution of concentration distribution after 4, 10, and 20 elements with alternately left and right twisting plates at 140° . [Reprinted by permission from O. S. Galaktionov, P. D. Anderson, G. W. M. Peters, and H. E. H. Meijer, “Morphology Development in Kenics Static Mixers (Application of the Extended Mapping Method),” *Can. J. Chem. Eng.*, **80**, 604–613 (2002).]

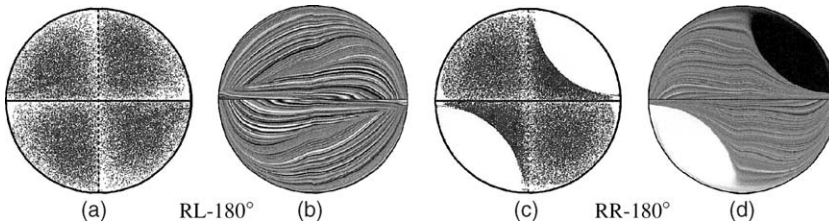


Fig. 7.44 Concentration distributional and Poincaré sections after eight elements side by side. (a) and (b) right–left 180° elements; (c) and (d) right–right 180° elements. [Reprinted by permission from O. S. Galaktionov, P. D. Anderson, G. W. M. Peters, and H. E. H. Meijer, “Analysis and Optimization of Kenics Mixers,” *Int. Polym. Process.*, **18**, 138–150 (2003).]

naked-eye resolution. By calculating Poincaré sections along the Kenics mixer, as shown in Fig. 7.44, the chaotic nature of the flow becomes visibly evident. The figure shows, side by side, the Poincaré section and the concentration distribution after eight elements with right–left twisting elements [parts (a) and (b)] and with right–right elements [parts (c) and (d)]. Clearly, the latter provides poor mixing. These computational techniques provide effective design and optimization tools, and alternate geometries can be quickly explored and analyzed, though care should be exercised, because as the particle trajectories are followed, at some point, precision may become a problem, even with refined mesh.

REFERENCES

1. I. Manas-Zloczower and Z. Tadmor, Eds. *Mixing and Compounding of Polymers*, Hanser, New York, 1994.
2. G. Matthews, *Polymer Mixing Technology*, Applied Science, London, 1982.
3. J. L. White, A. Y. Coran, and A. Moet, *Polymer Mixing* Hanser, Munich, Germany, 1998.
4. H. F. Irving and R. L. Saxton, “Mixing in High Viscosity Materials,” in *Mixing, Vol. 2, Theory and Practice*, V. H. Uhl and J. B. Gray, Eds., Academic Press, New York, 1967, Chapter 8.
5. R. S. Brodkey, “Fluid Motion and Mixing,” in *Mixing, Vol. 1*, V. H. Uhl and J. B. Gray, Eds., Academic Press, New York, 1966, Chapter 2.
6. R. S. Spencer and R. N. Wiley, “The Mixing of Very Viscous Liquids,” *J. Colloid Sci.*, **6**, 133 (1951).
7. J. T. Bergen, G. W. Carrier, and J. A. Krumbansh, “Criteria for Mixing and Mixing Process,” paper presented at the 14th Society of Plastic Engineers National Technical Conference, Detroit, January 1958.
8. J. M. McKelvey, *Polymer Processing*, Wiley, New York, 1962; also (a) Chapter 9.
9. G. Brothman, N. Woldan, and S. M. Feldman, *Chem. Metal. Eng.*, **52**, 102 (1945).
10. W. D. Mohr, R. L. Saxton, and e. H. Jepson, “Mixing in Laminar Flow Systems,” *Ind. Eng. Chem.*, **49**, 1855–1856 (1957).
11. L. Erwin, “New Fundamental Considerations on Mixing in Laminar Flow,” paper presented at the Society of Plastics Engineers 36th Annual Technical Conference, Washington, D.C., 1978, p. 488.

12. H. Aref, "Stirring Chaotic Advection," *J. Fluid Mech.*, **143**, 1–21 (1984).
13. H. Aref, "The Development of Chaotic Advection," *Phys. Fluids*, **14**, 1315–1325 (2002).
14. H. Aref and S. Balachandrar, "Chaotic Advection in Stokes Flow," *J. Phys. Fluid*, **29**, 3516–3521 (1986).
15. J. Chaiken, R. Chevray, M. Tabor, and Q. M. Tan, "Experimental study of Lagrangian Turbulence in Stokes Flow," *Proc. Royal Soc. London A* **408** 165–174 (1986).
16. J. Chaiken, C. K. Chu, M. Tabor, and Q. M. Tan, "Lagrangian turbulence and Spatial Complexity in a Stokes Flow," *J. Phys. Fluids*, **30**, 687–99 (1987).
17. W. L. Chien, H. Rising, and J. M. Ottino, "Laminar Mixing and Chaotic Mixing in Several Cavity Flows," *J. Fluid Mech.*, **170**, 335 (1986)
18. J. M. Ottino, "The Mixing of Fluids," *Sci. Am.*, **200**, 56–67 (1989)
19. J. M. Ottino, *The Kinematics of Mixing: Stretching, Chaos and Transport*, Cambridge University Press, Cambridge, 1989.
20. S. Wiggins and J. M. Ottino, "Foundation of Chaotic Mixing," *Philos. Proc. R. Soc. London A*, **362**, 837–970 (2004).
21. R. I. Danescu and D. A. Zumbrunnen, "Production of Electrically Conducting Plastics Composites by Three-Dimensional Chaotic Mixing of Melts and Powder Additives," *J. Vinyl Addit. Technol.*, **6**, 26–33 (2000).
22. D. A. Zumbrunnen and C. Chibber, "Morphology Development in Polymer Blends Produced by Chaotic Mixing at Various Compositions," *Polymer*, **43**, 3267–3277 (2002).
23. D. M. Bigg and S. Middleman, "Laminar Mixing of a Pair of Fluids in a Rectangular Cavity," *Ind. Eng. Chem. Fundam.*, **13**, 184 (1974).
24. F. H. Harlow and J. E. Welch, "Numerical Calculation of Time Dependent Viscous Incompressible Flow of Fluid with Free Surface," *Phys. Fluids*, **8**, 2182–2189 (1965).
25. J. H. Hildebrand and R. L. Scott, *The Solubility of Non-Electrolytes*, 3rd ed., Reinhold, New York, 1950; reprinted by Dover, New York, 1964.
26. H. Burrell and B. Immergut, "Solubility Parameter Values," IV-341 in *Polymer Handbook*, J. Brandrup and E. H. Immergut, Eds., Wiley-Interscience, New York, 1966.
27. P. J. Flory, "Thermodynamics of High Polymer Solutions," *J. Chem. Phys.*, **10**, 51 (1942).
28. M. L. Huggins, "Theory of Solutions of High Polymers," *J. Am. Chem. Soc.*, **64**, 1712 (1942).
29. H. E. H. Meijer, "Processing for Properties," in *Material Science and Technology*, R. W. Cahn, P. Haasen, E. J. Kramer, Eds., Wiley-VCH, Weinheim, Germany, 1997.
30. H. H. Meijer and J. M. H. Janssen, "Mixing of Immiscible Liquids," in *Mixing and Compounding of Polymers*, I. Manas-Zloczower and Z. Tadmor, Eds., Hanser, Munich, Germany 1994; also J. M. H. Janssen, Ph.D. Dissertation, Technical University of Eindhoven, Eindhoven, The Netherlands, 1993.
31. Lord Rayleigh, "On the Capillary Phenomena of Jets," *Proc. R. Soc.*, (London), **29**, 71–97 (1879).
32. C. Weber, *Z. Angew. Math. Mech.*, **11**, 136 (1931).
33. S. Tomotika, "On the Instability of a Cylindrical Thread of a Viscous Liquid Surrounded by Another Viscous Fluid," *Proc. R. Soc. London*, **A150**, 322–337 (1935).
34. J. M. H. Janssen, "Emulsions: The Dynamic of Liquid-Liquid Mixing," in *Material Science and Technology*, Vol. 18, R. W. Cahn, P. Haasen, E. J. Kramer, Eds., Wiley-VCH, Weinheim, Germany, 1997.

35. G. I. Taylor, "The Viscosity of a Fluid Containing Small Drops of Another Fluid," *Proc. R. Soc.*, **A138**, 41 (1932).
36. G. I. Taylor, "The Formation of Emulsions in Definable Fields of Flow," *Proc. R. Soc.*, **A146**, 501–523 (1934).
37. F. D. Rumscheidt and S. G. Mason, "Particle Motion in Sheared Suspensions. XII. Deformation and Burst of Fluid Drops in Shear and Hyperbolic Flow," *J. Colloid Sci.*, **16**, 238–261 (1961).
38. H. P. Grace, *Chem. Eng. Comm.* **14**, 2225 (1971).
39. A. M. Gessler, W. M. Hess, and A. I. Medalia, "Reinforcement of Elastomers with Carbon Black: Part 1. The Nature of the Carbon Black; Part 2. Effect of Incorporating Carbon Black in Elastomers; and Part 3. The Phenomenon of Reinforcement," *Plast. Rubber. Process.*, (1978).
40. W. R. Bolen and R. E. Colwell, "Intensive Mixing", *Soc. Plastics Eng. J.*, **14**(8), 24–28 (1958).
41. I. Manas-Zloczower, "Dispersive Mixing of Solid Additives," in *Mixing and Compounding of Polymers*, I. Manas-Zloczower and Z. Tadmor, Eds., Hanser, Munich, Germany, 1994.
42. I. Manas-Zloczower, A. Nir, and Z. Tadmor, "Dispersive Mixing in Internal Mixers – A Theoretical Model Based on Agglomerate Rupture," *Rubber Chem. Technol.*, **55**, 1250–1285 (1982).
43. H. Rumpf, "The Strength of Granules and Agglomerates," in *Agglomeration*, W. A. Knepper, Ed., Wiley-Interscience, New York 1962.
44. H. C. Hamaker, *Physica*, **4**, 1058 (1937).
45. A. Nir and A. Acrivos, "On the Creeping Motion of Two Arbitrary-sized Touching Spheres in a Linear Shear Field," *J. Fluid Mech.*, **59**, 209–223 (1973).
46. I. Y. Z. Zia, R. G. Cox, and S. G. Mason, "Ordered Aggregates of Particles in Shear Flow," *Proc. R. Soc.*, **A300**, 421–441 (1967).
47. (a) I. Manas-Zloczower and D. L. Feke, "Analysis of Agglomerate Rupture in Linear Flow Fields," *Int. Polym. Process.*, **4**, 3–8 (1989); also (b) A. Scurati, I. Manas-Zloczower, and D. L. Feke, *Proc. ACS Rubber Division Meet.*, Atlanta, GA, 2002.
48. V. Collin and E. Peuvrel-Disdier, "Disperion Mechanisms of Carbon Black in an Elastomer Matrix," *Elastomery*, Vol. 9 (2005) Special Edition JSSN PL 1427-3519; see also V. Collin and E. Peuvrel-Disdier, presentation at the Conference of European Rubber Research "Practical Improvements of Mixing Processer," Paterborn, Germany, January 25-26 (2005), pp. 219–241.
49. N. R. Schott, B. Weinstein, and D. LaBombard, "Motionless Mixers in Plastics Processing," *Chem. Eng. Prog.*, **71**, 54–58 (1975).
50. C. M. Marshall and P. Geyer, US Patent 2,744,287.
51. H. List, *Kunststoffe*, **40**, 185 (1950); also, Swiss Patent 247,704 (1947) and U.S. Patent 2,505,125 (1950).
52. E. H Ahlefeld, A. J. Baldwin, P. Hold, W. A. Rapetski, and H. R. Scharer, U.S. Patent 3,154,808 (1964), also, U.S. Patent 3,239,878 (1966).
53. T. Okada, K. Taniguchi and K. Kamimori, US Patent, 3,802,670 (1974).
54. K. Inoue, K. Ogawa, T. Fukui. T. Asai, and S. Hashizume U.S. Patent 4,332,481 (1982).
55. P. V. Danckwerts, "Theory of Mixtures and Mixing," *Research* (London), **6**, 355–361 (1953); see also P. V. Danckwerts, "General Aspects of Mixtures and Mixing," paper presented at the Symposium on Mixing of Thick Liquids, Pastes, and Slurries, British Society of Rheology, London, September 1953; cf. N. Wookey, "Mixing of Thick Liquids, Pastes and Slurries", *Nature*, **172**, 846–847 (1953).

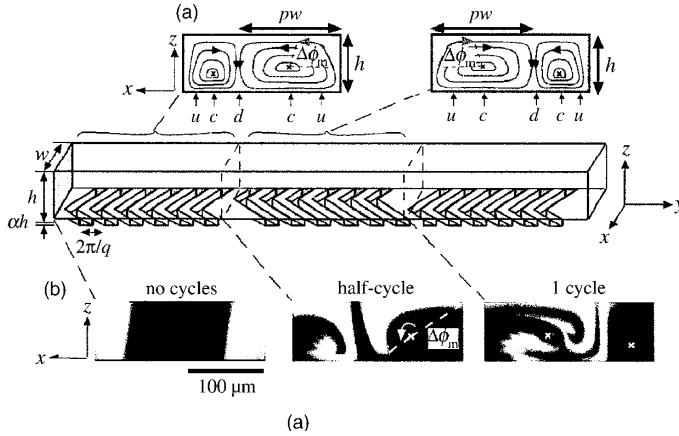
56. G. Lidor and Z. Tadmor, "Theoretical Analysis of Residence Time Distribution Functions in Plasticating Screw Extruders," *Polym. Eng. Sci.*, **16**, 450–462, (1976).
57. I. Manas Zloczower, A. Nir and Z. Tadmor, "Dispersive Mixing in Internal Mixers—A Theoretical Model Based on Agglomerate Rupture," *Rubber Chemistry Technology*, **55**, 1250–1285 (1982).
58. I. Manas-Zloczower and Z. Tadmor, "The Dispersive Mixing in Rubber and Plastics—A Review," *Rubber Chem. Technol. Rev.*, **57**, 583–670 (1984).
59. I. Manas-Zloczower and Z. Tadmor, "Scale-up of Internal Mixers," *Rubber Chem. Technol.*, **57**, 48–54 (1984).
60. I. Manas-Zloczower, A. Nir and Z. Tadmor, "Dispersive Mixing in Roll-Mills," *Polym. Compos.*, **6**, 222–231 (1984).
61. I. Manas-Zloczower and Z. Tadmor, "The Distribution of Number of Passes over the Flights in Single Screw Melt Extruders," *Adv. Plast. Technol.*, **3**, 213, (1983).
62. Z. Tadmor, "Passage Distribution Functions and Their Application to Dispersive Mixing of Rubber and Plastics," *AIChE J.*, **34**, 1943 (1988).
63. Z. Tadmor, "Number of Passage distribution Functions," in *Mixing and Compounding of Polymers – Theory and Practice*, I. Manas-Zloczower and Z. Tadmor, Eds., Hanser, New York, 1994, Chapter 5.
64. R. Shinnar, S. Katz, and P. Naor, *Interpretation of Tracer Experiments in Recirculating Systems, and Application of Renewal Theory*, unpublished report, Department of Chemical Engineering, City College, City University, New York (1970).
65. D. R. Cox, *Renewal Theory*, Methuen, London; also, Wiley, New York (1962)
66. U. Mann and E. J. Crosby, "Cycle Time Distribution in Circulating Systems," *Chem. Eng. Sci.*, **29**, 623–627 (1973).
67. U. Mann, E. J. Crosby, and M. Rubinovitch, "Number of Cycles Distribution in Circulating Systems," *Chem. Eng. Sci.*, **29**, 761–765 (1974).
68. B. Julesz, "Experiments in the Visual Perception of Texture," *Sci. Am.*, **232**, 34–43 (1975).
69. W. Feller, *An Introduction to Probability Theory and Its Applications*, Vol. 1, Wiley, New York, 1950.
70. W. Clump, "Mixing of Solids," in *Mixing*, Vol. II, V. H. Uhl and J. B. Gray, Eds., Academic Press, New York, 1967, Chapter 10.
71. J. R. Bourne, "The Mixing of Powders, Pastes, and Non-Newtonian Fluids," Industrial Research Fellow Report No. 2, The Institute of Chemical Engineers, London, 1969.
72. L. T. Fan and R. H. Wang, "On Mixing Indices," *Powder Technol.*, **11**, 27–32 (1975).
73. P. V. Danckwerts, "The Definition and Measurement of Some Characteristics of Mixtures," *Appl. Sci. Res.*, **A3**, 279–296 (1952).
74. N. Nadav and Z. Tadmor, "Quantitative Characterization of Extruded Film Textures," *Chem. Eng. Sci.*, **28**, 2115–2126 (1973).
75. W. Wang, I. Manas-Zloczower and M. Kaufman, "Characterization of Distributive Mixing in Polymer Processing Equipment Using Renyi Entropies," *Int. Polym. Process.*, **16**, 315–322 (2001).
76. W. Wang, I. Manas-Zloczower, and M. Kaufman, "Entropic Characterization of Distributive Mixing in Polymer Processing Equipment," *AIChE J.*, **49**, 1637–1644 (2003).
77. C. E. Shannon, "A Mathematical Theory of Communication," *Bell Syst. Tech. J.*, **27**, 379 (1948).
78. A. Renyi, *A Probability Theory*, North-Holland, Amsterdam, 1973.

79. K. Alemanskin, I. Manas-Zloczower, and M. Kaufman, "Index for Simultaneous Dispersive and Distributive Mixing Characterization in Processing Equipment," *Int. Polym. Process.*, **19**, 327–333 (2004).
80. K. Alemanskin and I. Manas-Zloczower, "Color Mixing in the Metering Zone of a Single Screw Extruder: Numerical Simulation and experimental Validation," *Polym. Eng. Sci.*, **45**, 1011–1020 (2005).
81. K. Alemanskin and I. Manas-Zloczower, "Entropic Analysis of Color Homogeneity," *Polym. Eng. Sci.*, **45**, 1031–1038. (2005).
82. R. Spencer and R. Wiley, "The Mixing of Very Viscous Liquids," *J. Colloid Sci.*, **6**, 133–145 (1951).
83. O. S. Galaktionov, P. D. Anderson, P. G. M. Kruijff, W. G. M. Peters, and H. E. H. Meijer, "A Mapping Approach for 3D Distributive Mixing Analysis," *Comput. Fluids*, **30**, 271–289 (2001).
84. G. F. Carey and Y. Shen, "Simulation of Fluid Mixing Using Least-square Finite Elements and Particle Tracing," *Int. J. Numer. Heat Fluid Flow*, **5**, 549–573 (1995).
85. B. C. Hutchinson, A. C. Rios, and T. A. Osswald, "Modeling the Distributive Mixing in Internal Batch Mixers," *Int. Polym. Process.* **14**, 315–321 (1999).
86. C. V. Hurt and B. D. Nichols, "Volume of Fluid (VOF) Methods for Dynamic of Free Boundaries," *J. Comput. Phys.*, **39**, 201–225 (1981).
87. O. S. Galaktionov, P. D. Anderson, G. W. M. Peters, and F. N. v.d. Vosse, "An Adaptive Front Tracking Technique for Three Dimensional Transient Flow," *Int. J. Numer. Methods. Fluids*, **32**, 201–218 (2000).
88. J. M. Hyman, "Numerical Methods for Tracking Interfaces," *Physica*, **12**, 396–407(1984); also, M. Rudman, "Volume Tracking Methods for Interfacial Flow Calculations," *Int. J. Numer. Heat Fluid Flow*, **24**, 671–691 (1997).
89. S. O. Unverdi and G. Tyggvason, "Computation of Multi-fluid Flow," *Phys. Fluids D*, **60**, 70–83 (1992).
90. O. S. Galaktionov, P. D. Anderson, W. G. M. Peters, and H. E. H. Meijer, "Analysis and Optimization of Kenics Mixers," *Int. Polym. Process.*, **18**, 138–150 (2003).
91. O. S. Galaktionov, P. D. Anderson, W. G. M. Peters, and H. E. H. Meijer, "Morphology Development in Kenics static Mixers (Application of the Extended Mapping Method)," *Can. J. Chem. Eng.*, **80**, 604–613 (2002).

PROBLEMS

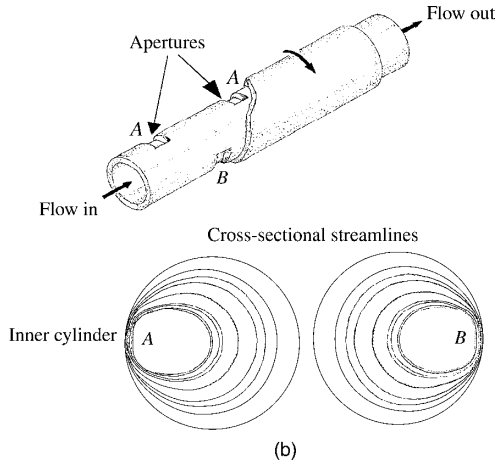
7.1 *Mixing Mechanisms* Consider a calendaring process for manufacturing PVC floor covering. The line consists of a ribbon-type blender in which the PVC is dry-blended, and an internal mixer that feeds a SSE equipped with a static mixer, feeding the first nip of the calender. What types of mixing mechanisms does the polymer experience? Specify the locations at which each mechanism occurs.

7.2 *Chaotic Mixer Designs* In discussing chaotic flow, we stressed that for two-dimensional flow, time-periodic variations that lead to nonintegrability of streamlines or to streamline crossing, are a prerequisite. This is not the case in three-dimensional flows. The accompanying figures (a–e) show a few imaginative designs, reviewed by Wiggins and Ottino (20), that have been suggested to induce chaotic mixing. Describe why and how these mixing devices lead to chaotic mixing.



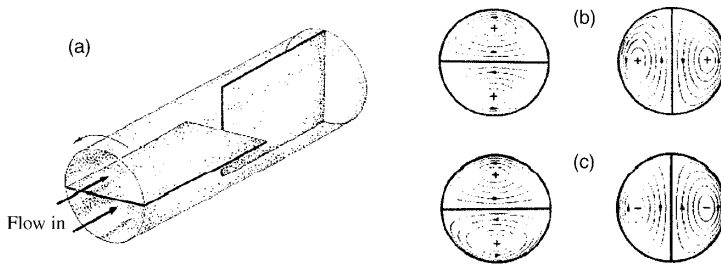
(a)

A micromixer suggested by Stroock et al., consisting of pressure flow in straight rectangular channels with ridges on one of the walls [Reprinted by permission from A. D. Stroock, S. K. W. Dertinger, A. Ajdari, I. Mezić, H. A. Stone, and G. M. Whitesides, “Chaotic Mixer for Microchannels,” *Science*, **295**, 364–651 (2002).]



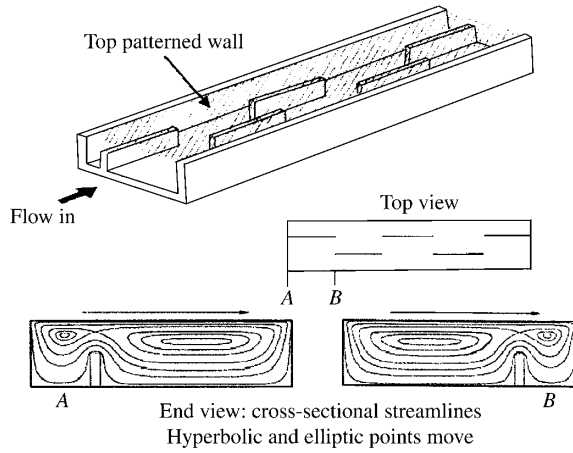
(b)

Pressure-driven flow in a rotating arc mixer suggested by Metcalfe et al., consisting of two closely spaced concentric cylinders, with the outer cylinder rotating and strategically located slits in the inner cylinder. The pressure-driven flow enters axially into the inner cylinder. [Reprinted by permission from G. Metcalfe, M. Rudman, A. Brydon, and L. Graham, “Numerical Mixing Experiments in a Rotating Cylinder Mixer,” *Proc. 6th World Cong. on Chemical Engineering*, Melbourne Australia, 2001.]



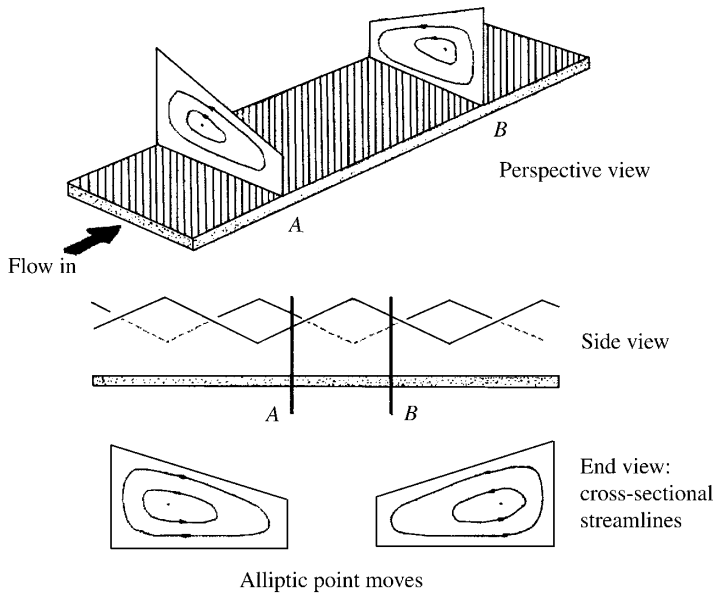
(c)

Pressure-driven flow in a simplified Kenics-type mixer consisting of a tube with alternating partitions.



(d)

Pressure-driven flow in a rectangular channel suggested by Jana et al. consisting of a rectangular channel with a moving ridged upper wall and alternating axial partitions. [Reprinted by permission from S. C. Jana, M. Tjahjadi, and J. M. Ottino, "Chaotic Mixing of Viscous Fluids by Periodic Changes in Geometry; The Baffled Cavity Flow," *AICHE J.*, **40**, 1769–1781 (1994).]



(e)

The micromixer shown in (a) with the wall with ridges replaced by an alternating cross-sectional area [Reprinted by permission from S. Wiggins and J. M. Ottino, "Foundations of Chaotic Mixing," *Philos. Trans. R. Soc. London*, **362**, 937–970, (2004).]

7.3 Increase in Interfacial Area in Homogeneous Flow The increase in interfacial area in a general homogeneous flow is given in Eq. E7.1-23. Prove that for simple shear flow, this equation reduces to Eq. E7.1-15.

(*Hint:* Recall that the angles formed by the principal axes of the strain spheroid with direction x (direction of shear), χ , $\chi + (\pi/2)$ are related to the total strain γ as follows

$$\gamma = 2 \cot 2\chi$$

and the principal elongational ratios are

$$\lambda_x = \cot \chi, \quad \lambda_y = \frac{1}{\lambda_x}, \quad \lambda_z = 1$$

The angle formed by the principal axes with the x direction in the initial state χ_0 is given by

$$\sin \chi_0 = \cos \chi$$

Next, express the angles α' and β' in terms of angles α_x , α_y , and χ_0 , and substitute in Eq. E7.1-23.)

7.4 The Distribution of Interfacial Area Elements at High Strains in Simple Shear Flow Consider randomly distributed and equal-sized interfacial area elements placed in a rheologically uniform medium in simple shear flow. After a given strain, the interfacial area elements vary in size; that is, a distribution of interfacial area elements evolves because of the flow. (a) Show that the variance of the distribution is

$$\left(\frac{\sigma}{\bar{A}}\right)^2 = \frac{\overline{A^2}}{(\bar{A})^2} - 1 = \frac{\gamma^2 + 12}{3\gamma^3}$$

where $\overline{A^2}$ is the mean of the square of the area elements and \bar{A} is the mean area

$$\bar{A} = \frac{1}{N} \sum_{i=1}^N A_i$$

where N is the number of area elements.

(b) It has been shown¹² that the mean square of interfacial area elements for any homogeneous deformation is given by

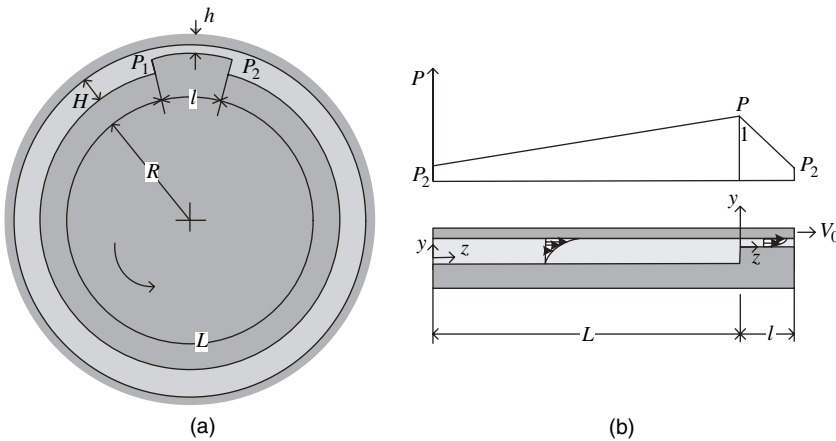
$$\overline{\left(\frac{A'}{A_0}\right)^2} = \frac{1}{3} \lambda_1^2 \lambda_2^2 \lambda_3^2 (\lambda_1^{-2} + \lambda_2^{-2} + \lambda_3^{-2})$$

12. A. S. Lodge, private communication, 1976.

where A_0 is the initial surface and λ_i are the principal elongational ratios. Show that the preceding equation for simple shear, together with Eq. E7.1-20, reduce to the results in part (a).

7.5 Deformation of a Sphere in Various Types of Flows A spherical liquid particle of radius 0.5 in is placed in a liquid medium of identical physical properties. Plot the shape of the particle (a) after 1 s and 2 s in simple shear flow with $\dot{\gamma} = 2 \text{ s}^{-1}$; (b) after 1 s and 2 s in steady elongational flow with $\dot{\epsilon} = 1 \text{ s}^{-1}$. (c) In each case, the ratio of the surface area of the deformed particle to the initial one can be calculated. What does this ratio represent?

7.6 Hydrodynamic Analysis of an Idealized Internal Mixer Consider the idealized mixer shown in the accompanying figure, consisting of two concentric cylinders in relative motion with a step change in clearance. Calculate the mean shear stress in the narrow gap.



7.7 Cohesive Forces in Dispersive Mixing Using the following information, estimate the cohesive forces holding carbon black particles together. Breakup of the agglomerates was obtained in an idealized internal mixer, as shown in the figure in Problem 7.6, with $V_0 = 25 \text{ cm/s}$. The carrier is LDPE at 150°C . The gap clearance is $h = 0.1 \text{ cm}$, $H = 1.0 \text{ cm}$; the clearance length is $l = 0.5 \text{ cm}$ and $L = 10.0 \text{ cm}$. The particle size is $5 \mu\text{m}$ in diameter. Assume a constant viscosity $0.05 \text{ lb}_f \cdot \text{s/in}^2$.

7.8 Roll-mill for Dispersive Mixing A laboratory roll-mill with 5-in diameter rolls and 0.05 in minimum clearance between the rolls is used for dispersive mixing of carbon black agglomerates in LDPE. Calculate the roll speed needed to break up 5 of the particles per pass, assuming that the critical shear stress needed for breakup is that obtained in Problem 7.12 in the narrow clearance, and that the amount of polymer on the rolls is 50% above the minimum. Assume the same constant viscosity as in Problem 7.7.

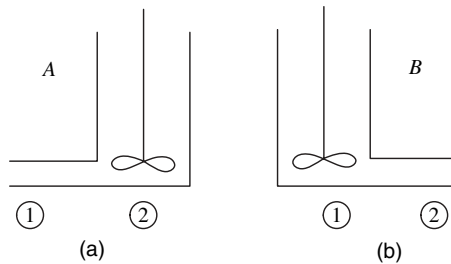
7.9 Relationship between the Mean Strain and the Mean Shear Rate Show that, for continuous, single-valued viscometric shear flows, the following relationship

holds:

$$\gamma = \bar{\gamma t} = \bar{t} \frac{1}{H} \int_0^H \dot{\gamma} dy$$

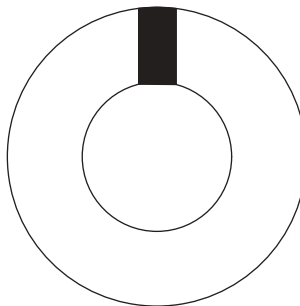
7.10 Purging a Tubular Die A “red” polymer is pumped through a tubular die. At time t , the inlet stream is switched over to a “white” polymer for purging the die. Assuming Newtonian fluids, identical viscosities and densities, and fully developed isothermal laminar flow, calculate the volume fraction of red polymer left in the die at the time the first traces of white polymer appear at the exit.

7.11 RTD in Two Systems in a Series The accompanying figure shows two combinations of a tubular vessel and a well-mixed stirred tank. (a) Assuming plug flow in the tube, prove that the RTDs in both combinations are identical. (b) Repeat (a), assuming laminar flow in the tube.



7.12 Derivation of RTD in a Continuously Stirred Tank Equation 7.3-18 gives the RTD function $F(t)$ in a CST. (a) Calculate $f(t) dt$. (b) The function $f(t) dt$ also expresses the probability that an entering fluid particle will leave at time t . Derive this function, using probability considerations. (c) Extend the derivation in (b) to N vessels in series.

7.13 The Two-cylinder Mixer Two concentric cylinders contain a viscous liquid. A vertical slice of fluid contains black dye, which does not affect the rheological properties. Two experiments are carried out: (a) the outer cylinder rotates clockwise at 1 rpm for 5 min.; (b) the outer cylinder rotates alternately clockwise and counterclockwise at 2 rpm, 15 s in each direction, for a total of 2.5 min. Which mode of motion leads to better mixing?



7.14 Strain Distribution Function in Poiseuille Flow (a) Derive the SDF $F(\gamma)$ for fully developed isothermal laminar flow of a Newtonian fluid in a tube. (b) Calculate the mean strain. (c) If the length of the tube is 1 m and its radius 0.01 m, what fraction of the exiting stream experiences a total strain of less than 100?

7.15 Strain Distribution Function in Parallel Plate Flow (a) Derive the SDF $F(\gamma)$ for the parallel-plate flow with a superimposed pressure gradient in the range $-1/3 < q_p/q_d < 1/3$. The velocity profile is given by

$$v_x = \left[\xi + 3\xi \frac{q_p}{q_d} (1 - \xi) \right] V_0$$

where $\xi = y/H$, and q_p and q_d are pressure and drag flow rates per unit width, respectively, and their ratio A is

$$A = \frac{q_p}{q_d} = \frac{1}{6} \left(-\frac{dP}{dx} \right) \frac{H^2}{V_0}$$

(b) Calculate the mean strain. (c) Plot the SDF with q_p/q_d as a parameter in the range $-1/3 < q_p/q_d < 1/3$.

7.16 The Strain Distribution Function of a Power Law Fluid in Pressure Flow between Parallel Plates Consider two infinitely wide parallel plates of length L gap H . Polymer melt is continuously pumped in the x direction. Assuming isothermal steady, fully developed flow, (a) show that $F(\xi)$ is given by

$$F(\xi) = \frac{2+s}{1+s} \left(1 - \frac{1}{2+s} \xi^{1+s} \right) \xi \quad 0 \leq \xi \leq 1$$

where $\xi = 2y/H$ (the coordinate system is placed at the center of the gap).

(b) Show that the total strain is related to ξ via

$$\gamma(\xi) = 2(1+s) \frac{L}{H} \frac{\xi^s}{1-\xi^{1+s}} \quad 0 \leq \xi \leq 1$$

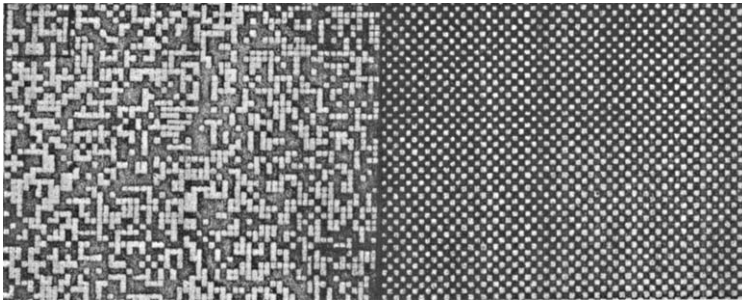
(c) Show that the mean strain $\bar{\gamma}$ is

$$\bar{\gamma} = \int_0^1 \gamma(\xi) f(\xi) d\xi = 2 \left(\frac{2+s}{1+s} \right) \frac{L}{H}$$

- (d) Show that the mean strain can also be calculated by using the following relationship

$$\bar{\gamma} = \bar{t} \int_0^1 \dot{\gamma}(\xi) d\xi$$

- 7.17 Random and Ordered Mixtures** The accompanying figure shows two samples of mixtures of black-and-white squares. One is a black-and-white checkered board and the other was obtained by tossing a coin for each square; if it showed heads, the square was colored black. (a) If we take a large number of black-and-white particles of equal numbers and place the mixture in a V-blender, which sample will the mixture resemble? (b) If we take a large number of small testing samples from sample 1 and sample 2, and measure the fraction of black particles in each sample, what type of distribution would be expected in each case? (c) What is the variance of each distribution?



- 7.18 Gross Uniformity and Texture** Do the two samples in the figure of Problem 7.17 share the same first-order statistics (i.e., are they “grossly uniform”)? (b) Do they have different textures? (c) Outline a computer program for evaluating the scale of segregation of the sample obtained by tossing a coin.

- 7.19 The Binomial Distribution** Consider a random mixture of minor particles in major particles of equal size. The fraction of minor particles in the mixture is p . We withdraw a large number of testing samples from the mixture, each containing exactly n particles. (a) Show that distribution of minor particles in the samples is given by Eq. 7.4-1. (b) Calculate the mean and the variance of the distribution.

- 7.20 The Coefficient of Correlation of a Two-composition System in Terms of Probabilities** Consider a two-composition texture of concentrations x_1 and x_2 shown in the figure below. Following a (mental) process of “dipole throwing,” we find that k_{11} of them fell with both ends on composition x_1 , k_{22} fell with both ends on composition x_2 , and k_{12} fell with one end on composition x_1 and the other on x_2 .

(a) Show that the mean concentration is given by

$$\bar{x} = \frac{2k_{11} + k_{12}}{2N}x_1 + \frac{2k_{22} + k_{12}}{2N}x_2$$

where $N = k_{11} + k_{22} + k_{12}$

(b) Show that the variance is given by

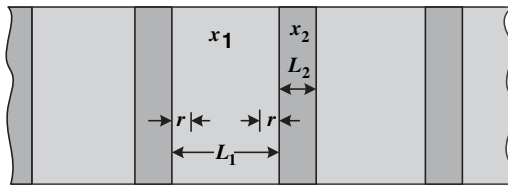
$$S^2 = \frac{(2k_{11} + k_{12})(2k_{22} + k_{12})}{2N} (x_1 - x_2)^2$$

(c) Using the results just obtained, show that the coefficient of correlation is given by

$$R(r) = \psi_{11} \frac{\phi_2}{\phi_1} + \psi_{22} \frac{\phi_1}{\phi_2} - \psi_{12}$$

where (for large number of dipoles) $\psi_{11} = k_{11}/N$, $\psi_{22} = k_{22}/N$, $\psi_{12} = k_{12}/N$, and

$$\frac{\phi_1}{\phi_2} = \frac{2k_{11} + k_{12}}{2k_{22} + k_{12}}$$



7.21 The Scale of Segregation of a Striped Texture Using the coefficient of correlation from the previous problem, show that the linear scale of segregation (perpendicular to the stripes) of the texture of the figure in Problem 7.21 is given by

$$\zeta = \int_0^{\zeta} R(r) dr = \frac{1}{2} \left(\frac{L_1 L_2}{L_1 + L_2} \right)$$

[Hint: The probabilities are evaluated by a (mental) process of “dipole throwing.” Thus the probability that one end of the dipole should fall on region I is $L_1/(L_1 + L_2)$. The probability that this point should fall not closer than a distance

r from either boundary is

$$\left(\frac{L_1}{L_1 + L_2}\right)\left(\frac{L_1 - 2r}{L_1}\right)$$

The probability that the other end should fall on region I is 1. Therefore, the foregoing equation gives the probability that these dipoles fall with both ends on region I. (*Note:* There are additional dipoles that fall on region I.)]

8 Devolatilization

- 8.1 Introduction, 409
- 8.2 Devolatilization Equipment, 411
- 8.3 Devolatilization Mechanisms, 413
- 8.4 Thermodynamic Considerations of Devolatilization, 416
- 8.5 Diffusivity of Low Molecular Weight Components in Molten Polymers, 420
- 8.6 Boiling Phenomena: Nucleation, 422
- 8.7 Boiling–Foaming Mechanisms of Polymeric Melts, 424
- 8.8 Ultrasound-enhanced Devolatilization, 427
- 8.9 Bubble Growth, 428
- 8.10 Bubble Dynamics and Mass Transfer in Shear Flow, 430
- 8.11 Scanning Electron Microscopy Studies of Polymer Melt Devolatilization, 433

8.1 INTRODUCTION

In the manufacturing process of most polymers, there is a need to separate and remove undesirable, residual volatile components such as solvents, monomers, and other low molecular weight components from the polymeric material. These volatiles are removed in one or more postreactor operations in order to recover the solvent and monomer, impart the polymer with the desired physical properties, meet environmental requirements, and eliminate residual odors and taste. In condensation polymerization, of course, the removal of volatiles is essential to drive the polymerization reaction and reach high molecular weights. Moreover, removal of volatiles, moisture and entrapped air is also essential for many types of down-stream compounding and processing equipment.

The elementary step of *devolatilization*, discussed in this chapter, refers to the removal of relatively low concentrations of volatiles of the order of 1% or less. Much of the research, which elucidated the devolatilization step, took place over the past two decades. Joseph A. Biesenberger, one of the pioneers of devolatilization research, published the first review on the subject in 1983 (1), and more recently, Ramon J. Albalak edited a volume devoted to this subject in 1996 (2).

Devolatilization is a mass transport operation. The molecules of the volatile components dissolved in the matrix of the polymeric melt must diffuse to liquid–vapor interfaces, and then be removed and collected. All devolatilization processes, irrespective of the complexity of the equipment in which they take place, are represented schematically by Fig. 8.1.

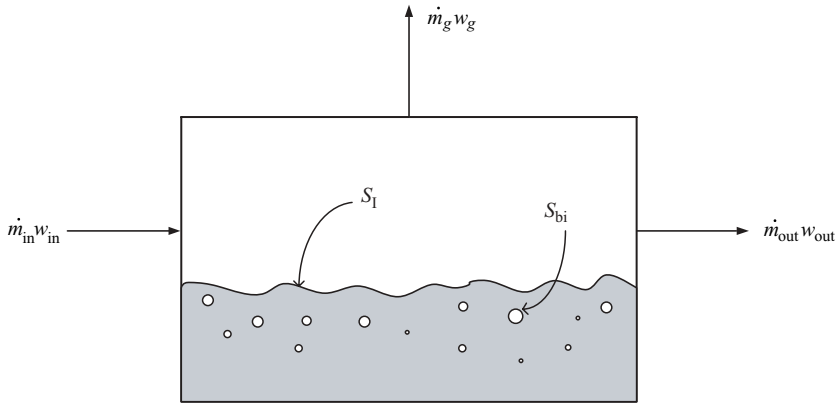


Fig. 8.1 Schematic representation of the devolatilization process. The hatched area represents the polymer melt being devolatilized, which is almost always subject to laminar flow. The bubbles shown are created by the boiling mechanism and by entrapped vapors dragged into the flowing/circulating melt by moving surfaces.

Under steady state operating conditions the macroscopic mass balance of the volatile component (Eq. 2.4-1) is given by

$$w_{in}\dot{m}_{in} - w_{out}\dot{m}_{out} - w_g\dot{m}_g = 0 \quad (8.1-1)$$

where \dot{m} represents mass flow rate and w represents mass fraction of the volatile component. It is convenient to express the mass flow rate of the evaporating volatile component $w_g\dot{m}_g$ in terms of interface transport flux (1), that is, flow rate per unit area of the volatile component normal to the interfacial

$$w_g\dot{m}_g = k_m S_m \quad (8.1-2)$$

where k_m is a mass transfer coefficient and S_m is the total interfacial area given by

$$S_m = S_I + \sum_{i=1}^N S_{bi} \quad (8.1-3)$$

where S_I is the interfacial area of the melt surface and S_{bi} is the interfacial area of bubble i .

The objective is to reduce volatiles to below 50–100-ppm levels. In most devolatilization equipment, the solution is exposed to a vacuum, the level of which sets the thermodynamic upper limit of separation. The vacuum is generally high enough to superheat the solution and foam it. Foaming is essentially a boiling mechanism. In this case, the mechanism involves a series of steps: creation of a vapor phase by nucleation, bubble growth, bubble coalescence and breakup, and bubble rupture. At a very low concentration of volatiles, foaming may not take place, and removal of volatiles would proceed via a diffusion-controlled mechanism to a liquid–vapor macroscopic interface enhanced by laminar flow-induced repeated surface renewals, which can also cause entrapment of vapor bubbles.

Alternatively, a third, low boiling-point additive such as water or inert gas can be added to strip the residual volatiles, which (a) provides more mass transfer area, (b) reduces diffusion distance for the molecules that we wish to remove, (c) increases the driving force for the separation because of the lower concentration of the volatile in the bubbles, and (d) the vaporization of the stripping agent offsets some of the heat generated by viscous dissipation. Of course, after separation we have to deal with a dilute mixture of the volatile in the stripping agent, which may need to be separated for recovery and/or environmental reasons.

In this chapter, subsequent to an introduction to devolatilization equipment, we review the thermodynamics of polymer solution equilibrium, which determines the *maximum* amount of volatiles that can be separated under a given set of processing conditions; the phenomena associated with diffusion and diffusivity of small molecules in polymeric melts, which affects the rate of mass transfer; the phenomena and mechanisms involving devolatilization and their modeling and the detailed and complex morphologies within the growing bubbles created during devolatilization of melts.

8.2 DEVOLATILIZATION EQUIPMENT

As noted earlier, the polymeric melt systems in devolatilization have very low volatile concentration and therefore very high viscosities. Consequently their handling normally requires equipment with rotating elements similar or identical to polymer processing machinery such as single and twin screw extruders (SSEs, TSEs). These extruders are equipped with “venting ports,” which expose the molten polymer to low absolute pressure levels, superheating the polymer–volatile mixture, and thus enabling the removal of the volatiles.

In industrial practice, high production postreactor streams, as well as compounding and reactive processing operations, need to be devolatilized. The devolatilization process significantly affects the manufacturing cost and is critical to the quality of the product. The equipment is complex and costly and also involves the recovery of the volatiles. Todd et al. (3) and Mehta (4) reviewed, in some detail, the commercial equipment used for devolatilization, which we briefly summarize later in this Section.

Dilute polymer solutions containing relatively large amounts of volatiles are devolatilized in ordinary, relatively low-cost, single or multiple stage *flash tanks*. The flash tank is fed via a preheater that superheats the solution. The vapors of the foaming–boiling solution are removed at the top of the tank by a vapor takeoff system, and the concentrated solution is removed at the bottom via a gear pump.

As viscosity increases with decreasing volatile content, the flash tank becomes inefficient as bubbles are entrapped and redissolved upon discharge. The *falling-strand devolatilizer*, shown schematically in Fig. 8.2, was developed to answer this problem, and represents an improvement over the ordinary flash tank. Here the polymer solution is pumped at high superheat into thin strands that fall gravitationally into the vacuum tank. Free of hydrostatic or shear-induced pressure fields, the bubbles nucleate, grow, coalesce, and rupture so that the volatiles are released before they get trapped in the melt of the cachepot.

As volatile levels drop further, yielding very concentrated polymer solutions, the viscosity increases to a level that requires *rotary equipment* for forward pumping of the solution, which imparts surface renewal and often entraps vapor bubbles, for improved mass and heat transfer as well. There is a wide variety of rotary equipment available, from advanced *ribbon* devolatilizers, *vertical-cone* devolatilizers, and *disk-ring* devolatilizers for moderately viscous solutions, to *single* and *twin screw* devolatilizers and *thin-film*

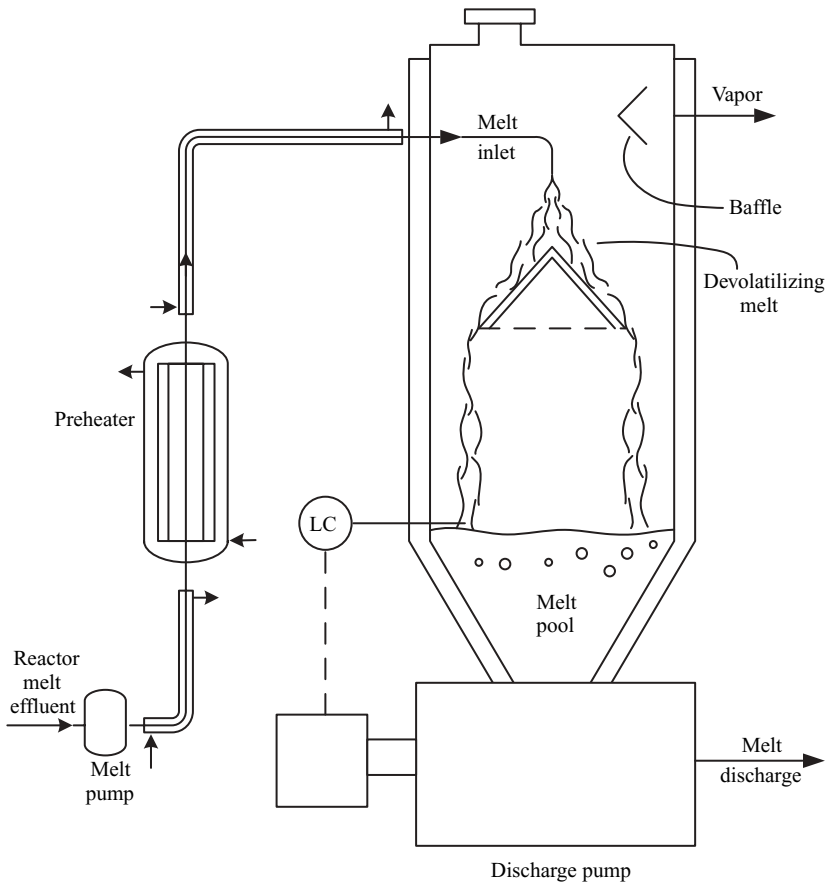


Fig. 8.2 A schematic view of a falling-strand devolatilizer.

devolatilizers for very high-viscosity solutions. Figure 8.3 shows a large, two-shaft reactor devolatilizer, and Fig. 8.4 shows a wiped thin-film evaporator.

In the case of devolatilization, industrial practice preceded theory, and the rich variety of equipment used in industry was developed without any thorough understanding of the molecular mechanisms by which devolatilization takes place. This, of course, is not an uncharacteristic phenomenon in technology, where practice often anticipates theory by providing “satisficing” design solutions.¹ These in turn become entrenched and reproduced in industry, even though there may perhaps be other better or even optimal and easily scalable design solutions.

1. The term *satisficing* was coined by the Nobel Prize-winning economist Herbert Simon, who suggested that in engineering (and management) as a *matter of principle* one should not look for an optimal solution, but only an adequate or *satisfactory* solution, since identifying the former may be a wasteful and time-consuming process with marginal added gain. Simon conveys a profound point regarding design and practice; however, this should not discourage us from the pursuit of theoretical understanding. The latter not only enhances our knowledge and may provide numerous other, possibly better, design solutions which, being theoretically driven, are more adaptable to industrial scale-up, but also enhances our understanding of current practices.

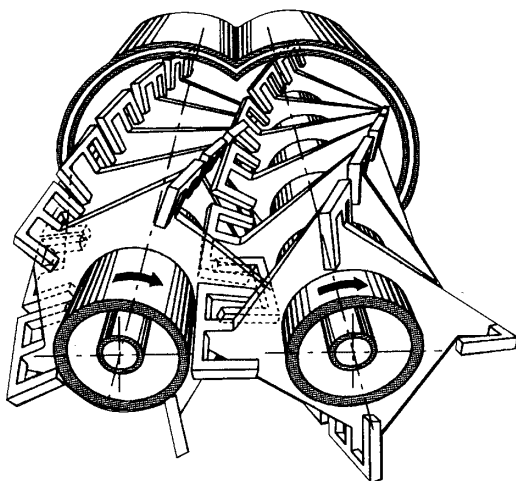


Fig. 8.3 Schematic representation of the List twin shaft co-rotating continuous mechanical and thermal processor. [Courtesy of the List Corporation.]

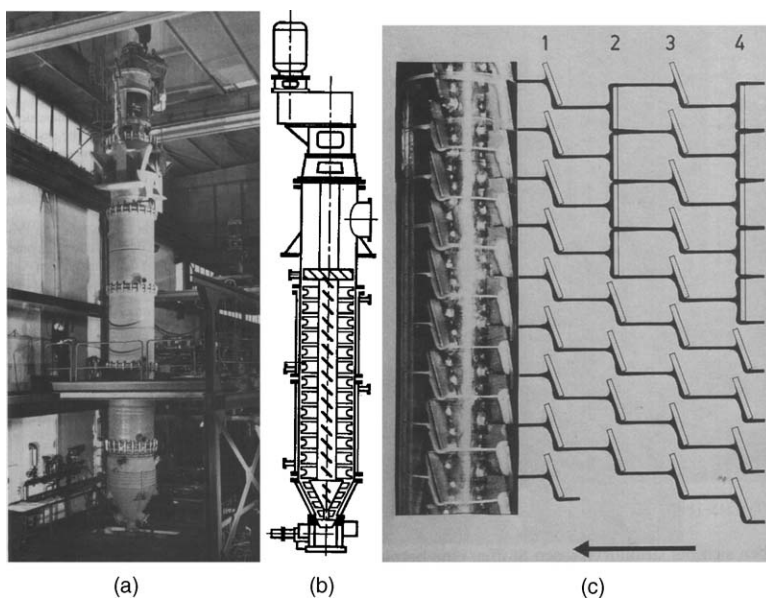


Fig. 8.4 Luwa Corporation Filmtruder (a) Filmtruder HS-1800. (b) Schematic representation of the Filmtruder. (c) Schematic representation of the falling- and wiped-film in the Filmtruder. [Courtesy Luwa Corporation.]

8.3 DEVOLATILIZATION MECHANISMS

Devolatilization of concentrated solution may start with an above atmospheric flash separation. This way the solvent and unreacted monomer can be easily and directly recycled. However, downstream all devolatilization equipment is operated under reduced

pressure or vacuum. This creates the superheat needed for separation and also makes the collection and condensation of the volatiles rather straightforward. In 1980, Newman and Simon (5) were the first to model theoretically the foaming mechanism in falling-film evaporators. They assumed a swarm of bubbles that grow, coalesce, rupture, and vacate their vapor content into the vapor space.

The pioneering researchers of devolatilization did not recognize, however, that at low volatile content when rotary equipment is used, in most cases, devolatilization takes place via a foaming-boiling process, with the vacuum level determining the supersaturation needed for bubble nucleation and growth. Rather, they initially conceived a molecular diffusion-controlled mechanism. Thus Latinen (6), who in 1962 was among the first to propose a theoretical mathematical model for devolatilization in SSEs, suggested that the mass transfer rate is controlled by molecular diffusion in the thin film deposited by the screw flight on the barrel surface in the partially filled vented region of the extruder, as shown in Fig. 8.5. The thin film, as it emerges from under the flight, is uniform in concentration C . As soon as the film surface is exposed to the vapor phase, its surface concentration drops to C^* , which is the volatile concentration in the solution at equilibrium with the vapor phase. This creates, for a short time period of one rotation, a high initial concentration gradient in the film, leading to possibly high mass transfer rates. Then the film is mixed with the rest of the solution in the rolling pool, and a new film, at a somewhat lower concentration, is deposited on the barrel. Therefore, by periodic *renewal* of the film, termed *surface renewal*, an overall high rate of mass transfer can be expected. This rate depends on the frequency of screw rotation, N , because the surface is renewed over a period of time of $1/N$, and on the

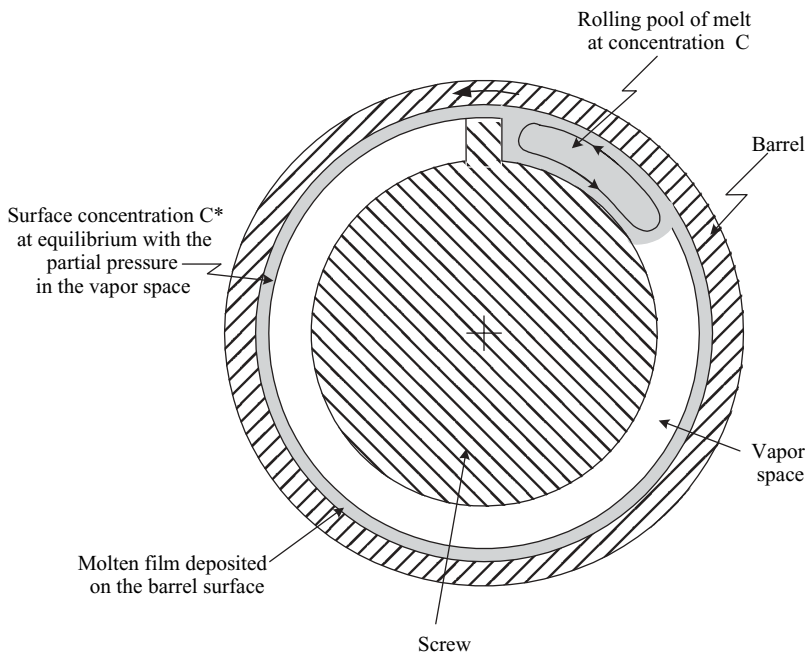


Fig. 8.5 Schematic representation of a screw section in the partially filled vented section of the extruder, according to Latinen (6).

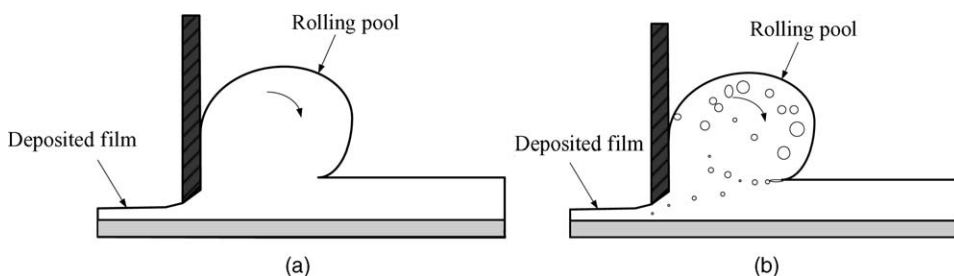


Fig. 8.6 (a) Schematic representation of the “rolling pool deposited film” mechanism. (b) The same mechanism, but with bubble formation and entrainment of vapor and noncondensable gas pockets, which act as nuclei in the boiling–foaming mechanism.

partial pressure of the volatile in the vapor space, which sets the value of C^* . According to this mechanism, the role of the vacuum level is limited only to setting the value of C^* . Of course, if the vapor phase would be swept with an inert gas, C^* could be reduced to practically zero without applying vacuum. The essence of this mechanism is shown in Fig. 8.6(a) consisting of a rolling pool and a deposited film exposed to low partial vapor pressure. However, we should note that pockets of vapor can become entrapped in the rolling pool, and provide the initial nucleation sites in wiped-film devolatilizers and extruders, as shown in Fig. 8.6(b).

Latinen (6) experimented with the separation of styrene from PS in a vented extruder. At the time, he did not have experimentally measured values of styrene diffusivity in molten PS and, therefore, from the experimentally measured separation he back-calculated the diffusivity. The values he attained were in the range of $10^{-9} \text{ m}^2/\text{s}$ at 200°C . Today we know that these values are at least one order of magnitude too high. Latinen compared the results he got to diffusivities in low-viscosity systems and they appeared to him to be too high as well, leading him to suggest possible explanations, such as melt surface roughness and foaming. He subsequently rejected the latter as being unlikely for such viscous solutions. Several others tried to improve the Latinen model (7,8) by accounting for the contribution of the rolling pool to the separation by diffusion, but they too obtained unreasonably high values for the back-calculated diffusivities, indicating that this mechanism is unsatisfactory for explaining the devolatilization mechanism.

The definite proof that, even at such low levels of volatiles, the devolatilization mechanism in vented SSEs is a foaming–boiling one came from the work of Biesenberger and Kessidis (9) in 1982, Mehta et al. (10) in 1984, and Tukachinsky et al. (11) in 1994.

Biesenberger and Kessidis repeated Latinen’s experiment in vented SSEs, but rather than applying vacuum over the vent, they flushed the vapor space with nitrogen. The separation they obtained was two orders of magnitude below the one obtained with vacuum and provided a reasonable match between the Latinen model and the real diffusivity values. Using the simple geometry of the co-rotating disk (CDP) processor, which enables accurate modeling as well as visual observation of the deposited film, Mehta et al. (10) concluded that, contrary to the surface renewal diffusion-controlled theory, the thinner the film, the poorer the separation efficiency. Moreover, they observed foaming on the deposited thin films on the disk surfaces. Finally, Tukachinsky et al. (11)

videotaped and observed the instantaneous foaming of 6000-ppm polystyrene–styrene solution in a 50-mm-diameter SSE upon the application of vacuum through an observation post in the barrel.

Yet in spite of all the evidence just presented, it is not impossible that at very low volatile levels the Latinen-type model may have some validity, but this likelihood appears to be small because foaming was observed at volatile concentrations as low as 50 ppm. Moreover, the likelihood further diminishes due to the fact that, as shown in Section 8.5, the diffusivity of small molecules in polymeric melts may drop by orders of magnitude, with dropping concentrations at these levels.

In the rolling pool-film configuration, however, normally nucleation, bubble growth and rupture take place primarily in the rolling pool. Nucleation is expected to be enhanced in the regions of stretching (negative pressure) in the rolling melt pool, and by entrainment of free, noncondensable gases at the pool–film junction where melt “folding” takes place by the moving solid surface, which creates microbubbles.

Bubble growth is enhanced by bubble deformation in the shear fields, and it was shown that the alternating pressure field existing in the rolling pool yields continuous bubble growth and bubble breakup. Bubble breakup in the shear fields increases the bubble population, and bubble rupture is induced in the bubbles close to the pool surface, where they release their content into the vacuum space. The total mass transfer surface significantly increases, because the sum total of bubble surfaces is much larger than that of the deposited film. For all these reasons, it is not surprising to find an increase in devolatilization efficiency with increasing speed of rotation.

In view of the foregoing discussion, and in order to better understand devolatilization in quantitative terms, in the following sections we will revisit elements of polymeric solution thermodynamics, briefly discuss diffusivity of small molecules in polymeric melts, review nucleation, bubble growth, bubble breakup, and bubble rupture theories, and elucidate them if possible in the shear-flow fields that occur in rotating-type devolatilizers. The chapter concludes with a discussion of experimental microscopic observations designed to “look” into the actual mechanisms taking place in boiling–foaming solutions, which led to surprising and unexpected results, and some suggestions for their theoretical formulation.

8.4 THERMODYNAMIC CONSIDERATIONS OF DEVOLATILIZATION

First we consider ideal solutions. An ideal solution is one where the solute and solvent molecules 1 and 2 have roughly the same size, shape, and force fields. An ideal solution obeys Raoult’s law:

$$P_1 = Y_1 P_1^0 \quad (8.4-1)$$

where Y_1 is the mole fraction of the solute, P_1 is the vapor pressure of the solute in equilibrium with the solution, and P_1^0 is the vapor pressure of the pure solute at the given temperature. Very dilute polymer solutions exhibit nearly ideal behavior. More concentrated solutions, however, exhibit large deviations from Raoult’s law. In one of the most notable early examples of polymer solution thermodynamics, Flory (12) and Huggins (13) independently dealt with this nonideal behavior. The result of this work is

the celebrated Flory–Huggins equation:

$$\ln\left(\frac{P_1}{P_1^0}\right) = \ln(1 - \phi_2) + \phi_2 + \chi_{12}\phi_2^2 \quad (8.4-2)$$

where ϕ_1 and ϕ_2 are the volume fractions of the solute and the polymer, respectively, and χ_{12} is the Flory–Huggins interaction parameter for a specific polymer–solvent system. This parameter is indicative of the similarity (affinity) of the two components and can be related to the solubility parameters δ_1 and δ_2 of the solute and polymer, respectively, by the following equation

$$\chi_{12} = \frac{V_1(\delta_1 - \delta_2)^2}{RT} \quad (8.4-3)$$

where V_1 is the *molar* volume of the solvent. Solubility parameters of common polymer–solvent systems are available in the literature (2,14). Values $\chi_{12} < 0.5$ denote mutual solubility, whereas, higher values denote increasing incompatibility. With Eq. 8.4-2, the interaction parameter can be computed from experimental measurement of vapor pressure over the solution. We note that, given the interaction parameter, the limiting solute concentration for phase separation can be obtained by setting $P_1/P_1^0 = 1$. This can be observed in Fig. 8.7, which plots P_1/P_1^0 vs. ϕ_1 with χ_{12} as a parameter. We note that phase separation takes place only at $\chi_{12} > 0.5$.

At very low solute concentrations ($\phi_2 \rightarrow 1$), Eq. 8.4-2 reduces to

$$\ln\left(\frac{P_1}{P_1^0}\right) = \ln(1 - \phi_2) + 1 + \chi_{12} \quad (8.4-4)$$

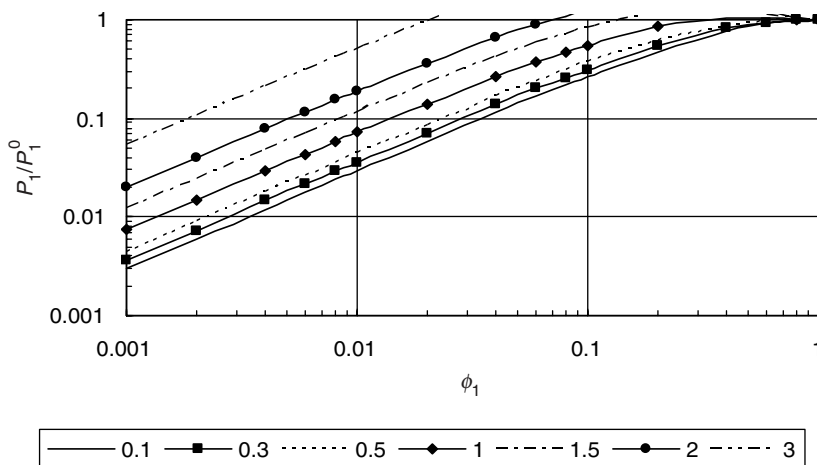


Fig. 8.7 The Flory–Huggins equation with χ_{12} as a parameter.

Equation 8.4-4 can be written with good approximation as

$$P_1 = \frac{\rho_2}{\rho_1} W_1 P_1^0 e^{(1+\chi_{12})} \quad (8.4-5)$$

where ρ_1 and ρ_2 are the solute and polymer densities, respectively, and W_1 is the weight fraction of the solute in the solution.

Solubility is very frequently expressed in the form of Henry's law, where P_1 is proportional to the weight fraction of the solute

$$P_1 = HW_1 \quad (8.4-6)$$

and H at low concentrations becomes

$$H = \frac{\rho_2}{\rho_1} P_1^0 e^{1+\chi_{12}} \quad (8.4-7)$$

The advantage of expressing H in terms of the Flory–Huggins parameter χ_{12} is that the latter is often insensitive to temperature, and may better reflect the dependence on concentration than H . Its disadvantage is that it does not apply near and above the critical temperature of the volatile component.

If the pressure over a solution is reduced below the partial pressure of the solvent over the solution, then the solution is said to be *superheated*. The *degree* of superheat is represented by the difference between the equilibrium partial pressure of the solvent over the solution and the total pressure (vacuum level) over the solution $P_1 - P_0$. The higher the vacuum level, the higher the superheat at a given concentration and temperature. Increasing the temperature at a fixed pressure level, of course, also increases the superheat.

Simon (15) suggests that, depending on the degree of superheat, there are three rate-limiting mechanisms for devolatilization. The first he calls "free boiling." This occurs at high degrees of superheat and low viscosities, namely, volatile rich conditions. Vapor bubbles are initiated at a high rate, grow, and burst. The second mechanism, he calls "bubble growth." Here the superheat is lower and the viscosity is higher; consequently, the rate-determining step is bubble nucleation and growth. The third mechanism takes place at very low superheat levels where few bubbles are formed and the rate-determining step is diffusion.

Increasing the temperature of the solution and reducing the pressure above the solution as much as possible can maximize the superheat. The former is bound by the thermal sensitivity of the polymers and the latter by technical and economic factors of the vacuum generating solvent separation and condensation systems.

Example 8.1 The Degree of Superheat and Vapor Volume for a Desired Separation

Level We consider a 10,000 ppm styrene–PS solution at 220°C, which has to be devolatilized to 1000 ppm. Disregarding the rate of devolatilization, we wish to determine the minimum superheat necessary in order to achieve the required separation. We assume that

$\rho_1 = \rho_2$, $\chi_{12} = 0.3$, and $P_1^0 = 450$ kPa. Using Eq. 8.4-5, we first obtain the partial pressure over the solution at 10,000 ppm:

$$P_1 = (0.01) \times (450 \times 10^3) \times e^{(1+0.3)} = 16.51 \text{ kPa}$$

or 123.8 mmHg. The partial pressure over the desired solution of 1000 ppm is given by:

$$P_1 = (0.001) \times (450 \times 10^3) \times e^{(1+0.3)} = 1.65 \text{ kPa}$$

or 12.4 mmHg. Therefore the minimum degree of superheat that is required is $16.51 - 1.65 = 14.86$ kPa or 111.5 mmHg.

Next we want to calculate the volume of vapors, at 1.65 kPa and 220°C, to be removed for each kilogram of solution. We will assume that the vapor behaves as an ideal gas. For each kilogram of solution we remove 9 g of solute. The molecular weight of styrene is 104.16, and therefore we remove $9/104.16 = 0.0864$ mol, which has a volume of:

$$V = \frac{nRT}{P} = \frac{0.0864(\text{mole}) \times 8.31(\text{J/mole K}) \times (273 + 220)(\text{K})}{1650(\text{Pa})} = 0.215 \text{ m}^3$$

Example 8.2 Vacuum Staging If the volatile concentration is relatively high, removal of all the volatiles at the vacuum level needed to accomplish the desired separation will result in large vapor volumes, and hence a larger and more expensive vacuum-pumping system. In such cases, vacuum staging will be advantageous. By staging, we can remove the bulk of the volatiles at a higher pressure level (low vacuum levels) and remove the leftover volatiles at the low final pressure (high vacuum). Progressive staging becomes even more important if more than 90% removal is required.

Generally, it can be shown (1,16) that the optimum pressure profile P_j over j stage separation, which minimizes the volume of vapor when the temperature is uniform, is given by

$$P_j = P_0 a^j \quad 1 \leq j \leq N$$

where

$$a = \left(\frac{P_N}{P_0} \right)^{1/N}$$

where P_j is the pressure level in stage j , and P_N is the pressure in the last stage that sets the final separation. For example, in a two-stage separation $a = (P_2/P_0)^{1/2}$, and the pressure in stage one will be $P_1 = P_0(P_2/P_0)^{1/2}$. Thus in the previous example, if in order to get the final separation we need a pressure of 1.65 kPa, then the pressure in the first stage should be $16.51(1.65/16.51)^{1/2} = 5.22$ kPa. The equilibrium weight fraction in stage one, via Eq. 8.4-5 is $W_1 = 5220/(450 \times 10^3 \times e^{(1+0.3)}) = 0.0032$. Thus, in the first stage we drop the volatile from 10,000 ppm to 3200 ppm, and in the second stage to the required 1000 ppm. From

these we can calculate the volumes to be removed in each stage, as shown in the following table:

	Feed	Stage 1	Stage 2
Weight fraction (ppm)	10,000	3200	1000
Partial pressure (kPa)	16.51	5.22	1.65
Removed weight (g/kg)		6.8	2.2
Removed (g · mol)		0.06825	0.02112
Removed volume (m ³ /kg)		0.0501	0.0513

Thus, the total vapor volume to be removed in a two-stage operation is 0.1023 m³/kg, as compared to 0.215 m³/kg, or about one-half the volume.

8.5 DIFFUSIVITY OF LOW MOLECULAR WEIGHT COMPONENTS IN MOLTEN POLYMERS

Larry Duda and Jim Vrentas were the first to systematically study the diffusion of small molecules in molten polymers, formulate a free volume-based theoretical model, and elucidate the sharp dependence of the diffusion coefficient on temperature and concentration.² Figure 8.8 shows diffusivities of toluene in polystyrene as a function of concentration and temperature. The values were computed using the Vrentas and Duda (17) free volume model and, as shown, coincide well with available data.

This model, based on the earlier work of Fujita (18), currently appears to be the most effective theory to describe diffusion both above and below T_g . It adopts the notion that all transport processes are governed by the availability of free volume in the system. *Free volume* is a useful concept representing a specific volume \hat{V}_{fv} present as holes of the order of molecular (monomeric) dimensions or smaller, which together with the specific volume of the molecules themselves, \hat{V}_0 , gives the total specific volume, \hat{V}

$$\hat{V} = \hat{V}_0 + \hat{V}_{fv} \quad (8.5-1)$$

As the temperature above T_g decreases, the kinetic energy of chain segments decreases as well and the volume contracts, sharply reducing the relative amount of free

2. This early work was started by Larry Duda and Jim Vrentas in the 1960s at the Dow Chemical Company, in a study of styrene polymerization reactors and downstream devolatilizers, and was triggered by the lack of any reliable data on diffusion coefficients of small molecules in molten polymers. Their study continued from the 1970s on at Pennsylvania State University, where the theoretical model based on Fujita's earlier work (18) was the subject of detailed experimentation, indicating the sharp temperature and concentration dependence of the coefficient. Fujita himself became interested in the diffusion problem while working on fish drying for the Japanese fishery department, at which time he observed a strong concentration dependence of the diffusion coefficient. (Larry Duda, private communication, 2002.)

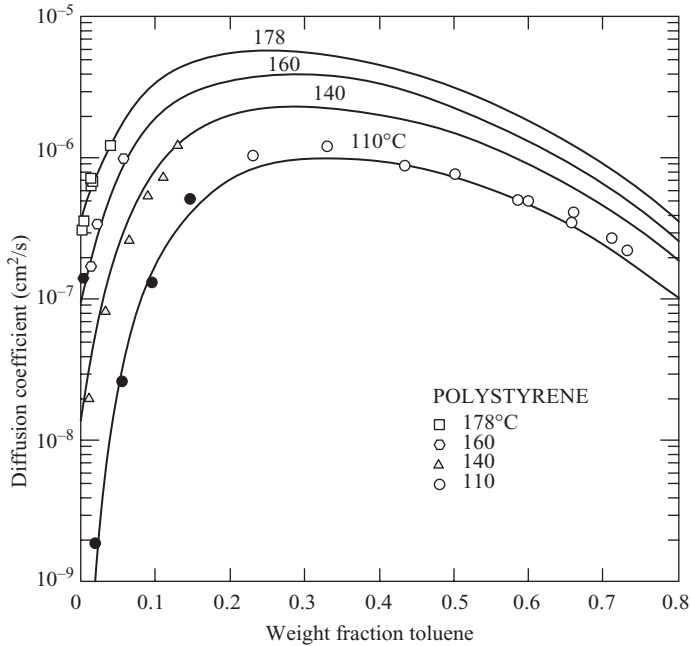


Fig. 8.8 Free volume theory prediction of mutual binary diffusion coefficient for the toluene–PS system based on parameters (19). [Reproduced by permission from J. L. Duda, J. S. Vrentas, S. T. Ju and H. T. Liu, “Prediction of Diffusion Coefficients,” *A.I.Ch.E. J.*, **28**, 279 (1982).]

volume between the polymeric chains approaching a constant value at T_g . Molecules diffuse by successive discrete jumps, provided a vacancy of sufficient size appears adjacent to the molecule and the molecule possesses sufficient energy to break the nearest-neighbor contacts. Assuming that the vacancy and energy availabilities are governed by a Boltzmann probability function, and that only that portion of the free volume is available for diffusion that is continuously redistributed by thermal energy, Vrentas and Duda derived the following expression for the diffusion coefficient of a solvent in polymers:

$$\mathcal{D} = (1 - \phi_1)^2 (1 - 2\phi_1\chi) \mathcal{D}_0 \exp(-E/RT) \exp\left\langle \frac{-\gamma(w_1 \hat{V}_1^* + w_2 \zeta \hat{V}_2^*)}{\hat{V}_{fh}^*} \right\rangle \quad (8.5-2)$$

where ϕ_1 is the solvent volume fraction; \mathcal{D}_0 is a constant preexponential term; E is the molar energy a molecule needs to overcome the attractive forces between nearest neighbors; γ is an overlap factor (between 0.5 and 1.0) to account for the fact that the same volume is available to more than one molecule; \hat{V}_1^* and \hat{V}_2^* are the smallest holes that need to form before a solvent and polymer segment, respectively, can make a jump; w_1 and w_2 are the weight fractions of solvent and polymer; ζ is the ratio of molar volumes for the solvent and polymer segment involved in a jump; and \hat{V}_{fh}^* is the hole free volume, namely, that portion of the free volume that is available for diffusion. A detailed procedure for computing the diffusivity and evaluating the various parameters is given by Zielinski and Duda (20).

8.6 BOILING PHENOMENA: NUCLEATION

When does a liquid boil? Clearly, boiling at constant pressure—say, atmospheric pressure—begins when we increase the temperature of a liquid or solution and the vapor pressure reaches a pressure of one atmosphere. Alternatively, the pressure over a liquid or solution at constant temperature must be reduced until it reaches the vapor pressure at that temperature (e.g., vacuum distillation). Yet it is well known that liquids can be superheated (and vapors supersaturated) without the occurrence of phase transfer. In fact, liquids must *always* be superheated to some degree for nucleation to begin and for boiling to start. That is, the temperature must be raised *above* the value at which the equilibrium vapor pressure equals the surrounding pressure over the liquid, or the pressure must be reduced below the vapor pressure value. As defined earlier, these differences are called the *degree of superheat*. When the liquid is superheated, it is metastable and will reach equilibrium only when it breaks up into two phases.

There is a thermodynamic upper limit to the degree of superheat of a homogeneous liquid system, above which the metastable state cannot exist. In fact, phase separation occurs and *homogeneous boiling* begins below this limit when the *kinetic* limit of superheat is reached. This happens when bubbles begin to nucleate within the homogeneous liquid at a significant rate. Homogeneous nucleation theories, developed by Blander and Katz (21), describe a process that leads to the formation of density fluctuations in the metastable liquid, creating vapor embryos that may either grow or disappear due to vaporization or condensation, respectively. According to these theories, which are based on a vast amount of earlier work reviewed in many available texts, the rate of homogenous nucleation J takes the form:

$$J = A e^{(-B)} \quad (8.6-1)$$

where A and B are groupings of thermodynamic properties as given (21) in the following expression:

$$J = 3.73 \times 10^{35} \left(\frac{\rho_l^2 \sigma}{M^3 B} \right)^{1/2} \left[\exp \frac{-1.182 \times 10^5 \sigma^3}{T_0 (P_e - P_0)^2} \right] \quad (8.6-2)$$

where J (#/cm³·s) is the rate at which nuclei are created in a unit volume; ρ_l (g/cm³) is the density of the liquid; σ (erg/cm²) is the surface tension; M (g/mol) is the molecular weight of the volatile component; B is a factor equal to 2/3 (and 1 for cavitation); T_0 (K) is the temperature; P_e (at) is the equilibrium vapor pressure at T_0 (K); and P_0 (at) is the pressure in the liquid. The pressure P_e is the actual pressure within the bubble and is not equal to the equilibrium vapor pressure of the liquid P_1^0 . They are related as follows

$$P_e = \eta P_1^0 \quad (8.6-3)$$

where

$$\eta = \exp \frac{v_l(P_0 - P_1^0)}{RT_0} \quad (8.6-4)$$

where v_l is the specific volume of the liquid.

The resulting expression, Eq. 8.6-2, has a weak temperature-dependent preexponential term, and a temperature sensitive exponential term. The latter contains the surface tension to the third power and the superheat to the second power. With increasing temperature the surface tension drops, and superheat increases, giving rise to an increase of orders of magnitude in J over a very narrow temperature range.

The computed kinetic limit of superheat of *n*-butane, for example, is 378.3 K and the experimentally measured³ value is 376.9 K. With ordinary liquids, the kinetic limit of superheat approaches the critical temperature ($T_{kls}/T_{crit} = 0.89$). However, under ordinary conditions, when the liquid is in contact with solid surfaces, it boils far below the kinetic limit of superheat. Thus, the boiling point of *n*-butane, for example, is 272.5 K. Similarly, the theoretical kinetic superheat of water is 300°C, while the ordinary boiling point of water is 100°C.

When the vapor phase is generated at a solid interface rather than in the bulk of the liquid, the process is known as *heterogeneous nucleation*. Heterogeneous nucleation theories on smooth surfaces yield similar expression to Eq. 8.6-1 for J , with modified groupings A' and B' that account for the contribution of geometry and energy of the solid surface (22).

Smooth surfaces in and of themselves do not substantially reduce the kinetic limit of superheat. However, ordinary surfaces have macroscopic and microscopic scratches—gouges, grooves, and pits of the order of 1–5 μm —and the preexistence of gas or vapor phases in these surface imperfections generates the nuclei in heterogeneous boiling. If the surfaces are not perfectly wetted by the liquid, as the case usually is, it may be expected that many of these cavities will contain entrapped gas, and hence act as bubble initiators, thereby reducing the kinetic limit of superheat to negligibly small values. Hence, the common experience that boiling starts at the solid wall of any kettle (where the superheat is even higher due to the outside heating sources).

Indeed, it has been proven experimentally that, if prior to heating, the liquid is pressurized to very high pressures, thereby dissolving the gas in these cavities into the liquid, the superheat needed for nucleation increases dramatically. Of course, in the presence of these bubble-generating cavities, the degree of superheat needed for boiling is significantly reduced. In addition, a liquid saturated at a given temperature (say at room temperature) with a gas such as air, will activate additional bubbles with increasing temperature, as a result of decrease in solubility with increasing temperature. The same happens when the pressure is reduced over a supersaturated and pressurized liquid, as is the case when a soda bottle is opened.

Finally, it is worth mentioning that the *cavitation* phenomenon observed in low viscosity liquids is also caused by (explosive) boiling induced by sudden reduction of pressure, such as that occurring in regions behind moving surfaces, such as impellers, or as the result of flow acceleration (Bernoulli effect) (23).

3. A common method to measure the kinetic limit of superheat is by the exploding drop technique. In this technique a small droplet of the liquid is placed in a column of another immiscible liquid and either the temperature is raised until homogenous boiling begins or the pressure is reduced.

8.7 BOILING–FOAMING MECHANISMS OF POLYMERIC MELTS

The devolatilization process of polymeric melts is generally a boiling–foaming⁴ mechanism that takes place within the bulk of the homogenous liquid phase. Thus, one would expect that homogenous nucleation theories should be applicable to devolatilization. However, these theories fail to give a satisfactory explanation for the boiling–foaming process at the temperature and pressures at which it is practiced. These theories for polystyrene–styrene systems, for example, predict that degrees of superheat far in excess of processing temperatures are required to attain observed nucleation rates. In fact, heterogeneous nucleation theories are not useful in predicting the experimental observation, either. Moreover, bubbles resulting from heterogeneous nucleation at the solid containing walls would by and large remain close to the wall and will not move quickly into the bulk because of the very high viscosities of the melt. The same holds true for bubbles originating from entrapped gasses and vapors in wall cavities and scratches, which are the major sources of heterogenous nucleation under ordinary conditions.

What, then, is the nucleation mechanism in the bulk of these viscous molten polymer solutions?

In a polymeric system, it would be reasonable to examine the possibility that the free volume concept described earlier, which explains so well phenomena like molecular diffusion and viscosity, might perhaps also explain nucleation phenomena. The critical radius r_e of a stable bubble can be obtained from a simple mechanical-force balance, yielding the Laplace equation:

$$r_e = \frac{2\Gamma}{P_e - P_0} \quad (8.7-1)$$

where Γ is the surface tension. Bubbles smaller than r_e will shrink and disappear and larger ones will grow. For a devolatilizing system of, say, 1000–10,000 ppm styrene in polystyrene (PS), the critical radius can be shown to be of the order of 1–12 μm (24). However, the free volume theories involve holes of the order of molecular dimensions and, as shown by Lee and Biesenberger (24) and Lee (25), the probability of finding free volume of the critical bubble size approaches zero.

Any explanation of nucleation in polymer melts at devolatilization conditions must also explain the experimental observation of the catalytic effect of shearing on bubble nucleation, whereby profuse foaming starts with the slightest shearing. Lee and Biesenberger investigated this phenomenon in some detail. They concluded that a melt saturated with entrained bubbles in a rolling-pool configuration, shown in Fig. 8.6(b), foams immediately following the application of vacuum, without being agitated or experiencing deformation. Otherwise, deformation, however slight, is required in addition to positive superheat (24). In deformation-induced nucleation, one should consider the possibility that shearing flow, which normally exists in devolatilizers, might shift the distribution of free volume toward the large end to give reasonable

4. The term foaming comes from the fact that the melt is very viscous and, when the devolatilization process begins, the melt fills up with bubbles that appear as foam. Sometimes, as in foaming processes, low boiling-point additives are added to enhance the process.

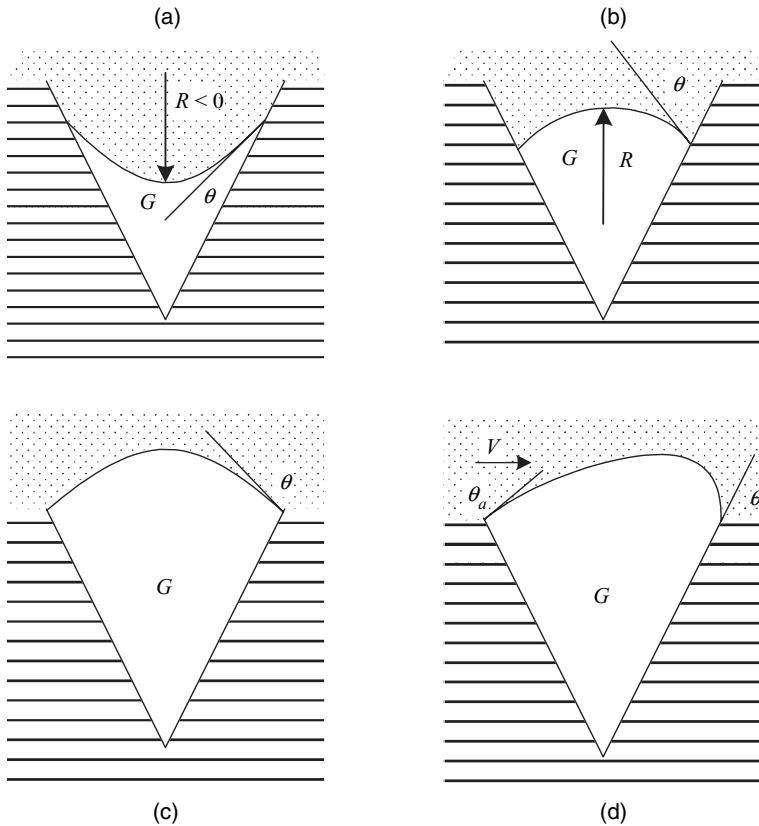


Fig. 8.9 Schematic representations of metastable cavity models.

probability for the existence of holes of the critical dimensions. However, Lee and Biesenberger ruled out this possibility as well, on the ground that very low shearing rates, well within the Newtonian range, sufficed to produce swarms of bubbles in their experiments.

They suggested explaining bubble nucleation by the preexistence of Harvey-type⁵ (26) heterogeneous germ-nuclei, or free-streaming nuclei, located within the cracks and crevices of microscopic particulate matter believed to be present in all liquids. It presumes that within these acute-angle cracks and crevices, pockets of gas or vapor can exist in equilibrium within the liquid indefinitely, until activated by superheat and shearing. Figure 8.9 illustrates conical-shaped crevices and various alternative configurations of gas pockets with negative and positive radii of curvature. In the former case, the surface tension partly supports the pressure of the liquid, and the pressure within the pocket, according to Eq. 8.7-1, is less than that in the liquid: $P_e < P_0$. The deeper the penetration, the smaller the radius of curvature will be, and the lower the pressure in the gas pocket will be, until an equilibrium state with the liquid prevails and stable pockets are created.

5. During World War II Harvey et al. investigated the well-known phenomenon of bubbles appearing in the blood and tissue of divers surfacing too quickly after deep diving.

Alternatively, it can be argued, as did Harvey et al., that the contact angle between the liquid and the hydrophobic surface in this case can reestablish itself as the meniscus moves, due to absorption or release of vapor, and therefore it is unstable. This could explain the existence of relatively large, stable pockets of vapor and/or air dispersed within the melt. Lee and Biesenberger (24) estimated that pockets of the size of $1\mu\text{m}$ could exist in the melt, and these fall within the range of critical nuclei for bubble formation. When superheat is applied, the pressure within the pockets exceeds that in the liquid and the radius of curvature becomes positive, as in Fig. 8.9(b) and 8.9(c).

Harvey et al. further argued that in order to detach a gas pocket from the solid surface, it is necessary to reduce the receding angle θ_r below a critical value. This, claim Lee and Biesenberger, implies a yield phenomenon that occurs when the pocket is swollen to the cavity mouth, where contact angles are likely to experience a sharp increase and dislodge the gas/vapor phase into a bubble [Fig. 8.9(d)]. Possibly, the role of shear in inducing nucleation may be related to this phenomenon. Indirect support for this proposition comes from their experimental work with LDPE and CCl_2F_2 as a volatile foaming agent, which revealed that the number of bubbles formed per unit volume increased linearly with the capillary number, expressing the ratio of laminar flow-induced shear forces on the bubble-to-surface tension forces (27):

$$\text{Ca} = \frac{R\mu\dot{\gamma}}{\Gamma} \quad (8.7-2)$$

where μ is the melt viscosity, Γ the surface tension, and $\dot{\gamma}$ the shear rate.

As in devolatilization, Harvey-type free-streaming nuclei are also invoked in explaining cavitation nucleation in water and low viscosity liquids. Brennen (28) points out that “many of the observations of the onset of cavitation appear to be the result of free stream nuclei rather than surface nuclei.” Indeed, he points out that cavitation nuclei number density distributions were measured by holography in water tunnels. This method, however, does not distinguish between the solid particles and microbubbles that may be present in the liquid, and the exact character of these free-streaming nuclei still needs to be elucidated. Moreover, a rather esoteric suggestion was made regarding continuous production of nuclei by cosmic radiation. Yet, Greenspan and Tschiegg (29) showed that removal of particles larger than $0.2\mu\text{m}$ from water raised its tensile strength to 200 bar, and Marschall et al. (30) showed that incorporating small spherical hydrophobic particles into the water significantly reduced the tensile strength of purified water. Furthermore, it was shown that imposing high pressure on water, which presumably dissolves the entrained gas pockets and destroys the nuclei, raises the tensile strength and kinetic limit of superheat of water. All this evidence seems to support the free-streaming nuclei theory, though no direct experimental observations on their nature have yet been made.

In devolatilization with viscous polymeric melts, it is difficult, of course, to carry out similar experiments and prove indirectly that free-streaming nuclei may play a similar role, but microscopic particles originating from the monomers and catalyst systems are likely to be found in the polymeric product. Moreover, it is well known that the addition of fine powders and solid particles induces foaming. Therefore, the Biesenberger–Lee proposition seems plausible.

As mentioned earlier, entrained free air cannot survive indefinitely in a liquid, but it can still play a role in the devolatilization process in rotary machinery, where the moving surface can drag free air into the melt, forming small bubbles that can serve as nuclei for

further bubble growth. At atmospheric pressures, air entrainment takes place at a critical modified capillary number of 1.18 (31):

$$Ca = \frac{\mu V}{\Gamma} \quad (8.7-3)$$

where V is the velocity of the solid surface. According to this criterion high viscosity induces gas entrainment, but it is questionable if this criterion holds at low pressures.

8.8 ULTRASOUND-ENHANCED DEVOLATILIZATION

In devolatilization, the superheat for nucleation and boiling, at a fixed temperature, is set by the absolute pressure (vacuum) that can be attained. The upper limit of the superheat is attained by setting absolute pressure to zero. Triaxial stretching of a liquid may reduce the ambient pressure to negative values. That can be achieved by imposing the liquid to an ultrasonic source. The acoustic field causes high-frequency stretching–compression stresses within the liquid which, in ordinary liquids, can result in bubble nucleation and acoustic cavitations (23). The bubble nucleation rate may be catalyzed by ultrasonic fields, possibly both as a result of the increased instantaneous superheat and the imposed deformation, which might overcome the yielding of the Harvey-type activated nuclei, as was suggested in shear fields. Tukachinsky et al. (32) studied the effect of ultrasonic fields on polymer strand devolatilization and observed a significant increase in separation, as shown in Fig. 8.10.

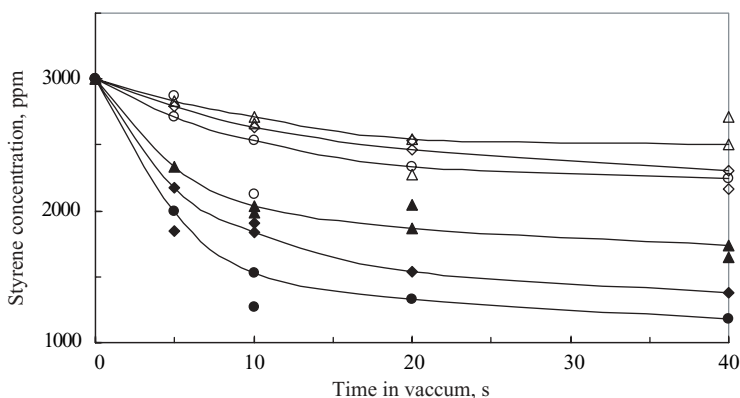


Fig. 8.10 Residual styrene concentration in PS extruded at 225°C. The open symbols refer to experiments without ultrasound, while the filled ones refer to experiments where ultrasound radiation was applied. The parameter is the absolute pressure in the chamber. Triangles: 150 mmHg; squares: 50 mmHg, and circles: 12 mmHg. [Reprinted by permission from A. Tukachinsky, Z. Tadmor, and Y. Talmon, “Ultrasound-enhanced Devolatilization in Polymer Melt,” *AIChE J.*, **39**, 359 (1993).]

8.9 BUBBLE GROWTH

Once a nucleus of a critical size is formed in a superheated solution, the volatile component in the liquid phase begins diffusing to the interface and vaporizing into the vapor space. Consequently the pressure in the bubble increases, and it will begin to grow in size. The rate of bubble growth is a complex and unsteady process affected by diffusion, heat transfer, and viscous forces. Depending on the system and conditions, one or more of these transport operations may be the rate-controlling step. Favelukis and Albalak (33) review a spectrum of solutions proposed in the literature for a single spherical bubble in a quiescent superheated Newtonian liquid of infinite extent, and discuss their relevance or rather lack of relevance to devolatilization. The latter is due to the fact that in devolatilization of polymeric liquids the liquid is non-Newtonian, there are swarms of bubbles, the liquid is sheared and therefore the bubbles are deformed, and, more importantly, microscopic studies, discussed below, indicate a far more complex mechanism than simple diffusion into the surface of a growing bubble.

Nevertheless, in order to get some insight into the mechanism of bubble growth, and following the classic derivation of Scriven (34), we derive here the particular case for the rate of growth of a single bubble in a quiescent infinite liquid (Fig. 8.11), with the viscous forces acting as the rate-controlling step.

The equation of continuity for an incompressible liquid, and with spherical symmetry, reduces to

$$\frac{\partial}{\partial r}(r^2 v_r) = 0 \quad (8.9-1)$$

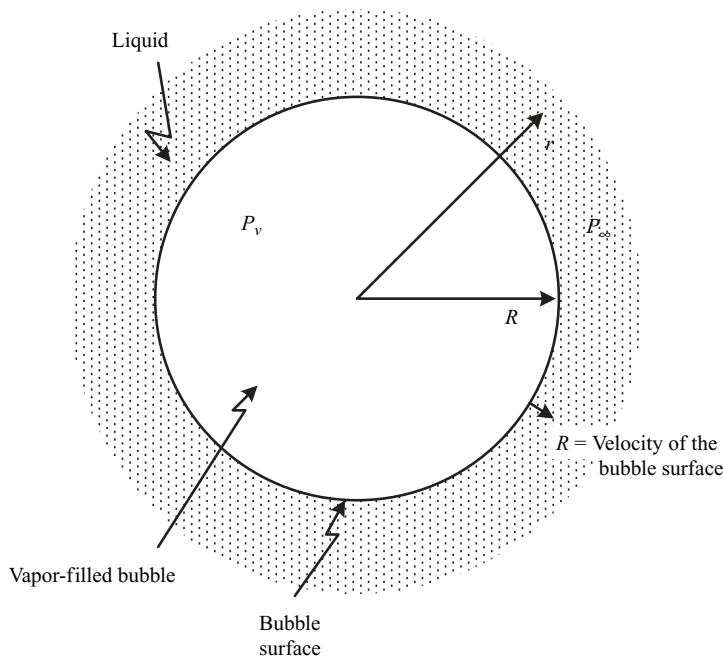


Fig. 8.11 Diffusion of volatiles into a growing bubble of radius R . The pressure inside the bubble is P_v , the pressure in the liquid far from the bubble surface is P_∞ , the bubble surface is moving radially at velocity \dot{R} .

which can be integrated to give

$$v_r r^2 = f(t) \quad (8.9-2)$$

Since $v_r r^2$ is a function of time alone, it must hold everywhere in the liquid, including at the surface of the bubble. The surface itself moves at velocity \dot{R} , while the liquid adjacent to the surface moves with velocity $v_r(R)$, which is different from that of the surface because some of the volatile material evaporates, and the mass flow rate is given by $4\pi R^2 \rho_L [\dot{R} - v_r(R)]$, which is the rate of vaporization of volatile material into the bubble. We now can write a mass balance over the bubble surface:

$$\frac{d}{dt} \left(\frac{4}{3} \pi R^3 \rho_G \right) = 4\pi R^2 \rho_L [\dot{R} - v_r(R)] \quad (8.9-3)$$

where ρ_L and ρ_G are the densities of the gas and liquid phases, respectively. Assuming constant density of the gas in the bubble Eq. 8.9-3 reduces to

$$v_r(R) = \dot{R}(\rho_L - \rho_G)/\rho_L = \varepsilon \dot{R} \quad (8.9-4)$$

Equation 8.9-2 suggests that the product of the radial velocity and the square of the radius is constant anywhere in the liquid phase, which gives the following continuity condition:

$$v_r r^2 = \varepsilon \dot{R} R^2 \quad (8.9-5)$$

Next we turn to the Navier–Stokes equation, which for creeping flow of incompressible liquids, neglecting inertial and gravitational forces, reduces to

$$0 = -\frac{\partial P}{\partial r} + \mu \left[\frac{1}{r^2} \frac{\partial^2}{\partial r^2} (r^2 v_r) \right] \quad (8.9-6)$$

Substituting Eq. 8.9-5 into Eq. 8.9-6 and integrating over the radius from the bubble surface to infinity results in

$$\frac{\partial P}{\partial r} = 0 \quad (8.9-7)$$

which after integrating from the surface of the bubble to infinity, gives

$$P_\infty - P_R = 0 \quad (8.9-8)$$

where P_∞ is the ambient pressure, and P_R is the pressure in the *liquid* phase at the bubble surface. Next we make a force balance at the bubble surface, much like with the Laplace

equation, but for this case involving bubble growth, we must add the viscous forces to the pressure drop to give

$$P_B - P_R - \tau_{rr} = 2\Gamma/R \quad (8.9-9)$$

where P_B is the uniform pressure in the bubble, Γ is the surface tension, and τ_{rr} is the radial component of the viscous stress tensor in the liquid, given by

$$\tau_{rr} = -2\mu \frac{\partial v_r}{\partial t} \quad (8.9-10)$$

Substituting Eq. 8.9-8 and Eq. 8.9-10 into Eq. 8.9-9 results in:

$$P_B - P_\infty - \frac{2\Gamma}{R} = \frac{4\mu}{R} \left(\frac{dR}{dt} \right) \quad (8.9-11)$$

which is a special case of the Rayleigh equation with the inertial terms neglected. At constant ambient and bubble pressure, Eq. 8.9-11 may be integrated with the initial condition of $R = R_0$ at time zero:

$$R(t) = R_{cr} + (R_0 - R_{cr}) \left[\exp \frac{(P_B - P_\infty)t}{4\mu} \right] \quad (8.9-12)$$

where

$$R_{cr} = \frac{2\Gamma}{P_B - P_\infty} \quad (8.9-13)$$

is the equilibrium critical radius of the bubble in the absence of viscous forces.

We therefore find that in this special case the bubble radius grows exponentially in time. The pressure drop is a forward-driving force for bubble growth and viscosity is a retarding force.

8.10 BUBBLE DYNAMICS AND MASS TRANSFER IN SHEAR FLOW

Much of the devolatilization takes place in rotating machines where, by and large, the bubbles formed are exposed to a shear field. We must therefore consider the effect of shear fields on bubble shape and mass transfer. It has been shown that the deformation of a bubble (inviscid droplet) in a Newtonian liquid in simple shear creeping flow is governed by a single dimensionless parameter, the capillary number Ca , expressing the ratio of shear to surface tension forces, defined in Eq. 8.7-2 with the equivalent radius a (radius of a sphere of equal volume) replacing R . At small deformations ($Ca \ll 1$) the bubble becomes an ellipsoid, oriented along

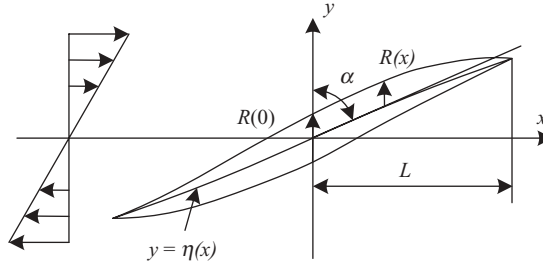


Fig. 8.12 Deformation of a bubble in simple shear flow at $Ca \gg 1$. $R(x)$ is the bubble radius as a function of coordinate x ; L is the half-length of the bubble; α is the inclination angle; and $y = \eta(x)$ is the position of the bubble centerline.

the principal axis of deformation of the undisturbed flow, with the G.I. Taylor deformation parameter D , equaling the capillary number Ca

$$D = \frac{l - b}{l + b} = Ca \quad (8.10-1)$$

where l and b are, respectively, the major and minor axes of the ellipse inclined 45° in the direction of flow.

In devolatilizing systems, however, $Ca \gg 1$ and the bubbles deform into slender S-shaped bodies, as shown in Fig. 8.12. Hinch and Acrivos (35) solved the problem of large droplet deformation in Newtonian fluids. They assumed that the cross section of the drop is circular, of radius a , and showed that the dimensionless bubble surface area, A^* , defined as the ratio of the surface area of the deformed bubble A to the surface area of a spherical bubble of the same volume, is approximated by (36):

$$A^* = \frac{A}{4\pi a^2} = 1.41 Ca^{1/4} \quad (8.10-2)$$

and the dimensionless half-length of the bubble L^* , and the slenderness ratio $R^*(0)/L$, where $R^*(0)$ is the dimensionless radius of the cross section at the center,

$$R^*(0) = \frac{R(0)}{a} = 0.578 Ca^{-1/4} \quad (8.10-3)$$

are given, respectively, by

$$L^* = \frac{L}{a} = 3.45 Ca^{1/2} \quad (8.10-4)$$

and

$$\frac{R^*(0)}{L^*} = \frac{R(0)}{L} = 0.167 Ca^{-3/4} \quad (8.10-5)$$

Canedo et al. (36) confirmed these predictions for bubbles in a Couette flow apparatus.

Favelukis et al. (37,38) dealt with the problem of droplet deformation in extensional flow with both Newtonian and non-Newtonian Power Law model fluids, as well as bubble breakup. For the Newtonian case, they find that as an inviscid droplet (or bubble) deforms, the dimensionless surface area is proportional to the capillary number

$$A^* = \frac{10}{3} \text{Ca} \quad (8.10-6)$$

Thus, extensional flow is more efficient in increasing surface area as compared to shear flow.

The breakup or bursting of liquid droplets suspended in liquids undergoing shear flow has been studied and observed by many researchers beginning with the classic work of G. I. Taylor in the 1930s. For low viscosity drops, two mechanisms of breakup were identified at critical capillary number values. In the first one, the pointed droplet ends release a stream of smaller droplets termed "tip streaming"; whereas, in the second mechanism the drop breaks into two main fragments and one or more satellite droplets. Strictly inviscid droplets such as gas bubbles were found to be stable at all conditions. It must be recalled, however, that gas bubbles are compressible and soluble, and this may play a role in the relief of hydrodynamic instabilities. The relative stability of gas bubbles in shear flow was confirmed experimentally by Canedo et al. (36). They could stretch a bubble all around the cylinder in a Couette flow apparatus without any signs of breakup. Of course, in a real devolatilizer, the flow is not a steady simple shear flow and bubble breakup is more likely to take place.

Bubble deformation in shear flow increases mass transfer because of the increase in surface area and because of convection. The latter brings volatile-rich liquid to the bubble surface. Favelukis et al. (39) studied the (identical but experimentally easier) reverse problem of *dissolution* of a gas bubble in a sheared liquid, both theoretically and experimentally, and they confirmed the increase of mass transfer with increasing shear rate. They also showed that the rate of dissolution, da/dt , where a is the equivalent radius of the bubble, is given by

$$\frac{da}{dt} \approx - \frac{RT(C_s - C_\infty)}{P} \mathcal{D}^{1/2} \dot{\gamma}^{1/2} \quad (8.10-7)$$

for a nearly spherical bubble ($\text{Ca} \ll 1$), and by:

$$\frac{da}{dt} \approx - \frac{RT(C_s - C_\infty)}{P} \mathcal{D}^{1/2} \dot{\gamma}^{3/8} a^{-1/8} \left(\frac{\mu}{\Gamma} \right)^{-1/8} \quad (8.10-8)$$

for a slender bubble ($\text{Ca} \gg 1$), where R is the universal gas constant, T is the absolute temperature, C_s is the concentration of the gas at the interface, and C_∞ is the concentration gas far from the interface, P is the bubble pressure, \mathcal{D} is the diffusivity, $\dot{\gamma}$ is the shear rate, μ is the viscosity, and Γ is the surface tension. Clearly, the rate of dissolution increases significantly at large Ca numbers with $3/8$ power of the shear rate. The same should be expected for bubble growth, and hence one could conclude that devolatilization efficiency ought to improve with increasing rotational speed.

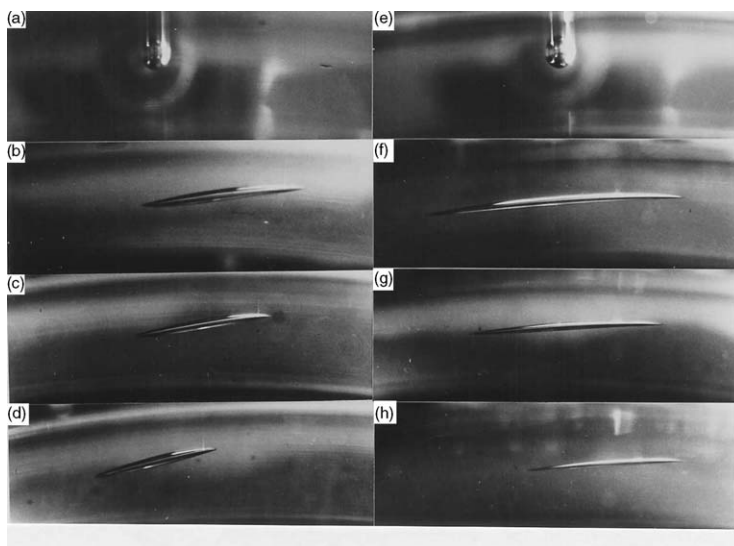


Fig. 8.13 Photograph of bubble deformation and bubble dissolution, in simple shear flow at room temperature, in a Newtonian low molecular-weight polyisobutylene (Chevron PB 24), in a Couette flow apparatus. Left: shear rate 5.5 s^{-1} , (a) $t = 0 \text{ min}$, $a = 1.2 \text{ mm}$; (b) $t = 1.5 \text{ min}$, $a = 1.14 \text{ mm}$; (c) $t = 5.5 \text{ min}$, $a = 0.98 \text{ mm}$; (d) $t = 7.5 \text{ min}$, $a = 0.92 \text{ mm}$. Right: shear rate 16.6 s^{-1} ; (e) $t = 0 \text{ min}$, $a = 1.2 \text{ mm}$; (f) $t = 1.1 \text{ min}$, $a = 1.15 \text{ mm}$; (g) $t = 5.1 \text{ min}$, $a = 0.93 \text{ mm}$; (h) $t = 8.0 \text{ min}$, $a = 0.80 \text{ mm}$: [Reprinted by permission from M. Favelukis, Z. Tadmor, and Y. Talmon, "Bubble Dissolution in Viscous Liquids in Simple Shear Flow," *AIChE J.*, **41**, 2637 (1995).]

Figure 8.13 shows the dissolution of bubbles in simple shear flow as a function of time and shear rate, confirming Eq. 8.10-7.

8.11 SCANNING ELECTRON MICROSCOPY STUDIES OF POLYMER MELT DEVOLATILIZATION

Albalak et al. (40) were the first to experimentally examine the devolatilization mechanism on a microscopic scale, and their results revealed a far more complex and subtle mechanism than what was expected by the straightforward foaming–boiling process they observed. PS with a known content of styrene was extruded in a modified melt-flow indexer. The thin melt strand was extruded into a temperature-controlled brass chamber connected to a vacuum pump, and after a prescribed time, was frozen by a spray of cooling water. After freezing, scanning electron micrograph (SEM) samples were prepared to examine the surface and the fractured cross section of the strands. The PS contained 2300 ppm styrene and was extruded in the temperature range of 170–235°C. The partial pressure of a 2300 pp styrene–PS solution at 170°C is of the order of 4 kPa (30 mmHg), and at 235°C, is 12 kPa (90 mmHg). Figure 8.14 shows a control sample extruded at 180°C into atmospheric pressure with no signs of foaming (as would be expected in the absence of superheat). However, when the strands were extruded into a high vacuum that created the necessary superheat for boiling, a series of characteristic features were observed. We discuss these in the following subsections.

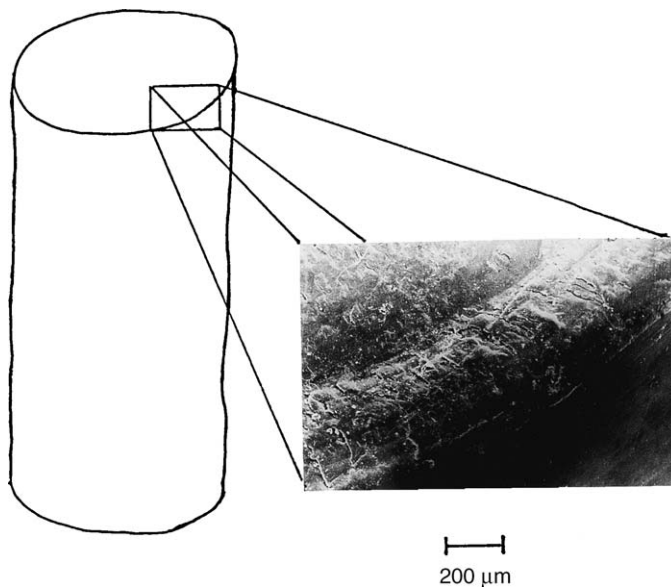


Fig. 8.14 PS–styrene sample extruded at 180°C into atmospheric pressure. The micrograph shows the smooth lateral surface and part of the cross section; there is no evidence of bubbles. [Reprinted by permission from R. J. Albalak, Z. Tadmor, and Y. Talmon, “Scanning Electron Microscopy Studies of Polymer Melt Devolatilization,” *AIChE J.*, **33**, 808–818 (1987).]

Macrobubbles

The first characteristic morphological feature was the appearance of *macrobubbles*, relatively large voids, randomly scattered spatially, of the order of 100 μm and above. These are shown on the lateral surface and cross section of the sample in Fig. 8.15. Postulating that the macrobubbles have their origins in outside sources, such as entrapped noncondensable gases or moisture, the authors concluded that they are the final stage of a growth process of vapor-filled bubbles in the natural course of boiling, as discussed later in this section.

Blisters

Perhaps the most striking morphological feature discovered were swarms of *blisters* on the inner surface of the macrobubbles, located both on the lateral surface and within the core of the strand, as shown in Figs. 8.16 and 8.17, respectively. These are thin, dome-shaped, vapor-filled pockets attached to the soft inner surface of the large macrobubbles. There are two types of blisters: *microblisters*, ranging in size from 1 to 3 μm diameter, and *miniblisters*, ranging in size from 10 to 15 μm diameters. Figure 8.17 shows microblisters and miniblisters side by side. The researchers hypothesized that this arrangement is not coincidental and that the miniblisters actually evolve from the microblisters. They suggested that a first generation of microblisters emerges through the soft surface of a macrobubble after having been formed as tiny boiling nuclei that grow into microbubbles under the surface. Being close to the surface in a melt that possesses significant tensile

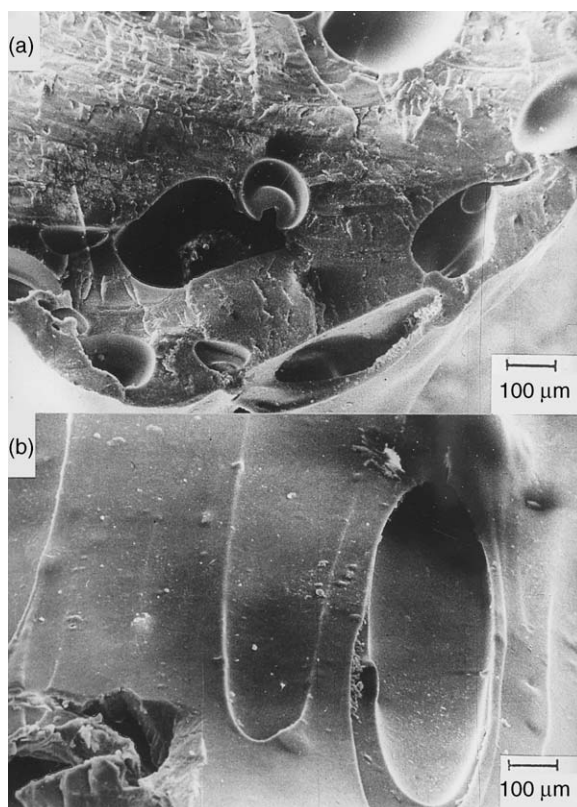


Fig. 8.15 PS–styrene sample extruded into 100-Pa pressure. (a) Cross section (170°C); (b) Lateral surface (180°C). Large macrobubbles are evident over both surfaces. [Reprinted by permission from R. J. Albalak, Z. Tadmor, and Y. Talmon, “Scanning Electron Microscopy Studies of Polymer Melt Devolatilization,” *AIChE J.*, **33**, 808–818 (1987).]

strength, these microbubbles naturally develop into blisters (much like when a stream of air is blown into a soap solution).

Once the newly formed styrene–vapor-filled microblisters grow to a maximum diameter of about 3 μm, at which stage the skin containing the vapor is too thin and weak to withstand the pressure difference, they burst, releasing the contained vapor into the macrobubble. This behavior is characteristic of microblisters that happen to break to the surface at relatively large distances ($>8\mu\text{m}$) from each other. However, microblisters emerging closer to each other may merge to form a larger “miniblisters” with a slightly thicker skin than that of the original microblister. In this manner, adjacent microblisters combine to form miniblisters, as clearly evident in Fig. 8.17. At some later stage, miniblisters also burst and the skin collapses, entraining small vapor-filled pockets that form nuclei for a new generation of microblisters, as can be clearly seen in Fig. 8.18.

According to this hypothesized mechanism, the process has an autocatalytic feature in that the bursting micro- and miniblisters create many new nuclei for new generations of microblisters. Moreover, the subsequent, quickly expanding macrobubble creates tensile

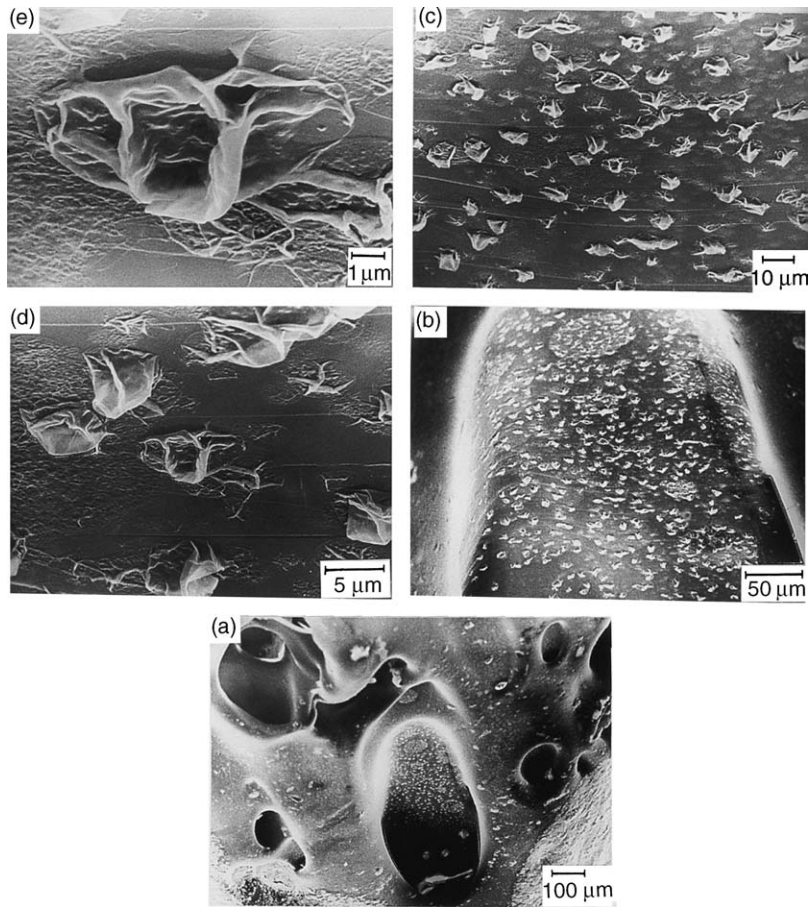


Fig. 8.16 Blisters in a macrobubble on the area of the lateral surface of a PS–styrene sample extruded at 200°C into 200-Pa pressure. (a) Lowest magnification shows macrobubbles and blister-covered inner surface. (b) Inner surface of macrobubbles at large magnification. (c) and (d) Randomly scattered collapsed blisters at increasing magnification, respectively. (e) A single collapsed blister. [Reprinted by permission from R. J. Albalak, Z. Tadmor and Y. Talmon, “Scanning Electron Microscopy Studies of Polymer Melt Devolatilization,” *AIChE J.*, **33**, 808–818 (1987).]

stress on the inner surface of the macrobubble, further accelerating the nucleation of new microbubbles under the soft surface. Thus, perhaps it is no wonder that such a ‘blistering’ devolatilization mechanism would yield relatively few macrobubbles at the expense of the rest of the core material.

Microblister Remains: Hair-like Fibers, Crusty Nodules, Stringy Fibers, and Spongy Surfaces

As the volatile content of the polymer is depleted, the blisters undergo a series of fascinating transformations until they fade away into the featureless soft inner surface of

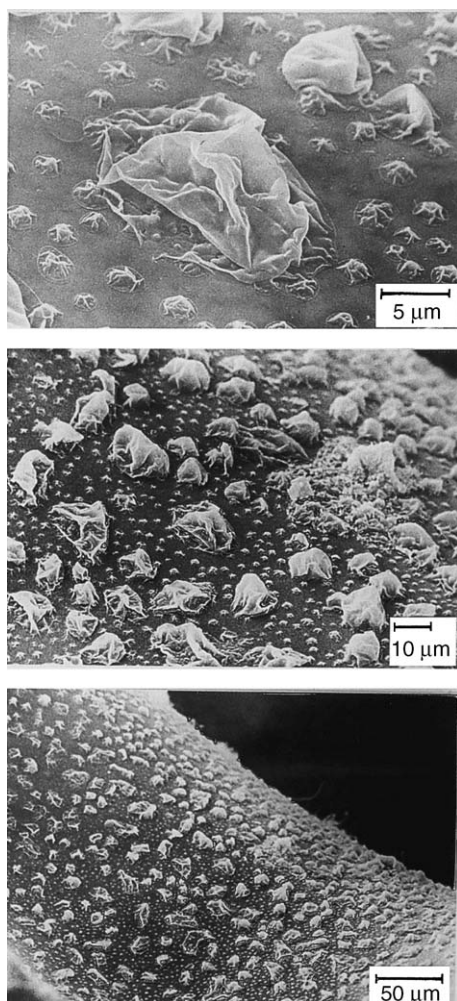


Fig. 8.17 Blisters in a macrobubble in the core of the strand of a PS–styrene sample extruded at 235°C into 300-Pa pressure. These magnifications show miniblisters and microblisters on the inner surface of a macrobubble within the core of the strand. [Reprinted by permission from R. J. Albalak, Z. Tadmor, and Y. Talmon, “Scanning Electron Microscopy Studies of Polymer Melt Devolatilization,” *AIChE J.*, **33**, 808–818 (1987).]

the macrobubble. Like the blisters, these are transient forms that quickly fade during the devolatilization process. Among the features observed were *hair-like fibers* that were 0.1–0.2 μm thick and about 3–5 μm long; *crusty nodule-like* structures; stringy fiber-like structures; spongy surfaces consisting of holes of about 1–3 μm.

The morphology remaining in a blister-inhabited area subsequent to the depletion of the volatile is shown in Fig. 8.19. The large circular tracks are those of miniblisters, while the smaller ones are those of the microblisters. Not all macrobubbles show the presence of blisters. Clearly, in the devolatilization process, after the volatiles are depleted

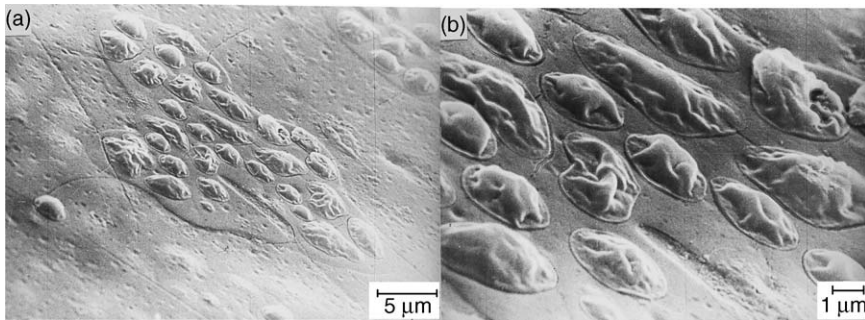


Fig. 8.18 Lateral surface of PS–styrene sample extruded at 170°C into 100-Pa pressure. Two magnifications of the same area show microblisters growing on the remains of collapsed miniblisters. [Reprinted by permission from R. J. Albalak, Z. Tadmor, and Y. Talmon, “Scanning Electron Microscopy Studies of Polymer Melt Devolatilization,” *AIChE J.*, **33**, 808–818 (1987).]

and before freezing of the samples took place, the surface might have healed itself to become smooth and featureless.

The preceding observations on the microscopic features of polymer melt devolatilization are not unique to the PS–styrene system, or to strand devolatilization. Similar, though somewhat less rich, features of blister-covered macrobubbles were observed with low-density polyethylene (PE), high-density PE and polypropylene (PP) systems (40,41). Furthermore, Tukachinsky et al. (11) discovered macrobubbles covered with microblisters in a 50-mm-diameter vented SSE, with PS showing more oblong shapes as a result of shearing. The onset of foaming with the application of vacuum was quicker with increased frequency of screw rotation, and the separation was more efficient.

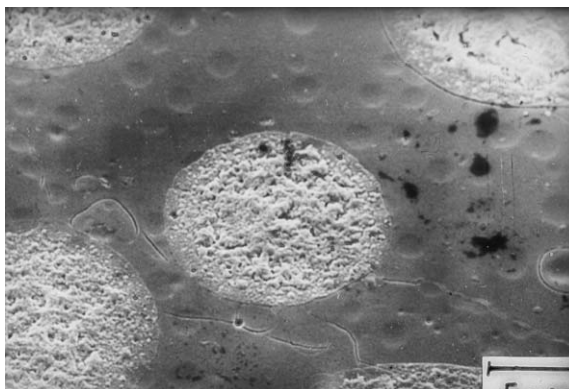


Fig. 8.19 Strand cross section of a PS–styrene sample extruded at 170°C and 100-Pa pressure. Coarse circular areas are the remains of miniblisters; small circular indentations are those of microblisters. [Reprinted by permission from R. J. Albalak, Z. Tadmor, and Y. Talmon, “Scanning Electron Microscopy Studies of Polymer Melt Devolatilization,” *AIChE J.*, **33**, 808–818 (1987).]

The foaming–boiling mechanism described previously may be characteristic not only to polymeric melts, but it may also be the inherent boiling mechanism of viscoelastic liquids in general.

Theoretical Formulation

Clearly, this mechanism is more complex than ordinary boiling mechanisms, and any theoretical formulation of devolatilization must take into account this complexity. An initial attempt to formulate semiquantitative elements of this mechanism was made by Albalak et al. (41). They proposed that once a nucleus of a macrobubble is created and the bubble begins to grow, the stretched inner surface of the bubble enhances the rate of nucleation just beneath the soft surface, thus generating new blisters, as shown schematically in Fig. 8.20.

Turning to Eq. 8.6-2, we note that the superheat appears in the denominator of the exponent term. As pointed out earlier, under ordinary conditions the maximum superheat of a given system at a fixed temperature can be obtained by reducing P_0 to a minimum value close to zero. However, further decrease in the local value of P_0 can be obtained by a cavitation process due to the tensile stresses generated in the moving boundaries of the macrobubble. Street (42) showed that the bubble surface is stretched (i.e., the $\tau_{\theta\theta}$ and $\tau_{\phi\phi}$ stress components are negative), and that for a viscoelastic liquid they are given by

$$\tau_{\theta\theta} = \tau_{\phi\phi} = - \left\{ \frac{2\mu_0\dot{R}}{R} + \left(\frac{4\mu_0\alpha^2\lambda_1}{1 - 2\alpha\lambda_1} \right) \left[1 - e^{-(1-2\alpha\lambda_1)(t/\lambda_1)} \right] \right\} \quad (8.11-1)$$

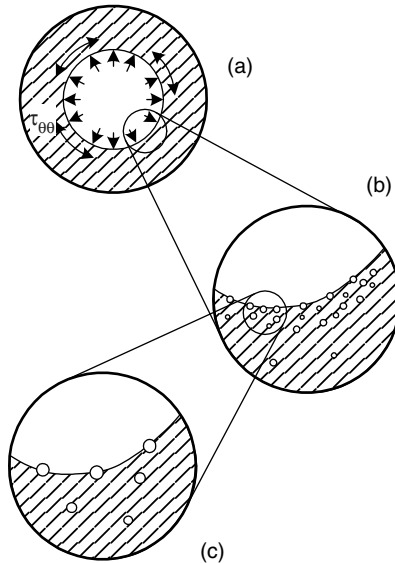


Fig. 8.20 Nucleation mechanism on the surface of a macrobubble. (a) A growing macrobubble generates angular stresses in the surrounding melt; (b) secondary microbubbles nucleate and form blisters; (c) detail of (b).

where μ_0 is the zero shear viscosity, λ_1 is the first relaxation time, and $\alpha = \dot{R}/R$, where R is the macrobubble radius. The order of magnitude of these stresses for a growing bubble was estimated to be (41) 10,000 Pa, as compared to a typical superheat of about 1000 Pa, suggesting a possibly significant role for these cavitation-like stresses on the growing bubble surface in enhancing nucleation rate. Yarin et al. (43) developed a modified nucleation-rate expression accounting for the surface stretching and possible mechanical degradation of the polymer and showed a significantly increasing rate of secondary nucleation with bubble growth.

REFERENCES

1. J. A. Biesenberger, *Devolatilization of Polymers*, Hanser, Munich; also, Macmillan, New York, 1983.
2. R. J. Albalak, Ed., *Polymer Devolatilization*, Marcel Decker, New York, 1996.
3. D. B. Todd, R. H. M. Simon, J. Lane, and J. A. Biesenberger, "Equipment" in *Devolatilization of Polymers*, Sec. II, J. A. Biesenberger, Hanser, Munich; Macmillan, New York, 1983.
4. P. S. Mehta, "An Overview of Devolatilizers," in *Polymer Devolatilization*, R. J. Albalak, Ed., Marcel Decker, New York, 1966.
5. R. E. Newman and R. H. S. Simon, "A Mathematical Model for Devolatilization Promoted by Bubble Formation," American Institute of Chemical Engineers paper presented at the Annual Meeting, Chicago, 1980.
6. G. A. Latinen, "Devolatilization of Viscous Polymeric Systems," *Adv. Chem. Ser.*, **34**, 235, (1962).
7. R. W. Coughlin and G. P. Canevari, "Drying Polymers during Screw Extrusion," *AIChE J.*, **15**, 560 (1969).
8. G. W. Roberts, "A Surface Renewal Model for Drying of Polymers during Screw Extrusion", *AIChE J.*, **16**, 878 (1970).
9. J. A. Biesenberger and G. Kessidis, "Devolatilization of Polymer Melts in Single Screw Extruders," *Polym. Eng. Sci.*, **22**, 832 (1982).
10. P. S. Mehta, L. N. Valsamis, and Z. Tadmor, "Foam Devolatilization in a Multi-channel Corrotating Disk Processor," *Polym. Process. Eng.*, **2**, 103 (1984).
11. A. Tukachinsky, Y. Talmon, and Z. Tadmor "Foam-enhanced Devolatilization of Polystyrene Melt in a Vented Extruder," *AIChE J.*, **40**, 670-675 (1994).
12. P. J. Flory, "Thermodynamics of High Polymer Solutions," *J. Chem. Phys.*, **10**, 51-61 (1942).
13. M. L. Huggins, "Some Properties of Solutions of Long-chain Compounds," *J. Phys. Chem. A.*, **46** (1), 151-158 (1942).
14. J. Brandrup and E. H. Immergut, *Polymer Handbook, Third Edition*, Wiley-Interscience, New York, 1989.
15. R. H. M. Simon, "Flash Evaporators and Falling Strand Devolatilizers" in *Devolatilization of Polymers*, J. A. Biesenberger, Ed., Hanser, Munich, 1983.
16. D. B. Todd, "Polymer Devolatilization," paper presented at the Society of Plastics Engineers Annual Technical Conference, San Francisco, 1974.

17. J. S. Vrentas and J. L. Duda, *J. Poly. Sci. Part B: Poly. Phys.*, **15**, 403 and 417 (1977).
18. H. Fujita, "Diffusion in Polymer Diluent Systems," *Fortschr. Hochpolym. Forsch.*, **3**, 1–47 (1961).
19. J. L. Duda, J. S. Vrentas, S. T. Ju, and H. T. Liu, "Prediction of Diffusion Coefficients for Polymer Solvent Systems," *AIChE J.*, **28**, 279 (1982).
20. J. M. Zielinski and J. L. Duda, "Solvent Diffusion in Polymeric Systems," in *Polymer Devolatilization*, R. J. Albalak, Ed., Marcel Dekker, New York, 1996.
21. M. Blander and J. L. Katz, "Bubble Nucleation of Liquids," *AIChE J.*, **21**, 833 (1975).
22. R. Cole, "Homogeneous and Heterogeneous Nucleation" in *Boiling Phenomena*, Vol. 1, S. Van Stralen, and R. Cole, Eds., McGraw-Hill, New York, 1979, Chapter 3.
23. R. T. Knapp, J. W. Daily, and F. G. Hammitt, *Cavitation*, McGraw-Hill, New York, 1970.
24. S. T. Lee and J. A. Biesenberger, "Fundamental Study of Polymer Melt Devolatilization. IV: Some Theories and Models for Foam-enhanced Devolatilization," *Polym. Eng. Sci.*, **29**, 782–790 (1989).
25. S. T. Lee, Ph.D. Thesis, Chem. Eng. Dept., Stevens Institute of Technology, Hoboken, NJ.
26. E. N. Harvey, D. K. Barnes, W. D. McElroy, A. H. Whitely, D. C. Pease, and K. W. Cooper, "Bubble Formation in Animals: I. Physical factors," *J. Cellular Comp. Physiol.*, **24**, 1 (1944).
27. S. T. Lee, "A Fundamental Study of Foam Devolatilization" in *Polymer Devolatilization*, R. J. Albalak, Ed., Marcel Dekker, New York, 1996, Chapter 6.
28. C. E. Brennen, *Cavitation and Bubble Dynamics*, Oxford University Press, Oxford, 1995.
29. M. Greenspan, and C. E. Tschiegg, *J. Res. Natl. Bur. Stand. C. Eng. Instrum.*, **71C**, 299–312 (1967).
30. H. B. Marschall, K. A. Mørch, A. P. Keller, and M. Kjeldsen, "Cavitation Inception by Almost Spherical Particles in Water," paper presented at the Fourth International Symposium on Cavitation, California Institute of Technology, Pasadena, CA, June 20–23, 2001.
31. W. L. Wilkinson, "Entrainment of Air by a Solid Surface Entering a Liquid/Air Interface," *Chem. Eng. Sci.*, **30**, 1227 (1975).
32. A. Tukachinsky, Z. Tadmor, and Y. Talmon, "Ultrasound-enhanced Devolatilization in Polymer Melt," *AIChE J.*, **39**, 359 (1993).
33. M. Favelukis and R. J. Albalak, "Fundamentals of Bubble Growth," in *Polymer Devolatilization*, R. J. Albalak, Ed., Marcel Dekker, New York, 1996.
34. L. E. Scriven, "On the Dynamics of Phase Growth," *Chem. Eng. Sci.*, **10**, 1 (1959).
35. E. J. Hinch and A. Acrivos, "Long Slender Drops in a Simple Shear Flow," *J. Fluid Mech.*, **98**, 305 (1980).
36. E. L. Canedo, M. Favelukis, Z. Tadmor, and Y. Talmon, "An Experimental Study of Bubble Deformation in Viscous Liquids in Simple Shear Flow," *AIChE J.*, **39**, 553 (1993).
37. M. Favelukis, O. M. Lavrenteva and A. Nir, "Deformation of a Slender Bubble in a non-Newtonian Liquid in an Extensional Flow," *Chem. Eng. Sci.*, **56**, 4643–4648 (2001).
38. M. Favelukis, O. M. Lavrenteva, and A. Nir, "Deformation and Breakup of a Non-Newtonian Slender Drop in an Extensional Flow," *J. Non-Newtonian Fluid Mech.*, **125**, 49–59 (2005).

39. M. Favelukis, Z. Tadmor, and Y. Talmon, "Bubble Dissolution in Viscous Liquids in Simple Shear Flow," *J. Non-Newtonian Fluid Mech.*, **41**, 2637–2641 (1995).
40. R. J. Albalak, Z. Tadmor, and Y. Talmon, "Scanning Electron Microscopy Studies of Polymer Devolatilization" *J. Non-Newtonian Fluid Mech.*, **33**, 808–818 (1987).
41. R. J. Albalak, Z. Tadmor, and Y. Talmon, "Polymer Melt Devolatilization Mechanisms," *J. Non-Newtonian Fluid Mech.*, **36**, 1313–1320 (1990).
42. J. R. Street, "The Rheology of Phase Growth in Elastic Liquids," *Trans. Soc. Rheol.*, **12**, 103 (1968).
43. A. L. Yarin, D. Lastochkin, Y. Talmon, and Z. Tadmor "Bubble Nucleation during Devolatilization of Polymer Melts," *AIChE J.*, **45**, 2590–2605 (1999).

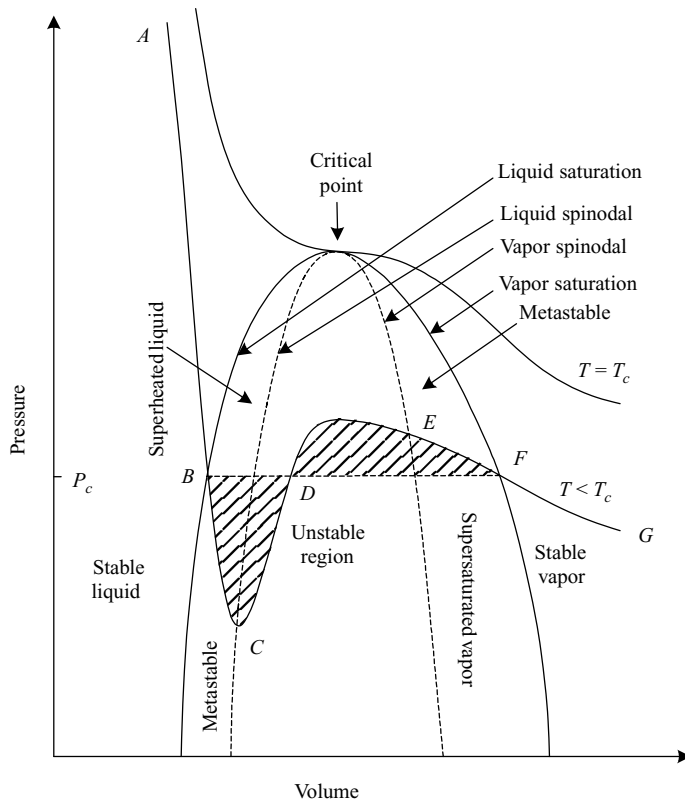
PROBLEMS

- 8.1 Equilibrium Concentration of the Solute over the Solution and the Degree of Superheat** Consider a 5000-ppm styrene-(PS) solution at 200°C ($\chi_{12} = 0.3$ and $P_1^0 = 450$ kPa) placed in a vacuum of 2 mmHg. Assuming identical densities, calculate the maximum final separation possible. What is the degree of superheat?
- 8.2 Determining the Flory–Huggins Interaction Parameter χ_{12}** Charge a 1-liter vessel with 250 g polymer ($\rho = 1.37$), heat, and evacuate to 1 torr. Add 3.6 mL nitromethane, agitate at 180°C at final pressure of 560 torr. What is χ_{12} for the polymer–nitromethane system?
- 8.3 Staging and Equilibrium** Methylene chloride (CH_2Cl_2) is to be removed from polymer ($\rho = 1.57$ g/cm³) containing 8.7% wt CH_2Cl_2 to a residual content of 100 ppm, $\chi_{12} = 0.56$. (a) How many stages should be considered? (b) At 150°C, what is the theoretical vacuum level required in the last stage? (c) Above what temperature should the first stage be maintained to obtain one order of magnitude solvent content reduction, yet keep this stage above atmospheric pressure, in order to avoid fouling large amounts of the devolatilized stream? (d) How much energy (kwh/kg polymer) must be put into the first stage if the feed is at 110°? Assume $C_p = 0.4$ cal/g°C for both solvent and polymer. (e) Calculate the equilibrium pressure and volume of vapor (m³/kg polymer) removed in each stage when the preceding devolatilizing process is attempted with $n = 1, 2, 3$, or 4 stages. Assume equilibrium in each stage at 150°C. Use the commonly used assumption $W_j/W_{j+1} = (W_0/W_f)^{1/n}$.
- 8.4 Single Screw Extruder Devolatilization Using Latinen's Model** Review the paper by Biesenberger and Kessidis* and discuss (a) the experimental method used

*J.A. Biesenberger and G. Kessidis, "Devolatilization of Polymer Melts in Single Screw Extruders," *Polym. Eng. Sci.*, **22**, 832 (1982).

by the authors to verify or disprove the Latinen model; (b) why the Latinen model cannot explain the rate of devolatilization in vacuum-vented screw extruders. (c) Suggest an alternative technique for choosing between a diffusion-controlled and a boiling-type devolatilization mechanism.

8.5 The Thermodynamic Pressure–Volume Diagram The accompanying figure shows a schematic pressure–volume–temperature diagram for a pure liquid. Trace lines on the diagram showing (a) supersaturation at fixed pressure in terms of temperature difference, and (b) supersaturation at fixed temperature in terms of pressure difference. (c) Explain the meaning of the spinodal line. (d) Explain the difference between the kinetic and thermodynamic limits of superheat.



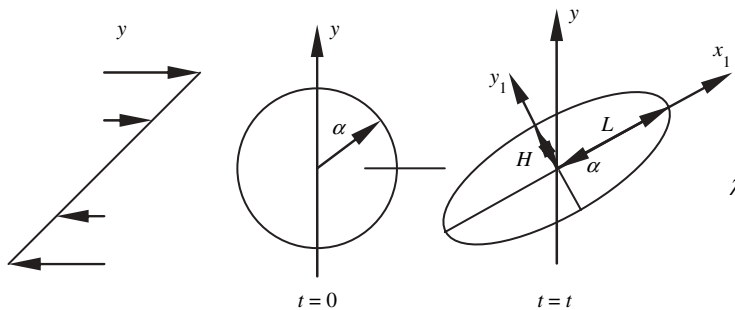
8.6 Homogeneous Nucleation (a) Using Eq. 8.6-2, calculate the rate of homogeneous nucleation of styrene as a function of temperature at atmospheric pressure and a temperature range from 145°C to 325°C. In calculating the pressure in the bubble, assume that it equals the vapor pressure (extrapolate it from lower temperature values). Use the Eötvös equation $\sigma = 2.1(\rho/M)^{2/3}(T_c - T - 6)$, where the surface tension is in erg/cm³, temperature is in °C, and density in g/cm³, to evaluate the surface tension as a function of temperature. The critical temperature

of styrene is 374°C , and the boiling point at atmospheric pressure is 145°C . Homogeneous boiling starts when the rate of nucleation is of the order of 10^6 nuclei per cubic centimeter per second. (b) Explain qualitatively why homogenous nucleation is unlikely in polymer melt devolatilization.

8.7 Bubble Growth A 1-mm radius bubble with internal pressure of 0.1 atm(g) (above atmospheric pressure) is placed in a polymeric liquid of viscosity 3.5×10^3 Ns/m² and surface tension 2.5×10^{-2} N/m at ambient pressure. Calculate the bubble radius as a function of time.

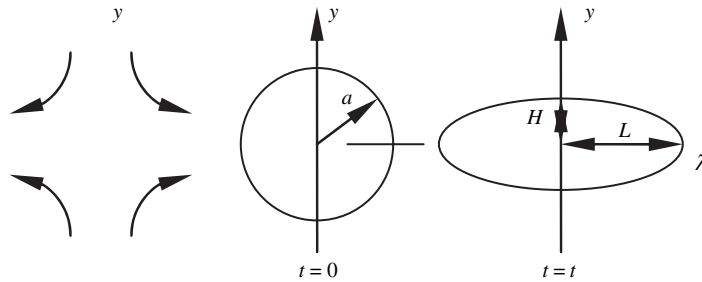
8.8 Bubble Deformation A 5-mm radius bubble is placed in a viscous liquid of 0.2 lb_Fs/in² and surface tension of 22 dyne/cm. Calculate the shape of the bubble, the half-length, and slenderness ratio of the bubble at shear rates 1, 10, and 100 s⁻¹.

8.9 Affine Deformation of a Liquid Droplet in Simple Shear Flow When a drop of liquid is suspended in another liquid undergoing shear or extensional flow, the drop will deform. If the strength of the flow exceeds some critical value, as discussed in the chapter, the drop will break into two or more fragments. In affine deformation the droplet deforms exactly as the surrounding liquid, which implies that the suspended droplet does not disturb the original velocity profile. The accompanying figure shows a two-dimensional drop placed in a simple shear flow $v_x = dx/dt = Gy$ and $v_y = dy/dt = 0$:



(a) Integrate the velocity profile and show that a point at time $t = 0$ placed at (x_0, y_0) is at time t at position $(x_0 + \tau y_0, y_0)$, where $\tau = Gt$ is a dimensionless time. (b) At time $t = 0$ a point on the surface of the drop satisfies the equation $x_0^2/a^2 + y_0^2/a^2 = 1$. Show that after time t the shape of the drop is given by $x^2 - 2\tau xy + (1 + \tau^2)y^2 = a^2$. (c) Show that the angle of the major axis of the ellipse with the x -axis is given by $\tan(2\alpha) = 2/\tau$. (d) Show that the shape of the ellipse can be expressed in terms of the semimajor L and semiminor H axes as $x_1^2/L^2 + y_1^2/H^2 = 1$.

8.10 Affine Deformation of a Liquid Droplet in Extensional Flow The shape of a droplet in extensional flow defined by $v_x = dx/dt = Gx$ and $v_y = dy/dt = -Gy$ is shown in the accompanying figure.



(a) Integrate the velocity profile and show that the original point (x_0, y_0) moves to the position $(x_0 \exp(\tau), y_0 \exp(-\tau))$ at time t , where $\tau = Gt$ is a dimensionless time. (b) Show that the shape of the ellipse is given by $\exp(-2\tau)x^2 + \exp(2\tau)y^2 = a^2$. (c) Show that the semimajor and semiminor axes are given by $L/a = \exp(\tau)$ and $H/a = \exp(-\tau)$.

8.11 Devolatilization of Residual Toluene Residual toluene is continuously removed from a polymer melt stream of 454 kg/h at 230°C and 0.006 weight fraction of toluene, at a vacuum of 20 torr. The density of the polymer is 0.98 g/cm³, and the Florry–Huggins interaction parameter is $\chi_{12} = 0.43$. (a) Calculate the equilibrium concentration, w_e . (b) If equilibrium is reached, that is, $w_f = w_e$, where w_f is the final concentration, calculate the separation efficiency $F_S = (w_0 - w_f)/w_0$. (c) If the final concentration $w_f = 2w_e$, calculate F_S . (d) Calculate for (c) the volumetric flow rate of the vacuum pump removing the volatiles.

8.12 Elastomer Solution Stagewise Devolatilization A stream of 1000 lb/h of an elastomer solution containing 18% wt hexane at 70°F is to be concentrated by heating under pressure and flashing, followed by a two-stage devolatilization to a residual concentration of 0.4% wt. The elastomer must not exceed 320°F to avoid degradation. The flash should not go below 5 psig to make solvent recovery easier and to reduce the potential hazard of air incursion under vacuum. Assume $\chi_{12} = 0.4$, density 1.0 g/cm³, and that the specific heat of the polymer is the same as for hexane. (a) Estimate the minimum hexane concentration possible under the flash constraints just given. (b) Estimate the process stream temperature following the flash. (c) Calculate the percentage of hexane removed in the flash. (d) Calculate the heat load for the heat exchanger upstream of the flash. (e) Estimate the surface area required. (f) Estimate the first vacuum-stage pressure if operated at 300°F. (g) Calculate the last vacuum-stage pressure, also at 300°F, assuming equilibrium is attained. (h) Calculate the energy loads for the two vacuum stages.

8.13 Devolatilizing Screw Extruder A 150-mm-diameter, square-pitched, single-flight screw extruder, with screw channel depth of 25 mm and 20-mm flight width is used to devolatilize a 1000-kg/h stream with 0.78-g/cm³ density at 200°C and 125 torr. (a) At what frequency of screw rotation will the channel be 30% or less full? (b) With water injection, if density is halved by formation of 1-mm bubbles, how much surface area (per meter length) is created? (c) How does

this surface compare with the available area before and after foaming? (d) Assuming a cubical array of the foam bubbles in the melt, what is the minimum film thickness?

- 8.14 *Silo Volatiles Composition*** Polymer flake is fed into a silo at 2820 kg/h containing 0.56% residual cyclohexane. (a) What sweep air rate should be employed to keep the effluent air at less than one-half of the lower explosion limit? (b) Is it permissible from an environmental point of view to release the effluents into the atmosphere?

9 Single Rotor Machines

- 9.1 Modeling of Processing Machines using Elementary Steps, 447
- 9.2 The Single Screw Melt Extrusion Process, 448
- 9.3 The Single Screw Plasticating Extrusion Process, 473
- 9.4 The Co-rotating Plasticating Disk Processor, 506

9.1 MODELING OF PROCESSING MACHINES USING ELEMENTARY STEPS

By dissecting polymer processing into *elementary steps*, and analyzing each step in isolation, we are able to uncover the underlying, basic mechanisms of each individual step, and its theoretical foundation. As we discussed in Section 2.11, this process is part of a systematic scientific methodology for modeling any complex system. In our case, the complex system is the polymer processing discipline as a whole. Along similar lines, we showed in Section 6.2 that the machines themselves can also be dissected or “deconstructed” into basic elements and building blocks, which capture the basic underlying mechanism or essence of a particular machine. We further showed in Section 6.2 that we can synthesize new machines by systematically and rationally recombining the building blocks in imaginative ways.

In this chapter and in Chapter 10, we *synthesize* or *design* prototype polymer processing machines using these elementary steps and building blocks. The uniqueness of each prototype machine is determined by the *building blocks* of the machine itself, and the particular combination of elementary steps and elementary-step mechanisms utilized to create it.

However, once we have conceptually designed the prototype machine, which involves selecting the elementary steps and the particular mechanisms we wish to use, and describing them in terms of mathematical subsystem models, we can assemble them into a comprehensive *mathematical model* of the whole machine and proceed through *simulation* to design-specific machines for given sets of requirements.¹

This chapter focuses on single rotor machines. Specifically, we analyze the single screw extruder (SSE) and the co-rotating disk processor (CDP). The former, based on two parallel plates in relative motion (building block 1 in Fig. 6.2) was chosen not only because it enjoys a dominant role in the processing industry, and therefore ought to be studied by all processing engineers, but also because of its inherent capability to perform *all* the elementary steps of polymer processing. Indeed, the versatility of the SSE, coupled with its design simplicity, is what makes it so useful. The CDP, based on jointly moving parallel

1. It is worthwhile noting that polymer processing was among the first engineering disciplines in which comprehensive mathematical modeling was used for the design of machines. This was pioneered by Imrich Klein and Donald I. Marshall in their book *Computer Programs for Plastics Engineers*, Reinhold, New York, 1968.

plates (building block 2 in Fig. 6.2), was chosen because it can also perform all the elementary steps in a radically different geometrical configuration, and the juxtaposition of these two very different machines helps gain better insight into each of them.

9.2 THE SINGLE SCREW MELT EXTRUSION PROCESS

Melt-fed SSEs are used in *post-reactor processing*. This involves three stages: (a) compounding of various additives into the polymer after it exits the reactor; (b) pressurization of the melt; and (c) pelletizing of the polymeric melt. The compounding takes place in either a batch mixer (e.g., Banbury-type internal mixer) or a continuous mixer (CM), feeding an SSE equipped with a pelletizing plate. An alternative solution calls for using a twin screw extruder (TSE) equipped with kneading elements that compounds, pressurizes, and pelletizes the polymeric melt.

In this section, we discuss the design of a melt extruder and derive the appropriate mathematical model. This will also introduce the reader to the plasticating extrusion process discussed in the following section.

Figure 9.1 shows a schematic view of a metering-type melt extruder, consisting of a deep channel feed section, a compression section, and a shallow metering section. The geometrical variables that must be specified to cut a screw are depicted in the figure, and they include the screw diameter, D_s , the total length and the flighted length, L , the length or number of turns in each geometrical section (feed, tapered, and metering), the lead, L_s , the feed depth, the metering depth, and the flight width, e . In addition, one must specify the shank and the bearing diameters, the keyway, the feed pocket, the front and rear radii, and the nose cone, but these do not affect simulation within the accuracy of the existing models.

The screw is placed within a barrel of diameter $D_b = D_s + 2\delta_f$, where δ_f is the radial flight clearance. This is shown schematically in Fig. 9.2. The figure shows a pelletizing extruder, but the discussion that follows is valid for *any* melt extruder equipped with any kind of die, and for the melt region in a plasticating extruder as well.

The *system* consists of three *subsystems*: the feed port, the screw, and the pelletizing plate, which are connected in *series*. Therefore, for steady state operation with atmospheric inlet and outlet conditions, the mass flow rate in each subsystem G_i is constant

$$G_i = G_0 \quad (9.2-1)$$

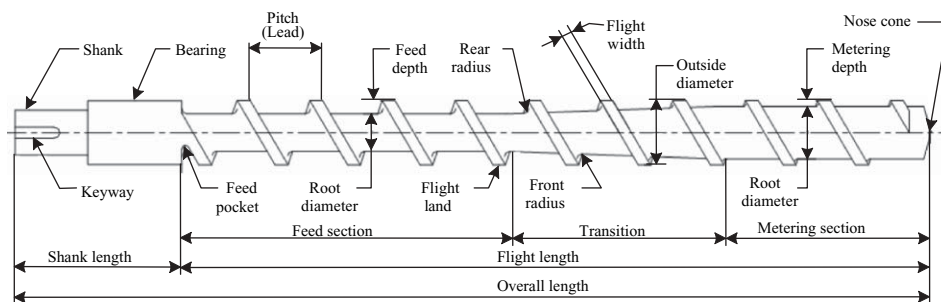


Fig. 9.1 A metering-type screw indicating the geometrical variables that must be specified for cutting a screw, and their common names.

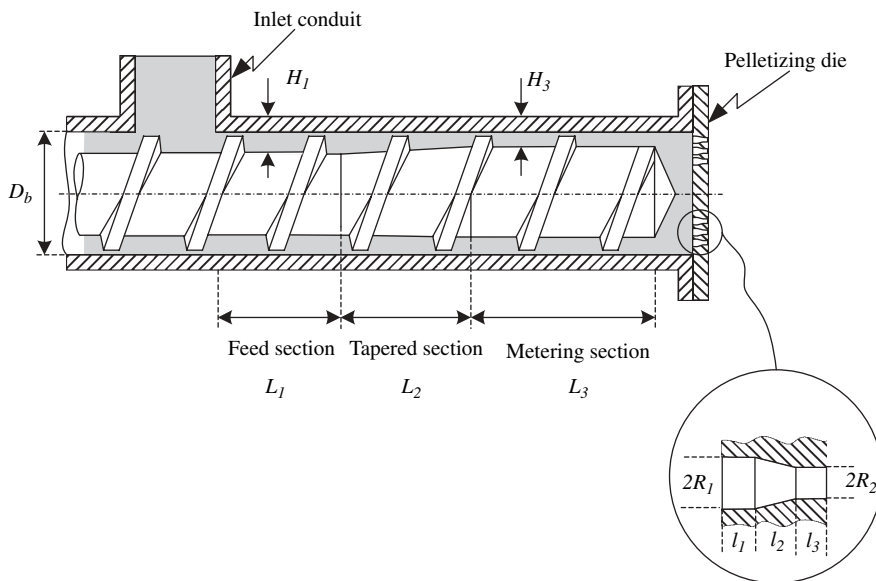


Fig. 9.2 Schematic view of a melt extruder. The extruder is equipped with a feed port and a pelletizing plate.

where G_0 is the throughput, and the sum of pressure changes over the entire process is zero

$$\Delta P_i = 0 \quad (9.2-2)$$

which implies that the pressure *rise* in the extruder equals the pressure *drop* over the pelletizing plate. In designing a pelletizing system, therefore, we first of all need to relate flow rate to pressure change over each subsystem. However, the mass flow rate or throughput and pressure changes are not the only operational variables of interest. Linked to the pressurization step are also bulk temperature changes and temperature distributions, which may affect the uniformity of the pellets, and of course power input through the shaft of the extruder, which determines the size of the drive system. We may also be interested in the mean strain, strain, and residence time distribution functions.

The assembled models of the subsystems provide relationships between the main process variables mentioned earlier (flow rate, pressure profile, temperature profile, power requirements, residence time), the relevant geometrical variables (i.e., design variables), the rheological and thermophysical properties of the melt, and the main operational variables (i.e., frequency of screw rotation or “screw speed,” barrel temperature profile, and die temperature settings). These relationships can, therefore, be used both for new machine design or for the analysis (optimization) of existing ones. In addition to the main process variables, there are other variables that may be worthwhile studying, such as cross die variation in temperature (leading to uneven pellets), flow-rate fluctuations, swelling and shape stability, and parameter sensitivity of the process. Chapter 12, on die forming, deals with some of these issues.

The Isothermal Newtonian Model for Constant Channel Depth Screw

We now proceed to the main task of subsystem modeling. The inlet flow to the extruder is simple gravitational flow through (generally) a tubular conduit. In such slow flows, the shear rate range is very low and the isothermal Newtonian assumption is valid. For a vertical tubular entrance, the flow rate is given by the Haagen–Poiseuille law (Table 12.2)

$$Q = \frac{\pi(P_0 - P_L)R^4}{8\mu L_0} \quad (9.2-3)$$

where $P_z = P_0 - \rho gz$, z is the downward distance in the inlet conduit of height L_0 . Therefore, for a melt column of height L_0 , $P_0 - P_L = \rho gL_0$, and

$$Q = \frac{\pi\rho gR^4}{8\mu} \quad (9.2-4)$$

Drag-induced pressurization in shallow screw channels was discussed in Section 6.3, and the flow rate is given in Eqs. 6.3-27 and 6.3-28. The former can be rewritten as

$$Q_s = \frac{1}{2}\pi ND_b \cos \theta_b W(H - \delta_f)F_d - \frac{WH^3}{12\mu} \frac{\Delta P_s}{L} \sin \bar{\theta}(1 + f_L)F_p \quad (9.2-5)$$

where Q_s is the volumetric flow rate in the extruder, L is the axial length of the screw, ΔP_s is the pressure rise over the screw from inlet to exit, and f_L is given in Eq. 6.3-28. Note that in Eq. 9.2-5, we use an average helix angle to convert helical length to axial length; whereas, for the barrel velocity, we use the helix angle at the barrel inner surface. In developing Eq. 6.3-27, it was assumed that a congruent velocity distribution exists in the channel, and therefore, we neglected the end effects. However, in Eq. 9.2-5, we applied it to a finite-length screw. This introduces an error called the oblique end effect, as shown schematically in Fig. 9.3. This error is discussed by Tadmor and Klein (1) and was originally suggested by Booy (2). For low L/D screws, it may be important, and both pressure and drag flows have to be multiplied by correction factors, which are only functions of L/D and θ .

Equation 9.2-5 can be represented by plotting the flow rate Q_s versus the pressure rise ΔP_s . Such plots, called *screw characteristics*, appear in Fig. 9.4. The intersection with the ordinate gives the drag-flow rate value and that with the abscissa, the maximum pressure at closed discharge. For isothermal flow of a Newtonian fluid in the absence of leakage flow,

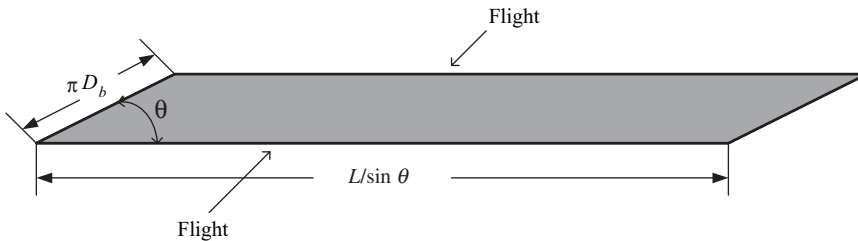


Fig. 9.3 Top view of an “unwound” screw channel indicating the oblique ends of the channel. The significance of this geometrical end-effect correction factor is of the order $\pi \sin \theta \cos \theta / (L/D)$.

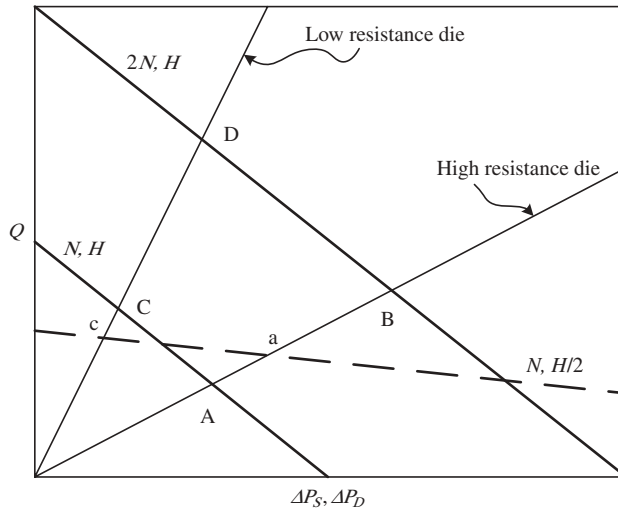


Fig. 9.4 Schematic views of screw characteristic lines for Newtonian fluids and isothermal flow. The points where the screw and die characteristic lines cross are the operating points of the extruder. The effect of the screw speed and the channel depth on the operating points is demonstrated.

the screw characteristics are straight lines with a negative slope of $-(WH^3/12\mu)(\sin \bar{\theta}/L) F_p$. Figure 9.4 illustrates the effect of two important variables on screw characteristics: frequency of screw rotation, or screw speed, as it is commonly referred to, and channel depth. Changing the former shifts the screw characteristic, whereas the latter affects both its level and slope.

A general equation for the isothermal pressure flow of an incompressible Newtonian fluid in a die (without moving parts like, e.g., wire coating dies), can be written as

$$Q_D = \frac{K}{\mu} \Delta P_D \tag{9.2-6}$$

where K is the *die constant* or “flow conductance” term, determined by the die geometry, and ΔP_D is the *pressure drop* over the die. For relatively simple dies, K can be calculated from basic principles (e.g., for the orifice die from Eq. 9.2-1 we find that $K = \pi R^4/8L_0$), but for more complex ones, it must be determined experimentally. Equipping an extruder with a valve is tantamount to a die with a variable K . Figure 9.4 shows two die characteristic lines, one at high die resistance and one at low die resistance. Clearly, the operating point of the former (C, D) is at higher flow rates and lower pressure drops than the latter (A, B). Note that reducing the channel depth may have a different effect with high and low resistance dies. In the case shown in Fig. 9.4, the flow rate increases with the former (operating point C shifts to c) and it drops with the latter (operating point A shifts to a). We noted in Section 6.3 that there is an optimum channel depth for maximum output or pressure, and in this schematic example, the two cases happen to fall on opposite sides of the optimum. Finally, it should be noted that, for non-Newtonian fluids and/or nonisothermal flow, the general

behavior remains the same, but the extruder and die characteristics, as shown later, will no longer be straight lines but curved ones.

By combining Eqs. 9.2-5 and 9.2-6, with $Q_S = Q_D = Q$ and $\Delta P_S = \Delta P_D = \Delta P$, the operating point of the extruder is obtained

$$Q = \frac{0.5\pi ND_b \cos \theta_b W (W - \delta_f) F_d}{1 + [WH^3 \sin \bar{\theta} (1 + f_L) F_p] / 12LK} \quad (9.2-7)$$

$$\Delta P = \frac{0.5\mu\pi ND_b \cos \theta_b W (H - \delta_f) F_d}{K + [WH^3 \sin \bar{\theta} (1 + f_L) F_p] / 12L} \quad (9.2-8)$$

These two equations, together with Eq. 9.2-4, form the complete model for the problem at hand.

This is the simplest model of a melt extruder–die system, but it qualitatively represents the behavior of *any* melt extruder–die combination, and it even provides good order of magnitude for them.

Example 9.1 Power and Temperature Consideration in Batch and Continuous Systems Before proceeding with the single screw modeling, we want to make a few general observations on temperature and power considerations in batch and continuous systems.

The temperature of an incompressible fluid element in a deforming medium is governed by the equation of thermal energy, Eq. 2.9-14. This excluding the reversible compression term, and in terms of specific heat, is

$$\rho C_v \frac{DT}{Dt} = -(\nabla \cdot \mathbf{q}) + (-\boldsymbol{\tau} : \nabla \mathbf{v}) \quad (E9.1-1)$$

which states that the change of the temperature of a fluid element in a flowing system is the sum of the heat gain (loss) by conduction and the rate of viscous dissipation in the element. Since viscosities of polymeric are high and thermal conductivities are low, efficient heat transfer must be secured to control the system at a desired temperature. The integral of the second over the volume of the system gives the total rate of conversion of mechanical energy into heat, E_v

$$E_v = \int_V (-\boldsymbol{\tau} : \nabla \mathbf{v}) dV \quad (E9.1-2)$$

In order to evaluate E_v we need to know the velocity and temperature fields as well as the rheology of the fluid.

For a batch system the macroscopic energy balance,² in the absence of kinetic and potential energy changes, reduces to

$$\frac{du}{dt} = \rho C_v M \frac{dT}{dt} = q_h + P_w \quad (E9.1-3)$$

2. The macroscopic energy balance is obtained by integrating Eq. 2.9-10.

where u is the internal energy, M is the mass in the system, q_h is the total heat added (removed) to the system, and P_w is the total power (rate of work) input. Note that for incompressible fluids $C_V = C_P$. Thus, all the input power is dissipated into heat and if isothermal conditions are desired, all the power input must be removed by conduction.

In a steady, continuous system, the macroscopic energy balance in terms of enthalpy \hat{h} (per unit mass) reduces to

$$\Delta\hat{h} = \hat{q}_h + \hat{P}_w \quad (\text{E9.1-4})$$

where $\hat{q}_h = q_h/G$ and $\hat{P}_w = P_w/G$, G being the mass flow rate. Now, the enthalpy can be expressed in terms of temperature and pressure

$$\Delta\hat{h} = \int_{T_1}^T C_P dT + \frac{\Delta P}{\rho} \quad (\text{E9.1-5})$$

Thus, from Eqs. E9.1-4 and E9.1-5 we obtain

$$\Delta T = \frac{1}{C_P} \left(\hat{q}_h + \hat{P}_w - \frac{\Delta P}{\rho} \right) \quad (\text{E9.1-6})$$

The macroscopic mechanical energy balance³ reduces to

$$\hat{P}_w = \hat{E}_v + \frac{\Delta P}{\rho} \quad (\text{E9.1-7})$$

or

$$P_w = E_v + (\Delta P)Q \quad (\text{E9.1-8})$$

where Q is the volumetric flow rate. Thus, the total power input is partly used to increase the pressure and the rest dissipated into heat (Eq. E9.1-2). In other words, the rate of energy dissipated into heat in a continuous processor is given by the total shaft power input less the product of the volumetric flow rate with the pressure rise. By substituting Eq. E9.1-7 into Eq. E9.1-6 we obtain the temperature change in terms of heat input (loss) and viscous dissipation

$$\Delta T = \frac{1}{C_P} (\hat{q}_h + \hat{E}_v) \quad (\text{E9.1-9})$$

Next we calculate the power input of a screw extruder. Equation E9.1-8 indicates that for calculating the total power we need to know the viscous energy dissipation and the pressure rise. To calculate the former according to Eq. E9.1-2, we need the complete velocity and temperature fields inside the machine. However, it is easier to calculate the total power input by multiplying the shear stress at any point on the barrel surface with the barrel velocity and integrating over the surface of the barrel. This will be equivalent to the total shaft power input. In tensor form, accounting for the direction of the shear stress and velocity, this is given by

$$P_w = \int_s (-[\mathbf{n} \cdot \boldsymbol{\tau}] \cdot \mathbf{v}) dS \quad (\text{9.2-9})$$

3. The macroscopic mechanical energy balance is obtained by integrating Eq. 2.9-11.

where S is the surface of the barrel, \mathbf{n} is the outward normal unit vector, $\boldsymbol{\tau}$ is the stress tensor at the barrel surface, and \mathbf{v} is the barrel velocity. Equation 9.2-9 for the simple model discussed previously reduces to

$$P_w = -[\tau_{yz}(H)V_{bz} + \tau_{yx}(H)V_{bx}]WZ \quad (9.2-10)$$

where Z is the total “unwound” channel length. The shear stress component $\tau_{yz}(H)$ is obtained from Eq. E2.5-20 by replacing V_0 by V_{bz} and q_p/q_d with $Q_p/Q_d = Q/Q_d - 1$, whereas, the $\tau_{yx}(H)$ is obtained by replacing V_0 by V_{bx} and setting $Q = 0$, since neglecting leakage over the flight, there is no net flow in the cross-channel direction.⁴ Substituting these into Eq. 9.2-10 results in

$$P_w = \mu \frac{\pi^2 N^2 D_b^2 WL}{\sin \theta H} \left(4 - 3 \cos^2 \theta_b \frac{Q}{Q_d} \right) \quad (9.2-11)$$

The total power input is at minimum under open discharge conditions ($Q = Q_d$) and is at maximum under closed discharge conditions ($Q = 0$). However, in addition to the power consumption in the channel, we must account for the power consumption in the flights,⁵ which is by no means negligible (1a).

The rate of power input dissipated into heat can be obtained from Eq. 9.2-11 by subtracting the term $Q\Delta P$, which is the power input for pressurization (Eq. E9.1-8), to give

$$E_v = \mu \frac{\pi^2 N^2 D_b^2 WL}{\sin \theta H} \left[4 - 6 \cos^2 \theta_b \frac{Q}{Q_d} + 3 \cos^2 \theta_b \left(\frac{Q}{Q_d} \right)^2 \right] \quad (9.2-12)$$

This expression can also be obtained by integrating the term $0.5\mu(\dot{\boldsymbol{\gamma}} : \dot{\boldsymbol{\gamma}})$ over the volume of the channel (Eq. E9.1-2).

Calculating the adiabatic temperature rise can make an approximate test of the validity of the isothermal assumption is obtained from Eq. E9.1-9

$$\Delta T = \frac{1}{C_p \rho Q} E_v \quad (9.2-13)$$

If ΔT is significant, we reject the isothermal assumption, but if it is small, local temperature effects may still be important.⁶

Without too much difficulty, we can extend the model to any screw design consisting of constant depth channels, and moderate tapers by using the taper correction factors of Eq. 6.4-4 separately for each section, and adding up the pressure drops (rises) according to Eq. 9.2.2. Thus, for a tapered channel, the drag and pressure flow terms are multiplied by the expressions $2/(1 + \zeta_0)$ and $2/\zeta_0(1 + \zeta_0)$, respectively, where $\zeta_0 = H_0/H_1$, with H_0

4. Note that, for calculating power, we neglect the effect of the leakage flow on the value of $\tau_{yx}(H)$, but we account for leakage flow for flow rate and pressure generation. This is not consistent, but acceptable in mathematical modeling of an engineering system because the former (depending in flight clearance) is less critical than the latter.

5. If we do this, we must make a minor correction to account for the loss of the barrel surface over the flight.

6. In Section 12.1 we show that in capillary flow average temperature rise may be very misleading, because even low values may hide large temperature rises at the capillary wall. The same may hold in this case, although the cross-channel circulatory flow brings about mixing of the melt-reducing cross-channel nonuniformities.

being the channel depth at the inlet and H_1 at the outlet, and H in Eq. 9.2-5 being replaced by H_0 .

Example 9.2 The Design of a HDPE Pelletizing Extruder Design an 18,000-lb/hr pelletizing extruder for high-density polyethylene (HDPE) melt at 450°F to generate 2500 psi head pressure. Assume a constant channel depth extruder with an axial length of 60 in. The melt density is 54 lb/ft³, the viscosity is 0.15 lb_s/in², and the specific heat is 0.717 Btu/lb°F.

Solution This is an open-ended problem, which has many possible solutions. We need to find the diameter of the barrel, the channel depth, and the screw speed needed to generate the head pressure. We shall assume a square pitched screw, and use British units (in, s, Btu, lb_f).

First we compute the volumetric flow rate

$$Q = \frac{18,000(\text{lb/h}) \times 1728(\text{in}^3/\text{ft}^3)}{3600(\text{s/h}) \times 54(\text{lb}/\text{ft}^3)} = 160(\text{in}^3/\text{s})$$

Next we turn to Eq. 9.2-5 and derive the optimum channel depth for the maximum pressure rise at fixed screw speed and barrel diameter. We rewrite Eq 9.2-5, neglecting the effect of the flight clearance and the shape factors, as follows

$$\frac{\Delta P \sin \bar{\theta}}{L} = \frac{6\mu\pi ND_b \cos \theta_b}{H^2} - Q \frac{12\mu}{WH^3}$$

Next, we take the derivative of this equation with respect to channel depth to obtain the optimum channel depth, H_{op}

$$\frac{d(\Delta P \sin \bar{\theta}/L)}{dH} = 6\mu \left(\frac{-2\pi ND_b \cos \theta_b}{H^3} + \frac{6Q}{WH^4} \right) = 0$$

to give

$$H_{\text{op}} = \frac{3Q}{\pi N W D_b \cos \theta_b}$$

It is easy to show that, with the optimum channel depth, $Q_d = 3Q/2$ and $Q_p = Q/2$.

We now take the drag and pressure flow terms in Eq. 9.2-5 and substitute the relevant numerical values. We assume a square pitched screw, neglecting the difference between mean and barrel surface helix angle, and neglecting shape factors and flight clearance. We further assume that flight width is 10% of the barrel diameter. We can make these simplifying assumptions because, at this point, we only wish to select the barrel diameter and the screw speed. The channel width can be expressed in terms of the screw diameter as follows:

$$W = D_b \cos \bar{\theta} - e = 0.953D_b - 0.1D_b = 0.853D_b$$

where we neglected the difference between the helix angle at the barrel surface and at the midchannel plane. Now, using Eq. 9.2-5, we can write for the drag flow term

$$Q_d = 1.5Q = 0.5\pi ND_b(0.853D_b) \cos \theta_b H_{\text{op}} = 1.28D_b^2 NH_{\text{op}}$$

and substitute $160 \text{ in}^3/\text{s}$ for the net flow rate to get

$$D_b^2(\text{in}^2)H_{\text{op}}(\text{in})N(\text{s}^{-1}) = 187.97(\text{in}^3/\text{s})$$

Next, we write the pressure flow term

$$Q_p(\text{in}^3/\text{s}) = 0.5Q = \frac{(0.853D_b)H_{\text{op}}^3(2500)(0.302)}{12(0.15)(60)} = 5.963 H_{\text{op}}^3 D_b$$

and the power input per unit volume is obtained from Eq. 9.2-12 divided by the channel volume $WLH_{\text{op}}/\sin \bar{\theta}$, which within the approximation we made, gives

$$e_v(\text{lb}_f \text{ in}/\text{in}^3 \text{ s}) = 2.38 \left(\frac{ND_b}{H_{\text{op}}} \right)^2$$

Note that the mean shear rate in the channel is given by

$$\bar{\dot{\gamma}} = \frac{\pi ND_b}{H_{\text{op}}}$$

The channel volume divided by the net volumetric flow rate gives the mean residence time

$$\bar{t}(s) = \frac{(0.853D_b)H_{\text{op}}(60/\sin \bar{\theta})}{160} = 1.0578D_b H_{\text{op}}$$

Finally, the mean temperature rise is given by

$$\Delta \bar{T}(\text{°F}) = 4.7795 \times 10^{-3} e_v(\text{lb}_f \text{ in}/\text{in}^3 \text{ s}) \bar{t}(s)$$

From the preceding equations, we can now select a barrel diameter, calculate the optimum channel depth, then the screw speed, the mean shear rate, and the power per unit volume. In the following table, the results are shown with barrel diameters from 8 in to 16 in.

D_b (in)	H_{op} (in)	$N(\text{s}^{-1})$	N (rpm)	$\bar{\dot{\gamma}}(\text{s}^{-1})$	e_v ($\text{lb}_f \text{ in}/\text{in}^3 \text{ s}$)	\bar{t} (s)	$\Delta \bar{T}$ (°F)
8	1.188	2.472	148	52.2	659	10.0	31.7
10	1.103	1.704	102	48.5	568	11.7	31.7
12	1.038	1.258	75	45.7	503	13.2	31.7
14	0.986	0.973	58	43.4	454	14.6	31.7
15	0.964	0.867	52	42.4	434	15.3	31.7
16	0.943	0.779	47	41.5	415	16.0	31.7

At first sight, based on the results we have, any of these extruders would be able to do the job. The 8-in extruder would need 7.5 turns to build up the required pressure, whereas the 16-in one will only need 3.75 turns. We note that both mean shear rate and specific power input per

unit volume drop significantly with increasing diameter, but the mean residence time increases, resulting in a constant mean temperature of about 31°F. This is quite a significant temperature rise, particularly if we take into account that the temperature over the channel height is not uniform, and may exhibit a significant local maximum that may be as high as twice the mean value. In actual operation, the barrel at this section may be cooled, somewhat reducing the mean temperature rise, but this does not eliminate the local maxima. In fact, overcooling, because of the interplay between convection and creation of a cool viscous melt layer near the barrel surface, may increase rather than decrease it. This is a rather important point, because temperature nonuniformities in a pelletizing extruder will yield unequal pellet sizes. Therefore, a reasonable first choice would be to select an extruder of 14 or 15 in diameters, where the shear rates and specific power inputs are low and the residence time reasonable. Subsequently, one would go to a more detailed solution without the simplifying assumptions introduced here, using a nonisothermal and non-Newtonian computer package.

Non-Newtonian and Nonisothermal Models

Distributed Parameter Models Both non-Newtonian and shear-thinning properties of polymeric melts in particular, as well as the nonisothermal nature of the flow, significantly affect the melt extrusion process. Moreover, the non-Newtonian and nonisothermal effects interact and reinforce each other. We analyzed the non-Newtonian effect in the simple case of unidirectional parallel plate flow in Example 3.6 where Fig.E 3.6c plots flow rate versus the pressure gradient, illustrating the effect of the shear-dependent viscosity on flow rate using a Power Law model fluid. These curves are equivalent to screw characteristic curves with the cross-channel flow neglected. The Newtonian straight lines are replaced with S-shaped curves.

Let us next consider the simple *isothermal* drag flow ($dP/dz = 0$) of a shear-thinning fluid in the screw channel. The cross-channel flow, induced by the cross-channel component of the barrel surface velocity, affects the down-channel velocity profile and vice versa. In other words, the two velocity profiles become coupled. This is evident by looking at the components of the equation of motion. Making the common simplifying assumptions, the equation of motion in this case reduces to

$$\frac{\partial \tau_{yz}}{\partial y} = 0 \quad (9.2-14)$$

and

$$\frac{\partial \tau_{yx}}{\partial y} = -\frac{\partial P}{\partial x} \quad (9.2-15)$$

Expressing the stress components in terms of the velocity gradients, we obtain the following two *coupled* differential equations

$$\frac{dv_z}{dy} = -\frac{C_1}{m} \left[\left(\frac{dv_x}{dy} \right)^2 + \left(\frac{dv_z}{dy} \right)^2 \right]^{(1-n)/2} \quad (9.2-16)$$

and

$$\frac{dv_x}{dy} = \frac{1}{m} \left[\left(\frac{dv_x}{dy} \right)^2 + \left(\frac{dv_z}{dy} \right)^2 \right]^{(1-n)/2} \left(\frac{dP}{dx} \right) (y - y_e) \quad (9.2-17)$$

where C_1 and y_e are integration constants to be evaluated from the boundary conditions $v_x(0) = V_z(0) = 0$, $v_x(H) = -V_b \sin \theta$, and $v_z(H) = V_b \cos \theta$. The constant C_1 is the shear stress component in the down-channel direction, and y_e is the channel height where the cross-channel velocity profile exhibits an extremum point. Clearly, the down-channel velocity profile $v_z(y)$, in spite of the constant shear-stress component value or absence of down-channel pressure gradient, is no longer linear. In physical terms, the cross-channel shear-rate distribution affects the non-Newtonian viscosity, which varies with y , hence, in the down-channel direction, the liquid responds as a rheologically nonhomogeneous liquid. Consequently, the deviation from linearity becomes a function of the helix angle; as the helix angle approaches a value of zero, the parallel-plate model is regained.

Next, we explore some nonisothermal effects on of a shear-thinning temperature-dependent fluid in parallel plate flow and screw channels. The following example explores simple temperature dependent drag flow.

Example 9.3 Nonisothermal Drag Flow of a Power Law Model Fluid Insight into the effect of nonisothermal conditions, on the velocity profile and drag flow rate, can be obtained by analyzing a relatively simple case of parallel-plate nonisothermal drag flow with the two plates at different temperatures. The nonisothermicity originates from viscous dissipation and nonuniform plate temperatures. In this example we focus on the latter.

We assume an exponential temperature dependence of the parameter m

$$m = m_0 e^{-a(T-T_0)} \quad (E9.3-1)$$

If $a = 0$, the non-Newtonian viscosity is temperature independent and the equations of motion and energy can be solved independently from each other; if, however, $a \neq 0$, they are coupled. Next, we assume that viscous dissipation is negligible $Br \rightarrow 0$, and that the moving plate at velocity V_0 is T_1 and the lower stationary plate is T_0 . The equations of motion and energy reduce to

$$\frac{d}{d\xi} \left[\left(\frac{du_z}{d\xi} \right)^n e^{b\Theta} \right] = 0 \quad (E9.3-2)$$

and

$$\frac{d^2\Theta}{d\xi^2} = 0 \quad (E9.3-3)$$

where $\Theta = (T - T_0)/(T_1 - T_0)$ and $b = -a(T_1 - T_0)$. The boundary conditions are $\Theta(0) = u_z(0) = 0$ and $\Theta(1) = u_z(1) = 1$. Solving Eqs. E9.3-2 and E9.3-3 yields the velocity and temperature profiles

$$u_z = \frac{1 - e^{-b'\xi}}{1 - e^{-b'}} \quad (E9.3-4)$$

and

$$\Theta = \zeta \quad (\text{E9.3-5})$$

where

$$b' = \frac{-a(T_1 - T_0)}{n} \quad (\text{E9.3-6})$$

Note that the temperature profile is linear, because we neglected viscous dissipation, but the velocity profile is nonlinear because of the temperature dependence of m . Integrating the velocity profile yields the flow rate per unit width

$$q = \frac{HV_0}{2} U_2 \quad (\text{E9.3-7})$$

where

$$U_2 = 2 \frac{1 - b' - e^{-b'}}{b'(e^{-b'} - 1)} \quad (\text{E9.3-8})$$

The factor $U_2 < 1$ for $b' < 0$ ($T_1 > T_0$); that is, flow rate drops if the temperature of the dragging surface is higher than the stationary wall, and vice versa. Since the shear stress is constant across the gap, in the former case, and the viscosity drops as we approach the moving plate, and, therefore, the shear rate must increase (so that the product is constant), and the velocity profile becomes convex. This effect, as we will see in the melting model discussed later, strongly affects the melting rate.

Now let us turn to the case of *nonisothermal* flow of a shear-thinning temperature-dependent polymer melts in combined pressure and drag flow. Colwell and Nicholls (3), explored nonisothermal effects of flow in the screw channels, neglecting the effect of cross-channel flow in parallel plate geometry. For a Power Law model fluid, their analysis parallels the nonisothermal effects considered in the preceding example, with pure drag flow replaced by combined pressure and drag flow. Figure 9.5 summarizes some of their results, plotting the “screw” characteristic (curve A). We note the typical S-shaped curve, but at nonisothermal conditions, the mean extrudate temperature varies slightly along the characteristic curve. There is interaction among heat transfer through the constant temperature walls, viscous dissipation, and the velocity profile, coupled through the temperature dependent viscosity. Colwell and Nichols (3) also calculated similar curves under adiabatic conditions, shown in Fig. 9.5 for high and low inlet temperatures. It is worth noting that the adiabatic screw characteristic curves exhibit maximum attainable pressures and a region of double values of flow rate for a given pressure rise.

Griffith (4), Zamodits and Pearson (5) and Yates (6) were the first to account for cross-channel flow of a temperature-dependent shear-thinning fluid, but they all assumed the flow to be two-dimensional and fully developed, both hydrodynamically and thermally [$v_x(y)$, $v_z(y)$, $T(y)$], by numerical solution using the finite difference method. Figure 9.6 shows some of Griffith’s results of isothermal Power Law model fluids in shallow channels, exhibiting the typical S-shaped curves, with increasing deviation from Newtonian behavior ($n < 1$), as well as a downward shift of the curves as a result of the cross-channel–down-channel coupling effect. This downward shift diminishes with diminishing helix angle. Griffith, who tested these results experimentally with a 1%

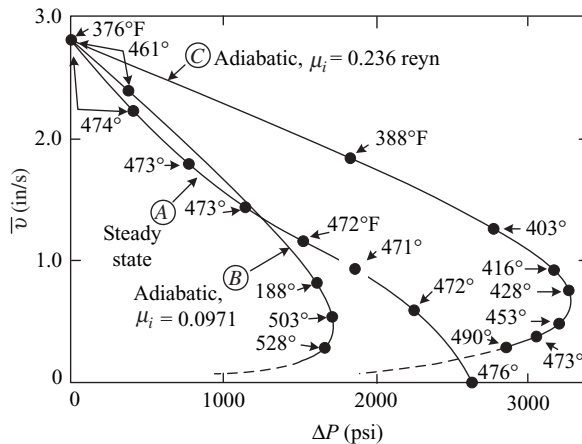


Fig. 9.5 Computed average velocities (proportional to volumetric flow rate) as a function of pressure drop. Length, 50 in; V_{bz} 5.66 in/s. Curve A, steady state; curve B, adiabatic high inlet temperature; curve C, adiabatic low inlet temperature. Note the double-valued flow rates at a given pressure rise in the adiabatic operation and the maximum pressure rise at finite flow-rate values. [Reprinted by permission from R. E. Colwell and K. R. Nicholls, “The Screw Extruder,” *Ind. Eng. Chem.*, **51**, 841–843 (1959).]

solution of a carboxyvinyl polymer in water extruded in a 2-in-diameter extruder, reported good agreement with theoretical predictions. These solutions, however, neglect the rather significant effect of the down-channel convection on temperature. This was accounted for in the work of Yates (6), and later that of Fenner (7,8) and Elbirli and Lindt (9).

With the great strides in computational fluid mechanics made over the past decades, the current trend is toward applying sophisticated *finite element* methods. These include both two- and three-dimensional (10–15) methods, which in principle allow the computation of two- or three-dimensional velocity and temperature fields with a variety of boundary

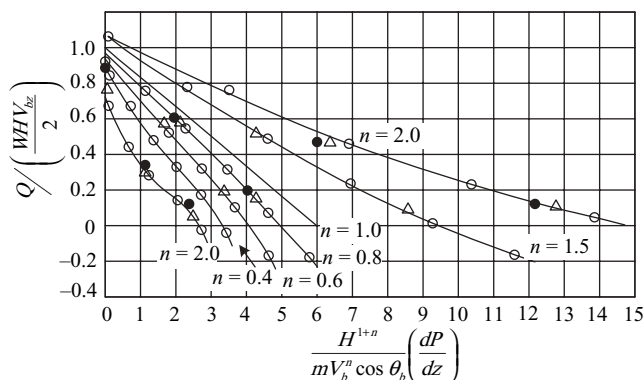


Fig. 9.6 Computed curves of dimensionless flow rate versus dimensionless pressure gradient for isothermal flow of a power law model fluid in shallow screw channels with the power law exponent n as a parameter, for helix angles θ_f as follows: O, 30°; Δ , 20°; \bullet , 10°; solid curves are for a helix angle 30°. Note that for $n < 1$, the reduced flow rate is less than 1, with the deviation diminishing with decreasing of the helix angle. [Reprinted with permission from R. M. Griffith, “Fully Developed Flow in Screw Extruders,” *Ind. Eng. Chem. Fundam.*, **1**, 180–187 (1962).]

conditions, while accounting for convection in both directions. Yet, convection terms, in particular the circulatory flow in the cross-channel direction, may give rise to numerical-stability problems. However, Syrjälä (16) recently computed very efficiently the three-dimensional fluid flow and heat transfer of a shear-thinning temperature-dependent fluid in a screw channel, accounting for convection in both the recirculation cross-channel flow, as well as the down-channel flow. He showed that the circulatory flow significantly alters the temperature, viscosity, and velocity profiles, as compared to two-dimensional solutions neglecting the cross-channel convection. Specifically, the temperature variation over the channel height is reduced by the recirculating flow, and the down-channel pressure profile deviates significantly from the two-dimensional computation. In real extruders, however, in addition to the recirculating flow, there is a series of additional factors and conditions that make accurate computation very difficult. For example, the leakage flow over the flight clearance, which both consumes significant power and may significantly alter the flow and temperature patterns in the screw channel; the nonprecise boundary conditions on the barrel surface; the root of the screw and the flights; the possibility of slip on the metal surfaces; and entrance and exit effects. Moreover, the polymeric material is frequently not a homogeneous fluid, but rather a filled or multicomponent system, such as a blend and alloy, or a reactive system with less well-defined rheological properties.

Still, sophisticated, exact, numerical, non-Newtonian and nonisothermal models are essential in order to reach the goal of accurately predicting final *product* properties from the total thermomechanical and deformation history of each fluid element passing through the extruder. A great deal more research remains to be done in order to accomplish this goal.

Lumped-parameter Models For *engineering design* of extruders, much simpler, lumped-parameter models may generally suffice. The main goal of the engineering design is to predict the pressure and mean melt temperature profiles along the extruder for a given screw geometry and output rate as a function of the operational parameters: screw speed, pressure at the die (or die characteristic), and barrel temperature profiles. In the models first proposed by Klein and Tadmor (17), the screw channel is divided into short axial segments, as shown in Fig. 9.7, where the inlet temperature and pressure are known from the calculation in the previous upstream segment. Within each segment, the temperature is

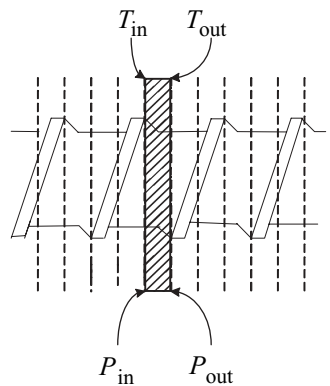


Fig. 9.7 The shaded area shows an axial slice of the screw with inlet melt temperature and pressure T_{in} and P_{in} and outlet temperature and pressure T_{out} , P_{out} .

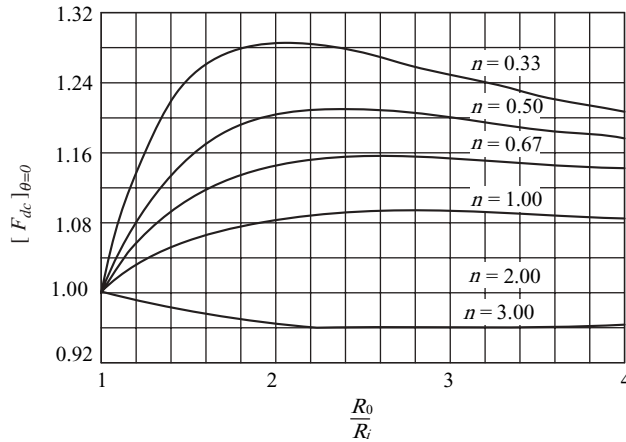


Fig. 9.8 Curvature correction factor for drag flow for a Power Law model fluid. $[F_{dc}]_{\theta=0}$ denotes the ratio of drag flow between parallel plates to drag (Couette) flow between concentric cylinders at equal gaps and moving surface velocities. The subscript $\theta = 0$ indicates that in screw extrusion this correction factor is rigorously valid only in the limit of a zero helix angle. [Reprinted by permission from Z. Tadmor and I. Klein, *Engineering Principles of Plasticating Extrusion*, Van Nostrand Reinhold, New York, 1970.]

assumed to be uniform and is equal to the mean temperature based on inlet and outlet temperatures: $(T_{in} + T_{out})/2$. Moreover, within each segment mean barrel and screw⁷ temperatures are assumed, as well as constant channel depth, which is the mean value between entrance and exit. Using isothermal non-Newtonian models, the pressure change across the segment is computed applying rheological properties at the mean temperature within the segment. Then, via an enthalpy balance including heat fluxes from the barrel, and screw and viscous dissipation, we calculate the temperature change in the segment. From these, T_{out} , P_{out} are calculated, and the shaft power input and torque in the segment. The computation is, of course, iterative within each segment (because the mean temperature and pressure depend on the exit values) as well as over the whole extruder in order to converge on the particular output at which the pressure rise in the extruder equals the pressure drop over the die.

The details of the fluid mechanical computations within each segment can vary in complexity. One rather useful approach was found to be the previously mentioned general modeling approach of “correcting” the separately computed drag and pressure flow terms for Power Law model fluids for shape (18), curvature (Figure 9.8) (19), and viscosity ratio at barrel and melt temperature⁸ (1d), and so on. The pressure-flow term is calculated using a Power Law model fluid. Of course, for a non-Newtonian fluid, drag and pressure flow cannot be superimposed as in the case of Newtonian fluids, but by introducing a “superposition correction factor” (1d), this error can be eliminated. These individual correction factors, in addition to providing some quantitative insight into the magnitude of the effects considered, were successfully applied to calculations by an appropriate

7. For “neutral” screws, that is, screws that are neither heated nor cooled through the shaft, it was found that the screw temperature at any given axial location equals that of the melt (1e).

8. The barrel temperature affects not only heat conduction into the barrel but it may strongly affect the drag capacity of the barrel; for example, if the barrel surface temperature is higher than the melt temperature, drag is reduced.

modeling scheme (1d,17). The analytical aspects of the foregoing procedure are given in great detail by Tadmor and Klein (1), and the computational aspects leading to computer program packages are given by Klein and Tadmor⁹(17).

The lumped-parameter model approach becomes particularly useful when dealing with the plasticating extrusion process discussed in the next subsection, where, in addition to melt flow, we are faced with the elementary steps of solids handling and melting.

Extensive Mixing and Residence Time Distribution in Screw Extruders

The velocity profiles for an isothermal Newtonian fluid in the screw channel were derived in Section 6.3. We concluded that the fluid particles circulate in the cross-channel direction while flowing down the channel. Thus, the flow path is a “helix within a helix.” This, as we will see below, leads to good laminar mixing and to narrow residence time distribution (RTD). Having narrow RTD which approaches plug-flow conditions, is a useful characteristic in a polymer processing machine to avoid the risk of thermal degradation of the long-term “tail” of the RTD. On the other hand, it also implies that inlet time fluctuations of composition should be *avoided* because the extruder is ineffective in “washing” out these fluctuations.

We now derive the RTD function $f(t) dt$ and the strain distribution functions $f(\gamma) d\gamma$ for isothermal Newtonian fluids in shallow screw channels.

The cross- and down-channel velocity profiles are (see Section 6.3):

$$u_x = \xi(2 - 3\xi) \quad (9.2-18)$$

and

$$u_z = \xi + 3\xi(1 - \xi) \frac{Q_p}{Q_d} \quad (9.2-19)$$

Thus, the operating conditions affect the down-channel velocity profile, but not the cross-channel velocity profile. At closed discharge conditions ($Q_p/Q_d = -1$), both the down-channel and cross-channel velocities vanish at $\xi = 2/3$, implying that the whole plane at this location is stagnant.

The Residence Time Distribution Function A fluid particle at height $\xi > 2/3$ will approach the “pushing flight” turnaround and move toward the trailing flight at height ξ_c . The relation between the two heights can be obtained by the following mass balance (neglecting leakage flow over the flights):

$$\int_0^{\xi_c} u_x d\xi = - \int_{\xi}^1 u_x d\xi \quad (9.2-20)$$

Substituting Eq. 9.2-18 into Eq. 9.2-20 yields

$$\xi_c^2 - \xi_c^3 = \xi^2 - \xi^3 \quad (9.2-21)$$

9. Note that in Reference 17, Table 1, which gives the coefficients for the regression analysis of the superposition correction error, there is a misprint: $C_{82} = -0.02029$ and not -0.2029 as listed.

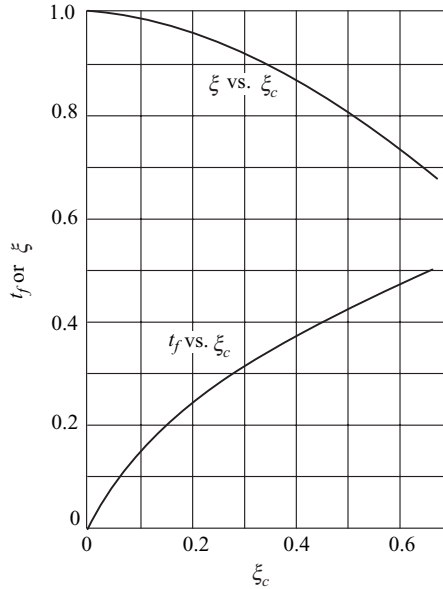


Fig. 9.9 Fluid particle position in the upper part of the channel, ξ , versus its position in the lower part of the channel, ξ_c , and the fraction of time t_f versus position ξ_c .

where $0 \leq \xi_c \leq \frac{2}{3}$ and $\frac{2}{3} \leq \xi \leq 1$.

Equation 9.2-21 can be solved to give

$$\xi = \frac{1}{2} \left(1 - \xi_c + \sqrt{1 + 2\xi_c - 3\xi_c^2} \right) \quad 0 \leq \xi_c \leq \frac{2}{3} \quad (9.2-22)$$

and

$$\xi_c = \frac{1}{2} \left(1 - \xi + \sqrt{1 + 2\xi - 3\xi^2} \right) \quad \frac{2}{3} \leq \xi \leq 1 \quad (9.2-23)$$

Figure 9.9 plots the relationship between ξ and ξ_c . In this analysis we disregarded the complex flow fields in the neighborhood of the flights, which are restricted to regions of the order of channel height distance from the flight. The exact flow fields can be obtained by standard numerical methods, which confirm the flow patterns previously described, though they indicate that in the lower corners small stagnant fluid regions appear where reverse circulation takes place.¹⁰

The residence time of a fluid particle at a given height in one cycle is obtained by dividing the channel width with the local cross-channel velocity given in Eq. 9.2-18. The residence time at ξ is different, of course, from that at ξ_c . It is easy to show that the

10. These solutions [e.g., O. R. Burggaf, "Analytical and Numerical Studies of the Structure of Steady Separated Flows," *J. Fluid Mech.*, **24**, 113–151 (1966)] were done with a rectangular channel. Real screws have rounded corners that most likely eliminate these stagnant pockets. However, we note that residence time and the strain distribution function are more sensitive to fine local flow structures than design equations relating pressure gradients and flow rates. Therefore, care should be exercised in using equations based on simple flow models.

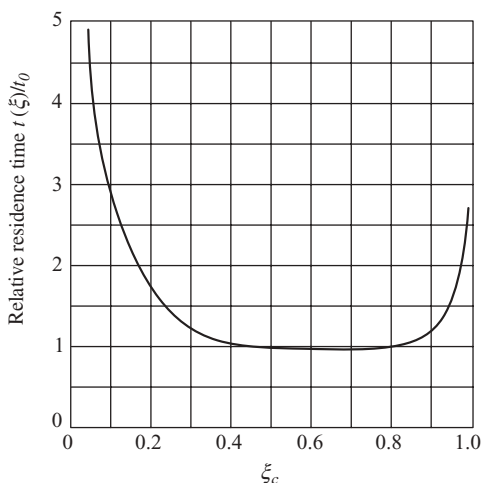


Fig. 9.10 The normalized residence time as a function of ξ .

fraction of time the fluid particle spends in the upper portion of the channel, $t_f(\xi)$, is given by

$$t_f(\xi) = \frac{1}{1 + \frac{|u_x(\xi)|}{|u_x(\xi_c)|}} = \frac{1}{1 - \frac{\xi(2 - 3\xi)}{\xi_c(2 - 3\xi_c)}} \quad (9.2-24)$$

Figure 9.10 plots $t_f \xi$ as a function of position. Results indicate that the further away the fluid particle is from $\xi = 2/3$, the shorter is the fraction of time it spends in the upper portion of the channel. The fluid particle, while alternating between layers ξ and ξ_c , also moves in the down-channel direction, as dictated by Eq. 9.2-19. The residence time of this fluid particle in an extruder of axial length l is

$$t = \frac{l}{V_b \bar{u}_l(\xi)} \quad (9.2-25)$$

where V_b is the barrel velocity relative to the screw and $\bar{u}_l(\xi)$ is the average velocity of the fluid particle in the axial direction given by

$$\bar{u}_l(\xi) = u_l(\xi)t_f(\xi) + u_l(\xi_c)[1 - t_f(\xi)] \quad (9.2-26)$$

The velocity profile in the axial direction is obtained from Eqs. 9.2-18 and 9.2-19 (see Section 6.3)

$$u_l(\xi) = 3\xi(1 - \xi) \left(1 + \frac{Q_p}{Q_d} \right) \sin \theta \cos \theta \quad (9.2-27)$$

Substituting Eq. 9.2-26 and 9.2-27 into Eq. 9.2-25, together with Eqs. 9.2-22 and 9.2-23, gives the residence time of a fluid particle circulating between locations ξ and ξ_c

$$t(\xi) = \left[\frac{l}{3V_b(1 + Q_p/Q_d) \sin \theta \cos \theta} \right] \frac{3\xi - 1 + \sqrt{1 + 2\xi - 3\xi^2}}{\xi \left[1 - \xi + \sqrt{1 + 2\xi - 3\xi^2} \right]} \quad (9.2-28)$$

for $2/3 \leq \xi \leq 1$. The minimum residence time is at $\xi = 2/3$

$$t_{\min} = \frac{3l}{2V_b(1 + Q_p/Q_d) \sin \theta \cos \theta} = \frac{3z}{2V_{bz}(1 + Q_p/Q_d)} \quad (9.2-29)$$

where z is the helical distance and V_{bz} the down-channel barrel-velocity component. Figure 9.10 plots the normalized residence time t/t_{\min} as a function of ξ .

Figure 9.10 indicates that over a broad region of the channel core, the residence time is close to the minimum, but as we approach the top or bottom of the channel, the residence time increases significantly. The importance of this, however, cannot be appreciated unless we derive the RTD function (20), which tells what *fraction* of the exiting flow rate that stays a given time t in the channel.

The fraction of flow rate in the upper portion of the channel between ξ and $\xi + d\xi$, corresponding to residence time t and $t + dt$, is

$$\frac{dQ}{Q} = \frac{V_{bz}WH}{Q} u_z(\xi) d\xi = \frac{V_{bz}WH}{Q} \left[\xi + 3\xi(1 - \xi) \frac{Q_p}{Q_d} \right] d\xi \quad (9.2-30)$$

and that in the corresponding lower portion of the channel is

$$\frac{dQ_c}{Q} = \frac{V_{bz}WH}{Q} u_z(\xi_c) |d\xi_c| = \frac{V_{bz}WH}{Q} \left[\xi_c + 3\xi_c(1 - \xi_c) \frac{Q_p}{Q_d} \right] |d\xi_c| \quad (9.2-31)$$

The total fraction of flow rate between time t and $t + dt$ is the sum of Eqs. 9.2-30 and 9.2-31, which is also the definition of the RTD function $f(t) dt$

$$f(t)dt = \frac{dQ + dQ_c}{Q} \quad (9.2-32)$$

By substituting Eqs. 9.2-30 and 9.2-31 into Eq. 9.2-32 and further deriving a relationship between $d\xi$ and $d\xi_c$ from Eq. 9.2-23, we get

$$d\xi_c = \frac{1 - 3\xi - \sqrt{1 + 2\xi - 3\xi^2}}{2\sqrt{1 + 2\xi - 3\xi^2}} d\xi \quad (9.2-33)$$

and noting that $|d\xi_c| = -d\xi_c$, we get

$$f(t)dt = \frac{3\xi [1 - \xi + \sqrt{1 + 2\xi - 3\xi^2}]}{\sqrt{1 + 2\xi - 3\xi^2}} d\xi \quad (9.2-34)$$

Equation 9.2-28 provides a unique relation between ξ and t ; thus, the RTD function $f(t) dt$ can be easily evaluated. We note that the RTD functions depend on only one dimensionless group $l/3V_b(1 + Q_p/Q_d) \sin \theta \cos \theta$ in Eq. 9.2-28, which is a simple multiplier and does not alter the *shape* of the RTD.

The mean residence time can be evaluated from Eq. 9.2-32 and Eq. 9.2-28 to give

$$\bar{t} = \int_{t_{\min}}^{\infty} tf(t) dt = \frac{4}{3} t_{\min} \quad (9.2-35)$$

where t_{\min} is given in Eq. 9.2-29.

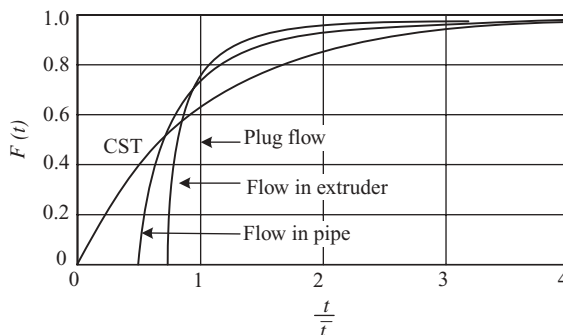


Fig. 9.11 The RTD function $F(t)$ versus reduced time t/\bar{t} for flow in screw extruder compared to plug flow, isothermal flow of Newtonian fluids in pipes, and a continuously stirred tank vessel (CST).

The cumulative RTD function $F(t)$ is obtained by integrating Eq. 9.2-24 while recalling that the fraction of flow rate with a residence time less than t is located in the region located between $\xi = 2/3$ and ξ :

$$F(t) = F(\xi) = \frac{1}{2} \left[3\xi^2 - 1 + (\xi - 1)\sqrt{1 + 2\xi - 3\xi^2} \right] \quad (9.2-36)$$

Once again $F(t)$ can be calculated from Eq. 9.2-36 in conjunction with Eq. 9.2-28. Figure 9.11 plots the RTD function $F(t)$ versus reduced time t/\bar{t} and compares it to the RTD function of Newtonian laminar flow in a pipe and that in a well-stirred vessel. The RTD function in the melt extruder is quite narrow, approaching plug-type flow. Only about 5% of the flow rate stays more than twice the mean residence time in the extruder.

Wolf and White (21) verified the theoretical RTD function experimentally with radioactive tracer methods. Figure 9.12 gives some of their results, indicating excellent agreement with theory. RTD functions in extruders using non-Newtonian Power Law model fluids have also been derived (22,23).

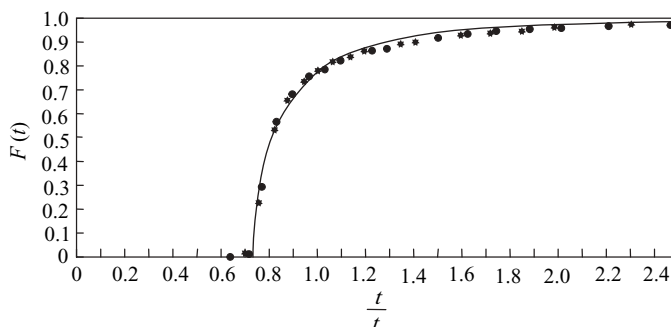


Fig. 9.12 Experimental verification of the RTD function in extruder by radioactive tracer techniques with a 44.2-mm-diameter, 24:1 L/D extruder, liquid polyester resin, and a radioactive manganese dioxide tracer: Asterisk, Experiment 1; ●, Experiment 2; smooth curve indicates theoretical prediction. [Reprinted by permission from D. Wolf and D. H. White, "Experimental Study of the Residence Time Distribution in Plasticating Screw Extruders," *AIChE J.*, **22**, 122–131 (1976).]

The Strain Distribution Functions In Chapter 7 we established the relation between interfacial area stretching and the total strain imposed on the fluid. The strain is the product of rate of strain and time, and therefore strain is a function of location in the channel. The strain distribution function (SDF) was defined in Chapter 7 as the fraction of exiting flow rate that experienced a given strain in the extruder. Following similar lines to the derivation of the RTD functions we now derive the SDF.

The rate of strain components are obtained from Eqs. 6.3-16 and 6.3-17 (simplified for shallow channels)

$$\dot{\gamma}_{yx}(\xi) = \frac{V_{bx}}{H} \frac{du_x}{d\xi} = \frac{2V_b \sin \theta}{H} (1 - 3\xi) \quad (9.2-37)$$

and

$$\dot{\gamma}_{yz}(\xi) = \frac{V_{bz}}{H} \frac{du_z}{d\xi} = \frac{2V_b \cos \theta}{H} \left[1 + 3(1 - 2\xi) \frac{Q_p}{Q_d} \right] \quad (9.2-38)$$

According to our model, these are the only components of the rate of strain tensor. Thus, we can write an expression for the magnitude of the rate of strain tensor (cf. Eq. 2.7-11)

$$\begin{aligned} \dot{\gamma}(\xi) &= \left(\dot{\gamma}_{yx}^2 + \dot{\gamma}_{yz}^2 \right)^{1/2} \\ &= \frac{V_b}{H} \left\{ 4(1 - 3\xi)^2 \sin^2 \theta + \left[1 + 3(1 - 2\xi) \frac{Q_p}{Q_d} \right]^2 \cos^2 \theta \right\}^{1/2} \end{aligned} \quad (9.2-39)$$

A corresponding expression for $\dot{\gamma}(\xi_c)$ is obtained by replacing ξ with ξ_c in Eq. 9.2-39. The direction of shear of a fluid particle differs at ξ and at ξ_c . This poses difficulties in evaluating the total strain experienced by a fluid particle circulating between these two positions, because depending on the specific position of ξ and the exact nature of the turnover at the flight, partial demixing may occur. The exact solution of the problem would require following the fluid particle in the true three-dimensional flow patterns, with the prerequisite of relating the increase of interfacial area to the invariants of the strain tensor. As a first approximation, however, we assume that total strains acquired in the upper and lower parts of the channel are additive. Thus, the total strain acquired by the fluid particle after time t is

$$\gamma(\xi) = \dot{\gamma}(\xi) t_f(\xi) t(\xi) + \dot{\gamma}(\xi_c) [1 - t_f(\xi)] t(\xi) \quad (9.2-40)$$

Substituting Eqs. 9.2.24, 9.2.28, and 9.2.39 into Eq. 9.2.40 gives

$$\gamma(\xi) = \frac{l}{3H} \left(\frac{1}{1 + Q_p/Q_d} \right) [E_1(\xi, \theta, Q_p/Q_d) + E_2(\xi, \theta, Q_p/Q_d)] \quad (9.2-41)$$

where

$$E_1(\xi, \theta, Q_p/Q_d) = \frac{2}{\cos \theta} \frac{t_f(\xi) \left[(1 - 3\xi)^2 + \frac{\cot^2 \theta}{4} \left(1 + 3 \frac{Q_p}{Q_d} - 6\xi \frac{Q_p}{Q_d} \right)^2 \right]^{1/2}}{\xi_c(1 - \xi_c) + [t_f(\xi)](\xi - \xi_c)(1 - \xi - \xi_c)} \quad (9.2-42)$$

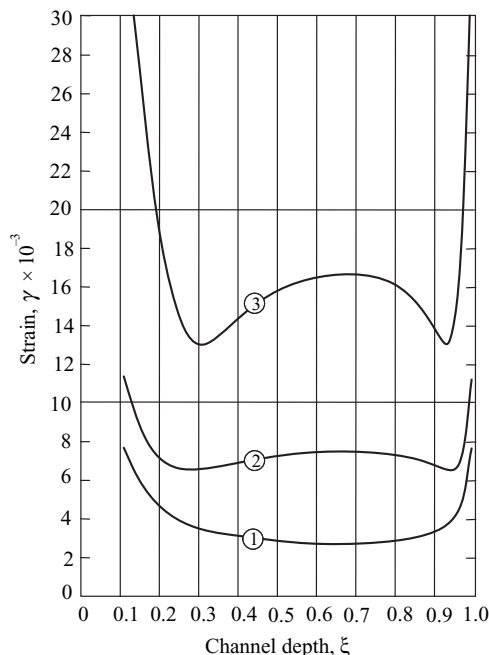


Fig. 9.13 Total strain as a function of position ξ in a screw channel. Calculations are based on a total axial length of 100 in, channel depth of 0.2 in, and 20° helix angle. Curve 1, $Q_p/Q_d = 0$; Curve 2, $Q_p/Q_d = -0.05$; and Curve 3, $Q_p/Q_d = -0.075(20)$.

and

$$E_2(\xi, \theta, Q_p/Q_d) = \frac{1}{\sin \theta} \frac{[1 - t_f(\xi)] \left[4(1 - 3\xi_c)^2 \tan^2 \theta + \left(1 + 3 \frac{Q_p}{Q_d} - 6\xi_c \frac{Q_p}{Q_d} \right)^2 \right]^{1/2}}{\xi_c(1 - \xi_c) + [t_f(\xi)](\xi - \xi_c)(1 - \xi - \xi_c)} \quad (9.2-43)$$

The time fraction $t_f(\xi)$ as a function of ξ and ξ_c is given in Eq. 9.2-24, and the relationship between ξ and ξ_c appears in Eq. 9.2-22. Thus, the total strain as a function of position t can be evaluated subject to the previously given assumption, without difficulties. Figure 9.13 presents the distribution of total strain as a function of ξ for various Q_p/Q_d values.

It is interesting to note that for pure drag flow the minimum strain is obtained (as expected) at $\xi = 2/3$, but when back pressure is applied ($Q_p/Q_d < 0$), the minimum strain is obtained elsewhere. Yet, like residence time, the total strain is rather uniform over a significant portion of the channel.

The SDF can be calculated by the same procedure used for the RTD function. For pure drag flow, where the minimum strain is obtained at $\xi = 2/3$, it is given by Eq. 9.2-36, with ξ uniquely related to γ in Eq. 9.2-40. For the more general case, however, the fraction of flow rate between $\xi = 2/3$ and ξ is *not* the fraction of flow rate experiencing a total strain of γ or less, as is evident from Fig. 9.13. First, the location of minimum γ must be established, then Eqs. 9.2-30 and 9.2-31 must be integrated over the appropriate limits. An alternative approach, which is also applicable to a plasticating extruder, in which the channel is broken up into small height increments and fluid particles are followed with

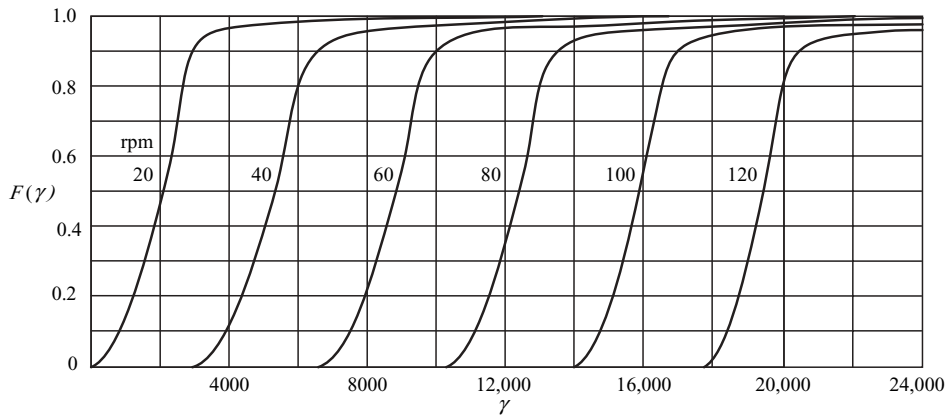


Fig. 9.14 Values of $F(\gamma)$ for a 6-in-diameter, 20:1 L/D extruder at constant flow rate (500 lb/h) with screw speed as a parameter. Simulation was made for a square pitched screw with a constant channel depth of 0.6 in. [Reprinted by permission from G. Lidor and Z. Tadmor, "Theoretical Analysis of Residence Time Distribution Functions and Strain Distribution Functions in Plasticating Extruders," *Polym. Eng. Sci.*, **16**, 450–462 (1976).]

time, was described by Lidor and Tadmor (24). Figure 9.14 gives the results of such computations for a 6-in-diameter plasticating extruder at 500 lb/h.

Melting is rapid at high screw speeds, and the SDF is essentially that of a melt extruder. Increasing the screw speed at constant flow rate implies an increase in back pressure, and we note a consequent shift of the SDF to higher strain ranges. Once again we observe that SDF in screw extruders is quite narrow. Hence, a good indication of the mixing performance can be obtained by calculating the mean strain $\bar{\gamma}$. The mean strain is proportional to l/H and a function of Q_p/Q_d and the helix angle θ . Figure 9.15 is a generalized plot of $\bar{\gamma}$ as a function of Q_p/Q_d , with the helix angle as a parameter. That the mean strain is proportional to l/H is borne out by engineering practice. Similarly, increasing the mean strain with increasing back pressure is also well supported by experience, and the same holds for the limited effect of the helix angle within the practical range of θ values.

Dispersive Mixing in Screw Extruders

While the common wisdom is that the SSE is a good extensive mixer, at least in the cross-channel direction, it is a poor dispersive mixer. This is not surprising because, as we showed in Chapter 7, good dispersion requires repeated passages of all fluid particles over high shear regions. However, in the single flighted SSE, the only high-shear zone is the flight clearance. Moreover, much of the material never passes or passes once or a few times over the flight and only small fractions pass it repeatedly. Finally, even the material that does pass the flights does not experience the stretching elongational flow, typical to shear regions in dispersive mixers, nor is it exposed to cool solid boundaries that are needed to maintain relatively low temperatures, and thus attain high shear stresses.

Next we derive a simple theoretical model to calculate the passage-distribution function (PDF) in a SSE¹¹ (25), assuming isothermal Newtonian fluids. We examine a small axial section of length Δl , as shown in Fig. 9.16.

11. In Reference 25 down-channel increments were used for the model. Here we use axial increments.

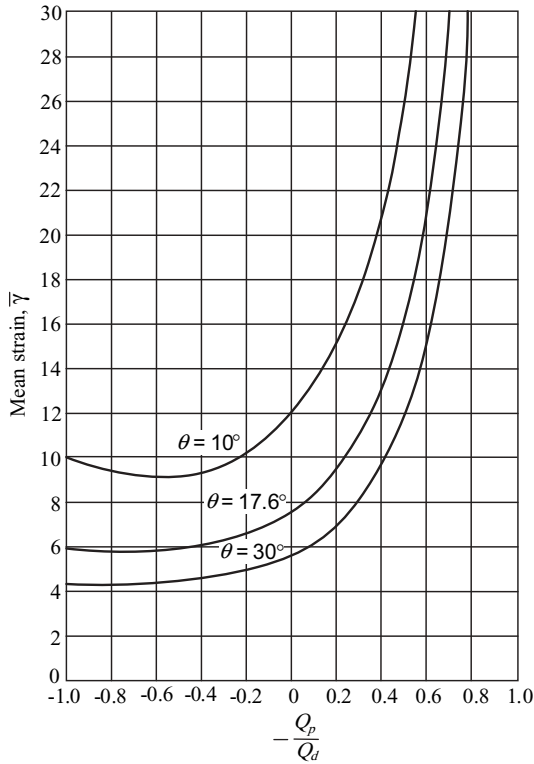


Fig. 9.15 Mean strain as a function Q_p/Q_d ratio with helix angle as a parameter for $l/H = 1$. When $Q_p/Q_d = -1$, γ goes to infinity; this condition corresponds to a closed discharge operation.

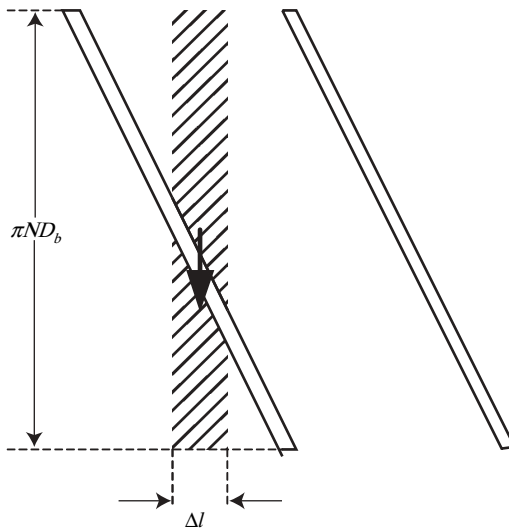


Fig. 9.16 An unwound single flighted screw, showing an axial increment of Δl .

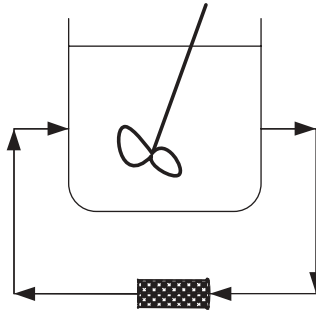


Fig. 9.17 Schematic representation of a well-stirred vessel with a recycling stream over a high-shear zone.

We recall that at closed discharge conditions fluid particles stay at a fixed axial position. This means that the fluid in the crosshatched incremental volume $\Delta V = \pi N \bar{D} H \Delta l$ does not leave it. Some fluid is dragged over the flight and recycled to the bulk, and since within the volume element the fluid circulates due to the drag of the barrel surface, we can model the system as a well-stirred tank with recycle, as shown in Fig. 9.17.

The PDF for this system, as shown in Chapter 7, is given by

$$g_k = \frac{\lambda^k}{k!} e^{-\lambda} \quad (9.2-44)$$

where $\lambda = t/\bar{t}$ is the ratio of the time elapsed to the mean circulation time in the vessel given by the ratio of the volume of the vessel to the volumetric flow rate over the flight. If we assume pure drag flow over the flight and neglect the flight width on the free volume this ratio is

$$\bar{t} = \frac{\pi \bar{D} H \Delta z}{\pi N D_b \Delta z \delta_f / 2} = \frac{2 H \bar{D}}{N D_b \delta_f} \quad (9.2-45)$$

We now extend the model to the positive net flow situation, and assume that the differential volume moves axially. Although the axial flow is not plug flow, this is not an unreasonable approximation because as we recall the RTD is rather narrow. In this case, the elapsed time t becomes the mean residence time in the extruder given by the ratio of screw channel volume and net flow rate

$$t = \frac{\pi L H \bar{D}}{Q} \quad (9.2-46)$$

Substituting Eqs. 9.2.45 and 9.2.46 into the definition of λ gives

$$\lambda = \frac{\pi N L D_b \delta_f}{2 Q} = \frac{Q_f}{Q} \quad (9.2-47)$$

where Q_f is defined as the drag flow rate of the flight along the whole extruder. Thus, neglecting the flight width λ is simply the ratio of flow rates over the flight and the net flow rate over the extruder.

Example 9.4 Passage Distribution in a 60-mm Single Flighted Screw Extruder Calculate the PDF in a 60-mm diameter 10/1 L/D melt extruder with 0.125-mm flight clearance, turning at 100 rpm and extruding 100 l/h. Neglect the effect of flight width on the volume of the channel.

Solution Using Eq. 9.2-47, we compute the value of λ

$$\lambda = \frac{\pi \times (100/60) \times (10 \times 0.06) \times 0.06 \times 0.125 \times 10^{-3}}{2 \times (100/3600) \times 10^{-3}} = 0.424$$

Turning to Eq. 9.2-44 and substituting λ , yields $g_0 = 0.654$; $g_1 = 0.277$; $g_2 = 0.059$; $g_3 = 0.008$, which implies that in this particular case that 65.4% does not pass over the flight, 27.7 passes once, 5.9% twice, and 0.8% three times, and so on. Good dispersion, as mentioned in Chapter 7, requires 20–30 passages over high-shear zones.

Clearly, the single flighted single screw is a poor dispersive mixer. However, it is possible to design special multiflighted single screws that can provide multiple passages over appropriately designed shearing flights (26,27).

9.3 THE SINGLE SCREW PLASTICATING EXTRUSION PROCESS

Most SSEs used in the plastics industry are “plasticating extruders,” that is, they are fed by solid pellets or powder. The solids are fed gravitationally into the hopper and the screw channel, where they are conveyed and compressed by a drag-induced mechanism, then melted, or “plasticated,” by a drag-induced melt removal mechanism. Pressurization and mixing take place side by side with the melting step. Hence, the plasticating extrusion process, shown in Fig. 9.18, consists of all four elementary steps: handling of particulate solids in Regions 1, 2, and 3; and melting, pumping, and mixing in Regions 3 and 4. The fifth elementary step, devolatilization, may also occur in Regions 3 and 4 through

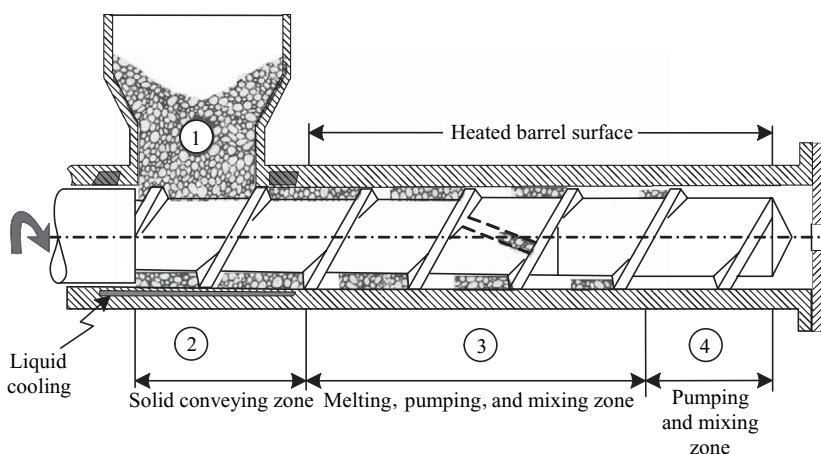


Fig. 9.18 Schematic representation of a plasticating screw extruder. The barrel is cooled in the hopper region and heated downstream. Typical plasticating SSE have length-to-diameter ratios of 24–26.

appropriate screw design (two-stage screw) and operating conditions, providing for a partially filled channel.

The Journey of a Polymer Particle in the Plasticating Extruder

It is easy to visualize the mechanisms that take place in the solids conveying zone of a screw extruder, and to develop appropriate mathematical models describing these mechanisms. This was done by Darnell and Mol (28) in 1956, and their model is discussed later in this section.

However, the melting or plasticating process that follows the solids conveying zone is a relatively complex one, and unlike the melt extrusion and solids conveying processes, the detailed physical melting mechanisms cannot be easily visualized, predicated, and modeled from basic principles without experimental investigation.

Indeed, the qualitative elucidation of the *melting mechanism* and its *quantitative* mathematical formulation by Tadmor (29) was done by observing and analyzing experimental samples obtained by Maddock using an ingenious experimental technique (30). This technique calls for abruptly stopping an extruder operating at steady state, chilling both barrel and screw (thereby solidifying the polymer in the screw channel), pushing out the screw from the barrel, unwinding the solidified helical ribbon of polymer from the screw (Fig. 9.19), and slicing thin representative sections perpendicular to the flights. To better visualize the details of the process, a small amount (3–5%) of colored polymer pellets is added as a tracer. This helps to distinguish between solids filled and molten regions. It also provides some information on flow patterns.

Figures 9.20–9.25 show the results of such “cooling” experiments obtained by Tadmor et al. (31) using the Maddock technique. The slices, sectioned every half-turn from the hopper to the die, are shown for each experiment. Next to each slice, the axial location in terms of the turn number (starting downstream from the hopper) is given. Figures 9.20–9.24 were obtained from a 2.5-in-diameter extruder with a metering-type screw having a 12.5 turns feed section with a channel depth of 0.370 in; a 10 turns compression section, and 4-turns-long metering section, 0.127-in deep. Results in Fig. 9.25 were obtained from an 8-in extruder with a metering-type screw. The polymers used and the operating conditions accompany each figure. Figure 9.19 illustrates the relative position of a typical “slice” or cross section. Thus the pushing flight is on the left and the trailing flight on the right; the barrel surface is on the top and the root of the screw on the bottom.

Analyzing the experimental results, we note that throughout most of the extruder, the solid and melt phases *coexist* side by side, and are clearly segregated from each other, with

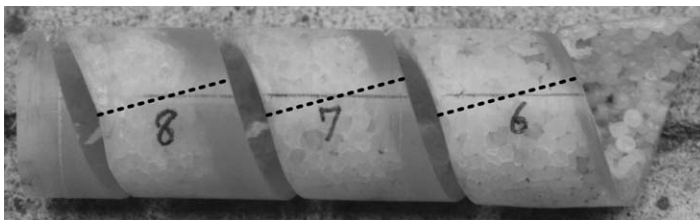


Fig. 9.19 Helical ribbon of LDPE, after it was taken off the screw following a cooling experiment. The numbers indicate turns downstream the hopper and cross sections for examination obtained by slicing it perpendicular to the flights, as shown by the broken line.

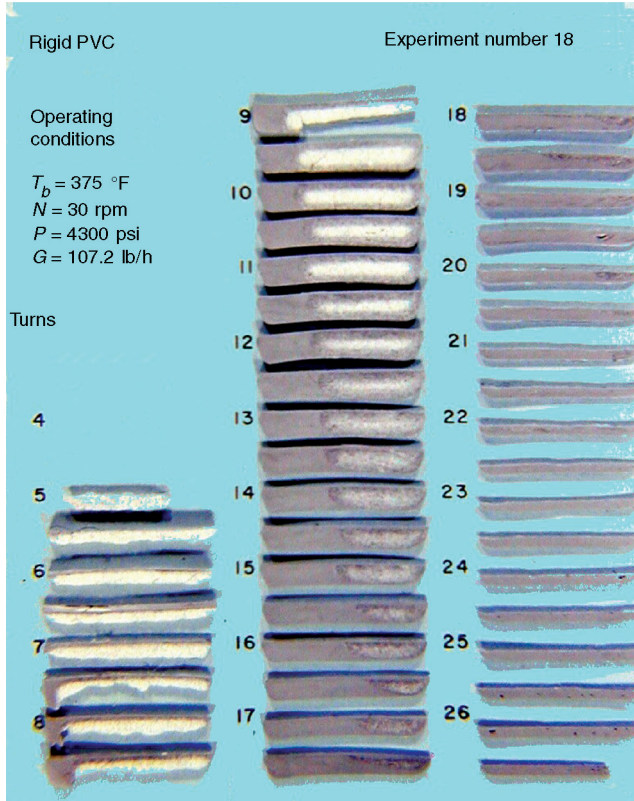


Fig. 9.20 Cross sections obtained from “cooling” experiments of a 2.5-in-diameter 26.5 length-to-diameter ratio screw extruder. Material: rigid PVC. Operating conditions are listed in the figure: T_b is the barrel temperature, N the screw speed, P the pressure at the die, and G the mass flow rate. Numbers denote turns from the beginning (hopper side) of the screw. The screw was of a metering type with a 12.5 turn feed section 0.37 in deep, a 9.5 turn transition section, and a 4.5 turn metering section 0.127 in deep. [Reprinted by permission from Z. Tadmor and I. Klein, *Engineering Principles of Plasticating Extrusion*, Van Nostrand Reinhold, New York, 1970. The experiments were carried out at the Western Electric Engineering Research Center, Princeton, NJ.]

the melt phase accumulating the pushing flight in a *melt pool* and the solids segregated at the trailing flight as a *solid bed*. The width of the melt pool gradually increases in the down-channel direction, whereas that of the solid bed generally decreases. The solid bed, shaped as a continuous long, helical ribbon of varying width and height, slowly turns in the channel (much like a nut on a screw) sliding toward the exit, while gradually melting. Upstream from the point where melting starts, the whole channel cross-section is occupied by the solid bed, which is composed, as the hopper is approached, of less compacted solids. The continuity of the solid bed provides an explanation for the capability of the screw extruder to generate melt that is free of air bubbles: the porous continuous solid bed provides uninterrupted air-filled passages from deep in the extruder all the way back to the hopper. Thus, particulate solids forming the solid bed move down-channel while the air is stationary.

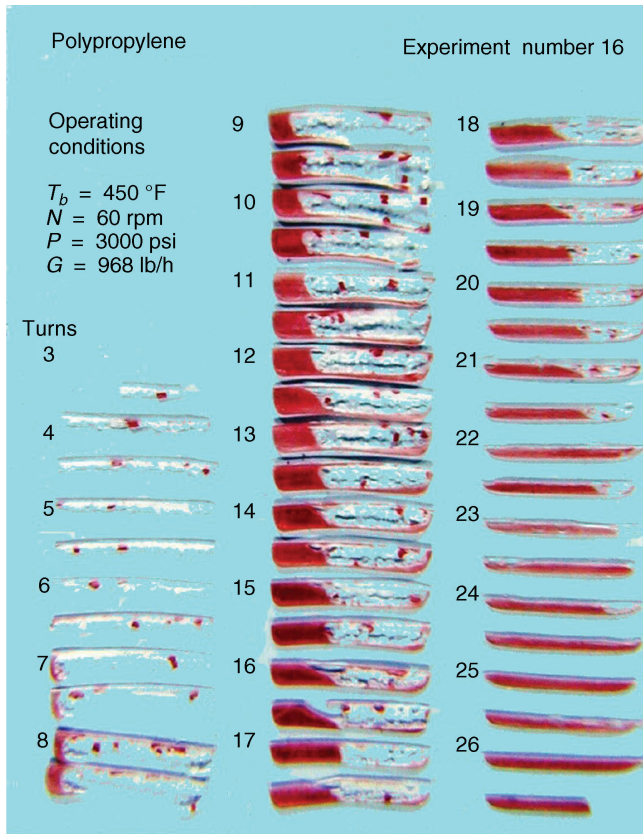


Fig. 9.21 Cross sections obtained from cooling experiments of a 2.5-in-diameter, 26.5 length-to-diameter ratio screw extruder. Material: PP. Operating conditions are listed in the figure ($G = 96.8$ lb/h). Symbols and screw descriptions as in Fig. 9.20.

Although the melting behavior in extruders just described appears to be quite general for amorphous and crystalline polymers, small and large extruders, and diverse operating conditions, it appears that, with certain PVC compounds, the melt pool accumulates at the trailing flight (32). Moreover, with large extruders, there was no segregated melt pool at the channel side, but rather a thickening layer of melt at the barrel surface was observed (33). Finally, dissipative mix-melting may take place in screw extruders under conditions that lead to high pressures in the feed zone. In this section, however, we concentrate on the commonly observed melting mechanism.

It should be noted that melting takes place along most of the extruder. Indeed, the production capacity of plasticating extruders is frequently determined by their plasticating capacity. Further visual analysis of the experimental results reveals a tendency of the melt pool to penetrate “under” the solid bed and, occasionally, to completely surround it; the continuity of the solid bed is frequently broken and a melt filled gap appears (e.g., turn 15.5, Fig. 9.23). This tendency for solid bed breakup seems to originate in the tapered sections of the extruder, and it appears to be a source of “surging” (i.e., fluctuation in time of temperature, pressure, and flow rate) of the extrudate at the die, as well as a source of entrapping some air bubbles into the melt stream.

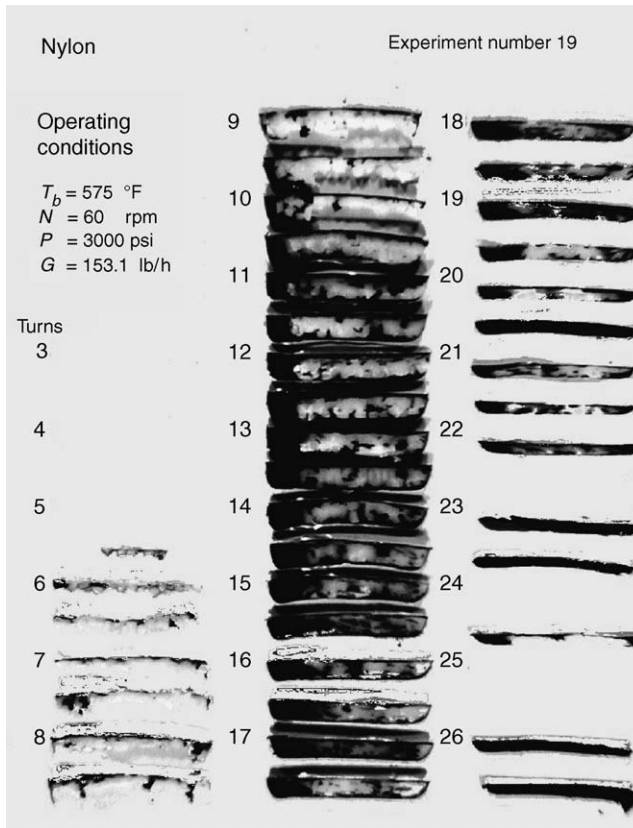


Fig. 9.22 Cross sections from “cooling” experiment. For details see Figs. 9.20 and 9.21. Material: nylon.

A close analysis of an individual cross section (Fig. 9.26) suggests further details on the physical mechanisms taking place in the screw channel. We observe a thin film of melt between the surface of the barrel and the solid bed. The relative motion of the barrel surface in the cross-channel direction drags the melt in the film into the melt pool, generating a cross-channel pressure gradient and a circulatory flow. This hydrodynamically generated pressure in the melt pool no doubt brings about the segregation of the solids at the trailing flight, and since melt is continuously removed by drag from the film, the solid bed must acquire a velocity component toward the barrel surface. But at the same time it also slides down channel; consequently, the size of the solid bed at a fixed position in the bed is continuously reduced until, at the end of melting, it completely disappears. At a fixed position in the screw channel, on the other hand, the size of the solid bed remains constant in time. Thus, all the elements have emerged for a *drag-induced melt removal, steady state, conduction melting mechanism*, discussed in Section 5.7. Moreover, the film region at the barrel surface is the only place where such a mechanism can develop. Recalling the significant difference between the rates of melting in conduction melting with and without melt removal, we can conclude that the melting at the root of the screw (even when there is melt penetration under the solid bed) as well as at the melt pool–solid bed interface, are second-order effects in most of the melting region.

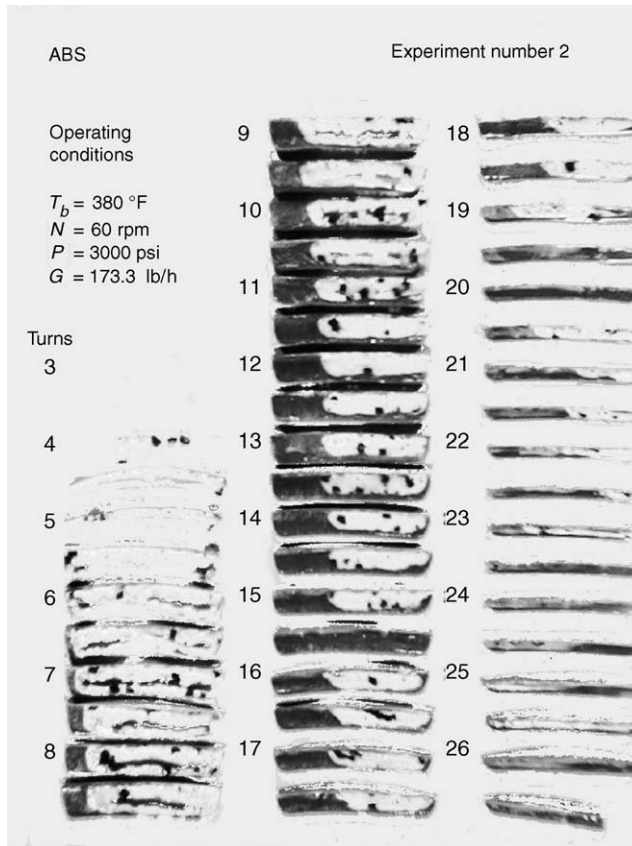


Fig. 9.23 Cross sections from the cooling experiments. See Figs. 9.20 and 9.21. Material: Acrylonitrile-Butadiene-Styrene (ABS).

With this overview on the physical mechanisms of melting in mind, we can proceed to examine the complete experience of the polymer in the extruder. We shall do this by launching a pellet and traveling with it throughout the extruder.

In the hopper, where only the elementary step of solids handling occurs, we commence a slow, somewhat erratic motion downward, repeatedly bumping into neighboring pellets and occasionally being hung up in a stable arch for short periods, until we reach the throat area. Here we observe the pellets in helical flight, being swept from underneath and pushed forward. The moment we are caught up by this flight and start rotating, our coordinate system changes. We now record our motion relative to the screw; hence, the barrel will appear to be rotating in the opposite direction. We find ourselves in a shallow channel confined between the flights, the roots of the screw, and the barrel surface.

We commence in slow motion down the channel, generally maintaining our position relative to the confining walls. As we move, the neighboring pellets exert an increasing force on our pellet, and the void between the pellets is gradually reduced. Most pellets are experiencing the same thing, except for those in contact with the barrel and those in contact with the screw. The former experience an intense frictional drag by the moving barrel surface, while the latter experience a frictional drag force in the up-channel direction by the screw surfaces.

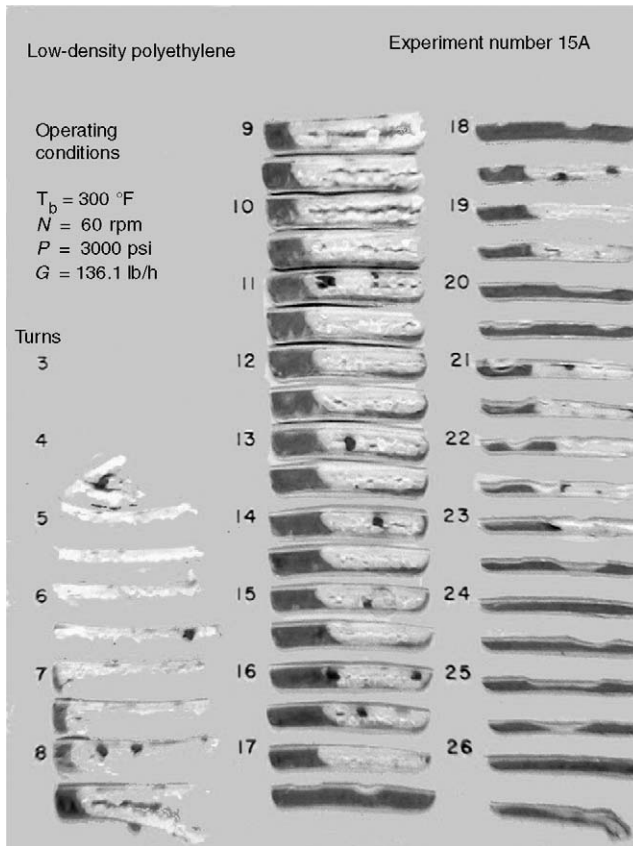


Fig. 9.24 Cross sections from cooling experiments. See Figs. 9.20 and 9.21. Material: Low density polyethylene (LDPE).

We know from Section 4.9 that this frictional drag at the barrel is the driving force of the solids conveying mechanism in the screw channel. Both these frictional processes result in heat generation, raising the polymer temperature, in particular the surface layer at the barrel surface. At some point, this temperature may exceed the melting point or softening range of the polymer, converting the frictional drag mechanism into a viscous drag mechanism. That is, the solids are conveyed forward in the channel by the shear stresses generated in the melt film.

A more common situation, however, is that before there is any significant frictional heating, an axial position is reached where the barrel is heated to well above the melting point, forcing the creation of a film of melt. In either case, this marks the end of that portion of the process in the extruder called the *solids conveying zone*, where only solids are present and the only elementary step that occurs is handling of solids.

By this time, we find our pellet somewhat deformed by the neighboring pellets, which have come together in a rather sturdy, but deformable, solid bed, which is moving in plug-like fashion down-channel. The thin film separating the bed from the barrel is sheared intensely. Heat is generated by this shearing action and conducted from the barrel to the solid bed. The temperature gradient is large because the barrel temperature drops to the melting point over a very thin film. As a result of this heat transfer, from this point on our

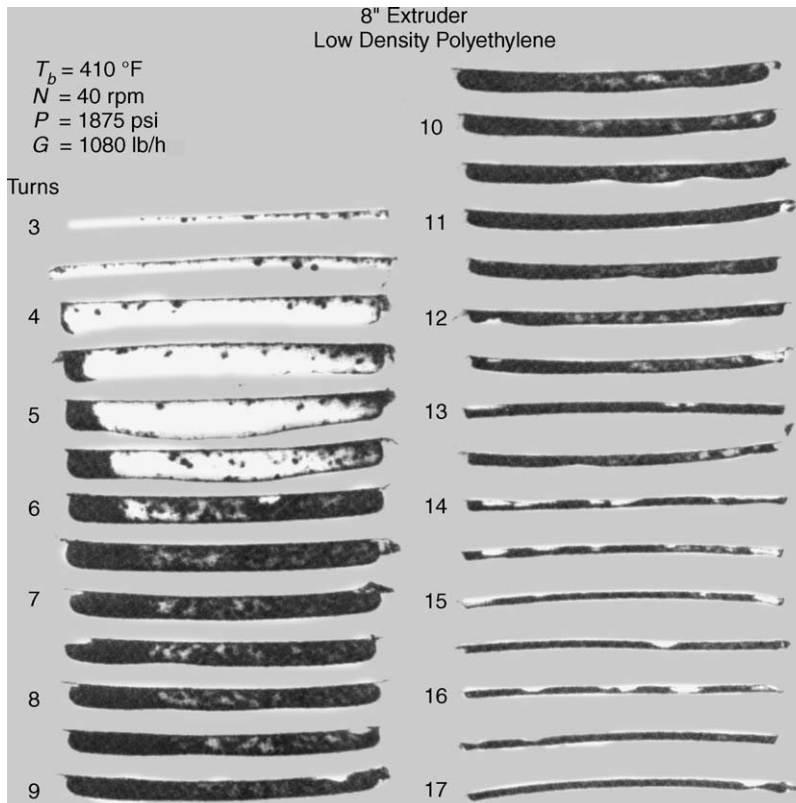


Fig. 9.25 Cross sections obtained from a “cooling experiment” of an 8-in-diameter extruder. Material and operating conditions indicated in the figure. [Reprinted by permission from Z. Tadmor and I. Klein, *Engineering Principles of Plasticating Extrusion*, Van Nostrand Reinhold, New York, 1970.]

pellet experiences a gradual rise in temperature. Since there is a small radial clearance between the tip of the flights and the barrel surface, until the melt film is thinner than the clearance, nothing drastic happens. This condition may continue for a few turns, during which the film thickens beyond the flight clearance. The flights then start to scrape the melt off the barrel and the melt starts accumulating at the pushing flight.

The portion of the process taking place from the end of the solids conveying zone to the point where the melt layer at the barrel surface first appears is called the *delay zone* (34). In this zone, the elementary step of melting occurs simultaneously with handling of solids. The melting mechanism, however, is contact melting without melt removal, but with heat generation in the molten film. In Fig. 9.20, the solids conveying zone ends at turn 3, where barrel heating starts, and the delay zone, which starts at this location, ends at turn 7, where the melt pool begins to form.

Returning to “our pellet,” we note the point where it reaches the end of the delay zone when the solid bed has acquired a small upward velocity toward the barrel surface. At some point in the extruder, our pellet will reach the melt film–solid bed interface, experiencing toward the end of this approach a quick (exponential) rise in temperature up to the melting point. After being converted into melt, our fluid particle is quickly swept

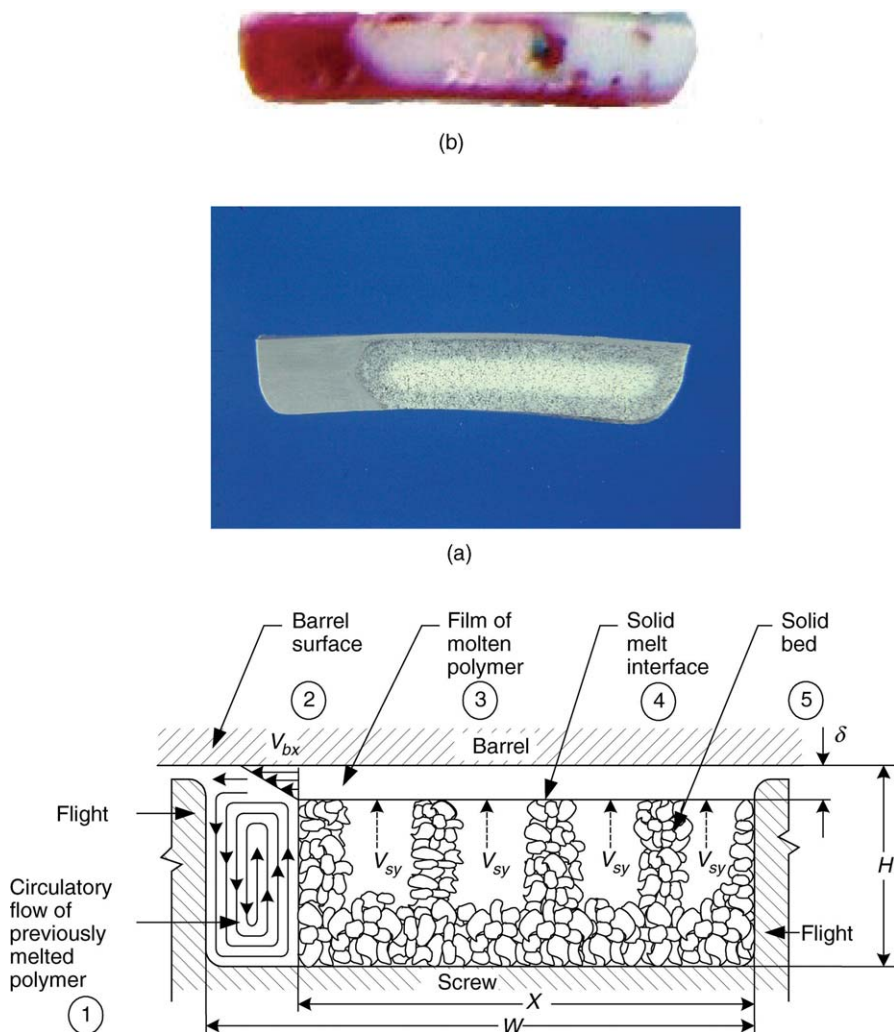


Fig. 9.26 Idealized cross-section compared to (a) the cross-section from a PVC “cooling” experiment and (b) the cross-section from an LDPE “cooling” experiment. [Reprinted with permission from Z. Tadmor and I. Klein, *Engineering Principles of Plasticating Extrusion*, Van Nostrand Reinhold Book Co., New York, 1970.]

into the melt pool. (For amorphous polymers, as the polymer softens, it moves both toward the barrel as well as toward the pushing flight.)

Once in the melt pool, the fluid particle settles at some position in the channel and commences the circulatory flow alternating between two positions. In the upper portion of the channel, it moves toward the pushing flight and down-channel relatively quickly, whereas in the lower portion of the channel, it moves toward the solid bed (which also slides down channel) or trailing flight (if melting is completed) and down channel relatively slowly. This continues until it leaves the screw channel.

In the melt pool, both the temperature and the pressure change; they generally increase. The portion of the process where melting takes place is called the *melting zone*, which lies

side by side with the *melt conveying zone*. The latter extends to the end of the screw. Clearly, then, in the melting zone, *all* elementary steps occur simultaneously; whereas in the melt conveying zone, as discussed in the preceding section, only pumping and mixing take place.

Modeling the Plasticating Extrusion Process

In addition to the modeling objectives listed for melt extruders (i.e., velocity, temperature, and pressure fields), which remain valid for plasticating extrusion, we add the following: gravitational flow behavior of particulate solids in hoppers, in particular pressure distribution, arching, and bridging; stress and temperature distribution of the compressed pellets into a deformable solid body in the solids conveying zone; length of the delay zone (i.e., the length from the axial location where polymer melts at the barrel surface, to the point where the melt is segregated into a melt pool at the pushing flight) and the evolution of the molten film at the barrel surface, as well as temperature and stress fields in the solid bed; length of the melting zone, rate of melting, mean width profile of the solid bed (solid bed profile, or SBP), stress and temperature distribution in the solid bed along the melting zone, mean temperature of the melt film flowing into the melt pool; power consumption in the solids conveying delay and melting zones; and surging conditions. We could generalize our modeling objectives to velocity, temperature, and stress fields in both solid and liquid phases, from which we could calculate all the other variables of interest. But in plasticating extrusion, more than in melt extrusion, it is very difficult to obtain a complete solution to this problem.

We now follow the modeling approach outlined for the melt extrusion process. We assume steady state conditions and a given mass flow rate; then, starting from the hopper, where initial conditions are known, calculations are made in finite steps, ending up at the die, with extrudate pressure, mean temperature, and solids content. If the flow rate at these conditions does not match that of the die, or if the calculations break down for some reason (e.g., insufficient solids conveying), calculations are repeated at a new mass flow rate.

The Solids Conveying Zone The conveying mechanism in screw extruders is one of drag-induced flow, as discussed in Section 4.9. Indeed, for shallow channels, we could turn directly to Eq. 4.9-7, which would form the solids conveying model. The feed section for screw extruders, however, is generally deep, and curvature effects are not negligible. Following Darnell and Mol (28), we derive a solids conveying model in a deep screw channel, subject to simplifying assumptions made in Section 4.9.

At steady state, the solid plug has a constant axial velocity V_{pl} and constant angular velocity $V_{p\theta}$, as shown in Fig. 9.27. The former is related to the mass flow rate by the following equation:

$$G = V_{pl}\rho_b \left[\frac{\pi}{4} (D_b^2 - D_s^2) - \frac{eH}{\sin \bar{\theta}} \right] \quad (9.3-1)$$

where D_b is the inside diameter of the barrel, $D_s = D_b - 2H$, H is the channel depth, e is the flight width, and $\bar{\theta}$ is the mean helix angle. The down-channel velocity of the solids is $V_{pl}/\sin \bar{\theta}$, which varies with channel depth. (Note that this velocity is equivalent to velocity u in Section 4.9.) It is more convenient to express the flow rate G in terms of the angle ϕ formed between the velocities of the solids and the barrel surface because

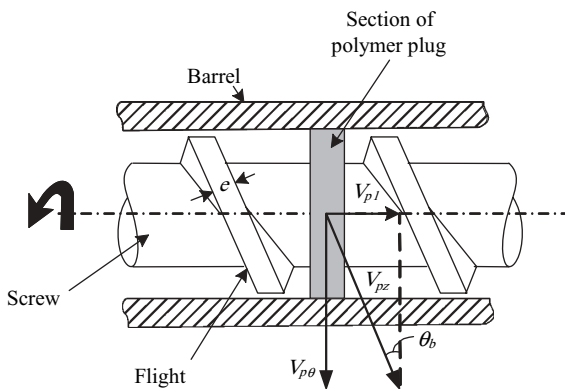


Fig. 9.27 Axial increment of the solid plug. Velocities given relative to a stationary screw: V_{pl} is the axial velocity of the plug, which is independent of the radial position; $V_{p\theta}$ and V_{pz} are the tangential and down-channel components of the plug surface velocity.

force and torque balances provide an expression for this angle. The relationship between V_{pl} , V_b , and the angle ϕ can easily be obtained, as shown in Fig. 9.28:

$$V_{pl} = V_b \frac{\tan \phi \tan \theta_b}{\tan \phi + \tan \theta_b} \tag{9.3-2}$$

where $V_b = \pi ND_b$ is the tangential velocity of the barrel surface. Clearly, at closed discharge conditions, $\phi = 0$ and $V_{pl} = 0$. Substituting Eq. 9.3-2 into Eq. 9.3-1, followed by rearrangements, results in

$$G = \pi^2 N H D_b (D_b - H) \rho_b \frac{\tan \phi \tan \theta_b}{\tan \phi + \tan \theta_b} \left[1 - \frac{e}{\pi (D_b - H \sin \theta)} \right] \tag{9.3-3}$$

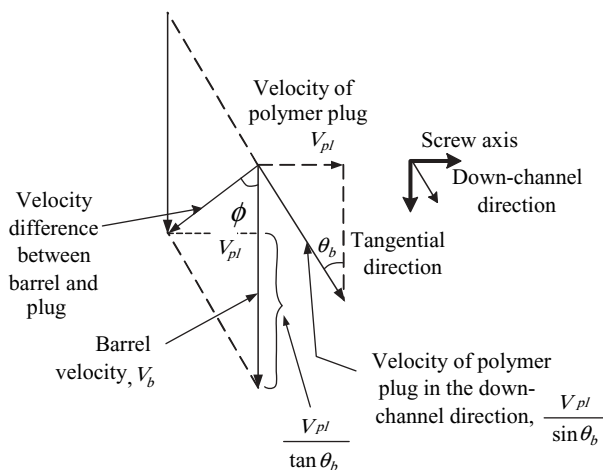


Fig. 9.28 Velocity vector diagram for calculating the velocity difference between barrel and solid plug. This is the velocity of the barrel surface observed by a viewer on the plug; the direction of its velocity relative to the viewer is ϕ .

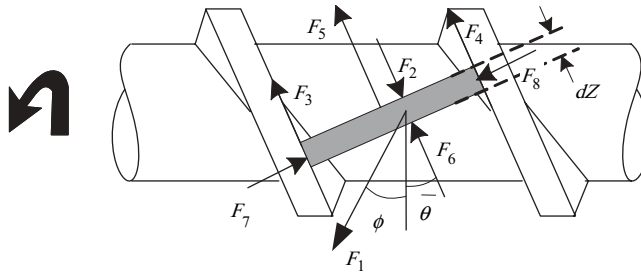


Fig. 9.29 Forces acting on a down-channel increment of the solid plug: F_1 is the forward dragging frictional force exerted on the plug by the barrel surface, $F_6 - F_2$ is the net force resulting from the down-channel pressure gradient, $F_3, F_4,$ and F_5 are the frictional retarding forces of the screw, and F_7 and F_8 are the normal forces by the flights on the plug.

Equation 9.3-3 can be used either to calculate ϕ from G , or vice versa. If bulk density changes cannot be neglected, the calculations should be performed in small axial increments.

Next we proceed with the force and torque balances. Since pressure builds up in the down-channel direction, the force and torque balances are made on a differential increment in the down-channel direction; this is illustrated in Fig. 9.29, where the various forces acting on the element are also depicted. These forces can be expressed in terms of the coefficients of friction, local geometry, and the differential pressure increment, which compensate for the other forces and torques. For an isotropic stress distribution, these are

$$\begin{aligned}
 F_1 &= f_b P W_b dz_b \\
 F_6 - F_2 &= H \bar{W} dP \\
 F_8 &= PH d\bar{z} \\
 F_7 &= PH d\bar{z} + F^* \\
 F_3 &= f_s F_7 \\
 F_4 &= f_s F_8 \\
 F_5 &= f_s P W_s dz_s
 \end{aligned}
 \tag{9.3-4}$$

where the subscripts b and s , respectively, denote the surfaces of the barrel and the root of the screw, and the overbar denotes the mean value over the channel depth. The motion of the plug consists of a pure translation in the axial direction and pure rotation in the angular direction. Hence, by calculating the components of all the forces in the axial and tangential directions, a force balance can be written in the former direction and a torque balance in the latter direction. By solving the two equations simultaneously, the force F^* is eliminated and, subsequent to considerable algebraic rearrangements, the following simple expression is obtained:

$$\cos \phi = K_s \sin \phi + M
 \tag{9.3-5}$$

or

$$\sin \phi = \frac{\sqrt{1 + K_s^2 - M^2} - K_s M}{1 + K_s^2}
 \tag{9.3-6}$$

where

$$K_s = \frac{\bar{D} \sin \bar{\theta} + f_s \cos \bar{\theta}}{D_b \cos \bar{\theta} - f_s \sin \bar{\theta}} \quad (9.3-7)$$

and

$$M = 2 \frac{H f_s}{W_b f_b} \sin \theta_b \left(K_s + \frac{\bar{D}}{D_b} \cot \bar{\theta} \right) + \frac{W_s f_s}{W_b f_b} \sin \theta_b \left(K_s + \frac{D_s}{D_b} \cot \theta_s \right) + \frac{\bar{W} H}{W_b Z_b f_b} \sin \bar{\theta} \left(K_s + \frac{\bar{D}}{D_b} \cot \bar{\theta} \right) \ln \frac{P_2}{P_1} \quad (9.3-8)$$

where P_1 is the initial pressure at $z = 0$ and P_2 is the pressure at any down-channel distance Z_b , where solids conveying is the only elementary step taking place. For a given flow rate, ϕ is obtained from Eq. 9.3-3, M is then calculated from Eq. 9.3-5, and the pressure rise, from Eq. 9.3-8. If a given pressure rise is needed, the process is reversed, with the angle ϕ being calculated from Eq. 9.3-6.

Finally, the total power consumption in the solids conveying zone is obtained by taking the product of the force between the barrel surface and solid plug F_1 and the barrel velocity in the direction of the force $\pi N D_b \cos \phi$

$$dP_w = \pi N D_b \cos \phi f_b W_b P dz_b \quad (9.3-9)$$

Integrating Eq. 9.3-9 after substituting the exponential relationship between P and Z_b , as expressed in Eq. 9.3-8, results in (35)

$$P_w = \pi N D_b W_b Z_b f_b \cos \phi \frac{P_2 - P_1}{\ln(P_2/P_1)} \quad (9.3-10)$$

Perhaps the most severe assumption in the Darnell and Mol model is the isotropic stress distribution. Recalling the discussion on compaction in Section 4.5, the stress distribution in the screw channel is expected to be complex. The first attempt to account for the nonisotropic nature of the stress distribution was made by Schneider (36). By assuming a certain ratio between compressive stresses in perpendicular directions and accounting for the solid plug geometry, he obtained a more realistic stress distribution, where the pressure exerted by the solids on the flights, the root of the screw, and the barrel surface are all different and less than the down-channel pressure. The ratio between the former and the latter is of the order of 0.3–0.4.

Another questionable assumption is that of constant temperature. Frictional forces lead to surface-heat generation. The total power introduced through the shaft is partly dissipated into heat at the barrel, flights, and root of the screw surfaces, and is partly used to generate pressure. However, most of the power is dissipated into heat at the barrel surface (Fig. 9.30). This quantity is given by the product of the force F_1 and the relative velocity between barrel surface and solid plug (35)

$$P_{wb} = \pi N D_b W_b Z_b f_b \frac{\sin \theta_b}{\sin(\theta_b + \phi)} \frac{P_2 - P_1}{\ln(P_2/P_1)} \quad (9.3-11)$$

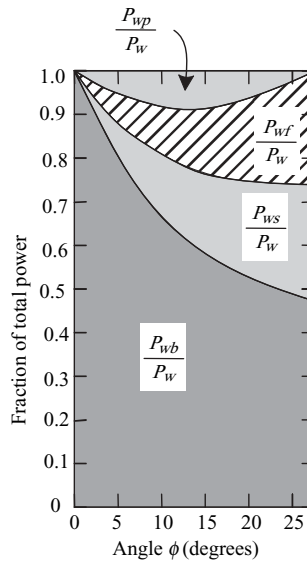


Fig. 9.30 Graphical representation of the various components of the total power consumption in the solids conveying zone of screw extruders for $H/D_b = 0.15$ and a constant f_s/f_b ratio as a function of the angle ϕ : P_{wb} , which is the major component of the power, is the power dissipated into heat at the barrel plug interface; P_{ws} and P_{wf} are the power dissipated on the root of the screw and flights, respectively; and P_{wp} is the power consumed for the pressurization of the plug. [Reprinted by permission from E. Broyer and Z. Tadmor, "Solids Conveying in Screw Extruders, Part I. A Modified Isothermal Model," *Polym. Eng. Sci.*, **12**, 12–24 (1972).]

This heat generated at the interface is partly conducted through the cooled barrel and partly conducted into the solid plug. Consequently, a temperature profile develops in the plug with a maximum temperature at the interface. If we neglect heat generation at the other surfaces, the problem reduces to a one-dimensional heat conduction problem soluble by methods discussed in Section 5.3. Since the rate of heat generation varies with axial location, numerical solution methods are needed. This was achieved by Tadmor and Broyer (37), with the results indicating that the solids surface temperature at the barrel increases exponentially. Clearly, once the melting point is reached, the frictional drag conveying mechanism changes into a viscous drag mechanism (34). This non-isothermal solids conveying mechanism explains the need for efficient barrel cooling in the solids conveying zone if high pressure generation is desired.

Finally, all solids conveying models require an estimate of the inlet pressure P_1 . One approach for evaluating P_1 is to assume that it equals the pressure under the granular material at the hopper base (35), which can be evaluated from the equations given in Section 4.3. This approach neglects the complex transition between the gravitational flow in the hopper and the drag-induced flow of the pluglike solid in the closed screw channel. However, it does connect the extruder performance to hopper design and loading level. The need for such a connection follows from experimental observations that, under certain conditions, small variations in solids height in the hopper bring about significant variation in extruder performance, such as, for example, pressure variations at the die. In such cases, keeping the solids height above a certain level eliminates pressure surging at the die. One possible reason for this behavior is the effect of solids height on the inlet pressure.

Another approach to the problem, proposed by Lovegrove and Williams (38,39), is to disregard the hopper and assume that the initial pressure in the solids conveying zone is the result of local gravitational and centrifugal forces. This is a reasonable assumption, considering the generally low level of pressure values in the inlet region. However, it fails to account for the effect mentioned previously, relating the hopper design and loading level to extrusion performance. Clearly, there is a need for additional experimental observation and a detailed mathematical model encompassing the hopper, the portion of the screw under the hopper, and the inlet region in the extruder, where the Darnell and Mol model does not apply.

For an effective solids conveying performance, pressure should rise over this zone. However the maximum theoretical conveying capacity is obtained by setting $P_2 = P_1$. Analysis of the solids conveying equations indicates that there is an optimum helix angle as well as an optimum channel depth for maximum conveying capacity or maximum pressure rise. We pointed out before that P_1 is low; consequently P_2/P_1 must be very high to obtain a substantial pressure level P_2 . Increasing P_1 by forced feeding (e.g., with a feeding screw in the hopper) will increase P_2 . Equation 9.3-8 indicates that the pressure profile in the solids conveying zone of screw extruders is exponential, as it is in shallow rectangular channels discussed in Section 4.9. Solids conveying is improved by increased f_b/f_s and by increasing the screw speed (ϕ is decreased for a given G), provided that isothermal conditions are maintained and the coefficients of friction remain constant. An accurate measurement of the latter, however, involves some experimental difficulties as discussed in Section 4.1.

Example 9.5 Solids Conveying in Screw Extruders LDPE is extruded in a 6.35×10^{-2} -m (2.5-in) diameter, 26.5 turns long SSE, with a square pitched ($L = D_b$) metering type of screw. The feed section is 12.5 turns long and 9.398×10^{-3} m (0.37 in) deep, the transition section is 9.5 turns long, and the metering section is 3.22×10^{-3} m (0.127 in) deep. Flight width is 6.35×10^{-3} m (0.25 in), and flight clearance is negligible. Hopper diameter is 0.381 m (15 in) and $K = 0.286$, with a converging conical section of 90° and discharge opening of 0.127 m (5 in), as in Fig. E9.5. The barrel temperature is maintained at 149°C (300°F), and heating starts three turns from the beginning of the flights, with the hopper opening occupying the first two turns, leaving one turn for solids conveying. At a screw

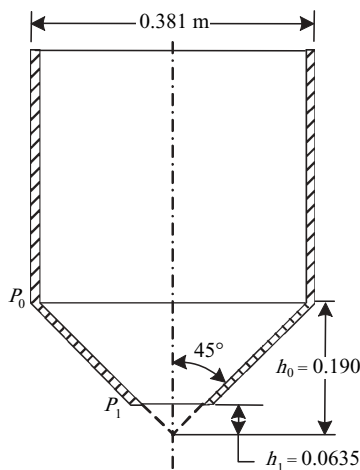


Fig. E9.5 A hopper consisting of cylinder over a truncated cone.

speed of 60 rpm, a mass flow rate of 67.1 kg/hr is obtained with polymer feed at 24°C (screw design and operating conditions correspond to the experiment reported in Fig. 9.24).

Calculate (a) the base pressure of the hopper, (b) pressure at the end of the solids conveying zone, and (c) power consumption in the solids conveying zone.

Assume isothermal operation and that the inlet pressure to the solids conveying zone equals the base pressure of a fully loaded hopper. Bulk density of the feed is 595 kg/m³, the static coefficient of friction in the hopper is 0.3, and the dynamic coefficients of friction on barrel and screw are 0.45 and 0.25, respectively.

Solution First we compute some geometrical data (needed both in this and the following example), summarized in the following table:

Variable	Feed Section	Transition Section	Metering Section
Helix angle at the barrel surface θ_b	17.65°	17.65°	17.65°
Mean helix angle $\bar{\theta}$	20.48°	Varies linearly	18.45°
Helix angle at the root of the screw θ_s	24.33°	Varies linearly	19.51°
Channel width at the barrel surface, W_b	5.416×10^{-2} m	5.416×10^{-2} m	5.416×10^{-2} m
Mean channel width, \bar{W}	5.314×10^{-2} m	Varies linearly	5.358×10^{-2} m
Channel width at the root of the screw, W_s	5.151×10^{-2} m	Varies linearly	5.350×10^{-2} m
Axial length	10.5 turns	9.5 turns	4 turns
Axial length	0.666 m	0.603 m	0.2886 m
Mean helical length, \bar{z}	2.270 m	-	0.800 m

(a) We commence calculations in the solids conveying zone. The initial pressure in the solids conveying zone P_1 is assumed to equal the pressure under the solids in the hopper. We can calculate it using Eq. 4.3-5. The value P_0 is evaluated assuming that the height of solids in the vertical part of the hopper is sufficient to result in at least 99% of the maximum pressure. Thus, from Eq. 4.3-5 we have

$$P_0 = \frac{(0.99)(595)(9.806)(0.381)}{(4)(0.3)(0.286)} = 6.412 \times 10^3 \text{ N/m}^2$$

A more accurate calculation of the pressure under the hopper accounting for the conical section outlined in the first edition of the book results in a lower pressure of $3.776 \times 10^3 \text{ N/m}^2$ (= 0.55 psi).

(b) The axial velocity of the plug V_{pl} from Eq. 9.3-1, neglecting the effect of pressure on bulk density, is

$$V_{pl} = \frac{61.7/3600}{(595) \left\{ \frac{\pi}{4} \left[(0.0635)^2 - (0.0447)^2 \right] - \frac{(0.00635)(0.003226)}{\sin(20.48)} \right\}}$$

$$= 0.0187 \text{ m/s}$$

The velocity of the barrel surface $V_b = \pi ND_b = 0.1995$ m/s. Hence, from Eq. 9.3-2, we obtain

$$\tan \phi = \frac{\tan \theta_b}{(V_b/V_{\rho i}) \tan \theta_b - 1} = \frac{\tan(17.65)}{(0.1995/0.0187) \tan(17.6) - 1} = 0.13288$$

and ϕ is 7.57° . Next K_s is evaluated from Eq. 9.3-7

$$K_s = \frac{(0.0541) \sin(20.48) + (0.25) \cos(20.48)}{(0.0635) \cos(20.48) - (0.25) \sin(20.48)} = 0.5859$$

and M is evaluated from Eq. 9.3-5

$$M = \cos(7.57) - 0.5859 \sin(7.57)$$

The pressure rise ratio P_2/P_1 over one turn of the solids conveying section ($Z_b = 0.0635/\sin 17.6^\circ = 0.209$ m); from downstream the hopper to the location where the barrel heating starts, is obtained from Eq. 9.3-8:

$$\begin{aligned} 0.9141 &= (2) \frac{(0.009398)(0.25)}{(0.05416)(0.45)} \sin(17.6) \left[(0.5859) + \frac{(0.0541)}{(0.0635)} \cot(20.48) \right] \\ &\quad + \frac{(0.05151)(0.25)}{(0.05416)(0.45)} \sin(17.6) \left[(0.5859) + \frac{(0.0447)}{(0.0635)} \cot(24.33) \right] \\ &\quad + \frac{(0.05314)(0.009398) \sin(20.48)}{(0.05416)(0.209)(0.45)} \left[(0.5859) + \frac{(0.0541)}{(0.0635)} \cot(20.48) \right] \ln \frac{P_2}{P_1} \\ &= 0.1676 + 0.34328 + 0.09813 \ln \frac{P_2}{P_1} \end{aligned}$$

and this gives $P_2 = 60.9P_1$.

Thus, the exit pressure from the solids conveying zone is $3.776 \times 10^3 \times 60.9 = 2.3 \times 10^5$ N/m² (33 psi). This result indicates that the solids conveying section functions properly and that higher outputs could be obtained at this screw speed before solids conveying limitations (e.g., "starving") were encountered. We should note, however, that the analysis of the solids conveying zone is very sensitive to the values of the coefficient of friction.

(c) The power consumption is calculated from Eq. 9.3-10

$$\begin{aligned} P_w &= (\pi)(1)(0.0635)(0.05416)(0.209)(0.45) \cos(7.57) \cdot \frac{(2.3 \times 10^5) - (3.776 \times 10^3)}{\ln 60.9} \\ &= 56.7 \text{ W} (= 0.076 \text{ hp}) \end{aligned}$$

The Melting Zone As we pointed out earlier, from the axial location where a melt film is formed at the barrel surface (either as a result of barrel heating or as a result of heat generation due to friction), to the axial location where a melt pool appears at the "pushing" flight, lies the *delay zone*. The conveying mechanism in this zone is one of viscous drag at the barrel surface, determined by the shear stresses in the melt film and,

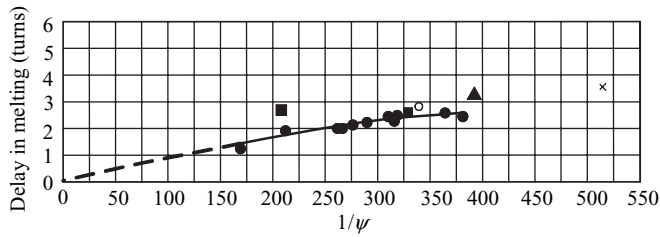


Fig. 9.31 Delay in melting expressed in “turns” from the point the barrel temperature exceeds the melting point (melt-film formed) to the point where a melt pool is segregated at the pushing flight, as obtained from cooling experiments versus calculated dimensionless group $1/\psi$. Solid curve for LDPE, ●; HDPE, ○; PP ▲; rigid PVC, ■; nylon, ×. [Reprinted by permission from Z. Tadmor and I. Klein, *Engineering Principles of Plasticating Extrusion*, Van Nostrand Reinhold, New York, 1970.]

generally, frictional (retarding) drag on the root of the screw and the flights (34). Thickness of the melt film increases with down-channel distance and attains a value of several times that of the flight clearance at the end of the zone. But to predict the exact axial location where it ends would require information on the strength and stress distribution in the solid bed. Figure 9.31 gives an approximate empirical correlation based on limited experimental data, relating the length of the zone expressed in turns and a dimensionless group ψ related to melting rate, discussed below.

As mentioned earlier, the melting mechanism in screw extruders was first formulated by Tadmor (29) on the basis of the previously described visual observations pioneered by Bruce Maddock. The channel cross section and that of the solid bed are assumed to be rectangular, as in Fig. 9.26. The prediction of the solid bed width profile (SBP), that is the width of the solid bed X as a function of down-channel distance z , is the primary objective of the model, which can be experimentally verified by direct observation via the “cooling experiment” of the kind shown in Figs. 9.20–9.25. As shown by Zhu and Chen (40), the solid bed can also be measured dynamically during operation by equipping the extruder with a glass barrel.

The SBP provides a wealth of information: (a) it gives the total length of melting; (b) it offers a detailed view of the melting process, its efficiency and the interaction with screw geometry; (c) it gives an indication of likelihood of surging (i.e., time variation in flow rate and temperature); (d) it provides the width profile of the melt pool needed to compute pressure and temperature profiles along the screw; and (e) it guides the design engineer in the selection of the best location for mixing elements and barrier flights.

The model assumes steady state, which implies that the SBP is constant in time, as are the velocity and temperature profiles in the solid and melt phases. It is further assumed that melting takes place *only* at the barrel surface, where a drag-induced melt removal mechanism exists. The solid bed is assumed to be homogeneous, deformable, and continuous. Next we assume that the *local* down-channel velocity of the solid bed is constant. Slow variations of this velocity (e.g., possible acceleration in the tapered section), as well as those of physical properties (e.g., density of the solid bed), operating conditions (e.g., barrel temperature), and geometry (e.g., channel depth) can easily be accounted for by a calculation procedure involving small, finite, down-channel increments. This can be viewed as an “extended lubrication approximation,” whereby changes in the direction of the main flow are assumed to be small as compared to changes in the perpendicular direction to this flow, and local changes are functions of local

conditions only. Finally, the fluid is assumed to be Newtonian, the local physical and thermophysical properties are assumed to be constant, and the solid bed–melt film interface is assumed to be a sharp interface at the melting point T_m .

The change in size of the solid bed over a small down-channel increment will depend on the rate of melting at the solid bed–melt film interface. Consider a small differential volume element, perpendicular to the solid–melt interface (Fig. 9.32). The solid bed has a local down-channel velocity V_{sz} and a local velocity component into the melt film of V_{sy} . The barrel surface velocity V_b is resolved into down-channel and cross-channel components V_{bz} and V_{bx} .

The relative velocity between barrel surface and solid bed is

$$\mathbf{V}_j = \mathbf{V}_b - \mathbf{V}_{sz} \quad (9.3-12)$$

or

$$|\mathbf{V}_j| = (\mathbf{V}_j \cdot \mathbf{V}_j) = (V_b^2 + V_{sz}^2 - 2V_b V_{sz} \cos \theta)^{1/2} \quad (9.3-13)$$

which determines the rate of viscous dissipation. For a linear velocity profile, the shear rate is V_j/δ , where δ is the local film thickness. The melt in the film, however, is removed only in the *cross-channel* direction, by the cross-channel velocity component of the barrel surface V_{bx} , which drags the melt into the melt pool, resulting in a reduction of solid-bed width. No such effective removal mechanism is possible in the down-channel direction; indeed, the film thickness variation in the down-channel direction is small.

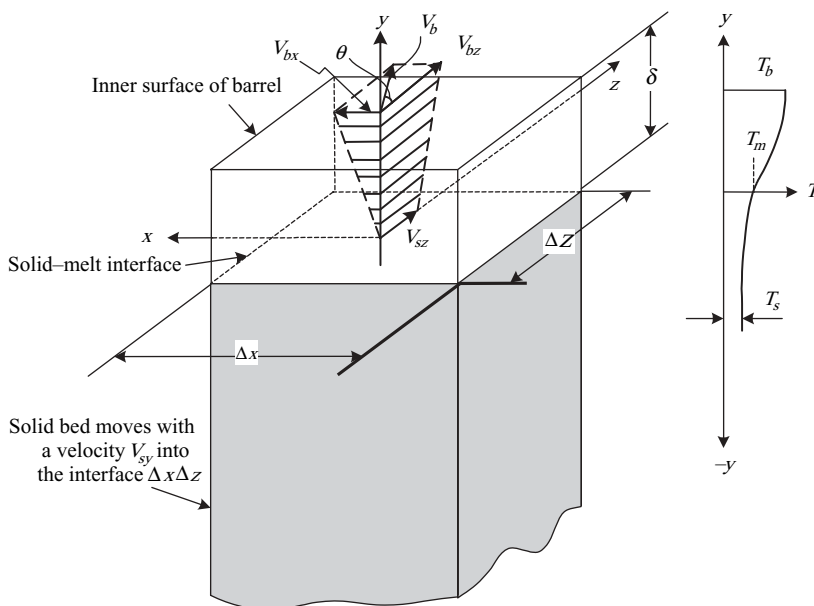


Fig. 9.32 A differential volume element perpendicular to the melt film–solid bed interface. Schematic view of temperature profile in the film and solid bed shown at right. Schematic views of velocity profiles (isothermal model) in the x and z directions are also shown.

In view of these assumptions, neglecting small changes in the down-channel direction over the differential element dz , we deal with a thin slice of solid bed that has a molten film, whose thickness varies in the x direction, and we regain the basic melting mechanism discussed in detail in Section 5.7. In particular, we can turn directly to Eq. 5.7-38, with solid-bed width, X , replacing W , T_b replacing T_0 , V_{bx} replacing V_0 in the first term, and V_j replacing V_0 in the second term, to obtain the rate of melting per unit down-channel distance

$$w_L(z) = \left\{ \frac{V_{bx}\rho_m [k_m(T_b - T_m) + (\mu/2)V_j^2] X}{\lambda + C_s(T_m - T_{s0})} \right\}^{1/2} \quad (9.3-14)$$

In this equation, the effect of convection on the temperature distribution in the melt film was neglected. This effect, however, is hardly negligible, and since equations with convection terms are hard to solve, we wish to include an approximate accounting for the effect.

Consider an imaginary model in which the newly melted polymer at the melt–solid interface is removed (by a Maxwell-type demon) and then brought to the location $x = 0$, heated up to the local melt temperature, and fed to the melt film. Thus, with convection into the film approximately taken care of in this fashion and the heat needed to heat up the melt from melt temperature to the cup-average temperature of the film accounted for. Moreover, with this approximation the film thickness can be assumed to remain constant with a fully developed velocity and temperature profile. The thermal energy needed to bring the “removed” melt from the melting point to the local melt-film temperature, which should be added to the heat of fusion, is given by $C_m\bar{\Theta}(T_b - T_m)$, where $\bar{\Theta}$ is the mean “cup” average temperature of the melt given in Eq. 5.7-33

$$\bar{\Theta} = \frac{2}{3} + \frac{\text{Br}}{12} \quad (9.3-15)$$

where Br is the Brinkman number defined in Eq. 5.7-28 which, for a Newtonian fluid, reduces to

$$\text{Br} = \frac{\mu V_j^2}{k_m(T_b - T_m)} \quad (9.3-16)$$

Deriving the rate of melting expression expressed in Eq. 9.3-14 under these conditions, we obtain the following expression

$$w_L(z) = \left\{ \frac{V_{bx}\rho_m [k_m(T_b - T_m) + (\mu/2)V_j^2] X}{2[\lambda + C_s(T_m - T_{s0}) + C_m\bar{\Theta}(T_b - T_m)]} \right\}^{1/2} \quad (9.3-17)$$

Comparing the two equations, we note that, in the denominator, we have the total thermal energy needed to bring the solid from inlet temperature to mean melt temperature, including heat of fusion, and a factor of $\sqrt{2}$. Thus, as expected, neglecting convection would result in an overestimation of the rate of melting.

Given the rate of melting in Eq. 9.3-17, we make the following differential mass balance in the down-channel direction

$$\rho_s V_{sz}(H - \delta)X|_z - \rho_s V_{sz}(H - \delta)X|_{z+\Delta z} = w_L(z) \Delta z \quad (9.3-18)$$

which at the limit of $\Delta z \rightarrow 0$, neglecting the change in film thickness in the down-channel direction, results in

$$-\frac{d(HX)}{dz} = \frac{w_L(z)}{\rho_s V_{sz}} \quad (9.3-19)$$

By substituting Eq. 9.3-17 into Eq. 9.3-19, we get

$$-\frac{d(HX)}{dz} = \frac{\Phi\sqrt{X}}{\rho_s V_{sz}} \quad (9.3-20)$$

where

$$\Phi = \left\{ \frac{V_{bx}\rho_m \left[k_m(T_b - T_m) + (\mu/2)V_j^2 \right]}{2[\lambda + C_s(T_m - T_{s0}) + C_m\bar{\Theta}(T_b - T_m)]} \right\}^{1/2} \quad (9.3-21)$$

For a constant channel depth, Eq. 9.3-21 can be integrated to give

$$\frac{X}{W} = \frac{X_1}{W} \left[1 - \frac{\psi(z - Z_1)}{2H} \right]^2 \quad (9.3-22)$$

where X_1 is the solid bed width at location $z = Z_1$, and ψ is a *dimensionless* number that characterizes the rate of melting given by

$$\psi = \frac{\Phi}{V_{sz}\rho_s\sqrt{X_1}} \quad (9.3-23)$$

If Z_1 is the location of the beginning of the melting zone, then $X_1 = W$. The SBP can be computed from Eq. 9.3-22. If conditions change in the down-channel direction (e.g., the barrel temperature), computations can be made in small, down-channel increments.

For tapered channels with constant taper

$$-\frac{dH}{dz} = A \quad (9.3-24)$$

Eq. 9.3-20 can be written as

$$\frac{d(HX)}{dH} = \frac{\Phi\sqrt{X}}{A\rho_s V_{sz}} \quad (9.3-25)$$

which can be integrated to give

$$\frac{X}{W} = \frac{X_1}{W} \left[\frac{\psi}{A} - \left(\frac{\psi}{A} - 1 \right) \sqrt{\frac{H_1}{H}} \right]^2 \quad (9.3-26)$$

where X_1 is the solid bed width at the down-channel location where the channel depth is H_1 . The down-channel location is obtained from Eq. 9.3-24.

Equations 9.3-22 and 9.3-26 are the basic equations of the melting model. We note that the solid-bed profile in both cases is a function of one *dimensionless* group ψ , which in physical terms expresses the ratio of the local rate of melting per unit solid–melt interface $\Phi\sqrt{X_1}/X_1$ to the local solid mass flux into the interface $V_{sz}\rho_s$, where ρ_s is the local mean solid bed density. The solid-bed velocity at the beginning of melting is obtained from the mass-flow rate

$$V_{sz} = \frac{G}{\rho_s HW} \quad (9.3-27)$$

where H is the channel depth at the beginning of melting. In Eq. 9.3-27 we neglected the effect of the melt film. The solid bed velocity was measured experimentally (1f) and proved to remain virtually constant in the feed and moderately tapered sections. In extreme cases, however, and in particular for large tapers and for low rates of melting, solid bed acceleration is possible, as discussed earlier.

A better insight into the nature of the melting model can be obtained by first considering melting in a constant depth channel, with constant ψ throughout the melting zone. The latter implies both constant physical properties and constant solid bed velocity. Equation 9.3-22 with $Z_l = 0$ and $X_1 = W$ reduces to

$$\frac{X}{W} = \left(1 - \frac{\psi z}{2H}\right)^2 \quad (9.3-28)$$

where ψ reduces in this case to

$$\psi = \frac{\Phi}{V_{sz}\rho_s\sqrt{W}} = \frac{\Phi\sqrt{WH}}{G} \quad (9.3-29)$$

Equation 9.3-28 indicates that the solid bed profile in a constant-depth channel is parabolic. The total (down-channel) length, Z_T , of melting is obtained from Eq. 9.3-28 by setting $X = 0$ to give

$$Z_T = \frac{2H}{\psi} \quad (9.3-30)$$

We therefore note that the length of melting is inversely proportional to ψ ; that is, it is proportional to mass flow rate and inversely proportional to the rate of melting. Clearly, through Φ in Eq. 9.3-21, the effect of the various operating conditions on the length of melting can be evaluated. Thus, an increase in screw speed at a constant flow rate brings about an increase in the rate of melting, both because melt removal is improved (V_{bx} increases), and because viscous dissipation increases. An increase in barrel temperature initially brings about an increase in the rate of melting because the conduction term $k_m(T_b - T_m)$ increases. But because further increases in the barrel temperature decrease the melt-film viscosity and the amount of viscous dissipation, there is an optimum barrel temperature for maximum melting rate. (There is, however, an additional reason for the existence of the optimum, as we shall see later.) Finally, an increase in solids feed temperature, T_{s0} , increases the rate of melting and reduces Z_T .

Similar conclusions are drawn by considering melting in a tapered section with initial channel depth H and taper $A = dH/dz$. In this case, Eq. 9.3-26 reduces to

$$\frac{X}{W} = \left[\frac{\psi}{A} - \left(\frac{\psi}{A} - 1 \right) \sqrt{\frac{H}{H - Az}} \right]^2 \quad (9.3-31)$$

and the total down-channel length, Z_T , of melting

$$Z_T = \frac{H}{\psi} \left(2 - \frac{A}{\psi} \right) \quad (9.3-32)$$

Comparing Eq. 9.3-32 to Eq. 9.3-30, we note that the length of melting in a tapered channel is always shorter than in a channel of constant depth.

Furthermore, the higher the taper, the shorter the melting, Z_T . But there is a limit to the taper that can be allowed, because a high taper may lead to conditions under which the solid bed width will tend to increase instead of decrease (the cross-sectional area, of course, always decreases), which may lead to plugging of the screw channel, solid bed acceleration, and surging conditions in general. It is common practice to characterize the tapered sections of screws by "compression ratio," that is, the ratio of the channel depth in the feed section to that in the metering section, although, from the preceding discussion, screw taper rather than compression ratio should be the value by which transition sections are characterized.

Figure 9.33 illustrates the effect of taper on the shape of the calculated SBP. The width of the solid bed drops if $A/\psi < 1$, it stays constant if $A/\psi = 1$, and it increases if $A/\psi > 1$. All these cases have been experimentally observed. An increase in solid bed width means that the reduction in channel depth is faster than the rate of melting. This condition frequently occurs in a tapered section following a constant depth feed section. Thus, at the beginning of the taper, $X < W$, and an increase in X is possible without generating either surging conditions or a breakdown of the drag removal melting mechanism. If, however, melting starts in a tapered section and conditions are such that $A/\psi > 1$, a stable drag removal melting mechanism, as described in this section, may not be attainable. Conceivably, under these conditions, other melting mechanisms may be triggered into action, such as the previously mentioned *dissipative mix-melting* discussed in Chapter 5.

Conditions that result in approximately constant solid bed width in the tapered section are desirable, and frequently used. Even moderate solid-bed width increases may often be tolerated. The experimentally measured SBPs of Figs. 9.20, 9.22, and 9.24 are plotted in Figs. 9.34–9.36. As predicted by the model, in all cases the solid bed drops continuously in the feed section (up to turn 12), it changes slope upon entering the tapered section, with plugging type conditions observed with nylon and stable constant width conditions observed with LDPE. In the metering section, experimental measurements are inaccurate because solid-bed breakup occurs, or because the bed is too narrow. These particular melting conditions are the combined result of operating conditions, screw design, and polymer properties.

The calculated SBPs in Figs. 9.34–9.36 are based on a model that is no different in concept from the one discussed previously, except that some of the simplifying assumptions were eliminated. In particular, a Power Law model fluid, with a temperature dependent parameter, replaces the Newtonian constant viscosity fluid assumption.

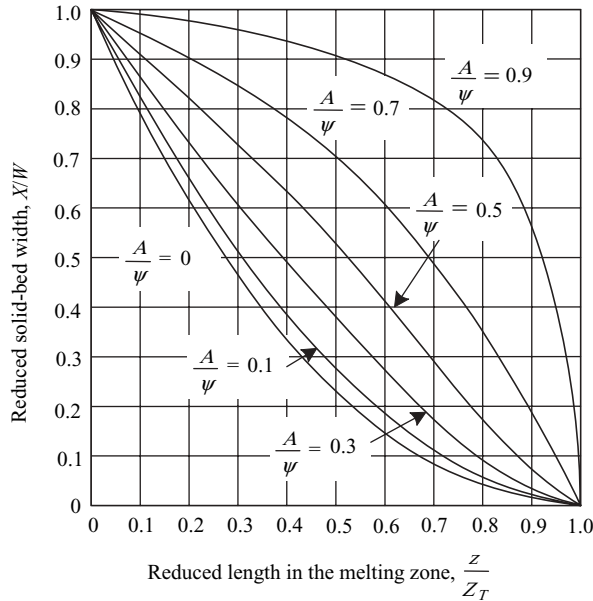


Fig. 9.33 Calculated SBP versus reduced length of melting in a single-section screw: $A/\psi = 0$ denotes a constant channel-depth section. The SBP becomes increasingly concave as A/ψ increases, either as a result of an increasing taper (i.e., increasing A) or a decreasing rate of melting (i.e., decreasing ψ). [Reprinted by permission from Z. Tadmor and I. Klein, *Engineering Principles of Plasticating Extrusion*, Van Nostrand Reinhold, New York, 1970.]

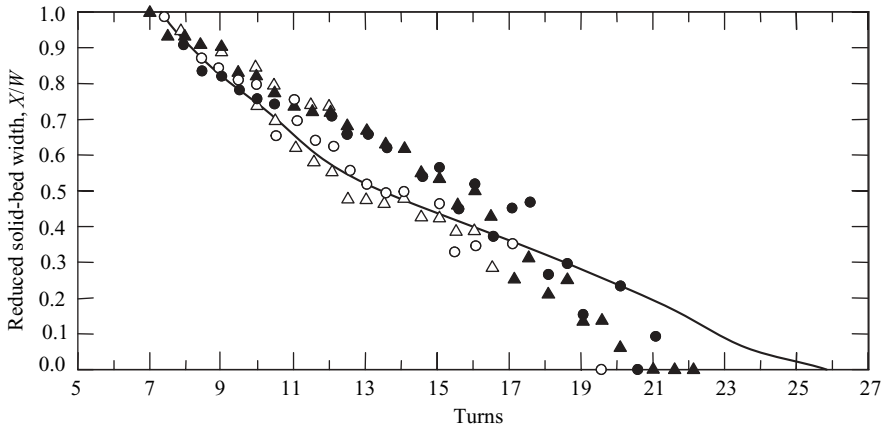


Fig. 9.34 Experimentally measured SBPs by “cooling” experiments as in Fig. 9.20 (PVC) and theoretically calculated SBP (solid curve). Circles and triangles denote two identical experiments. Solid circles and triangles denote solid-bed width at the barrel surface (maximum); open circles and triangles represent the solid-bed width at the root of the screw (minimum). Operating conditions as follows: $T_b = 375^\circ$; $N = 30$ rpm; $P = 4300$ psi; $G = 107.2$ lb/h. [Reprinted by permission from Z. Tadmor and I. Klein, *Engineering Principles of Plasticating Extrusion*, Van Nostrand Reinhold, New York, 1970.]

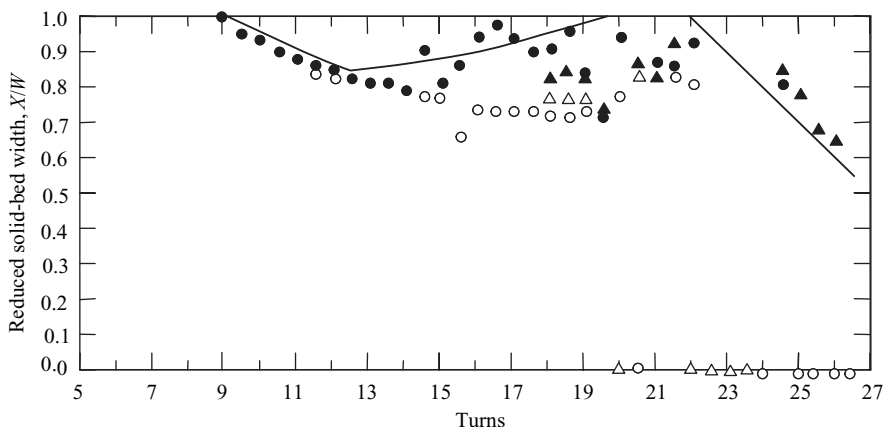


Fig. 9.35 Experimentally measured SBPs, by “cooling” experiments as in Fig. 9.22 (nylon) and theoretically calculated SBP (solid curve). Circles and triangles as in Fig. 9.34. Note the increasing solid-bed width in the tapered section. Operating conditions as follows: $T_b = 575^\circ\text{F}$; $N = 60$ rpm; $P = 3000$ psi; $G = 53.1$ lb/h. [Reprinted by permission from Z. Tadmor and I. Klein, *Engineering Principles of Plasticating Extrusion*, Van Nostrand Reinhold, New York, 1970.]

Moreover, flight clearance and curvature effects were also accounted for. Figure 9.37 indicates that, in this particular case, the simple Newtonian model provides a reasonable estimate, although it overestimates the rate of melting. Note that the predicted curve should approach the closed circles and triangles, which are the measured solid bed width at the melt film, rather than the open circles and triangles, which are the corresponding values at the root of the screw. As observed experimentally, the width near the root of the screw is reduced as a result of melt pool circulation.

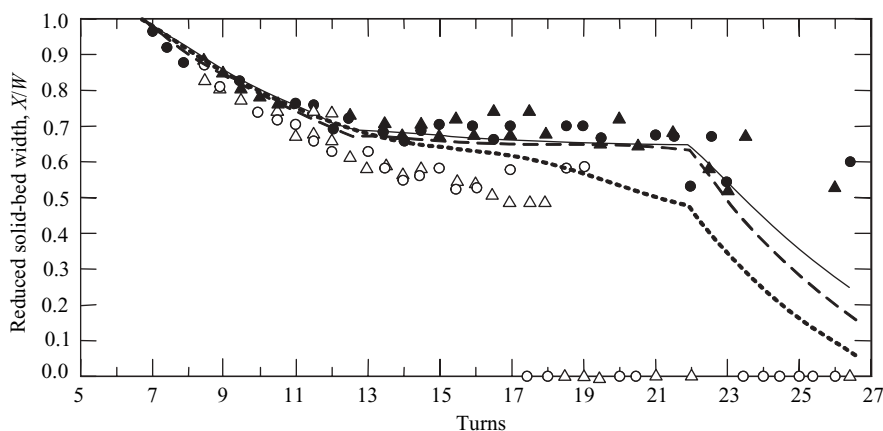


Fig. 9.36 Experimentally measured SBPs by “cooling” experiments as in Fig. 9.24 (LDPE) and theoretically calculated SBP (solid curve). Circles and triangles as in Fig. 9.34. Upper broken curve is the result of the calculation of the SBP in Example 9.6. Lower broken curve is the result of a simplified Newtonian model. Operating conditions as follows: $T_b = 300^\circ\text{F}$; $N = 60$ rpm; $P = 3000$ psi; $G = 136.1$ lb/h. [Reprinted by permission from Z. Tadmor and I. Klein, *Engineering Principles of Plasticating Extrusion*, Van Nostrand Reinhold, New York, 1970.]

In the melting model already described, the assumption of constant viscosity is particularly troublesome, since very large variations of viscosity are expected because of the large temperature variations. The rate of drag removal melting for a Power Law model fluid with temperature dependent viscosity is given in Eq. 5.7-55. The corresponding value of Φ , once again accounting for convection (31), is

$$\Phi = \left\{ \frac{V_{bx}\rho_m U_2 [k_m(T_b - T_m) + U_1]}{2[C_s(T_m - T_{s0}) + \lambda + C_m\bar{\Theta}(T_b - T_m)]} \right\}^{1/2} \quad (9.3-33)$$

and the film thickness δ is

$$\delta = \left\{ \frac{[2k_m(T_b - T_m) + U_1]X}{\rho_m V_{bx} U_2 [C_s(T_m - T_{s0}) + \lambda + C_m\bar{\Theta}(T_b - T_m)]} \right\}^{1/2} \quad (9.3-34)$$

where U_2 is given by Eq. 5.7-51 (see Example 9.3)

$$U_2 = 2 \frac{(1 - b' - e^{-b'})}{b'(e^{-b'} - 1)} \quad (9.3-35)$$

and b' is defined¹² as

$$b' = \frac{-a(T_b - T_m)}{n} \quad (9.3-36)$$

and U_1 is given by in Eq. 5.7-53

$$U_1 = 2m_0 V_j^{n+1} \bar{\delta}^{1-n} \frac{(e^{-b'} + b' - 1)}{(b')^2} \left(\frac{b'}{1 - e^{-b'}} \right)^{n+1} \quad (9.3-37)$$

Equation 9.3-37 for constant viscosity Newtonian fluid ($n = 1$, $\mu = m_0$, and $a = 0$) reduces to μV_j^2 . Finally, the mean temperature of the film $\bar{\Theta}$ is given by Eq. 5.7-57

$$\bar{\Theta} = \frac{b'/2 + e^{-b'}(1 + 1/b') - 1/b'}{b' + e^{-b'} - 1} \quad (9.3-38)$$

Modifications of this model, including a nonlinear temperature profile in the melt film, channel curvature effects, and an approximate method to account for the flight clearance effect, are presented by Tadmor and Klein (1), together with expressions for power calculations. Numerous other improvements of the melting model have been suggested in the literature (33,41-46). A detailed discussion of these, however, is beyond the scope of this text.

Example 9.6 Melting in Screw Extruders The screw geometry and operating conditions for the LDPE extrusion experiment (Figs. 9.24 and 9.36) were given in Example 9.5. Calculate the SBP, using the Power Law model with temperature-dependent viscosity and linear temperature profile.

12. Note that for $T_b > T_m$, $b' < 0$ and is identical to A_4 in Reference 1.

We assume that the polymer melt follows the Power Law model in the shear-rate and temperature ranges of interest

$$\eta = 5.6 \times 10^4 e^{-0.01(T-110)} \dot{\gamma}^{-0.655}$$

where η (N·s/m²) is the non-Newtonian viscosity, T (°C) is the temperature, and $\dot{\gamma}$ (s⁻¹) the shear-rate. The melt density as a function of pressure and temperature follows the empirical relationship

$$\rho_m = 852.7 + 5.018 \times 10^{-7} P - 0.4756 T$$

where ρ_m (kg/m³) is the density, P (N/m²) the pressure, and T (°C) the temperature. The melting point of the polymer T_m is 110°C, its thermal conductivity k_m is 0.1817 W/m°C, and heat capacity C_m is 2.596 kJ/kg°C. The density of the solid polymer is 915.1 kg/m³, its heat capacity C_s is 2.763 kJ/kg°C, and the bulk density of the feed at atmospheric pressure is 595 kg/m³. The heat of fusion is 129.8 kJ/kg.

Solution In this example we know the location of the beginning of the melting zone from experimental data. As Fig. 9.24 indicates, melting starts at turn number 7. Hence, we can proceed with the SBP calculation without evaluating the length of the delay zone. The first step is calculating Φ from Eq. 9.3-33. In the expression for Φ , we have the variables U_2 , U_1 , and $\bar{\theta}$, which we calculate from Eqs. 9.3-35, 9.3-37, and 9.3-38, respectively, with b' evaluated from Eq. 9.3-36:

$$b' = \frac{-(0.01)(149 - 110)}{(0.345)} = -1.1304$$

hence, U_2

$$U_2 = (2) \frac{1 + (1.1304) - e^{1.1304}}{(-1.1304)(e^{1.1304} - 1)} = 0.814$$

The physical meaning of this result is that the drag removal action of the barrel is reduced by a factor of 0.814 as a result of the temperature profile in the film on which the shear thinning effect is superimposed.

The down-channel velocity of the solid bed is obtained from Eq. 9.3-27

$$V_{sz} = \frac{(67.1/3600)}{(915.1)(0.009398)(0.05314)} = 0.0408 \text{ m/s}$$

The velocity of the barrel surface is

$$V_b = \pi(1)(0.0635) = 0.1995 \text{ m/s}$$

The absolute value of the velocity difference $V_b - V_{sz}$ from Eq. 9.3-13 is

$$\begin{aligned} V_j &= \left[(0.1995)^2 + (0.0408)^2 - (2)(0.1995)(0.0408) \cos(17.65) \right]^{1/2} \\ &= 0.161 \text{ m/s} \end{aligned}$$

To calculate U_1 from Eq. 9.3-37, we must simultaneously solve Eqs. 9.3-34 and 9.3-37 with the aid of Eq. 9.3-38

$$U_1 = (2)(5.6 \times 10^4)(0.161)^{1.345} \delta^{0.655} \frac{[e^{1.1304} - (1.1304) - (1)] \left(\frac{1.1304}{e^{1.1304} - 1} \right)^{1.345}}{(1.1304)^2}$$

$$= 3163.8\delta^{0.655}$$

The mean dimensionless temperature $\bar{\Theta}$ from Eq. 9.3-38

$$\bar{\Theta} = \frac{e^{1.1304} \left[(1) - (1.1304)^{-1} \right] + (1.1304)^{-1} - (1.1304)/2}{e^{1.1304} - 1.1304 - 1} = 0.700$$

In Equation 9.3-34, for δ we face a difficulty with the density, whose value is a function of pressure and temperature. The pressure varies with the down-channel location, which couples the melting with melt conveying. This is a *weak* coupling, however, and we shall use a constant density at a mean temperature of $T = (0.7)(149 - 110) + 110 \approx 137^\circ\text{C}$ and estimated mean pressure of $6.89 \times 10^6 \text{ N/m}^2 (= 1000 \text{ psi})$. Thus with $\rho_m = 791 \text{ kg/m}^3$, Eq. 9.3-34 results in

$$\delta = \left\{ \frac{[(2)(0.1817)(149 - 110) + U_1]X}{(0.1995) \sin(17.65)(0.814)(791)[(2763)(110 - 24) + (129.8 \times 10^3) + (2596)(0.638)(149 - 110)]} \right\}^{1/2}$$

$$= 2.438 \times 10^{-4} [(14.17 + U_1)X]^{1/2}$$

Next, we solve U_1 and δ simultaneously for a few X values. Results are given in the following table:

X (m)	U_1 (N/s)	δ (m)
0.055	16.07	3.144×10^{-4}
0.035	13.46	2.398×10^{-4}
0.025	11.81	1.965×10^{-4}

We note that the value of δ is very small compared to the channel depth. Next, from Eq. 9.3-33 we obtain

$$\Phi = \left\{ \frac{(0.1995) \sin(7.65)(791)(0.814)[(0.1817)(149 - 110) + 0.5U_1]}{(2)(2763)(110 - 24) + (129.8 \times 10^3) + (2596)(0.638)(149 - 110)} \right\}^{1/2}$$

$$= 4.7474 \times 10^{-3} (14.17 + U_1)^{1.5} \text{ kg/s} \cdot \text{m}^{1.5}$$

By comparing U_1 values from the table to the value of 14.17, we note that viscous dissipation and heat conduction are about equal in this case.

Since melting starts in the feed section, we use Eq. 9.3-22 to compute the SBP. Melting starts at turn 7, and the constant channel feed section ends at turn 12.5. There are, therefore, 5.5 turns of constant channel depth that are left for melting to take place. Since Φ depends on U_1 , which is a function of X , we make the calculation in increments. For this example, we take increments

one turn long and evaluate δ , U_2 , and Φ at conditions prevailing at the entrance of the increment. A more accurate calculation procedure would involve the evaluation of these variables at conditions prevailing in the middle of each increment. In this example, this involves the solid bed width X appearing in the expression for δ . Hence, iterative calculation procedures are needed for this purpose. Such a procedure can easily be carried out on a computer. We calculate ψ from Eq. 9.3-23 subsequent to solving for U_1 and Φ by interpolation in the table (for the interpolation, we use $\delta_1/\delta_2 = X_1/X_2$). Results of the computations are tabulated below. When the SBP is calculated with Eq. 9.3-22, in the first increment, we use $X_1/W = 1$, and then the exit solid bed width of the upstream increment equals the inlet solid-bed width in the following increment:

Increment		Inlet Conditions				X/W End of Increment
Start (turns)	End (turns)	X_1 (m)	U_1 (N/s)	Φ (Kg/s·m ^{1.5})	ψ	
7	8	5.416×10^{-2}	15.99	0.0261	3.0006×10^{-3}	0.934
8	9	5.060×10^{-2}	15.64	0.0259	3.0862×10^{-3}	0.871
9	10	5.717×10^{-2}	15.28	0.0257	3.1173×10^{-3}	0.810
10	11	4.389×10^{-2}	14.71	0.0255	3.2616×10^{-3}	0.752
11	12	4.074×10^{-2}	14.14	0.0253	3.3521×10^{-3}	0.697
12	12.5	3.774×10^{-2}	13.79	0.0251	3.4617×10^{-3}	0.670

In the tapered section, we follow the same procedure in principle, but use Eq. 9.3-26 to calculate the SBP. The mean taper is

$$A = \frac{(9.398 \times 10^{-3}) - (3.226 \times 10^3)}{(9.5)(6.35 \times 10^{-2})/\sin(19.51)} = 3.4169 \times 10^{-3}$$

Results are shown in the following table:

Increment		Channel Depth $\times 1000$			Inlet Conditions				X/W End of Increment	
Start (turns)	End (turns)	Start H_1 (m)	End H_2 (m)	H_1/H_2	X_1 (m) $\times 100$	U_1 (N/s)	Φ (Kg/sm ^{1.5})	$\psi \times 1000$		
12.5	14.5	9.3980	8.0986	1.1604	3.628	13.61	0.025	3.519	1.030	0.667
14.5	16.5	8.0986	6.7993	1.1911	3.612	13.60	0.025	3.525	1.032	0.663
16.5	18.5	6.7993	5.4999	1.2362	3.592	13.57	0.025	3.534	1.034	0.658
18.5	20.5	5.4999	4.2005	1.3093	3.563	13.54	0.025	3.546	1.038	0.651
20.5	22.0	4.2005	3.2260	1.3020	3.525	13.49	0.025	3.562	1.042	0.643

From turn 22 to turn 26.5, we once again have a constant channel section, which is computed by the same procedure as in the feed section. The channel depth in Eq. 9.3-22 is that of the metering section.

Increment		Inlet Conditions				X/W End of Increment
Start (turns)	End (turns)	X_1 (m)	U_2 (N/s)	Φ (Kg/s·m ^{1.5})	ψ	
22	23	3.482×10^{-2}	13.44	0.0249	3.580×10^{-3}	0.502
23	24	2.720×10^{-2}	21.14	0.0243	3.955×10^{-3}	0.381
24	25	2.065×10^{-2}	11.10	0.0239	4.448×10^{-3}	0.279
25	26.5	1.511×10^{-2}	10.02	0.0233	5.087×10^{-3}	0.158

The fraction of unmelted polymer leaving the screw is obtained from the last X/W value. The fraction of unmelted polymer in the extrudate is G_s/G , where

$$\frac{G_s}{G} = \frac{(X/W)\bar{W}HV_{sz}\rho_s}{G} = \frac{(0.158)(3.585 \times 10^{-2})(3.226 \times 10^{-3})(0.0408)(915.1)}{67.1/3600} = 0.055$$

Such a level of unmelted polymer can frequently be tolerated, because the screen pack and the die itself provide additional opportunities for melting and mixing.

Figure 9.36 plots the calculated SBP as a broken curve compared to experimental data. We note that the agreement is generally good except in the metering section where, as a result of the solid bed breakup, experimental data are scattered. The parabolic drop in constant depth sections, the sharp break in the slope of the SBP upon entering the tapered section, as well as the approximately constant solid-bed width (which is the combined result of channel taper and operating conditions) are all clearly evident in the experimental results and were predicted by the model. The solid curves are the result of computations with a more accurate model accounting for flight clearance and channel curvature effects (approximately offsetting each other in this example), as well as nonlinear temperature distribution in the film of melt and reevaluation of the rheological parameters at the local conditions. Nevertheless, the example demonstrates that calculations with a relatively simple model provide useful results.

Melt Conveying In a plasticating extruder, two distinct melt conveying regions can be found. One is downstream of the melting zone after the completion of melting, where the models derived in the preceding section can be applied without modifications. In addition, melt conveying occurs in the melt pool, which extends side by side with the solid bed profile. Here, the width of the melt pool changes in the flow direction. Moreover, the mass-flow rate of melt also changes as a result of the influx from the melt film. Both these quantities, as well as the mean melt-film temperature, are obtained from the melting model. Hence, the melt conveying model can be applied approximately to calculate local pressure gradients and temperature changes over small, finite axial increments using the mean local flow rate and melt pool size (1,47). The result of these calculations is the pressure and melt temperature profile over the length of the extruder.

Simulation of the Complete Process Having broken down the extrusion process into a series of submodels (solids flow in the hopper, solids conveying, melting and melt conveying), we are now in a position to combine these intimately interconnected submodels into a complete whole model, capable of simulating the whole plasticating extrusion process. This, however, requires a great deal of computation, which was made possible and convenient in the 1960s,

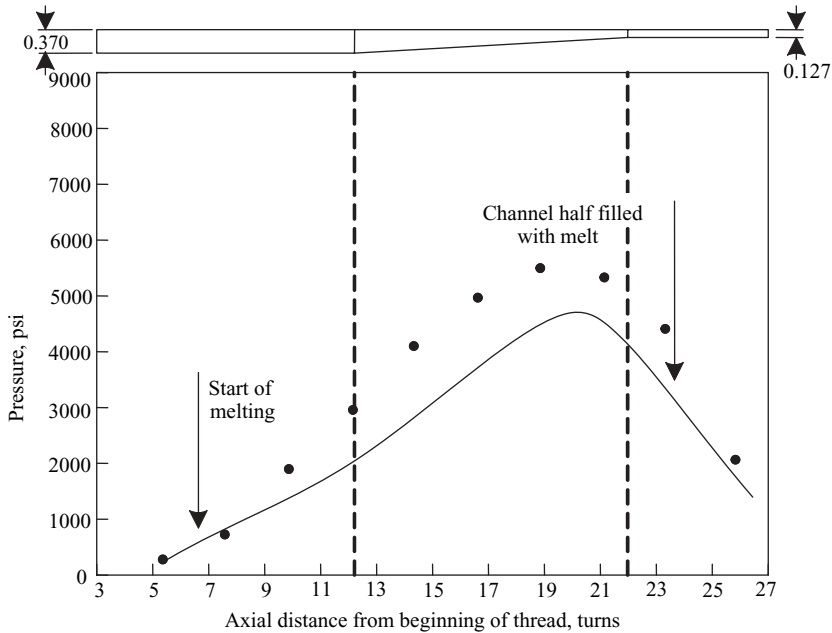


Fig. 9.37 Simulated and measured pressure profiles for an LDPE extruded in a 2.5-in-diameter, 26.5 length-to-diameter ratio extruder, with a metering-type screw having 12.5 feed section with channel depth of 0.37 in and 4.5 turns of metering section of depth of 0.1275. The flow rate is 136 lb/h, the screw speed 60 rpm, and the barrel temperature was set at 300°F. The SBP is shown in Fig. 9.24. The screw geometry is shown at the top of the figure. Simulation was carried out by the first computer simulation package for plasticating extrusion developed by the Western Electric Princeton Engineering Research Center team (17). [Reprinted by permission from Z. Tadmor and I. Klein, *Engineering Principles of Plasticating Extrusion*, Van Nostrand Reinhold, New York, 1970.]

when the theoretical model of melting was developed, by the revolutionary advent of digital computers. Indeed, the simulation of the plasticating extrusion process pioneered by the Western Electric Engineering Research Center team (17) was among the first *computer-aided design* (CAD) engineering software packages. Since that time numerous commercial computer simulation packages for extrusion have been developed and marketed.

Figure 9.37 presents the pressure profile of the experiment described in Fig. 9.24, simulated by the first complete extruder computer simulation package for plasticating extrusion developed by the Western Electric, Princeton Engineering Research Center team (17). As indicated, the simulated pressure profile agrees well with the measured one.¹³ The program, of course, simulates the whole process, predicting, in addition to the pressure profile, among others the SBP, the melt temperature profile, residence times and strain, degree of fill in vented regions, power consumption (and power breakdown for the various functions), and expected temperature surging at the die.

13. It is worth noting that the simulation of the pressure profile is the most sensitive from all other simulated variables. Under many operating conditions minor changes in input data as, for example, geometry (e.g., flight clearance and metering channel depth), or operating conditions (e.g., screw speed) can result in very large variations in the predicted pressure values. Therefore, a parameter sensitivity study should be carried out to better judge the accuracy of predictions.

In this class of models, it is assumed that the melting step strongly affects the melt pumping step, but the possible impact of the latter on the former is neglected. In effect, the melt in the pool exerts pressure and viscous drag on the solid bed, which, together with the viscous drag over the melt film, the root of the screw, and the trailing flight, determine the stress distribution in the solid bed. Such an analysis coupling the two phases has been attempted (33,46), and in principle, it may provide the means to predict solid deformation, acceleration, and breakup.

Mixing in plasticating extruders is closely related to melting. In the melt channel, laminar mixing takes place, as is evident in the uniform color in the previously described melting experiments. Clearly, however, mixing can only be completed after all solids melt. In a well-designed ordinary screw extruder this should happen only toward the end of the screw leading to exit composition fluctuations in time and space as well as temperature fluctuations. However, both the effectiveness of melting and that of mixing can be significantly improved by mixing sections and barrier-type screws, as described in the following subsection.

Finally, we comment on residence distribution in plasticating extruders. Tracer measurement will indicate a relatively narrow RTD, because the solid moves as a plug and the RTD of the melt pool is quite narrow as well, as discussed earlier. But what matters for polymers is the RTD in a *molten state*. This, as shown by Lidor and Tadmor (24), may be quite wide, as is the SDF.

Screw Designs

The classic plasticating screw consisted of three sections: a deep-channel feed section, a tapered melting section, and a shallow metering section. The feed section must be deep enough to accommodate the low bulk density plastics pellets, to generate the necessary torque to convey the solids, and to generate sufficient pressure to compact the bed into a solid bed. The barrel in the feed section is cooled to sustain frictional drag by the barrel surface. Sometimes axial or helical grooves are machined into the barrel to create an effective higher coefficient of friction and thus increase the solids conveying efficiency. Much of the melting takes place in the relatively long tapered section. The decrease in channel depth is needed not to compensate for the increasing density of the solids, as is sometimes claimed, but to improve the melting efficiency. This is clearly suggested by the melting mechanism and the melting model supports it quantitatively. Finally the metering section, which really does not exclusively *meter* the flow rate, as this is determined jointly by the upstream sections and the metering section. Nor does it exclusively generate the pressures at the die—as often pressure drops in this region—but being shallow it can homogenize reasonably well the melt that contains partially molten regions left over from the melting zone, and bring them to a more uniform temperature. This function of the metering section can be improved by inserting into the channel “mixing pins,” as shown in Fig. 9.38, or by a variety of mixing heads attached to the screw, as shown in Fig. 9.39.

The elucidation of the melting mechanism has triggered a productive period of innovation in screw design. Most of these screw designs are *barrier*-type screws, that is, an auxiliary flight is added such that it starts at the “pushing flight” and ends at the “trailing flight”; thus, it separates the solids from the melt in the main screw channel. The auxiliary flight has a larger flight clearance than the primary flight. This way, solids entering the screw channel cannot generally leave the screw without having to pass over the flight clearance of the auxiliary flight. Thus, solids are barred from leaving the screw.

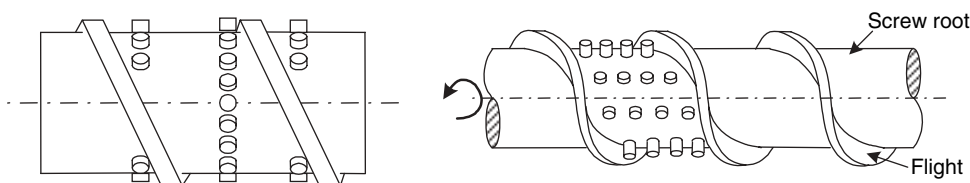


Fig. 9.38 Two arrangements of mixing pins in the screw channel.

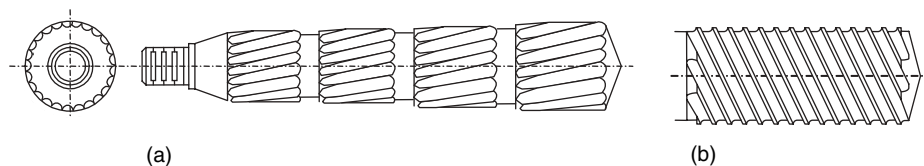


Fig. 9.39 Various mixing heads. (a) Torpedo extension. (b) Dulmage screw.

There are many barrier-type screws that differ from each other by the channel depth profiles of the melt and solids channels, by the helix angles, profiles, and the number of flights. We briefly review here just a few of these types of screw. The first barrier-screw design is due to C. Maillefer¹⁴ and is shown in Fig. 9.40, in which the auxiliary channel follows roughly the solid-bed profile. Clearly, at certain conditions the auxiliary flight can restrict flow rate, but at all times it prevents solids from leaving the screw.

The MC-3 screw, shown in Fig. 9.41, developed by the Waldron Hartig Division of the Midland Ross Corporation, improves upon the Maillefer screw, maintaining from a certain down-channel point a constant helix angle of the auxiliary flight, with increasing depth in the melt channel (to accommodate the increasing melt flow rate), and a diminishing solids conveying channel, until the converge. The Dray and Laurence screw is very similar, but the helix angle of the primary channel is increased up to a point to create more space for the melt channel, as is the Kim Screw, in which the helix angle is continuously increased.

The Efficient screw of the Feed Screws Division, New Castle Industries, shown in Fig. 9.42, has a constant helix angle in the feed section, but at the point the auxiliary flight begins the helix angle increases, providing space for the new barrier flight and the melt channel. After the width of the new melt channel is established, the flights remain parallel through the transition section. Toward the end of the melting zone the open-ended melt channel merges with the solids channel.

Finally, the Union Carbide Bruce Maddock Fluted Screw Section, shown in Fig. 9.43, is really a compressed barrier-type screw, whereby the mixture of melt and solids enters a set

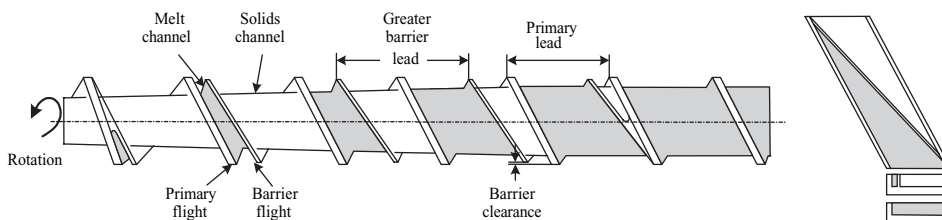


Fig. 9.40 Schematic view of the Maillefer barrier type screw.

14. C. Maillefer, *Mod. Plast.*, **40**, 132 (1963).

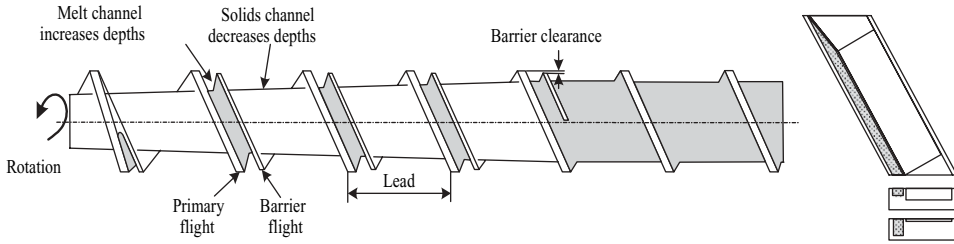


Fig. 9.41 Schematic view of the MC-3 of the Waldron Hartig Division of the Midland Ross Corporation. Smooth gray color indicates melt.

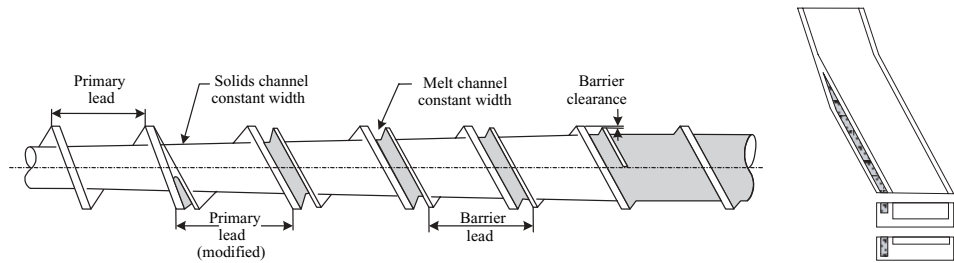


Fig. 9.42 Schematic view of the Efficient barrier-type screw by the Feed Screws Division, New Castle Industries. Smooth gray color indicates melt.

of parallel axial flutes or channel and is dragged by the barrel across barrier flights to a set of parallel exit flutes. The barrier flights do not separate solids from the melt, but merely prevent solids from leaving until they are melted. The pressure loss over the Maddock device, which was analyzed theoretically by Klein and Tadmor (49), is small and in certain conditions it may generate pressure. The device is frequently located at the end of the screw like a mixing head, or about two-thirds of the way downstream from the feed port.

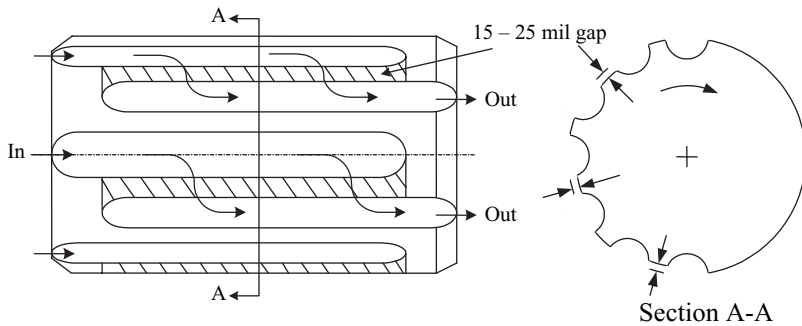


Fig. 9.43 The Union Carbide Maddock Fluted Mixing Screw Section.

9.4 THE CO-ROTATING DISK PLASTICATING PROCESSOR

Sections 9.2 and 9.3 discussed the elementary steps that make up the important and widely used screw extrusion process. The common and outstanding feature of all the elementary steps taking place in the screw channel is that they are induced by drag brought about by a single moving surface—that of the barrel. Solids are conveyed and compressed by the

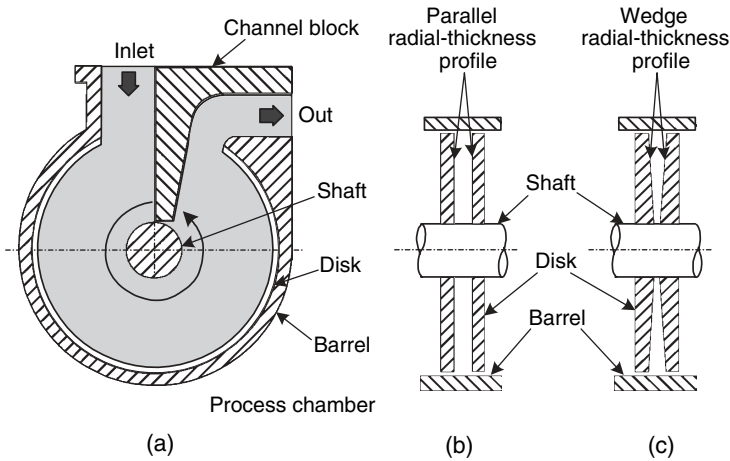


Fig. 9.44 (a) Schematic view of a co-rotating disk configuration. The disks are attached to the rotating shaft and enclosed in a housing. The channel block separates between inlet and outlet. (b) Parallel disk geometry and (c) wedge-shaped disk geometry.

frictional drag of the barrel surface; they are melted in a drag removal melting step, and the melt is pressurized and mixed by drag-induced flow. The other main surface of the channel, the stationary root of the screw, has no useful operational function except as a geometrical boundary. In fact, the efficiency of the elementary steps is even retarded by it.

In Section 6.2, however, we saw that, at least for pumping, there is a plethora of alternative geometrical configurations capable of generating pressure by a drag-induced mechanism. Specifically, in Section 6.6 we examined the *co-rotating disk* configuration based on Building Block 2 from Fig. 6.2 of jointly moving parallel plates. Table 6.1 summarized the design equation of such a pump.

In this section we examine the plasticating co-rotating disk configuration functioning as a complete plastics processor¹⁵ in which all the elementary steps take place (49–51). This configuration demonstrates that it is possible to process (i.e., to melt, mix, devolatilize, and pump) polymers in machines other than screw-based ones, whether single or twin. This, we believe, will help the reader to better understand screw machines as well. In addition, it provides yet another demonstration of how to mathematically model processing machines.

In screw extruders, as we have seen, the processing takes place in the helical channel formed between the screw and the barrel. In a co-rotating disk processor (CDP), on the other hand, processing takes place in flat doughnut-shaped *processing chambers* formed by two neighboring disk surfaces, the inner surface of the barrel, the shaft to which the disks are attached, and the *channel block* attached to the barrel, with very small clearance to the disk surfaces. It thus blocks the channel and separates inlet from outlet, as shown in Fig. 9.44. Processing chambers can be connected in series, parallel, or any other

15. The CDP was developed by the Farrel Corporation in Ansonia, CT, and sold under the trade name Diskpack. Although over a dozen machines were manufactured, sold, and used in industry, the line was discontinued. A retrospective analysis of this development, which is instructive regarding the uphill battle of many engineering innovations that radically depart from the traditional practices, is given in Z. Tadmor, "Machine Invention, Innovation and Elementary Steps," *Adv. Polym. Technol.*, **21**, 87–97 (2002).

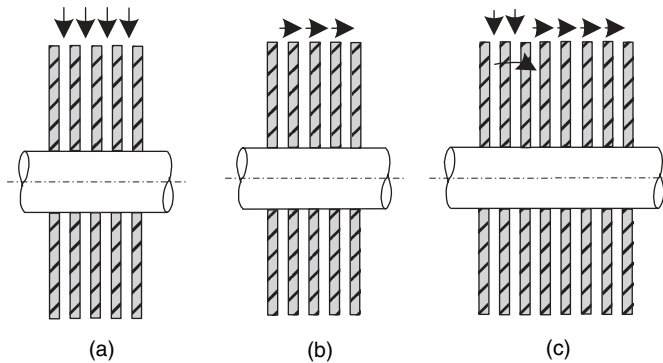


Fig. 9.45 Multiple disks attached to the shaft with (a) processing chambers connected in parallel, (b) processing chambers connected in series, and (c) combined parallel and series connection.

combination, as shown in Fig. 9.45. Generally, each chamber is designed to perform one of the elementary steps.

Example 9.7 Schematic Design of a Diskpack Co-rotating Disk Compounder Before discussing the mechanism and modeling of the various elementary steps in the processing chambers, and in order to gain a better understanding of this machine concept, we discuss the structure of a co-rotating disk compounder manufactured by the Farrel Corporation under the trade name Diskpack. This is shown schematically in Figure E9.7a.

This figure shows a schematic but representative design of a Diskpack compounder with 12 processing chambers. In this particular design, solids are fed in parallel into six melting chambers. The molten material is transferred through an axial transfer channel machined into the housing upstream of the channel block to a single mixing chamber (7). This mixing chamber is equipped with three mixing blocks (A, B, and C). Mixing blocks are similar to channel blocks, but have larger, wedge-shaped clearances to enable molten material to pass, thereby undergoing high shear stress. The channel block, which is 90° off the prior one forces the melt into another transfer channel, feeding two additional mixing–venting chambers in parallel (8 and 9). These chambers have a secondary port, either for adding additives or venting. In the latter case, a spreading insert (marked A) deposits the melt on the disk surfaces. Before exiting, the melt is mixed with yet another mixing block (B). Next the melt from the mixing–venting chambers is fed into a mixing–homogenizing chamber (10), also equipped with three mixing blocks (A, B, and C). Finally, the melt is transferred to a wedge-shaped pumping chamber, which normally operates partially filled, because a fraction of the circumference suffices to generate the pressure needed to extrude the melt through the die. Outboard of the pumping chamber, there is yet another chamber that collects any leakage through the viscoseals isolating the pumping chamber, and feeds it back to the pump. The melting chambers are generally wedge-shaped and wide enough to accept traditional solids feeding. The mixing chambers are parallel and the mixing blocks may come in a variety of shapes and be easily removed or replaced. Finally, the pump is wedge-shaped and narrow. The disks are hollow and can be temperature controlled with hot oil fed through the shaft via a rotary joint.

A 350-mm 12-chamber machine is shown in Fig. E9.7b. Unlike the case in the SSE described in the previous section, the journey of a polymer particle in a multichannel CDP is more predictable. Not only do the particles proceed through a sequence of chambers that is predetermined in the design stage, but in addition, each chamber is dedicated to a specific elementary step, as indicated in Example 9.7. This, of course, makes modeling and simulation easier.

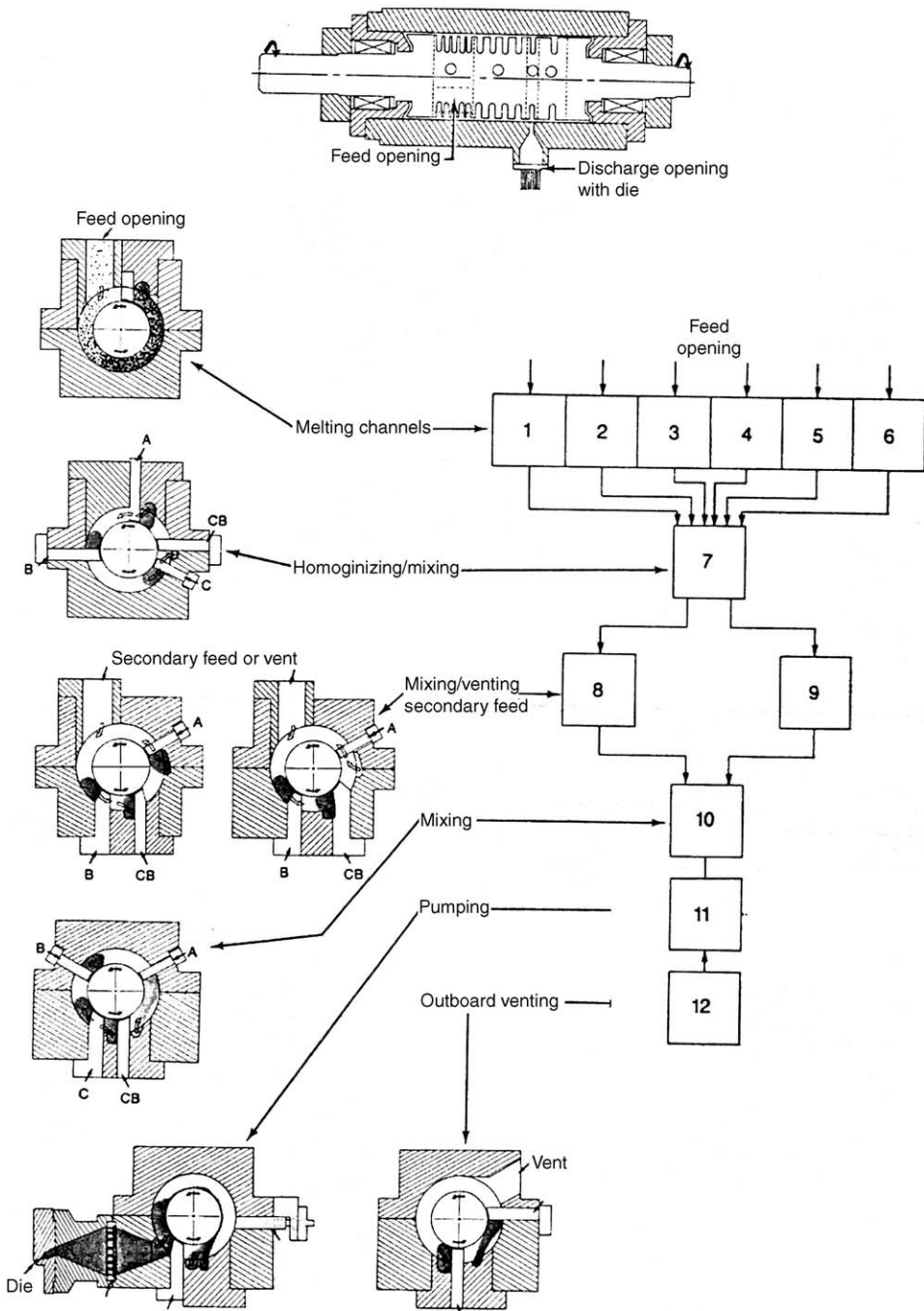


Fig. E9.7a A schematic but representative design of a 350-mm-diameter, 12-chamber Diskpack compounder. The rotor is shown at the top and the cross section of each separate chamber is shown in the sequence of the processing path. Each cross section shows the housing, the inlet and outlet, and the various inserts attached to the housing. [Courtesy of Farrel Corporation, Ansonia, CT.]



Fig. E9.7b Photograph of a 350-mm-diameter co-rotating disk Diskpack¹⁶ compounder manufactured by the Farrel Corporation with a tested production capacity of 3000 lb/h. [Courtesy of Farrel Corporation, Ansonia, CT.]

Plasticating First we observe that, in a CDP, there is no solids conveying section or chamber, because the disks are heated and the pellets that come in contact with the rotating disks quickly melt. The solids are compressed into a solid bed as in the SSE, occupying $2\pi\varepsilon$ of the circumference, as shown in Fig. 9.46.

We invoke the drag removal melting mechanism with thin films of melt created at the hot disk surfaces. The thickness of the film grows toward the exit, as shown in Fig. 9.47,

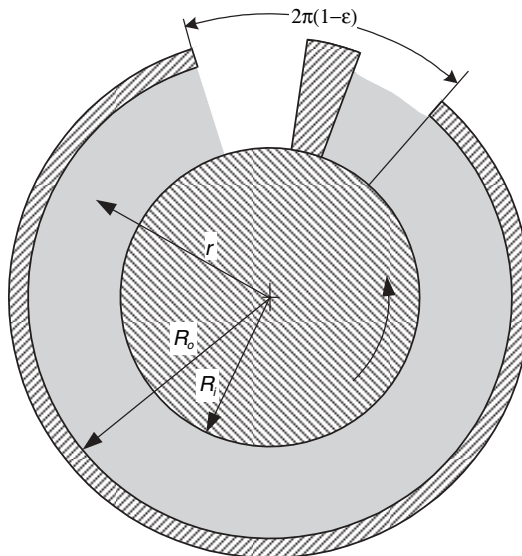


Fig. 9.46 A co-rotating disk melting chamber with solids filling up much of the channel.

16. This particular Diskpack machine had only four melting chambers.

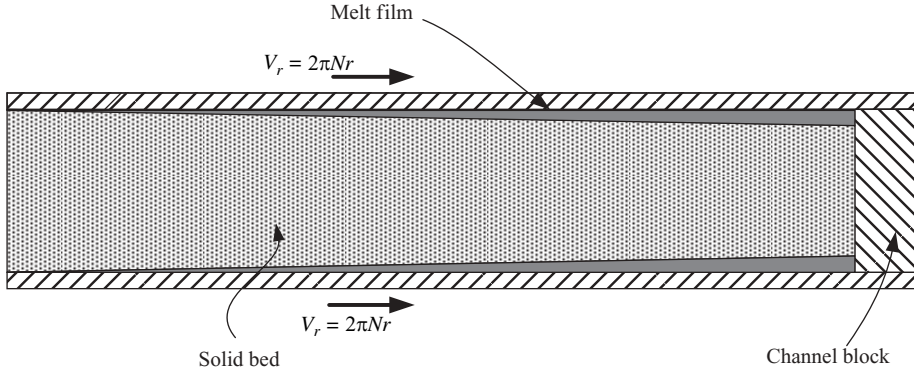


Fig. 9.47 Schematic representation of the drag removal melting mechanism along a plane of constant radius. Pressure builds by the drag exerted by the rotating disks with a maximum value at the channel block. The melt from the melt pool is discharged radially into a transfer channel to the next chamber.

which depicts schematically the solid bed along a constant radius. Pressure builds toward the channel block and, consequently, the melt in the exit region acquires a radial velocity component toward the exit. This melting model was experimentally observed by Tadmor et al. (50) for LDPE, HDPE, and Polypropylene (PP) with pelletized feed, using a freezing technique similar to the one used for elucidating the melting mechanism in SSEs.

We now derive a simple mathematical model for calculating the rate of melting in a melting chamber. The outer and inner radii of the disk are R_o and R_i , respectively, and the gap between them is H ; the solid bed occupies $2\pi\varepsilon$ of the circumference; the disk speed N is constant, the disk temperature is T_d ; the molten polymer is Newtonian with constant viscosity μ ; the solids and melt have densities and specific heat ρ_s, c_s and ρ_m, c_m , respectively; the melting point is T_m ; and the heat of fusion is λ . We now turn to Eq. 5.7-36, with W replaced by $2\pi r\varepsilon$, and the velocity V_0 by $2\pi rN$, to get the *rate of melting per unit distance in the r direction* (kg/(s·m))

$$\begin{aligned}\omega_r &= 2 \left\{ \frac{4\varepsilon\pi^2 r^2 N \rho_m [k_m(T_d - T_m) + 2\pi^2 r^2 N^2 \mu]}{\lambda + C_s(T_m - T_s)} \right\}^{1/2} \\ &= 4\pi r \sqrt{\frac{\varepsilon N \rho_m}{\lambda + C_s(T_m - T_s)}} \sqrt{[k_m(T_d - T_m) + 2\pi^2 r^2 N^2 \mu]}\end{aligned}\quad (9.4-1)$$

The *total rate of melting* (kg/s) is given by integrating ω_r :

$$\omega_T = \int_{R_i}^{R_o} \omega_r dr \quad (9.4-2)$$

Substituting Eq. 9.4-1 into Eq. 9.4-2 and integration, results in:

$$\begin{aligned}\omega_T &= \frac{2}{3\mu\pi N^2} \sqrt{\frac{\varepsilon\rho_m N}{\lambda + C_s(T_m - T_s)}} \\ &\quad \left\{ [2\mu\pi^2 N^2 R_o^2 + k_m(T_d - T_m)]^{3/2} - [2\mu\pi^2 N^2 R_i^2 + k_m(T_d - T_m)]^{3/2} \right\}\end{aligned}\quad (9.4-3)$$

Example 9.8 The Melting Rate in a Co-rotating Disk Chamber In this example we calculate the rate of melting of LDPE in a parallel chamber of width 0.75 in, outer radius of 3.75 in, inner radius 2.25 in as a function of disk speed with disk temperature set at 450°F. The viscosity is 0.035 lb_fs/in², the melting point is 231°F, the heat of fusion is 55.8 Btu/lb, the thermal conductivity of the melt is 0.105 Btu/ft°F·h, the specific heat of the melt and solids are 0.62 and 0.66 Btu/lb°F, respectively, and the solids and melt densities are 57 and 48 lb/ft³, respectively.

Solution Substituting the given parameters into Eq. 9.4-3 in suitable units and assuming an inlet temperature of 86°F gives:

$$\omega_T = \frac{2 \times 60^2}{(3\pi \times 0.036 \times N^2)} \left[\frac{0.75 \times 48N \left(\frac{1}{12^3 \times 60} \right)}{(55.8 + 0.66 \times (231 - 86)) \times 60244} \right]^{1/2}$$

$$\left\{ \left[2 \times 0.036\pi^2 \times 3.75^2 N^2 \left(\frac{1}{60} \right)^2 + 0.105 \times (400 - 231) \left(\frac{60244}{12 \times 3600} \right) \right]^{1/2} \right.$$

$$\left. - \left[2 \times 0.036\pi^2 \times 2.25^2 N^2 \left(\frac{1}{60} \right)^2 + 0.105 \times (400 - 231) \left(\frac{60244}{12 \times 3600} \right) \right]^{1/2} \right\}$$

This can be rewritten as

$$\omega_T = 0.13088787N^{-3/2} \left\{ [27.75826 \times 10^{-4}N^2 + 24.746059]^{1/2} \right.$$

$$\left. - [9.992974 \times 10^{-4}N^2 + 24.746059]^{1/2} \right\}$$

The rate of melting versus disk speed is shown in Fig. E9.8

However, experimental studies (50), using either powder feed or pelletized feed with some recycled melt over the channel block into the feed port, have not exhibited drag removal melting but a dissipative mix-melting mechanism, discussed in Chapter 5. As

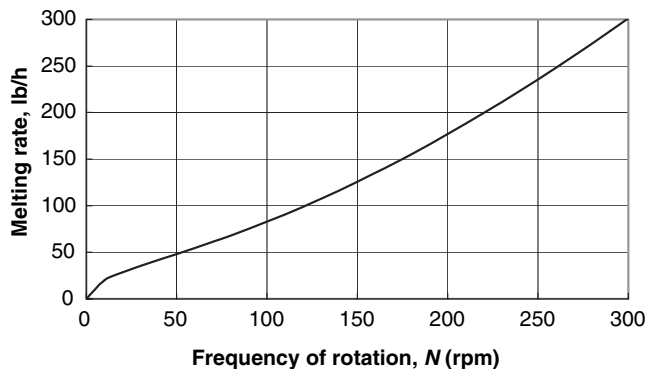


Fig. E9.8 Simulated rates of melting of LDPE in a 7.5-in-diameter co-rotating disk as a function of disk speed with the disk temperature as a parameter.

pointed out there, this melting mechanism is very efficient, although it creates a nonuniform plasticated melt with some entrapped air bubbles. The entrapped bubbles, however, can be removed in downstream chambers that also homogenize the melt. The interesting point is that, unlike in other machines, in this machine the dissipative mix-melting mechanism can be triggered by enabling melt recycle, at a desired rate, which is determined by the radial clearance of the channel block.

Mixing The extensive mixing in a co-rotating disk chamber was studied both theoretically and experimentally. The velocity profiles as predicted by the theoretical model described in Section 6.6 were verified experimentally (52), and the evolution of the interfacial area was studied using color tracers (53).

The velocity profile in a parallel channel given in Eq. 6.6-23 can be written in dimensionless form in terms of the pressure and drag flow rates as follows (52):

$$u_\theta = 1 - \frac{[(s + 2)/(s + 1)](R_d/r)^{s+2}(Q_p/Q_d)}{2\{(\alpha^{1-s} - 1)/[(s - 1)(1 - \alpha^2)]\}}(1 - \xi^{s+1}) \tag{9.4-4}$$

where $u_\theta = v_\theta/2\pi Nr$ is the dimensionless velocity, $\xi = 2z/H$, $s = 1/n$, where n is the Power Law exponent, $\alpha = R_s/R_d$, and Q_d and Q_p are the drag- and pressure-flow rates given by

$$Q_d = \pi NHR_d^2(1 - \alpha^2) \tag{9.4-5}$$

and

$$Q_p = \frac{H^2R_d}{2(s + 2)} \frac{(\alpha^{1-s} - 1)}{(s - 1)} \left[\frac{H}{2mR_d} \frac{\partial P}{\partial \theta} \right]^s \tag{9.4-6}$$

Mixing chambers are relatively wide and, therefore, the pressure and drag flows are close to each other. A good feel for the mixing condition can be obtained by examining the velocity profiles at various radial positions, as shown in Fig. 9.48. Clearly, the disks drag the fluid toward the channel block, where it must turn around and flow backward in the

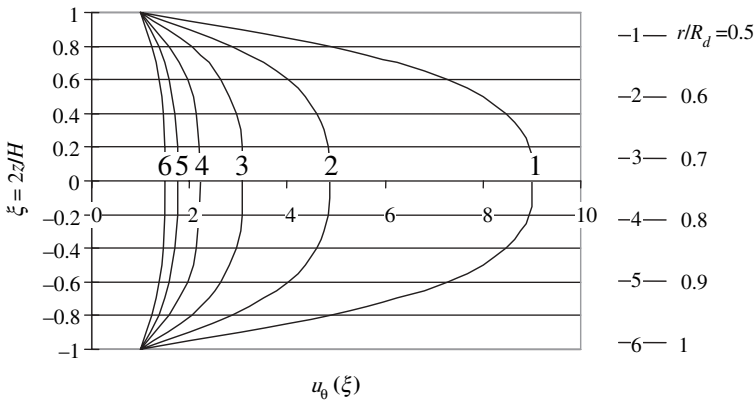


Fig. 9.48 Velocity profiles for a Power Law model fluid with $s = 2$, $\alpha = 0.5$ at various r/R_d values: 0.5, 0.6, 0.7, 0.8, 0.9, and 1.0, with $Q_p/Q_d = -1$.

center region of the channel. This circulatory flow at a fixed radius induces good extensive mixing. In a wedge-shaped chamber, under closed discharge conditions, fluid particles in a certain radial position stay at that plane. But in a parallel channel above a certain critical radius r^* , there is a net forward flow, whereas, below that value, there is a net backflow. The critical radius is given by

$$r^* = R_d \left[\frac{1}{2} \left(\frac{2n+1}{n+1} \right) \left(\frac{Q_p}{Q_d} \right) \frac{(1-s)(1-\alpha^2)}{(1-\alpha^{-s})} \right]^{n/(n+1)} \quad (9.4-7)$$

This implies that, superimposed on the circulatory flow at a fixed radius, there is an overall circulation perpendicular to the constant r plane. This overall circulation helps in randomizing the composition non-uniformity.

David and Tadmor (54) studied experimentally the evolution of the interfacial area using Thiokol rubber with a color tracer, and their findings are shown in Fig. 9.49. At one

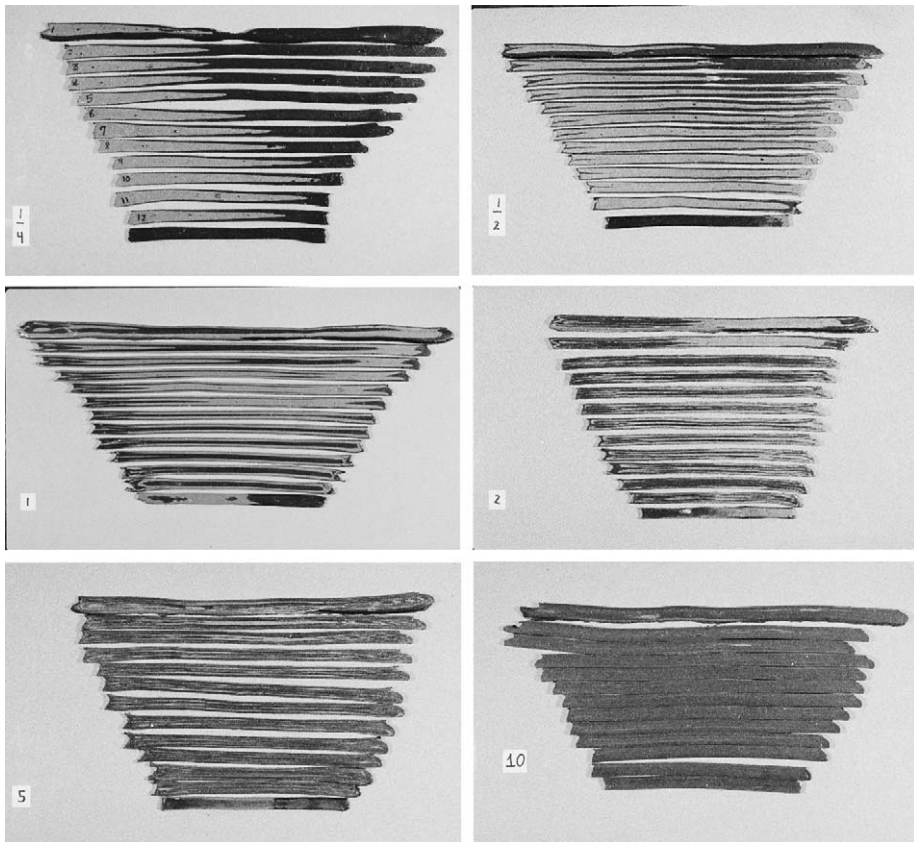


Fig. 9.49 The evolution of the interfacial area of a viscous Thiokol rubber in a 26.6-cm parallel-disk mixing chamber with $\alpha = 0.5$, with the number of turns. The rubber filled up half the chamber with one-quarter cream color (at the channel block at the left side) and one-quarter black. The numbers on the figure indicate the number of turns from 1/4 to 10. [Reprinted by permission from B. David and Z. Tadmor, "Laminar Mixing in Co-rotating Disk Processors," *Int. Polym. Process.*, **3**, 38-47 (1988).]

quarter of a turn, the disks drag the black material at the disk surfaces all the way to the channel. At half a turn, the black material turns around and begins to penetrate the cream material, creating new striations and interfacial area. At one turn, the black material at the center reaches the feed end. With increasing turns we observe more striations and, due to the overall circulation, we notice, for example, at five turns, more black in the lower regions. After only 10 turns, the mixture appears homogeneous to the naked eye. The smaller the melt pool, the more striations will be created for the same number of turns.

Dispersive mixing requires high shear stresses. These can be obtained by inserting shearing pins into the chamber with a prescribed clearance and shape, where the number of passages over the high shear region (at no recycle) equals the number of pins (55).

Devolatilizing Devolatilization in a co-rotating disk chamber can be achieved by spreading the melt on the disk surfaces in a chamber under high vacuum, and collecting the foamed film in a circulating pool at the channel block where bubble rupture takes place. The partly devolatilized melt can then be fed into another chamber in series, and so on. Fig. 9.50 shows a setup of three consecutive devolatilizing chambers.

The separation efficiency of a single chamber is given by

$$\varepsilon = 1 - \frac{c_{out} - c_e}{c_{in} - c_e} \tag{9.4-8}$$

where c_{out} and c_{in} are the exit and inlet concentrations, respectively, and c_e is the equilibrium concentration at the imposed vacuum level. In a multiple-chamber setup with identical conditions in each, it is easy to show that the overall separation efficiency is given by

$$E_n = 1 - (1 - \varepsilon)^n \tag{9.4-9}$$

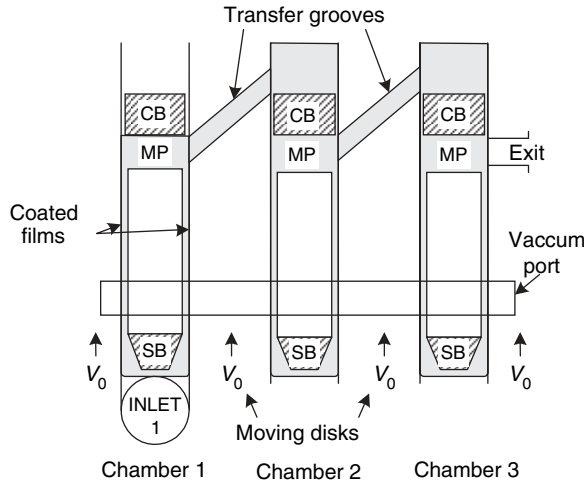


Fig. 9.50 Schematic view of a three-chamber co-rotating disk devolatilizer. The molten inlet feed is deposited on the disk surface of the first chamber by a spreading block (SB). The film is exposed to vacuum via the vacuum port. The melt is collected at the channel block (CB) and forced to flow over the top of the disk to the feed port of the second chamber. Similarly, the melt is fed into the third chamber from where the devolatilized melt exists.

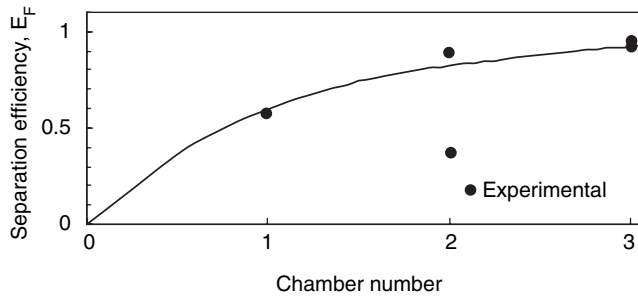


Fig. 9.51 Separation efficiency in consecutive chambers of 450°F PS melt fed at 42 lb/h into 0.54-in-wide chambers at 50-torr absolute pressure, with disks rotating at 30 rpm. [Reprinted by permission from P. S. Mehta, L. N. Valsamis, and Z. Tadmor, "Foam Devolatilization in a Multichannel Co-rotating Disk Processor," *Polymer Process Eng.*, **2**, 103–128 (1984).]

Devolatilization in a co-rotating disk chamber was studied by Mehta et al. (56). They used a melt-fed, 7.5-in-diameter co-rotating disk devolatilizer, with three 1-in-wide chambers connected in series, and with $\alpha = 0.566$ and $\varepsilon = 93^\circ$ as shown in Fig. 9.50. The polymer devolatilized was polystyrene (PS) with 1500–3000 ppm styrene. Figure 9.51 shows the efficiency of separation in the consecutive chambers. The efficiencies measured were 58%, 88%, and 94%, in one, two, and three chambers, respectively. These results conform reasonably well with Eq. 9.4-9.

Finally, Fig. 9.52 shows the overall efficiency of separation as a function of disk speed with flow rate as a parameter. Efficiency increases with flow rate (in spite of decreasing residence time), just as SSEs and TSEs, indicating that foaming, which was visually observed to take place, is quick, and the increased separation is most likely due to better bubble rupture and volatile release in the highly sheared melt pools.

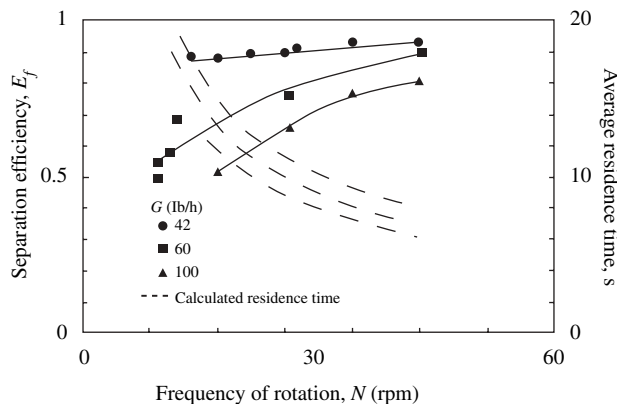


Fig. 9.52 Separation efficiency of a three-chamber co-rotating disk devolatilizer of 450°F PS melt containing 1500–3000 ppm styrene, fed at 42-lb/h into 0.54-in-wide chambers at 50-torr absolute pressure, as a function of disk speed and with flow rate as a parameter. Broken curves show calculated residence times. [Reprinted by permission from P. S. Mehta, L. N. Valsamis, and Z. Tadmor, "Foam Devolatilization in a Multichannel Co-rotating Disk Processor," *Polym. Process Eng.*, **2**, 103–128 (1984).]

REFERENCES

1. Z. Tadmor and I. Klein, *Engineering Principles of Plasticating Extrusion*, Reinhold, New York, 1970; (a) p. 234; (b) p. 310; (c) p. 328; (d) Chapters 6 and 8; (e) p. 186; (f) p. 90; (g) p. 133.
2. M. L. Booy, "Influence of Oblique Channel Ends on Screw Pump Performance," *Polym. Eng. Sci.*, **7**, 5–16 (1967).
3. R. E. Colwell and K. R. Nicholls, "The Screw Extruder," *Ind. Eng. Chem.*, **51**, 841–843 (1959).
4. R. M. Griffith, "Fully Developed Flow in Screw Extruders," *Ind. Eng. Chem. Fundam.*, **1**, 180–187 (1962).
5. H. Zamodits and J. R. A. Pearson, "Flow of Polymer Melts in Extruders. Part I. The Effect of Transverse Flow and of Superposed Steady Temperature Profile," *Trans. Soc. Rheol.*, **13**, 357–385 (1969); see also B. Martin, J. R. A. Pearson, and B. Yates, "On Screw Extrusion. Part I. Steady Flow Calculations," University of Cambridge, Department of Chemical Engineering, Polymer Processing Research Center, Report No. 5, 1969.
6. B. Yates, "Temperature Development in Single Screw Extruders," Ph.D. Thesis, University of Cambridge, Cambridge, 1968.
7. R. T. Fenner, "The Design of Large Hot Melt Extruders," *Polymer*, **16**, 298–304 (1975).
8. R. T. Fenner, in *Computational Analysis of Polymer Processing*, J. R. A. Pearson, and S. M. Richardson, Eds., Applied Science, London, 1983.
9. B. Elbirlı and J. T. Lindt, "A Note on the Numerical Treatment of the Thermally Developing Flow in Screw Extruders," *Polym. Eng. Sci.*, **24**, 482–487 (1984).
10. K. P. Choo, M. L. Hami, and J. F. T. Pittman, "Deep Channel Operating Characteristics of Single Screw Extruder," *Polym. Eng. Sci.*, **21**, 100–104 (1981).
11. D. Roylance, "Use of Penalty Finite Element Analysis of Polymer Melt Processing," *Polym. Eng. Sci.*, **20**, 1029–1034 (1980).
12. R. Y. Chang, C. W. Hsu, W. H. Yang, W. L. Yang, and D. C. Hsu, "Three Dimensional Numerical Analysis of the Single Screw Plasticating Extrusion Process," *SPE ANTEC Tech. Papers.*, **47**, 173–175 (2001).
13. E. E. Agur and J. Vlachopoulos, "Numerical Simulation of a Single Screw Plasticating Extruder," *Polym. Eng. Sci.*, **22**, 1084–1094 (1982).
14. J. F. T. Pittman and K. Rashid, "Heat Transfer in Recirculating Extruder Channel Flow," *J. Polym. Eng.*, **5**, 1–48 (1985).
15. M. Viriyayuthakorn and B. Kassahun, "A Three Dimensional Model for a Plasticating Extrusion Screw Design," *SPE ANTEC Tech. Papers*, **30**, 81 (1984).
16. S. Syrjälä, "On the Analysis of Fluid Flow and Heat Transfer in the Melt Conveying Section of a Single Screw Extruder," *Num. Heat Trans.*, Part A, **35**, 25–47 (1999).
17. I. Klein and Z. Tadmor, "Operating Characteristics of a Plasticating Extruder," in *Computer Programs for Plastics Engineers*, I. Klein and D. I. Marshall, Eds., Reinhold, New York, 1968, Chapter 6.
18. S. Middleman, "Flow of Power Law Fluids in Rectangular Ducts," *Trans. Soc. Rheol.*, **9**, 83 (1965).
19. Z. Tadmor, "Non-Newtonian Tangential Flow in Cylindrical Annuli," *Polym. Eng. Sci.*, **6**, 202–212 (1966).
20. G. Pinto and Z. Tadmor, "Mixing and Residence Time Distribution in Melt Extruders," *Polym. Eng. Sci.*, **10**, 279–288 (1970).
21. D. Wolf and D. H. White, "Experimental Study of the Residence Time Distribution in Plasticating Extruders," *AIChE J.*, **22**, 122–131 (1976).
22. M. Hirshberger, "Two-Dimensional Non-Newtonian Flow in Rectangular Channels," M. S. Thesis, Department of Chemical Engineering, Technion–Israel Institute of Technology, Haifa, 1972.

23. D. Bigg and S. Middleman, "Mixing in Screw Extruders: A Model for Residence Time Distribution and Strain," *Ind. Eng. Chem. Fundam.*, **13**, 66 (1974).
24. G. Lidor and Z. Tadmor, "Theoretical Analysis of Residence Time Distribution Functions in Plasticating Screw Extruders," *Polym. Eng. Sci.*, **16**, 450–462 (1976).
25. I. Manas-Zloczower and Z. Tadmor, "The Distribution of Number of Passes over the Flights in Single Screw Melt Extruders," *Adv. Plast. Tech.*, **3**, 213 (1983).
26. Z. Tadmor, "Machine Invention, Innovation and Elementary Steps," *Adv. Polym. Technol.*, **21**, 87–97, (2002); also presented at the Fundamental Forums "Invention and Innovation" session at the 2001 ANTEC at Dallas, TX.
27. Z. Tadmor, "Screw Elements Having Shearing and Scraping Devices," U.S. Patent 5,356,208, October 18, 1994; European Patent 0619173; German Patent 69327519.7-08, Great Britain Patent 133 19134 3.
28. W. H. Darnell and E. A. J. Mol, "Solids Conveying in Extruders," *Soc. Plast. Eng. J.*, **12**, 20–28 (1956).
29. Z. Tadmor, "Fundamentals of Plasticating Extrusion. I. A. Theoretical Model for Melting," *Polym. Eng. Sci.*, **6**, 185–190 (1966).
30. B. H. Maddock, "A Visual Analysis of Flow and Mixing in Extruder Screws," *Tech. Papers, Vol. V, 15th Annu. Tech. Conf.*, Society of Plastics Engineers, New York, January 1959; also, B. H. Maddock, "A Visual Analysis of Flow and Mixing in Extruder Screws," *SPE J.*, **15**, 383–389 (1959).
31. Z. Tadmor, I. J. Duvdevani, and I. Klein, "Melting in Plasticating Extruders—Theory and Experiments," *Polym. Eng. Sci.*, **7**, 198–217 (1967).
32. G. Menges and K. P. Klenk, "Melting and Plasticating of Unplasticized PVC Powder in the Screw Extruder," *Kunststoffe (German Plastics)*, **57**, 598–603 (1967).
33. J. T. Lindt, "A Dynamic Melting Model for Single Screw Extruders," *Polym. Eng. Sci.*, **16**, 284–291 (1976).
34. L. Kacir and Z. Tadmor, "Solids Conveying in Screw Extruders. Part I. The Delay Zone," *Polym. Eng. Sci.*, **12**, 387–395 (1972).
35. E. Broyer and Z. Tadmor, "Solids Conveying in Screw Extruders. Part I. A Modified Isothermal Model," *Polym. Eng. Sci.*, **12**, 12–24 (1972).
36. K. Schneider, "Technical Report on Plastics Processes in the Feeding Zone of an Extruder" (in German), Institute of Plastics Processing (IKV), Aachen, Germany, 1969.
37. Z. Tadmor and E. Broyer, "Solids Conveying in Screw Extruders. Part II. Non Isothermal Model," *Polym. Eng. Sci.*, **12**, 378–386 (1972).
38. J. G. A. Lovegrove and J. G. Williams, "Solids Conveying in a Single Screw Extruders: the Role of Gravity Forces," *J. Mech. Eng. Sci.*, **15**, 114–122 (1973); also, "Solids Conveying in a Single Screw Extruder: a Comparison of Theory and Experiments," *J. Mech. Eng. Sci.*, **15**, 195–199 (1973).
39. J. G. A. Lovegrove and J. G. Williams, "Pressure Generation Mechanism in the Feed Section of Screw Extruders," *Polym. Eng. Sci.*, **14**, 589–594 (1974).
40. F. Zhu and L. Chen, "Studies on the Theory of Single Screw Plasticating Extrusion. Part I: A New Experimental Method for Extrusion," *Polym. Eng. Sci.*, **31**, 1113–1116 (1991).
41. C. I. Chung, "New Ideas About Solids Conveying in Screw Extruders," *Soc. Plast. Eng.*, **26**, 32–44 (1970).
42. C. I. Chung, "A New Theory for Single Screw Extrusion. Part I and Part II," *Mod. Plast.*, **45**, 178 (1968).
43. R. Hinrich and L. U. Lilleleht, "A Modified Melting Model for Plasticating Extruders," *Polym. Eng. Sci.*, **10**, 268–278 (1970).

44. R. C. Donovan, "A Theoretical Melting Model for Plasticating Extruders," *Polym. Eng.*, **11**, 247–257 (1971).
45. J. R. Vermeulen, P. G. Scargo, and W. J. Beek, "The Melting of a Crystalline Polymer in a Screw Extruder," *Chem. Eng. Sci.*, **26**, 1457–1465 (1971).
46. I. R. Edmundson and R. T. Fenner, "Melting of Thermoplastics in Single Screw Extruders," *Polymer.*, **16**, 48–56 (1975).
47. J. Shapiro, A. L. Halmos, and J. R. A. Pearson, "Melting in Single Screw Extruders," *Polymer.*, **17**, 905–918 (1976).
48. I. Klein and Z. Tadmor, "Operating Characteristics of a Plasticating Extruder," in *Computer Programs for Plastics Engineers*, I. Klein and D. I. Marshall, Eds., Reinhold, New York, 1968, Chapter 6, Secs. 1 and 2.
49. Z. Tadmor and I. Klein, "Design of Certain Fluted Mixing Sections of Extruder Screws," *Polym. Eng. Sci.*, **13**, 382–389 (1973).
50. Z. Tadmor, U.S. Patents 4,142,805 and 4,194,841.
51. Z. Tadmor, P. Hold, and L. N. Valsamis, "A Novel Polymer Processing Machine—Theory and Experimental Results," *SPE ANTEC Tech. Papers.*, **25**, 193–202 (1979).
52. P. Hold, Z. Tadmor, and L. N. Valsamis, "Applications and Design of a Novel Polymer Processing Machine," *SPE ANTEC Tech. Papers.*, **25**, 205–211 (1979).
53. I. Edelist and Z. Tadmor, "Velocity Profiles in Corotating Disk Processors," *Polym. Process. Eng.*, **1**, 1 (1983).
54. B. David and Z. Tadmor, "Extensive Mixing in Corotating Processors," *Int. Polym. Process.*, **3**, 38–47 (1988).
55. L. N. Valsamis, A. M. Mekkaui, G. S. Donoian, P. S. Mehta, and Z. Tadmor, "Mixing, Dispersion and Blending in Corotating Disk Processors," *SPE ANTEC Tech. Papers.*, **30**, 987–992 (1984).
56. P. S. Mehta, L. N. Valsamis, and Z. Tadmor, "Foam Devolatilization in a Multichannel Corotating Disk Processor," *Polym. Process Eng.*, **2**, 103–128 (1984).

PROBLEMS

- 9.1 Analysis of a Melt Extrusion Process** Consider the extrusion process shown in Fig. 9.2 for pelletizing 8000 kg/h of polymer melt. The 40-cm-diameter and 12 L/D extruder has a square-pitched metering-type screw. The feed section is three turns long and 7.5 cm deep, and the metering section is six turns long and 2.5 cm deep. The flight width is 3 cm and the flight clearance is negligible. Neglecting the breaker plate and screen pack, the die consists of a 3-cm-thick pelletizing plate with 1000 holes over its surface of geometry, shown in Fig. 9.2, with $l_1 = l_2 = l_3 = 1$ cm, $R_1 = 0.5$ cm, and $R_2 = 0.25$ cm. The extruded polymer is an incompressible Newtonian fluid with a viscosity of 10^3 Ns/m² and a density of 0.75 g/cm³. Calculate (a) the screw speed needed to obtain the required output and the resulting head pressure; (b) the power; and (c) the mean strain and residence time in the extruder. In addition, (d) specify if the isothermal assumption is valid, and (e) estimate the minimum size of a tubular inlet conduit for gravitational feeding.
- 9.2 Design of a Melt Extruder** Design a 300-lb/h extruder pumping molten nylon at 400°F to generate 1200 psi head pressure. Assume a constant channel depth screw with axial length of 10 in. The melt density is 62.0 lb/ft³, the viscosity is 0.38 lb_f-s/in², and the specific heat is 0.35 Btu/lb°F.

9.3 The Superposition Correction Factor Combined drag and pressure flow between parallel plates (or concentric cylinders¹⁷) of a Newtonian fluid at isothermal conditions leads to a flow-rate expression that is the linear sum of two independent terms, one for drag flow and another for pressure flow:

$$Q = Q_d + Q_p$$

The former vanishes when the velocity of the moving plate is zero, and the latter vanishes in the absence of a pressure gradient. (a) Explain on physical and mathematical grounds why the solution of the same flow problem with a non-Newtonian fluid, for example, a Power Law model fluid, no longer leads to the same type of expressions. (b) It is possible to define a superposition correction factor ε as follows

$$Q = \varepsilon(Q_d^* + Q_p^*)$$

where Q_d^* and Q_p^* are *hypothetical* drag and pressure flow terms, each calculated with a Power Law model, assuming the other equals zero. Thus, $Q_d^* = Q_d$ as the pure drag flow term, and Q_p^* is the pure pressure flow term of a Power Law model fluid. Show that ε in parallel-plate flow is a function of only Q/Q_d and n . Restrict your analysis to a positive-pressure gradient and no extremum in the velocity profile. (c) Explain how, by using a generalized plot of E , one can calculate in a straightforward manner the pressure gradient for a given geometry, plate velocity, and net flow-rate requirement.

9.4 Viscous Seals Vertical extruders with the feed end of the screw protruding into the hopper at the top, and the drive attached to the discharge end of the screw at the bottom, have the advantage of good feeding and high torque input capability. This is because the drive is on the side where the channel depth is shallow, and consequently the root of the screw has a higher diameter; however, it has the disadvantage of leakage at the high pressure end, because the screw at the discharge end becomes a shaft attached to a drive. The shaft rotates in a slider bearing where substantial leakage can occur, depending upon the clearance. One way to reduce the leakage or stop it completely is to cut a reverse flight on the shaft. Thus, the bearing with the shaft turns into a screw extruder that pumps the leaking polymer melt back into the high-pressure discharge region. This is called a *viscous dynamic seal*. This design can be viewed as two extruders pointing head-on to each other. The main extruder has a certain throughput and generates a pressure P ; the dynamic seal, if no leakage is allowed, generates the same P at zero flow-rate condition. Design a dynamic seal on a 2-in shaft to prevent leakage for $P = 1000$ psi. Assume a Newtonian fluid of viscosity $0.05 \text{ lb}_f\text{-s/in}^2$ and isothermal conditions.

9.5 Solids Conveying of Nylon in Screw Extruders Consider a 1.991-in-diameter screw with 2-in lead, 1.375-in root diameter, and 0.2-in flight width, conveying nylon pellets with bulk density of 0.475 g/cm^3 and a coefficient of friction of 0.25. Assuming no pressure rise, calculate the solids conveying rate (g/rev) at the following conditions: (a) no friction between the screw and the solids; (b) no friction

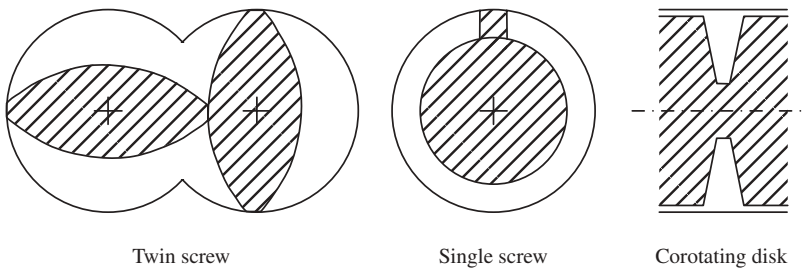
17. Z. Tadmor and I. Klein, *Engineering Principles of Plasticating Extrusion*, Van Nostrand-Reinhold, New York, 1970, p. 323.

on the screw flights; (c) no friction on the trailing flight; and (d) friction on all contacting surfaces. (e) Compare the experimentally measured value by Darnell and Mol (28) of 14.9 g/rev with your results.

9.6 Solid Bed Profile in Screw Extruders Determine the solid-bed profile and length of melting of LDPE extruded in a 2.5-in-diameter, single flighted screw extruder with the following screw geometry and operating conditions: Feed section, 3.2 turns and 0.5-in channel depth; compression section, 12 turns with linear taper; and metering section, 12 turns and 0.125-in channel depth. The flight width is 0.25 in and the flight clearance is negligible. The operating conditions are 82 rpm screw speed, 150°C constant barrel temperature, and 120-lb/h flow rate. Use the polymer physical property data in Example 9.6 and assume that melting starts one turn before the end of the feed section.

9.7 The Rotating Flight Extruder The flight on the screw forms a helical spiral. Consider a processing machine consisting of a detached flight freely rotating on a smooth shaft in a lightly fitted barrel. The difference between this “extruder” and the conventional one is that the root of the screw is stationary relative to the flights, just like the barrel. (a) Derive a theoretical model for pumping (equivalent to the simple Newtonian melt SSE model). (b) Derive a theoretical model for melting (equivalent to the simple Newtonian melting model in screw extruders), assuming that screw temperature in this zone equals the barrel temperature. (c) Derive a theoretical model for solids conveying. (d) How do the theoretical predictions of the rotating flight extruder compare to an equivalent size screw extruder? (e) Discuss the engineering feasibility of the rotating flight extruder.

9.8 Wiped Surface and Heat Transfer Surface The accompanying figure shows the cross section of an SSE, a co-rotating intermeshing TSE, and a co-rotating disk processor. (a) Show the surfaces that the polymer comes in contact with. (b) Which of these surfaces are “wiped”. (c) Which of them are temperature controlled? (d) Based on your findings, analyze the advantages and disadvantages of these machines regarding the risk of polymer degradation and efficiency of temperature control.

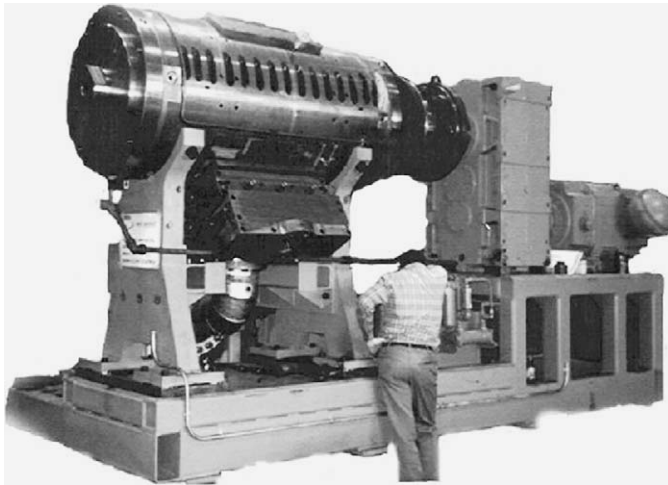


9.9 Melting in a Jointly Moving, Parallel Plate Configuration Figure 9.47 is also a schematic representation of a jointly moving, parallel-plate melter. Derive a mathematical model for this device, assuming that the plates are at constant temperature T_b , the melting process is steady (i.e., the molten polymer is continuously removed), the plate velocity is V_b , the molten material is Newtonian, and physical and thermophysical properties are constant and temperature independent.

9.10 Melting in a Co-rotating Disk Chamber Calculate the rate of melting in kg/s of a polymer fed at room temperature into a co-rotating disk chamber with an outer

diameter of 175 mm and an inner diameter of 100 mm, with $\varepsilon = 0.75$ rotating at 100 rpm and disk temperature 230°C. The melting point is 130°C, Newtonian viscosity of the melt is 400 Ns/m², the heat of fusion is 200 kJ/kg, the thermal conductivity is 0.101 J/m·s·°C, the melt density is 950 kg/m³, and the specific heat of the solid is 2.3 kJ/kg·°C.

- 9.11 Co-rotating Disk Scraped-surface Heat Exchanger**¹⁸ (see accompanying figure) The heating and cooling of very viscous liquids is carried out in scraped-surface heat exchangers, in which the viscous liquid is deposited on the heat transfer surfaces and is repeatedly scraped and replaced by fresh material. A co-rotating disk processor chamber in which a viscous liquid or polymeric melt is deposited by a spreader on the disk surfaces and then scraped off by the channel block is, in fact, a scraped-surface heat exchanger (see photo below). (a) Show that the heat-transfer surface to volume ratio of a double-pipe heat exchanger is given by $A/V = 2/R$, where R is the radius of the heat-transfer surface. (b) Show that, for a multiple-disk co-rotating scraped-surface heat exchanger, the heat transfer to volume surface is $A/V = [2(1 - \alpha^2)/l] + (1 - \alpha)/R$, where α is the shaft radius to barrel radius and l is the axial separation between centerlines. (c) Compare the surface-to-volume ratios of (a) and (b) for a 20-cm-radius heat exchanger with $l = 3$ cm and $\alpha = 0.5$. (d) Assuming the molten film deposited on the disk is a semi-infinite medium, show that the heat-transfer coefficient is given by $h_i = 2(k\rho C_p N/\pi)^{1/2}$ (e) Plot the heat transfer coefficient for $k = 0.10$ Btu/hr·ft²·°F, $C_p = 0.46$ BTU/lb·°F, $\rho = 48$ lb/ft³.



Photograph of a 550-mm-diameter Diskpack scraped-surface heat exchanger designed for reducing melt temperature from 400°F to 250°F for high Melt Index (MI) PE at 6000 lb/h. All 10 chambers were fed in parallel. The hot melt was spread on the cooled disk walls by self-adjusting floating spreaders. [Courtesy of the Farrel Corporation, Ansonia, CT.]

18. Z. Tadmor, "Co-rotating Disk Scraped-Surface Heat Exchanger," *Food Technol.*, **39**, 67–74 (1985).

10 Twin Screw and Twin Rotor Processing Equipment

- 10.1 Types of Twin Screw and Twin Rotor-based Machines, 525
- 10.2 Counterrotating Twin Screw and Twin Rotor Machines, 533
- 10.3 Co-rotating, Fully Intermeshing Twin Screw Extruders, 572

We discussed the principles of melting mechanisms of twin screw extruders (TSEs) in Sections 5.1 and 5.9, and melt pumping in Section 6.8, where we also discussed basic TSE configurations and geometry. In this chapter, we discuss, and when possible analyze, the overall processing performance. We do this in a broader family of polymer processing equipment, which utilizes two power-transmitting elements such as screws or rotors¹ operating adjacent to each other and rotating in the same or opposite directions in a common barrel.

Most twin screw-based machines are in fact extruders, and perform the same elementary polymer processing steps as single screw extruders (SSEs). However, because of the unique *time-varying* screw-to-screw interactions that take place in them, which are absent in single screw-based machines, *additional* physical mechanisms emerge that primarily and particularly affect the elementary steps of *melting* and *mixing*. Due to these additional mechanisms, the twin-screw machines offer important advantages over single screw machines, enabling them to carry out the melting and mixing steps more efficiently and uniformly. Specifically, melting can take place in a manner involving the *entire mass* of the compressed particulates, which results in very rapid and uniform melting over a very short ($1\text{--}2 L/D$) axial length, and hence narrow residence time distribution (RTD) in the molten state.² Consequently, a large amount of mechanical energy is needed in this axial rotor section to provide for the enthalpy of heating and melting. Equally important, mixing in many TSEs benefits from the existence of *three-dimensional*, time-varying, extensional melt “folding” chaotic flows, generated by screw-to-screw interactions. The result is very fine and rapid dispersive mixing that, in the case of immiscible blends, is independent of the component viscosity ratio and rapid and uniform distributive mixing, requiring *less twin shaft mechanical energy* input, since extensional flow kinematics are very efficient for distributive mixing.

1. Most of these machines are based on two adjacent screws, but some, like the continuous mixers, have a different geometry, which is better defined as consisting of two rotors.

2. Recall that in the SSE, some of the polymer melts early in the extruder and some at the very end, and hence, the RTD in the molten state is rather broad.

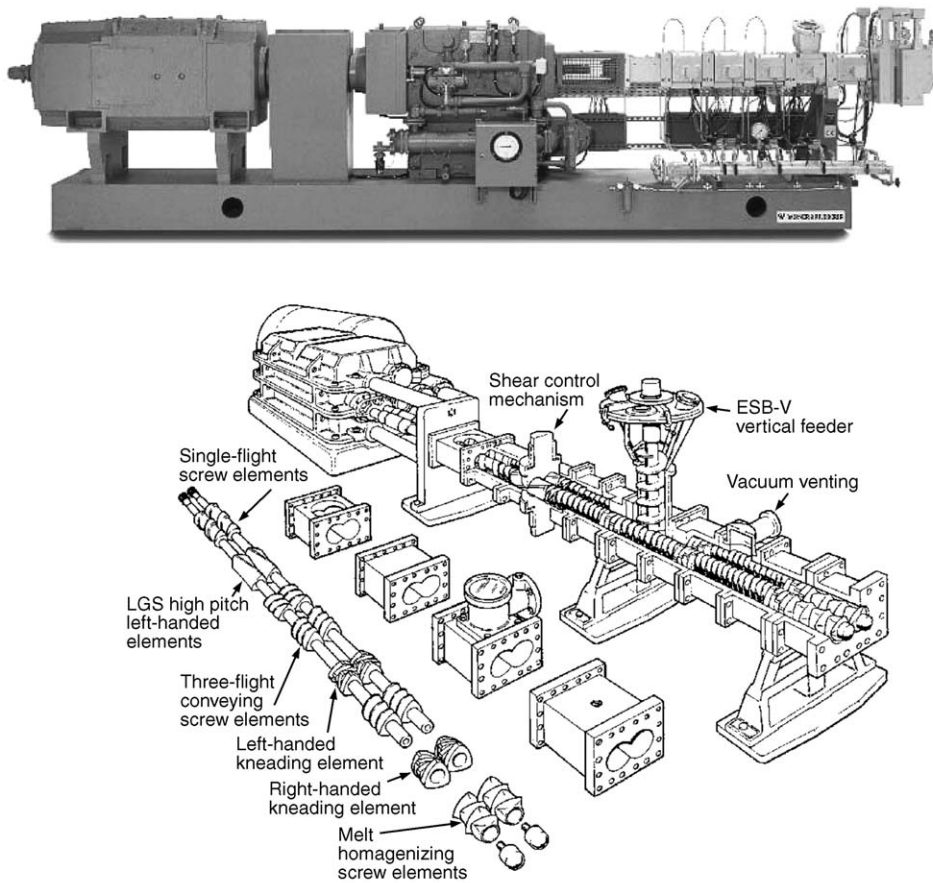


Fig. 10.1 Photograph and schematic representation of the modular screw-element sequences and barrel sections of an intermeshing, co-rotating TSE. [Courtesy of Coperion Werner and Pfleiderer Corp.]

Typically, the TSE is custom designed to fit the process and product requirements by utilizing a wide array of interchangeable screw elements and screw element sequences “skewered” onto polygonal shafts. This capability, together with the wide use of segmented barrel sections, enables twin screw-based machines to specify or fit the location of any of the elementary steps, as well as the downstream introduction of additional component feed streams, or removal of volatiles at the needed locations. The versatility of screw and barrel design in twin screw-based machines is shown schematically in the exploded view of a common variant of such equipment, the intermeshing, co-rotating TSE, in Fig. 10.1

Customized and flexible screw-element and barrel segment designs, and fast and efficient melting and mixing (both dispersive and distributive) in most TSEs make such equipment very well suited and almost exclusively used for the following polymer processing operations:

- Very high rate postpolymerization reactor product melting and mixing with stabilizer additives in postpolymerization reactor “finishing” operations.

- Polymer compounding of multicomponent/two-phase polymer systems.
- Reactive polymer processing.

The first operation was briefly discussed in Chapter 5, and we expand on it in this chapter, while the last two polymer processing operations are discussed in more detail in Chapter 11.

10.1 TYPES OF TWIN SCREW AND TWIN ROTOR-BASED MACHINES

A wide variety of both *co-rotating* and *counterrotating* twin screw and twin rotor-based extruders are commercially available. White (1) described and discussed the historical evolution of the design and function of most of them. Herrmann et al. (2) presented the “classic” schematic representation of all the possible variants of co- and counterrotating extruders. Todd (3) presented a concise schematic representation, shown in Fig. 10.2, while Agassant et al. presented both a more complete classification, as well as the different types of flow channels in twin screw-based machines, as shown in Figs. 6.41. As indicated in this figure, the *degree* of intermesh in co-rotating devices can be designed to be *partial* or *full*, the latter leading to the *self-wiping* capability by the screw pair.

Tangential counterrotating machines are available in both matched (shown) and staggered screw flight configurations. Both designs create screw-to-screw interaction flows and material exchanges, and result in very good distributive mixers and polymer modification reactors (4). The *intermeshing, counterrotating TSE* is essentially a “positive displacement” device, where the material is conveyed downstream in confined, helical, C-shaped channels (5),

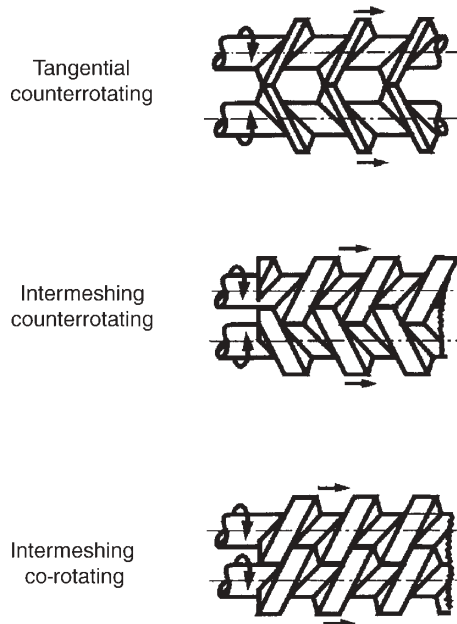


Fig. 10.2 Classification of TSEs. [Reprinted by permission from D. B. Todd, “Introduction to Compounding,” in *Plastics Compounding—Equipment and Processing*, D. B. Todd, Ed., Hanser, Munich, 1998.]

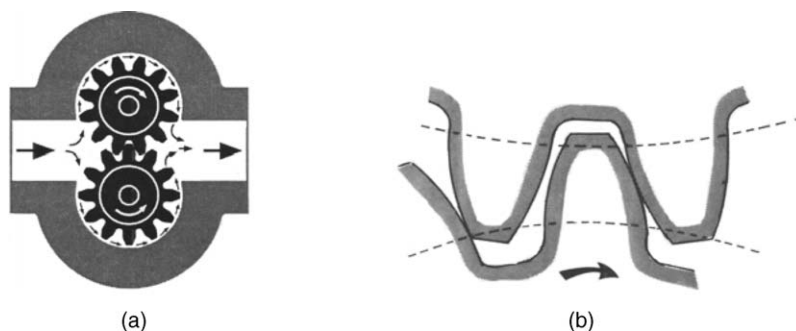


Fig. 10.3 Schematic representation of a gear pump. (a) Cross-sectional view [Reprinted by permission from D. Smith, P. Stoughton, C. Morgan, and G. Hovis, “Auxiliary Equipment” in the *SPE Guide on Extrusion Technology and Troubleshooting*, J. Vlachopoulos and J. R. Wagner, Jr., Eds., SPE, 2001]; and (b) tooth configuration showing the tooth-to-tooth interlock, creating the isolated “pockets” conveying the polymer charge in positive displacement.

shown in Figs. 6.46 and 6.47. Because the twin screws are counterrotating, feeding is facilitated. The volumetric flow rate is proportional to the speed of the counterrotating, intermeshing screws, as in the widely used gear pumps shown in Fig. 10.3(6).

Both positive displacement pumping devices are *rotational speed limited*, in that, at higher speeds, the pressures generated in the calender-like intermesh regions can generate very high shear and extensional rates and pressures, which may cause the melt films diametrically opposite to the intermesh to fail and deprive the machine of the lubrication benefit by the melt. A typical upper rotational speed limit is, for the *classic* intermeshing counterrotating extruders (as well as gear pumps), less than 150 rpm. This compares unfavorably with intermeshing, co-rotating TSEs, which are only torque limited and capable of very high rotational speeds of over 1000 rpm.

There is another limitation of these machines: the only site generating extensional flow, beneficial to both distributive and dispersive mixing, is the intermesh region, which affects only a small fraction of the polymer melt charge. As we will see later, in our introduction to the intermeshing, co-rotating TSEs, twin screw designs which generate extensional flows in more than one region of the cross-sectional area available to the polymer stream are clearly preferable in carrying out the elementary mixing steps. Thus, a *new class* of intermeshing, counterrotating TSEs has been developed that have *multilobal screw elements* to create multisite, elongational flows (7) similar to those generated by kneading elements in co-rotating intermeshing extruders. Such machines make wide use of screw element sequences and barrel sections, which are process and material appropriate. With segmented screw element pairs, such as the hexalobal, counterrotating mixing screw elements shown in Fig. 10.4, and using larger intermesh clearances, counterrotating TSEs can achieve good mixing, and operate at high rotational speeds and throughput rates.

The continuous mixer (CM) is a counterrotating, nonintermeshing *twin-rotor* machine. The Farrel Continuous Mixer (FCM) was the first CM developed (1964) by Ahlefeld et al. (8). It has rotor designs along the principles of the Banbury³ high-intensity batch mixer.

3. “Banbury” is a registered trademark of the Farrel Co., Ansonia, CT.

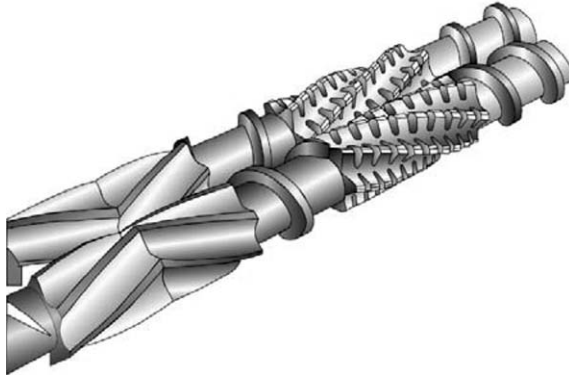


Fig. 10.4 Hexalobal, intermeshing, counterrotating twin-screw mixing screw elements. [Reprinted by permission from W. C. Thiele, “Counterrotating Intermeshing Twin Screw Extruders,” in *Plastics Compounding—Equipment and Processing*, D. B. Todd, Ed., Hanser, Munich, 1998.]

The latter, shown in Fig. 10.5, is still used extensively in the rubber compounding industry. The Banbury mixer consists of a figure-eight, cross-sectional-shaped mixing chamber with a spiral-lobed rotor in each chamber. The shape of the rotor is such that it induces axial flow and mixing along the rotors toward the center. The mixture is fed (using a variety of process-appropriate, ingredient-addition protocols) through a vertical chute in which an

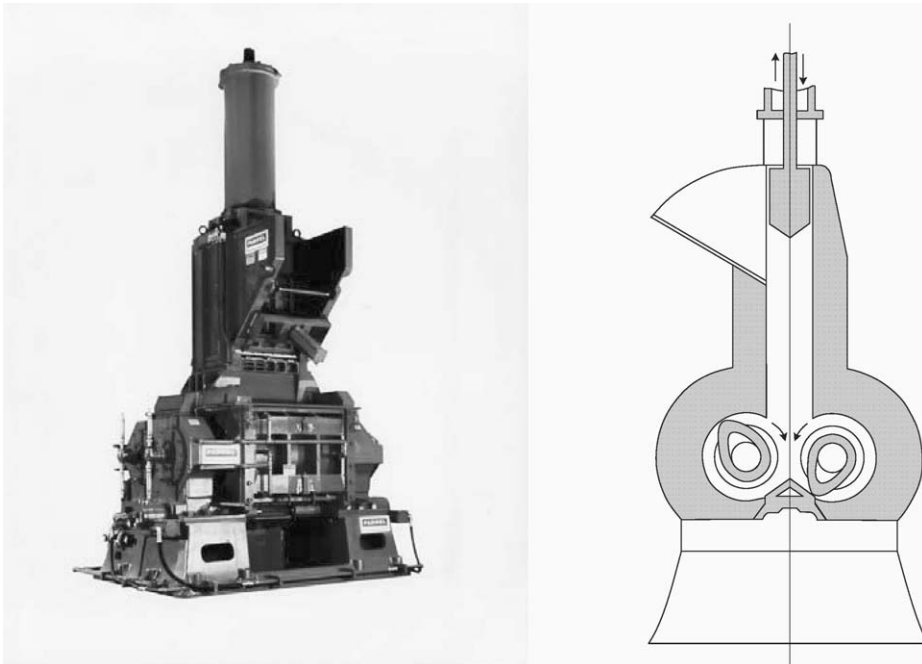


Fig. 10.5 Photograph and cross-sectional schematic representation of a Banbury high-intensity internal batch mixer. The photograph shows the two elements of the drive: the electrical motor and the gear reducer. Their large size is due to the very large power requirements of the mixer. [Photograph courtesy of the Farrel Company, Ansonia, CT.]

air- or hydraulic-driven ram can descend to seal the internal mixing chamber and force the mixture into the space between the rotors. The lower face of the ram is shaped in such a way that it becomes part of the chamber. Chamber sealing is critical to keeping the nanosized carbon black from getting out of the mixer and contaminating the room.⁴ Dispersive mixing takes place in the clearances between the rotor and the barrel, and between the two counterrotating rotors in the trailing apex region. Distributive mixing is promoted by the axial twists of the rotor flight tips, as previously noted. The mixers operate about 70% full to enhance distributive mixing. The homogenized charge is discharged through a slide or “drop door” at the bottom of the chamber.

Soon after its introduction⁵, the CM family of compounders came into widespread use as a rapid and high production rate machine used in thermoplastic compounding operations, because of its ability to both melt and mix at the required compounding production rates of 500–800 kg/h. Larger-size machines (ca. 300 mm · D) were also developed for the thermoplastics “finishing” operations as “mega” melter/mixers, achieving rates as high as 50 ton/h. For both applications, the rotational speeds are in the range of 400 to 1200 rpm. The CMs do not generate pressure, and therefore are always combined downstream with either a discharge extruder or a gear pump.

The top and cross-sectional views of a single stage FCM are shown in Fig. 10.6 (9). Note that the rotor shafts are supported at both ends. It is worth noting the following CM design characteristics: first, the high shear rate, tight clearance between the rotor-tip land area and the barrel is responsible for consuming much of the shaft mechanical energy by melting compressed polymer particulates, mainly by frictional energy dissipation (FED), and, further downstream, by viscous energy dissipation (VED), and plastic energy dissipation (PED) to eliminate the solids in the melt–solids suspension which *partially* fill the CM mixing chamber; second, the rotor-to-rotor, partial intermesh available cross-sectional area varies a great deal during each of the rapid rotations, creating considerable compressing/expanding extensional flows, both responsible for the CM’s capacity to affect very rapid and efficient mixing; third, the two rotor wings, upstream and downstream of the apex, create strong axial flows leading to back mixing and three-dimensional chaotic flows; and finally, CMs have practically no pumping capability, necessitating the use of single screw melt extruders fed at just above atmospheric pressures for compounding applications, and gear pumps for the finishing operation applications. The tandem CM/SSE processing system for compounding applications is shown in Fig. 10.7

The fully intermeshing, co-rotating TSEs shown in Fig. 10.1 are by far the most widely used twin screw–based processing equipment. They were developed in the 1940s by

4. Fernley Banbury conceived the “Banbury Mixer” to replace the open roll mill mixing of rubber which covered everything, including the operators, with black dust. In fact, he intended to place the rolls in a closed environment. But since it was not possible to “cut-and-turn” the rubber in a closed chamber, as is done in two roll mill mixing to create axial mixing, he had to give the rolls a geometry that would induce axial mixing. He did this quite successfully and the Banbury mixers are in wide use to the present day. Perhaps, with the burst of other nanosized additives to the processing scene, the internal mixer may find additional applications.

5. The development of the FCM was undertaken with the intention of replacing the batch Banbury mixing with continuous operation mixing. However, it did not achieve the quality of batch mixing required by the rubber industry, and was not adopted by that industry. Yet just at the time when the development was concluded, high production volume of polypropylene (PP) and high density polyethylene (HDPE) came on board. These polymers emerge from the reactor in powder form and need immediate postreactor melting and compounding to convert them into useful pellets. The FCM, with its high melting and adequate mixing capacity, was readily adopted for this application.

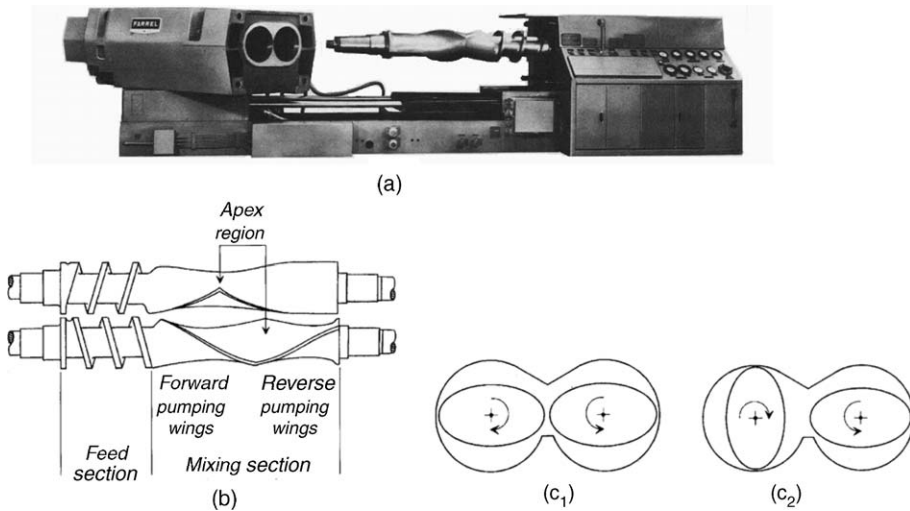


Fig. 10.6 The single-stage FCM. (a) Size 15 FCM with chamber opened and rotated hydraulically; (b) top view of staged apex twin rotors and the axial zones for carrying out the solids feed handling and the melting and mixing elementary steps; (c) cross-sectional view of two rotor orientations, tip-to-tip (c_1) and tip-to-flat (c_2). [Reprinted by permission from E. L. Canedo and L. N. Valsamis, “Farrel Continuous Mixer Systems for Plastics Compounding,” in *Plastics Compounding—Equipment and Processing*, D. B. Todd, Ed., Hanser, Munich, 1998.]

Erdmenger at Bayer A.G., who obtained a German patent in 1951 (10). They were further developed, under license, by Werner & Pfeleiderer in the 1950s (11). The co-rotating, intermeshing skewered screw elements are self-wiping, which reduces the residence time of barrel wall melt films, and come in two forms: the screw conveying elements and the kneading paddle sequences, staggered to approximate conveying screw segments.

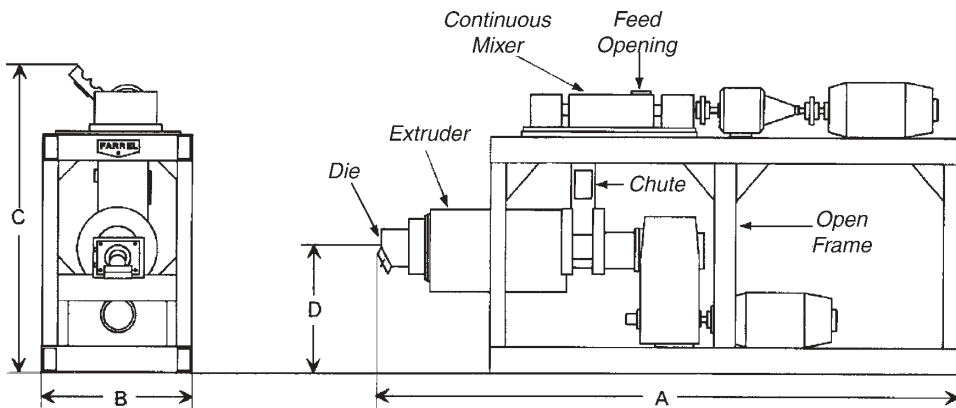


Fig. 10.7 Schematic view of the CM/single screw extruder combination used in polymer compounding operations. The *chute*, connecting the two processing machines, transfers the molten and mixed stream at low pressures to the throat of the melt pump SSE, which generates the pressure needed for pelletization. [Reprinted by permission from E. L. Canedo and L. N. Valsamis, Farrel Continuous Mixer Systems for Plastics Compounding in *Plastics Compounding—Equipment and Processing*, D. B. Todd, Ed., Hanser, Munich, 1998.]

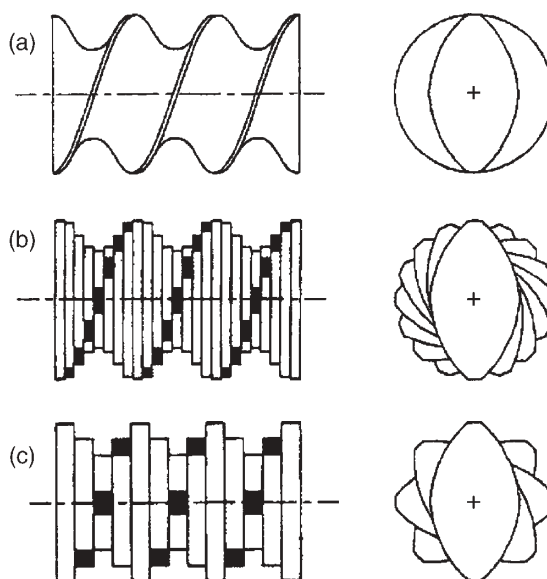


Fig. 10.8 Fully intermeshing, co-rotating elements in configurations matching square-pitch screws. (a) Forward screw conveying elements with different numbers of lobes; (b) forward staggered kneading paddles (a.k.a., disk elements) representing “leaky” screw elements, and (c) neutral configuration. [Reprinted by permission from D. B. Todd, “APV (Baker Perkins) Systems,” in *Plastics Compounding—Equipment and Processing*, D. B. Todd, Ed., Hanser, Munich, 1998.]

Single, bi-, tri-, and tetralobe screw profiles are shown in Fig. 6.42, and staggered bilobal kneading paddles are shown in Fig. 10.8(b)(3). The thinner each of the staggered paddles, the closer the paddle sequence comes to approximate the function of conveying screw elements, by affording smaller interpaddle spaces for polymer melt to leak backwards in the presence of a positive pressure gradient. Staggered kneading paddle sequences are specified by three numbers in the following order: the stagger angle, the number of paddles, and the total length of the sequence or “block.”⁶

Both screw and staggered kneading disk sequences (blocks) can be built to convey polymer melts in the forward or reverse (backward) directions. They are shown schematically as forward/reverse (a.k.a., right- and left-handed) pairs in Fig. 10.9 (12). Both configurations provide a *flow barrier* at the axial position, joining the forward and reverse sequences. The physically obvious consequence at this juncture is the following: the pressure drop required to overcome the flow barrier must be provided by the forward drag flow of a specific length of filled forward screw or staggered paddle element sequence. Clearly, screws provide a stronger barrier, one that requires larger drag-induced pressure buildup by a longer filled section than the “leaky” kneading element forward/reverse pairs. Even stronger flow barriers, often utilized as “melt seals” before devolatilization sections in intermeshing, co-rotating TSEs, are the overlapping full-bore blister rings and a barrel valve (13) used in conjunction with them, as shown in Fig. 10.10. It is noteworthy that radial or axial barrel valves regulate on-line pressure buildup independently of any other process, material, or design variables, so they provide an added

6. For example, the Coperion (formerly-Werner & Pfleiderer) designation “KB 45/5/40” denotes a kneading block (KB) 40 mm long, made of five kneading paddles, staggered 45° part.

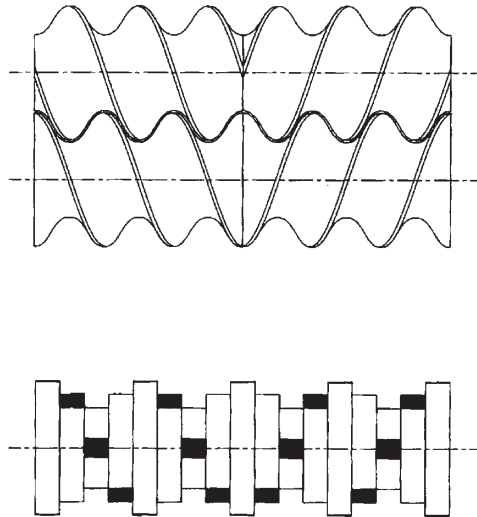


Fig. 10.9 Forward and reverse screw and kneading element sequences, both of which provide holdback capability.

variable for regulating the degree of fill and the mechanical energy dissipated in heating up the melt upstream of the valve (13,14).

We turn now to the most important capability of co-rotating kneading disks when they are full with the polymer stream, first pointed out by Todd (15). Figure 10.11 consists of five snapshots of a pair of co-rotating, bilobe kneading disks. The time-sequence of the snapshots documents the evolution of one of the three cross-sectional area pockets, the one that is shaded, A_s , available to be filled by the polymer charge. Of course, the disks have an axial thickness, H , and, thus, the volume available to the polymer charge is $(A_s H)$. As the pair of kneading disks co-rotate, A_s varies with time: first *expanding* from the minimum

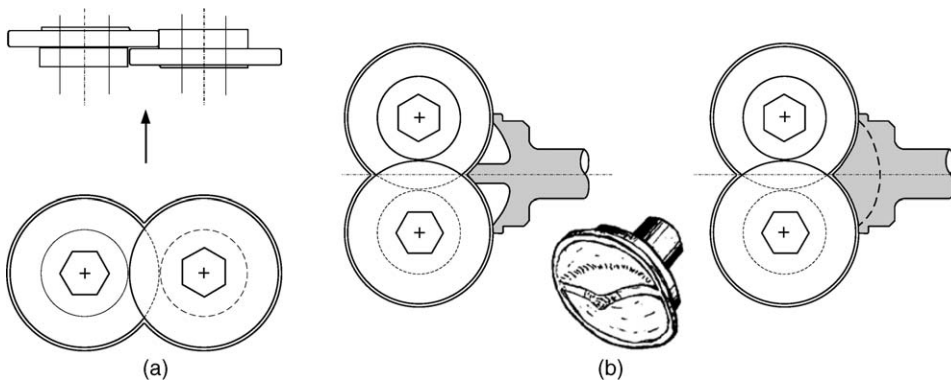


Fig. 10.10 (a) Top and side views of a pair of full-bore blister rings (orifice plugs), and (b) schematic of the Todd barrel valve and barrel cross sections in the fully open and closed positions: there is a bypass channel in the barrel immediately above the intersection of the blister rings and the barrel valve is rotatable in this bypass channel to vary the restriction of flow. [Reprinted by permission from D. B. Todd, “The APV (Baker Perkins) Systems,” in *Plastics Compounding—Equipment and Processing*, D. B. Todd, Ed., Hanser, Munich, 1998.]

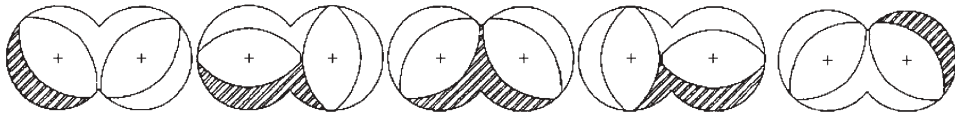


Fig. 10.11 Snapshots of the repetitive expansion/contraction of each of the cross-sectional area “pockets” between a pair of kneading disks and the barrel of fully intermeshing, co-rotating extruders. The evolution of the expansion/contraction is followed for one of the three “pockets,” the one shaded, $A_s(t)$.

cross section it started to the maximum in the third snapshot, and then *contracting* to the minimum, this time in the right lobe of the barrel. If this pair of co-rotating disks is part of full forwarding or reverse kneading disk sequences, then one can see that as A_s expands from the first to the third snapshot, the material from adjacent upstream and downstream disk pairs will keep the pair full since, because of the stagger, the communicating cross-sectional areas of the upstream and downstream neighboring pairs will be contracting. Similarly, when A_s is contracting from the third to the fifth snapshot, our pair of disks will be providing material to the upstream and downstream neighbors. It is important to note that:

1. The *mixing* ramifications of this “repetitive” pairwise and axially staggered expansion/contraction of the cross-sectional area are:
 - (a) Time-varying axial flow and back mixing.
 - (b) Time-varying extensional and folding chaotic flows and “global” mixing by such flows as discussed in Chapter 7.
2. The *melting* ramifications of the “relentless” compressive deformations on packed particulates filling the kneading elements are that the rapid and volumewise melting mechanisms of FED and in particular, PED are introduced, inducing melting in very short axial distance segments, as discussed in Section 5.8.

It is important to note that similar beneficial mixing flows and solid polymer particulate charge deformations to those discussed earlier also occur in the multilobal variants of the counterrotating, “intermeshing” TSEs, as well as in CMs. We used the co-rotating, fully intermeshing twin screw kneading element pairs, because the relentless expansion/contraction cycles can best be demonstrated with them.

Finally, before embarking on the discussion and analysis of specific types of screw-based machines, we must state that not all of the elementary step mechanisms taking place in twin screw-based machines are completely understood as physical phenomena and, thus, cannot be adequately modeled and simulated, despite the explosive growth in accessible computing power and advances in Computational Fluid Mechanics (CFM). Funatsu et al. (16) correctly pointed out that numerical simulation of some elementary steps in twin screw-based machines is still difficult to carry out with predictive numerical treatment, because their understanding is currently under development and incomplete. This is true for plastic deformation of packed polymer particulates (17,18), melting and phase transition processes (17–21), and interface deformation and evolution (22,23). Therefore, three-dimensional numerical studies of twin screw-based machines are now limited to compositionally homogenized melts in filled mixing and pumping zones.

10.2 COUNTERROTATING TWIN SCREW AND TWIN ROTOR MACHINES

In this section we discuss the following counterrotating, twin rotor-based equipment: the fully intermeshing TSE, the tangential TSE, the multilobal compounders, the CM FCMs, and the Banbury-type batch intensive mixer. We will comment on all the elementary steps taking place in them, and do so quantitatively, when possible.

Flow and Mixing in Counterrotating, Intermeshing Twin Screw Extruders

We mentioned earlier that the classic intermeshing, counterrotating TSEs are essentially positive displacement continuous pumps, delivering the polymer charge at a constant rate, which is independent of the die pressure flow restriction. We also mentioned that the positively displaced material travels in an axial series of confined, *helical, C-shaped* pockets. While the term *confined* is only approximate, as we will see later, the positive displacement nature of melt pumping is both physically correct and amenable to rather simple flow analysis, which we presented in Section 6.8 (assuming, for simplicity, isothermal flow of a Newtonian fluid, Eqs. 6.8-15–6.8-34). Let us now expand this discussion to include particulate solids transport, melting, partially filled chambers, and leakage flows in both partially and filled chambers.

Counterrotating, intermeshing TSEs are typically gravity-fed. Provided that the barrel throat and screw under the hopper are adequately cooled, feeding is facilitated by the counterrotation of the two screws. The particulates fill C-shaped helical chambers in a consecutive fashion. Thus, in contrast to the single-screw *continuous* solid beds, the solid bed here is *divided* by the intermeshing flights of the other screw, and is transported downstream by positive displacement. There is little difference in pressure levels and particulate bulk-density levels between adjacent C-shaped chambers. Limited frictional drag-induced pressurization is possible only within individual isolated chambers. Thus, with constant downstream screw geometry, and taking into consideration that the particulate bulk density is appreciably smaller than the melt density, the C-shaped chambers can only be partially filled upon melting, becoming fully filled further downstream, as we will see later. To obtain better filling, these extruders can be designed with different screw geometries under the hopper, for example, a greater pitch and more screw starts, which are aimed at providing for a constant *mass flow rate* rather than a constant volumetric flow rate, in the downstream direction.

Melting begins and is completed inside each of the C-shaped chambers. The downstream melting length is of the order of one diameter, almost an order of magnitude shorter than that of the typical melting length of SSEs. Janssen (24) conducted screw-pulling experiments similar to those we presented in connection with the SSEs' melting mechanism presented in Chapter 9. He extruded PP powder, of 0.65 g/cc bulk density and 0.72 g/cc melt density, in a double-flighted 47-mm extruder. The melting experiments were carried out at two low rotational speeds of 4.3 and 10.2 rpm, using two dies, one resulting in a 50-psi and the other in 2700-psi die pressure drop. He observed that melting lengths inside the more or less isolated C-shaped chambers were smaller than typical SSE lengths. This is not surprising, since the rotational speeds were very low, resulting in long exposures to conductive heating aided by the internal C-shaped chamber circulatory flow, as discussed in Section 6.8. Furthermore, two melting mechanisms were observed and attributed to the different die pressures used, from the examination of polished C-segment cross sections along the downstream direction, shown schematically in Fig. 10.12.

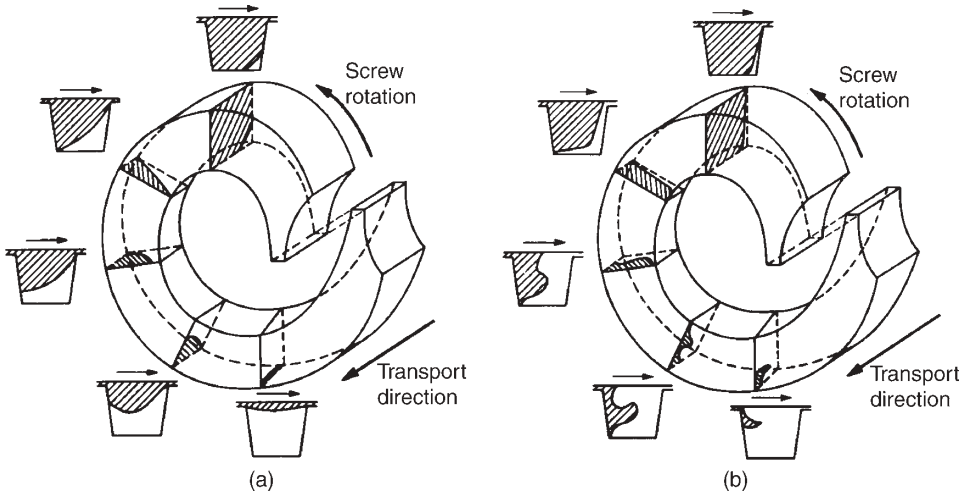


Fig. 10.12 Schematic representation of two melting mechanisms observed by Janssen (24) with PP processed in a double-flighted 47-mm counterrotating TSE operating at low rotational speeds. (a) Melting when the die pressure was set at the low value of 50 psi, where chamber-to-chamber leak pressure backflows are negligible. (b) Melting under the high die pressure of 2700 psi, which enables leak backflows, which result in chamber solid bed compaction and introduce the possibility of dissipative mix melting. [Reprinted by permission from L. P. B. M. Janssen, *Twin Screw Extrusion*, Elsevier Scientific, Amsterdam, 1978.]

The cross-sectional view of melting evolution, starting from the bottom and proceeding clockwise in Fig. 10.12, represents the first and last stages of melting in downstream successive chambers during the same experiment. In Fig. 10.12(a) the melting mechanism is indicative of drag-assisted conductive melting provided by the barrel under a low die pressure of 50 psi. Note that no melt pool is created at the pushing-screw flight. Rather, the melt created by the mechanism just discussed penetrates into the incompletely packed particulate bed, creating a well. This 'well', in turn, is deformed toward the pulling flight at later melting stages by the circulatory melt flow to form a melt wedge that grows until the completion of melting. In Fig. 10.12(b), melting conducted under a high die pressure of 2700 psi indicates that during the early stages of melting with this mechanism, melt from the downstream chamber *leaks* back into the chamber just upstream, compacting the particulate bed. That is, in this mechanism, the chambers in the melting zone are not isolated, but communicate through chamber-to-chamber leak pressure backflows. We will see later that, at large die pressure drops, these very important leak flows extend to many C-shaped chambers upstream of the die. The melting process continues by long-exposure-conductive, barrel-solid, and melt-solid melting, as well as *mild* dissipative mix melting (DMM), discussed in Chapter 5. This last melting contributor is small because of the two very low rotational speeds employed during the experiments. For this reason, melting under the low die pressure, as in Fig. 10.12(a), started at the fifth chamber from the hopper and ended at the seventh, often resulting in a chamber partially filled with melt, while, at the high die pressure, melting started at the fifth and ended in the ninth chamber. It is expected that at an order-of-magnitude higher screw speed, but still under the operational limits of counterrotating, intermeshing, TSEs DMM mechanisms, play a more dominant and beneficial melting role. Indeed, this appears to be so. White and co-workers (25–27)

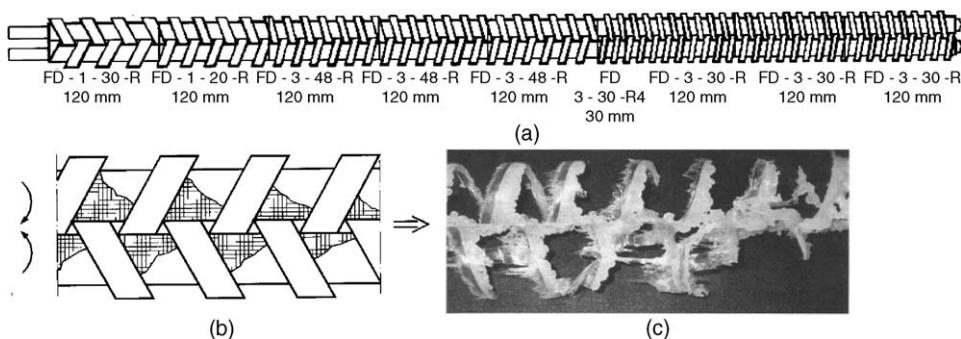


Fig. 10.13 Melting of low density polyethylene (LDPE) (Equistar NA 204-000) in a starve-fed, fully intermeshing, counterrotating Leistritz LMS 30.34 at 200 rpm and 10 kg/h. (a) The screw element sequence used; (b) schematic representation of the melting mechanism involving pellet compressive deformation in the calender gap; (c) the carcass from screw-pulling experiments. [Reprinted by permission from S. Lim and J. L. White, “Flow Mechanisms, Material Distribution and Phase Morphology Development in Modular Intermeshing counterrotating TSE,” *Int. Polym. Process.*, **9**, 33 (1994).]

have experimentally examined the melting behavior in *starve-fed*, fully intermeshing (thick-flighted), counterrotating extruders, such as the one shown in Fig. 10.13(a), operating at 100–200 rpm, and found that melting starts a short distance downstream from the hopper, far away from the melt-filled C-shaped chambers, and is complete in less than three diameters. They attribute melting primarily to PED of the pellets in the interscrew “calender-like” gap, where they are dragged by the counterrotation and undergo a compressive/squeezing plastic deformation, as shown schematically in Fig. 10.13(b). This pellet-dragging process continues until the entire pellet bed is depleted, Fig. 10.13(c), that is, here PED replaces the mechanism of conductive melting with drag-induced melt removal, which is responsible for melting in SSEs, discussed in Chapter 5.

Following the completion of melting, under low die pressures the chamber will typically be partially filled, while melt will occupy the entire chamber under high die pressures, ΔP_{die} , due to pressure backflows. Assuming that the melt viscosity and screw geometry are constant, the number of fully filled chambers, n_f , is

$$n_f = \frac{\Delta P_{\text{die}}}{\Delta P_c} \quad (10.2-1)$$

where the denominator represents each of the equal interchamber pressure drops. Thus, the transition from the partially to the fully filled zone takes place within one pitch, after the die pressure drop has been “exhausted.” Of course, the preceding equation is approximate, since the viscosity will decrease downstream due to increases in temperature, themselves intensifying with increasing operating die pressures (24). Concerning interchamber leak flows, Janssen (24) states that, although the theoretical volumetric pumping capability of the fully filled metering chambers (see Section 6.8) is

$$Q_{th} = 2mNV_c \quad (10.2-2)$$

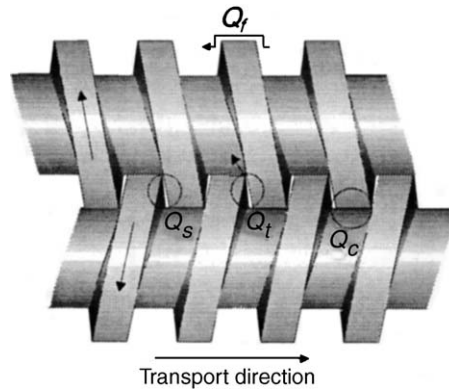


Fig. 10.14 The location of four gaps in “fully” intermeshing, counterrotating extruders though which leak flows can take place. [Reprinted by permission from A. J. van der Goot, O. Poorter, and L. P. B. M. Janssen, “Determination of the Degree of Fill in a Counterrotating TSE,” *Polym. Eng. Sci.*, **38**, 1193 (1998).]

where m is the number of screw starts, N the rotational speed, and V_c the chamber volume, the real pumping capacity is

$$Q = Q_{th} - Q_l \quad (10.2-3)$$

where Q_l represents the sum total of all the leakage flows over a cross section of the extruder. Four different leakage flows were identified by Janssen et al. (24,28) and van der Goot et al. (29) in fully intermeshing, counterrotating extruders, as shown in Fig. 10.14: over the flight gap, Q_f ; the tetrahedron gap, Q_t ; the calender gap, Q_c ; and the side gap, Q_s . They are caused by the drag of the moving surfaces and the interchamber pressure differences, ΔP_{c_i} , which, at first approximation, are taken to be the same in every filled chamber. Thus, they have the familiar generic form

$$Q_l = AN + B \frac{\Delta P_c}{\eta} \quad (10.2-4)$$

in which A and B are constants of the equipment geometric (design) variables, specific for each type of leak flow. They can be calculated approximately for isothermal flows, and using effective viscosities, η , from equations derived by Janssen (24,28).

The degree of fill in the partially filled zone, α_f , is (26)

$$\alpha_f = \frac{Q}{Q_{th}} \quad (10.2-5)$$

and, since ΔP_c in partially filled chambers is zero, the effective leak flow volumetric rate $Q_{l,pfz}$ is

$$Q_{l,pfz} = AN \quad (10.2-6)$$

and

$$\alpha_f = \frac{Q + Q_{l,pfz}}{Q_{th}} \quad (10.2-7)$$

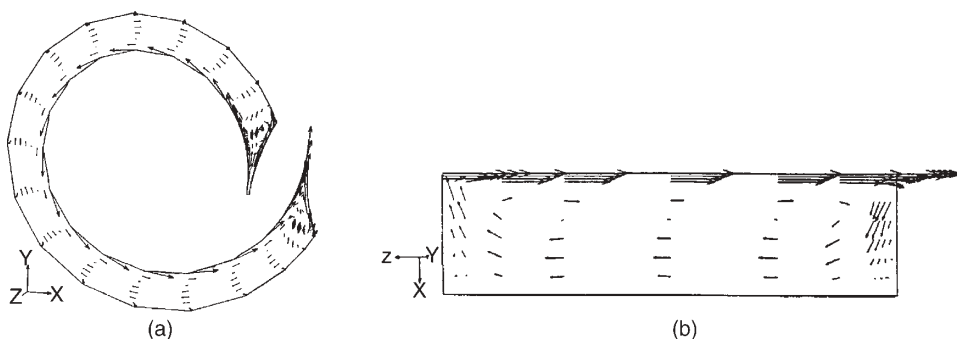


Fig. 10.15 (a) Velocity profile in the down-channel direction on a helically wound plane in the middle of the C-shaped chamber; (b) projection of the velocity field on a plane perpendicular to the helical plane of the C-shaped chamber. [Reprinted by permission from T. Li and I. Manas-Zloczower, "A Study of Distributive Mixing in Counterrotating TSEs," *Int. Polym. Process.*, **10**, 314 (1995).]

The preceding expressions are approximate and based on the assumption of isothermal one-dimensional flow of a Newtonian fluid. Speur et al. (30) studied the full calender gap, two-dimensional flows using finite element methods (FEM), and concluded that the presence of vortices depends on the magnitude of the calender-gap leak flow.

Li and Manas-Zloczower (31) used the CFM commercial "FIDAP" FEM package to simulate the three-dimensional isothermal flow patterns and distributive mixing in three consecutive filled, closed C-shaped chambers of fully intermeshing, counterrotating extruders, having the dimensions of Leistritz 30.34 (30 denotes the centerline distance and 34 the barrel diameter in mm units). An equal pressure drop per C-shaped chamber was applied for the calculations. The melt was assumed to be Power Law above $\dot{\gamma}_0$ and Newtonian below it. The design, process, and material variables are given by the authors.

The velocity in the down-channel direction, Fig. 10.15(a), indicates that most of the fluid undergoes circulatory flow, as expected. A circulatory flow is also generated in the plane perpendicular to the helical surface of the C-shaped chambers, Fig. 10.15(b). Velocity vectors indicating calender-gap leakage flows, Q_c , are shown, without using them to obtain leakage flow rates. The interaction between the two circulatory flows eliminates the possibility of a stagnant layer at $y/H = 2/3$.

Li and Manas-Zloczower also studied numerically the dynamics of distributive mixing by tracking the evolution of particle positions, originally gathered as randomly placed clusters, as shown in Fig. 10.16. The evolution of particle position distribution just discussed indicated a fast initial distributive mixing, which levels off but at reasonably high values. This is also borne out through the computation of distributive mixing efficiency measures, such as the length stretch, λ , used by the authors.

Comparison of Flow and Mixing in Open C-Shaped Channels of Counterrotating and Co-rotating Twin Screws Katziguara et al. (32) conducted three-dimensional FEM numerical studies in fully filled, melt conveying, thin-flighted, that is, open C-shaped channels of both counterrotating and, for comparison, co-rotating TSEs. The two screw configurations studied are shown in Fig. 10.17. In the first of a series of systematic numerical studies made by the group, they calculated the velocity field and, from this, the spatial distribution of tracer particles and the residence time distribution. They also

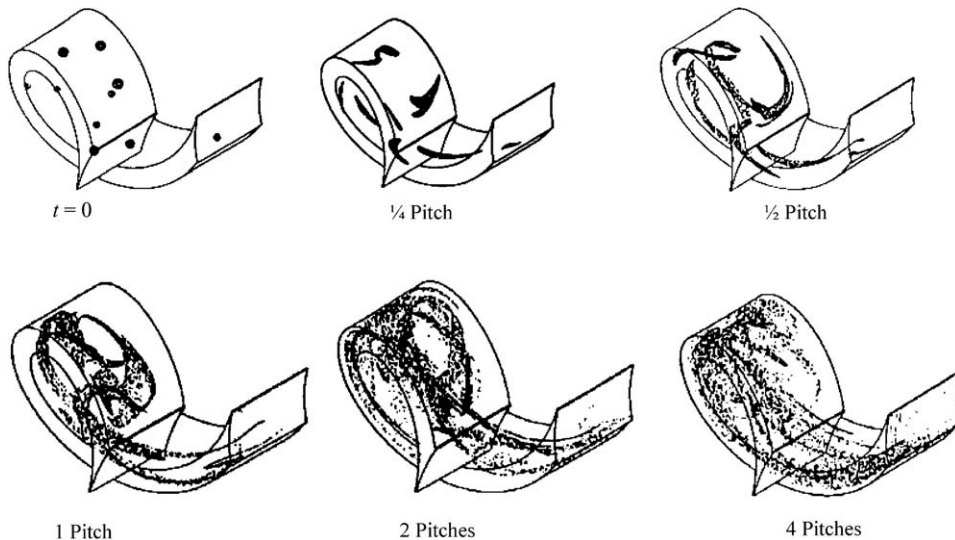


Fig. 10.16 The evolution of the spatial distribution of 10,000 particles initially clustered in 10 randomly placed clusters in the C-shaped chamber. The fraction or number of pitches denotes the axial advance of the material in the chamber due to the counterrotation. [Reprinted by permission from T. Li and Ica Manas-Zloczower, "A Study of Distributive Mixing in Counterrotating TSEs," *Int. Polym. Process.*, **10**, 314 (1995).]

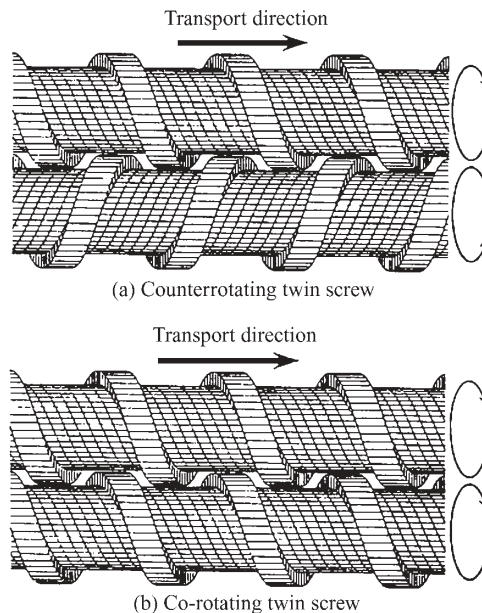


Fig. 10.17 The counter- and co-rotating thin-flight, open C-shaped channels used in the three-dimensional FEM study of Katziguara et al. (32). The two-screw configurations are identical except for the sense of rotation. [Reprinted by permission from T. Katziguara, Y. Nagashima, Y. Nakano, and K. Funatsu, "A Numerical Study of TSEs by 3-D Flow Analysis – Development of Analysis Technique and Evaluation of Mixing Performance for Full Flight Screws," *Polym. Eng. Sci.*, **36**, 2142 (1996).]

obtained the stress field responsible for dispersive mixing. The numerical simulation was conducted assuming isothermal, steady, incompressible, non-Newtonian, Carreau-type fluid flow, in fully filled channels, with no slip at the walls, neglecting inertia and gravitational forces, and assuming fully developed flow far away from the nip region.

The fully filled channel and the isothermal assumptions are not realistic in that, in practice, channels are partially filled and the flow is nonisothermal. The constitutive equation and the equations of change used are:

$$\tau = 2\eta\dot{\gamma} \tag{10.2-8}$$

$$\eta = \eta_0 \left[1 + (\lambda\Pi\dot{\gamma})^2 \right]^{(n-1)/2} \tag{10.2-9}$$

$$\nabla \cdot \mathbf{v} = 0 \tag{10.2-10}$$

$$-\nabla P + \nabla \cdot \tau = 0 \tag{10.2-11}$$

A low density polyethylene was used with Carreau model parameters: $\eta_0 = 19,500\text{Pa} \cdot \text{s}$; $\lambda = 5.5 \text{ s}$; $n = 0.52$. The screw speed was 100 rpm and the pertinent geometric parameters appear in Fig. 10.18 with their numerical values are listed in Table 10.1

The numerical analysis domain can be reduced to the one-pitch segment shown in Fig. 10.19 and further reduced to the midregion containing the intermesh zone, based on the assumption that the flow is fully developed far from the intermeshing zone. In other words, the channel flow region, which is far from the nip region, is omitted. The boundary conditions used were: the flow at cross sections *A* and *B* are fully developed and obtained

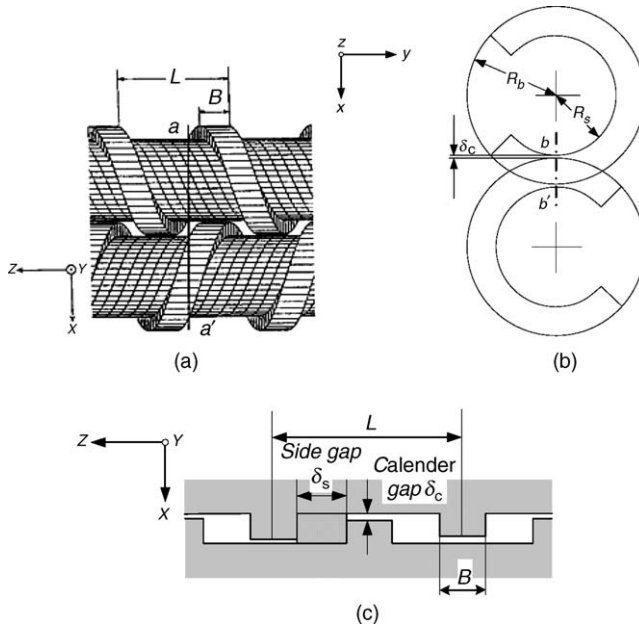


Fig. 10.18 Definition of the geometric parameters. (a) Screw configuration; (b) *a*–*a'* (*x*–*y*) plane; (c) *b*–*b'* (*x*–*z*) plane. [Reprinted by permission from T. Katziguara, Y. Nagashima, Y. Nakano, and K. Funatsu, “Numerical Study of Twin Screw Extruders by 3-D Flow Analysis – Development of Analysis Technique and Evaluation of Mixing Performance for Full Flight Screws,” *Polym. Eng. Sci.*, **36**, 2142 (1996).]

TABLE 10.1 Values of the Geometric Parameters in Fig. 10.18

Pitch	L (mm)	40
Flight width	B (mm)	10
Barrel radius	R_b (mm)	20
Screw radius	R_s (mm)	15
Side gap	δ_s (mm)	10
Calender gap	δ_C (mm)	0.5
Helix angle	θ (deg)	17.65

the same way as in a SSE; and the flows in the domain boundaries C and D are the same as that in the central crosssection of the C-shaped channel in the opposite screw, cross section E , because of the steady periodic condition. The computational scheme used was as follows: An initial guess was made for cross sections C and D , and the whole domain field was calculated using this guess. The obtained flow for cross section E was then used for C and D for a second iterative step, and iterations continued until convergence.

The coordinate system employed moves in the axial direction with the apparent forward velocity of the screw, that is, 40 mm/s, ensuring that the analysis domain will be time invariant. In this coordinate system, a given point can be observed to move in the direction parallel to the flight. It should be noted that in this coordinate system, down-channel velocity components may appear as having negative values. Velocity fields for the counterrotating channels were obtained at two planes perpendicular to the screw axes: plane (I) at the midpoint of the side gap, and plane (II) at the midpoint of the calender gap. They are shown in Fig. 10.20. The axial velocity contour and velocity vectors at plane (I) are shown in Fig. 10.21. The corresponding axial velocity contours and vector at the calender gap, plane (II), are shown in Fig. 10.22. Half of the cross section is shown since symmetry exists. At the calender gap, plane (II), the tight clearance decreases the axial velocity field over the entire cross section, as compared to those at plane (I). The contours at plane (II) are y -axis symmetric (closed C-shaped chambers) with negligible axial velocities at the gap, while for the side gap, the symmetry axis for the contours is different, involving both lobes of the barrel. All axial velocities are downstream positive at both planes of the counterrotating screws.

Turning, for comparison, to the co-rotating screws with identical geometrical parameters, let us examine once again the axial velocity contours and velocity vectors

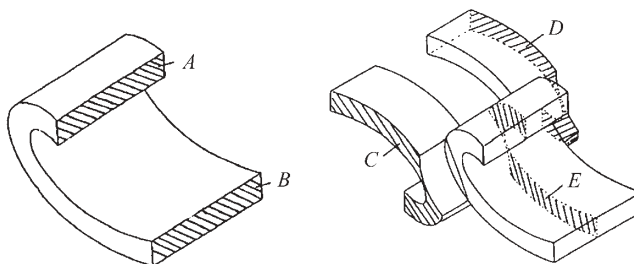


Fig. 10.19 The analysis domain and identification of the cross sections used in the discussion on boundary conditions below. [Reprinted by permission from T. Katziguara, Y. Nagashima, Y. Nakano, and K. Funatsu, "Numerical Study of Twin Screw Extruders by 3-D Flow Analysis – Development of Analysis Technique and Evaluation of Mixing Performance for Full Flight Screws," *Polym. Eng. Sci.*, **36**, 2142 (1996).]

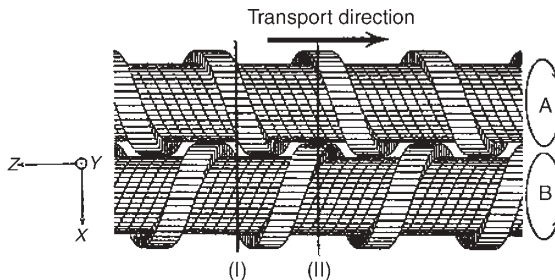


Fig. 10.20 Axial location of the two planes perpendicular to the counterrotating screws, where velocity fields were calculated. Plane (I) is at the middle of the side, and plane (II) at the middle of the calender gaps. [Reprinted by permission from T. Katziguara, Y. Nagashima, Y. Nakano, and K. Funatsu, “Numerical Study of Twin Screw Extruders by 3-D Flow Analysis – Development of Analysis Technique and Evaluation of Mixing Performance for Full Flight Screws,” *Polym. Eng. Sci.*, **36**, 2142 (1996).]

at plane (I), midway to the co-rotating side gap, and at plane (II), midway to the co-rotating calender gap. They are shown in Fig. 10.23. We note that negative upstream velocities exist at both planes, and at plane (I) in the side gap region, a very high axial velocity gradient contributes to axial mixing. The velocity vectors at plane (I) also indicate that there is material transfer from lobe to lobe at the side-gap plane (II).

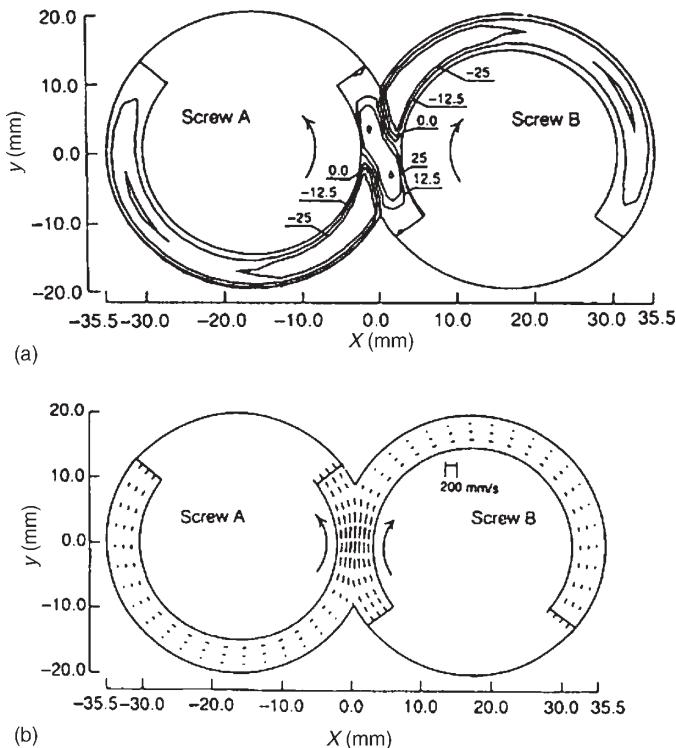


Fig. 10.21 Plane (I): (a) Contours of the axial velocity; (b) velocity vectors at the side gap region, in (mm/s). [Reprinted by permission from T. Katziguara, Y. Nagashima, Y. Nakano, and K. Funatsu, “Numerical Study of Twin Screw Extruders by 3-D Flow Analysis – Development of Analysis Technique and Evaluation of Mixing Performance for Full Flight Screws,” *Polym. Eng. Sci.*, **36**, 2142 (1996).]

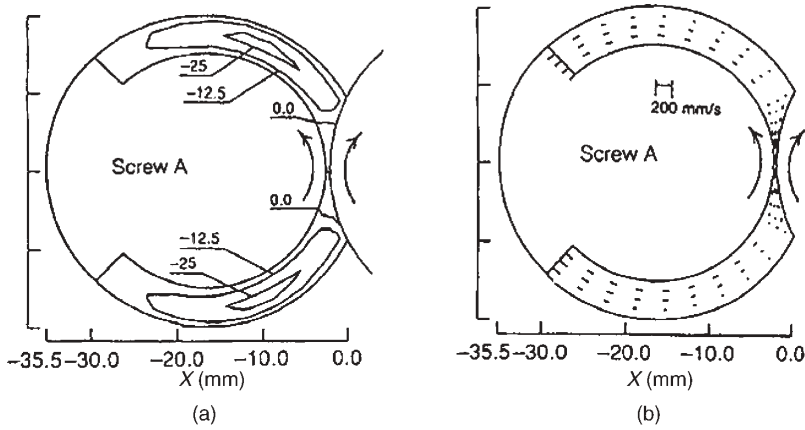


Fig. 10.22 Plane (II) at the calender gap: (a) contours of axial velocity; (b) velocity vectors, in (mm/s). [Reprinted by permission from T. Katziguara, Y. Nagashima, Y. Nakano, and K. Funatsu, “Numerical Study of Twin Screw Extruders by 3-D Flow Analysis – Development of Analysis Technique and Evaluation of Mixing Performance for Full Flight Screws,” *Polym. Eng. Sci.*, **36**, 2142 (1996).]

The flow rates, Q , for the counter- and co-rotating screw pumps in Fig. 10.17, the two leak flow, Q_C and Q_S , shown in Fig. 10.24, as well as the flow from screw A to screw B, Q_{AB} . Flows Q , Q_{AB} , Q_C , and Q_S are listed in Tables 10.2 and 10.3.

The pumping ability of the thin-flighted, filled co-rotating screw is about 1.4 times that of the counterrotating screw. The side-gap flow with the counterrotating screw is 90% of the

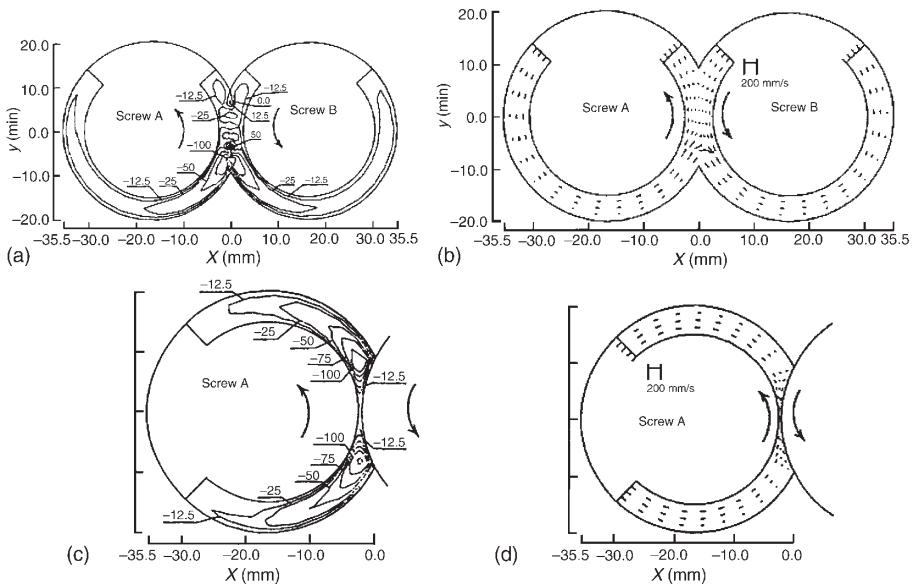


Fig. 10.23 Co-rotating channels. (a) Contours of axial velocity at plane (I); (b) velocity vector at plane (I); (c) contours of axial velocity at plane (I); (d) velocity vectors at plane (II), in (mm/s). [Reprinted by permission from T. Katziguara, Y. Nagashima, Y. Nakano, and K. Funatsu, “Numerical Study of Twin Screw Extruders by 3-D Flow Analysis – Development of Analysis Technique and Evaluation of Mixing Performance for Full Flight Screws,” *Polym. Eng. Sci.*, **36**, 2142 (1996).]

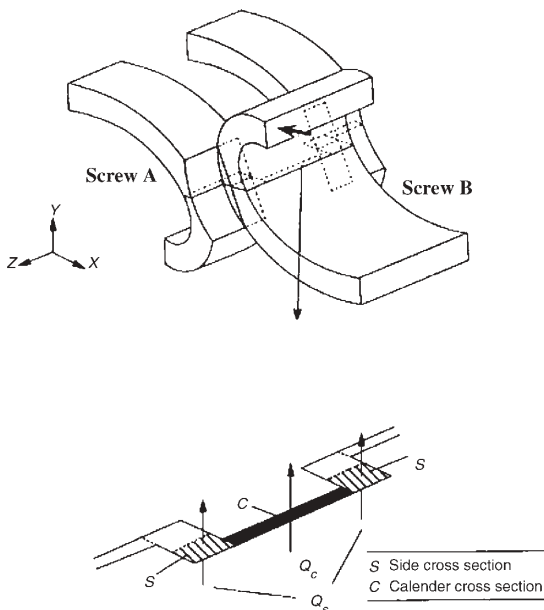


Fig. 10.24 Identification of the calender and side-gap cross sections and leak flows Q_s and Q_c . [Reprinted by permission from T. Katziguara, Y. Nagashima, Y. Nakano, and K. Funatsu, “Numerical Study of Twin Screw Extruders by 3-D Flow Analysis – Development of Analysis Technique and Evaluation of Mixing Performance for Full Flight Screws,” *Polym. Eng. Sci.*, **36**, 2142 (1996).]

TABLE 10.2 Flow Rate and Average Velocity in the Transport Direction

	Flow Rate (cm ³ /s)	Average Velocity (cm/s)
Counterrotating	10.84	1.408
Co-rotating	15.14	1.670

total flow, the calender gap flow is 5%, and the cross-screw flow around 1%, that is, there is no material transfer from screw to screw. By contrast and for comparison, with the co-rotating screws, the calender-gap leak flow is around 1% of the total, and the side-gap leak flow is 20%, both less than in the counterrotating screws, but the cross-screw flow is 83%, denoting very effective screw-to-screw distributive mixing. The contrast in the magnitude of Q_{AB} is supported by the numerical determination of the evolution of spatial distribution of tracers in the rotational direction in both counter- and co-rotating filled channels. Figure 10.25 presents such results for tracer particles aligned in 15 lines along the channel-width

TABLE 10.3 Flow Rates of Various Kinds of Leakage Flows

	Q_c/Q	Q_s/Q	Q_{AB}/Q
Counterrotating	0.058	0.910	0.016
Co-rotating	0.015	0.194	0.831

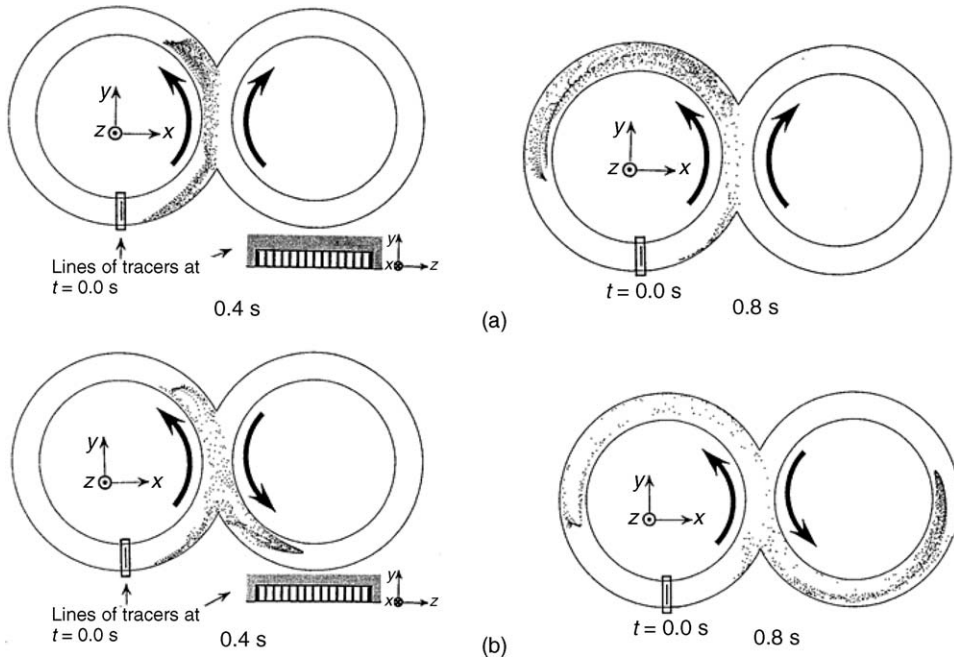


Fig. 10.25 Evolution of the spatial distribution of tracer particles initially placed at the location of the left lobe, as shown for (a) counterrotating, and (b) co-rotating filled channels. [Reprinted by permission from T. Katziguara, Y. Nagashima, Y. Nakano, and K. Funatsu, “Numerical Study of TSEs by 3-D How Analysis-Development of Analysis Technique and Evaluation of Mixing Performance for Full Flight Screws” *Polym. Eng. Sci.*, **36**, 2142 (1996).]

direction, as shown, each line having 80 particles in the y direction. All particles are projected on the cross section perpendicular to the screw axes and are also distributed in the axial direction. We find that most, if not all, of the particles stay in the initial lobe with counterrotating screws, while a considerable number of them are transferred to the other screw. These results suggest that the co-rotating screws can achieve effective distributive mixing from screw to screw, and from Fig. 10.23, also better axial mixing. This attribute is important to reactive extrusion, which requires distributive mixing of miscible components.

Finally, Katziguara et al. calculated the isothermal flow stress field, whose strength, locally, is the driving force of dispersive mixing of agglomerates. The invariant stress measured used is

$$\sigma = \sqrt{(\tau_{\max})_{xy}^2 + (\tau_{\max})_{yz}^2 + (\tau_{\max})_{zx}^2} \tag{10.2-12}$$

where $(\tau_{\max})_{xy}$ denotes the maximum shear stress in the x - y plane and can be obtained as

$$(\tau_{\max})_{xy} = \sqrt{4\tau_{xy}^2 + (\tau_{xx} - \tau_{yy})^2} \tag{10.2-13}$$

therefore

$$\sigma = \sqrt{4(\tau_{xy}^2 + \tau_{yz}^2 + \tau_{zx}^2) + (\tau_{xx} - \tau_{yy})^2 + (\tau_{yy} - \tau_{zz})^2 + (\tau_{zz} - \tau_{xx})^2} \tag{10.2-14}$$

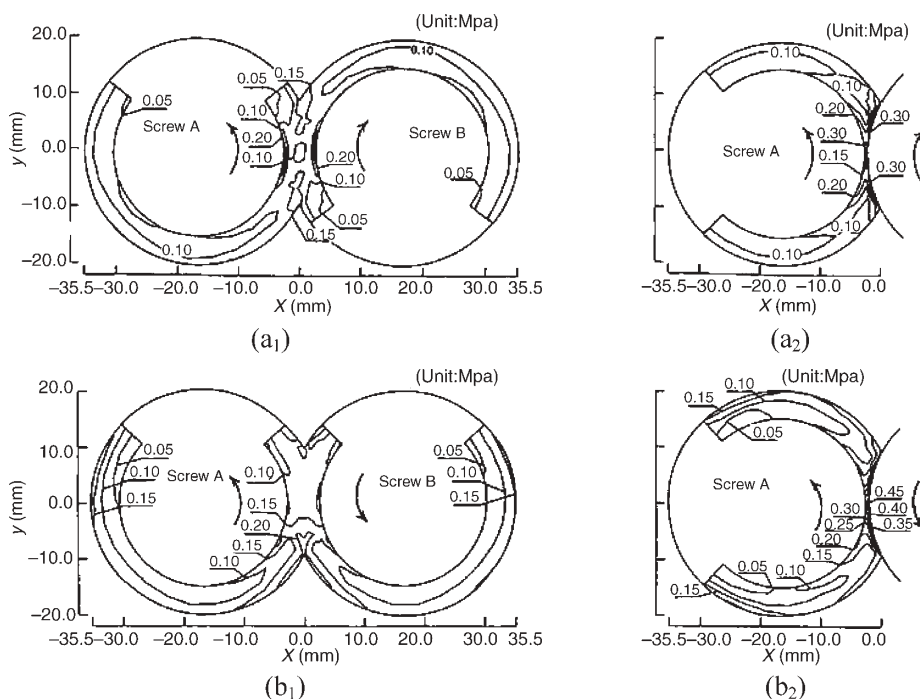


Fig. 10.26 The stress measure, σ , contours. (a₁) Counter-, side gap, plane (I). (a₂) Counter-calender gap, plane (II). (b₁) Co-plane (I) and (b₂) Co-plane (II). [Reprinted by permission from T. Katziguara, Y. Nagashima, Y. Nakano, and K. Funatsu, "Numerical Study of Twin Screw Extruders by 3-D Flow Analysis – Development of Analysis Technique and Evaluation of Mixing Performance for Full Flight Screws," *Polym. Eng. Sci.*, **36**, 2142 (1996).]

Figure 10.26 shows the contours of the stress measure, σ , in Mpa in the two planes used in the numerical evaluation of the velocity fields: plane (I) in the side gap and plane (II) in the calender gap in both the counter- and co-rotating filled screw channels. Higher stress contours are found on the flight in the calender gap region in both counter- and co-rotating screws. Additionally, the stresses at plane (I) for both counter- and co-rotating channels are very similar. Thus, from a dispersive stress field point of view, both are the same, while from their distributive mixing abilities, the co-rotating screws are clearly superior.

Devolatilization in Counterrotating Twin Screw Extruders

Sakai and Hashimoto (33) presented experimental results on devolatilization of a mixture of octane/hexane in linear low density polyethylene (LLDPE) from 10% to 0.01%, as well as a rubber slurry of 42% chloroprene and of 58% slurry in carbon tetrachloride in a JSW TEX 65 counterrotating, intermeshing, TSE. The LLDPE mixture was prepared in SSE upstream, where the octane/hexane was added to the melt with a plunger pump, which maintained constant concentration and was fed directly under pressure into the feed throat of the counterrotating, vented, TSE.

Venting takes place in these devices without the risk of vent-port fouling. The counterrotation of the screws forces the bubble-rich melt to remain inside the extruder and away from the vent port. On the other hand, in fully intermeshing extruders, because

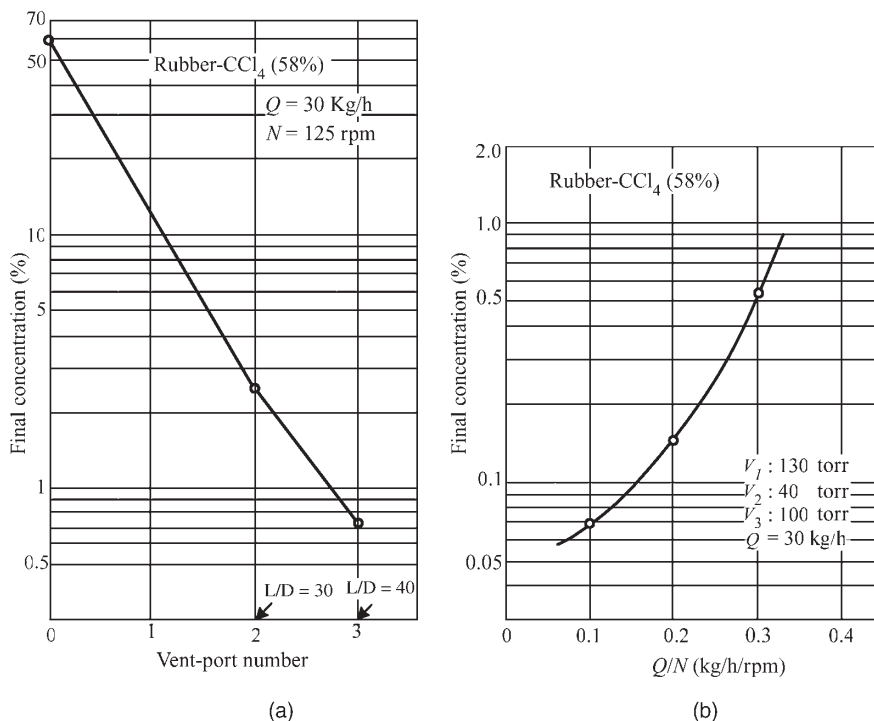


Fig. 10.27 Devolatilization of a 42% polychloroprene-58% CCl₄ in a JSW TEX 65 counter rotating, intermeshing TSE. (a) The effect of increasing the number of vent ports at $Q = 30$ kg/h and $N = 125$ rpm. (b) The effect of decreasing Q/N ratio, at constant Q . [Reprinted by permission from T. Sakai and N. Hashimoto, "Application of Novel Counter-rotating Intermeshed Twin Extruder for a Degasing Operation." *SPE ANTEC Tech Papers*, **32**, 860 (1986).]

the C-shaped chambers are more or less isolated, devolatilization can take place only below the vent port itself (12). For this reason Sakai used two and three vent ports in the experiments, in order to increase the number of stages (see Chapter 8), thus decreasing the final solvent concentration. Figure 10.27(a) shows the beneficial effects of multiple vent ports for the rubber slurry. Additionally, since the surface of a single C-shaped chamber is limited, compared to that in a co-rotating, intermeshing vent section between two melt seals, increasing the screw rotational speed N at constant flow rate Q will be beneficial, since the rate of melt/solvent rate renewal will be increased. This is shown in Fig. 10.27, again for the rubber slurry.

Reactive Processing in Counterrotating Twin Screw Extruders

Dey and Biesenberger (34) have reported results of reactive extrusion of methyl methacrylate in a counterrotating, fully intermeshing, Leistritz 30.34 TSE. Five single-flighted, 6-mm pitch, 120-mm-long screw elements followed by two triple-flighted, 30-mm pitch, 120-mm-long screw elements were used, with barrel temperature and screw rotational speed as the processing variables. Benzoyl peroxide was used as the initiator and the feed was a polymethyl-methacrylate prepolymer, to reduce the quantity of heat to be removed due to the polymerization exotherm, which is significant. Isothermal differential

scanning calorimetry (DSC) experiments were conducted to obtain the temperature-dependent polymerization rate constants. The molecular weight was determined by solution viscometry after obtaining the Mark–Howink constants from Water Associates, $\alpha = 0.69$ and $k = 1.04 \times 10^{-4} \text{ dl/g}$. They treated each of the C-shaped chambers as a batch reactor, which is approximate in that chambers “communicate” through gap pressure and drag flows, as discussed earlier. Although Dey and Biesenberger obtained high levels of conversion and high MW reactive extrusion products with some experiments, there were instances of unplanned and unexpected runaway reactions, as well as results that indicated that the rate of the heat generated by the polymerization was appreciably larger than that which can be removed by convective cooling at the barrel surface (see Section 11.2, where, for thematly stable processes, $t_G/t_r < 10^{-1}$). The 34-mm extruder used was air cooled, providing a poor heat-transfer coefficient. Larger extruders would tend to behave more “adiabatically” because of the smaller surface-to-volume ratio, creating more adverse conditions for thermal uniformity and stability inside the reactor vessels that are the C-shaped channels.

Gadzenveld and Janssen (35–38) and Gadzenveld et al. (39) have modeled the fully intermeshing, counterrotating extruder as a reactor, and used it for a number of polymerizing systems with both free radical and condensation-type reactions. Their model considers two extruder reactor zones: partially filled C-shaped chambers upstream, and completely filled chambers downstream, composing the metering zone where pressure is built up against the die pressure. All four leakage flows through the screw-to-screw and screw-to-barrel gaps allow for communication between chambers, and contribute to mixing of reactants. That is, in this zone, the volumetric displacement of the screws is greater than the actual output volume rate, the difference being the backward leakage mixing flows, which affect the chamber flow profiles and, thus, mixing and residence time distribution in each chamber (40). The numerical model of Gadzenveld and Janssen considers all the C-shaped chambers as a series of perfectly mixed continuous stirred tank reactors (CSTRs) “moving on a conveyor belt.” The partially filled ones communicate only through drag-induced gap flows. The mass balance in the j th chamber is

$$\frac{dM_j}{dt} = \frac{d(\rho_j \varepsilon V_j)}{dt} = \{Q_{t,i} \rho_{j+1} + 2Q_{f,i} \rho_{j+2} + 2m(Q_{t,i} + Q_{s,i}) \rho_{j+2m}\} - \{Q_{t,o} + 2Q_{f,o} + 2m(Q_{c,o} + Q_{s,o})\} \rho_j \quad (10.2-15)$$

where V_j is the volume of the j th chamber; ε is the filling degree of the chamber; ρ_j is the density of the material in the j th chamber; and Q_t , Q_f , Q_C , and Q_S are the leakage flows, where subscripts i and o denote inflow or outflow. In the balance, the variation of density during the polymerization reaction can be incorporated. In the model, however, this variation is neglected.

This simple model is schematically represented for single flighted screws in Fig. 10.28. The model is based on the overall balances for enthalpy, mass, and concentration that can be derived for each individual chamber moving through the extruder. Assuming constant density, the preceding equation reduces to

$$\frac{d(\varepsilon V_j)}{dt} = \{Q_{t,i} + 2Q_{f,i} + 2mQ_{c,i} + 2mQ_{s,i}\} - \{Q_{t,o} + 2Q_{f,o} + 2m(Q_{c,o} + Q_{s,o})\} \quad (10.2-16)$$

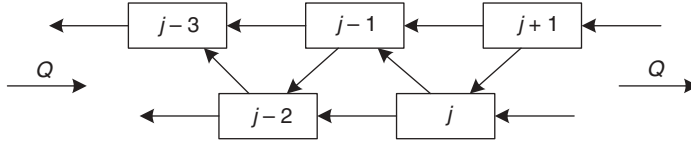


Fig. 10.28 Flow diagram representation of the reaction model of Gadzenveld et al. (39). Each box represents a C-shaped chamber, and the arrows represent the total leak flows from chamber to chamber.

Considering a free radical polymerization, the second relevant balance to the model is that of the monomer concentration over the j th chamber

$$V_j \varepsilon \frac{dc_j}{dt} = -\varepsilon V_j \dot{r} + \{Q_{t,i} c_{j+1} + 2(Q_{f,i} c_{j+2}) + 2m(Q_{t,i} + Q_{s,i}) c_{j+2m}\} - \{Q_{t,o} + 2Q_{f,o} + 2m(Q_{c,o} + Q_{s,o})\} \quad (10.2-17)$$

where \dot{r} is the reaction rate and c_j is the concentration of monomer in the j th chamber.

The energy balance is coupled to the monomer concentration balance by the reaction term, as this depends on the monomer concentration and the temperature. The energy balance equals

$$V_j \varepsilon \rho C_p \frac{dT_j}{dt} = -\varepsilon V_j \dot{r} \Delta H_r + \rho C_p [\{Q_{t,i} T_{j+1} + 2(Q_{f,i} T_{j+2}) + 2m(Q_{t,i} + Q_{s,i}) T_{j+2m}\} - \{Q_{t,o} + 2Q_{f,o} + 2m(Q_{c,o} + Q_{s,o})\} T_j] + hA(T_w - T_j) \quad (10.2-18)$$

where c_p is the specific heat, ΔH_r the reaction enthalpy, T_j the temperature in the chamber observed, h the heat transfer coefficient, A the heat exchanging surface of the chamber, and T_w the temperature of the wall at the position of the chamber.

The coordinate system is attached to the moving chamber whose velocity, V_c , is the product of the rotational speed, N , and the pitch axial length, L

$$V_c = NL(x) \quad (10.2-19)$$

Thus, the position of the chamber in the extruder is at any time, t

$$x(t) = N \int_0^t L(x) dt \quad (10.2-20)$$

and for constant pitch

$$x(t) = NLt \quad (10.2-21)$$

The fully filled length is determined by the die pressure, the viscosity of the reacting material, and the leakage flows. The die pressure is a model input parameter. Speur (41) arrived at an empirical model for the heat transfer coefficient, h , based on an energy balance over a single chamber interacting with its neighbors. Experimental results fitted well with the following relation,

$$h = 410 \left(\frac{N}{0.174} \right)^{1.65 - 2.3z_r} \quad (10.2-22)$$

where h is in $\text{watt/cm}^2 \cdot \text{K}$ and α_r is the relative throughput, the ratio of the process to the theoretical volumetric rates.

The rheological model used for the reacting stream is that of Stuber (42), based on known empirical generic behavior of polymer solutions. The basis of the model is

$$\eta_0(c, \bar{M}_w, T) = F\zeta \quad (10.2-23)$$

in which

$$F = K \left[1 + a_1(c\bar{M}_w)^{0.5} + a_2(c\bar{M}_w) \right]^{3.4} \quad (10.2-24)$$

and

$$\zeta = \exp \left[(b_0 + b_1c + b_2c^2) \left(\frac{1}{T} - \frac{1}{T_{\text{ref}}} \right) + b_3c^3 \right] \quad (10.2-25)$$

where c is the polymer concentration in weight percent, \bar{M}_w is the weight average molecular weight of the polymer in thousands, K , a_1 , a_2 , b_0 , b_1 , b_2 , and b_3 are constants, and T and T_{ref} are temperatures in degrees kelvin. The parameter T_{ref} adjusts the concentration dependence of the viscosity model at low concentrations. As T_{ref} decreases, the concentration dependence for low concentrations decreases.

The preceding model is for the zero shear viscosity, η_0 . The model does not include the shear rate dependence of viscosity. This is actually not a limiting assumption, since the viscosity changes (increases) with increasing polymer concentration are much greater than those due to shear thinning. The reaction studied was the free radical polymerization of *n*-butyl methacrylate. In the early stages, where a dilute polymer solution represents the reacting material, the polymerization is first order in the monomer concentration. At higher polymer concentrations, the polymer chain mobility becomes limited and the termination steps become *diffusion controlled*, resulting in a reduced combined termination rate constant, k_t . This leads to an increase of free radicals and, thus, loss of steady state due to the increase of the number of propagating chains, which, due to the propagation exotherm, increases the propagation rate constants, leading to the "gel" or Trommsdorff effect (43), where the weight average \bar{M}_w increases to a critical value, \bar{M}_{wcr} . Marten and Hamielec (44) developed an empirical kinetic model based on the free volume theory, leading to the following expression for k_t :

$$\frac{k_t}{k_{t0}} = \left(\frac{\bar{M}_{wcr}}{\bar{M}_w} \right)^a \exp \left[-A \left(\frac{1}{V_F} - \frac{1}{V_{Fcr}} \right) \right] \quad (10.2-26)$$

where a is a concentration dependent constant, A is a constant, and V_F is the free volume, which can be calculated by the following equation:

$$V_F = [0.025 + \alpha_p(T - T_{gp})] \frac{V_P}{V_T} + [0.025 + \alpha_m(T - T_{gm})] \frac{V_M}{V_T} \quad (10.2-27)$$

where the subscripts p and m denote polymer and monomer, and $\alpha = \alpha_l - \alpha_g$, α_l is the expansion coefficient for the liquid state, α_g the expansion coefficient for the

glassy state, T_g the glass transition temperature, V the volume, and V_r the total volume.

The critical free volume is determined by

$$K_3 = \bar{M}_{\text{merl}}^m \exp(A/V_{\text{Fcr}}) \quad (10.2-28)$$

where K_3 is a constant that is dependent on temperature and determined empirically, m is arbitrarily set equal to 0.5, and A is a constant.

The combination of the equations leads, for a bulk polymerization above the glass transition temperature, to a general rate expression:

$$\frac{dx}{dt} = k_p \left(\frac{f_{kd}}{k_{t0}} \right)^{0.5} \frac{(1-x)}{(1-\varepsilon x)} I_0^{0.5} \exp(-k_d t/2) \times \left(\frac{\bar{M}_w}{M_{\text{wcr}}} \right)^a \exp\left(\frac{A}{2} \left(\frac{1}{V_F} - \frac{1}{V_{\text{Fcr}}} \right) \right) \quad (10.2-29)$$

where k_d is the reaction constant for the decomposition of the initiator, f is the efficiency factor of the initiator, k_{t0} is the initial termination constant, x is the degree of conversion, ε is the volume contraction factor $(d_p - d_m)/d_p$, d_p is the density of the polymer, d_m is the density of the monomer, I_0 is the initial initiator concentration, and t is the time.

The relationship between the molecular weight and conversion for this polymerization was arrived at empirically, and is approximate, but functional (45)

$$\bar{M}_w = 781 \cdot \text{conversion} - 6500 \quad (10.2-30)$$

The previous two equations enable the solution of the reaction kinetics for the polymerization of *n*-butyl methacrylate, together with the reaction-specific constants given by the authors (39). The agreement between experimental data and model predictions of this rather simplified CSTR-based model is good, as shown in Fig.10.29(a)–10.29(d).

Counterrotating, Tangential, Nonintermeshing Twin Screw Extruders

Counterrotating, tangential, nonintermeshing (CRNI) TSEs were developed by the Welding Engineers Company (46,47). Their designs were expanded and modified in order to take advantage of their inherent capabilities in the areas of compounding, devolatilization, and reactive extrusion (48–50). Common currently used designs, such as the one shown schematically in Fig. 10.30, exhibit capabilities that have both similarities and differences when compared to single screw and *intermeshing* TSEs (12). Note that one screw is longer than the other, the extra length serving as a single screw melt pump. Also note that, in Fig. 10.30, the flights of the two counterrotating screws are in a *matched*-screw configuration. Figure 10.31 shows the matched-, as well as the staggered-screw configuration, also commonly used because it imparts different process capabilities, as we discuss later. The elementary steps of particulate solids feeding and pressurization, melting, mixing, and devolatilization are all carried out in the twin screw segment of the extruder. Those of melt pressurization and pumping, together with additional laminar shear mixing, are carried out in the downstream, single screw section. The longer screw is equipped on the drive side with a stronger thrust bearing to support the single screw pressure generation used to force the melt through the (pelletizing) die.

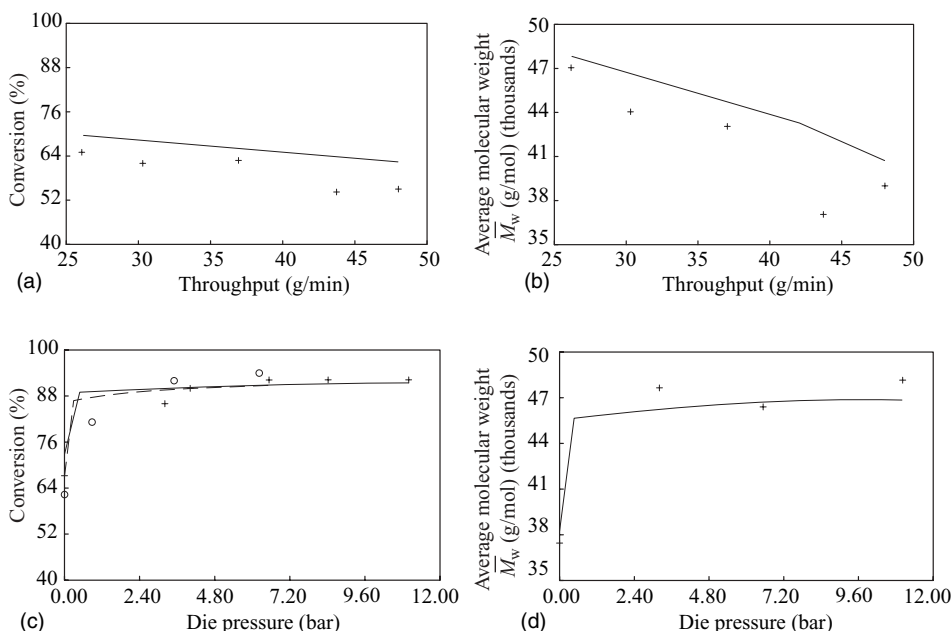


Fig. 10.29 Comparison between the experimental data on the reactive extrusion product of *n*-butyl methacrylate in a counterrotating, fully intermeshing extruder. (a, b) The dependence of conversion and \bar{M}_w on throughput; (c, d) the dependence of conversion and \bar{M}_w on die pressure. (+, O) experimental point, (–) model prediction. [Reprinted by permission from K. J. Gadzenveld et al., “The Modeling of Counterrotating TSEs as Reactors for Single-component Reactions,” *Chem. Eng. Sci.*, **49**, 1639 (1994).]

Since the counterrotating screws do not intermesh, axial screw-to-screw tolerance is not critical. This allows CRNI TSEs to be built with very long screws ($L/D \sim 100$), a design feature particularly useful for reactive processing, since the residence time increases, without undue viscous dissipation-generated-melt temperature increase, because the screws are not intermeshing. Relative screw-to-screw timing is also not critical. Thus, the longer screw, which twists, because of the extra shearing forces on the surface of its single-screw portion, more at any given axial position than the shorter, is acceptable. From a screw design

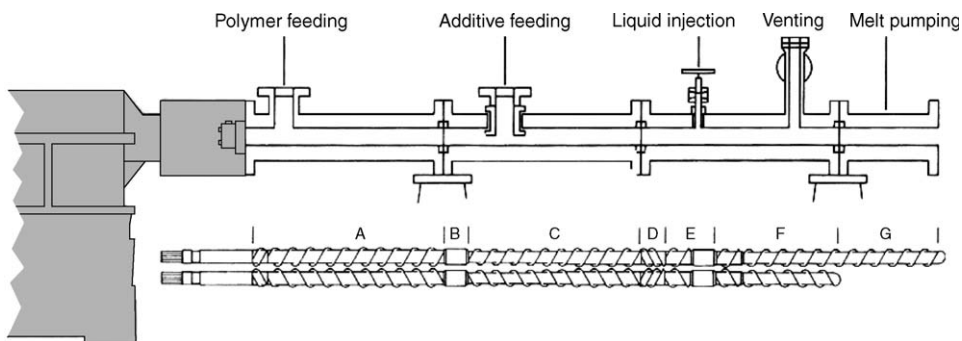


Fig. 10.30 Counterrotating, tangential, nonintermeshing TSE. (Schematic, Courtesy of Welding Engineers.)

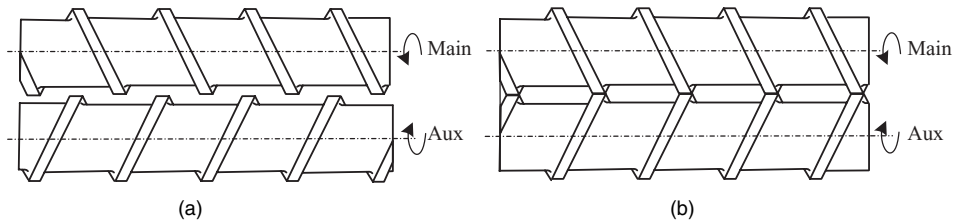


Fig. 10.31 (a) Staggered- and (b) matched-screw flights in a counterrotating, nonintermeshing TSE. The axial offset of staggered is a design variable.

point of view, screw versatility can be obtained by replacing complete shaft segments, connected to others with triple-start threaded screws, rather than individual elements, keyed on polygonal shafts, as in the case with intermeshing, co-rotating TSEs; see Fig. 10.1.

The two apices, where the two barrel lobes meet, are commonly truncated to promote axial mixing. The truncation ability eliminates some common fabrication and mechanical problems in twin-screw equipment. Finally, tight melt sealing is difficult to achieve, because of the “open” design features of the tangential TSEs.

We now discuss the elementary steps of processing as they occur in the twin screw segment of the CRNI tangential extruders; melt pumping in the single screw segment was covered in Chapter 9.

CRNI TSEs are almost always starve-fed to allow for the long lengths needed for mixing, reactive extrusion, and devolatilization. Starve feeding also decouples the feed rate from the screw speed. The needs of multiple feed ports are easy to accommodate because of sufficient equipment length; see Fig. 10.30. The volume available for feeding is quite large because of the tangential positioning of the screws. It is determined by the barrel and screw root diameter and the screw pitch, and, as shown in Fig. 10.32, is greater than that of intermeshing extruders, where it is determined by the centerline-to-diameter ratio, which is less than unity.

The partially filled counterrotating screws advance the free-flowing particulates against the region of the pushing flights by metal-particulate frictional forces. The

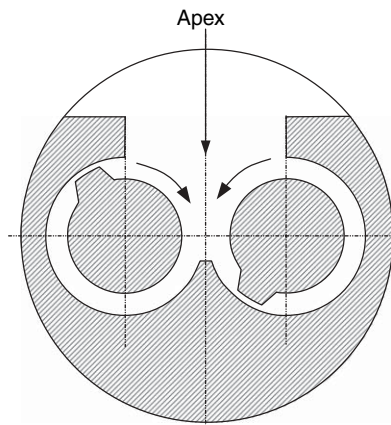


Fig. 10.32 Cross-sectional view of the feed throat region of a CRNI TSE.

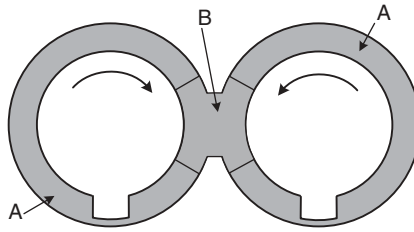


Fig. 10.33 Cross-sectional view of regions in the melting zone of CRNI TSEs where melting mechanisms may be different. [Reprinted by permission from R. J. Nichols and F. Kher-adi, “Melting in CRT Twin Screw Extruders,” *Mod. Plast.*, **61**(2), 70 (1984).]

barrel–particulate kinematic friction coefficient, as in the feed zone of SSEs, has to be larger than that between the screw and particulates. There is interchange of particulates at the tangential interscrew plane, which is larger for the staggered than for the matched screw arrays. In both cases, the net flux of such particulates interchange is zero.

The elementary step of melting cannot take place in this partially filled transport zone. These screw segments, which represent flow restrictors, or “dams” (B), or a pair of reverse screws (D)—are provided in Fig. 10.30. They create a compacted particulate solid bed that can now undergo melting utilizing mechanisms that depend on whether the screw arrays are matched or staggered. The similarity between the single and CRNI TSEs with matched screw arrays in the melting zone is shown schematically in Fig. 10.33 (51). Away from the tangent plane between the two counterrotating screws (regions (A) in Fig. 10.33), the dominant or prevailing melting mechanism is *conductive melting with drag-induced melt removal*, taking place at a molten thin film in the packed-bed barrel region and forming a melt pool, as in SSEs. This is indicated schematically in Fig. 10.34, by the “herring-bone,” side-by-side melt pool and packed-bed regions, for the *matched* screw array. On the other hand, in the screw-to-screw tangent region (B) in Fig. 10.33, both the melt and the packed solid beds from the two screws meet, allowing for the possibility of intermixing between the otherwise segregated solid particulates and melt, to form a solids-rich or, further downstream, a melt-rich suspension. If this takes place, then the melting mechanism is *dissipative mix-melting*.

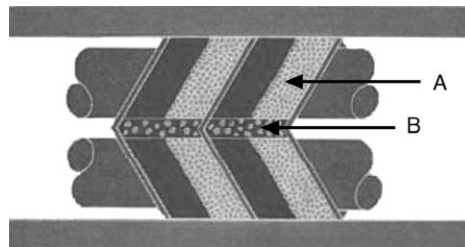


Fig. 10.34 Schematic representation of the two regions in the melting zone of CRNI TSEs with matched screw arrays. In the two regions (A), away from the tangent interscrew plane, the melting mechanism is that of SSEs. In the interscrew plane, a melt–particulates suspension undergoes dissipative mix-melting. [Reprinted by permission from R. J. Nichols and F. Kher-adi, “Melting in CRT Twin Screw Extruders,” *Mod. Plast.*, **61**, 70 (1984).]

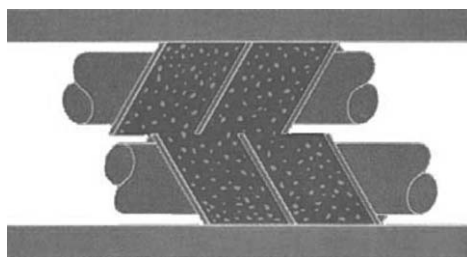


Fig. 10.35 Idealized representation of the solid–melt suspension formed in the melting zone of CRNI twin extruders with staggered screw arrays. The mechanism of melting will be dissipative mix-melting. [Reprinted by permission from R. J. Nichols and F. Kher-adi, “Melting in CRT Twin Screw Extruders,” *Mod. Plastics*, **61**(2), 70 (1984).]

Nichols and Kher-adi (51), conducting screw-pushing carcass analysis melting experiments, observed that the dominant mechanism in a matched-screw array, CRNI extruders resulted in a segregated melt pool and packed particulate beds, as is the case in SSEs. They, however, observed shorter melting lengths than in single screws with the same design and processing conditions. They attributed this to the contributions of the mix-melting mechanism in region (B). When examining the carcasses obtained from the melting zone with *staggered* screw arrays, they found that no coherent and segregated melt pool was formed. Rather, they observed interspersed regions of melt and particulates, represented in an idealized fashion in Fig. 10.35. It is reasonable that such a suspension forms with staggered screw arrays. The mechanism may be as follows: initially, melting of the compacted particulate beds in both screws occurs by conductive heating with drag-induced melt removal. This results in a molten film and the formation of a small melt pool in each screw by the scraping of the pushing flights. These pools meet the packed bed of the opposite screw, setting conditions for the formation of a solids-rich suspension in both flights, leading to dissipative mix-melting. This mechanism is driven by the viscous energy dissipation of the molten phase and deformation of solids, as well as conductive heating of solids. These are all due to the flow in the filled-channel regions (A) and (B), with material transferred from screw to screw because of the stagger, and leakage flow in the truncated barrel apex. Satija and Tucker (52) also observed dissipative mix-melting over a range of processing conditions.

Kaplan and Tadmor (53) (see Section 6.8) were the first to develop a theoretical model for melt conveying in the tangential, nonintermeshing twin screw pump. Their simplified “three parallel plate” model has two continuous plates representing the two stationary screws (since the observer is on them), on either side of a series of moving, slitted mid plates, as shown in Fig. 6.56. The slits represent region (B) and the interrupted plates, region (A) in Fig. 10.33. Nichols (54) conducted melt-conveying experiments with matched and staggered screw arrays, in a 2-in CRNI extruder using dimethylsiloxane, and found that the three parallel plate model overestimates the throughput rates of both staggered and matched arrays. He attributed this to the truncated barrel apexes, which allow back-leakage flows. Figure 10.36 shows the screw characteristic operating lines for staggered and matched arrays and for two different channel depths and two different values of f , the fraction of closed barrel, that is, a measure of the degree of apex truncation. Staggered arrays with open transverse and down-channel, screw-to-screw configuration have limited pressurization capabilities compared to the matched screw characteristics.

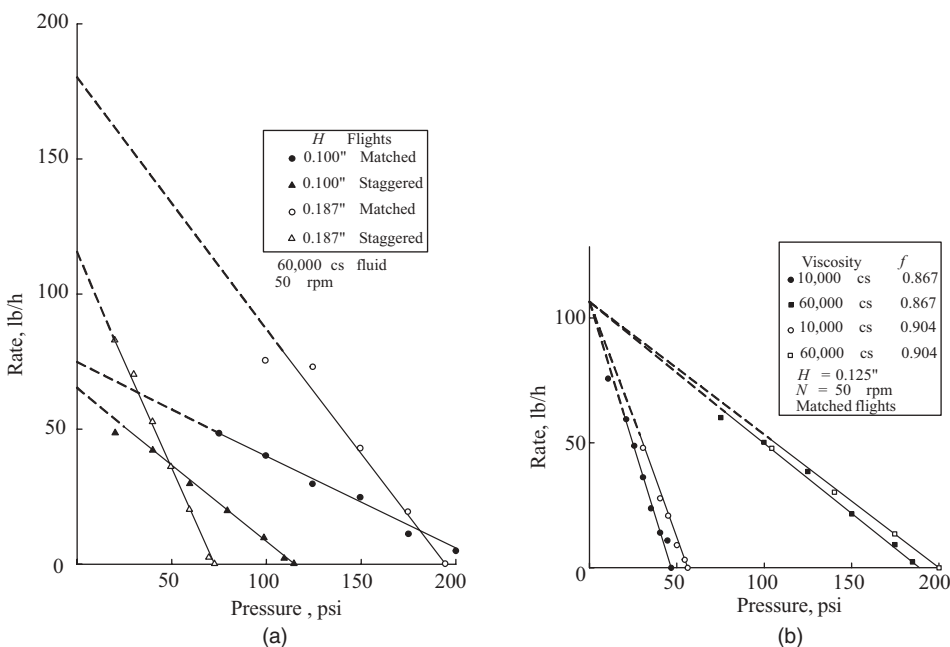


Fig. 10.36 Experimental screw-characteristic operating lines for a 2-in CRNI staggered and matched-screw array at room temperature using polydimethylsiloxane. (a) Comparison of the pumping capabilities of staggered and matched arrays at two different channel depths, H . (b) The effect of the fraction of closed barrel, f , on the matched-array screw characteristics for two fluid viscosities. [Reprinted by permission from R. J. Nichols, “Pumping Characteristics of Counter-rotating TSEs,” *SPE ANTEC Tech. Papers*, **29**, 130 (1983).]

Both staggered and matched screw characteristics show increased sensitivity with increasing channel depth, as expected. Figure 10.36(b) demonstrates the significance of the barrel apex truncation in allowing leakage backflows in this region.

Improved fluid mechanical models to better fit the experimental data were proposed by Nichols (55) and by Nguyen and Lindt (56), the latter being an FEM two- and three-dimensional model, achieving good fit with experimental results. More recently, Bang et al. (57) and, as previously referred to, Li and Manas-Zloczower (31) as well as Katziguara et al. (32) have developed three-dimensional FEM solutions of fully filled CRNI flight channels. As in the fully intermeshing full channels discussed earlier, Li and Manas-Zloczower tracked the evolution of particles fed continuously and steadily in the hopper of melt filled, thin-flighted, matched CRNI screw-array channels. They found that distributive mixing is efficient, resulting in uniform quasi-steady state particle distributions, such as the one shown in Fig. 10.37 at an axial cross section.

Bang et al. (57) conducted experiments with a 34-mm Leistritz LSM tangential CRNI extruder using LDPE with Power Law constants $m = 3200\text{Pa} \cdot \text{s}^n$ and $n = 0.45$ at 180°C . The extruder was outfitted with several pressure transducers. Additionally, screw-pulling experiments were carried out to determine the filled length upstream of the die, and three-dimensional FEM isothermal flow simulations were carried out. In general, the agreement between computational and experimental results was good. The screw melt conveying segments shown in Fig. 10.38 were studied. The screw characteristic curves for

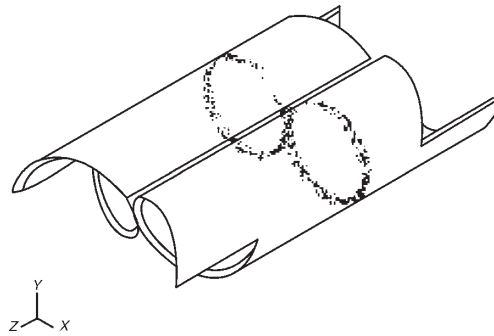


Fig. 10.37 Cross-sectional view of a quasi-steady state distribution of particles in thin-flighted tangential CRNI channels. From such distributions, several measures of distributive mixing can be computed. [Reprinted by permission from T. Li and I. Manas-Zloczower, "A Study of Distributive Mixing in Counterrotating TSEs," *Int. Polym. Process.*, **10**, 314 (1995).]

these elements were plotted in terms of the dimensionless flow rate, Q^* , and channel pressure gradient $(\Delta P/L)^*$, where

$$Q^* = \frac{Q}{(2\pi NR_b)R_b^2} \quad (10.2-31)$$

$$(\Delta P/L)^* = \frac{(\Delta P/L)R_b}{m(2\pi N)^n} \quad (10.2-32)$$

Figure 10.39 depicts the dimensionless screw-characteristic curves for the thin and thick, forward conveying screw array channels. Included, for comparison, are the simulated curves, which indicate good predictive agreement with the experimental results. The pressurization capability of the matched arrays is about three times that of the staggered arrays for the thin-flighted, and about twice for the "tighter," thick-flighted arrays. Furthermore, as expected from the existence of restricted flow paths, the melt-conveying pressure sensitivity of the thick-flighted channels is appreciably smaller than that in the thin-flighted channels.

As mentioned in Section 10.1, the counterrotating, the fully intermeshing, the thin-flighted intermeshing, and the nonintermeshing TSEs are all low-energy input devices. The first, because the calendaring gap tightness limits the rotational speed to the range of 100–150 rpm, and the second and third because of the existence of open channels, which

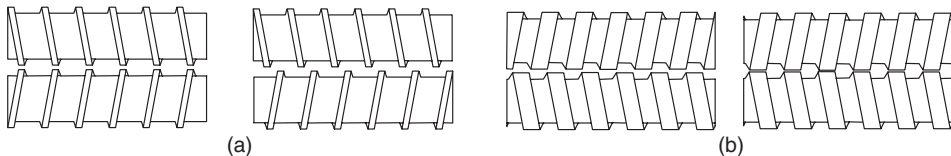


Fig. 10.38 The examples of Leistritz melt conveying, modular CRNI screw elements studied by White and associates. (a) Thin flighted forward matched and staggered; (b) thick-flighted, reverse matched and staggered. [Reprinted by permission from D. S. Bang, M. H. Hong, and J. L. White, "Modular Tangential Counterrotating TSEs: Determination of Screw Pumping Characteristics and Composite Machine Behaviour," *Polym. Eng. Sci.*, **38** 485 (1998).]

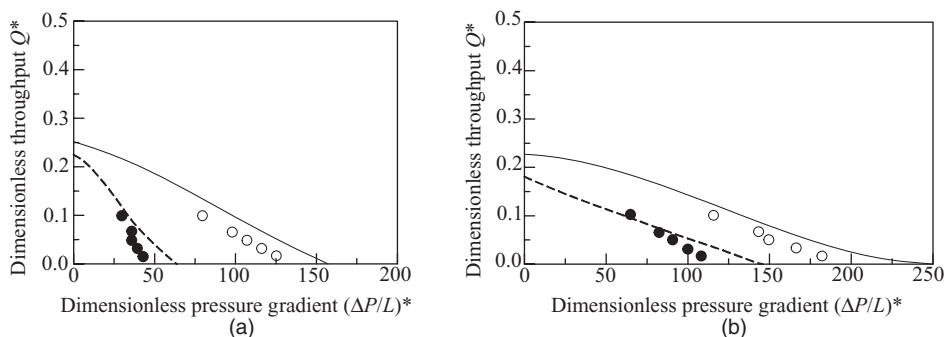


Fig. 10.39 Dimensionless screw-characteristic curves for forward melt-conveying, tangential CRNI modular segments in matched and staggered configurations. (a) Thin-flighted screws; (b) thick-flighted screws; (●) for staggered; (○) for matched. [Reprinted by permission from D. S. Bang, M. H. Hong, and J. L. White, “Modular Tangential Counterrotating TSEs: Determination of Screw Pumping Characteristics and Composite Machine Behaviour,” *Polym. Eng. Sci.*, **38**, 485 (1998).]

result in weak stress fields, even at high rotational speeds, but strong distributive flow fields.

Thiele (7) and Martin (58) discuss a new class of counterflight melting and mixing elements which impart mechanical energy at levels which are comparable to the kneading elements in co-rotating, intermeshing, self-wiping TSEs. In ‘counterflight’ elements, energy is dissipated by deforming or forcing squeezing flows in lobes, whose cross-sectional areas are in constant periodic change because of the counterrotation. Figure 10.40 demonstrates this point. The bilobal kneading element pair shown in Fig. 10.11 is functional only with co-rotating shafts. On the other hand, the modified bilobal pair in Fig. 10.40 can operate in both co- and counterrotating modes. If the number of lobes is increased, as shown schematically by the cross-sectional view of a hexalobal pair of mixing elements, it can operate only in counterrotation.

To allow for high speeds of 300–500 rpm, open-flighted elements are utilized to drag polymer melts over their flights. Thus, the number of interlobal mixing events taking place in hexalobal elements, which is the product of the number of lobes and the rotational speed, is very large. Indeed, versatile hexalobal designs, such as that shown in Fig. 10.41, make excellent distributive and dispersive mixing elements. Such counterflight elements can be used in conjunction with traditional counterrotating segments, but with wider calender gap clearances to allow for higher rotational speeds (58). There are no reported FEM simulations in the literature to describe the flow in fully filled counterflight multilobal element channels.

The Continuous Mixer

The principal characteristics of the CM were discussed briefly in Section 10.1, and discussed in detail by Valsamis and Canedo (59). The CM is a counterrotating, nonintermeshing twin rotor device that affects rapid and efficient melting and mixing of single- or multicomponent polymer systems. The rotors are supported at both ends by conventional bearings. At the feed end, the bearing is isolated from the particulate charge

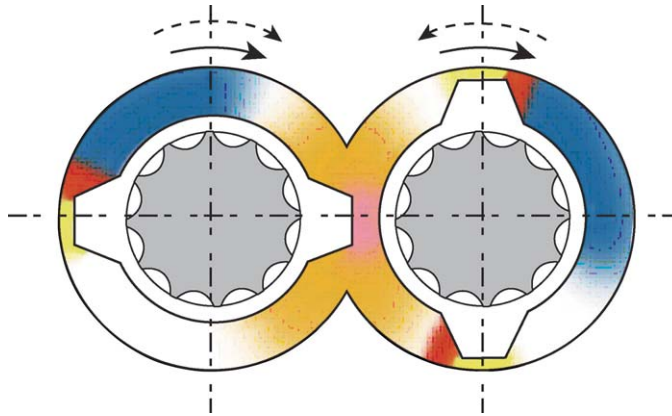


Fig. 10.40 A pair of bilobal elements that operate either in co- or counterrotation and impart mechanical energy in deforming solids or forcing flow in melts filling the available interelement volume. The shear intensity is depicted by the color code going from white to red with increasing intensity. [Courtesy of C. Martin, American Leistritz Extrusion Corp.]

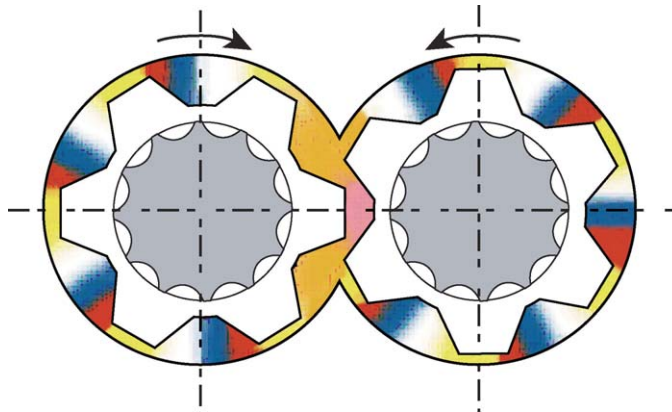


Fig. 10.41 Cross-sectional view of a pair of hexalobal mixing elements of counterrotating, intermeshing TSEs. [Courtesy of C. Martin, American Leistritz Extrusion Corp.]

with a powder (labyrinth) seal, and at the discharge end with a dynamic melt seal.⁷ Rotors are drilled for circulating cooling fluid. Short single-flighted or double-flighted screws, which extend upstream from the hopper opening, deliver the material in starve-fed, controlled mass-flow rate fashion to the mixing chamber. The rotors, shown in Fig. 10.6, are made of two helically twisted wings, approximately 180° apart, with the wings of each rotor twisted in opposite directions. Each wing has a forward and a backward (reverse) pumping section, the reverse being shorter and often twisted by a slightly different angle, in order to provide for forward net pumping. The apex of a wing is offset from the apex of the complementary wing of the same rotor and from the wings of the other rotor. The rotors are housed in cylindrical enclosures, the chamber halves, which communicate with

7. The dynamic seal is a reverse extruder created by machining small multiple-screw channels onto the rotor end rotating in the closed housing. Because of the helix angle, they will pump melt back into the mixing chamber.

each other along the entire mixing chamber. Feed and melt discharge openings are located at the intersection of the chamber halves.

Solids conveying is carried out by the two counterrotating, short starve-fed screws, which are double-flighted in large-size melters/mixers to accommodate high feed rates, often of low bulk density feeds. Particulates are in a moderately fluidized state and are dragged forward by barrel-particulate frictional forces. Screw cooling is important to avoid increased frictional (adhesive) forces between the screw walls and particulates. CMs are effective melters, yet there is only limited published research on the melting mechanisms in these machines. However, based on their high rates of melting, one can surmise that they must employ one or more high mechanical energy dissipating mechanisms of frictional, plastic, and viscous energy dissipation (FED, PED, and VED, respectively), as discussed in Section 5.8. This conclusion is qualitatively substantiated by Valsamis and Canedo (59), who presented the only experimental melting investigation in a full mixing-chamber 2-in-diameter FCM, by carrying out carcass analysis of a 50:50 LDPE/PE immiscible blend.

Example 10.1 Elements of a Plausible Melting Mechanism in Continuous Mixers

The Valsamis–Canedo experiments (60) revealed that extensive melting occurs rather early in the mixing section. Clearly, the energy dissipated at the entrance region of the mixing section is large enough to fuse and partly melt the particulates. This can only be accomplished by the two melting mechanisms that involve polymer particulates, namely FED and PED. It appears, therefore, that the solids are dragged by the rotors toward the converging entrance regions of the “leading faces” of the rotors, the rolling pool regions of Fig. E10.1, where they get compressed and sheared. When they reach the rotor wing-tip clearance region, these compressed particulates are forced to undergo shear deformation at a high rate of the order of $\dot{\gamma}_{\text{app}} \sim \pi D_{\text{max}}/h$, where h is the wing tip–barrel clearance and D_{max} is the wing tip rotor diameter.

Next we assume that the particulate solids at the beginning of the mixing chamber fill the “rolling pool” until the point of the minimum rotor diameter. The maximum degree of particulate bed densification and compaction, as it is forced through

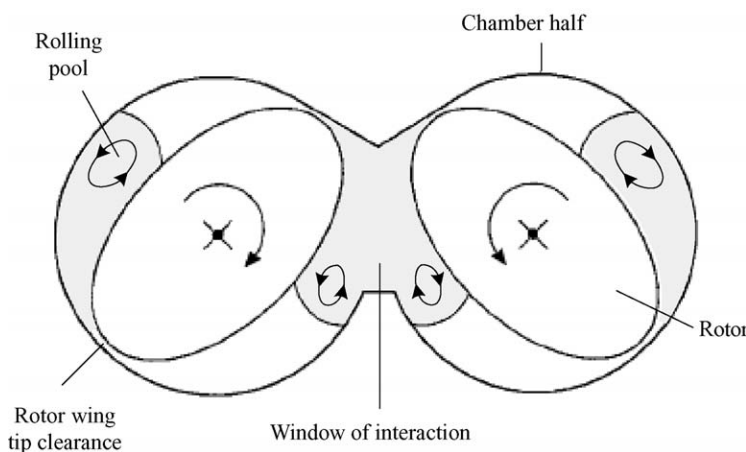


Fig. E10.1 Cross section of the mixing chamber of an FCM, identifying the regions of deformation and flow that are responsible for melting and mixing.

the converging region, is h/H_0 , where H_0 is the maximum and h is the minimum clearance between the barrel and the rotors. Typically, $h/H_0 \sim 10^{-1}$, while the ratio of the particulate solid bulk density to the density of the monolithic solid polymer, the densification measure, is $\rho_b/\rho_s \sim 0.5$. Thus, it is reasonable to assume that a rather significant compressive, squeezing particulate deformation may occur in this region. It follows, then, that PED may at least be operative in deforming and softening the contact regions from particulate to particulate throughout the bed, thus increasing their effective friction coefficient.

In addition, shear deformation is imposed on the particulate bed in the converging rolling pool region. Shear deformation of compressed particulates will result in the creation of velocity differences between adjacent particles. For simplicity, let us consider the shear deformation at the rotor wing tip clearance region. Each particle is subjected to a normal force by its neighbors, F_N , due to the bed compression. The velocity difference between the moving rotor wing-tip surface and the stationary barrel is $\pi D_{\max} N$. Assuming a linear circumferential velocity profile, the difference in velocity of one circumferential layer of particles to the next one in the radial direction is

$$\Delta v = \pi D_{\max} N (d_p/h) \quad (\text{E10.1-1})$$

where d_p is the average particulate diameter, and $d_p/h \sim 10^{-2}$.

Thus, the power dissipated locally by FED is of the order of

$$\dot{W}_{\text{FED}} \sim \pi D_{\max} N (d_p/h) f F_N \quad (\text{E10.1-2})$$

where f is the interparticle friction coefficient. No investigation has yet been made of the roles of PED and FED in the initiation of the rapid volumewise melting in CMs. We believe, based on the physical arguments previously presented, that both PED and FED contribute to the melting mechanisms operating at the beginning of the mixing chamber; of the two, FED will most likely be the dominant one. Together, they apparently produce enough melt to create a solids-rich suspension immediately downstream, which undergoes vigorous dissipative mix-melting in the “window of interaction” region, where complex circumferential, radial rotor-to-rotor, and axial flows, due to the opposing wing-tip twists, take place. In this region, however, not only does dissipative mix-melting take place, but also effective distributive mixing due to the prevailing chaotic flows.

At this juncture it is important to note the rather profound difference between an SSE with L/D values of 22–36, and those continuous mixers with L/D values of 5–10. In the former, which operates at lower frequencies of rotation, the elementary steps of processing occur in a more sequential fashion, with only partial overlap, while in continuous mixers, which operate at higher frequencies of rotation, there is significant overlap and concurrence of elementary steps along most of the axial length. This attribute enables CMs to be rapid and efficient melting and mixing twin rotor devices, but renders the development of theoretical models for their functioning more difficult.

Another difference between the extruders and continuous mixers, pointed out by Valsamis and Canedo, is that, in the former, channel solids and melt flow dominate, and flow over screw flights is a secondary effect (except for power calculations). In contrast, the circumferential flow in CMs (and internal mixers) over the wing tips is the *major* flow component. Thus, while wing tips and screw flights appear to be equivalent machine elements, their role and function are quite different. The wing tips provide high shear

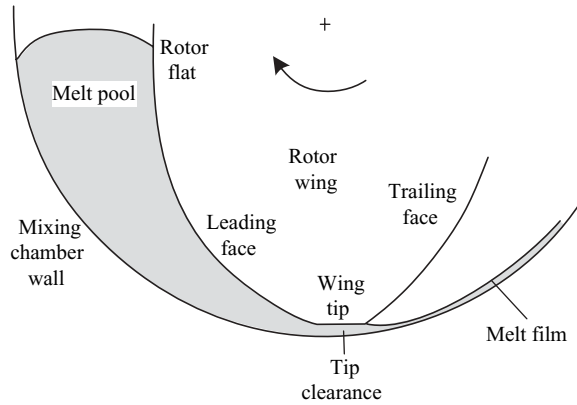


Fig. 10.42 Cross-sectional view of the CM mixing chamber near one of the rotor-wing sections, identifying relevant flow regions and mixer design parameters.

stress regions for the melt to repeatedly pass over circumferentially and, because of their helical twists, force axial circulation. On the other hand, continuous mixers, with their “window of interaction” region promoting rotor-to-rotor interaction and material interchange, are similar to most of the other TSEs, whether co- or counterrotating, as pointed out in Section 10.1.

Wedge Flow Analysis

Considerable research attention has been focused on circumferential flow simulation in narrowing gap wedge-type geometries characteristic to batch and continuous mixers, as well as to mixing regions of TSEs, shown schematically in Fig. 10.42. Bolen and Colwell (61) and Bergen (62) presented early analyses, and Meissner, et al. (63,64) and Wagenknecht et al. (65), were the first to use the lubrication approximation for the calender-like wedge-dynamic pressurization flows involved for non-Newtonian melts in nonisothermal flows. Kim and White used a modified flow-analysis network (FAN) (66) and Cheng and Manas-Zloczower (67,68) and Wong and Manas-Zloczower (69), a two-dimensional FEM model, which, for computational necessity, can only describe *full* mixing chambers.

In this section, we present a simple, one-dimensional lubrication approximation analysis, assuming isothermal conditions and Newtonian melts, along the lines of Section 6.4, dealing with non-parallel plate dynamic pressurization applications with knife coating, calendering, and two roll-mill flows (59). Such analysis, in spite of its simplicity, gives good insight and provides analytical results. Moreover, the lubrication approximation with common CM rotor-design approach angles of 10–20° results in relatively minor errors (5–10%), and the effect of shear thinning can be estimated and taken into account.

The cross-sectional view of the CM mixing chamber in the rotor-wing section is shown schematically in Fig. 10.42. The gap between the rotor and the chamber wall varies from the minimum gap, h , to the maximum gap, H_0 , given, respectively, by

$$h = \frac{1}{2}(D_0 - D_{\max}) \quad (10.2-33)$$

$$H_0 = \frac{1}{2}(D_0 - D_{\min}) \quad (10.2-34)$$

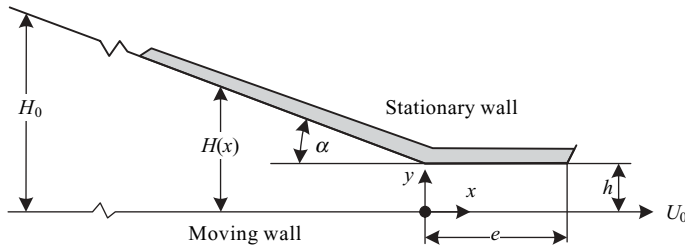


Fig. 10.43 Linear wedge model of the mixing chamber near a wing tip.

where D_0 is the mixer-section barrel diameter, D_{max} the rotor diameter at the wing tip, and D_{min} the diameter at the rotor flat. In the wing tip vicinity, the flow field geometry can be approximated by a wedge at an angle α , the leading face wedge angle, and a parallel plate wing tip clearance, as shown in Fig.10.43. The wedge spacing H , with the stationary coordinate system placed at the entrance to the wing tip, is given by

$$H = \begin{cases} h - x \tan \alpha & -E_0 < x < 0 \\ h & 0 < x < e \end{cases} \quad (10.2-35)$$

where

$$|E_0| = \frac{H_0 - h}{\tan \alpha} \quad (10.2-36)$$

The drag of the moving wall in the wedge section builds up pressure, which is then lost over the parallel plate section. We now derive expressions for the flow rate in the tip region and its dependence on wedge geometry and the velocity fields in the wedge region.

For incompressible isothermal flow of a Newtonian fluid, making the lubrication approximation and the no-slip condition, the equations of continuity and motion become

$$\frac{dv_x}{dx} + \frac{dv_y}{dy} = 0 \quad (10.2-37)$$

$$\frac{dP}{dx} = \mu \frac{\partial^2 v_x}{\partial y^2} \quad (10.2-38)$$

with the boundary conditions $v_x(0) = \pi ND_0 = U_0$ and $v_y(0) = 0$ for all x , and $v_x(H) = v_y(H) = 0$ for $-E_0 < x < 0$ and $v_x(h) = v_y(h) = 0$ for $0 < x < e$. Pressure at planes $x \leq -E_0$ and $x \geq e$ is zero (atmospheric).

In the parallel plate wing tip region, in terms of the pressure and drag flows per unit width, we obtain (see Example 2.5 and Section 6.3)

$$q = \int_0^h v_x(0, y) dy = (q_d + q_p) \quad (10.2-39)$$

where q_d and q_p are the drag and pressure flows per unit width, respectively. The drag flow is given by

$$q_d = \frac{1}{2} U_0 h \quad (10.2-40)$$

and by defining $G_N = q_p/q_d$, we can write Eq. 10.2-39 as

$$q = \frac{1}{2}U_0h(1 + G_N) \quad (10.2-41)$$

Solving for the velocity components in the wedge region, we obtain

$$v_x = \left[1 - 3 \left(1 - (1 + G_N) \frac{h}{H} \right) \frac{y}{H} \right] \left(1 - \frac{y}{H} \right) U_0 \quad (10.2-42)$$

and by using the equation of continuity, given in Eq. 10.2-37, we can derive the following expression for the v_y component:

$$v_y = \tan \alpha \left[2 - 3(1 + G_N) \frac{h}{H} \right] \left(1 - \frac{y}{H} \right) \left(\frac{y}{H} \right)^2 U_0 \quad (10.2-43)$$

By inserting Eq. 10.2-42 into Eq. 10.2-38, we obtain the pressure fields in the wedge region

$$P(x) = \frac{3\mu U_0}{h} \cot \alpha \left[2 - (1 + G_N) \left(\frac{h}{H(x)} + \frac{h}{H_0} \right) \right] \left(\frac{h}{H(x)} - \frac{h}{H_0} \right) \quad (10.2-44)$$

and, in the tip region (see Example 2.5) we obtain

$$P(x) = \frac{6\mu U_0 G_N}{h^2} (e - x) \quad (10.2-45)$$

Equations 10.2-44 and 10.2-45 are equal at $x = 0$, where $H(x) = h$, which yields

$$G_N = \frac{(1 - h/H_0)^2}{1 + 2(e/h) \tan \alpha - (h/H_0)^2} \quad (10.2-46)$$

Thus, we find that, for Newtonian fluid, the pressure-to-drag-flow ratio in the tip region is dependent only on geometric variables. Valsamis and Canedo (59) point out that, for most of the practical designs, $0.25 < G_N < 0.50$, that is, the wedge dynamic pressurization increases the flow rate over the wing tip by 25–50%.

Turning to the velocity fields, we can find from Eq. 10.2-42 that v_x is zero at

$$\frac{y}{H(x)} = \frac{1}{3 \left[1 + (1 + G_N) \frac{h}{H(x)} \right]} \quad (10.2-47)$$

From this equation, by setting $h = H(x) = H_s$ we obtain the stagnation point

$$H_s = \frac{3}{2} (1 + G_N) h \quad (10.2-48)$$

shown in Fig. 10.44. Thus, for $H < H_s$, we find that in both Regions I and II, the melt moves forward in the positive x direction. However, for $H > H_s$, we find Region III near

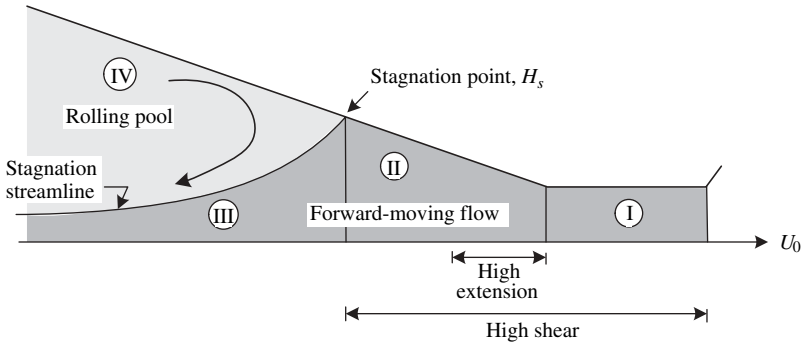


Fig. 10.44 Flow regions in the model wedge.

the moving wall, in which the melt also moves forward, and above it we find Region IV with a rolling, circulating melt pool. Thus, a stagnation streamline exists, as indicated in Fig. 10.44, $y = y_s(x)$, which can be evaluated by recognizing that the flow rate in Region III must equal q , the flow rate over the wing tip parallel plate Region I. Thus, the *net* flow in the rolling pool is zero, and thus

$$\int_{y_s(x)}^{H(x)} v_x dy = 0 \tag{10.2-49}$$

Substituting Eq. 10.2-42 into Eq. 10.2-49 yields

$$y_s(x) = \frac{\frac{1}{2}(1 + G_N)h}{1 - (1 + G_N)[h/H(x)]} \tag{10.2-50}$$

The v_x component of the velocity field along the streamline can be obtained by substituting Eq. 10.2-50 into 10.2-42, to give

$$v_s = v_x|_s = \frac{1 - \frac{3}{2}(1 + G_N)(h/H)^2}{1 - (1 + G_N)(h/H)} \tag{10.2-51}$$

The $v_x(y)$ velocity profiles for Regions III and IV are shown in Fig. 10.45. Using Eq. 10.2-43, we can compute the whole velocity field and plot the velocity vector field. However, we must recall that the model assumed the lubrication approximation and neglected all acceleration and inertia effects.

Turning to the pressure profile $P(x)$ given in Eq. 10.2-44, we note that it reaches a maximum value of

$$P(x)|_M = \frac{3\mu U_0}{(1 + G_N)h} \cot \alpha \left[1 - (1 + G_N) \frac{h}{H_0} \right]^2 \tag{10.2-52}$$

at the axial location corresponding to H_M , where

$$H_M = (1 + G_N)h \tag{10.2-53}$$

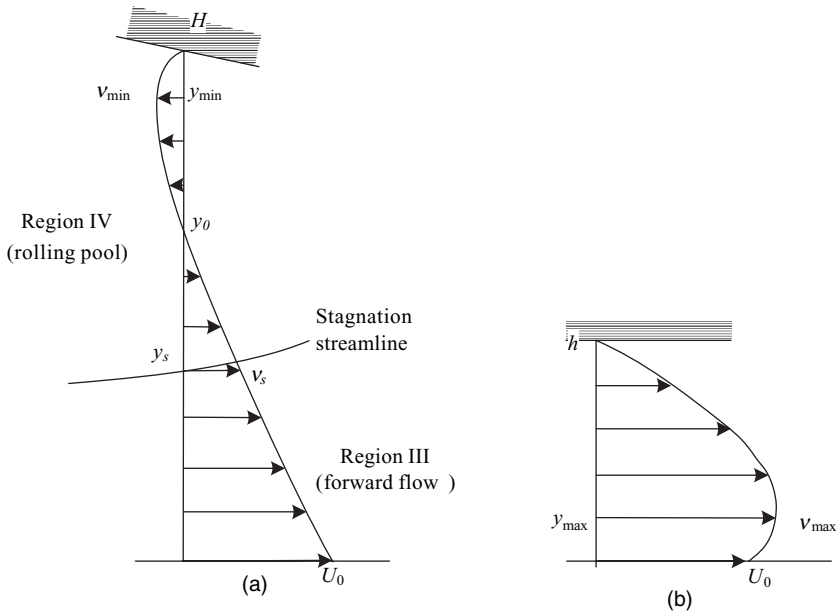


Fig. 10.45 The velocity profiles $v_x(y)$. (a) For Regions III and IV; (b) for Region I.

The dimensionless pressure profile is plotted against the dimensionless x direction in Fig. 10.46. Note that the maximum value is attained upstream of the parallel tip section, and $P(x)$ is the only parameter that can be measured with relative ease in an FCM by placing a transducer at the mixer section of the barrel wall. Valsamis and Canedo (59), working with HDPE and a non-Newtonian melt being processed in 4-in-diameter FCM, reported qualitative agreement with the predictions, and the same order of magnitude of the maximum pressure given by Eq. 10.2-52.

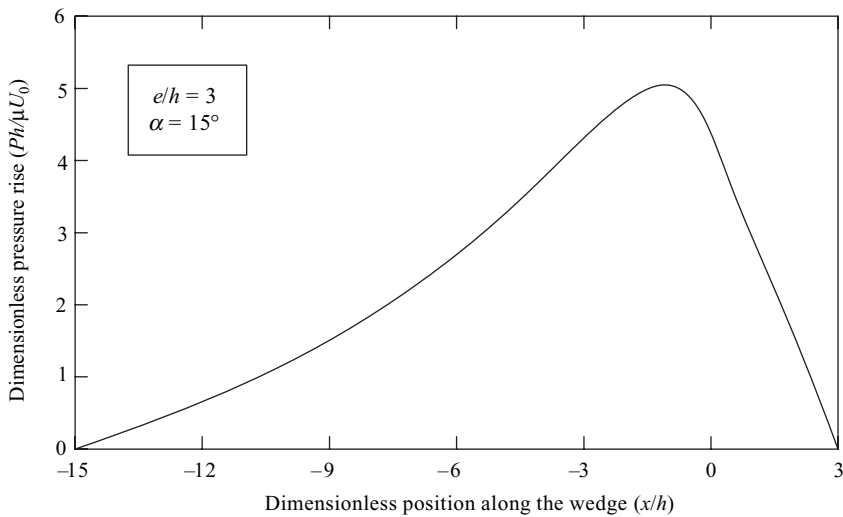


Fig. 10.46 The dimensionless pressure profile developed in Regions I–IV by dynamic drag pressurization.

In addition to the Newtonian fluid, Valsamis and Canedo (70) also used the Carreau constitutive equation to solve the continuity equation (Eq. 10.2-37) together with the following form of the equation of motion

$$\frac{dP}{dx} = \frac{\partial}{\partial y} \left(\frac{\eta_0}{[1 + (\lambda\dot{\gamma}^*)^2]^{\frac{1-n}{2}}} \right) \tag{10.2-54}$$

where, for computational simplicity, they used the Newtonian shear rate $\dot{\gamma}^*$ obtained by differentiating v_x with respect to y , Eq. 10.2-42,

$$\dot{\gamma}^* = \left| 1 - 3 \left[1 - (1 + G_N) \frac{h}{H} \right] \left(1 - \frac{2h}{H} \right) \right| \frac{U_0}{H} \tag{10.2-55}$$

obtained the numerical solution and non-Newtonian $G = q_p/q_d$ values shown in Fig. 10.47. Valsamis and Canedo found that the non-Newtonian $G = q_p/q_d$ parameters, when used with the Newtonian expressions for the pressure, $P(x)$. Equations 10.2-44 and 10.2-45, give results that agree more closely with experimentally obtained $P(x)$ data.

The preceding computational model was extended to allow for nonisothermicities, through the use of the Carreau–Yasoda model (71)

$$\eta = \frac{\eta_0 e^{-\beta(T-T_R)}}{[1 + (\lambda\dot{\gamma})^2]^{(1-n)/2}} \tag{10.2-56}$$

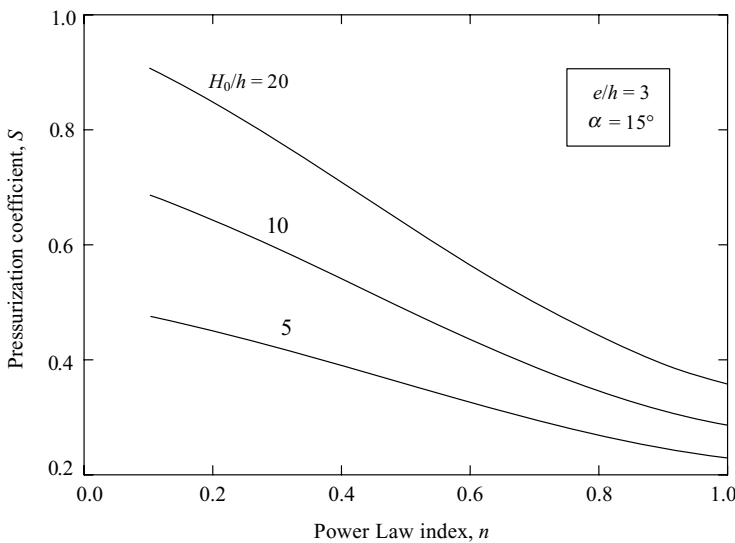


Fig. 10.47 The effect of the Power Law index in the Carreau model, and the melt-pool size for a characteristic model wedge with $e/h = 3$ and $\alpha = 15^\circ$ on the non-Newtonian q_p/q_d parameters. [Reprinted by permission from L. N. Valsamis and E. L. Canedo, “Mixing in the Farrel Continuous Mixer” in *Mixing and Compounding of Polymers*, I. Manas-Zloczower and Z. Tadmor, Eds., Hanser, Munich, 1994.]

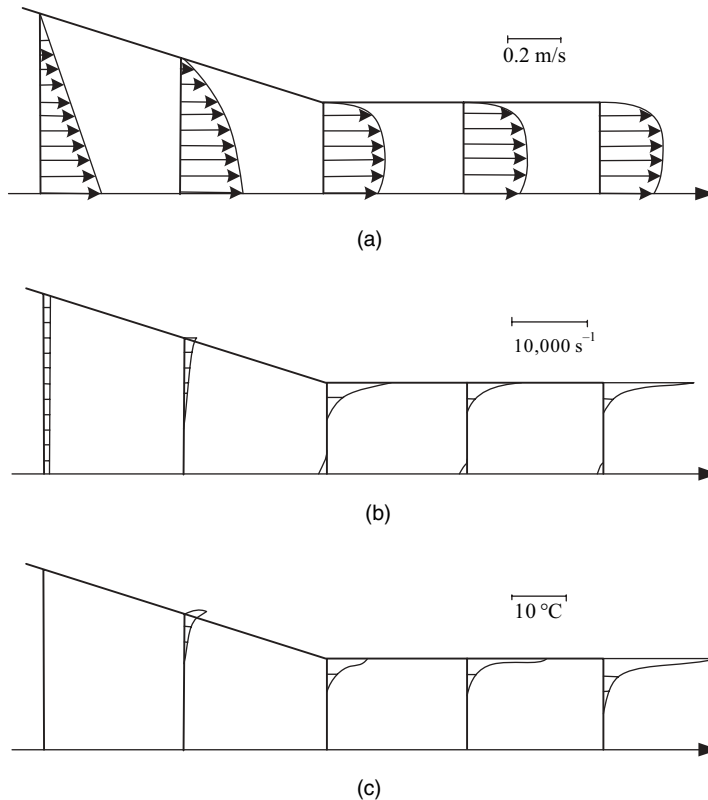


Fig. 10.48 Numerical simulation results of nonisothermal flow of HDPE, Melt Flow Index MFI = 0.1 melt obeying the Carreau–Yagoda model for a typical FCM model wedge of $e/h = 3$ and $= 15$. (a) Velocity; (b) shear rate; and (c) temperature profiles [Reprinted by permission from E. L. Canedo and L. N. Valsamis, “Non Newtonian and Non-isothermal Flow between Non-parallel Plate – Applications to Mixer Design,” *SPE ANTEC Tech. Papers*, **36**, 164 (1990).]

The equations of continuity, motion, and energy, using the constitutive equation (Eq. 10.2-56), were solved numerically only for Regions I and II, where most heat is generated, invoking the lubrication approximation, and assuming that conduction takes place only in the y (radial) direction and that there is no convective heat transfer. The boundary conditions used were an adiabatic rotor and constant chamber temperature. Calculated results are shown in Fig. 10.48. The results indicate very large shear rates, but a moderate temperature rise, due to VED in the melt layer occupying one-third of the tip clearance closest to the rotors, because of the short residence time. Such results are important for the estimation of the total shaft energy converted into heat in the axial section of the mixing chamber, which is partially filled with polymer melt, and not the first upstream part, where melting occurs.

The original CM was extended by a number of polymer processing equipment manufacturers to include in-line, axial, two single screw pressurization and melt pumping elements feeding a gear pump. The advantage of the axial discharge continuous mixer over CMs is, of course, pressurization capability, while the drawbacks are the loss of the discharge bearing and the ability to cool the rotors. The loss of the discharge support

bearing can become limiting, especially for large size, high capacity, postreactor finishing applications.

The two counterrotating rotors in the mixing chambers are under dynamic forces which are due, on the one hand, to the hydrodynamic separating forces generated in the region of the window of interaction, which are largest in the transition region from the feed screws to the mixing chamber, and, on the other hand, the lubrication hydrodynamic lift forces generated at the wedge and tip clearance regions, which oppose the separating forces to degrees that depend on the rotor orientation and the wing tip helical twist. Under these two opposing forces, as well as their own weight, the two rotor shafts respond in a dynamic deflection mode, which may become the cause of metal-to-metal contact and wear, especially between the screws and barrels in the dual, single screw discharge pumps.

The dynamic analysis of the shaft deformation problem requires the simultaneous solution of the real fluid mechanical problem, that is, a partially filled mixing chamber with an axially changing solids content, and the solid mechanics problem of deformation of the variable cross-section, counterrotating shafts. This is not feasible at this time, because of the inability of FEM CFM schemes to handle these partially filled chamber flows. Although not examined, this problem can be addressed by combining the full mixing chamber fluid mechanical simulations, such as by Manas-Zloczower (67–69,72) and Ishikawa et al. (73), with the solid mechanics shaft deformation CAD packages. On the other hand, Ishikawa et al., as part of the series of three-dimensional FEM investigations, obtained numerical results on the velocity, temperature, and pressure fields of the second stage of the LCM 100G, a 100-mm barrel diameter CM, developed by Kobe Steel. The LCM 100G and the second-stage rotors are shown schematically in Fig. 10.49. Since the second stage is usually operated *almost filled*, the FEM simulation results, which hold only for filled mixer chambers, are quite relevant. For this reason, they compare them with experimentally obtained pressure and temperature results on the actual mixing chamber barrel at positions shown in Fig. 10.50.

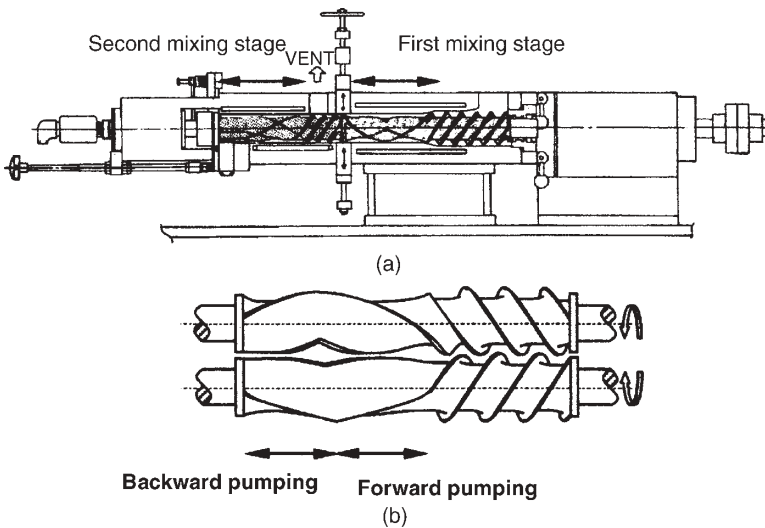


Fig. 10.49 The LCM 100G CM. (a) Schematic representation; (b) the second stage LCM rotors.

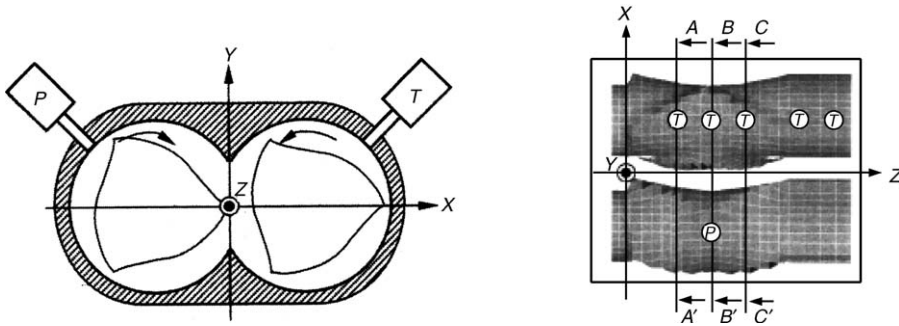


Fig. 10.50 Location of the pressure gauge (*P*) and the thermocouples (*T*) at the five axial barrel positions. The three cross sections *A–A'*, *B–B'* and *C–C'* are used for contour plots of the numerical results. [Reprinted by permission from T. Ishikawa, S. Kihara, K. Funatsu, T. Amaiwa, and K. Yano, “Numerical Simulation and Experimental Verification of Nonisothermal Flow in Counterrotating Nonintermeshing Continuous Mixers,” *Polym. Eng. Sci.*, **40**, 365 (2000).]

The simulation is for a shear thinning fluid and nonisothermal flow. The equations of change are

$$\nabla \cdot \mathbf{v} = 0 \tag{10.2-57}$$

$$-\nabla P + \nabla \cdot \boldsymbol{\tau} = 0 \tag{10.2-58}$$

$$\rho C_p \mathbf{v} \cdot \nabla T = k \nabla^2 T + \boldsymbol{\tau} : \nabla \mathbf{v} \tag{10.2-59}$$

The constitutive equation is

$$\boldsymbol{\tau} = 2\eta \dot{\boldsymbol{\gamma}} \tag{10.2-60}$$

where

$$\eta = H(T)F(\dot{\boldsymbol{\gamma}}H(T)), \quad II\dot{\boldsymbol{\gamma}} = \sqrt{2II\dot{\boldsymbol{\gamma}}} \tag{10.2-61}$$

$$F = \eta_0 [1 + \lambda_c^2 (2II\dot{\boldsymbol{\gamma}})]^{(n-1)/2} \tag{10.2-62}$$

$$H(T) = \exp[-\beta(T - T_a)] \tag{10.2-63}$$

The HDPE melt used has the rheological and thermomechanical parameters listed in Table 10.4. The boundary conditions employed are listed in Table 10.5. There was no

TABLE 10.4 Material Data of High Density Polyethylene

Carreau model parameter	λ	1.360
Carreau model parameter	n	0.296
Zero shear rate viscosity	η_0 [Pa · s]	52,930
Arrhenius' law parameter	β [1/K]	0.01
Reference temperature	T_a [K]	503.0
Density	ρ [kg/m ³]	752.0
Specific heat	C_p [J/(kg · K)]	1,900
Thermal conductivity	κ [W/(m · K)]	0.225

TABLE 10.5 Boundary Conditions

Inlet cross section	Constant flow rate (375, 455, 500 kg/h)
Barrel inner surface	No slip
Rotor surface	Tangential velocity by screw rotation
Outlet cross section	Outflow

mixing-chamber barrel temperature control, the rotational speed was 420 rpm, and the three flow rates used were 375, 455, and 500 kg/h. The calculated average temperatures and their measured counterparts at the five axial thermocouple positions are shown in Fig. 10.51. As expected, decreasing the flow rate at constant rpm increases the temperature rise. The computed values, although in general agreement with the experimentally measured ones, are, however, less sensitive to flow rate. Figure 10.52 plots the temperature contours at cross section B–B' for 500 kg/h. The difference between the maximum and minimum temperatures is 17°C. The temperatures are highest at the adiabatic rotor surfaces, and lowest at the cooling chamber barrel wall. Figure 10.53 plots the velocity vectors at plane (B–B') and the axial velocity contours at cross-sections (B–B') and (C–C') at 500 kg/h.

High velocity vectors are obtained everywhere, and in particular at the window of interaction region. As expected, positive $dP/d\theta$ vales are calculated behind each of the wing tip gap regions. Small axial positive and negative velocities, due to small axial pressure drops, are calculated at (B–B') the transition between the forward- and backward-pumping rotor sections. However, at (C–C'), while axial velocities are only about 5–15% of the circumferential, negative values are calculated in the large gap areas due to the backward-pumping mechanism of the helically twisted wings in this section.

The opposite occurs at the forward-pumping section (A–A'). However, axial velocities, although still beneficial for distributive mixing, are an order of magnitude of the

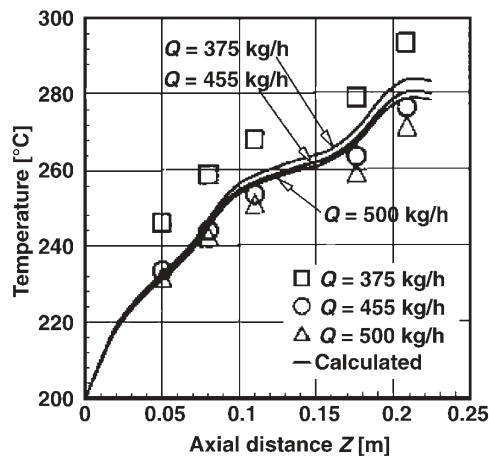


Fig. 10.51 Comparison between the calculated (average) and experimental temperatures at five axial positions. The entrance melt temperature was assumed to be 200°C. [Reprinted by permission from T. Ishikawa, S. Kihara, K. Funatsu, T. Amaiwa, and K. Yano, “Numerical Simulation and Experimental Verification of Nonisothermal Flow in Counterrotating Nonintermeshing Continuous Mixers,” *Polym. Eng. Sci.*, **40**, 365 (2000).]

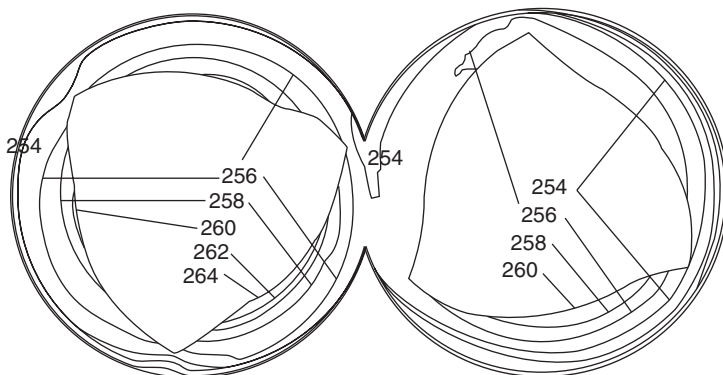


Fig. 10.52 Calculated temperature contours at cross section (B–B′) at 500 kg/h. [Reprinted by permission from T. Ishikawa, S. Kihara, K. Funatsu, T. Amaiwa, and K. Yano, “Numerical Simulation and Experimental Verification of Nonisothermal Flow in Counterrotating Nonintermeshing Continuous Mixers,” *Polym. Eng. Sci.*, **40**, 365 (2000).]

circumferential velocities, which are responsible for melting, heating, and dispersive mixing. Finally, Ishikawa et al. calculated the pressure as a function of the circumferential angle, and compared it with the experimentally obtained pressure transducer trace at (B–B′). The results are shown in Fig. 10.54.

Calculated results show a repetitive peak at 0° (120°), while the pressure transducer trace registers three peaks. Since the wing tip passes in front of the gauge every 120°, the

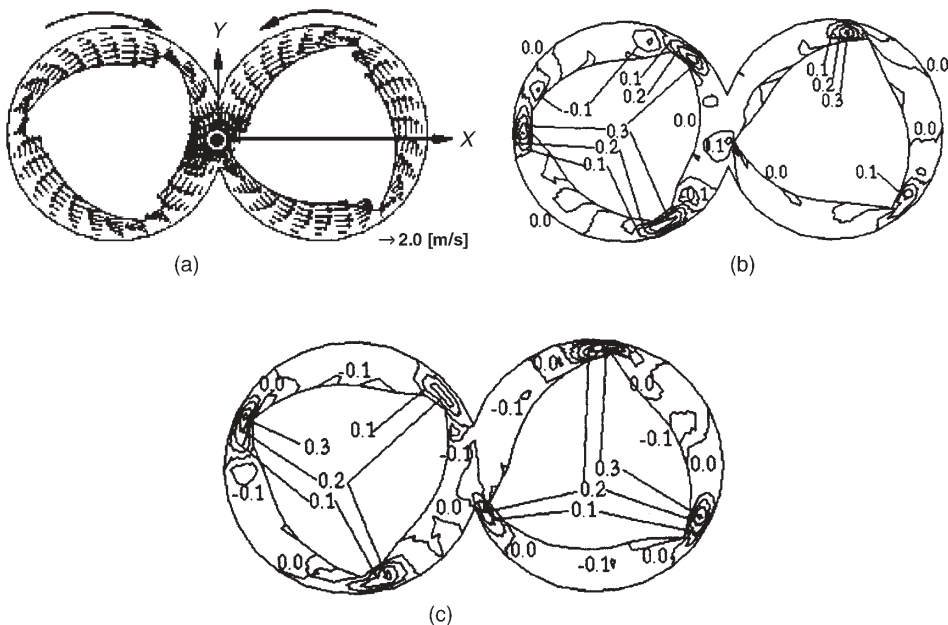


Fig. 10.53 Mixing-chamber melt velocities at cross sections (B–B′) and (C–C′). (a) Velocity vectors at (B–B′); (b) axial velocity contours at (C–C′); (c) axial velocity contours at (C–C′); all at 500 kg/h. [Reprinted by permission from T. Ishikawa, S. Kihara, K. Funatsu, T. Amaiwa, and K. Yano, “Numerical Simulation and Experimental Verification of Nonisothermal Flow in Counterrotating Nonintermeshing Continuous Mixers,” *Polym. Eng. Sci.*, **40**, 365 (2000).]

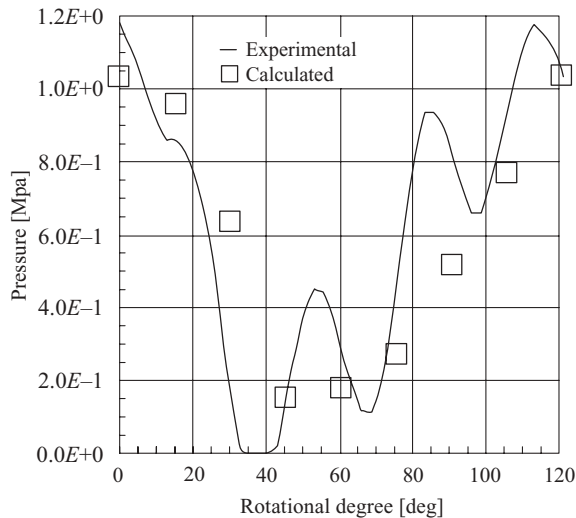


Fig. 10.54 Comparison between calculated and experimental values of $P(\theta)$ at (B–B') and 500 kg/h. [Reprinted by permission from T. Ishikawa, S. Kihara, K. Funatsu, T. Amaiwa, and K. Yano, "Numerical Simulation and Experimental Verification of Nonisothermal Flow in Counterrotating Nonintermeshing Continuous Mixers," *Polym. Eng. Sci.*, **40**, 365 (2000).]

two extra local maxima are most probably due to small unfilled regions in the chamber. Other than that, there seems to be good agreement between calculated and measured pressure values. In summary, simulating an almost fully filled second-stage LCM mixer chamber with the robust three-dimensional FEM scheme of the Funatsu group, which assumes full chambers, proves to be useful to engineering practice. Yet for predicting total energy consumption and for answering scale-up questions, we need a better understanding of the melting step.

10.3 CO-ROTATING, FULLY INTERMESHING TWIN SCREW EXTRUDERS

We have introduced some of the main design features and attributes of the Co-TSEs in Section 10.1. We devote this section to the discussion of the elementary steps of processing as they occur in these devices. We note the following references, chapters in edited texts that provide detailed information on the design features and capabilities of equipment provided by the major Co-TSE manufacturers: Andersen of Coperion Werner and Pfleiderer (74,75), Sakai of Japan Steel Works (76,77), Todd of APV-Baker Perkins (12,78), and Mack of Berstorff (79). Anderson (75), in an overview of Co-TSE design and functions, points out that the two most important equipment parameters are (a) the outer-to-inner diameter ratio (OD/ID), shown for bilobal screws and kneading elements in Fig. 10.55, and (b) the specific torque, defined as the ratio of the torque, M , to the cube of the screw-to-screw centerline distance, C_L . The gap between adjacent screw elements is the minimum required for mechanical safety. Thus, it is assumed to be zero in evaluating C_L . Since the crest of one screw (kneading disk) traces the root and flank of the mating screw, one screw wipes its associated mate.

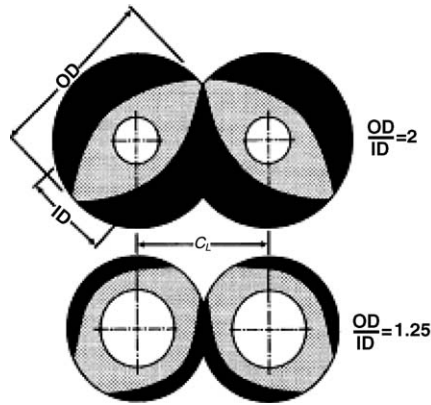


Fig. 10.55 Two extremes of OD/ID ratios for two-lobe machines.

The OD/ID ratio defines the free volume, which can be filled by the polymer. Thus, the larger the OD/ID, the larger the equipment capacity, but as can be seen in Fig. 10.55, the smaller the available shaft diameter for torque transmission, the lower the applied average shear rate. Thus, the design challenge for building a high rate Co-TSE, that is, one with high OD/ID, is to be able to supply it with high specific torque, which relates to the power provided to the free volume. If this is achieved, then the Co-TSE can operate at higher degrees of fill, high rates, and lower rpm, resulting in lower discharge temperatures. This trend has been developing over the last 30 years or so, as can be seen in Table 10.6, which lists the evolution of Coperton Werner and Pfeleiderer Co-TSEs with both increased OD/ID and specific torque, $M/(C_L)^3$.

The Megacompounder, developed in 1995 by Heidemeyer (80), achieved the highest specific torque and OD/ID ratio (for the entire spectrum of available machine sizes and barrel diameter, 32–380 mm) by utilizing 24 shaft splines to transmit the shaft energy to the screw/kneading elements, instead of the usual one-to-six keys. The 30% increase in specific torque from the Super- to the Megacompounder required gear box redesign for delivering greater power and this, together with specific screw configurations, allowed for rotational speeds of up to 1200 rpm. Finally, it is desirable to have the two important parameters of OD/ID and $M/(C_L)^3$ constant over the available size range of any given type

TABLE 10.6 Comparison of the Six Generations of ZSK Machines

	Z	OD/ID	$M/(C_L)^3$
1. ZSK-standard	3	1.22	3.7–3.9
2. ZSK-variable	3	1.22	4.7–5.5
1. ZSK-standard	3	1.22	3.7–3.9
3. ZSK-variable	2	1.44	4.7–5.5
4. ZSK-compact	2 or 3	1.22 or 1.44	7.2–8.0
5. ZSK supercompounder	2	1.55	8.7
6. ZSK megacompounder	2	1.55	11.3
7. ZSK mega plus	2	1.55	13.6

Note: OD = screw outer diameter; ID = screw inner diameter; α = centerline distance; M = torque/shaft; Z = number of flights (75).

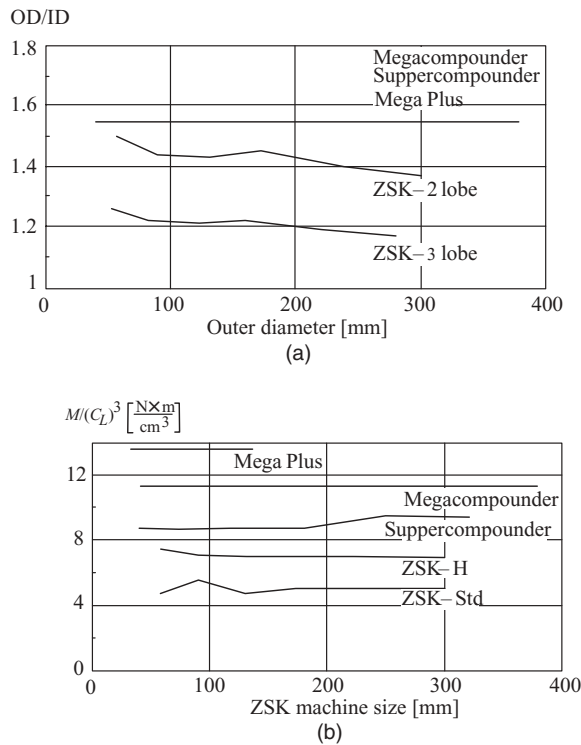


Fig. 10.56 Different ZSK generations over a range of barrel diameters. (a) Values of OD/ID; (b) values of the specific torque available. [Reprinted by permission from P. G. Andersen, “The Werner and Pfleiderer Twin Screw Co-rotating Extruder System,” in *Plastics Compounding*, D. B. Todd, Ed., Hanser, Munich (1998); P. G. Andersen, private communication.]

of equipment, for example, supercompounders. The reason being that scale-up become easier because both the feed intake capabilities and power acquirement do not change.

The latest ZSK Mega Plus generation, developed with further gear box improvements, achieves a 13.6 specific torque value maintaining OD/ID at 1.55. Currently, the largest size Mega Plus ZSK is 133 mm. Figure 10.56 provides data on the values of these two parameters for several generations of Coperion ZSK Co-TSEs.

As mentioned in the introduction to this chapter, Co-TSEs are modular in barrel components, with individual rotating shaft elements and element sequences associated with each of the barrel segments in order to achieve a specific primary process goal, such as affecting melting. Typical types of barrel segments are shown in Fig. 10.57. Each barrel segment is 4 L/D long, and typical total machine lengths are in the range of 24–40 L/D for compounding; for large-size postreactor finishing operations, long L/D are necessary. Co-TSEs are used to carry out reactive processing to provide enough time to the dispersed and/or mixed reactant so that $t_{\text{react}}/t_{\text{res}} \sim 10^{-1}$ (see Section 11.2). One of ‘Todd’s rules’⁸ is that “each elementary step in co-rotating, intermeshing TSEs takes 4 L/D (one barrel section) to be completed.” Thus, for solids transport, melting, additives feeding, mixing,

8. D. B. Todd, private communication.

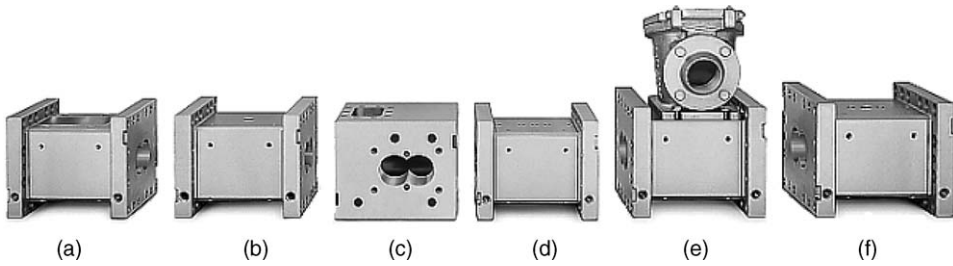


Fig. 10.57 Typical 4 L/D Co-TSE barrel segments. (a) Feed throat; (b) melting; (c) downstream feed section; (d) mixing; (e) devolatilization; (f) pumping and limited pressurization. [Courtesy of P. Andersen Coperion Werner and Pfleiderer, Ramsey, NJ.]

devolatilization, and pumping, we need a minimum of 24 L/D length. For large postreactor extruders, which primarily melt and pelletize powders, $L/D \sim 20$.

Feeding and Transport of Particulates and Additives in Co-rotating, Twin Screw Extruders

As is common with twin screw equipment, Co-TSEs are starve-fed by metering feeders, that is, their solids conveying capacity exceeds that of the downstream requirements, making feed rate independent of the *screw speed*. This makes screw speed an *independent variable*, and permits the control of residence time, degree of fill, and specific energy input (kw-h/kg). This, of course, at the expense of having to use feed metering equipment. Optimal equipment capability utilization is reached when all of the available power is fully utilized at the feed intake upper limit. Feeders must be capable of adjusting the operating feed-rate setting to within 1–2% over a 10-s period. This is because the typical residence time within a process section, where an elementary step takes place, is about 10 s. With feeders having such capabilities, there is no need for preblending. The feed-throat diameters are usually 1.5 D , allowing for the accommodation of very low bulk-density powders. Only with the very large-capacity finishing line extruders can feeding of powders at rates of 50–100 t/h be troublesome, because the stream of excluded air exiting the feed throat causes feed fluidization.

Todd (3) notes that (1) in *single-stage* compounding processes and extruders, all dry feed components are metered in a single feed throat; liquid additives may be injected through downstream ports. Non-abrasive additives at low concentrations (e.g., pigments) can be co-fed with the polymers. (2) In *multi-stage* compounding processes and extruders, feed ingredients, such as the preceding, are fed and melted in the first melting section (zone). Downstream this zone, a section of feed screws, running starved, passes by the second feed part, where ingredients such as the following are introduced, typically through a side-entering feeder: long fibers to be mixed with the melted polymer(s), thus minimizing (not avoiding) fiber length attrition and machine wear; polymers with much lower viscosities than those fed in the feed stage. If large concentrations of such low-viscosity polymers are required by the blend application, more than one port can be used for sequential addition of such low viscosity polymer to avoid “scalping,” leading to incomplete mixing or phase inversion (see Section 11.3); and liquid, low-viscosity additives that would cause first single-stage powder feed to agglomerate. Again, more than one port may be required for higher concentrations; abrasive solid additives, whereby the

molten first-stage polymer(s) provide lubrication protection to the machine; additional low density particulate feeds to achieve higher throughput if feed throat feeding capacity is exceeded; and finally, reactive liquid ingredients in low concentrations, which are introduced through a barrel tap fitted, small-diameter tube by a liquid-metering pump. The exit tip may extend into the melt if it is introduced in a rotating disk region (81) so that the reacting ingredient enters the bulk of the flowing melt to be distributively mixed. High pitch screw conveying elements (e.g., 2.0 D) are typically used in the feed zone. For low bulk-density feed, TSE manufacturers have transformed self-wiping feed screw element profiles into square-channel profiles, allowing for up to 40% increase in free volume and powder conveying capacity (75).

Melting in Co-rotating Twin Screw Extruders

Melting in Co-TSEs takes place primarily and most commonly in kneading elements that are full of compacted particulates because of a flow restriction, such as reverse kneading or screw elements; the restriction creates a certain filled length and generates the needed pressurization for the melt (or partially molten polymer) to flow through the restriction. The evolution of melting in such filled kneading-element channels was studied experimentally by Kim (82) and Gogos et al. (17) utilizing carcass analysis, and is shown schematically in Fig. 5.14. Their conclusions as to the genesis and evolution of melting appear as comments in that figure. They found that interparticle FED, defined by Eq. 5.9-1 with evidence of it shown in Fig. 5.15, takes place early and does not require full compaction. At full compaction, PED, defined by Eqs. 5.9-2 and 5.9-3, becomes a *dominant* melting mechanism. It is caused by the “mandatory” and repetitive compressive/squeezing deformations brought about by the kneading elements (see Fig. 5.16).

Kim (82) estimated PED from compressive experiments on molded disks of a number of materials, as shown in Fig. 5.17. High modulus, yielding, amorphous polymers such as PS dissipate a large amount of mechanical energy, compared to lower modulus, polycrystalline polymers, as shown again in Fig. 5.17. Iso-PED and corresponding iso- ΔT_{adiab} contours can be obtained from a number of cylindrical specimens compressed to various strains at various initial temperatures, as shown in Fig. 5.18(a) and 5.18(b). From such plots, the expected ΔT_{adiab} from one or more successive ϵ_i deformations can be obtained, as shown in Fig. 5.19, for PS compressed to successive $\epsilon_0 = 1$ deformations.

The experimental work of Kim (82) and later on of Gogos, Qian, Todd, and Kim (83–86) demonstrated the dominant role of PED, *not only in initiating but also appreciably advancing* melting almost to completion for high modulus, yielding under compression polymers, such as PS. Thus, they created a simplified but physically reasonable model for predicting the course of melting, by assuming that the compacted particulate assembly can be reasonably represented as a “solids continuum” undergoing *repeated* and *spatially uniform* deformations and deformation rates determined by geometric and process variables, and getting heated/melted in the fashion shown in Fig. 5.19. With this approach, they were able to make good engineering estimates of the actual melting length in full Co-TSE kneading elements. This simple model is as follows:

1. First, the average “transit time,” t_{transit} , needed by the charge to go over one lobe is calculated

$$t_{\text{transit}} = \frac{V_{\text{avail}}}{\dot{m}/\rho_b} \quad (10.3-1)$$

where

$$V_{\text{avail}} = 3.08HDL_{\text{lobe}} \quad (10.3-2)$$

and where D = OD of the bilobal element, \dot{m} is the mass flow rate, and H is the maximum channel depth, that is, the difference between OD and ID of the kneading element. Thus,

$$t_{\text{transit}} = 3.08H \cdot D \cdot L_{\text{lobe}}\rho_b/\dot{m} \quad (10.3-3)$$

2. Second, the number of rotations that takes place during the transit time of the charge over one lobe, N_R , is given as

$$N_R = t_{\text{transit}}RPS \quad (10.3-4)$$

where RPS is the operating rotational speed (rev/s).

4. With the preceding, the number of compressions experienced by the charge during its entire transit over one lobe, N_C , is

$$\begin{aligned} N_C &= \frac{4}{3}N_R \\ &= \frac{4}{3} \cdot t_{\text{transit}} \cdot RPS \\ &= \frac{4}{3} \times 3.08HDL_{\text{lobe}}\rho_bRPS/\dot{m} \\ &= 4.1HDL_{\text{lobe}}\rho_bRPS/\dot{m} \end{aligned} \quad (10.3-5)$$

Thus, the number of PED-producing, kneading element pair compressions that the particulate charge is subjected to during its transit time over one lobe decreases with increasing mass flow rate and increases with increasing rotational speeds, increasing bulk density (degree of compaction), increasing diameter and maximum channel depth (related to (OD/ID)) and finally, it increases with increasing lobe length. There is another effect caused by increasing the lobe length L_{lobe} , which is shown schematically in Fig. 10.58. As the axial length (width) of the lobe is increased, the edge effects of reduced pressure generated become less important and the wide lobe becomes a more effective compressive “device.”

The effectiveness of PED to melt PS is shown in Fig. 10.59 as the melting evolution of the carcass of PS being melted by *two forward* wide-lobe kneading sequences $2 \times [45/5/42]$, followed by *one reverse* narrow-lobe sequence 45/5/14 (R) at 180°C, 180 rpm and 6.9 kg/h. The Co-TSE used was the Twin Screw Mixing Element Evaluator (TSMEE[®]) developed by the Polymer Mixing Study of PPI, which has the Coperion Werner and Pfeiderer ZSK 30 design parameters: 30.65-mm barrel diameter, 21.0-mm screw-root diameter, 26.2-mm centerline distance, and length of one lobe of 8.4 mm. Under these processing conditions, PS undergoes three compressions during its transit time over one lobe. Experimentally, practically complete melting is observed in one lobe, Fig. 10.59(a).

Figure 10.59(b) indicates that as few as three $\varepsilon = 1$, spatially uniform compressions of PS are capable of heating it past its T_g . Thus, there is good agreement between the

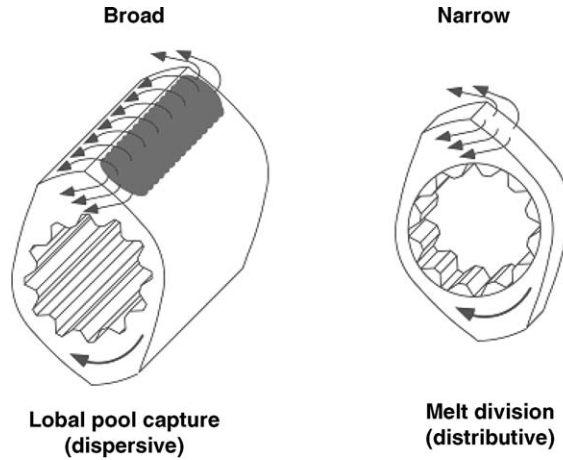


Fig. 10.58 The effect of increasing kneading-lobe length on its compressive and squeezing capabilities. [Courtesy of C. Martin, American Leistritz Corp.]

experimental and simple PED model results. Kim and Gogos (85) conducted a number of carcass analysis, PP melting experiments at varying barrel temperature, mass flow rate, rotational speed, and width of the lobe. The results are shown in Table 10.7. The agreement between experimental carcass analysis results and those calculated by the PED model is good. The observed melting lengths are either the same or shorter than the predicted ones.

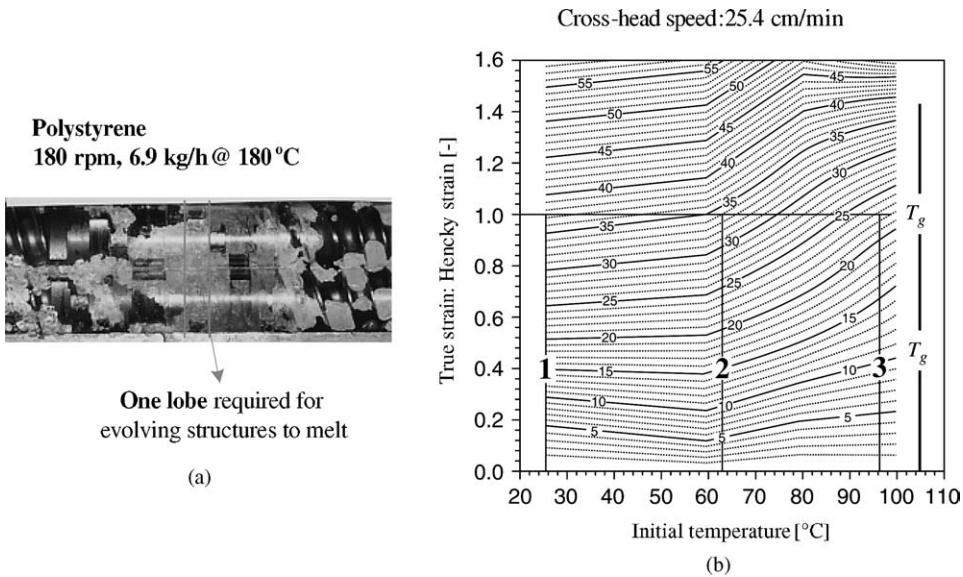


Fig. 10.59 (a) Picture of the carcass of the compressed PS pellet bed in the melting region of the TSMEE, indicating that PS reaches T_g in one lobe axial distance. (b) Iso-adiabatic temperature increases during compressive deformation experiments on cylindrical PS samples at various initial temperatures, indicating that three $\epsilon = 1$ compressions can bring PS to its glass transition temperature. [Reprinted by permission from M. H. Kim, Ph.D Dissertation, Department of Chemical Engineering, Stevens Institute of Technology, Hoboken, NJ, 1999.]

TABLE 10.7 Comparison of the Experimentally Obtained Melting Lengths with those Calculated by the Simple PED Model of Kim and Gogos (86)

Experimental Conditions $T_b/\dot{m}/\text{rpm}/\text{screw type}$	Melt Temperature °C	Solid-Plug Velocity	Holding Time per Lobe	Predicted Number of Lobes	Observed Number of Lobes
150/5/60/s1	163	0.14	5.93	3	3
140/10/60/s1	166	0.28	2.96	6	4
180/10/60/s1	185	0.28	2.96	6	4
140/10/120/s1	187	0.28	2.96	3	2
180/10/120/s1	195	0.28	2.96	3	3
140/40/240/s1	187	1.13	0.74	6	4
180/40/240/s1	190	1.13	0.74	6	5
140/5/60/s2	174	0.14	2.82	6	4
180/5/60/s2	185	0.14	2.82	6	5
140/40/240/s2	197	1.13	0.35	13	10
180/40/240/s2	199	1.13	0.35	13	12

Note: Basel PP 6523 (MFI = 4), $L_1 = 8.4$ mm, $L_2 = 40$ mm kneading lobe lengths.

The reason for this discrepancy is that the PED model does not include the melting mechanism of VED, which, as shown in Fig. 5.14, takes place primarily in the melt-rich suspension stage of melting. Kim et al. found that their PED model works very well with polystyrene (PS) which, because of its tough ductile behavior under compression, generates very high PED values; Fig. 5.17 indicates a bulk temperature increase of around 30°C for a single $\varepsilon = 1$ compression. Furthermore, as seen in Fig. 5.1, the specific enthalpy needed to heat PS to $T = T_g$ is about 100 kJ/kg. Under these conditions, with only a few compressive deformations needed to plasticate (bring to a temperature above T_g) PS, VED cannot establish itself as a contributing melting mechanism; it does, however, above the glass transition temperature.

The physical reality is very different for PP: its melting temperature range is around 165°C, and the specific enthalpy needed to melt it is about 500 kJ/kg, five times that needed for PS to reach T_g (Fig. 5.1). Furthermore, as indicated in Fig. 5.17, the adiabatic temperature increase for a single $\varepsilon = 1$ compression of a room temperature cylindrical sample is only 8–10°C. Thus, a larger number of compressions is needed, at least an order of magnitude higher, to melt PP. Under these conditions, soon after some initial PED heating and local melt generation, VED contributes to melting in a significant way, becoming dominant at the melt-rich stage. Recently Wetzel et al. (87,88), working with a well-instrument 34-mm Co-TSE, filled with a glass window, attempted to separate the contributions of FED, PED, and VED during the evolution of melting, by introducing pulsed increases in the feed rate. Their results are preliminary, but represent a promising experimental technique to understand the relative roles of these dissipative melting mechanisms, which will aid in the development of a comprehensive model for melting in full kneading elements.

Qian et al. (18) have recently studied the evolution of melting of polymer blends composed of an amorphous high modulus (PS) component and a semicrystalline low modulus (LLDPE) component in Co-TSE full kneading elements. They observed that over a concentration range of 10–50%, the weaker modulus LLDPE melts faster than the higher modulus PS. Furthermore, when the semicrystalline component has a low melt

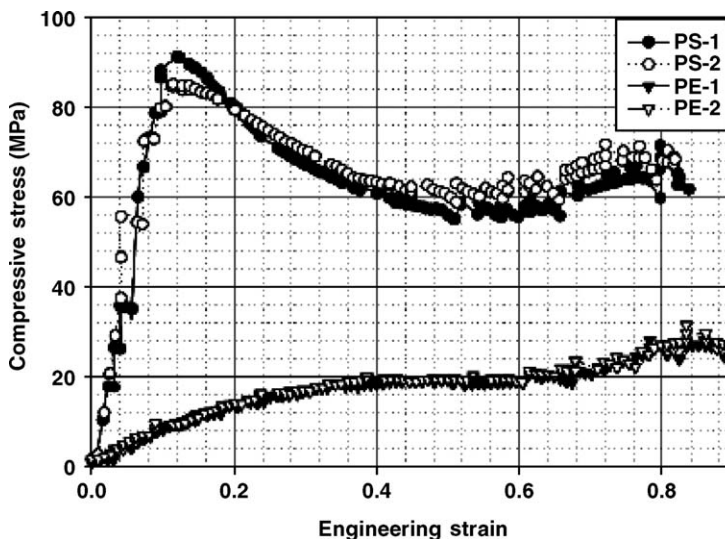


Fig. 10.60 Compressive stress–strain behavior of PS and LLDPE at 25°C and crosshead speed of 25.4 mm/min. At a compressive stress level of 20 MPa the deformation of the soft LLDPE is large, in the dissipative region and nearly twenty times the PS deformation, which is of the order of 0.04, in the elastic nondissipative range. [Reprinted by permission from B. Qian, D. B. Todd, and C. G. Gogos, “Plastic Energy Dissipation (PED) and its Role in Heating/Melting of Single Component Polymers and Multi-component Polymer Blends,” *Adv. Polym. Techn.*, **22**, 85–95 (2003).]

viscosity, the amorphous component has very good chances of transiting the kneading-element melting zone without being completely melted. Of course, as noted earlier, when melting each of the individual components alone, PS melts faster, over a smaller full kneading element length than semicrystalline polymers, due to the very strong PED contribution to melting, as shown on Fig. 10.60, which depicts the individual stress–strain curves of PS and LLDPE. Examining this figure, we note that, if the two materials were stacked as two identical disks, one on top of the other, and a compressive deformation were applied on the stacked pair, then by the time a compressive stress level of 20 MPa was reached, under the conditions indicated, the deformation of LLDPE would be about twenty times larger than that of PS. Furthermore, at this stress level, the small PS deformation is in the “elastic” nondissipative range, while that of the LLDPE is past the yield point, dissipative, and giving rise to PED heating. Under such stacked-disk conditions, the LLDPE component will heat up and melt first, before the PS. In kneading elements full of a mixture of PS and LLDPE pellets we do not have a simple two-disk stack of the two components. Nevertheless, the forced cross-sectional area reduction resulting from the kneading element corotation will compress the randomly packed blend and, as stresses increase, the weaker LLDPE will deform much more than PS, resulting to the observed earlier melting of LLDPE.

Potente and Melish (89), Bawiskar and White (90,91), Zhu, Narh, and Geng (92) and Vergnes et al. (93) have developed one-dimensional melting simulation models that are based on viscous energy dissipation and conduction being responsible for the rapid melting in Co-TSE’s. The polymer charge being melted is a suspension of pellets, whose concentration diminishes with the evolution of melting. We deal briefly here with the work

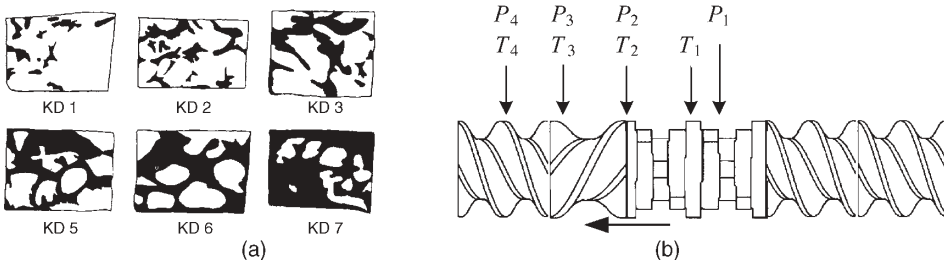


Fig. 10.61 (a) Evolution of the packed solids/melt mixtures obtained by carcass analysis during melting of PP in the 90° stagger kneading block shown in (b). The Co-TSE used was Cletral 45 mm running at 300 rpm and 100 kg/h. Polypropylene Solvay Eltex HL 001 750 μm beads. [Reprinted by permission from B. Vergnes, G. Souveton, M. L. Deacour, and A. Ainsler, “Experimental and Theoretical Study of Polymer Melting in a Co-TSE,” *Int. Polym. Process.*, **16**, 351 (2001).]

of Vergnes et al., which makes good use of experimental carcass analysis results. First, they discuss and accept, but disregard the “genesis” of the initial heating of pellets and the initial melt formation brought about by PED. Then they treat the initial, highly concentrated and inhomogeneous solids/melt mixture, Fig. 10.61(a), as a concentrated suspension, that is, an idealized “continuum” fluid suspension, shown in Fig. 10.62. The melting model of Vergnes et al. assumes that this idealized uniform suspension is characterized simply by a solid, concentration-dependent viscosity, which has the general form valid for monodispersed size spheres (94–97)

$$\frac{\eta_{\text{susp}}}{\eta_{\text{pol}}} = (1 + \alpha\phi)^\beta \tag{10.3-6}$$

where $\alpha = 1/\phi_m$ and ϕ_m is the maximum packing, and β is a particle-to-particle interaction parameter.

The flow on the suspension visualized and simplified in the model just discussed generates VED and heats the pellets, but *does not* deform them. Thus, they do not include the dissipative mix-melting (DMM) melting mechanism, only VED. However, with the proper parameter adjustments, they are able to make fair predictions of the overall melting

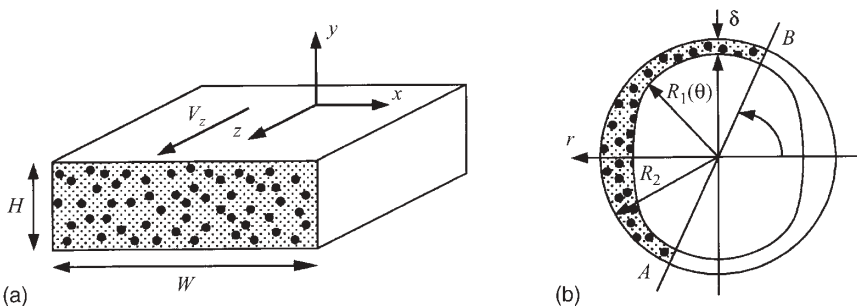


Fig. 10.62 Schematic description of (a) the solid/liquid mixture in the screw channel, and (b) around a kneading disk (93).

lengths. Their model first computes the number of uniform-sized solid particulate spheres of radius R_0 , corresponding to the initial volume fraction of particulates, ϕ_0 :

$$M = \frac{3\phi_0\Delta V}{4\pi R_0^3} \quad (10.3-7)$$

where $\Delta V = A_f \cdot \Delta z$ and A_f is the available cross-sectional area between a pair of kneading elements. The radius of the spheres decreases as they are heated by the flowing suspension exhibiting VED, via convective heat transfer. The sphere radii become zero at complete melting. What is needed to complete the model is, first, an evaluation of the relative viscosity as a function of f ; second, the flow field and expressions for the average shear rate, $\dot{\gamma}$, and $VED = \eta_{\text{rel}}(\phi)\dot{\gamma}^2 = W(z)$; third, the average melt temperature increase over Δz ; and fourth, the reduction of the pellet radii because of convection heat transfer.

It is worth noting that the method used by Vergnes et al. in experimentally obtaining the relative viscosity equation parameters, α and β in Eq. 10.3-6. They worked with two almost identical PP homopolymers, one in 4-mm mean pellet diameter form, and the other in the form of small, 750- μm -diameter beads (Solvay Eltex HL 101). A 21-mm Co-TSE was fitted with a rheometric slit of length $L = 52$ mm, width $w = 28$ mm, and an adjustable gap spacing $1.5 \leq h \leq 2.5$ mm. The polypropylene in pellet form was fed at the feed throat and melted. Just before the die, a second feed port introduced the PP in bead form at various rates, resulting in different effective ϕ values. Two pressure transducers at the die were used to record the slit pressure drop $\Delta P(\phi)$. The relative viscosity was then expressed as

$$\eta_{\text{rel}} = \frac{\eta(\phi)}{\eta_0} \quad (10.3-8)$$

The main assumption made in the preceding relative viscosity evaluation is that no PP bead size reduction and no shape change took place in the slit. This is reasonable only if the heating characteristic time R_0^2/α_{th} is small compared to the average residence time in the slit. Here, α_{th} is the thermal diffusivity, which is in the range of 10^{-3} cm^2/s . The heating time for the 750- μm -diameter beads is then around 1.5 s. Thus, for their assumption of rigid spheres going through the slit rheometer to hold, the average slit velocities must be greater than 5 mm/s. Their experimental results yielded values for the suspension rheological parameters $\alpha = -1.11$ and $\beta = -0.51$. The velocity field in the kneading elements is approximated by that around one isolated kneading disk in the manner developed by Werner (98). The results obtained with such a model are shown in Fig. 10.63, and for the screw and kneading element sequence in Fig. 10.61(b). It is evident that neither the PED model of Kim and Gogos nor the VED model of Vergnes et al. nor other investigators are physically *fully* exhaustive in that they are incapable of describing the evolution of melting in full kneading elements in terms of all the melting mechanisms taking place alone and in parallel until all particulates melt.

Jung and White (99) expressed PED in the following interesting way: They considered a bed of compacted pellets with material points inside the pellets. They then applied the energy equation applicable for this system (100)

$$\rho c_p \left[\frac{\partial T}{\partial t} + (\mathbf{v} \cdot \nabla) T \right] = -\nabla \cdot \mathbf{q} + \sum_i \sum_j \sigma_{ij} \frac{\partial v_i}{\partial x_j} \quad (10.3-9)$$

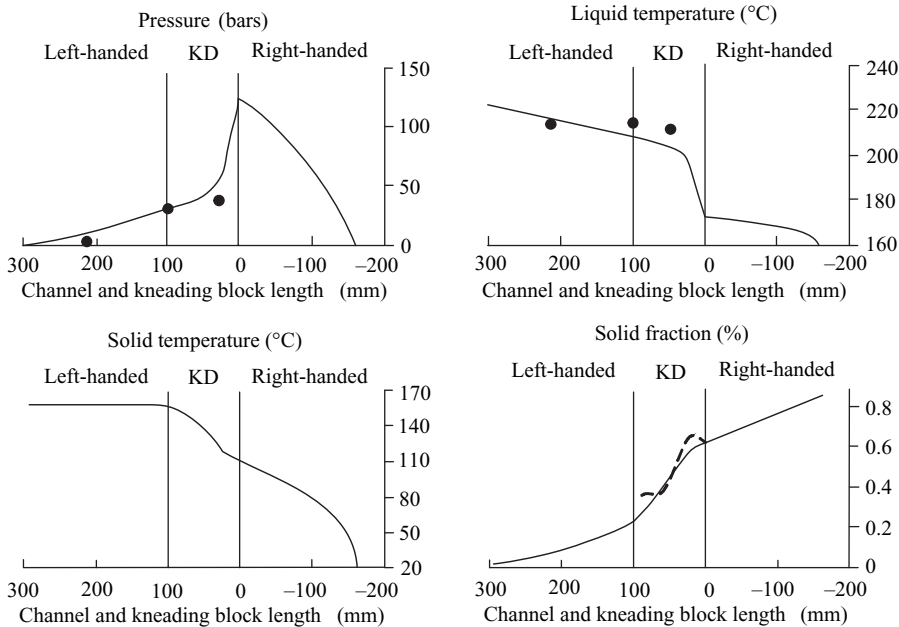


Fig. 10.63 Computation of melting process (screw sequence in Fig. 10.61(b), $N = 300 \text{ min}^{-1}$, $Q = 100 \text{ kg/h}$); dotted line and black symbols are experimental values. [Reprinted by permission from B. Vergnes, G. Souveton, M. L. Deacour, and A. Ainsier, “Experimental and Theoretical study of Polymer Melting in a Co-TSE,” *Int. Polym. Process.*, **16**, 351 (2001).]

and integrated it over the pellet, so that it applies to a moving pellet with diameter D , resulting in

$$\rho c_p V_p \frac{d\bar{T}_p}{dt} = h A_p (\bar{T}_p - T_s) + \sum_{ij} \bar{\sigma}_{ij} \frac{dv_i}{dx_j} V_p \quad (10.3-10)$$

where V_p and A_p are the volume and surface area of the pellet, \bar{T}_p is the mean pellet temperature, h is the heat transfer coefficient, and T_s is the surface temperature. The last term on the right side is PED, or what they call “bulk interior melting.” They then neglected the convective heat transfer term and assumed that the deformation the pellet undergoes is *uniaxial extension*, although in the processing machines pellets undergo compressive deformation, a difference that is very important if one considers PS, which is brittle in tension and tough ductile in compression. Under these assumptions

$$\frac{d\bar{T}_p}{dt} = \frac{1}{\rho c_p} \left(\frac{F}{A'_p} \right) \frac{1}{L_p} \left(\frac{dL_p}{dt} \right) \quad (10.3-11)$$

$$\bar{T}_p(t) - \bar{T}_p(0) = \int_0^t \frac{1}{\rho c_p} \left(\frac{F}{A'_p} \right) \frac{1}{L_p} \left(\frac{dL_p}{dt'} \right) dt' \quad (10.3-12)$$

where (F/A'_p) is taken to be the *tensile yield stress*, shown for LLDPE in Fig. 10.64, and A'_p and L_p are the deformed cross-sectional area and length of the pellet.

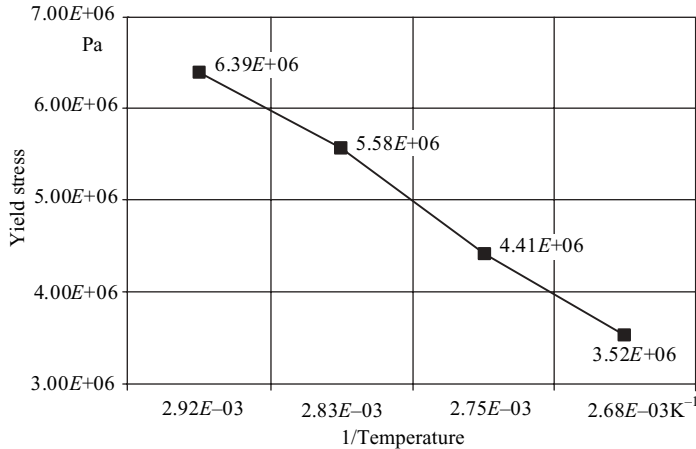


Fig. 10.64 The temperature dependent tensile yield stress for LLDPE (Dow, Dowlex 2045) obtained at Instron crosshead speed of 20 in/min. [Reprinted by permission from H. Jung and J. L. White, "Investigation of Melting Phenomena in Modular Co-TSEs," *Int. Polym. Process.*, **18**, 127 (2003).]

The temperature increase of a pellet by this rather simplified treatment can be calculated knowing ρ , c_p , estimating dL_p/dt , and thus A'_p , and evaluating experimentally $(F/A'_p)(\bar{T}_p)$. This treatment is similar to that of Kim and Gogos in its ability to estimate pellet heating by PED in a simple fashion, needing only the experimental evaluation of the large deformation mechanical behavior of polymer solids.

Flow and Pressurization in Co-rotating Twin Screw Extruders

We now turn to flow and pressurization affected by Co-TSE full-screw and kneading-conveying elements. In Section 6.8 we noted the simple flow rate expressions for isothermal flow of Newtonian fluids in full Co-TSE conveying screw channels, similar in form to those in single screw, full-melt pumps, but containing in both the pressure and drag flow terms, shape factors to account for the channel contour and for the presence of the transition space between the screws where drag flow vanishes, because of the opposing sense of rotation of the screws there (see Eqs. 6.8-12 to 6.8-14). Todd (101) presents calculated values for the drag flow A_t and pressure flow B_t parameters in the flow rate expression

$$Q = A_t N - B_t \Delta P / \eta L \quad (10.3-13)$$

which are listed in Table 10.8 for both kneading and screw elements. They provide *qualitative engineering estimates*.

Considerable work in the three-dimensional simulation of flow in the full conveying screw and kneading elements has been carried out since 1990, when Gotsis et al. (102) treated a Newtonian fluid, isothermal flow, and the problem of time dependence of the geometry of the channels by constructing a three-dimensional mesh covering the entire space inside the barrel, which could be occupied either by the melt or the kneading disks or screws, checking at each step for the space occupied by melt. Lawal and Kalyon (103) extended this work to calculate the intensity of segregation using particle tracers. Wang et al. (104) used FEM for Power Law fluids flowing isothermally, in a number of Coperion

TABLE 10.8 Drag and Pressure Flow Constants for a 50.8-mm Twin Screw Extruder (78)

Bilobal Kneading-paddles Configurations			
Offset Angle	Paddle Width	A_t (cm ³)	B_t (cm ⁴)
30	12.7	51.5	0.53
45	6.3	18.7	0.19
45	12.7	31.1	0.34
45	25.4	36.4	0.60
60	6.3	5.7	0.23
60	12.7	17.9	0.36
60	25.4	22.9	0.49
90	12.7	0.0	0.43

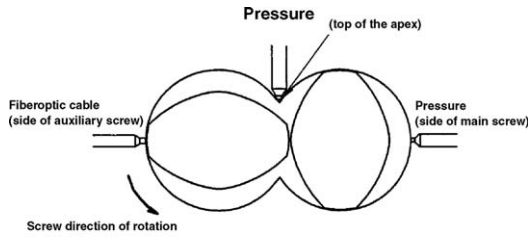
Screw Configurations		
HELIX ANGLE	A_t	B_t
6.1	12.4	0.021
18	41	0.118

elements. Kiani et al. (105,106) used a spectral-element method for a three-dimensional, quasi-steady-state solution of the continuity and motion equations, using periodic boundary conditions. Yang (107) and Cheng and Manas-Zlowcower (108) addressed the transient nature of the flow by reasonably assuming creeping flow, thus approximating the transient flow as a sequence of steady flows at intermediate times. Experimental results of the dynamic pressure profiles by McCullough and Hilton (109) and Christiano and Lindenfelzer (110) reinforced the importance of the intermeshing region and the three-dimensional velocity field there, including strong intermeshing, regional axial squeeze flows. They provided the impetus for intensified investigations by a number of researchers. The first to address the need to compare three dimensional FEM full kneading-element computational results with experimentally obtained dynamic pressure profiles was the group of Hrymak, Bravo et al. (111) and Jaffer et al. (112). The numerical results hold for a quasi-steady-state solution of isothermal full kneading-channels flow of a Carreau model melt.

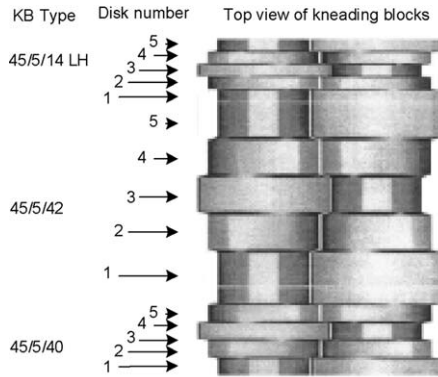
McCullough and Hilton equipped the ZSK 30 barrel with five evenly spaced ports every 30 mm along the top and bottom of the center apex region, and three ports along the sides, spaced every 60 mm. The twin screw assembly was mounted on a movable lathe bed, allowing the barrel and ports to be moved wherever needed along the screw elements to obtain the dynamic pressure data. The transducer locations and kneading element block used are shown in Fig. 10.65. The transducers were capable of responding quickly at 800 MPa/s. Experimentally, it was found that pressure fluctuated as much as 160 MPa/s.

The numerical determination of pressures at the apex and side was as follows: Nine calculated pressure points (see Fig. 10.66), were interpolated in a cross pattern to cover a 1-mm-diameter circle, which corresponds to the exposed area to the transducer.

Figure 10.67(a) and 10.67(b) depict the experimental and simulation pressure profiles at the apex region and the side port of kneading element 5 of the 45/5/20 kneading block, respectively [see Fig. 10.65(b)]. In both cases, of course, it is the motion of the rotors that generate the pressure profiles. The side port fluctuations are of the same nature as those of the flight tip in the CMs and calenders, essentially converging/diverging geometry



(a)



(b)

Fig. 10.65 Experimental apparatus used by McCullough and Hilton (109). (a) Transducer circumferential locations, (b) kneading block used for the ZSK 30 barrel. [Reprinted by permission from V. L. Bravo, A. N. Hrymak, and J. D. Wright, “Numerical Simulation of Pressure and Velocity Profiles in Kneading Elements of a Co-TSE,” *Polym. Eng. Sci.*, **40**, 525–541 (2000).]

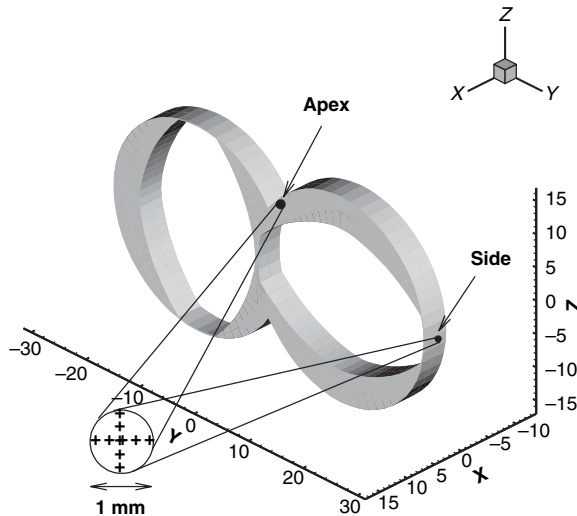


Fig. 10.66 Schematic representation of the mode of numerical determination of pressure at the apex and side pressure port. [Reprinted by permission from V. L. Bravo, A. N. Hrymak, and J. D. Wright, “Numerical Simulation of Pressure and Velocity Profiles in Kneading Elements of a Co-TSE,” *Polym. Eng. Sci.*, **40**, 525–541 (2000).]

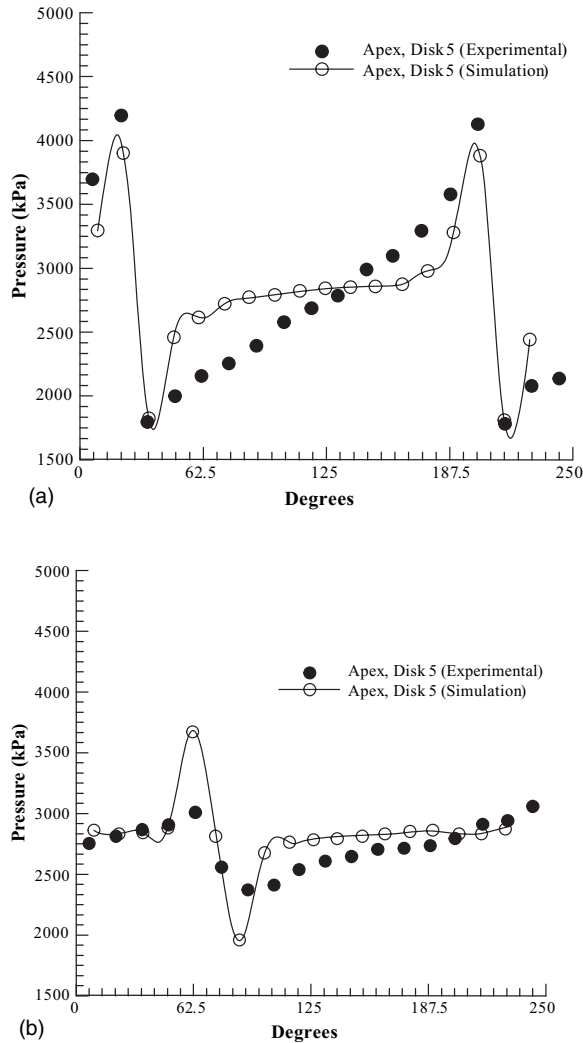


Fig. 10.67 Experimental and simulated pressure profiles obtained with kneading disk 5 of the 45/5/20 element sequence shown in Fig. 10.65(b). (a) Apex region and transducer; (b) wide channel region and side port. [Reprinted by permission from V. L. Bravo, A. N. Hrymak, and J. D. Wright, "Numerical Simulation of Pressure and Velocity Profiles in Kneading Elements of a Co-TSE," *Polym. Eng. Sci.*, **40**, 525-541 (2000).]

resulting in drag flow pressurization. The experimental extremes are 3 and 2.3 MPa, while the calculated are 3.7 and 1.8 MPa, clearly overestimated. In the wider gap region, the agreement is quite good. Turning to the much higher pressure, fluctuations at the apex region originate from the encounter of the two kneading elements, as shown in Fig. 10.68. A small chamber is created and then reduced in size until it disappears, another small chamber appears again and increases in size until it communicates with the wide channels of both sides of the chamber, creating low pressure, which draws melt into it, since pressure "valleys" of one pair coincide with pressure peaks in the up- and downstream neighbors, generating axial backflows. These expansions and contractions, like those

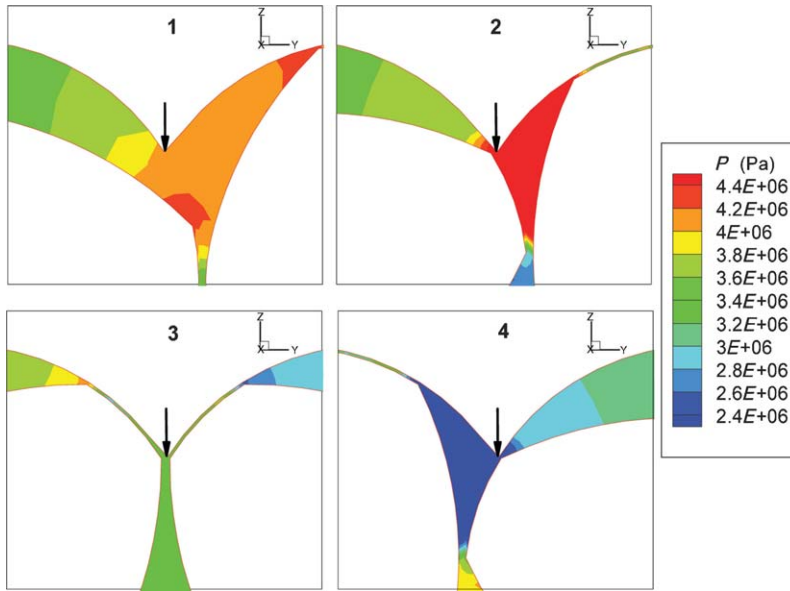


Fig. 10.68 The available expansion–contraction area in the apex region responsible for the dynamic pressure generated at the apex port. [Reprinted by permission from V. L. Bravo, A. N. Hrymak and J. D. Wright, “Numerical Simulation of Pressure and Velocity Profiles in Kneading Elements of a Co-TSE,” *Polym. Eng. Sci.*, **40**, 525–541 (2000).]

causing PED in kneading elements full of particulate solids, now cause effective distributive mixing. As with our PED discussion, the width of the kneading disks is expected to generate stronger backflows. Although the model predictions by Bravo et al. (111) are close to those experimentally obtained, the authors attribute these discrepancies to noninclusion of transient terms in their quasi-steady state three-dimensional FEM, and nonisothermicities present in the experiments give lower pressure drops. Furthermore, the neglect of extensional viscosities is also significant in view of the presence of strong compressive extensional flows.

In 2000 Ishikawa et al. (113) of the Funatsu group conducted three-dimensional FEM nonisothermal simulations for full Co-TSE kneading- and screw-element blocks, without making use of the quasi-steady state assumption. Their results were also compared with those obtained experimentally using a Japan Steel Works TEX 30 (30 mm) machine with 90° stagger angle, bilobal kneading disks. The polymer used was PP, whose rheological behavior fitted with a nonisothermal Carreau model. The pressure and temperature were measured at the circumferential and axial locations shown in Fig. 10.69. The pressure profile 90° away from the apex indicating converging–diverging plate-drag pressurization, shown in Fig. 10.70, is similar to the one obtained by Bravo et al., Fig. 10.67(b), but with better agreement between computed and experimental values, as is expected; nonisothermal and transient flow effects are included in this work. The pressure contours at the cross-sections A–A', B–B', and C–C', with A–A' being the upstream one, are depicted in Fig. 10.71 and are in line with the results in Fig. 10.70. Furthermore, the dP/dz axial pressure gradients change at a fixed circumferential position with the axial position. For example, in the region behind the upper right tip, the $(P|_{A-A'}P|_{B-B'})$ value is negative, while $(P|_{B-B'}P|_{C-C'})$ is positive. On the other hand, in front of the right tip, the

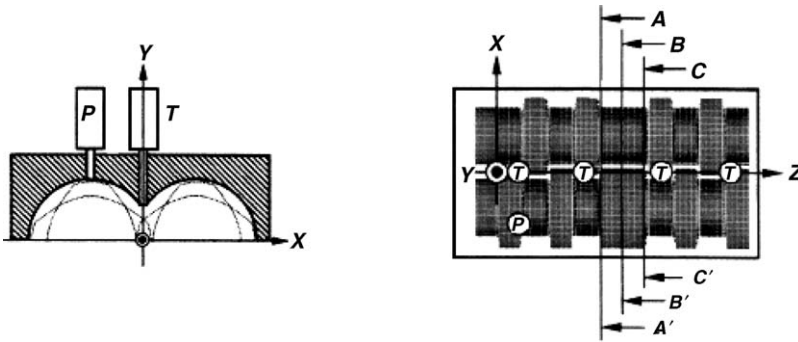


Fig. 10.69 Locations of the thermocouple and pressure transducers used by Ishikawa et al. (113). Numerical velocity, pressure, and temperature field at cross-sections A–A', B–B', and C–C'. [Reprinted by permission from T. Ishikawa, S. I. Kihara, and K. Funatsu, "3-D Numerical Simulations of Nonisothermal Flow in Co-Rotating Twin Screw Extruders," *Polym. Eng. Sci.*, **40**, 357 (2000).]

pressure gradient is positive between A–A' and B–B', while it is negative from B–B' to C–C'. These pressure gradients attest to the presence at various circumferential locations of forward and backward axial flows, which are the hallmark of the screw-to-screw interactive effects, and are of large importance to rapid chaotic mixing. The circumferential velocities are an order of magnitude larger than the axial velocities. The directions of the calculated axial velocities correspond to the calculated pressure gradients, since axial flows are pressure driven. Typical temperature contours are shown in Fig. 10.72 at cross-section B–B' obtained at 200 rpm. The calculated intermesh region values are the highest, higher than those in flight-gap regions. Nevertheless, the temperature field is rather flat, with a maximum

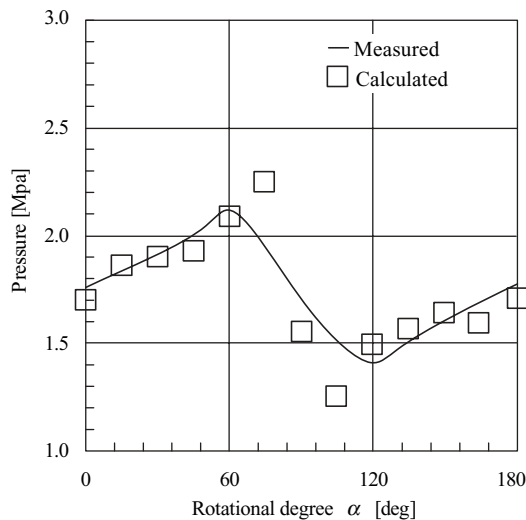


Fig. 10.70 Comparison between experimental and computational pressure profile results. [Reprinted by permission from T. Ishikawa, S. I. Kihara, and K. Funatsu, "3-D Numerical Simulations of Nonisothermal Flow in Co-Rotating Twin Screw Extruders," *Polym. Eng. Sci.*, **40**, 357 (2000).]

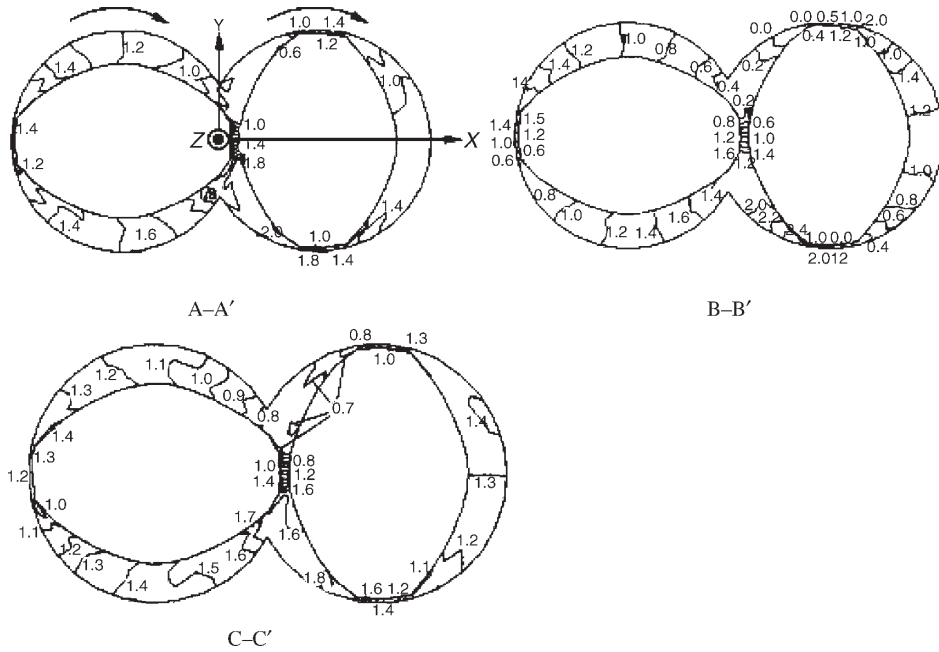


Fig. 10.71 Pressure contours computed at the three axial cross sections A-A' (upstream), B-B', and C-C' (downstream). [Reprinted by permission from T. Ishikawa, S. I. Kihara, and K. Funatsu, "3-D Numerical Simulations of Nonisothermal Flow in Co-Rotating Twin Screw Extruders," *Polym. Eng. Sci.*, **40**, 357 (2000).]

temperature difference of 7°C. The total experimentally obtained axial difference, see Fig. 10.69, is only around 8–10°C. Non-isothermicities in the range of 20°C were measured and calculated for 400 rpm. Since 2000, Funatsu et al. have continued their extensive three-dimensional FEM simulations of nonisothermal flow of shear thinning, Carreau model polymer melts flowing in the following full channels, with screw geometrical and operational variables indicated in Table 10.9 (114).

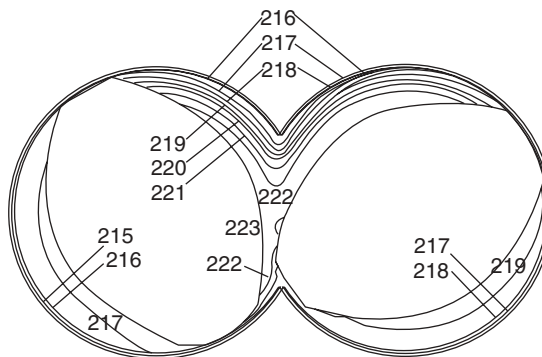


Fig. 10.72 Temperature field at cross section obtained by Ishikawa at 200 rpm. [Reprinted by permission from T. Ishikawa, S. I. Kihara, and K. Funatsu, "3-D Numerical Simulations of Nonisothermal Flow in Co-Rotating Twin Screw Extruders," *Polym. Eng. Sci.*, **40**, 357 (2000).]

TABLE 10.9 Twin Rotor, Screw, and Kneading Element Configurations and Typical Dimensions and Operating Conditions Used for Full Channel Three-dimensional FEM Flow Analysis by Funatsu et al. (114)

Subjects	Geometry	Full-Flighted Screw Elements										Mixing Elements				
		Single Flighted Rectangle			Self-cleaning			Rotors		Kneading Blocks		Shielding Disks				
		Counterrotating	Co-rotating	Single-flighted	Double-flighted	Discontinuous	Continuous	Two-tip	Three-tip	Blister rings						
Geometry Number	[Unit]	I	II	III	IV	V	VI	VII	VIII	IX	X					
Barrel radius	R_B [mm]	20.0	20.0	20.0	20.0	20.0 ~ 36.5	20.0	20.0	15.0 ~ 23.5	20.0	30.0 ~ 90.0					
Flight radius	R_F [mm]	—	19.5	—	—	19.5 ~ 36.0	—	18.75 ~ 19.75	14.6 ~ 22.3	19.5	29.0 ~ 88.9					
Screw root radius	R_S [mm]	15.0	15.0	15.0	10.0	12.5 ~ 23.5	—	12.5	10.5 ~ 23.0	16.0	18.0 ~ 55.0					
Flight width (disk width)	W [mm]	10.0	2.0 ~ 5.3	0.8, 2.7	—	—	—	4.15	7.8 ~ 10.0	10.0	11.0 ~ 33.0					
Flight (tip) clearance	δ_s [mm]	10.0	0.2 ~ 3.5	—	—	—	—	—	0.4 ~ 0.7	0.5	1.0 ~ 1.7					
Calendar gap	δ_c [mm]	0.5	0.5 ~ 1.0	1.0	—	0.5 ~ 2.0	—	0.75	0.7 ~ 1.0	1.0	1.2 ~ 2.1					
Pitch	P [mm]	40.0	11.0	10.0	10.0	30.0 ~ 56.0	—	—	45.0 ~ 50.0	50.0	—					
Forward screw length	L_F [mm]	—	—	—	—	—	—	40.0	—	—	—					
Backward screw length	L_B [mm]	—	—	—	—	—	—	40.0	—	—	—					
Intermediate length	L_M [mm]	—	—	—	—	—	—	0.0	0.8	—	—					
Disk gap	δ [mm]	—	—	—	—	—	—	—	0.1 ~ 1.5	0.1	1.0 ~ 4.5					
Stagger angle	ψ [deg]	—	—	—	—	—	—	—	30 ~ 90	30 ~ 90	—					
Rotational speed	N [rpm]	60.0	60.0	60.0	60.0	60.0 ~ 1300.0	—	60.0	60.0 ~ 1300.00	60.0	86.0 ~ 150.0					

[Reprinted with permission from K. Funatsu, S.I. Kihara, M. Miyazaki, S. Katsuki and T. Kajiwara, "3-D Numerical Analysis of the Mixing Performance for Assemblies with Filled-Zone of Right- and Left-handed Double-Flighted Screw and Kneading Blocks in TSEs," *Polym. Eng. Sci.*, **42**, 707 (2002).]

TABLE 10.10 Computational Capabilities (●) and Possible Simulations (○) of the Full Twin Rotor, Screw, and Kneading Element Channels of Funatsu et al. (114)

Twin-screw Element	Geometric Configurations	Velocity		Leakage		Shear		Pressure		Residence Time		Marker Tracking		Temperature Distr.	Reaction	Cited Refs
		Distr.	Flows	Stress Distr.	Drop	Time Distr.	Animation	Animation								
1 Single-flighted (SF)	Rectangular channel	●	●	●	●	●	●	●	●	●	○	○	○	○	○	(117)
	Self-cleaning	●	●	●	●	●	●	●	●	●	○	○	○	○	○	(118)
2 Double-flighted (DF)	Self-cleaning	●	●	●	●	●	●	●	●	●	○	○	○	○	○	(119)
3 Rotor	Continuous	●	●	●	●	●	●	●	●	○	○	○	●	○	○	(73)
	Discontinuous	●	●	●	●	●	●	●	●	○	○	○	○	○	○	
4 Kneading blocks (KB)	Two-tip	●	●	●	●	●	●	●	●	●	●	●	●	●	●	
	Right-handed (R) stagger angle	●	●	●	●	●	●	●	●	●	●	●	●	●	●	
	Neutral (N) stagger angle	●	●	●	●	●	●	●	●	●	●	●	●	●	●	(113)
	Left-handed (L) stagger angle	●	●	●	●	●	●	●	●	●	●	●	●	●	●	
	Right-handed (R) stagger angle	●	●	●	●	●	●	●	●	●	●	●	●	○	○	
	Neutral (N) stagger angle	●	●	●	●	●	●	●	●	●	●	●	●	○	○	(115)
Left-handed (L) stagger angle	●	●	●	●	●	●	●	●	●	●	●	●	○	○		
5 Disk	Shielding disks (Blister rings)	●	●	●	●	●	●	●	●	●	●	●	○	○	○	(120)
6 Element assembly (EA)	3 pitches (EA3-R, N, L)	●	●	●	●	●	●	●	●	●	●	●	●	●	○	In press
	DF/R + KB/R + DF/R	●	●	●	●	●	●	●	●	●	●	●	●	●	○	
	DF/R + KB/N + DF/R	●	●	●	●	●	●	●	●	●	●	●	●	●	○	
	DF/R + KB/L + DF/R	●	●	●	●	●	●	●	●	●	●	●	●	○	○	(114)
10 pitches (EA 10)	DF/R + KB/N + DF/L + DF/R	●	●	●	●	●	●	●	●	●	●	●	○	○	○	
	DF/R + KB/L + DF/L + DF/R	●	●	●	●	●	●	●	●	●	●	●	○	○	○	
2DF/R + 3KB/R + 2KB/N + KB/L + 2DF/R	DF/R + KB/N + DF/R + DF/R	●	●	●	●	●	●	●	●	●	●	●	○	○	○	
	DF/R + KB/L + DF/R + DF/R	●	●	●	●	●	●	●	●	●	●	●	○	○	○	
10 pitches (EA 10)	DF/R + KB/L + DF/R + DF/R	●	●	●	●	●	●	●	●	●	●	●	○	○	○	
	DF/R + KB/L + DF/R + DF/R	●	●	●	●	●	●	●	●	●	●	●	○	○	○	(121)

Source: Reprinted by permission from K. Funatsu, S. I. Kihara, M. Miyazaki, S. Katsuki, and T. Kajiwara, *Polym. Eng. Sci.*, **42**, 707 (2002).

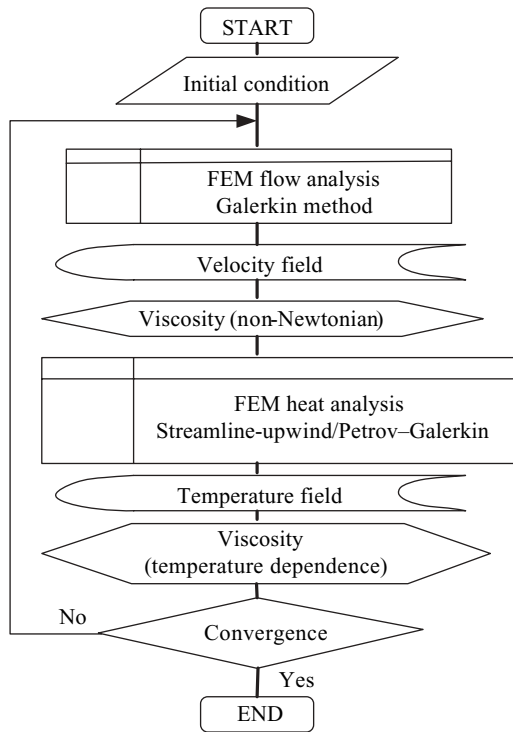


Fig. 10.73 Schematic of the three-dimensional FEM nonisothermal flow analysis flow diagram employed by the Ishikawa et al. (113). [Reprinted by permission from T. Ishikawa, S. I. Kihara and K. Funatsu, “3-D Numerical Simulations of Nonisothermal Flow in Co-Rotating Twin Screw Extruders,” *Polym. Eng. Sci.*, **40**, 365 (2000).]

The computational capabilities of the Funatsu et al. modeling are listed in Table 10.10 with reference to the publication reporting their computational work. Some of the following are evident from the Tables 10.9 and 10.10. All common twin-rotor polymer processing equipment and screw-, rotor-, or kneading-element types, as well as element sequences have been treated:

1. Much computational effort has been devoted to the *full-channel* Co-TSE kneading-element and element sequences.
2. The majority of simulations deal with *isothermal* flows, though the computational format of this computational group is shown in Fig. 10.73.
3. There is more attention paid to examining the *distributive mixing* abilities of each of the full-channel geometries examined, through marker tracking computational animation (114–116).
4. Finally, reactive processing in full nonisothermal, twin-rotor channel flows has not been solved for all but full bilobal kneading-disk sequences and screw-mixing elements (SME) (116).

It is certain that, in the near future, as is partially true at present, polymer processing engineers who are involved in the design of twin-rotor processing equipment and process

results analysis will be aided by CFM simulation packages, which will shed light on the melt mixing and reactive processing capabilities of such equipment

REFERENCES

1. J. L. White, *Twin Screw Extrusion*, Hanser, Munich, 1990.
2. K. Eise, H. Herrmann, S. Jakopin, U. Burkhardt, and H. Werner, "An Analysis of Twin Screw Extruder Mechanisms," *Adv. Polym. Tech.*, **1** (2), 18–39 (1981).
3. D. B. Todd, "Introduction to Compounding," in *Plastics Compounding—Equipment and Processing*, D. B. Todd, Ed., Hanser, Munich, 1998.
4. R. C. Kowalski, "Case Histories of Industrial Studies of Extruder Reactions," in *Reactive Extrusion, Principles and Practices*, M. Xanthos, Ed., Hanser, Munich, 1992.
5. Z. Tadmor and C. G. Gogos, *Principles of Polymer Processing*, Wiley-Interscience, New York, 1979, Chapter 10.
6. D. Smith, P. Stoughton, C. Morgan, and G. Hovis, in *The SPE Guide on Extrusion Technology and Troubleshooting*, J. Vlachopoulos and J. R. Wagner, Jr., SPE, Danbury, CT, 2001, Chapter 5.
7. W. C. Thiele, "Counter-rotating Intermeshing Twin Screw Extruders," in *Plastics Compounding—Equipment and Processing*, D. B. Todd, Ed., Hanser, Munich, 1998.
8. E. H. Ahlefeld, A. J. Baldwin, P. Hold, W. A. Rapetski, and H. R. Scharer, U.S. Patent 3,154,808 (1964); U.S. Patent 3,239,878.
9. E. L. Canedo and L. N. Valsamis, "Selecting Compounding Equipment Based on Process Considerations," *Int. Polym. Process.*, **9**, 225 (1994); in *Plastics Compounding—Equipment and Processing*, D. B. Todd, Ed., Hanser, Munich, 1998.
10. R. Erdmenger, German Patent 813,154 (1951); U. S. Patent 2,670,188 (1954).
11. P. G. Andersen, "The Werner and Pfeleiderer Twin-Screw Corotating Extruder System," in *Plastics Compounding—Equipment and Processing*, D. B. Todd, Ed., Hanser, Munich, 1998.
12. D. B. Todd, "Compounding in Twin Screw Extruders," in *Two-phase Polymer Systems*, L. A. Utracki, Ed., Hanser, Munich, 1991.
13. D. B. Todd, U.S. Patent 4,136,968 to Baker Perkins (1979); also, D. B. Todd, "Energy Dissipated in Twin Screw Extruders," *SPE ANTEC Tech. Papers*, **26**, 220 (1980).
14. H. Herrmann, H. J. Nettelbrecker, and A. Dreiblatt, "Quality Assurance and Improvement in On-line Controlled Compounding," *SPE ANTEC Tech. Papers*, **33**, 157 (1987).
15. D. B. Todd, "Drag and Pressure Flow in Twin Screw Extruders," *SPE ANTEC Tech. Papers*, **35**, 168 (1989); also, D. B. Todd, "Drag and Pressure Flow in Twin Screw Extruders," *Int. Polym. Process.*, **6**, 143 (1991).
16. K. Funatsu, S.-I. Kihara, M. Miyazaki, S. Katsuki, and T. Kajiguara, "3-D Numerical Analysis on the Mixing Performance for Assemblies with Filled Zone of Right-handed and Left-handed Double-flighted Screws and Kneading Blocks in Twin-screw Extruders," *Polym. Eng. Sci.*, **42**, 707–723 (2002).
17. C. G. Gogos, Z. Tadmor, and M.-H. Kim, "Melting Phenomena and Mechanisms in Polymer Processing Equipment," *Adv. Polym. Technol.*, **17**, 285–305 (1998).
18. B. Qian, D. B. Todd, and C. G. Gogos, "Plastic Energy Dissipation and its Role on Heating/Melting of Single-component Polymers and Multi-component Polymer Blends," *Adv. Polym. Technol.*, **22**, 85–95 (2003).
19. U. Sundararaj and C. W. Macosko, R. J. Rolando, and H. T. Chan, "Morphology Development in Polymer Blends," *Polym. Eng. Sci.*, **32**, 1814–1832 (1992).

20. S. Bawiskar and J. L. White, "Melting Model for Modular Self Wiping Co-rotating Twin Screw Extruders," *Polym. Eng. Sci.*, **38**, 727–740 (1998).
21. B. Vergnes, G. Souveton, M. L. Delacour, and A. Ainsler, "Experimental and Theoretical Study of Polymer Melting in a Co-rotating Twin Screw Extruder," *Int. Polym. Process.*, **16**, 351–362 (2001).
22. D. M. Anderson, G. B. McFadden, and A. A. Wheeler, "Diffuse-interface Methods in Fluid Mechanics," *Annu. Rev. Fluid Mech.*, **30**, 139 (1998).
23. P. D. Anderson, O. S. Galaktionov, G. W. M. Peters, F. N. Van de Vosse, and H. E. H. Meijer, "Mixing of Non-Newtonian Fluids in Time-periodic Cavity Flows," *J. Non-Newtonian Fluid Mech.*, **93**, 265–280 (2000).
24. L. P. B. M. Janssen, *Twin Screw Extrusion*, Elsevier Scientific, Amsterdam, 1978.
25. S. Lim and J. L. White, "Flow Mechanisms, Material Distribution and Phase Morphology Development in a Modular Intermeshing Counterrotating Twin Screw Extruder of Leistritz Design," *Int. Polym. Process.*, **9**, 33–45 (1994).
26. J. W. Cho and J. L. White, "Melting and Blending in a Modular Corotating/Counter-rotating Twin Screw Extruder," *Int. Polym. Process.*, **11**, 21–28 (1996).
27. K. Wilczynski and J. L. White, "Experimental Study of Melting in an Intermeshing Counter-Rotation Twin Screw," *Int. Polym. Process.*, **16**, 257–262 (2001).
28. L. P. B. M. Janssen and J. M. Smith, *Kunststoffe*, **66**, 724 (1976).
29. A. J. van der Goot, O. Poorter, and L. P. B. M. Janssen, "Determination of the Degree of Fill in a Counterrotating Twin Screw Extruder," *Polym. Eng. Sci.*, **38**, 1193–1198 (1998).
30. J. A. Speur, H. Mavridis, J. Vlachopoulos, and L. P. B. M. Janssen, "Flow Patterns in the Calendar Gap of a Counterrotating Twin Screw Extruder," *Adv. Polym. Technol.*, **7**, 39–48 (1987).
31. T. Li and I. Manas-Zloczower, "A Study of Distributive Mixing in Counter-rotating Twin Screw Extruders," *Int. Polym. Process.*, **10**, 314–320 (1995).
32. T. Katziguara, Y. Nagashima, Y. Nakano, and K. Funatsu, "Numerical Study of Twin-screw Extruders by Three-dimensional Flow Analysis—Development of Analysis Technique and Evaluation of Mixing Performance for Full Flight Screws," *Polym. Eng. Sci.*, **36**, 2142–2152 (1996).
33. T. Sakai and N. Hashimoto, "Application of Novel Counter-rotating Intermeshed Twin Extruder for Degassing Operation," *SPE ANTEC Tech. Papers*, **32**, 860–863 (1986); also T. Sakai, N. Hashimoto, and N. Kobayashi, "Experimental Comparison between Counter-rotation and Co-rotation on the Twin Screw Extrusion Performance," *SPE ANTEC Tech. Papers*, **33**, 146–151 (1987).
34. S. K. Dey and J. A. Biesenberger, "Reactive Extrusion of Methyl Methacrylate," *SPE ANTEC Tech. Papers*, **33**, 133 (1987).
35. K. J. Gadzenveld and L. P. B. M. Janssen, "Scale-up of Counter-rotating Closely Intermeshing Twin Screw Extruders without and with Reactions," *Polym. Eng. Sci.*, **30**, 1529–1536 (1990).
36. K. J. Gadzenveld and L. P. B. M. Janssen, "A Mixing Model for Multicomponent Reactions in Twin Screw Extruders Applied to the Polymerization of Urethanes," *Polym. Eng. Sci.*, **32**, 457–466 (1992).
37. K. J. Gadzenveld and L. P. B. M. Janssen, "The Grafting of Maleic Anhydride on High Density Polyethylene in an Extruder," *Polym. Eng. Sci.*, **32**, 467–474 (1992).
38. K. J. Gadzenveld and L. P. B. M. Janssen, "Twin Screw Extruders as Polymerization Reactors for a Free Radical Homo Polymerization," *Can. J. Chem. Eng.*, **71**, 411–418 (1993).
39. K. J. Gadzenveld, J. E. Capel, D. J. van der Wal, and L. P. B. M. Janssen, "The Modeling of Counterrotating Twin Screw Extruders as Reactors for Single-component Reactions," *Chem. Eng. Sci.*, **49**, 1639–1649 (1994).

40. H. A. Jongbloed, R. K. S. Mulder and L. P. B. M. Janssen, "The Co-polymerization of Methacrylates in a Counterrotating Twin Screw Extruder," *Polym. Eng. Sci.*, **35**, 588 (1995).
41. J. A. Speur, Ph.D. Thesis, Department of Chemical Engineering, University of Groningen, Groningen, The Netherlands, 1988.
42. N. P. Stuber, Ph.D. Thesis, Department of Chemical Engineering, University of Minnesota, Minneapolis 1986.
43. E. Trommsdorff, H. Holle, and P. Lagally, *Macromol. Chem.*, **1**, 280 (1947).
44. F. L. Marten and A. E. Hamielec, "High Conversion Diffusion-controlled Polymerization," *ACS SYMP. SER.*, (10), 34–70 (1979).
45. K. J. Gadzenvelt, Ph.D. Thesis, Department of Chemical Engineering, University of Groningen, Groningen, The Netherlands, 1992.
46. L. J. Fuller, U.S. Patent 2,441,222 (1948).
47. L. J. Fuller, U.S. Patent 2,615,199 (1952).
48. L. F. Street, U.S. Patent 2,733,051 (1956).
49. L. F. Street, U.S. Patent 3,078,511 (1963).
50. R. H. Skidmore, U.S. Patent 3,985,348 (1976).
51. R. J. Nichols and F. Kher-adi, "Melting in CRT Twin Screw Extruders," *Mod. Plast*, **16** (2), 70 (1984).
52. S. Satija and C. S. Tucker, "Effect of Screw Root Profile on PMMA Melting in Counterrotating Non-intermeshing Twin Screw Extruder," *SPE ANTEC Tech. Papers*, **40**, 248–255 (1994).
53. A. Kaplan and Z. Tadmor, "Theoretical Model for Non-intermeshing Twin Screw Extruders," *Polym. Eng. Sci.*, **14**, 58–66 (1974).
54. R. J. Nichols, "Pumping Characteristics of Counterrotating Tangential Twin Screw Extruders," *SPE ANTEC Tech. Papers*, **29**, 130–133 (1983).
55. R. J. Nichols, "Modeling Performance Characteristics of Counterrotating Tangential Twin Screw Extruders," *SPE ANTEC Tech. Papers*, **30**, 6–9 (1984).
56. K. Nguyen and J. Lindt, "Finite Element Modeling of a Counterrotating, Non-intermeshing Twin Screw Extruder," *Polym. Eng. Sci.*, **29**, 709–714 (1989).
57. D. S. Bang, M. H. Hong, and J. L. White, "Modular Tangential Counterrotating Twin Screw Extrusion: Determination of Screw Pumping Characteristics of Modules and Composite Machine Behavior," *Polym. Eng. Sci.*, **38**, 485–498 (1998).
58. C. Martin, "Counterrotating Twin Screw Extruders", in *Extrusion Toolbox*, Society of Plastics Engineers, Danbury, CT, (2004).
59. L. N. Valsamis and E. L. Canedo, "Mixing in the Continuous Farrel Mixer," in *Mixing and Compounding of Polymers*, I. Manas-Zloczower and Z. Tadmor, Eds., Hanser, Munich (1994).
60. L. N. Valsamis and E. L. Canedo, "Effect of Rotor Geometry and Operating Conditions on Mixing Performance in Continuous Mixers: An Experimental Study," *SPE ANTEC Tech. Papers*, **37**, 629–632 (1991).
61. W. R. Bolen and R. E. Colwell, *SPE J.*, **14** (3), 24 (1958).
62. J. T. Bergen, "Mixing and Dispersive Processes," in *Processing of Thermoplastic Materials*, E. C. Bernhardt, Ed., Reinhold, New York (1959).
63. K. Meissner and E. O. Reher, *Plaste Kautsch.*, **26**, 272 (1979).
64. K. Meissner, J. Bergmann, and E. O. Reher, *Plaste Kautsch.*, **27**, 147 (1980).
65. U. Wagenknecht, K. Meissner, E. O. Reher, and B. Polsterdorf, *Plaste Kautsch.*, **35**, 175 (1988).

66. M. H. Kim and J. L. White, "Simulation of Flow in a Farrel Continuous Mixer," *Int. Polym. Process.*, **7**, 15–19 (1992).
67. J. J. Cheng and I. Manas-Zloczower, "Hydrodynamic Analysis of a Banbury Mixer 2-D Flow Simulations for the Entire Mixing Chamber," *Polym. Eng. Sci.*, **29**, 1059–1065 (1989).
68. J. J. Cheng and I. Manas-Zloczower, "Flow Field Characterization in a Banbury Mixer," *Int. Polym. Process.*, **5**, 178–183 (1990).
69. T. W. Wong and I. Manas-Zloczower, "Numerical Studies of the Flow Field in Partially Filled Mixing Equipment," *SPE ANTEC Tech. Papers*, **38**, 1788–1793 (1992).
70. E. L. Canedo and L. N. Valsamis, "Non-Newtonian, Non-isothermal Flow between Non-parallel Plates in Relative Motion. Applications to Mixer Design," *SPE ANTEC Tech. Papers*, **36**, 164–167 (1990).
71. R. B. Bird, R. C. Armstrong, and O. Hassager, *Dynamics of Polymeric Liquids*, Vol. 1, *Fluid Mechanics*, Second Edition, Wiley, New York, 1987.
72. C. H. Yao and I. Manas-Zloczower, "Influence of Design on Dispersive Mixing Performance in an Axial Discharge Continuous Mixer–LCMAX 40," *Polym. Eng. Sci.*, **38**, 936–946 (1998).
73. T. Ishikawa, S. Kihara, K. Funatsu, T. Amaiwa, and K. Yano, "3-D Numerical Simulations and Nonisothermal Flow in Co-rotating Twin Screw Extruders," *Polym. Eng. Sci.*, **40**, 357–364 (2000).
74. P. G. Andersen, "Mixing Practices in Co-rotating Twin Screw Extruders," in *Mixing and Compounding of Polymers*, I. Manas-Zloczower and Z. Tadmor, Eds., Hanser, Munich (1994).
75. P. G. Andersen, "The Werner and Pfleiderer Twin Screw Co-rotating Extruder System," in *Plastics Compounding*, D. B. Todd, Ed., Hanser, Munich (1998).
76. T. Sakai, "Intermeshing Twin Screw Extruders," in *Mixing and Compounding of Polymers*, I. Manas-Zloczower and Z. Tadmor, Eds., Hanser, Munich (1994).
77. T. Sakai, "Intermeshed TEX Twin Screw Extruder: JSW Compounding System," in *Plastics Compounding*, D. B. Todd, Ed., Hanser, Munich (1998).
78. D. B. Todd, "APV (Baker Perkins) Systems," in *Plastics Compounding*, D. B. Todd, Ed., Hanser, Munich (1998).
79. M. Mack, "Co-rotating Intermeshing Twin Screw Extruder: Berstorff's System," in *Plastics Compounding*, D. B. Todd, Ed., Hanser, Munich (1998).
80. P. Heidemeyer, German Patent Application 195,36289.6 (1995).
81. R. Potluri, D. B. Todd, and C. G. Gogos, *Proc. 11th Polymer Mixing Study Semi-annual Meeting*, Polymer Processing Institute, Hoboken, NJ (1995).
82. M. H. Kim, Ph.D. Dissertation, Department of Chemical Engineering, Stevens Institute of Technology, Hoboken, NJ (1999).
83. B. Qian and C. G. Gogos, "The Importance of Plastic Energy Dissipation (PED) to the Heating and Melting of Polymer Particulates in Intermeshing Co-rotating Twin Screw Extruders," *Adv. Polym. Tech.*, **19**, 287–299 (2000).
84. C. G. Gogos, B. Qian, D. B. Todd, and M. H. Kim, "A Predictive Melting Model for Polymer Particulates in Co-rotating Twin Screw Extruders," *SPE ANTEC Tech. Papers*, **47**, 134–138 (2001).
85. M. H. Kim and C. G. Gogos, "Melting Phenomena and Mechanism in Co-rotating Twin Screw Extruder," *SPE ANTEC Tech. Papers*, **47**, 145–149 (2001).
86. C. G. Gogos and B. Qian, "Plastic Energy Dissipation during Compressive Deformation of Individual Polymer Pellets and Polymer Particulate Assemblies," *Adv. Polym. Tech.*, **21**, 287–298 (2002).
87. M. D. Wetzel, C. K. Shih, D. A. Denelsbek, and S. L. Latimer, "Quantification of Melting using the Pulse Perturbation Technique, Part I," *SPE ANTEC Tech. Papers*, **51**, 347 (2005).

88. M. D. Wetzel, C. K. Shih, D. A. Denelsbek, and S. L. Latimer, "Quantification of Melting using the Pulse Perturbation Technique Part II," *SPE ANTEC Tech. Papers*, **51**, 354 (2005).
89. H. Potente and U. Melish, "Theoretical and Experimental Investigations of the Melting of Pellets in Co-rotating Twin Screw Extruders," *Int. Polym. Process.*, **11**, 101 (1996).
90. S. Bawiskar and J. L. White, "A Composite Model for Solid Conveying, Melting, Pressure and Fill Factor Profiles in Modular Co-rotating Twin Screw Extruders," *Int. Polym. Process.*, **12**, 331 (1997).
91. S. Bawiskar and J. L. White, "Melting Model for Modular Self Wiping Co-rotating Twin Screw Extruders," *Polym. Eng. Sci.*, **38**, 727–740 (1998).
92. L. Zhu, K. A. Nahr, and X. Geng, "Modeling of Particle-dispersed Melting Mechanism and Its Application in Corotating Twin Screw Extrusion," *J. Polym. Sci. Part B: Polym. Phys.*, **39**, 2461–2468 (2001).
93. B. Vergnes, G. Souveton, M. L. Deacour, and A. Ainsler, "Experimental and Theoretical Study of Polymer Melting in a Co-rotating Twin Screw Extruder," *Int. Polym. Process.*, **16**, 351–362 (2001).
94. J. Mewis and C. W. Macosko, *Rheology: Principles, Measurements and Applications*, C. W. Macosko, Ed. Wiley, New York (1994).
95. P. J. Carreau, D. C. R. DeKee, and R. P. Chabra, *Rheology of Polymeric Systems: Principles and Applications*, Hanser, Munich (1997).
96. I. M. Krieger and T. J. Dougherty, "A Mechanism for Non-Newtonian Flow in Suspensions of Rigid Spheres," *Trans. Soc. Rheol.*, **3**, 137–152 (1959).
97. R. Roscoe, in *Flow Properties of Dispersed Systems*, J. J. Hermans, Ed., Interscience, New York (1953).
98. H. Werner, Ph.D. Thesis, University of Munich, Munich, Germany (1976).
99. H. Jung and J. L. White, "Investigation of Melting Phenomena in Modular Co-rotating Twin Screw Extrusion," *Int. Polym. Process.*, **18**, 127–132 (2003).
100. C. Truesdell and R. A. Tupin, "The Classical Field Theories," in *Handuch der Physik*, Springer-Verlag, Berlin (1960).
101. D. B. Todd, "Drag and Pressure Flow in Twin Screw Extruders," *Int. Polym. Process.*, **6**, 143–147 (1991).
102. A. D. Gotsis, Z. Ji, and D. M. Kalyon, "3-D Analysis of the Flow in Co-rotating Twin Screw Extruders," *SPE ANTEC Tech. Papers*, **36**, 139–142 (1990).
103. A. Lawal and D. M. Kalyon, "Mechanisms of Mixing in Single and Co-rotating Twin Screw Extruders," *Polym. Eng. Sci.*, **35**, 1325–1338 (1995).
104. Y. Wang, J. L. White, and W. Szydlowski, "Flow in a Modular Intermeshing Co-rotating Twin Screw Extruder," *Int. Polym. Process.*, **4**, 262–269 (1989).
105. A. Kiani and H. J. Samann, "The Influence of Curvature on the Simulation of Flow in a Tangential Counter-rotating Twin Screw Extruder," *SPE ANTEC Tech. Papers*, **39**, 2758 (1993).
106. A. Kiani, P. Heidemeyer, and R. Pallas, "Study of Flow and RTD in a ZSK Twin Screw Extruder," *SPE ANTEC Tech. Papers*, **43**, 94–99 (1997).
107. H. H. Yang, Ph.D. Thesis, Chemical Engineering Department, Case-Western Reserve University, Cleveland (1993).
108. J. J. Cheng and I. Manas-Zloczower, "Hydrodynamic Analysis of a Banbury Mixer 2-D Flow Simulations for the Entire Mixing Chamber," *Polym. Eng. Sci.*, **29**, 1059–1065 (1989).
109. T. W. McCullough and B. T. Hilton, "The Extrusion Performance of Co-rotating, Intermeshing Twin Screw Extruder Screw Elements—An Experimental Investigation," *SPE ANTEC Tech. Papers*, **39**, 3372–3379 (1993).

110. J. P. Christiano and M. Lindenfelzer, "Investigation of Mixing Patterns in Co-rotating Fully Intermeshing Twin Screw Extruders Mixing Elements Using Dynamic Pressure Distributions," *SPE ANTEC Tech. Papers*, **43**, 78–83 (1997).
111. V. L. Bravo, A. N. Hrymak, and J. D. Wright, "Numerical Simulation of Pressure and Velocity Profiles in Kneading Elements of a Co-rotating Twin Screw Extruder," *Polym. Eng. Sci.*, **40**, 525–541 (2000).
112. S. A. Jaffer, V. L. Bravo, P. E. Wood, A. N. Hrymak, and J. D. Wright, "Experimental Validation of Numerical Simulations of the Kneading Disc Section in a Twin Screw Extruder," *Polym. Eng. Sci.*, **40**, 892–901 (2000).
113. T. Ishikawa, S. I. Kihara, and K. Funatsu, "3-D Numerical Simulations of Nonisothermal Flow in Co-rotating Twin Screw Extruders," *Polym. Eng. Sci.*, **40**, 357–364 (2000).
114. K. Funatsu, S. I. Kihara, M. Miyazaki, S. Katsuki, and T. Kajiwara, "3-D Numerical Analysis on the Mixing Performance for Assemblies with Filled Zone of Right-handed and Left-handed Double-flighted Screws and Kneading Blocks in Twin Screw Extruders," *Polym. Eng. Sci.*, **42**, 707–723 (2002).
115. M. Yoshinaga, S. Katsuki, M. Miyazaki, L. Liu, S. I. Kihara and K. Funatsu, "Mixing Mechanism of Three-tip Kneading Block in Twin Screw Extruders," *Polym. Eng. Sci.*, **40**, 168–178 (2000).
116. T. Ishikawa, T. Amano, S. I. Kihara, and K. Funatsu, "Flow Patterns and Mixing Mechanisms in the Screw Mixing Element of a Corotating Twin-screw Extruder," *Polym. Eng. Sci.*, **42**, 925–939 (2002).
117. T. Kajiwara, Y. Nagashima, Y. Nakano, and K. Funatsu, "Numerical Study of Twin-screw Extruders by Three-dimensional Flow Analysis—development of Analysis Technique and Evaluation of Mixing Performance for Full Flight Screws," *Polym. Eng. Sci.*, **36**, 2142–2152 (1996).
118. L. Liu, H. Higashi, Y. Nagashima, T. Kajiwara, and K. Funatsu, *Seikei-Kakou*, **9**, 169 (1997).
119. L. Liu, M. Yoshinaga, S. Kihara, and K. Funatsu, *Seikei-Kakou*, **11**, 250 (1999).
120. M. Miyazaki, M. Yamaura, T. Takayama, S. Kihara, and K. Funatsu, "3-D Flow Simulation of Shielding Disk in Twin Screw Extruders," *Proc. 16th Ann. Meet. Polym. Process. Soc.*, Shanghai, China, 2000, pp. 268–269.
121. K. Funatsu, S. Katsuki, and S. Kihara, *J. Soc. Chem. Eng., 31st Ann. Meet.*, Vol. II, (in Japanese) Yonezawa, Japan, 1998, p. 272.

PROBLEMS

10.1 *Engineering Estimates of the Drag- and Pressure-Flow Terms of the "Screw Characteristic Lines" of Co-TSE Conveying Screws and Kneading Elements* Todd* presents the calculated values of the A_t and B_t geometric parameters for conveying screw and kneading elements of Co-TSEs needed for engineering estimates of "screw characteristic lines," Eq. 10.3-13, also listed on Table 10.8

$$Q = A_t N - B_t \Delta P / \eta L$$

Examine the assumptions, carry out two sample calculations, one for kneading- and another for conveying-screw elements, and discuss the range of applicability and limitations of these engineering estimates.

* D. B. Todd, "Drag and Pressure Flow in Twin Screw Extruders," *Int. Polym. Process.*, **6**, 143 (1991).

10.2 Comparison of Melting Rates of Polypropylene in Single and Twin Screw Extruders Polypropylene was melted in both a single- and a co-rotating intermeshing twin-screw extruder. The experimental conditions and the results analysis of the carcasses by screw pulling to determine the axial lengths in which melting takes place are as follows:

- (a) SSE: 2.5-in D, square pitch, 26.5 L/D with 12.5 turns of feed section 0.37 in deep, a 9.5-turn transition section, and a 4.5-turn metering section 0.127 in deep. Melting was carried out at 96.8 lb/h at 60 rpm with $T_{\text{barrel}} = 450^\circ\text{F}$ and a die pressure of 3000 psi. The melting process starts at turn 7 and ends at turn 24 (see Fig. 9.21).
 - (b) TSE: 30-mm D, $D_o - D_i = 4.7\text{ mm}$, $L_{\text{lobe}} = 8.4\text{ mm}$ operating at 10 kg/h, 60 rpm, and $T_{\text{barrel}} = 140^\circ\text{C}$. The observed melting length was approximately $4 \times L_{\text{lobe}} \sim 30 - 35\text{ mm}$; second row of Table 10.7.
- (1) Calculate the time it takes to melt PP in both the single- and twin-screw extruders, under the condition, indicated.
 - (2) Based on the observed total number of lobes needed for melting of PP under the conditions stated in part (b), what is the total number of compressions needed for complete melting of PP?
 - (3) Comment on the difference between the estimated and observed number of lobes, 6 vs. 4 for Exp 4, Table 10.7, second row of Table 10.7.

10.3 PED-Based Melting Estimates in a ZSK-30 and a ZSK 300 The PED-based melting model was discussed in Section 10.3. The model was used by Qian and Gogos to calculate the melting capabilities, under typical operating conditions, of two Coperion Co-TSEs: the laboratory-scale 30-mm ZSK 30 and the large production-scale ZSK-300 (Fig. 10.56). Their results appear on the following table:

Number of Compacted Particulate Compressions Occurring during the Passage over a $1(L/D)$ Kneading Block

	ZSK-30	ZSK-300
Barrel diameter (D , mm)	30	300
Channel depth (H , mm)	4.7	40.75
Mass flow rate (kg/h)	20	35,000
Bulk density (g/cm^3)	1	1
Screw speed (rpm)	300	300
Average t_{transit} to go over one (L/D) (s)	2.3	1.2
Number of rotations per one (L/D) transit	11.7	5.8
Number of compressions per one (L/D) transit	15.7	7.7

- (a) Verify the results of these calculations using Eqs. 10.3-1 to 10.3-5. (b) In which of the two Co-TSEs is the assumption that melting arises totally from PED and not conductive melting from the barrel? (c) Specify the operating conditions at which the ZSK-30 must be operated, for the melting results to be scalable to the 300 Megacompounder. (d) Does the PED model provide an explanation for the extraordinary melting capabilities of the 300 Megacompounder for melting such

high throughput of PE within the 10–20 of residence time? Estimate whether VED alone can provide enough mechanical energy dissipation to enable this melting rate.

- 10.4 Throughput Rate Calculations for a Solids Single Screw Feeder Feeding a Co-TSE** A single-screw feeder is used for controlled feed rate of a 30-mm Co-TSE. The experimentally obtained feed rates with LDPE pellets at different screw speeds are give in the following table:

Screw Speed (rpm)	Throughput (kg/h)
9.27	3.80
19.44	7.60
48	18.76
96	37.51
144	56.72
192	75.02
207	80.89

Calculate the feeding screw throughput rate capacity assuming plug-flow and LDPE pellet bulk density of 0.45 g/cc. The geometrical variables of the feeder screw are: barrel diameter, $D_1 = 1.66$ in; screw root diameter, $D_2 = 0.325$ in; and lead, $L = 1.2$ in. Examine and discuss the difference between the observed and calculated throughput rate feeder capabilities, as it relates to the “plug” velocity assumption.

- 10.5 Estimation of the Order of Magnitude of the FED Generated during a Single Pass of a Compacted Particulate Solid Bed over the Rotor Wing-Tip Clearance of a CM** In Example 10.1, the *local* interparticle mechanical power dissipated into heat \dot{W}_{FED} (watts) by FED during the passage of a compressed polymer particulates bed over the rotor wing-tip clearance region, is estimated by Eq. E10.1-2

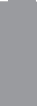
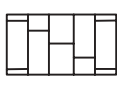
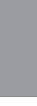
$$\dot{W}_{\text{FED}} \sim \pi D_{\text{max}} N (d_p/h) f \cdot F_N$$

where $D_{\text{max}} = 300$ mm; $h = 7.5$ mm; wing-tip width $w = 25$ mm; particulate size $d_p = 300$ microns; $f = 0.5$; and a barrel transducer pressure recording during the passage of the rotor wing tip of $P = 10^7$ Pa. Calculate the FED power dissipated per unit during a single pass over the wing tip just downstream the feed section of the FCM, Fig. 10.6(b)

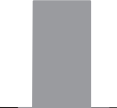
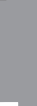
- 10.6 VED-Based Estimate of the Mixing Zone Power Requirements of a CM** Engineering estimates of the power requirement for the mixing section of CMs are difficult to make, even with 3D FEM fluid mechanical models, because CMs operate partially full, a physical state with free boundaries, which cannot be handled by such simulations. Thus, often such estimates are based on the power consumed during the flow of the polymer melt in the wing-tip region, making a parallel-plate approximation. The rationale behind this estimate is the realization that this region creates the highest shear-rate flows, due to the small clearance h between the rotor lip and the barrel. Calculate (a) the mechanical energy dissipated per pass per unit wing-tip length for a polyethylene melt with effective Newtonian viscosity

$\mu_{eff} = 300 \text{ Pa}\cdot\text{s}$ flowing in isothermal flow in the wing-tip region of $h = 7.5 \text{ mm}$, $W = 25 \text{ mm}$, $D_{max} = 300 \text{ mm}$ at a rotor speed $N = 300 \text{ rpm}$.

10.7 Effects of the Co-TSE Kneading-Disk Sequence Stagger Angle and Disk Width on Melt Distributive and Dispersive Mixing Andersen (75) presents the effects of the stagger angle in a sequence of forwarding kneading disks, as well as the effect of their width using the two schematic representations in the accompanying figure.

ELEMENT	DISTRIBUTIVE MIXING	DISPERSIVE MIXING
		
		
		

Effect of disk width on distributive mixing

ELEMENT	DISTRIBUTIVE MIXING	DISPERSIVE MIXING
		
		
		

Effect of disk sequence stagger on distributive and dispersive mixing

Discuss the validity and usefulness of the preceding qualitative figures in terms of Fig. 10.11 and this chapter's discussion on melt flow, pressurization and chaotic mixing in Co-TSEs.

10.8 Vent-Port Staging Analysis of a 42% polychloroprene – 58% CCl_4 Undergoing Devolatilization in a JSW TEX 65 Counter-TSE Examine the experimental results obtained by Sakai et al. (33), shown on Fig. 10.27 in terms of equilibrium stage analysis. The results indicate that the incoming 58% CCl_4 stream concentration is reduced to just above 7000 ppm after the second vent port downstream of the feed port. What does vent port equilibrium analysis?

- What does equilibrium stage analysis preset for this system?
- Are there any problems associated with the fact that the feed stream in a rubber slurring with a high CCl_4 concentration of 58%, requiring high amounts of CCl_4 to be removed in the first stage?

11 Reactive Polymer Processing and Compounding

- 11.1 Classes of Polymer Chain Modification Reactions, Carried out in Reactive Polymer Processing Equipment, 604
- 11.2 Reactor Classification, 611
- 11.3 Mixing Considerations in Multicomponent Miscible Reactive Polymer Processing Systems, 623
- 11.4 Reactive Processing of Multicomponent Immiscible and Compatibilized Immiscible Polymer Systems, 632
- 11.5 Polymer Compounding, 635

One can view *polymerization* as the “structuring” of monomeric molecules into macromolecular structures and *polymer processing* as the “structuring” of polymeric molecules, since it results in products of specific macromolecular orientation and morphology distributions. These two processes require very different types of process equipment and are carried out at different manufacturing facilities. *Reactive polymer processing*, in the broadest sense, is the execution of both processes simultaneously, in equipment normally associated with polymer processing. In reactive polymer processing we go either from monomer to polymer, or more often, from polymer to *modified* polymer, to shaped and structured finished products (1). Extruders, both single and twin rotor, have unique advantages in that they are capable of handling high viscosity reacting systems. On the other hand, extruders also have limitations, which must be considered when selecting equipment for a given reacting polymer stream. Following Todd (2), the advantages are easy handling and melting of polymeric particulates; rapid laminar distributive and dispersive mixing of the reactants; good temperature and residence-time distribution control; the ability to react in one or more stages under appreciable pressure levels; and also the ability to remove by the devolatilization elementary step (3) volatile unreacted species, or reaction by-products. Finally, such devices are very good drag pressurization devices and affect easy viscous melt discharge and shaping. The two main limitations are (a) difficulty in handling large heats of reaction, and (b) the high equipment cost, because of the need that the process provide for long reaction times. It is because of these two limitations that only few classic polymerization reactions are carried out in continuous reactive polymer equipment and go from monomer to finished polymer. On the other hand, single and twin rotor processing equipments are uniquely suited as *reactors* for carrying out *polymer chain modification reactions*. In this chapter, we concentrate on such reactive polymer systems, which create novel, value-added, or “designer pellet polymers,” needed to meet specific product properties.

The equipment in which reactive polymer processing is carried out, is in fact a *chemical reactor*. The performance, design, analysis, and control of such reactors have been dealt

with extensively in the chemical engineering literature (4). We follow the standard chemical engineering reactor design approach, pointing out both the similarities and the profound differences between classic chemical engineering *low viscosity* reactor design and that which is necessary in *high viscosity* reactors as the ones used in reactive processing. The main differences between the two are the conditions required for achieving adequate mixing: in low-viscosity reactors, with their turbulent flow regimes, mixing times for achieving composition uniformity, although they have to be addressed, are short compared to the *characteristic reaction times*. Whereas in high viscosity reactors, in which only laminar creeping flows are attainable, we have to secure efficient low-energy-consuming distributive flow kinematics to achieve mixing times that are commensurate to the reaction times of the reacting components. In this chapter we make use of the *ratios of characteristic times* of the competing processes of mixing, diffusion, reaction, and heat generation/transfer, pioneered by Biesenberger and Sebastian (5).

11.1 CLASSES OF POLYMER CHAIN MODIFICATION REACTIONS, CARRIED OUT IN REACTIVE POLYMER PROCESSING EQUIPMENT

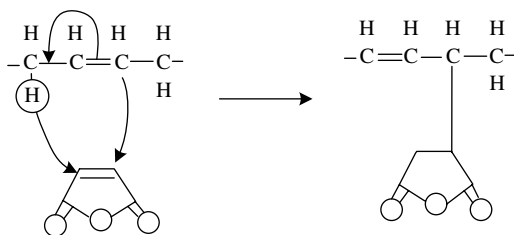
There are many polymer chain modification reactions of different types that have been carried out on polymer melts processed in single and twin rotor extruders. This activity, (4–6) in the analysis of polymerization reactors, driven by market forces seeking to create value-added polymers from commodity resins, started in the mid-1960s in industrial research laboratories (7). Indeed much of the early work is to be found in the patent literature.¹ Although in recent times more publications, both industrial and academic can be found in the open literature, there is still a good deal of industrial secrecy, because the products of reactive polymer processing are of significant commercial value to industry. Below we will deal briefly with two important examples of such reactions.

Chain Functionalization Reactions

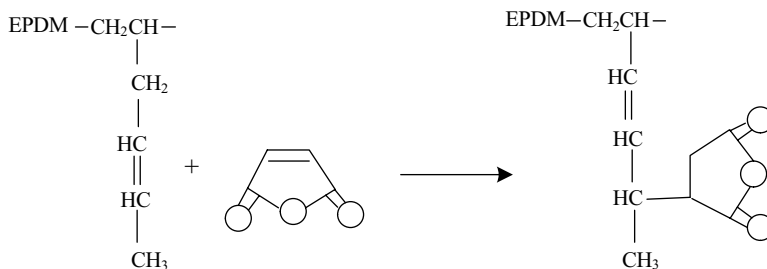
Chain functionalized polymers or graft copolymers are of great technological importance. They are used as compatibilizing agents for immiscible polymer blends (8) and adhesive layers between polymer–polymer co-extruded surfaces (8). Currently, of all polymers sold, about 30% are in the form of compatibilized immiscible blends (9–12). Next we discuss a few examples of chain functionalization.

Reactive polymer processing has been used extensively in the manufacture of carboxyl-containing polymers (8). The *carboxylation of unsaturated polymers* with maleic anhydride (MAH) proceeds through the “ene” reaction where succinic anhydride is attached to the polymer with a shift of the double bond to the adjacent site.

1. Kowalski (7), commenting on the early period of work in this area, stated as follows: “At Exxon Chemical we measured the level worldwide interest in reactive extrusion via a patent and literature survey for the period 1966–1983. We found a total of more than 600 different patents granted to 150 companies—many Japanese. In comparison only 57 papers were found in the open literature, mostly by extruder vendors . . . only three papers were from the above 150 companies!”

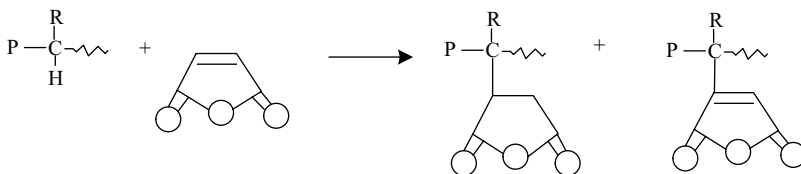


The carboxylated ethylene-propylene-diene elastomeric terpolymer (EPDM) with MAH (13)



is one of the components of producing the impact modified Dupont SuperTough™ Nylon 6-6 compatibilized polymer blend. The blend components are: EPDM-MAH-Nylon-EPDM, EPDM and Nylon 6-6 (Zytel™ST) (14,15). The two amine groups of Nylon 6-6 (one at each end) are capable of reacting and cross-linking the EPDM, creating the compatibilizing first blend component in the preceding formula. The dispersed 20% elastomeric phase is of the order of one micron and is the main toughening agent.

Hydroxylation of saturated polymers can also take place in polymer processing equipment. As a first example, MAH in the presence of a free-radical initiator will attach succinic or anhydride groups on the saturated chain (16)



Although this reaction does not involve MAH homopolymerization, the reaction conditions used are those promoting homopolymerization. Thus, the MAH homopolymerization mechanism has to be understood in order to properly carry out the MAH carboxylation of saturated polymers in the presence of a free radical initiator. In other words, maleation of polyolefins represents a rather complex reaction, involving dimethyl formamide (DMF) to inhibit the undesirable MAH homopolymerization (17) and diamyl peroxide (DCP) to partially cross link the polyolefins being maleated (18). About 0.2% of the MAH is grafted onto polyolefins using peroxide (POX) concentrations of 100–500 ppm. We discuss the decomposition rate requirements in Section 11.2 in a process scheme shown in Fig. 11.1. Higher levels of POX achieve higher bonded MAH concentrations, but result in chromophoric reactions, which are product-undesirable. Colorless maleated polyolefins can be produced at concentrations greater than 0.2% in

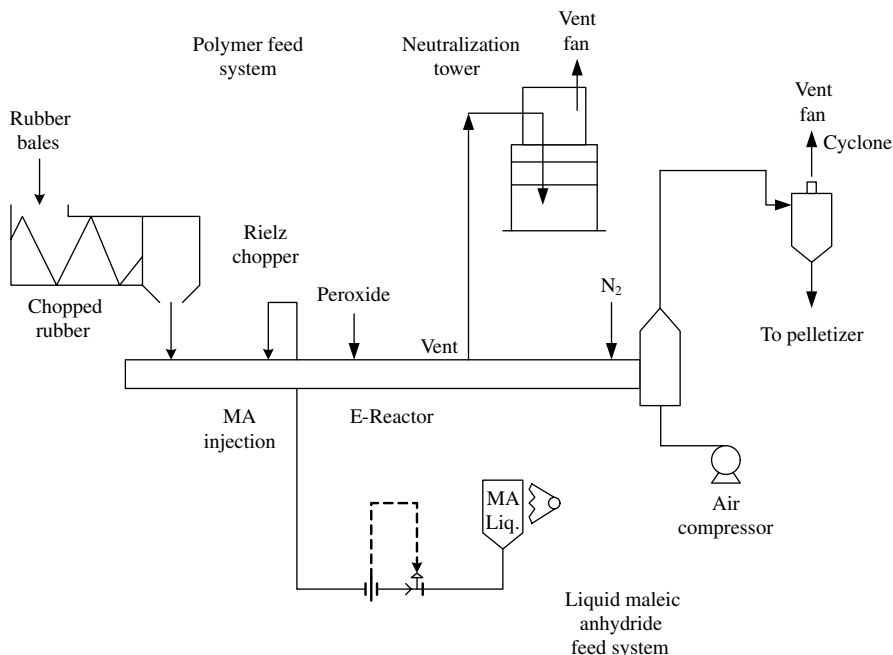
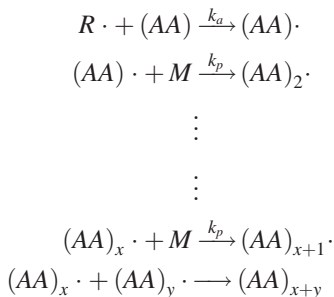
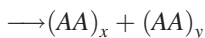


Fig. 11.1 Maleic anhydride graft process for baled EP rubber. [Reprinted by permission from R. C. Kowalski, "Fit the Reactor to the Chemistry," in *Reactive Extrusion*, M. Xanthos, Ed., Hanser, New York, 1992.]

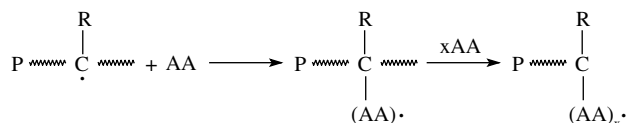
dilute solution; it is obvious, therefore, that maleation, carried out in reactive polymer processing equipment taking place under evolving degrees of mixedness and in nonuniform temperature fields that are difficult to control, is a more complex reaction scheme. We will be discussing the roles and control of the competing phenomena of laminar mixing, temperature increases, diffusion, and reaction in Sections 11.2 and 11.3. Saturated polymers are also commonly carboxylated with acrylic acid (AA) monomer, which is itself polymerizable, since the reaction takes place in the presence of a free-radical initiator. The result is a graft copolymer, where the polyacrylic acid is the graft, produced simultaneously with polyacrylic acid. The mechanisms are, for homodimerization (19,20):



or



The simultaneous and desired grafting of polyacrylic acid onto the saturated host polymer proceeds as:



followed by the termination step(s).

Common saturated polymers-forming copolymers with AA are HDPE, PP and ethylene-propylene copolymer (EPR), the last being a grafted elastomer. All are blend compatibilizers, high density polyethylene (HDPE)-g-AA, PP-g-AA, and EP-g-AA. Producing these copolymers through reactive processing is the only reaction route available, because copolymerization between AA and the olefin monomers just given is not possible since the polar AA reacts and inactivates the metal-based olefin polymerization catalysts (8).

Polymer Macromolecular Chain Modification Reactions

Soon after the Ziegler-Natta catalyst enabled the commercial production of isotactic polypropylene (PP), it became apparent that it was a difficult polymer to melt process, especially in producing thin fibers at acceptable rates. Kowalski (21) carrying out retarded elastic melt recovery experiments with an instrument developed by Bryce Maxwell showed that PP has an unusually high melt elasticity that results in both extrudability problems and extruded products with high levels of retained orientation. Later, Kowalski and his co-workers at Esso Research and Engineering (22–25) extruded PP using a “reverse” temperature profile by setting high barrel temperatures of 370–425°C at the single screw extruder (SSE) melting zone. Such high temperatures near the feed zone will generate oxygen free radicals from the air in the particulates solid bed. Such free radicals may initiate a β chain scission reaction at the ternary carbon backbone sites of the PP melt. Since chain scission is more likely to occur with longer PP chains, the product of the preceding reaction will be of lower weight-average molecular weight (\bar{M}_w) and narrower molecular weight distribution (MWD). In turn, these polymer chain modifications have a profound effect on both melt viscosity and melt elasticity, as shown in Fig. 11.2, where melt flow rate (MFR), indicative of viscosity and extrudate swell, indicative of melt elasticity, are plotted against MW and MWD (21,9). It is evident from this figure that the *entire viscoelastic behavior* is affected by the chain “degradation path,” that is, each of the five curves on Fig. 11.2, where the parameter MFR is indicative of the viscous nature and the extrudate swell is indicative of the elastic nature of the PP viscracked melts. They are plotted against \bar{M}_w and MWD. It is evident on this figure that the entire viscoelastic behavior is affected in every one of the degradation paths, that is, each of the five curves on Fig. 11.2. It is for this reason that the free radical polymer chain modification of PP carried out by reactive processing is commonly referred to in practice as “controlled rheology” (CR-PP) or viscracking processes. In practice, the *amount and rate* of the free radical POX initiator can be controlled, as can the *protocol and mode of addition* of the POX stream, mixed with the feed, or introduced as a diluted or undiluted liquid at an appropriate axial position, usually after melting is completed. It must be noted, though, that the presence of oxygen and process stabilizers (free-radical scavengers) may interfere through radical

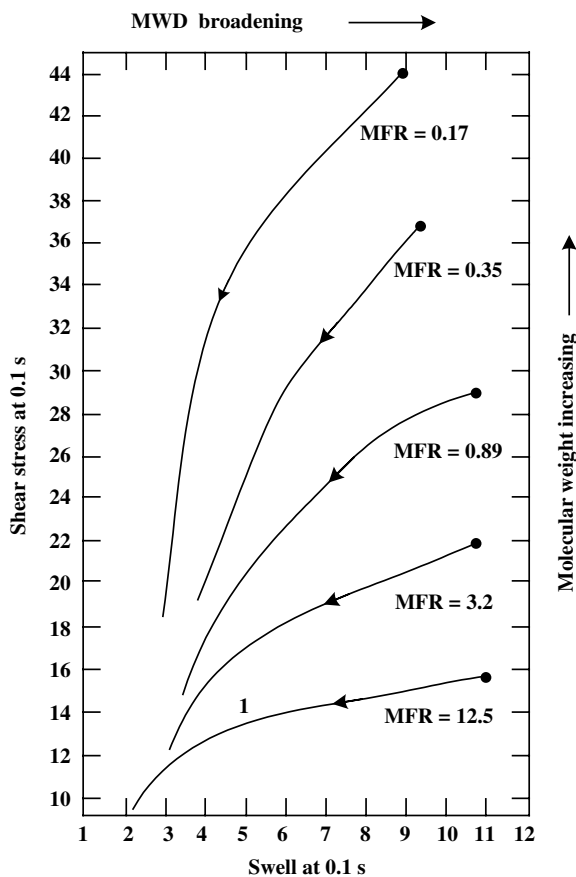


Fig. 11.2 The effect of the PP controlled rheology (CR) or “viscracking” process on the “viscoelastic grid”; each curve represents a PP macromolecular “degradation path.” [Reprinted by permission from R. C. Kowalski, “Fit the Reactor to the Chemistry,” in *Reactive Extrusion*, M. Xanthos Ed., Hanser, New York, 1992.]

competing reaction (26). Hence, closed-loop viscracking control schemes, based on the linear relationship between POX concentrations and MFR, have been developed by industry (27–29) as well as by academic research (30,31). Of course, in-line or on-line measurement of MFR is required in these control schemes. Information on the “process technology” of CR–PP processes can be found in Xanthos (26), and the accepted PP degradation reaction with peroxides ROOR is given by Dorn (32) and Tzoganakis, Vlachopoulos, and Hamielec (33).

Since the peroxide decomposition may be the rate-controlling reaction step in the preceding, it is of paramount importance to choose the peroxide that has the “required” decomposition rate at the real or expected melt processing temperatures. Such rates for dialkylperoxides are determined from decomposition kinetic data carried out in dilute decane or dodecane solutions in the form of half-lives, $t_{1/2}$, which is the time required for the decomposition of 50% of the POX (34), as shown in Figure 11.3.

High temperature and low reactivity host substances (e.g., polymers) are known to favor secondary decompositions, leading to other active radicals and nonreactive volatiles

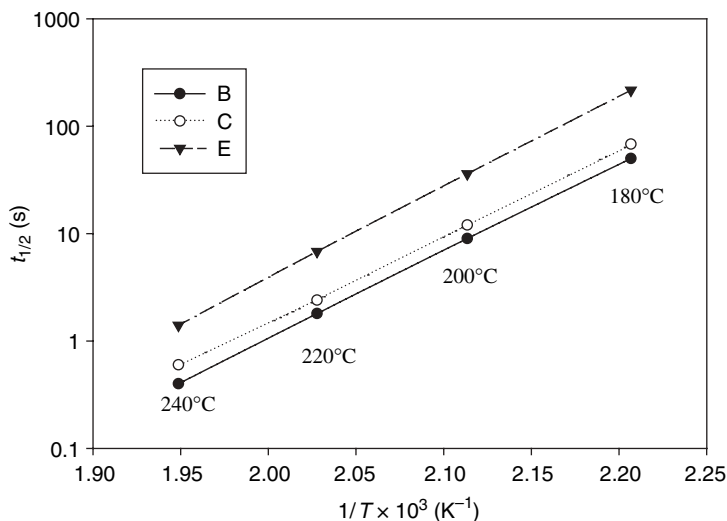


Fig. 11.3 Arrhenius plots of the half-lives of three different POX showing that despite the difference in half-lives among them, their activation energies are of the same value and equal to 155 KJ/mol.

(32). Thus, is it not surprising that the dilute solution, half-lives shown in Fig. 11.3 are different from the experimentally obtained effective half-lives in molten flowing polymers, which may be 2 to 5 times longer than the dilute solutions $t_{1/2}$ (34,35). An additional reason for this difference is the gradual and, at times, incomplete laminar mixing of the POX in polymer melts, compared to the “instantaneous” and homogeneous mixing obtained with very low-viscosity diluents, such as decane. We discuss this further in Section 11.2. Finally, half-lives, $t_{1/2}(T)$ are important to the semiquantitative *specification* of the required residence time of the polymer in *molten form*, that is, the “age” of the melt from the time of its formation to the die exit at the prevailing processing temperatures. For 99% POX decomposition, the average residence time of the melt in the reactive polymer processing equipment must be of the order of six to seven times its half-life at the process temperature.

Recalling the profound differences in the melting mechanisms in SSEs and in co-rotating twin-screw extruders (Co-TSE) (Chapter 5), we see that the latter one creates all of the melt almost instantaneously, resulting in a very narrow “melt age distribution,” while in SSE the age distribution is very broad. Thus, Co-TSEs and twin rotor *melting* devices [e.g., continuous mixers (CMs)] are better suited to be “reactors” of polymer melts, as is reflected in the current industrial reactive polymer processing practice.

Experiments conducted in laboratory-scale batch-intensive mixers can be suitable for following the kinetics of CR-PP. PP pellets or powder are introduced and are completely melted in these hot co-rotating batch devices, under a blanket of nitrogen. Following melting, the POX is introduced all at once and is mixed into the polymer melt. The ensuing PP degradation will cause the torque required to drive the mixer shafts at the process speed to drop, due to the reduction of the melt viscosity of the reacting melt. Figure 11.4 shows the torque reduction rate, which is very similar to the POX (Lupersol 101) decomposition in dodecane (36). The result that the kinetics of the controlling POX decomposition in an isothermal dilute solution environment is the same as the viscracking kinetics in a melt

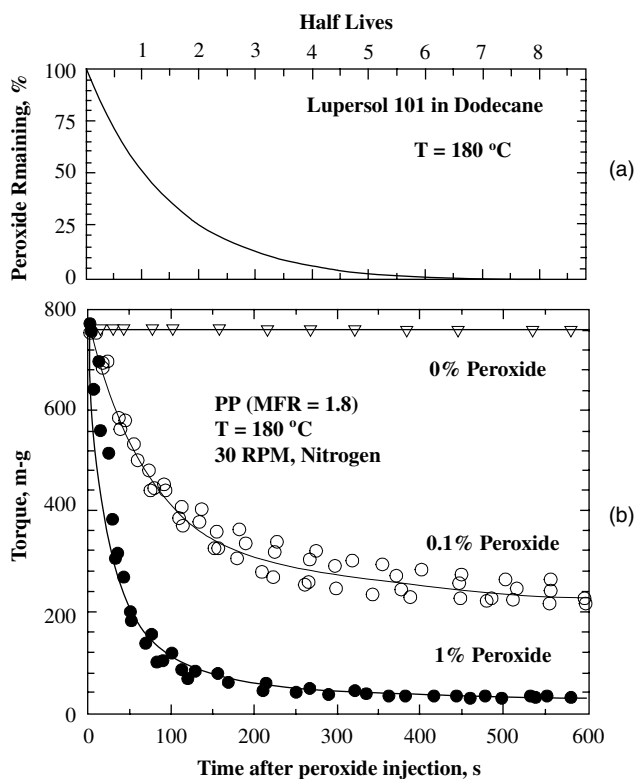


Fig. 11.4 Comparison of (a) the POX decomposition rate in dodecane at 180°C with (b) the rate of reduction of the batch mixer torque, that is, reduction of the viscosity of the reacting PP, indicates that the two are identical; the POX decomposition is *rate controlling* and the CR-PP reactions are practically complete after 6–7 POX half-lives. [Reprinted by permission from D. W. Yu, “Polyolefin Blends Modified through Peroxide Initiated Reactions,” Ph.D Dissertation, Department of Chemical Engineering, Stevens Institute of Technology, Hoboken, NJ, 1991.]

continuously mixed at 180°C and 30rpm indicates that (a) the mixing rate in the batch mixer is fast, compared to the Lupersol decomposition rate, and (b) there is little melt temperature increase during this reactive processing.

Ryu et al. (37) and Xanthos et al. (38) prepared thin films of sintered PP, 200–300 micron diameter, precoated at room temperature with POX “E”. The films were allowed to react in a constant-temperature oven and samples were withdrawn and analyzed to determine \bar{M}_W and MWD. It was found that the reduction rates of the \bar{M}_W and MWD became essentially zero after six to seven half-lives of POX “E” as measured in dodecane. The conclusion is, since there is no mixing during reaction, the diffusion rate of the POX coating onto the PP particulates is not rate controlling, that is, CR-PP for those coated 200–300- μm PP powder particulates is not diffusion controlled. In reactive processing one should strive for process conditions and reaction kinetics where the reactive polymer processing environment is uniform, resulting in uniform product. We discuss this in Sections 11.2 and 11.3.

Finally it is instructive to present the resulting macromolecular chain modifications (MWD) and their effect on the rate-dependent viscosity during viscracking, as shown in

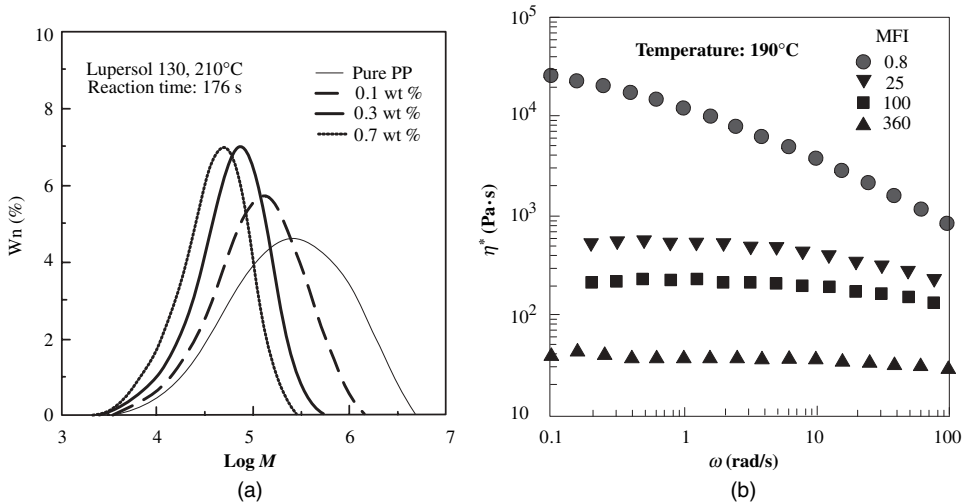


Fig. 11.5 (a) the MWD of a 0.8 MFR PP before and “viscracking” using three different POX E concentrations (b) the corresponding dynamic viscosities and MFR values of the original and three “viscracked” polypropylenes [Reprinted by permission from S. H. Ryu, C. G. Gogos, and M. Xanthos, “Kinetic Studies on the Peroxide Initiated Polypropylene Controlled Degradation,” *SPE ANTEC Tech. Papers*, **35**, 879–881 (1989).]

Figure 11.5 (37). At high POX concentrations, η^* at low frequencies can be reduced 100- to 1000-fold, and the polymer melts become essentially Newtonian. Such CR-PP products are very easily spinnable.

Another example of chain modification reactive processing reactions are those that induce *controlled long chain branching* or (*light cross-linking*). Such reactions are carried out in the molten state in order to obtain specific melt rheological properties needed for specific polymer shaping methods. As an example, long chain branching incorporation onto (linear) polyethylene terephthalate (PET) chains, imparts sufficient levels of melt elasticity to the long chain branched PETs and make them suitable for extruding foamed or blow molded products (39), both of which require appreciable levels of melt elasticity.

11.2 REACTOR CLASSIFICATION

Chemical reactors are normally classified into *batch* and *continuous* reactors. In *batch* reactors all the species of the “batch” of compounds placed into the reactor have the same *residence time*, since the reactor forms a “closed system” with no material exchange with the surroundings. If the reactive fluids are agitated and are of monomeric level viscosities, then the resulting turbulent flow imparts *uniform* and practically *instantaneous mixing*. Turbulent flow is also necessary, but not sufficient, to achieve an efficient heat transfer and obtain a uniform batch reactor temperature field. For this to happen, first the heat of reaction has to be relatively small to moderate and second, the rate of heat conducted via both internal and “jacketed” vessel wall coolers has to be larger or much larger than the rate of reaction heat generation.

Batch Reactor Analysis

In batch reactors, for thermally simple types of reactions, that is, ones that can be attributed to a single reaction step, generally applicable to the propagation step of polymerization reactions, we can write the following thermal energy balance (6)

$$\frac{dT}{dt} = \frac{(-\Delta H_r)\dot{r}}{\rho C_p} - \frac{hA}{\rho C_p V}(T - T_c) \quad (11.2-1)$$

where $(-\Delta H_r)$ is the heat released by the reaction, \dot{r} the reaction rate, h the overall heat transfer coefficient between fluid and coolant, A the heat transfer area, V the batch reactor volume, and T_c the coolant temperature. Equation 11.2-1 can be rewritten in dimensionless form as

$$\frac{d\hat{T}}{dt} = \frac{(-\Delta H_r)\dot{r}_{\text{ref}}\hat{r}}{\rho C_p T_{\text{ref}}} - \frac{hA}{\rho C_p V}(\hat{T} - \hat{T}_c) \quad (11.2-2)$$

where the dimensionless temperature is defined as

$$\hat{T} = \frac{T - T_{\text{ref}}}{T_{\text{ref}}} \quad (11.2-3)$$

and the dimensionless reaction rate is defined as

$$\hat{r} = \frac{\dot{r}}{\dot{r}_{\text{ref}}} \quad (11.2-4)$$

where T_{ref} is a reference temperature and \dot{r}_{ref} is the rate of reaction at the reference temperature.

The two right-hand terms of Eq. 11.2-2 have units of reciprocal time. Physically, they are the inverse of the *characteristic times* for heat released by the reaction, t_G , and for heat removal, t_R . These can be written as

$$t_G = \frac{\rho C_p T_{\text{ref}}}{(-\Delta H_r)\dot{r}_{\text{ref}}} \quad (11.2-5)$$

and

$$t_R = \frac{\rho C_p V}{hA} = \frac{\rho C_p R_H}{h} \quad (11.2-6)$$

where $R_H = V/A$ is a "hydraulic radius." The ratio of these characteristic times gives good estimates on the thermal behavior of the reactor. Thus, Eq. 11.2-2 becomes

$$\frac{d\hat{T}}{dt} = t_G^{-1}\hat{r} - t_R^{-1}(\hat{T} - \hat{T}_c) \quad (11.2-7)$$

If $t_G/t_R < 1$, the temperature field is expected to be nonuniform and the average batch-reactor temperature increases with time; whereas, if $t_G/t_R > 1$, the temperature field is

expected to be uniform and time independent, which, of course, is a desirable reactor condition to achieve from the point of view of both reaction control and product uniformity.

A very important characteristic of polymerization reactors is their thermal stability as discussed by Sebastian (6). Chain addition polymerizations are *thermally simple* reactions, in that the polymerization exotherm is attributable almost in its entirety to the chain propagation step. For chain addition polymerization reactors the rate of reaction \dot{r} is proportional to the product of the square root of initiator concentration, c_i , and to monomer concentration, c_m

$$\dot{r} = \dot{r}_p = k_{ap} c_i^{1/2} c_m \quad (11.2-8)$$

where \dot{r}_p is the rate of propagation, and k_{ap} the apparent reaction rate. By assuming that k_{ap} has an Arrhenius-type dependence on temperature characterized by the activation energy E , and substituting Eq. 11.2-8 into Eq. 11.2-7, results in

$$\frac{d\hat{T}}{dt} = t_G^{-1} \hat{r}_p - t_R^{-1} (\hat{T} - \hat{T}_c) \quad (11.2-9)$$

where

$$\hat{r}_p = e^{(\hat{E}\hat{T}/(1+\hat{T}))} \hat{c}_i^{1/2} \hat{c}_m \quad (11.2-10)$$

and the dimensionless activation energy and concentration are defined, respectively, as

$$\hat{E} = E/RT_{\text{ref}} \quad \text{and} \quad \hat{c}_k = c_k/c_{k0} \quad (11.2-11)$$

Next, following Semenov (40) we define another dimensionless temperature Θ , which is the product of the dimensionless temperature define in Eq. 11.2-3 with the dimensionless activation energy

$$\Theta = \frac{E}{RT_{\text{ref}}} \left(\frac{T - T_{\text{ref}}}{T_{\text{ref}}} \right) = \hat{E}\hat{T} \quad (11.2-12)$$

and in terms of Θ , Eq. 11.2-9 can be written as

$$\frac{d\Theta}{dt} = t_{AD}^{-1} \exp\left(\frac{\Theta}{1 + \varepsilon\Theta}\right) \hat{c}_i^{1/2} \hat{c}_m - t_R^{-1} (\Theta - \Theta_c) \quad (11.2-13)$$

where

$$t_{AD} = \hat{E}^{-1} t_G = \varepsilon t_G \quad (11.2-14)$$

Semenov noted that when $t_G/t_R \lll 1$, explosions may occur even before there is any appreciable depletion of the reactants, that is, when the dimensionless initiator and monomer concentrations are nearly unity and when $T_{\text{ref}} \approx T_0 \approx T_c$, where T_0 is the initial temperature. These conditions constitute the *early runaway approximation*

described by

$$\frac{d\Theta}{dt} \sim \exp\left(\frac{\Theta}{1 + \varepsilon\Theta}\right) - a\Theta \quad (11.2-15)$$

where the ignition parameter, a , is the ratio of two characteristic times

$$a = \frac{t_{AD}}{t_R} = \varepsilon \frac{t_G}{t_R} = \varepsilon \frac{h}{(-\Delta H_r)\dot{r}_o R_H} \quad (11.2-16)$$

The dimensionless heat generation term $r_G = \Theta/(1 - \varepsilon\Theta)$ is plotted as a function of the dimensionless temperature $\Theta = \hat{T}/\varepsilon$ for various values of the inverse dimensionless activation energy, ε , in Fig. 11.6.

We note two important features on this graph. First, the transition from stable to potentially “runway” conditions increases dramatically with decreasing ε , that is, increasing the reaction constant activation energy; in the limit at $\varepsilon \rightarrow 0$ we have explosive conditions. Second, the transition from stable to potentially unstable reactions occurs when the dimensionless at $\Theta = \hat{T}/\varepsilon \sim 1$. Furthermore, for $\Theta = 10^{-1}$ the reaction is stable with $\Theta/(1 + \varepsilon\Theta) = 1$ and for $\Theta \geq 10^1$ there is a significant increase (of the order of 10^4 to 10^{10}) in the dimensionless heat-generation term, denoting the potential of unstable, runaway reactions.

Chain addition polymerizations have a typical value of $\varepsilon \approx 4 \times 10^{-2}$, and for such batch reactions r_G increase 10^6 times from $\Theta = 10^{-1}$ to $\Theta = 10$, with the plateau region at Θ values that are 10^{10} times higher. It is for this reason that chain addition polymerization reactions, although experimentally studied, as with methyl methacrylate (41,42), are rarely carried out in reactive polymer processing equipment.

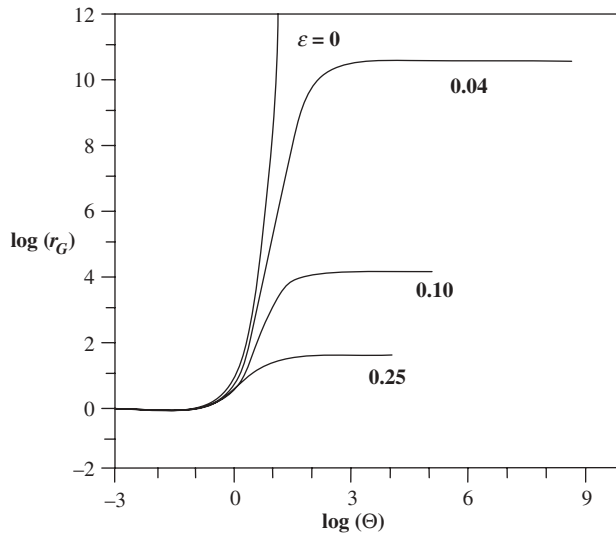


Fig. 11.6 Dimensionless heat generation rates for various values of the dimensionless activation energy. [Reprinted by permission from D. H. Sebastian, “Non-Isothermal Effects in Polymer Reaction Engineering,” in *Temperature Control Principles for Process Engineers*, E. P. Dougherty, Ed., Hanser, Munich, 1993.]

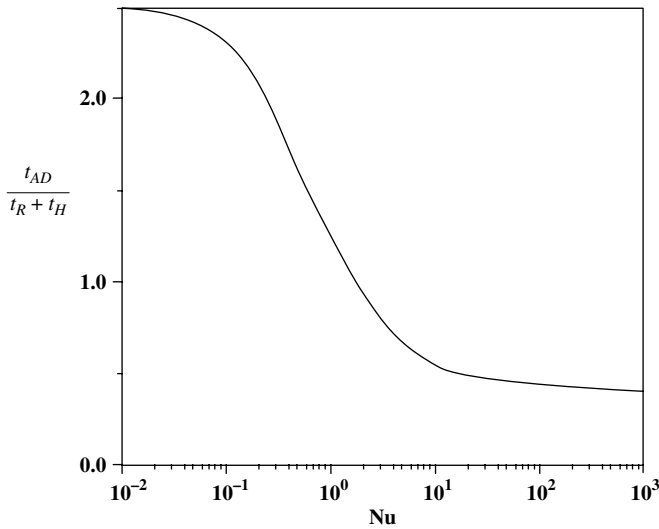


Fig. 11.7 Runaway boundary as a function of Nu number. [Reprinted by permission from D. H. Sebastian, “Non-Isothermal Effects in Polymer Reaction Engineering,” in *Temperature Control Principles for Process Engineers*, E. P. Dougherty, Ed., Hanser, Munich, 1993.]

Sebastian (2,6) following Frank-Kamenetskii (43) arrived at the results depicted on Fig. 11.7, where the Nusselt (Nu) dimensionless number $Nu = hR_H/k$, k is the thermal conductivity, t_H is the characteristic time for removing the reaction-generated heat by conduction

$$t_H = \frac{\rho C_p R_H^2}{k} = \frac{R_H^2}{\alpha_T} \quad (11.2-17)$$

where $\alpha_T = k/\rho C_p$ is the thermal diffusivity. The heat removal in this case is a series process of the fluid conducting to the vessel followed by convective heat transfer to the surroundings. For this case a combined heat removal time is defined below

$$T_R = t_R + t_H \quad (11.2-18)$$

and the Nusselt number is

$$Nu = \frac{t_H}{T_R} \quad (11.2-19)$$

The ratio of the adiabatic heat generation characteristic time to that of heat removal is now $a = t_{AD}/(t_R + t_H)$ and related to the Nusselt number. For the chain addition polymerization this relation is shown graphically in Fig. 11.7.

It is noteworthy that the transition from large to small ignition parameter a transition is practically complete from $Nu \sim 10^{-1}$ to $Nu \sim 10$, and that the transition occurs when a is nearly unity. Both these results, because of their simplicity and because of the fact that they can be generalized to all competing processes, are very useful in understanding the results of the effects of competing processes—in this instance, the adiabatic reaction-generated heat characteristic time to the total heat-removal characteristic time. The

preceding simplified reaction kinetics and reactor behavior models cut to the core of illustrating competing phenomena in reactors. As suggested by Sebastian, the reader should not be deceived by this apparent simplicity. These models do not trivialize the results, but rather capture the essence that distinguishes principal cases of reaction and reactor behavior *without* obscuring the principles in intractable mathematics. Thus they are equally useful in determining dynamic similarity (44) in the process of scale-up as they are in reactor analysis and design.

The foregoing analysis holds for homogeneous single-phase reactions, but can also be applied to nonhomogenous, dispersed-phase morphology consisting of spatially well-distributed small spherical domains. Such systems can be considered, approximately, to be “pseudocontinua.” In the preceding analysis of thermally simple propagation reactions in batch reactors, t_m , the mixing characteristic time was assumed to be essentially zero because of the prevailing turbulent flow in the early reaction stages. We now address reactors where mixing is a most important consideration: The polymer processing equipment–reactor is used primarily to modify polymer chains in the molten state; thus, the resulting flows are laminar, mixing times can be considerable, and mixing spatial uniformity can be problematic to product stream quality.

Linear Continuous Flow Reactors

Most reactive polymer processing operations take place in single or twin rotor-type steady continuous-processing equipment or “reactors.” Following Biesenberger (3), all continuous flow reactors can be designated as either linear continuous flow reactors (LCFRs), or back-mixed flow reactors (BMFR). In LCFR, shown schematically in Fig. 11.8, $L \gg H$ and the dominant flow direction axial. The axial distance downstream the feed inlet, z , corresponds to the time, t , in a batch reactor; that is, the reacting stream in a LCFR “ages” along the z direction as the batch material does with time.

The *plug flow reactor* (PFR) is conceptually the simplest example of a LCFR: all fluid elements have the same axial velocity, and therefore they have the same residence time or “age” at the exit, which would correspond to the batch reactor time. But, unlike the batch reactor in the CPFRR there is no mixing of the species except by diffusion. Figure 11.9(a) schematizes a CPFRR.

Tubular flow reactors (TFR) deviate from the idealized PFR, since the applied pressure drop creates with viscous fluids a laminar shear flow field. As discussed in Section 7.1, shear flow leads to mixing. This is shown schematically in Fig. 11.9(a) and 11.9(b). In the former, we show laminar distributive mixing whereby a thin disk of a *miscible* reactive component is deformed and distributed (somewhat) over the volume; whereas, in the latter we show laminar dispersive mixing whereby a thin disk of *immiscible* fluid, subsequent to being deformed and stretched, breaks up into droplets. In either case, diffusion mixing is superimposed on convective distributive mixing. Figure 11.9(c) shows schematically the

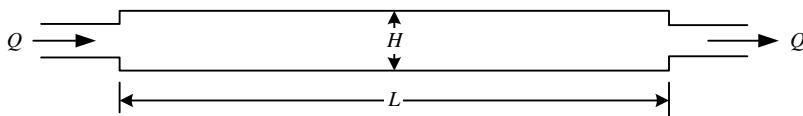


Fig. 11.8 Schematic representation of continuous flow reactors of length L , characteristic height H , and steady flow rate, Q .

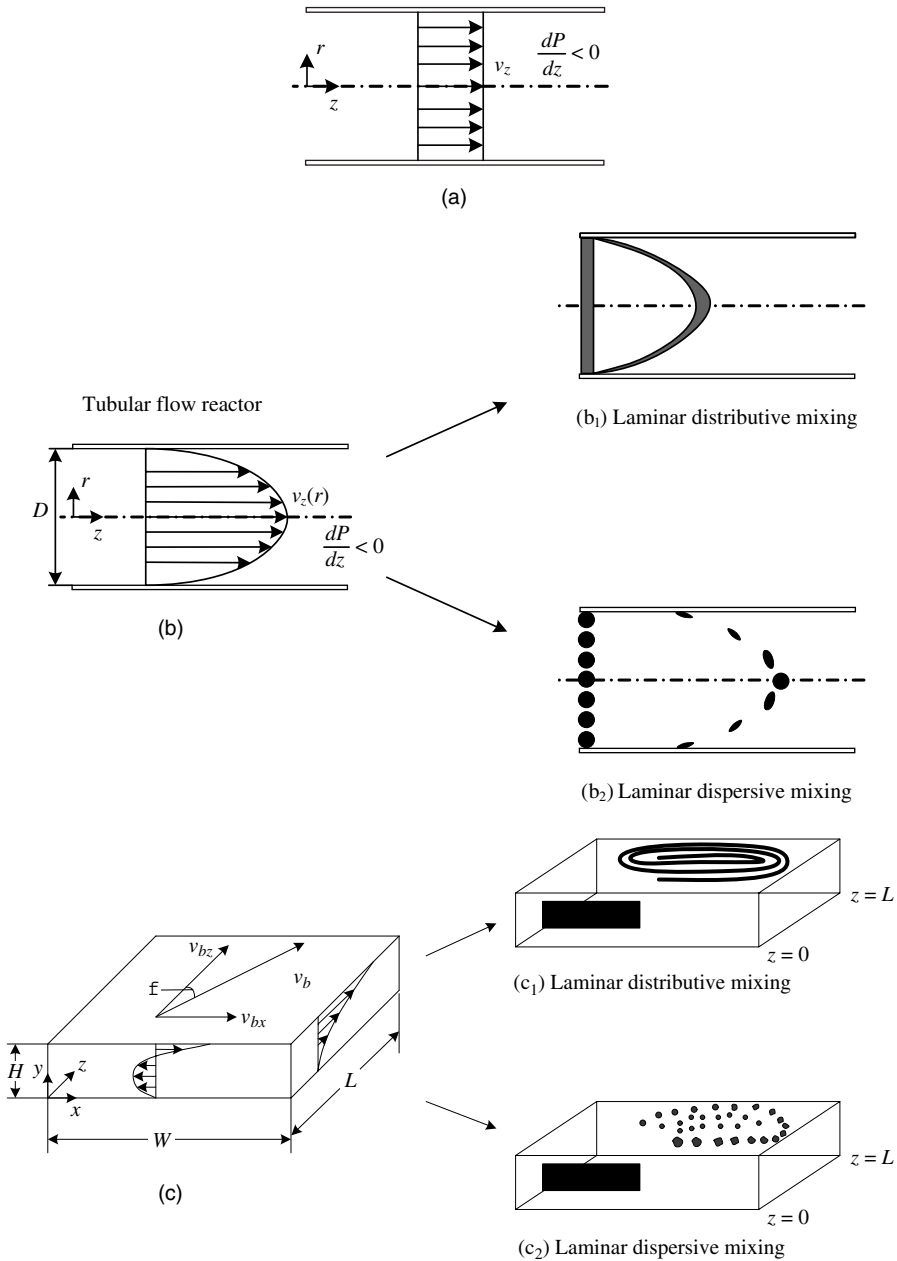


Fig. 11.9 Types of linear continuous-flow reactors (LCFRs). (a) Continuous plug flow reactor (CPFR) resembling a batch reactor (BR) with the axial distance z being equivalent to time spent in a BR. (b) A tubular flow reactor (TFR) with (b₁) miscible thin disk of reactive component deformed and distributed (somewhat) by the shear field over the volume, and (b₂) immiscible thin disk is deformed and stretched and broken up into droplets in a region of sufficiently high shear stresses. (c) SSE reactor with (c₁) showing laminar distributive mixing of a miscible reactive component initially placed at $z = 0$ as a thin slab, stretched into a flat coiled strip at $z = L$, and (c₂) showing dispersive mixing of an immiscible reactive component initially placed at $z = 0$ as a thin slab, stretched and broken up into droplets at $z = L$.

prevailing down-channel and cross-channel velocity profiles in the metering section of an SSE, with (c_1) showing laminar distributive mixing of a miscible reactive component initially placed at $z = 0$ as a thin slab, stretched into a flat coiled strip at $z = L$, and with (c_2) showing dispersive mixing of an immiscible reactive component initially placed at $z = 0$ as a thin slab, stretched and broken up into droplets at $z = L$.

The SSE is an important and practical LCFR. We discussed the flow fields in SSEs in Section 6.3 and showed that the helical shape of the screw channel induces a cross-channel velocity profile that leads to a rather narrow residence time distribution (RTD) with cross-channel mixing such that a small axial increment that moves down-channel can be viewed as a reasonably mixed differential batch reactor. In addition, this configuration provides self-wiping between barrel and screw flight surfaces, which reduces material holdback to an acceptable minimum, thus rendering it an almost ideal TFR.

If the striation thickness, r , becomes smaller than $(r)_{\text{crit}}$, which satisfies the relation below

$$t_{D_{\text{crit}}} = \frac{r_{\text{crit}}^2}{\mathcal{D}_{AB}} \ll t_{\text{res}} \quad (11.2-20)$$

then the ratio of the diffusion and residence characteristic times

$$\frac{t_{D_{\text{crit}}}}{t_{\text{res}}} \ll 1 \quad (11.2-21)$$

and the major portion of the LCFR is molecularly mixed. Since the rate of reaction changes continuously along the reactor as a result of concentration and temperature changes, some metric is required to represent the typical reactor characteristic, such as the familiar half-life. Sebastian (6) suggested that based on feed conditions we can devise a *characteristic* reaction time without solving any equations as follows:

$$t_r = \left(\frac{c}{\dot{r}} \right) \Big|_0 \quad (11.2-22)$$

where c is the reactive species concentration, for example, POX concentration in PP controlled-rheology reactive processing. For simple n th-order kinetics, $\dot{r} = kc^n$

$$t_r = \frac{1}{kc^{n-1}} \Big|_0 \quad (11.2-23)$$

which for first-order kinetics reduces to

$$t_r = \frac{1}{k} \quad (11.2-24)$$

and for second-order kinetics reduces to

$$t_r = \frac{1}{kc_0} \quad (11.2-25)$$

Equation 11.2-25 is the formal definition of *half-life*, the time the second-order reaction takes to reduce the initial concentration to half the initial c_0 . Following the methodology of

gaining insights for reactive polymer processing systems by examining the ratios of characteristic times of competing phenomena taking place in such reactors, we define the Damkohler dimensionless number, Da , as

$$Da = \frac{t_{\text{res}}}{t_r} = \left(\frac{V}{Q} \right) \left(\frac{\dot{r}}{c} \right) \Big|_0 \quad (11.2-26)$$

where V is the reactor volume and Q the volumetric flow rate.

In Fig. 11.10 the ratio of $c(t)/c_0$ is plotted against Da for well-mixed BR and LCFR with half-, first-, and second-order kinetics systems. Again, we observe that although each case has different concentration histories and flow conditions, we can have the following simple rule-of-thumb analysis for complex reactive processing systems: reactions are roughly half complete at $Da = 1$; they are practically complete at $Da = 10$; and the systems are essentially unreacted at $Da = 0.1$. The entire dynamic state of the reaction is in the region $10^{-1} < Da < 10$; this is a similar conclusion to that on Fig. 11.7 earlier in this section.

Furthermore, using the conditions for “complete” conversion of $Da \approx 10$, Sebastian (6) noted that, one can solve for any parameter in the Da number, given values of others, to provide a simple linearization of a potentially complicated kinetic analysis. One can generalize this simple approach and obtain adequate analysis of complex systems with competing physical phenomena, one “driving” and the other “resisting”

$$0.1 \leq \frac{t_{\text{resisting}}}{t_{\text{driving}}} \leq 10 \quad (11.2-27)$$

Examples of the preceding for reactive systems, other than Da , are t_D/t_{mix} and t_r/t_D , both giving rise to molecularly mixed systems.

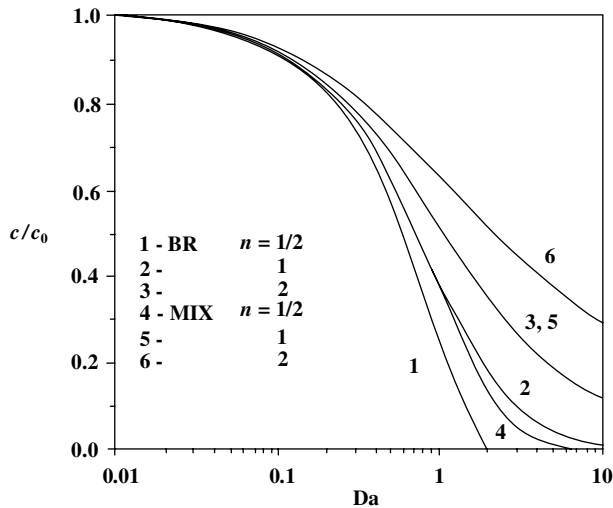


Fig. 11.10 The reduction of the initial reactant concentration as a function of the Da number, showing the unifying ability of the use of characteristic time ratios. The curves are solutions to the kinetic expressions for batch and LCFR with half-, first-, and second-order kinetics. [Reprinted by permission from D. H. Sebastian, “Non-Isothermal Effects in Polymer Reaction Engineering,” in *Temperature Control Principles for Process Engineers*, E. P. Dougherty, Ed., Hanser, Munich, 1993.]

Back-Mixed Continuous Flow Reactors

Following Biesenberger (3) “back-mixing” in a reactor is defined as *mixing of molecules in advanced stages of the reactor*, that is, low reactant and high product content, *with those in early stages*, that is, high reactant and low product concentrations. The main prerequisite for an ideally back-mixed reactor and continuous reacting stream is *complete and instantaneous mixing*, as is the case in the classic chemical engineering well-known *continuous stirred tank reactor (CSTR)*. In such a reactor the exit probability of fluid particles, independent of its “age,” is constant. Complete and instantaneous mixing can normally be achieved in low viscosity systems. Since the degree of mixing in CSTRs is instantaneous and the degree of mixedness is molecular and spatially uniform, the only requirement of reaction completion is

$$Da = \frac{\bar{t}}{t_r} = \frac{V}{Q} \left(\frac{\dot{r}}{c} \right) \Big|_0 \geq 10 \quad (11.2-28)$$

In a CSTR, as discussed in Section 7.3, the RTD is *exceptionally wide*, that is, the age, and thus the degree of reaction in the existing stream, at any time is very broad: 60% of the exiting stream has resided in the CSTR for a time less than the mean residence time, \bar{t} and 10% less than $0.15\bar{t}$. For the reaction completion requirement given in Eq. 11.2-28 to be satisfied for this 10% young age exit element, $Da|_{10\%} = 0.15\bar{t}/t_r > 10$. Thus, CSTRs must have a mean residence time of $\bar{t} > 67t_r$, and thus, they may not be desirable for all types of reactions.

It had widely been held by conventional wisdom, and reasonably so, that CSTR conditions cannot be achieved with high viscosity fluids in laminar flow fields, which as shown on Fig. 11.11, generally have narrower RTDs. However, in the early 1990s Biesenberger and Todd, working with Lu (45–47), and later on with Greci (48), developed a laminar flow reactor physically resembling a LCFR, but one that achieves results close to those of a CSTR. For this reason they called it the *Back-mixed extruder*. The cumulative RTD function, evaluated experimentally by Lu (45), and shown in Fig. 11.12, is very close and slightly narrower than the theoretical CSTR.

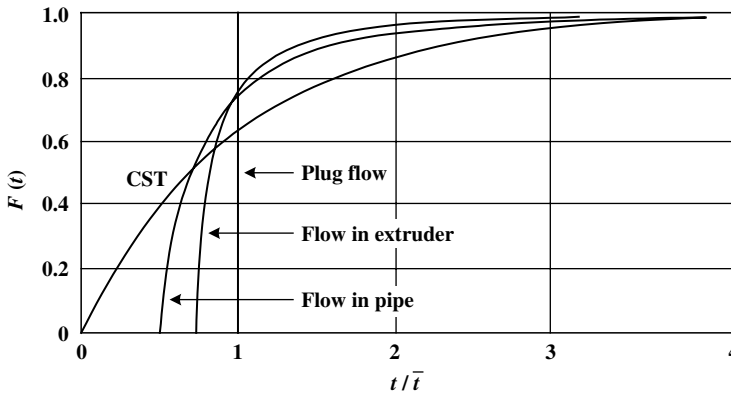


Fig. 11.11 The cumulative RTD function $F(t)$ versus dimensionless time, t/\bar{t} for the metering zone of an SSE compared to plug flow, pipe flow (for Newtonian and isothermal conditions), and the very broad CSTR.

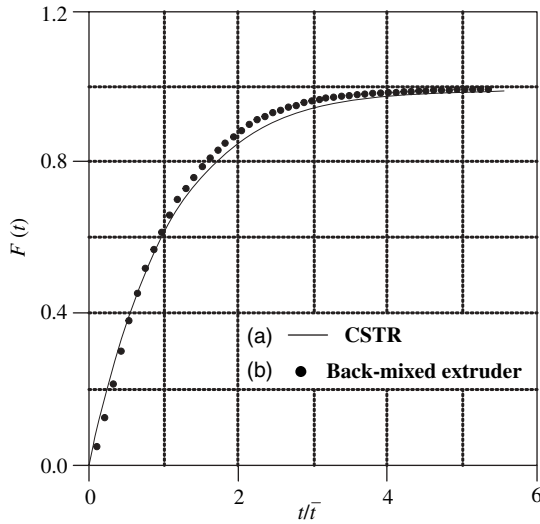


Fig. 11.12 Comparison between the theoretical cumulative RTD function for (a) CSTR and (b) the back-mixed extruder. [Reprinted by permission from Y. Lu, Ph.D Dissertation, Department of Chemical Engineering, Stevens Institute of Technology, Hoboken, NJ, 1993.]

The back-mixed extruder is a variant of the conventional nonintermeshing (tangential) counterrotating TSE represented on Fig. 11.13(a); both counterrotating screws in this LCFR create a dominant downstream flow with no back mixing and with some mixing screw-to-screw flow. By contrast, the two counterrotating screws of the back-mixed reactor

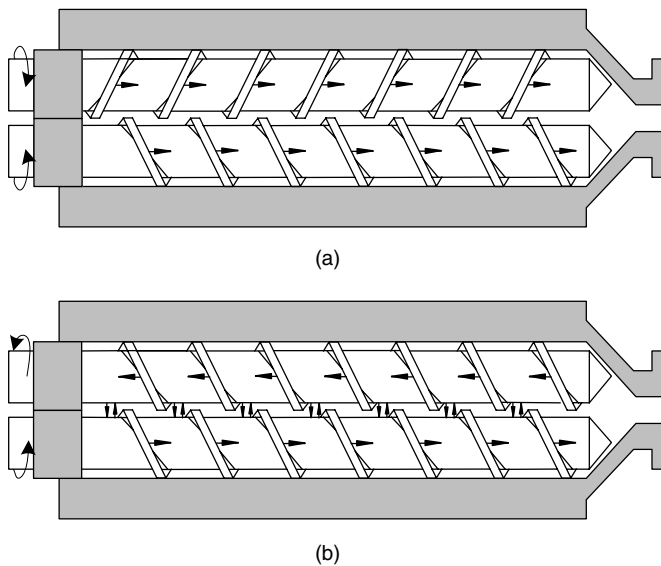


Fig. 11.13 Schematic representation of the twin-screw flow directions in (a) the conventional counterrotating nonintermeshing TSE, and (b) its “back-mixed extruder” variant. [Reprinted by permission from Y. Lu, Ph.D Dissertation, Department of Chemical Engineering, Stevens Institute of Technology, Hoboken, NJ, 1993.]

convey the material one forward and the other backward, as shown on Fig. 11.13(b). Such forward-backward flows occurring in parallel and side by side create the CSTR-type back-mix conditions. But, although this is an important feature of the back-mixed extruder, there is another feature, equally important, and it concerns the screw-to-screw material exchange, potentially leading to chaotic flows, and therefore well-mixed systems, represented by the vertical and reciprocal arrows between the two screws in Fig. 11.13(b). To understand the origins of these screw-to-screw material-exchange mixing flows we turn to Fig. 11.14 (45). The pressure “profiles” $P_b(z)$ for the backward- and $P_f(z)$ for the forward-pumping flows are created because of the circulatory cross-flows in each of the screws. Their slopes are $dP_f/dz < 0$ and $dP_b/dz > 0$. Therefore, the difference $P_b - P_f$ varies with z and can be negative or positive, and it is a function of the frequencies of rotation of the screws. When $P_b - P_f > 0$ melt in the backward-pumping screw at *that z location* is pushed into the forward-pumping screw flight. Of course, melt transfer from the forward- to the backward-pumping screw flight occurs at a z location when $P_b - P_f < 0$.

With the preceding arguments we see that the flow is three-dimensional with the added “dimension” of time periodicity, which as pointed out in Section 7.2, is a required condition for generating chaotic flows, as is the case in a two-dimensional cavity flow with periodic boundary conditions (49–51). Although apparently no fluid mechanical simulation has been done, there is strong experimental evidence of “instantaneous” mixing throughout the back-mixed extruder volume (45), and no composition drift is observed in copolymerization of two monomers with different reactivities, as expected only from a reaction occurring in a CSTR (48). Finally, in conventional tangential counter-rotating, either matched or staggered, TSEs the experimentally obtained $F(t)$ functions, as shown on Fig. 11.15, are very close to each other and very similar to that of

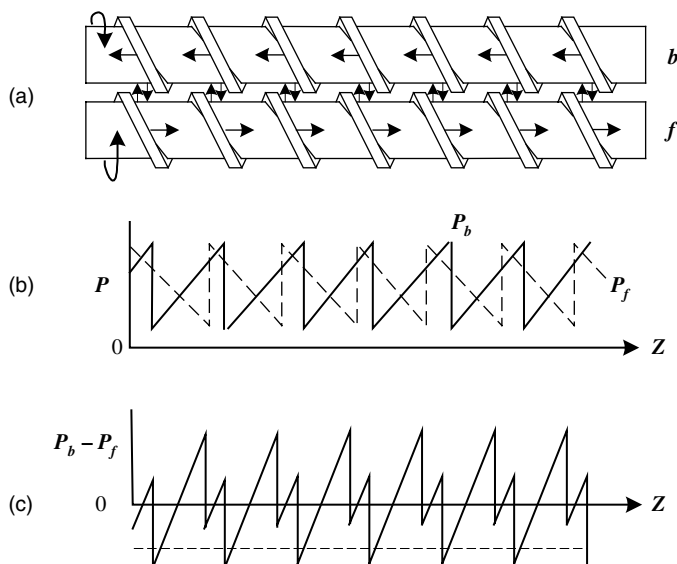


Fig. 11.14 Schematic representation of the local pressure and pressure difference at the “interface” between the two screws in the back-mixed extruder. The pressure difference changes periodically with varying amplitudes and frequencies. [Reprinted by permission from Y. Lu, Ph.D Dissertation, Department of Chemical Engineering, Stevens Institute of Technology, Hoboken, NJ, 1993.]

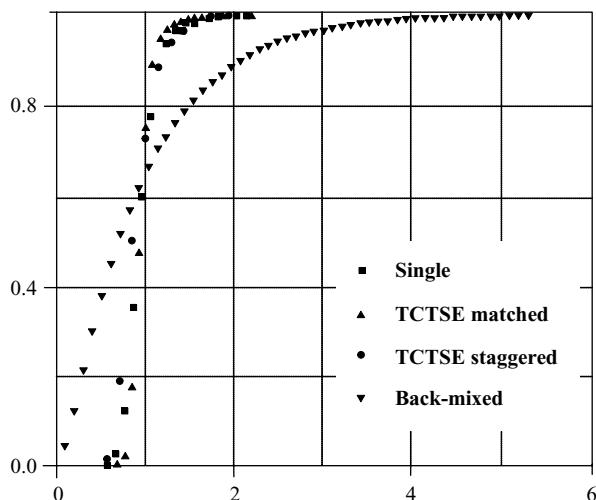


Fig. 11.15 RTD cumulative functions of a single screw; tangential counter-rotating twin-screw extruder (TCTSE) under matched and staggered conditions, and the back-mixed extruder reactor. [Reprinted by permission from Y. Lu, Ph.D Dissertation, Department of Chemical Engineering, Stevens Institute of Technology, Hoboken, NJ, 1993.]

the metering zone of the SSE, denoting parallel pumping along the two forward-pumping screws with no back mixing. Similarly there is experimental evidence of lack of “global,” CSTR-like back mixing in co-rotating, intermeshing TSEs. There is “local” and limited-range back-mixing only in full kneading elements, due to the expansion–contraction squeezing flow that forces limited flows in the kneading elements of the next kneading element neighbors to the front and back of that element, as discussed in by Brouwer et al. (52). Thus both conventional counter- and co-TSEs, as well SSEs, are LCFRs.

11.3 MIXING CONSIDERATIONS IN MULTICOMPONENT MISCIBLE REACTIVE POLYMER PROCESSING SYSTEMS

Following the preceding discussions on the various types of reactors for reactive processing, we now discuss the requirements for attaining completed reactions, uniform reactor environment, and uniform reaction product.

First and foremost, the laminar mixing flow created in the reactive processing equipment, must reduce the striation thickness to a level where the diffusion characteristic time, $t_D = r^2/\mathcal{D}_{AB}$, is small compared to the reaction characteristic time. Since the molecular diffusivities of low molecular weight components in polymeric melts (see Section 8.3) are very small and of the order of 10^{-6} cm²/s, the striation thickness must be reduced to the micron level in order to get a characteristic time t_D of the order of 1 s. Shear flow can accomplish this in reasonable mixing times because the striation thickness is inversely proportional to the total shear (see Section 7.3)

$$r = \frac{r_0}{\gamma} \approx \frac{r_0}{\dot{\gamma}t_{\text{mix}}} \quad (11.3-1)$$

and therefore the diffusion characteristic time is inversely proportional to the square of the total shear:

$$t_D = \frac{r^2}{\mathcal{D}_{AB}} = \frac{r_0^2}{\mathcal{D}_{AB}} \left(\frac{1}{\dot{\gamma}}\right)^2 = \frac{t_{D_0}}{\dot{\gamma}t_{\text{mix}}} \tag{11.3-2}$$

This becomes evident from Figure 11.16, which gives the $t_D = 1$ s iso- t_D curves in the $\dot{\gamma}$ - t_{mix} space for three initial t_{D_0} values of 10^1 , 10^2 , and 10^3 s. It is evident that for typical processing shear rates of $50 < \dot{\gamma} < 100 \text{ s}^{-1}$ at the t_{mix} needed to achieve $t_D = 1$ s, and thus molecular mixing, are in the range of 1 s to 20 s. It is important to note that the iso- $t_D = 1$ s curves flatten out with decreasing shear rate. For example, for $t_{D_0} = 10^2$, $t_D = 1$ s is reached in about 1 s for $\dot{\gamma} = 100 \text{ s}^{-1}$ and in about 10 s at $\dot{\gamma} = 10 \text{ s}^{-1}$.

Thus, in nonuniform shear rate flows, as in drag- and pressure-induced LCFRs a binary miscible blend element flowing in regions of very low shear rate, for example, $\zeta = y/H \approx 2/3$ in the metering zone of the SSE (see Chapter 6), may exit the linear reactor with a striation thickness that has hardly changed from its initial t_{D_0} value, and since with polymer blends $10^3 < t_{D_0} < 10^6$, the reaction and resulting LCFR product will be quite nonuniform. Furthermore, as shown in Fig. 11.11, in the metering zone of SSEs the residence time is close to the minimum over a broad region of the channel *core*, with 75% of the exiting flow rate having experienced a residence time of less than the mean value, and only 5% of the flow rate stays more than twice the mean value.

The second requirement, for reactions that are *not* diffusion controlled to reach completion, is that the Damkohler number be larger than 10. The previous discussion and Fig. 11.12 strongly indicate that for SSEs, where at $t = 0.75\bar{t}$ there is an almost vertical ascent of $F(t)$, we use $Da = 0.75\bar{t}/t_r > 10$ as the requirement for completion.

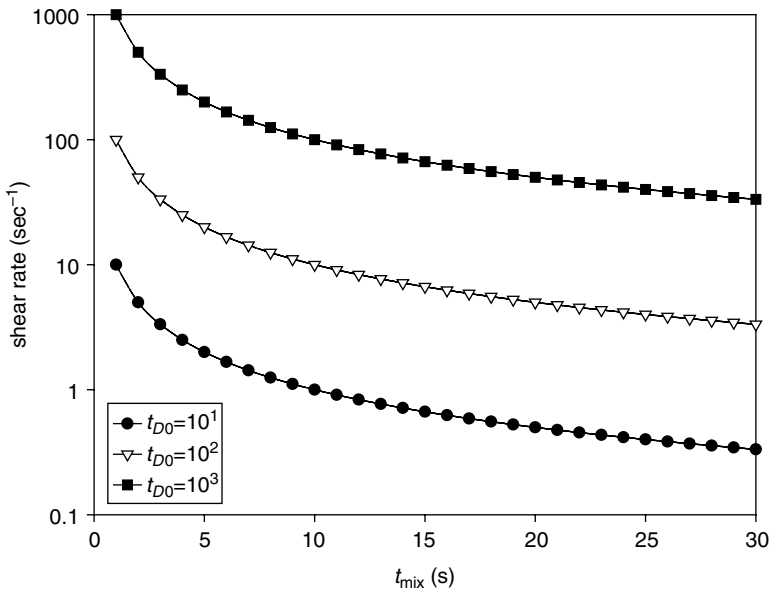


Fig. 11.16 Iso- $t_D = 1$ s curves for various $t_{D_0} = s_0^2/D_{AB}$ values, indicating that diffusion times of one second can be reached in short times for typical processing shear flow rates.

Example 11.1 Chain Modification (Branching and Partial Cross-linking) of PET with Triglycidyl Isocyanurate (TGIC) Dhavalkikar (39) conducted the reaction cited in the Example title on samples placed between the rheometrics mechanical spectrometer (RMS) parallel disks in the temperature-controlled chamber under nitrogen. He followed the reaction dynamics chemorheologically by measuring, in-line, the in- and out-of-phase dynamic moduli $G'(t)$ and $G''(t)$; they are indicative of the elastic and viscous nature of the molten reactive samples.

The reactive PET/TGIC 2.5-cm-diameter and 0.5-cm-thick disks were prepared by the following two methods: (a) a predried PET and 2000-ppm TGIC were dissolved in a few drops of hexafluoroisopropanol (HFIP); a thin film was cast and vacuum dried for 48 hours, resulting in a 2.5-cm diameter 0.05-cm thin sheets; ten of these sheets were stacked between the two parallel disks of the RMS where the reaction took place at 270°C after 300 s of sample heating in the RMS chamber; (b) the second method involved making spatially uniform, but microsegregated blends of 0.89-mm dried PET and 0.15 mm TGIC particulates; these blends were compression sintered into 2.5-cm by 0.5-cm disks, which were allowed to react in the RMS chamber, again under nitrogen.

The results obtained are shown in Fig. E11.1a. The elastic G' and loss (viscous) G'' moduli both increase with increasing branching and high cross-linking chain modification of PET by TGIC as expected, because the preceding macromolecular changes increase both the elastic and viscous responses. But there is a *notable difference*, between the responses of the homogeneous (solution) and the initially heterogeneous (powder) samples. As expected, the homogeneous sample, after the needed time for thermal equilibrium, shows the expected response of a first-order kinetics of branching $dc_{\text{TGIC}}/dt = kc_{\text{TGIC}}$, through which the reaction kinetic constant at 270°C is found to be $k = 3 \times 10^{-3} \text{ s}^{-1}$.

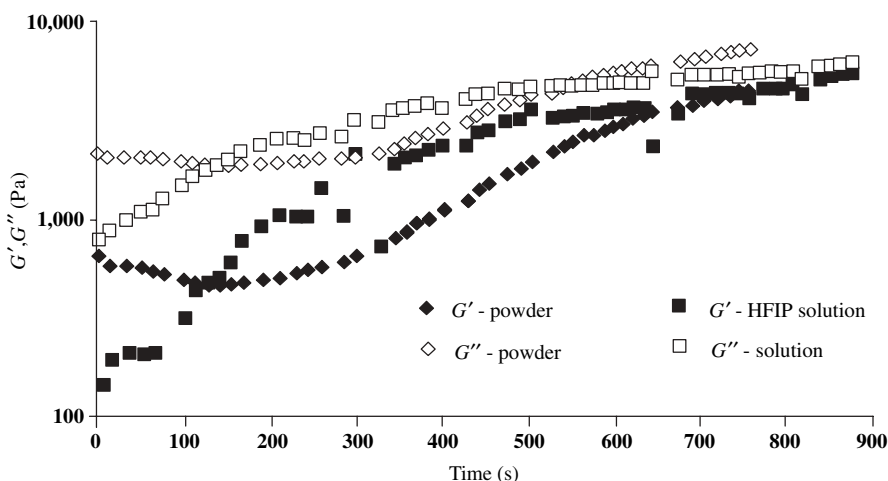


Fig. E11.1a The in-phase G' and out-of-phase G'' moduli of the PET/TGIC samples, one molecularly mixed (solution) and the other made of compressed and initially segregated PET. As expected, the homogeneous sample, after the required time for thermal equilibrium, shows the expected response of first-order kinetics. [Reprinted by permission from R. Dhavalkikar and M. Xanthos, "Monitoring the Evolution of PET Branching Through Chemorheology," *Polym. Eng. Sci.*, **44**, 474 (2004).]

On the other hand, the initially heterogeneous “powder” (actually composed of 0.89-mm average-size particulates) sample response is virtually unchanged for the first 300 s, denoting the absence of a spatially uniform reaction and, thus, G' as well as G'' are dominated by the unreacted regions of PET and TGIC. The obvious conclusion is that for this microsegregated system the reaction will not take place uniformly before the required t_D of TGIC diffusing to the core of the PET particulates, (0.89/2) mm inwards.

For $10^{-6}\text{-cm}^2/\text{s} < \mathcal{D}_{AB} < 10^{-4}\text{ cm}^2/\text{s}$, the characteristic time of diffusion falls in the range $200\text{ s} < t_D < 2000\text{ s}$. Thus, the observed “delay” time for the onset of the uniform reaction $t_D \approx 300\text{ s}$ supports the assumption of a diffusion-controlled reaction for the initially segregated reactive system. Furthermore, the initial slopes of $G'(t)$ and $G''(t)$ for the homogeneous samples are larger than those of the segregated counterparts, 300 s later. This is because, for the latter, some nonuniform reaction is taking place in the mixed-sample regions with, presumably, the same reaction constant. Jeong and Gogos (53) analyzed these chemorheological results, simulating the following three cases

1. PET/TGIC reaction only (“solution” sample)

$$\frac{dc}{dt} = kc_{\text{TGIC}} \quad (\text{E11.1-1})$$

2. Diffusion of TGIC into PET only (initially segregated “powder” sample)

$$\frac{\partial c}{\partial t} = \mathcal{D}_{AB} \frac{\partial^2 c}{\partial x^2} \quad (\text{E11.1-2})$$

3. Coupled diffusion and reaction (actual initially segregated)

$$\frac{\partial c}{\partial t} = \mathcal{D}_{AB} \frac{\partial^2 c}{\partial x^2} + kc \quad (\text{E11.1-3})$$

From Eq. E11.1-1, as mentioned earlier, the value of $k = 300\text{ s}$ fits the “solution” data and with this k value one determines the time-dependent and spatially uniform drop in TGIC concentration, as shown on Fig. E11.1b. The reaction is complete in about 500 s, in agreement with experimental results. To appreciate the effect of the reaction in the coupled diffusion-reactions of the initially segregated “powder” sample, the pure diffusion of TGIC into PET is examined, Eq. E11.1-2. The results are plotted in Fig. E11.1c. The diffusion process, using $\mathcal{D}_{AB} = 10^{-6}\text{ cm}^2/\text{s}$ is effectively complete in 500–900 s, close to the rough t_D calculation just given.

Turning now to the results of Eq. E11.1-3, the coupled diffusion-reaction process demonstrates the effect of reaction in depleting the TIGC concentrations, especially at longer t_{res} in the initially segregated sample, as shown in Fig. E11.1d.

Jeong and Gogos proceeded to answer the following question: If, instead of applying on the initially segregated sample an oscillatory deformation $\gamma = \gamma_0 \sin \omega t$, a steady shear flow $\gamma(t) = \dot{\gamma} \cdot t$ was applied, by rotating the top RMS disk, the effect of such a flow, according to Eq. E11.1-3, would be to reduce the initial striation thickness, r_0 , with time $r(t) = r_0/(1 + \dot{\gamma}t)$ and consequently reduce the diffusion time from t_D to $t_D(t) = r^2(t)/D_{AB}$. The results of solving the coupled diffusion-reaction process (Eq. E11.1-3) in the presence of a steady shear-flow field, which reduces continuously the

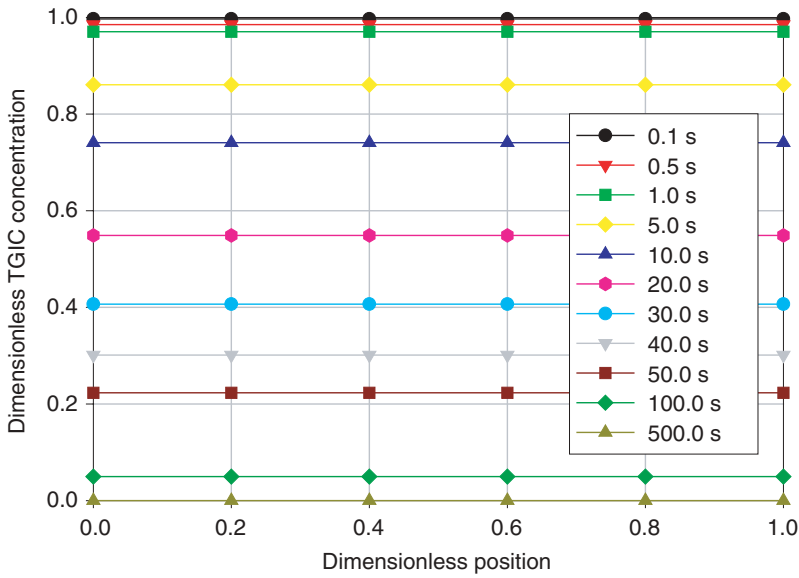


Fig. E11.1b Results of Eq. E11.1-1 with $k = 300$ s. The uniform sample reaction at 270°C is complete in 500 s.

striation thickness and diffusion time, are shown on Fig. E11.1e for $\dot{\gamma} = 1\text{ s}^{-1}$, that is, $\gamma = t$.

Comparing the preceding results with those of Fig. E11.1d, where the striation thickness is constant, demonstrates the *dramatic decrease of the reaction time*, with a modest $\dot{\gamma} = 1\text{ s}^{-1}$ shear flow.

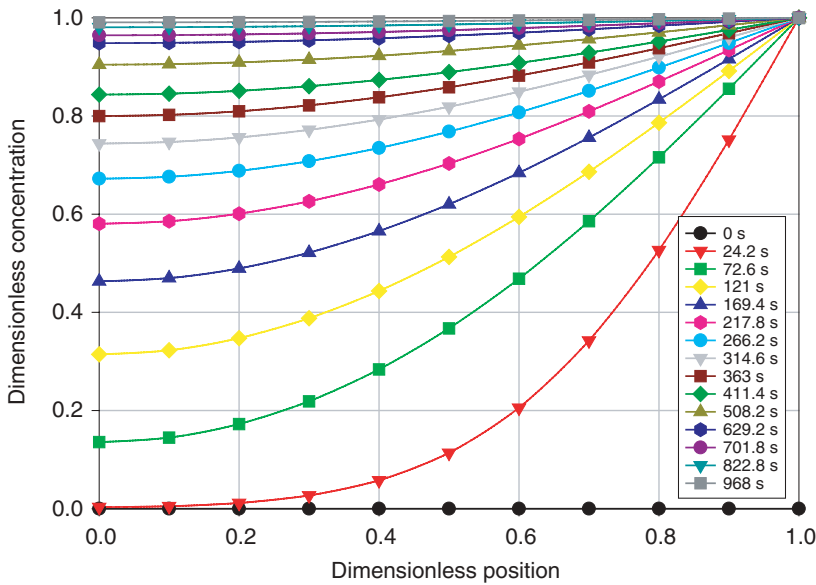


Fig. E11.1c Results of Eq. E11.1-2 for the pure diffusional process of TGIC in PET.

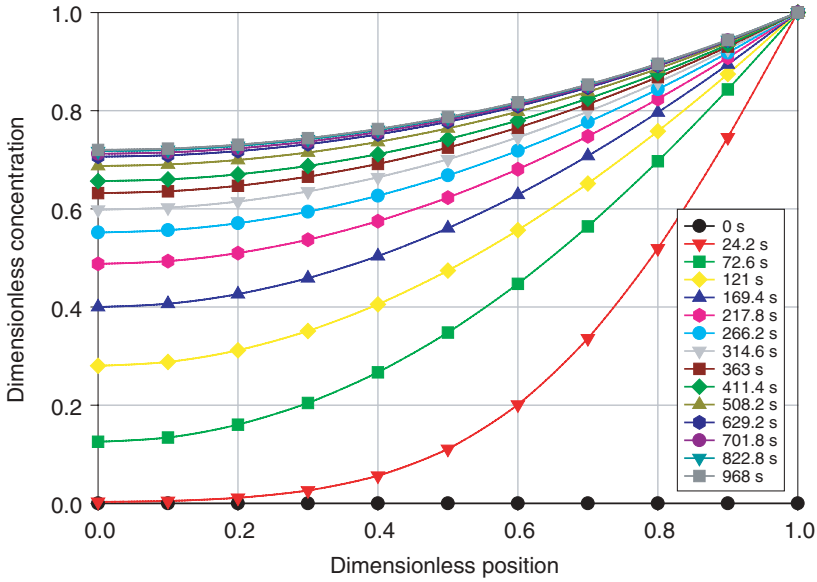


Fig. E11.1d Results of Eq. E11.1-3 for the coupled diffusion-reaction process of the initially segregated “powder” sample.

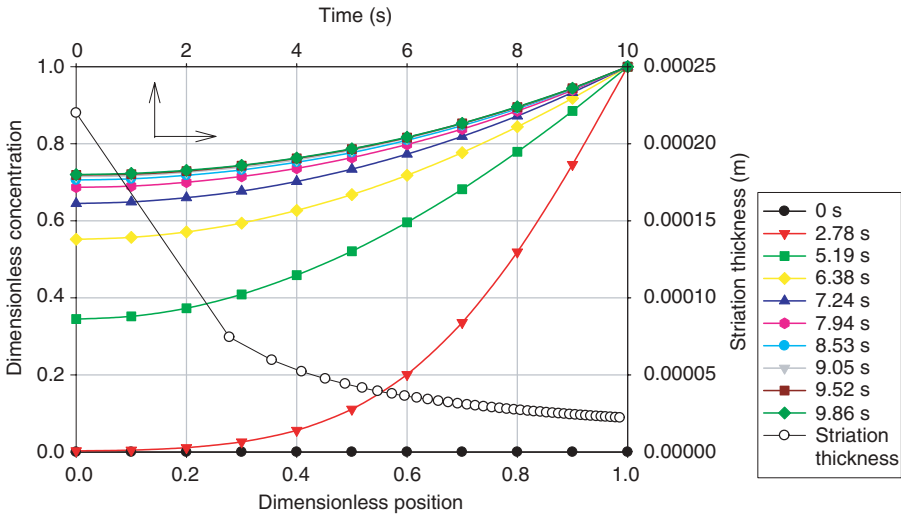


Fig. E11.1e The coupled diffusion-reaction process while applying a steady torsional parallel-disk flow of $\dot{\gamma} = 1 \text{ s}^{-1}$ to the initially segregated sample.

Example 11.2 Investigation of the Effects of Interfacial Cross-linking, Diffusion, and Area Generation Rates on Multilayer Miscible (PE-8% GMA)/PE-4% MAH) Films on the Extensional Rheometry of Such Films. Saito and Macosko (54) prepared multilayer films of two low density polyethylene (LDPE) miscible copolymers: a random copolymer of

ethylene and 8% glycidyl methacrylate (PE-GMA) and an LDPE randomly grafted with 4% maleic anhydride (MAH) (PE-MAH). The 256-layer films were produced in layer multiplication dies of Schrenk and Alfrey (55) at 220°C with a die residence time of 180 s and then cooled to room temperature, T_{room} . Strips were cut whose ends were clamped by the Rheometrics extension rheometer (RME) grips (56), allowed to come to thermal equilibrium under a blanket of nitrogen at 140°C, and then forced to undergo constant extensional strain-rate deformations at 0.01–0.05 s⁻¹. The length, width, and thickness of the strip ($l(t), W(t), H(t)$) (see Chapter 3) vary with time as follows:

$$\begin{aligned} l(t) &= l_0 \exp(\dot{\epsilon}t) \\ W(t) &= W_0 \exp\left(-\frac{1}{2}\dot{\epsilon}t\right) \\ H(t) &= H_0 \exp\left(-\frac{1}{2}\dot{\epsilon}t\right) \end{aligned} \quad (\text{E11.2-1})$$

If, during the extensional multilayer film deformation, the interfacial layers remain continuous, then the interfacial area *per unit film volume*, A_I , increases exponentially. For N layers

$$A_I(t) = \frac{N-1}{H_0} \exp\left(\frac{1}{2}\dot{\epsilon}t\right) \quad (\text{E11.2-2})$$

Because the consecutive stacked film layers are miscible, it is expected that a typical two-layer sample can be represented morphologically, as shown on Fig. E11.2a. The thickness of the interface layer, δ_I , increases with time, provided that the adjacent layers are molten, as is the case during the residence in the die (220°C), as well as during the time of thermal conditioning and stretching in the RME (140°C). Assuming an Arrhenius-type temperature dependence of the diffusivity (57),

$$\mathcal{D}_{AB}(T) = \mathcal{D}_{AB_0} \exp\left(-\frac{E_D}{RT}\right) \quad (\text{E11.2-3})$$

with $E_D = 24$ kJ/mole for PE, they converted the 180-s residence in the die to an equivalent (longer) time at 140°C and added the 180-s conditioning time in the RME; they

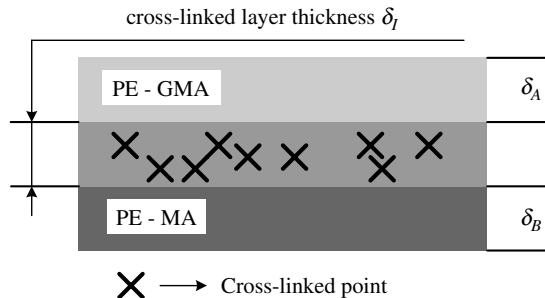


Fig. E11.2a Schematic representation of an adjacent pair of PE-GMA/PE-MAH layers. δ_I , the reacting interphase with cross-linked (branched) LDPE increases with time because of diffusion, at the expense of both δ_A and δ_B ; note that $\delta_A + \delta_I + \delta_B = \delta_{A_0} + \delta_{B_0}$

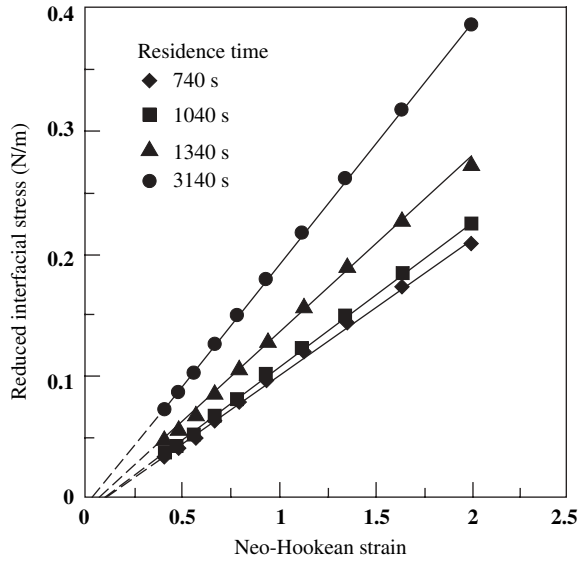


Fig. E11.2b Interfacial stress versus Neo-Hookean strain for three samples of different total residence times at 140°C, showing, δ_l thickening. [Reproduced by permission from T. Saito and C. W. Macosko, “Interfacial Cross-linking and Diffusion via Extensional Rheometry,” *Polym. Eng. Sci.*, **42**, 1–9 (2002).]

estimated the residence time at 140°C to be 740 s before any extensional deformation in the RME. Increasing the total residence time increases, δ_l , and, since the interphase is a cross-linked PE, the elongational stress–strain measured by the RME increases with total residence time, as shown on Fig. E11.2b. The measured force (stress) of the deforming multilayer film is

$$F_{\text{multilayer}} = \left\{ \frac{1}{2}N \left(\delta_a - \frac{1}{2}\delta_i \right) \sigma_a + \frac{1}{2}N \left(\delta_b - \frac{1}{2}\delta_i \right) \sigma_b + (N - 1)\delta_i \sigma_i \right\} W(t) \quad (\text{E11.2-4})$$

where N is the number of layers, σ is the tensile stress, δ is the layer thickness, W is the width, and a , b , and i are the subscripts denoting each polymer and the cross-linked interlayer, respectively. Since $\delta_i < \delta_{a,b}$ and $\sigma_i \gg \sigma_{a,b}$, Eq. E11.2-4 can be simplified to

$$F_{\text{multilayer}} = \left\{ \frac{1}{2}N(\delta_a \sigma_a + \delta_b \sigma_b) + (N - 1)\delta_i \sigma_i \right\} W(t) \quad (\text{E11.2-5})$$

The independent contributions of PE-GMA, A , and PE-MAH, B , depend on their volume fractions ϕ_A and ϕ_B and therefore:

$$\frac{1}{2}N(\delta_a \sigma_a + \delta_b \sigma_b)W(t) = \phi_a F_a(t) + \phi_b F_b(t) \quad (\text{E11.2-6})$$

where F_a and F_b are measured independently and are shown on Fig. E11.2c together with the ten times larger force of the multilayer film.

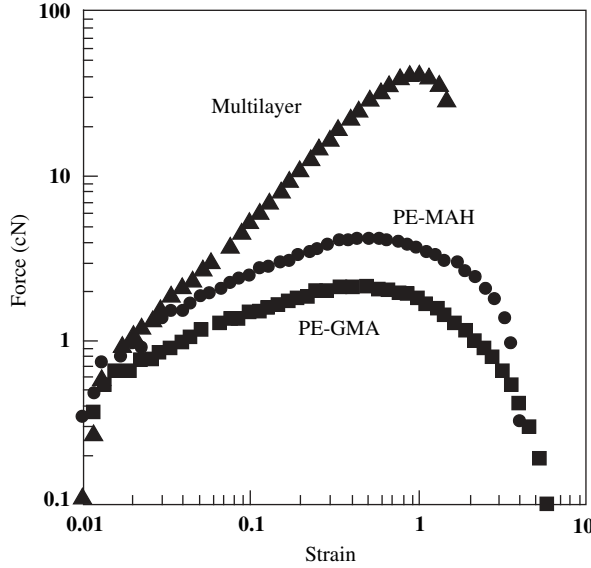


Fig. E11.2c Extensional stress–strain response of the PE-GMA, PE-MAH, and 256 multilayer films at 140°C and extension rate of 0.1 s⁻¹. [Reproduced by permission from T. Saito and C. W. Macosko, “Interfacial Cross-linking and Diffusion via Extensional Rheometry,” *Polym. Eng. Sci.*, **42**, 1–9 (2002).]

The contribution of all the δ_I cross-linked interlayers is found from the difference between Eqs. E11.2-5 and E11.2-6

$$F_I(t) = (N - 1)\delta_I\sigma_I W(t) = F_{\text{multilayer}} - [\phi_A F_A(t) + \phi_B F_B(t)] \quad (\text{E11.2-7})$$

From the first part of the preceding equation the tensile stress per unit width of any interlayer is

$$\delta_I\sigma_I(t) = \frac{F_I(t)}{(N - 1)W(t)} \quad (\text{E11.2-8})$$

Using Eq. E11.2-1 and Eq. E11.2-8 the “reduced” interfacial stress can be calculated and plotted on Fig. E11.2b for various residence times at 140°C. There the “Neo-Hookean” strain ε^{NH}

$$\varepsilon^{NH} = \exp(2\dot{\varepsilon}t) - \exp(-\dot{\varepsilon}t) = \frac{l^2(t)}{l_0} - \frac{l_0}{l(t)} \quad (\text{E11.2-9})$$

If a Neo-Hookean constitutive equation is used to describe the tensile behavior of the cross-linked interlayer

$$\sigma(t) = G\varepsilon(t)^{NH} \quad (\text{E11.2-10})$$

then $\delta_I\sigma_i = \delta_i E \varepsilon(t)^{NH}$. The modulus E was evaluated from tensile experiments of well cross-linked PE-MAH and PE-GMA samples and found to be 1.6×10^5 Pa. Using this value with

the 740 s, curve of Fig. E11.2b, which plots the reduced interfacial stress, $\sigma_i \delta_i$, we evaluate the interfacial thickness to be 0.7 μm . In addition, 740 s is the time in the RME before the start of the extensional deformation. From the curves, at higher times in the RME, we can obtain the increase in the interlayer thickness, which was found to grow in a diffusion-controlled manner with time.

In this example of “model” reactive polymer processing of two immiscible blend components, as with Example 11.1, we have three characteristic process times: t_D , t_r , and the time to increase the interfacial area, all affecting the RME results. This example of stacked miscible layers is appealing because of the simple and direct connection between the interfacial layer and the stress required to stretch the multilayer sample. In Example 11.1 the initially segregated samples do create with time at 270°C an interfacial layer around each PET particulate, but the torsional dynamic steady deformation torques can not be simply related to the thickness of the interfacial layer, δ_i . However, the initially segregated morphology of the “powder” samples of Example 11.1 are more representative of real particulate blend reaction systems.

11.4 REACTIVE PROCESSING OF MULTICOMPONENT IMMISCIBLE AND COMPATIBILIZED IMMISCIBLE POLYMER SYSTEMS

As discussed in Chapter 1, the majority of “new” polymers have been blends of existing commodity or engineering polymers. Blends account for roughly 30% of all polymer sales (12). Most polymer pairs used in blends are practically *immiscible* and, as such, in principle their morphology and properties are unstable. Thus, commercial blends are made by *reactively* forming a block copolymer at the interface during reactive polymer processing operations. The interfacial reactions require that the homopolymer blend components are functionalized. We have reviewed some of them in Section 11.1 and there are a number of specific and informative general references (11,12,58). Block copolymers, synthesized in polymerization reactors, are functioning much like a “third” surfactant-type component of the blend, since one part of the block is immiscible to one component, while the other immiscible with the second blend component (59,60). They therefore, “compatibilize” the two immiscible components. These compatibilizers improve blend morphology and stability, but because of viscosity differences, their addition may sometimes lead to the formation of compatibilizer micelles inside one of the homopolymer, creating the so-called “salami” morphologies (61,62).

Blends are produced by the intensive mixing that takes place in the processing equipment. In Chapter 7 we dealt with mixing of both miscible and immiscible blends. With *miscible systems*, we discussed both the mechanisms and rates of mixing (rates of interfacial area increase), which are relatively straightforward, since they depend primarily on the flow kinematics. In discussing mixing of immiscible blends we concentrated, not so much on the rates of droplet and filament breakup, but on the physical mechanisms associated with the breakup process, and with the final morphology in both shear and extensional flows. In the next section, we discuss the rates of melt droplet and filament breakup, through “carcass” analysis in compounding equipment, mainly twin rotor devices, and relate it to both the melting and mixing phenomena, deformations, and flows in such equipment.

In dealing with the reactive processing (blending) of multicomponent immiscible systems we must, however, also consider chemical reaction rates. Thus, we have to

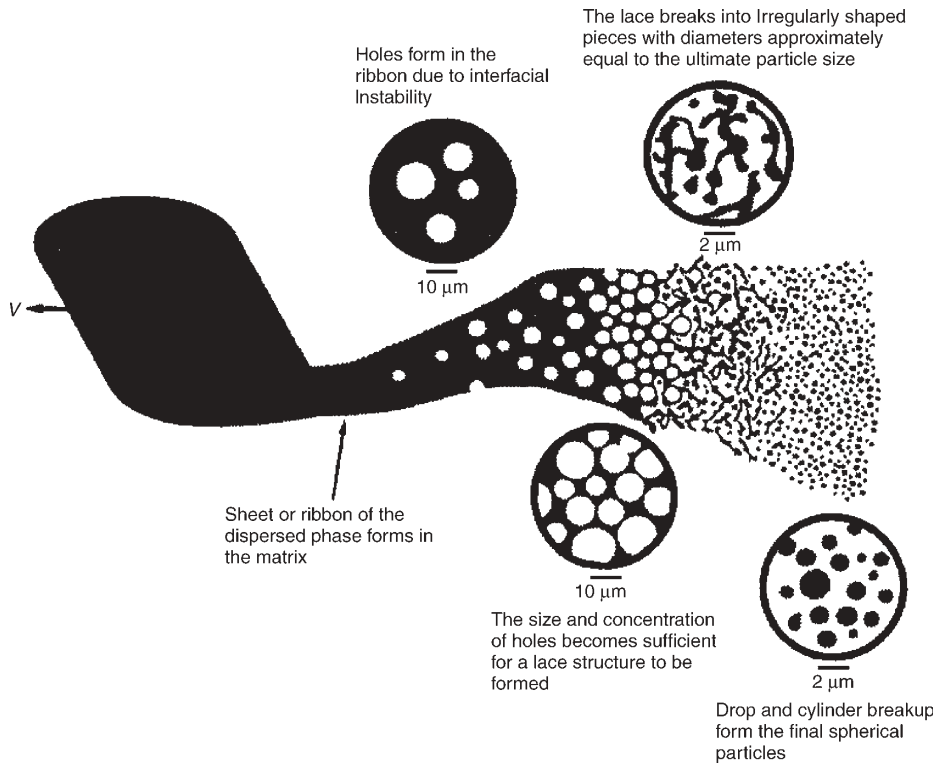


Fig. 11.17 The melting mechanism of immiscible blends, showing in cartoon form the evolution of blend morphology during and following melting in twin rotor devices. [Reprinted by permission from C. E. Scott and C. W. Macosko, "Morphology Development During the Initial Stages of Polymer-polymer Blending," *Polymer*, **36**, 461-470, (1995).]

consider *three* characteristic times: the melt dispersive *mixing* characteristic time, t_{mix} , from the time of melting of the blend components to the time of attainment of a final and stable morphology; the *reaction* time, $t_r(T)$, and the time it takes to achieve the very limited *diffusion* needed for the reaction, t_D , at the interface, creating exceedingly thin, but beneficial, interphases. Scott and Macosko (63) studied the evolving blend morphologies in a Co-TSE, with the results shown in "cartoon" form in Fig. 11.17 and in batch-intensive mixers by taking samples at various mixing times and analyzing them with scanning electron micrography (SEM) (64). Five model blends were used. In all of them the minor dispersed phase was DuPont Nylon Zytel 330, which is a partially aromatic amorphous Nylon [polyamide (PA)] capped at both ends with reactive amine groups. Five matrices were used in the blends of 20% Zytel 330: three are not reactive and immiscible, and two are reactive and initially immiscible. They are: (a) functionalized polystyrene (PS) through copolymerization with 1% vinyl oxazoline and reactive with the amine groups of PA; (DOW RPS X U.S. 4005601) (PS-Ox); (b) styrene-maleic anhydride copolymer (ARCO Dylark 29), with a reported reactive MAH content of 17% (SMA); (c) Dow's PS (Styron 666D), not reactive with Zytel 330; (d) amorphous low MW copolyester (Eastman Chemical Kodar 6763), nonreactive with the amine end-capped PA (PETG), and (e) Dow general-purpose polycarbonate, also nonreactive with the end-capped PA (PC).

It was found (64) that for all five systems, reactive and nonreactive, the melting mechanism giving rise to the evolution of the blend morphology is identical in the initial stages of mixing, namely, the formation of molten *sheet*, *lace*, *filaments*, and finally *droplets*, as schematically shown in Fig. 11.17. In terms of ratios of characteristic times, the identical initial morphology of both reactive and nonreactive blends requires that $t_{\text{mix}}/t_r \leq 10^{-1}$. At longer mixing times, however, after the formation of dispersed PA droplets it is observed that the mean droplet diameter is 5–10 times *smaller* and *stable* for the reactive blends, because of the compatibilizing products of the chemical reaction at the interface. One can conclude from these results that, for the two reactive blends just cited, *mixing is not controlling* the morphology development down to the droplet level, since the morphology evolution completion time is very small; at longer times droplets will decrease in size as the concentration of the interfacial reactions increases, decreasing the interfacial tension. Furthermore, Marič and Macosko (65) working with aminoterminated PS and anhydride-terminated polydimethylsiloxane (PDMS) blends, observed that this reactive immiscible blend gives a fine and stable droplet morphology that is insensitive to the mixing device used; nonreactive blends, on the other hand, have mixing device-sensitive morphologies.

We have previously used the term “interfacial reaction” to describe mixing between two reactive blend components. In reality, as we have seen in the Example 11.2, there is an interphase that is formed on the surface of the dispersed phase where molecules of both components can be found and react (66,67). If the nonfunctionalized blend components have high immiscibility, then the thickness, δ_I , of the interphase around the droplets, as well as the volume of the interphase, V_I , will be small and, thus, the probability of the functional groups to react forming compatibilizing products will be low, giving rise to coarse and not very stable morphologies. Helfand (66) defines δ_I as

$$\delta_I = \frac{2\langle b \rangle}{\sqrt{6}\chi_{AB}} \quad (11.4-1)$$

where $\langle b \rangle$ is the mean segment length of the formed block copolymer, and χ_{AB} is the Flory–Huggins interaction parameter between components *A* and *B* (68):

$$\chi_{AB} = \frac{\bar{V}}{RT}(\delta_A - \delta_B)^2 \quad (11.4-2)$$

where \bar{V} is the molar volume and δ_A and δ_B are the solubility parameters. The mean length $\langle b \rangle$ can be calculated from chain dimensions data and estimated as the geometric mean of the homopolymer segment lengths b_A and b_B (69,70)

$$\langle b \rangle = (b_A b_B)^{1/2} \quad (11.4-3)$$

Macosko and his co-workers have estimated δ_I for a number of immiscible uncompatibilized polymer pairs in the Table 11.1.

A blend between two highly immiscible polymers, 20% PDMS in Nylon 6 (PA6) has a very thin interphase thickness of 2Å, as shown on Table 11.1, and, as a result a coarse dispersed morphology of about 10µm. Similarly coarse morphology is obtained when PDMS is blended with PA 6 amine-functionalized at each chain end to form PA 6/diamine.

TABLE 11.1 Calculated Interphase Thicknesses δ_I for Four Pairs of Immiscible Polymers

Blend Component	$\delta_I(A)$	T ($^{\circ}C$)
PS/PDMS	10	200
PS/PI	23	180
PS/PMMA	68	180
PA6/PDMS	2	235

Apparently, with a very small interphase thickness the two end-cap groups are too few and not easily accessible to affect compatibilization. On the other hand, when four anhydride (An) groups are attached, randomly on each PDMS chain, then the blend of 20% PDMS/4-An and PA 6/di-amine have a very fine and stable morphology (ca 0.5 μm). Thus, the amount of interfacial reaction product, although diminished by small δ_I values of the unmodified polymer components, is promoted by the larger number and more “accessible” functional groups in either or both of the reactive components. Finally, Macosko and co-workers (62) have estimated that the minimum fraction of the interphase that has to be covered by reacted compatibilization products to achieve fine and stable morphologies is about 0.2.

11.5 POLYMER COMPOUNDING

As stated in Chapter 1, polymer processing is the engineering activity concerned with operations carried out on polymeric materials or material systems to increase their utility. While the early objective of the field was the shaping (forming) of finished products, polymer processing has long dealt with and made large technological strides by using the processing equipment to carry out compounding and chemical reactions in order to achieve macromolecular modifications, creation of multicomponent and multiphase structures, and morphology stabilization. All these lead toward technologically and commercially desired “value added” products. Figure 1.9 depicts schematically the transformation of feed streams of polymers, additives, and reactants into microstructured “designer pellets,” which are, in turn, used in shaping products with enhanced properties.

Compounding is associated mainly with the dispersive and distributive mixing of additives into a single polymer matrix, or the creation of stable physical blends of two or more polymers. Often, before entering the compounding equipment, solid components are surface modified to improve dispersive mixing during compounding and products with enhanced mechanical properties. Also in physical blend compounding, interfacial modifiers and compatibilizers are introduced to achieve stable and finely dispersed blends. Reactive processing, on the other hand, utilizes chemical reactions that modify the macromolecular structure of polymers to achieve the same designer pellets as in compounding. The only difference between compounding and reactive processing is that interfacial modifications are through reactions that, subject to the associated heats of reactions, are carried out *in situ* in the processing equipment. The equipment of choice for carrying out both reactive processing and compounding are twin rotor devices. The reasons for this choice, as discussed in Chapter 10, are their ability to achieve rapid melting and efficient chaotic laminar mixing.

Polymer Additives and Modifiers Used in Compounding

In earlier chapters we mentioned that all commercial plastics are compounds of polymerization reactor-generated macromolecules and a number of additives and modifiers that impart chemical stability, facilitation of processing and fabrication, as well as desired product properties. Although arriving at a specific additives formulation package may be the result of accumulated practical experience, specific and general statements can be made concerning their role or functionality in affecting dispersive and distributive mixing, as well as their effect on processing material variables, such as the viscoelastic nature of the processed stream, at least after mixing is complete and uniform. Mascia (71) and Mascia and Xanthos (72) and recently Xanthos (73,74) have suggested that additives and modifiers be classified according to their *function*, *miscibility*, and *concentration*. We follow this classification in Tables 11.2, 11.3, and 11.4, as presented by Xanthos (73).

The additives in the tables below can be either *rigid* (fillers, reinforcing agents, inorganic flame retardants, pigments, etc.) or *deformable* (polymeric impact modifiers, compatibilizers, dyes, etc.). For rigid particulate additives, as discussed in Chapter 7, the dominant mixing mechanism determining compounding quality is *dispersive mixing*, which depends on many operational and physical property variables, such as the cohesive strength of the particle, its shape, size, and size distribution, and the volume fraction of the additive. In addition, the surface area and surface treatment to alter surface tension and improve wetting and particulate adhesion to the matrix play an important role. For *deformable additives* deformation and breakup by the polymer matrix depends on

TABLE 11.2 Examples of Additives that Modify Mechanical Properties, Electrical Conductivity, and Flame Retardancy

Functions	Examples
Fillers/reinforcements	
Inorganics	Oxides (glass, MgO, SiO ₂ , Al ₂ O ₃) Hydroxides (Al(OH) ₃) Salts (CaCO ₃ , BaSO ₄ , CaSO ₄ , phosphates) Silicates (talc, mica, kaolin, woolastonite) Metals (boron, steel fibers)
Organics	Carbon-graphite, cellulose, PA, PET, PE, PVA and aramid fibers, wood starch
Plasticizers	Phthalate esters, trialkyl phosphates, adipates, chlorinated paraffins, high molecular-weight polyesters, epoxy derivatives
Impact modifiers	EPR, EPDM, NBR, NR, EVA, MBS, CPE, various elastomers
Cross-linking agents	Organic peroxides, rubber curatives
Flame retardants and smoke suppressants	Sb ₂ O ₃ , chlorinated paraffins, Al(OH) ₃ , Mg(OH) ₂ , organophosphate esters, MoO ₃ , zinc barate, brominated organic compounds, molybdate salts
Conductive additives	Carbon black, carbon-graphite fibers, metals, metallized fillers/reinforcements

Source: Reprinted by permission from M. Xanthos, "The Physical and Chemical Nature of Plastics Additives," in *Mixing and Compounding of Polymers*, I. Manas-Zloczower and Z. Tadmor, Eds. Hanser 1994.]

TABLE 11.3 Examples of Processing and Antiaging Additives

Functions	Examples
Processing Additive	
Stabilizers	Primary antioxidants (sterically hindered phenols, <i>sec</i> -arylamines) hydroperoxide decomposers (organophosphites, thioesters), acid absorbers (lead salts, Ca/Ba-Ba/Cd-Ba/Sn salts, organotin, epoxidized oils)
Lubricants	High molecular weight fatty acids and derivatives, paraffin waxes, metal soaps, ester and amide waxes, silicones, polyfluorocarbons
Flow and fusion promoters	PMMA and acrylate ester copolymers, MBS
Thixotropic agents	Fumed silica, clays
Antiaging	
Antioxidants	Sterically hindered phenols, <i>sec</i> -aromatic amines, phosphates, thioethers
Metal deactivators	Chelating agents (hydrazones, oxamindes, hydrazides, phosphates, phosphines)
Light Stabilizers	Pigments (carbon black, iron oxides), UV absorbers (hydroxyphenones, benzotriazoles), excited-state quenchers (organic Ni complexes), free-radical scavengers Hindered amine light stabilizers [piperidines, hindered amine light stabilizers (HALS)]
Biostabilizers	Copper quinolinolate, phenoxarsines, phthalimides, thio compounds

Source: Reprinted by permission from M. Xanthos, "The Physical and Chemical Nature of Plastics Additives," in *Mixing and Compounding of Polymers*, I. Manas-Zloczower and Z. Tadmor Eds. Hanser, New York, 1994.

TABLE 11.4 Examples of Surface Modifiers, Optical Property Modifiers, and Blowing Agents

Functions	Examples
Surface modifiers	
Antistats	Ethoxylated amines and quaternary ammonium salts, phosphate esters, glycerides
Antifoggers	Fatty chain glycol and polyether surfactants
Antiblocking agents, slip additives	Silica, amide waxes, oleamide
Antiwear additives	Graphite, MoS ₂ , polytetrafluoroethylene (PTFE)
Wetting agents	Ionic and nonionic surfactants
Adhesion promoters	Silanes, titanates, block and graft copolymers
Optical property modifiers	
Pigments	<i>Inorganic</i> : Ti, Fe, and Cr oxides, Cd, Ba, and Pb sulfides, sulfates, and chromates <i>Organic</i> : carbon black, phthalocyanines, quinacridones, flavanthrones, azo pigments
Dyes	Anthraquinones, azo and bisazo compounds, nigrosines
Nucleating agents	SiO ₂ , talc, sodium benzoate, polymers
Blowing agents	
Physical	Hydrocarbons, halocarbons, CO ₂ , N ₂
Chemical	Bicarbonates, azodicarbonamide, benzene sulfonylhydrazides, tetrazoles

Source: Reprinted by permission from M. Xanthos, "The Physical and Chemical Nature of Plastics Additives" in *Mixing and Compounding of Polymers*, I. Manas-Zloczower and Z. Tadmor Eds., Hanser, 1994.

interfacial tension—which influences miscibility—volume fraction, and the viscosity and elasticity ratios of the additives to the matrix at processing conditions. The *distributive mixing* aspect of compounding depends primarily, almost exclusively, on the flow field generated by the compounding equipment in partially and fully filled sections.

Effects of Additives and Modifiers on the Rheology and Processing of Compounded Systems

The effect of additives and modifiers on product properties will not be discussed here because it is beyond the scope of this textbook. We must emphasize, however, that the ultimate objective of compounding additives and modifiers in polymer matrices is to obtain specific multicomponent and multiphase structures and morphologies needed to obtain certain desired product properties. We will only discuss their effects on the compounded systems rheology and, mainly, the shear flow viscosity, and their effects on compounding equipment and processes.

The Rheology of Solid Particulate-Filled Polymer Matrices

For polymer matrices filled with particulate additives of dimensional aspect ratio near unity, that is, nearly spherical, the rheological behavior at low volume fraction concentrations $\phi_v < 10\%$ resembles the shear thinning nature of the unfilled polymer matrix, except that the viscosity is higher and increases with particulate concentration. In other words, as expected from suspension theory, the suspended particulates do not interact strongly and do not form a particulate *network structure*. At higher particulate volume fractions, on the other hand, such suspended particulate networks are formed and become stronger, increasingly dominating the rheology of the suspension. The above are illustrated in Fig. 11.18 for PS–carbon black filled melts (75).

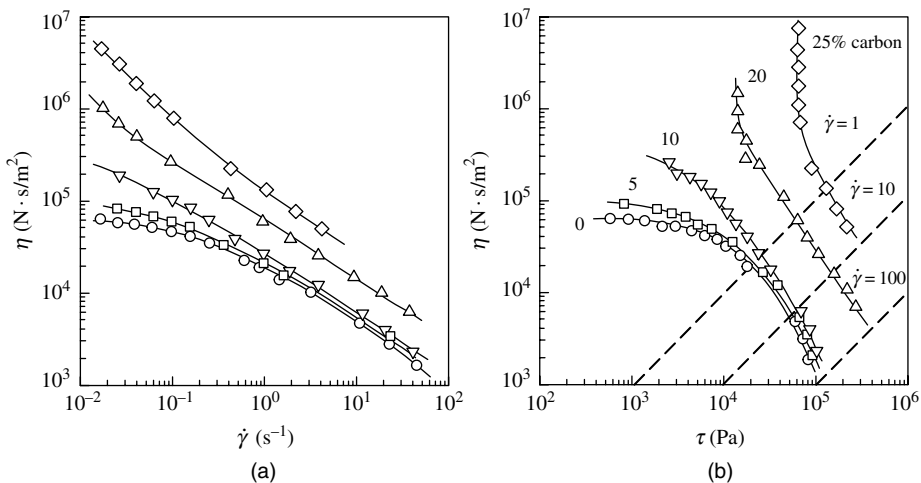


Fig. 11.18 (a) The steady state shear rate and (b) shear stress-dependent viscosity of carbon black filled PS melts; $\bar{M}_w = 214,000$, carbon black surface area is $124 \text{ m}^2/\text{g}$. [Reprinted by permission from V. M. Lobe and J. L. White, "An Experimental Study of the Influence of Carbon Black on the Rheological Properties of a Polystyrene Melt," *Polym. Eng. Sci.*, **19**, 617 (1979).]

We observe that at 5% volume concentration carbon black has a very small effect: shear thinning is preserved and no yield is exhibited. On the other hand, at and above 20% and in the very low shear rate region $10^{-2} < \dot{\gamma} < 1 \text{ s}^{-1}$ network yielding is evident, as well as very large viscosity increases—two orders of magnitude higher than the polystyrene matrix at $\dot{\gamma} = 10^{-2} \text{ s}^{-1}$. It is noteworthy that at processing shear rates, which generally are above 10 s^{-1} , the network structure of the carbon black particulates is destroyed: at the onset of flow the network is strained until it yields; thus, the rate of network junctions' destruction is much larger than the rate of creation. At steady state, normal shear thinning is established, indicating that now the rheological nature of the matrix dominates. Also noteworthy is that at the two higher loadings, the viscosity increase with increasing ϕ is more pronounced.

Figure 11.19(a) and 11.19(b) plot relative viscosities of suspensions of monodispersed-size spheres in Newtonian liquids. Figure 11.19(a) was constructed by Bigg (76) from data obtained by Lewis and Nielsen (77), who investigated the viscosity of glass-sphere suspensions in Aroclor Type 1254, a Monsanto chlorinated bisphenyl liquid with Newtonian viscosity of 80 poise at 25°C. As we will see later, Lewis and Nielsen investigated the effect of glass sphere agglomeration on suspension viscosity. Rutgers (78) has also presented similar results.

Figure 11.19(b) plots the steady state ratio of the viscosities of suspensions of spherical particles in Newtonian liquids, μ_s , to the viscosity of the Newtonian fluid, μ_f . It was constructed by Thomas (79) using the data of a number of investigators. A variety of uniform-sized particles having diameters of 1–400 μm were used. They included PS and

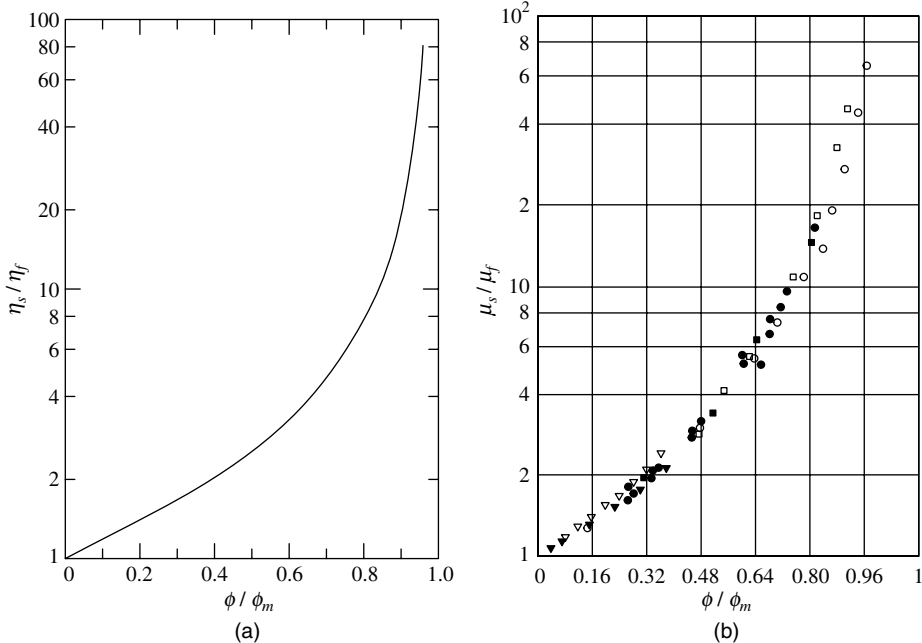


Fig. 11.19 Viscosity of suspensions of spherical particles in Newtonian fluids. (a) Curve constructed by Bigg. [Reprinted by permission from D. M. Bigg, "Rheological Behavior of Highly Filled Polymer Melts," *Polym. Eng. Sci.*, **23**, 206 (1983).] (b) Curves presented by Thomas (79).

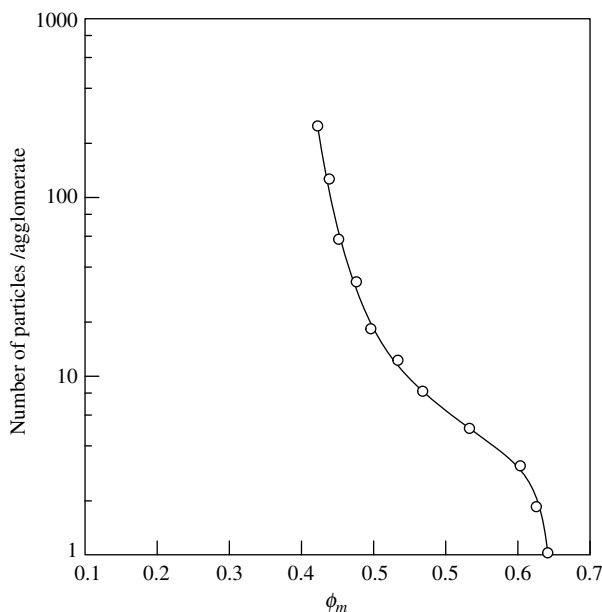


Fig. 11.20 Relationship between the number of spherical particulates in an average agglomerate and ϕ_m , plotted by Bigg from data by Lewis and Nielsen (77), on glass spheres in Aroclor with various degrees of agglomeration. [Reprinted by permission from D. M. Bigg, "Rheological Behavior of Highly Filled Polymer Melts," *Polym. Eng. Sci.*, **23**, 206 (1983).]

polymethyl methacrylate (PMMA) beads, rubber latex, and glass spheres. To avoid settling, either the density of the suspending medium was adjusted or a medium of high viscosity was used. The maximum packing density was determined by extrapolating a plot of $1/[(\mu_s/\mu_f) - 1]$ vs. ϕ to zero, giving $\phi_m = 0.625$, very close to that of randomly packed spheres of equal size. Frankel and Acrivos (80) have developed and reviewed theories describing the viscosity behavior of concentrated Newtonian fluid suspensions. Thus ϕ_m is an important parameter in determining the viscosity of filled systems. It depends on the particle size distribution and shape of the fillers, plus the degree of agglomeration. Small size fillers, with large surface-to-volume ratios agglomerate under the influence of interparticle forces. Agglomeration decreases the maximum packing volume fraction, as shown on Fig. 11.20. Thus, agglomeration increases the viscosity of particulate filled melts.

Surface treatment of fillers normally reduces the interparticle forces, the degree of agglomeration, which in turn increases the maximum packing density, ϕ_m , and decreases the viscosity at any given level. This is shown on Fig. 11.21 for LDPE filled with uncoated and stearic acid-coated CaCO_3 (81,82) and for PP filled with uncoated and titanate-coated CaCO_3 (83,84). The viscosity is reduced by coating CaCO_3 with a physical coupling agent (stearate) or a reactive coupling agent (titanate), where X is the reactive group. Both compounds are bifunctional with one end adhering to the matrix and the other to the particulate filler. In the case of titanate coated CaCO_3 there is an apparent suppression of the yield stress. It is generally observed that filled polymer melts are "less elastic" than their matrices, resulting in lower extrudate swell and depressed melt fracture (81). Indeed, the results in Fig. 11.21(b) indicate that at constant stress the first normal stress coefficient decreases appreciably with the addition of CaCO_3 , and this is evidence of the decrease in

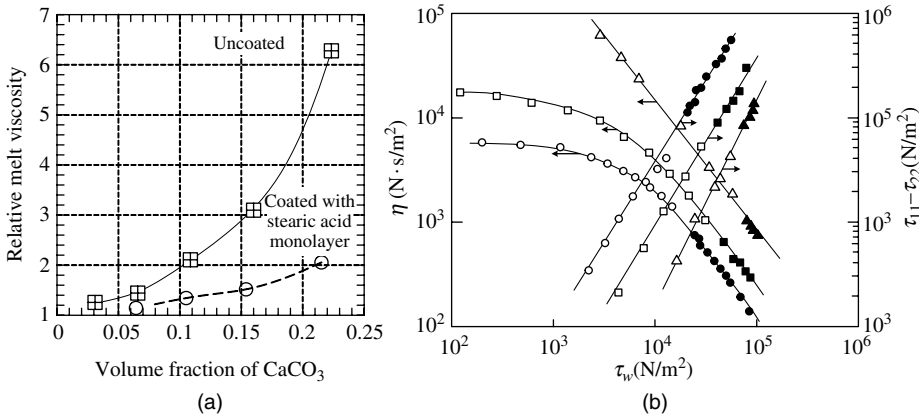


Fig. 11.21 Increases in viscosity brought about by (a) the deagglomerating effect of coating CaCO₃ filler particulates with calcium stearate [reprinted by permission from Y. Bomal and P. Goddard, "Melt Viscosity of CaCO₃-filled Low Density Polyethylene: Influence of Matrix-filler and Particle-particle Interactions," *Polym. Eng. Sci.*, **36**, 237–243 (1996)], and (b) a titanate RO-Ti-(OX)₃. Viscosity and first normal stress difference vs. shear stress for CaCO₃-filled polypropylene with titanate coupling agent TTS (isopropyl triisostearyl titanate) at 200°C. (○ ●) PP; (△ ▲) PP/CaCO₃; (□ ■) PP CaCO₃/TTS. Data with open symbols were obtained with a Weissenberg rheogoniometer, and data with closed symbols were obtained with the Han slit/capillary rheometer. [Reprinted by permission from C. D. Han et al., "Effects of Coupling Agents on the Rheological Properties Processability and Mechanical Properties of Filled PP," *Polym. Eng. Sci.*, **21**, 196 (1981).]

elasticity. The reason behind the smaller decrease in N_1 with the titanate-coated CaCO₃ shown in the figure may be related to better matrix-particulate adhesion.

Next we turn to *anisotropic fillers* such as glass fibers and explore their effect on the rheology of polymer matrices. Fibers, like spherical particulates cause an increase in viscosity and a decrease in elasticity. They are also coated with coupling agents to decrease agglomeration and increase adhesion between the fibers and the matrix. This is especially desirable for glass fiber reinforced final products. They decrease solid state debonding from both thermoplastic polymers, thus becoming true load-bearing components of such composite structures. But unlike nearly spherical fillers, randomly suspended rodlike *fibers* get oriented during flow start-up. In nondilute fiber-filled polymer matrices fiber orientation is in the direction of flow, with a distribution similar to that of rodlike fillers in Newtonian fluids (82). Fiber motions in non-Newtonian fluids have been the main focus of theoretical studies (83–86). Experimental steady state glass fiber orientation distributions in viscometric pressure flow are shown on Fig. 11.22. Fiber orientation distribution is narrow and below 5° away from the shear plane at low shear rates, and it narrows to even smaller angles with increasing shear rate. Thus, there is a major fiber network destruction that results in lowering the viscous energy dissipation and allowing the matrix to be the major contributor to the shear thinning behavior of the glass-filled melt (87–89). This is shown on Fig. 11.23 for a 30% wt glass-filled LDPE melt.

We note that in the entire range of processing shear rates (10¹–10³ s⁻¹) the viscosity of the glass-filled melt seems to be dominated by the matrix in its shear-thinning property, but has an absolute value of about 50% higher than the matrix at this loading level. The filler aspect ratio (i.e., length to diameter ratio) affects the low shear rate viscosity of glass-filled melts, as shown on Fig. 11.24 for a series of loadings with a low viscosity Nylon-6. Above

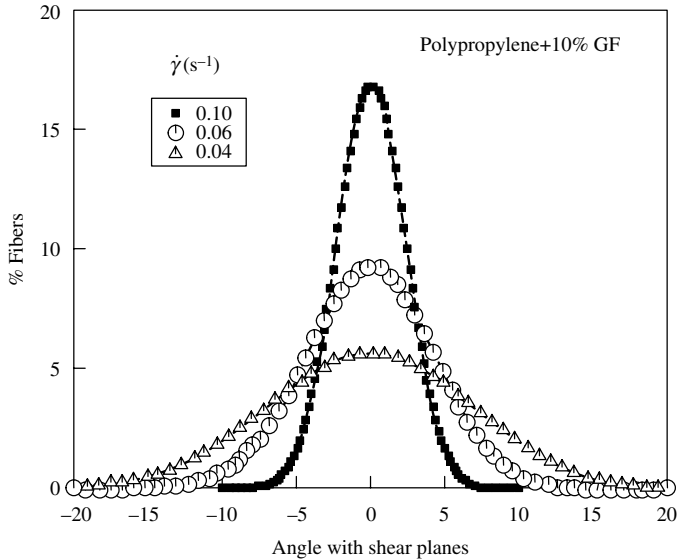


Fig. 11.22 Steady state fiber orientation with respect to shear planes for GF-filled PP. [Reprinted by permission from A. T. Mutel, Ph.D. Thesis, Department of Chemical Engineering, McGill University, Montreal, Canada (1989).]

fiber L/D ratio of 10 and shear rates up to about 1 s^{-1} the effect is more pronounced, indicating possible network formation. Furthermore, Nylon-6 with longer fibers is more shear thinning than the Newtonian matrix and matrix filled with shorter fibers. This is an indication of the destruction of remnants of long-fiber networks, albeit weak.

The flow-induced destruction of networks of both near-spherical and rodlike particulates suspended in polymer matrices can be reversed with time in quiescent conditions. It is of limited interest, since it may take hours, which will cause thermal degradation. Larson (90)

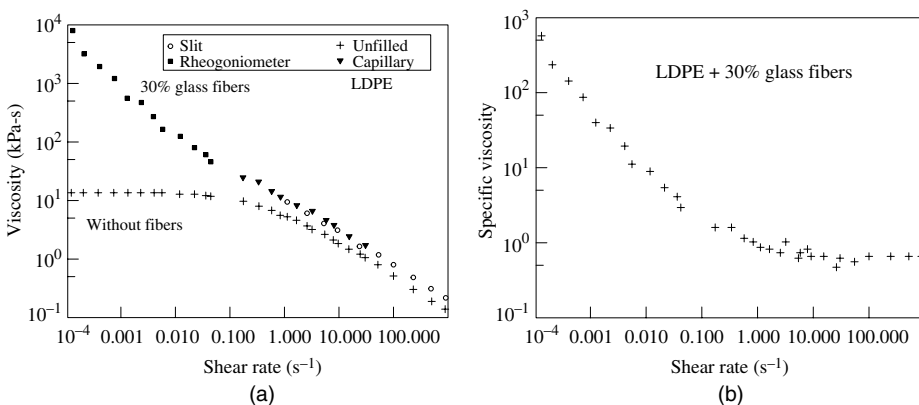


Fig. 11.23 (a) The shear flow viscosity of the matrix and 30% wt glass-filled PP, and (b) the specific viscosity, equal to the ratio of the glass-filled LDPE to the unfilled LDPE viscosities at the same shear rate. [Reprinted by permission from H. M. Laun, "Orientation Effects and Rheology of Short Glass Fiber-reinforced Thermoplastics," *Colloid Polym. Sci.*, **262**, 257 (1984).]

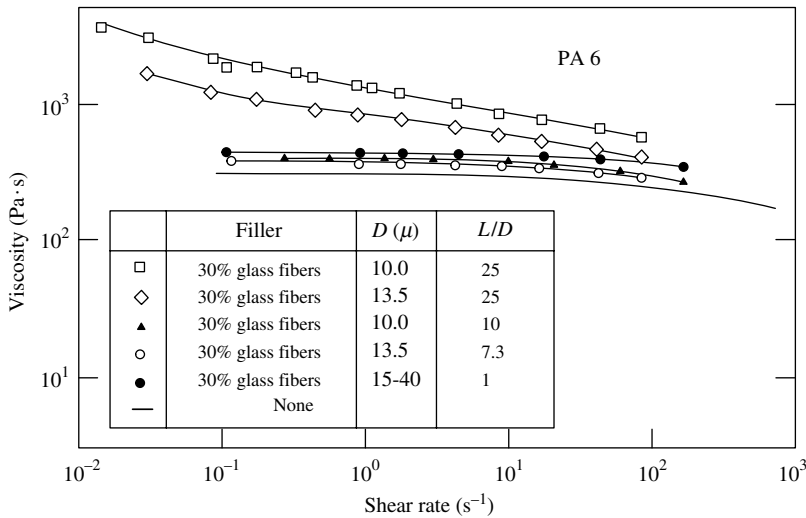


Fig. 11.24 The effects of the fiber aspect ratio, at constant 30% wt loading, on glass-filled polyamide-6. [Reprinted by permission from H. M. Laun, "Orientation Effects and Rheology of Short Glass Fiber-reinforced Thermoplastics," *Colloid Polym. Sci.*, **267**, 257 (1984).]

estimates that the diffusion time, $t_D \approx \eta d^3/k_b$ for a 1- μm -diameter particle in a melt of viscosity 10^3 Pa·s is very long, of the order of 10 h! This phenomenon is *thixotropy*, which is shear-thinning with time at constant deformation rate.

Finally, at higher particulate loadings, above 50% vol, the rheological behavior of filled melts is dominated by particle-to-particle interactions, due to both interparticle forces and physical flow-caused movement hindrances of the suspended particulates, particularly during pressure flows. One consequence of this is the creation of a particulate-free wall film that creates a lubricity slip layer and pluglike flows. Such slip velocities have to be considered in flow rate versus pressure drop design expressions, as well as the viscometric rheological characterization (91).

In summary, the following effects of particulates on the viscosity of filled melts are observed: at very low shear rates and with $\phi_v > 0.1$ –0.2, very large effects are observed, indicative of the presence of interparticle networks; the destruction of these networks at the entire processing shear-rate region results in the fact that the matrix shear-thinning nature is preserved, but with viscosities increasing with increasing ϕ_v ; coating particulates with bifunctional coupling agents decrease agglomeration, increasing ϕ_m , and therefore decreasing the shear viscosity; at higher ϕ_v particulate-free wall-slip layers are formed during flow, resulting in wall-slip velocities; filled melts are less elastic, resulting in low extrudate swelling and delayed onset of melt fracture; finally, filled melts are thixotropic. The preceding collection of rheological attributes of particulate-filled polymer melts renders them to be "complex" fluids.

Compounding of Particulate-Filled Systems

Let us now turn to the question of the consequences of the previously discussed rheological behavior to polymers compounding operations. In continuous compounding equipment we have to answer this question for each of the elementary steps involved.

Solids Handling Feeding and solids transport can benefit from coating particulates with physical and chemical coupling agents, since they reduce agglomeration and make particulates free flowing, but feeding polymer pellets or stabilized reactive powder with solid particulates of different size and density may result in feed-constituent segregation. In general, feeding of dry particulate ingredients requires preblending, which is carried out in simple ribbon blenders with the blend transferred to a metering feeder in twin rotor compounders and a gravity or force feeder in a SSE. However, feeding large amounts of filler may also be carried out by preblending via separately metered joint feeding, or by sequential addition of the filler through feed ports after melting has taken place (92). Feeding a mix of a liquid additive with solid particulates is facilitated by preparing a concentrate in an intensive mixer, for example, a Henschel mixer. The high speed rotors generate very vigorous flow, coating, and collisions, leading to a rise in temperature and absorption of the liquid component by the solid particulates, often resulting in a free-flowing system.

Feeding fibers together with polymer pellets or powder does lead to feeding complications as well as component segregation. Furthermore, the high fiber aspect ratio together with their abrasive nature will result in excessive machine wear in those channel segments that are full of solids (solids transport and early melting sections). For these reasons continuous glass rovings or “chopped” fibers are fed or “stuffed” at a location downstream of the melting section, as shown on Fig. 11.25 (93), requiring only deagglomeration and dispersive mixing by the laminar flow stresses. Within the machine, downstream from the feeding port, near-spherical particulates may get agglomerated or

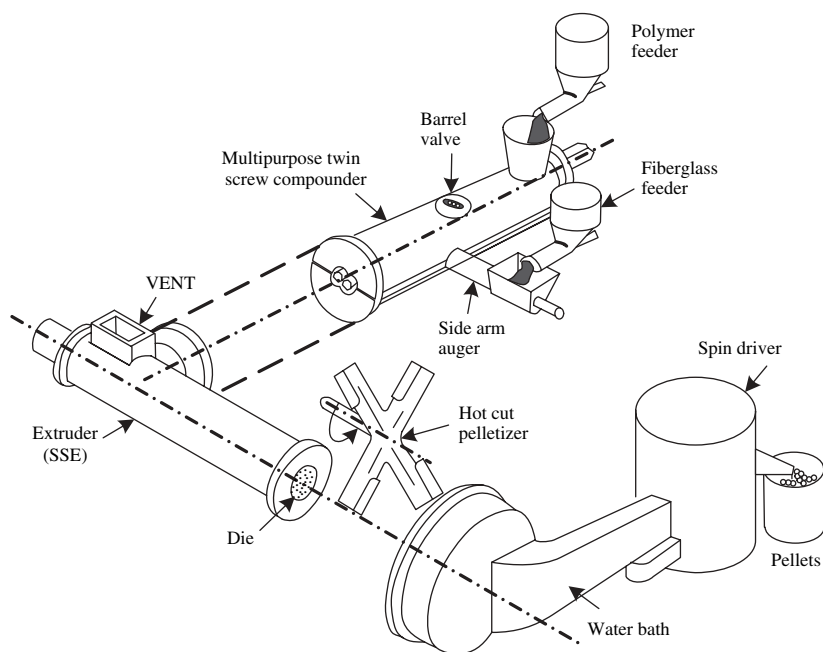


Fig. 11.25 Schematic of twin-screw compounding system for producing glass-reinforced polymer pellets. [Reprinted by permission from D. B. Todd and D. K. Baumann, “Twin Screw Reinforced Plastics Compounding,” *Polym. Eng. Sci.*, **18**, 321–325 (1978).]

“briquetted” by compressive forces, thus hindering the tasks of dispersive mixing following melting. On the other hand, very small and “fluffy” particulate additives, such as carbon black, are pelletized into moderate density 0.3–0.5-g/cm³ pellets and transported in bulk or bags. The process conditions must “navigate between *Scylla* and *Charybdis*”² (94) in making pellets with enough cohesive strength to endure bulk handling, but weak enough to be dispersed by laminar flow stresses during compounding. Additives that will be compounded with water sensitive polymers (e.g., polyamides and polyesters) must be thoroughly dried, and a nitrogen blanket is required for compounding into polymers sensitive to oxidative degradation (e.g., LDPE).

The presence of particulate fillers in polymer systems, which are compounded in twin rotor equipment, does not affect *solids transport*, since that section of the device is partially filled and, in the case of co-rotating twin extruders, self-wiping. By contrast, in single-rotor processing equipment, compressed-particulate solids beds are formed soon after gravity-fed hoppers. They slide in a pluglike fashion downstream, under the frictional forces at the barrel–solid bed interface. There, the filler particulates in contact with the barrel, bring about a higher apparent coefficient of friction, $f_{w,ps}$ above that without the filler, f_w . This results in an increase in frictional forces, which in turn leads to increased transport capability, to increased torque and power consumption, as well as more machine wear since most fillers are abrasive. The extra frictional force is

$$F(z) = P(z)A_{ps}(z)(f_{w,ps} - f_w) \quad (11.5-1)$$

where $A_{ps}(z)$ is the area of effective contact between particulates and the barrel. The extra mechanical power is

$$\dot{W}(z) = F(z)(V_b - V_{\text{plug}}) \quad (11.5-2)$$

where V_{plug} is the solids bed plug velocity (see Section 4.9). Higher \dot{W} will generate, in a shorter down-channel distance, the thickness needed for melting to begin, and thus reduce the length of the “delay zone,” discussed in Chapter 9. The preceding effects increase with increasing filler loadings.

Melting The effects of particulate fillers on melting are appreciable in both single and twin rotor compounding equipment. In single rotor devices, melting occurs by *conduction* with *drag-induced melt removal* (see Section 5.7). The two heating contributors are conduction from the barrel and viscous energy dissipation (VED) generated in the sheared molten film (see Eq. 5.7-38 for “Newtonian” melts). The VED source term increases linearly with viscosity. Turning to Fig. 11.18 we observe at a shear-rate value of 10² s⁻¹ an order-of-magnitude increase in the viscosity at 20% by volume of carbon black–filled PS compared to PS. Since in compounding it is reasonable to assume that VED is the dominant contributor, the melting rate also may increase by an order of magnitude.

2. Ulysses had been warned by Circe of the two monsters Scylla and Charybdis. Scylla dwelt in a cave high up on the cliff, from whence she was accustomed to thrust forth her long necks (for she had six heads), and in each of her mouths to seize one of the crew of every vessel passing within reach. The other terror, Charybdis, was a gulf nearly on a level with the water. Thrice each day the water rushed into a frightful chasm, and thrice was disgorged. *The Odyssey* by Homer.

Similar, but lower increases are observed on Fig. 11.21(a), with 20% loading of uncoated CaCO_3 giving a fivefold viscosity increase and a twofold increase with the coated filler in LDPE. The denominator in Eq. 5.7-38 represents the amount of thermal energy needed to raise the temperature of the feed to the processing melt temperatures. Note that the filler does not have to undergo melting; thus, the needed thermal energy may be lower, also contributing to higher melting rates.

In twin rotor compounding equipment melting takes place very rapidly in the melting section, which is filled by compacted particulate-filled polymers. The initial melting mechanisms (see Section 5.9) are frictional energy dissipation (FED) and plastic energy dissipation (PED). After partial melting, the unmelted pellets/powder form “suspensions” in the particulate-filled fresh melt. Thus, VED in the molten regions now becomes an important melting contributor. The presence of particulates has the following effects: an appreciable increase of the FED, since frictional forces between deforming filler-coated assemblies are larger, or much larger, than with only polymer particulate assemblies; thus FED, which is usually much smaller than PED in unfilled systems becomes a strong contributor to melting at the polymer-particulate surfaces. This, coupled with PED, stemming from solid pellet deformations, results in more rapid melting both initially and during the VED stage. This is shown on Fig. 11.26 for a system of PP powder filled with only 2% by weight of clay melted in the Twin Screw Melting Element Evaluator³ (TSMEE) and a Brabender internal mixer (95). The melting length in the TSMEE is reduced by 17% and the melting peak in the Brabender internal mixer is reduced from 18 s to 6 s. It is also noteworthy that addition of 5% PE wax lubricant increases the melting length, for example, for PP powder from 1.6 L/D to 2.2. L/D .

Dispersive Mixing The objective of dispersive mixers is to break down agglomerates. This is discussed in detail in Section 7.1. Yet, as mentioned earlier in this section, particulate fillers may undergo agglomeration by the high-frequency pressure generated by the kneading paddles, and if this happens it will generally be difficult to deagglomerate in the downstream mixing section. The degree of agglomeration, or rather the lack of dispersive deagglomeration, at any uniform global concentration will affect the mechanical properties of the product as well as its visual appearance when analyzed at small enough scale of examination.

An example of agglomeration in a CaCO_3 -filled PP sample is shown on Fig. 11.27 (96). The SEM photograph shows that the 8% filled (by volume) sample is packed with agglomerates of different sizes. The degree of agglomeration can be appreciated by the fact that an agglomerate of size $d_1 \approx 15 \mu\text{m}$, contains approximately 10^6 primary CaCO_3 particles of size $d_2 \approx 0.15 \mu\text{m}$. Yet, the main function of mixers is to disperse the agglomerates into smaller agglomerates, or preferably into the primary particles and distribute them throughout the volume of a batch mixer, or the discharge of a continuous mixer.

In Section 7.1 we show that the criterion for a spherical agglomerate breakup in viscous flow depends on parameter Z defined as:

$$Z = \frac{8}{9} \chi \mu \dot{\gamma} \left(\frac{\varepsilon}{1 - \varepsilon} \right) \frac{d}{C_0} \quad (11.5-3)$$

3. The TSMEE is an experimental device developed to study melting and mixing in twin rotor mixers during the Polymer Mixing Study conducted at the Polymer Processing Institute (95).

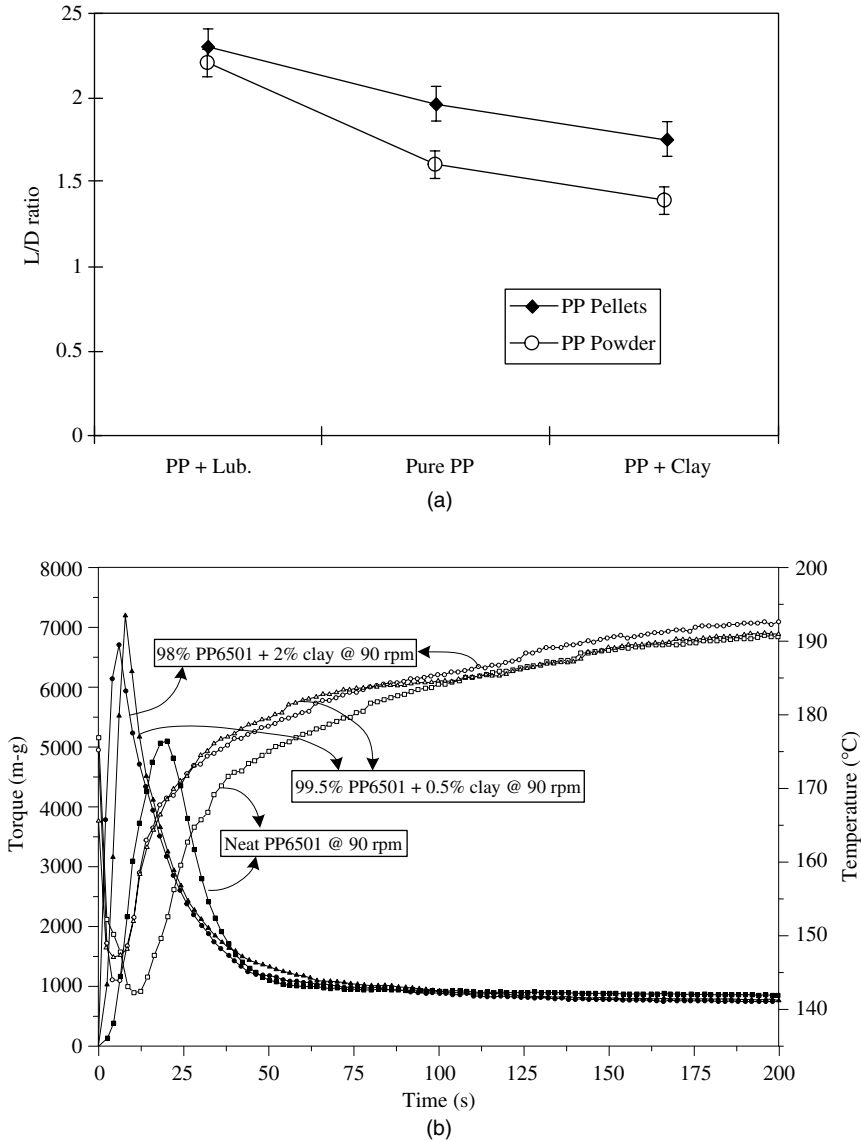


Fig. 11.26 (a) The length-to-diameter ratio, L/D , required for melting of PP Montell (6523) pellets and the same powder: PP only, PP with 2% wt clay, and PP with 5% wt PE wax lubricant. (b) The evolution of torque and temperature in a Brabender internal mixer for neat and clay-filled powder. [Reprinted by permission from M. Kim and C. G. Gogos, "The Roles of Clay and PE Wax Lubricants on the Evolution of Melting in PP Powder and Pellets," *Proceedings of the 11th Polymer Mixing Study Meeting*, Polymer Processing Institute, Hoboken, NJ (1995).]

Agglomerate breakup will occur at $Z > 2$ in shear flow; in biaxial extensional and uniaxial extensional flow, it will occur at $Z > 1$ and $Z > 0.5$, respectively. Breakup does not depend on agglomerate size, but on the size of the primary particle. Clearly, the smaller the primary particle is, the higher the shear stresses needed to reach breakup. It is worth noting

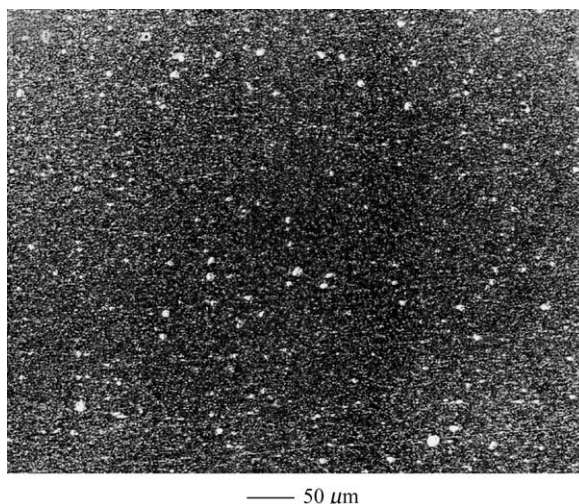


Fig. 11.27 Scanning electron micrograph of calcium carbonate-filled polypropylene: the primary particle size is $0.15\ \mu\text{m}$; the volume fraction of filler 0.08. [Reprinted by permission from Y. Suetsugu, "State of Dispersion-Mechanical Properties Correlation in Small Particle Polymer Composites," *Int. Polym. Process.*, **5**, 184 (1990).]

that the dimensionless number Z is the agglomerate equivalent of the capillary number. Both are parameters representing the ratio of hydrodynamic surface forces acting to break up the particle/droplet to the cohesive forces that hold them together. In agglomerates these are van der Waals forces between the primary particles; whereas, in droplets it is the surface tension.

We have shown in Section 7.1 that hard agglomerate breakup requires fairly high shear stresses. Yet, because of power and heat transfer limitations, mixers for both rubbers and plastics, continuous or batch, cannot be designed to impose high stress levels throughout the mixer volume. All dispersive mixers are therefore designed to have the following characteristics: (a) high stress regions of relatively small volume with good heat-removal characteristics; (b) a flow pattern that circulates the fluid repeatedly through the high shear regions; and (c) an overall geometrical configuration that ensures very good distributive mixing, frequently stemming from chaotic flow patterns in the mixers. In classic Banbury-type batch mixers, the high-stress region is the radial clearance between the tip of the rotating blades and the wall of the mixer. In the continuous twin screw-type of mixers it is the clearance between the tip of a flight or a kneading-type element and the barrel surface, or any other geometrical configuration with narrow clearance.

Clearly, if these conditions are met, different fluid particles experience a different number of passes (for a given time in a batch mixer, or over a certain length in a continuous one), and we can only compute the probability of a fluid particle to experience a given number of passages. This is what the number of passage distribution (NPD) functions discussed in Section 7.3 accomplish. Now, having the criterion of breakup, and assuming midplane cleavage when it occurs, and using the NPD functions, Manas-Zloczower, Nir, and Tadmor (97) derived a complete model for batch mixers.

They adopted the well-stirred vessel with recirculation as a model for internal Banbury-type mixers. They derived the NPD function, combined it with a physical and hydrodynamic model to describe the rupture of an individual freely suspended axisymmetric solid particle, and derived the ultimate particle size distribution of the solid. They tested the model with experimental results on carbon black dispersion in rubber and showed very good agreement. The good agreement was attributed to the capture by the NPD function of the key element of the very complex mixing process. Indeed they suggested (98) as a mixer scale-up criterion the mean number of passages coupled with securing a given threshold shear stress value in the high shear region between the tip of the rotor and the chamber wall.

Example 11.3 The Two-Zone Theoretical Model for Agglomerate Dispersion in a Batch Intensive Mixer

In this example we calculate the agglomerate size distributions, a function of mixing time in a dispersive batch mixer following the two-zone model developed by Manas-Zloczower et al. (97,98). According to this model the mixer of volume V is divided into two functional zones: *Zone 1* occupies virtually all of the mixer and it is considered to be a stirred tank, implying uniform composition at all times; whereas, *Zone 2* occupies the small narrow gap high shear regions. A constant steady stream q exits the first zone, passes through the high-shear second zone, and is recirculated to the first zone. We assume constant shear stress drag flow in the gap. Therefore, since we have shown in Section 7.1 that for agglomerates with uniform porosity rupture is independent of size, there are only two outcomes for agglomerates passing in Zone 2: they either rupture or not. Of course, dispersive mixing occurs only in the former case. We further assume that the rupture of agglomerates is a repetitive process until the ultimate particle size is reached, which can no longer rupture. The initial agglomerates are spherical in diameter size, D_0 , and when they rupture two equal size spherical smaller agglomerates are formed of size D_1 , and so on. Thus, the size of the agglomerate after $k + 1$ ruptures is given by

$$D_{k+1} = \frac{D_k}{2^{1/3}} \quad (\text{E11.3-1})$$

and in terms of the initial size

$$D_k = \frac{D_0}{2^{k/3}} \quad (\text{E11.3-2})$$

Initially a fluid particle in the mixer contains a volume fraction v_0 of agglomerates of size D_0 . After the fluid particle passes *Zone 2* once, it will contain the same volume fraction of particles of size D_1 , and so on. But, as discussed in Section 7.3, at any time, t , we find fluid particles in *Zone 1* that never passed through *Zone 2*, fluid particles that passed once, twice, or k times. Therefore, as soon as mixing begins, at any given mixing time, t , we find a *distribution* of agglomerate sizes in the mixer. In Section 7.3 we showed that the volume fraction of fluid that has experienced k passes in a recirculating stirred vessel is given by

$$g_k = \left[\frac{1}{k!} \left(\frac{t}{\bar{t}} \right)^k \right] e^{-t/\bar{t}} \quad (\text{E11.3-3})$$

where \bar{t} is the mean residence time in Zone 1, between passes through Zone 2, and is given by

$$\bar{t} = \frac{V}{q} \quad (\text{E11.3-4})$$

Equation E11.3-3 provides the required size distribution of the agglomerates, because the direct correspondence between the number of passes in Zone 2 and the resulting agglomerate size as given in Eq. E11.3-2. Thus, at a given mixing time, t , the fraction of fluid volume that never passed Zone 2, and, therefore, contains only agglomerates of size D_0 , according to Eq. E11.3-3 decreases exponentially with time:

$$g_0 = e^{-t/\bar{t}} \quad (\text{E11.3-5})$$

The volume fraction that contains agglomerates that passed through Zone 2 once and, therefore contains agglomerates of size of D_1 , is

$$g_1 = \left(\frac{t}{\bar{t}}\right) e^{-t/\bar{t}} \quad (\text{E11.3-6})$$

We note that the volume fraction of fluid with agglomerates of this size begins with zero and passes through a maximum at a mixing time $t/\bar{t} = 1$ and then drops exponentially. Similarly, all fractions at $k > 1$ will exhibit the same type of behavior, but with the maxima at increasingly longer mixing times.

The quality requirements of dispersive mixing generally require that the fraction of agglomerate above a critical size be below a certain set value. For carbon black dispersion in rubber, for example, generally the requirement is that the fraction of agglomerates above $10 \mu\text{m}$ be less than 1%. In terms of distribution function the mixing time needed to meet such a criterion is given by

$$\sum_{i=0}^L g_i = \sum_{i=0}^L \left(\frac{1}{i!}\right) \left(\frac{t}{\bar{t}}\right)^i e^{-t/\bar{t}} < \psi \quad (\text{E11.3-7})$$

where L is the minimum number of passes needed to reach the critical size of the agglomerate, and ψ is the quality criterion (e.g., 0.01 for carbon black). If, for example, $L = 10$, and the mean residence time is 10 s, the mixing time needed to meet a criterion of $\psi = 0.01$ is $t = 529$ s. That is, 8.8 min are needed to secure that 99% of the agglomerates experience more than 10 passages.

From the preceding equations, we can also calculate the discreet agglomerate size distribution at any mixing time. The total initial number of agglomerates is

$$N_0 = \frac{v_0 V}{4\pi D_0^3/3} \quad (\text{E11.3-8})$$

The number of initial-size agglomerates decreases with time, as given by Eq. E11.3-5:

$$N_0(t) = N_0 e^{-t/\bar{t}} \quad (\text{E11.3-9})$$

In a fluid particle that passes k times the *size* of the particle according to Eq. 11.3-2 reduces to D_k , and the *number* of particles doubles every pass to $N_k = 2^k N_0$. Thus, the number of agglomerates of size D_k in the mixer at time t is

$$\begin{aligned} N_k(t) &= 2^k N_0(0) g_k \\ &= 2^k N_0(0) \left[\frac{1}{k!} \left(\frac{t}{\bar{t}} \right)^k \right] e^{-t/\bar{t}} \end{aligned} \quad (\text{E11.3-10})$$

The fraction of agglomerate of size k is

$$Y_k = \frac{N_k(t)}{\sum_0^L N_k(t)} \quad (\text{E11.3-11})$$

There is a series of additional factors that we have not taken into account in this example. These, however, do not change the concept, but make the model somewhat more complicated.

The first factor is that the agglomerates are not necessarily spherical in shape. A more general representation would be to assume that they are spheroids in shape with fore and aft symmetry. This case was treated in detail by Manas-Zloczower et al. (97). These particles enter the high shear zone in random orientation, and therefore some may rupture and others will pass without rupturing. The fraction of particles that rupture in a given set of condition can be calculated.

The second factor is that the flow field is not pure drag flow, because upstream from the high shear zone there is a tapered region that generates pressure and affects the flow field. The pressure is necessary to prevent slip in the narrow gap. Moreover, elongational flow develops in the tapered section, which by itself helps separate closely spaced particles and even leads to rupture. Clearly, if the flow field in the narrow-gap is a combination of drag and pressure flow, the shear stress will no longer be uniform and consequently not all agglomerates may rupture, because some may pass the narrow gap region at locations where the shear stress is below the critical value. This factor can be incorporated into the model, too.

The third factor is the nonuniform temperature field in the gap, because the outside wall is cooled to secure high enough stresses in the gap, but the rotor is not cooled; moreover, viscous dissipation generates heat. All these led to a nonuniform stress field, which once again affects performance.

Finally, the fourth factor in the size-dependent cohesion of agglomerates (99), discussed in Section 7.1.

Example 11.4 Revisiting the SSE as a Dispersive Mixer In Section 9.2 we discussed the Manas-Zloczower and Tadmor (100) NPD model for an SSE, which indicates that the common SSE is an inherently poor dispersive mixer. In this example we examine the NPD in an SSE with a larger flight clearance providing for more circulation over the flight. The model is based on a continuous-plug-like flow system with recirculation shown schematically in Fig. E11.4 where an axial slice of material considered a well-mixed tank, with recirculation over the flight, moves along the axis of the SSE.

The NPD is given by Eq. 9.2-44 (which is equivalent to Eq. E11.3-3) where $\lambda = t/\bar{t}$ is given in Eq. 9.2-47, and it is the ratio of residence time in the extruder (given by the ratio of free volume of the screw to SSE volumetric flow rate, V/Q) to the mean circulation time over the flight zone (given by the ratio of the free volume of the screw to the total (drag) flow rate

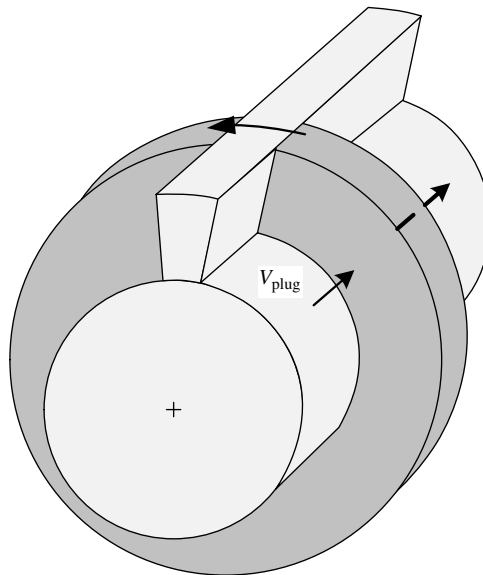


Fig. E11.4 A shaded axial slice of the screw extruder of volume v , which is assumed to move axially in a plug-like mode. The barrel drags melt from the well-mixed annular region over the flight back to the annular well-mixed region.

over the flight, V/Q_f). If we neglect the effect of the flight width on the free volume of the screw, λ is given by Eq. 9.2-47

$$\lambda = \frac{Q_f}{Q} \tag{E11.4-1}$$

As an example consider a single-flighted 60-mm diameter extruder with length-to-diameter ratio of 20 and a relatively large flight clearance of 0.05 cm to allow high rates of flow over the flight (and thus increase the number of passages) with the screw rotating at 60 rpm and extruding 50 l/h melt.

The flow rate of the flight from Eq. 9.2-47 is

$$Q_f = \frac{1}{2} \pi \left(\frac{60}{60} \right) (20 \times 0.06)(0.06)(0.5 \times 10^{-3}) = 0.565 \times 10^{-4} m^3/s$$

And the volumetric flow rate is

$$Q = 50l/h = \frac{50 \times 10^{-3}}{3600} = 0.13889 \times 10^{-4} m^3/s$$

Which results in $\lambda = 4.068$ and the NPD is

g_0	1.71%
g_1	6.96%
g_2	14.15%
g_3	19.20%
g_4	19.50%
g_5	15.87%
g_6	10.76%

Results indicate that although only 1.7% of the exiting flow rate never passes the flight, 61.5% of the material passes less than five times. Keeping in mind that for good dispersion we need some 25 passages, clearly the SSE is a poor dispersive mixer. Moreover, the melt in the screw channel, though mixed by the circulatory flow pattern that ensues in the channel, cannot be considered well-mixed and chances are that much of the same melt is recirculated; the velocity profile in the flight clearance is not pure drag flow, but because of temperature effect it is distorted, reducing the flow rate across the flight; the barrel is hot and the melt is heated further by viscous dissipation, reducing shear stresses in the flight; and, finally, there is no tapered entrance into the narrow flight gap, generating pressure to avoid slip in the flight. In view of all this one cannot expect that the SSE be dispersive mixers. However, using a very different screw geometry and design, as shown by Tadmor (101), SSEs can be converted into dispersive mixers.

Finally, along similar lines, Canedo and Valsamis (102) analyzed and modeled the nonintermeshing twin rotor Farrell Continuous Mixer (FCM) as a continuous plug-flow system with recirculation. These authors calculate the average number of passages in the FCM machine to be in the range of 20–50, despite the relative short residence time of the material. By modeling flow over the clearance they compute the maximum shear stress, and they propose to quantify mixing performance of continuous mixers in terms of the maximum shear stress, the mean number of passages, and the mean residence time. Dispersive mixing requirements with fiber additives are more complex. On the one hand, we wish to wet and break bunches of fibers into individual fibers and then distribute them throughout the volume. Yet, the need of dispersion must be carefully balanced with the risk of fiber length breakdown. Indeed, brittle fiber additives suffer length breakdown mainly during melting, but also during the subsequent mixing flows, as seen on Fig. 11.28, tracking the breakdown of glass fibers in an SSE (103). For this reason fibers are fed (stuffed) at a feed location downstream melting in both single- and twin-rotor continuous compounders. Figure 11.29 (104) depicts the original fiber length distribution of magnesium oxysulfate (MOS) whiskers in the extruder when MOS is dry-blended with PP pellets (feed A) and those when MOS is fed after melting has taken place (feed B). In the former, fiber breakdown is much larger than in the latter. Nevertheless, fiber feeding after melting also results in appreciable length breakdown. Turkovich and Erwin (103) found no significant effect of processing variables and filler concentration (in the range of 1% to 20%) of 6-mm glass fibers on breakdown of the fiber; this indicates that for the given initial length and for the equipment size used, fiber–fiber interactions are not responsible for the breakdown. Gogos et al. (105) studied the effect of preheating 10–15-mm-long pulltruded polyamid pellets containing 50% wt E-glass fibers, during injection molding. Figure 11.30 shows clearly the benefits of feed preheating by analyzing “carcass” samples taken at the screw tip, which contained almost an order of magnitude more fibers that were over 6 mm long. This was attributed to melting under lower shearing stresses. Of course, during the mold filling flow considerable glass-fiber attrition will take place.

Distributive Mixing Distributive mixing of solid particulate fillers is, to a first approximation, the same as with homogeneous melts: the flow kinematics, not laminar stresses dictate it, with chaos-conductive stretching and folding patterns being the most efficient (see Section 7.1). In the SSE distributive mixing can be greatly improved by a host of mixing elements. These are being extensively used not only because they improve distributive mixing, but primarily because they help complete the melting process, which

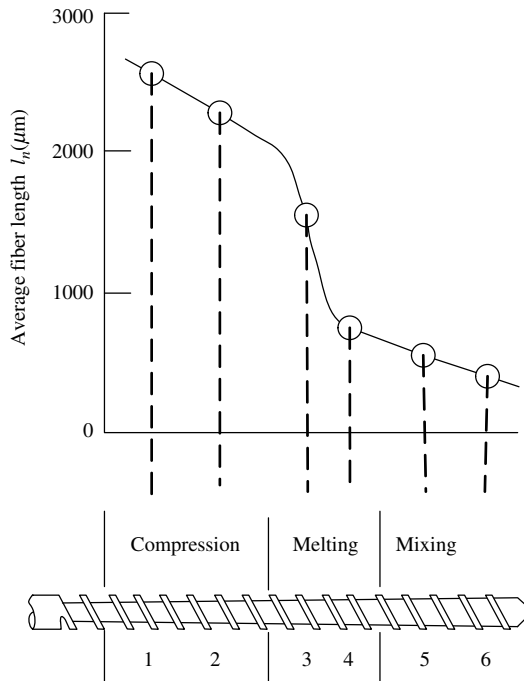


Fig. 11.28 The number average fiber length at various axial positions of an injection molding screw. DuPont Alathon 2010 pellets preblended with 3.2 mm chopped fibers and extruded in a 0.75 in diameter, 20.1 L/D , with 3:1 compression ratio extruder. [Reprinted by permission from R. von Turkovich and L. Erwin, "Fiber Fracture in Reinforced Thermoplastic Processing," *Polym. Eng. Sci.*, **23**, 743 (1983).]

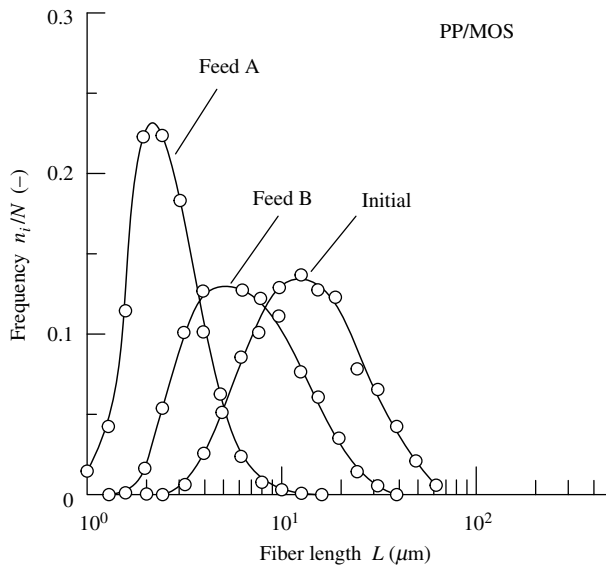


Fig. 11.29 Fiber-length distribution of MOS and feeding protocol for MOS-filled PP containing ethylene-propylene copolymer. [Reprinted by permission from Y. Suetsugu, "The Effect of Mixing on Some Properties of Compounds and Composites," in *Mixing and Compounding of Polymers*, I. Manas-Zloczower and Z. Tadmor, Eds., Hanser, Munich, 1994.]

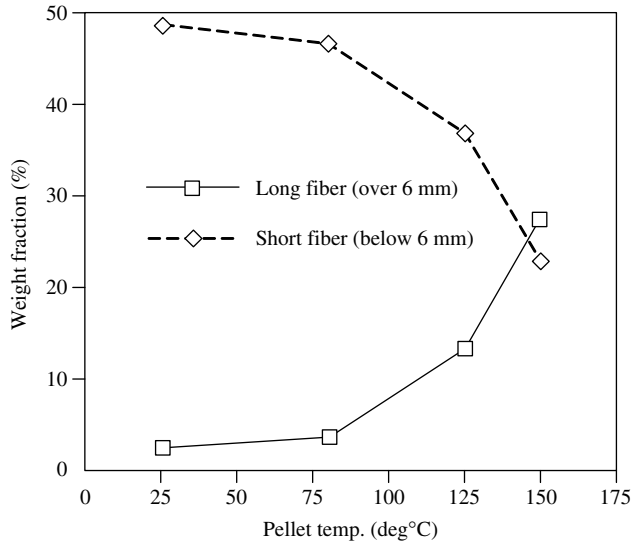


Fig. 11.30 Effect of preheating 50% by weight E-glass fiber-filled polyamide pulltruded pellets on fiber lengths at the screw tip of a 300-ton 23.86-oz reciprocating injection molding machine. [Reprinted by permission from C. G. Gogos, C. K. Yoon, and J. Brizzolara, "Injection Molding Process Development for Long Fiber Reinforced Thermoplastics," *SPE ANTEC Tech. Papers*, **40**, 384 (1994).]

if uncompleted, is the major source of both composition and thermal nonuniformity. An extruder having a screw equipped with suitable mixing sections, though it lacks the dispersive capability of twin-rotor mixers, is a very good compounder. Rauwendaal (106) reviewed the commonly used mixing elements in SSEs. A single-rotor extruder with exceptionally good distributive capability is the Ko-kneader-type rotating and reciprocating machine (107). The barrel in these machines has rows of pins and the screw flights are slotted to allow the barrel pins to pass through the flight slots. This results in stretching and folding flows by the relative and reciprocating motions of barrel pins and screw slots (108). Andersen (109) relates distributive mixing in co-rotating TSEs to mixing practices and distributive mixing elements, which generate stretching and folding chaotic flows, as well as splitting and recombination, leading to spatial redistribution of the compounded stream. As discussed in Chapter 10, simulations of the stretching and folding flows in full kneading elements in co-rotating TSEs have been carried out by a number of investigators, notably, Kiani and Samann (110) and Bravo et al. (111).

Compounding of Polymer Blends

Commercially available important *miscible* polymer blends are rare, the most notable and commercially important example being General Electric's original NorylTM polyphenylene oxide (PPO)/PS composition (112). Producing such blends commercially in compounding equipment is best carried out with chaotic flows following melting of the two components. With no interfacial forces, the two components flow with shear rates that are inversely proportional to their viscosities, since $\tau = \eta_A \dot{\gamma}_A = \eta_B \dot{\gamma}_B$. Thus, unless there is a very large

disparity in the viscosities, for example, a ratio greater than 100, chaotic flows will normally create small and spatially uniform striation thicknesses within short mixing times, t_m , enabling molecular diffusion to complete mixing on a molecular level. Twin rotor continuous and, of course, batch equipment are capable of creating rapid and uniform distributive mixing, and thus they are the preferred equipment for this type of compounding.

However, the majority of commercial blends is *immiscible* and are either physically or chemically *compatibilized* to improve and maintain, or rather to “lock in” the morphology developed during compounding and forming flows. The two components are morphologically segregated, coexisting as (a) *dispersions* at low “minor” component concentrations; (b) *cocontinuous* at nearly equal component concentration or *phase-inverted suspensions*, where the “major” is dispersed because the minor-to-major viscosity ratio is very small; and (c) composite-droplet, or “salami,” or droplet-within-droplet morphologies (113–116). The compatibilizing component(s), being amphiphilic, is (are) concentrated at the *interfaces* between the two polymer components.

It is axiomatic that compounding laminar flows are the cause of component domain breakup, since laminar stresses are the sources for breakup. On the other hand, their specific effects cannot be easily quantified because the flows are mostly nonviscometric and most often time-varying, the blend components are viscoelastic, and the stress transfer across the interfaces is ill-understood as a result of “dynamic” nonequilibrium interfacial tension. In addition, the domain cohesive strength, resisting laminar stress dispersion, has in addition to the surface stresses due to interfacial tension, as discussed in Section 7.1, plus a second component due to “melt strength” of the whole bulk of the dispersed domain. Thus, both the evolution of morphology during compounding and its final state are difficult to predict. Nevertheless, the mechanisms described in Section 7.1 do provide insight into the nature of the process. These are sequential liquid droplet breakup at some critical capillary number and extension of the dispersed phase into filaments and subsequent breakup of the filament into droplet, as depicted in Fig. 7.23. It is the latter that is the dominant mechanism in creating polymer blends.

In both batch and continuous mixers the elongational flow, conducive to filament stretching and breakup, occurs at the tapered entrance regions to narrow gaps between blades and wall and between kneading elements of the co-rotating intermeshing twin screw compounders. Past the narrow gap the material is mixed with the bulk. Thus, the global model for blending compounders is identical conceptually to the “two-zone” model of dispersion of solids previously discussed⁴ in which material circulates between a *strong* zone, where affine stretching and thread breakup in flow take place, and a *weak* zone, where thread breakup at rest continues and drop coalescence may take place. Thus, the mechanism of liquid breakup is more complex than that of solid breakup. In the latter case, the criterion for agglomerate breakup is a simple yes/no, depending on the stress levels in the gap, and there is no size dependence; whereas, in liquid breakup local time scales in the gap and beyond play a distinctive role and breakup is size dependent. Yet, as shown by Janssen and Meijer (117), this complex mechanism can be modeled with reasonable accuracy.

The most commonly used equipment for continuous blending is the co-rotating intermeshing TSEs. In these machines the kneading flows produce two-dimensional

4. The name “two-zone model” was coined by H. E. H Meijer in his chapter “Processing for Properties” in R. W. Cahn, P. Haasen, and E. J. Kramer, Eds., *Material Science and Technology*, Vol. 18, Wiley-VCH, New York, 1997.

sheets, which progress to become ligaments and then fine droplets. The SSE is more limited in its capability to process blends for the same reasons it is limited in dispersive mixing. As pointed out earlier for dispersive mixing, certain screw designs (101) should at least partially overcome this limitation.

We conclude this chapter by reviewing in some detail an experimental mixing program entitled “Polymer Mixing Study,” which was led by one of the authors.⁵ The study focused on the central complexities of compounding polymeric blends during melting and mixing. Two experimental laboratory-size compounders were developed and used to study the mixing mechanisms in continuous compounders. One was the *Single Screw Mixing Element Evaluator* (SSMEE)TM and the other the *Co-rotating Twin Screw Mixing Element Evaluator* (TSMEE)TM. Both experimental devices share the following features:

1. They are designed with split barrels, each half having extensive cooling channels; these two features enable quick quenching of the processed stream and easy opening of the barrel for morphological examination of the solidified “carcass” to study the evolution of dispersive mixing.
2. They can operate in two mixing modes: the first is the *melt–melt mixing* (M–M) mode, where the two blend components are fed into two separate ports as melts, using two SSE pumps. The two melt streams are mixed at the entrance of the mixing element to be evaluated for a given component blend. The second is the *dissipative-mix melting* (DMM) mode, where the two blend components are fed in pellet or powder form as a dry blend to be melted and mixed by the melting/mixing element used. Thus, in the DMM mode, the device can also be used to evaluate melting performance.
3. Downstream from the mixing element section there are two separate inverse SSEs (see Section 6.2) that have the helical channel machined into the barrel, thus needing only rotating shafts to convey the material. Two pressure transducers, one diameter apart, record the pressure built up at closed discharge, a parameter that can be used to measure the viscosity of the molten blend at various shear rates. This “rheometry” section is the forerunner of the *Helical Barrel Rheometer* (HBR)TM of the Polymer Processing Institute (118).
4. A portion of the exiting stream of the molten blend is diverted into the Flow CellTM, where Nomarsky reflection microscopy is carried out in a thin slit, the bottom plate of which is reflective polished steel and the top is a quartz window. The microscope, the rapid image data acquisition device, and analyzer are capable of producing dispersion data down to sizes of one micrometer. The TSMEE is shown schematically for both the (M–M) and DMM) modes in Fig. 11.31 (119–121).

These experimental mixers enabled the study of the role of the rheological properties of the individual blend components on the mechanisms and rates of dispersive mixing. Three commercial polymers: Dow Chemical Company polystyrene (PS686) and low density polyethylene (PE 132) and Chevron low density polyethylene (PE 1409) were used in the study. Figure 11.32 (a) shows the viscosities of the three polymers at 200°C (121). PS 685

5. This industrially cosponsored program was carried out through the 1990s at the Polymer Processing Institute at New Jersey Institute of Technology, Hoboken, NJ, and directed by one of the authors.

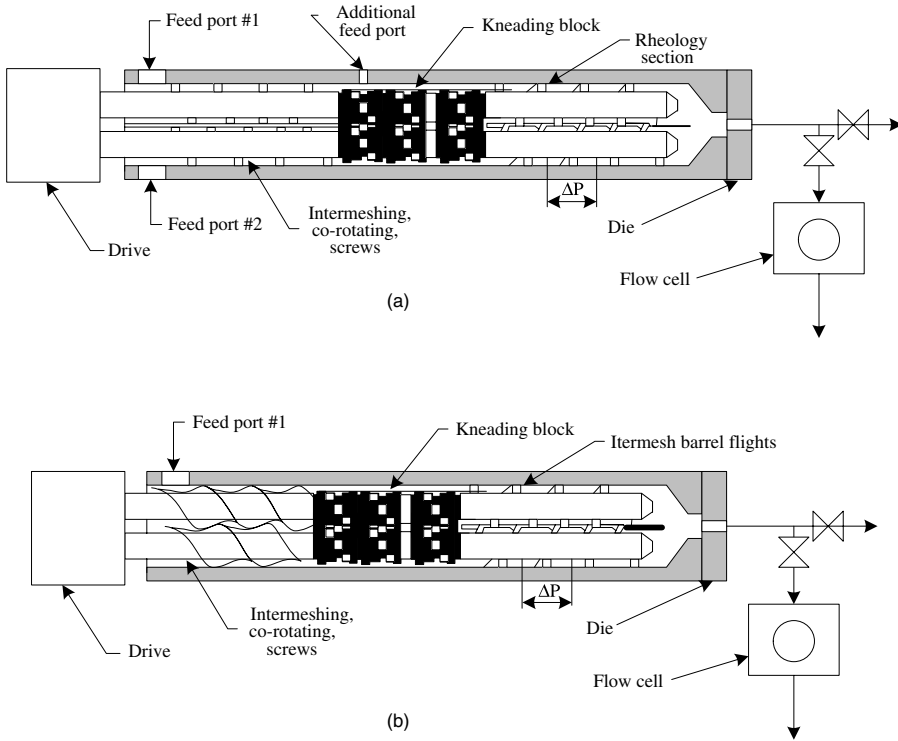


Fig. 11.31 Schematic representation of the Twin Screw Mixing Element Evaluator (TSMEE) in (a) the melt-melt (M-M) mode, and (b) the dissipative mix-melting (DMM) mode. The last section of both the M-M and DME modes consists of two separate HBRs. The mixing element sequences are a “design” variable. [Reprinted with permission from *Proceedings of the Sixth Semi-annual Meeting of the Polymer Mixing Study*, Polymer Processing Institute, Hoboken, NJ (1993).]

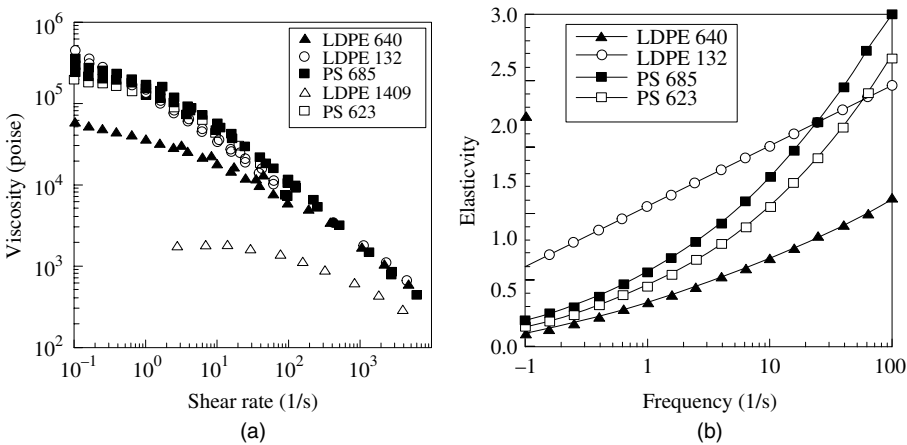


Fig. 11.32 The rheological properties of the polymer resins used in the polymer mixing study at 200°C. (a) The shear viscosity. (b) The elasticity parameter $(\frac{\tau_{11} - \tau_{22}}{\tau_{12}})$. [Proceedings of the Sixth Semi-annual Meeting of the Polymer Mixing Study, Polymer Processing Institute, Hoboken, NJ (1993).]

and PE132 are *equiviscous*. On the other hand, PE 1409 has a much lower viscosity as compared to PS 685. Furthermore, as shown in Fig. 11.32(b), PS 685 and PE 132 are elastic, while PE 1409 is almost totally nonelastic. The blends PS 685/PE 132 are *rheologically matched*, while those of PS 685/PE1409 are *rheologically mismatched*, yet they are both equally immiscible. The following PS/LDPE blends were used to study the “rheology driven” dispersion mechanisms (121):

Blend 1	10% PS	90% PE 1409
Blend 2	10% PS	90% PE132
Blend 3a	90% PS	10% PE 1409
Blend 3b	98% PS	2% PE 1409
Blend 3c	75% PS	25% PE 1409

The TSMEE in the M–M mixing mode was used with three kneading blocks of 5/45/42 forwarding elements. Experiments were conducted at two melt temperatures, 180° and 140°C, and two rotor speeds, 60 and 120 rpm. The results and conclusions that emerged from the study are discussed in the following subsections.

Equiviscous Blend 2 Earlier we postulated that the compression/expansion cycles in fully melt-filled kneading elements of Co-TSEs in fact superpose a periodic axial stretching flow to the steady flow generated by the shaft rotation (110,111). This results in time-varying velocity components in both the axial and radial directions, which, in turn, produce a two-dimensional stretching flow, which is effective for dispersive mixing. We have observed experimentally the effect of the flow pattern just described at the blend microstructure level when analyzing blend “carcasses.” Morphology images taken from samples of equiviscous systems have shown clear evidence of this complex nature of the flow as evidenced by the affine deformation of the minor phase. The minor, following the matrix flow field, undergoes stretching and folding before breaking into smaller domains, as shown in Fig. 11.33. This affine deformation of the dispersed phase was observed *only* in the equiviscous Blend 2. The dispersion mechanism for this blend in the stretching/folding flow field is by the sequential formulation of sheets with holes that reduce the interfacial area, ligament formation, and stretching of the ligaments, which leads to breakup formation of fine droplets, as seen on Fig. 11.34. The rate of dispersive mixing in this equiviscous blend is very rapid, as shown on Fig. 11.35, becoming complete by the eighth lobe, that is, half way into the middle kneading block.

Also noteworthy is the appreciable *coalescence* caused by the shear flows in the single screws, of the “rheology” section of the TSMEE following the mixing element section. Flow of dispersed immiscible blends involves continuous breakdown and coalescence of the dispersed domains (122). Shear flows, where droplet-to-droplet collisions are frequent—in contrast to extensional flows—favor coalescence over dispersion. The presence of compatibilizers shifts the balance toward reduced coalescence rate. Macosko et al. (123) attribute this to the entropic repulsion of the compatibilizer molecules located at the interface as they balance the van der Waals forces and reduce coalescence, as shown on Fig. 11.36.

The addition of a very small amount of styrene-isoprene-styrene (SIS) triblock compatibilizer, introduced as a compounded pellet with PS 685, suppresses the shear flow-induced coalescence appreciably, as seen by comparing Fig. 11.35 with Fig. 11.37. On the other hand, there is no effect of this very small amount of SIS on the dispersion rate.



Fig. 11.33 Dispersed PS 685 streaks of ligaments and droplets in the equiviscous Blend 2. PS is flowing/deforming in an affine fashion in the expected stretching and folding pattern. Experiments were conducted at 180°C and 120 rpm. [Reprinted with permission from *Proceedings of the Tenth Semi-annual Meeting of the Polymer Mixing Study*, Polymer Processing Institute, Hoboken, NJ (1995).]

When the melt–melt mixing temperature is reduced to 140°C and at 120 rpm, there is still stretching of PS, but the stretched morphology is different; not smooth, but rather jagged PS domains stretched into jagged “finger-like” ligaments, followed by shedding of droplets. This is shown on Fig. 11.38. The fact that at 140°C PS is a rubbery melt, in

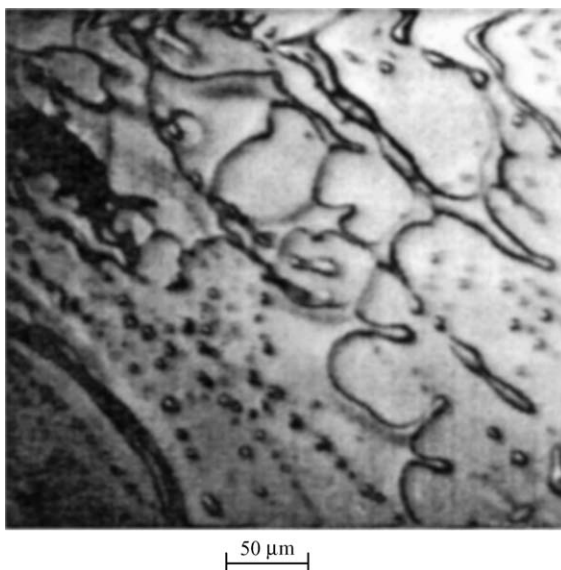


Fig. 11.34 The dispersive mixing mechanism of the equiviscous Blend 2 at 180°C and 120 rpm. Repeated stretching and folding is evident, which result in sheets that have holes, ligaments, and droplets. [Reprinted with permission from *Proceedings of the Eighth Semi-annual Meeting of the Polymer Mixing Study*, Polymer Processing Institute, Hoboken, NJ (1994).]

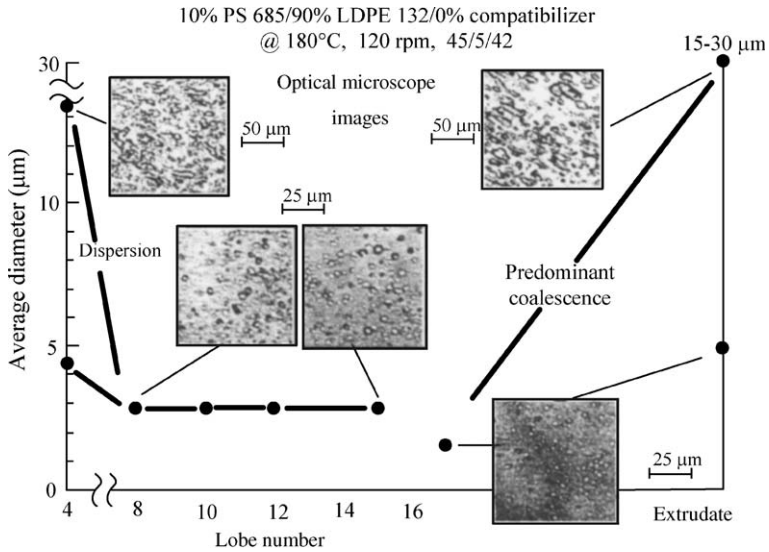


Fig. 11.35 Dispersion rate of Blend 2 obtained through carcass analysis: TSMEE at 180°C and 120 rpm. [Reprinted with permission from *Proceedings of the Tenth Semi-annual Meeting of the Polymer Mixing Study*, Polymer Processing Institute, Hoboken, NJ (1995).]

the Williams–Landel–Ferry (WLF) regime (124), explains the PS domain’s resistance to form smooth sheets and ligaments. Figure 11.39 tracks the evolution of dispersion and 140°C. Compared to Blend 2 dispersed at 180°C, shown on Fig. 11.37, the dispersed morphology is coarser and with a wide size distribution. It was also found that, when

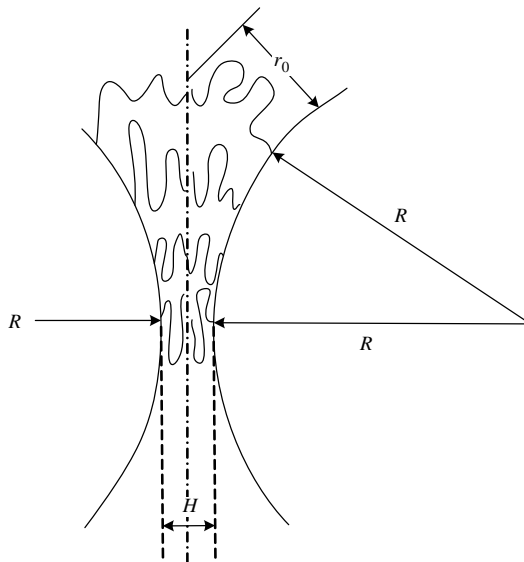


Fig. 11.36 Schematic representation of the effect of compatibilizer chains between two dispersed droplets. The entropic decrease near the pinch distance H repulses “the droplets,” decreasing coalescence.

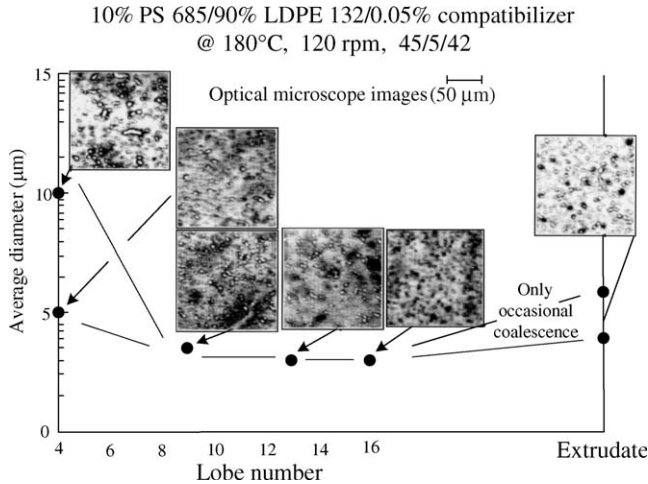


Fig. 11.37 Suppression of shear flow-induced coalescence by incorporating a very low concentration of SIS triblock compatibilizer into the equiviscous Blend 2. [Reprinted by permission from the *Proceedings of the Tenth Semi-annual Meeting of the Polymer Mixing Study*, Polymer Processing Institute, Hoboken, NJ (1995).]

operating the TSMEE in the *dissipative mix-melting* mode at 180°C and 120 rpm, the morphology obtained is closer to that in Fig. 11.39, mix-melting carried out at 140°C. For the equiviscous Blend 2, M-M mixing results in finer morphologies than those obtained at the same conditions with dissipative mix-melting. On the other hand,



Fig. 11.38 Blend 2 at 140°C and 120 rpm. Early morphology development reveals rough PS surfaces and “fingers” indicative of the rubber-like nature of PS at 140°C. [Reprinted by permission from the *Proceedings of the Seventh Semi-annual Meeting of the Polymer Mixing Study*, Polymer Processing Institute, Hoboken, NJ (1993).]

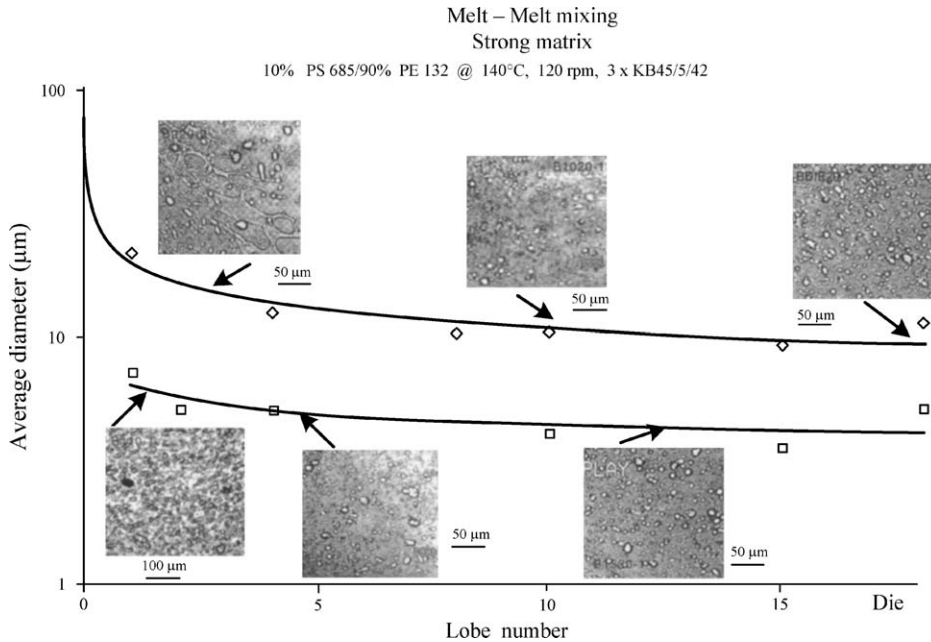


Fig. 11.39 Melt–melt dispersive mixing Blend 2 in the TSME at 140°C and 120 rpm. [Reprinted by permission from the *Proceedings of the Thirteenth Semi-annual Meeting of the Polymer Mixing Study*, Polymer Processing Institute, Hoboken, NJ (1996).]

incorporation of 1–5% SIS compatibilizer into Blend 2 mixed in the dissipative mix-melting made at 180°C and 120 rpm makes the morphology finer, much like the one shown on Fig. 11.37. At this level of compatibilizer the transfer of laminar stresses improves and the interfacial tension decreases, both conducive to finer dispersions.

Weak Matrix Blend 1 Blend 1 consists of a high viscosity and elasticity rheologically robust PS resin, in a low-viscosity inelastic rheologically weak LDPE. The viscosity ratio $\eta_d/\eta_m \approx 50$. The composition of this blend does not favor good dispersion, because the dispersed PS has both bulk elastic strength and high surface tension that resists breakup, and the matrix has a weak Newtonian viscosity. Thus, only extensional flows, whose dispersing ability is only weakly dependent on the viscosity ratio, would achieve dispersive mixing. Figure 11.40 shows the extrudate emerging from the SSME using a 3.5 L/D Maddock mixing element, at 140°C and 90 rpm. A gross unmixed lump of the rubbery PS, about 100 μm in size, attests to the fact that, even after passing through the “barrier” region of this dispersive mixer with a flow that has some elongational component, the prevailing shear flow in the mixing element is unable to affect dispersion. Single rotor devices are not compounding equipment of choice for dispersing systems like Blend 1. With the TSME in the M–M mixing mode, two-dimensional extensional flows are generated in full kneading disks. The results at the following operating conditions—140°C and 60 rpm; 140°C and 120 rpm; 180°C and 120 rpm—are shown in Fig. 11.41(a)–Fig. 11.41(c), respectively. Under all three operating conditions there is strong evidence of

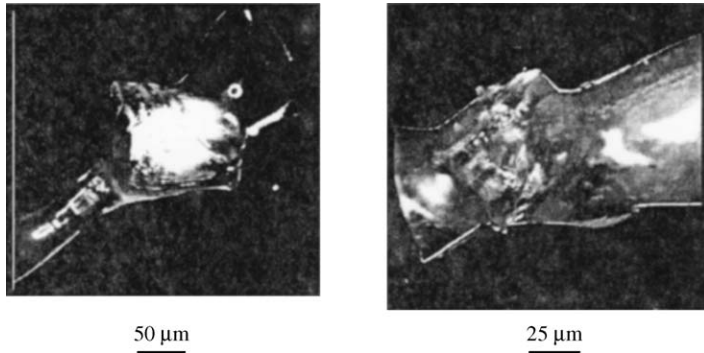


Fig. 11.40 Extrudate of Blend 1 emerging from the SSMEE with a 3.5 *L/D* Maddock mixer operating at 140°C and 90 rpm. [Reprinted by permission from the *Proceedings of the Fourth Semi-annual Meeting of the Polymer Mixing Study*, Polymer Processing Institute, Hoboken, NJ (1992).]

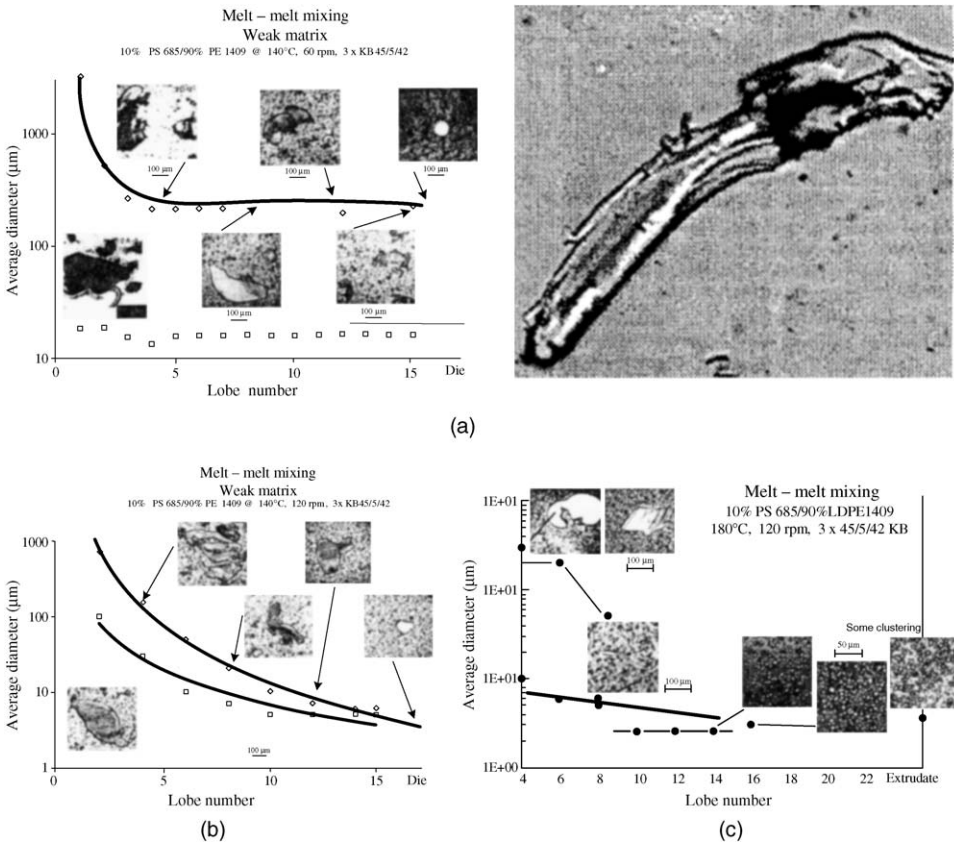


Fig. 11.41 Evolution of the dispersed morphology along the TSMEE mixing element at three operating conditions of the weak matrix Blend 1: (a) 140°C and 60 rpm; (b) 140°C and 120 rpm; (c) 180°C and 120 rpm. [Reprinted by permission from the *Proceedings of the Thirteenth Semi-annual Meeting of the Polymer Mixing Study*, Polymer Processing Institute, Hoboken, NJ (1996).]

dispersion by “brittle” fracture. Initially in the PS breakup, the domains are being stretched and form *fragments with sharp edges*. This is most prevalent at 140°C and 60 rpm; with the brittle features becoming milder and more toward thick stretched sheets only with increasing melt temperature. That is, brittle fracture becomes less dominant as the Deborah number, $De = \lambda/t_{exp}$, becomes smaller, rendering the dispersed domain less elastic.

For both the 140°C dispersive experiments there is evidence of small–large size bimodal dispersion with a fair number of “escapees,” that is, large undispersed PS regions, present in the extrudate. This is, of course, a practically unacceptable dispersion, albeit common with weak matrix blends. At 180°C, Fig. 11.41(c), bimodal dispersion is present only in the early lobes where large sheets and droplets coexist. The sheets and extrudate escapees disappear because PS is now less elastic. It is worth noting in this figure that the degree of coalescence is smaller than with Blend 2, possibly due to the ease with which droplets avoid “collisions” in the low viscosity shear flow. On the other hand, clustering of neighboring droplets, which were not forced to coalesce by strong matrix laminar shear stresses becomes more prominent, possibly because the low matrix viscosity allows quiescent diffusional droplet motion. Finally, using the TSMEE in the dissipative mix melting mode at 180°C and 120°C we obtain both strong brittle fracture features, but the presence of PS extrudate escapees persists with dispersion bimodal results, as seen on Fig. 11.42. PED melting, taking place in the dissipative mix-melting mode with the weak

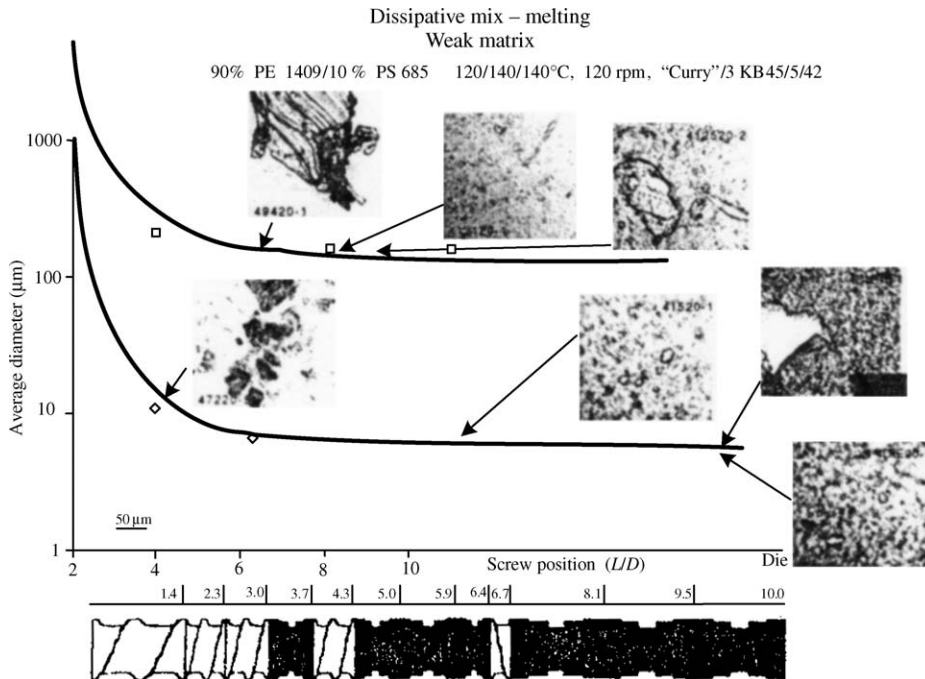


Fig. 11.42 Weak matrix Blend 1. Evolution of dispersed morphology in dissipative mix-melting mode at 180°C and 120°C. [Reprinted by permission from the *Proceedings of the Thirteenth Semi-annual Meeting of the Polymer Mixing Study*, Polymer Processing Institute, Hoboken, NJ (1996).]

matrix Blend 1 is inefficient, resulting in chunks of cooler PS domains entering the TSMEE mixing element. This is the reason for being plagued with such escapees in industrial scale compounding of weak matrix blends compounded in twin rotor equipment.

Let us examine the preceding from the point of view of the PED melting phenomena taking place in the PS/LDPE pellet blend system. In contrast with the PED melting of the single component PS, where its high modulus creates high PED heating/melting rates and complete melting over a short kneading element distance, PS/LDPE blends were found to melt differently. The stiffer polymer, which normally melts faster (i.e., has a much shorter melting length in the full kneading element region of the Co-TSE) when melted alone, is not the faster melting component in blends. This is because in blends, not unlike stacked cylinders of the blend components undergoing unconfined compressive deformation, the softer component LDPE is the component that responds first and predominantly to the forced applied deformations caused by the kneading element corotation. Thus, LDPE “absorbs” most of the plastic deformation energy, melts, and surrounds the mostly unmolten PS. Melting of the PS particulate suspension in LDPE can now take place primarily by VED. If the viscosity of the molten LDPE matrix is high (as is the case with Blend 2), the PS will melt completely; if the viscosity is low (as in Blend 1), PS melting will be incomplete, resulting in “escapees.” In conclusion, we can state that the relative rates of the *initial* heating/melting of the blend components depend inversely on their individual modulus and mechanical strength at high deformation levels; furthermore, complete melting of the strong modulus component occurs only when the melt viscosity of the weak modulus component, which melts first, is high, promoting vigorous VED. This mechanism is corroborated by the compressive stress–strain behavior of two stacked molded disks, one PS and one LLDPE, and is depicted in Fig. 11.43 (125). As the stack is

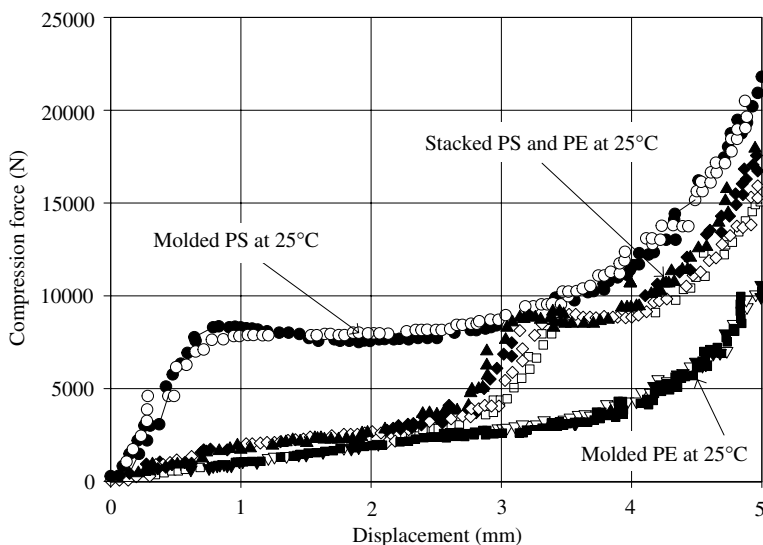


Fig. 11.43 The compressive force versus displacement of stacked PS and LLDPE cylinders at 25°C. Note that initially the stack deformation force tracks that of the more deformable LLDPE, before, at 3 mm, beginning to deform the PS cylinder. [Reprinted by permission from B. Qian, D. B. Todd, and C. G. Gogos, “Plastic Energy Dissipation and Its Role on Heating/melting of Single-component Polymers and Multi-component Polymer Blends,” *Adv. Polym. Technol.*, **22**, 85 (2003).]

compressed it is only the weaker modulus LLDPE that deforms and gets heated by PED, while PS is not affected, and it is only when the LLDPE is almost fully flattened that PS deformation starts. With the weak matrix Blend 1 in full kneading disks, PS will be deformed after PE 1409 is melted. But, as previously discussed, the PS pellets now will be suspended in a low viscosity matrix that will allow for reduced PED and certainly greatly reduced VED because of the low LDPE 1409 viscosity; the result is incompletely heated and incompletely melted PS particulates that become “escapees.”

Blends 3 (a,b,c) Rheologically Robust Matrix and Weak Dispersed Components Since PE 1409 is a low viscosity nearly Newtonian polymer melt, its dispersive behavior is uncomplicated and more Newtonian like. Blend 3a forms a small (3–5- μm) droplet dispersion morphology, and Blend 3b is even finer (1–2 μm), becoming, only below 2% concentration, less subject to flow-induced coalescence. The TSMEE-obtained dispersions are finer than those from the SMEE, with a variety of kneading elements (126). What is noteworthy about these blends is the early stages of the dispersion process, shown on Fig. 11.44, obtained with Blend 3a using the TSMEE at 180°C and 120 rpm.

The low viscosity PE 1409 breaks up into large “odd looking” domains which, when they break up to sizes around 10 μm , become rounder, progressively becoming fine droplets of size 2–3 μm , by the repeated breakdown mechanisms indicated on Fig. 7.23. Finally, Blend 3c forms phase-inverted morphology in the SSME, as shown on Fig. 11.45, where the minor low viscosity, dark region PE 1409, engulfs the major PS. In shear devices sequential addition of low-viscosity blend components is required to achieve fine dispersions; whereas, TSMEEs do not have this limitation to the same extent.

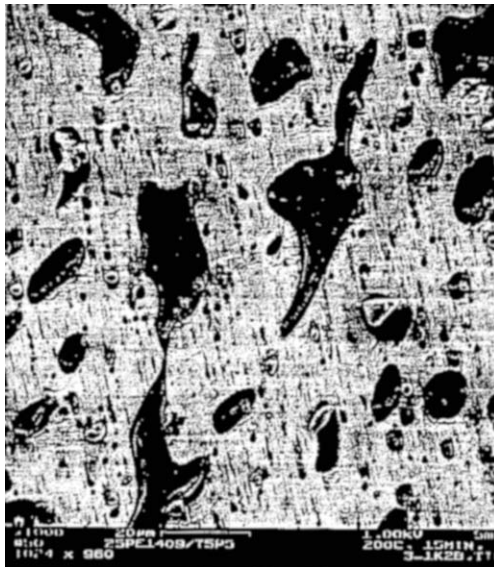


Fig. 11.44 Early-stage morphology developed with Blend 3a in the TSMEE at 180°C and 120 rpm. [Reprinted by permission from the *Proceedings of the Sixth Semi-annual Meeting of the Polymer Meeting Study*, Polymer Processing Institute, Hoboken, NJ (1993).]

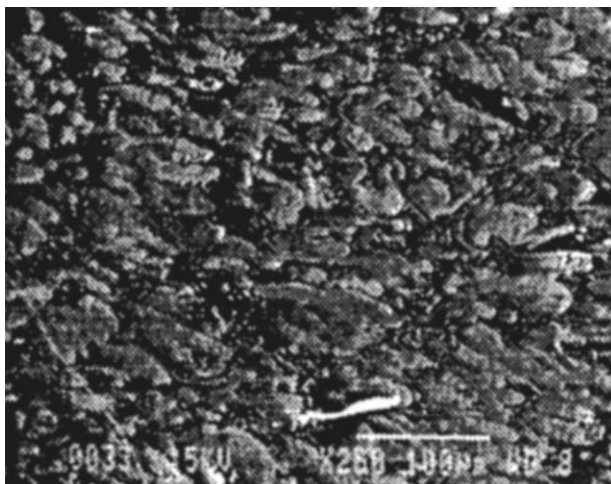


Fig. 11.45 Blend 3a morphology developed in the SSME at 180°C and 80 rpm. SEM image of the carcass. [Reprinted by permission from the *Proceedings of the Sixth Semi-annual Meeting, Polymer Mixing Study*, Polymer Processing Institute, Hoboken, NJ (1993).]

REFERENCES

1. J. A. Biesenberger and C. G. Gogos, Guest Eds., *Polymer Topics Issue on Reactive Polymer Processing*, *Polym. Eng. Sci.*, **20**, 837 (1980).
2. D. B. Todd, "Features of Extruder Reactors," in *Reactive Extrusion*, M. Xanthos, Ed., Hanser, New York, 1992, Chapter 5.
3. J. A. Biesenberger, Ed., *Devolatilization of Polymers*, Hanser, Munich, 1983.
4. J. A. Biesenberger, "Principles of Reaction Engineering," in *Reactive Extrusion*, M. Xanthos, Ed., Hanser, New York, 1992, Chapter 6.
5. J. A. Biesenberger and D. H. Sebastian, *Principles of Polymerization Engineering*, Wiley, New York, 1983.
6. D. H. Sebastian "Non-Isothermal Effects in Polymer Reaction Engineering," in *Temperature Control Principles for Process Engineers*, E. P. Dougherty, Ed., Hanser, Munich, 1993.
7. R. C. Kowalski, "Fit the Reactor to the Chemistry," in *Reactive Extrusion*, M. Xanthos, Ed., Hanser, New York, 1992.
8. N. G. Gaylord, "Reactive Extrusion in the Preparation of Carboxyl – containing Polymers and their Utilization as Compatibilizers," in *Reactive Extrusion*, M. Xanthos, Ed., Hanser, New York, 1992, Chapter 3.
9. R. C. Kowalski, "Fit the Reactor to the Chemistry," in *Reactive Extrusion*, M. Xanthos, Ed., Hanser, New York, 1992.
10. S. Datta and D. J. Lohse, *Polymeric Compatibilizers: Uses and Benefits in Polymer Blends*, Hanser, New York, 1996.
11. H. R. Brown, "Strengthening Polymer-Polymer Interfaces," in *Polymer Blends Volume 2: Performance*, D. R. Paul and G. B. Bueknall, Eds., Wiley, New York, 2000, Chapter 23.
12. L. A. Utracki, *Polymer Alloys and Blends*, Hanser, New York, 1989.
13. N. G. Gaylord, "Poly(maleic Anhydride)," *J. Macromol. Sci.-Rev. Macromol. Chem.*, **C13**(2), 235–261 (1975).
14. B. N. Epstein, U.S. Patent 4,174,538, DuPont (1979); U.S. Patent 4,172,859, DuPont (1979).

15. B. N. Epstein and R. U. Pagilagan, U.S. Patent 4,410,661, DuPont (1983).
16. R. A. Steinkamp and T. J. Grail, U.S. Patent 3,862,265, Exxon Res. and Eng. (1975): US 3,953,655, Exxon Res. and Eng. (1976).
17. N. G. Gaylord and J. Y. Koo, "Participation of Cationic Intermediates in Radical-induced Homopolymerization of Maleic Anhydride," *J. Polym. Sci. Polym Lett. Ed.*, **19**, 107–112 (1981).
18. N. G. Gaylord and R. Mehta, "Peroxide-catalyzed Grafting of Maleic Anhydride onto Molten Polyethylene in the Presence of Polar Organic Compounds," *J. Polym. Sci.: Part A: Polym. Chem.*, **26**, 1189–1198 (1988).
19. P. J. Flory, *Principles of Polymer Chemistry*, Cornell University Press, Ithaca, NY, 1953.
20. G. Odian, *Principles of Polymerization, Second Edition*, Wiley, New York, 1981.
21. R. C. Kowalski, Ph.D. Dissertation, Department of Chemical Engineering, Polytechnic Institute of Brooklyn, Brooklyn, NY, 1983.
22. J. C. Statton, J. P. Keller, R. C. Kowalski, and J. Harrison, U.S. Patent 3,551,943, Esso (1971).
23. R. C. Kowalski, U.S. Patent 3,563,972, Esso (1971).
24. J. Beauxis and R. C. Kowalski, U.S. Patent 3,593,011 Esso Res. and Eng. Co. (1971).
25. R. C. Kowalski, J. W. Starrison, J. C. Staton, and J. P. Kener, U.S. Patent 3,608,001, Esso (1971).
26. M. Xanthos, "Process Analysis from Reaction Fundamentals," in *Reactive Extrusion*, M. Xanthos, Ed., Hanser, New York, 1992.
27. A. Dreiblatt, H. Herrmann, and H. J. Nettelbrecker, "ON-line Quality Control for Improved Compounding," *Plast. Eng.*, **43**, 31–34 (1987).
28. J. Curry, S. Jackson, B. Stroehrer, and A. VanderVeen, "Free Radical Degradation of Polypropylene," *Chem. Eng. Prog.*, **84**, 43–46 (1988).
29. J. G. Andersen and M. J. Kenny, *SPE RETEC: Polyolefins VI, Tech. Papers*, Huston, TX, 1988, p.186.
30. T. Hertlein and H. G. Fritz, *Kunstst. Ger. Plast.*, **78**, 606 (1988).
31. A. Pabedinskas, W. R. Clmett, and S. T. Balke, "Process Control for Polypropylene Degradation during Reactive Extrusion," *Polym. Eng. Sci.*, **29**, 993–1003 (1989).
32. M. Dorn, "Modification of Molecular Weight and Flow Properties of Thermoplastics," *Adv. Polym. Tech.*, **5**, 82–98 (1995).
33. C. Tzoganakis, J. Vlachopoulos, and A. E. Hamielec, "Production of Controlled-rheology Polypropylene Resins by Peroxide Promoted Degradation during Extrusion," *Polym. Eng. Sci.*, **28**, 170–180 (1988).
34. Atochem, Product Bulletin, "Half-life: Peroxide Selection Based on Half-life," Buffalo, NY (1990).
35. Pennwalt Corp., Lucidal Division Product Bulletin "DialkylPeroxides," Buffalo, NY (1989).
36. D. W. Yu, Ph.D Dissertation, Department of Chemical Engineering, Stevens Institute of Technology, Hoboken, NJ 1991.
37. S. H. Ryu, C. G. Gogos, and M. Xanthos, "Kinetic Studies on the Peroxide Initiated Polypropylene Controlled Degradation," *SPE ANTEC Tech. Papers*, **35**, 879–881 (1989).
38. M. Xanthos, C. G. Gogos, and S. H. Ryu, "Kinetic Studies on the Peroxide Initiated Polypropylene Controlled Degradation," *Proc. Polym. Process Soc., Meeting*, Paper 7F, Amherst, MA, 879–882 (August 1989).
39. R. Dhavalkikar, Ph.D. Dissertation, Department of Chemical Engineering, New Jersey Institute of Technology, Newark, NJ 2002; also, R. Dhavalkikar and M. Xanthos, "Monitoring the Evolution of PET Branching through Chemorheology," *Polym. Eng. Sci.*, **44**, 474 (2004).
40. W. N. Semenov, *Some Problems in Chemical Kinetics and Reactivity*, Princeton University Press, Princeton, NJ, 1958, p. 87.

41. S. K. Dey, Ph.D Dissertation, "Reactive Extrusion of Methyl Methacrylate," Department of Chemical Engineering, Stevens Institute of Technology, Hoboken, NJ, 1987.
42. S. K. Dey and J. A. Biesenberger, "Reactive Extrusion of Methyl Methacrylate," *SPE, ANTEC Tech. Papers*, **45**, 133–135 (1987).
43. D. A. Frank-Kamenetskii, *Diffusion and Heat Exchange in Chemical Kinetics*, Princeton Univ. Press, Princeton, NJ, 1955, pp. 202–266.
44. T. Vomkarman, *Nachr. Ges. Wiss. Gottingen, Math-physic. K1* (1930).
45. Y. Lu, Ph.D. Dissertation, Department of Chemical Engineering, Stevens Institute of Technology, Hoboken, NJ, 1993.
46. Y. Lu, J. A. Biesenberger, and D. B. Todd, "A Backmix Drag-flow Reactor," *SPE. ANTEC, Tech. Papers*, **51**, 27–29 (1993); also Y. Lu, J. A. Biesenberger, and D. B. Todd, "Continuous Polymerization in a back-mixed Drag Flow reactor," *SPE. ANTEC Tech. Papers*, **52**, 113–115 (1994).
47. J. A. Biesenberger and D. B. Todd, U.S. Patent 5, 372,418 (1994).
48. J. Greci and D. B. Todd, "Effect of Conversion on Chain Addition Copolymerizations Performed in a Backmixed Drag Flow Extruder Reactor," *Int. Polym. Process.*, **15**, 147–156 (2000).
49. J. M. Ottino, C. W. Leong, H. Rising, and P. D. Swanson, "Morphological Structures Produced by Mixing in Chaotic Flows," *Nature*, **333**, 419–425 (1988).
50. J. M. Ottino, *The Kinematics of Mixing: Stretching, Chaos and Transport*, Cambridge University Press, London, 1989.
51. F. H. Ling and S. Widagdo, *Polymer Mixing Study*, Vol. 1, Polymer Processing Institute, 1991.
52. T. Brouwer, D. B. Todd, and L. P. B. M. Janssen, "Flow Characteristics of Screws and Special Mixing Enhancers in a Co-rotating Twin Screw Extruder," *Int. Polym. Process.*, **18**, 26 (2002).
53. B. Jeong and C. G. Gogos, "Reactive Extrusion of Initially Segregated Miscible Blends with a Time Reducing Striation Thickness," Submitted *Adv. Polym. Technol.* (2005).
54. T. Saito and C. W. Macosko, "Interfacial Crosslinking and Diffusion via Extensional Rheometry," *Polym. Eng. Sci.*, **42**, 1–9 (2002).
55. W. J. Schrenk and T. Alfrey, "Some Physical Properties of Multilayered Films," *Polym. Eng. Sci.*, **9**, 393–399 (1969).
56. J. Meissner and J. Hostettler, "A New Elongational Rheometer for Polymer Melts and Other Highly Viscoelastic Liquids," *Rheol. Acta*, **33**, 1–21 (1994).
57. J. Klein, D. Fletcher, and L. J. Fetters, "Dynamics of Entangled Star-branched Polymers," *Faraday Symp. Chem.*, **18**, 159–171 (1983).
58. D. R. Paul and C. B. Bucknall, Eds., *Polymer Blends Vols. I and II*, Wiley, New York, 2000.
59. S. H. Anastasiades, I. Ganantz, and J. T. Koberstein, "Compatibilizing Effect of Block Copolymers Added to the Polymer/polymer Interface," *Macromolecules*, **22**, 1449–1453 (1989).
60. W. Hu, J. T. Koberstein, J. P. Lingelser, and Y. Gallot, "Interfacial Tension Reduction in Polystyrene/Poly(dimethylsiloxane) Blends by the Addition of Poly(styrene-b-dimethylsiloxane)," *Macromolecules*, **28**, 5209–5214 (1995).
61. G. Kim and M. Libera "Microstructural Analysis of Compatibilizer Distribution in LDPE/PS Blends with SIS," *Proceed. Eleventh Semi-annual Polymer Mixing Study*, Polymer Processing Institute, Hoboken, NJ, 1996.
62. C. W. Macosko, P. Gueram, A. K. Khandpur, A. Nakayama, and P. Marechal, "Compatibilizers for Melt Blending: Premade Block Copolymers," *Macromolecules*, **29**, 5590–5598 (1996).
63. C. E. Scott and C. W. Macosko, "Morphology Development during the Initial Stages of Polymer-polymer Blending," *Polymer*, **36**, 461–470, (1995).

64. C. E. Scott and C. W. Macosko, "Model Experiments Concerning Morphology Development during the Initial Stages of Polymer Blending," *Polym. Bull.*, **26**, 341–348 (1991).
65. M. Marič and C. W. Macosko, "Improving Polymer Blend Dispersion in Mini-mixers," *Polym. Eng. Sci.*, **41**, 118–130 (2001).
66. E. Helfand and Y. Tagami, "Theory of the Interface between Immiscible Polymers. II," *J. Chem. Phys.*, **56**, 3592 (1972).
67. J. Noolandi and K. M. Hong, "Interfacial Properties of Immiscible Homopolymer Blends in the Presence of Block Copolymers," *Macromolecules*, **15**, 482–492 (1982).
68. J. Brandrup and E. H. Immergut, Eds., *Polymer Handbook*, Third Edition, Wiley, New York, 1985.
69. L. J. Fetters, D. J. Lohse, D. Richter, T. A. Witten, and A. Zirkel, "Connection between Polymer Molecular Weight, Density, Chain Dimensions, and Melt Viscoelastic Properties," *Macromolecules*, **27**, 4639–4647 (1994).
70. M. Marič, N. Ashuror, and C. W. Macosko, "Reactive Blending of Poly-(dimethylsiloxane) with Nylon 6 and Poly(styrene): Effect of Reactivity on Morphology," *Polym. Eng. Sci.*, **41**, 631–642 (2001).
71. L. Mascia, *The Role of Additives in Plastics*, Edward Arnold, London, 1972.
72. L. Mascia and M. Xanthos, "An Overview of Additives and Modifiers for Polymer Blends: Facts, Deductions, and Uncertainties," *Adv. Polym. Technol.*, **11**, 237–248 (1992).
73. M. Xanthos, "The Physical and Chemical Nature of Plastics Additives," in *Mixing and Compounding of Polymers*, I. Manas-Zloczower and Z. Tadmor Eds. Hanser, Munich, 1994.
74. M. Xanthos *Functional Fillers for Plastics*, Wiley-VCH, New York, 2005.
75. V. M. Lobe and J. L. White, "An Experimental Study of the Influence of Carbon Black on the Rheological Properties of a Polystyrene Melt," *Polym. Eng. Sci.*, **19**, 617–624 (1979).
76. D. M. Bigg, "Rheological Behavior of Highly Filled Polymer Melts," *Polym. Eng. Sci.*, **23**, 206–210 (1983).
77. T. B. Lewis and L. E. Nielsen, "Viscosity of Dispersed and Aggregated Suspensions of Spheres," *Trans. Soc. Rheol.*, **12**, 421–443 (1968).
78. I. L. Rutgers, *Rheol. Acta.*, **2**, 202, (1962); also, I. L. Rutgers, *Rheol. Acta.*, **2**, 305, (1962).
79. D. G. Thomas, "Transport Characteristics of Suspension: VIII. A Note on the Viscosity of Newtonian Suspensions of Uniform Spherical Particles," *J. Colloid Sci.*, **20**, 267–277 (1965).
80. N. A. Frankel and A. Acrivos, "On the Viscosity of a Concentrated Suspension of Solid Spheres," *Chem. Eng. Sci.*, **22**, 847–853 (1967).
81. Y. Bomal and P. Goddard, "Melt Viscosity of Calcium-carbonate-filled Low Density Polyethylene: Influence of Matrix-filler and Particle-particle Interactions," *Polym. Eng. Sci.*, **36**, 237–243 (1996).
82. G. Wypych, "Effects of Fillers on Rheological Properties of Filled Materials," in *Handbook of Fillers, Second Edition*, Plastic Design Library, Toronto, Canada, 1999, Chapter 9.
83. C. D. Han, *Multiphase Flow in Polymer Processing*, Academic Press, New York, 1981.
84. C. D. Han, T. Van-den Weghe, P. Shete, and J. R. Haw, "Effects of Coupling Agents on the Rheological Properties, Processability, and Mechanical Properties of Filled Polypropylene," *Polym. Eng. Sci.*, **21**, 196–204 (1981).
85. Y. Iso, D. L. Kuch, and C. Cohen, "Orientation in Simple Shear Flow of Semi-dilute Fiber Suspensions 1. Weakly Elastic Fluids," *J. Non-Newt. Fluid Mech.*, **62**, 115–134 (1996).
86. L. G. Leal, "The Motion of Small Particles in Non-Newtonian Fluids," *J. Non-Newt. Fluid Mech.*, **5**, 33–78 (1979).
87. A. T. Mutel, Ph.D. Thesis, Department of Chemical Engineering, McGill University, Montreal, Canada, 1989.

88. H. M. Laun, "Orientation Effects and Rheology of Short Glass Fiber-reinforced Thermoplastics," *Colloid Polym. Sci.*, **262**, 257–269 (1984).
89. A. T. Mutel and M. R. Kamal "Rheological Properties of Fiber-reinforced Polymer Melts," in *Two-phase Polymer Systems*, L. A. Utracki, Ed., Hanser, New York, 1991.
90. R. G. Larson, *The Structure and Rheology of Complex Fluids*, Oxford University Press, Oxford, 1999.
91. P. Yaras, U. Yilmazer, and D. M. Kalyon, "Ustable Flow of Concentrated Suspensions in Tube Flow," *SPE ANTEC Tech. Papers*, **39**, 2604–2606 (1993); also B. Aral and D. M. Kalyon, "Time-dependent Development of Wall Slip in Shear Flows of Concentrated Suspensions," *SPE ANTEC Tech. Papers*, **39**, 2607–2610 (1993).
92. D. B. Todd, "Introduction to Compounding," in *Plastics Compounding*, D. B. Todd, Ed., Hanser, Munich, 1998.
93. D. B. Todd and D. K. Baumann, "Twin Screw Reinforced Plastics Compounding," *Polym. Eng. Sci.*, **18**, 321–325 (1978).
94. G. Wypych, *Handbook of Fillers, Second Edition*, Plastics Design Library, 1999.
95. M. Kim and C. G. Gogos, "The Roles of Clay and PE Wax Lubricants on the Evolution of Melting in PP Powder and Pellets," *Proc., 11th Polymer Mixing Study Meeting*, Polymer Processing Institute, Hoboken, NJ (1995).
96. Y. Suetsugu, "State of Dispersion – Mechanical Properties Correlation in Small Particle Filled Polymer composites," *Int. Polym. Process.*, **5**, 184–190 (1990).
97. I. Manas-Zloczower, A. Nir, and Z. Tadmor, "Dispersive Mixing in Internal Mixers—A Theoretical Model Based on Agglomerate Rupture," *Rubber Chem. Technol.* **55**, 1250–1285 (1982); also, I. Manas-Zloczower, I. Nir, and Z. Tadmor, "Dispersive Mixing in Roll-mills," *Polym. Compos.*, **6**, 222 (1985).
98. I. Manas-Zloczower and Z. Tadmor, "Scale-up of Internal Mixers," *Rubber Chem. Technol.*, **57**, 49–54 (1984).
99. V. Collin and E. Peuvrel-Disdier, "Disperion Mechanisms of Carbon Black in an Elastomer Matrix," *Elastomery*, Vol. 9 (2005) Special Edition JSSN PL 1427-3519; see also V. Collin and E. Peuvrel-Disdier, presentation at the Conference of European Rubber Research "Practical Improvements of Mixing Processer," Paterborn, Germany, January 25-26 (2005), pp. 219–241
100. I. Manas-Zloczower and Z. Tadmor, "The Distribution of Number of Passes over the Flights in Single Screw Melt Extruders," *Adv. Plasti. Technol.*, **3**, 213–221 (1983).
101. Z. Tadmor, "Screw Elements Having Shearing and Scraping Devices" U.S. Patent 5,356,208, October 18, 1994; also, Z. Tadmor, "Machine Invention, Innovation and Elementary Steps," *Adv. Polym. Technol.*, **21**, 87–97, 2002.
102. E. L. Canedo and L. N. Valsamis, "Modeling Mixing in Continuous Mixers," *SPE ANTEC Tech. Papers*, **35**, 116 (1989).
103. R. Turkovich and L. Erwin, "Fiber Fracture in Reinforced Thermoplastic Processing," *Polym. Eng. Sci.*, **23**, 743–749 (1983).
104. Y. Suetsugu, "The Effect of Mixing on Some Properties of Compounds and Composites," in *Mixing and Compounding of Polymers*, I. Manas-Zloczower and Z. Tadmor, Eds., Hanser, Munich, 1994.
105. C. G. Gogos, C. K. Yoon, and J. Brizzolara, "Injection Molding Process Development for Long Fiber Reinforced Thermoplastics," *SPE ANTEC Tech. Papers*, **40**, 384 (1994).
106. C. Rauwendaal, "Mixing in Single Screw Extruders," in *Mixing and Compounding of Polymers*, I. Manas-Zloczower and Z. Tadmor, Eds., Hanser, Munich, 1994.
107. C. Rauwendaal, "Mixing in Reciprocating Extruders," in *Mixing and Compounding of Polymers*, I. Manas-Zloczower and Z. Tadmor, Eds., Hanser, Munich, 1994.

108. R. Brzowski, T. Kumazawa, and J. L. White, "A Model of Flow in the Mixing Section of the List KoKneader," *Int. Polym. Process.*, **6**, 136 (1991).
109. P. G. Andersen, "Mixing Practices in Corotating Twin Screw Extruders," in *Mixing and Compounding of Polymers*, I. Manas-Zloczower and Z. Tadmor, Eds., Hanser, Munich, 1994.
110. A. Kiani and H. J. Samann, "Transient Flow Calculation of Co-rotating Twin Screw Extruders," *SPE ANTEC Tech. Papers*, **39**, 2758–2762 (1993).
111. V. L. Bravo, A. N. Hrymak, and J. D. Wright, "Numerical Simulation of Pressure and Velocity Profiles in Kneading Elements of a Co-rotating Twin Screw Extruder," *Polym. Eng. Sci.*, **40**, 525–541 (2000).
112. A. F. Yee, "Mechanical Properties of Mixtures of Two Compatible Polymers," *Polym. Eng. Sci.*, **17**, 213–219 (1977).
113. B. D. Favis, "Factors Influencing the Morphology of Immiscible Polymer Blends in melt Processing," in *Polymer Blends*, Vol. I, D. R. Paul and C. B. Bucknall, Eds., Wiley-Interscience, New York, 1999.
114. D. R. Paul and J. W. Barlow, "Polymer Blends (or Alloys)," *J. Macromol. Sci., Rev. Macromol. Chem.*, **C18**, 109–168 (1980).
115. G. N. Avgeropoulos, F. C. Weissert, P. H. Biddisow, and G. G. A. Böhm, "Heterogeneous Blends of Polymers. Rheology and Morphology," *Rubber Chem. Technol.*, **49**, 93–104 (1976).
116. L. A. Utracki, "On the Viscosity-concentration Dependence of Immiscible Polymer Blends," *J. Rheol.*, **35**, 1615–1637 (1991).
117. J. M. H. Janssen and H. E. H. Meijer, "Dynamics of Liquid-liquid Mixing: A 2-zone Model," *Polym. Eng. Sci.* **35**, 1766–1780 (1995).
118. D. B. Todd, C. G. Gogos, and D. N. Charalambopoulos, U.S. Patent 5,708, 197 (1998).
119. C. G. Gogos, M. Esseghir, B. David, D. B. Todd, and D. H. Sebastian, "The Mixing Element Evaluator," *SPE ANTEC Tech. Papers*, **39**, 1542–1545 (1993).
120. C. G. Gogos, M. Esseghir, D.W. Yu, D. B. Todd, and J. E. Curry, "The Twin-screw Mixing Element Evaluator: On-line Performance Evaluation of Modular Twin-Screw Mixing Elements," *SPE ANTEC Tech. Papers*, **40**, 270–276 (1994).
121. M. Esseghir, D.W. Yu, and C. G. Gogos "Rheology-driven Mixing Mechanisms in TSMEE Kneading Blocks," *SPE ANTEC Tech. Papers*, **41**, 1994 (1995).
122. N. Tokita, "Analysis of Morphology Formation in Elastomer Blends," *Rubber Chem. Technol.*, **50**, 292–300 (1977).
123. C. W. Macosko, P. Guégan, A. K. Khandpur, A. Nakayama, P. Marechal, and T. Inoue, "Compatibilizers for Melt Blending: Premade Block Copolymers," *Macromolecules*, **29**, 5590–5598 (1996).
124. M. L. Williams, R. F. Landel, and J. D. Ferry, "The Temperature Dependence of Relaxation Mechanisms in Amorphous Polymers and Other Glass-forming Liquids," *J. Am. Chem. Soc.*, **77**, 3701–3707 (1955).
125. B. Qian, D. B. Todd, and C. G. Gogos, "Plastic Energy Dissipation and Its Role on Heating/melting of Single-component Polymers and Multi-component Polymer Blends," *Adv. Polym. Technol.*, **22**, 85–95 (2003).
126. M. Esseghir and D. W. Yu, *Proc. 4th Semi-annual Meet. of the Polymer Mixing Study*, Polymer Processing Institute, Hoboken, August 1992.

PROBLEMS

11.1 Complete POX Decomposition Requirements at Various Temperatures If we define, functionally, complete POX decomposition to be after a reaction time, t_f , at

constant reaction temperature, when the POX concentration $C(t_f) \cong 4 \times 10^{-2}[C_0]$. (a) Calculate t_f for POXs B and E on Fig. 11.3 at 180° and 240°C. (b) Calculate t_f for POX B in a dilute solution of decane in a reaction vessel, where the temperature is increased at the following rate: $T(t) = 180 + At$, where $A = 2 \times 10^{-1} [^{\circ}\text{C} \cdot \text{s}^{-1}]$. Use the reported $t_{1/2}$ activation energy.

11.2 Rate-Controlling Phenomena in Reactive Processing Figure 11.4 indicates that the rate of decomposition in dodecane at 180°C of a commonly used POX in PP viscracking, Lupersol 101 is very close to the rate of decrease of the torque of a PP melt mixed with this POX in a laboratory scale Brabender internal laminar mixer. The reduction of the Brabender rotor torque is related to the reduction of the effective melt viscosity, due to the reduction of \bar{M}_w and narrowing of the MWD, both consequences of the *controlled rheology polypropylene* (CR-PP) or viscracking reaction. (a) The text states that this similarity in the reduction rates of the POX concentration in dodecane and torque in the Bradender indicates that the POX decomposition kinetics is *rate controlling* the CR-PP reaction. What is meant by this statement? (b) In view of the kinetics of decomposition presented for the three POXs on Fig. 11.3, and keeping in mind their constant decomposition activation energy, would you expect POX decomposition to be *rate controlling* with the PP-Lupersol 101 reaction carried out at 240°C? If not, what would be the most probable rate-controlling process? What would be the effect of increasing the rotor speed? (c) At the POX concentration levels used with the reaction depicted on Fig. 11.4, what would you expect the order of magnitude of (t_G/t_R) , Eqs. 11.2-5 and 11.2-6 to be?

11.3 Physical Significance and Reactive Processing Consequences of Process Characteristic Time Ratios A number of reactive processing characteristic times were presented in Sections 11.2–11.4. Following Biesenberger and Sebastian (5) and Sebastian (6), our discussion of reactive processing utilizes considerations of the physical significance of *ratios* of competing process characteristic times of processes involved in reactive polymer processing. Discuss the following ratios of characteristic times; in particular on how and why their order-of-magnitude values determine the rate-controlling processes in reactive processing, as well as how they affect process stability: (a) t_G/t_R or $t_G/(t_R + t_H)$ (b) $Da = t_{\text{res}}/t_r$ (c) t_D/t_r (d) t_D/t_{res} (e) t_D/t_{mix}

11.4 Advantages and Limitations of Polymer Processing Equipment as Polymer System “Reactors” Consider the following reacting systems involving polymers. Conduct the necessary literature⁶ searches on the reaction mechanisms, kinetics, and heats of reaction for each system and discuss it as a candidate to be carried in polymer processing equipment, considering both batch and continuous processors. (a) Polymerization of methylmethacrylate monomer into high MW PMMA. (b) Polymerization of PMMA prepolymer into high MW PMMA. (c) Condensation polymerization of PET. (d) Halogenation (both chlorination and bromination) of polyolefins. (e) Grafting of AA onto PE or PP.

6. An excellent source of references on reactions carried out in polymer processing equipment is S. B. Brown, “Reactive Extrusion: A Survey of Chemical Reaction of Monomers and Polymers, during Extrusion Processing,” in *Reactive Processing*, M. Xanthos, Ed., Hanser, Munich, 1992.

- 11.5 *Carrying out Controlled Rheology Polypropylene (CR-PP) Viscracking Reactions in Single Screw and Twin Screw Extruders*** Historically the early CR-PP reactions were carried in SSEs with the POX mixed into the feed PP reactor granules or in a smaller-scale reactive extrusion process by mixing PP-POX masterbatch pellets with PP pellets. Currently, this process is carried out, almost exclusively, in TSEs and most often by coating the PP particulates with the required amount of POX. You are asked to: (a) Discuss the differences in carrying out the CR-PP reaction in SSEs and Co-TSE, from the points of view of the different melting and mixing mechanisms in each. (b) Which of the preceding “reactors” will yield lower \bar{M}_w and narrower MWD viscracked PP product? Why? (c) If the POX were to be introduced in both extruders as a separate reactant stream *after* melting, which of the two will yield a lower \bar{M}_w and narrower MWD? Will the difference become larger or small at higher melt temperatures? Why?
- 11.6 *Estimation of the Effective Diffusivity of POX in PP Melts*** Ryu et al. (37), as discussed in Section 11.1, coated 200–300 μm diameter PP granules with POX, compressed them to prepare thin films and used the films to carry out CR-PP reactions by placing them in a constant-temperature oven, withdrawing the samples after specified reaction times, and obtaining \bar{M}_w and MWD; POX “E,” (see Fig. 11.3) was used. They found no measurable macromolecular structure changes after reaction times of (6–7) $t_{1/2}$ of POX “E.” They concluded that the process of diffusion of POX “E” into the PP melt was not rate controlling. (a) What is the basis for this conclusion? (b) Can one obtain an estimate of the effective diffusivity of POX “E” in the PP melt by specifying the order of magnitude of the ratio of diffusion to reaction characteristics times (t_D/t_r)?
- 11.7 *Effect of Compositional Nonuniformities on the “Unifying” Ability of Characteristic Time Ratios to Analyze the Dynamic State of Reactions*** Figure 11.10, plotting the dimensionless initial reactant concentration as a function of the Damkohler number, $Da = t_{res}/t_r$ for both batch and continuous reactors. This analysis assumes a well-mixed reacting system. (a) What will the effects of poor mixing be and how will they influence this analysis? (b) What is the maximum allowable striation thickness between the reacting species for the system to be considered well mixed?
- 11.8 *Physicochemical Mechanisms Responsible for the Beneficial Actions of Polymer Additives*** Tables 11.2–11.4 list examples of common polymer additives by their beneficial action(s) to the polymers during processing and products during their product life.
1. You are invited to search for and examine the physicochemical mechanisms responsible for such beneficial actions for the following additives: (a) Sterically hindered phenol antioxidants; (b) Carbon black, as a light stabilizer (e.g., rubber tires); (c) Carbon black, as an electrically conductive additive; (d) Silanes, as glass fiber–coating adhesion promoter with thermosets and thermoplastic reinforced systems; (e) Quaternary ammonium salts as antistatic agents; (f) Azodicarbonamide as a chemical blowing agent; (g) CO_2 as a physical blowing agent; (h) Hydrocarbons as physical blowing agents (e.g., LDPE foams)

2. Are there critical maximum distances between adjacent dispersed additive sites, above which the additives are not effective? Discuss, with example(s).

11.9 *Modeling Melt-Full Kneading Elements by the Two-Zone Theoretical Model* The two-zone model to treat dispersive mixing was developed by Manas-Zloczower et al.⁷ for internal batch mixers. An example of this work is presented in this chapter, Example 11.3 and, as extended to the continuous SSE, viewed as a dispersive mixer, in Example 11.4. You are invited to consider the melt-full, kneading elements, Fig. 10.11, from a two-zone dispersive mixer point of view. Comment on the gradual and cyclical reduction/extension of the available cross-sectional area between a pair of opposing kneading disks and the barrel.

11.10 *Fiber Length Attrition during the Single Screw Extrusion of PE Pellets Mixed with 3.2-mm Chopped Glass Fibers* Figure 11.28 presents experimental results of von Turkovich and Erwin (103) on the fiber number average length attrition along the single screw in the downstream direction of solids conveying, compression, melting, and metering/mixing sections. (a) What analytical procedures can be used to measure the number average fiber length using the SSE carcass along the screw length? (b) Comment on the observed results, that is, what fiber breaking phenomena are at play at each section? (c) Would you expect different results in a larger SSE, say a 4-in-diameter, where the channel dimensions are an order of magnitude larger than the fiber and pellet dimensions? (d) Will the glass-fiber attrition rate be different if they were coated with a silane compound?

7. *Rubber Chem. Technol.*, **55**, 1250–1285 (1982); *Polym. Compos.*, **6**, 222 (1985).

12 Die Forming

- 12.1 Capillary Flow, 680
- 12.2 Elastic Effects in Capillary Flows, 689
- 12.3 Sheet Forming and Film Casting, 705
- 12.4 Tube, Blown Film and Parison Forming, 720
- 12.5 Wire Coating, 727
- 12.6 Profile Extrusion, 731

Dies, as used in polymer processing, are metal flow channels or restrictions that serve the purpose of imparting a specific *cross-sectional shape* to a stream of polymer melt that flows through them. They are primarily used in the extrusion process to *continuously* form polymer products such as tubes, films, sheets, fibers, and “profiles” of complex cross-sectional shapes. Dies are positioned at the exit end of the melt-generating or -conveying equipment and, generally speaking, consist of three functional and geometrical regions:

1. The *die manifold*, which serves to distribute the incoming polymer melt stream over a cross-sectional area similar to that of the final product but different from that of the exit of the melt conveying equipment.
2. The *approach channel*, which streamlines the melt into the final die opening.
3. The *die lip*, or final die opening area, which is designed to give the proper cross-sectional shape to the product and to allow the melt to “forget” the generally nonuniform flow experience in regions 1 and 2.

Figure 12.1 shows these regions schematically for a sheet-forming die. The shape of both the manifold and approach channels may vary in the cross-die x direction, to permit achievement of the design goals just outlined, that is, melt distribution and delivery to the die lips area at uniform pressure. Minor adjustments of the die-lip opening are often required to correct for temperature gradients along the die, as well as bending of the die under the applied pressure.

The engineering objectives of die design are to achieve the desired shape within set limits of dimensional *uniformity* and at the *highest possible production rate*. This chapter discusses both objectives, but the question of die-formed product uniformity deserves immediate amplification. To understand the problem, we must distinguish between two types of die-formed product nonuniformity: (a) nonuniformity of product in the machine direction, direction z [Fig. 12.2(a)], and (b) nonuniformity of product in the cross-machine direction, direction x [Fig. 12.2(b)]. These dimensional nonuniformities generally originate from entirely different sources. The main source of the former is the variation

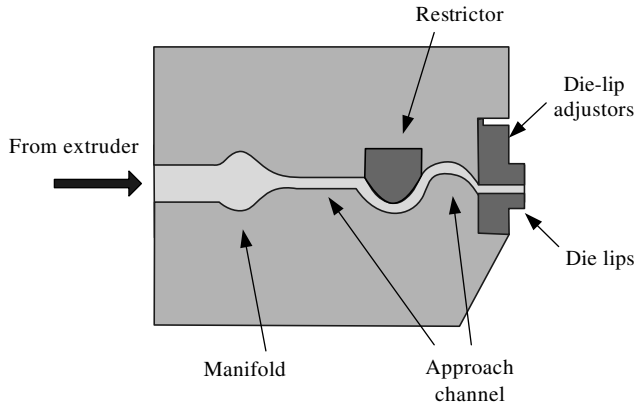


Fig. 12.1 Schematic representation of a sheet die, including manifold, approach channel, and die lip regions. The restrictor bar is incorporated so that the die can be used with different polymers of varying viscosities.

over time of the inlet stream temperature, pressure, and composition (when mixtures are extruded through the die). The latter is generally due to improper die design. From the discussion on residence time distribution (RTD) in Chapter 7 it is evident that the capability of eliminating inlet concentration variations depends on the RTD function. A

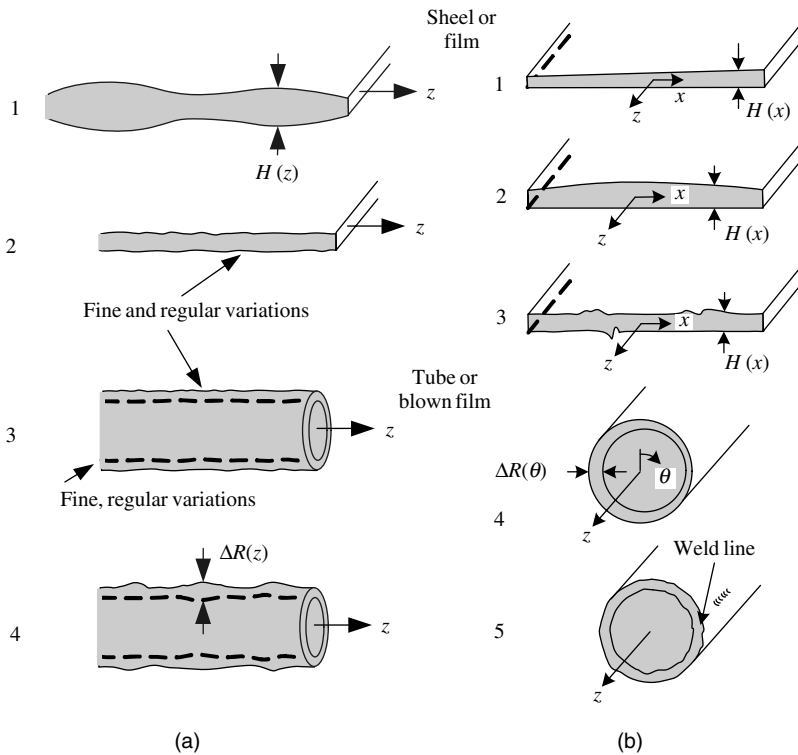


Fig. 12.2 Die-formed product nonuniformities in (a) the machine direction, and (b) the cross-machine direction.

step change in inlet concentration in the plug-flow system will be reflected unchanged at the exit. Back-mixing will reduce outlet concentration variation. Therefore, narrow RTD functions, as in pressure-type flow dies, cannot be expected to eliminate concentration or temperature variation by mixing. Hence, we must ensure adequate inlet uniformity in time, of both temperature and pressure. These depend on the melt generating and conveying equipment preceding the die. In terms of the extrusion operation, improper solids conveying, solid bed breakup, incomplete melting, inefficient mixing due to deep metering channels (all for set extrusion conditions), or the absence of a mixing or barrier device, may result in a *time variation* of the pressure and temperature of the melt being delivered to the die; this will certainly cause machine direction non-uniformities. Figure 12.3 gives examples of acceptable and unacceptable temperature and die inlet pressure variations for a melt stream of low density polyethylene (LDPE). The level of variations that can be tolerated depends on both the product specifications and the temperature sensitivity of the viscous and elastic responses of the melt.

It is also worth noting in Fig. 12.3 that the two engineering objectives of die forming—namely, uniformity of product and maximum throughput rate—are competing ones. That is, a high throughput rate can be achieved at the expense, in general, of machine direction product uniformity, at set processing conditions. Additionally, there exists an intrinsic upper limit in the throughput rate set by the phenomenon of melt fracture, observed with all polymer melts and discussed in Section 12.2.

Machine direction product nonuniformities always accompany melt fracture, and this is why the phenomenon marks the throughput upper limit to die forming. These nonuniformities can be intense or mild, depending on the die *streamlining*, but they are always high frequency disturbances in the product thickness. Other causes for machine

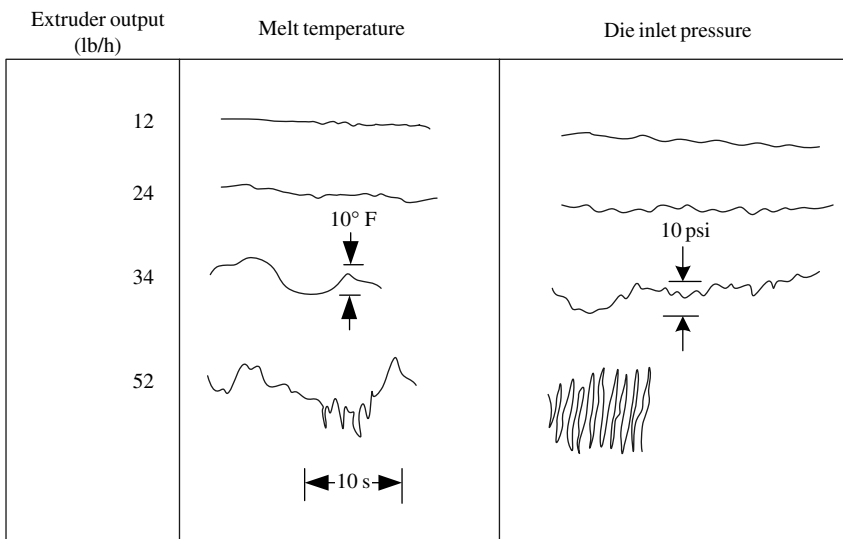


Fig. 12.3 Types of actual melt temperature and die inlet pressure variations obtained with LDPE. The last two would result in product nonuniformities in the machine direction. [Reprinted by permission from H. B. Kessler, R. M. Bonner, P. H. Squires, and C. F. Wolf, *Soc. Plast. Eng. J.*, **16**, 267 (1960).]

direction nonuniformities can be found in the die design that creates stagnation areas where the melt gets trapped and periodically surges forward, and in the post-die forming, cooling, and stretching operations, which may vary with time or may be subject to periodic instabilities.

Product nonuniformities in the cross-machine direction are, as just pointed out, due to *poor die design* or are intrinsic to particular types of dies. Any number of die-related causes can be responsible for the types of nonuniformities in Fig. 12.2(b): inappropriate design of any one of the three die regions [Fig. 12.2(b) 1–4], inadequate temperature control of the die walls [Fig. 12.2(b), 1, 2, 4]; bending of the die walls by the flow pressure [Fig. 12.2(b), 2], and finally the presence of obstacles in the flow channels for die-support purposes [Fig. 12.2(b), 5].

In principle, all types of cross-machine direction nonuniformities can be remedied by proper die design, which can be achieved in part through the development of *die design equations*, which form the mathematical model of the die flow. This chapter discusses the origin, form, and limitations of such models as they apply to dies of various types.

Before getting to that, however, we examine in detail the flow of polymer melts in capillaries. There are two reasons for revisiting capillary flow, after having discussed it in Chapter 3. First, capillary flow is characterized by all the essential problems found in any die forming flow: flow in the entrance, fully developed, and exit regions; therefore, the conclusions reached from the study of capillary flow can, and will be, generalized for all pressure flows. Second, capillary flow has been more widely studied by both rheologists and engineers than any other flow configuration. We pay particular attention to the problems of entrance pressure drop, viscous heat generation, extrudate swelling, and extrudate melt fracture.

Finally, in discussing die flow models, we take into account the results presented in connection with capillary flow, but we also look at the details of the flow in each particular die. Die flow models should provide quantitative answers to questions of the following type: (a) if a tube of given dimensions, uniform in the cross-machine direction, is to be extruded at a given rate and with a specific polymer, what should the die design (or designs) be, and what would the resulting pressure drop be? (b) How do the design and pressure drop depend on the processing variables and melt rheology?

12.1 CAPILLARY FLOW

Figure 12.4 depicts schematically the experimental setup used in capillary flow studies. The primary application of the discussion that follows is in capillary viscometry, which is useful to die design. The ratio R_r/R should be greater than 10, so that the pressure drop due to the flow in the reservoir can be neglected.¹ The reservoir radius cannot be too large, though, because the time required for uniform heating of the solid polymer load would be too long (see Fig. 5.6). Long heating cannot be used for sensitive polymers such as polyvinyl chloride (PVC), which readily degrade thermally.

It is useful at this point to consider the “polymer melt experience” as it flows from the reservoir into, through, and out of the capillary tube. In the entrance region shown in

1. In careful viscometric studies, this pressure drop is never neglected; the pressure reading at zero reservoir height, as found by extrapolation, is used for the value of P_0 .

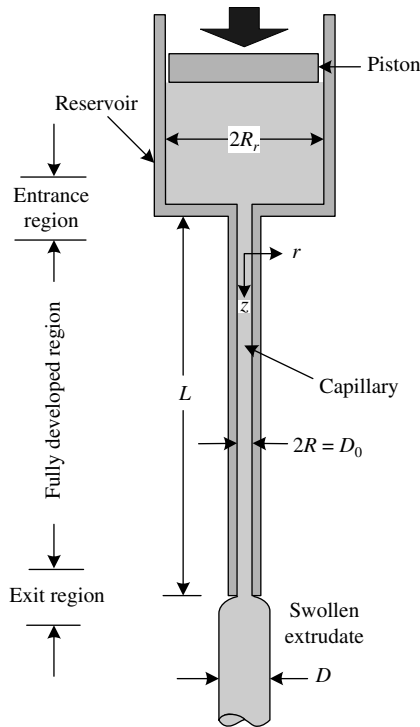


Fig. 12.4 Experimental setup for capillary flow showing reservoir, entrance, fully developed, and exit regions.

Fig. 12.4, the melt is forced into a converging flow pattern and undergoes a large axial acceleration, that is, it stretches. As the flow rate is increased, the axial acceleration also increases, and as a result the polymer melt exhibits stronger elastic response, with the possibility of rupturing, much like “silly putty” would, when stretched fast. Barring any such instability phenomena, a fully developed velocity profile is reached a few diameters after the geometrical entrance to the capillary.

The flow in the capillary, which for pseudoplastic fluids is characterized by a rather “flat” velocity profile, imparts a shear strain on the melt near the capillary walls. The core of the melt, if the capillary L/R is large and the flow rate is small, can undergo a partial strain recovery process *during* its residence in the capillary. At the exit region, the melt finds itself under the influence of no externally applied stresses. It can thus undergo delayed strain recovery, which, together with the velocity profile rearrangement to one that is pluglike in the exit region, results in the phenomenon of extrudate swelling.

The “polymer melt experience” briefly described above is complex and varied; it involves steady, accelerating, fully developed, and exit flows and strain recovery. It is not surprising, then, that this apparently simple experiment is used to study not only the viscous but also the elastic nature of polymer melts.

Entrance and Exit Capillary Pressure Losses; the Bagley Correction

In the fully developed flow region, the assumptions of steady and isothermal flow, constant fluid density, and independence of the pressure from the radius, resulted in the conclusion

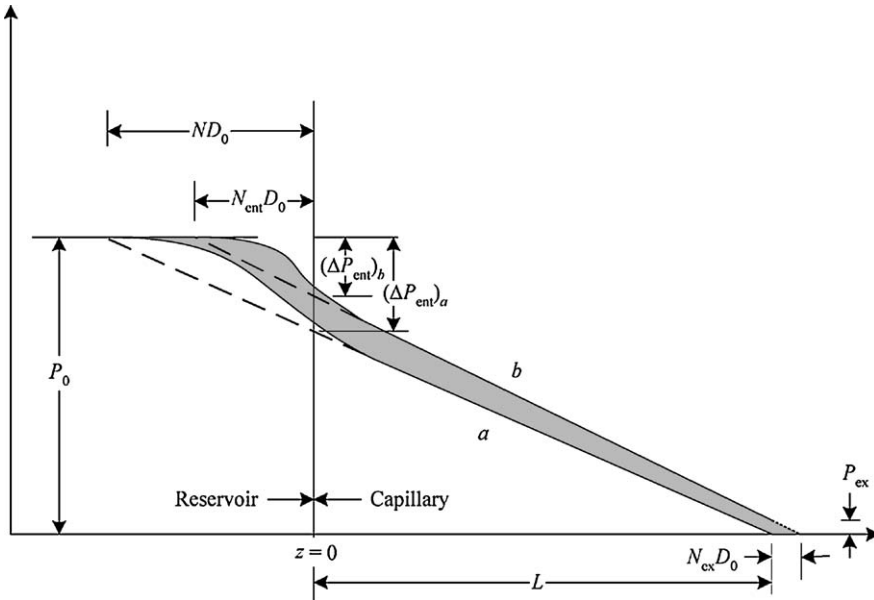


Fig. 12.5 Schematic representation of the capillary pressure along its axis: Curve *a*, without P_{ex} ; Curve *b*, in the presence of P_{ex} .

that $-dp/dz = \Delta P/L$. This conclusion is obviously not correct near the capillary entrance where, because of the converging flow, extra velocities (v_r) and velocity gradients (dv_z/dz , dv_r/dr , etc.) are present. Although the flow pattern is not known precisely, we know that a higher pressure drop is needed to support the additional velocity gradients for any viscous or viscoelastic fluid. Schematically, then, the pressure profile can be represented as in Fig. 12.5 (Curve *a*). Thus, $-dp/dz = \Delta P/L^* = \Delta P/(L + ND_0)$, where $N > 0$ is the entrance loss correction factor that must be evaluated experimentally. The entrance, or Bagley correction (1), N must be considered in the calculation of the shear stress at the wall

$$\tau_w^* = \frac{(P_0 - P_L)D_0}{4L^*} = \frac{D_0}{4} \left(\frac{\Delta P}{L + ND_0} \right) \tag{12.1-1}$$

where τ_w^* is the corrected shear stress at the wall for fully developed flow. The stress at the capillary wall is given by

$$\tau_w^* = -\eta \dot{\gamma}_{12}(R) = \eta \dot{\gamma}_w^* \tag{12.1-2}$$

From the Rabinowitsch equation E3.1-10, $\dot{\gamma}_w^*$ is given by

$$\dot{\gamma}_w^* = \frac{3}{4}\Gamma + \frac{\tau_w^*}{4} \frac{d\Gamma}{d\tau_w^*} \tag{12.1-3}$$

where $\Gamma = 32Q/\pi D_0^3$. Combining the equations for $\dot{\gamma}_w^*$ and τ_w^* , we see that $\tau_w^* = g(\Gamma)$.

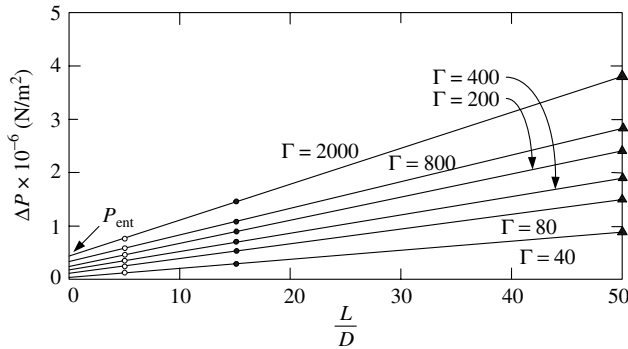


Fig. 12.6 Bagley plots for a polystyrene (PS) melt at 200°C, from which $N(\Gamma)$ can be evaluated; ΔP at $L/D_0 \rightarrow 0$ is the entrance pressure drop ΔP . [Reprinted by permission from J. L. White, *Appl. Polym. Symp.*, No. 20, 155 (1973).]

Equation 12.1-1 can be rearranged as follows:

$$\frac{L}{D_0} = -N + \frac{\Delta P}{4g(\Gamma)} \quad (12.1-4)$$

where $g(\Gamma)$ is a function of the Newtonian shear rate at the wall. Equation 12.1-4 forms the basis of the so-called Bagley plots (1) (Fig. 12.6) through which $N(\Gamma)$ is evaluated graphically and the corrected wall shear stresses are determined using Eq. 12.1-1. Experimental evidence indicates that the P versus L/D_0 curves at constant Γ are not straight, but curve upward at high L/D_0 values. This phenomenon has been attributed in the literature both to the relaxation of normal stresses (2), and probably, to a large extent, to the effect of the hydrostatic pressure on melt viscosity (3–5), which can be expressed as

$$\mu(P) = \mu(P_0) \exp[\beta(P - P_0)] \quad (12.1-5)$$

where β is related to polymer melt compressibility and is of the order of $5 \times 10^{-9} \text{ (N/m}^2\text{)}^{-1}$. It should be emphasized that, although the preceding treatment may give better values for the fully developed region, the same is not true for its entrance region, where the actual τ_w^* values are large. Despite the previously mentioned experimental facts, the Bagley correction $N(\Gamma)$ is *functionally useful* in that it eliminates the effect of L/D_0 from the capillary flow curves. Problem 12.1(b) indicates the error involved in neglecting ΔP_{ent} with various L/D_0 capillaries.

Also worth noting in connection with the foregoing discussion is the experimental observation of a nonzero gauge pressure at the capillary exit P_{ex} (Curve *b* of Fig. 12.5). Thus one must take into consideration end corrections, both entrance and exit, and not only entrance corrections alone, as was done by Bagley. Sakiades (6) was the first to report the existence of P_{ex} for polymer solutions, and Han and his co-workers have studied it extensively using polymer melts (7–9). It has been found that $P_{\text{ex}}/\Delta P_{\text{ent}}$ is between 0.15 and 0.20, and that, although ΔP_{ent} does not depend on L/D_0 , P_{ex} decreases up to $L/D_0 = 10$, then remains constant (9).

With these observations in mind (see Curve *b*, Fig. 12.5), we can rewrite Eq. 12.1-1

$$\tau_w^* = \frac{\Delta P D_0}{4L^*} = \frac{D_0}{4} \left(\frac{\Delta P}{L + N_{\text{ent}} D_0 + N_{\text{ex}} D_0} \right) \quad (12.1-6)$$

where N_{ent} is the entrance capillary length correction and N_{ex} the exit capillary length correction. If $(P_{\text{ex}}/\Delta P_{\text{ent}}) \ll 1$, then $N = N_{\text{ent}}$; if P_{ex} is included, it is found that $N_{\text{ent}} < N$. Problem 12.2 indicates that, for high density polyethylene (HDPE) the data improvements obtained with the inclusion of P_{ex} are slight; ΔP_e is the sum of P_{ex} and ΔP_{ent} .²

Viscous Heat Generation

One of the assumptions made in solving the flow in the fully developed region of the capillary was that of constant fluid temperature throughout the flow region. This is not a valid assumption for the flow of very viscous fluids at high rates of shear in which a nonuniform temperature field is created. As we have already mentioned in connection with the thermal-energy balance (Section 2.2), the rate of viscous heating per unit volume e_v is

$$e_v = -(\boldsymbol{\tau} : \nabla \mathbf{v}) = -\frac{1}{2}(\boldsymbol{\tau} : \dot{\boldsymbol{\gamma}} + \boldsymbol{\tau} : \boldsymbol{\omega}) \quad (12.1-7)$$

with $\boldsymbol{\tau} : \boldsymbol{\omega} = 0$ as a scalar product of a symmetric and antisymmetric matrix. Thus, for a Newtonian fluid

$$e_{v,N} = \frac{\mu}{2} \dot{\boldsymbol{\gamma}} : \dot{\boldsymbol{\gamma}} \equiv \mu \Phi_v \quad (12.1-8)$$

while for a Power Law fluid

$$e_{v,PL} = \frac{m}{2} \left[\sqrt{\frac{1}{2}(\dot{\boldsymbol{\gamma}} : \dot{\boldsymbol{\gamma}})} \right]^{n-1} (\dot{\boldsymbol{\gamma}} : \dot{\boldsymbol{\gamma}}) \equiv m \Phi_v^{(n+1)/2} \quad (12.1-9)$$

In the fully developed region of the capillary, the flow is described by

$$\dot{\boldsymbol{\gamma}} = \begin{pmatrix} 0 & 0 & \frac{dv_z}{dr} \\ 0 & 0 & 0 \\ \frac{dv_z}{dr} & 0 & 0 \end{pmatrix} \quad (12.1-10)$$

2. The Rosand Viscometer [Malvern Instruments Ltd., Enigma Business Park, United Kingdom] consists of two identical parallel barrels and two equal-length plungers that are driven by the same constant velocity drive. Each of the plungers has its own pressure transducers. One of the barrels is fitted with a zero-length (knife-edge) capillary and the other with one of $10 < L/D < 20$. When all the melt has been emptied from the barrel, the pressure registered by the plunger with the knife-edge capillary, represents a direct experimental value of ΔP_{ent} .

Thus, Eqs. 12.1-8 and 12.1-9 become, respectively,

$$e_{v,N} = \mu \left(\frac{dv_z}{dr} \right)^2 \quad (12.1-11)$$

$$e_{v,PL} = m \left[\left(\frac{dv_z}{dr} \right)^2 \right]^{(n+1)/2} \quad (12.1-12)$$

where

$$\mu = \mu_0 e^{\Delta E/RT} \quad (12.1-13)$$

and

$$m = m_0 e^{\Delta E/RT} \quad (12.1-14)$$

Figure 12.7 gives the velocity gradients of a Newtonian and a Power Law fluid with $\mu = m$; isothermal flow is assumed. It is clear that, for Power Law fluids, viscous heating may be intense near the capillary wall, whereas the central portion of the fluid is relatively free of this effect.

The mathematical solution of the nonisothermal flow problem in the fully developed region of the capillary, even with the simplifying assumption of constant fluid density, involves the simultaneous solution of the momentum and energy balances, which have the general forms discussed in Section 2.2, subject to the appropriate boundary conditions. The two equations must be solved simultaneously, because they are coupled through the temperature-dependent viscosity (Eq. 12.1-13). Nahme (10) was the first investigator to look into this coupled-transport problem. Brinkman (11) made the first significant contributions to the understanding of the problem (the Brinkman number), although his solution is limited by the assumption of constant viscosity.

The problem of viscous heat generation of a Newtonian fluid with temperature-dependent transport properties was solved by Turian and Bird (12), and the first numerical solution is credited to Gerrard, Steidler, and Appeldoorn (13). Using a perturbation procedure, Turian solved the problem of a Power Law fluid with temperature-dependent viscosity and conductivity, flowing in Couette and cone and plate flows (14). Morrette and Gogos (15), using a numerical solution, examined the flow of PVC compounds that are subject to thermal degradation, and viscosity changes because of it. For this system, the coupled momentum and energy balances are

$$-\frac{dP}{dz} + \frac{1}{r} \frac{d}{dr} \left[r m_0 e^{\Delta E/RT} \left| \frac{dv_z}{dr} \right|^{n-1} \frac{dv_z}{dr} \right] = 0 \quad (12.1-15)$$

$$\rho C_p v_z \frac{dT}{dz} = \frac{1}{r} \frac{\partial}{\partial r} \left(r k \frac{\partial T}{\partial r} \right) + m_0 e^{\Delta E/RT} \left| \frac{dv_z}{dr} \right|^{n-1} \left(\frac{dv_z}{dr} \right)^2 \quad (12.1-16)$$

Results obtained by the latter investigators indeed show what is expected from Eqs. 12.1-15 and 12.1-16: temperature rises are intense and significant for the layer of the PVC melt near the capillary wall, where $e_{v,PL}$ has high values. As Fig. 12.8 indicates,

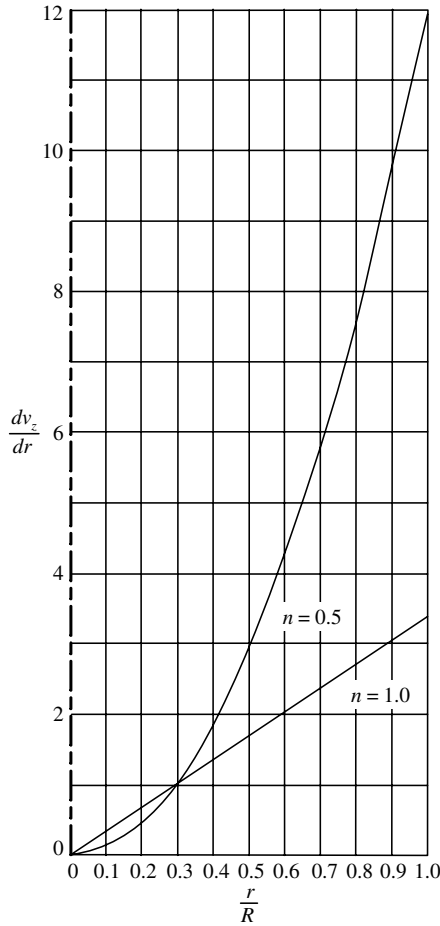


Fig. 12.7 Velocity gradients in a capillary for incompressible Newtonian and Power Law fluids: $\mu = m = 10^5 \text{ N} \cdot \text{s/m}^2$; $\Delta P = 5000 \text{ psi} = 3.45 \times 10^7 \text{ N/m}^2$; $R = 0.1 \text{ cm}$; $L = 5 \text{ cm}$.

about 50 % of the temperature rise occurs in the first tenth of the capillary length when m has a high value, since the temperature of the entering melt is low. Two cases were considered, those of isothermal and adiabatic capillary walls, because actual flows lie between these two extremes.

A good experimental method has yet to be devised to measure the temperature of highly viscous fluids flowing at high flow rates. Thermocouple measurements (16–18) have not been successful because they disrupt the flow field and become heated by the viscous fluid flowing past their surface.

Cox and Macosko (19) have reported experimental results on measurements of the melt-surface temperature upon exit from the capillary using infrared pyrometry, which senses the radiation emitted by the hot polymer melt surface. Their work also included the numerical simulation of viscous heating in a capillary, a slit, and an annular die, using a method resembling that of Gerrard et al. (13). They used a boundary condition at the die wall in between the isothermal and adiabatic case, $-k(\partial T/\partial r) = h(T - T_0)$ at the wall, where T_0 is the die temperature “far” from the melt–die interface as well as the inlet melt

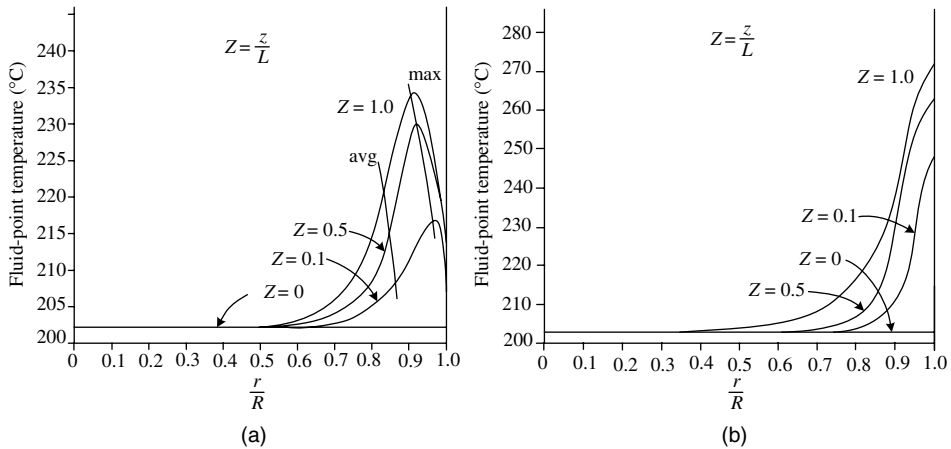


Fig. 12.8 Computed temperature profiles for a PVC melt. (a) Isothermal capillary wall. (b) Adiabatic wall. [Reprinted by permission from R. A. Morrette and C. G. Gogos, "Viscous Dissipation in Capillary Flow of Rigid PVC and PVC Degradation," *Polym. Eng. Sci.*, **8**, 272 (1968).]

temperature. Some of their results for ABS Cyclac T appear in Figs. 12.9–12.11. The data and numerical results depicted in these figures suggest the following:

1. Large temperature rises due to viscous heating do indeed occur in melt capillary flow at moderate and high shear rates. These must be estimated and taken into account whenever temperature sensitive polymers are extruded and whenever the extrudate surface quality and extrudate properties are of critical importance.

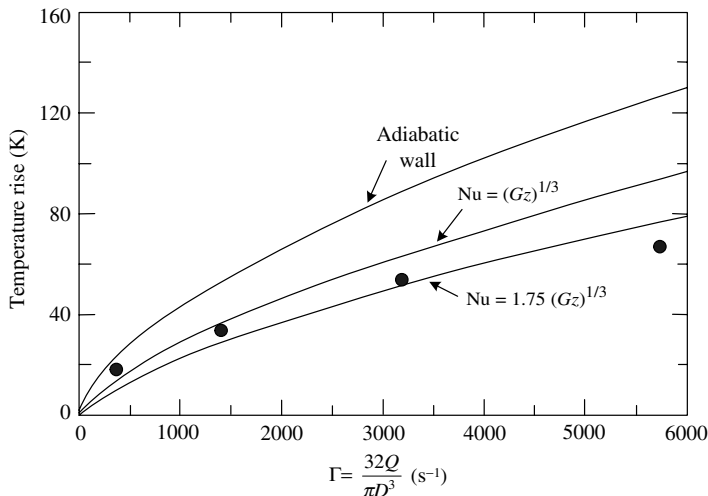


Fig. 12.9 Melt surface temperature rise at the capillary exit, calculated for ABS Cyclac T and measured (●) with an infrared pyrometer: $T_0 = 505$ K, $D_0 = 0.319$ cm, $L/D_0 = 30$. The relationships $Nu = C(Gz)^{1/3}$ are used to estimate h . [Reprinted by permission from H. W. Cox and C. W. Macosko, "Viscous Dissipation in Die Flow," *AIChE J.*, **20**, 785 (1974).]

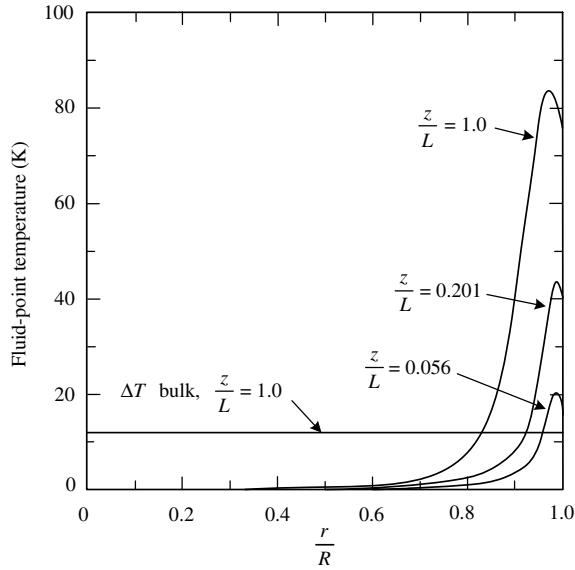


Fig. 12.10 Temperature profiles (calculated) for ABS Cylolac T in tube flow using $Nu = 1.75(Gz)^{1/3}$ to estimate h ; $D_0 = 0.319$ cm; $L/D_0 = 30$; $T_0 = 505$ K; $\Gamma = 5730$ s⁻¹. [Reprinted by permission from H. W. Cox and C. W. Macosko, “Viscous Dissipation in Die Flow,” *AIChE J.*, **20**, 785 (1974).]

- At least as far as estimating the surface-temperature rise, the simple dimensionless relationship concerning heat transfer at the wall suffices:

$$Nu = C(Gz)^{1/3} \tag{12.1-17}$$

where $Nu = hD_0/k$, $Gz = \dot{m}c_p/kL$, \dot{m} is the mass flow rate, and $C = 1.75$ for satisfactory fit with the data. The temperature at the capillary wall is never the

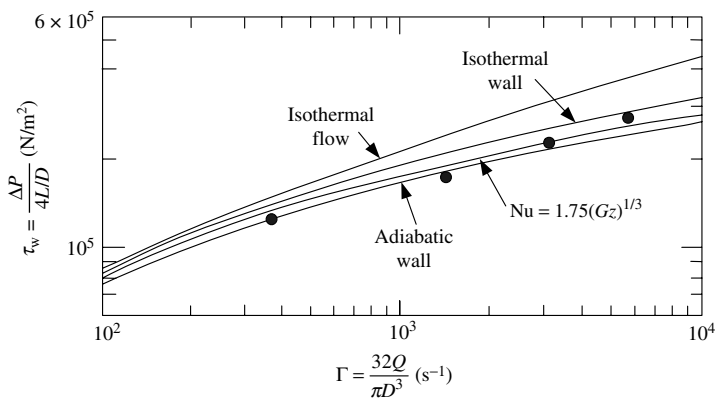


Fig. 12.11 Uncorrected shear stress versus Newtonian wall shear rate for ABS Cylolac T; measured and calculated using various thermal boundary conditions. $D_0 = 0.319$ cm; $L/D_0 = 30$; $T_0 = 505$ K. [Reprinted by permission from H. W. Cox and C. W. Macosko, “Viscous Dissipation in Die Flow,” *AIChE J.*, **20**, 785 (1974).]

maximum; this occurs at about 9/10 the capillary radius. The temperature field at the exit, $T(r, L)$ will influence the swelling and drawing behavior of the extrudate.

3. About 50 % of the temperature rise occurs near the capillary entrance, $z \leq 0.2L$. Thus, shortening the capillary length does not decrease the temperature rise due to viscous heating, proportionally.
4. The bulk temperature rise, ΔT_b (Fig.12.10), does not seem to serve any useful purpose in that it is much smaller than the maximum and is heavily influenced by the central core of the fluid, which does not significantly heat up; ΔT_b is a quantity often calculated and presented as the reason for not having to worry about viscous heating. A simple estimate of ΔT_b is obtained by assuming that the entire mechanical energy degenerates to heating the melt. It seems, therefore, that one must consider and deal with the nonisothermal nature of any type of pressure flow when the calculated value of ΔT_b exceeds 4–5 °C.

Galili and Takserman-Krozer (20) have proposed a simple criterion that signifies when nonisothermal effects must be taken into account. The criterion is based on a perturbation solution of the coupled heat transfer and pressure flow isothermal wall problem of an incompressible Newtonian fluid.

The pressure drop calculated assuming the relationship $Nu = 1.75(Gz)^{1/3}$ for estimating h is smaller than the calculated ΔP , assuming isothermal flow. For the conditions depicted in Fig. 12.11, at $\Gamma = 10^3 \text{ s}^{-1}$ the isothermal pressure drop is about 30 % higher than the measured value. This fact must be taken into account in the design of extrusion dies, so that gross die overdesign can be avoided, as well as in capillary viscometry.

12.2 ELASTIC EFFECTS IN CAPILLARY FLOWS

So far in this chapter we have looked into the viscous phenomena associated with the flow of polymer melts in capillaries. We now turn to the phenomena that are related to melt elasticity, namely: (a) swelling of polymer melt extrudates; (b) large pressure drops at the capillary entrance, compared to those encountered in the flow of Newtonian fluids; and (c) capillary flow instabilities accompanied by extrudate defects, commonly referred to as “melt fracture.”

These phenomena have been the subject of intensive study during the last 50 years and still represent major problems in polymer rheology. From a processing point of view they are very important, since melt fracture represents an upper limit to the rate of extrusion, and swelling and the large pressure drops must be accounted for in product considerations and in the design of the die and processing equipment.

Extrudate Swelling

Extrudate swelling refers to the phenomenon observed with polymer melts and solutions that, when extruded, emerge with cross-sectional dimensions appreciably larger than those of the flow conduit. The ratio of the final jet diameter to that of the capillary D/D_0 , for Newtonian fluids varies only from 1.12 at low shear rates to 0.87 at high rates. Polymer

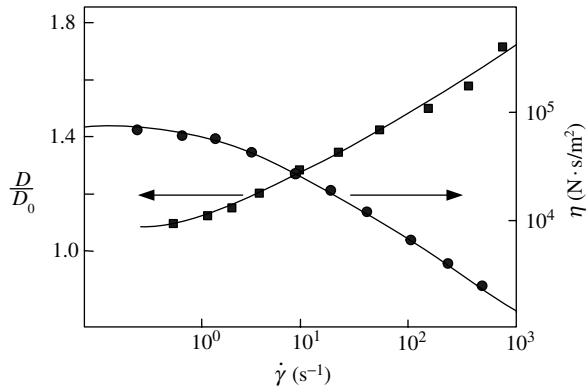


Fig. 12.12 Comparison of the viscosity and swelling ratio dependence on shear rate for a polystyrene melt of $\bar{M}_w = 2.2 \times 10^5$ and $\bar{M}_w/\bar{M}_n = 3.1$. [Reprinted by permission from W. W. Graessley, S. D. Glasscock, and R. L. Crawley, "Die Swell in Molten Polymers," *Trans. Soc. Rheol.*, **14**, 519 (1970).]

melts exhibit the same low shear rate D/D_0 value in the Newtonian plateau region, but swell 2–4 times the extrudate diameter at higher shear rates (21,22). Figure 12.12 gives the shear-rate dependent D/D_0 for melts, together with $\eta(\dot{\gamma})$. Extrudate swelling increases are accompanied by $\eta(\dot{\gamma})$ decreases.

Experimentally, as indicated in Fig. 12.13, we find that D/D_0 depends on the shear stress at the wall τ_w (a flow variable) and the molecular weight distribution (MWD) (a structural variable) (22). The length-to-diameter ratio of the capillary (a geometric variable) also influences D/D_0 . The swelling ratio at constant τ_w decreases exponentially with increasing L/D_0 and becomes constant for $L/D_0 > 30$. The reason for this decrease can be explained qualitatively as follows. Extrudate swelling is related to the ability of polymer melts and solutions to undergo delayed elastic strain recovery, as discussed in

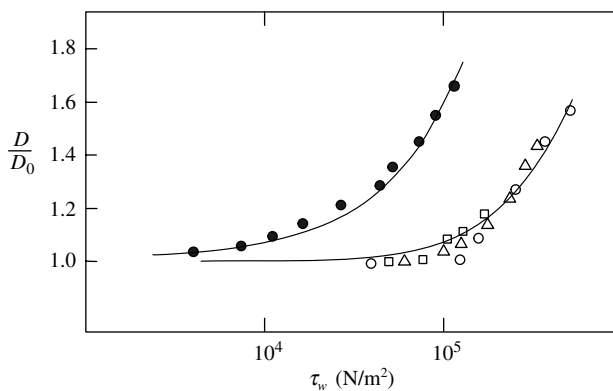


Fig. 12.13 Extrudate swelling data for polystyrene melts: ●, broad molecular weight sample; ○, □, △, narrow distribution sample data at various temperatures. [Reprinted by permission from W. W. Graessley, S. D. Glasscock, and R. L. Crawley, "Die Swell in Molten Polymers," *Trans. Soc. Rheol.*, **14**, 519 (1970).]

Section 3.1. The more strained and the more entangled the melt is at the capillary exit, the more it will swell.³

From this point of view, the decrease of swelling with increasing L/D_0 is due to two causes. First, along the capillary, the melt recovers from the tensile deformations suffered at the capillary inlet, which is due to the axial acceleration in that region. Second, the shear strain imposed on the melt while in the capillary may bring about disentanglements. Polymer melts and solutions are entangled and, under quiescent conditions, are characterized by a high entanglement density value. In this sense they possess a "structure." During shear flow, the entanglement density is reduced, and so is the ability of the fluid to undergo strain recovery. Thus the value of D/D_0 at very long L/D_0 values reflects the ability of the viscoelastic liquid to recover from shear strains only. The melt exiting from a very short capillary is much more entangled and recovers better from both shear and tensile strains.

In view of the foregoing discussion, it is not surprising that the magnitude of the first normal stress difference, which measures the extra tension in the flow direction during the flow in a long capillary, reflects the magnitude of extrudate swelling. Such a relationship has indeed been suggested by Tanner (23), who applied Lodge's theory of free recovery following steady shearing flows (24). For long capillaries, Tanner obtains

$$\frac{D}{D_0} = 0.1 + (1 + S_R^2)^{1/6} \quad (12.2-1)$$

The constant 0.1 is empirical; S_R , the recoverable shear strain, is

$$S_R = \frac{\tau_{11} - \tau_{22}}{2\tau_{12}} = \frac{\Psi_1 \dot{\gamma}_w}{2\eta} \quad (12.2-2)$$

where the stresses are evaluated at the wall shear rate $\dot{\gamma}_w$. The shear stress and normal stress differences can be measured experimentally or they can be calculated with the aid of indirect experimental measurements and either continuum or molecular theories. For example, Tanner used the Bernstein–Kearsler–Zappas (BKZ) theory and Bird et al. (25) the Goddard–Miller theory. When the Rouse molecular theory is used, the steady-state shear compliance J_R is (26)

$$J_R = 0.4 \frac{\bar{M}_w}{\rho RT} \cdot \frac{\bar{M}_z \bar{M}_{z+1}}{\bar{M}_w^2} \quad (12.2-3a)$$

for PS, Graessley et al. (22) found

$$J_0 = \frac{2.2J_R}{1 + 2.1 \times 10^{-5} \rho \bar{M}_w} = \frac{S_R}{\tau_w^*} \quad (12.2-3b)$$

3. Solutions of rigid polymer molecules (e.g., poly-*p*-phenylene terephthalate) may also exhibit extrudate swelling because they too are *entropy elastic*: molecules exit the capillary in a fairly oriented state and become randomly oriented downstream.

where ρ is in g/cm^3 . Thus, for high \bar{M}_w

$$J_0 = \frac{0.4 \times 10^5}{\rho^2 RT} \cdot \frac{\bar{M}_z \bar{M}_{z+1}}{\bar{M}_w^2} \quad (12.2-3c)$$

These relationships indicate that S_R and, according to Eq.12.2-1, D/D_0 , depend on the MWD. We recall that this was also observed by Graessley.

Equation 12.2-1 has been semiquantitatively successful in predicting extrudate swelling (25). However, White and Roman (27) have shown experimentally with a number of polymers that D/D_0 is not a function of S_R only. Furthermore, they demonstrated that the success of the Tanner equation depends on the method of measurement of D/D_0 .

As Fig.12.14 reveals, extrudate swelling values can differ by as much as 30%, depending on the measurement method. The Tanner equation compares best with the results obtained on extrudates frozen in air. The work of White and Roman is important to processing because, in such operations, extrudate swelling occurs under postextrusion conditions that are poorly specified and always nonequilibrium. The solution of the extrudate swelling problem can, in principle, be found by using macroscopic mass and momentum balances over a control volume bound by the capillary exit plane and another at a downstream position where the velocity profile is flat (28). This method has been successfully applied to the solution of extrudate swelling in Newtonian jets (Problem 12.3). The results obtained by such balances in polymers do *not* agree with experiments.

A detailed analysis of extrudate swell by macroscopic balances was carried out by Bird et al. (29), who distinguished between two regimes: a low Reynolds number regime and a high Reynolds number regime. In the latter regime, good analysis can be done using only macroscopic mass and momentum balances, but in the former regime (which includes polymer swelling), the macroscopic mechanical energy balance has to be included in the analysis because of the significant effect of the viscous dissipation term. This renders

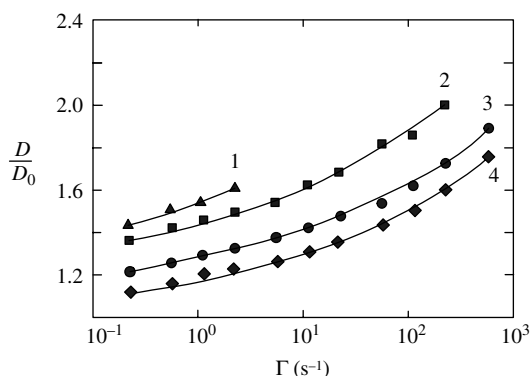


Fig. 12.14 Effect of the method of measurement on the value of D/D_0 for HDPE. Curve 1, frozen extrudates; Curve 2, extrudates annealed at 160°C in hot silicon oil; Curve 3, photographs of extrudates emerging from capillary; Curve 4, photographs of extrudates in hot silicon oil. [Reprinted by permission from J. L. White and J. F. Roman, "Extrudate Swell During the Melt Spinning of Fibers-Influence of Rheological Properties and Take-up Force," *J. Appl. Polym. Sci.*, **20**, 1005 (1976).]

the analysis more difficult, as it requires detailed knowledge of the jet free-surface shape, the distance downstream to fully developed flow, the velocity rearrangement in the die, the Reynolds number, and a new dimensionless group, including the primary normal-stress difference function Ψ_1 .

Whipple's careful experimental study of the velocity profile in the region before and after the capillary exit is an initial step in answering some of these needs. He found that polymer melts "anticipate" the swelling phenomenon, in that, just before the exit, axial decelerations and radial velocity components are observed. Thus the exit velocity profile is not the same as in the fully developed region and the flow there is not viscometric.⁴

Example 12.1 Recoverable Strain Graessley et al. (22) found that, with polystyrene extrudate velocities of 1–3 mm/s in the temperature range of 160°–180°C, about 90% of the final D/D_0 value was reached at an axial distance of 0.1 cm past the capillary exit. The rest of the swelling was completed in the next three centimeters. We wish to calculate the "recoverable strain" at 0.1 cm.

Recoverable strain can also be defined as the tensile strain needed to pull a fully swollen extrudate until its diameter is that of the capillary (22).⁵ Assuming constant density $\pi D_2 L/4 = \pi D_0 L_0/4$, or $L_0/L = S_R = (D/D_0)^2$. At 0.1 cm past the capillary exit $S_R = 0.81(D/D_0)^2$, and at 3 cm, it is $(D/D_0)^2$. Therefore, at 0.1 cm, 19% of the recoverable tensile strain that the extrudate is capable of undergoing is still present. In other words, if no further swelling were allowed, $0.19(D/D_0)^2$ would be the value of the average "frozen-in" strain in the extrudate.

Entrance Flow Patterns

Earlier in this chapter, in discussing the Bagley correction in capillary viscometry, we pointed out the necessity of eliminating entrance pressure drops to get the correct value of the wall shear stress τ_w^* . As Fig. 12.6 indicates, the level of entrance pressure drops is large for polymer melts and solutions. Figure 12.15 gives specific evidence of the magnitude of the ratio of entrance pressure drop to the shear stress at the wall; this is shown for a number of materials. According to Eq. 12.1-1, we obtain that $\Delta P_{\text{ent}}/\Delta P_{\text{cap}} = (D_0/4L^*) (\Delta P_{\text{ent}}/\tau_w^*)$. Thus, for LDPE flowing in an $L/D_0 = 2.4$ capillary, $\Delta P_{\text{ent}}/\Delta P_{\text{cap}} = 1$ at a value of $\Gamma = 2 \text{ s}^{-1}$, according to Fig. 12.15. The value of the entrance pressure drop becomes larger than the total capillary pressure drop at higher shear rates. It follows then that, in polymer processing, where the length-to-opening ratios are small and shear rates are high, entrance pressure drops must be included in calculations of the die pressure in die design equations. Entrance pressure drops are, of course, observed with all fluids in regions of conduit cross-sectional changes. This is because the conduit shape and the rheological response of the fluid create extra velocity gradients that, to be sustained, need to be "fed" by stress terms, which give rise to extra pressure drops (i.e., $[\nabla \cdot \tau] = -\nabla P$ in the equation of motion). Newtonian fluids in laminar flow in contracting regions exhibit streamlines that radiate in waves in the entire entrance region, as has been shown by Giesekus (31). This simple flow pattern, together with the simple rheological response of

4. The experimental fact that nonviscometric flow prevails at the capillary exit must be taken into account in the discussion of P_{ex} (9) mentioned earlier.

5. Here we use the "engineering strain," $\varepsilon = l(t)/l_0$, and not the "true strain" used in Eq. 3.1-3.

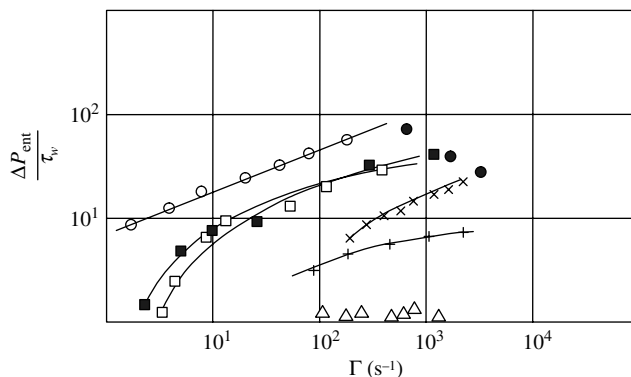


Fig. 12.15 The ratio of entrance pressure drop to shear stress at the capillary wall versus Newtonian wall shear rate, Γ . ■, PP; □, PS; ○, LDPE; +, HDPE; ●, 2.5% polyisobutylene (PIB) in mineral oil; ×, 10% PIB in decalin; △, NBS-OB oil. [Reprinted by permission from J. L. White, "Critique on Flow Patterns in Polymer Fluids at the Entrance of a Die and Instabilities Leading to Extrudate Distortion," *Appl. Polym. Symp.*, No. 20, 155 (1973).]

Newtonian fluids, gives rise to relatively small entrance pressure losses that have been calculated by Weissberg (32) to be

$$\Delta P_{e,N} = \frac{3\mu Q}{2R^3} \quad (12.2-4)$$

where Q is the volumetric flow rate and R is the capillary radius.

Polymer melts and solutions, on the other hand, are rheologically more complex fluids and, even under simple radiating flows in the entrance region, would need more stress components to sustain them; thus there are larger entrance pressure drops. Additionally, the entrance flow patterns with polymer melts and solutions are typically more complex.⁶

Entrance vortices are observed (Fig. 12.16) with the viscoelastic fluid flowing into the capillary from a "wine glass" region (33). Not all polymers exhibit vortices—HDPE and isotactic polypropylene (PP) do not—and all polymer melts and solutions behave like Newtonian fluids at very low shear rates where the viscosity has reached the "Newtonian plateau." As the flow rate is increased, vortices are formed, leading to the conclusion that radiating flow is not compatible with the equation of motion and the constitutive equation describing these fluids. Furthermore, increasing the flow rate results in increasing the vortex size (34).

The large entrance pressure losses are a consequence of the large vortices, which effectively increase the capillary length. Large vortices imply small entrance angles α , as Fig. 12.16 suggests.⁷ In turn, small entrance angles give rise to a small elongational extension rate in the region of the wine glass stem. This apparently has led Lamb and Cogswell (35) to relate the entrance angle α to the elongational viscosity $\bar{\eta}$, arguing that

6. The viscous contribution to the total entrance pressure loss is very small. [C. D. Han, "Influence of the Die Entry Angle in the Entrance Pressure Drop, Recoverable Elastic Energy and Onset of Flow Instability in Polymer Melt Flow," *AIChE J.*, **17**, 1480 (1970).]

7. It follows then that the capillary entrance angle affects the value of ΔP_{ent} . Han (37) has shown that, for HDPE, ΔP_{ent} decreases with increasing entrance angle, up to 60° , then remains constant from 60° to 180° .

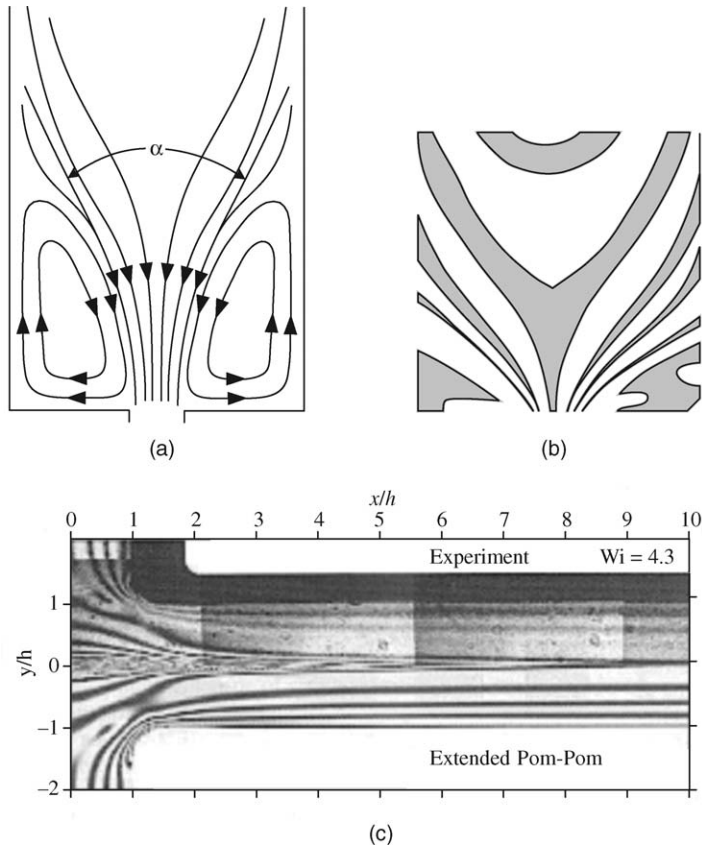


Fig. 12.16 Entrance flow patterns in molten polymers. (a) Schematic representation of the “wine glass” and entrance vortex regions with the entrance angle. [Reprinted by permission from J. L. White, “Critique on Flow Patterns in Polymer Fluids at the Entrance of a Die and Instabilities Leading to Extrudate Distortion,” *Appl. Polym. Symp.*, No. 20, 155 (1973).] (b) Birefringence entrance flow pattern for a PS melt. [Reprinted by permission from J. F. Agassant, et al., “The Matching of Experimental Polymer Processing Flows to Viscoelastic Numerical Simulation,” *Int. Polym. Process.*, **17**, 3 (2002).]

melts with high elongational viscosity would favor small elongational rates, and thus small entrance angles. The relationship proposed is

$$\alpha = \tan^{-1} \frac{2\eta}{\bar{\eta}} \quad (12.2-5)$$

The ratio of shear to elongational viscosities becomes smaller with increasing deformation rates, giving rise to smaller entrance angles and, consequently, larger entrance vortices, as observed experimentally.

Ballenger and White (34) relate the entrance angle α in degrees to the ratio of the entrance pressure loss to the capillary wall-shear stress, $\Delta P_{\text{ent}}/\tau_w^*$

$$\alpha = 178.5(0.9644)^{\Delta P_{\text{ent}}/\tau_w^*} \quad (12.2-6)$$

The relationship is experimental. LaNieve and Bogue (36) have related the entrance pressure losses of polymer solutions to the viscosity and primary normal stress difference coefficient. Thus, the works of Ballenger and LaNieve, taken together, seem to imply that the entrance angle (thus the size of the entrance vortices) depends on both the viscosity and the first normal stress difference coefficient. White and Kondo (38) have shown experimentally that, for LDPE and PS

$$\alpha = f \left[\frac{(\tau_{11} - \tau_{22})_w}{(\tau_{12})_w} \right] \quad (12.2-7)$$

Equations 12.2-6 and 12.2-7 seem to imply that the entrance (or “ends”) pressure losses are simply related to the first normal stress difference function at the capillary wall. Indeed they find that

$$\frac{\Delta P_e}{(\tau_{11} - \tau_{22})_w} \cong 2 \quad (12.2-8)$$

A better understanding of the exact origins of the entrance pressure loss in polymer melts requires the experimental determination of the precise flow field in that region. Until such work and the subsequent analysis have been completed, it suffices to state that entrance pressure losses with polymer melts are large, since these fluids are viscoelastic and exhibit large extensional viscosity values. For die design purposes, we must have experimentally available data, such as those obtained with zero-length capillaries, or with a number of different L/D_0 capillaries by extrapolations to $L/D_0 = 0$.

Extrudate Melt Fracture

In the flow of molten polymers through capillaries and other dies, a striking phenomenon is observed of shear stresses at the wall of the order of 10^5 N/m². As the flow rate is increased, there is a *critical stress* level at and above which the emerging polymer stream exhibits irregular distortion. This distortion contributes evidence for some irregularity or resistability in flow.

The preceding observations originated with Tordella (39), who not only investigated the field of unstable polymer melt pressure flow but has written lucidly on it, coining the term “melt fracture” for the just-described phenomena. The phenomenon was first studied by Spencer and Dillon (40), who found that the critical wall shear stress is independent of the melt temperature, and inversely proportional to the weight average molecular weight. These conclusions have remained essentially valid to date. Aside from the review by Tordella (39), two more review papers should be mentioned: one general article on polymer processing instabilities by Petrie and Denn (41), and more recently, a thorough review of the many facets of melt fracture by Denn (42).

Looking at the melt fracture of specific polymers, we see many similarities and a few differences. Polystyrene extrudates begin to spiral from smooth at $\tau_w^* \approx 10^5$ N/m², and at higher shear stresses, they are grossly distorted. Visual observations show a wine glass entrance pattern with vortices that are stable at low stress values and spiral into the capillary and subsequently break down, as τ_w^* is increased. Clearly, melt fracture is an entrance instability phenomenon for this polymer.

Similar observations have been made with polypropylene, with two qualitative differences. The flow entrance angle is very large, almost 180° , and the observed spiraling of the extrudate is very regular. LDPE extrudates transit from smooth to dull or matte at subcritical values of τ_w^* . With increasing shear stress, they begin to spiral over a narrow range of τ_w^* , and subsequently become grossly distorted.

Corresponding to smooth and matte extrudates, very small entrance angles but stable patterns are observed at the capillary entrance. This flow pattern spirals in the capillary at high stresses, and at the critical shear stress, the wine glass stem flow lines are grossly disrupted. With the exception of the appearance of the matte extrudate surface, which is an exit fracture phenomenon as has been demonstrated by Cogswell and Lamb (43) and Vinogradov (44), and which will be further discussed below, LDPE behaves in the melt fracture region similarly to PS and PP.

In the three polymers just named, two more observations are worth mentioning. First, at the melt fracture onset, there is no discontinuity in the flow curve (τ_w^* vs. $\dot{\gamma}_w^*$). Second, as expected, because the entrance is the site of the instability, increasing L/D_0 decreases the severity of extrudate distortions.

HDPE exhibits extrudates that are smooth at low τ_w^* values, and display "sharkskin" (a severe form of matte) and regular, helical screw thread surface patterns in the subcritical stress region (Fig. 12.17), followed by grossly distorted shapes, which are accompanied by large pressure fluctuations at constant flow rates. That is, in the distorted extrudate region, there is a discontinuity in the flow curve. At higher stresses (flow rates), the extrudate surface becomes smooth again, a fact that may be utilized in fast shaping operations such as wire coating and blow molding of HDPE. The distortions either are not affected or become amplified with increasing L/D_0 (45).



Fig. 12.17 Scanning electron micrograph of HDPE extruded at a shear rate slightly lower than the oscillation region, showing "sharkskin." [Reprinted by permission from N. Bergem, "Visualization Studies of Polymer Melt Flow Anomalies in Extruders," *Proceedings of the Seventh International Congress on Rheology*, Gothenberg, Sweden, 1976, p. 50.]

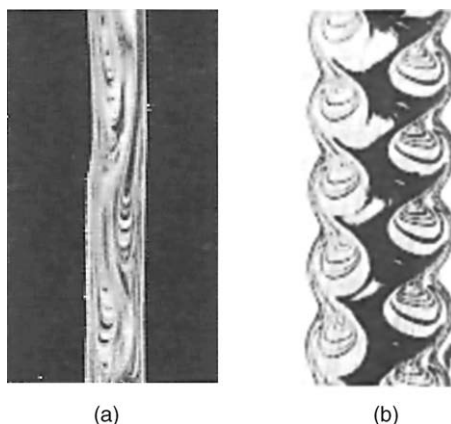


Fig. 12.18 Flow patterns above the oscillating region of HDPE. (a) Microtome cut along the cylinder axis of HDPE solidified inside a capillary die showing that the flow patterns are formed at the die entrance. (b) Microtome cut of the HDPE extrudate resulting under the same conditions as in (a). [Reprinted by permission from N. Bergem, “Visualization Studies of Polymer Melt Flow Anomalies in Extruders,” *Proceedings of the Seventh International Congress on Rheology*, Gothenberg, Sweden, 1976, p. 50.]

The entrance flow pattern at low flow rates corresponding to the matte or smooth extrudates is stable with a very wide wine glass entrance angle ($\alpha \sim 180^\circ$). Bagley and Birks (33) have observed only high-frequency oscillations into the capillary at the critical shear stress region, whereas White (34), Oyanagi (46), and Bergem (47) have reported spiraling flow patterns into the die, well into the distorted extrudate regions.

The site of the sharkskin distortion is again the die exit, and so is the screw thread pattern. The site of, and the mechanism for the gross extrudate distortion are problems that have no clear answers. The work of White and Ballenger, Oyanagi, den Otter, and Bergem clearly demonstrates that some instability in the entrance flow patterns is involved in HDPE melt fracture. Clear evidence for this can be found in Fig. 12.18. Slip at the capillary wall, to quote den Otter, “does not appear to be essential for the instability region, although it may occasionally accompany it.”

The idea of slip at the wall was first proposed by Tordella and later gained popularity because it can be used to explain the discontinuity in the HDPE flow curve (48) and the fact that, at shear stresses above the discontinuity, the extrudate becomes smooth again (the melt is continuously slipping at the wall). Den Otter (45) has found evidence of slip in the flow of linear elastomers. Thus, it is possible that, through molecular disentanglement at a certain stress level, a low viscosity layer is formed at the die entrance which, if it is at the periphery, would result in the flow patterns of Fig. 12.18. If disentanglement is involved for the entrance region, there is no reason to exclude it in the capillary where a surface layer of low viscosity film would be formed, acting as an effective lubricant (see section 2.11).

With the discovery and development of metallocene-based LLDPEs with narrow MWD and high molecular weight, there has been a flurry of investigations with these polymers, because they exhibit sharkskin melt fracture at quite low and industrially limiting production rates. The objective of such studies is to increase the rate of production with

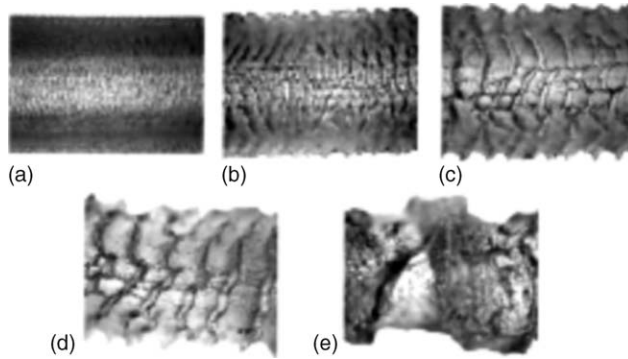


Fig. 12.19 Cold postextrusion micrographs as a function of the flow rate. The processing conditions were $T = 177^\circ\text{C}$ and no PPA. Each image is actually a composite of two micrographs in which the side and top are focused. The relative errors in throughputs are $0.05 Q =$ (a) 1.0, (b) 2.2, (c) 3.8, (d) 6.3, and (e) 11 g/min. The width of each image corresponds to 3 mm. [Reprinted by permission from K. B. Migler, “Extensional Deformation, Cohesive Failure, and Boundary Conditions during Sharkskin Melt Fracture,” *J. Rheol.*, **46**, 383–400 (2002).]

sharkskin-free extrudates. The incorporation of two processing additives, fluoroelastomers (49) and boron nitride (50) achieves this, but at the expense of adulterating the base polymers. Thus, the studies continue to probe two basic questions relating sharkskin in LLDPE extrudates: first, where is the location of origin of this flow instability and, second, what is the cause with LLDPEs.

Migler et al. (49) observe that (a) the fracture phenomena progress with increasing flow rate from smooth, to sharkskin, to grossly deformed extrudates, as shown in Fig. 12.19; (b) the onset of sharkskin is *not associated with slip* at the capillary wall just upstream of the exit, as shown by the velocity profiles on Fig. 12.20 measured with

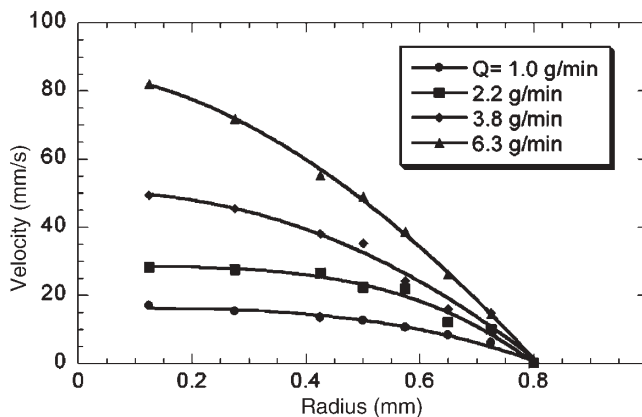


Fig. 12.20 Flow velocimetry as a function of the radial position of the polyethylene *inside* the capillary die for a series of flow rates. Measurements were taken at $x = -0.2$ mm (no PPA). [Reprinted by permission from K. B. Migler, “Extensional Deformation, Cohesive Failure, and Boundary Conditions during Sharkskin Melt Fracture,” *J. Rheol.*, **46**, 383–400 (2002).]

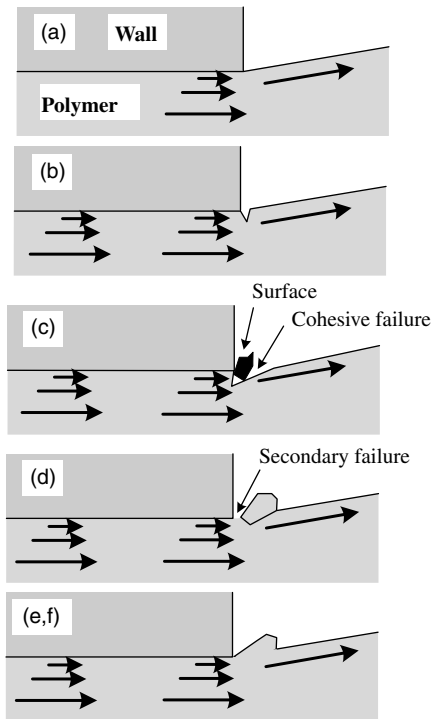


Fig. 12.21 Sketch of the kinetics of the sharkskin instability, side view. [Reprinted by permission from K. B. Migler, “Extensional Deformation, Cohesive Failure, and Boundary Conditions during Sharkskin Melt Fracture,” *J. Rheol.*, **46**, 383–400 (2002).]

particle-tracking velocimetry through a quartz capillary. Thus, the phenomenon originates at the capillary exit, as was first presented in clear physical terms by Cogswell (51); (c) the cause appears to be *cohesive failure* of the polymer melt at the capillary exit corner, as shown schematically in Fig. 12.21(b); this splits the extrudate into a core and a surface layer, as shown in Fig. 12.21(c).

As the extrudate proceeds downstream, there is a secondary failure that creates the sharkskin ridge [Fig. 12.21(d)]. Following the *ridge creation*, whose amplitude increases with flow rate (Fig. 12.19), there is an axial movement of the core downstream, till the repetition of the cycle [Fig. 12.21(e,f)]; the period of the ridge-core repetition is also flow rate dependent.

The cohesive failure is brought about by the sudden and large axial acceleration of the melt layer next to the capillary wall, as shown by Migler et al. (49) in Fig. 12.22(a). Figure 12.22(b) shows that the addition of a fluoroelastomer (PPA) additive allows the formation of a slip that is larger upstream from the exit, as shown on Fig. 12.23, which reduces the axial acceleration and the level of extensional deformation and rate.

Recently, Muliawan et al. (52), who have been studying melt fracture, and in particular sharkskin extrudate instabilities over the last decade, have presented interesting experimental results relating the extensional stress–Hencky strain behavior of polymer melts to their sharkskin (exit) and gross (capillary entrance) melt fracture behavior. For the purposes of this discussion, results obtained with two Nova Chemicals

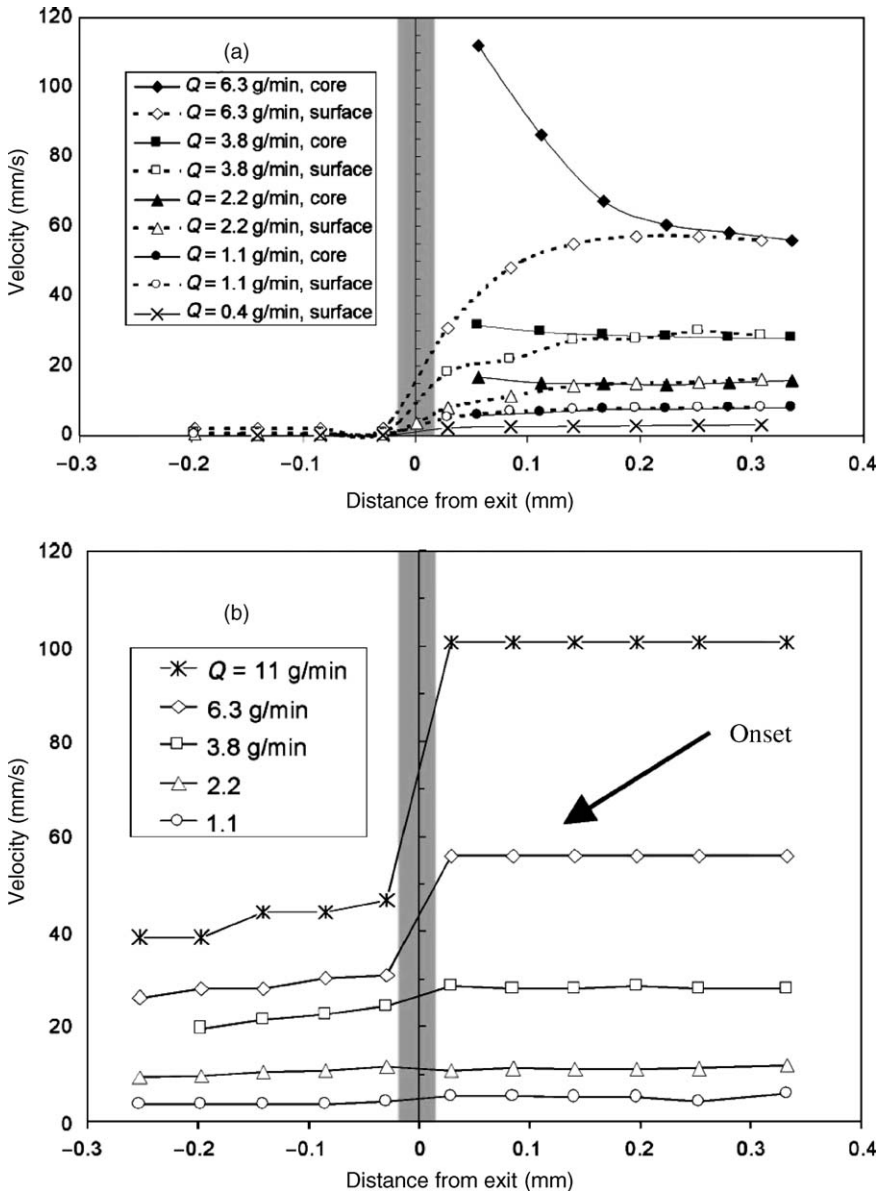


Fig. 12.22 Velocity of the polymer in the vicinity of the wall as it makes the transition from inside to outside the capillary die. For $x < 0$ (inside the die), measurements were made of slow-moving particles, that is, those nearest the wall. For $x > 0$ (outside the die), the measurements were made at the air–polymer interface. The flow rate at which the onset of sharkskin is observed is noted. (a) Without the polymer process additive. For the higher flow rates, we show the velocity of both the core and the surface regions. (b) With the polymer process additive. [Reprinted by permission from K. B. Migler, “Extensional Deformation, Cohesive Failure, and Boundary Conditions during Sharkskin Melt Fracture,” *J. Rheol.*, **46**, 383–400 (2002).]

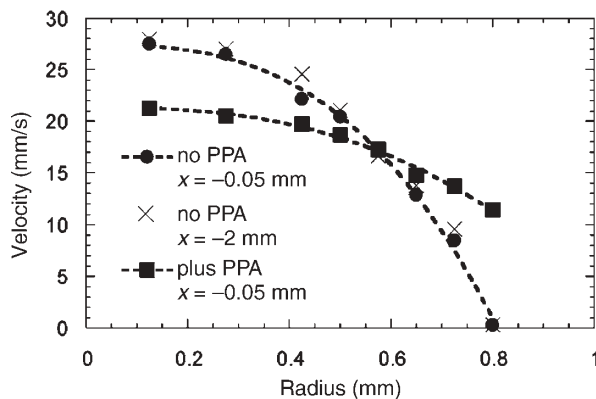


Fig. 12.23 Flow velocimetry as a function of the radial position of the polyethylene *inside* the capillary die for a $Q = 2.2$ g/min [the same as in Fig. 12.19(b)]. The measurements were taken at $x = -0.05$ and -2 mm upstream of the exit. Also shown is the case with PPA. [Reprinted by permission from K. B. Migler, "Extensional Deformation, Cohesive Failure, and Boundary Conditions during Sharkskin Melt Fracture," *J. Rheol.*, **46**, 383–400 (2002).]

Corporation film-grade Ziegler-Natta linear low density polyethylenes will be presented. They are Resin E, Nova FP-015-A, MFI = 0.55, $\rho = 0.9175$ g/cc, and Resin C, Nova PF-120-F, MFI = 1.00, $\rho = 0.9170$ g/cc. Their capillary-flow behavior in terms of apparent shear stress vs. apparent shear rate are shown on Fig. 12.24. The melt fracture onset is also noted in Figure 12.24 and the data presented in the table below, indicate that resin E undergoes both sharkskin and gross melt fracture at lower apparent shear rates and stresses.

Critical Shear Rates and Stresses for All Resins in Capillary Die Extrusion at 170°C

Sample I.D.		Critical Shear Rate (s^{-1}) and Stress (MPa) for the Onset of	
		Sharkskin	Gross melt
C (LLDPE FP-120-F)	Apparent shear rate	100	1100
	Apparent shear stress	0.24	0.42
E (LLDPE FP-015-A)	Apparent shear rate	40	700
	Apparent shear stress	0.20	0.39

The extensional melt behavior was assessed with the new SER Universal Testing Platform from X-pansion Instruments, described by Sentmanat (53,54) and shown in Fig. 12. 25. The obtained tensile stress of the two resins at 170°C and extensional rate of 20 s $^{-1}$ are shown on Fig. 12.26. It is evident that Resin E has a higher modulus and higher tensile stress values, at a given strain below yield, than Resin C. From this, and the experimental data discussed previously, we see that the values of the critical shear rate and shear stress for the onset of sharkskin fracture are inversely proportional to the magnitude of the tensile stress of the resins. This suggests that the rapid increase

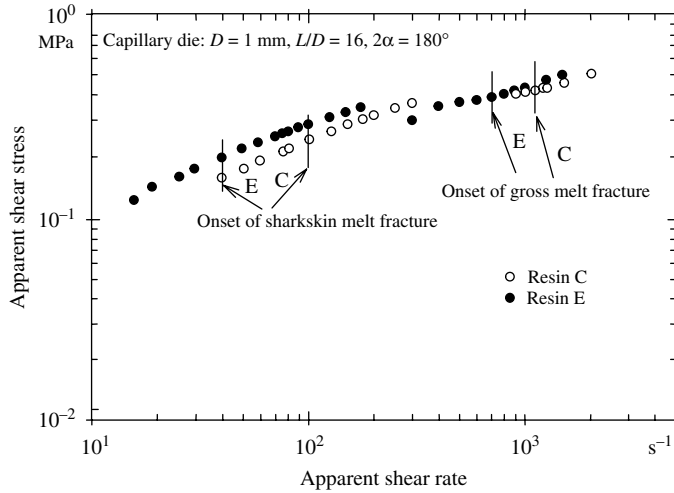


Fig. 12.24 Flow curves of LLDPE resins E and C, indicating the onset of sharkskin and gross melt fracture for each resin. $T = 170^\circ\text{C}$, capillary: $D = 1$ mm, $L/D = 16$, with entrance angle $2\alpha = 180^\circ$. [Reprinted by permission from E. G. Muliawan, S. G. Hatzikiriakos, and M. Sentmanat, "Melt Fracture of Linear Polyethylene," *Int. Polym. Process.*, **20**, 60 (2005).]

in extensional stresses leads to an earlier "rupture" of the melt at the capillary exit wall circumference, where *elongational stresses and strains* are the highest, with subsequent rupture propagation toward the center, where they are the lowest. Extensional rheological data on branched low density polyethylene by Sentmanat and Hatzikiriakos (55) indicate that the presence of long chain branches retards tensile stress growth to much higher strains, due to the dissipative interaction of the polymer branch entanglements prior to the main chain stretch. This, they claim, is the reason that sharkskin melt fracture is not observed with LDPEs.

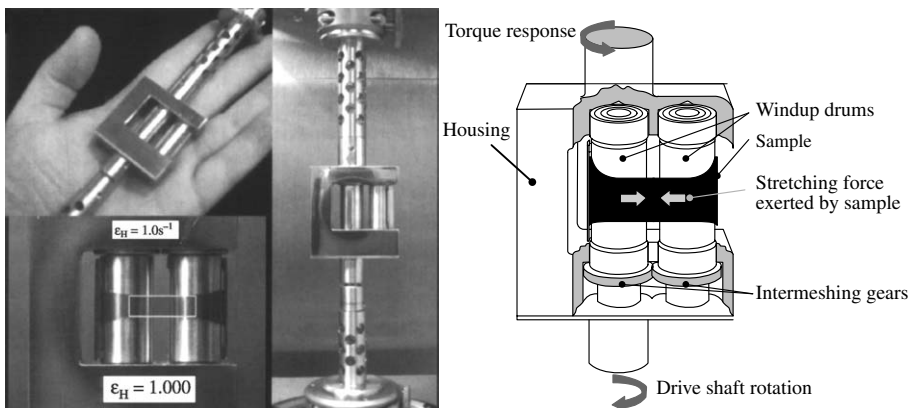


Fig. 12.25 The Universal testing platform fitted on a rotational Rheometrics RDA II rheometer host station. The two counterrotating cylinders where the film is mounted cause the application of the extensional strain. [Reprinted by permission from E. G. Muliawan, S. G. Hatzikiriakos, and M. Sentmanat, "Melt Fracture of Linear Polyethylene," *Int. Polym. Process.*, **20**, 60 (2005).]

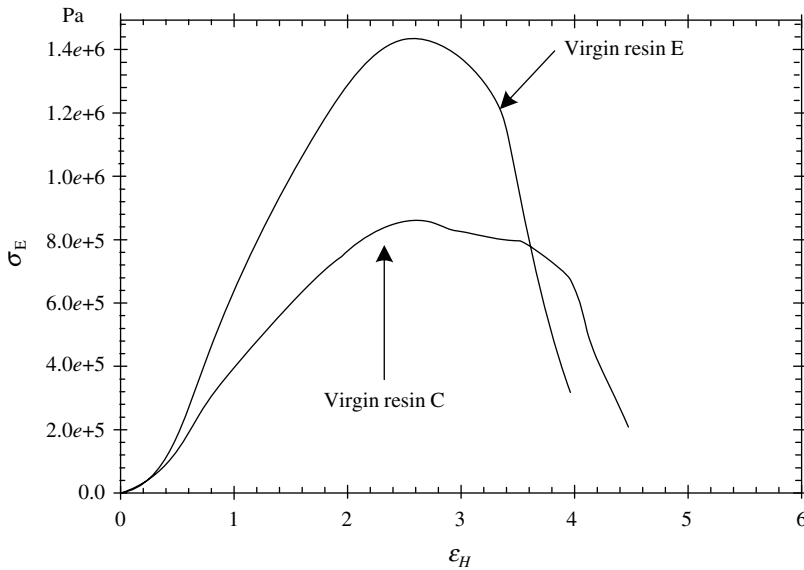


Fig. 12.26 True tensile stress–Hencky strain curves for resins C and E at Hencky strain rate of 20 s^{-1} and temperature of 170°C . [Reprinted by permission from E. G. Muliawan, S. G. Hatzikiriakos, and M. Sentmanat, “Melt Fracture of Linear Polyethylene,” *Int. Polym. Process.*, **20**, 60 (2005).]

Gogos et al. (56) conducted extensive studies on the morphological features of the surface melt fractured extrudates of metallocene catalyzed LLDPE in pelletizing dies. They concluded that the morphological evidence, Fig. 12.27, suggested strongly that surface melt fracture of LLDPE is due to cohesive (“peel”) strength failure of the melt layer *next to the wall at the die exit* of the pelletizing die, under the burden of local high shear *and* extensional stresses, as Cogswell (51) suggested in 1977. The objective of their study was to develop pelletizing dies that *extend* the shear rate range of surface melt fracture-free extrudates, *without the use of processing aids*. They were able to meet this objective by developing “integrally heated” die plates, which heat the die exit corner region to unusually high temperatures (up to 200°C higher than the melt bulk temperature) (57). Thus, while the bulk melt temperature is unaffected, a very low viscosity melt layer is formed next to the wall of the die exit-corner region, forming a melt slip layer and rendering the exiting extrudate “immune” to cohesive failure. With such integrally heated pelletizing dies, they were able to obtain smooth extrudates at nominal calculated shear stress levels of 0.65 MPa , well above the critical sharkskin surface melt fracture levels with LLDPE (see Fig. 12.24). Smooth, sharkskin-free extrudates were obtained at flow rates as high as three times those with conventional conductively heated pelletizing dies, both in air and under water, as shown on Fig. 12.28. Similarly, beneficial effects were observed with Ziegler catalyzed LLDPE resins, LLDPE with and without processing aids, and with dies made of stainless steel and brass. Such integrally heated dies hold the promise of substantially increasing the current operating rates in postreactor finishing operations, which are limited by the onset of sharkskin melt fracture.

We now turn to the gross melt fracture behavior. Estimates of the prevailing extensional rates at the capillary entrance indicate that their value corresponding to the critical gross melt fracture conditions is larger than the 20 s^{-1} used in this work. Nevertheless, since

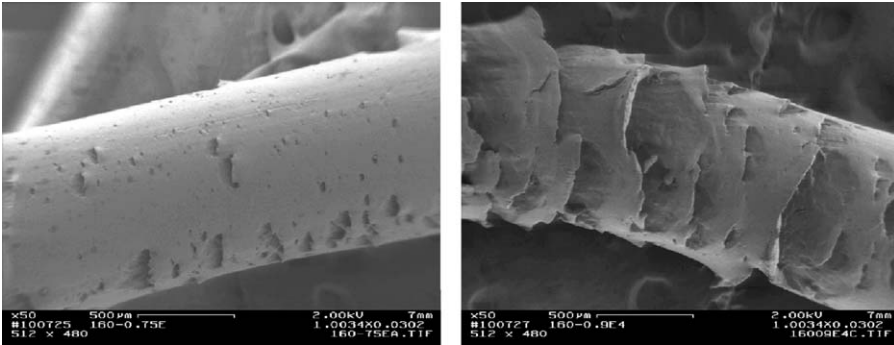


Fig. 12.27 Surface morphological features of mLLDPE (ExxonMobil Exceed™ 350D60) extrudates obtained at 160 °C with a tungsten carbide die: $D = 0.767$ and $L = 25.5$ mm just above and in the sharkskin melt fracture flow-rate region. [Reprinted by permission from C. G. Gogos, B. Qian, D. B. Todd, and T. R. Veariel, “Melt Flow Instability Studies of Metallocene Catalyzed LLDPE in Pelletizing Dies,” *SPE ANTEC Tech. Papers*, **48**, 112–116 (2002).]

20 s^{-1} is the highest attainable value with this instrument at present, the tensile stress versus Hencky strain at this rate is used to explain the inverse relation between the modulus and the tensile stress values and the critical shear rate for the onset of gross melt fracture, as previously shown. Resin E has the higher tensile modulus, thus the higher increase in extensional stress, with this polymer reaching its critical gross melt fracture stress at an earlier (lower) rate. Thus, for exit and entrance melt fracture phenomena, the strain dependent, high strain rate, extensional stress behavior appears to be an indicator, if not a predictor, of the early shear-rate and shear-stress susceptibility of LLDPEs to such instabilities.

12.3 SHEET FORMING AND FILM CASTING

Polymer flat film sheets are formed continuously by extruding a polymer through a more or less rectangular sheeting die, which is quite wide with a small opening. Because the extruder outlet is by necessity circular, and the die rectangular, two fluid particles feeding

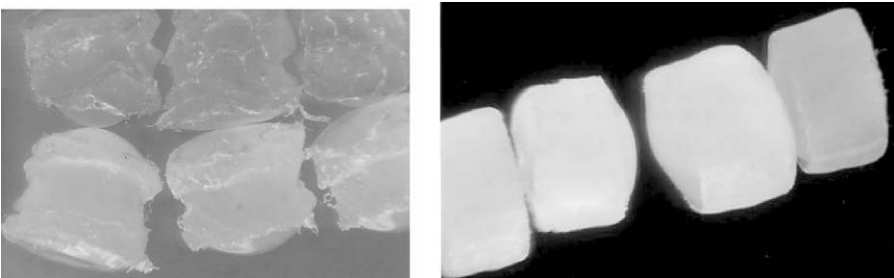


Fig. 12.28 Melt-fractured pellets extruded at 8 kg/h per die hole (3.2 mm in diameter) from a conventional underwater pelletizing die (left) and smooth pellets extruded under the same conditions at 24 kg/h per die hole from the same underwater pelletizing die when locally heated to high temperature (right) (57).

two arbitrarily chosen die positions will have gone through different flow histories, and this may result in a nonuniform flow rate through the die, dependent on the position along the die width. As seen in Fig. 12.29(b), the triangular region exists for that purpose, providing width-dependent flow resistance.

Additionally, the role of the relaxation region is to help erase the width-dependent upstream flow history. Thus the design and the choice of the flow passages from the extruder to the die per se are of great importance. A number of sheeting-die designs representing different practical as well as theoretical solutions are currently in use.

Upon exiting the die, the sheet extrudate will swell to a level determined by the polymer, the melt temperature, the die length-to-opening ratio, and the shear stress at the die walls. Additionally, flow instabilities will occur at values of the corrected shear stress at the wall, of the order of, but higher than 10^5 N/m^2 , as found by Vlachopoulos and Chan (58), who also concluded that, for PS, HDPE, and LDPE, the critical S_R in slits is 1.4 times higher than in tubes of circular cross section. Aside from these differences, the information presented in Section 12.1 and 12.2 applies to slit flow.

Polymer sheets are cooled without stretching by convected cold air (or an inert gas), by immersion into a fluid bath, or by passage over chilled rolls. Flat films are usually stretched and oriented uniaxially and cooled by either of the methods previously mentioned. Films are also cast and cooled on rolls for optimal clarity purposes.

Die Design Equations

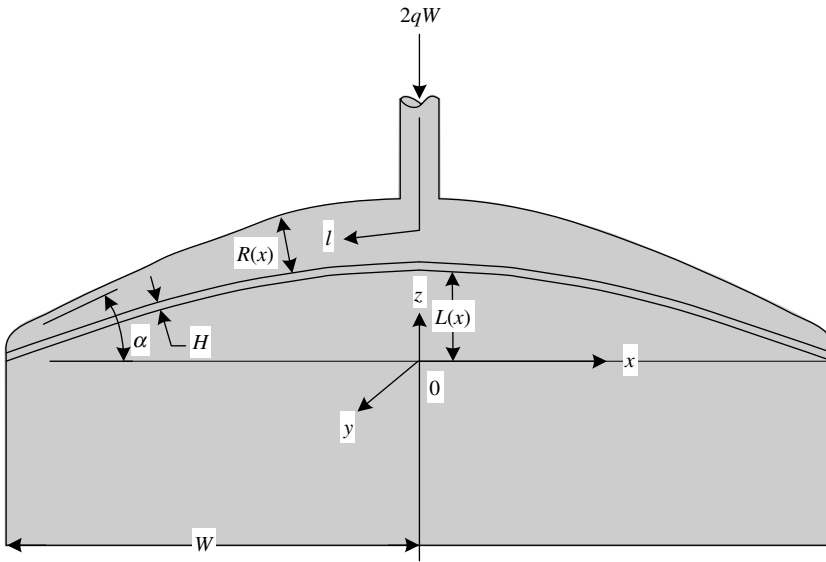
The most common mechanical sheet die designs are the center-fed “T” and the “coat hanger.” In both cases, the melt is fed into the center of the manifold, which has a circular or bead-shaped cross section. The manifold distributes the melt into the approach channel through a slit opening running along its entire length. The names T and coat hanger refer to the angle the manifold makes with the flow direction (Fig. 12.29).

Sheet die design equations were first developed by Carley (59) for T-shaped dies using Newtonian fluids. Pearson (60), whose basic approach we now elucidate, extended the design equations to Power Law fluids. The proper die design delivers a given polymer melt under specified conditions through a constant die opening at a constant rate and temperature (cross-machine direction uniformity). Here, we trace the development of a die design equation that has this design objective.⁸

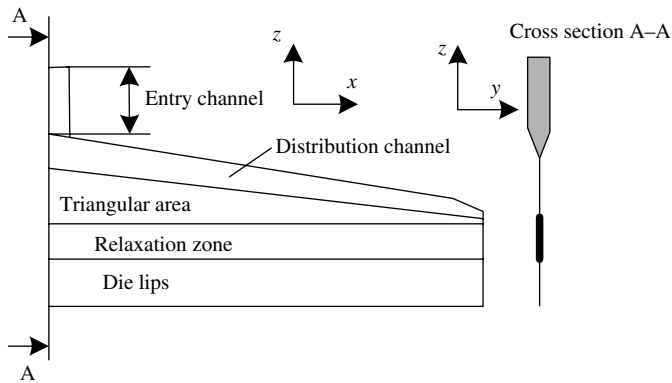
Figure 12.29 presents the geometrical features of the coat-hanger die, on which the design equation will be developed. The manifold is a tubular, variable radius channel of curved axis l . The slit opening H is constant. The only geometric restriction is that the manifold be of a small curvature, so that the lubrication approximation can be applied in the manifold region. Also, for the same reason, $dR(x)/dx \ll 1$.

Assuming that the pressure at the manifold entrance is constant and that the problem is isothermal, we have a constant flow rate entering the die (machine direction uniformity). Our objective is to ensure cross-machine direction uniformity, that is, constant flow rate at

8. In practice, die design does not concern itself simply with the design of the flow passages to control the flow and produce a uniform extrudate—the only aspect we deal with—but also with mechanical design to ensure rigidity of the die under the operating temperatures and pressures, and with chemical and abrasion resistance to the polymers being formed. It also involves the design of an adequate temperature control system, especially in sheeting dies where the surface-to-volume ratio is very large.



(a)



(b)

Fig. 12.29 Schematic representations of the coat-hanger die design.

$z = 0$. But since the slit opening is constant,

$$\frac{dP}{dz} = a = \text{constant} \tag{12.3-1}$$

This holds everywhere in the parallel-plate flow region formed by the slit, where z -constant lines are isobars as a consequence. Integrating Eq.12.3-1 yields

$$[L(0) - L(x)]a = P_0 - P'(l) \tag{12.3-2}$$

where $P'(l)$ is the manifold pressure at position l , and P_0 is the manifold entrance (delivery) pressure; x and l are related geometrically through the shape of the manifold.

Differentiating Eq. 12.3-2 with respect to l results in the following relationship between the pressure gradient in the manifold, its shape, and the pressure gradient in the slit region:

$$\frac{dP'}{dl} = a \frac{dL}{dl} \quad (12.3-3)$$

The preceding relation is the general design equation satisfying the objective set in the beginning of this section. It holds for any fluid. Thus, let us give it a usable form by considering a Power Law fluid flowing in this die. Turning first to the parallel plate region formed by the slit, the z -component momentum equation reduces to

$$-\frac{dP}{dz} - \frac{d\tau_{yz}}{dy} = 0 \quad (12.3-4)$$

For a Power Law fluid, $\tau_{yz} = -m|dv_z/dy|^{n-1} dv_z/dy$, and using the appropriate boundary conditions in this assumed fully developed flow, we obtain, after integration (note that flow is in the negative z direction)

$$v_z(y) = \frac{n}{n+1} \left(\frac{1}{m} \frac{dP}{dz} \right)^{1/n} \left(\frac{H}{2} \right)^{(n+1)/n} \left[\left(\frac{2|y|}{H} \right)^{(n+1)/n} - 1 \right] \quad (12.3-5)$$

or

$$v_z(y) = \left(\frac{1}{1+s} \right) \left(\frac{1}{m} \frac{dP}{dz} \right)^s \left(\frac{H}{2} \right)^{1+s} \left[|\xi|^{1+s} - 1 \right] \quad (12.3-6)$$

where $s = 1/n$ and $\xi = 2y/H$. Integrating over the gap opening, we obtain the following relationship between the pressure drop and the flow rate per unit width, q , taken to be positive in the negative z direction:

$$a = \frac{dP}{dz} = 2^{n+1} (2+s)^n m \frac{q^n}{H^{2n+1}} \quad (12.3-7)$$

For the flow inside the manifold of a circular cross-section⁹ channel, we assume that, locally, we have fully developed tube (capillary) flow. That is, we disregard the channel curvature, the channel tapering off, and the effects of the leak flow into the slit region. The following relationship was derived previously (see Table 12.3):

$$-\frac{dP'}{dl} = \left(\frac{3+s}{\pi} \right)^n 2m \frac{Q^n(l)}{R(x)^{3n+1}} \quad (12.3-8)$$

9. As Fig. 12.1 indicates, the manifold cross section may be bead shaped and not circular. Thus, pressure flow in an elliptical cross-section channel may be more appropriate for the solution of the manifold flow. Such a problem, for Newtonian incompressible fluids, has been solved analytically. (J. G. Knudsen and D. L. Katz, *Fluid Dynamics and Heat Transfer*, McGraw-Hill, New York, 1958). See also, Table 12.4 and Fig. 12.51.

From a mass balance point of view, the flow rate in the manifold at any point $Q(l)$ provides for the melt that flows in the slit region from that point on to the end of the manifold. Specifically,

$$Q(l) = Q(x) = q(W - x) \quad (12.3-9)$$

Combining Eqs. 12.3-8 and 12.3-9 gives

$$-\frac{dP'}{dl} = \left(\frac{3+s}{\pi}\right)^n 2m \frac{[q(W-x)]^n}{R(x)^{3n+1}} \quad (12.3-10)$$

Inserting Eqs. 12.3-7 and 12.3-10 into the general design equation 12.3-3, we obtain the specific design equation for Power Law fluids:

$$\frac{2^n(2+s)^n}{H^{2n+1}} \left(\frac{dL}{dl}\right) + \left(\frac{3+s}{\pi}\right)^n 2m \frac{[q(W-x)]^n}{R(x)^{3n+1}} = 0 \quad (12.3-11)$$

Given the product width $2W$ and the rheological parameter n , there are two geometric (die design) parameters available: for a given manifold axis curvature, dL/dl or dL/dx , there exists a manifold radial taper profile $R(x)$ that results in a uniform pressure at any $z = \text{constant}$ line. In particular, $P(0) \neq f(x)$; this, together with the fact that $H \neq f(x)$, guarantees the design objectives. Conversely, for a given $R(x)$ there exists an $L(l)$ or $L(x)$ that ensures the die design objectives. Generally, for simplicity of construction, constant dL/dl is used. Note that the preceding expression provides the value of the radius at the center $R(0)$, which is necessary for designing a die.

It is worth noting that *not* all $R(x)$ and $L(l)$ or $L(x)$ are acceptable solutions. Any solution that proposes a steeply curving manifold axis or a steeply tapering manifold radius would interfere with the lubrication approximation made during the solution. Furthermore, some solutions may be unacceptable from a machining point of view or because of die-strength considerations. Finally, some designs may be preferable over others, either because the die design equation applies to them more rigorously (the design is such that the assumptions made are reasonable), or because construction is easier. In the first case, more confidence can be placed in the design, and in the second, the die can be made more economically.

Figure 12.29 shows that the die does not end at the plane $z = 0$. Because polymer melts are viscoelastic fluids, it extends to downstream to the end of the die lip region so that a uniform “recent” flow history can be applied on all fluid elements. In deriving the die design equation, we disregarded the viscoelasticity of the melts, taking into account only their shear thinning character.

Example 12.2 Coat Hanger Die Design We specify the coat hanger die manifold radius along the entire width of the die, if the manifold axis is straight and makes an angle $\alpha = 5^\circ$ with the x coordinate (see Fig. 12.29). The slit opening is set at $H = 0.05$ cm, the half-width $W = 100$ cm, and the Power Law index of the polymer melt $n = 0.5$.

From Eq. 12.3-11 the following expression for $R(x)$ is obtained

$$R(x)^{3n+1} = -\frac{[(3+s)/\pi]^n H^{2n+1} (W-x)^n}{2^n(2+s)^n (dL/dl)}$$

where $dL/dl = -\sin \alpha = -0.0872$. Thus, for $n = 0.5$ the preceding equation reduces to

$$R(x) = 0.175(W - x)^{0.2}$$

Thus, the manifold radius at the center is $R(0) = (0.175)(2.51) = 0.44$ cm, and the value close to the edge at 90 cm is $R(90) = (0.175)(1.58) = 0.277$ cm. The manifold tapered tube is open to form the slit opening over an angle β such that $\sin[\beta(x)/2] = (H/2)/R(x)$. Thus at $x = 0$ $\beta(0) = 13^\circ$ and at $x = 90$ cm $\beta(90) = 21^\circ$. This design results in a very slight taper of the radius of the manifold, about 2×10^{-3} . Also worth noting is that the maximum value of the manifold radius is only about nine times the slit opening. Finally the taper decreases slightly with decreasing n , while the dependence of the manifold radius on H increases with decreasing n . The manifold radius becomes infinite at $\alpha = 0$ and is very sensitive to α when it has small values. Note that the solution is independent of m .

Other flat film die design equations have been proposed in the literature. The one advanced by McKelvey and Ito (61) has as a design objective the flow rate uniformity along the die width. This is achieved by varying the final die lip opening. Thus, although the resulting flow rate is independent of the width direction, the film or sheet thickness is *not*. Additionally, the wall shear rate for a Power Law fluid

$$\dot{\gamma}_w = \frac{2(s+2)q}{H^2(x)} \quad (12.3-12)$$

will be width dependent, allowing extrudate swelling to vary.

The die design equation proposed by Pearson (60) utilizes a constant die lip opening, but an approach-channel-taper that varies with the die width. Thus, in the region between the manifold and the die lip opening both the pressure and flow fields are two-dimensional. This may affect the flow in the die lip region, since the fluid is viscoelastic with memory of this recent upstream flow experience.

The following criticisms apply to all the die design equations for sheet forming that have been proposed so far:

1. The manifold and slit flows are treated independently, disregarding the disturbances in both flow fields as a result of the transition flow from the manifold to the slit, including "entrance" losses. To reduce the latter, tapered, wedge-shaped manifolds are used.
2. The flow is assumed to be isothermal. In any real sheet forming operation, some temperature gradients, both in the melt and along the die, will be present (19).
3. The die lip deflection under the pressure applied by the flow is neglected. This could be accounted for, at least approximately, by rather straightforward beam calculations and iterative procedures, as suggested by Pearson (60).
4. The die designs developed or mentioned previously are for a specific polymer and specific processing conditions. Nonuniform sheets of another polymer would result if substitutions were made. The same holds true for the same polymer extruded at a different temperature.

For these reasons, die lip opening adjustor bolts are provided with every sheeting die to make fine adjustments. Usually these adjustments are made manually. Because the die flows are

often quite fast and manual corrections of sheet thickness nonuniformities result in material waste, feedback systems have been devised to adjust lip openings automatically. Multiple extruders can be used for very wide dies, or a screw may be placed in the manifold of a T die.

If “machine direction” thickness uniformity is a problem, it can best be remedied with the use of a gauge detector (beta gauge) that is part of a control system adjusting the speed of the take-up device, to correct for thickness nonuniformities. Small period variations are very difficult to remedy in this fashion.

It can generally be said that the approach to developing die design equations, irrespective of the basic die type, is the following:

1. Simplify the actual flow by assuming that it is a series of well-identified viscometric flows.
2. By applying one or more mass balances, relate the volumetric flow rates in each of the viscometric flows.
3. Allowing for one or more die geometric parameters to be variable, state one or more “extrudate uniformity conditions” that, when satisfied (solved for), will determine the geometric variables given previously as functions of other geometric, process, material constants.

Obviously, this method of developing die design equations implies that there is no unique die design to achieve product uniformity in the cross-machine direction. Multiple alternative designs—and thus die design equations—exist because one has an a priori choice of what geometric variables will be allowed to “float.” Sun and Gupta (62) examined computationally the effect of including the extensional viscosity in the coat-hanger die flow of Dow LDPE 132i. They used the Sarkar–Gupta model (63), whose four rheological parameters were evaluated from entrance pressure measurements. They found that the inclusion of the elongational viscosity has only a minor influence on the velocity field at the die exit, but that it increased the die lip pressure drop by 10–15%, with subsequent increases in the viscous energy dissipation and flow nonisothermicities.

Multilayer flat films and sheets can be formed by coextrusion, consisting of two layers (AB), three (such as ABA), five (such as ABCBA), and up to eleven layers. Each layer and particular multilayer configuration is selected for its contribution to one or more film/sheet product properties, such as gas barrier, adhesion, abrasion, and chemical resistance.

There are two basic methods of producing multilayer films and sheets, both using more than one extruder. The first uses a *multimanifold die*, where the different layers are separately distributed along the full width before being merged to form the multilayer just upstream from the die lips; although expensive, such coextrusion systems can accommodate polymers with very different rheological behaviors. The second uses a *single manifold* being fed by a *feed-port* system, as shown schematically in Fig. 12.30. The specific multilayer assembling is created by the feed block.

There are two important multilayer flow instability phenomena. The first is an interface that changes, migrating spatially and progressively downstream in both the x and y directions, as shown in Fig. 12.31. It has been established that this instability becomes more pronounced with increasing viscosity ratios (64). The second manifests itself with the onset of wavelike irregularities at the interface, which, because of the prevailing periodicity of below 1 μm , result in loss of see-through optical clarity (65).

Schrenk et al. (66) were among the first to report and study this interfacial instability, which they attributed to exceeding a critical value of interfacial shear stress. This criterion

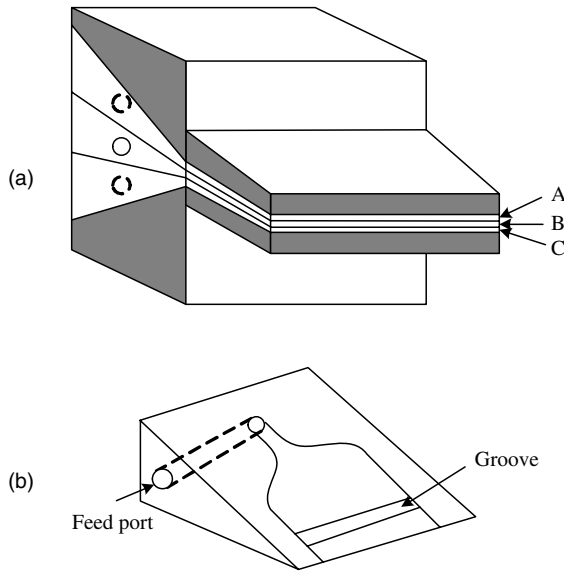


Fig. 12.30 Schematic showing the velocity profile in the three-layer coextrusion through a rectangular channel. [Reprinted by permission from C. D. Han, *Multiphase Flow in Polymer Processing*, Academic Press, New York, 1981.]

is akin to the critical wall shear stress at the onset of melt fracture. Mavridis and Shroff (65) on the other hand have shown that the adjacent layers' *difference* of the “recoverable shear” (67), that is, a difference in their elasticity, is also important and, quite possibly, controlling. Thus, this instability is a concern in the *die lip region* of multilayer flow, where the shear stress and elasticity levels are very high at the prevailing production rates.

We present briefly the two polymer melt coextrusion flow in the die lip region, following Han (64), without any of the instabilities just discussed. This flow region is

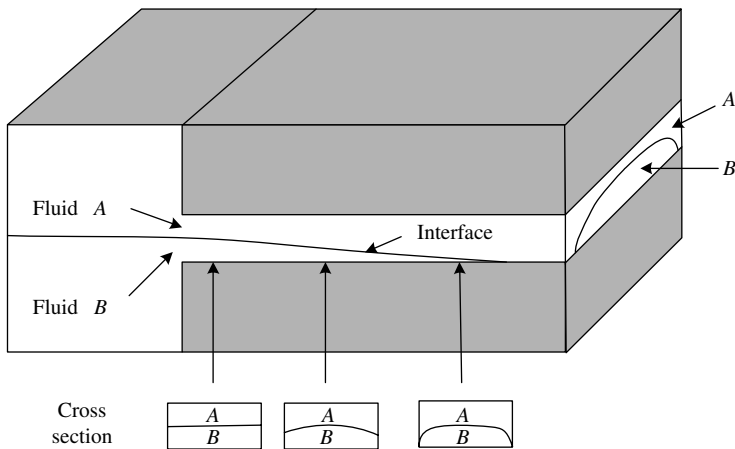


Fig. 12.31 Schematic showing the phase interface, which changes progressively as two polymer melts flow, side by side, through a rectangular channel. [Reprinted by permission from C. D. Han, *Multiphase Flow in Polymer Processing*, Academic Press, New York, 1981.]

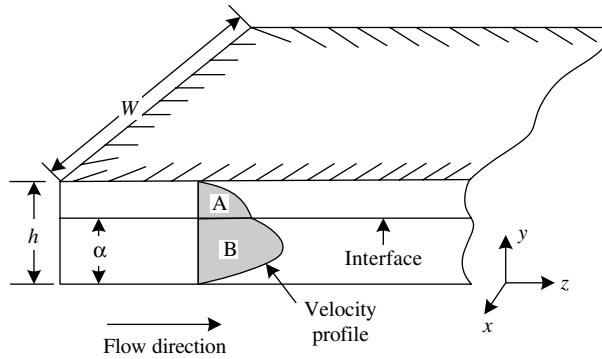


Fig. 12.32 Schematic showing the velocity profile in the two-layer coextrusion through a rectangular channel. [Reprinted by permission from C. D. Han, *Multiphase Flow in Polymer Processing*, Academic Press, New York, [1981.]

shown in Fig. 12.32. For a steady, isothermal flow of two Power Law fluids, A and B, floating in the die-lip region, where $h \ll W$, also known as a Hele–Shaw flow, there is only one velocity component $v_z = f(y)$, thus,

$$-\partial P/\partial z + \partial \tau_{yz}/\partial y = 0 \quad (12.3-13)$$

Integrating gives for phase A

$$\tau_{yz,A} = -\zeta(y - \lambda), \quad 0 \leq y \leq \alpha \quad (12.3-14)$$

and, for phase B

$$\tau_{yz,B} = -\zeta(y - \lambda), \quad \alpha \leq y \leq h \quad (12.3-15)$$

in which ζ is the pressure gradient defined by

$$\zeta = -\partial P_A/\partial z = -\partial P_B/\partial z = \text{const.} \quad (12.3-16)$$

Note that Eq. 12.3-14 implies that the pressure gradients in both phases are the same. This was verified experimentally by Yu and Han (68). Note further that λ is an integration constant, which corresponds to the position at which the maximum in velocity (and hence, the minimum in shear stress) occurs.

In order to obtain the velocity profile and then to calculate the volumetric flow rate, we use

$$\tau_{yz,A} = m_A \dot{\gamma}^{n_A} \quad (12.3-17)$$

where m_A and n_A are the Power Law constants for phase A, and $\dot{\gamma}$ is the velocity gradient defined as

$$\dot{\gamma} = \left| \frac{dv_{z,A}}{dy} \right| \quad 0 \leq y \leq \alpha \quad (12.3-18)$$

Similarly, for phase B we have

$$\tau_{yz,B} = m_B \dot{\gamma}^{n_B} \quad (12.3-19)$$

where m_B and n_B are the Power Law constants for phase B , and $\dot{\gamma}$ is the velocity gradient defined by

$$\dot{\gamma} = \left| \frac{dv_{z,B}}{dy} \right| \quad \alpha \leq y \leq h \quad (12.3-20)$$

Now, combining Eqs. 12.3-14 and 12.3-17 and integrating the resulting expression, we obtain

$$v_{z,A} = \left(\frac{\zeta}{m_A} \right)^{s_A} \left(\frac{1}{s_A + 1} \right) \left\{ \lambda^{s_A+1} - |\lambda - y|^{s_A+1} \right\} \quad 0 \leq y \leq \alpha \quad (12.3-21)$$

Similarly, combining Eqs. 12.3-15 and 12.3-19 and integrating the resulting expression, we obtain

$$v_{z,B} = \left(\frac{\zeta}{m_B} \right)^{s_B} \left(\frac{1}{s_B + 1} \right) \left\{ (h - \lambda)^{s_B+1} - (y - \lambda)^{s_B+1} \right\} \quad \alpha \leq y \leq h \quad (12.3-22)$$

where

$$s_A = 1/n_A \quad s_B = 1/n_B \quad (12.3-23)$$

It should be noted that Eqs. 12.3-21 and 12.3-22 contain a constant λ , yet to be determined with the aid of the boundary condition:

$$\text{at } y = \alpha, \quad \tau_{yz,A} = \tau_{yz,B} \quad (12.3-24)$$

That is, the equation

$$\begin{aligned} & \left(\frac{\zeta}{m_A} \right)^{s_A} \left(\frac{1}{s_A + 1} \right) \left\{ \lambda^{s_A+1} - |\lambda - \alpha|^{s_A+1} \right\} \\ & = \left(\frac{\zeta}{m_B} \right)^{s_B} \left(\frac{1}{s_B + 1} \right) \left\{ (h - \lambda)^{s_B+1} - (\alpha - \lambda)^{s_B+1} \right\} \end{aligned} \quad (12.3-25)$$

must be solved for λ . The solution of Eq. 12.3-25 requires a trial-and-error procedure, using some kind of successive iteration scheme. Note, however, that in determining the parameter λ from Eq. 12.3-25, the interface position (see Fig. 12.32) has to be specified.

The volumetric flow rates, Q_A and Q_B , can be obtained from:

$$Q_A = w \left(\frac{\zeta}{m_A} \right)^{s_A} \left(\frac{1}{s_A + 1} \right) \left\{ \lambda^{s_A+1} \alpha - \frac{\lambda^{s_A+2}}{s_A + 2} - \frac{(\alpha - \lambda)^{s_A+2}}{s_A + 2} \right\} \quad (12.3-26)$$

$$Q_B = w \left(\frac{\zeta}{m_B} \right)^{s_B} \left(\frac{1}{s_B + 1} \right) \left\{ (h - \lambda)^{s_B+1} (h - \alpha) - \frac{(h - \lambda)^{s_B+2}}{s_B + 2} + \frac{(\alpha - \lambda)^{s_B+2}}{s_B + 2} \right\} \quad (12.3-27)$$

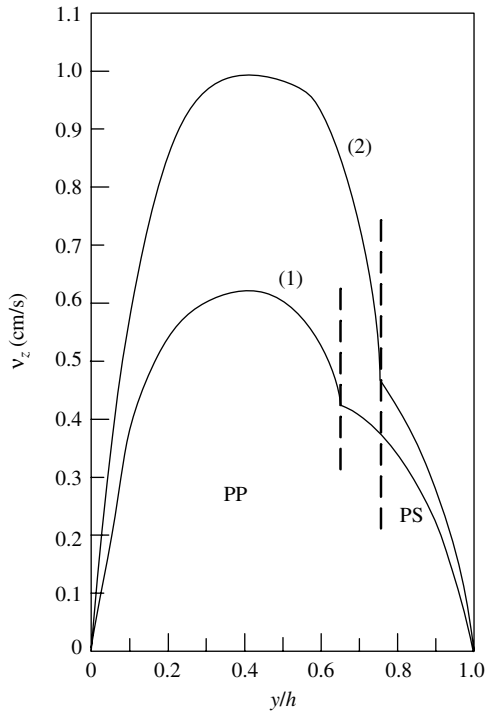


Fig. 12.33 Theoretically predicted velocity profiles in the two-layer (PP/PS) coextrusion through a rectangular channel: (1) $-\partial P/\partial z = 2.46 \times 10^7 \text{ N/m}^3$; $Q = 19.8 \text{ cm}^3/\text{min}$; (2) $-\partial P/\partial z = 2.74 \times 10^7 \text{ N/m}^3$; $Q = 26.9 \text{ cm}^3/\text{min}$; The Power Law constants used are, for PP: $m = 0.724 \times 10^4 \text{ N s}^n/\text{m}^2$, $n = 0.451$; and, for PS: $m = 2.127 \times 10^4 \text{ N s}^n/\text{m}^2$, $n = 0.301$. [Reprinted by permission from C. D. Han, *Multiphase Flow in Polymer Processing*, Academic Press, New York, 1981.]

Figure 12.33 gives velocity profiles for the PP/PS system, which were obtained with the aid of Eqs. 12.3-21 and 12.3-22, using volumetric flow rates and pressure gradients determined experimentally in a rectangular channel. Figure 12.34 gives plots of viscosity versus shear stress for the PP and PS employed. It is seen that the polymer melts obey a Power Law model for $\dot{\gamma} > 10 \text{ s}^{-1}$.

It should be pointed out that, in computing velocity profiles such as those given in Fig. 12.30, one needs information about the position of interface α (i.e., the relative layer thickness) in the die. Yu and Han (68) used computed values of the volumetric flow ratio, Q_A/Q_B , as a guide for determining the values of α by comparing them with the experimentally determined values of Q_A/Q_B . Note that Eqs. 12.3-26 and 12.3-27 yield.

$$\frac{Q_A}{Q_B} = \frac{(\zeta/m_A)^{s_A}}{(\zeta/m_B)^{s_B}} \left(\frac{s_B + 1}{s_A + 1} \right) \left\{ \frac{\lambda^{s_A+1} \alpha - [\lambda^{s_A+2}/(s_A + 2)] - [(\alpha - \lambda)^{s_A+2}/(s_A + 2)]}{(h - \lambda)^{s_B+1} (h - \alpha) - [(h - \lambda)^{s_B+2}/(s_B + 2)] + [(\alpha - \lambda)^{s_B+2}/(s_B + 2)]} \right\} \quad (12.3-28)$$

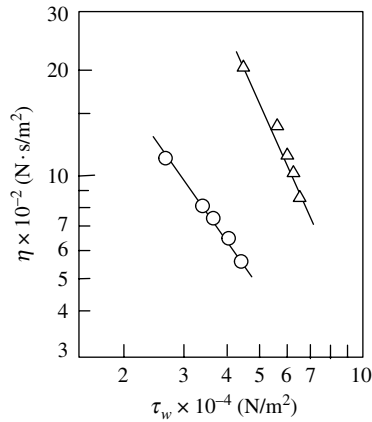


Fig. 12.34 Viscosity versus shear stress for the polymers ($T = 200^\circ\text{C}$) used in the computations that yielded the velocity profiles given in Fig. 12.30: (Δ) PS; (\circ) PP. [Reprinted by permission from C. D. Han, *Multiphase Flow in Polymer Processing*, Academic Press, New York, 1981.]

It is seen that the volumetric flow ratio Q_A/Q_B is not equal to the layer thickness ratio $\alpha/(h - \alpha)$ as one might expect. Q_A/Q_B is a complicated function that depends on the pressure gradient ζ , the Power Law constants of each phase (n_A , m_A , n_B , and m_B), and the parameters α and λ . Therefore, for a given fluid system and flow conditions, where the pressure gradient ζ and flow rates (Q_A and Q_B) are specified, the interface position α can be determined from Eq. 12.3-28, when the predicted value of Q_A/Q_B agrees with the experimentally determined one, provided Eq. 12.3-25 is satisfied. In other words, Eqs. 12.3-25 and 12.3-28 can be used for determining values of α and λ .

We now turn to the treatment of the die lip coextrusion analysis of Mavridis and Shroff (65). Their analysis treats the flow of an arbitrary number of layers of melts that are viscoelastic, flowing in a one-dimensional nonisothermal flow, shown in Fig. 12.35 and

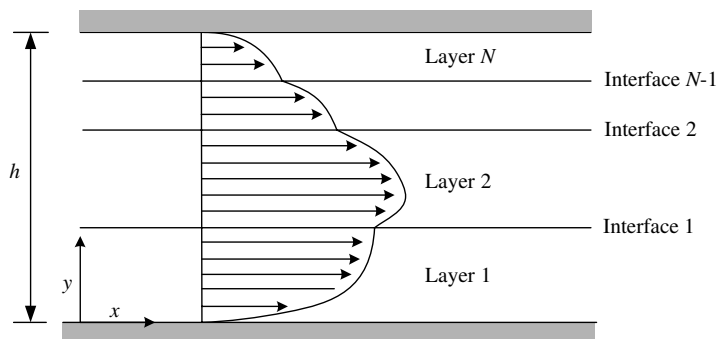


Fig. 12.35 Schematic of flow geometry in N -layer coextrusion.

described as follows:

$$Q_i = \int_{l_{i-1}}^{l_i} v_z dy \quad i = 1, \dots, N \quad (12.3-29)$$

$$\tau_{zy} = \left(-\frac{\partial P}{\partial z} \right) (y - y_{\max}) \quad (12.3-30)$$

$$\rho C_p v_z \frac{\partial T}{\partial z} = k \frac{\partial^2 T}{\partial y^2} + \eta \dot{\gamma}^2 \quad (12.3-31)$$

These equations are solved numerically under the assumptions of velocity, shear stress, and temperature continuity at all interfaces. They use the Sabia 4-parameter viscosity model (69), because of its ability to include the Newtonian plateau viscosity, which is important for multilayer extrusion, because of the existence of low shear-rate viscosities at the interfaces.

$$\ln \left(\frac{\eta}{\eta_0} \right) = \left(\frac{\eta}{\eta_0} - A \right) \ln \left[1 + \left(\frac{\dot{\gamma}}{\dot{\gamma}_0} \right)^B \right] \quad (12.3-32)$$

where the parameters η and η_0 are both temperature dependent. Furthermore, in order to explore the role of the melt elasticity of adjacent layers to the wavelike interfacial disturbances, they evaluated the discrete relaxation spectra, back-calculated from dynamic measurements. They then used the Leonov Model (70) to obtain the shear stress

$$\tau_{12}(\dot{\gamma}) = 2 \sum_i G_i \frac{\lambda_i \dot{\gamma}}{1 + X_i} \quad (12.3-33)$$

and first normal stress difference

$$\tau_{11} - \tau_{22} = \sqrt{2} \sum_i G_i \frac{X_i - 1}{(1 + X_i)^{1/2}} \quad (12.3-34)$$

where

$$X_i = (1 + 4\lambda_i^2 \dot{\gamma}^2)^{1/2} \quad (12.3-35)$$

Finally, they calculated the recoverable strain of each of the polymers used, and the difference between two adjacent layers, ΔS_R , that is, the difference in their elasticity

$$\Delta S_R = S_{R,A} - S_{R,B} = \left(\frac{\tau_{11} - \tau_{22}}{2\tau_{12}} \right)_A - \left(\frac{\tau_{11} - \tau_{22}}{2\tau_{12}} \right)_B \quad (12.3-36)$$

Three polymers were used: one grade of polyester and two grades of EVA. Furthermore, two three-layer systems were investigated: 5% polyester–90% EVA₁–5% Polyester, and 5% polyester–90% EVA₂–5% polyester. The viscosity $\eta(\dot{\gamma})$ and first normal stress

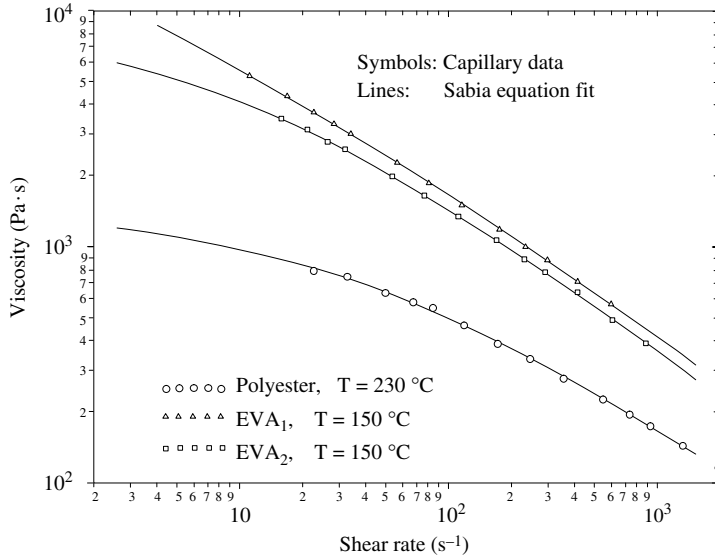


Fig. 12.36 Capillary viscosity data and Sabia equation fit. [Reprinted by permission from H. Mavridis and R. N. Shroff, “Multilayer Extrusion: Experiments and Computer Simulation,” *Polym. Eng. Sci.*, **34**, 559 (1994).]

difference $(\tau_{11} - \tau_{22})(\dot{\gamma}^2)$ of the three polymers are shown in Fig. 12.36 and Fig. 12.37. The polyester is the least viscous and least elastic of the three polymers used, and EVA₁ is more viscous and elastic than EVA₂. Three experiments were conducted with EVA₁ and three with EVA₂ at conditions that result in different interfacial stresses, with their

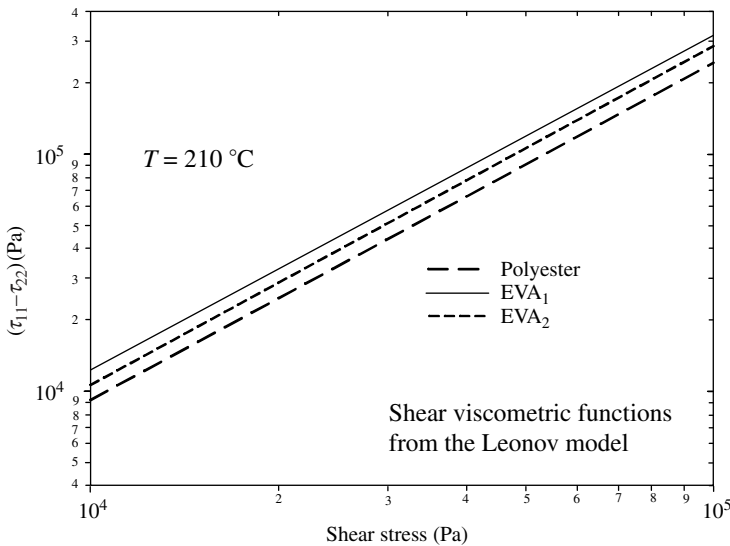


Fig. 12.37 First normal stress difference vs. shear stress, as predicted by the Leonov model. [Reprinted by permission from H. Mavridis and R. N. Shroff, “Multilayer Extrusion: Experiments and Computer Simulation,” *Polym. Eng. Sci.*, **34**, 559 (1994).]

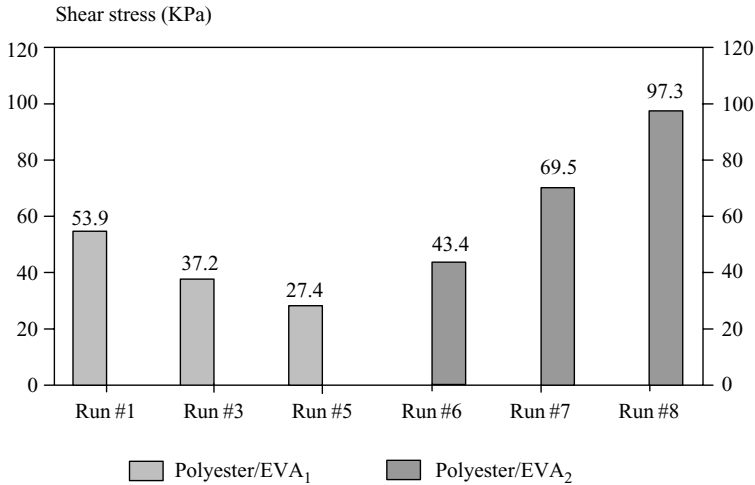


Fig. 12.38 Predicted interfacial shear stress at the polyester/EVA interface. [Reprinted by permission from H. Mavridis and R. N. Shroff, "Multilayer Extrusion: Experiments and Computer Simulation," *Polym. Eng. Sci.*, **34**, 559 (1994).]

calculated values shown in Fig. 12.38. Also, Fig. 12.39 shows the ΔS_R values at the interface for all experiments.

As mentioned previously, the "see-through" clarity of the coextruded films deteriorates with the presence and extent of the wavelike interfacial instability. Quantitative

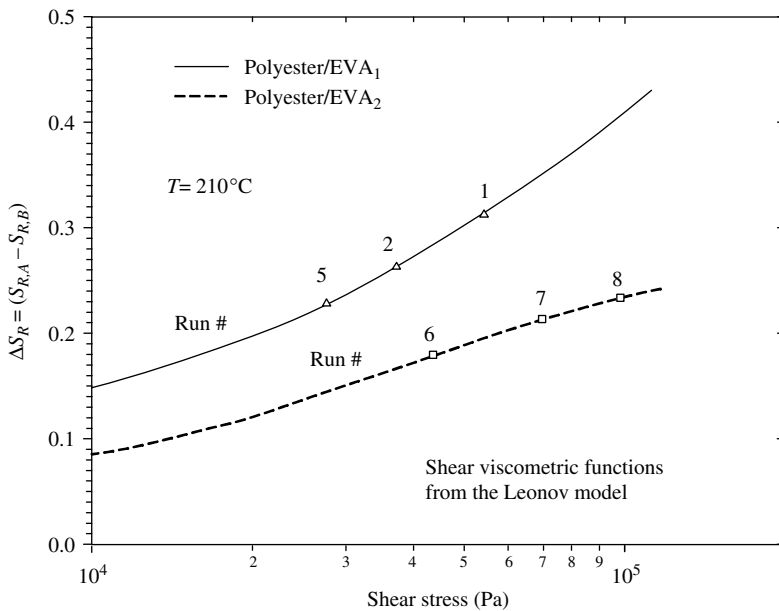


Fig. 12.39 Difference in stress ratio vs. interfacial shear stress, for polyester/EVA₁ (solid line) and polyester/EVA₂ (dashed line). [Reprinted by permission from H. Mavridis and R. N. Shroff, "Multilayer Extrusion: Experiments and Computer Simulation," *Polym. Eng. Sci.*, **34**, 559 (1994).]

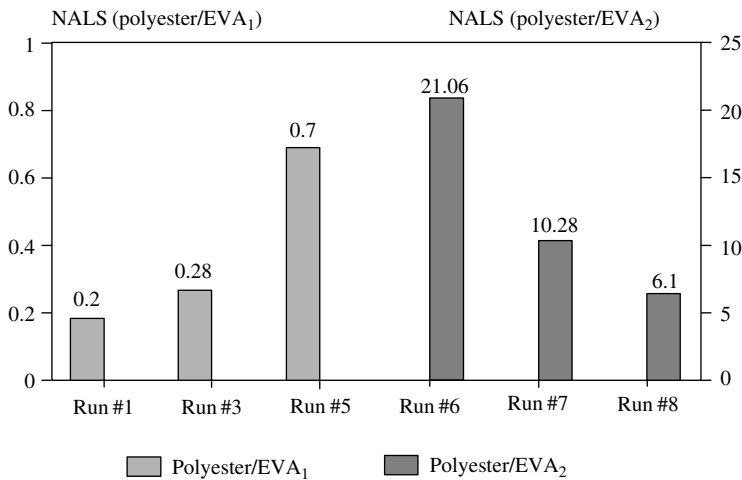


Fig. 12.40 Narrow angle scattering measurements of the coextruded films. [Reprinted by permission from H. Mavridis and R. N. Shroff, “Multilayer Extrusion: Experiments and Computer Simulation,” *Polym. Eng. Sci.*, **34**, 559 (1994).]

measures for see-through clarity are obtained with narrow-angle light-scattering (NALS) measurements of the transmittance of light through the film (ASTM D-1746). NALS values for all the experiments are shown in Fig. 12.40, with 100 denoting perfect clarity.

The NALS ratings of all the EVA₁ films are an order of magnitude lower than those with EVA₂. This cannot be explained by the Schrenk (66) criterion of a critical interfacial shear stress, as we see in Fig. 12.38. On the other hand, the differences of the recoverable strain values at the interface between polyester/EVA₁ and polyester/EVA₂ shown in Fig. 12.39 correlate better with the obtained NALS results: the higher the ΔS_R , that is, the larger the melt elasticity difference between polyester and EVA, the more severe the interfacial instability. In other words, the work of Mavridis and Shroff suggests that the instability is elastic in nature. Such insight would allow for the reduction of the instability through the in-line reactive extrusion long chain branching modification of the polyester melt, which will increase its elasticity, S_R .

The flat film and sheet coextrusion analyses mentioned earlier can be easily extended to the treatments of the wire coating and film blowing coextrusion processes.

12.4 TUBE, BLOWN FILM, AND PARISON FORMING

Plastic tube and tubular films are formed continuously by extruding a polymer through an annular die. The annular flow channel is formed by the outer die body and the die mandrel. A number of annular die designs are currently employed. In the first, the mandrel is supported mechanically onto the outer die body by a number of “fins” called “spider legs”; Fig. 12.41 illustrates this type of die. The flow is axisymmetric, and the only serious problem encountered in the cross-machine direction uniformity of the extruded product is that of “weld” lines and streaks caused by the presence of the spider legs, which split the flow.

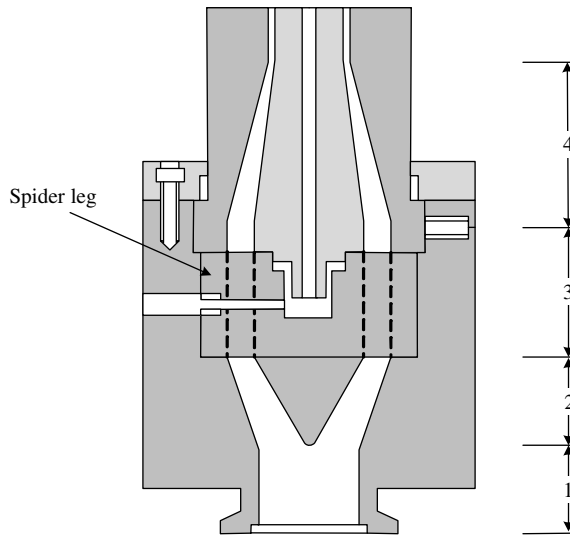


Fig. 12.41 Typical spider-type tube or blown film die.

Even though these obstacles are far away from the die lip region, the polymer melt, at normal extrusion speeds, is unable to “heal” completely. That is, the macromolecules comprising the two layers that were split by the spider legs do not establish the entanglement level characteristic of the bulk at the prevailing shear rate and temperature.

This is another ramification of incomplete response of polymers, because the “experimental time” is smaller than the relaxation time of the system of macromolecules. As expected, weld lines are mechanically weak and have optical properties that differ from those of the bulk, making them visible. Furthermore, they result in film or tube gauge nonuniformities, probably because of the different degree of swelling of the melt in the neighborhood of the weld line. They also induce cross-machine pressure nonuniformities. To overcome these problems, basic cross-head die designs (Fig. 12.42) have been devised in which the mandrel is mechanically attached to the die body in such a way that obstacles are not presented to the flow in the annular region.

Unlike the coat hanger flat film dies, no simple final film adjustment is possible by lip flexing. Consequently, the order of magnitude of thickness accuracy in tubular dies is $\pm 10\%$ as compared to $\pm 5\%$ in flat sheet and film dies. This larger margin of accuracy in blown film dies is compensated by die rotation, which permits the distribution of the thickness variation across the entire width of the product.

For flow simulation in spiral mandrel dies, software simulation packages (e.g., SPIRALCAD^(TM) by Polydynamics, Inc.) are used. The molten polymer flow is simulated from the die ports as it moves along and leaks from the spiral channels in the gap between the body and the mandrel. It predicts the flow, pressure, and temperature distributions throughout the die and the thickness variation in the final annular extruded film. Regions of heavy or light gauge film can easily be identified and design modifications made accordingly.

In the cross-head type of dies, the melt is split at the inlet to the manifold and recombines 180° from the inlet. Moreover, the flow is not axisymmetric, and fluid particles flowing around the mandrel have a longer distance to travel than those that do not.

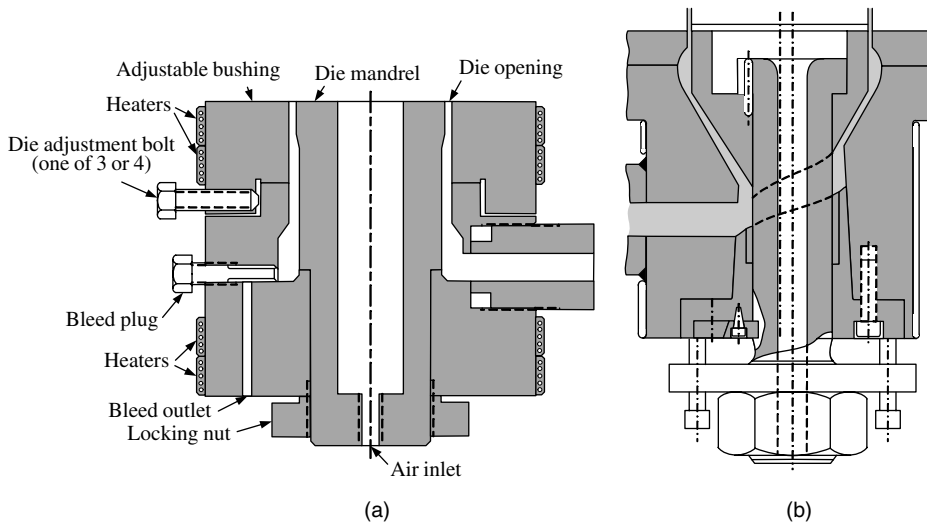


Fig. 12.42 Schematic representation of tubular dies. (a) Side-fed manifold die. (b) Blown-film die.

Consequently, if the die gap were uniform, the flow rate 180° away from the die entrance would be smaller, resulting in nonuniform thickness.

There are a number of ways to reduce this nonuniformity. The mandrel can be placed eccentrically in the die, allowing for a wider gap at the remote end from the lead port. Such a design can, in principle, provide uniform flow rate, but shear rate and temperature histories will remain nonuniform. In another solution [Fig. 12.42(b)], an insert directs the flow at the far end upward, reducing the flow length around the mandrel and eliminating slow flow (stagnant) regions. In addition, the mandrel is also eccentric.

Finally, Fig. 12.43 shows a spiral mandrel die, currently in common use for film blowing, which allows greater design flexibility in obtaining a uniform flow rate, uniform shear rate and temperature histories, and elimination of weld lines. The feed is distributed into separate flow tubes called *feed ports*. Each of these ports feeds the polymer in a spiral groove cut into the mandrel. The spiral decreases in cross-sectional area, whereas the gap between the mandrel and the die increases toward the exit. The result is a mixing or “layering” of melt originating from the various ports.

Tubes and blown films can be produced as multilayer structures by employing multiple extruders and coextrusion manifolds and dies. Figure 12.44 is a schematic representative of a conventional and new spiral coextrusion die. The designs can be used for both blown-film and blown-molding parison dies. In the extrusion of tubes, such as rigid PVC or PE pipe, the extrudate passes over a water-cooled mandrel and enters a cold-water bath whose length depends on the tube thickness; the tube leaves the bath well below its T_m (if it is crystalline) or T_g (if it is amorphous) and is sectioned to the desired lengths.

Next we discuss the problem of estimating the total pressure drop in tubular dies, and we trace the development of the die design equation.

Estimation of Pressure Drop in Tubular Dies

We know that the tubular die flow channel is composed of a series of more or less annular flow regions, which are straight, tapering, of almost uniform cross section, or interrupted

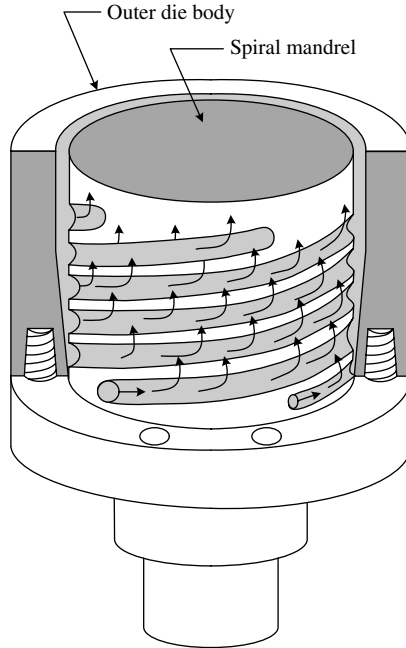


Fig. 12.43 Schematic representation of a spiral mandrel die.

by obstacles. Thus, although exact solutions of the flow in them may require numerical methods, we can arrive at a number of useful and simple engineering expressions by examining the steady isothermal flow between two straight concentric cylinders of constant radii R_o and R_i .

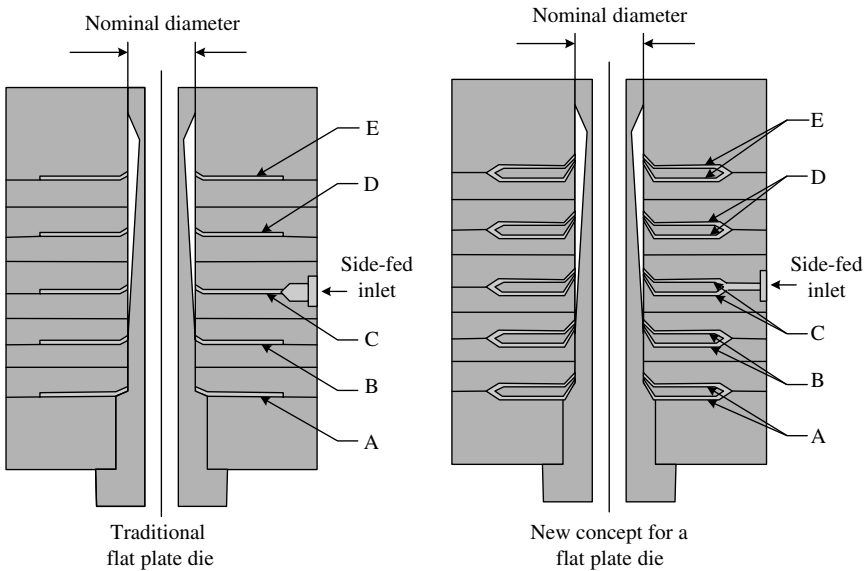


Fig. 12.44 Schematic representation of multilayer extrusion dies.

Consider the annular flow region $R_i \leq r \leq R_o$, $0 \leq z \leq L$, and $0 \leq \theta \leq 2\pi$. An incompressible Power Law fluid is flowing under steady and isothermal conditions because of the pressure drop $\Delta P = P_0 - P_L$. The flow is assumed to be fully developed. Under these assumptions the z -component momentum equation becomes

$$\frac{dP}{dz} = -\frac{1}{r} \frac{d}{dr} (r\tau_{rz}) \quad (12.4-1)$$

When Eq. 12.4-1 is coupled with the Power Law constitutive equation for this flow

$$\tau_{rz} = -m \left| \frac{dv_z}{dr} \right|^{n-1} \left(\frac{\partial v_z}{\partial r} \right) \quad (12.4-2)$$

the following expression is obtained

$$\left(\frac{r}{m} \right) \frac{dP}{dz} = \frac{d}{dr} \left(r \left| \frac{dv_z}{dr} \right|^{n-1} \frac{dv_z}{dr} \right) \quad (12.4-3)$$

Let r^* be the radial position where the velocity is maximum; that is, $dv_z/dr = 0$. Then in region I, $R_i \leq r \leq r^*$, $dv_z^I/dr \geq 0$, and Eq. 12.4-3 becomes

$$\left(\frac{r}{m} \right) \frac{dP}{dz} = \frac{d}{dr} \left[r \left(\frac{dv_z^I}{dr} \right)^n \right] \quad (12.4-4)$$

where $v_z^I(r)$ is the velocity in this region. The accompanying boundary conditions are $v_z^I(R_i) = 0$ and $dv_z^I/dr = 0$ at $r = r^*$. Similarly, in region II, $r^* \leq r \leq R_o$, $dv_z^II/dr \leq 0$, and Eq. 12.4-3 becomes

$$\left(\frac{r}{m} \right) \frac{dP}{dz} = -\frac{d}{dr} \left[r \left(-\frac{dv_z^II}{dr} \right)^n \right] \quad (12.4-5)$$

having the following boundary conditions: $v_z^II(R_o) = 0$ and $dv_z^II/dr = 0$ at $r = r^*$. Equations 12.4-4 and 12.4-5 can be directly integrated with the foregoing boundary conditions, and the location r^* can be obtained by setting $v_z^I(r^*) = v_z^II(r^*)$. This problem was solved by Fredrickson and Bird (71), and the resulting flow rate–pressure drop relationship is

$$Q = \left(\frac{\pi R_o^3}{s+2} \right) \left[\frac{R_o \Delta P}{2mL} \right]^s \left(\frac{\beta-1}{\beta} \right)^{2+s} F(n, \beta) \quad (12.4-6)$$

where $\beta = R_o/R_i$ and $F(n, \beta)$ is the shear dependency and geometry-dependent function appearing in Fig. 12.45.

For values of $0.4 \leq R_i/R_o \leq 1.0$, which represent relatively narrow annuli, the function F becomes independent of the degree of shear thinning of the melt. At the limit $\beta \rightarrow 1.0$, Table 12.2 can be used to relate the volumetric flow rate to the axial pressure drop, since the geometrical situation corresponds to the flow between parallel plates.

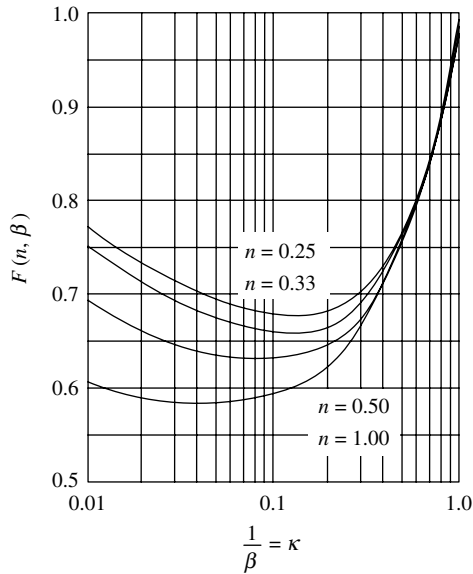


Fig. 12.45 The function $F(n, \beta)$ for the flow of Power Law fluids in an annular region. [Reprinted by permission from A. G. Fredrickson and R. B. Bird, "Non Newtonian Flow in Annuli," *Ind. Eng. Chem.*, **50**, 347(1958).]

In this case

$$Q = \left(\frac{\pi R_o^3}{s+2} \right) \left[\frac{R_o \Delta P}{2mL} \right]^s \left(\frac{\beta-1}{\beta} \right)^{2+s} \left(\frac{1+\beta}{2\beta} \right) \quad (12.4-7)$$

where in Table 12.2 $W = \pi(R_i + R_o)$. Thus, the pressure drop in straight concentric annular sections of tubular dies can be obtained fairly easily using Eq. 12.4-6 with the help of Fig. 12.40, or with Eq. 12.4-7 for very narrow annuli.

It should be recalled that, in annular pressure flows, as in all pressure flows, an error is introduced by using the Power Law model fluid because of inaccuracies in the low shear rate regions. Moreover, the assumption of isothermicity also introduces errors and can lead to an overestimation of $P_0 - P_L$.

Cox and Macosko (19) have measured increases in melt surface temperature of the order of 10° – 20°C with LDPE flowing in an $L = 0.1$ m, $R_i/R_o = 0.5$ annulus at 190°C , and Newtonian wall shear rates of about 200 s^{-1} . Such temperature increases would reduce the melt viscosity, especially near the exit of the annulus.

For tapering annular flow channels (regions 2 and 4 of the spider-type die in Fig. 12.41), we can calculate the pressure drop by making the lubrication approximation and using either Eq. 12.4-6 or Eq. 12.4-7, depending on the width of the annulus. In both cases, $\beta = \beta(z)$ and $H = H(z)$. We can use values of β and H that are averaged over the entire length, or we can solve Eq. 12.4-6 or Eq. 12.4-7 over small axial length increments ΔL_i , with corresponding β_i or H_i , then summing up the partial pressure drops. For thin tapered annuli, which can be represented by two almost parallel plates, one can use the Reynolds lubrication equation (Eq. 2.11-11).

In converging or diverging sections of annular dies, the fluid elements are subjected to axial and radial accelerations. Neglecting the radial special accelerations (for small tapers), the z -component equation of motion reduces to

$$\rho v_z \frac{\partial v_z}{\partial z} = -\frac{dP}{dz} - \left[\frac{1}{r} \frac{\partial}{\partial r} (r\tau_{rz}) + \frac{\partial \tau_{zz}}{\partial z} \right] \quad (12.4-8)$$

For very viscous fluids the inertial term $\rho v_z(\partial v_z/\partial z)$ is negligible, thus

$$\frac{dP}{dz} = -\frac{1}{r} \frac{\partial}{\partial r} (r\tau_{rz}) - \frac{\partial \tau_{zz}}{\partial z} \quad (12.4-9)$$

For converging channels the first term on the right-hand side of Eq. 12.4-9 increases with increasing axial distance, and because of this, dP/dz is not a constant but is z -dependent. For a viscous fluid, the value of $\partial \tau_{zz}/\partial z$ is given by the relation

$$\tau_{zz} = -\bar{\eta} \frac{\partial v_z}{\partial z} \quad (12.4-10)$$

A value for $\partial v_z/\partial z$ averaged over the spacing H can be used for approximate calculations. This quantity, since $q = \bar{v}_z(z)H(z)$, is

$$\frac{\partial \bar{v}_z}{\partial z} \cong \frac{\partial}{\partial z} \left(\frac{q}{H(z)} \right) = \frac{\partial}{\partial z} \left(\frac{q}{H_0 - Az} \right) = -\frac{Aq}{(H_0 - Az)^2} \quad (12.4-11)$$

where A is the taper. Considering the result of the preceding equation, as well as Eq. 12.4-10, we conclude that the contribution of the second term of the right-hand side of Eq. 12.4-9 is never zero for tapered channels. For more exact calculations, the dependence of $\partial v_z/\partial z$ on the thickness direction must be taken into account.

Worth and Parnaby (72) have considered the contribution of the elasticity of the polymer melt G to the term τ_{zz} . Using a Maxwell-type constitutive equation (Eq. 3.3-9), they find

$$\tau_{zz} - \tau_{rr} \cong \tau_{zz} = \frac{\tau_{rz}^2}{G} \quad (12.4-12)$$

Since $\tau_{zz} = f(z)$ for tapered dies, $\partial \tau_{zz}/\partial z$ is nonzero. For reasonable taper values, they find these elastic forces to contribute less than 10% of the viscous pressure drop. They have also calculated the drag and pressure forces on the mandrel.

Turning to the cross-fed tubular dies, we note that, to develop die design expressions, we must model the two-dimensional flow in the z - and θ -directions. This is a task of considerable difficulty. Pearson (73) was the first to model the flow for narrow dies. The flow region was "flattened," and the two-dimensional flow in rectangular coordinates between two plates was considered. The plate separation was allowed to vary in the approach channel so that the resulting output is constant. The final die lip opening is constant, formed by the concentric cylinders.

The resulting design equations are complicated, and their solution is computationally demanding. Nevertheless, design expressions for both Newtonian and Power Law fluids in

isothermal flow can be obtained. Gutfinger, Broyer, and Tadmor (74) solved this problem using the flow analysis network (FAN) method discussed in Chapter 13. This approximate but relatively simple numerical method is particularly well suited for two-dimensional slow flow problems in narrow gaps. The results obtained with the FAN method are identical to those of Pearson, but they can be achieved with much less computational effort.

As mentioned earlier, there is an additional role that the approach and die lip regions must play. In these regions, the polymer melt must be given an opportunity to lose all its “memory” of the cross-flow, nonuniform strain history. Worth and Parnaby (72) call these regions the “relaxation zone,” and by assuming that the melt responds as a simple linear viscoelastic Voigt fluid model, the authors calculate roughly the minimum length for a desired level of relaxation of the strains applied at the entrance.

It is worth noting that, although in principle tube and tubular blown film dies are similar, in practice they are quite different in function, size, and complexity. Blown film dies are much longer, have a very small die lip opening, and are subject to more stringent product uniformity criteria because there is no “sizing” equipment downstream. Furthermore, blown film products are almost exclusively LDPE, and occasionally HDPE and PP. On the other hand, HDPE and rigid and plasticized PVC are the common polymers for pipes and tubes.

12.5 WIRE COATING

Wire and cable coating dies are used in the extrusion process for primary insulation of single conducting wires as well as the jacketing or sheathing of a group of wires already insulated electrically, for mechanical strength and environmental protection purposes.

The bare wire is unwound, sometimes by a controlled tension device, and is preheated to a temperature above the T_g or T_m of the polymer to be extruded; this is done so that the layer next to the bare wire adheres to it, and to drive moisture or oils off the conductor surface. The wire is fed in the back of the cross-head die and into a “guider tube.” Upon exiting the guider, it meets the molten plastic, which covers it circumferentially. Since the wire speed, which is controlled by a capstan at the end of the line, is usually higher than the average melt velocity, a certain amount of “drawdown” is imposed on the melt anywhere from a value slightly greater than unity to 4.

After exiting the die, the coated wire is exposed to an air or gas flame for the purpose of surface annealing and melt relaxation, which also improves the coating gloss. It then enters a cooling trough, where the cooling medium is usually water. The length of the trough depends on the speed of the wire, the diameter of the wire or cable, and the insulation thickness; it increases with increasing level of these parameters. As expected, the cooling trough length is longer for crystalline polymers, since the crystallization process is exothermic. For undersea cables, cooling troughs not only provide for almost 300 ft of linear travel, but are also divided into several compartments containing water of successively cooler temperatures (typically of a total range 80°–100°C), to avoid fast cooling of the jacket surface, which could cause void formation or thermal stresses.¹⁰

10. Cross-linkable LDPE, used in insulating power cables, requires long residence in steam “curing tubes” 100–300 m long.

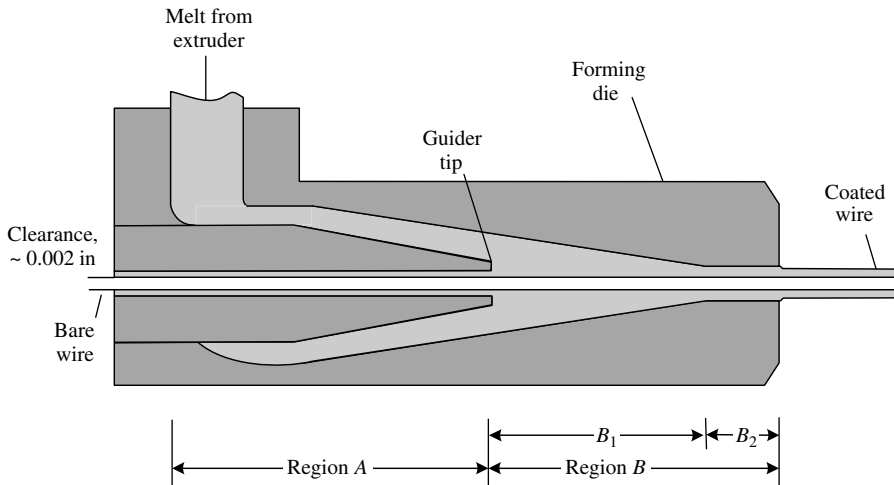


Fig. 12.46 Detailed schematic representation of the pressure type of wire-coating die.

Upon exiting the cooling trough, the wire passes over the capstan, where its tension is controlled and further cooling can be provided. It then passes through a capacitance-measuring device that detects flaws as well as thickness variations. These variations provide information for adjusting the pulling device speeds or the extruder screw speeds. Since defective wire is difficult to reprocess, because the product is a composite, the process is closely monitored. In addition, great care is taken to design the coating die properly.

Two types of cross-head dies are used for wire and cable coating. The first type is an annular flow or tubing die, where a thin-walled tube is extruded and the molten tube drawn onto the conductor by vacuum after it leaves the die. The vacuum is applied through the clearance between the conductor and the guide, which is usually of the order of 0.2 mm. Tubing dies are commonly used for jacketing cables or coating very thin wires with polymer melts that are very viscous.

The second type of cross-head die used is the “pressure” type, where the polymer melt contacts the conductor *inside* the die; Fig. 12.46 gives details of such a die. The clearance between the guide and the conductor must be quite small, of the order of 0.05 mm, because at the guide tip, the melt is under some pressure. This type of die is quite commonly used for wire coating. From a flow analysis point of view, the pressure die can be broken down into two regions, as in Fig. 12.46. The flow situation in region A is the same as that in the approach channel of side-fed tubular dies discussed in the previous section. Thus, making the lubrication approximation, the pressure drop in this region can be estimated using Eq. 12.4-6.

In region B, one of the containing walls is the conductor wire, which is moving with a high velocity V . Thus, the flow is both drag and pressure induced. In the streamline region B, the flow can be treated locally as a combined drag and pressure flow in an annulus of the local thickness (lubrication approximation). Such a flow truly exists in region B₂. Thus, solving the annular drag and pressure flow will help us in the analysis of the entire region B.

Example 12.3 The Absence of Melt Fracture in Wire Coating Let us consider the question of why the wire coating process can operate at very high wire speeds and a shear rate of $10^4\text{--}10^5\text{ s}^{-1}$, given the thin coating thicknesses, without the onset of melt fracture. Referring to the die lip region of the wire-coating die shown schematically below, consider the following specific process: $L = 10\text{ mm}$, $H = 1\text{ mm}$, $R_i = 0.5\text{ mm}$, a polymer with melt viscosity (constant) $\mu = 100\text{ Pa}\cdot\text{s}$, melt density $\rho = 750\text{ kg/m}^3$, heat capacity of the melt $C_p = 2.33 \times 10^3\text{ J/(kg}\cdot\text{K)}$, pressure difference between the exit and the entrance $\Delta P = P_{\text{ent}} - P_{\text{atm}} = 0.1\text{ MPa}$, initial melt temperature $T_0 = 200^\circ\text{C}$, activation energy: $\Delta E = 6\text{ kcal/mol} = 6 \times 4.1868\text{ kJ/mol}$, and the wire being pulled with a velocity $V = 1200\text{ m/min}$.

What will the resulting polymer coat thickness be, assuming that the solid density is 0.95 g/cc ?

Solution This flow is z -axisymmetric. We, thus, select a cylindrical coordinate system, and make the following simplifying assumptions: Newtonian and incompressible fluid with constant thermophysical properties; no slip at the wall of the orifice die; steady-state fully developed laminar flow; adiabatic boundaries; and negligible of heat conduction.

Thus:

$$q_r|_{r=R_i} = q_r|_{r=R_o} = 0 \quad \text{or} \quad \left. \frac{\partial T}{\partial r} \right|_{r=R_i} = \left. \frac{\partial T}{\partial r} \right|_{r=R_o} = 0 \tag{E12.3-1}$$

The equation of continuity with the preceding assumptions gives $\partial v_z / \partial z = 0$.

The equation of motion in the cylindrical coordinates reduces to

$$\frac{\partial P}{\partial z} = -\frac{1}{r} \frac{\partial}{\partial r} (r\tau_{rz}) \tag{E12.3-2}$$

where

$$\tau_{rz} = -\mu \frac{\partial v_z}{\partial r} \tag{E12.3-3}$$

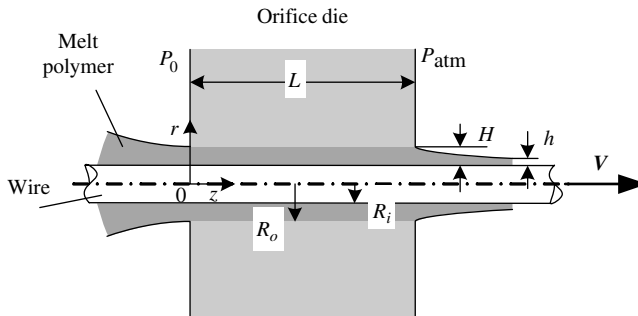


Fig. E12.3 A schematic of the die lip region of a wire coating die.

Equation E12.3-2 can be rewritten with $(\partial P/\partial z) = (\Delta P/L)$ as:

$$\frac{\Delta P}{L} = \frac{\mu}{r} \frac{\partial}{\partial r} \left(r \frac{\partial v_z}{\partial r} \right) \quad (\text{E12.3-4})$$

Integrating Eq. E12.3-4 with respect to r in company with velocity boundary conditions of $v_z|_{r=R_i} = V$ and $v_z|_{r=R_o} = 0$ gives

$$v_z(\rho) = V + (\rho^2 - 1)\Psi V - [V + (\alpha^2 - 1)\Psi V] \frac{\ln \rho}{\ln \alpha} \quad (\text{E12.3-5})$$

where $\rho = r/R_i$, $\alpha = R_o/R_i$ and the dimensionless parameter $\Psi = (R_i^2 \Delta P)/(4\mu LV)$

The equation of energy reduces to

$$\rho C_v \frac{\partial T}{\partial t} = \mu \left(\frac{\partial v_z}{\partial r} \right)^2 \quad (\text{E12.3-6})$$

Making Eq. E12.3-6 dimensionless with new variables, $u = v_z/V$, $\rho = r/R_i$, and operators $\partial/\partial r = (1/R_i)(\partial/\partial \rho)$ results in,

$$\frac{\partial T}{\partial t} = \frac{\mu}{\rho C_v} \left(\frac{V}{R_i} \right)^2 \left(\frac{\partial u}{\partial \rho} \right)^2 \quad (\text{E12.3-7})$$

where

$$u(\rho) = 1 + (\rho^2 - 1)\Psi - [1 + (\alpha^2 - 1)\Psi] \frac{\ln \rho}{\ln \alpha} \quad (\text{E12.3-8})$$

$$\frac{\partial u}{\partial \rho} = 2\rho\Psi - [1 + (\alpha^2 - 1)\Psi] \frac{1}{\rho \ln \alpha} \quad (\text{E12.3-9})$$

$$\left(\frac{\partial u}{\partial \rho} \right)^2 = \left\{ 4\Psi^2 \rho^2 - \left[\frac{4\Psi + 4(\alpha^2 - 1)\Psi^2}{\ln \alpha} \right] + \left[\frac{1 + (\alpha^2 - 1)\Psi}{\ln \alpha} \right]^2 \frac{1}{\rho^2} \right\} \quad (\text{E12.3-10})$$

Integrating Eq. E12.3-7 with respect to t can obtain the melt temperature profile of any point in the die, under the assumptions made

$$T - T_0 = \frac{\mu}{\rho C_v} \left(\frac{V}{R_i} \right)^2 \left\{ 4\Psi^2 \rho^2 + \left[\frac{1 + (\alpha^2 - 1)\Psi}{\ln \alpha} \right]^2 \frac{1}{\rho^2} - \left[\frac{4\Psi + 4(\alpha^2 - 1)\Psi^2}{\ln \alpha} \right] \right\} t \quad (\text{E12.3-11})$$

The melt residence time of each layer in the die is actually dependent of radius coordinate ρ , that is

$$t(\rho)_{\text{res}} = \frac{L}{u(\rho)V} \quad (\text{E12.3-12})$$

Inserting Eq. E12.3-12 into Eq. E12.3-11 gets the melt temperature increase of each layer of melt fluid throughout the die.

$$(T(\rho) - T_0)_{\text{exit}} = \frac{\mu L}{\rho C_v V u(\rho)} \left(\frac{V}{R_i} \right)^2 \left\{ 4\Psi^2 \rho^2 + \left[\frac{1 + (\alpha^2 - 1)\Psi}{\ln \alpha} \right]^2 \frac{1}{\rho^2} - \left[\frac{4\Psi + 4(\alpha^2 - 1)\Psi^2}{\ln \alpha} \right] \right\} \quad (\text{E12.3-13})$$

We now discuss the residence times and temperature increases of layers close to the die wall using the preceding equations: At $r = R_o - 0.1$ mm and $r = R_o - 0.01$ mm, the residence time and the temperature increase of the two layers are, respectively, 0.008 s, 77°C and 0.082 s, 704°C. On the other hand, on the core surface ($r = R_i$), the residence time is 0.0005 s, and the temperature increase only 38°C. It is obvious that the closer the melt layer is to the die wall, the residence time is longer and the melt temperature during transit increases in an exponential fashion. Despite the very high temperature increases, the residence time of the melt layers near the wall is short and much shorter than the degradation induction time $\theta(T)$ (see Fig. E5.1(a), which is for unplasticized PVC). Thus, degradation is not likely to occur, and the wall melt layer has such a small viscosity that it precludes melt fracture.

If the melt viscosity is considered as a function of temperature, then the momentum and energy equations will have to be solved simultaneously. Nevertheless, the results concerning the temperature increase of the melt layers near the wall will be only slightly different from that just given. The resulting polymer coat thickness can be calculated by equating the volumetric flow rates inside and outside the die, namely:

$$Q_{\text{inside}} = \rho_{\text{melt}} \pi R_i^2 V \left\{ \frac{(\alpha^2 - 1)}{2 \ln \alpha} - 1 + \left[\frac{(\alpha^2 - 1)}{\ln \alpha} - (\alpha^2 + 1) \right] \frac{(\alpha^2 - 1)}{2} \Psi \right\} \quad (\text{E12.3-14})$$

$$Q_{\text{onwire}} = \rho_{\text{solid}} \pi V (2R_i h + h^2) \quad (\text{E12.3-15})$$

Solving for h , the polymer melt-coating thickness, we obtain $h = 0.45$ mm. Thus, taking into account the density increase upon solidification, the solid polymer coat thickness is $h_s = 0.37$ mm.

12.6 PROFILE EXTRUSION

Profiles are all extruded articles having a cross-sectional shape that differs from that of a circle, an annulus, or a very wide and thin rectangle (flat film or sheet). The cross-sectional shapes are usually complex, which, in terms of solving the flow problem in profile dies, means complex boundary conditions. Furthermore, profile dies are of nonuniform thickness, raising the possibility of transverse pressure drops and velocity components, and making the prediction of extrudate swelling for viscoelastic fluids very difficult. For these reasons, profile dies are built today on a trial-and-error basis, and final product shape is achieved with “sizing” devices that act on the extrudate after it leaves the profile die.

The problem of steady, isothermal flow in straight axis channels of noncircular cross section has received considerable theoretical attention. The results of such studies (usually numerical solutions) indicate that, for Newtonian fluids, flow involving the axial velocity component alone satisfies the equations of continuity and motion (75–77).

The same statement can be made about *inelastic* non-Newtonian fluids, such as the Power Law fluid, from a mathematical solution point of view. In reality, most non-Newtonian fluids are viscoelastic and exhibit normal stresses. For fluids such as those (i.e., fluids described by constitutive equations that predict normal stresses for viscometric flows), theoretical analyses have shown that secondary flows are created inside channels of nonuniform cross section (78,79). Specifically it can be shown that a zero second normal stress difference is a necessary (but not sufficient) condition to ensure the absence of secondary flow (79). Of course, the analyses of flows in noncircular channels in terms of constitutive equations—which, strictly speaking, hold only for viscometric flows—are expected to yield qualitative results only. Experimentally low Reynolds number flows in noncircular channels have not been investigated extensively. In particular, only a few studies have been conducted with fluids exhibiting normal stresses (80,81). Secondary flows, such as vortices in rectangular channels, have been observed using dyes in dilute aqueous solutions of polyacrylamide. Interestingly, these secondary flow vortices (if they exist) seem to have very little effect on the flow rate.

Let us examine more closely some of the problems that arise in designing profile extrusion dies whose origin is to be found in the flow patterns. We consider the square-tube flow patterns calculated for a Power Law fluid of $n = 0.5$ (Fig. 12.47). Although the velocity profiles are symmetric, they are still θ -dependent, θ being the angle in the

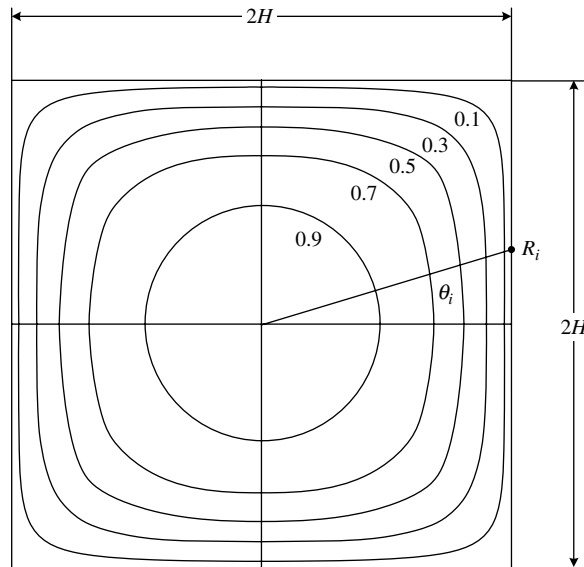


Fig. 12.47 Isovelocity contours v/V_0 of a power law fluid flowing in a square channel, $n = 0.5$. [Reprinted by permission from F. Röthemeyer, *Kunststoffe*, **59**, 333 (1969).]

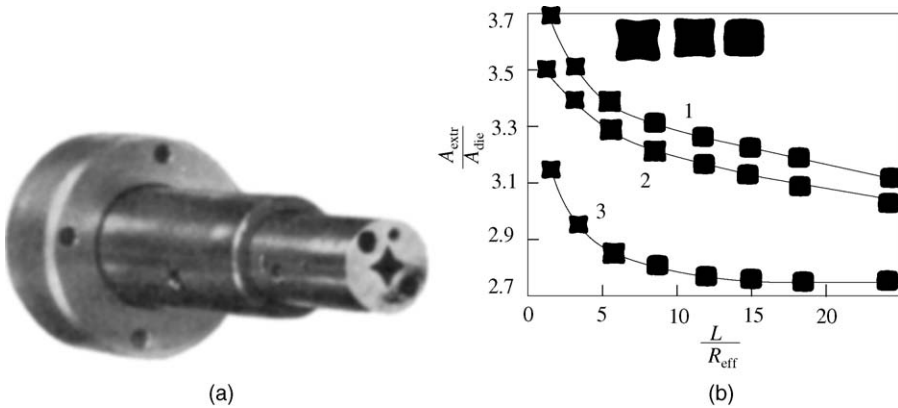


Fig. 12.48 (a) Profile die shape used in obtaining the results in (b). (b) Plot of A_{extr}/A_{die} vs. L/R_{eff} for LDPE, $R_{eff} = (2A_{die}/\text{perimeter of die})$. Curve 1, $T = 196^\circ\text{C}$, $\Gamma_{eff} = 40/\pi R_{eff}^3 = 79 \text{ s}^{-1}$; Curve 2, $T = 189^\circ\text{C}$, $\Gamma_{eff} = 56 \text{ s}^{-1}$; Curve 3, $T = 180^\circ\text{C}$, $\Gamma_{eff} = 30 \text{ s}^{-1}$. [Reprinted by permission from F. Röhthemyer, *Kunststoffe*, **59**, 333 (1969).]

cross-sectional plane. Furthermore, it is evident that the velocity gradient dv_z/dr , where r is an “effective radius” coordinate, also depends on the angle θ . Therefore, in each quadrant, for every value of the angle θ , there is a different velocity gradient variation with r . At $\theta = 0$ and $\theta = \pi/2$, the velocity gradients are high, since $r = H$, while at $\theta = \pi/4$, where $r = \sqrt{2}H$, the velocity gradients are small. It follows then that, if a polymer melt were flowing in a channel of square cross section, the extrudate would *swell more* at the vicinity of the center than of its sides, because of the high prevailing shear rates; the resulting extrudate shape would then show a “bulge” outward at the sides.

What is important from a die-designing point of view is that the cross-sectional shapes of the die and the extrudates are *different*. Simply put, to produce a square cross-section extrudate, one needs a die that looks like a four-cornered star [Fig. 12.48(a)], whose sides are concave. The curvature of the walls of the die used depends on the variation of extrudate swelling with shear stress for the polymer used. The differences in the shapes and magnitudes of the cross-sectional areas are primarily due to the θ -dependence of the degree of extrudate swelling.

As Fig. 12.48(b) indicates, the degree of swelling and the shape of the extrudate vary with increasing L/D of the die. First, the ratio of areas of the extrudate and the die decreases with increasing L/R_{eff} ; this effect was also observed with circular dies. It is again attributed to the loss of memory by the melt of the entrance deformations.

The second effect is quite interesting and significant. At very short L/R_{eff} values, a though the degree of swelling is large, the extrudate shape is closer to that of the die than it is at large L/R_{eff} values. The reason for this phenomenon is the following: at short capillary lengths, the stress field is probably not fully established, at least as far as establishing reasonable shear strains that are independent of the axial distance, thus the effects of the varying velocity gradients and recoverable strains at the various θ_i are not fully felt. Furthermore, at short L/R_{eff} values, entrance tensile strains predominate and mark the effects of the θ -dependent flow and recoverable shear strain fields. From a die design point of view, though, it seems that short profile dies,

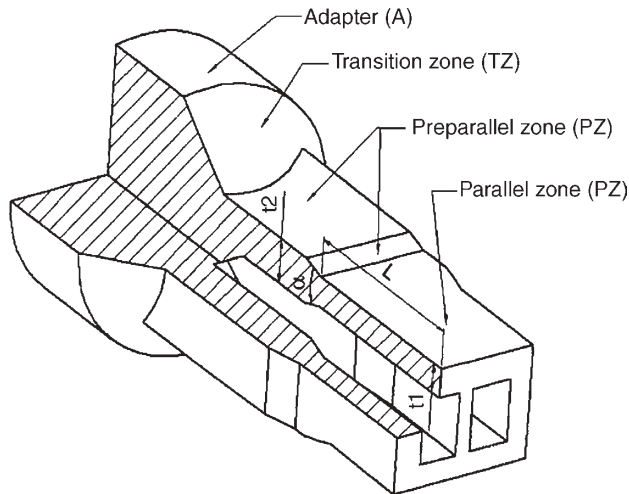


Fig. 12.49 Flow channel of a profile extrusion die: identification of its main zones and geometrical controllable parameters considered in the definition of the preparallel zone (PPZ).

in addition to resulting in small pressure drops, also form extrudates of shapes closer to that of the die.

Streamlining of the complex profile dies is as necessary as with any other die shape, but obviously more difficult. For this reason, plate dies (82) made up of thin plates inserted in a die housing one behind the other, are common. The channel cross-sections in the individual plates differ in such a way as to streamline the polymer melt into the final plate. This construction makes both die modifications and die machining easier. In such complex dies, even approximate design expressions have not been developed yet; in practice, the repeated filing off of metal in the approach plates achieves the desired shape.

The availability of powerful three-dimensional flow computer simulation packages and personal computers capable of handling them is gradually transforming profile die design from an empirical trial-and-error process to one where design optimization benefits from computational results. Sebastian and Rakos (83) were the first to utilize realistic computational fluid-mechanical results in the design of profile dies.

Siencz et al. (84,85), and Nóbrega et al. (86,87) divided a given profile die into distinct axial zones, each having variable and controllable geometric parameters, as shown in Fig. 12.49. Furthermore, after carrying out the three-dimensional nonisothermal flow simulation for a given geometry, the “quality” of the result was assessed through the use of an *objective function*, in which for Nóbrega et al. (86), combines two criteria: the flow balance and the segment length to metal thickness ratio (L/t). Two optimization methods are then utilized to arrive at the optimal profile die geometry: the SIMPLEX method and one that starts with a trial geometry, suggested by the mold maker, taking advantage of relevant experience, together with mesh refinement, to arrive at an optimal profile die geometry. Computational results are shown in Fig. 12.50.

Although such numerical die design optimization techniques significantly improve the flow uniformity and reduce the level of internal stresses leading to extrudate distortion,

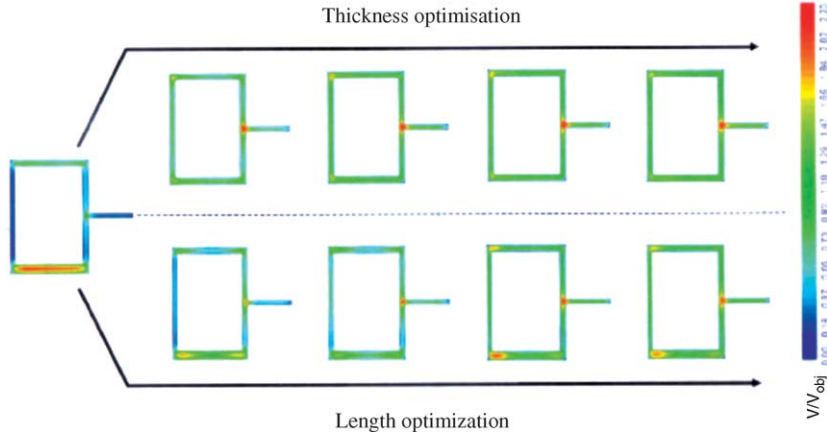


Fig. 12.50 Contours of the ratio V/V_{obj} corresponding to some steps of the optimization procedure employed by Nóbrega et al. (86,87) [Reprinted by permission from J. M. Nóbrega, O. S. Carneiro, P. J. Oliveira, F. T. Pinho, “Flow Balancing in Extrusion Dies for Thermoplastic Profiles, Part III Experimental Extrusion,” *Intern. Polym. Process.*, **19**, 225 (2004).]

they still have to be combined with final experimental geometry adjustments. Furthermore, the viscoelastic profile extrudate swelling is not addressed, requiring further geometry adjustments, as discussed earlier. Thus, the net gain in using computational die designs is the elimination of some or many trial-and-error geometries from the initial to the final versions.

Before closing this chapter, we feel that it is useful to list in tabular form some isothermal pressure–flow relationships commonly used in die flow simulations. Tables 12.1 and 12.2 deal with flow relationships for the parallel-plate and circular tube channels using Newtonian (N), Power Law (P), and Ellis (E) model fluids. Table 12.3 covers concentric annular channels using Newtonian and Power Law model fluids. Table 12.4 contains volumetric flow rate–pressure drop (die characteristic) relationships only, which are arrived at by numerical solutions, for Newtonian fluid flow in eccentric annular, elliptical, equilateral, isosceles triangular, semicircular, and circular sector and conical channels. In addition, Q versus ΔP relationships for rectangular and square channels for Newtonian model fluids are given. Finally, Fig. 12.51 presents shape factors for Newtonian fluids flowing in various common shape channels. The shape factor M_0 is based on parallel-plate pressure flow, namely,

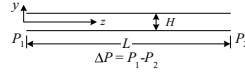
$$Q_{ch} = Q_{pp}M_0 \tag{12.6-1}$$

where

$$Q_{pp} = \frac{\Delta P B d^3}{12\mu L} \tag{12.6-2}$$

Q_{ch} is the volumetric flow rate in any of the channels appearing in the figure and B and d are specified for each channel in the figure.

TABLE 12.1 Parallel-Plate Pressure Flow:



$(\mathbb{N})^a \tau_{yz} = -\mu \frac{dv_z}{dy}$	$(\mathbb{P})^a \tau_{yz} = -m \left \frac{dv_z}{dy} \right ^{n-1} \frac{dv_z}{dy}$
$\tau_{yz}(y) = \left(\frac{\Delta P}{L} \right) y$	$\tau_{yz}(y) = \left(\frac{\Delta P}{L} \right) y$
$\tau_w = \tau_{yz} \left(\frac{H}{2} \right) = \frac{H \Delta P}{2L}$	$\tau_w = \tau_{yz} \left(\frac{H}{2} \right) = \frac{H \Delta P}{2L}$
$-\dot{\gamma}_{yz}(y) = \left(\frac{\Delta P}{\mu L} \right) y$	$-\dot{\gamma}_{yz}(y) = \left(\frac{\Delta P}{mL} y \right)^s \quad y \geq 0$
$\dot{\gamma}_w = -\dot{\gamma}_{yz} \left(\frac{H}{2} \right) = \frac{H \Delta P}{2\mu L}$	$\dot{\gamma}_w = -\dot{\gamma}_{yz} \left(\frac{H}{2} \right) = \left(\frac{H \Delta P}{2mL} \right)^s$
$v_z(y) = \frac{H^2 \Delta P}{8\mu L} \left[1 - \left(\frac{2y}{H} \right)^2 \right]$	$v_z(y) = \frac{H}{2(s+1)} \left(\frac{H \Delta P}{2mL} \right)^s \left[1 - \left(\frac{2y}{H} \right)^{s+1} \right] \quad y \geq 0$
$v_z(0) = v_{\max} = \frac{H^2 \Delta P}{8\mu L}$	$v_z(0) = v_{\max} = \frac{H}{2(s+1)} \left(\frac{H \Delta P}{2mL} \right)^s$
$\langle v_z \rangle = \frac{2}{3} v_{\max}$	$\langle v_z \rangle = \left(\frac{s+1}{s+2} \right) v_{\max}$
$Q = \frac{WH^3 \Delta P}{12\mu L}$	$Q = \frac{WH^2}{2(s+2)} \left(\frac{H \Delta P}{2mL} \right)^s$

$$(\mathbb{E})^a \tau_{yz} = -\eta(\tau) \frac{dv_z}{dy} \quad \eta(\tau) = \frac{\eta_0}{1 + (\tau/\tau_{1/2})^{\alpha-1}} \quad \tau = |\tau_{yz}|$$

$$\tau_{yz}(y) = \left(\frac{\Delta P}{L} \right) y$$

$$\tau_w = \tau_{yz} \left(\frac{H}{2} \right) = \frac{H \Delta P}{2L}$$

$$-\dot{\gamma}_{yz}(y) = \left(\frac{\Delta P}{\eta_0 L} \right) y \left[1 + \left(\frac{\Delta P y}{\tau_{1/2} L} \right)^{\alpha-1} \right]$$

$$\dot{\gamma}_w = -\dot{\gamma}_{yz} \left(\frac{H}{2} \right) = \frac{H \Delta P}{2\eta_0 L} \left[1 + \left(\frac{H \Delta P}{2\tau_{1/2} L} \right)^{\alpha-1} \right]$$

$$v_z(y) = \frac{H^2 \Delta P}{8\eta_0 L} \left\{ \left[1 - \left(\frac{2y}{H} \right)^2 \right] + \left(\frac{2}{1+\alpha} \right) \left(\frac{H \Delta P}{2L\tau_{1/2}} \right)^{\alpha-1} \left[1 - \left(\frac{2y}{H} \right)^{\alpha+1} \right] \right\}$$

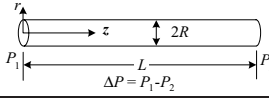
$$v_z(0) = v_{\max} = \frac{H^2 \Delta P}{8\eta_0 L} \left[1 + \left(\frac{2}{1+\alpha} \right) \left(\frac{H \Delta P}{2L\tau_{1/2}} \right)^{\alpha-1} \right]$$

$$\langle v_z \rangle = \frac{2}{3} v_{\max} \left[1 + \left(\frac{3}{2+\alpha} \right) \left(\frac{H \Delta P}{2L\tau_{1/2}} \right)^{\alpha-1} \right] / \left[1 + \left(\frac{2}{1+\alpha} \right) \left(\frac{H \Delta P}{2L\tau_{1/2}} \right)^{\alpha-1} \right]$$

$$Q = \frac{WH^3 \Delta P}{12\eta_0 L} \left[1 + \left(\frac{3}{2+\alpha} \right) \left(\frac{H \Delta P}{2L\tau_{1/2}} \right)^{\alpha-1} \right]$$

^a (\mathbb{N}) Newtonian fluid; (\mathbb{P}) Power Law model fluid; (\mathbb{E}) Ellis fluid.

TABLE 12.2 Circular-Tube Pressure Flow:



$\textcircled{N} \tau_{rz} = -\mu \frac{dv_z}{dr}$	$\textcircled{P} \tau_{rz} = -m \left \frac{dv_z}{dr} \right ^{n-1} \frac{dv_z}{dr}$
$\tau_{rz}(r) = \left(\frac{\Delta P}{2L} \right) r$ $\tau_w = \tau_{rz}(R) = \frac{R\Delta P}{2L}$ $-\dot{\gamma}_{rz}(r) = \left(\frac{\Delta P}{2\mu L} \right) r$ $\dot{\gamma}_w = -\dot{\gamma}_{rz}(R) = \frac{R\Delta P}{2\mu L}$ $v_z(r) = \frac{R^2 \Delta P}{4\mu L} \left[1 - \left(\frac{r}{R} \right)^2 \right]$ $v_z(0) = v_{\max} = \frac{R^2 \Delta P}{4\mu L}$ $\langle v_z \rangle = \frac{1}{2} v_{\max}$ $Q = \frac{\pi R^4 \Delta P}{8\mu L}$	$\tau_{rz}(r) = \left(\frac{\Delta P}{2L} \right) r$ $\tau_w = \tau_{rz}(R) = \frac{R\Delta P}{2L}$ $-\dot{\gamma}_{rz}(r) = \left(\frac{\Delta P r}{2mL} \right)^s$ $\dot{\gamma}_w = -\dot{\gamma}_{rz}(R) = \left(\frac{R\Delta P}{2mL} \right)^s$ $v_z(r) = \frac{R}{1+s} \left(\frac{R\Delta P}{2mL} \right)^s \left[1 - \left(\frac{r}{R} \right)^{s+1} \right]$ $v_z(0) = v_{\max} = \frac{R}{1+s} \left(\frac{R\Delta P}{2mL} \right)^s$ $\langle v_z \rangle = \left(\frac{s+1}{s+3} \right) v_{\max}$ $Q = \frac{\pi R^3}{s+3} \left(\frac{R\Delta P}{2mL} \right)^s$

$\textcircled{E} \tau_{rz} = -\eta(\tau) \frac{dv_z}{dr}$	$\eta(\tau) = \frac{\eta_0}{1 + (\tau/\tau_{1/2})^{\alpha-1}} \quad \tau = \tau_{rz} $
$\tau_{rz}(r) = \left(\frac{\Delta P}{2L} \right) r$ $\tau_w = \tau_{rz}(R) = \frac{R\Delta P}{2L}$ $-\dot{\gamma}_{rz}(r) = \left(\frac{\Delta P}{2\eta_0 L} \right) r \left[1 + \left(\frac{\Delta P r}{2\tau_{1/2} L} \right)^{\alpha-1} \right]$ $\dot{\gamma}_w = -\dot{\gamma}_{rz}(R) = \frac{R\Delta P}{2\eta_0 L} \left[1 + \left(\frac{R\Delta P}{2\tau_{1/2} L} \right)^{\alpha-1} \right]$ $v_z(r) = \frac{R^2 \Delta P}{4\eta_0 L} \left\{ \left[1 - \left(\frac{r}{R} \right)^2 \right] + \left(\frac{2}{1+\alpha} \right) \left(\frac{R\Delta P}{2L\tau_{1/2}} \right)^{\alpha-1} \left[1 - \left(\frac{r}{R} \right)^{\alpha+1} \right] \right\}$ $v_z(0) = v_{\max} = \frac{R^2 \Delta P}{4\eta_0 L} \left[1 + \left(\frac{2}{1+\alpha} \right) \left(\frac{R\Delta P}{2L\tau_{1/2}} \right)^{\alpha-1} \right]$ $\langle v_z \rangle = \frac{1}{2} v_{\max} \left[1 + \left(\frac{4}{3+\alpha} \right) \left(\frac{R\Delta P}{2L\tau_{1/2}} \right)^{\alpha-1} \right] \bigg/ \left[1 + \left(\frac{2}{1+\alpha} \right) \left(\frac{R\Delta P}{2L\tau_{1/2}} \right)^{\alpha-1} \right]$ $Q = \frac{\pi R^4 \Delta P}{8\eta_0 L} \left[1 + \left(\frac{4}{3+\alpha} \right) \left(\frac{R\Delta P}{2L\tau_{1/2}} \right)^{\alpha-1} \right]$	

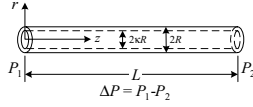


TABLE 12.3 Concentric Annular Pressure Flow:

$$\textcircled{N}^a \quad \tau_{rz} = -\mu \frac{dv_z}{dr}$$

$$\tau_{rz}(r) = \frac{\Delta PR}{2L} \left[\left(\frac{r}{R} \right) - \left(\frac{1 - \kappa^2}{2 \ln(1/\kappa)} \right) \left(\frac{R}{r} \right) \right]$$

$$-\dot{\gamma}_{rz}(r) = \frac{\Delta PR}{2\mu L} \left[\left(\frac{r}{R} \right) - \left(\frac{1 - \kappa^2}{2 \ln(1/\kappa)} \right) \left(\frac{R}{r} \right) \right]$$

$$\tau_{w1} = \tau_{rz}(R) = \frac{\Delta PR}{2L} \left[1 - \frac{1 - \kappa^2}{2 \ln(1/\kappa)} \right]$$

$$\tau_{w2} = \tau_{rz}(\kappa R) = \frac{\Delta PR}{2L} \left[\kappa - \frac{1 - \kappa^2}{2 \ln(1/\kappa)} \left(\frac{1}{\kappa} \right) \right]$$

$$\dot{\gamma}_{w1}(r) = -\dot{\gamma}_{rz}(R) = \frac{\Delta PR}{2\mu L} \left[1 - \left(\frac{1 - \kappa^2}{2 \ln(1/\kappa)} \right) \right]$$

$$\dot{\gamma}_{w2}(r) = -\dot{\gamma}_{rz}(\kappa R) = \frac{\Delta PR}{2\mu L} \left[\kappa - \left(\frac{1 - \kappa^2}{2 \ln(1/\kappa)} \right) \left(\frac{1}{\kappa} \right) \right]$$

$$v_z(r) = \frac{\Delta PR^2}{4\mu L} \left[1 - \left(\frac{r}{R} \right)^2 + \left(\frac{1 - \kappa^2}{2 \ln(1/\kappa)} \right) \ln \left(\frac{r}{R} \right) \right]$$

$$v_z(\lambda R) = v_{\max} = \frac{\Delta PR^2}{4\mu L} \{ 1 - (\lambda^2) [1 - \ln(\lambda^2)] \} \quad \lambda^2 = \frac{1 - \kappa^2}{2 \ln(1/\kappa)}$$

$$\langle v_z \rangle = \frac{\Delta PR^2}{8\mu L} \left[(1 + \kappa^2) - \left(\frac{1 - \kappa^2}{2 \ln(1/\kappa)} \right) \right]$$

$$Q = \frac{\pi \Delta PR^4}{8\mu L} \left[(1 - \kappa^4) - \frac{(1 - \kappa^2)^2}{2 \ln(1/\kappa)} \right]$$

$$\textcircled{P}^b \quad \tau_{rz} = -m \left| \frac{dv_z}{dr} \right|^{n-1} \left(\frac{dv_z}{dr} \right) \quad \rho = \frac{r}{R} \quad s = \frac{1}{n} \quad \tau_{rz}(\lambda R) = 0$$

$$v_z^I(r) = R \left(\frac{\Delta PR}{2mL} \right)^s \int_{\kappa}^{\rho} \left(\frac{\lambda^2}{\rho} - \rho \right)^s d\rho \quad \kappa \leq \rho \leq \lambda$$

$$v_z^{II}(r) = R \left(\frac{\Delta PR}{2mL} \right)^s \int_{\kappa}^{\rho} \left(\rho - \frac{\lambda^2}{\rho} \right)^s d\rho \quad \lambda \leq \rho \leq 1$$

λ is evaluated numerically for the preceding equations using the boundary condition.

$$v_z^I(\lambda R) = v_z^{II}(\lambda R)$$

$$Q = \frac{\pi R^3}{s + 2} \left(\frac{R \Delta P}{2mL} \right)^s (1 - \kappa)^{s+2} F_1(n, \kappa)$$

$F_1(n, \kappa) = F(n, \beta)$ is given in graphical form in Fig. 12.45, when $\kappa = 1/\beta$.
 Very thin annuli ($\kappa \rightarrow 1$), $F_1(n, \kappa) \rightarrow 1$

TABLE 12.3 (Continued)

$$\textcircled{E}^c \tau_{rz} = -\eta(\tau) \frac{dv_z}{dr} \quad \eta(\tau) = \frac{\eta_0}{1 + (\tau/\tau_{1/2})^{\alpha-1}} \quad \tau = |\tau_{rz}|$$

$$Q = \frac{\tau_{1/2} \pi R^3}{\eta_0} \left\{ \frac{\Delta PR}{2\tau_{1/2}} \left[\lambda^4 \ln \frac{1}{\kappa} - \lambda^2 (1 - \kappa^2) + \frac{1}{4} (1 - \kappa^4) \right] + \left(\frac{\Delta PR}{2\tau_{1/2}} \right)^\alpha \left(\sum_{i=0}^{\alpha-1} \varepsilon_{i, i \neq (\alpha+3)/2} \lambda^{2i} + F \lambda^{\alpha+3} \right) \right\}$$

$$\varepsilon_i = \binom{\alpha+1}{i} (-1)^i \left(\frac{1 + (-1)^{\alpha} \kappa^{\alpha+3-2i}}{\alpha+3-2i} \right)$$

$$F = \binom{\alpha+1}{(\alpha-1)/2} (-1)^{(\alpha-1)/2} \ln \left(\frac{1}{\kappa} \right) \quad \alpha \text{ odd}$$

$$F = 2 \sum_{i=0}^{\alpha/2-1} \binom{\alpha+1}{i} (-1)^i \left(\frac{1}{2i-\alpha+1} \right) \quad \alpha \text{ even}$$

$$\textcircled{E} \tau_{rz} = -\eta(\tau) \frac{dv_z}{dr} \quad \eta(\tau) = \frac{\eta_0}{1 + (\tau/\tau_{1/2})^{\alpha-1}} \quad \tau = |\tau_{rz}|$$

Approximately^d

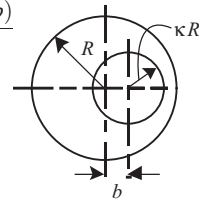
$$Q = \frac{\pi R^4 \Delta P \varepsilon^3}{6\eta_0 L} \left[1 + \frac{3}{\alpha+2} \left(\frac{\Delta P \varepsilon R}{2\tau_{1/2} L} \right)^{\alpha-1} \right] \left(1 - \frac{1}{2} \varepsilon + \frac{1}{60} \varepsilon^2 + \dots \right)$$

where $\varepsilon = 1 - \kappa$. This approximate solution is valid for $\kappa > 0.6$

TABLE 12.4 Flows in Selected Conduits

Ⓝ Eccentric annulus pressure flow^a

$$Q = \frac{\pi \Delta P}{8\mu L} \left\{ R^4 (1 - \kappa^4) - \frac{(R + \kappa R + b)(R + \kappa R - b)(R - \kappa R + b)(R - \kappa R - b)}{\delta - \omega} - 4b^2 \kappa^2 R^2 \left[1 + \frac{\kappa^2 R^4}{(R^2 - b^2)} + \frac{\kappa^4 R^8}{[(R^2 - b^2)^2 - \kappa^2 R^2 b^2]} + \dots \right] \right\}$$



where

$$\omega = \frac{1}{2} \ln \frac{F + M}{F - M} \quad \delta = \frac{1}{2} \ln \frac{F - b + M}{F - b - M}$$

$$F = \frac{R^2 - \kappa R^2 + b^2}{2b} \quad M = \sqrt{F^2 - R^2}$$

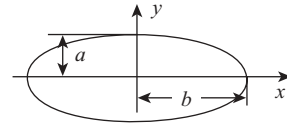
(Continued)

TABLE 12.4 (Continued)

Ⓝ Elliptical channel pressure flow^a

$$v_z(x, y) = \frac{\Delta P a^2 b^2}{2\mu L(a^2 + b^2)} \left(1 - \frac{x^2}{b^2} - \frac{y^2}{a^2} \right)$$

$$Q = \frac{\pi \Delta P}{4\mu L} \frac{a^3 b^3}{a^2 + b^2}$$



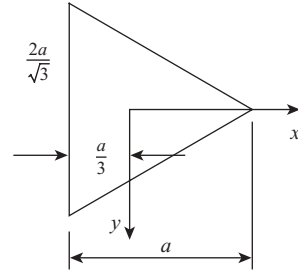
Ⓝ Triangular channel pressure flow

1. Equilateral triangle^a

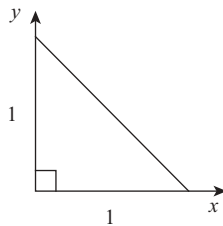
$$v_z(x, y) = -\frac{\Delta P}{4a\mu L} \left[x^3 - 3xy^2 - a(x^2 + y^2) + \frac{4}{27}a^3 + \dots \right]$$

$$Q = \frac{\Delta P a^4}{20\sqrt{3}\mu L}$$

$$\frac{Q_{\text{e.t.}}}{Q_{\text{tube}} \Big|_{\text{equal area}}} = 0.72552 \quad \frac{a^2}{\sqrt{3}} = \pi R^2$$



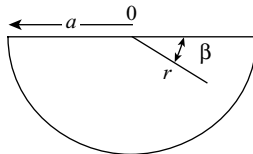
2. Isosceles triangle (right)^b



$$v_z(x, y) = \frac{16l^2 \Delta P}{\pi^4 \mu L} \left[\sum_{i=1,3} \sum_{j=2,4} \frac{j \sin(i\pi x/l) \sin(j\pi y/l)}{i(j^2 - i^2)(i^2 + j^2)^2} + \sum_{i=2,4} \sum_{j=1,3} \frac{i \sin(i\pi x/l) \sin(j\pi y/l)}{j(i^2 - j^2)(i^2 + j^2)^2} \right]$$

Ⓝ Semicircular channel pressure flow^b

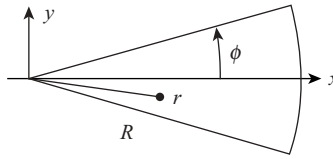
$$v_z(r, \beta) = \frac{\Delta P}{L\mu} a^4 \sum_{i=1,3,5} \left[\frac{4r^2}{a^4} \frac{1}{i\pi(4 - i^2)} - \frac{4r^i}{a^{i+2}} \frac{1}{i\pi(4 - i^2)} \right] \sin i\beta$$



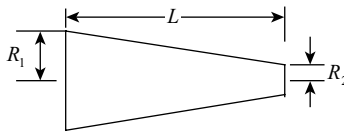
Ⓝ Circular section channel pressure flow^c

$$v_z(x, y) = \frac{\Delta P}{2\mu L} \left[\frac{x^2 \tan^2 \phi - y^2}{1 - \tan^2 \phi} + \frac{16R^2(2\phi)^2}{\pi^3} \sum_{i=1,3,\dots}^{\infty} (-1)^{(i+1)/2} \left(\frac{r}{R} \right)^{i\pi/2\phi} \frac{\cos(i\pi\phi)/2\phi}{i \left[i^2 - (4\phi/\pi)^2 \right]} \right]$$

TABLE 12.4 (Continued)



(N) Conical channel pressure flow



$$Q = \frac{3\pi\Delta P}{8\mu L} \left[\frac{R_1^3 R_2^3}{R_1^2 + R_1 R_2 + R_2^2} \right]$$

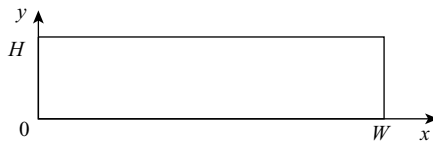
(P) Conical channel pressure flow^d (by the lubrication approximation)

$$Q = \frac{n\pi R_1^3}{3n + 1} \left(\frac{R_1 \Delta P a_{13}}{2mL} \right)^s$$

where

$$a_{13} = \frac{3n(R_1/R_2 - 1)}{R_1/R_2 [(R_1/R_2)^{3n} - 1]}$$

(N) Rectangular channel pressure flow^e



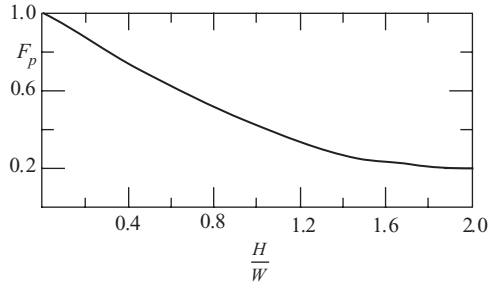
$$v_z(x, y) = \frac{\Delta P}{\mu L} \left\{ \frac{y^2}{2} - \frac{yH}{2} + \frac{4H^2}{\pi^3} \sum_{i=1,3,\dots}^{\infty} \frac{\cosh[(i\pi/2H)(2x - W)]}{i^3 \cosh(i\pi W/H)} \sin\left(\frac{i\pi y}{H}\right) \right\}$$

$$Q = \frac{WH^3}{12\mu} \left(\frac{\Delta P}{L} \right) \left[1 - \frac{129H}{\pi^5 W} \sum_{i=1,3,\dots}^{\infty} \frac{1}{i^5} \tanh\left(\frac{i\pi W}{2H}\right) \right] = \frac{WH^3}{12\mu} \left(\frac{\Delta P}{L} \right) \cdot F_p$$

(Continued)

TABLE 12.4 (Continued)

F_p is given graphically as follows:



^a J. Happel and H. Brenner, *Low Reynolds Number Hydrodynamics*, Prentice Hall, Englewood Cliffs, NJ, 1965, Chapter 2.

^b S. M. Marco and L. S. Han, *Trans. Am. Soc. Mech. Eng.*, **56**, 625 (1955).

^c E. R. G. Eckert and T. F. Irvine, *Trans. Am. Soc. Mech. Eng.*, **57**, 709 (1956).

^d J. M. Mckelvey, V. Maire, and F. Haupt, *Chem. Eng.*, 95 (September 1976).

^e M. J. Boussinesq, *J. Math. Pure Appl.*, Ser. 2, **13**, 377 (1868).

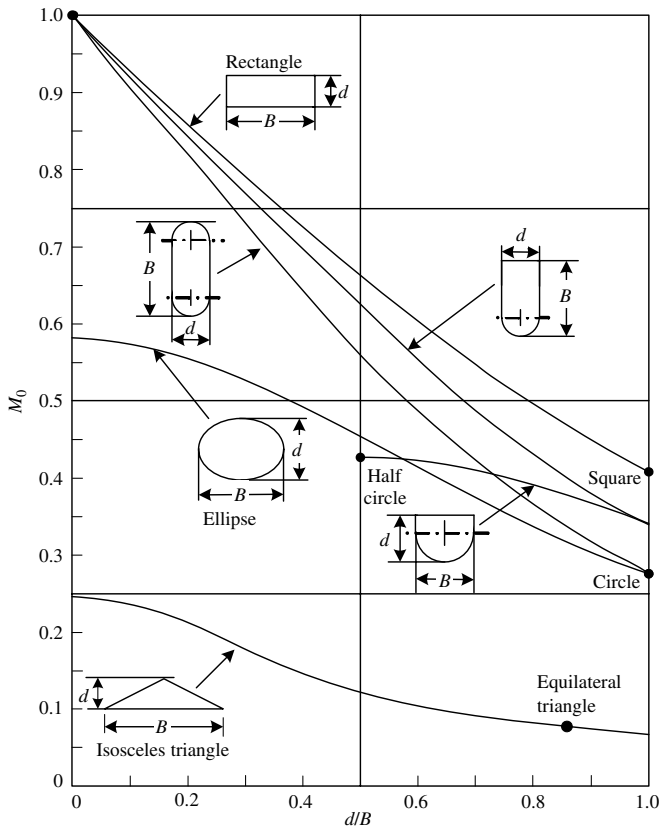


Fig. 12.51 Graphical representation of shape factor M_0 used in Eq. 12.6-1 [Reprinted by permission from G. P. Lahti, *Soc. Plast. Eng. J.*, 619 (1963).]

REFERENCES

1. E. B. Bagley, "End Corrections in the Capillary Flow of Polyethylene," *J. Appl. Phys.*, **28**, 624 (1957).
2. C. McLuckie and M. Rogers, "Influence of Elastic Effects of Capillary Flow of Molten Polymers," *J. Appl. Polym. Sci.*, **13**, 1049 (1969).
3. N. Hirai and H. Eyring, "Bulk Viscosity of Polymeric Systems," *J. Polym. Sci.*, **37**, 51 (1959).
4. I. J. Duvdevani and I. Klein, "Analysis of Polymer Melt Flow in Capillaries Including Pressure Effects," *Soc. Plast. Eng. J.*, **23**, 41–45 (1967).
5. P. H. Goldblatt and R. S. Porter, "A Comparison of Equations for the Effect of Pressure on the Viscosity of Amorphous Polymers," *J. Appl. Polym. Sci.*, **20**, 1199 (1976).
6. B. C. Sakiades, "Equilibrium Flow of a General Fluid through a Cylindrical Tube," *AIChE J.*, **8**, 317 (1962).
7. C. D. Han, M. Charles, and W. Philippoff, "Measurements of the Axial Pressure Distribution of Molten Polymers in Flow through a Circular Tube," *Trans. Soc. Rheol.*, **13**, 453 (1969).
8. C. D. Han, "On Silt- and Capillary-Die Rheometry," *Trans. Soc. Rheol.*, **18**, 163 (1974).
9. C. D. Han, *Rheology in Polymer Processing*, Academic Press, New York, 1976, Chapter 5.
10. R. Nahme, *Ing. Arch.*, **11**, 191 (1940).
11. H. C. Brinkman, "Heat Effects in Capillary Flow I," *Appl. Sci. Res.*, **A2**, 120–124 (1951).
12. R. M. Turian and R. B. Bird, "Viscous Heating in the Cone-and-Plate Viscometer. II. Temperature Dependent Viscosity and Thermal Conductivity," *Chem. Eng. Sci.*, **18**, 689 (1963).
13. J. E. Gerrard, R. E. Steidler, and J. K. Appeldoorn, "Viscous Heating in Capillaries," *Ind. Eng. Chem. Fundam.*, **4**, 332 (1965).
14. R. M. Turian, "Viscous Heating in the Cone-and-Plate Viscometer. III," *Chem. Eng. Sci.*, **20**, 771 (1965).
15. R. A. Morrette and C. G. Gogos, "Viscous Dissipation in Capillary Flow of Rigid PVC and PVC Degradation," *Polym. Eng. Sci.*, **8**, 272 (1968).
16. D. E. Marshall, I. Klein, and R. H. Uhl, "Measurement of Screw and Plastic Temperature Profiles in Extruders," *Soc. Plast. Eng. J.*, **20**, 329 (1964).
17. J. Van Leeuwen, "Stock Temperature Measurement in Plastifying Equipment," *Polym. Eng. Sci.*, **7**, 98–109 (1967).
18. H. T. Kim and E. A. Collins, "Temperature Profiles of Polymer Melts in Tube Flow. Conduction and Shear Heating Corrections," *Polym. Eng. Sci.*, **11**, 83 (1971).
19. H. W. Cox and C. W. Macosko, "Viscous Dissipation in Die Flow," *AIChE J.*, **20**, 785 (1974).
20. N. Galili and R. Takserman-Krozer, "Heat Effect in Viscous Flow through a Pipe," *Israeli Tech.*, **9**, 439 (1971).
21. H. P. Schreiber and E. B. Bagley, "Melt Elasticity in Fractionated HDPE," *Polym. Lett.*, **1**, 365 (1963).
22. W. W. Graessley, S. D. Glasscock, and R. L. Crawley, "Die Swell in Molten Polymers," *Trans. Soc. Rheol.*, **14**, 519 (1970).
23. R. I. Tanner, "A Theory of Die Swell," *J. Polym. Sci.*, **A-28**, 2067 (1970).
24. A. S. Lodge, *Elastic Liquids*, Academic Press, New York, 1964, p. 131.
25. S. I. Abdel-Khalik, O. Hassager, and R. B. Bird, "Prediction of Melt Elasticity from Viscosity Data," *Polym. Eng. Sci.*, **14**, 859 (1974).
26. J. D. Ferry, *Viscoelastic Properties of Polymers*, Wiley, New York, 1971; also, S. Middleman, *Fundamentals of Polymer Processing*, McGraw-Hill, New York, 1977, p. 472.
27. J. L. White and J. F. Roman, "Extrudate Swell During the Melt Spinning of Fibers—Influence of Rheological Properties and Take-up Force," *J. Appl. Polym. Sci.*, **20**, 1005 (1976).

28. A. B. Metzner, W. T. Houghton, R. A. Sailor, and J. L. White, "A Method for the Measurement of Normal Stresses in Simple Shearing Flow," *Trans. Soc. Rheol.*, **5**, 133 (1961).
29. R. B. Bird, R. K. Prud'homme, and M. Gottlieb, "Extrudate Swell as Analyzed by Macroscopic Balances," The University of Wisconsin, Rheology Research Center Report RRC-35, 1975.
30. B. Whipple, "Velocity Distributions in Die Swell," Ph.D. Dissertation, Washington University, St. Louis, MO, 1974.
31. H. Giesekus, "Verschiedene Phänomene in Strömungen Viskoelastischer Flüssigkeiten durch Düsen," *Rheol. Acta*, **8**, 411 (1969).
32. H. L. Weissberg, "End Corrections for Slow Viscous Flow through Long Tubes," *Phys. Fluids*, **5**, 1033 (1962).
33. E. B. Bagley and R. M. Birks, "Flow of Polyethylene into a Capillary," *J. Appl. Phys.*, **31**, 556 (1960).
34. T. F. Ballenger and J. L. White, "The Development of the Velocity Field in Polymer Melts into a Reservoir Approaching a Capillary Die," *J. Appl. Polym. Sci.*, **15**, 1849 (1971).
35. P. Lamb and F. N. Cogswell, paper presented at the International Plastics Congress on Processing Polymer Products, Amsterdam, 1966.
36. H. L. LaNieve III, and D. C. Bogue, "Correlation of Capillary Entrance Pressure Drops with Normal Stress Data," *J. Appl. Polym. Sci.*, **12**, 353 (1968).
37. C. D. Han, "Influence of the Die Entry Angle in the Entrance Pressure Drop, Recoverable Elastic Energy and Onset of Flow Instability in Polymer Melt Flow," *J. Appl. Polym. Sci.*, **17**, 1403 (1973).
38. J. L. White and A. Kondo, "Rheological Properties of Polymer Melts and Flow Patterns During Extrusion through a Die Entry Region," *J. Appl. Polym. Sci.*, in press.
39. J. P. Tordella, in *Rheology*, Vol. 4, F. R. Eirich, Ed., Academic Press, New York, 1969, Chapter 3.
40. R. S. Spencer and R. D. Dillon, *J. Colloid Interface Sci.*, **3**, 163 (1940).
41. C. J. S. Petrie and M. M. Denn, "Instabilities in Polymer Processing," *AIChE J.*, **22**, 209 (1976).
42. M. M. Denn, "Extrusion Instabilities and Wall Slip," *Annu. Rev. Fluid Mech.*, **33**, 265–287 (2001).
43. F. N. Cogswell and P. Lamb, *Plast. Today*, 33 (1969).
44. G. V. Vinogradov A., Ya. Malkin, Yu. G. Yanovskii, E. K. Borisenkova, B. V. Yarlykov, and G. V. Berezhnaya, "Viscoelastic Properties and Flow of Narrow Distribution PIB and Polyisoprene," *J. Polym. Sci.*, **A2 10**, 1061 (1972).
45. J. L. den Otter, "Mechanisms of Melt Fracture," *Plast. Polym.*, **38**, 155 (1970).
46. Y. Oyanagi, "A Study of Irregular Flow Behavior of HDPE," *Appl. Polym. Symp.*, **20**, 123 (1973).
47. N. Bergem, "Visualization Studies of Polymer Melt Flow Anomalies in Extrusion," *Proc 7th Int. Congr. on Rheology*, Gothenburg, Sweden, 1976, p. 50.
48. L. L. Blyler, Jr., and A. C. Hart, Jr., "Capillary Flow Instability of Ethylene Polymer Melts," *Polym. Eng. Sci.*, **10**, 193 (1970).
49. K. B. Migler, Y. Son, F. Qiao, and K. Flynn, "Extensional Deformation, Cohesive Failure, and Boundary Conditions during Sharkskin Melt Fracture," *J. Rheol.*, **46**, 383–400, (2002).
50. M. Seth, S. G. Hatzikiriakos, and T. Clere, "Gross Melt Fracture Elimination: The Role of Surface Energy of Boron Nitride Powders," *Polym. Eng. Sci.*, **42**, 743–752 (2002).
51. F. N. Cogswell, "Stretching Flow Instabilities at the Exits of Extrusion Dies," *J. Non-Newton. Fluid Mech.*, **2**, 37–47 (1977).
52. E. G. Muliawan, S. G. Hatzikiriakos, and M. Sentmanat, "Melt Fracture of Linear PE," *Int. Polym. Process.*, **20**, 60–67 (2005).

53. M. L. Sentmanat, SER-HV AO1, *Universal Testing Platform Instrument Manual*, X-Pansion Instruments 2003.
54. M. L. Sentmanat, "A Novel Device for Characterizing Polymer Flows in Uniaxial Extension," *SPE ANTEC Tech. Papers*, **61**, 992 (2003).
55. M. Sentmanat and S. G. Hatzikiriakos, "Mechanism of Gross Melt Fracture Elimination in the Extrusion of Polyethylenes in the Presence of Boron Nitride," *Rheol. Acta*, **43**, 624–633 (2004).
56. C. G. Gogos, B. Qian, D. B. Todd, and T. R. Veariel, "Melt Flow Instability Studies of Metallocene Catalyzed LLDPE in Pelletizing Dies," *SPE ANTEC Tech. Papers*, **48**, 112–116 (2002).
57. T. R. Veariel, B. Qian, C. G. Gogos, and D. B. Todd, Patent Application #2005-0074609, ExxonMobil Chemical Co, Published April 7, 2005.
58. J. Vlachopoulos and T. W. Chan, "A Comparison of Melt Fracture Initiation Conditions in Capillaries and Slits," *J. Appl. Polym. Sci.*; also, J. Vlachopoulos, M. Horie, and S. Lidorikis, "An Evaluation of Expressions Predicting Die Swell," *Trans. Soc. Rheol.*, **16**, 669 (1972).
59. J. F. Carley, "Flow of Melts in Crosshead-Slit Dies; Criteria for Die Design," *J. Appl. Phys.*, **25**, 1118 (1954).
60. J. R. A. Pearson, "Non-Newtonian Flow and Die Design. Part IV. Flat Film Die Design," *Trans. J. Plast. Inst.*, **32**, 239 (1964).
61. J. M. McKelvey and K. Ito, "Uniformity of Flow from Sheet Dies," *Polym. Eng. Sci.*, **11**, 258 (1971).
62. Y. Sun and M. Gupta, "Elongational Viscosity on the Flow of a Flat Die," *Int. Polym. Process.*, **18**, 353 (2003).
63. D. Sarkar and M. Gupta, "Further investigation of the effect of elongational viscosity on entrance flow," *J. Reinf. Plast. Comp.*, **20**, 1473–1484 (2001).
64. C. D. Han, *Multiphase Flow in Polymer Processing*, Academic Press, New York, 1981, Chapter 7.
65. H. Mavridis and R. N. Shroff, "Multilayer Extrusion: Experiments and Computer Simulation," *Polym. Eng. Sci.*, **34**, 559–569 (1994).
66. W. J. Schrenk, N. L. Bradley, T. Alfrey, and H. Maack, "Interfacial Flow Instability in Multilayer Coextrusion," *Polym. Eng. Sci.*, **18**, 620–623 (1978); also, W. J. Schrenk and T. Alfrey, "Co-extruded Multilayer Films and Sheets," in *Polymer Blends* Vol. 2, D. R. Paul and N. Seymour, Eds., Academic Press, New York, 1978.
67. J. M. Dealey and K. F. Wissbrun *Melt Rheology and Its Role in Plastics Processing*, Van Nostrand Reinhold, New York (1990).
68. T. C. Yu and C. D. Han, "Stratified Two-phase Flow of Molten Polymers," *J. Appl. Polym. Sci.*, **17**, 1203–1225 (1973).
69. R. Sabia, "On the Characterization of Non-Newtonian Flow," *J. Appl. Polym. Sci.*, **7**, 347–355 (1963).
70. A. I. Leonov, "On a Class of Constitutive Equations for Viscoelastic Liquids," *J. Non-Newt. Fluid Mech.*, **25**, 1–59 (1987).
71. A. G. Fredrickson and R. B. Bird, "Non-Newtonian Flow in Annuli," *Ind. Eng. Chem.*, **50**, 347 (1958).
72. R. A. Worth and J. Parnaby, "The Design of Dies for Polymer Processing Machinery," *Trans. Inst. Chem. Eng.*, **52**, 368 (1974).
73. J. R. A. Pearson, "Non-Newtonian Flow and Die Design. Part I," *Trans. J. Plast. Inst.*, **30**, 230 (1962).
74. C. Gutfinger, E. Broyer, and Z. Tadmor, "Analysis of a Cross Head Film Blowing Die with the Flow Analysis Network (FAN) Method," *Polym. Eng. Sci.*, **15**, 385–386 (1975).
75. O. Yandoff, *Acad. Sci., Paris*, **223**, 192 (1946).

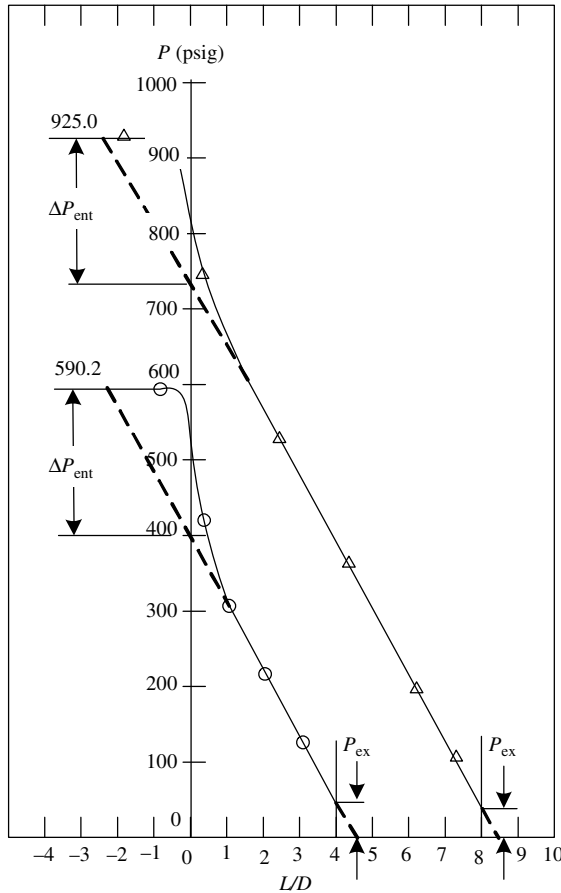
76. R. S. Schechter, "On the Steady Flow of a Non-Newtonian Fluid in Cylinder Ducts," *AICHE J.*, **7**, 445 (1961).
77. J. A. Wheeler and E. H. Wissler, "Steady Flow of Non-Newtonian Fluids in Square Duct," *Trans. Soc. Rheol.*, **10**, 353 (1966).
78. A. E. Green and R. S. Rivlin, "Steady Flow of Non-Newtonian Fluids through Tubes," *Quant. Appl. Math.*, **14**, 299 (1956).
79. J. G. Oldroyd, "Some Steady Flows of the General Elastic-viscous Liquid," *Proc. Roy. Soc.*, **A283**, 115 (1965).
80. H. Giesekus, "Sekundärströmungen in viskoelastischen Flüssigkeiten bei stationärer und periodischer Bewegung," *Rheol. Acta*, **4**, 85-101 (1965).
81. A. G. Dodson, P. Townsend, and K. Walters, "Non-Newtonian Flow in Pipes of Non-Circular Cross Section," *Comp. Fluids.*, **2**, 317-338 (1974).
82. S. Matsuhisa, *Jpn Plast. Age*, **12**, 25 (1974).
83. D. H. Sebastian and R. Rakos, "Interactive Software Package for the Design and Analysis of Extrusion Profile Dies," *Adv. Polym. Tech.*, **5**, 333-339 (1985).
84. J. Sienz., S. D. Bullman, and J. F. T. Pittman, paper presented at the 4th ESAFORM Conference, Liege, Belgium, (2001).
85. I. Szarvasy, J. Sienz, J. F. T. Pittman, and E. Hinton, "Computer Aided Optimisation of Profile Assessment," *Int. Polym. Process.*, **18**, 235 (2003).
86. J. M. Nóbrega, O. S. Carneiro, P. J. Oliveira, and F. T. Pinho, "Flow Balancing in Extrusion Dies for Thermoplastic Profiles, Part I: Automatic Design," *Int. Polym. Process.*, **18**, 298 (2003).
87. J. M. Nóbrega, O. S. Carneiro, F. T. Pinho, and P. J. Oliveira, "Flow Balancing in Extrusion Dies for Thermoplastic Profiles, Part III: Experimental Extrusion," *Int. Polym. Process.*, **19**, 225-235 (2004).

PROBLEMS

- 12.1 Bagley Corrections** (a) Given the "raw" capillary flow data for two capillaries, plot both $[\Delta P/(4L/D_0)]$ and $\Delta P/4[L/D_0 + N(\Gamma)]$ vs. Γ , showing that the flow curves of the former depend on L/D_0 , while the latter is L/D_0 independent. (b) Consider the experimental point $L/D_0 = 50$ and $\Gamma = 2000 \text{ s}^{-1}$ on Fig. 12.6. What would the magnitude of the error be in evaluating the shear stress at the wall, if the Bagley entrance correction is neglected? Repeat the calculation for $L/D_0 = 6$, $\Gamma = 2000 \text{ s}^{-1}$.

Capillary A		Capillary B	
$L = 0.500 \text{ in}$	$D_0 = 0.0625 \text{ in}$	$L = 2.005 \text{ in}$	$D_0 = 0.0501 \text{ in}$
$\Delta P(\text{psi})$	$\Gamma (\text{s}^{-1})$	$\Delta P(\text{psi})$	$\Gamma (\text{s}^{-1})$
125.7	7.68	578.6	14.87
149.2	15.36	844.5	29.73
227.7	38.40	1353.1	74.34
394.7	76.81	1886.4	148.67
610.3	153.61	2645.8	297.34
972.6	384.03	3943.6	743.35
1298.7	768.07	5103.1	1486.71
1688.2	1536.13	6479.9	2973.41

12.2 Relative Magnitude of ΔP_{ent} and P_{ex} In the accompanying figure, Han¹¹ presents capillary flow data on HDPE at 180°C with which a Bagley plot can be constructed for $\Gamma = 327.7 \text{ s}^{-1}$. (a) Assuming $P_{ex} = 0$, show that for the shear rate $N = 3.3$ and that for $L/D_0 = 4$ and 8, respectively, τ_w^* is 20.21 and 20.46 psi. (b) Taking into account the measured ΔP_{ent} and P_{ex} values, show that $\tau_w^* = (\Delta P - \Delta P_{ent} - P_{ex})D_0/4L$ and that τ_w^* values are in this case 21.19 and 21.42 psi for $L/D_0 = 4$ and 8, respectively. That is, including P_{ex} (which is not readily available experimentally), increases the value of τ_w^* by 5%.



12.3 Newtonian and Power Law Fluids Extrudates A Newtonian and a Power Law model fluid are extruded from a long horizontal pipe of diameter D_0 . Show that in the absence of gravity, the ratio of the extrudate diameter D to the tube diameter is given by 0.87 and $[(2n + 1)/(3n + 1)]^{1/2}$ for the Newtonian and Power Law model, respectively.

12.4 Estimation Extrudate Swell of a Polymer Tenite 800 LDPE is extruded from a long horizontal pipe of diameter D_0 . Using Eqs. 12.2-1 and 12.2-2 and the

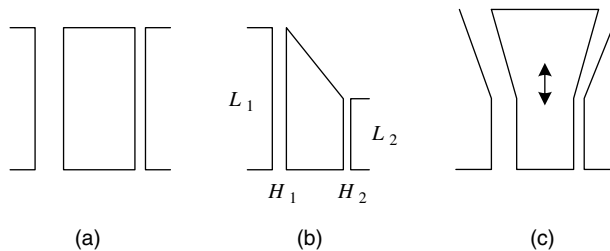
11. C. D. Han, "On Silt and Capillary-Die Rheometry," *Trans. Soc. Rheol.*, **18**, 163 (1974).

rheological data on Fig. 3.10, calculate the extrudate swell as a function of shear rate at the wall at 160° and 200°C.

- 12.5 Maximum Flow-Rater Production of Flat Sheets** Calculate the maximum flow rate per unit width, q_{max} , for producing a smooth fracture-free sheet with a die of 0.05-cm opening for HDPE – Alathon 7040, LDPE – Alathon 1540 at 473 K; PS – Dylene 8, ABS and HIPS at 483 K. Use the Power Law model and the rheological constants below. q_{max} has to be such that $\tau_w \leq \tau_{crit} \approx 10^5 \text{ N/m}^2$.

Polymers	T (K)	m ($\text{N} \cdot \text{s}^n/\text{m}^2$)	n
HDPE–Alathon 7040	473	4.68×10^3	0.59
LDPE–Alathon 1540	473	4.31×10^3	0.47
PS–Dylene 8	483	2.83×10^4	0.25
ABS	483	3.93×10^4	0.25
HIPS	483	3.61×10^4	0.19

- 12.6 Die for Extruding a Square Extrudate** (a) Explain why a die with a square cross section cannot produce an extruded product with a square cross section. (b) What cross section should the die have to produce a square-shaped product?
- 12.7 Design Graphs for Dies of Various Shapes, but the Same Cross-Sectional Area** (a) Use Eqs. 12.6-1 and 12.6-2 and Fig. E5.1(a) to construct Q vs. ΔP graphs for dies that have the same cross-sectional area and the following shapes: circle, ellipse, rectangle, and a rectangle with two rounded-off sides in the shape of half-circles. Use a Newtonian fluid. (b) How can the equivalent Newtonian fluid concept help you extend these shapes for non-Newtonian fluids?
- 12.8 Design of Profile Extrusion Dies**¹² In designing a die for extruding a product that has thick and thin sections, we must secure equal extrudate velocities in both the thin and thick sections. The design in the accompanying figure shows schematically a die with one thin and one thick section. (a) Show that for such a product design A is not appropriate. (b) Calculate the lengths L_1 and L_2 (for given H_1 and H_2) in design B, which give uniform extrudate velocity at equal entrance pressure. (c) Discuss design C, and prove that if the mandrel can move axially, this die can accommodate, in principle, any polymer melt of different rheological properties.

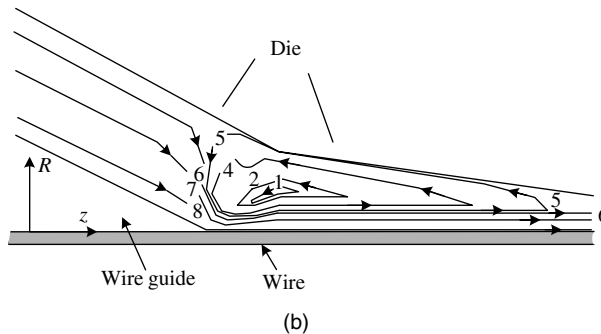
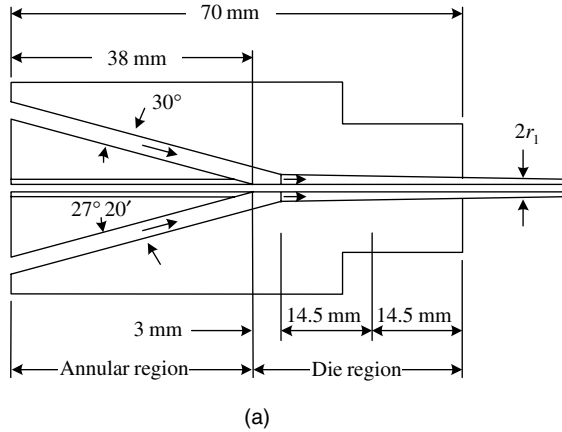


- 12.9 Wire Coating Die** A wire coating-die, with the wire velocity of V and annular thickness of H , results in a coating thickness h at a given pressure drop. Develop an

12. F. N. Cogswell, "The Scientific Design of Fabrication Processes; Blow Molding," *Plast. Polym.*, October, (1971).

isothermal Newtonian model for calculating the coating thickness for a given pressure drop.

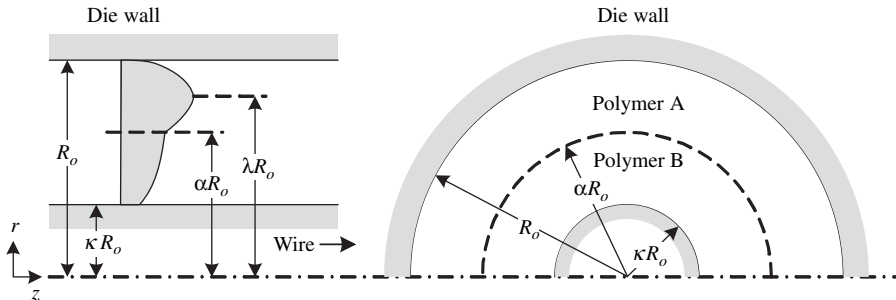
- 12.10 Wire-Coating Pressure Dies: The Lubrication Approximation** An example of the wire coating pressure die is shown on Fig. 12.46. Past the guider tip the die contracts with a small taper. Consider a cross section of this region to be formed by two nonparallel plates of spacing $H(z)$, that is, disregard the curvature. The bottom plate is moving with the wire velocity V . (a) Use the lubrication approximation to obtain an expression for dP/dz . (b) Does this result support, qualitatively, the velocity field obtained by Tanner shown in the accompanying figure.



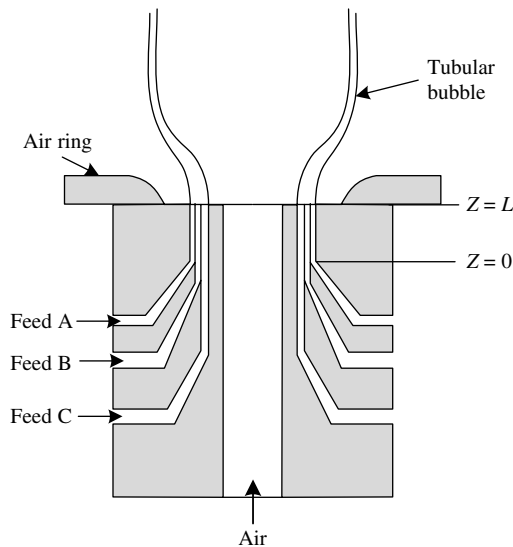
- 12.11 Coextrusion of Flat Sheets**¹³ A sheet die is fed by two extruders that deliver two polymer melts at the same temperature, but each having Power Law constants m_1, n_1 and m_2, n_2 . Fluid 1 is the more viscous of the two. The two streams meet in the channel approach region of the die. That is, the die has separate manifolds and restrictors for each of the melts, but a common approach and die-lip region. Let the more viscous fluid occupy the region $0 \leq y \leq K$, where $K < H/2$, the half-thickness. Following a solution approach similar to that of Section 12.3 for evaluating the position of the maximum in the velocity profile, obtain expressions for the velocity profile if the fluids are HDPE–Alathon 7040 and PP–E612 flowing at 210°C (see Appendix A).

13. C. D. Han, "On Silt and Capillary-Die Rheometry," *Trans. Soc. Rheol.*, **18**, 163 (1974).

12.12 Wire-Coating Coextrusion Die Flow In the wire-coating coextrusion process two different polymer melts are brought together into a cross-head block that guides the two melts to flow in a concentric annular manner over a fast-moving wire. Consider the steady and isothermal combined drag and pressure annular flow of two Power Law melts A and B depicted in the accompanying figure, where the velocity maximum occurs in melt A. Following the methodology developed by Han and Rao¹⁴ in Section 12.3, develop the expressions that specify the velocity profiles in both melts and the radial position of the interface, if the magnitudes of the respective volumetric flow rates of the two melts are known.



12.13 Blown-Film Coextrusion Die Flow Consider the stratified concentric steady and isothermal flow of three Power Law melts A, B, and C in the region $0 \leq Z \leq L$ in the accompanying figure. Following Han¹⁵ methodology, formulate the expressions for obtaining the velocity profiles across all three melts, for known values of the three flow rates.



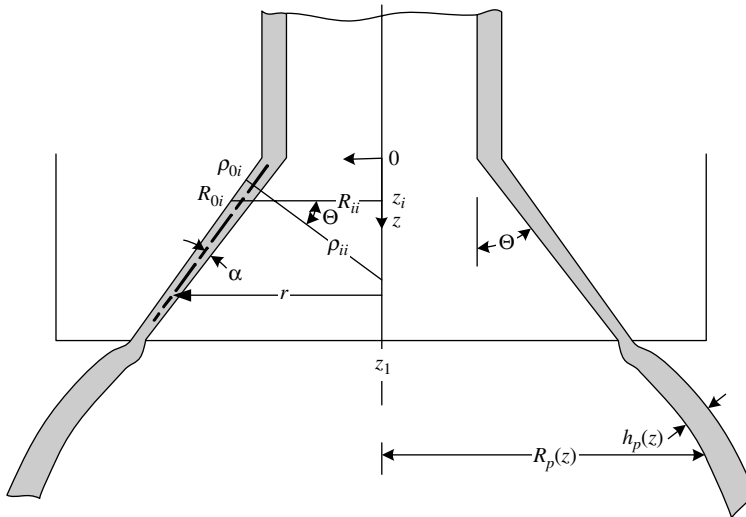
14. C. D. Han, *Multiphase Flow in Polymer Processing*, Academic Press, New York, 1981, Chapter 7; also, C. D. Han and D. A. Rao, "Studies on Wire coating Extrusion. II. The Rheology of Wire Coating Coextrusion," *Polym. Eng. Sci.* **20**, 128 (1980).

15. C. D. Han, "Multiphase Flow in Polymer Processing," Academic Press, New York, 1981, Chapter 7.

12.14 Effect of the Power Law Index on the Coat-Hanger Die Design Utilizing the coat-hanger die design equation for Power Law fluids, developed in Section 12.3, examine whether the design arrived at for the hypothetical $n = 0.5$ polymer melt in Example 12.3 will produce a uniform sheet with the following two polymers: HIPS LX-2400 (ex-Monsanto) m ($T = 443 \text{ K}$) $= 7.6 \times 10^4 \text{ (N}\cdot\text{s}^n/\text{m}^2)$ and $n = 0.20$, and for Nylon Capron TM 8200 (Ex-Allied Chemical Corp.) m ($T = 503 \text{ K}$) $= 1.95 \times 10^3 \text{ (N}\cdot\text{s}^n/\text{m}^2)$ and $n = 0.66$. If not, what design(s) will give a uniform sheet from an $H = 0.05\text{-cm}$ slit opening?

12.15 Pressure Drop Estimation in Spiral Dies¹⁶ Consider a spiral mandrel die similar to the one shown on Fig. 12.43. You are asked to develop a mathematical model for calculating the pressure drop flow rate relationship needed to pump a polymer melt of known rheological properties (represented, for example, by Power Law constants m and n). Neglect any “coupling” between the helical flow inside the grooves and axial flow between the flat cylindrical surfaces. Also neglect the taper between the cylindrical surfaces. Express your results in terms of m , n , Q , number and size of the ports and helical grooves, their helical angle, as well as the cylindrical surface spacing and overall length. Make use of Fig. E5.1(a).

12.16 Flow in the Parison Die Exit Region The flow in the diverging exit region of a parison die, shown in the accompanying figure, cannot be easily simulated, both because of the geometrical complexities involved and because the melt response is not known for such nonviscometric flow. Consider the die exit flow as the superposition of annular pressure flow in the z direction and planar extensional flow with stretching in the θ direction. Set up the appropriate equations to hold for small axial increments Δz .



16. B. Proctor, “Flow Analysis in Extrusion Dies,” *Soc. Plast. Eng. J.*, **28** (1972).

12.17 Estimation of Entrance Pressure–Pressure Losses from the Entrance Flow Field¹⁷ Consider the entrance flow pattern observed with polymer melts and solutions in Fig. 12.16(a). The flow can be modeled, for small values of α , as follows: for $|\theta| \leq \alpha/2$ the fluid is flowing in simple extensional flow and for $\alpha/2 \leq |\theta| \leq \pi/2$ the flow is that between two coaxial cylinders of which the inner is moving with axial velocity V . The flow in the outer region is a combined drag–pressure flow and, since it is circulatory, the net flow rate is equal to 0. The velocity V can be calculated at any upstream location knowing α and the capillary flow rate. Use this model for the entrance flow field to get an estimate for the entrance pressure drop.

17. A. E. Everage, Jr., and R. L. Ballman, “An Energy Interpretation of the flow Patterns in Extrusion through a Die Entry Region,” paper presented at the 47th Annual Meeting of the Society of Rheology, New York, 1977.

13 Molding

- 13.1 Injection Molding, 753
- 13.2 Reactive Injection Molding, 798
- 13.3 Compression Molding, 811

The injection molding, compression molding, and casting-shaping operations all entail forcing the polymer into a cavity and reproducing its shape. In the process of casting, the cavity is filled by gravitational flow with a low viscosity liquid (reacting monomer or prepolymer) and, following polymerization the liquid solidifies. In compression molding, a prepolymer solid mass is heated up or melted and forced to undergo a squeezing flow by hot mold surfaces that close to form a final shape. The prepolymer usually cross-links and permanently assumes the shape of the closed cavity. In the injection molding process, a polymer melt is forced through an orifice (gate) into a closed, cold mold, where it solidifies under pressure in the shape of the mold cavity.

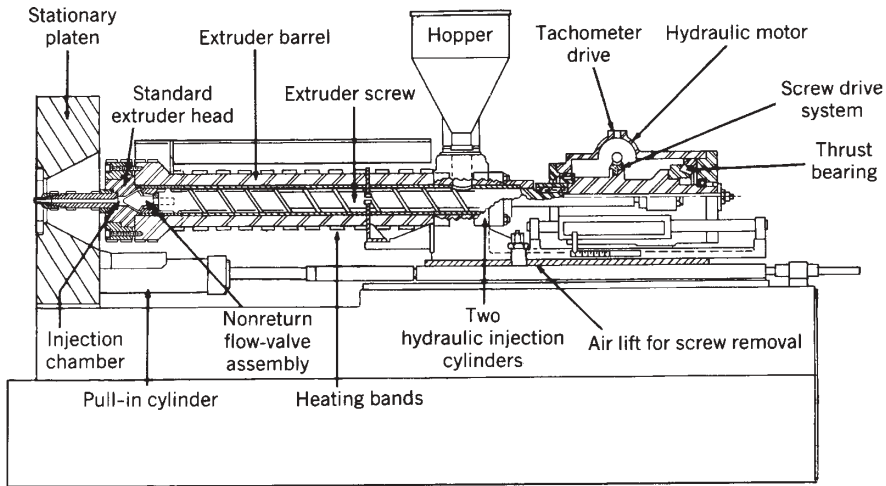
Two polymers can be used in sequence to fill the mold, forming skin–core sandwich molded articles. Air can also be introduced in partially melt-filled molds, and pressurized to form a polymer skin–air core sandwich structure, through the gas-assist injection-molding process. In all injection molding processes, the polymer is melted, mixed, and injected from the injection unit of the machine.

Finally, in the reaction injection-molding (RIM) process, low-viscosity reacting monomers or prepolymers are intimately mixed just before being injected into a hot cavity, where they react further and solidify. The RIM process, then, is a variation of the casting process, where highly reactive liquid systems are injected quickly, rather than being allowed to flow by gravity, into complex shape cavities, where they quickly react and solidify.

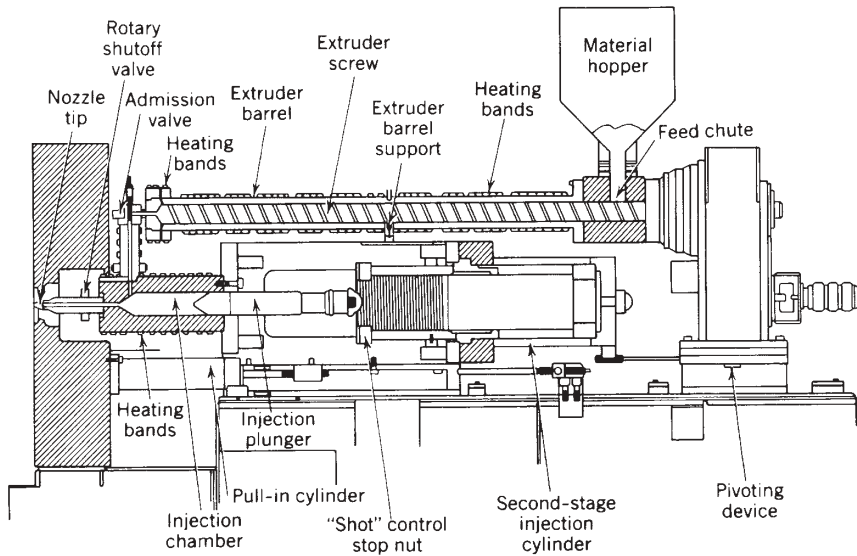
In this chapter we focus on injection molding, which, along with die forming, is one of the two most important shaping steps. We also discuss reaction injection molding and compression molding. From a process analysis point of view, the basic problems this chapter addresses are (a) nonisothermal and transient flow of polymer melts, followed by *in situ* cooling and solidification, and (b) nonisothermal and transient flow of reacting (polymerizing) liquids followed by *in situ* polymerization and heat transfer.

13.1 INJECTION MOLDING

Injection molding involves two distinct processes. The first comprises the elementary steps of solids transport, melt generation, mixing, and pressurization and flow, which are carried



(a)



(b)

Fig. 13.1 (a) Reciprocating-screw machine, injection end. (b) Two-stage screw-plunger machine. [Courtesy of HPM Division of Koehring Company.]

out in the injection unit of the molding machine; the second is the product shaping and “structuring,” which takes place in the mold cavity. Most injection molding machines are the in-line, reciprocating-screw type, as illustrated in Fig. 13.1(a). Two-stage injection molding machines, shown in Fig. 13.1(b) are also used; the polymer melt is produced in an extruder and exits into a reservoir connected to a hydraulic piston device, which is cyclically pressurized to deliver the melt into the cold mold cavity.

The theoretical analysis of the injection unit involves all the facets of steady, continuous, plasticating screw extrusion, with the added complication of a transient

operation resulting from the intermittent screw rotation, on which axial motion is superimposed. In the injection unit the melting step is the dominant one regarding design and operation. Experimental work on melting in injection units (1) revealed a melting mechanism similar to that in plasticating screw extrusion, which was then used to formulate a mathematical model for the melting process (2). The product of the injection unit is the polymer melt accumulating in front of the screw. Melt homogeneity affects the filling process and final product quality. However, we assume that the same quality of well-mixed and uniform temperature melt is produced by the injection unit during each cycle, as well as from one cycle to the next.

To inject the polymer melt into the mold, the melt must be pressurized. This is achieved by the forward thrust of the screw (a) or the piston (b), both of which act as rams. Hence we have static mechanical pressurization, as discussed in Section 6.7, which results in positive displacement flow.

The injection “molding cycle” is shown schematically in Fig. 13.2, indicating the simultaneous positions and states of the screw, the mold and the process. A typical injection mold is made of at least two parts, one of which is movable so that it can open and close during different parts of the molding cycle, as shown in Fig. 13.3(a) and 13.3(b). The entire mold is kept at a constant temperature below T_g or T_m . The melt exits the nozzle of the injection unit and flows through the *sprue*, *runner*, and *gate* into the mold cavity. Each of these structural elements of the mold performs well-defined functions and affects the molding operation. Thus the sprue forms the overall entrance into the mold. It should not generate large resistance to flow, yet at the same time the melt in it should

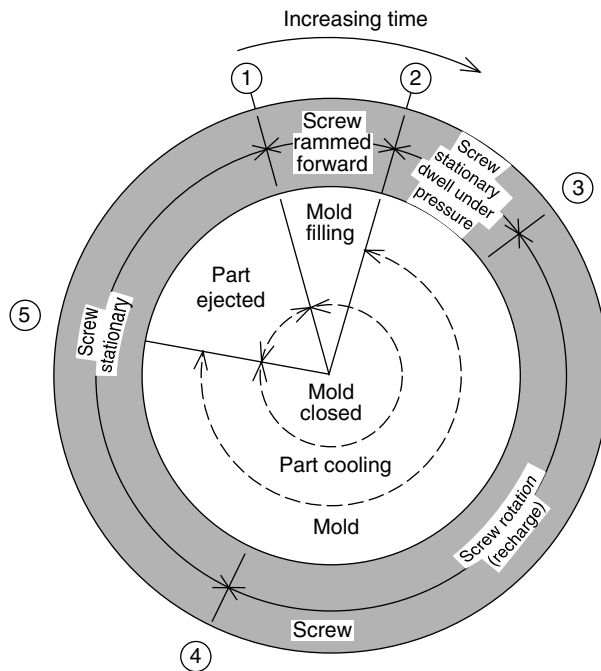


Fig. 13.2 The injection molding cycle. [Reprinted by permission from R. C. Donovan, “An Experimental Study of Plasticating in a Reciprocating-Screw Injection Molding Machine,” *Polym. Eng. Sci.*, **11**, 353 (1971).]

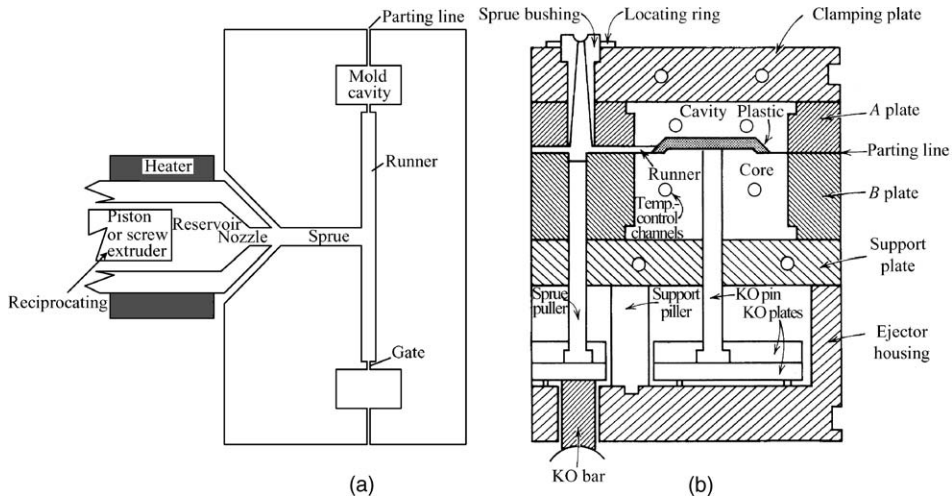


Fig. 13.3 (a) Schematic view of injection molding tooling showing the tip of the injection system and its connection to the mold. Melt passes from the reservoir through the nozzle, the sprue, and the runner system, entering the mold cavities through the gate. (b) Two-plate mold. [Courtesy of Robinson Plastic Corporation.]

quickly solidify upon completion of injection and should be extracted from it without difficulty. The sprue should also form a streamlined transition between the nozzle and runner system. All these functions are attainable by a short, diverging conical shape.

The function of the runner system is to bring the hot melt to the cavities. This should be done with the minimum of material and pressure-drop “waste.” Therefore the runner conduit length must be kept to a minimum, and the cross section should be *optimally* set for low pressure drop, low material waste, and relatively slow cooling, avoiding premature solidification and “short shots.” Generally, the runner is about 1.5 times the characteristic thickness of the molded part, and it is of circular cross section to minimize heat loss as well as to facilitate easy machining. Polymer saving and faster cycles occasionally can be achieved by hot-runner systems where the polymer in the runners is prevented from solidifying through heating units built around them in the mold plate housing them in hot-runner molds. Alternatively, particularly with large parts, it is sufficient to insulate the runner system from the mold. In both cases, the sprue can, in effect, be eliminated from the design.

The gate controls the flow of the polymer melt into the mold. Its size, shape, and position are affected by a number of considerations. First, a narrow gate is desirable from the standpoint of ease of separation of the molded part from the runner system, as well as solidification after the completion of melt injection, to isolate the cavity from the rest of the system. Of course, early solidification must be prevented. Moreover, narrow gates may be detrimental to the finished product because they also bring about large shear rates and stresses (above the melt fracture region), and consequent excessive temperature rise. When the stress level must be reduced, divergent fan gates are used, spreading the flow. Generally speaking, the gate length is about half the characteristic thickness of the section

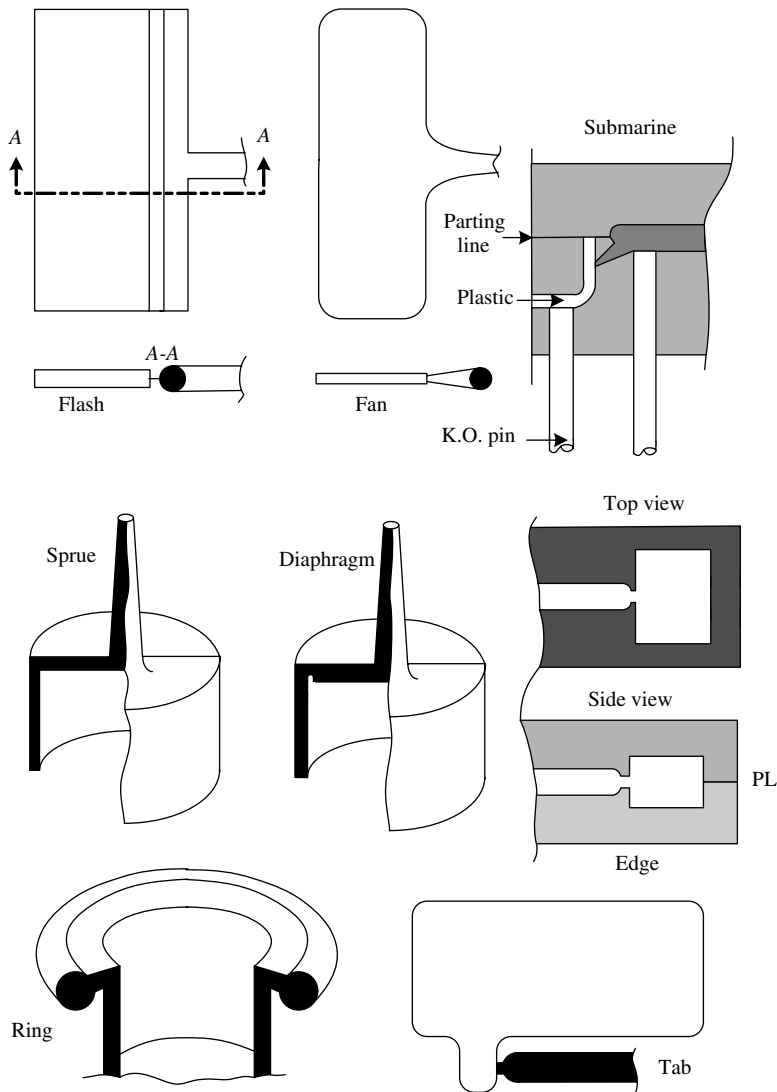


Fig. 13.4 Typical gate designs and locations. [Reprinted by permission from I. Rubin, *Injection Molding—Theory and Practice*, Wiley, New York, 1972.]

where the gate is attached (usually the heavy sections). It is positioned such that the emerging stream impinges on the opposite wall. Figure 13.4 presents typical gate designs and locations. In multiple-cavity molds, gates (and runners) also serve the function of balancing flow such that all cavities fill simultaneously. Further discussion of sprue, runner, and gate design considerations can be found in the literature (3,4). The detailed mathematical modeling of the flow of polymer melts through these conduits is not easy, and involves most of the complexities of the cavity filling problems, which we discuss below.

Example 13.1 Flow in an Idealized Runner System We consider a straight tubular runner of length L . A melt following the Power Law model is injected at constant pressure into the runner. The melt front progresses along the runner until it reaches the gate located at its end. We wish to calculate the melt front position and the instantaneous flow rate as a function of time. We assume an incompressible fluid in isothermal and fully developed flow, and make use of the pseudo-steady state approximation.

With the preceding assumption, the *instantaneous* flow rate $Q(t)$, at given constant inlet pressure, P_0 , and instantaneous fill length, $Z(t)$ at time, t , is given by (see Example 3.4 or Table 12.2):

$$Q(t) = \frac{\pi R^3}{s+3} \left(\frac{RP_0}{2mZ(t)} \right)^s \quad (\text{E13.1-1})$$

The position $Z(t)$ is obtained from a mass balance

$$Z(t) = \frac{1}{\pi R^2} \int_0^t Q(t) dt \quad (\text{E13.1-2})$$

Differentiating the preceding equation, we obtain

$$\frac{dZ(t)}{dt} = \frac{Q(t)}{\pi R^2} \quad (\text{E13.1-3})$$

Finally, substituting the flow rate expression into the preceding equation, followed by integration, gives

$$Z(t) = \left(\frac{1+n}{1+3n} \right)^{n/(1+n)} R \left(\frac{P_0}{2m} \right)^{1/(1+n)} t^{n/(1+n)} \quad (\text{E13.1-4})$$

and the flow rate is

$$Q(t) = \pi R^3 \left(\frac{1+n}{1+3n} \right)^{n/(1+n)} \left(\frac{n}{1+n} \right) \left(\frac{P_0}{2m} \right)^{1/(1+n)} t^{-\frac{1}{1+n}} \quad (\text{E13.1-5})$$

It is interesting to note that the “penetration depth” $Z(t)$ is proportional to the radius R . This implies that the ratio of penetration depths of the same material in two conduits of different radii is given by $Z_1/Z_2 = R_1/R_2$, and for constant P_0 is dependent only on geometry and not the rheological behavior of the fluid. We next consider a polymer melt with $m = 2.18 \times 10^4 \text{ N} \cdot \text{s}^n/\text{m}^2$ and $n = 0.39$, and calculate $Z(t)$ and $Q(t)$ for an applied pressure $P_0 = 20.6 \text{ MN}/\text{m}^2$ in a runner of dimensions $R = 2.54 \text{ mm}$ and $L = 25.4 \text{ cm}$. The expressions for $Z(t)$ and $Q(t)$ for the values just given become

$$Z(t) = 0.188t^{0.281} \quad (\text{E13.1-6})$$

$$Q(t) = \frac{1.07 \times 10^{-6}}{t^{0.719}} \quad (\text{E13.1-7})$$

Values of $Z(t)$ and $Q(t)$ are listed in the following table for various times:

t (s)	Z (m)	Q (m^3/s)
0	0	∞
0.5	0.155	1.76×10^{-6}
1	0.188	1.06×10^{-6}
1.5	0.211	0.8×10^{-6}
2	0.228	0.65×10^{-6}
2.88	0.253	0.5×10^{-6}

These results clearly indicate that we should expect a very high flow rate initially, followed by a rapidly dropping flow rate, $Q(t)$ as the runner fills up. The first half of the runner is filled in 10% of the total runner fill time. From the equation for $Q(t)$ given earlier (under the assumptions made), it is easy to show that, for a constant flow rate, a linear increase in the applied pressure is required. In practice, the initial part of the mold filling cycle is one of increasingly applied pressure and almost constant flow rate. If the mold is easy to fill, this situation will persist until mold filling is completed. On the other hand, if the mold flow resistance is high (as, for example, in Fig. 13.5), the pressure will reach its maximum available value and will remain constant for the rest of the filling time, while the flow rate decreases with time. In the real nonisothermal case, once the flow rate reaches low values, the melt has time to cool by conduction to the cold walls, its viscosity increases exponentially, and the flow stops completely, resulting in "short shots."

For comparison purposes, the numerical simulation results of nonisothermal runner filling are given in the following table (5). For the same conditions, using a flow activation energy value of 6 kcal/g · mole. It is clear from the tabulation, and especially from the nonisothermal-to-isothermal flow ratio, that the polymer is cooling rapidly in the runner and that a "short shot" will result soon after 1 s. Huang's (5) simulation indicates that a "frozen skin" was formed at 0.7 s in the axial region of 2–4 cm from the entrance.

t (s)	Z (t)	Q (t)	$Z(t)/Z(t) _{T=\text{const.}}$ (%)	$Q(t)/Q(t) _{T=\text{const.}}$ (%)
0.5109	0.111	1.10×10^{-6}	0.77	0.63
0.9703	0.140	0.51×10^{-6}	0.74	0.48

After the cavity has been filled, the injection pressure is maintained to "pack" a small additional amount of melt into the cavity and to compensate for the thermal contraction of the polymer during the cooling and solidification stages. Packing increases the cavity pressure rapidly and appreciably. When the externally applied pressure is removed (by retracting the reciprocating screw or piston of the injection-molding machine), backflow out of the cavity takes place, unless the polymer in the gate has solidified or unless such flow is prevented by a one-way valve. At the end of the backflow, if there is any, only cooling of the polymer takes place, together with minute contraction-induced local flows. When the polymer has solidified sufficiently to withstand the forces of ejection, the mold is opened and the molded article is removed from the cavity with the aid of the ejection "knock out" (KO) pins.

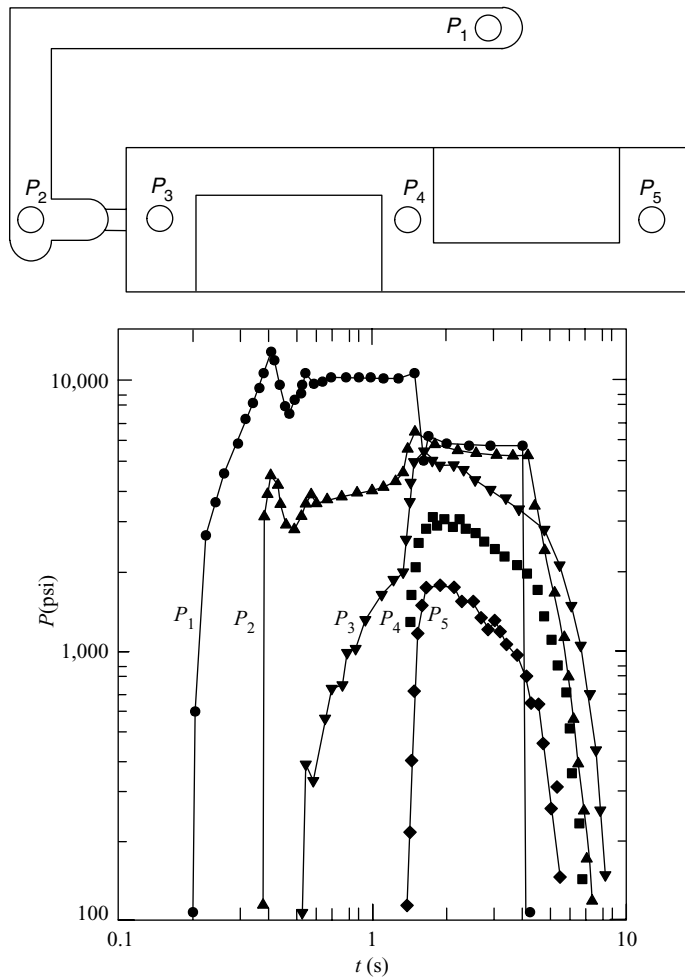


Fig. 13.5 Experimental pressure traces during mold filling of a rectangular cavity shown on the top with polystyrene at 400°F. P_1 is the pressure at the nozzle, P_2 the pressure at the end of the runner outside the gate, and P_3 – P_5 are cavity pressures at the locations indicated. Pressure traces P_4 and P_5 are questionable because of an unintentional preloading of the transducers upon mold closing. [Reprinted by permission from W. L. Krueger and Z. Tadmor, "Injection Molding into Rectangular Cavity with Inserts," *Proc. Society of Plastics Engineering 36th Annu. Tech. Conf.*, Washington, DC, 1978, pp. 87–91.]

A detailed study of mold filling was done by Krueger and Tadmor (6). The various stages of the injection process was followed by pressure gauges in the mold, as shown in Fig. 13.5. In this experiment polystyrene (PS) was injected into a shallow rectangular cavity with inserts as shown in the figure. Pressure transducers were placed in the nozzle, runner, and mold cavity; their output was scanned every 0.02 s and retrieved by a computer. The nozzle pressure was set by machine controls to inject at a constant 10,000 psi and, upon mold filling, to hold the pressure at 5500 psi.

Appreciable pressure overshoots and undershoots are noticeable. The pressure trace at the end of the runner system (P_2) at lower levels follows the pattern of the nozzle pressure.

The two become equal upon cessation of flow when the mold is full. The difference $P_1 - P_2$ indicates the pressure drop over the sprue and runner system. The pressure drop across the gate is given approximated by $P_2 - P_3$. We note that just downstream of the gate, the pressure P_3 increases with time throughout the filling process (from about 0.4 s to 1.3 s). As Example 13.1 pointed out, such a pressure trace approaches conditions of constant filling rate. This is supported by ram position measurements, which were also retrieved at 0.02-s intervals. We further note that, upon mold filling, when P_5 sharply increases, there is also a steep increase in all the pressures except the nozzle pressure, which is then reduced to 5500 psi.

During the “hold” time, the three pressure transducers within the cavity record different pressures in spite of the absence of appreciable pressure drops due to flow. This is probably the result of skin formation and solidification preventing true core pressure (liquid) recordings. All cavity pressures drop gradually upon solidification, and this gradual pressure drop continues after gate solidification. Of particular practical interest is the residual pressure at the time the mold is opened. If it is near zero, there is the real danger that, with further cooling to room temperature, the part will either be smaller than the cavity or will show “sink marks.” On the other hand, if the residual pressure is high, the part cannot be easily ejected from the mold and will be “scarred” or deformed during the process.

From the short description of the molding cycle, it is clear that flow, viscous heat generation (filling flow rates are very high), heat transfer, and melt stress relaxation occur to varying degrees of intensity simultaneously. The transport phenomena involved are coupled, and since the solidification times can be comparable to the polymer relaxation times [Deborah number (De) ~ 1], molded articles solidify under strained conditions, that is, they contain “frozen-in” strains. Such internal strains greatly affect the properties and morphology of molded articles. Thus, we can use the injection molding process to “structure” polymers. We will examine the various stages of injection molding separately.

Mold Filling

It is now clear that there is no simple answer to the question of what are the optimal conditions for the proper molding of a specific polymer in a given mold cavity. Figure 13.6, however, illustrates an empirical answer, showing an experimentally determined “molding area” processing window on the melt temperature–injection pressure plane. Within this area the specific polymer is *moldable* in the specific cavity. The area is bounded by four curves. Below the bottom curve, the polymer is either a solid or will not flow. Above the top curve, the polymer degrades thermally. To the left of the “short shot” curve, the mold cannot be completely filled, and to the right of the “flash” curve, the melt flows in the gaps formed between the various metal pieces that make up the mold, creating thin webs attached to the molded article at the parting lines.

Another practical approach to the question of moldability, especially in comparing one polymer with another, is the use of a standard spiral mold cavity and the measurement, under prescribed molding conditions, of the spiral length filled (7).

Because mold filling is a complex process, flow visualization studies have been useful and necessary, both for the actual mold design and for the mathematical simulation of the process. The first important experimental contributions were made by Gilmore and Spencer (8,9) whose work forms the basis of a review chapter by Beyer and Spencer (10). Ballman et al. (11–13) conducted mold filling experiments in the early 1960s. A decade later, a time that marks the beginning of serious efforts to solve

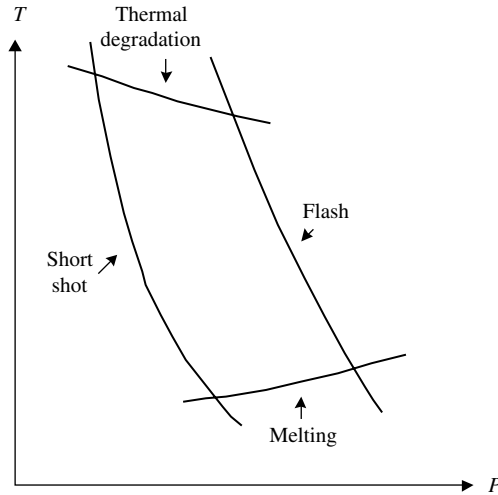


Fig. 13.6 Schematic “molding area” or “molding window” diagram that can be determined for a given polymer and mold cavity.

the injection molding problem, a new wave of mold-filling flow visualization studies were reported by Aoba and Odaira (14), Kamal and Kenig (15), White and Dee (16), and Schmidt (17). These studies revealed that the mode of filling at moderate flow rates is an orderly forward flow, as shown schematically in Fig. 13.7(a) for a constant

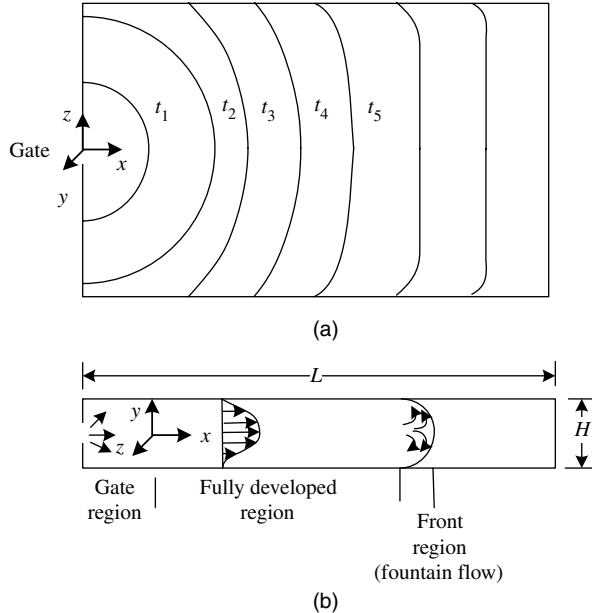


Fig. 13.7 Schematic representation of the flow patterns during the filling of an end-gated rectangular mold whose width is much greater than its thickness. (a) Width direction flow fronts at various times. (b) Velocity profiles in the fully developed region, and schematic representation of the fountain effect in the front region.

depth rectangular cavity. During the early stages of filling, the flow is radial and the melt “front” circular (in this top view). The flow character changes as the melt front advances away from the gate, whereby the predominant velocity component is now v_x and the front shape is either flat for isothermal filling or curved for filling into cold molds (16).

In mold cavities with inserts and nonuniform thickness distribution, the flow pattern is more complicated. This problem was investigated by Krueger and Tadmor (6) using a thin, rectangular 1.5×6 -in cavities like the one shown in Fig. 13.5. Inserts of various shapes and sizes could be placed in different locations in the mold, creating either obstacles to the flow or regions of different thickness. PS was injected, and the position and shape of the advancing front could be traced by a series of short shots, as shown in Fig. 13.8.

Figure 13.8(a) shows the trace of the advancing front recorded from the experimental molded pieces in Fig. 13.8(b). The solid lines are the experimentally measure advancing front lines obtained from the short shots, the simulated results discussed later are marked by the \times signs, and the broken curve shows the weld lines clearly visible in the finished products.

In Fig. 13.8, Sample 1 shows that the outline (shape) of the front is circular in the deep section and becomes somewhat distorted upon entering the thinner region. The flow is split by the T insert and reunites past the insert, forming a weld line. The location and the shape of the weld line are determined by the flow profile around the insert. The insert strongly affects the direction of the advancing front which, as we see later, determines the direction of molecular orientation. We would expect, therefore, a highly nonuniform orientation distribution in such a mold.

In Fig. 13.8, Sample 2, the insert was placed in the thin section close to the gate, completely changing the weld line location and shape, as well as the advancing melt profiles (consequently, the orientation distribution). Figure 13.8, Sample 3, shows an S-shaped deep section connected by a thin web. We note that the penetration lengths in the deep and shallow sections of the mold, which are being simultaneously filled, qualitatively follow the predictions of Example 13.1, where for $P = \text{constant}$, $Z(t)$ is proportional to the cross-sectional thickness of the channel, and, to a first approximation, is independent of the rheological properties of the melt. This is, in fact, what is observed (6). There is also formation of two weld lines, where the second weld line branches out sideways upon entering the deep section.

Figure 13.8, Sample 4, shows flow in an S-shaped cavity without weld line formation. Finally, Fig. 13.8, Sample 5, shows flow around square and circular inserts, with pronounced weld line formation. These results draw attention to the complex flow patterns occurring even in relatively simple molds. In particular, it is interesting to note the shape of weld lines, which are important not only because they sometimes form visual defects in the product, but also because they generally represent “weak” regions in properties. In general, we can state that weld lines are formed whenever advancing melt fronts “meet,” that is, whenever their outward normals are opposite or converging. The former case occurs in double gate filling and immediately past cavity obstacles, whereas the latter occurs when the front is composed of two segments and there is a discontinuity in the shape of the advancing front.

As mentioned in Section 12.4, weld line interfaces can be characterized by an appreciably different (lower) entanglement level as compared to the bulk of the material. The formation and properties of the weld lines can be explained in view of the detailed

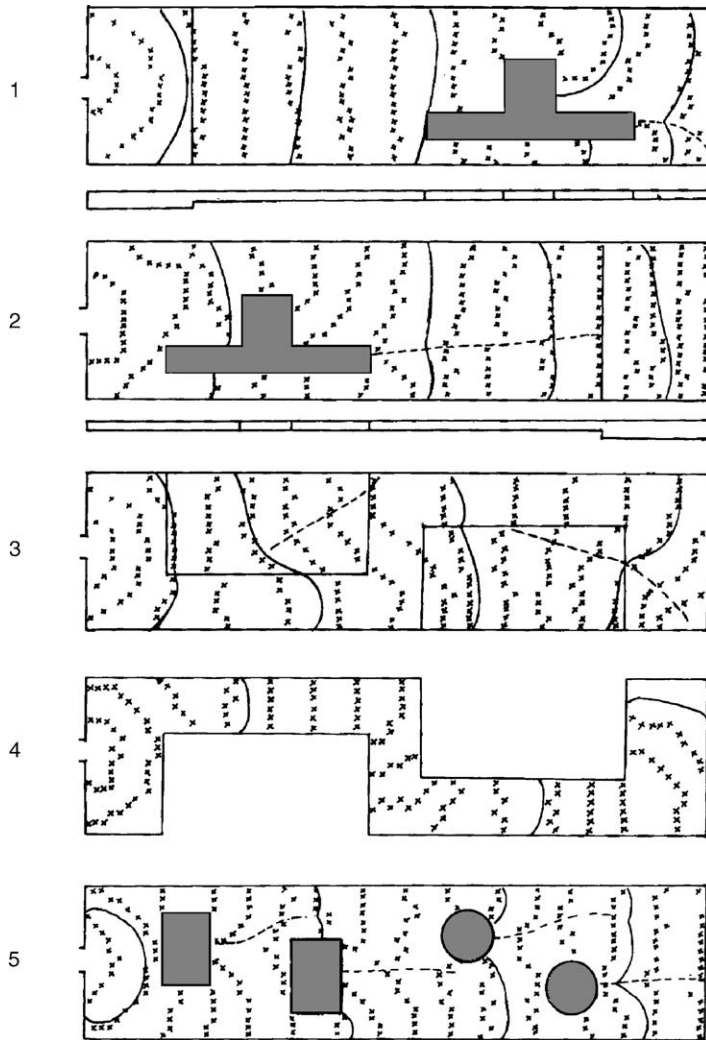


Fig. 13.8(a) Experimental (solid lines) and simulated (\times) advancing front profiles in a shallow rectangular cavity with inserts of various shapes. Experimental profiles were obtained by short shots (6), as shown in Fig. 13.8(b). Cavity dimensions are 3.8×15.2 cm (1.5×6 in). Sample 1: A T-shaped insert completely obstructing the flow, and a step reduction in thickness as indicated in the figure. The deep section was 0.335 cm and the thin section varied from 0.168 to 0.180 cm. (In the simulations, the actual thickness distribution was determined by measuring the injection molded samples corrected for contraction, but not for mold distortion.) Sample 2: the reverse of Sample 1, but the shallow section has a uniform thickness of 0.166 cm. Sample 3 contained two rectangular web inserts, giving rise to a correspondingly shallow section, 0.35 cm thick. Sample 4 had two rectangular inserts blocking flow, giving rise to an S-shaped cavity of thickness ranging from 0.165 cm to 0.173 cm. Sample 5 had two rectangular and two circular inserts obstructing the flow with the rest of the cavity at uniform thickness of 0.323 cm. The broken curves denote visually observable weld lines. [Reprinted by permission from W. L. Krueger and Z. Tadmor, "Injection Molding into Rectangular Cavity with Inserts," *Proc. Soc. of Plastics Engineers, 36th Annu. Techn. Conf.*, Washington, DC, 1978, pp. 87–91.]

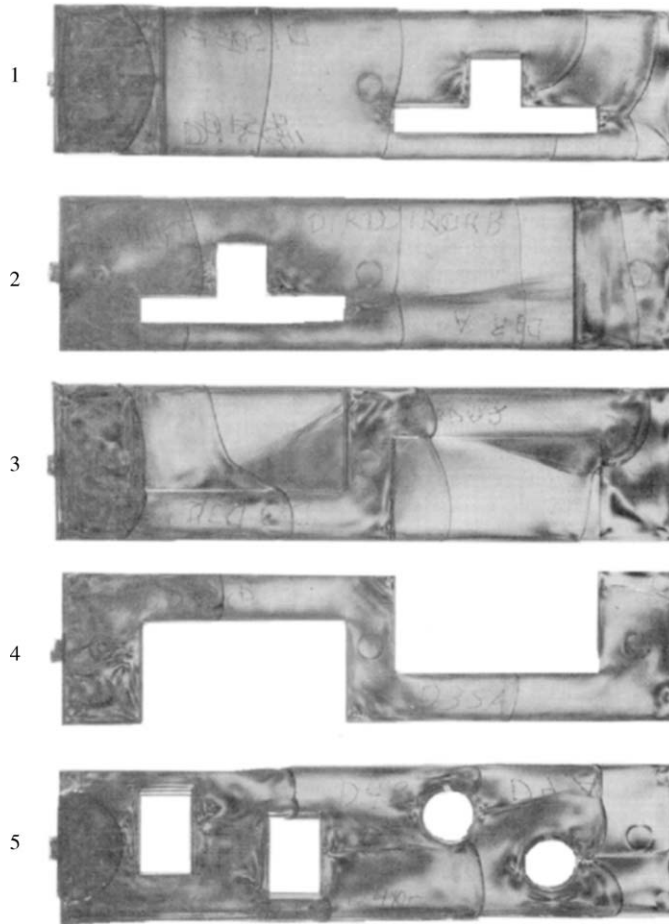


Fig. 13.8(b) Photographs of superimposed short shots using polarized light. [Reprinted by permission from W. L. Krueger and Z. Tadmor, "Injection Molding into Rectangular Cavity with Inserts," *Proc. Society of Plastics Engineers, 36th Annu. Techn. Conf.*, Washington, DC, 1978, pp. 87–91.]

flow pattern at and near the advancing front, which is different from that in the bulk. In the front region, the melt at the center of the thickness direction, which moves with the maximum velocity of the parabolic-like velocity profile, spills out or *fountains* out to the mold wall to form the surface of the molded article at that location, as in Fig. 13.7(b). This is the only way of filling the region near the wall of the mold, where there is no slip. Thus, in the front region, the central core decelerates from the maximum velocity at the centerline upstream from the front, to the mean velocity at which the front advances. As it decelerates in the direction of flow, x , it acquires a velocity component in the thickness direction, y .

The term *fountain effect* or *fountain flow* was coined and discussed by Rose (18), and it is essentially the reverse of the flow observed near a plunger emptying a fluid out of a channel of the same cross section. The two-dimensional flow in the

front region is important in determining the quality and morphology of the surface of the molded article as well as the nature of weld lines. We shall return to weld line morphology following the discussion of the flow pattern in the melt front.

When the gate faces a mold wall that is far away, and when the filling flow rate is very high, the phenomenon of “jetting” is observed. The melt emerging from the gate forms a jet that rapidly advances until it is stopped by the mold wall opposite to it. Both melt fractured and smooth melt jets have been observed. There are two modes of mold filling under jetting conditions. In the first mode, jetting continues after the jet tip has touched the opposite wall and the jet folds over many times, starting at the impingement surface and continuing toward the gate. When the cavity is almost full of the folded melt jet, regular filling and compression of the folded jet occurs. Thus the filling is in the backward direction. In the second mode of filling, jetting stops after impingement of the jet tip on the opposite wall, and regular forward filling commences. In both cases, weld lines may present problems with respect to the optical and mechanical properties of the molded article.

It has been experimentally observed that jetting can occur whenever the dimension of the fluid stream is smaller than the smallest dimension in the plane perpendicular to the flow (19). It is thus related both to the gate size and to the degree of extrudate swelling of the melt, rather than to the level of the axial momentum. Filled polymers, which swell less than unfilled melts, exhibit jetting at lower filling rates. Two “cures” for jetting are commonly practiced. First, the gate is positioned so that the emerging melt impinges on a *nearby* wall; second, “fan” gates are used, which increase one of the dimensions of the exiting melt stream, thus decreasing its momentum.

Mold Filling Simulations

A complete mold filling simulation would require the calculation of the detailed velocity and temperature profiles throughout the mold flow region, including the position and shape of the advancing front. This would suffice, in principle, to determine orientation distribution affecting the article morphology, which evolves upon cooling and solidification. Such a complete model, if available, would be instrumental in assisting the theoretical mold design, as well as in optimizing molding conditions for specified property requirements.

The complete problem, of course, is extremely complex even for a relatively simple mold, and is hardly soluble for intricate molds. Fortunately, however, a great deal of information and insight can be obtained by simulating (i.e., modeling) selected aspects of the filling problem in isolated “flow regions.” Each of these regions requires a unique approach and mathematical tools. Considering the mold filling visualizations in Fig. 13.7(b), we distinguish among the following regions.

1. *The “fully” developed region.* During the filling process most of the melt flows in an almost fully developed flow in a narrow-gap configuration between cold walls. The nature of this flow determines filling time and part core orientation, as well as the occurrence of short shots. A great deal of insight can be obtained by analyzing one-dimensional flow (either radial, spreading disk, or rectilinear) of hot melt between cold walls. The coupling of the momentum and energy equation eliminates analytical solutions, and finite difference methods can be used.

2. *The close neighborhood of the front region.* As pointed out earlier, this region determines both surface properties (skin formation) and weld line formations. Hence, a detailed analysis of the front region is warranted. This region can be simulated either by approximate analytical or detailed numerical models.
3. *The gate region.* This region is dominant at the beginning of mold filling. It contributes less as the melt front advances and, because fresh melt is hot in this region, melt memory of the flow experience in this region soon decays.

We discuss some of these regions in detail below. In addition, we concern ourselves with the *overall* flow pattern during filling. Recall that the manner in which a mold is filled—that is, the location of the advancing melt front—affects the weld-line location and the orientation distribution and may be responsible for poor mold filling conditions.

The Fully Developed Region A number of mathematical simulations of the flow and heat transfer in the fully developed region have been reported (11,15,20–25). Here we follow the work of Wu et al. (23), who simulated the filling of a center gated disk (Fig. 13.9). A frozen surface layer (frozen “skin”) can be formed during the filling process, which forces the fluid to flow through a channel of reduced cross section. Assuming constant thermophysical properties, quasi-steady-state, $\partial v_r / \partial t = 0$, and neglecting $\tau_{\theta\theta}$ and τ_{rr} in the r -momentum equation, as well as the axial conduction in the energy equation, these balance expressions become

$$\frac{d\tau_{zr}}{dz} = \frac{dP}{dr} \quad (13.1-1)$$

$$\rho C_p \left(\frac{\partial T}{\partial t} + v_r \frac{\partial T}{\partial r} \right) = k \frac{\partial^2 T}{\partial z^2} - \tau_{\theta\theta} \frac{v_r}{r} - \tau_{zr} \frac{\partial v_r}{\partial z} \quad (13.1-2)$$

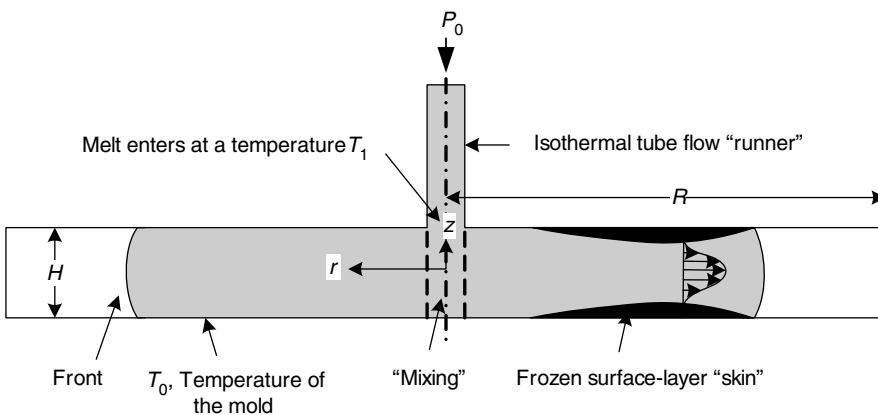


Fig. 13.9 Cross-sectional view of a center-fed, disk-shaped mold cavity. Indicated schematically are the frozen-skin layer that can form during filling, as well as the “nipple”-shaped velocity profile.

The term $\tau_{\theta\theta}v_r/r$ is significant only at small values of r . Inserting the Power Law constitutive equation

$$\tau_{zr} = -m \left| \frac{dv_r}{dz} \right|^{n-1} \frac{dv_r}{dz} \quad (13.1-3)$$

where $m = m_0 \exp(\Delta E/RT)$ and n is a constant. The radial pressure drop is given (22) by the following equation

$$\left| \frac{dP}{dr} \right| = \left[\frac{Q(t)}{4\pi r \int_0^{H/2} (z^{1+s}/m^s) dz} \right]^n \quad (13.1-4)$$

The velocity can be obtained by integration of Eq. 13.1-1 and using Eq. 13.1-4

$$v_r(r, z, t) = - \left| \frac{dP}{dr} \right|^s \int_{H/2}^z \left(\frac{z}{m} \right)^s dz \quad (13.1-5)$$

For the numerical calculation of the pressure drop, as well as the velocity field, one must iterate the pressure at every radial position until the flow rate in the cavity is the same as that across the tube entrance. In both Eqs. 13.1-4 and 13.1-5, the consistency index m varies with z , since the temperature varies in the thickness direction. Two boundary conditions used in the energy equation are of interest. At the advancing front $r = r_{ik}$, the heat transferred to the air in the mold dictates that the term $2r_{ik} h(T_{ik} - T_a)/(r_{ik}^2 - r_{ik-1}^2)$ be included in the right-hand side of Eq. 13.1-2, where h is the heat-transfer coefficient to the air. At the mold wall

$$k \left(\frac{\partial T}{\partial z} \right)_{z=H/2} = h \left[T_0 - T \left(r, \frac{H}{2}, t \right) \right] \quad (13.1-6)$$

where T_0 is the mold bulk temperature and h is a heat-transfer coefficient that is taken to be equal to k_{mold}/d , where d is the distance from the mold surface to the depth where the mold temperature is, T_0 . The energy equation is transformed into a difference equation using an implicit formula and solved by the Crank–Nicolson (26) or by methods discussed by O'Brien et al. (27). The grid size used can be logarithmically decreasing with increasing z , so that the details of the rapidly changing temperature and velocity can be revealed.

The simulation results indicate that as far as filling time calculations are concerned, the important variable is the ratio of the rate of heat generated by viscous dissipation to that lost by heat transfer to the cold walls. As a matter of fact, when the ratio is close to unity, fair estimates of filling times can be obtained by assuming isothermal flow.

The flow front is found to advance at an ever decreasing rate, when the disk-shaped cavity is fed at a constant tube-entrance pressure (see Example 13.1). Correspondingly, the filling pressure builds up at an ever-increasing rate if the front is to advance at a constant filling rate. As mentioned earlier, a constant filling rate can be assumed if the mold is easy to fill. Realistically, the flow rate is constant for the early part of filling, and drops during

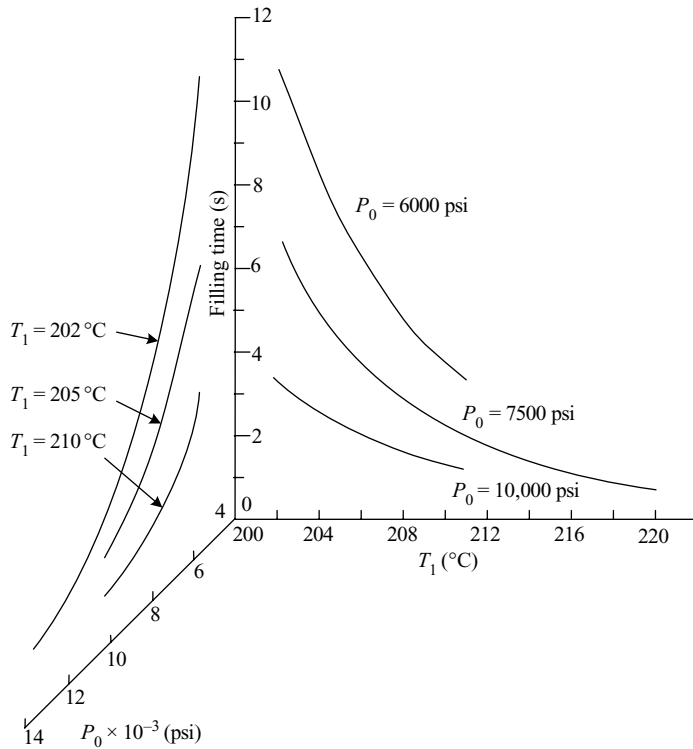


Fig. 13.10 Filling time versus entrance melt temperature at three constant injection pressures and filling time versus injection pressure at three constant entrance melt temperatures. Mold dimensions are $R = 9$ cm, $H = 0.635$ cm. The polymer is unplasticized polyvinyl chloride (PVC) of $n = 0.50$, $m(202^\circ\text{C}) = 4 \times 10^4$ ($\text{N} \cdot \text{s}^n/\text{m}^2$), $A = 6.45 \times 10^{-8}$, $\Delta E = 27.8$ (kcal/g · mole), $\rho = 1.3 \times 10^3$ (kg/m^3), $C_p = 1.88 \times 10^3$ ($\text{J}/\text{kg} \cdot \text{K}$), and $k = 9.6 \times 10^{-2}$ ($\text{J}/\text{m} \cdot \text{s} \cdot \text{K}$). [Reprinted by permission from P. C. Wu, C. F. Huang, and C. G. Gogos, "Simulation of the Mold Filling Process," *Polym. Eng. Sci.*, **14**, 223 (1974).]

the latter part. The filling time versus melt temperature at the mold entrance, as well as versus injection pressure, is plotted in Fig. 13.10 for an unplasticized polyvinyl chloride (PVC) resin.

The slope of the filling time versus melt temperature curves depends on the activation energy for flow, that is, the temperature sensitivity of the consistency index m . On the other hand, the slope of the filling time versus injection pressure curves depends on the value of the Power Law model index n . The temperature profiles at the instant of complete fill for the same mold and resin entering the mold at 202°C and 15,000 psi are shown in Fig. 13.11. A number of features are interesting. First, almost isothermal conditions prevail in the thickness region from the center of the mold halfway to the wall. This is because the velocity profile is almost flat and heat transfer is negligible. Appreciable and rapid conductive cooling occurs only *very* near the mold cavity wall.

If 150°C is taken to be a temperature level where PVC has a practically infinite viscosity, then an effective thin frozen skin is formed for $r > 2.5$ cm. At lower injection

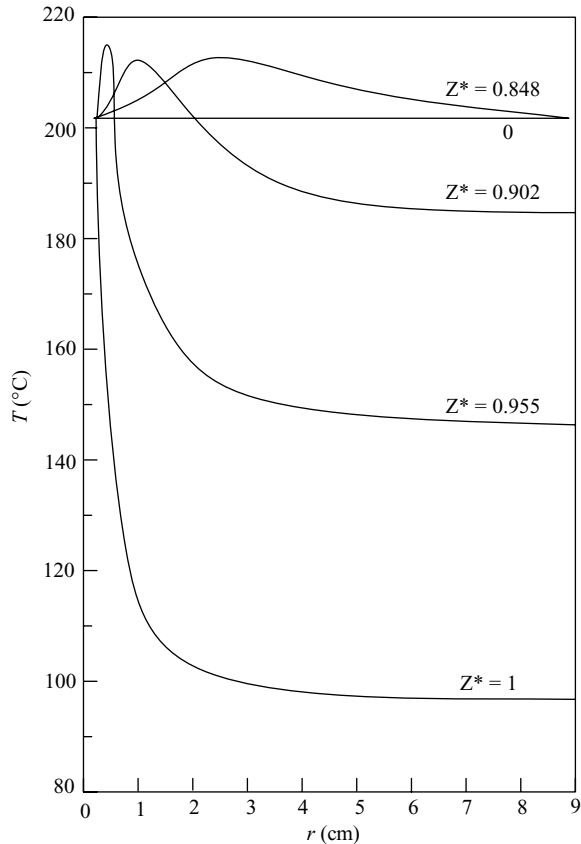


Fig. 13.11 Temperature distribution at the instant of fill as a function of radial distance and at various values of $Z^* = z/(H/2)$, for PVC at 15,000 psi, $H = 0.635$ cm, $t = 1.45$ s; $R = 9$ cm, $T_1 = 202^\circ\text{C}$, $T_0 = 30^\circ\text{C}$. [Reprinted by permission from P. C. Wu, C. F. Huang, and C. G. Gogos, "Simulation of the Mold Filling Process," *Polym. Eng. Sci.*, **14**, 223 (1974).]

pressures, thicker frozen skin layers are formed. The dependence of the frozen-skin profile on molding variables is indicated in Fig. 13.12, where the frozen skin at the moment of fill is plotted under the conditions specified. Its thickness decreases with increasing pressure, melt, and mold temperature and mold thickness. The shape of the frozen skin profile is characterized by a maximum (a "pinch" region). Near the entrance, fresh hot melt keeps the skin to a minimum, and near the front, the melt near the walls is still hot because it originates from the center region. It is the pinch region, in which flow would stop first, that would be responsible for short shots at low injection pressures. It is also worth noting that the shape of the frozen skin creates both an axial stretching flow and a z -component velocity. This is particularly true in the gate region. The problem has been discussed by Barrie (28). In the disk cavity, the stretching flow discussed earlier offsets the assumption of neglecting the term dv_r/dr .

The Front Region The front region was analyzed by Tadmor (29) in an attempt to model the experimentally observed molecular orientation distribution in molded articles.

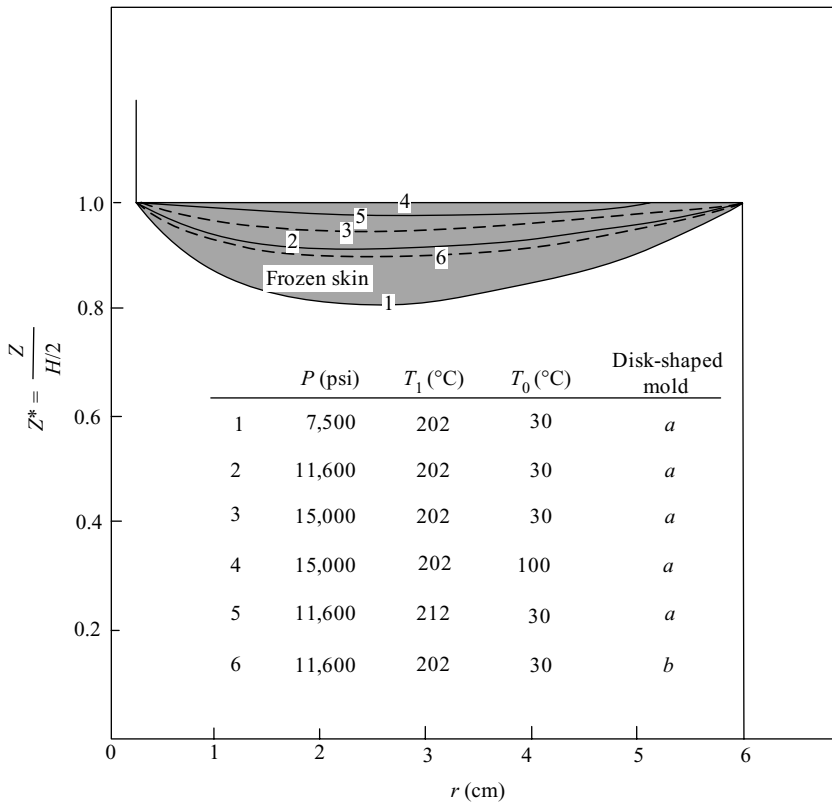


Fig. 13.12 Frozen skin profiles in two disk-shaped center-fed molds (*a*: $R = 6$ cm, $H = 0.5$ cm; *b*: $R = 6$ cm, $H = 0.3$ cm). Rigid (unplasticized) PVC was considered in the simulation. The frozen-skin region is defined by $T < 150^{\circ}\text{C}$ (5). [Reprinted by permission from P. C. Wu, C. F. Huang, and C. G. Gogos, "Simulation of the Mold Filling Process," *Polym. Eng. Sci.*, **14**, 223 (1974).]

Figure 13.13 shows such a distribution measured by Menges and Wübken (30) for amorphous PS. They measured the shrinkage of microtomed molded samples at elevated temperatures. Figure 13.13(a) shows the longitudinal (flow direction) orientation distribution at two injection rates. The characteristic features of the orientation distribution are a maximum orientation at the wall that vanishes at the center with a local maximum near the wall. In Fig. 13.13(b), the longitudinal orientation at the wall and secondary maximum orientation are in close proximity, and the transverse orientation drops continuously from a maximum value at the surface.

Tadmor (29) suggested that both the orientation in the close neighborhood of the wall and the transverse orientation originate from the fountain-type flow (18) in the advancing front region, whereas the source of the orientation in much of the bulk of the material results by-and-large from the shear flow upstream from the front. Figure 13.14 shows a numerical simulation by Mavridis et al. (31) of the velocity field in the advancing front from a coordinate system moving at the average velocity, where the fountain flow is clearly visible.

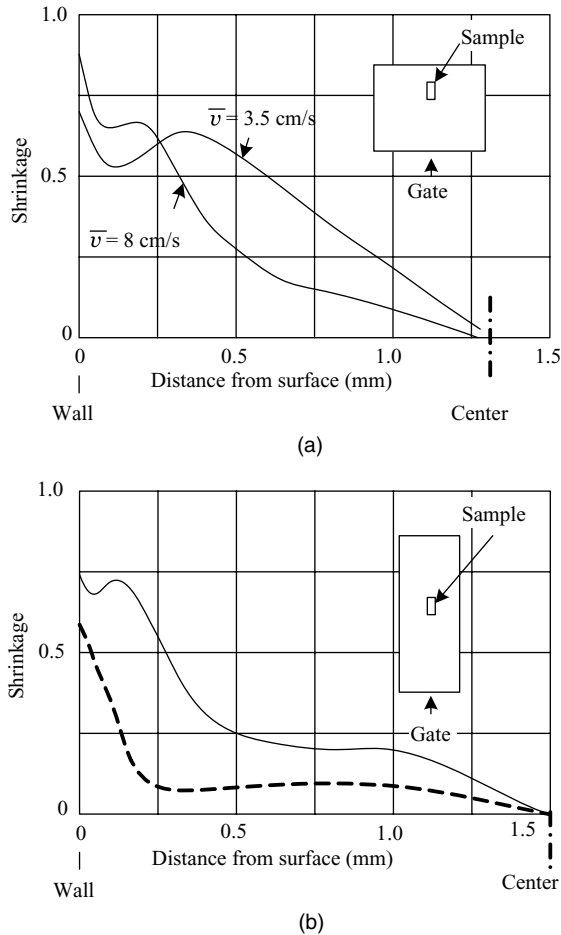


Fig. 13.13 Shrinkage distributions of injection molded amorphous PS (a) at two injection rates: longitudinal direction, (b) solid curves, longitudinal direction; broken curve, transverse direction. [Reprinted with permission from G. Menges and G. Wübken, "Influence of Processing Conditions on Molecular Orientation in Injection Molds," *Soc. Plastics Eng., 31st Annual Technical Conference*, Montreal, Canada, 1973.]

Figure 13.15 shows schematically the changing shape of a square-shaped fluid particle as it approaches the advancing front. It decelerates in the direction of flow and accelerates in the perpendicular direction. Thus, the fluid particles are stretched perpendicular to the direction of flow. By assuming a steady extensional flow in the y direction, Tadmore developed a semiquantitative model for the orientation distribution. The velocity profile in a coordinate system located on the advancing front and moving with it at the mean velocity $\langle v \rangle$, is $v_x = -\dot{\epsilon}_{pl}x$, $v_y = \dot{\epsilon}_{pl}y$, and $v_z = 0$, where $\dot{\epsilon}_{pl}$ is the steady rate of elongation (this velocity profile also describes incompressible stagnation potential flow). The molecular orientation is a function of the *rate* of elongation, which can be estimated by assuming that the maximum velocity $v_{x,max}$, upstream of the advancing front, drops to the mean front velocity $\langle v \rangle$ within a certain distance. Assuming this distance to be of the order of the gap

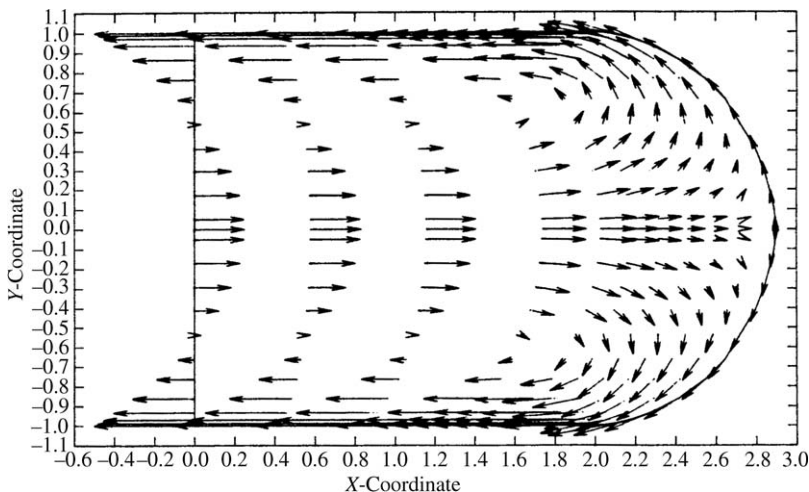


Fig. 13.14 Numerical simulation of the velocity field behind an advancing liquid front, moving at constant speed inside a two-dimensional channel. Calculations were carried out with a standard, general purpose FEM program. [Reprinted by permission from H. Mavridis, A. N. Hrymak and J. Vlachopoulos, “A Finite Element Simulation of the Fountain Flow,” *Polym. Eng. Sci.*, **26**, 449 (1986).]

thickness, which is quite reasonable on the basis of Fig. 13.14, we obtain the following estimated rate of elongation:

$$\dot{\epsilon}_{pl} = \frac{dv_y}{dy} = -\frac{dv_x}{dx} = \frac{\langle v \rangle - v_{max}}{H} \tag{13.1-7}$$

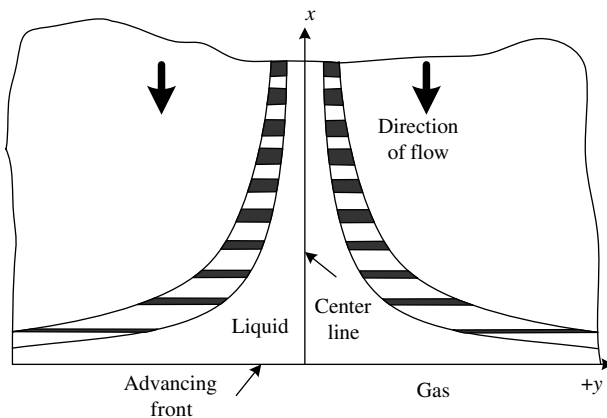


Fig. 13.15 Schematic representation of the flow pattern in the central portion of the advancing front between two parallel plates. The coordinate system moves in the x direction with the front velocity. Black rectangles denote the stretching deformation the fluid particles experience. [Reprinted by permission from Z. Tadmor, “Molecular Orientation in Injection Molding,” *J. Appl. Polym. Sci.*, **18**, 1753 (1974).]

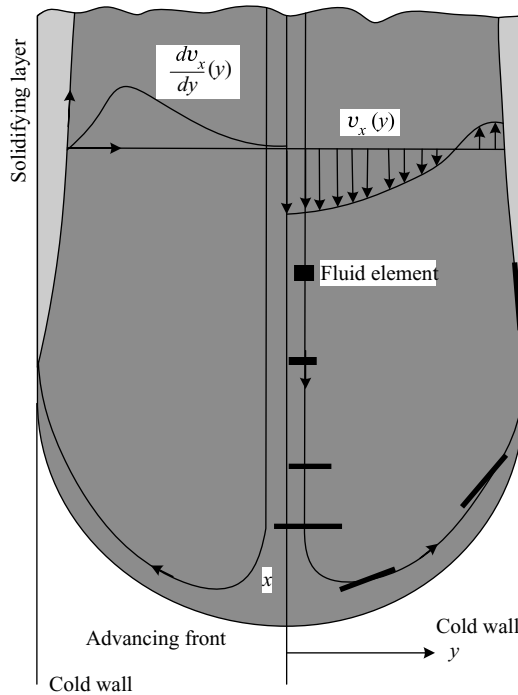


Fig. 13.16 Schematic representation of the flow pattern in the advancing front between two parallel cold walls. Black rectangles denote the stretching and orientation of a fluid particle approaching the central region of the front. The curved shape of the front causes fluid particles initially oriented in the y direction to end up on the wall, oriented in the x direction. The velocity profile upstream from the front is in the x direction and is viewed from a coordinate system located on the front. [Reprinted by permission from Z. Tadmor "Molecular Orientation in Injection Molding," *J. Appl. Polym. Sci.*, **18**, 1753 (1974).]

Note that $\langle v \rangle < 0$ and $v_{\max} < 0$, since they are in the negative x direction and hence, $\dot{\epsilon}_{\text{pl}} > 0$. If v_{\max} is taken from the fully developed flow of a Power Law model fluid between parallel plates, then

$$-\dot{\epsilon}_{\text{pl}} = \left(\frac{n}{n+1} \right) \frac{\langle v \rangle}{H} \quad (13.1-8)$$

Clearly, according to this model the rate of elongation increases with injection rate, with decreasing gap and increasing n . Because the shape of the front is not flat but, as shown in Fig. 13.16, bends "backward" and becomes *tangent* to the walls at $y = \pm H/2$, the fluid elements that were oriented by the fountain flow in the y direction are deposited on the cold wall with an x -direction orientation.

Thus, as the result of the fountain type of flow, an oriented polymer layer originating from the central core of the advancing front and experiencing a steady elongation rate given in Eq. 13.1-8 is deposited on the cold wall of the mold, where it solidifies upon contact with the cold wall, retaining its elongational orientation. Molecular relaxation occurs further away from the surface into the skin layer, reducing this orientation. The

final orientation distribution in the skin layer will be a function of the cooling rate and the spectrum of relaxation times. The fountain-type flow mechanism and the orientation model just described suggest that in narrow-gap flow, skin-layer orientation is unidirectional in the direction of the front advances. If, however, the cross section of the flow is deep, the fountain-type flow leads to biaxial orientation, that is, orientation in the x -longitudinal and z -transverse directions.

Further away from the surface, the fully developed shear flow behind the front is responsible for any molecular orientation that may be present in the final product. Shear orientation, is a function of shear rate, which varies over the gap. As discussed earlier, in a fully developed flow in molds with cold walls, $\dot{\gamma}$ is almost zero in the immediate vicinity of the wall, exhibits a maximum *near* the wall, and is very low in the central core. Thus the initial shear orientation distribution at any particular location in the mold is approximately determined by the local shear-rate distribution at the moment of fill. Shear orientation therefore is unidirectional in the direction of flow. This initial shear orientation relaxes to various degrees, depending on the cooling rate and the relaxation spectrum. A complete orientation distribution can be approximately obtained by superimposing the elongational and shear orientations. The result, depending on the relative magnitude of the two orientation sources, may be complex, as is the case in Fig. 13.13(a). Alternatively, if the shear orientation is dominant, a maximum orientation is exhibited at a short distance from the wall where the shear rate was maximum. Clearly, the transverse orientation distribution [broken line in Fig. 13.13(b)] exhibits no secondary maximum, lending support to the assumption that it originates from the elongational type of flow in the advancing front. We should note that the relative significance of the orientation sources, as well as the detailed distribution, depend on polymer properties (ability to orient during and relax upon cessation of flow), injection conditions (filling rate, melt, and mold temperatures), and mold geometry.

Finally, by assuming that there is a quantitative relationship between shrinkage due to orientation and mean molecular end-to-end distance, following the framework of the previously described model, and assuming a bead-spring molecular model developed by Warner and Christiansen and Bird (32), Tadmor (29) obtained orientation distributions that, with a reasonable choice of parameters, agreed semiquantitatively with experimental measurements (30). The flow pattern and temperature distribution in the advancing melt, both in the bulk of the liquid and the frontal region, affect not only molecular orientation distribution, but are also frozen in strains and crystallinity distributions that have a decisive effect on the properties of the final product. Therefore, a great deal of work has been done on modeling such flows with Newtonian and non-Newtonian fluids.

Mavridis et al. (31), as previously pointed out, not only solved the flow pattern using FEM, but also dealt with the consequences of the deformation history experienced by the fluid elements on the frozen strains of injection molded parts. Dietz, et al. (33) demonstrated that birefringence measurements during and after filling can be useful in obtaining information about the filling flow kinematics. Birefringence measurements are related to the stress field through the stress optical law, $\Delta n = C\sigma$, where C is the "universal" stress optical coefficient for amorphous matter. The stress, in turn, is related to the flow kinematics by assuming the appropriate constitutive relations for flow and stress relaxation. Conversely, one can check the validity of assumed velocity fields and constitutive relations by comparing the predicted birefringence to that obtained by experiments.

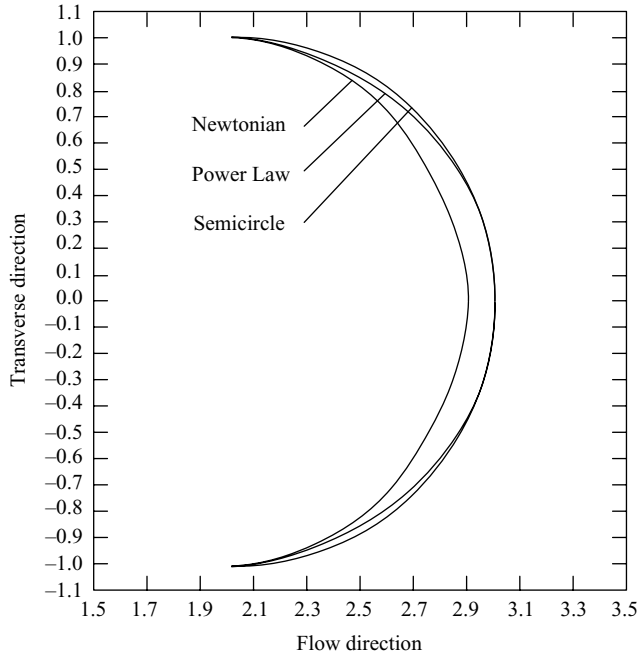


Fig. 13.17 Comparison of advancing front shapes for Newtonian and Power Law fluids (planar geometry). Power Law parameters: $m = 10,000 \text{ Pa} \cdot \text{s}^n$, $n = 0.5$, $\dot{\gamma}_w = 500 \text{ s}^{-1}$. [Reprinted by permission from H. Mavridis, A. N. Hrymak, and J. Vlachopoulos, "A Finite Element Simulation of Fountain Flow," *Polym. Eng. Sci.*, **26**, 449 (1986).]

Gogos and Huang (34) and Huang (35) used the "marker and cell" method to investigate the melt front flow. Assuming isothermal Newtonian and Power Law fluid behavior, they obtained fountain-type flow patterns. Furthermore, their results are in good agreement with the experimental work of Schmidt (17) for nonisothermal flows, where V-shaped streaks of tracer polymer introduced at midplane were observed. Similar results were obtained by Friedrichs and Guçeri (36) using a hybrid three-dimensional and two-dimensional numerical technique to handle the three-dimensional advancing front flow and the Hele–Shaw flow behind it. Mavridis et al. (31), as pointed out earlier, used a finite-element methods (FEM) scheme developed by Mitsoulis and Vlachopoulos (37) to study the isothermal fountain flow of Newtonian and Power Law fluids. They followed the iterative method of Orr and Scriven (38) to find the location and shape of the melt front, and found that the difference between the calculated Newtonian and Power Law front shapes is small. As is seen in Fig. 13.17, the front is very close to a semicircle for Power Law fluids. Recently, Chung and Kwon (39) used a rigorous three-dimensional FEM analysis, utilizing the pseudoconcentration method at the advancing melt front capturing technique (40,41).

Figure 13.18 gives an example of the predicted flow field viewed from a reference frame moving with the velocity of the flow front for a center-gated disk mold. By this method, using a fiber-filled material, Dinh and Armstrong (42) succeeded in predicting fiber orientation distributions closer to the experimentally measured ones than those of assuming a Hele–Shaw flow throughout.

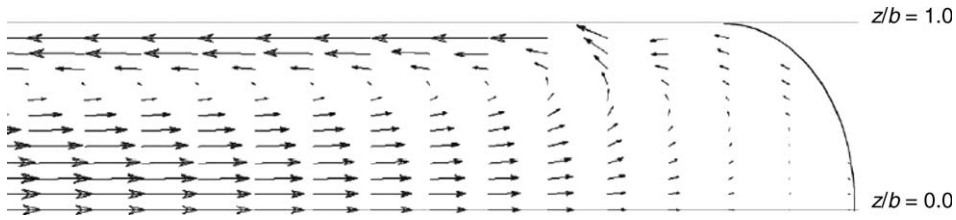


Fig. 13.18 Predicted velocity field showing fountain flow around the melt front region for non-Newtonian fiber suspension flow at about half the outer radius of the disk. The reference frame is moving with the average velocity of melt front, and the length of arrow is proportional to the magnitude of the velocity. The center corresponds to $z/b = 0$ and wall is $z/b = 1$, where z is the direction along the thickness and b is half-gap thickness. [Reprinted by permission from D. H. Chung and T. H. Kwon, "Numerical Studies of Fiber Suspensions in an Axisymmetric Radial Diverging Flow: The Effects of Modeling and Numerical Assumptions," *J. Non-Newt. Fluid Mech.*, **107**, 67–96 (2002).]

Extensive experimental and simulation investigations (43–45) consistently show that the rheological melt properties do not affect the shape of the advancing front, as indicated in Fig. 13.17. The reason for this may be attributed to conservation of mass, and not the momentum, governing the flow-front kinematics (46). Thus, the following fourth-order approximate expression (47) for the velocity field of an end-fed wide-slit mold with respect to an observer moving with the front velocity $v_x \neq \dot{z}$ may be of general use for obtaining particle tracking information in the flow front domain, which is taken to be of length equal to the slit spacing H .

$$\frac{v_x}{\bar{v}_x} = -(0.5 - 6z^2/H^2) \times [1 - 1.45 \exp(-5x/H) \sin(0.76 + 2x/H)] - 0.53(1 - 80z^4/H^4) \exp(-5x/H) \sin(2x/H) \quad (13.1-9)$$

$$\frac{v_z}{\bar{v}_x} = z/H(1 - 4z^2/H^2)[3.63 \exp(-5x/H) \sin(0.76 + 2x/H) - 1.45 \exp(-5x/H) \cos(0.76 + 2x/H)] - 2z/H(1 - 16z^4/H^4)[1.32 \exp(-5x/H) \sin(2x/H)] \quad (13.1-10)$$

The dimensionless residence time is

$$\bar{t}_r = \frac{t_r \bar{v}_x}{H/2} \quad (13.1-11)$$

with dimensions scaled with $H/2$, and is shown in Fig. 13.19. The folding point or plane is the dimensionless z_u position where, from the moving observer frame used, the velocity $v_x(z)$ can be considered negative.

Elucidating the flow pattern in the advancing front also helps to better understand the weld-line formation when two fronts collide. Figure 13.20 depicts the various stages of flow during weld line formation. When they meet, the two fronts are made of polymer molecules that are aligned with the front shape. Thus, they will meet tangentially. Following the first contact, a stagnation-type flow fills the two wedge-shaped regions next to the two mold walls. This flow further stretches the free boundaries of the two fronts and

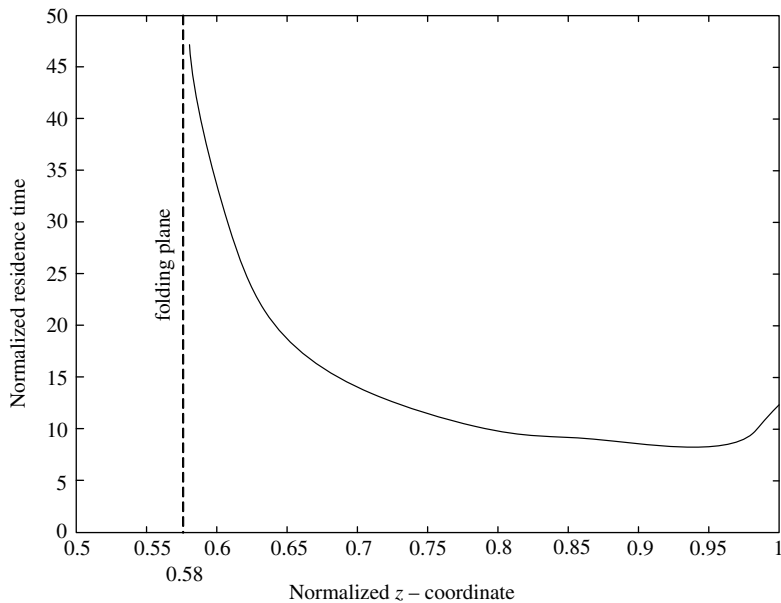


Fig. 13.19 Normalized residence time ($\bar{t}_r = t_r \bar{v}_x / (H/2)$) as a function of normalized position ($\bar{z}_u = z_u / (H/2)$), where a particle leaves the flow front domain; the dashed line indicates the position of the folding point. [Reprinted by permission from G. W. M. Peters, P. J. L. van der Velden, H. E. H. Meijer, and P. Schoone, "Multilayer Injection Molding," *Int. Polym. Process.*, **9**, 258–265 (1994).]

has a tendency to resist the packing flow that is necessary to avoid small sink marks at the weld line.

Front Instabilities During mold filling flow instabilities, which apparently originate from the advancing front, may occur. Bogaerds et al. (47) reviewed flow instabilities that normally occur above a critical filling rate, treating them analytically and experimentally. The general nature of such instabilities are surface defects, characterized by shiny and dull bands periodically appearing and alternating from top to bottom surfaces. They are roughly perpendicular to the flow direction, as shown in Fig. 13.21. The defects are called *tiger stripes*, *flow marks*, or *ice lines*. Under any name, they limit the use of molded parts with such defects in unpainted products requiring uniform surface appearance, such as car bumpers. For homopolymers, such as PP, the dull bands appear in scanning electron micrographs (SEM) to have a striated topology of hills and valleys (48–50). Hamada and Tsunasawa (51) showed that in polymer blends such as polycarbonate/acrylonitrile-butadiene-styrene (PC/ABS), the shiny bands are PC-rich and the dull (cloudy) ones, ABS-rich. Furthermore, they found that in the shiny bands, the blend morphology indicated a symmetric flow pattern approaching the free surface. On the other hand, when the flow front passed through the region where the cloudy band was being formed, the flow pattern was not symmetric. Other investigators (49,50,52–54) have also concluded that the surface defects are due to *unstable flows in the fountain flow region*. The cause of such unstable fountain flows, shown schematically in Fig. 13.22, is most often thought to be *slip* at the wall. This unstable flow mechanism was first demonstrated experimentally by Rielly

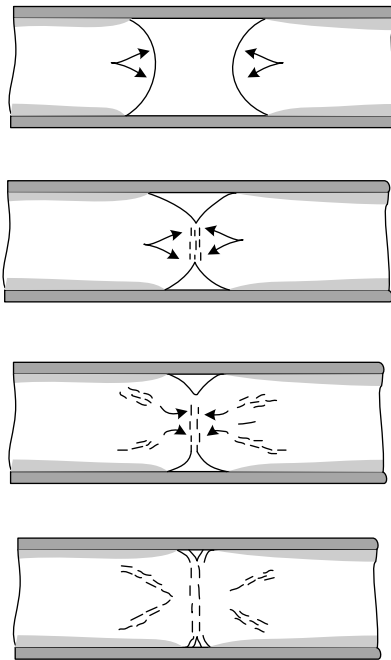


Fig. 13.20 Schematic representation of the impingement and the subsequent flows in the weld-line region: gray areas indicate cold regions of the melt; dashed lines denote regions undergoing extensional flow. [Reprinted by permission from S. Y. Hobbs, "Some Observations on the Morphology and Fracture Characteristics of Knit Lines," *Polym. Eng. Sci.*, **14**, 621 (1974).]

and Price (54) at high fill rates: when a small, red, oil/lubricant-based crayon mark was made on one of the flat mold surfaces, upon mold filling, a red transfer mark would appear on the *opposite wall downstream*, with progressively fainter red marks on alternating walls downstream as the mold was being filled. The wall-slip explanation for this phenomenon is based on the very low viscosity of the crayon, which causes a melt front *slip velocity* on

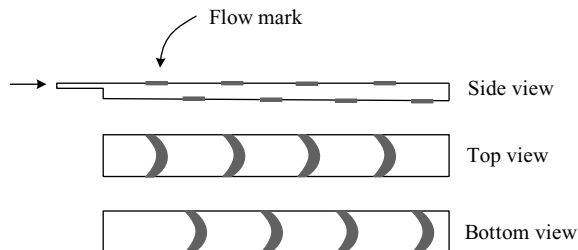


Fig. 13.21 Schematic representation of the surface defects that appear periodically and alternate in location on opposite sides of a flat mold. [Reprinted by permission from A. C. B. Bogaerds, G. W. M. Peters, and F. P. T. Baaijens, "Tiger Stripes: Instabilities in Injection Molding," in *Polymer Processing Instabilities*, S. G. Hatzikiriakos, and K. B. Migler, Eds., Marcel Dekker, New York, 2005.]

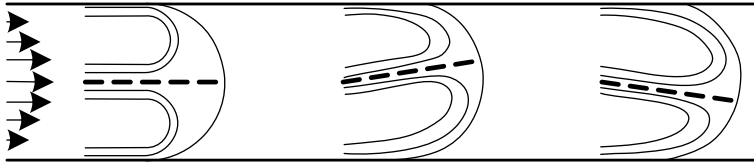


Fig. 13.22 Schematic representation of stable (left) and unstable (two right) fountain flows as causes of surface defects. [Reprinted by permission from A. C. B. Bogaerds, G. W. M. Peters, and F. P. T. Baaijens, “Tiger Stripes: Instabilities in Injection Molding,” in *Polymer Processing Instabilities*, S. G. Hatzikiriakos and K. B. Migler, Eds., Marcel Dekker, New York, 2005.]

one of the walls. Since the other side of the front sticks on the wall, it causes the slipping side to transfer to the opposite wall, transferring with it part of the crayon mark (55). Bulters and Schepens (48,49) used a two-color molding technique and high fill rates to obtain the short-shot flow patterns shown in Fig. 13.23. The black core melt, instead of becoming the surface layer on both walls, as would be expected in a symmetric fountain flow, is first swept to the bottom side and then flipped to the top.

Bogaerds et al. (47) developed a *linear* flow stability analysis “toolbox” in conjunction with the single-mode extended pom-pom (XPP) constitutive equation (56–58). Their analysis did not show the periodic nature of the flow-front motion observed experimentally with instabilities. On the other hand, their simulations do show that the onset of the linear instability can be postponed by increasing the number of the pom-pom-bearing arms of the XPP model, which would render in the melt increased, strain-hardening behavior.

Multicomponent Systems The flow kinematics of the multicomponent system is of considerable interest in molding. Vos et al. (59) used multilayer polymer tracers to study experimentally and to simulate the fountain and reverse fountain flows occurring in the driven and driving piston regions of the simple capillary experimental device shown in

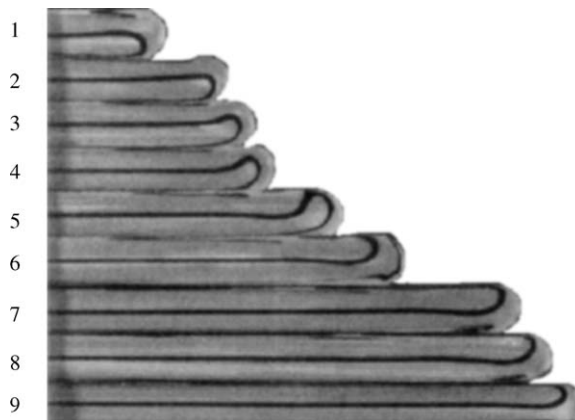


Fig. 13.23 Two-color, PP injection, high-rate mold-filling short shots documenting fountain flow instability. [Reprinted by permission from A. C. B. Bogaerds, G. W. M. Peters, and F. P. T. Baaijens, “Tiger Stripes: Instabilities in Injection Molding,” in *Polymer Processing Instabilities*, S. G. Hatzikiriakos and K. B. Migler, Eds., Marcel Dekker, New York, 2005.]

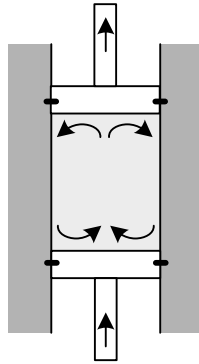


Fig. 13.24 Schematic representation of the fountain and reverse fountain flows at the driving and driven pistons.

Fig. 13.24. Solid cylindrical slices of the same polymer, but stacked in two alternating colors, as shown in Fig. 12.25 are heated and melted to 200° – 260°C , causing them to flow in a circulatory pattern under the force of the driving piston $F_p - F_g$. The fountain and reverse fountain flows, with no slip at any of the three melt-containing walls, were studied for two polymer melts: Dow PS 634 and DMS ABS Ronfalin FX50. PS at 230°C is quasi-Newtonian for $\dot{\gamma} < 10 \text{ s}^{-1}$, while ABS has a Power Law behavior even at $\dot{\gamma} = 10 \text{ s}^{-1}$, as shown in Fig. 13.26. The “marker” layer deformations are *very* different for the two rheologically different polymers, as shown on Figs. 13.27 and 13.28. Furthermore, the agreement between experimental and simulation results, using the Carreau model for PS and a Bingham fluid model for ABS, is good. The shear-thinning nature of PS is exhibited both experimentally and computationally in Fig. 13.27. An FEM, variable mesh-density method was used with different boundary conditions, to account for leakage at the two piston corners. The pluglike flow behavior of ABS could be obtained computationally only

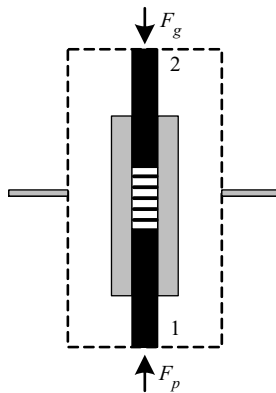
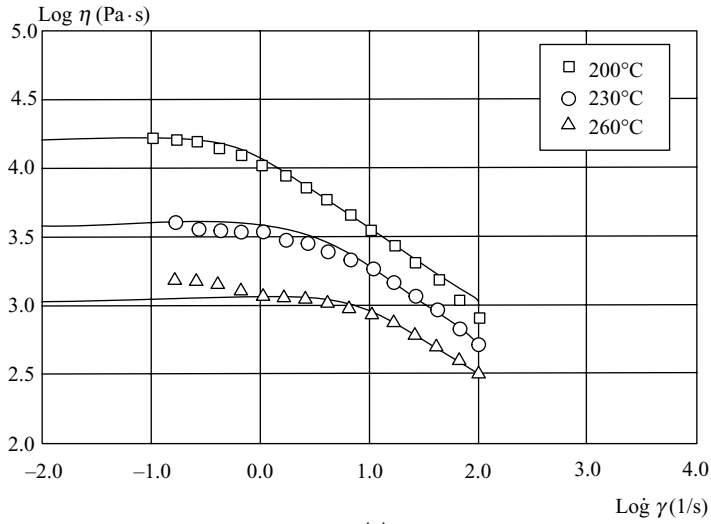
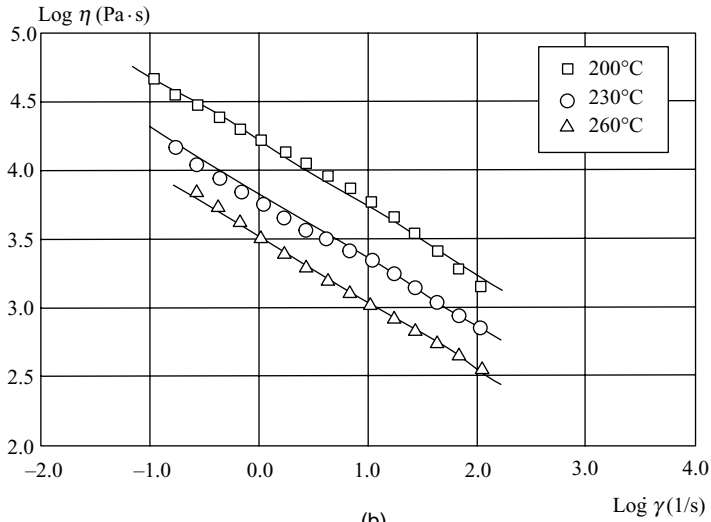


Fig. 13.25 Experimental setup on an apparatus for displacing a multilayered, two-color melt by the driving piston force ($F_p - F_g$). [Reprinted by permission from E. Vos, H. E. H. Meijer, and G. W. M. Peters, “Multilayer Injection Molding,” *Int. Polym. Process.*, **6**, 42–50 (1991).]



(a)



(b)

Fig. 13.26 Experimental flow curves for PS and ABS. Lines represent fits with a Carreau, for PS, and Power Law, for ABS, constitutive equations. [Reprinted by permission from E. Vos, H. E. H. Meijer, and G. W. M. Peters, “Multilayer Injection Molding,” *Int. Polym. Process.*, **6**, 42 (1991).]

when a Bingham fluid is used, indicating the presence of yield behavior in the circulating flow inside the chamber. The Bingham fluid model used is

$$\eta = \eta_b \left[1 + \left(\frac{\tau_y}{\eta_b} \right) \dot{\gamma}^{-1} \right] \tag{13.1-12}$$

where τ_y is the yield stress and η_b is the viscosity at high shear rates.

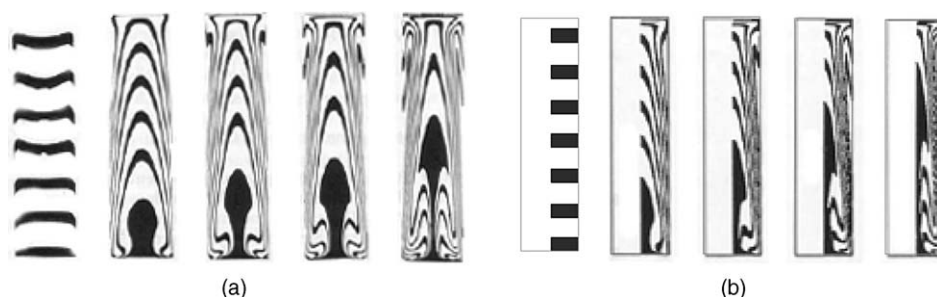


Fig. 13.27 Deformation of PS at different displacements: 0, 22, 33, 44, and 55 mm. (a) Experimental. (b) Calculated using the Carreau model ($T = 230^{\circ}\text{C}$). [Reprinted by permission from E. Vos, H. E. H. Meijer, and G. W. M. Peters, "Multilayer Injection Molding," *Int. Polym. Process.*, **6**, 42 (1991).]

Peters et al. (46) incorporated particle tracking by means of labels into the FEM software program developed at Eindhoven University of Technology and used by Vos et al. (59), whose results were discussed previously. They simulated the coinjection process, where two different colors of the same polymer DuPont PA (Zytel 101 L N C-10) are sequentially injected into an end-gated mold with four ribs, shown in Fig. 13.29 (a). Since particle tracking provides the deformation history of every fluid element that enters the mold it enables the prediction of the occurrence and the location of the technologically important problem of "layer breakthrough," where the second melt breaks through the first via the fountain flow, and ends up at the outer layer of the coinjection molded product, which is not acceptable for coinjection. The agreement between the simulated and experimentally obtained breakthrough regions for the rib mold in Fig. 13.29(a) is good, as shown in Fig. 13.29(b) and 13.29(c). Once again, the importance of the fountain flow is demonstrated.

Coinjection Molding

In 1967, Imperial Chemical Industries (ICI) developed the "sandwich" or coinjection molding process for producing structural foam products. In this process, the first melt is

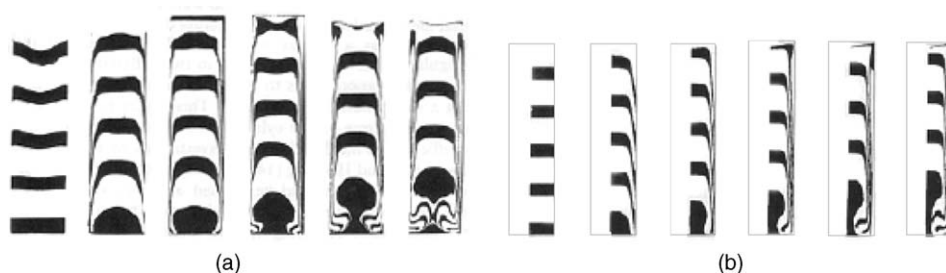


Fig. 13.28 Deformation of ABS at different piston displacements: 0, 11, 22, 33, 44, and 55 mm. (a) Experimental. (b) Calculated using a Bingham fluid model ($T = 230^{\circ}\text{C}$). [Reprinted by permission from E. Vos, H. E. H. Meijer, and G. W. M. Peters, "Multilayer Injection Molding," *Int. Polym. Process.*, **6**, 42 (1991).]

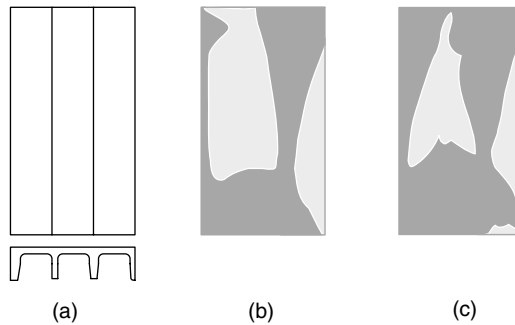


Fig. 13.29 (a) The four-ribbed, end-fed rectangular tray mold used by Peters et al. (46) for coinjection molding experiments and simulations; (b) numerically determined “breakthrough” areas by the second melt; (c) experimentally obtained “breakthrough” areas. [Reprinted by permission from G. W. M. Peters, P. J. L. van der Velden, H. E. H. Meijer, and P. Schoone “Multilayer Injection Molding,” *Int. Polym. Process.*, **9**, 258 (1994).]

injected into the mold until it fills it partway. At this point the second melt, which is the same polymer as the first, but contains a foaming agent, is injected behind the first, pushing its core forward and, because of the fountain flow, creating a skin made of the first melt. When the mold is filled and the polymers undergo cooling, the internal pressure is reduced and foaming takes place, resulting in the formation of a structural foam product—foamed core and solid skin. Before the gate freezes, the first polymer is injected again to purge the sprue of the second melt, in preparation for the next molding cycle. These sequential steps of the process are shown schematically in Fig. 13.30, where the changeover from one melt to the other is carried out by shifting a valve. Two melt-generating devices are needed. This can be achieved either with two injection molding machines or with two extruders feeding into the reservoir of a ram positive-displacement hydraulic injection unit. When utilizing hot runner molds, the two melt streams are directed into the mold via separate channels, which remain hot and separate until they reach the gate area, where they flow in a concentric nozzle arrangement similar to the common, machine-based coinjection process in Fig. 13.30. Coinjection molding has found application in “green” products where the second, foaming agent-containing melt is a recycled grade of the “virgin” melt. Two different polymers can be used in this process to take advantage of the following benefits: lower-cost parts, higher strength, reinforcing agent-containing core, sound absorbing core, and reduced cooling times, especially in thick parts, when the injection temperature of the core is lower. However, at least one of the two different polymers must contain a compatibilizing agent with the first in order to achieve interfacial bonding.

Gas-Assisted Injection Molding

The gas-assisted injection molding process involves the high-pressure injection of a gas into a partially filled mold. Under the gas pressure, the polymer *core* melt is driven downstream of the mold and, because of the fountain flow, a continuous melt skin is formed until the mold is filled. The result of this process is a product with a polymer skin and a gas core. In this process, the gas pressure is maintained while the polymer skin melt is cooling, transmitting the required packing pressure to the skin. Having gates that are not polymer filled, this process is more effective than the application of the packing melt

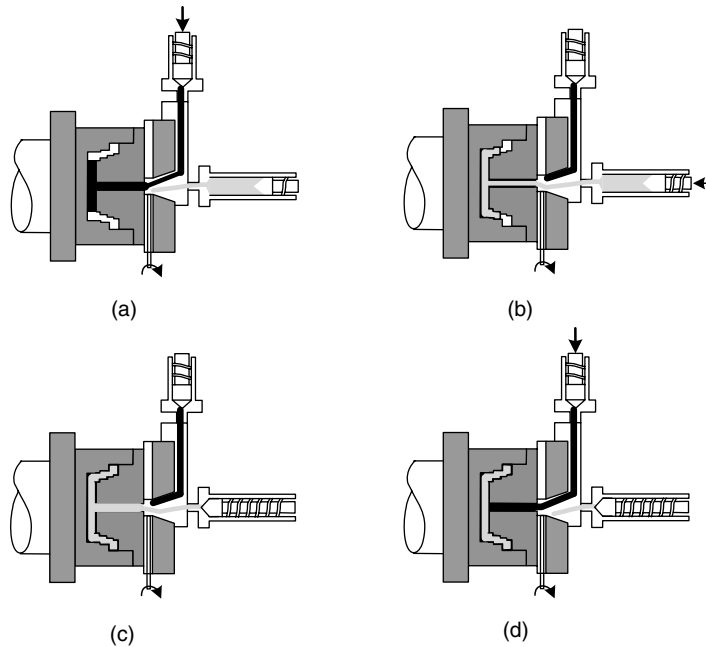


Fig. 13.30 Four stages of coinjection molding. (a) Short shot of skin polymer melt (shown in dark shade) is injected into the mold. (b) Injection of core polymer melt until cavity is nearly filled, as shown in (c). (d) Skin polymer is injected again, to purge the core polymer away from the sprue. [Reprinted by permission from Design Center, School of Engineering, Santa Clara University, Santa Clara, CA.]

pressure in conventional injection molding, especially for thick product parts, resulting in the absence of surface sink marks. Once the polymer skin has completely solidified, the gas pressure is released, the mold opened and the product ejected. The process stages are shown in Fig. 13.31. In visualizing and understanding the gas-assisted injection molding process, it is important to note that the *viscosity of the gas is immensely lower* than that of the polymer melt it is displacing, and that the gas is compressible. Thus, the pressure gradient in the gas core is zero, as it advances in the direction of the least resistance, which involves hot melt-containing thick part regions. As a result, this process yields more uniform polymer skins compared to those of coinjection-molding products, as shown schematically in Fig. 13.32. Other consequence of the use of compressed gas include a more uniform packing pressure distribution, a reduction in injection and packing pressures, and reduction of the molding cycle due to shorter required cooling times. Because of these advantageous consequences, gas-assisted injection molding allows for forming of thick products, which is technologically very significant. On the other hand, low injection and packing pressures may result in limited reproduction of textured mold surfaces, in surface marks due to the incompressible melt to compressible gas switchover, and, finally, uncontrolled gas penetration.

The problem of gas-assisted displacement of Newtonian fluids along capillaries was first examined by Fairbrother and Stubbs (60). Later, Marchessault and Mason (61) measured the coating thickness after gas penetration ($R_0 - R_b$) as well as the “fractional

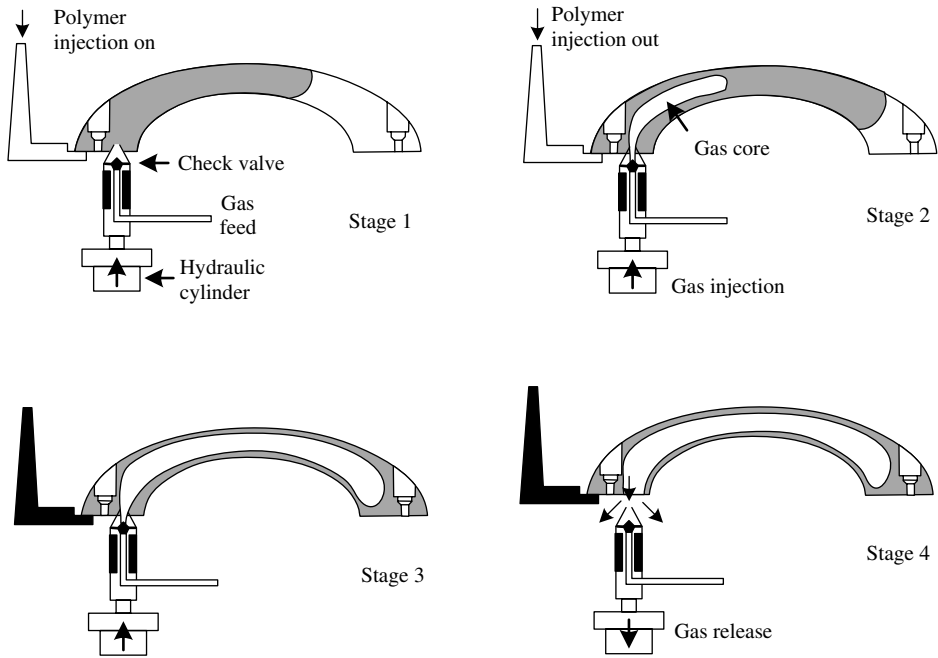


Fig. 13.31 Schematic representation of the stages of the gas-assisted injection molding process for a container handle.

coverage,” defined as

$$m = \frac{(R_0^2 - R_b^2)}{R_0^2} \tag{13.1-13}$$

where R_0 and R_b are the capillary wall and the fluid-bubble radii. Their experiments were expanded by Taylor (62) who examined a large number of Newtonian fluids in the capillary number region $10^{-3} < Ca < 1.9$, where

$$Ca = U_b \mu / \Gamma \tag{13.1-14}$$

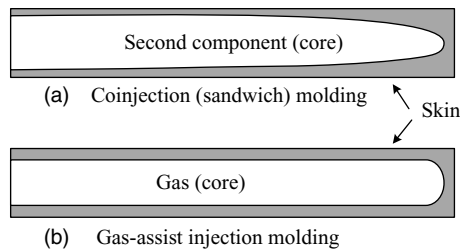


Fig. 13.32 Schematic comparison of the skin thickness distributions in co- and gas-assisted injection molded parts due to the negligible gas viscosity.

where U_b is the constant bubble velocity used in the experiments, μ is the Newtonian viscosity, and Γ is the gas–liquid interfacial tension. Ca is the ratio of the viscous forces driving the creation of new interfacial surface to that of the resisting surface tension. In the absence of gravitational contributions, that is, the Bond number $Bo = \rho g R_0^2 / \Gamma \ll 1$, the Ca number is the only controlling dimensionless number. This is what Taylor and later Cox (63) found experimentally: a single curve of fractional coverage, m , versus Ca was obtained for a variety of Newtonian fluids and capillary radii, reaching an asymptote of $m = 0.6$ at $Ca > 10$. Westborg and Hassager (64) used a Galerkin formulation to solve the problem of a Newtonian fluid by a gas bubble for the region $10^{-2} < Ca < 1$ and compared their results with those of Fairbrother and Stubbs (60) and Taylor (62). The agreement was quite good.

Turning to the problem of the penetration of long gas bubbles in tubes with non-Newtonian fluids, a physical situation that is more akin to gas-assisted injection molding, Poslinski et al. (65,66) concluded both experimentally and through FEM computational work with shear thinning fluids, that the fractional coverage, m , has asymptotic values lower than those of Newtonian fluids, and that the asymptote is lower with lower Power Law index fluids. Finally, Huzyak and Koelling (67), and Gauri and Koelling (68) were the first to investigate, both through thorough experiments, including particle tracking velocimetry (PTV), and FEM (POLYFLOW) simulations, the effect of the viscoelasticity on the coating thickness and fractional coverage, m , during displacement of melts by long gas bubbles for the wide range of the capillary number $10^{-2} < Ca < 10^2$. For Newtonian fluids, their experimental and POLYFLOW simulation work predictions coincide with the experimental results of Taylor (62), as shown in Fig. 13.33.

The simulation results are shown in Fig. 13.34 for the Newtonian, Amoco Polybutene (PB) H-100 of weight average molecular weight $\bar{M}_w = 10^3$ and a constant viscosity up to 10 s^{-1} of $19 \text{ Pa} \cdot \text{s}$. The fluid flow in the liquid being displaced by the gas bubble is viewed from a Lagrangian perspective, where the bubble is stationary and the tube wall is

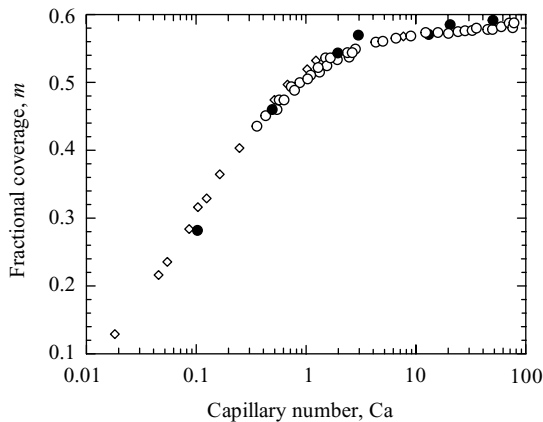


Fig. 13.33 Fractional coverage predicted by simulations (solid circles) in comparison with the experiments of Taylor (62) (open diamond) and Huzyak and Koelling (67). [Reprinted by permission from V. Gauri and K. W. Koelling, “Gas-assisted Displacement of Viscoelastic Fluids: Flow Dynamics at the Bubble Front,” *J. Non-Newt. Fluid Mech.*, **83**, 183–203 (1999).]

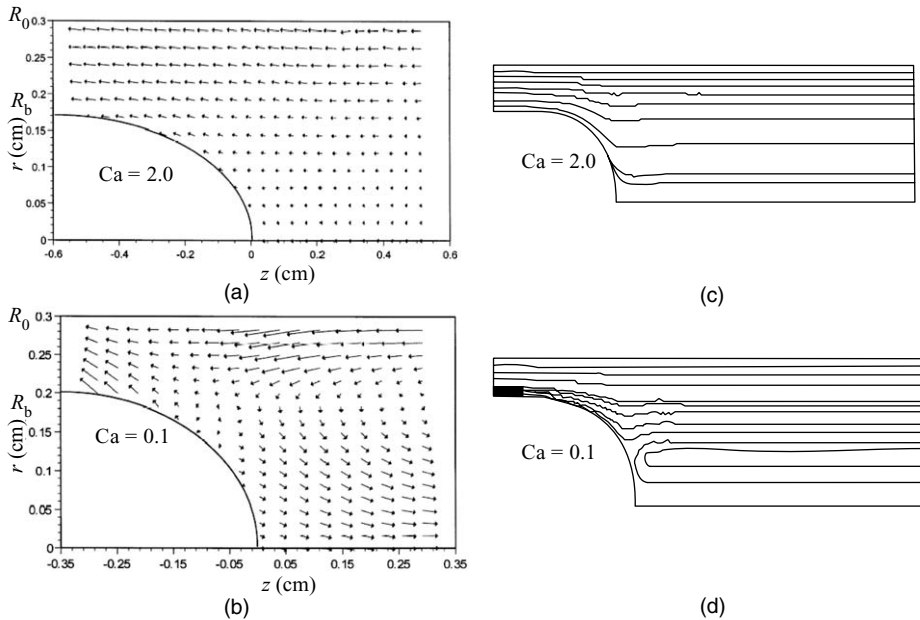


Fig. 13.34 Velocity vectors from PTV experiments with the Newtonian PB H-100. (a) $Ca = 2.0$; (b) $Ca = 0.1$; FEM POLYFLOW streamlines for the same fluid; (c) $Ca = 2.0$; (d) $Ca = 0.1$. [Reprinted by permission from V. Gauri and K. W. Koelling, "Gas-assisted Displacement of Viscoelastic Fluids: Flow Dynamics at the Bubble Front," *J. Non-Newt. Fluid Mech.*, **83**, 183–203 (1999).]

moving backwards with the bubble advance velocity. At the free surface, the interfacial tension is $2.95 \times 10^{-2} \text{ Nm}^{-1}$ for PB H-100 and 2.41 Nm^{-1} for the Boger fluid, discussed later. The pressure-related, normal force is an imposed process variable at the free surface. A reverse fountain-like flow in front of the advancing bubble (the frame of reference) is observed at low Ca , while a bypass flow is observed with stagnant layers near the bubble apex at higher Ca values. The shear ratios in front of the bubble are in the range of $0\text{--}0.75 \text{ s}^{-1}$.

Hyzyak and Koelling (67), and Gauri and Koelling (68) used a Boger fluid to study the effects of viscoelasticity. The fluid is 31 wt % Exxon Vistanex L-120 of $M_w = 1.2 \times 10^6$ in a Newtonian solvent of 95 wt % Amoco PB H-100 and 5 wt % tetradecane. It exhibits a constant viscosity of $12.5 \text{ Pa} \cdot \text{s}$ and a nonzero, first normal stress coefficient, Ψ_1 . That is, it is Newtonian and at the same time elastic and can be modeled with a four-mode Giesekus constitutive equation (69). The velocity vectors obtained are similar to those of Newtonian fluids. On the other hand, the fractional coverages, both experimentally and computationally, are increasing with increasing De , and are 30% higher than the Newtonian at $De = 4$, as shown in Fig. 13.35

For the Boger fluid $De = \lambda \dot{\gamma}_w$, $\lambda = \Psi_1(w)/2\mu$, $\dot{\gamma}$ is the shear rate and the subscript (w) denotes the fluid shear rate at the fluid–bubble interface. The increase in the fractional coverage for Boger fluids at $De > 1$ was attributed to their elastic nature, in particular their extensional flow thickening. Higher De values are obtained at high imposed capillary numbers, that is, higher U_b . Under such conditions, the computed flow, close to the stagnation point at the centerline, right behind the bubble, is purely extensional, with a

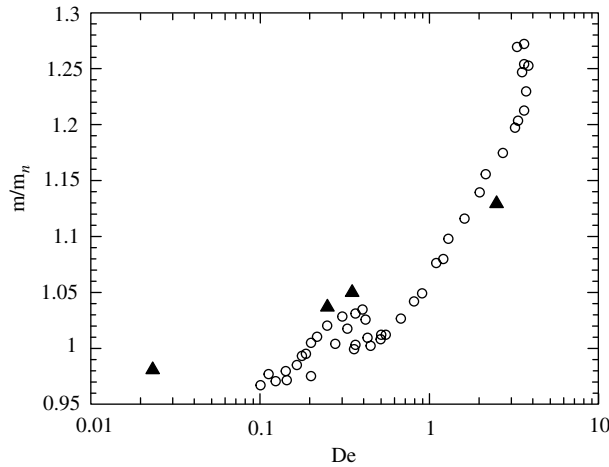


Fig. 13.35 Fractional coverage results for the Boger fluids (open circles) compared to experiments (solid triangles). [Reprinted by permission from V. Gauri and K. W. Koelling, “Gas-assisted Displacement of Viscoelastic Fluids: Flow Dynamics at the Bubble Front,” *J. Non-Newt. Fluid Mech.*, **83**, 183–203 (1999).]

value of the Giesekus parameter (69) $R = 1$. This parameter is

$$R = \frac{\dot{\gamma} - \omega}{\dot{\gamma} + \omega} \quad (13.1-15)$$

where $\dot{\gamma}$ and ω are the scalar local shear rate and vorticity, respectively.

Koelling et al. (70) conducted nonisothermal, pressurized gas-bubble Newtonian fluid-displacement experiments. The fluid used was PB H-300. It was injected into a capillary tube maintained at 60°C. The tube was then transferred in a different temperature bath at 0°C. The penetrating gas was then injected after different delay times, t . The longer the delay time, the deeper the cooling penetration thickness will be, since it is dependent on the Fourier number,

$$F_0 = \frac{\alpha t}{R_0^2} \quad (13.1-16)$$

where α is the thermal diffusivity of the fluid.

The hydrodynamic fractional coverage for the 60° to 0°C switchover under various F_0 values is shown in Fig. 13.36. It is to be noted that, even at $F_0 = 0$, the fluid is being cooled during gas penetration. This explains why m is close to, but higher than, the isothermal $m = 0.6$ value. The increase in m with increasing F_0 continues, since the cooler and the more viscous the fluid layers near the wall are, the more difficult the displacement would be, so the bubble advances through a narrowed, cylindrical, hotter melt passage. A maximum is reached as F_0 is further increased and m approaches the isothermal $m = 0.6$ at $F_0 \sim 1.0$, when an almost uniform 0°C fluid temperature is established. That is, the experimental conditions revert back to isothermal simulations, and are capable of predicting the results shown in Fig. 13.36, once the activation energy for flow, which is

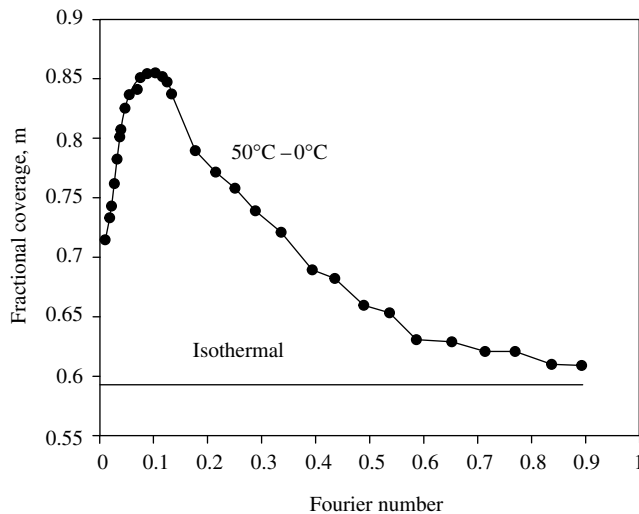


Fig. 13.36 The fractional coverage during nonisothermal gas-penetration experiments in PB-300, where the gas was injected after different $F_0 = \alpha t/R_0^2$, that is, dimensionless delay times, following the step bath temperature switchover from 60° to 0°C . [Reprinted by permission from K. W. Koelling, V. Gauri, M. Tendulkar, R. Kaminski, and O. Becker, "Understanding the Controlling Mechanisms of Gas-assisted Injection Molding through Visualization," *SPE ANTEC Tech Papers*, **43**, 3697 (1997).]

$\Delta H/R = 8.525 \text{ K}^{-1}$ for PB H-300, is known. Finally, we note that the nonisothermal temperature profiles here exist only in the absence of a phase transition, which occurs in the gas-assisted injection-molding process, at least with semicrystalline polymers.

The Overall Flow Pattern

The most characteristic feature of injection molds is geometrical complexity. In such molds there is a need to predict overall flow pattern, which provides information on the sequence in which different portions of the mold fill, as well as on short shots, weld line location, and orientation distribution. The more complex a mold, the greater this need is. The irregular complexity of the geometry, which forms the boundary conditions of the flow problem, leads naturally to FEMs, which are inherently appropriate for handling complex boundary conditions.

In principle, the pressure, velocity, and temperature distribution can be determined by such methods. The problem, however, can be greatly simplified by restricting the flow to the narrow-gap type of configurations in which locally fully developed flow can be assumed at any instant of time. Many molded articles have a generally thin-walled structure where such an analysis is relevant. The FEM formulation of the two-dimensional narrow-gap flow problem would closely follow that of anisotropic seepage problems analyzed by Zienkiewicz et al. (71). A simple lattice-type FEM formulation called *flow analysis network* (FAN) was suggested for this problem by Broyer et al. (72), assuming isothermal non-Newtonian flow. Krueger and Tadmor (6) simulated with this model the filling of rectangular molds with inserts (Fig. 13.8). A computational grid of 18×72 was used. The time-dependent gate pressure used in the simulations were based on the

experimental pressure traces at location P_3 (Fig. 13.5), neglecting the pressure drop from the gate outlet to this location. The temperature was also measured at the same location, and its mean value was used in the simulations. Figure 13.8(a) plots simulation results. Calculated advancing front profiles are marked by \times symbols (sudden jumps in values are the result of the rather coarse grid size) labeled by corresponding filling times. Experimental front profiles obtained by short shots are denoted by solid lines, and experimental (visually observable) weld line locations by dotted lines. The agreement between predicted and measured front profiles is surprisingly good, considering the restrictive isothermal flow assumption in the model and the possible front distortion in short shots. The theoretical model does not account for side-wall effects, which clearly appear to restrict flow in the experimental profile. Reasonable agreement was also obtained in predicting mold filling times (6). The good prediction of the advancing front profiles indicates that no large melt temperature drop occurred during filling under the conditions used, and suggests that theoretical prediction of orientation distribution and weld-line locations may be possible.

Finally, simulation studies indicate that the overall flow pattern and the front shapes are only weak functions of the viscous nature of the liquids used; Newtonian liquids exhibit almost the same front patterns as pseudoplastic melts. Such behavior is implied by the results of Example 13.1. This finding was supported experimentally by studies that utilized high-speed movie photography during the injection of low viscosity Newtonian fluids in a transparent mold (6). The implications of such findings are twofold: from a modeling point of view we can use at first approximation a simple Newtonian constitutive equation to predict the position of the advancing front and its shape. Moreover, we can also study filling patterns of very complex molds with low viscosity Newtonian fluids in transparent molds experimentally with reasonable accuracy. Of course, filling times and pressures are highly dependent on the rheological properties of the melt used. For a more reliable and accurate simulation, there are complete simulation packages for mold filling that can be of great value in the process of mold design and exploration of operating conditions on the process. Example 13.2 shows some results with one such package, MoldFlowTM.

Cooling of the Molded Part

Melt cooling takes place from the start of the injection-molding cycle; that is, because, with the exception of the case of hot runner molding, the entire mold is near room temperature. We saw earlier that during filling temperature gradients appear in both the flow and transverse directions, and a “frozen skin” develops whose average thickness decreases with increasing entering melt temperature and injection rate. At the end of the filling stage, cooling of the melt is the predominant phenomenon. However, because of the resulting specific volume decrease, a small amount of melt must be “packed” into the mold to compensate. Furthermore, if the injection pressure is removed before the gate freezes (or in the absence of a one-way valve), backflow can occur because of the prevailing high pressure in the mold cavity. Finally, during cooling, minor secondary flows occur, which, being at a relatively low temperature, may result in appreciable macromolecular orientation. These flows are triggered by temperature gradients, causing the melt to flow from the hot region to the cold to compensate for the volume contraction. Thus, secondary flows are expected to occur in regions of abrupt decreases in the cross-sectional dimension. Whenever such flows are *not* possible, usually due to lack of material, voids are formed in the bulk of the molded article. From an overall point of view, the

TABLE 13.1 The Equation of State of Spencer and Gilmore and the Experimental Data

$$(P + \pi)(\hat{V} - \omega) = RT$$

where $\hat{V} = \hat{V}(T, P)$ is the specific volume, π = "internal pressure," ω = specific volume at 0 K, R = material constant.

Polymer	R (psi · cm ³ /g K)	ω (cm ³ /g)	π (psi)
PS (atactic)	11.60	0.822	27.000
PMMA (Lucite HM 140)	12.05	0.734*	31.300
PE (du Pont P1000 PM1)	43.00	0.875*	47.600

*Values uncertain owing to lack of reliable values of equilibrium densities

necessary requirement for avoiding void formation is that the mass of the polymer injected is greater than or equal to the product of the atmospheric density times the cavity volume.

In specifying the transport equations that simulate the cooling and solidification of molded parts, we neglect the packing, back flow, and secondary flows that take place during that stage of molding and contribute convectively to the heat transfer. Kuo and Kamal (73) have simulated cavity packing for the following two cases: fast flows that end in rapid decelerations, and negligible thermal contractions during packing and slow-filling flows, where deceleration is negligible but thermal contractions are controlling. In both cases, the equation of state of Spencer and Gilmore (Table 13.1) was used. For an end-fed rectangular mold cavity of a small thickness compared to the other two dimensions, we expect temperature gradients in the flow and thickness direction at the end of the filling, such as those in Fig. 13.10. Thus, for a cavity such as that in Fig. 13.7, the energy equation describing mold cooling is

$$\rho C_p \frac{\partial T}{\partial t} = k \left[\frac{\partial^2 T}{\partial y^2} + \frac{\partial^2 T}{\partial x^2} \right] \quad (13.1-17)$$

The temperature field at the end of filling is taken as the initial condition for the preceding equation. The boundary conditions are (where l is the mold length)

$$\left. \begin{aligned} \left(\frac{\partial T}{\partial y} \right) (0, x, t) &= 0 \\ \left(\frac{\partial T}{\partial y} \right) \left(\frac{H}{2}, x, t \right) &= -\frac{h}{k} \left[T \left(\frac{H}{2}, x, t \right) - T_0 \right] \\ \left(\frac{\partial T}{\partial y} \right) (y, 0, t) &= -\frac{h}{k} [T(y, 0, t) - T_0] \\ \left(\frac{\partial T}{\partial y} \right) (y, l, t) &= -\frac{h}{k} [T(y, l, t) - T_0] \end{aligned} \right\} \quad (13.1-18)$$

This problem can be solved numerically for the case of constant thermophysical properties.

The next section discusses the solution and its results in covering reactive molding. As Chapter 5 discussed, the solution of solidification with crystallization can be treated by stating Eq. 13.1-17 twice, once for the melt and once for the polycrystalline solid, taking into account the heat released during the first-order transition by a thermal balance at the interface. Alternatively, Eq. 13.1-17 can be used for both phases if C_p , ρ , and k are allowed to vary continuously over the entire temperature range. Finally, the conduction in the direction of flow can be neglected, since the gradients in that direction are, in general, smaller than the transverse gradients. In this case, the term $k\partial^2 T/\partial x^2$ is zero, and only the first two boundary conditions of Eq. 13.1-18 have to be used.

Injection Molding Structuring

There is a broad potential of structuring in injection molding, because the flow field in filling the mold is rapid and complex and can be varied by varying the process variables. Furthermore, the heat transfer can be fast and efficient, at least for the molecules near the surfaces of the mold. In other words, the probability of freezing molecular orientation brought about by flow is high near the surface layers and low near the core, enabling the formation of the sandwich type of structure.

From our earlier discussion in this chapter we expect to have the following macromolecular orientation, starting from the center of the thickness and proceeding outward: (a) near the center, no orientation at all because the shear velocity gradients are zero; (b) moving away from the center, an increasing amount of shear flow orientation due to the shear gradients that pass through a maximum value, and due to the faster cooling as we approach the wall; (c) near the wall, we expect only some shear flow orientation (shear gradients are low), in addition to some extensional flow orientation due to the fountain flow; and (d) in the wall region, only extensional flow orientation, due to the fountain effect. Although there is no question that shear flow occurs during filling, experimental evidence must be brought forth in support of the fountain flow, since it is so important to the resulting morphology.

We cite two experimental investigations, one by Schmidt (17) and the other by Thamm (74). In Schmidt's work, colored tracer particles, which entered the mold at the center of the mold thickness while the mold was partly filled, were found deposited at the mold walls at a later time, and at an axial distance beyond that of the front at the time of the tracer entrance (the approximate locations of such particles on the mold wall were predicted by Huang (35) who simulated the melt front flow region problem during filling). Thamm, investigating the morphology of injection molded blends of PP and ethylene-propylene-diene terpolymer (EPDM), found that near the mold surface, the EPDM profiles are either elongated for flat narrow molds or disk shaped for more squarelike molds. The EPDM particles in this case act as deformable tracer particles. Thus, from Schmidt's work we see that center particles catch up with the surface and flow to the wall, and from Thamm's evidence, we can deduce that the flow is either that of simple extension for narrow flat molds, or biaxial extension for square molds. Figure 13.37 demonstrates the extensional nature of the front region flow as the EPDM "tracer" particles are deformed on either side of the weld line. In light of this, the crystalline morphology reported by Kantz, Newman, and Stigale (75), Clark (76), and others can be understood fairly clearly. At the surface layer row, nuclei are formed by chains aligned in the direction of flow (extensional flow) on which lamellae grow in

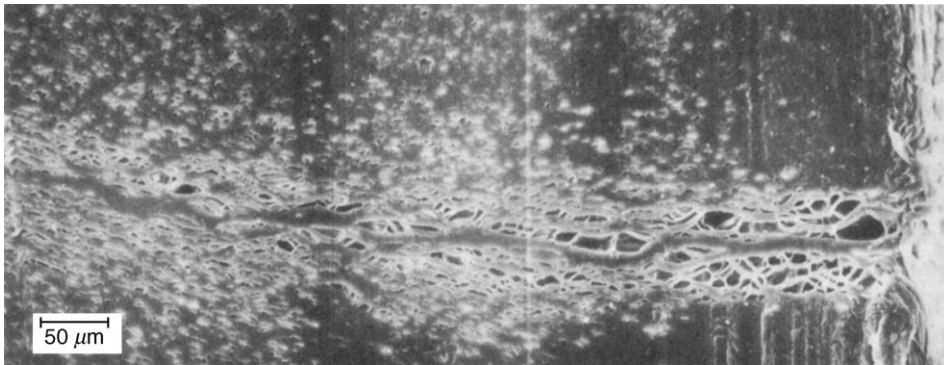


Fig. 13.37 Scanning electron photomicrograph of a weld line formed during the injection molding of a polypropylene–15% EPDM blend. Surface is hexane-extracted to remove EPDM. [Reprinted by permission from, R. C. Thamm, *Rubber Chem. Technol.*, **50**, 24 (1977).]

the plane perpendicular to the filling direction. At the layer just below, row nucleation still persists, but there the lamellae are perpendicular to the mold surface, but randomly oriented with respect to the filling direction. Shear flow orientation in combination with the prevailing temperature gradients is probably responsible for this morphology. Recall that both shear and elongational flows are capable of producing chain orientation that is intense enough to create row nucleation. Spherulitic morphology, indicative of little or no orientation, is observed in the core region. Figure 13.38 shows such variation of crystalline morphology with thickness. Similar morphologies have been reported by Hobbs (77) at and behind weld lines. This is expected in light of our previous discussion. We note in passing that if nucleating agents were added, the effect of row nuclei would be masked by profuse nucleation on the surfaces of the nucleating agents. Furthermore, the spherulitic core morphology would be grainy. The desirability of adding nucleating agents depends on the mechanical properties that are sought.

For amorphous polymers, the skin will be oriented, thus ductile, whereas the core region, being unoriented, will be brittle. Furthermore, the mechanical properties will be anisotropic, since the orientation is predominant in the filling direction. This anisotropy can be overcome for cup-shaped injection-molded articles. The male part of the mold can be rotated during filling, giving rise to additional orientation in the θ direction. This double orientation has been termed *helicoidal* by Cleereman (78), who suggested the process. Figure 13.39 illustrates the resulting impact strength.

For decades now, a great deal of work has been conducted in studying injection molding, both from the mathematical simulation and structuring-morphology points of view. The stage seems to be set for the next step forward, namely, the complete prediction of the properties of any given injection molded product, given the macromolecular specification of the polymer and the design and operating conditions used in molding it. This is the ultimate goal of polymer processing: to combine the power of computational continuum mechanics and molecular dynamics packages with powerful, molecular theory-based constitutive equations, equations of state and crystallization rates, and

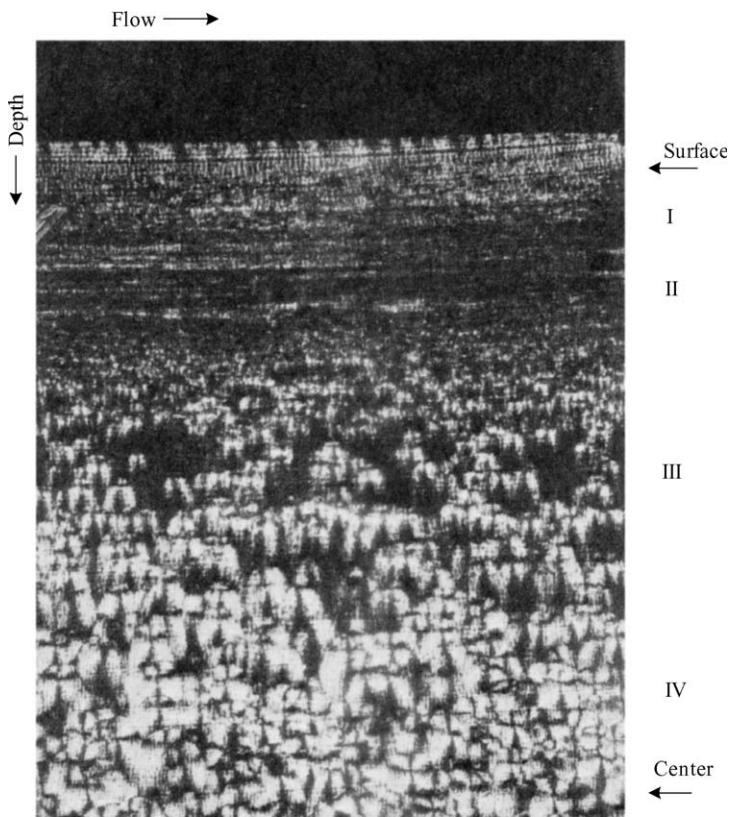


Fig. 13.38 Birefringence microscopy study of a cross section of molded HDPE, depicting various morphological regions. [Reprinted by permission from V. Tan, paper presented at the International Conference on Polymer Processing, MIT, Cambridge, MA, August 1977.]

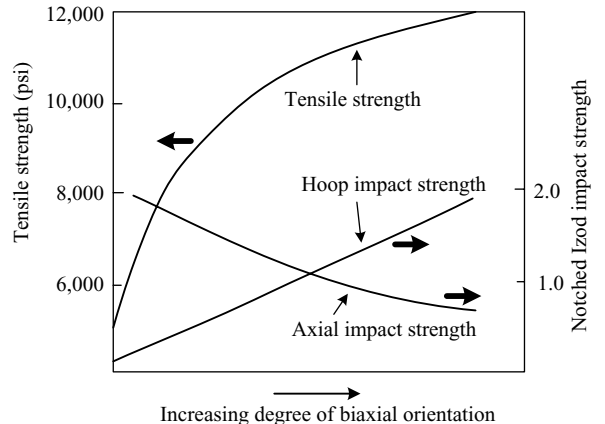


Fig. 13.39 Mechanical properties of biaxially (helicoidally) oriented PS. [Reprinted by permission from K. J. Cleereman, "Injection Molding of Shapes of Rotational Symmetry with Multiaxial Orientation," *Soc. Plast. Eng. J.*, 23, 43 (1967).]

morphology theories, to arrive at an a priori specification of molded product properties. Once this is achieved, polymer processing will be equally adept both in process and product scientific design and engineering. For the time being, however, this goal has not yet been reached. Nevertheless, as discussed in Section 1.4, we can find important progress being made in this direction in the intense and focused multidisciplinary macromolecular engineering research, which is being carried out at several leading universities and research centers.

Computer Simulation Package Analysis

Example 13.2 Simulation of Mold Filling Using the MoldFlow™ Simulation Package We have previously described the various elements of the mold filling process, beginning with the hot melt flow through the sprue, runner, and gate into the cold mold. The details of the flow in an advancing front were discussed, as well as the way this front fills the mold and determines molecular orientation and the weld lines, and finally the cooling process. As in the case of plasticating extrusion, where the conveying, melting, mixing, and pumping of solids take place partly sequentially and partly concurrently, and which requires a complete computer simulation package to describe the process as a whole (Section 9.3), in injection molding we also need a complete computer simulation package to describe the entire process. In this Example, we present simulation with the MoldFlow™ Simulation Package.

Figure E13.2a shows the geometry of a tray that is to be molded from DuPont Zytel® 101F DAM PA66 and injected at 290°C into 90°C mold. The gate is located at the bottom center of the mold. The computations were carried out with 34×28 elements. Some of the computed parameters are given in the following table and meshing in Fig. E13.2b:

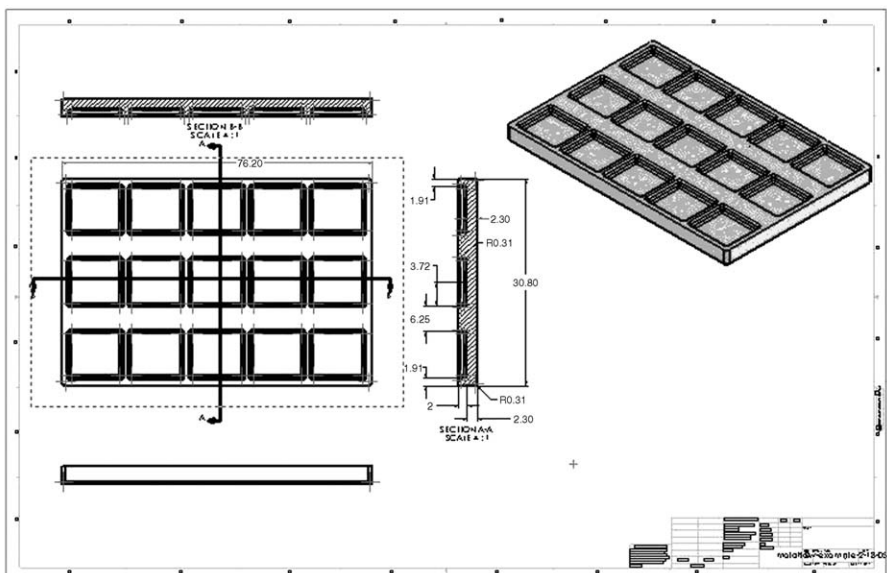


Fig. E13.2a A fifteen-compartment flat tray with wall thickness of 2.5 mm.

Injection time (s)	1.0
Nominal flow rate (cm ³ /s)	12.8
Packing pressure profile (MPa) Duration (s),	
0	0.9
10	0.9
Cooling Time (s)	20.0
Total volume of the part and cold runners (cm ³)	12.8
Switchover pressure (MPa)	1.2

The results of the simulation are shown in Figs. E13.2c to E13.2m. By using color coding the designer gets an immediate and in-depth view of the whole process, which would be very difficult if not impossible to get from a numerical output. Indeed, in modern computerized fluid mechanics the visual representation plays a key role in studying a problem and is an inherent part of the solution. The vast amount of detailed data that can be obtained from the simulation of a complex process cannot be absorbed without appropriate visual two- or three-dimensional representation.

Figure E13.2c shows the fill time. As expected in this center-gated mold, the center region fills up first and the outer edges last, by a factor of 2:1.

Figures E13.2d and E13.2e show the melt front and bulk temperature distribution.

Figure E13.2f plots the pressure profile at the injection location.

The next two figures, Figs. E13.2g and E13.2h, show the thickness of the fraction of frozen layer, and regions of trapped air. Both are important for designing a good mold.

Figure E13.2i shows the average velocity at the end of fill, which determines, to a large extent, core orientation [E13.2j], whereas skin orientation, as discussed earlier, is determined by the normal of the advancing front shown in Fig. E13.2k.

Finally, Fig. E13.2l shows the recommended ram speed, and Fig E13.2m shows the weld-line locations.

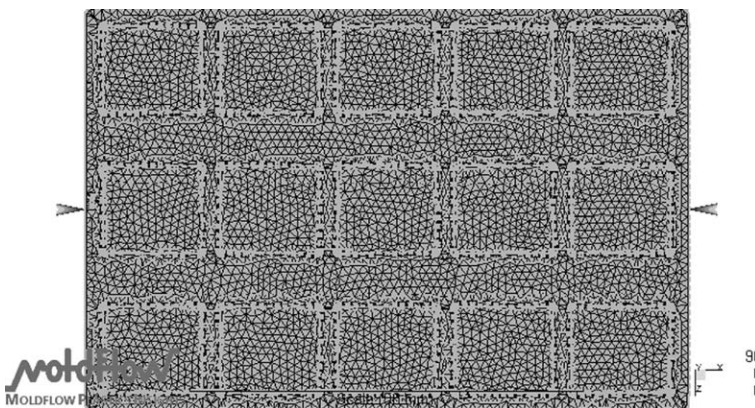


Fig. E13.2b The FEM cells generated by the program for the simulation.

13.2 REACTIVE INJECTION MOLDING

Injection molding has been used to form objects ranging in weight from a fraction of a gram to several kilograms. As the size of the article to be molded increases, two problems arise in injection molding: (a) generating enough homogeneous melt in the injection molding machine, and (b) maintaining sufficient clamping pressure to keep the mold closed during the filling and packing stages of the injection molding operation. The latter problem becomes serious when the projected area of the molded part is large and requires enormous mold presses.

The reaction injection molding (RIM) process was developed to bypass both of these problems. In this process, two or more low viscosity, $0.1\text{--}1.0\text{-Pa}\cdot\text{s}$ liquid streams, which react when brought together, are mixed prior to being injected into large cavities (79). Some of the polymerization reaction (which may result in linear, branched, or cross-linked polymers) occurs during the filling stage. The bulk of the reaction, however, takes place after filling and even after removal from the hot mold. Thus, the injection pressures needed for filling molds in the RIM process are generally small. As the polymerization proceeds after filling, heat is generated by the reaction, which increases the specific volume of the polymer system. On the other hand, a specific volume decrease of the order of 10% accompanies polymerization. Thus, packing flows would be necessary, which would require high pressures, since the viscosity of the reacting system increases with increasing molecular weight or degree of cross-linking. To eliminate the necessity of packing, a small amount of a foaming agent is introduced into one of the streams. The resulting foaming action ensures that the RIM article will conform to the shape of the cavity. In this way, very large and complex-shaped cavities can be formed using a rather small injection pressure, of the order of $1\text{--}10\text{MN/m}^2$, and small clamping presses with inexpensive molds.

Obviously a key to the success of the RIM process has to be economically fast rates of polymerization. Otherwise the process is not competitive to injection molding, but comparable to casting. It follows, then, that not all polymer systems are good candidates for the RIM process. The most commonly used polymer system since the commercial inception of the process in the early 1970s is that of linear and cross-linked polyurethanes, where di- or trialcohols and di- or tri-isocyanates are the two main reacting species. Fiber-filled polyesters also have been used. Other systems used include polyureas, nylon 6 (ring opening), polyesters, polyacrylamides, and epoxies. Table 13.2 lists the principal differences between the injection molding and the RIM processes.

Since RIM involves reaction between miscible reactants, the process equipment must provide for: (a) fine control of the temperature of both reactant streams, (b) very accurate stoichiometric metering of the reactants, and (c) nearly instantaneous intimate mixing of the reactants within a "mixhead" prior to being delivered to the hot mold. Figure 13.40 is a schematic representation of the polyurethane RIM process. Jacketed and stirred isocyanate and polyol tanks with gas dispersed in them keep the reactants at process temperature. Low-pressure pumps recirculate both streams (see right tank) between the delivery piping and the tanks. Heat exchangers keep the reactants in the pipe channels at process temperatures so that, when the valves to the two metering cylinders are opened, both reactants are at process temperature. When the cylinders are filled, the reactants undergo high-pressure (rate) recirculation until they are directed to the mixhead, where they

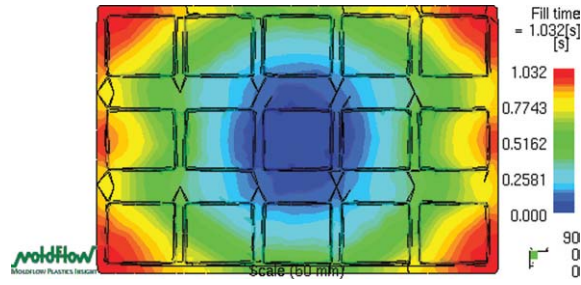


Fig. E13.2c Fill time.

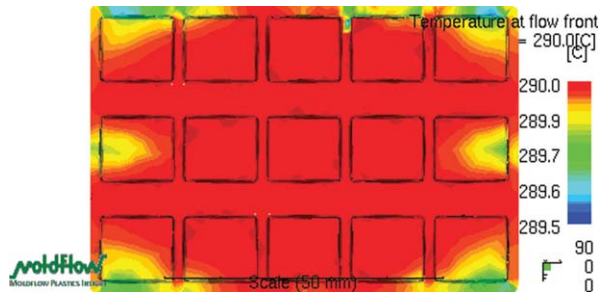


Fig. E13.2d Temperature at flow front.

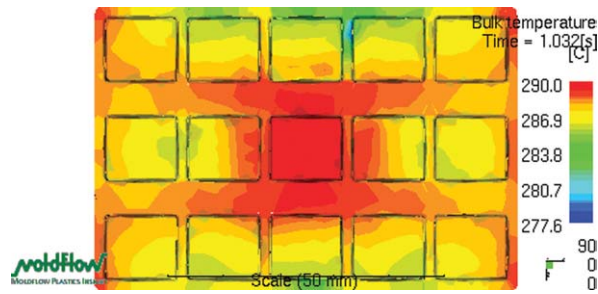


Fig. E13.2e Bulk temperature.

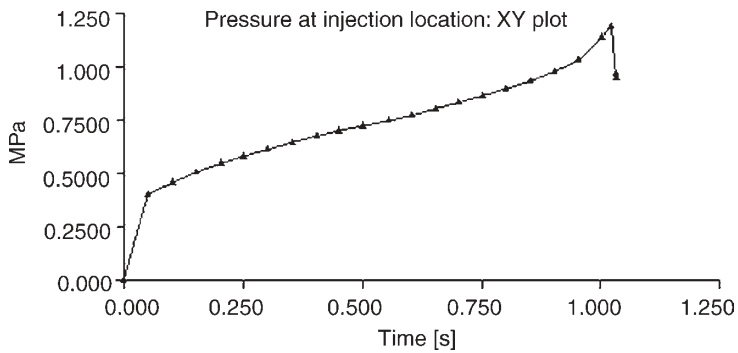


Fig. E13.2f Pressure at injection location.

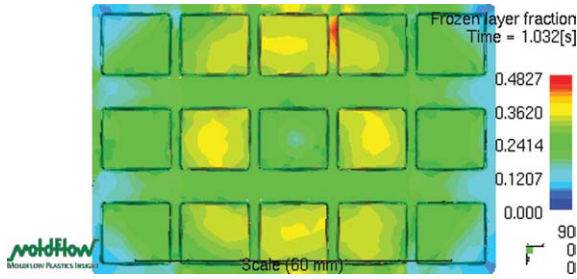


Fig. E13.2g The fraction of frozen layer at the end of injection.

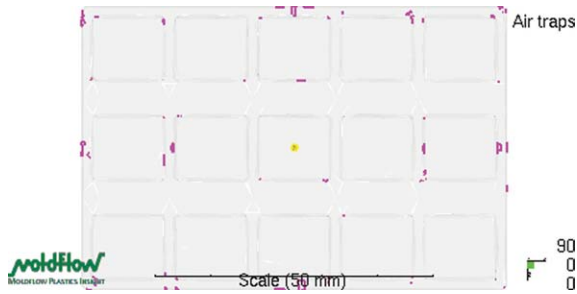


Fig. E13.2h Air traps locations.

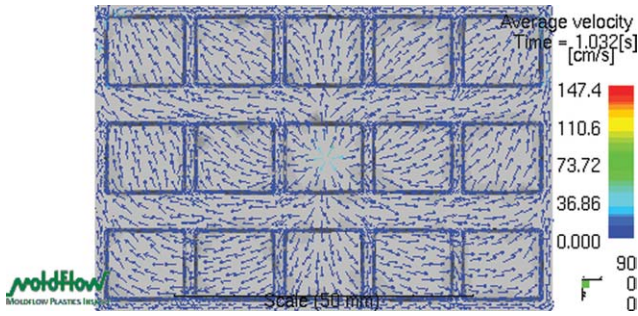


Fig. E13.2i Average velocity at the end of fill.

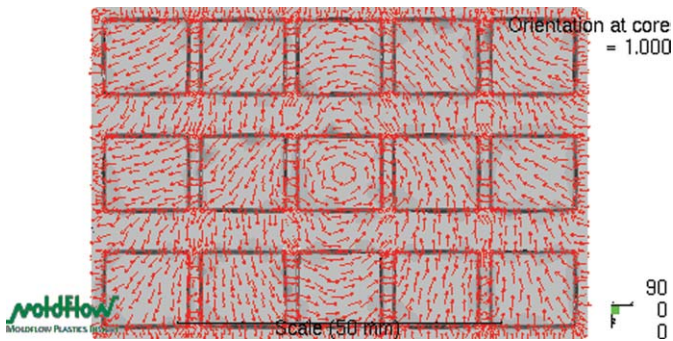


Fig. E13.2j Core orientations.

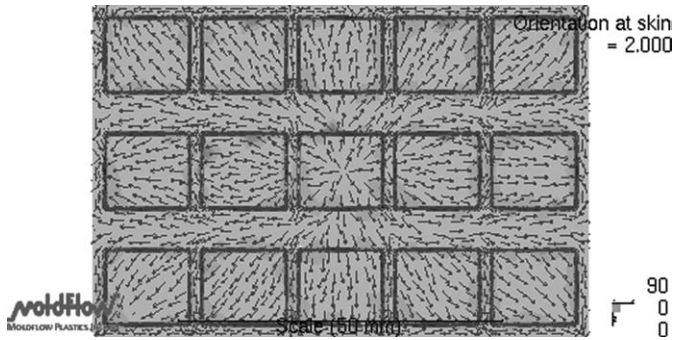


Fig. E13.2k Skin orientation..

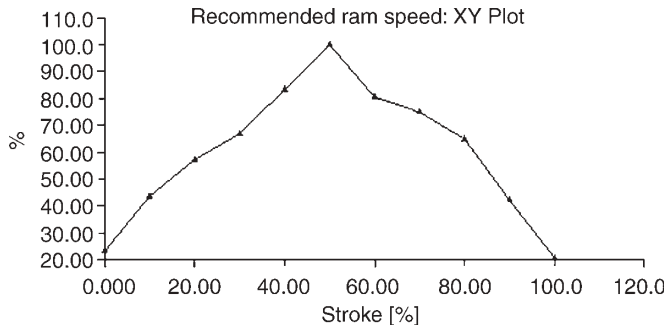


Fig. E13.2l Recommended ram speed..

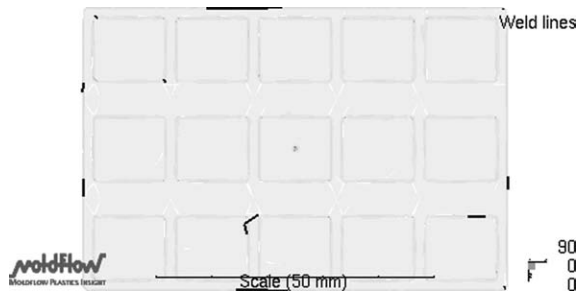


Fig. E13.2m Weld line location..

TABLE 13.2 Comparison between Typical RIM and Thermoplastic Injection Molding (TIM)*

	RIM	TIM
Temperature		
reactants	40°C	200°C
mold	70°C	25°C
Material viscosity	1 Pa · s	10 ² –10 ⁴ Pa · s
Injection pressure	100 bar	1000 bar
Clamping force (for 1 m ² surface part)	50 ton	3000 ton

*C. W. Macosko, *RIM Fundamentals of Reaction Injection Molding*, Hanser, Munich, 1989.

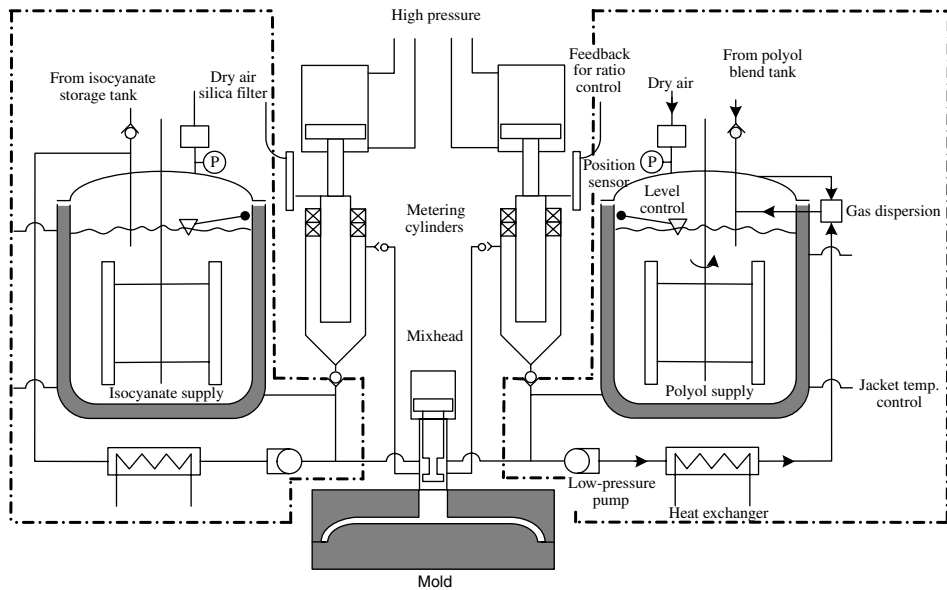


Fig. 13.40 Schematic representation of a typical RIM machine. The machine can be divided into three basic parts: (1) low-pressure recirculation or conditioning (bounded by the dotted lines); (2) high-pressure metering; and (3) the impingement mixhead. The mold is usually considered separately. The figure shows the machine in low-pressure recycle mode. [Reprinted by permission from C. W. Macosko, *RIM Fundamentals of Reaction Injection Molding*, Hanser, Munich, 1989.]

undergo impingement mixing, which is capable of creating very small striation thicknesses. Consequently, the ratio of the characteristic diffusion times $t_d = \bar{r}^2 / \mathcal{D}_{AB}$ is smaller than the characteristic reaction time of the particular polyurethane reactants used at process temperature, $t_r = ([c]/\dot{r})_0$, where $[c]$ is reactive species concentration, and \dot{r} is the rate of reaction, both at $t = 0$. The impingement mixing and self-cleaning features of a mixhead are shown in Fig. 13.41 (80,81)

The success of high velocity jet impingement mixing in reducing the striation thickness of the impinging reactant streams from 1–3 mm to about $100 \mu\text{m}$ nearly instantaneously, and within a very small volume and readily cleanable mixhead, has been the key to the development of RIM. With a striation thickness of $100 \mu\text{m}$, the reactant diffusivity required for good diffusional mixing in one second, is $\mathcal{D}_{AB} = 10^{-4} \text{ cm}^2/\text{s}$. The mixed reactants flow out of the small mixhead chamber into the mold through a runner and gate. Impingement mixing with RIM reactants was first studied by Menges et al. (81) and later by Malguarnera et al. (82,83), by Macosko and Suh (84), Lee and Macosko (85), and Lee et al. (86). The studies are experimental, with dimensional analysis of the results. Tucker and Suh (87) took the fine-scale features of the reactants in the mixhead, l_m , to be of the same order as the scale of turbulence given by the Kolmogoroff microscale, l_k

$$l_k \sim (v^3 P_m)^{1/4} \quad (13.2-1)$$

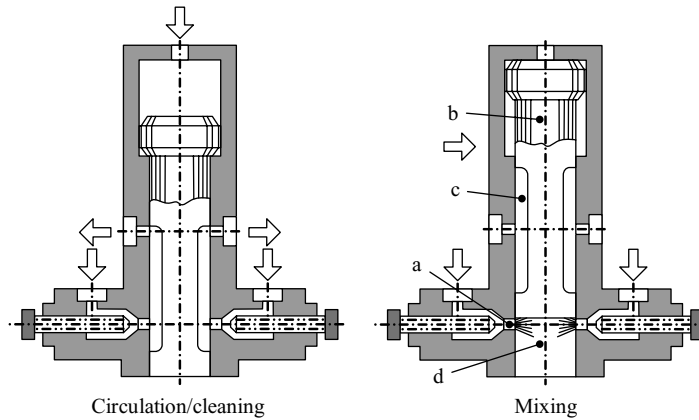


Fig. 13.41 The Keulerber and Pahl (1970) mixhead. In the closed or recirculation position, reactants recirculate through grooves (c) along the cylindrical cleanout piston (b). In the open position, reactants flow at high velocity through circular orifices (a), impinge in the chamber (d), and flow out to the mold cavity (diagram from G. Oertel, 1985 (80)). [Reprinted by permission from C. W. Macosko, *RIM Fundamentals of Reaction Injection Molding*, Hanser, Munich, 1989.]

where $\nu = \mu/\rho$ is the reactant kinematic viscosity and P_m is the rate of turbulent energy dissipation:

$$P_m \sim V^3/D \quad (13.2-2)$$

where V is the average reactant jet velocity in the nozzles leading to the mixhead and D is the nozzle diameter. Thus, noting $l_m \sim l_k$ one obtains

$$l_m/D \sim [v^3/V^3 D^3]^{1/4} \quad (13.2-3)$$

or

$$l_m/D \sim \text{Re}^{-3/4} \quad (13.2-4)$$

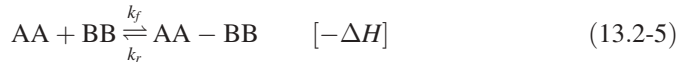
Experimentally it has been found that the Re_{crit} for impingement mixing for onset of turbulence is around 140. This value seems to be insensitive to the impinging jet angle of incidence (82). Furthermore, the $\text{Re}^{-3/4}$ dependence seems to hold until the range $140 < \text{Re} < 250 \sim 500$ (83).

From a process simulation point of view, in addition to impingement mixing, there are two main problems: (a) nonisothermal and transient flow with chemical reaction, prevalent during the filling stage of the process, and (b) conductive heat transfer with heat generation due to the polymerization reaction. We discuss these two problems next, using the case of

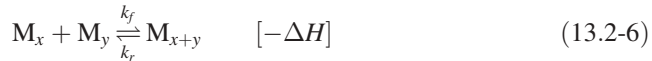
linear polyurethane being molded in a long, rectangular, thin mold that is fed by a “gate” occupying the entire feed surface.

Mold Filling by a Reactive Liquid

Domine and Gogos (88–90) considered a very long, very wide, and thin mold being fed by a constant temperature mixture of AA, BB molecules. Both types are bifunctional and the feed has a molecular weight M_0 . The polymerization, assumed to be reversible, proceeds by the reaction of A-ends with B-ends, and follows idealized step polymerization (condensation) kinetics without the generation of a small molecule (91). Specifically, we have



Setting $(AA - BB)_x = M_x$, we can write the general reversible condensation reaction



Equation 13.2-5 is second order in A- or B-ends and first order in A–B links. The rate of change of the concentrations c_A , c_B , and c_{AB} are

$$\left. \begin{aligned} \frac{dc_A}{dt} &= -k_f c_A c_B + k_r c_{AB} \\ \frac{dc_B}{dt} &= -k_f c_A c_B + k_r c_{AB} \\ \frac{dc_{AB}}{dt} &= -k_f c_A c_B - k_r c_{AB} \end{aligned} \right\} \quad (13.2-7)$$

thus, $dc_A/dt = dc_B/dt = -dc_{AB}/dt$ and for $c_A = c_B$, $c_{A0} = c_{B0}$, $c_{AB0} = 0$, and $c_{AB} = c_{A0} - c_A$, and we can write Eq. 13.2-7 as

$$\frac{dc_A}{dt} = -k_f c_A^2 + k_f [c_{A0} - c_A] \quad (13.2-8)$$

Defining the reaction conversion ϕ as

$$c_A = c_{A0}(1 - \phi) \quad (13.2-9)$$

Eq. 13.2-8 becomes

$$\frac{d\phi}{dt} = k_f c_{A0}(1 - \phi)^2 - k_r \phi \quad (13.2-10)$$

For a flowing system with a velocity $v_x = v_x(x, y, t)$ undergoing the chemical reaction just given, $d\phi/dt = D\phi/Dt$. Thus, Eq. 13.2-10 becomes

$$\frac{\partial \phi}{\partial t} + v_x \frac{\partial \phi}{\partial x} = k_f c_{A0}(1 - \phi)^2 - k_r \phi \quad (13.2-11)$$

The boundary and initial conditions are

$$\begin{aligned}\phi(0, y, t) &= 0 \\ \phi(x, y, 0) &= 0\end{aligned}\quad (13.2-12)$$

Both reaction-rate constants are assumed to obey the Arrhenius temperature dependence

$$\left. \begin{aligned}k_f &= k_{f0} \exp\left(\frac{-E_{fr}}{RT}\right) \\ k_r &= k_{r0} \exp\left(\frac{-E_{rr}}{RT}\right)\end{aligned}\right\} \quad (13.2-13)$$

The forward and reverse reaction activation energies are related to the heat of reaction as follows (89);

$$E_{rr} - E_{fr} = -\Delta H \quad (13.2-14)$$

The reaction also has a characteristic temperature, where $k_f = k_r$. For this reacting system the number and weight average molecular weights are (91)

$$\bar{M}_n = \frac{M_0}{1 - \phi} \quad (13.2-15)$$

$$\bar{M}_w = M_0 \left[\frac{1 + \phi}{1 - \phi} \right] \quad (13.2-16)$$

To solve the filling flow and heat-transfer problem with the reacting system just given, we need to specify the x -direction momentum and energy balances. Following Domine and Gogos (88–90), the x -momentum equation during filling is

$$\rho \frac{\partial v_x}{\partial t} = -\frac{\partial P}{\partial x} + \eta \frac{\partial^2 v_x}{\partial y^2} + \frac{\partial \eta}{\partial y} \frac{\partial v_x}{\partial y} \quad (13.2-17)$$

The boundary conditions for Eq. 13.2-17 are

$$\begin{aligned}\frac{\partial v_x}{\partial y}(x, 0, t) &= 0 \\ v_x\left(x, \frac{H}{2}, t\right) &= 0 \\ \frac{\partial \eta}{\partial y}(x, 0, t) &= 0 \\ \frac{\partial v_x}{\partial t}(0, y, t) &= 0 \\ \frac{\partial P}{\partial x}(0, y, t) &= 0\end{aligned}\quad (13.2-18)$$

The viscosity is given by the Carreau fluid equation, which for melts is

$$\eta = \frac{\eta_0}{[1 + (\lambda\dot{\gamma})^2]^{(1-n)/2}} \quad (13.2-19)$$

where

$$\lambda = \frac{\lambda_0 \eta_0 (\overline{M}_w)^{0.75}}{\rho T} \quad (13.2-20)$$

and λ_0 is a curve-fitting parameter. The zero shear viscosity is primarily a function of the weight-average molecular weight

$$\eta_0 = \alpha_i (\overline{M}_w)^{\beta_i} \exp\left(\frac{\Delta E}{RT}\right) \quad (13.2-21)$$

where α_i are material parameters, and

$$\Delta E = \delta_i \exp\left(\frac{-\varepsilon_i}{\overline{M}_n}\right) \quad (13.2-22)$$

and $i = 1, 2$, and denote the two regions of no entanglement and entanglement, respectively. Specifically, for $i = 1$, $\overline{M}_w < M_e$ (91)

$$\begin{aligned} \beta_1 &= 1 \\ \delta_1 &= \Delta E_0 \exp\left(\frac{\varepsilon_1}{M_0}\right) \\ \varepsilon_1 &= M_0 \left(\frac{M_e + M_0}{M_e - M_0}\right) \ln\left(\frac{\Delta E}{\Delta E_0}\right) \end{aligned} \quad (13.2-23)$$

For $i = 2$, $\overline{M}_w > M_e$

$$\begin{aligned} \beta_2 &= 3.4 \\ \delta_2 &= \Delta E \\ \varepsilon_2 &= 0 \end{aligned} \quad (13.2-24)$$

The energy equation for the filling stage is for constant density and thermal conductivity:

$$\rho C_p \left(\frac{\partial T}{\partial t} + v_x \frac{\partial T}{\partial x} \right) = k \frac{\partial^2 T}{\partial y^2} + \eta \left(\frac{\partial v_x}{\partial y} \right)^2 + \frac{\partial \phi}{\partial t} (-\Delta H) \quad (13.2-25)$$

The boundary conditions for Eq. 13.2-25 are

$$\begin{aligned} \frac{\partial T}{\partial y}(x, 0, t) &= 0 \\ \frac{\partial T}{\partial y}\left(x, \frac{H}{2}, t\right) &= -\frac{h}{k} \left[T\left(x, \frac{H}{2}, t\right) - T_w \right] \\ T(0, y, t) &= T_0 \\ \frac{\partial T}{\partial t}(0, y, t) &= 0 \end{aligned} \quad (13.2-26)$$

where T_w is the mold temperature and T_0 is the temperature of the feed, both time independent.

Section 13.1 indicated that the fountain flow in the front region could be neglected in the simulation of the mold filling process and calculations of the time-dependent front position and filling pressure. In RIM, unfortunately, this is no longer true, because the fluid viscosity depends on the molecular weight, and to know the molecular weight of any fluid element at any time, we must know where the fluid has been since entering the mold. Domine (88) tracked fluid particles as they move from the central region of the front toward the front mold wall in a manner similar to that of the fountain flow.

The species balance relation Eq. 13.2-8 is transformed to a difference equation using the forward difference on the time derivative and the backward difference on the space derivative. The finite difference form of the x -momentum equation (Eq. 13.2-25) is obtained by using the forward difference on all derivatives, and is solved by the Crank–Nicolson method. The same is true for the energy equation (Eq. 13.2-26).

The results of the simulation show that for reaction rates that are common in the conventional RIM process, the chemical reaction cannot be ignored during the filling step. In other words, RIM *is not casting*. Appreciable conversion and nonisothermicity can be obtained during filling. Figure 13.42 gives the conversion and temperature fields at the moment of fill. Both temperature and conversion increase with increasing flow direction distance; this is simply the result of larger residence times. It is worth noting that the fountain flow taking the reactive fluid from the center and depositing it on the wall makes both profiles flatter. As the feed reaction constant and the fill time increase, there is more chance for chemical reaction during filling.

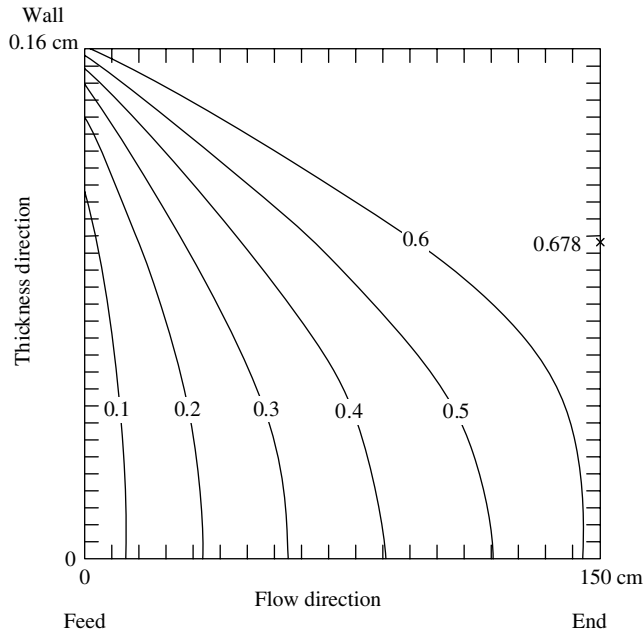
Figure 13.43 presents the results of such increases, for the case where the product of ($k_f \times t_{\text{fill}}$) is four times that of the preceding case. Conversion levels exceeding 90% are obtained, giving rise to a rather thick “reacted skin,” as Fig.13.43(b) indicates by the line for velocity of 10 cm/s. Furthermore, there is a pinching effect on the flow midway in the flow direction, which results in a nipple-like velocity profile with very high velocity gradients and viscous energy dissipation (VED) levels. As a matter of fact, for the system studied, there appears to be an upper limit in the feed-condition reaction-rate constant because of local thermal problems that arise by way of high chemical and viscous heat generation terms. This problem can be reduced by increasing the thermal conductivity of the reacting system (by incorporating conductive additives) and by making the system more shear thinning (perhaps by the addition of dissolved elastomer). At any rate, the effects of both the material and process variables must be studied in order to understand the filling step of the RIM process. A study of this kind was carried out by Domine (88).

Peters et al. (46) utilized their fourth-order approximation of the fountain flow velocity field, Eqs. 13.1-9 and 13.1-10, and the particle tracking numerical technique they incorporated, to calculate the temperature and conversion fields in that region. They assumed that the very flow front material particles experience an adiabatic thermal history, which is reasonable.

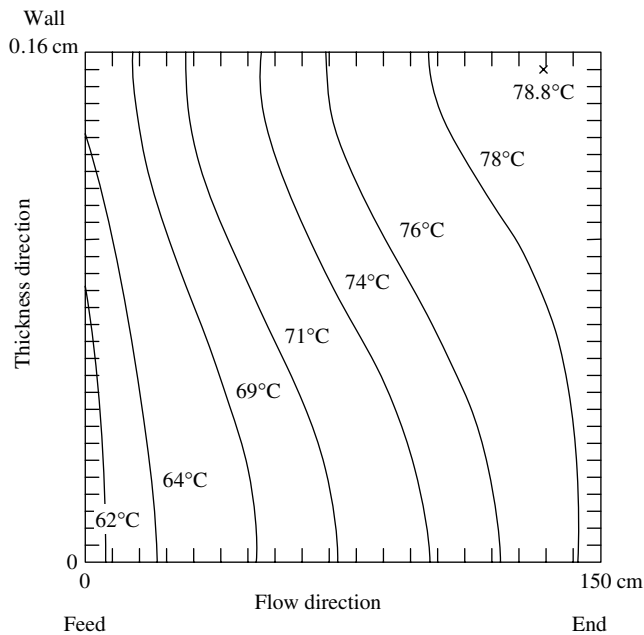
At the end of the filling stage, only heat transfer with chemical reaction occurs, which can be described by the following species and energy balance equations:

$$\frac{d\phi}{dt} = k_f c_{A0} (1 - \phi)^2 - k_r \phi \quad (13.2-27)$$

$$\rho C_p \frac{\partial T}{\partial t} = k \frac{\partial^2 T}{\partial y^2} + k \frac{\partial^2 T}{\partial x^2} + \frac{\partial \phi}{\partial t} (-\Delta H) \quad (13.2-28)$$



(a)



(b)

Fig. 13.42 Simulation results of the RIM process involving a linear step polymerization: $T_0 = T_w = 60^\circ\text{C}$, $k_f = 0.5 \text{ L/mole} \cdot \text{s}$, $t_{\text{fill}} = 2.4 \text{ s}$. (a) Conversion contours at the time of fill. (b) Temperature contours at the time of fill. [Reprinted by permission from J. D. Domine and C. G. Gogos, "Computer Simulations of Injection Molding of a Reactive Linear Condensation Polymer," paper presented at the *Society of Plastics Engineers, 34th Annu. Tech. Conf.*, Atlantic City, NJ, 1976. (Also published in the *Polym. Eng. Sci.*, **20**, 847–858 (1980); volume honoring Prof. B. Maxwell).]

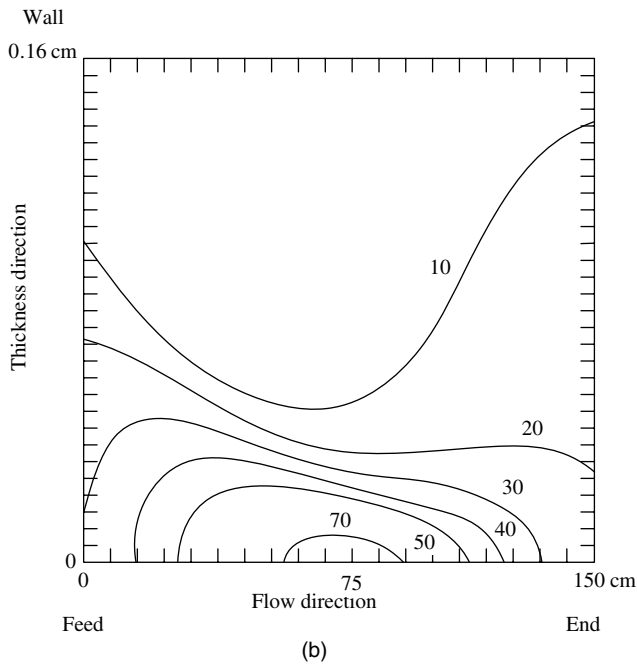
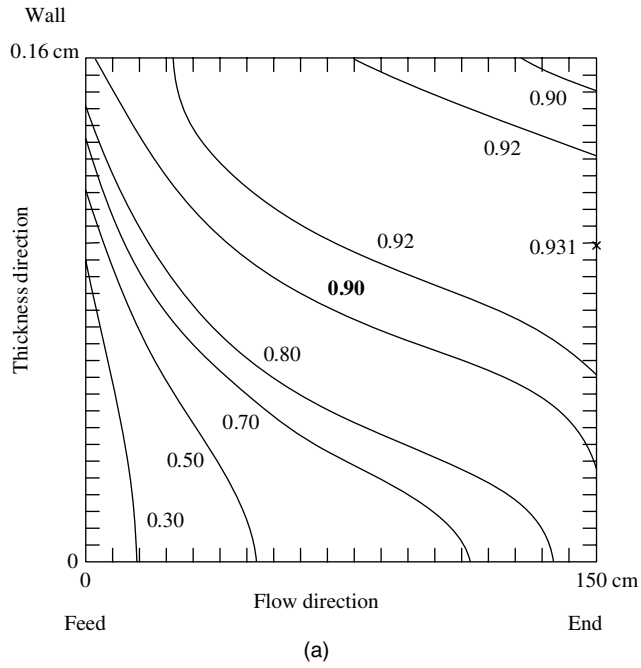


Fig. 13.43 Simulation results of the RIM process involving a linear step polymerization: $T_0 = T_w = 60^\circ\text{C}$, $k_f = 1.0\text{L/mole}\cdot\text{s}$, $t_{\text{fill}} = 4.8\text{ s}$. (a) Conversion contours at the time of fill. (b) Temperature contours at the time of fill. [Reprinted by permission from J. D. Domine and C. G. Gogos, "Computer Simulations of Injection Molding of a Reactive Linear Condensation Polymer," paper presented at the *Society of Plastics Engineers, 34th Annu. Tech. Conf.*, Atlantic City, NJ, 1976. (Also published in the *Polym. Eng. Sci.*, **20**, 847–858 (1980); volume honoring Prof. B. Maxwell.)]

The axial conduction, which was neglected in Eq. 13.2-28 as being smaller than axial convection, is now included. The two preceding equations hold for $t \geq t_{\text{fill}}$. The temperature boundary conditions for an adiabatic feed surface are

$$\begin{aligned}\frac{\partial T}{\partial x}(0, y, t) &= 0 \\ \frac{\partial T}{\partial x}(l, y, t) &= -\frac{h}{k}[T(l, y, t) - T_w] \\ \frac{\partial T}{\partial y}\left(x, \frac{H}{2}, t\right) &= -\frac{h}{k}\left[T\left(x, \frac{H}{2}, t\right) - T_w\right] \\ \frac{\partial T}{\partial y}(x, 0, t) &= 0\end{aligned}\quad (13.2-29)$$

Since the energy balance involves second-order derivatives in both the x and y directions, the alternating direction implicit (ADI) method is used (92). This method requires three time levels of temperature and involves the solution of the equation twice, once in each direction.

The “postfill cure” and heat transfer continues until the thickness–average tensile modulus is high enough at every x position for the part to be removed. The tensile modulus is dependent on the number average molecular weight (89). Through this procedure the *de-mold time* is obtained. The de-mold time for the case corresponding to Fig. 13.42 is 62.4 s, compared to 12 s for the case corresponding to Fig. 13.43. The low de-mold time in the latter case is the result of the thick reacted skin formed during the filling process, as mentioned previously.

Analyses such as the foregoing are necessary to understand the interrelations among the chemical, process, and rheological variables in RIM.

Thermoplastic Foam Injection Molding

In thermoplastic foam injection molding, which is, in principle, a RIM-like process, a gas is introduced into the molten polymer in the injection molding machine (93), or a gas-producing compound (usually in fine powder form) is mixed with the polymer pellets or powder prior to processing. In either case, upon injection into the mold, the gas can be released from the solution because of the prevailing low pressures, especially as the advancing front is approached. The product formed can have a very dense “skin” and a foamed “core” that has a 20–50% density of the unfoamed polymer. The surface contains only a few voids because of the phenomenon of skin formation. Nevertheless the surface is not void-free because of the low pressures during the fountain-flow phenomenon. Typical density profiles of thermoplastic structural foam articles indicate that the solid surface skin is usually about one-quarter of the half-thickness. The density decreases *rapidly* to a constant low value in the core region.

These facts justify the statement made previously that this process is similar to RIM, since physicochemical reactions occur concurrently with mold filling. On the other hand, in contrast to RIM, gas generation can occur *well before* the melt reaches the mold, necessitating the consideration of the chemical reaction during the melting, melt storage, and pumping steps of the process [i.e., inside the injection molding machine (94–96)]. The principles of bubble nucleation and growth in a polymer melt, which are relevant to this process as well, were discussed in Chapter 8.

13.3 COMPRESSION MOLDING

In the compression molding process, a thermoplastic or partially polymerized thermo-setting polymer is placed in a heated cavity, usually in a preheated and preformed shape vaguely corresponding to that of the cavity; the mold begins to close and pressure is applied to the preform, forcing it to further heat up close to the mold temperature, and flow to fill the mold cavity. In the process, the polymer undergoes complete polymerization (cross linking). Then the mold is opened, the part is ejected, and the cycle starts again. This process wastes very little material (no runners and sprue) and can produce large parts. However, it is difficult to produce parts with very close tolerances because the final size of the compression molded article depends on the *exact* amount of the preform. Furthermore, the process does not easily lend itself to molding of intricate parts with deep undercuts.

Figure 13.44 represents the various stages of the compression molding cycle from the point of view of the plunger force needed to close the mold at a constant rate. In the first region, $t \leq t_f$, the force increases rapidly as the preform is squeezed and heated. At t_f , the polymer is presumably in the molten state and, as such, is forced to flow into the cavity and fill it. Filling terminates at t_c , when compression of the polymer melt takes place, to compensate for the volume contraction that results from the polymerization reaction. The bulk of the chemical reaction occurs after t_c . We now comment on each of the steps of the compression molding process.

During the preform-heating part of the cycle, the main problems to be considered are heat transfer and flow (or elastic deformation) of the compressed particulate matter. Referring to Fig. 13.45, the heat transfer problem can be described with the following form of the energy equation:

$$\rho C_p \frac{\partial T}{\partial t} = k \frac{\partial^2 T}{\partial z^2} \quad (13.3-1)$$

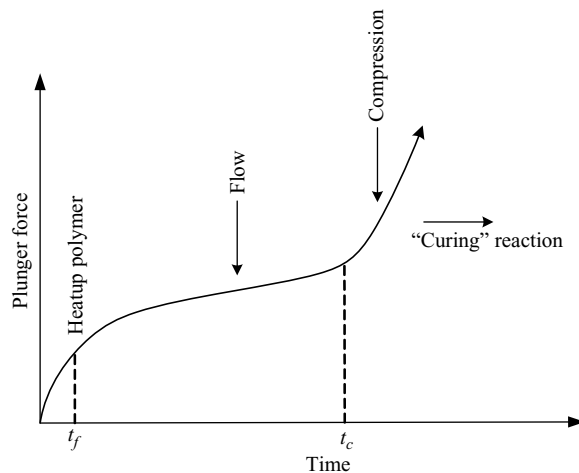


Fig. 13.44 Schematic representation of the plunger force applied during compression molding to move the plunger at a constant speed. The various stages of the process are depicted.

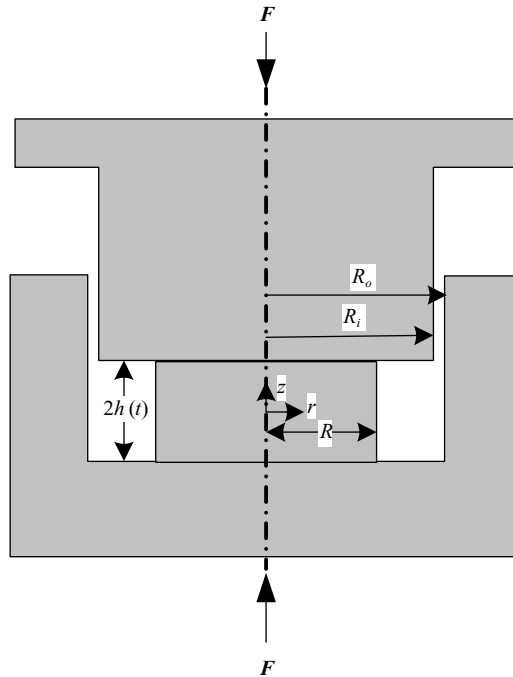


Fig. 13.45 The geometry and coordinate frame used for the simulation of the compression-molding process of a cup-shaped cavity.

where the following assumptions have been made: the convective and dissipative effects associated with v_r are negligible, as is the radial conductive heat transfer, and the thermophysical properties are taken to be constant. The temperature of the preform is constant at the start of the process, and the boundary conditions are

$$\begin{aligned} \frac{\partial T}{\partial z}(0, t) &= 0 \\ \frac{\partial T}{\partial z}[h(t), t] &= -U[T(h(t), t) - T_w] \end{aligned} \quad (13.3-2)$$

where U is the ratio of the heat transfer coefficient to the thermal conductivity. Furthermore, because of the plunger motion,

$$h(t) = h_0 - \dot{h}t \quad (13.3-3)$$

The heat transfer problem just discussed can be solved in a fashion similar to the one used in Section 5.3, to yield $T(z, t)$. In principle, once the temperature field is known in the preform at any time before t_f , the plunger force can be calculated. The preform can be taken as a solid that slips at the mold surface and has a temperature-dependent compressive modulus. At any time $t < t_f$, each layer of the preform will deform by an amount such that (a) the force on *every* layer of thickness Δz is the same (and equal to the unknown quantity), and (b) the sum of the compressive deformations of all the layers equals the deformation imposed on the preform by the plunger at the given time. The force

can also be estimated by assuming that the preform is a viscous liquid with a temperature-dependent viscosity undergoing an overall constant rate squeezing flow. The problem can then be solved in a manner similar to that in Example 6.14. An average temperature value can be used, or each layer can be considered to flow at a rate such that (a) the force on every layer is independent of z , and (b) the sum of all the squeezing rates is equal to the one applied by the plunger \dot{h} .

Assuming that $T(z, t_f) = T_w$, we can deal with the flow problem alone for $t_f < t < t_c$. Referring to Fig. 13.45, as long as the preform radius is less than R_0 , we can treat the problem as an isothermal radial flow of an incompressible fluid flowing between two disks that approach each other at a constant rate \dot{h} . Recapturing the results for the velocity field, pressure distribution, and plunger force needed to squeeze an isothermal Power Law fluid at a constant slow or moderate squeeze rate, we have

$$v_r(z, r, t) = \frac{h^{1+s}}{1+s} \left(-\frac{1}{m} \frac{\partial P}{\partial r} \right)^s \left[1 - \left(\frac{z}{h} \right)^{1+s} \right] \quad (13.3-4)$$

where the pressure gradient can be obtained from

$$P = P_a + \frac{m(2+s)^n}{2^n(n+1)} \frac{(-\dot{h})R^{n+1}}{h^{2n+1}} \left[1 - \left(\frac{r}{R} \right)^{n+1} \right] \quad (13.3-5)$$

The plunger force F_N can be calculated from the preceding equation to give

$$F_N = \frac{\pi m(2+s)^n}{2^n(n+3)} \frac{(-\dot{h})^n R^{3+n}}{h^{2n+1}} \quad (13.3-6)$$

Since the fluid is incompressible and nonreactive at this stage, its volume is constant, implying that

$$h(t)R^2(t) = C_1 \quad (13.3-7)$$

Thus, the Scott Equation 13.3-6 becomes

$$F_N = \frac{\pi m(2+s)^n}{2^n(n+3)} \frac{(-\dot{h})^n R^{5(n+1)}}{C_1^{2n+1}} \quad (13.3-8)$$

When the radius of the flowing preform reaches the value of R_o , the fluid is forced to flow in the annular space $R_o - R_i$. For a constant squeeze rate, the rate of increase of the axial annular distance \dot{l} occupied by the melt is

$$-\pi R_i^2 \dot{h}(t) = \pi(R_o^2 - R_i^2) \dot{l} \quad (13.3-9)$$

For small annular spacing $\Delta R \ll 1$, and Eq. 13.3-9 can be written as

$$\dot{l} = \dot{h} \left(\frac{\bar{R}}{2\Delta R} \right) \quad (13.3-10)$$

Once annular flow occurs, there is an additional force term acting on the plunger. The pressure at $r = R_i$ is not atmospheric but that which is needed to support the flow in the annulus. To calculate this pressure, we first turn to the volumetric flow rate in the annular region, which is

$$Q = \pi(R_o^2 - R_i^2)\dot{l} \quad (13.3-11)$$

For a thin annulus, $\Delta R \ll \bar{R}$, the plunger travel rate \dot{h} is very small compared to \dot{l} , and the annular flow can be considered to be a pressure, not a combined pressure and drag flow. For a thin annulus, Eq. 13.3-11 reduces to

$$Q = 2\pi\bar{R}\Delta R\dot{l} \quad (13.3-12)$$

For isothermal annular pressure flow of an incompressible Power Law fluid, Fredrickson and Bird (97) have calculated the following relationship between Q and ΔP

$$Q = \frac{\pi R_o^3}{s+2} \left(\frac{R_o \Delta P}{2ml} \right)^s (1-\kappa)^{s+2} F(n, \kappa) \quad (13.3-13)$$

where $1/\beta = \kappa = R_i/R_o$. Figure 12.45 plots $F(n, \kappa)$. For a thin annulus, $F(n, \kappa) \rightarrow 1$ and Eq. 13.3-13 reduces to

$$Q = \frac{\pi R_o^3}{s+2} \left(\frac{R_o \Delta P}{2ml} \right)^s (1-\kappa)^{s+2} \quad (13.3-14)$$

Therefore, to calculate the added pressure at $r = R_i$, we use Eqs. 13.3-11 and 13.3-13 for a wide annulus, or Eqs. 13.3-12 and 13.3-14 for a thin annulus. For the latter case, we write

$$P(R) - P_{\text{atm}} = \frac{2ml}{R_o^{3n+1}} \frac{[2(s+2)\bar{R}\Delta R\dot{l}]^n}{(1-\kappa)^{+2n}} \quad (13.3-15)$$

When this is multiplied by the plunger area and added to the right-hand side of Eq. 13.3-6, the plunger force is obtained for the case where annular flow takes place in a cup-shaped cavity in compression molding. Similar expressions can be obtained for the entire flow stage $t_f < t < t_c$, during the compression molding of other shapes, by making use of the quasi-steady state and, when needed, the lubrication approximation.

The reaction stage of the compression molding process can be described by Eqs. 13.2-27 and 13.2-28, employed in the simulation of the postfilling reaction stage in the RIM process. Of course, Eq. 13.2-27 is applicable only to a linear and reversible step polymerization. Furthermore, we have assumed that the melt is at a uniform temperature at the beginning of the reaction. Therefore, in Eq. 13.2-28 conduction should occur only in the thickness direction. Broyer and Macosko (98) have solved the problem of heat transfer numerically with a cross-linking polymerization reaction that is more representative of the compression molding process. For a thin rectangular mold of half-thickness h and temperature T_w , as well

as n th-order kinetics and constant thermophysical properties, the governing equations in dimensionless form are

$$-\frac{dc_A^*}{dx} = k^* c_A^{*n} \exp B \left[\frac{\Delta T'_{ad} T^*}{\Delta T'_{ad} T^* + 1} \right] \tag{13.3-16}$$

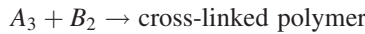
and

$$-\frac{dT^*}{dt^*} = \frac{\partial^2 T^*}{\partial y^{*2}} + k^* c_A^{*n} \exp B \left[\frac{\Delta T'_{ad} T^*}{\Delta T'_{ad} T^* + 1} \right] \tag{13.3-17}$$

where $c_A^* = c_A/c_{A0}$, $t^* = \alpha t/h^2$, $y^* = y/h$, h is the half-thickness of the polymerizing slab, $k^* = c_{A0}^{n-1} h^2 A e^{-B}/\alpha$, $B = E/RT_0$, E is the reaction activation energy, and A is the frequency factor, $T^* = (T - T_0)/(T_{ad} - T_0)$, and the adiabatic temperature rise is

$$\Delta T'_{ad} = \frac{T_{ad} - T_0}{T_0} = \frac{\Delta H c_{A0}}{\rho C_p T_0} \tag{13.3-18}$$

where ΔH is the heat of reaction, c_A is the concentration of the A functional group in the trifunctional group-bifunctional group step reaction



The system of Eqs. 13.3-17 and 13.3-18 can be solved for the adiabatic, isothermal, or constant wall flux cases using the Crank–Nicolson method. The thermomechanical and reaction data for such systems were evaluated by Lifshitz, Macosko, and Mussatti (99) at 45°C for a polyester triol and a chain extended 1,6-hexamethylene diisocyanate (HDI) with dibutyltin as a catalyst. Figure 13.46 gives the temperature profiles for the isothermal-wall case. Because of the high heat of polyurethane formation and the low conductivity of

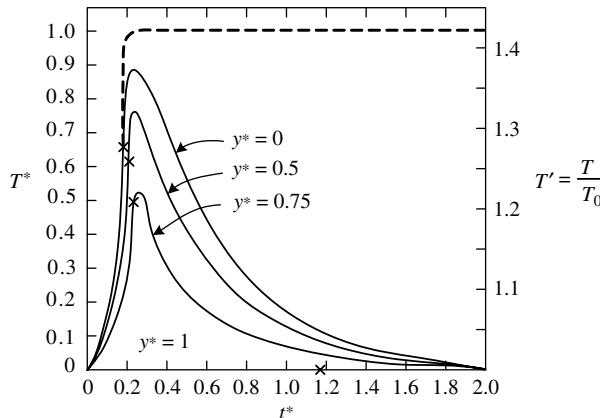


Fig. 13.46 Temperature distribution in a reacting polyurethane slab; isothermal-wall simulations. Dotted line denotes the adiabatic temperature rise and \times 's indicate gel points. $k^* = 1$, $n = 1$, $\Delta T'_{ad} = 0.423$, and $B = 18.7$, $\phi_{gel} = 0.707$. [Reprinted by permission from E. Broyer and C. W. Macosko, "Heat Transfer and Curing in Polymer Reaction Molding," *AICHE J.* **22**, 268 (1976).]

the system, the center of the slab shows nearly an adiabatic temperature rise. The peaks come also closer to the adiabatic temperature when k^* is increased.

The extent of the reaction ϕ can be related to the \bar{M}_w for the triol-HDI-polyurethane system under equal stoichiometry (100) as follows:

$$\bar{M}_w = \frac{\frac{2}{3}(1 + \phi^2)M_{A_3}^2 + (1 + 2\phi^2)M_{B_2}^2 + 4\phi M_{A_3}M_{B_2}}{\left(\frac{2}{3}M_{A_3} + M_{B_2}\right)(1 - 2\phi^2)} \quad (13.3-19)$$

The “gel point” is defined as the condition when \bar{M}_w goes to infinity, which occurs at $\phi \equiv \phi_{\text{gel}} = (1/2)^{1/2} = 0.707$. It follows from Fig. 13.46 that the center of the slab will gel faster than the skin. A more uniform extent of reaction can be achieved by maintaining the mold walls at a higher temperature, assuming that this does not result in excessive surface reaction and interference with the filling and the compression processes. Knowing the temperature, the conversion, and the MWD as a function of thickness and reaction time is essential in determining the required compression-mold cycle or the time and temperature in the postcuring step, if it is necessary.

REFERENCES

1. R. C. Donovan, D. E. Thomas, and L. D. Leversen, “An Experimental Study of Plasticating in a Reciprocating-Screw Injection Molding Machine,” *Polym. Eng. Sci.*, **11**, 353 (1971).
2. S. D. Lipshitz, R. Lavie, and Z. Tadmor, “A Melting Model for Reciprocating Screw Injection Molding Machines,” *Polym. Eng. Sci.*, **14**, 553 (1974).
3. G. B. Thayer, J. W. Mighton, R. B. Dahl, and C. E. Beyer, “Injection Molding,” in *Processing of Thermoplastic Materials*, E. C. Bernhardt, Ed., Reinhold, New York, 1959, Chapter 5.
4. I. I. Rubin, *Injection Molding-Theory and Practice*, Wiley-Interscience, New York, 1972.
5. C. F. Huang, “Numerical Simulations of the Filling Process with a Cup-shaped Mold,” M.S. Thesis, Department of Chemical Engineering, Stevens Institute of Technology, Hoboken, NJ, 1974.
6. W. L. Krueger and Z. Tadmor, “Injection Molding into a Rectangular Cavity,” *Polym. Eng. Sci.*, **20**, 426–431 (1980).
7. F. C. Caras, “Spiral Mold for Thermosets,” *Mod. Plast.*, **41**, 140 (1963).
8. G. D. Gilmore and R. S. Spencer, “Role of Pressure, Temperature and Time in the Injection Molding Process,” *Mod. Plast.*, **27**, 143 (April 1950); also, R. S. Spencer and G. D. Gilmore, “Residual Strains in Injection Molded Polystyrene,” *Mod. Plast.*, **28**, 97 (December 1950).
9. R. S. Spencer and G. D. Gilmore, “Some Flow Phenomena in the Injection Molding of PS,” *J. Colloid Sci.*, **6**, 118 (1951).
10. C. E. Beyer and R. S. Spencer, “Rheology in Molding,” in *Rheology*, Vol. 3, F. R. Eirich, Ed., Academic Press, New York, 1960.
11. R. L. Ballman, T. Shusman, and H. L. Toor, “Injection Molding-Flow into a Cold Cavity,” *Ind. Eng. Chem.*, **51**, 847 (1959).
12. R. L. Ballman and H. L. Toor, “Injection Molding: A Rheological Interpretation - Part 1,” *Mod. Plast.*, **37**, 105 (September 1959); also R. L. Ballman, T. Shusman, and H. L. Toor, “Injection Molding: A Rheological Interpretation - Part 2,” *ibid.*, **37**, 115 (October 1959).

13. G. B. Jackson and R. L. Ballman, "The Effect of Orientation on the Physical Properties of Injection Moldings," *Soc. Plast. Eng. J.*, **16**, 1147–1152 (1960).
14. T. Aoba and H. Odaïra, Flow of Polymer Melt in Injection Mold, *Proc. of the 14th Japanese Congr. on Materials Research*, Kyoto, Japan, 1970, p. 124.
15. M. R. Kamal and S. Kenig, "The Injection Molding of Thermoplastics. Part I. Theoretical Model," *Polym. Eng. Sci.*, **12**, 294 (1972).
16. J. L. White and H. B. Dee, "Flow Visualization of Injection Molding Polyethylene and Polystyrene Melts in Sandwich Molding," *Polym. Eng. Sci.*, **14**, 212 (1974).
17. L. R. Schmidt, "A Special Mold and Tracer Technique for Studying Shear and Extensional Flows in a Mold Cavity during Injection Molding," *Polym. Eng. Sci.*, **14**, 797 (1974).
18. W. Rose, "Fluid-Fluid Interfaces in Steady Motion," *Nature*, **191**, 242–243 (1961).
19. K. Oda, J. L. White, and E. S. Clark, "Jetting Phenomena in Injection Mold Filling," *Polym. Eng. Sci.*, **16**, 585 (1976).
20. J. R. A. Pearson, *Mechanical Principles of Polymer Melt Processing*, Pergamon Press, Oxford, 1966, p. 128.
21. D. H. Harry and R. G. Parrott, "Numerical Simulation of Injection Mold Filling," *Polym. Eng. Sci.*, **10**, 209 (1970).
22. J. L. Berger and C. G. Gogos, "A Numerical Simulation of the Cavity Filling Process with PVC," *SPE ANTEC Tech. Papers*, **17** (1971); also, J. L. Berger and C. G. Gogos, "A Numerical Simulation of the Cavity Filling Process with PVC in Injection Molding," *Polym. Eng. Sci.*, **13**, 102–112 (1973).
23. P. C. Wu, C. F. Huang, and C. G. Gogos, "Simulation of the Mold Filling Process," *Polym. Eng. Sci.*, **14**, 223 (1974).
24. B. R. Laurencena and M. C. Williams, "Radial Flow of Non-Newtonian Fluids between Parallel Plates," *Trans. Soc. Rheol.*, **18**, 331 (1974).
25. G. Williams and H. A. Lord, "Mold Filling Studies for the Injection Molding of Thermoplastics," *Polym. Eng. Sci.*, **15**, 553 (1975).
26. J. Crank and P. Nicolson, "A Practical Method for Numerical Evaluation of Solutions of Partial Differential Equations of the Heat-conducting Type," *Proc. Cambridge Philos. Soc.*, **43**, 50 (1947).
27. G. G. O'Brien, M. A. Hyman, and S. Kaplan, "A Study of the Numerical Solution of Partial Differential Equations," *J. Math. Phys.*, **29**, 223–251 (1951).
28. I. T. Barrie, "Understanding How an Injection Mold Fills," *Soc. Plast. Eng. J.*, **27** (8), 64–69 (1971).
29. Z. Tadmor, "Molecular Orientation in Injection Molding," *J. Appl. Polym. Sci.*, **18**, 1753–1772 (1974).
30. G. Menges and G. Wübken, "Influence of Processing Conditions on Molecular Orientation in Injection Molds," *SPE ANTEC Tech. Papers*, **19**, 519 (1973).
31. H. Mavridis, A. N. Hrymak, and J. Vlachopoulos, "A Finite Element Simulation of Fountain Flow," *Polym. Eng. Sci.*, **26**, 449–454 (1986).
32. H. R. Warner, Jr., "Kinetic Theory and Rheology of Dilute Suspensions of Finitely Extendible Dumbbells," *Ind. Eng. Chem. Fundam.*, **11**, 379–387 (1972); also, R. L. Christiansen and R. B. Bird, "Dilute Solution Rheology: Experimental Results and Finitely Extensible Nonlinear Elastic Dumbbell Theory," *J. Non-Newt. Fluid Mech.*, **3**, 161–177 (1977/1978).
33. W. Dietz, J. L. White, and E. S. Clark, "Orientation Development and Relaxation in Molding of Amorphous Polymers," *Polym. Eng. Sci.*, **18**, 273–281 (1978).
34. C. G. Gogos and C. F. Huang, "The Process of Cavity Filling Including the Fountain Flow in Injection Molding," *Polym. Eng. Sci.*, **26**, 1457–1466 (1986).

35. C. F. Huang, Ph.D. Dissertation, Department of Chemical Engineering, Stevens Institute of Technology, Hoboken, NJ, 1978.
36. B. Friedrichs and S. I. Güçeri, "A Novel Hybrid Numerical Technique to Model 3-D Fountain Flow in Injection Molding Processes," *J. Non-Newt. Fluid Mech.*, **49**, 141–173 (1993).
37. E. Mitsoulis and J. Vlachopoulos, "The Finite Element Method for Flow and Heat Transfer Analysis," *Adv. Polym. Technol.*, **4**, 107–121 (1984).
38. F. M. Orr and L. E. Scriven, "Rimming Flow: Numerical Simulation of Steady, Viscous, Free-surface Flow with Surface Tension," *J. Fluid Mech.*, **84**, 145–165 (1978).
39. D. H. Chung and T. H. Kwon, "Numerical Studies of Fiber Suspensions in an Axisymmetric Radial Diverging Flow: the Effects of Modeling and Numerical Assumptions," *J. Non-Newt. Fluid Mech.*, **107**, 67–96 (2002).
40. E. Thompson, "Use of Pseudo-concentrations to Follow Creeping Viscous Flows during Transient Analysis," *Int. J. Numer. Meth. Fluids*, **6**, 749–761 (1986).
41. G. A. A. V. Haagh and F. N. V. D. Vosse, "Simulation of Three-dimensional Polymer Mould Filling Processes Using a Pseudo-concentration Method," *Int. J. Numer. Meth. Fluids*, **28**, 1355–1369 (1998).
42. S. M. Dinh and R. C. Armstrong, "A Rheological Equation of State for Semi-concentrated Fiber Suspensions," *J. Rheol.*, **28** (3), 207–227 (1984).
43. A. C. Garcia, "Reactive Mold Filling Modeling," Ph.D. Thesis, Chemical Engineering Department, University of Minnesota, Minneapolis, 1991.
44. S. K. Goyal, E. Chu, and M. R. Kamal, "Non-isothermal Radial Filling of Center-gated Disc Cavities with Viscoelastic Polymer Melts," *J. Non-Newt. Fluid Mech.*, **28**, 373–406 (1988).
45. D. J. Coyle, J. W. Blake, and C. W. Macosko, "Kinematics of Fountain Flow in Mold Filling," *AIChE J.*, **33**, 1168–1172 (1987).
46. G. W. M. Peters, P. J. L. van der Velden, H. E. H. Meijer, and P. Schoone, "Multilayer Injection Moulding," *Int. Polym. Process.*, **9**, 258 (1994).
47. A. C. B. Bogaerds, G. W. M. Peters, and F. P. T. Baaijens, "Tiger Stripes: Instabilities in Injection Molding" in *Polymer Processing Instabilities*, S. G. Hatzikiriakos and K. B. Migler, Eds., Marcel Dekker, New York, 2005.
48. M. Bulters and A. Schepens, "The Origin of the Surface Defect 'Slip-stick' on Injection Moulded Products," *Proc. Annu. Meet.*, American Institute of Chemical Engineering, Los Angeles, CA, 2000.
49. M. Bulters and A. Schepens, "The Origin of the Surface Defect 'Slip-stick' on Injection Moulded Products," *Proc. 16th Annu. Meet., Polymer Processing Society*, Shanghai, 2000, pp. 144–145.
50. M. C. O. Chang, "On the Study of Surface Defects in the Injection Molding of Rubber-modified Thermoplastics," *SPE ANTEC Tech. Papers*, **40**, 360–367 (1994).
51. H. Hamada and H. Tsunasawa, "Correlation between Flow Mark and Internal Structure of Thin PC/ABS Blend Injection Moldings," *J. Appl. Polym. Sci.*, **60**, 353–362 (1996).
52. S. Y. Hobbs, "The Development of Flow Instabilities during the Injection Molding of Multicomponent Resins," *Polym. Eng. Sci.*, **36**, 1489–1494 (1996).
53. B. Monasse, L. Mathieu, M. Vincent, J. M. Haudin, J. P. Gazonnet, V. Durand, J. M. Barthez, D. Roux, and J. Y. Charneau, "Flow Marks in Injection Molding of Polypropylene: Influence of Processing Conditions and Formation in Fountain Flow," *Proc. 15th Annual Meeting, Polymer Processing Society*, Hertogenbosch, 1999.
54. F. J. Rielly and W. L. Price, "Plastic Flow in Injection Molds," *SPE J.*, **17**, 1097–1101 (1961).
55. M. M. Denn, "Extrusion Instabilities and Wall Slip," *Ann. Rev. Fluid Mech.*, **33**, 265 (2001).
56. R. S. Graham, T. C. B. McLeish, and O. G. Harlen, "Using the Pom-pom Equations to Analyze Polymer Melts in Exponential Shear," *J. Rheol.*, **45**, 275–290 (2001).

57. N. J. Inkson, T. C. B. McLeish, O. G. Harlen, and D. J. Groves, "Predicting Low Density Polyethylene Melt Rheology in Elongational and Shear Flows with 'Pom-pom' Constitutive Equations," *J. Rheol.*, **43**, 873–896 (1999).
58. W. M. H. Verbeeten, G. W. M. Peters, and F. P. T. Baaijens, "Differential Constitutive Equations for Polymer Melts: The Extended Pom–pom Model," *J. Rheol.*, **45**, 823–843 (2001).
59. E. Vos, H. E. H. Meijer, and G. W. M. Peters, "Multilayer Injection Molding," *Int. Polym. Process.*, **6**, 42–50 (1991).
60. F. Fairbrother and A. E. Stubbs, *J. Chem. Soc.*, **1**, 527 (1935).
61. R. N. Marchessault and S. G. Mason, "Flow of Entrapped Bubbles through a Capillary," *Ind. Eng. Chem.*, **52**, 79–84 (1960).
62. G. I. Taylor, "Deposition of a Viscous Fluid on the Wall of a Tube," *J. Fluid Mech.*, **10**, 161–165 (1961).
63. B. G. Cox, "On Driving a Viscous Fluid Out of a Tube," *J. Fluid Mech.*, **14**, 81–96 (1962).
64. H. Westborg and O. Hassager, "Creeping Motion of Long Bubbles and Drops in Capillary Tubes," *J. Colloid Interface Sci.*, **133**, 135–147 (1989).
65. A. J. Poslinski, P. R. Oehler, and V. R. Stokes, "Isothermal Gas-assisted Displacement of Viscoplastic Liquids in Tubes," *Polym. Eng. Sci.*, **35**, 877–892 (1995).
66. A. J. Poslinski and D. J. Coyle, "Steady Gas Penetration through Non-Newtonian Liquids in Tube and Slit Geometries: Isothermal Shear-Thinning Effects," *Proc. Polymer Processing Society, 10th Annu. Meet.*, Akron, Ohio (1994), pp. 219–220.
67. P. C. Huzyak and K. W. Koelling, "The Penetration of a Long Bubble through a Viscoelastic Fluid in a Tube," *J. Non-Newt. Fluid Mech.*, **71**, 73–88 (1997).
68. V. Gauri and K. W. Koelling, "Gas-assisted Displacement of Viscoelastic Fluids: Flow Dynamics at the Bubble Front," *J. Non-Newt. Fluid Mech.*, **83**, 183–203 (1999).
69. H. Giesekus, *Rheol. Acta*, **2**, 122 (1962).
70. K. W. Koelling, V. Gauri, M. Tendulkar, R. Kaminski, and O. Becker, "Understanding the Controlling Mechanisms of Gas-assisted Injection Molding through Visualization," *SPE ANTEC Tech. Papers*, **43**, 3697–3701 (1997).
71. O. C. Zienkiewicz, P. Mayer, and Y. K. Cheung, "Solution of Anisotropic Seepage Problems by Finite Elements," *Proc. Am. Soc. Civ. Eng.*, **92**, EM1, 111–120 (1964).
72. E. Broyer, C. Gutfinger, and Z. Tadmor, "A Theoretical Model for the Cavity Filling Process in Injection Molding," *Trans. Soc. Rheol.*, **19**, 423 (1975).
73. Y. Kuo and M. R. Kamal, "Flows of Thermoplastics in the Filling and Packing Stages of Injection Molding," paper presented at the International Conference on Polymer Processing, MIT, Cambridge, MA, August 16, 1977.
74. R. C. Thamm, "Phase Morphology of High-Impact-Strength Blends of EPDM and Polypropylene. Knit-line Behavior," *Rubber Chem. Technol.*, **50**, 24–34 (1977).
75. M. R. Kantz, H. H. Newman, Jr., and F. H. Stigale, "The Skin-Core Morphology and Structure-Properties Relationships in Injection Molded PP," *J. Appl. Polym. Sci.*, **16**, 1249 (1972).
76. E. S. Clark, "Morphology and Properties of Injection Molded Crystalline Polymers," *Appl. Polym. Symp.*, **24**, 45–53 (1974).
77. S. Y. Hobbs, "Some Observations in the Morphology and Fracture Characteristics of Knit-lines," *Polym. Eng. Sci.*, **14**, 621 (1974).
78. K. J. Cleereman, "Injection Molding of Shapes of Rotational Symmetry with Multiaxial Orientation," *Soc. Plast. Eng. J.*, **23**, 43 (October 1967).
79. R. Keuerleber and F. W. Pahl, U.S. Patent 3,706,518, Kraus Maffei, Germany (1972).
80. G. Oertel, Ed., *Polyurethane Handbook*, Hansen, Munich, 1985, Chapter 4.
81. G. Menges, K. Schwanitz, J. C. Petersen, and V. Schulte, *Kunststoff–Rundschau*, **10**, 435 (1973).

82. S. C. Malguarnera, M.S.Thesis, Department of Mechanical Engineering, MIT, Cambridge, MA, 1976.
83. S. C. Malguarnera and N. P. Suh, "Liquid Injection Molding I. An Investigation of Impingement Mixing," *Polym. Eng. Sci.* **17**, 111–115 (1977).
84. C. W. Macosko, *RIM Fundamentals of Reaction Injection Molding*, Hansen, Munich, 1989.
85. L. J. Lee and C. W. Macosko, *SPE ANTEC Tech. Papers*, **24**, 151 (1978); also, L. J. Lee, Ph.D. Thesis, Chemical Engineering Department, University of Minnesota, Minneapolis, 1979.
86. L. J. Lee, J. M. Ottino, W. E. Ranz, and C. W. Macosko, "Impingement Mixing in Reaction Injection Molding," *Polym. Eng. Sci.*, **20**, 868–874 (1980).
87. C. L. Tucker III and N. P. Suh, "Mixing for Reaction Injection Molding. I. Impingement Mixing of Liquids," *Polym. Eng. Sci.*, **20**, 875–886 (1980).
88. J. D. Domine, "Computer Simulation of the Injection Molding of a Liquid Undergoing a Linear Step Polymerization," Ph.D. Thesis, Department of Chemical Engineering, Stevens Institute of Technology, Hoboken, NJ, 1976.
89. J. D. Domine and C. G. Gogos, "Computer Simulations of Injection Molding of a Reactive Linear Condensation Polymer," *SPE ANTEC Tech. Papers*, **22**, (1976).
90. J. D. Domine and C. G. Gogos, "Simulation of Reactive Injection Molding," *Polym. Eng. Sci.*, **20**, 847–858 (1980).
91. G. Odian, *Principles of Polymerization*, McGraw-Hill, New York, 1970; also, T. G. Fox and V. R. Allen, "Dependence of the Zero Shear Melt Viscosity and the Related Friction Coefficient and Critical Chain Length on Measurable Characteristics of Chain Polymers," *J. Chem. Phys.*, **41**, 344–352 (1964).
92. D. W. Peaceman and H. H. Rachford, Jr., "The Numerical Solution of Parabolic and Elliptic Differential Equations," *J. SIAM*, **3**, 28–41 (1955).
93. R. G. Angell, Jr., U.S. Patent 3,268,636 (to Union Carbide) (1966).
94. J. L. Throne, "Note on the Mechanical Strength of Self-skinning Foams," *J. Cell. Plast.*, **8**, 208–210 (1972).
95. J. L. Throne and R. G. Griskey, "Structural Thermoplastic Foam – A Low Energy Processed Material," *Polym. Eng. Sci.*, **15**, 747 (1975).
96. P. L. Durrill and R. G. Griskey, "Diffusion and Solution of Gases in Thermally Softened or Molten Polymers. Part I," *AIChE J.*, **12**, 1147 (1966).
97. A. G. Fredrickson and R. B. Bird, "Non-Newtonian Flow in Annuli," *Ind. Eng. Chem.*, **50**, 347 (1958).
98. E. Broyer and C. W. Macosko, "Heat Transfer and Curing in Polymer Reaction Molding," *AIChE J.*, **22**, 268 (1976).
99. S. D. Lifshitz, C. W. Macosko, and F. G. Mussatti, *SPE ANTEC Tech. Papers*, **21**, 239 (1975).
100. C. W. Macosko and D. R. Miller, "A New Derivation of Post-gel Properties Network Polymer," *Macromolecules*, **9**, 206 (1976).

PROBLEMS

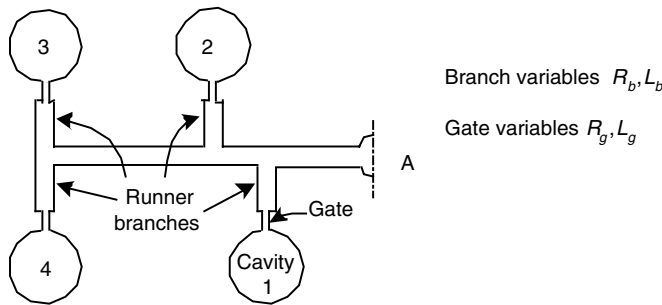
- 13.1 Injection Mold Runner Filling at a Constant Flow Rate** Using the viscosity data and runner dimensions used in Example 14.1 calculate the required injection pressure to fill the entire runner at a constant rate of $1.2 \times 10^{-6} \text{ m}^3/\text{s}$.
- 13.2 Filling of an Injection Mold Runner of Noncircular Cross Section** Consider the filling of a runner, the cross section of which is formed by three rectangle sides and a semicircle. The filling takes place at a constant applied injection pressure of

20 MN/m². The dimensions of the runner cross section (see Fig. 12.51) are $d/B = 0.8$ and $B = 5.0$ mm, while its length is 25 cm. (a) Assuming that the polymer melt has a viscosity which is shear rate independent and equal to 6×10^3 N·s/m², and making the pseudo-steady state assumption, calculate $Q(t)$ and $Z(t)$.

13.3 Relative Pressure Drops in the Runner and Gate in Injection Molding Consider the pressure traces on Fig. 13.5, as well as the location of the pressure transducers. Assuming that the filling process is isothermal, neglecting the “elbows” in the runner and the distance of P_3 from the gate, calculate P_1-P_2 (runner pressure drop) and P_2-P_3 (gate pressure drop) at 0.7 s. The runner distance from P_1 to P_2 is 8.0 in, its width is 0.43 in, and the thickness 0.317 in. The gate dimensions are 0.25 in wide, 0.07 in long, and 0.089 in deep. The rheological properties of the PS melt used are $\ln \eta = A_0 + A_1 \ln \dot{\gamma} + A_{11}(\ln \dot{\gamma})^2 + A_2 T + A_{22} T^2 + A_{12} T \ln \dot{\gamma}$, where $\dot{\gamma}$ is in s⁻¹, and T in °F, and η in lb_f·s/in.² The coefficients are $A_0 = 0.14070 \times 10^2$, $A_1 = -0.80596 \times 10^0$, $A_{11} = -0.22504 \times 10^{-1}$, $A_2 = -0.44972 \times 10^{-1}$, $A_{22} = 0.38399 \times 10^{-4}$, $A_{12} = 0.99782 \times 10^{-3}$. Compare your answers to the P_1-P_2 and P_2-P_3 transducer values appearing in Fig. 13.5.

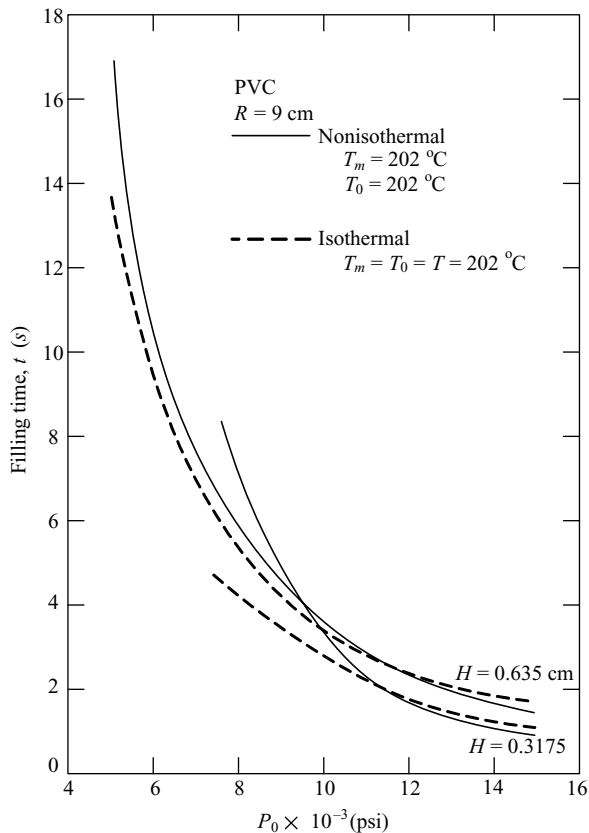
13.4 “Packing” Flow during Injection Molding Based on the pressure values recorded in Fig. 13.5 and assuming that during the period 1.5 s < t < 3 s no appreciable skin has been formed at the positions of the transducer P_1 , P_2 , and P_3 , obtain an estimate of the “packing flow rate” both from P_1-P_2 or P_2-P_3 . Use the runner and gate dimensions given in Problem 13.3. The fluid can be assumed to be Newtonian at these slow flow rates with a viscosity evaluated from the rheological data in Problem 13.3. Check your answer by calculating the corresponding thermal contraction of the melt in the mold in the period of 1 s. The thermal expansion coefficient of the PS melt is 6×10^{-4} K⁻¹, the entering melt temperature is 400°F and the mold temperature is 75°F.

13.5 Design of a Multiple-Cavity Runner System Multicavity molds need multiple runners and gates. The accompanying figure shows one half of a center-fed eight-cavity mold, which shows one half of the mold and cavities. The design objective is to start and end filling the cavities simultaneously to attain uniform properties and to avoid flash, on the one hand, and partially filled cavities, on the other. Consider the runner-cavity system shown in the figure. Assuming equal-length branches and gates, develop design equations for the system that will predict the location of the penetrating melt and the pressure at the branching points and gates, as a function of time. Assume that the injection pressure is constant at point A, that flow is isothermal, and the fluid is incompressible and Newtonian.



13.6 The ‘Molding Area’ in Injection Molding (a) Discuss the dependence of each of the curves making up the molding area in Fig. 13.6 on polymer parameters such as T_g , T_m , $m(T)$, n , k , $m(P)$, and $T_m(P)$, and thermal degradation. (b) Apply the preceding ideas to three polymers—PVC, nylon, and HDPE—whose properties appear in Appendix A.

13.7 The Assumption of Isothermal Cavity Filling As we have seen, good estimates of filling rates can be obtained by assuming that the cavity filling flow is isothermal. The success of this assumption is illustrated in Fig. 13.8 (a), where the predicted positions of the short shots are compared with the experimental ones.¹ In an attempt to investigate when the isothermicity assumption is good, Wu et al.² compared isothermal and nonisothermal calculated filling times for two molds (see figure). The material parameters for the PVC used in the simulations are shown on Fig. 13.10. (a) Discuss the results in terms of the “balance” between heat generated and heat lost during filling. (b) How do the isothermal and nonisothermal velocity profiles look and what physical conditions interrelate them? What can you conclude from this condition about the temperature field? (c) How would the results be for LDPE?



1. W. L. Krueger and Z. Tadmor, “Injection Molding into a Rectangular Cavity,” *Polym. Engin. Sci.*, **20**, 426–431 (1980).

2. P. C. Wu, C. F. Huang, and C. G. Gogos, “Simulation of the Mold Filling Process,” *Polym. Eng. Sci.*, **14**, 223 (1974).

- 13.8 Overall Flow-Pattern Simulation** (a) Develop a computer model to simulate, with the FAN³ method, the filling of a shallow mold, assuming constant gate pressure, isothermal flow, and incompressible Newtonian fluid. (b) Simulate the filling of the mold in Fig. 13.8, Case 1, identify the shape of the advancing front at various times, and the location and shape of the weld lines.
- 13.9 The Assumption of Constant Frozen-Skin Thickness** Barrie,⁴ considering the filling flow of large area articles, suggests that they be treated as isothermal flows between two plates not of the actual separation h , but $(h - 2\Delta x)$, where Δx is the frozen-skin thickness. The Δx is taken to be independent of the flow distance. Evidence supporting this assumption is brought from structural foam molding, where the solid skin thickness does not vary much. Empirical estimates of Δx indicate that $\Delta x \propto \tau^{1/3}$, where $\tau = Ah/Q$, A is the area covered during filling, and Q is the filling rate. On the other hand, from heat-transfer calculations, we find that $\Delta x \propto \tau^{1/2}$. Prove the second relationship.
- 13.10 Sandwich Injection Molding** In the ICI sandwich molding process, two injection machines are used to fill a mold. First, a melt fills a fraction of the mold from 10% to 20%, and immediately following, the second injection machine injects a melt with a foaming agent. It is observed that the first melt forms the surface area of the entire mold. Explain the flow mechanism—sketching it out at its various stages—that makes this process possible. (A similar process has been used to mold articles of “virgin” polymer skin and recycled core.⁵)
- 13.11 Squeezing Flow** A disk-shaped 5-cm-diameter and 1-cm-thick molten polymer preform with $m = 5 \times 10^4 \text{ N s}^n/\text{m}^2$, $n = 0.5$ at 200°C is placed between two plates. A 10 kg weight is placed on the upper plate. Calculate the preform thickness and diameter as a function of time.

3. E. Broyer, C. Gutfinger, and Z. Tadmor, “A Theoretical Model for the Cavity Filling Process in Injection Molding,” *Trans. Soc. Rheol.*, **19**, 423 (1975).

4. I. T. Barrie, *Soc. Plast. Eng. J.*, **27**, 64(1971); also, I. T. Barrie “An Application of Rheology to the Injection Molding of Large-Area Articles,” *Plast. Polym.*, 47–51 (1970).

5. G. Williams and H. A. Lord, “Mold Filling Studies for the Injection Molding of Thermoplastics,” *Polym. Eng. Sci.*, **15**, 553 (1975).

14 Stretch Shaping

- 14.1 Fiber Spinning, 824
- 14.2 Film Blowing, 836
- 14.3 Blow Molding, 841

In this chapter we discuss three common and important stretch or extensional flow-based shaping operations: *melt fiber spinning*, *tubular film blowing*, and *blow molding*. These operations take place downstream from the die. Another stretch-flow-type shaping method is thermoforming, which involves deformation of previously shaped polymer sheets or films into a desired shape. Since the principles of thermoforming are very similar to those of parison inflation discussed later in this chapter, we do not dwell on this shaping method.

Fiber spinning is a uniaxial extensional deformation process, which is the principal method of manufacturing synthetic fibers for the textile industry. It also provides a good example of the enormous significance of “structuring” polymeric chains during shaping for imparting unique properties to a product. In fact, fiber spinning is the quintessential example of the goal of modern polymer processing as a multidisciplinary activity, better termed “macromolecular engineering,” whose objective, as discussed in Chapter 1, is: “to bridge the gap between science and technology in material processing using modeling and computation of the full thermomechanical history during formation to quantitatively predict properties” (1).

Film blowing and blow molding are shaping operations that produce most plastics films, bags, and bottles, respectively. Both processes involve two-dimensional elongational deformation of the polymer melt. Thermoforming is a versatile, relatively inexpensive shaping method used extensively for packaging applications, which also involves two-dimensional extensional deformation. In all these processes, the purpose of a mathematical analysis is to describe the kinematics and dynamics of the process, to predict the nature and source of instabilities that are characteristic of these unconfined deformation processes, and, as just stated, hopefully predict a priori final properties based on the thermal and deformational history.

14.1 FIBER SPINNING

Until the 20th century mankind was limited to natural fibers such as wool, cotton, linen, and for the rich, silk. The first man-made fiber was artificial silk rayon (1910), which was based on cellulose. The big jump came with the invention of nylon by Wallace Carothers, with commercial production starting in 1939, followed in the 1950s by acrylics (which, when mixed with cotton, produced the “wash-and wear” textiles), polyesters, and many others.

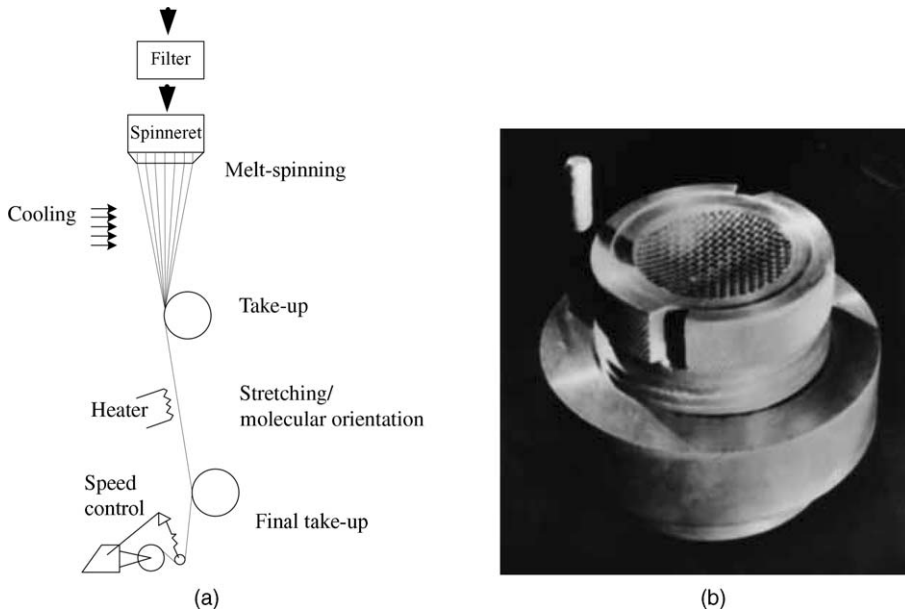


Fig. 14.1 (a) Schematic representation of the melt fiber spinning process. (b) Photograph of a spinneret. [Fiber-world Classroom Website.]

The melt spinning of fibers begins with the melting and pumping of solid pellets by a screw extruder (normally followed by a gear pump for accurate flow-rate control) into a die with multiple holes called a *spinneret*. The extruded strands are drawn and the solidified fibers are wound up and subsequently cold-drawn further, as shown schematically in Fig. 14.1(a). The design of a commercial spinneret is shown in Fig. 14.1(b). In addition to melt spinning, there are two other spinning methods: *wet spinning*, in which the polymer is dissolved in a solvent and extruded through a spinneret immersed in a chemical solution, and *dry spinning*, which also extrudes a solution of the polymer the solvent of which evaporates upon exiting the spinneret. These are used for polymers that cannot be melt-spun. However, in this chapter we discuss only the ubiquitous and most commercially important melt spinning.

In analyzing the melt spinning process, we consider a single strand as it emerges from the spinneret and is drawn by the take-up roll, as shown in Fig. 14.2. There is no clear point of demarcation where post-die extrudate swelling ends and melt stretching begins. The two phenomena occur simultaneously, especially near the die exit, where the rapid rate of swelling ordinarily occurs. Experimental data from actual melt-spinning runs indicate that the melt strand cross-sectional area decreases hyperbolically from the spinneret exit to the take-up rolls (2). Figure 14.3 gives typical melt strand area and radius axial profiles. The melt drawdown region extends to about 200 cm from the spinneret exit. There is no specific indication of where the melt strand begins to solidify (“frost line”).

The final properties of the fiber, such as tenacity,¹ modulus, luster, and flex loss, are determined by the spinning process. This is because, as the molten filament moves from

1. Tenacity equals the breaking strength (grams) divided by denier. Denier is the weight in grams of 9000 meters of filament.

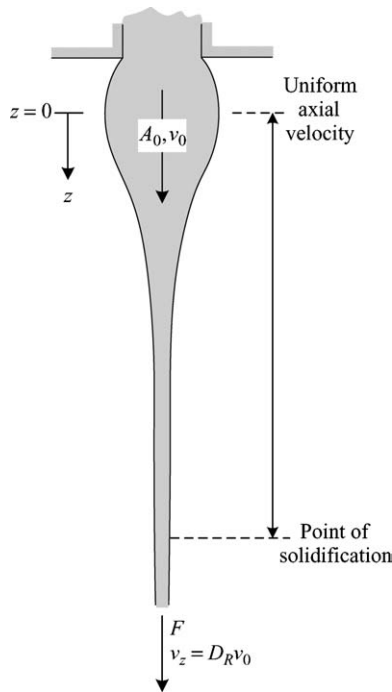


Fig. 14.2 A single strand emerging from the spinneret which undergoes die swell, then cooling to a point of solidification, drawn by the take-up roll.

the spinneret exit to the take-up roll, it is simultaneously stretched and cooled, thus orienting the polymer chains (Fig. 14.4) and crystallizing the polymer; this is repeated with the subsequent drawing and orientation in the solid state. Therefore, the spinning process is, in fact, not only a fiber forming step, but a “structuring” one as well. Early

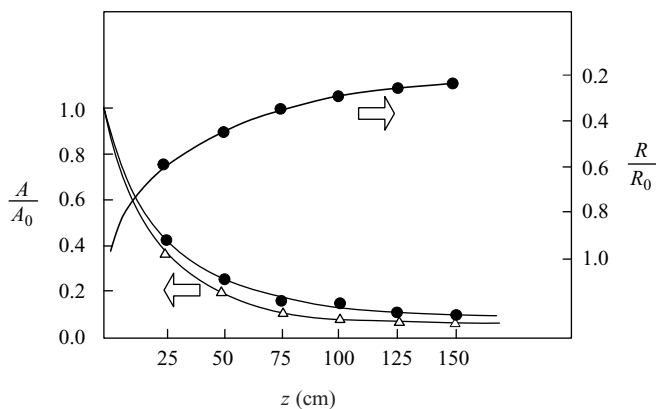


Fig. 14.3 Melt strand area and radius profiles in the melt drawdown region: ● nylon 6 at 265°C and take-up velocity of 300 m/min; △, polypropylene (PP) at 262°C and take-up velocity of 350 m/min. [Reprinted with permission from H. F. Mark, in *Rheology*, Vol. 4, F. R. Eirich, Ed., Academic Press, New York, 1969.]

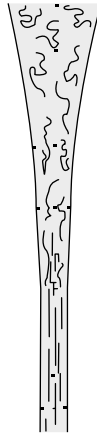


Fig. 14.4 Schematic view of orientation development along the spinline.

work on structuring during fiber spinning was done by Dees and Spruiell (3), who studied structure development with linear high density polyethylene fiber spinning and modeled it as shown in Fig. 14.5. They reported that the observed orientation function behavior during melt spinning can be explained with a morphological model, assuming that at low

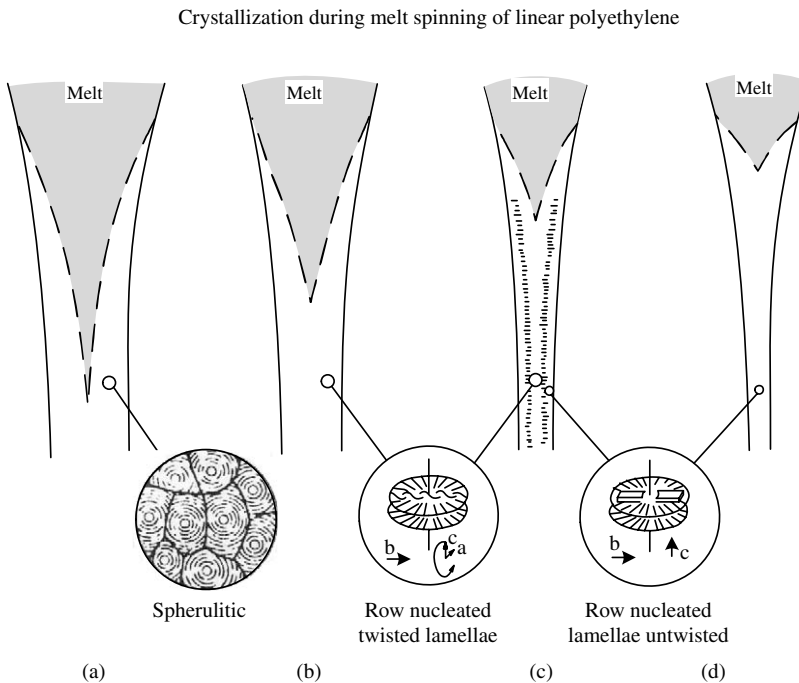


Fig. 14.5 Morphological model of structures developed in as-spun HDPE. Take-up velocities are (a) very low; (b) low; (c) medium; and (d) high. [Reprinted by permission from J. E. Spruiell and J. L. White, "Structure Development during Polymer Processing: Studies of the Melt Spinning of Polyethylene and Polypropylene Fibers," *Polym. Eng. Sci.*, **15**, 660 (1975).]

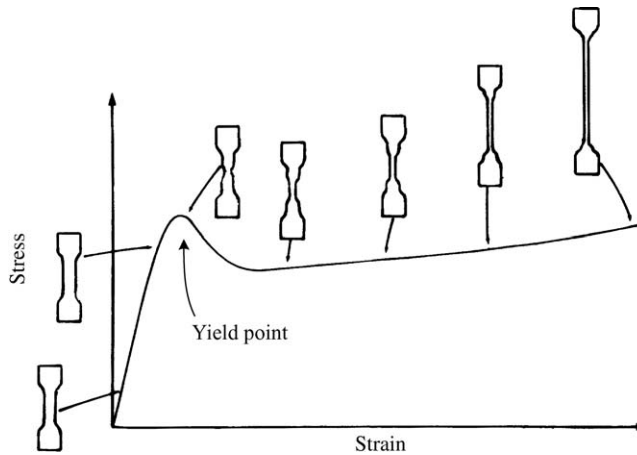


Fig. 14.6 Schematic stress–strain curves for a semicrystalline polymer. The shape of tensile specimens at several stages is indicated. [Reprinted by permission from J. M. Schultz, *Polymer Materials Science*, Prentice Hall, Englewood Cliffs, NJ, 1974.]

spinline stresses or take-up velocities, spherulitic structures are obtained. Increasing the take-up velocity results in row nucleated twisted lamellae, and at even higher speeds, in row nucleated untwisted lamellae.

As noted in Fig. 14.1(a), commercial fibers of semicrystalline polymers are always cold-drawn after spinning to achieve further structuring through further macromolecular orientation and crystalline morphological changes, many of which are retained because of the low temperature of the cold-drawing processes. A typical stress–strain curve for a polycrystalline polymer at a temperature $T_g < T < T_m$ appears in Fig. 14.6.

The onset of yielding and necking of fibers, as well as films and tensile bar specimens, is the result of the ability of polycrystalline “composites” to accommodate stress-induced destruction of the crystalline units. In this process both the amorphous and the crystalline phases are involved. A “molecular” descriptive model of the morphological changes initiated with necking, and propagated by cold drawing, indicated in Fig. 14.7, consists of the following steps:

1. The lamellae slip rigidly past one another. Lamellae parallel to the direction of draw cannot slip; thus, spherulites become anisotropic. At this stage, at which necking begins, the strain is accommodated almost entirely by the interlamellar amorphous component.
2. Since the amorphous “ties” are almost completely extended, slip-tilting of the lamellae is induced.
3. Lamellar breakup occurs through chain pulling and unfolding; the chains pulled still connect the fragments of the lamellae.
4. The lamellar fragments slip further in the direction of draw and become aligned. They now form fibrils of alternating crystal blocks and stretched amorphous regions, which may also contain free chain ends, and some chain folds. Thus, the lamellae break into fragments that end up stacked in the axial direction. Tie molecules that connect these fragments in the draw direction provide the strength of the microfibrils in the fiber. Thus the goal in a fiber structuring operation is to employ the values of the parameters of spinning and drawing processes, which increase the fraction of tie molecules.

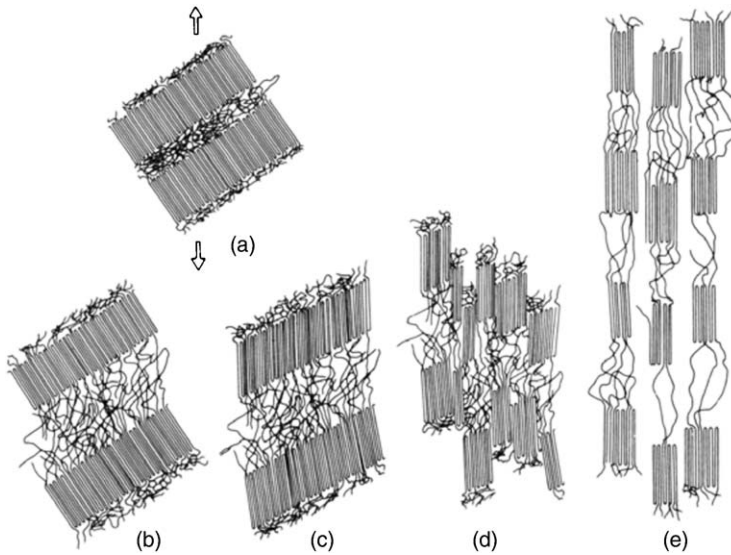


Fig. 14.7 Steps in the deformation of semicrystalline fiber, shown schematically. [Reprinted by permission from J. M. Schultz, *Polymer Materials Science*, Prentice Hall, Englewood Cliffs, NJ, 1974.]

It is evident from the preceding that the important cold drawing variables are not only the rate of extension, determining $t_{\text{exp}} = 1/\dot{\epsilon}$, and the temperature; determining the relaxation time, λ , but also the initial crystalline morphology, that is, the morphology obtained during the spinning process (see Fig. 14.5). Capaccio and Ward (4) demonstrated the important role played by the initial crystalline morphology in obtaining ultrahighly drawn and ultrahigh stiffness high density polyethylene (HDPE) fibers and films. A HDPE of $\bar{M}_n = 13,350$ and $\bar{M}_w = 67,800$, cooled from 160°C and quenched at 110°C , possessed an initial morphology such that, when drawn at 75°C at 10 cm/min , it can be extended to a draw ratio of 30. The cold-drawn sample had a specific Young's modulus in tension $E = 68 \times 10^9\text{ N/m}^2$, an order of magnitude higher than of conventionally drawn HDPE. For comparison, "E" glass fibers have a specific Young's modulus of $35\text{ (N/m}^2\text{)}$ and Kevlar fibers, $92\text{ (N/m}^2\text{)}$. It should be noted, however, that the theoretical estimates of Young's modulus for fully extended HDPE chains range from 240 N/m^2 to 350 N/m^2 (4). Thus, further structuring improvements are possible, in principle.

The mathematical formulation of the fiber-spinning process is meant to simulate and predict the hydrodynamics of the process and the relationship between spinning conditions and fiber structure. It involves rapid extensional deformation, heat transfer to the surrounding quenching environment, air drag on the filament surface, crystallization under rapid axial-orientation, and nonisothermal conditions.

Example 14.1 A Semiempirical, Simplified, One-Dimensional, Nonisothermal Model [C. D. Han, *Rheology in Polymer Processing*, Academic Press, New York, 1976, Section 12.3.1.] Assuming steady state and further assuming that there is only one nonvanishing velocity component $v(z)$, which is a function of only z , and that temperature varies only in the z direction, the equation of motion reduces to

$$v_z \frac{dv_z}{dz} = -v_z \frac{d}{dz} \left(\frac{\tau_{zz}}{\rho v_z} \right) - 2 \left(\frac{\pi v_z}{\rho G} \right) F_D + g_z \quad (\text{E14.1-1})$$

where $G = \rho\pi R^2 v_z$ is the mass flow rate and F_D is the air drag force per unit area given by:

$$F_D = \left(\frac{0.843}{\pi R^2}\right) \left(\frac{\rho_a}{\rho}\right) G v_z \left[\frac{\pi \rho \mu_a (L-z)}{\rho_a G}\right]^{0.915} \quad (\text{E14.1-2})$$

indicating that extension rate is controlled by tensile stresses, air drag on the fiber, and gravitational forces. Similarly, the equation of energy reduces to

$$\frac{dT}{dz} = -\frac{2}{C_v} \left(\frac{\pi}{\rho G v_z}\right)^{1/2} [h(T - T_a) + \sigma \varepsilon (T^4 - T_a^4)] \quad (\text{E14.1-3})$$

In this equation, h is the heat transfer coefficient given by

$$\frac{hR}{k_a} = 0.21(1 + K) \left(\frac{2R\rho_a v_z}{\mu_a}\right)^{0.334} \quad (\text{E14.1-4})$$

where K is an adjustable parameter and the subscript a refers to ambient air. According to Eq. E14.1-3 the temperature drop of the fiber depends on heat transfer to the ambient air and radiation losses. Han coupled these transport equations with an empirical ‘‘Power Law in tension’’ constitutive equation containing a temperature-dependent viscosity

$$\tau_{zz} = -3\alpha e^{\beta/T} \left[k_1 + k_2 \left(\frac{dv_z}{dz}\right)^{n-1} \right] \frac{dv_z}{dz} \quad (\text{E14.1-5})$$

where

$$\alpha = \eta_0 e^{\Delta E/RT_0} = \eta_0 e^{-\beta/T_0} \quad (\text{E14.1-6})$$

This system of equations is solved numerically. The results obtained are physically reasonable up to the axial position where crystallization commences, where the rate of cooling slows down because of the exothermic solidification phenomenon and the rheological properties change sharply.

Many of the early models were one-dimensional, in which the field equations were averaged over the filament cross section. Kase and Matsuo (5,6) were the first to consider nonisothermal (in the stretching direction) fiber stretching. Matovich and Pearson (7) studied Newtonian, shear thinning and second order fluids. Denn et al. (8,9) modeled the process with upper-convected Maxwell constitutive equation. Papanastasiou et al. (10) studied isothermal viscoelastic spinning. Bell and Edie (11), using a finite element method (FEM), computed the two-dimensional temperature profile, assuming a one-dimensional velocity profile and measures of orientation, to obtain the internal stress distribution (12). The single component models were extended by Kulkarni and Beris (13) and Doufas et al. (14) to two component models, accounting for stress-induced crystallization.

A detailed two-dimensional numerical analysis of nonisothermal spinning of viscoelastic liquid with phase transition was carried out recently by Joo et al. (15). They used a mixed FEM developed for viscoelastic flows (16) with a nonisothermal version of the Giesekus constitutive equation (17), the Nakamura et al. (18) crystallization kinetics

model, and the dependence of the crystallization rate on temperature and molecular orientation according to Ziabicki (19). They simulated amorphous polystyrene and fast-crystallizing nylon-6.6. The results indicate that although the kinematics in the thread line are approximately one-dimensional, as assumed by most researchers, the significant radial temperature nonuniformity leads to radially nonuniform viscoelastic stresses, which result in radially nonuniform molecular orientation and strong radial variation of crystallinity.

The polystyrene simulation followed the experiments of Bell and Edie (12) with good agreement. Figure 14.8 shows the simulation results for fiber spinning nylon-6.6 with a draw ratio of 40. The figure demonstrates the wealth of information provided by the model. It shows the velocity, temperature, axial normal stress, and crystallinity fields along the threadline. We see the characteristic exponential-like drop in diameter with locally (radially) constant but accelerating velocity. However, results map out the temperature, stress, and crystallinity fields, which show marked variation radially and axially.

Recent advances in molecular dynamics simulations enabled Levine et al. (20) to take modeling one step further, to the molecular level. They succeeded in simulating from first principles the structure formation of 100 carbon atom polyethylene during uniaxial extension, under a variety of conditions. Figure 14.9 shows the dynamics of extensional deformation below the melting point, beautifully indicating the dynamic development of orientation and order.

Figure 14.10 shows the simulation results of nonisothermal crystallization, during simultaneous deformation and cooling through the melting point, as is the case in fiber spinning, indicating the formation of homogeneous, deformation-induced crystallization nuclei.

The foregoing analyses show, as pointed out earlier, that fiber spinning is perhaps the first process approaching the goal of modern polymer processing as macromolecular engineering. That is, developing a multiscale approach to simulate manufacturing processes using the governing continuum-level equations and operating conditions. Material-specific parameters for those equations are generated from molecular dynamics simulations, to ensure consistent, predictive ability. Crystal growth rates are generated using parameters derived entirely from first principles molecular modeling, over a large range of temperatures and molecular weight. This is shown schematically in Fig. 14.11.

So far, we assumed that the spinning process is stable. In practice, however, spinning instabilities may constrain spinning rates and even curb the possibility of spinning a fiber. Indeed, not all polymers can be melt-spun. Some polymers are easier to spin than others. The *spinnability* of a polymer is related to the stability of the process (21,22), particularly the ability of polymer melts to be drawn without breaking, due to either capillary failure resulting from surface tension-induced breakup into droplets, “necking” and ductile failure (23) characteristic to extension-thinning polymers, and/or cohesive fracture (24,25) exhibited by extension-thickening polymers.

A typical instability is *draw resonance*. Physically, the occurrence of draw resonance can be viewed as follows. In the region between the spinneret exit and the take-up rolls there can be a time variation of the total extrudate mass: although the rate of mass entering this region is constant, the rate it leaves is not controlled, since only the take-up speed is regulated, not the fiber diameter. Thus, if the strand thins out near the take-up rolls, the diameter of the strand above it will increase, creating (from the spinneret exit) a thick–thin strand. But the thick portion soon reaches the take-up rolls. Mass leaves the region at a high rate and the strands thin out upstream, creating a thin–thick strand. The process can repeat itself. This may explain the experimental reports that if solidification occurs before

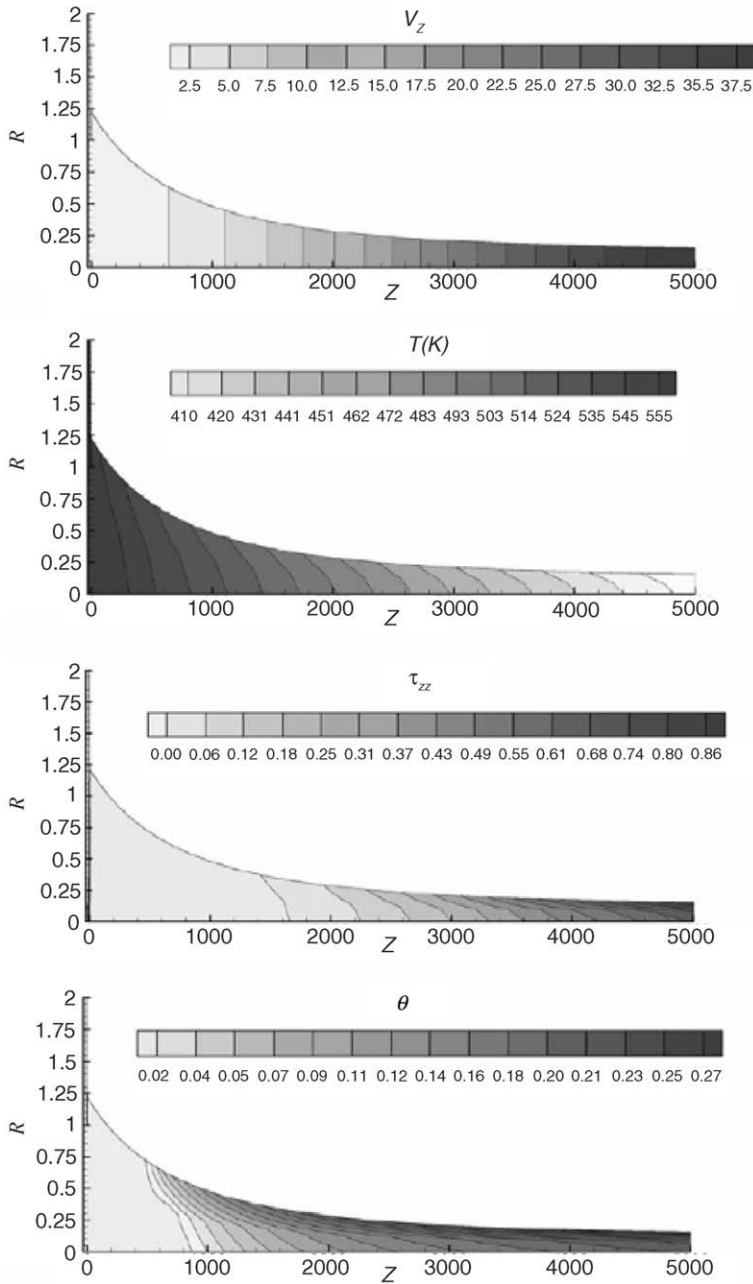


Fig. 14.8 Simulation results for velocity, temperature, axial normal stress, and crystallinity fields for low-speed spinning of nylon-6.6. [Reprinted with permission from Joo et al., “Two-dimensional Numerical Analysis of Nonisothermal Melt Spinning with and without Phase Transition,” *J. Non-Newton. Fluid Mech.*, **102**, 37–70 (2002).]

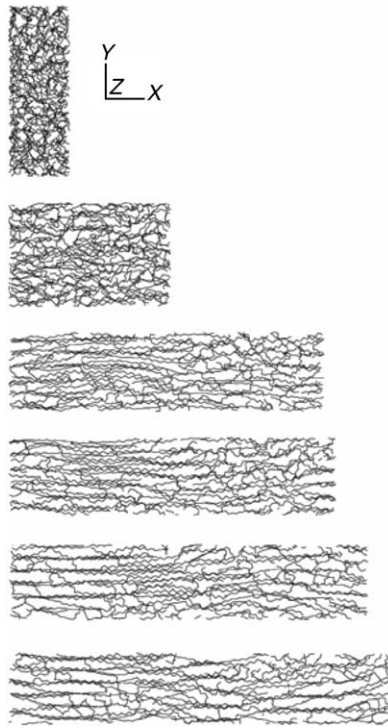


Fig. 14.9 Snapshots of a system of twenty 100 carbon atom long polyethylene chains deformed at 300 K. The initial slab at the top rapidly deforms with the applied stress in the x dimension of the slab, roughly doubling in the first 500 ps to $\lambda = 2.64$ (second image from the top); then the rate of deformation is slower and doubles again in 1500 ps to $\lambda = 5.15$ (third image from the top). Beyond this point the cell deforms even more slowly to reach a final deformation of $\lambda = 6.28$ (bottom image). In absolute values, the initial cell of dimensions $1.88 \times 5.32 \times 5.32$ nm deforms to $11.8 \times 2.23 \times 1.96$ nm. [Reprinted by permission from M. C. Levine, N. Waheed, and G. C. Rutledge, "Molecular Dynamics Simulation of Orientation and Crystallization of Polyethylene during Uniaxial Extension," *Polymer*, **44**, 1771–1779, (2003).]

the take-up rolls, no resonance is observed (26), as well as the observation of increased resonance period with increased residence time in the spinline (21).

Isothermal draw resonance is found to be independent of the flow rate. It occurs at a critical value of draw ratio (i.e., the ratio of the strand speed at the take-up rolls to that at the spinneret exit). For fluids that are almost Newtonian, such as polyethylene terephthalate (PET) and polysiloxane, the critical draw ratio is about 20. For polymer melts such as HDPE, polyethylene low density (LDPE), polystyrene (PS), and PP, which are all both shear thinning and viscoelastic, the critical draw ratio value can be as low as 3 (27). The maximum-to-minimum diameter ratio decreases with decreasing draw ratio and decreasing draw-down length.

The experimental and theoretical literature on instabilities in fiber spinning has been reviewed in detail by Jung and Hyun (28). The theoretical analysis began with the work of Pearson et al. (29–32), who examined the behavior of inelastic fluids under a variety of conditions using linear stability analysis for the governing equations. For Newtonian fluids, they found a critical draw ratio of 20.2. Shear thinning and shear thickening fluids

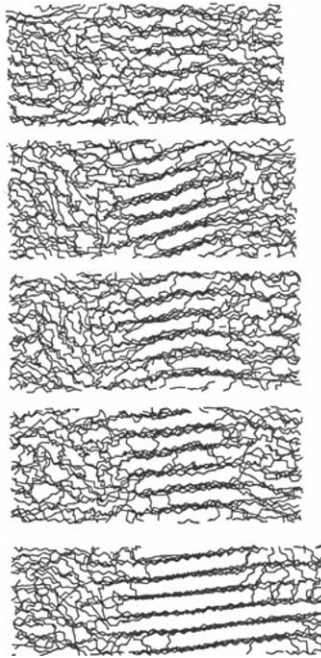


Fig. 14.10 Chain configurations from a nonisothermal deformation simulation. From top to bottom, the images were taken at 374, 368, 364, 360 K, and 290 K, corresponding to 7.6, 8.2, 8.6, 9.0, and 16.0 ns. [Reprinted by permission from M. C. Levine, N. Waheed, and G. C. Rutledge, “Molecular Dynamics Simulation of Orientation and Crystallization of Polyethylene during Uniaxial Extension,” *Polymer*, **44**, 1771–1779, (2003).]

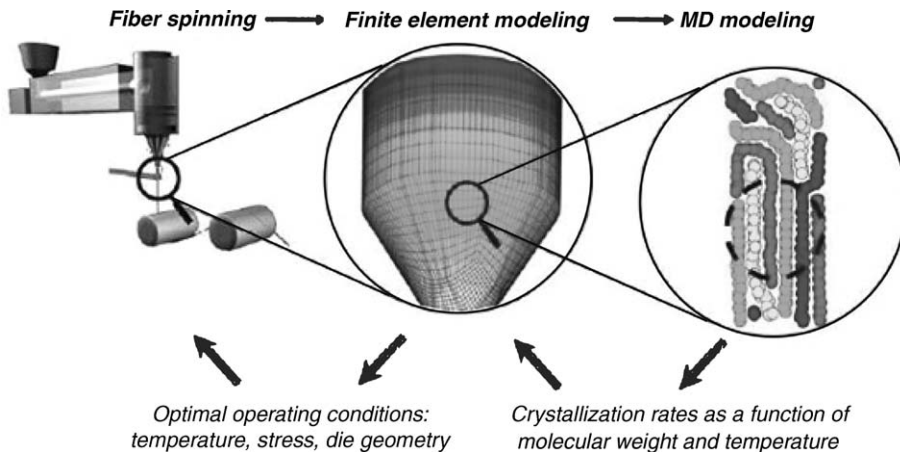


Fig. 14.11 Schematic representation of fiber spinning process simulation scheme showing the multiple scale simulation analysis down to the molecular level. This is the goal of the Clemson University–MIT NSF Engineering Research Center for Advanced Engineering Fibers and Films (CAEFF) collaboration. CAEFF researchers are addressing fiber and film forming and structuring by creating a multiscale model that can be used to predict optimal combinations of materials and manufacturing conditions, for these and other processes.

exhibit critical draw ratios that are smaller or larger, respectively, than 20.2. At the same time, Denn et al. (8,33–36) systematically carried out both infinitesimal (linearized) and finite amplitude analyses of the isothermal draw resonance problem. They found that Newtonian fluids are stable to finite amplitude disturbances for draw ratios of less than 20.2. Linearized stability analysis revealed that for fluids that obey a White–Metzner-type constitutive equation, the critical draw ratio depends on the Power Law index n and the viscoelastic dimensionless number N

$$N = 3^{(1-s/2)} \left(\frac{m}{G}\right)^s \left(\frac{V_0}{L}\right) \quad (14.1-1)$$

where $s = 1/n$, L is the spinline length, G is the tensile modulus, and V_0 is the spinneret velocity. The results appear in Fig. 14.12. Of interest is the “nose” region of the curves, which indicates that one could eliminate the draw resonance phenomenon by an *increase* in the draw ratio. Also of interest is the work of Han (37), who finds experimentally that as the temperature level is decreased in isothermal spinning, draw resonance occurs at lower draw ratios. This seems reasonable from the figure. In the “nose” region, decreasing the temperature increases G and decreases m , which in turn decreases N , bringing about lower draw ratio values.

White et al. (38,39) presented experimental and theoretical (isothermal linear stability analysis) results that indicate the following: first, that polymer melts respond similarly to uniform elongational flow and to melt spinning; second, that polymers whose elongational viscosity $\bar{\eta}^+(t, \dot{\epsilon})$ increases with time or strain result in a stable spinline, do not exhibit draw resonance, and undergo cohesive failure at high draw ratios. A prime example of such behavior is LDPE. On the other hand, polymer melts with a decreasing $\bar{\eta}^+(t, \dot{\epsilon})$

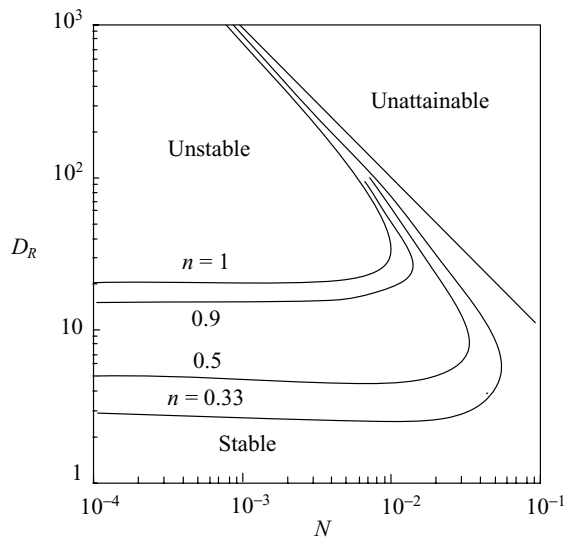


Fig. 14.12 Results of the linearized stability analysis for a White–Metzner-type fluid, indicating the dependence of the critical draw ratio on n and N . [Reprinted by permission from R. J. Fisher and M. M. Denn, “A Theory of Isothermal Melt Spinning and Draw Resonance,” *AIChE J.*, **22**, 236 (1976).]

exhibit draw resonance at low draw ratios and break in a ductile fashion (after “necking”) at high draw ratios. Typical polymers in this category are HDPE and PP.

The preceding analyses were based on steady state solution of the governing equations, and examining the response of the system to applied sinusoidal perturbations. However, for the study of the *dynamics* of the instability, and for tracing the physical sources of instability, transient time-dependent solutions are needed. Hyun et al. (40,41) developed such solutions by tracing and analyzing kinematic traveling waves on the spinline from the spinneret to the take-up. Their simulation shows good agreement with the experiments (28).

14.2 FILM BLOWING

Most films and bags, in sizes varying from a sandwich bag to large films covering building sites, are made by the ingenious and deceptively simple process of film blowing. This process is shown schematically in Fig. 14.13(a), and a photograph of the process is shown in Fig. 14.13(b). A relatively small diameter tubular film is extruded upwards; upon exit it is blown up, with air introduced below the die, into a larger tubular film and then picked up by a pair of nip rolls that seal the bubble. An external stream of chilled air cools and solidifies the film at a certain upstream location called the *freeze line*, where $T_f = T_m$. In this process the film is stretched biaxially, thereby improving its mechanical properties. The blow up ratio, R_f/R_0 , determined by the pressure level within the bubble, sets the (tangential) circumferential stretching, and the speed of take-up by the nip rolls sets the axial stretching.

The film thickness produced by film blowing ranges from $10\ \mu\text{m}$ to $100\ \mu\text{m}$ and the rates of production are very high. The most common plastic films produced by this method are branched LDPE, linear low density polyethylene (LLDPE), and linear HDPE films. By using more than one extruder, multilayer films can also be manufactured. To appreciate the

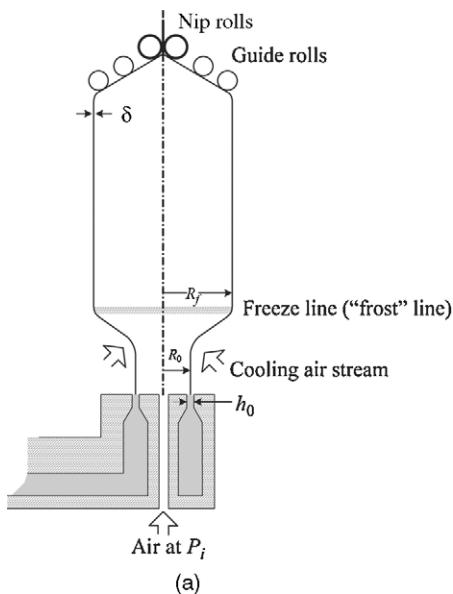


Fig. 14.13 (a) Schematic representation of the tubular blown film forming operation. (b) Photograph of a coextruded blown film die followed by blown film with external and internal cooling. [Courtesy of Windmoeller & Hoelscher (Lincoln RI).]

elegant engineering simplicity of this process, we have to compare it to the more complicated and expensive die forming flat film process, where the melt is extruded through a slit die onto chilled take-up rolls. The latter process, while more expensive, has the advantage of producing optically clear films, because of the profuse nucleation induced by the quenching abilities of the chilled rolls. Yet, as the mathematical analysis discussed below demonstrates, the film blowing process is not simple at all, particularly when we consider the multiplicity of steady states and bubble instabilities that may arise which, in addition to cooling rates, place upper limits on production rates.

The first milestone in modeling the process is credited to Pearson and Petrie (42–44), who laid the mathematical foundation of the thin-film, steady-state, isothermal Newtonian analysis presented below. Petrie (45) simulated the process using either a Newtonian fluid model or an elastic solid model; in the Newtonian case, he inserted the temperature profile obtained experimentally by Ast (46), who was the first to deal with nonisothermal effects and solve the energy equation to account for the temperature-dependent viscosity. Petrie (47) and Pearson (48) provide reviews of these early stages of mathematical foundation for the analysis of film blowing.

Han and Park (49–51) used a coupled force and thermal energy balances to take care of the nonisothermal nature of the process and accounted for the non-Newtonian nature of the viscosity. Gupta (52) presented experimental results that were used by several investigators. Kanai and White (53,54) carried out detailed experimentation as well as theoretical analysis of both the kinematics and the dynamics of the process and the effect of the cooling rate on crystallization. Heat transfer and bubble cooling were studied by Sidiropoulos and Vlachopoulos (55–58), who used numerical simulation to study air flow around the bubble, investigated the effect of internal bubble cooling, and studied the temperature gradient in the blown film. Finally, Campbell et al. (59) carried out a full aerodynamic analysis of the cooling air around the bubble.

The early attempts to account for the viscoelastic nature of the fluid encountered mathematical difficulties in the numerical solutions. Yet later, Luo and Tanner (60) expanded the Petrie model to viscoelastic nonisothermal flow using the convected Maxwell and Leonov (61) models, and compared results to experiments done by Gupta (52). Cain and Denn (62) carried out a detailed analysis of both Newtonian and viscoelastic fluids. For the latter, they used the upper convected Maxwell model and the Marrucci (63) model. They found that multiple solutions of the governing equations are possible even for the Newtonian fluid, with the existence of more than one steady state bubble profile for a given set of operating conditions. Furthermore, they found several types of instabilities. A recent, detailed review of film blowing instabilities is given by Jung and Hyun (28).

Following the principles of the Petrie model, and recalling that the film thickness δ is much smaller than the radius $\delta/R \ll 1$, we invoke the “thin-film approximation,” which implies that field equations are averaged over the thickness and that there are no shear stresses and moments in the film. The film is regarded, in fact, as a thin shell in tension, which is supported by the longitudinal force F_z in the bubble and by the pressure difference between the inner and outer surfaces, ΔP . We further assume steady state, a clearly defined sharp freeze line above which no more deformation takes place and an axisymmetric bubble. Bubble properties can therefore be expressed in terms of a single independent spatial variable, the (upward) axial position from the die exit,² z . The object

2. To be exact, the origin of variable z is located not at the die exit, but just past the die-exit swell region (21).

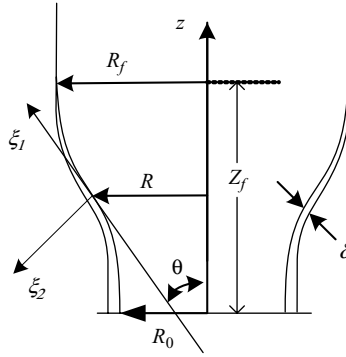


Fig. 14.14 The melt exits the die at $z = 0$; the radius of the bubble R and the thickness δ are a function of z . The coordinate system ξ_i is embedded into the inner surface of the bubble.

of the analysis is to predict the dependent variables, including the bubble radius, film thickness, film temperature (in the nonisothermal case), and local values of stresses as a function of the axial distance, z .

We first derive the kinematics of the deformation. The flow situation is shown in Fig. 14.14. Coordinate z is the vertical distance in the center of the axisymmetric bubble with the film emerging from the die at $z = 0$. The radius of the bubble R and its thickness δ are a function of z . We chose a coordinate system ξ_i embedded in the inner surface of the bubble. We discussed extensional flows in Section 3.1 where we defined the velocity field of extensional flows as

$$v_i = a_i \xi_i \tag{14.2-1}$$

In this case, as pointed out earlier, the extension is planar, but unequal in directions ξ_1 and ξ_3 . In order to derive the rate of deformation tensor components, we need to define the flow field in terms of the dependent variables δ and R . We note that in direction “2” at $\xi_2 = \delta$, we can write

$$v_2 = a_2 \delta = \frac{d\delta}{dt} \tag{14.2-2}$$

Writing a_2 in terms of δ , from the kinematics of extensional flow, we have

$$\dot{\gamma}_{22} = 2a_2 = \frac{2}{\delta} \frac{d\delta}{dt} \tag{14.2-3}$$

We can rewrite Eq. 14.2-3 as follows

$$\dot{\gamma}_{22} = 2a_2 = \frac{2}{\delta} \frac{d\delta}{d\xi_1} \frac{d\xi_1}{dt} \tag{14.2-4}$$

where

$$\frac{d\xi_1}{dt} = v_1 \tag{14.2-5}$$

And from geometrical considerations, we find that

$$\frac{d\delta}{d\xi_1} = \frac{d\delta}{dz} \frac{dz}{d\xi_1} = \cos\theta \frac{d\delta}{dz} \quad (14.2-6)$$

Substituting Eqs. 14.2-6 and 14.2-5 into Eq. 14.2-4, we get

$$\dot{\gamma}_{22} = \frac{2}{\delta} v_1 \cos\theta \frac{d\delta}{dz} \quad (14.2-7)$$

The volumetric flow rate Q is given by

$$Q = 2\pi R \delta v_1 \quad (14.2-8)$$

Substituting it into Eq. 14.2-7, we obtain

$$\dot{\gamma}_{22} = \left(\frac{Q \cos\theta}{\pi R \delta} \right) \frac{1}{\delta} \frac{d\delta}{dz} \quad (14.2-9)$$

The film circumference at any given z where the bubble radius is R , is $l = 2\pi R$, and the velocity v_3 is given by

$$v_3 = \frac{dl}{dt} = 2\pi \frac{dR}{dt} = 2\pi \frac{dR}{d\xi_1} \frac{d\xi_1}{dt} \quad (14.2-10)$$

Substituting Eq. 14.2-5 into Eq. 14.2-10 and recalling that $dz/d\xi_1 = \cos\theta$, we get

$$v_3 = 2\pi v_1 \cos\theta \frac{dR}{dz} \quad (14.2-11)$$

Next we substitute Eq. 14.2-8 into Eq. 14.2-11 and with Eq. 14.2-1, get

$$v_3 = \frac{Q \cos\theta}{\delta} \frac{1}{R} \frac{dR}{dz} = 2\pi R a_3 \quad (14.2-12)$$

Recalling that $\dot{\gamma}_{33} = 2a_3$, we obtain

$$\dot{\gamma}_{33} = \left(\frac{Q \cos\theta}{\pi R \delta} \right) \frac{1}{R} \frac{dR}{dz} \quad (14.2-13)$$

Finally, we obtain the third component of the rate of deformation tensor $\dot{\gamma}_{11}$ from the equation of continuity $\Sigma a_i = 0$ or $\Sigma \dot{\gamma}_{ii} = 0$ to give

$$\dot{\gamma}_{11} = - \frac{Q \cos\theta}{\pi R \delta} \left(\frac{1}{\delta} \frac{d\delta}{dz} + \frac{1}{R} \frac{dR}{dz} \right) \quad (14.2-14)$$

Having the components of the rate of deformation tensor, we can turn to the components of the stress tensor assuming a Newtonian fluid

$$\boldsymbol{\pi} = P\boldsymbol{\delta} - \mu\dot{\boldsymbol{\gamma}} \quad (14.2-15)$$

Setting $\pi_{22} = 0$ because no external forces act in this direction, we can extract P from the previous equation after substituting Eq. 14.2-9, to obtain

$$P = \frac{\mu Q \cos \theta}{\pi R \delta^2} \frac{d\theta}{dz} \quad (14.2-16)$$

From the foregoing, the two other normal stress components can be evaluated

$$\pi_{11} = \frac{Q\mu \cos \theta}{\pi R \delta} \left(\frac{2}{\delta} \frac{d\theta}{dz} + \frac{1}{R} \frac{dR}{dz} \right) \quad (14.2-17)$$

$$\pi_{33} = \frac{Q\mu \cos \theta}{\pi R \delta} \left(\frac{1}{\delta} \frac{d\theta}{dz} - \frac{1}{R} \frac{dR}{dz} \right) \quad (14.2-18)$$

To solve for $\delta(z)$ and $R(z)$, one needs to state the force balance equations for the blown film. The simplest form of these equations, disregarding inertial and gravity forces, are the classic thin-film equations. The forces per unit length in the film in the ζ_1 and ζ_3 directions are $F_L/2\pi R = \delta\pi_{11}$ and $F_H/\zeta_1 = \delta\pi_{33}$, respectively; thus from the thin film equation, we get

$$\Delta P = -\delta \left(\frac{\pi_{11}}{R_L} + \frac{\pi_{33}}{R_C} \right) \quad (14.2-19)$$

where $R_C = R\sqrt{1 + \dot{R}^2} = R/\cos \theta$ and $R_L = -(1 + \dot{R}^2)^{3/2}/\ddot{R} = -\sec^3 \theta/\ddot{R}$ are the radii of curvature with $\dot{R} = dR/dz$ and $\ddot{R} = d\dot{R}/dz$. Next we make a force balance in the z direction on a portion of the bubble bound by two planes, one at z and the other at the freeze line $z = Z_f$, where the radius is R_f , and the force F_z , acting in the axial direction on the bubble for $z \geq Z_f$, is

$$F_z = -(2\pi R \cos \theta)\delta\pi_{11} + \pi\Delta P(R_f^2 - R^2) \quad (14.2-20)$$

By substituting Eq. 14.2-17 and 14.2-18 into Eqs. 14.2-19 and 14.2-21, we obtain two differential equations, one for the radius and the other for the thickness. In terms of the dimensionless parameters $r = R/R_0$, $w = \delta/R$, and $\zeta = z/R_0$

$$2r^2(A + r^2B)\ddot{r} = 6\dot{r} + r(1 + \dot{r}^2)(A - 3r^2B) \quad (14.2-21)$$

where $\dot{r} = dr/d\zeta$ and $\ddot{r} = d\dot{r}/d\zeta$, and is subject to boundary conditions $r(0) = 1$ and $\dot{r}(\zeta_f) = 0$, and

$$\dot{w} = -w \left[\frac{\dot{r}}{2r} + \frac{(1 + \dot{r}^2)(A + r^2B)}{4} \right] \quad (14.2-22)$$

where $\dot{w} = dw/d\zeta$, and dimensionless groups A and B are

$$A = \frac{R_0 F_z}{\mu Q} - B \left(\frac{R_f}{R_0} \right)^2 \quad (14.2-23)$$

$$B = \frac{\pi R_0^3 \Delta P}{\mu Q} \quad (14.2-24)$$

subject to boundary conditions $w(0) = \delta_0/R_0$.

Note that in order to solve these equations, the position of the freeze line Z_f and the value δ_0 at the die exit (post-die exit swelling) must be known. Neither quantity can be specified a priori. Cain and Denn (62) discuss the numerical solution of these equations for various rheological models. The two differential equations are decoupled, and after solving Eq. 14.2-22 for the radius profile, which most investigators solve by using a fourth-order Runge-Kutta method, the results can be inserted into Eq. 14.2-22 to obtain the thickness profile. In the former, a final bubble radius at the freeze line is assumed and the initial bubble radius at the origin is computed. Then the freeze-line radius is adjusted until the desired initial radius is achieved. Cain and Denn simulations, using the rich experimental data collected by Gupta (52), show a complex, multiple, steady state behavior even for the Newtonian isothermal model. Han and Park (50) carried out LDPE film blowing experiments and, using a modified model described earlier with a Power Law-type temperature-dependent viscosity and heat transfer calculation, showed good agreement between simulation and experiments (64).

Bubble instability is one of the complications of this process. Only recently did this matter receive theoretical attention. As pointed out by Jung and Hyun (28), there are three characteristic bubble instabilities: axisymmetric draw resonance, helical instability, and metastability where the bubble alternates between steady states, and the freeze line moves from one position to another. Using linear stability analysis, Cain and Denn (62) showed that multiple steady state solutions are possible for the same set of conditions, as pointed out earlier. However, in order to study the dynamic or time-dependent changes of the process, transient solutions are needed. This was recently achieved by Hyun et al. (65), who succeeded in quite accurately simulating the experimentally observed draw resonance (28).

14.3 BLOW MOLDING

Blow molding is a very important polymer processing method, borrowed from the glass industry, for manufacturing hollow articles such as small bottles for household products and personal care, dairy products and beverages, containers for industrial goods or chemicals, fuel tanks, drums, car dashboards, and so on (66–68). There are three basic types of blow molding processes: *extrusion*, *injection*, and *stretch blow molding*. Classic extrusion blow molding involves first the forming of a molten tube, called the *parison*. The parison is engaged between two mold halves and, upon their closing, is inflated like a balloon by compressed air, to conform to the interior shape of the chilled mold, as shown in Fig. 14.15. The polymer quickly solidifies upon contact with the cold mold, and the finished hollow article is ejected.

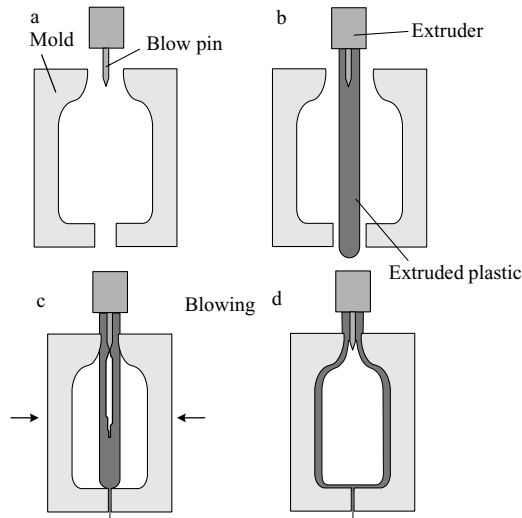


Fig. 14.15 Schematic representation of the blow molding process. (a) The extruder head with the blowing pin and open mold; (b) the extrusion of the parison; (c) the mold closed with the parison pinched in the bottom and sealed at the top; (d) the inflated parison forming a bottle.

The *extrusion blow molding* process can be continuous or intermittent, as shown in Fig. 14.16. The former, employed commonly for parts less than 1 gal, has a continuously rotating screw extruder, extruding parisons through one or more dies. The latter may use either an accumulator head with a piston-driven extrusion forming of the parison, or a reciprocating screw, such as the one used in injection molding.

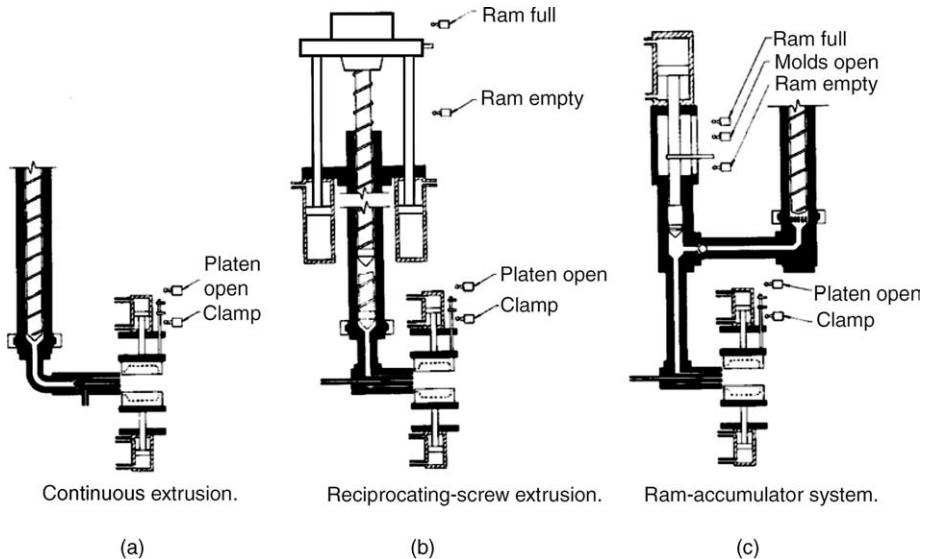


Fig. 14.16 Schematic view of (a) continuous extrusion blow molding; (b) reciprocating screw blow molding; and (c) ram-accumulator blow molding. [Reprinted by permission from *Modern Plastics Encyclopedia*, McGraw-Hill, New York, 1976–1977.]

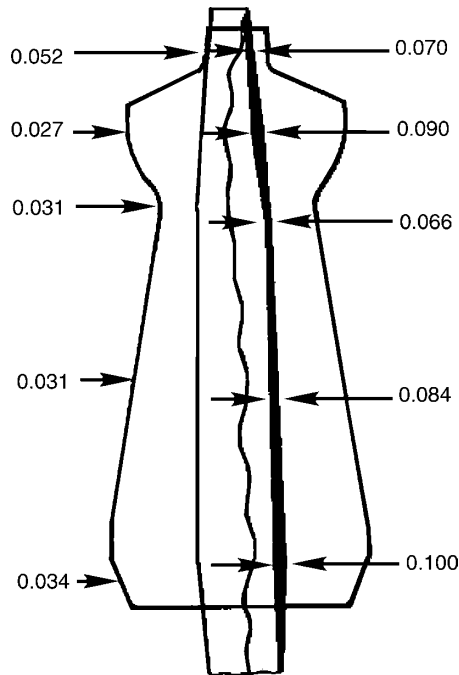


Fig. 14.17 Example of a parison thickness variation by parison “programming.” [Reprinted by permission from *Modern Plastics Encyclopedia*, Vol. 53, McGraw-Hill, New York, 1976–1977.]

The intermittent-parison production methods are more suited to the nature of the blow molding process; greater flexibility and control are possible in the forming itself, which is the heart of the process. The inflation step is fast, and little flexibility is allowed in the control of the “bubble” thickness. Thus, by controlling the rate of extrusion during parison forming (which results in different degrees of swelling of the extrudate), the thickness of the parison can be programmed to result in a product of more-or-less uniform thickness. Figure 14.17 shows a parison of programmed thickness. The same result can be obtained by varying the annular die gap and extruding the polymer at a constant rate. Parison forming is very sensitive to both shear and extensional rheological properties, hence to temperature.

It is possible to blow mold several layers of material by coextrusion blow molding processes. By appropriate material selection, the various parts of the structure can be optimized for the best balance between properties and cost.

In the *injection blow molding* process, the parison is formed by injection molding of the preshaped parison onto a steel rod, as shown in Fig. 14.18. The rod with the molded thread already completed is moved to the blowing station, where the article is inflated free of scrap. The parison thickness distribution is determined in the injection mold without the need of further control. Some axial orientation is introduced during injection, resulting in an article with partial biaxial orientation.

A process that greatly improves blow molded product properties is that of *injection stretch blow molding*, which introduces biaxial orientation in crystallizable polymers. There are two variants of this process involving the molding of a preform as the first step. The thermomechanical paths of the two process variants are shown in Fig. 14.19. In the

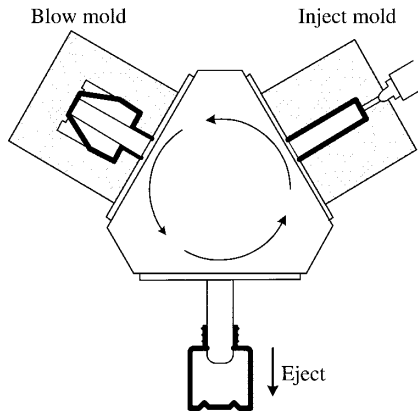


Fig. 14.18 Schematic of the three-position injection blow-molding rotary machine. The third position is easily accessible for removing the blow-molded article. [Reprinted by permission from *Modern Plastics Encyclopedia*, Vol. 53, McGraw-Hill, New York, 1976–1977.]

two-step process, the preform is molded, cooled and transported to the stretch blow molding station, where it is *reheated* (thermally conditioned) to a temperature, T_s , above T_g , but well below T_m , and stretched with an axially moving rod, while simultaneously being blown in a mold. In the one-step process the preform is *cooled* to the stretching temperature T_s , and then is stretched and blown in the same molding station to conform in shape with the mold. Although thermally efficient, the one-step process is not process efficient, since it ties up the equipment during the parison cooling time period, which cannot be very small, since a preformwide uniform temperature must be attained before

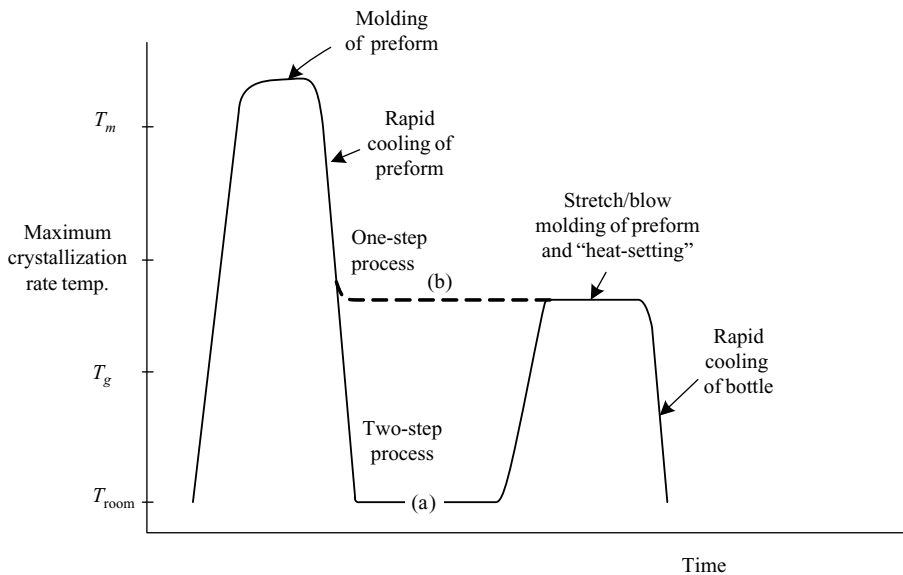


Fig. 14.19 Thermomechanical histories of the two variants of the injection stretch blow molding process; (a) the two-step, and (b) the less common one-step.

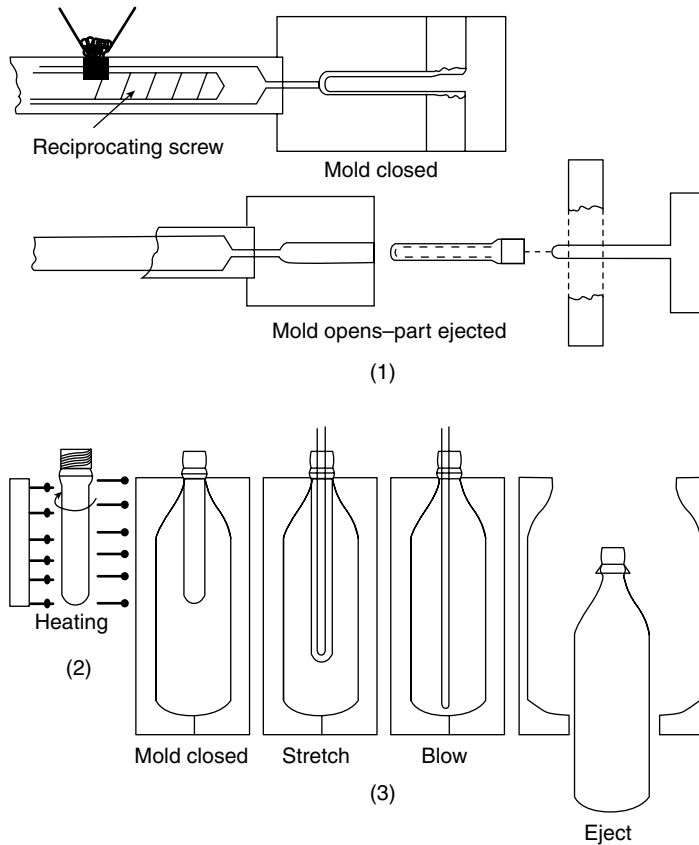


Fig. 14.20 Schematic representation of the injection stretch blow-molding process. Step (1) producing preforms may be carried out in different location from the stretch blow molding process. [Reprinted by permission from Schmidt et al., “Experimental Study and Numerical Simulation of the Injection Stretch/Blow Molding Process,” *Polym. Eng. Sci.*, **38**, 1399 (1998).]

the stretching and blowing step. Thus, the two-step process is the most common and is typically used to produce PET carbonated beverage bottles, which represent a very large volume market. The stages of the two-step process are shown in Fig. 14.20. The reason for thermally conditioning the preform in both process variants to the previously given temperature range, $T_g < T_s < T_m$, is to allow for crystallization during the biaxial stretch blow molding as shown in Fig. 14.21. In this way, deformation-induced crystallization is promoted *both* during the stretch blow molding stage and the heat-setting stage, if a hot mold is used. Following Druin (68), standard PET carbonated beverage bottles are produced by heating the preform to 95°–105°C and stretch blow molding it into a cold mold (3°–10°C), producing a deformation-induced crystallinity of 25%. The resulting product T_g is 73°C, and the O_2 and CO_2 permeability is reduced to half that of an nonoriented amorphous PET film.

If the preheated preform is stretched and blown into a *hot* mold, for example, 100–110°C and held there for a short period, the resulting T_g is in the range of 88°C, allowing for “hot fill” capabilities of such bottles, increasing the crystallinity to the 28–30% level and further decreasing the O_2 permeability to one-third that of an nonoriented amorphous

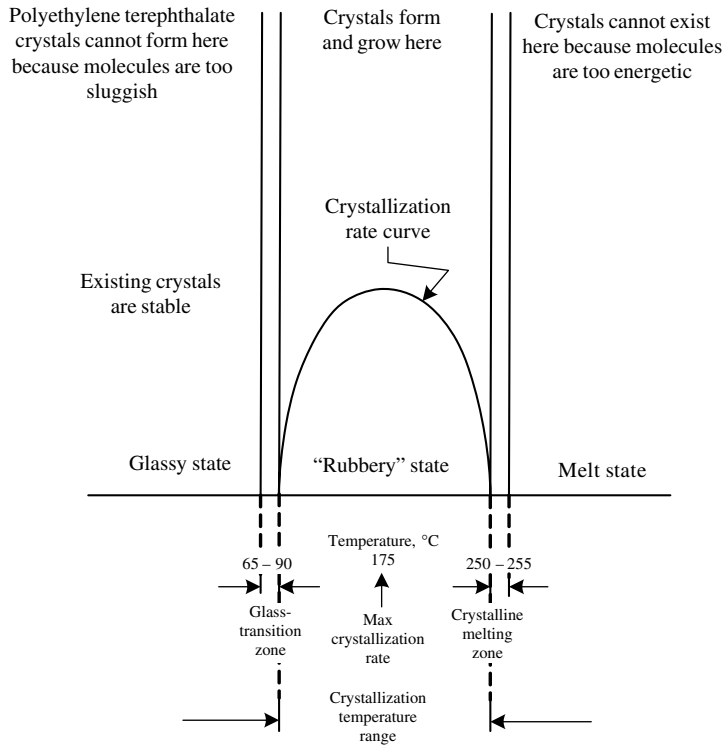


Fig. 14.21 Schematic representation of the crystallization behavior of PET relative to the stretch blow molding process. [J. S. Schaul, "Drying and Injection Molding PET for Beverage Bottle Preform," *SPE ANTEC Tech. Papers*, **26**, 534 (1980).]

PET film. The overall improvement in "barrier" properties of PET upon biaxial deformation, followed by heat-setting, is the *combined* result of higher deformation-induced crystallization and orientation. The role of crystallinity may be more significant than that of orientation, because it reduces both the diffusion rate (increasing the permeant's path "tortuosity") as well as its solubility, while orientation reduces only the diffusion rate.

Figure 14.22 plots the oxygen permeability of PET nonoriented sheets and biaxially oriented bottles as a function of the degree of crystallinity. Indeed, the effect of crystallinity is larger than that of biaxial orientation. But in practical terms, nonoriented sheets crystallize much more slowly than the biaxially oriented bottle walls, because deformation-induced orientation proceeds at higher rates at any temperature between T_g and T_m . That is, the schematically represented "crystallization rate" curve in Fig. 14.21 extends vertically upwards.

The real "structuring" benefit, then, of the stretch blow molding-induced biaxial deformation is to create the needed degree of crystallinity during the very short stretch blowing and heat-setting times, which makes the process commercially viable. Finally, the deformation-induced nonspherulitic crystalline morphology not only increases the modulus of elasticity, but also the impact strength of the stretch blow molded bottles. Thus, the structuring achieved during stretch blow molding for plastic materials has opened up the vast market for bottling pressurized supersaturated carbonated drinks, at

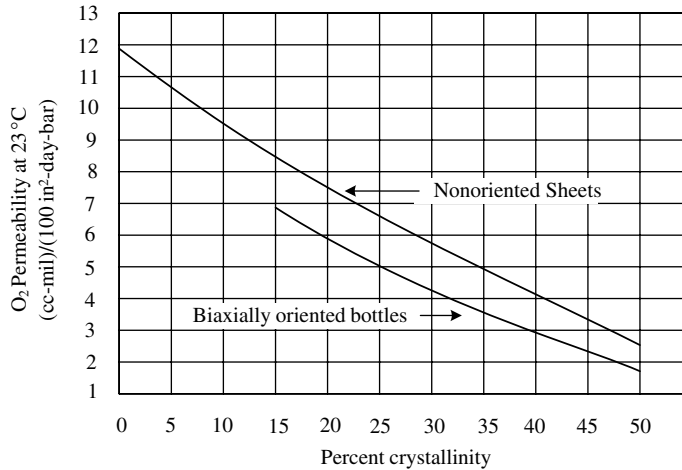


Fig. 14.22 Oxygen permeability of nonoriented PET sheets and biaxially oriented PET bottles as a function of crystallinity. [M. Salame, paper presented at the *Bev-Pak 1992 Conference*, Atlanta, GA March 23–25 (1992).]

the expense of both glass and aluminum containers, which have product-appropriate strength (though glass is brittle and thus breakable) and permeability, but are costlier to fabricate.

Finally, it is worth mentioning the more recent three-dimensional blow molding in which a robot arm optimally positions the parison in the mold cavity, to minimize trim-off, and to produce complex shapes, such as automotive parts.

Parison Formation

If the ratio of the final postinflation diameter to parison diameter is constant along the parison length (cylindrical shape), then the parison thickness should be uniform along its length. If, however, it varies, the parison should be thicker at axial locations where the diameter ratio is larger. Only under such conditions can acceptable product strength levels be reached with minimum product weight. To accomplish thickness control of the parison, special dies have been designed. In a typical reciprocating screw blow molding die head (Fig. 14.23), the choke screw D is adjustable to compensate for batch-to-batch or polymer-to-polymer viscosity variations. The choke ring I is adjustable to eliminate circumferential melt pressure variations. It also forms an annular channel that is narrow enough to ensure reduction of the effects of the varying melt flow histories of the incoming melt. The centering screw J is used for the final adjustments, which ensure that there is no angular dependence of the parison thickness or diameter.

The final die gap is a conical section, slightly tapering, annular channel. The cone angle Θ is appreciable (Fig. 14.24) and is an important die design variable in determining the parison diameter, diameter profile, and thickness. Furthermore, an angle $\theta > 0$ allows convenient die gap adjustment through slight axial mandrel position changes.

Figure 4.25 shows other possible parison die designs: diverging, converging, and straight, that also allow for flow rate control. An appreciable value of the diverging or converging angle renders the flow in the conical die land gap nonviscometric, consisting of both shear and planar extensional flows. This makes extrudate swell prediction

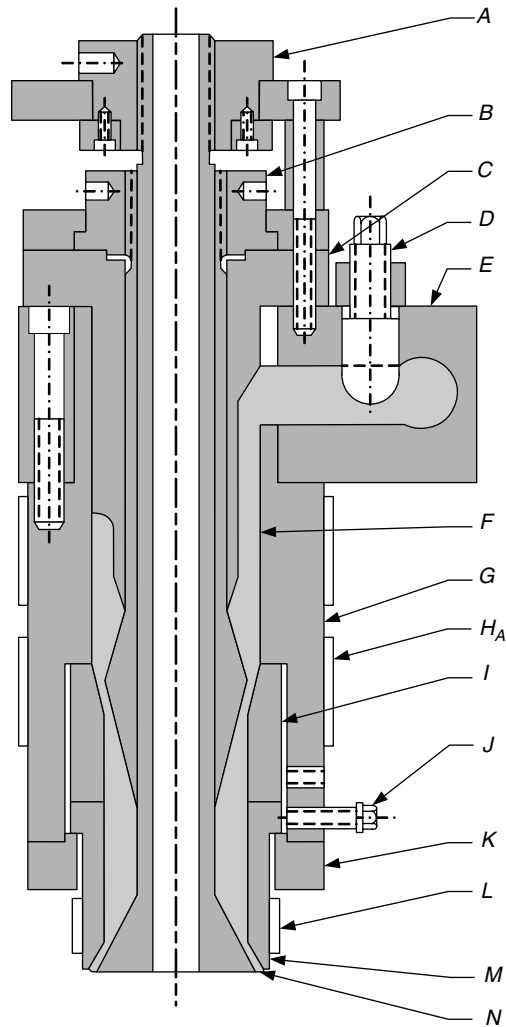


Fig. 14.23 Typical blow molding die: A, choke adjusting nut; B, mandrel adjustment; C, feed throat; D, choke screw; E, die head; F, plastic melt; G, die barrel; H, heater band; I, choke ring; J, centering screw; K, clamp ring; L, die heater; M, die; N, mandrel. [Reprinted by permission from J. D. Frankland, "A High Speed Blow Molding Process," *Trans. Soc. Rheol.*, **19**, 371 (1975).]

more difficult, in particular since the polymers that are suitable for the blow molding process are generally strongly elastic with a high extensional viscosity to avoid parison sagging and to undergo stable parison blowing to form final products. Moreover, in annular extrudate swell, in addition to the thickness swell (equivalent to radial swell in capillary flow), we must also deal with the diameter swell, as indicated in Fig. 14.18, both of which are affected by sagging due to gravitational forces; hence they are time-dependent and also affected by nonuniform temperature due to cooling of the parison. It is not surprising, therefore, that numerical methods are still somewhat limited, and semiempirical methods based on experimental measurements need to be used in process and die design.

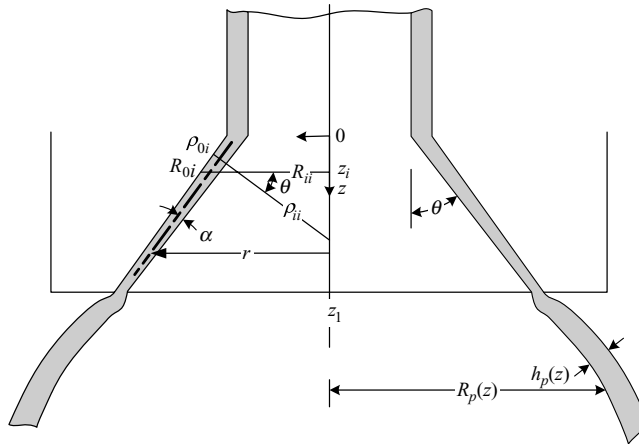


Fig. 14.24 Detailed cross-sectional representation of the die exit and the parison formed in the blow molding process, with the key design variables and the thickness and outer diameter swell.

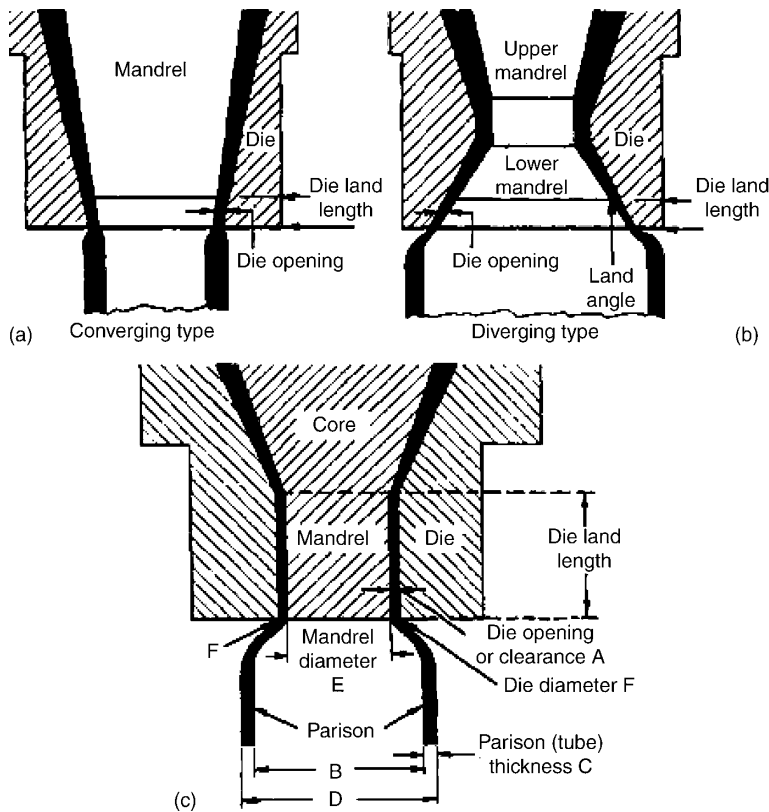


Fig. 14.25 Schematic parison die designs: (a) convergent; (b) divergent, and (c) straight. [Reprinted by permission from A. Gracia-Rejon, R. W. DiRaddo, and M. E. Ryan, “Effect of Die Geometry and Flow Characteristics on Viscoelastic Annular Die Swell,” *J. Non-Newt. Fluid Mech.*, **60**, 107–128 (1995).]

A simple and straightforward experimental method to determine parison shape and thickness distribution was suggested by Sheptak and Beyer (69), who developed a mold that pinched off the extruded parison in several axial segments, enabling the measurement of the weight and the lay-flat width of each segment. Kamal et al. (70) derived a time-dependent relationship between diameter and thickness swell based on experimental data. Kamal and Kalyon (71) correlated between area swell and capillary swell. Gracia-Rejon et al. (72) explored the effect of the die geometry (e.g., diverging versus converging, die contraction ratio, inclination angle, and length of tapered section) and flow characteristic on viscoelastic annular swell of HDPE using the commercial POLYFLOW FEM program and the Kaye-Bernstein-Kearsley-Zappas (K-BKZ) constitutive model. They found that diameter and thickness swell depend on the extent of elongational and shear deformation history in the die and, of course, the rheological characteristics of the polymer. Orbey and Dealy (73) also explored the effect of die design on annular swell values for both converging and diverging dies, and they (74) developed a lumped parameter model to predict the length and shape of the parison on the basis of experimental swell data and storage modulus of the resin. Wagner and Kalyon (75) studied parison shape and thickness distribution experimentally using cinematography and a transparent mold with a range of polyamide resins. They observe differences in behavior that cannot be easily related to the rheological properties of the resins. As Fig. 14.26(a), 14.26(b), and 14.26(c) indicates there are great differences in swell behavior between the resins. The straight nylon [Fig. 14.26(a)] shows greater nonuniformity along the axis. Diameter swell increases from 1.1 to 1.3, whereas the weight and thickness swell undergo a minimum, due to drawdown or sag and strain recovery. The addition of 12% glass fiber significantly reduces swell, with diameter swell slightly above 1 and the weight and thickness swell below 1 due to drawdown, this, in spite of measuring similar primary normal stress difference and storage modulus for the two resins. The polyolefin modified resin shows the largest swell ratio and minimal drawdown, indicating higher melt strength resisting drawdown.

Laroche et al. (76), who developed an integrated numerical model for the blow molding process, observe that computation of the annular die swell using differential viscoelastic constitutive models were found to overpredict the measured swell levels. Integral constitutive models, such as the K-BKZ constitutive equation, have proved to be more reliable. They deal with parison formation by a numerical Lagrangian scheme, whereby the parison is subdivided into axial increments and followed from emergence from the die to the end of the cycle. In each one, deformation due to swell and sagging is obtained using empirical relations.

Tanue et al. of the Funatsu computational group (77) using an FEM formulation and a Giesekus constitutive model (17), predicted the parison swell and shape within 20% accuracy, though it appears that they neglected gravitational effects. A number of viscoelastic constitutive equations (e.g., K-BKZ, Larson) for computing HDPE annular extrudate swell in large parisons were explored by Otsuki et al. of the same group (78), indicating very different responses with the different models, and great sensitivity to differences in resin properties at relatively small deformation.

The SIMBLOW³ integrated FEM simulation commercial software for the extrusion blow molding process also uses the K-BKZ fluid (79), which accounts for shear thinning,

3. The Plamedia Research Corporation (Tokyo, Japan)

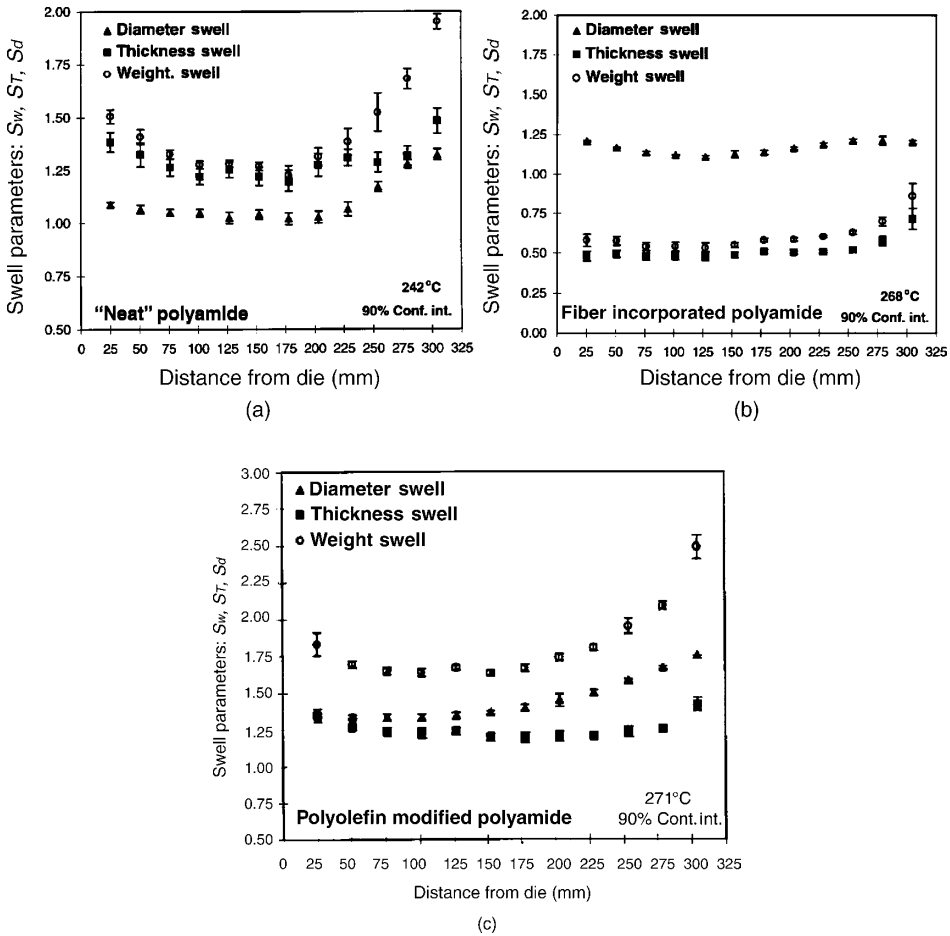


Fig. 14.26 Diameter (S_D , thickness (S_T), and weight (S_W) swell of a parison extrudate from a commercial blow-molding machine equipped with CCD camera equipment and parison pinch-off mold based on the design of Shepak and Beyer (69). (a) A chain extended multibranch polyamide-6 resin; (b) the former with 12% glass fiber of 10 μm diameter 60:1 L/D ; and (c) polyolefin modified polyamide-6 with some carbon black. [Reprinted by permission from A. H. Wagner and D. Kalyon, "Parison Formation and Inflation Behavior of Polyamide-6 During Extrusion Blow Molding," *Polym. Eng. Sci.*, **36**, 1897–1906 (1996).]

normal stresses in shear flow, and elastic behavior. It is a special case of the Lodge rubber-like liquid constitutive equations (Eqs. 3.4-4 and 3.4-5)

$$\tau(t) = \int_{-\infty}^t \left[\sum_i G_i \exp\left(-\frac{t-t'}{\lambda_i}\right) h(\gamma) [\gamma[1](t', t), -\mathbf{I}] \right] dt' \quad (14.3-1)$$

where $\gamma[1]$ is the Finger tensor and H_i is the dynamic damping function to account for nonlinearity in the relaxation spectrum (G_i, λ_i) (80). The evaluation of the material rheological parameters needed in Eq.14.3-1 requires the following characterization experiments: dynamic mechanical, steady shear, and transient uniaxial elongational flow.

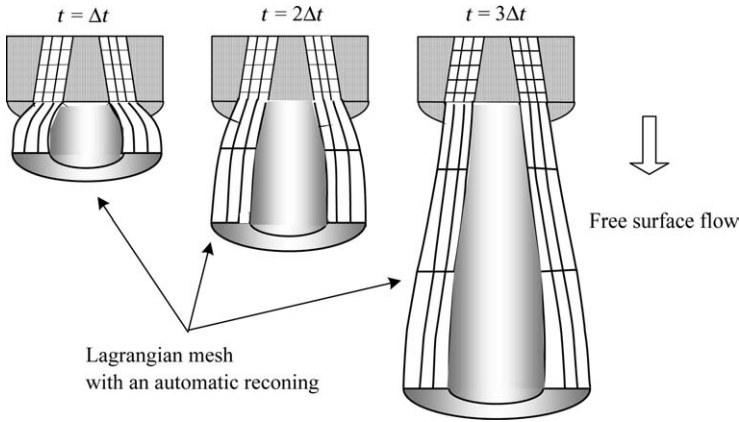


Fig. 14.27 Lagrangian mesh used in the FEM in the post-die extruded parison. [Reprinted by permission from the Plamedia Research Corporation, Tokyo, Japan.]

The momentum and energy equations are then cast in an Eulerian FEM mesh inside the conical die and a Lagrangian mesh in the parison being formed, as shown in Fig. 14.27. Typical results obtained with SIMBLOW are depicted qualitatively in Fig. 14.28. A conical parison is formed initially, which, under the body force of gravity, turns vertical downwards. The gradual thickening of the parison is due to the axial programmed parison core movement.

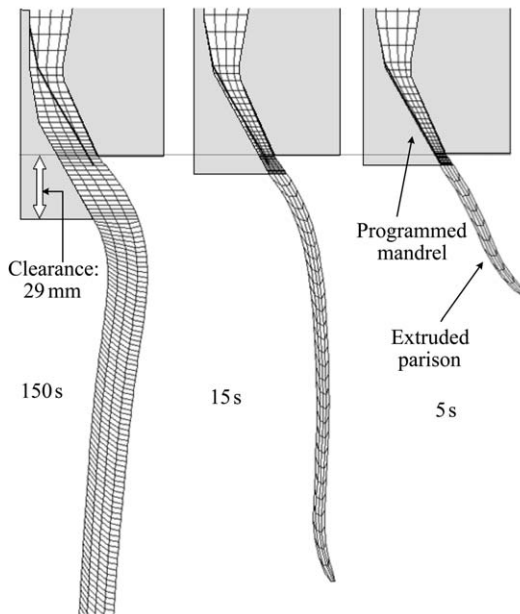


Fig. 14.28 Parison shape and thickness profile of the parison at different times with programmed mandrel and a region of partially confined extrudate. [Reprinted by permission from the Plamedia Research Corporation, Tokyo, Japan.]

Parison Inflation

The parison is inflated fast, within seconds or less, at a predetermined rate such that it does not burst while expanding. It is a complex process that involves expansion of a nonuniform membrane-like element. Because the extension ratio is high (above 10), it is difficult to calculate the final thickness distribution. Naturally, much of the recent theoretical research on parison stretching and inflation (as in the case with thermoforming) focuses on FEM methods and the selection of the appropriate rheological constitutive models to predict parison shape, thickness, and temperature distribution during the inflation.

FEM is the only practical tool to handle the problem. Not surprisingly, this method was first applied to membranes or thin shells in the field of structural analysis, a field where, in fact, FEM was pioneered, with a much later penetration to fluid mechanics and polymer processing. Indeed, Oden and Sato (81) were the first to apply FEM to examine the three-dimensional membrane inflation problem. Two other engineering fields that apply a similar FEM approach are metal sheet forming and glass bottle blowing (82).

Parison inflation models use a Lagrangian framework with most of them employing the thin-shell formulation and various solidlike or liquid constitutive equations, generally assuming no-slip upon the parison contacting the mold. The first attempts to simulate polymeric parison inflation were made by Denson (83), who analyzed the implications of elongational flow in various fabrication methods, as discussed in the following example.

Example 14.2 Inflation of a Cylindrical Uniform Parison Assuming Simple Planar Extensional Flow Following Denson (83), an approximate description of the inflation of a cylindrical parison of uniform radius R_i and thickness h_i to that R_0 and h_0 can be obtained by assuming that (a) the flow is a planar extension; (b) the flow is isothermal; and (c) $h/r \ll 1$, so that the hoop stress $\tau = -[PR(t)/h(t)]$. Experimentally, planar extensional viscosity at very low strain rates (which clearly is a poor approximation for blow molding processes) can be expressed as

$$\bar{\eta}_{pl} = K(\dot{\epsilon}_{pl})^{n-1} \quad (\text{E14.2-1})$$

The tangential elongational stress component $\tau_{\theta\theta}$ is given by

$$\tau_{\theta\theta} = -\frac{PR(t)}{h(t)} = -K(\dot{\epsilon}_{pl})^{n-1}\dot{\epsilon}_{pl} \quad (\text{E14.2-2})$$

Since

$$\dot{\epsilon}_{pl} = \frac{1}{R(t)} \frac{dR(t)}{dt} \quad (\text{E14.2-3})$$

and for an incompressible material we have

$$V = 2\pi R(t)h(t)L = \text{const.} \quad (\text{E14.2-4})$$

we obtain the expression

$$\frac{dR}{dt} = CP^s R^{2s+1} \quad (\text{E14.2-5})$$

where $s = 1/n$ and

$$C = \left(\frac{2\pi L}{VK} \right)^s \quad (\text{E14.2-6})$$

Equation E14.2-5 can be solved for any time-dependent or constant inflation pressure to give the radial value as a function of time. For example, if P is constant, the parison inflation time is

$$t = \frac{1}{2sCP^s} \left[\left(\frac{1}{R_i} \right)^{2s} - \left(\frac{1}{R_0} \right)^{2s} \right] \quad (\text{E14.2-7})$$

However, since extentional viscous flow behavior is expected to occur only below a certain critical strain rate given by $\dot{\epsilon} = (2\lambda_{\max})^{-1}$, and the blow-molding inflation rates are high, the preceding approximation may only hold at high temperatures, where the maximum relation time is small.

Petrie and Ito (84) used numerical methods to analyze the dynamic deformation of axisymmetric cylindrical HDPE parisons and estimate final thickness. One of the early and important contributions to parison inflation simulation came from DeLorenzi et al. (85–89), who studied thermoforming and isothermal and nonisothermal parison inflation with both two- and three-dimensional formulation, using FEM with a hyperelastic, solidlike constitutive model. Hyperelastic constitutive models (i.e., models that account for the strains that go beyond the linear elastic into the nonlinear elastic region) were also used, among others, by Charrier (90) and by Marckmann et al. (91), who developed a three-dimensional dynamic FEM procedure using a nonlinear hyperelastic Mooney–Rivlin membrane, and who also used a viscoelastic model (92). However, as was pointed out by Laroche et al. (93), hyperelastic constitutive equations do not allow for time dependence and strain-rate dependence. Thus, their assumption of quasi-static equilibrium during parison inflation, and overpredicts stresses because they cannot account for stress relaxation; furthermore, the solutions are prone to numerical instabilities. Hyperelastic models like viscoplastic models do allow for strain hardening, however, which is a very important element of the actual inflation process.

Vantal et al. (94) and Rodriguez-Villa et al. (95) used viscoplastic models. Wang et al. (96) also used a viscoplastic model, but assumed the material's behavior at elevated temperatures to be strain-rate-dependent, and a non-Newtonian creeping material model to specify the strain rate-sensitive characteristic of the material, strain hardening, and temperature dependence. They applied the model to PET stretch blow molding, and simulated three cases: inflation without stretching, stretching followed by inflation, and simultaneous stretching and inflation. Their conclusion is that the first case cannot be used to produce a real product, the second case can lead to wrinkling, and only the third case resulted in stable and smooth deformation.

With viscoelastic models used by an increasing number of researchers, time and temperature dependence, as well as strain hardening and nonisotropic properties of the deformed parison can, in principle, be accounted for. Kouba and Vlachopoulos (97) used the K-BKZ viscoelastic constitutive equation to model both thermoforming and parison membrane stretching using two-dimensional plate elements in three-dimensional space. Debbaut et al. (98,99) performed nonisothermal simulations using the Giesekus constitutive equation.

Shrivastava and Tang (100) used a viscoelastic constitutive equation with special reference to thermoforming, whereas Laroche et al. (101) developed an integrated numerical model for the complete blow molding process, and simulated the blow molding of a gas tank. The viscoelastic deformations during parison formation and inflation were modeled by a K-BKZ constitutive equation, and the thermal dependence was accounted for by the Williams–Landel–Ferry (WLF) equation. Temperature variations during parison formation that affect the inflation were taken into account. They found good agreement with commercial size blow molding machine products.

Schmidt et al. (102) carried out a detailed experimental study of PET blow molding with a well-instrumented machine and compared the results with theoretical predictions using FEM and an Oldroyd B constitutive equation. They measured and calculated internal gas pressure, coupled it with the thermomechanical inflation and performed experiments and computations with free parison inflation.

Parison cooling is an integral part of the process that has been treated by a number of researchers (103–105). The principles are based on contact solidification without deformation, as discussed in Chapter 5. A special complication is the frictional heat generation in injection blow molding between the rod and the parison.

REFERENCES

1. J. F. Agassant, P. Coates, M. Denn, D. Edie, C. G. Gogos, K. S. Hyun, M. Kamal, H. Meijer, W. Michaeli, D. H. Sebastian, Z. Tadmor, J. Vlachopoulos, J. L. White, and M. Xanthos, (Organizing Committee), “Touchstones of Modern Polymer Processing,” Workshop Held at the Polymer Processing Institute at New Jersey Institute of Technology, Newark NJ, May 10–12, 2002. The quote is due to Han Meijer.
2. H. F. Mark, in *Rheology*, Vol. 4, F. R. Eirich, Ed., Academic Press, New York, 1969, Chapter 7.
3. J. R. Dees and J. E. Spruiell, “Structure Development During Melt Spinning of Linear Polyethylene Fiber,” *J. Appl. Polym. Sci.* **18**, 1053 (1974).
4. G. Capaccio and I. M. Ward, “Ultra-high Modulus Linear Polyethylene through Controlled Modulus Weight and Drawing,” *Polym. Eng. Sci.*, **15**, 219–224 (1975).
5. S. Kase and T. Matsuo, “Studies on Melt Spinning, I. Fundamental Equations on the Dynamics of Melt Spinning,” *J. Polym. Sci.*, Part A, **3**, 2541 (1965).
6. S. Kase and T. Matsuo, “Studies on Melt Spinning, Part II. Steady State and Transient Solutions of Fundamental Equations Compared with Experimental Results, Fundamental Equations on the Dynamics of Melt Spinning,” *J. Appl. Poly. Sci.*, **11**, 251–287 (1967).
7. M. A. Matovich and J. R. A. Pearson, “Spinning a Molten Threadline,” *Ind. Eng. Fundam.*, **8**, 512 (1969).
8. M. M. Denn, C. J. S. Petrie, and P. Avenas, “Mechanics of Steady Spinning of Viscoelastic Liquids,” *AIChE J.*, **21**, 791(1975).
9. R. J. Fisher and M. M. Denn, “A Theory of Isothermal Melt Spinning and Draw Resonance,” *AIChE J.*, **22**, 236–246 (1976).
10. T. C. Papanastasiou, C. W. Macosko, L. E. Scriven, and Z. Chen, “Fiber Spinning of Viscoelastic Liquid,” *AIChE J.*, **33**, 834–842 (1987).
11. P. W. Bell and D. D. Edie, “Calculated Internal Stress Distribution in Melt-spun Fibers,” *J. Appl. Polym. Sci.*, **33**, 1073–1088 (1987).
12. P. W. Bell and D. D. Edie, “Measured Orientation and Internal Stress Distribution in Melt-spun Fibers,” *J. Appl. Polym. Sci.*, **33**, 1089–1102 (1987).

13. J. A. Kulkarni and A. N. Beris, "Lattice-based Simulation of Chain Conformation in Semicrystalline Polymers with Application to Flow Induced Crystallization," *J. Non-Newt. Fluid Mech.*, **82**, 331–336 (1999).
14. A. K. Doufas, A. J. McHugh, and C. Miller, "Simulation of Melt Spinning Including Flow-induced Crystallization. Part I. Model Development and Predictions," *J. Non-Newt. Fluid Mech.*, **92**, 27–66 (2000).
15. Y. L. Joo, M. D. Smith, R. C. Armstrong, R. A. Brown, and R. A. Ross, "Two-dimensional Numerical Analysis of Non-isothermal Melt Spinning with and without Phase Transition," *J. Non-Newt. Fluid Mech.*, **102**, 37–70 (2002).
16. R. Guennete and M. Fortin, "A New Mixed Finite Element Method for Computing Viscoelastic Flows," *J. Non-Newt. Fluid Mech.*, **77**, 153–190 (1998).
17. H. Giesekus, "A Simple Constitutive Equation for Polymer Fluids Based on the Concept of Deformation-dependent Tensorial Mobility," *J. Non-Newt. Fluid Mech.*, **11**, 60–109 (1982).
18. K. Nakamura, K. Katayama, and T. Amano, "Some Aspects of Non-isothermal Crystallization of Polymers. Part II. Consideration of Isokinetic Conditions," *J. Appl. Polym. Sci.*, **17**, 1031–1041 (1982).
19. A. Ziabicki, *Fundamentals of Fiber Formation*, Wiley, New York, 1976.
20. M. C. Levine, N. Waheed, and G. C. Rutledge, "Molecular Dynamics Simulation of Orientation and Crystallization of Polyethylene during Uniaxial Extension," *Polymer*, **44**, 1771–1779 (2003).
21. Y. Ide and J. L. White, "The Spinnability of Polymer Filaments," *J. Appl. Polym. Sci.*, **20**, 2511–2531 (1976).
22. C. J. S. Petrie and M. M. Denn, "Instabilities in Polymer Processing," *AIChE J.*, **22**, 209 (1976).
23. Y. Ide and J. L. White, "Investigation of Failure during Elongational Flow of Polymer Melts," *J. Non Newt. Fluid Mech.*, **2**, 281–298 (1977).
24. J. L. White and Y. Ide, "Instabilities and Failure in Elongational Flow of Melts in Isothermal Spinning of Fibers," *J. Appl. Polym. Sci.*, **22**, 3057–3074 (1978).
25. S. Lee, B. M. Kim, and J. C. Hyun, "Dichotomous behavior of Polymer Melts in Isothermal Mel Spinning," *Korean J. Chem. Eng.*, **12**, 345–351 (1995).
26. S. Kase, "Studies in Melt Spinning, IV. On the Stability of Melt Spinning," *J. Appl. Polym. Sci.*, **18**, 3279 (1974).
27. G. F. Cruz-Saenz, G. J. Donnelly, and C. B. Weinberger, "Onset of Draw Resonance during Isothermal Melt Spinning," *AIChE J.*, **22**, 441 (1976).
28. H. W. Jung and J. C. Hyun, "Fiber Spinning and Film Blowing Instabilities," in *Polymer Processing Instabilities – Control and Understanding*, S. G. Hatzikiriakos and K. B. Migler, Eds., Marcel Dekker, New York, 2004, Chapter 11.
29. J. R. A. Pearson and Y. T. Shaw, "Stability Analysis of the Fiber Spinning Process," *Trans. Soc. Rheol.*, **16**, 519–533 (1972).
30. Y. T. Shaw and J. R. A. Pearson, "On the Stability of Non-isothermal Fiber Spinning – General Case," *Ind. Eng. Chem. Fundam.*, **11**, 150–153 (1972).
31. J. R. A. Pearson and Y. T. Shaw, "On the Stability of Isothermal and Non-isothermal Fiber Spinning of Power Law Fluids," *Ind. Eng. Chem. Fundam.*, **13**, 134–138 (1974).
32. J. R. A. Pearson, Y. T. Shaw, and R. D. Mhaskar, "On the Stability of Fiber Spinning of Freezing Fluids," *Ind. Eng. Chem. Fundam.*, **15**, 31–37 (1976).
33. R. J. Fisher and M. M. Denn, "Finite-amplitude Stability and Draw Resonance in Isothermal Spinning," *Chem. Eng. Sci.*, **30**, 1129–1134 (1975).
34. R. J. Fisher and M. M. Denn, "Mechanics of Nonisothermal Polymer Melt Spinning," *AIChE J.*, **23**, 23–28 (1977).

35. J. C. Chang and M. M. Denn, "Sensitivity of the Stability of Isothermal Melt Spinning to Rheological Constitutive Assumptions," in *Rheology: Applications*, Vol. 3., G. Astarita, G. Marrucci, and L. Nicolais, Eds., Plenum Publishing, New York 1980, pp.9–13.
36. J. C. Chang, M. M. Denn, and F. T. Geyling, "Effect of Inertia, Surface Tension and Gravity on the Stability of Isothermal Drawing of Newtonian Fluids," *Ind. Eng. Chem. Fundam.*, **20**, 147–149 (1981).
37. C. D. Han, *Rheology in Polymer Processing*, Academic Press, New York, 1976, Section 12.3.1.
38. I. J. Chen, G. E. Hagler, L. E. Abbott, D. C. Bogue, and J. L. White, "Interpretation of Tensile and Melt Spinning Experiments in LDPE and HDPE," *Trans. Soc. Rheol.*, **16**, 473 (1972).
39. J. L. White and Y. Ide, "Instabilities and Failure in Elongational Flow and Melt Spinning of Fibers," *J. Appl. Polym. Sci.* **22**, 3057–3074 (1978).
40. B. M. Kim, J. C. Hyun, J. S. Oh, and S. J. Lee, "Kinematic Waves in the Isothermal Melt Spinning of Newtonian Fluids," *AIChE J.*, **42**, 3134–3169 (1996).
41. H. W. Jung, H.-S. Song, and J. C. Hyun, "Draw Resonance and Kinematics Waves in Viscoelastic Isothermal Spinning," *AIChE J.*, **46**, 2106–2111 (2000).
42. J. R. A. Pearson and C. J. S. Petrie, "The Flow of a Tubular Film. Part 1. Formal Mathematical Presentation," *J. Fluid Mech.*, **40**, 1–19 (1970).
43. J. R. A. Pearson and C. J. S. Petrie, "The Flow of a Tubular Film. Part 2. Interpretation of the Model and Discussion of Solutions," *J. Fluid Mech.*, **42**, 609–625 (1970).
44. J. R. A. Pearson and C. J. S. Petrie, *Plast. Polym.*, **38**, 85 (April 1970).
45. C. J. S. Petrie, "A Comparison of Theoretical Predications with Published Experimental Measurements on the Blown Film Process," *AIChE J.*, **21**, 275–282 (1975).
46. W. Ast, "Der Abkälvorgang beim Herstellen von Blasfolien aus Polyäthylen Niedriger Dichte," *Kunststoffe*, **63**, 427 (1973).
47. C. J. S. Petrie, in *Computational Analysis of Polymer processing*, J. R. A. Pearson and S. M. Richardson, Eds., Applied Science Publishers, New York, 1983, Chapter 7.
48. J. R. A. Pearson, *Mechanics of Polymer Processing*, Applied Science Publishers, New York, 1985.
49. C. D. Han and J. Y. Park, "Studies on Blown Film Extrusion, I. Experimental Determination of Elongational Viscosity," *J. Appl. Polym. Sci.*, **19**, 3257 (1975).
50. C. D. Han and J. Y. Park, "Studies on Blown Film Extrusion, II. Analysis of the Deformation and Heat Transfer Process," *J. Appl. Polym. Sci.*, **19**, 3277 (1975).
51. C. D. Han and J. Y. Park, "Studies on Blown Film Extrusion, III. Bubble Instability. Analysis of the Deformation and Heat Transfer Process," *J. Appl. Polym. Sci.*, **19**, 3291 (1975).
52. R. K. Gupta, Ph.D. Thesis, Department of Chemical Engineering, University of Delaware, Newark, NJ 1980.
53. T. Kanai and J. L. White, "Kinematics, Dynamics and Stability of the Tubular Film Extrusion of Various Polyethylenes," *Polym. Eng. Sci.*, **24**, 1185–1201 (1984).
54. T. Kanai and J. L. White, "Dynamics, Heat Transfer, and Structure Development in Tubular Film Extrusion of Polymer Melts: A Mathematical Model and Prediction," *J. Polym. Eng.*, **5**, 135 (1985).
55. V. Sidiropoulos and J. Vlachopoulos, "An Investigation of Venturi and Coanda Effects in Blown Film Cooling," *Int. Polym. Process.*, **15**, 40 (2000).
56. V. Sidiropoulos and J. Vlachopoulos, "The Effect of Dual-orifice Air-ring Design on Blown Film Cooling," *Polym. Eng. Sci.*, **40**, 1611–1618 (2000).
57. V. Sidiropoulos and J. Vlachopoulos, "Numerical Study of Internal Bubble Cooling in Film Blowing," *Int. Polym. Process.*, **16**, 48–53, (2001).

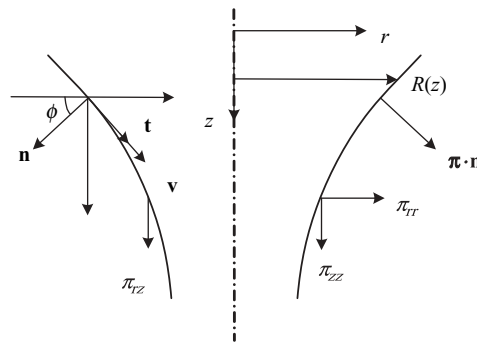
58. V. Sidiropoulos and J. Vlachopoulos, "Temperature Gradients in Blown Film Bubbles," *Adv. Polym. Technol.*, **24**, 83–90 (2005).
59. G. A. Campbell, N. T. Obot, and B. Cao "Aerodynamics in the Blown Film Process," *Polym. Eng. Sci.*, **32**, 751 (1992).
60. X.-L. Luo and R. I. Tanner, "A Computer Study of Film Blowing," *Polym. Eng. Sci.*, **25**, 620–629 (1985).
61. A. I. Leonov, "Nonequilibrium Thermodynamics and rheology of viscoelastic polymer media," *Rheol. Acta*, **15**, 85–98 (1976).
62. J. J. Cain and M. M. Denn, "Multiplicity and Instabilities in Film Blowing," *Polym. Eng. Sci.*, **28**, 1527–1541 (1988).
63. D. Acierno, F. P. La Mantia, G. Marrucci, and G. Titomanlio, "A Non-linear Viscoelastic Model with Structure-dependent Relaxation Times: I. Basic Formulation," *J. Non-Newt. Fluid Mech.*, **1**, 125–146 (1976).
64. C. D. Han, *Rheology in Polymer Processing*, Academic Press, New York, 1976, fig. 9.14.
65. J. C. Hyun, H. Kim, J. C. Lee, H. S. Song, and H. W. Jung, "Transient Solutions of the Dynamics in Film Blowing Processes," *J. Non-Newt. Fluid Mech.*, **121**, 157–162 (2004).
66. G. N. Beall and J. L. Throne, *Hollow Plastics Parts: Manufacturing and Design*, Hanser, New York, 2004.
67. D. V. Rosato, A. V. Rosato, and D. P. DiMatia, *Blow Molding Handbook*, Second Edition, Hanser, Munich, 2003.
68. M. L. Druin, "PET Properties and Performance Requirements," paper presented at the Polyester Packaging - The Critical Path Ahead Conference, sponsored by Packaging Strategies, Inc., Newark, NJ, May 28–30 (1997).
69. N. Sheptak and C. E. Beyer, "Study of Parison Formation, including the Effects of Swell and Drawdown," *Soc. Plastics Eng. J.*, **32**, 190–196 (1965).
70. M. R. Kamal, V. Tan, and D. Kalyon, "Measurement and Calculation of Parison Dimensions and Bottle Thickness Distribution during Blow Molding," *Polym. Eng. Sci.*, **21**, 331–338 (1981).
71. M. R. Kamal and D. M. Kalyon, "An Experimental Investigation of Capillary Extrudate Swell in Relation to Parison Swell Behavior in Blow Molding," *Polym. Eng. Sci.*, **26**, 508–516 (1986).
72. A. Gracia-Rejon, R. W. DiRaddo, and M. E. Ryan, "Effect of Die Geometry and Flow Characteristics on Viscoelastic Annular Die Swell," *J. Non-Newt. Fluid Mech.*, **60**, 107–128 (1995).
73. N. Orbey and J. M. Dealy, "Isothermal Swell of Extrudate from Annular Dies; Effects of Die Geometry, Flow Rate, and Resin Characteristics," *Polym. Eng. Sci.*, **24**, 511–518 (1984).
74. J. M. Dealy and N. Orbey, "A Model for Parison Behavior in the Extrusion Blow Molding Process," *AIChE J.*, **31**, 807–811 (1985).
75. A. H. Wagner and D. Kalyon, "Parison Formation and Inflation Behavior of Polyamide-6 during Extrusion Blow Molding," *AIChE J.*, **36**, 1897–1906 (1996).
76. D. Laroche, K. K. Kabanemi, L. Pecora, and R.W. DiRaddo, "Integrated Numerical Modeling of the Blow Molding Process," *Polym. Eng. Sci.*, **39**, 1223–1233 (1999).
77. S. Tanue, T. Kajiwara, K. Funatsu, K. Terada, and M. Yamabe, "Numerical Simulation of Blow Molding – Prediction of Parison Diameter and Thickness Distribution in the Parison Formation Process," *Polym. Eng. Sci.*, **36**, 2008–2017 (1996).
78. Y. Otsuki, T. Kajiwara, and K. Funatsu, "Numerical Simulations of Annular Extrudate Swell Using Various Types of Viscoelastic Models," *Polym. Eng. Sci.*, **39**, 1969–1981 (1999).
79. B. Bernstein, E. A. Kearsley, and L. J. Zappas, "A Study of Stress Relaxation with Finite Strain", *Trans. Soc. Rheol.* **7**, 391–410 (1963).

80. M. H. Wagner, T. Raible, and J. Meissner, "Tensile Overshoot in Uniaxial Extension of LDPE Melt," *Rheol. Acta*, **18**, 427–428 (1979).
81. J. T. Oden and T. Sato, "Finite Strains and Displacements of Elastic Membranes by the Finite Element Method," *Int. J. Solids and Struct.*, **3**, 471–488 (1967).
82. J. M. A. Cesar de Sa, "Numerical Modeling of Glass Forming Processes," *Eng. Comput.*, **3**, 266–275 (1986).
83. C. D. Denson, "Implications of Extensional Flow in Polymer Fabrication Processes," *Polym. Eng. Sci.*, **13**, 125 (1973).
84. C. J. S. Petrie and K. Ito, "Prediction of Wall Thickness of Blow Molded Containers," *Plast. Rubber Process.*, **5**, 68–72 (1980).
85. H. G. deLorenzi and H. F. Nied, "Finite Element Simulation of Thermoforming and Blow Molding," *SPE ANTEC Tech. Papers*, **33**, 418–420 (1987).
86. H. G. deLorenzi and H. F. Nied, "Blow Molding and Thermoforming of Plastics: Finite Element Modeling," *Compu. Struct.* **26**, 197–206 (1987).
87. H. G. deLorenzi, H. Nied, and C. A. Taylor, "Simulation and Analysis of Blow Molding Using the Finite Element Method," *SPE ANTEC Tech. Papers*, **34**, 797–799 (1988).
88. H. F. Nied, C. A. Taylor, and H. G. deLorenzi, "Three-dimensional Finite Element Simulation of Thermoforming," *Polym. Eng. Sci.*, **30**, 1314–1322 (1990).
89. H. G. deLorenzi and H. F. Nied in *Progress in Polymer Processing*, A. I. Isayev, Ed., Hanser Verlag, Munich, 1991.
90. J. M. Charrier, S. Shrivastava, and R. Wu, "Free and Constrained Inflation of Elastic Membranes in Relation to Thermoforming - non-axisymmetric Problems," *J. Strain Anal.*, **24**, 55–74 (1989).
91. G. Marckmann, E. Verron, and B. Peseux, "Finite Element Analysis of Blow Molding and Thermoforming Using a Dynamic Explicit Procedure," *Polym. Eng. Sci.*, **41**, 426–439 (2001).
92. E. Verron, G. Marckmann, and B. Peseux, "Dynamic Inflation of Non-Linear Elastic and Viscoelastic Rubber-like Membranes," *Int. J. Num. Meth. Eng.* **50**, 1233–1251 (2001).
93. D. Laroche, K. K. Kabanemi, L. Pecora, and R. W. Diraddo, "Integrated Numerical Modeling of the Blow Molding Process," *Polym. Eng. Sci.*, **39**, 1223–1233 (1999).
94. M. H. Vantal, B. Monasse, and M. Bellet, *Numiform*, **95**, 1089 (1995).
95. A. Rodriguez-Villa, J. F. Agassant, and M. Bellet, "Finite Element Simulation of the Extrusion Blow-Molding Process," *Numiform*, **95**, 1053 (1995).
96. S. Wang, A. Makinouchi, and T. Nakagawa, "Three-dimensional Viscoplastic FEM Simulation of a Stretch Blow Molding Process," *Adv. Polym. Technol.*, **17**, 189–202 (1998).
97. K. Kouba and J. Valchopoulos, "Modeling of Thermoforming and Blow Molding," *Theoretical and Applied Rheology, Proc. XIth Cong. Rheology*, Brussels, Belgium, August 17–21, 1992.
98. B. Debbaut, B. Hocq, and J. M. Marchal, "Numerical Simulation of the Blow Molding Process," *SPE ANTEC Tech. Papers*, **39**, 1870–1872 (1993).
99. B. Debbaut, B. Hocq, J. M. Marchal, Y. Jiang, and V. Legat, "Blow Molding: a 3D Approach," *Proc. III World Congr. on Computational Mechanics*, IACM, Chiba, Japan, 1994, pp. 1580–1581.
100. S. Shrivastava and J. Tang, "Large Deformation Finite Element Analysis of Non-linear Viscoelastic Membranes With Reference to Thermoforming," *J. Strain Anal.* **28**, 31 (1993).
101. D. Laroche, K. K. Kabanemi, L. Pecora, and R. W. DiRaddo, "Integrated Numerical Modeling of the Blow Molding Process," *Polym. Eng. Sci.*, **39**, 1223–1233 (1999).
102. F. M. Schmidt, J. F. Aggasant, and M. Bellet, "Experimental Study and Numerical Simulation of the Injection Stretch/Blow Molding Process," *Polym. Eng. Sci.*, **38**, 1399–1407 (1998).
103. M. F. Edwards, P. K. Suvanaphen, and W. L. Wilkinson, "Heat Transfer in Blow Molding Operations," *Polym. Eng. Sci.* **19**, 910 (1979).

104. M. F. Edwards, S. Georghiades, and P. K. Suvanaphen, *Plast. Rubber. Compos. Process. Appl.*, **1**, 161 (1981).
105. M. R. Kamal and D. Kalyon, "Heat Transfer and Microstructure in Extrusion Blowmolding," *Polym. Eng. Sci.*, **23**, 503–509 (1983).

PROBLEMS

14.1 Isothermal Fiber Spinning of a Newtonian Melt⁴ In carrying out this analysis, neglect (i) any heat transfer to the surrounding air, that is, assume that the fiber drawing is completed over a very short distance downstream from the spinneret and then quenched in a liquid medium; (ii) the air-drag forces as well as the surface-tension forces that arise from the rapid generation of new surface during drawing. The relevant stresses, velocity, surface vectors \mathbf{t} and \mathbf{n} , and coordinates are shown in the accompanying figure for a representative section of the fiber being drawn in air.



where $\pi_{il} = P + \tau_{li}$ and $\pi_{ij} = \tau_{ij}$ ($i \neq j$). Assume that $v_z = v_z(r, z)$, $v_r = v_r(r, z)$, $P = P(r, z)$, and Newtonian constitutive equation $\pi_{zz} = P - 2\mu(\partial v_z/\partial z)$

- (a) Derive the following expression for the z -component velocity and resulting fiber radius

$$R(z) = R_0 \exp \left[-\frac{1}{2} z \frac{\ln D_R}{L} \right]$$

where $D_R = V_L/V_0$, V_0 and R_0 are values at the spinneret exit, and L is the length of the drawdown region

- (b) If nylon 6–6 is extruded at a volumetric flow rate of $0.1 \text{ cm}^3/\text{s}$, at 285°C and drawn under isothermal conditions in a chamber of $L = 400 \text{ cm}$, $D_R = 100$, with a take up speed of 1000 m/min , and if the extrudate swell diameter is three times that of the spinneret diameter, calculate: (1) the maximum stretching rate of the drawn nylon 6–6 melt, and (2) the maximum tensile stress in the melt and the force needed to draw the fiber

4. D. G. Baird and D. I. Collias, *Polymer Processing*, Wiley, New York, 1998, Chapter 9; also, S. Middleman, *Fundamentals of Polymer Processing*, McGraw-Hill, New York, 1997, Chapter 9.

14.2 Relative Importance of the Various Terms in the Analysis of the Isothermal Fiber Spinning of a Newtonian Melt Use the data and result of Problem 14.1(b) to evaluate the importance in the isothermal fiber spinning of a Newtonian melt analysis (nylon 6-6 at 285°C) of the inertial terms and gravity relative to the viscous stress terms. Using Eq. E14.1-2 for F_D , evaluate the importance of the air-drag force term.

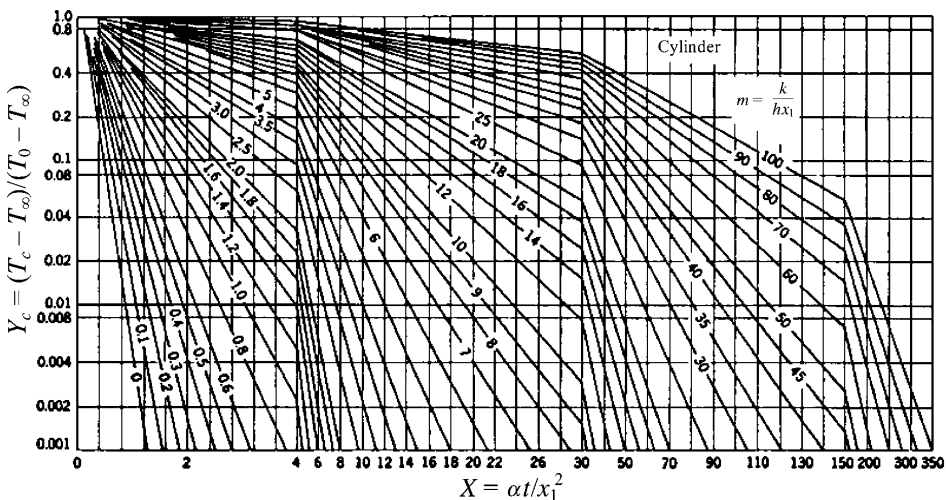
14.3 Isothermal Fiber Spinning of a Power Law Melt Derive the following expression for the axial velocity $v_z(z)$ resulting from the steady isothermal fiber spinning of a Power Law melt

$$v_z(z) = v_0 \left[1 + \left(D_R^{(n-1)/n} - 1 \right) \frac{z}{L} \right]^{n/(n-1)}$$

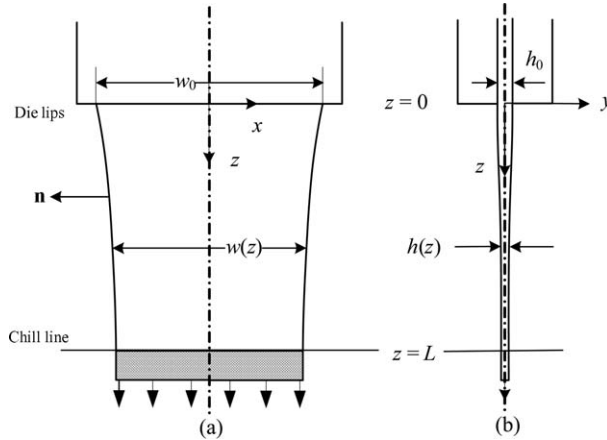
Use the assumption made in Problem 14.1

14.4 Transport Equations for Nonisothermal Fiber Stretching Starting from the momentum and thermal energy balances, derive Eqs. E14.1-1 and E14.1-3, which are used for the description of the nonisothermal stretching of molten polymer fibers. (a) Discuss in detail the assumptions made, and specifically discuss the nature of F_D and its inclusion in the momentum balance (e.g., “Where did it come from?”); the relative magnitude of gravity (use real $\bar{\eta}$ and $\dot{\epsilon}$ data); the form of the entire Eq. 14.1-3 and the absence of radial temperature gradients. (b) What additional complexities to the solution of the problem would the inclusion of dT/dr bring?

14.5 Estimation of $T(r = 0, t)$ in Melt-Spun Fibers (a) From $T(x_1, \alpha t)$ values of the accompanying figure (x_1 is the characteristic length equivalent to the radius of the cylinder) calculate the centerline temperature of a HDPE melt strand exiting the spinneret at 240°C at a take-up speed of 50 m/min, a mass flow rate of 1.93 g/min, at distances 50 cm and 10 cm below the spinneret plate. Assume that no change in phase occurs and that the heat-transfer coefficient is $10^{-3} \text{ cal/cm}^2 \cdot \text{s} \cdot \text{K}$, $k = 8 \times 10^{-4} \text{ cal/cm} \cdot \text{s} \cdot \text{K}$, $\rho = 0.75 \text{ g/cm}^3$, $C_p = 0.5 \text{ cal/g}$, and the cooling-medium temperature is 25°C. (b) What can you conclude about the magnitude of dT/dr relative to dT/dz ?



14.6 Isothermal Film Casting of a Newtonian Melt⁵ The film casting process is shown schematically on the accompanying figure.



For very thin films $|\nabla h \ll 1|$, both h and w decrease with increasing z . The analysis of this case for a Newtonian melt being film cast nonisothermally has been treated by Pearson [J. R. A. Pearson, *Mechanics of Polymer Processing*, Elsevier, New York, 1985]. (a) For thicker films the deformation of the melt can be considered as one where only $h = h(z)$ and $w = w_0$. Use the continuity and z -momentum equations, neglecting inertial terms, gravity, and air-drag forces, to obtain the following expressions for $h(z)$ and $v_z(z)$:

$$h(z) = h_0 \exp\left(\frac{-z\rho F}{\bar{\eta}_{pl}\dot{m}}\right) = h_0 D_R^{-z/L}$$

$$v_z(z) = v_{z0} \exp\left(\frac{-z\rho|F|}{\bar{\eta}_{pl}\dot{m}}\right) = v_{z0} D_R^{-z/L}$$

where

$$D_R = \exp\left(-\frac{\rho FL}{\bar{\eta}_{pl}\dot{m}}\right)$$

F is the force necessary to draw the film, ρ is the melt density, and $\bar{\eta}_{pl} = 4\mu$, thus, $\pi_{zz} = -4\mu(dv_z/dz)$.

(b) Prove that the following relationship holds for isothermal and Newtonian fiber spinning and film casting:

$$\frac{[\ln D_R]_{\text{spin.}}}{[\ln D_R]_{\text{cast.}}} = \frac{4}{3}$$

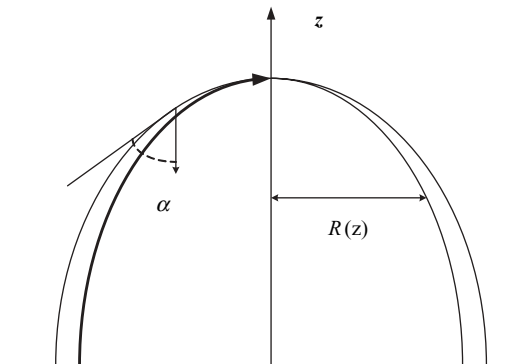
5. D. G. Baird and D. I. Collias, *Polymer Processing*, Wiley, New York, 1998, Chapter 9.

14.7 Free Sheet Blowing Free bubble blowing of heat-softened polymeric sheets is a good test for thermoformability of polymers.⁶ The bubble behaves as a membrane with rotational symmetry, as shown in the accompanying figure. The shape of the membrane is specified by a meridian curve $r(z)$ and the thickness distribution $\delta(z)$. The two principal radii of curvature of the surface R_L and R_C , in the meridian (longitudinal) and circumferential (hoop) directions, respectively, are related to $r(z)$ as follows:

$$R_C = r\sqrt{1 + (dr/dz)^2} \quad R_L = \frac{[1 + (dr/dz)^2]^{3/2}}{d^2r/dz^2}$$

By symmetry, the two principal directions of stress (and strain) are in the meridian direction, π_{11} , and the circumferential direction π_{33} . The third principal stress is zero. Show that if body and acceleration forces are neglected, the following equilibrium equations are obtained for thin membranes:

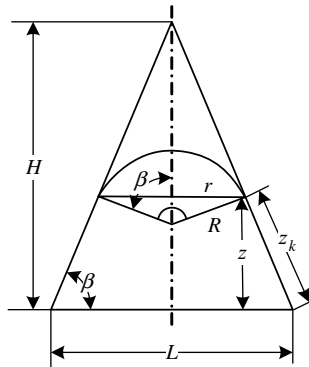
$$\Delta P = -\delta \left(\frac{\pi_{11}}{R_L} + \frac{\pi_{33}}{R_C} \right) - \frac{d}{dz} (r\delta\pi_{11} \cos \theta) = r \left(\frac{dr}{dz} \Delta P \right)$$



14.8 Wall Thickness Distribution in a Conical Mold Consider a thermoforming process of heat-softened polymeric sheet of thickness h_0 into a cold conical mold, as shown in the accompanying figure. Assuming incompressible polymer, elastic deformation, uniform spherical bubble thickness at the time of contacting the conical mold, frictionless contact, and immediate freezing of the plastic upon contact, show the thickness distribution is given by:

$$\frac{h}{h_0} = \frac{1 + \cos \beta}{2} \left(1 - \frac{z_k}{H} \sin \beta \right)^{\sec \beta - 1}$$

6. L. R. Schmidt and J. F. Carley, "Biaxial Stretching of Heat Softened Plastic Sheets: Experiments and Results," *Polym. Eng. Sci.*, **15**, 51–62 (1975).



14.9 Wall Thickness—Thermoforming a Cup Consider a cup 6 cm in diameter throughout its height and 10 cm high, which has to be made out of a 1.5-mm-thick molten high impact polystyrene (HIPS) sheet. Derive an expression for the thickness distribution assuming that the free bubble is of spherical shape until its top reaches the mold bottom, once the bubble touches the mold, no further deformation occurs, and the thickness of the free bubble at any stage of its deformation is spatially uniform. Once the melt touches the bottom of the mold, the deformation that fills the corners can be represented by spherical sections of successively smaller radii and centers that move diametrically to the corners.

14.10 Blown Film Deformation during Folding by the “Tent” and the Nip Rolls⁷ In the film blowing process the solidified round film bubble comes into contact with a series of guides (slats or rollers) that form the “tent,” and gradually collapses into a folded configuration between the nip rolls. Folding the bubble and feeding it into the nip rolls impose a deformation on the film, which is a function of the angle θ in the plane of the cross section of the bubble. The deformation results from the fact that each “fiber” of the film, that is, at each θ , travels a distance $L(\theta)$ that is different from the last round cross section to the nip rolls. Derive an expression for this deformation. What effect does it have on the wrapping step following the slitting?

7. William Arruda, private communication.

15 Calendering

- 15.1 The Calendering Process, 865
- 15.2 Mathematical Modeling of Calendering, 867
- 15.3 Analysis of Calendering Using FEM, 873

15.1 THE CALENDERING PROCESS

Two-roll mills and calenders belong to the earliest group of equipment used for processing natural rubber. They were introduced in the 1830s by Edwin Chaffee and Charles Goodyear in the United States, as described in Section 1.1. The number of rolls of a calender is determined by the nature of material processed and the product. Rubber can be calendered on a two-roll calender, with four-roll calenders generally used for double coating of substrates [Fig. 15.1(a)]. However, the surface quality requirements of calendered thermoplastic polymer require four-roll calenders [Figs. 15.1(b), 15.1(c)]. Therefore, when calendering polymers, the material passes three nip regions. The first pass is the “feed” pass, the second, the “metering” pass, and the third, the “sheet formation, gauging, and finishing” pass (1). Calenders with five rolls in various arrangements are also used.

Transfer from one roll to the next is accomplished by some combination of differentials in roll speed, temperature, and surface finish (2). The width of the sheet (when the speed of both rolls is equal) changes at each nip in inverse proportion to the decrease in thickness. The production rate of a calendering line, when not limited by the mixing and melting capacity upstream, is determined primarily by the size and surface requirements of the product and the properties of the polymer (1). Thus, heavy sheets of 0.25 mm and up can be produced at 60 m/min without difficulty. Even higher speeds are possible if the sheet is posttreated (e.g., embossed, top coated). However, certain rigid, glossy, roller-polished sheets are produced at much lower rates of 10–35 m/min. Thin flexible films can be produced at 100 m/min at the roll and 125 m/min at the winder. The higher speed at the winder is due to a drawdown process that helps in producing thin films (0.04 mm and below); films of such thickness would be hard to separate from the roll.

Calender sizes range up to 90 cm (36 in) in diameter and 250 cm (97 in) wide, with polymer throughputs up to 4000 kg/h. The surface temperature of the rolls is carefully controlled by using drilled rolls—that is, axially drilled holes all around the periphery—in which a temperature-controlling liquid is circulated.

The calendering process is commonly used for shaping high melt viscosity thermoplastic sheets and is particularly suitable for polymers susceptible to thermal degradation or containing substantial amounts of solid additives. This is because the calender can convey large rates of melt with a small mechanical energy input (compared to an extruder).

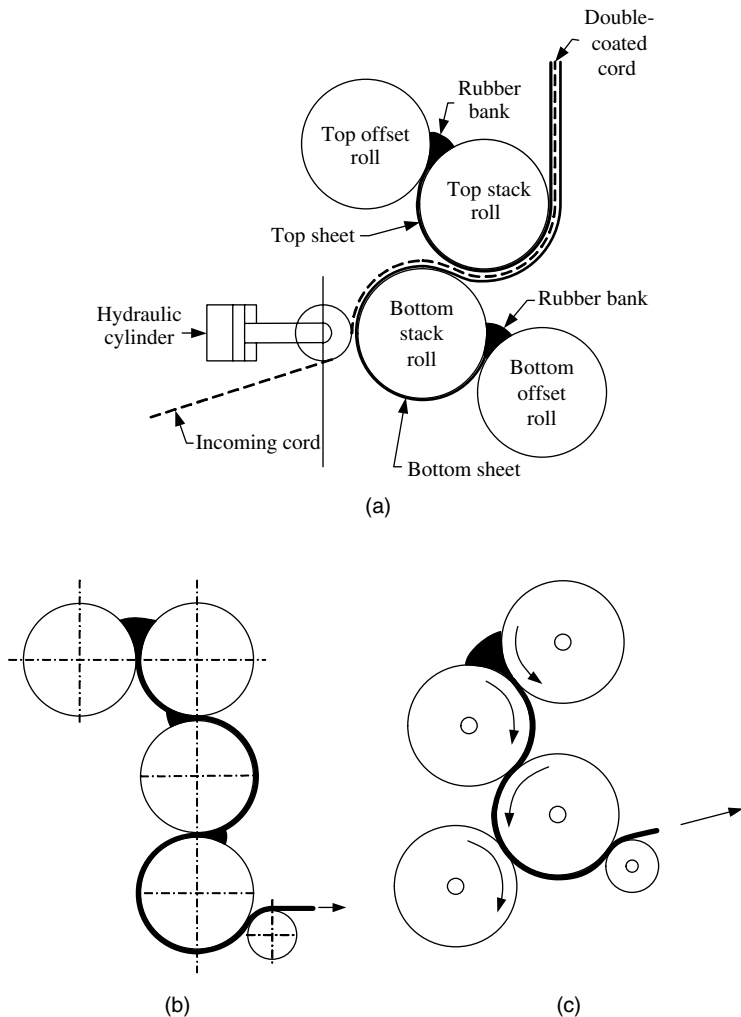


Fig. 15.1 (a) A four-roll, inclined “Z” calender for double casting of tire cord. (b) A four-roll, inverted “L” calender. (c) A four-roll “Z” calender.

The thickness of the calendered product must be uniform in both the machine and cross-machine directions. Any variation in gap size due to roll dimensions, setting, thermal effects, and roll distortion due to high pressures developing in the gap, will result in product nonuniformity in the cross-machine direction. Eccentricity of the roll with respect to the roll shaft, as well as roll vibration and feed uniformity, must be tightly controlled to avoid nonuniformity in the machine direction. A uniform empty gap size will be distorted in operation because of hydrodynamic forces, developed in the nip, which deflect the rolls. The resulting product from such a condition will be thick in the middle and thin at the edges, as shown in Fig. 15.2.

Three common methods, which are commonly referred to as *roll-crown*, *roll-crossing*, and *roll-bending*, are employed to compensate for this deformation. Roll-crown indicates that the roll diameter at the center is slightly greater than at the edges. In principle, by applying an appropriate roll diameter and profile, roll deflection can be exactly

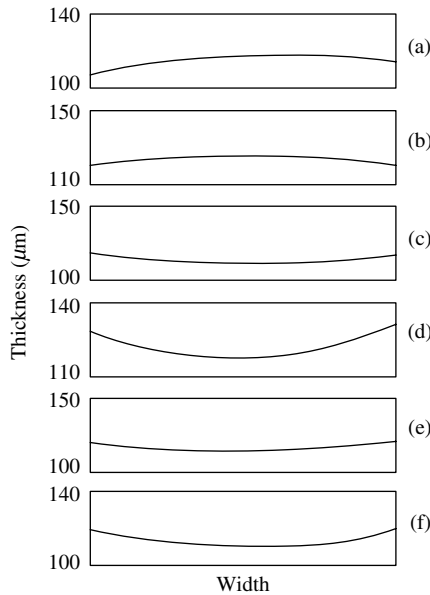


Fig. 15.2 Effect of roll-crossing and -bending on web uniformity in a calender 1.8 m wide. (a) No crossing or bending. (b) Crossing, 4 mm; no bending. (c) Crossing, 8 mm; no bending. (d) Crossing, 12 mm; no bending. (e) No crossing, bending of 10 Mp. (f) No crossing, bending of 16 Mp. [Reprinted by permission from D. Katz, “An Inquiry on the Behavior of Bingham Materials in Calender Processing,” M. S. Thesis, Department of Mechanics, Technion—Israel Institute of Technology, Haifa, 1973.]

compensated for *given* operating conditions. Roll-crossing and roll-bending provide means for continuous adjustment of gap size distribution. Roll-crossing results in a wider gap at the edges and can easily be visualized as giving the same effect as increasing the roll-crown. In roll-bending, a bending moment is applied on both ends of the roll by two additional bearings, which can increase or decrease the bending due to hydrodynamic forces.

Figure 15.2 shows the effect of roll-crossing and roll-bending on product uniformity. An exact knowledge of the hydrodynamic pressure distribution in the nip is therefore necessary for predicting by structural analysis the exact gap thickness distribution, as well as the load on the bearings; we discuss this in Section 15.4. Accurate gap thickness control and stringent roll temperature uniformity requirements are indicative of the sensitivity of the product quality to minor variations in conditions. It is not surprising, therefore, that a calender line takes a long time, sometimes hours, to “stabilize,” that is, to reach steady state. Consequently calender lines are best utilized in long production runs. The ruggedness and basic simplicity of the machine elements involved are fully compatible with such long runs.

15.2 MATHEMATICAL MODELING OF CALENDERING

A comprehensive mathematical model of the calendering process should consist of a coupled hydrodynamic and roll structural analysis, heat transfer in the deforming polymer

and the rolls, and product response to drawdown. By taking into account the rheological properties of the material, feed conditions, and operating conditions, such as roll speeds and temperatures, gap separation, roll-crossing and -bending, the following matters can be ascertained: the exact nature of the flow in the nip, the width variation from nip to nip, and the thickness and temperature distribution, as well as the effect of these conditions on the transfer of the material from roll to roll, and the onset of instabilities. Such a model would assist the calender designer in selecting roll size, gap separation, roll-crown, -crossing, and -bending requirements, and operating conditions for given production rates and quality requirements.

The first step in developing such a model (cf. Section 6.4) is to gain a clear *qualitative* picture on the exact nature of the flow mechanism. A viscoelastic melt is fed into the first nip in strips. The melt accumulates in the center zone of the nip area and simultaneously undergoes flow into the nip and sideways; the drag-induced flow leads to pressure buildup, which inevitably produces pressure gradients in the machine and cross-machine directions, resulting in the flow above. Experimental evidence of such a pressure distribution is given by Unkrüer (3), who reports on detailed calendering studies of polyvinyl chloride (PVC) and polystyrene (PS).

Figure 15.3 gives pressure profiles at three cross-machine locations. Thus, a complex three-dimensional flow field is set up with an a priori, unspecified free boundary. Axial flow (cross-machine direction) continues throughout the nip zone all the way to the exit, but the rate varies because of the varying gap size. That is, in the narrow region of the nip, drag flow in the direction of rotation is predominant as compared to cross-machine pressure flow.

According to Marshall (2), it can be assumed that the increase in width is virtually limited to the entrance zone up to where the peak pressure is obtained. The actual flow in the nip area is further complicated because the gap clearance varies axially as a result of built-in roll-crowns, hydrodynamic flexing, and bending of the rolls. All these factors should bring about a flow distribution in the nip area that results in

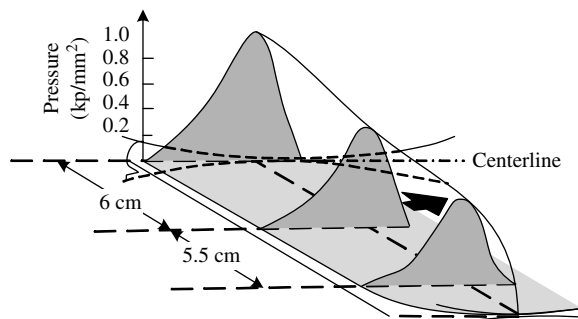


Fig. 15.3 Pressure profiles in the calender gap at various cylinder axial positions, with rigid PVC (Vestolit Z 1877) at equal roll speeds of 5 cm/s and roll temperature of 185°C: minimum gap, 0.6 mm; roll diameter, 30 cm; width, 50 cm. Note the drop in pressure in the cross-machine direction with distance from the centerline, which drops to zero at the end of the rolled web. [Reprinted by permission from W. Unkrüer, Doctoral Thesis, IKV, Technischen Hochschule, Aachen, 1970.]

uniform flow rate per unit width. Minor variations of pressure profiles in the direction of rotation will cause variations in detachment locations, and hence, thickness variations.

In light of the preceding qualitative picture, we can understand recent developments in a modified calendering process, where an extruder equipped with a simple and short sheet forming die feeds the nips uniformly throughout the nip width of only one pair of calender rolls. The sheet forming die therefore performs the functions of the first nip—namely, spreading out the material and feeding it at a more or less uniform rate to the second nip.

The functions of the second and third nips are a further reduction of the thickness and of the flow rate nonuniformities in both the machine and cross-machine directions. The rolling banks in all nips act as reservoirs that can accommodate and attenuate flow rate fluctuations. Thus, no sharp qualitative distinction should be made between the functions of the three nips; it is the relative significance of the various functions that changes from nip to nip. All nips “meter” flow rate, reduce thickness, and “wash out” variations in thickness and flow rate to various degrees (just as in plasticating screw extruders, flow rate is determined by the whole length of the screw, not merely by the “metering” section). Clearly there is no simple analytical mathematical solution to this three-dimensional flow in a complex geometry (variable gap thickness in two directions) with rheologically complex fluids under nonisothermal conditions.

Most models proposed in the literature are based on Gaskell’s (4) model, which was discussed in detail in Section 6.4. This is a one-dimensional, rather restrictive model. Recall that to use the model, we must know the location X_1 where the sheet detaches from one of the rolls (X_1 is uniquely related to X_2 , the upstream location where the rolls come in contact with the polymer). This is tantamount to an a priori knowledge of the exiting sheet thickness, $2H_1$. The latter, however, for a given flow rate, Q , depends on the exiting sheet width W_1

$$Q = 2H_1 W_1 U \quad (15.2-1)$$

where U is the velocity of the roll surface. But W_1 cannot be predicted from a one-dimensional model (which implicitly assumes infinitely wide rolls), hence as McKelvey (5) pointed out, X_1 (or H_1) must be considered to be an experimentally determined parameter of the model. This, of course, restricts the predictive capability of the model. To overcome this problem, the previously discussed cross-machine flow must be incorporated into the model.

This, however, is not the only limitation of the Gaskell model. As discussed in Section 6.4, this model fails to predict the experimentally observed flow patterns in the inlet region because it neglects the effect of the incoming melt stream on the flow in the bank, as well as the non-Newtonian and viscoelastic effects. Consequently, the model does not satisfactorily predict the observed pressure profiles, as shown by Bergen and Scott (6), Unkrüer (3), and others.

Following Gaskell’s work, a great deal of effort was invested by numerous researchers in the field to improve on his model. Most of this effort, however, basically concentrated on solving the Gaskell model with more realistic, constitutive equations and attempts to account for nonisothermal effects. In the original Gaskell model, a purely viscous (nonelastic and time-independent) fluid model is assumed, with specific

solutions for Newtonian and Bingham Plastic fluids, and a brief treatment of nonsymmetric calenders. McKelvey (5) and Brazinsky et al. (7) extended the model to Power Law fluids (as discussed in Section 6.4), and Alston and Astill (8) investigated fluids whose shear rate dependent viscosity can be represented by a hyperbolic tangent function.

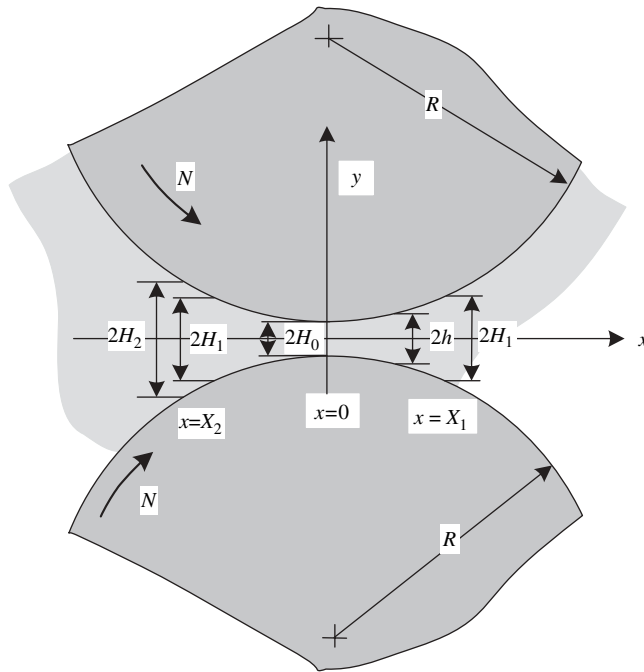
Flow of viscoelastic fluids in the roll geometry was considered by Paslay (9) and Tokita and White (10), and by Chong (11); Paslay's analysis is essentially based on a three constant Oldroyd model.¹ He analyzes the interrelations of the parameters of the constitutive equation with flow kinematics, but neglects the normal stresses in the equation of motion. Tokita and White (10) relate experimental observations on milling of elastomers to rheological parameters of a second order Rivlin–Ericksen asymptotic expansion fluid, and point out the significance of the Deborah number $De = \dot{\gamma}\lambda \cong (V/L)\lambda$ in milling and calendaring, where V and L are characteristic velocity and gap size. Following their analysis, Example 15.1 briefly explores the significance of normal stresses in calendaring. However velocity and pressure profiles were not obtained by them.

Chong (11) analyzed a Power Law model fluid, a three-constant Oldroyd fluid and a modified second order Rivlin–Ericksen fluid. He incorrectly stated that the shear rate and the shear stress attain maximum values at minimum clearance location, and in integrating for the velocity profile with the Power Law model fluids, did not properly account for the sign of the pressure gradient. The velocity profile for the Oldroyd fluid cannot be obtained analytically. Therefore Chong obtained an approximate pressure distribution by assuming Newtonian flow kinematics, and he analyzed the flow pattern with the Rivlin–Ericksen flow equation in terms of dimensionless groups only. He also measured the separating force at various calendaring conditions for cellulose acetate. Like Tokita and White (10), he found, upon analyzing experimental data of calendaring cellulose acetate, that the Deborah number is an important number in determining the onset of a nonuniform internal strain pattern, called *nerve* in calendaring. Calendaring defects with PVC were studied in detail by Agassant et al. (12), who also measured separating force, torque power, and reservoir height-to-gap ratio (H_2/H_0) as a function of calendaring conditions.

With regard to constitutive equations, White (13) notes that, in view of the short residence time of the polymer in the nip region (of the order of magnitude of seconds), it would be far more realistic to use a constitutive equation that includes viscoelastic transient effects such as stress overshoot, a situation comparable to that of squeezing flows discussed in Section 6.6.

Example 15.1 The Significance of Normal Stresses We consider the calender geometry of Fig. 6.22 (shown here) and make the same simplifying assumptions as in Section 6.4, but instead of a Newtonian or Power Law model fluid, we assume a CEF model that exhibits normal stresses in viscometric flows. By accepting the lubrication approximation, we assume that locally we have a fully developed viscometric flow because there is only one velocity component v_x , which is a function of only one spatial variable y .

1. The three constant Oldroyd model is a nonlinear constitutive equation of the differential corrotational type, such as the Zaremba–Fromm–Dewitt (ZFD) fluid (Eq. 3.3-11). [For details, see R. B. Bird, R. C. Armstrong, and O. Hassager, *Dynamics of Polymeric Liquids*, Second Edition, Vol. 1, Wiley, New York, 1987, Table 7.3-2.]



An analysis similar to that carried out in Section 6.5 leads to the following, nonvanishing stress components

$$\tau_{xx} = -(\Psi_1 + \Psi_2)\dot{\gamma}^2 \tag{E15.1-1}$$

$$\tau_{yy} = -\Psi_2\dot{\gamma}^2 \tag{E15.1-2}$$

where $\dot{\gamma} = |\dot{\gamma}_{yx}|$ is the shear rate and

$$\dot{\gamma}_{yx} = \frac{dv_x}{dy} \tag{E15.1-3}$$

which is assumed to be independent of x locally. The three components of the equation of motion then reduce to

$$\frac{\partial P}{\partial x} = -\frac{\partial \tau_{yx}}{\partial y} \tag{E15.1-4}$$

$$\frac{\partial P}{\partial y} = -\frac{\partial \tau_{yy}}{\partial y} \tag{E15.1-5}$$

$$\frac{\partial P}{\partial z} = 0 \tag{E15.1-6}$$

Comparing with the solution in Section 6.4, we observe that instead of a single differential equation for the velocity profile, two coupled (through $\dot{\gamma}$) differential equations are obtained. However, the kinematics can be well approximated by assuming $\partial P/\partial y = 0$, which then will

lead to the same velocity profile given in Section 6.4. Moreover, we note that the pressure at the roll surface will differ from that of the simple model by a term $-\Psi_2\dot{\gamma}^2$. Since Ψ_2 is found to be negative, this normal stress contribution adds to the pressure at the roll surface. Hence, it is the secondary normal difference function that plays a role in calculating the forces on the calender roll. This can probably be assumed to be small.

The present analysis was based on the lubrication approximation; that is, we neglected changes in the x direction. If this assumption is lifted, we are faced with a flow field in which two nonvanishing velocities exist that are functions of two spatial coordinates, $v_x(x, y)$, $v_y(x, y)$. This is clearly a nonviscometric flow situation, and the Criminale–Ericksen–Filbey (CEF) equation is not applicable. White (13) made an order of magnitude evaluation of normal stress effects for this more realistic flow situation. In this case, the equation of motion reduces to

$$-\frac{\partial P}{\partial x} = \frac{\partial \tau_{yx}}{\partial y} + \frac{\partial \tau_{xx}}{\partial x} \quad (\text{E15.1-7})$$

and

$$-\frac{\partial P}{\partial y} = \frac{\partial \tau_{yx}}{\partial x} + \frac{\partial \tau_{yy}}{\partial y} \quad (\text{E15.1-8})$$

which can be combined by respective differentiation into one equation

$$\frac{\partial^2 \tau_{yx}}{\partial y^2} - \frac{\partial^2 \tau_{yx}}{\partial x^2} + \frac{\partial^2}{\partial x \partial y} (\tau_{xx} - \tau_{yy}) = 0 \quad (\text{E15.1-9})$$

Expressing the various terms in Eq. E15.1-9 at the roll surface as orders of magnitude, we get

$$\frac{\tau_w}{H_0^2}; \quad \frac{\tau_w}{R^2}; \quad \frac{\tau_{xx} - \tau_{yy}}{H_0 R} \quad (\text{E15.1-10})$$

where H_0 and R are gap clearance and roll radius, respectively. If $R \gg H_0$, the second term is negligible. The third term, which reflects the primary normal stress difference, is also negligible, provided

$$\frac{R}{H_0} \tau_w \gg \tau_{xx} - \tau_{yy} \quad (\text{E15.1-11})$$

The preceding condition is met at low shear rates, but it begins to break down with increasing shear rate when $\tau_{xx} - \tau_{yy}$ increases rapidly, as indicated in Fig. E3.2b.

In the Gaskell model, the flow geometry is simplified to facilitate the solution (see Eq. 6.4-13). This geometrical simplification can be avoided either by using bipolar coordinates or finite element methods (FEMs). Both provide a convenient way to treat calenders of unequal rolls and unequal speeds. The former approach was taken by Finston (14), Takserman-Krozer et al. (15), and Bekin et al. (16), whereas the latter was chosen by Kiparissides and Vlachopoulos (17). Finally, the Gaskell model is isothermal, whereas in calendaring, significant nonisothermal effects arise because of viscous dissipation and heat conduction to the temperature-controlled rolls.

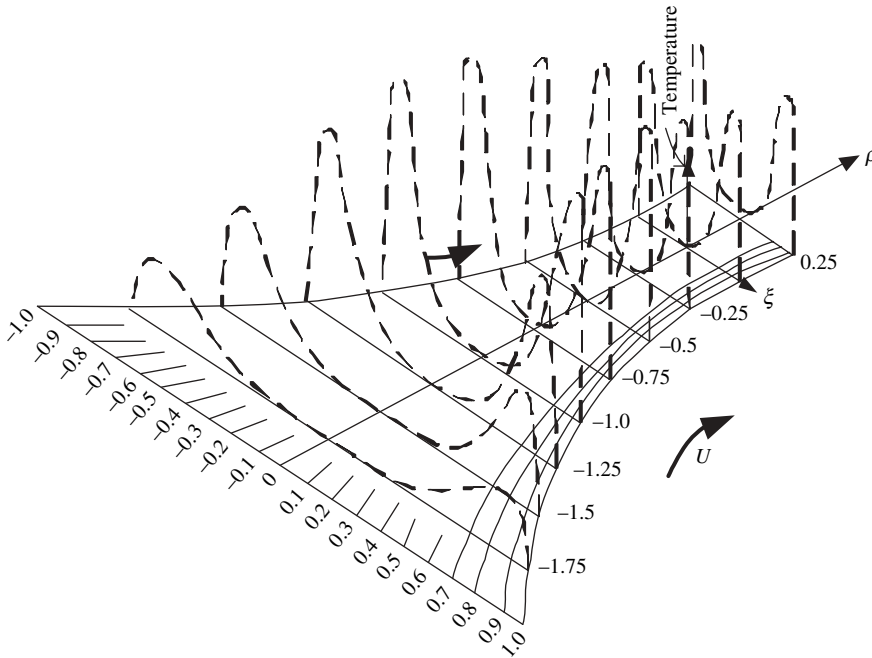


Fig. 15.4 Schematic temperature distribution based on data given by Torner (18).

Finston (14) was the first to deal with viscous heating of Newtonian fluids. Torner (18) reported on an experimental study by Petrusanskii and Stachaev (19) on the calendering of styrene-butadiene rubber (SBR) on a 12×32 -cm calender. Figure 15.4 is a schematic view of the reported temperature profiles. Characteristic to the temperature profiles is the existence of two maxima in the vicinity of the rolls. This is the combined effect of a shear rate profile with a maximum value at the roll surface and heat conduction to the temperature-controlled roll surface. The temperature profile has a minimum at the center plane. The temperature profiles change in the machine direction, with a gradual temperature rise at the center plane and more complex behavior in the vicinity of the rolls. It should be noted that these temperature profiles do not refer to recirculating regions in the entry to the calender gap. Temperature effects were also studied by Bekin et al. (16), using bipolar coordinates and temperature dependent fluid viscosity.

15.3 ANALYSIS OF CALENDERING USING FEM

The FEM, which was originally developed for structural analysis of solids, has been very successfully applied in the past decades to viscous fluid flow as well. In fact, with the exponentially growing computer power, it has become a practical and indispensable tool for solving complex viscous and viscoelastic flows in polymer processing (20) and it is the core of the quickly developing discipline of computational fluid mechanics (cf. Section 7.5).

One of the first applications of FEM in polymer processing is a result of the work of Vlachopoulos and Kiparissides (21,22). Some of the computed results obtained by this

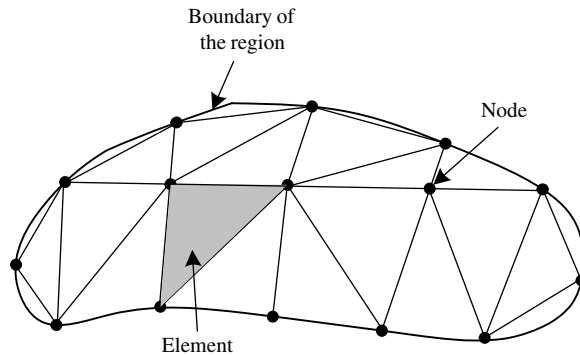


Fig. 15.5 Two-dimensional region represented as an assemblage of triangular elements.

method are discussed later in this chapter. The use of FEM in calendering has the added advantage that it can, in principle, be combined with a structural FEM analysis of the rolls accounting for roll deflections.

The principles and applications of FEM are described extensively in the literature (e.g., 23–26). FEM is a numerical approximation to continuum problems that provides an *approximate*, piecewise, continuous representation of the unknown field variables (e.g., pressures, velocities).

The continuous region or body is subdivided into a *finite* number of subregions or *elements* (Fig. 15.5). The elements may be of variable size and shape, and they are so chosen because they closely fit the body. This is in sharp contrast to finite difference methods, which are characterized by a regular size mesh, describable by the coordinates that describe the boundaries of the body.

The crossing of two curves bounding adjacent elements form *nodes*. The values of the field variables at the nodes form the desired solution. Common shapes of finite elements are triangular, rectangular, and quadrilateral in two-dimensional problems, and rectangular, prismatic, and tetrahedral in three-dimensional problems. Within each element, an interpolation function for the variable is *assumed*. These assumed functions, called *trial functions* or *field variable models*, are relatively simple functions such as truncated polynomials. The number of terms (coefficients) in the polynomial selected to represent the unknown function must at least equal the degrees of freedom associated with the element. For example, in a simple one-dimensional case [Fig. 15.6(a)], we have two degrees of freedom, P_i and P_j , for a field variable $P(x)$ in element e . Additional conditions are needed for more terms (e.g., derivatives at nodes i and j or additional internal nodes).

The chosen function must satisfy certain additional requirements. Not only must it be continuous throughout the element, but also compatible across element interfaces. In the simple case [Fig. 15.6(b)], this means $P_a = P_b$ at the node m is common to elements a and b . Thus the coefficients of a selected trial function can be expressed in terms of the (unknown) values of the field variables at the nodes. For a two-dimensional case we can write for the field variable u ,

$$u^{(m)}(x, y) = \sum_{i=1}^r N_i(x, y) u_i^{(m)} \quad (15.3-1)$$

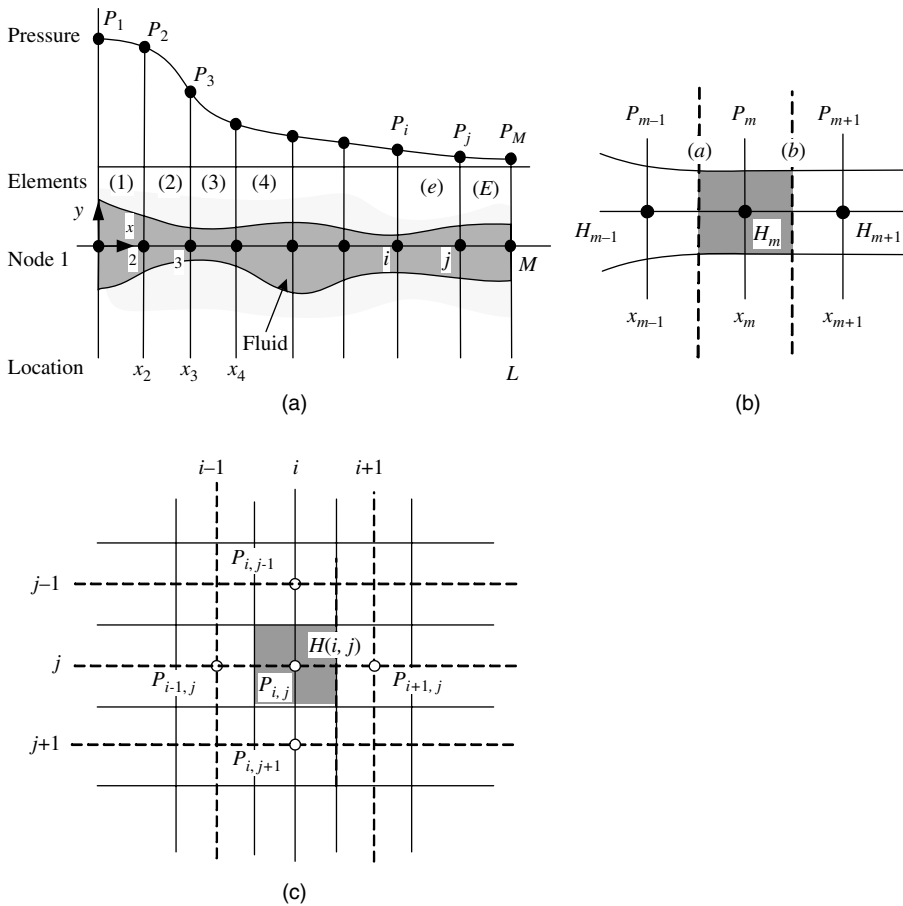


Fig. 15.6 (a) Side view of two infinite plates with a variable gap in the x direction. The region of interest $0 < x < L$ is broken up into E elements forming M nodes. A schematic pressure profile for one-dimensional pressure flow is plotted on the top. (b) Details of two neighboring elements a and b with the common node m . (c) Two-dimensional square elements representing flow analysis network model.

where the superscript denotes that the field is for the m th element, r is the number of nodes associated with this element, $u_i^{(m)}$ are the nodal values of the variable u , and $N_i(x,y)$ is the *shape function*. The function $N_i(x,y)$ is determined by the shape of the element, the location of the nodes, and the number of terms in the polynomial. Again, the objective is the numerical evaluation of u_i . The common approach to obtaining this is to set up the finite element equations either by “variational” methods or by “residual” methods, such as the *Galerkin method*. These, together with appropriate boundary conditions, result in a set of linear or nonlinear algebraic equations with the nodal variables u_i as unknowns.

Structural analysis, initially developed on an intuitive basis, later became identified with variational calculus, in which the Ritz procedure is used to minimize a *functional* derived mathematically or arrived at directly from physical principles. By substituting the final solutions into the variational statement of the problem and minimizing the latter, the FEM equations are obtained. Example 15.2 gives a very simple demonstration of this procedure.

However, in many cases (general non-Newtonian flow problems being among them), a variational principle either does not exist or its existence is not obvious. Nevertheless, these problems can often be defined by a set of differential equations (e.g., the equations of continuity and motion with a constitutive equation), together with their boundary conditions. In such cases, weighted residual methods such as the collocation and the Galerkin methods produce a simpler and direct formulation of the FEM equations (27). In the Galerkin method, the approximate interpolation function is substituted into the governing differential equations, multiplied by the weighting function, which is the relevant shape function, and integrated over the body. The resulting expressions are set to zero, leading to a set of algebraic equations.

Inherent in the FEM is the flexibility in dealing with complex geometries as well as mixed boundary conditions (e.g., stress and velocity boundary conditions as in a die-swell problem). Moreover, computationally, the FEM is not difficult to carry out. Not only can a continuous domain of complex boundary be easily broken down into well-fitting finite elements, but the inherent possibility exists of using elements of various sizes and shapes. This permits a refined solution in critical regions (corners, sudden changes in geometry, etc.) without the penalty of excessive computation in the rest of the regions, as would be the case with the more limited finite difference methods. Finally, it is noted by Oden et al. (28) that by certain function choices, the standard finite difference processes can be included in the general finite-elements concept.

Example 15.2 FEM Formulation of Isothermal Steady Pressure Flow in Narrow but Variable Thickness Gap of a Newtonian Fluid The governing differential equation is the Reynolds equation given for a two-dimensional flow in Eq. 2.11-11. To demonstrate the FEM formulation, we consider the one-dimensional flow case, for which Eq. 2.11-11 reduces to

$$\frac{d}{dx} \left(\frac{H(x)^3}{\mu} \frac{dP}{dx} \right) = 0 \quad (\text{E15.2-1})$$

We have retained the viscosity because we want to treat approximately the non-Newtonian fluids case later. If the function $H(x)$ is known, preceding the differential equation can be solved analytically or numerically for $P(x)$ in a straightforward method without turning to FEM. Our purpose here, however, is to demonstrate the FEM method and, following Myers (29), we do so in a step-by-step fashion.

The flow configuration appears in Fig. 15.6(a). The one-dimensional conduit of length L is broken down into E elements, bounded by M nodes. Our objective is to set up the FEM equations that will give the pressure values P_i .

The first step is to derive the *variational statement* of the problem. This can be done with the aid of the Lagrange–Euler equation

$$\frac{\partial F}{\partial P} - \frac{d}{dx} \left(\frac{\partial F}{\partial \dot{P}} \right) = 0 \quad (\text{E15.2-2})$$

which must be satisfied for the following *functional* I

$$I = \int_0^L F(x, P, \dot{P}) dx \quad (\text{E15.2-3})$$

to be an *extremum*. Comparison of Eqs. E15.2-1 and E15.2-2 gives the following expressions for F :

$$\frac{\partial F}{\partial P} = 0 \quad (\text{E15.2-4})$$

and

$$\frac{\partial F}{\partial \dot{P}} = \frac{H^3}{\mu} \dot{P} \quad (\text{E15.2-5})$$

Integration of Eqs. E15.2-4 and E15.2-5, respectively, gives

$$F = K_0 + f(\dot{P}) \quad (\text{E15.2-6})$$

and

$$F = \frac{H^3}{2\mu} (\dot{P})^2 + g(P) \quad (\text{E15.2-7})$$

Comparing Eqs. E15.2-6 and E15.2-7, we note $g(P) = K_0$ and $f(\dot{P}) = (H^3/2\mu)(\dot{P})^2$; thus, F can be written as

$$F = K_0 + \frac{1}{2} \frac{H^3}{\mu} (\dot{P})^2 \quad (\text{E15.2-8})$$

Hence, the variational statement of this problem reduces to obtaining the extremum of the functional

$$I = \int_0^L \left[K_0 + \frac{1}{2} \frac{H^3}{\mu} (\dot{P})^2 \right] dx \quad (\text{E15.2-9})$$

that is, we are searching for the unknown *function* $P(x)$ that, when substituted into Eq. E15.2-9, gives an extremum for I . To evaluate I , we break it down into E subintegrals corresponding to the E elements

$$I = I^{(1)} + I^{(2)} + \dots + I^{(E)} = \sum_{e=1}^E I^{(e)} \quad (\text{E15.2-10})$$

The integral $I^{(e)}$ over a typical finite element is

$$I^{(e)} = \int_{x_i}^{x_j} \left[K_0 + \frac{1}{2} \frac{H^3}{\mu} (\dot{P})^2 \right] dx \quad (\text{E15.2-11})$$

We now *assume* a linear trial function for the variation of the pressure within each element

$$P^{(e)} = C_1^{(e)} + C_2^{(e)} x \quad (\text{E15.2-12})$$

We thus have two coefficients, and since we have two degrees of freedom—the (unknown) nodal values of the pressures—we can express the former in terms of the latter, and Eq. E15.2-12 can be written as

$$P^{(e)} = \left(\frac{x_j - x}{x_j - x_i} \right) P_i + \left(\frac{x - x_i}{x_j - x_i} \right) P_j \quad (\text{E15.2-13})$$

Note that Eq. E15.2-13 is of the same form as Eq. 15.3-1. Next we take the derivative of $P^{(e)}$ given in Eq. E15.2-13 with respect to x

$$\dot{P} = \frac{dP^{(e)}}{dx} = \frac{P_j - P_i}{x_j - x_i} \quad (\text{E15.2-14})$$

and substitute it into Eq. E15.2-11 which, after integration, gives

$$I^{(e)} = K_0(x_j - x_i) + \frac{1}{2} \frac{H^3}{\mu} \frac{(P_j - P_i)^2}{(x_j - x_i)} \quad (\text{E15.2-15})$$

We have assumed in the foregoing integration that μ is constant within the element and equal to the average value in it.

Next we differentiate $I^{(e)}$ with respect to the nodal pressures P_i and P_j

$$\frac{\partial I^{(e)}}{\partial P_i} = - \frac{H^3}{\mu} \frac{P_j - P_i}{x_j - x_i} \quad (\text{E15.2-16})$$

and

$$\frac{\partial I^{(e)}}{\partial P_j} = \frac{H^3}{\mu} \frac{P_j - P_i}{x_j - x_i} \quad (\text{E15.2-17})$$

where $I^{(e)}$ is a function of P_i and P_j only, whereas I (in Eq. E15.2-10) is a function of P_1, P_2, \dots, P_M . To find the extremum of I , we must differentiate I with respect to all P_i , and set the results equal to zero, obtaining M equations. Thus, differentiating Eq. E15.2-10 with respect to a typical nodal pressure P_m , we get

$$\frac{\partial I}{\partial P_m} = \frac{\partial I^{(1)}}{\partial P_m} + \frac{\partial I^{(2)}}{\partial P_m} + \dots + \frac{\partial I^{(E)}}{\partial P_m} = 0 \quad (\text{E15.2-18})$$

But the pressure P_m appears only in two neighboring elements, as Fig. 15.6(b) shows. For element a we set $i = m - 1$ and $j = m$ in Eqs. E15.2-16 and E15.2-17, and for element b we set $i = m$ and $j = m + 1$ in the two previous equations, resulting in

$$\frac{\partial I^{(a)}}{\partial P_m} = \left(\frac{H^3}{\mu} \right)^{(a)} \frac{P_m - P_{m-1}}{x_m - x_{m-1}} \quad (\text{E15.2-19})$$

and

$$\frac{\partial I^{(b)}}{\partial P_m} = - \left(\frac{H^3}{\mu} \right)^{(b)} \frac{P_{m+1} - P_m}{x_{m+1} - x_m} \quad (\text{E15.2-20})$$

where the superscripts a and b on H^3/μ indicate that mean local values are used. Adding Eqs. E15.2-19 and E15.2-20, and equating the sum to zero, we get

$$\left(\frac{H^3}{\mu} \right)^{(a)} \frac{P_m - P_{m-1}}{x_m - x_{m-1}} + \left(\frac{H^3}{\mu} \right)^{(b)} \frac{P_m - P_{m+1}}{x_{m+1} - x_m} = 0 \quad (\text{E15.2-21})$$

Since m is any interior nodal point, Eq. E15.2-21 is a set of $M - 2$ algebraic equations, the solution of which provides the required pressure field (profile).

As a numerical example, consider a linearly decreasing gap broken down into four equal length elements. The gaps at the entrance and at the exit are 1 and 0.5 cm, respectively. Thus $H_1 = 1$, $H_2 = 0.875$, $H_3 = 0.75$, $H_4 = 0.625$, and $H_5 = 0.5$. The inlet pressure is 1 atm, and the exit pressure is zero. The resulting equations from Eq. E15.2-21, with constant viscosity, are

$$\begin{aligned} -1.53618 + 2.53618P_2 - P_3 &= 0 \\ -1.6506P_2 + 2.6506P_3 - P_4 &= 0 \\ -1.8257P_3 + 2.8257P_4 &= 0 \end{aligned}$$

which, upon solution, give $P_2 = 0.897$, $P_3 = 0.738$, and $P_4 = 0.477$. The exact analytical solutions obtained by integrating Eq. E15.2-1 are $P_2 = 0.8980$, $P_3 = 0.7407$, and $P_4 = 0.480$, which agree well with the FEM solution using only four elements.

Equation E15.2-21 can also be derived by a “controlled volume” approach. Consider the a element confining node m in Fig. 15.6(b) (shaded area). For an incompressible fluid and under the same assumptions as earlier we can make the following flow rate balance

$$\underbrace{\frac{1}{12} \left(\frac{H^3}{\mu} \right)^{(a)} \frac{P_{m-1} - P_m}{x_m - x_{m-1}}}_{\text{Rate of flow into element}} = \underbrace{\frac{1}{12} \left(\frac{H^3}{\mu} \right)^{(b)} \frac{P_m - P_{m+1}}{x_{m+1} - x_m}}_{\text{Rate of flow out of element}} \quad (\text{E15.2-22})$$

The FEM formulation of two-dimensional problems is not different in principle from the simple one-dimensional case just described. For two-dimensional problems, however, the algebra becomes involved and matrix notation is required to keep it manageable.

Example 15.3 The Flow Analysis Network Method Clearly Eq. E15.2-22 is identical to Eq. E15.2-21. This is the basis for the flow analysis network (FAN) method developed by Tadmor et al. (30) to solve two-dimensional steady or quasi-steady state flow problems in injection molds and extrusion dies. In two-dimensional flows the pressure distribution is obtained by dividing the flow region into an equal-sized mesh of square elements

[Fig. 15.6(c)]. At the center of each element there is a node. The nodes of adjacent elements are interconnected by links. Thus, the total flow field is represented by a network of nodes and links. The fluid flows out of each node through the links and into the adjacent nodes of the network. The local gap separation determines the “resistance” to flow between nodes. Making the quasi-steady state approximation, a mass (or volume) flow rate balance can be made about each node (as done earlier for one-dimensional flow), to give the following set of algebraic equations

$$X_{i,j}(P_{i,j} - P_{i+1,j}) + X_{i-1,j}(P_{i,j} - P_{i-1,j}) + Z_{i,j}(P_{i,j} - P_{i,j+1}) + Z_{i,j-1}(P_{i,j} - P_{i,j-1}) = 0 \quad (\text{E15.3-1})$$

where $X_{i,j}$ and $Z_{i,j}$ are “flow conductances” in the x and z directions, respectively:

$$X_{i,j} = \frac{1}{12\mu} \left(\frac{H_{i,j} + H_{i+1,j}}{2} \right)^3 \quad (\text{E15.3-2})$$

and

$$Z_{i,j} = \frac{1}{12\mu} \left(\frac{H_{i,j} + H_{i,j+1}}{2} \right)^3 \quad (\text{E15.3-3})$$

This two-dimensional formulation of the flow problem is identical in concept to the “discrete element method” or “lattice models” of classic structural analysis. Physically, the FEM concept differs from the lattice analogy in that the elements themselves are two- or three-dimensional bodies (31). The FAN method, however, is a straightforward, simple method, which was extended to deal with non-Newtonian fluids by replacing the Newtonian viscosity with an “equivalent Newtonian viscosity” (32). The latter is uniquely related to the local shear stress at the wall, which in turn depends on the local pressure gradient. Both can be converged upon by repeated solutions of the set of algebraic equations for P_{ij} , while in each iteration, the viscosities are recalculated. This method was applied by Tadmor et al. to cross-head die flow (33), mold filling (34), and flow in non-intermeshing twin screw extruders (35). White et al. (36) extended the method and applied it to intermeshing corotating twin screw extrusion flow. Both are two-dimensional, the first being steady while the second is assumed to be quasi-steady.

Mitsoulis, Vlachopoulos, and Mirza (37) were the first to lift the lubrication approximation in calendering flows and use FEM computational packages to obtain the flow and temperature fields in the bank and nip regions, with which we can calculate the pressure distribution, roll-separating force, torques, and power consumption to drive the rolls, as well as the nip entry and exit locations and the exit sheet thickness. They did the analysis for a Newtonian and a Power Law model fluid, with rheological constants representing a rigid PVC melt, which also exhibits slip (38). The FEM results are in fair agreement with experiments, but give only axysymmetric circulatory flows in the melt pool upstream from the nip. Park et al. (39) used the viscoelastic integral type Kaye-Bernstein- Kearsy-Zappas (K-BKZ) fluid model to simulate the converging flow using an FEM. Luo (40) used a finite volume method (FVM) and the integral K-BKZ to calculate the converging flow. Both groups of investigators did not integrate their fluid-mechanical results with the resulting roll deformations.

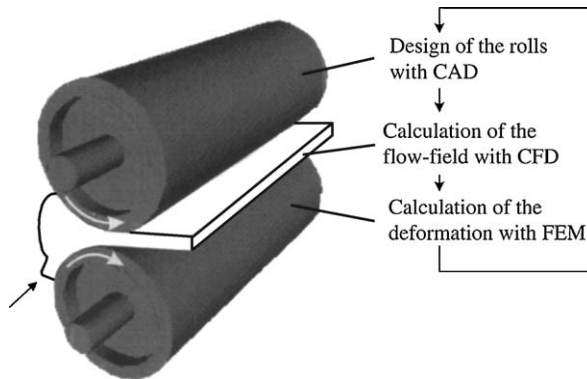


Fig. 15.7 Iterative computational scheme used by Mewes et al. [Reprinted by permission from D. Mewes, S. Luther, and K. Riest, “Simultaneous Calculation of Roll Deformation and Polymer Flow in the Calendering Process,” *Int. Polym. Process.*, **17**, 339–346 (2002).]

Recently, Mewes (41) utilized the FVM CFX4 computational package of Luo (40) and integrated it with the ANSYS solids structural FEM model to calculate the resulting roll deformations. The rolls were designed using a computer-aided design (CAD) program. Their iterative computational scheme is shown in Fig. 15.7.

The calender roll diameter profiles are designed using the CAD Pro/Engineer program and the isothermal flow field is calculated using the computational fluid mechanics FVM. With the resulting stress field as boundary conditions, the deformation of the rolls is calculated using ANSYS. If the resulting gap thickness determined by the initial diameter axial profile, flow, and axial separation force profile do not yield a uniform gap thickness, then the CAD design is changed as many times as it takes to obtain a gap spacing for the calendered material thickness that is uniform, that is, independent of the axial roll distance.

Conducting iterative flow calculations per se for given initial roll design was not carried out, since this requires large computational times. Three constitutive equations were used by Mewes et al: the K-BKZ with a damping function formulation by Papanastasiou et al. (42) for the polymer melt [a low density polyethylene (LDPE)]; a three-dimensional Hooke’s law for multiaxial strains (43) and the relation between the Poisson ratio (ν), shear (G), and tensile (E) moduli $G = E/2(1 + \nu)$ for the steel; and a Mooney–Rivlin hyperelastic model (44) for the cross-linked elastomer lining of one of the rolls. All the rheological parameters have to be evaluated. Details of the constitutive equations, parameters, and the computational details are given in the paper by Mewes et al. (41).

Computed values of the primary normal stress difference of a low molecular weight polyisobutylene (PIB) melt we compared with experimentally obtained values, using bire fringence techniques, as shown on Fig. 15.8; they indicate good agreement.

The effect of changing the longest relaxation time of the K-BKZ and the primary normal stress difference is shown in Fig. 15.9.

Fig. 15.10(a) represents schematically the roll deformation along the roll axes, z , caused by the flow of a K-BKZ fluid. Figure 15.10(b) plots the initial roll-diameter profile

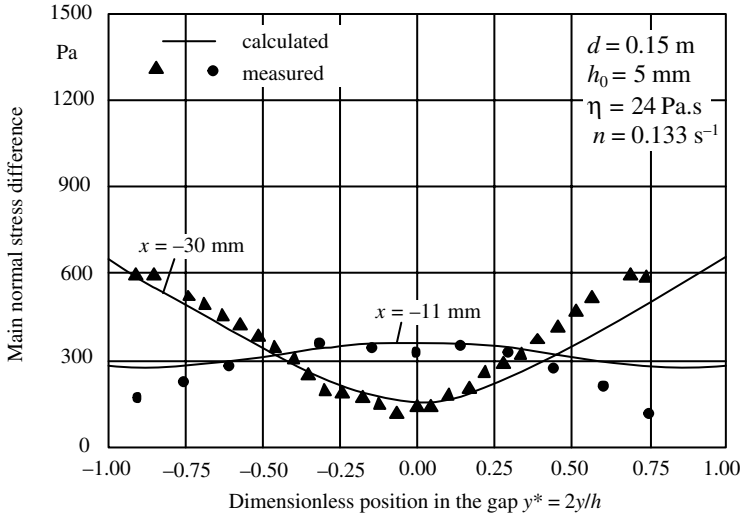


Fig. 15.8 Calculated and measured differences of the primary normal stresses in the calender gap for two different planes; $y_{(x=0)} = H_0/2$. [Reprinted by permission from D. Mewes, S. Luther, and K. Riest, “Simultaneous Calculation of Roll Deformation and Polymer Flow in the Calendering Process,” *Int. Polym. Process.*, **17**, 339–346 (2002).]

(“tangential deviation”), the roll deformation due to flow, and the resulting, almost constant gap thickness. The desired constant gap thickness is due to the compensating deformation and initial rolls profiles, as seen in the figure. Finally, for a pair of rolls, one of which is “rigid” steel and the other coated with a deformable, hyperelastic fluid elastomer,

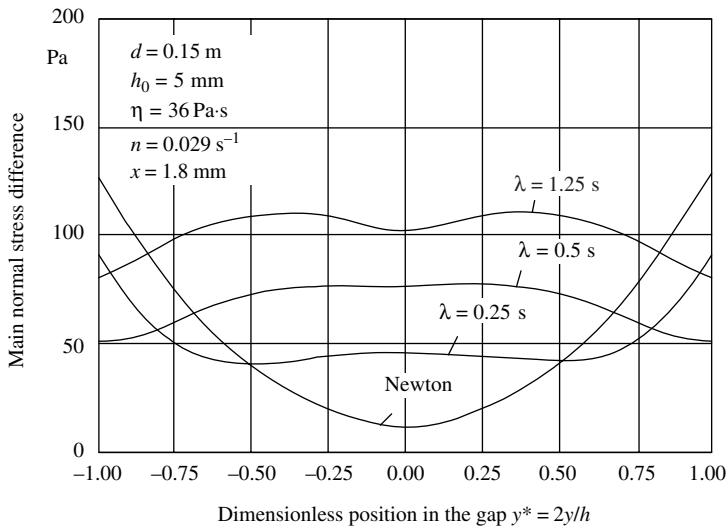


Fig. 15.9 Primary normal stress differences in the calender gap calculated with the K-BKZ model for different relaxation times. [Reprinted by permission from D. Mewes, S. Luther, and K. Riest, “Simultaneous Calculation of Roll Deformation and Polymer Flow in the Calendering Process,” *Int. Polym. Process.*, **17**, 339–346 (2002).]

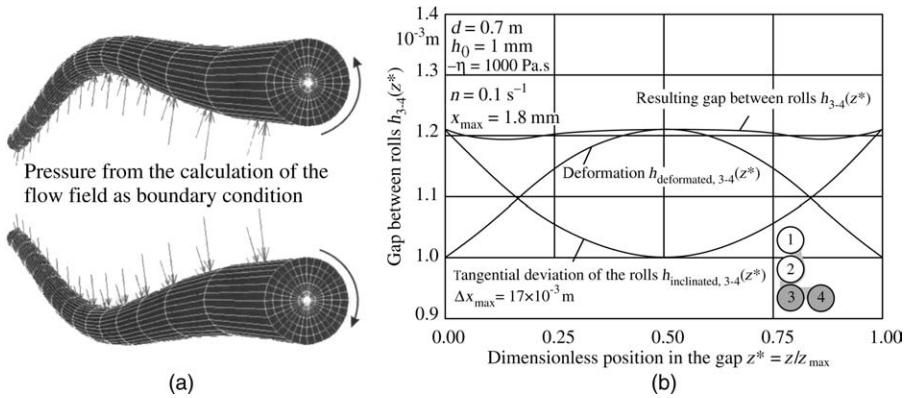


Fig. 15.10 (a) Representation of the deformation between rolls 3 and 4 of a calender design used by Mewes et al. (41); not to scale (b) calculated gap uniformity, resulting from the initially imposed roll diameter and the roll deformation for rolls 3 and 4. [Reprinted by permission from D. Mewes, S. Luther, and K. Riest, “Simultaneous Calculation of Roll Deformation and Polymer Flow in the Calendering Process,” *Int. Polym. Process.*, **17**, 339–346 (2002).]

the flow stresses in the nip deform the elastomer coats. Figure 15.11 depicts the calculated von Mises stresses

$$\sigma_{\text{Mises}} = \sqrt{\frac{1}{2} [(\sigma_1 - \sigma_2)^2 + (\sigma_2 - \sigma_3)^2 + (\sigma_3 - \sigma_1)^2]}$$

in the elastomeric coat and the flow pressure buildup, both in the circumferential direction.

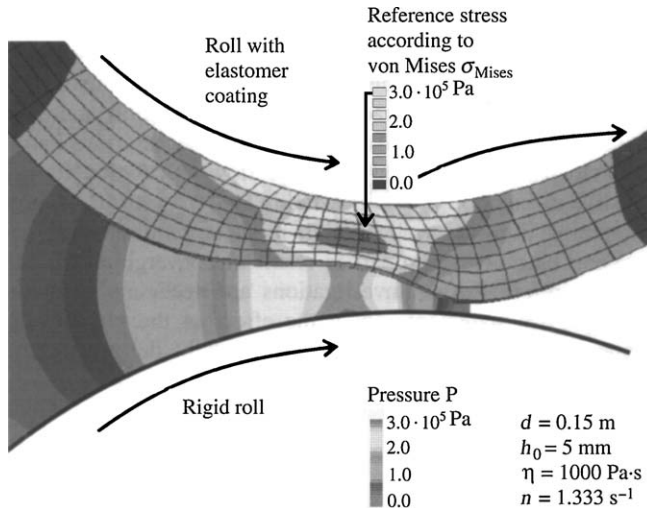


Fig. 15.11 Representation of the pressure in the flow field and the deformation of the elastomer coating. [Reprinted by permission from D. Mewes, S. Luther, and K. Riest, “Simultaneous Calculation of Roll Deformation and Polymer Flow in the Calendering Process,” *Int. Polym. Process.*, **17**, 339–346 (2002).]

The ANSYS program is used to calculate the deformations and stresses in the elastomeric coat.

The preceding work demonstrates the benefits of combining CAD design, computational fluid mechanics (in this case a FVM CFX4), and a solids deformation ANSYS program to solve the “complete” calendering program and, thus, arrive at a computer roll design that points to a promising uniform sheet production for a given polymer melt and operating conditions. Of course, more realistic solutions, such as the simulation of the nonisothermal flow and roll temperature case, are obtainable with sufficient computing power.

REFERENCES

1. G. W. Eighmy, Jr., “Calendering,” in *Modern Plastics Encyclopedia*, McGraw-Hill, New York, 1977, p. 234.
2. D. I. Marshall, “Calendering,” in *Processing of Thermoplastics Materials*, E. C. Bernhardt, Ed., Reinhold, New York, 1959, Chapter 6.
3. W. Unkrüer, “Beitrag zur Ermittlung des Druckverlaufes und der Fliessvorgänge im Walzspalt bei der Kalanderverarbeitung von PVC Hart zu Folien,” Doctoral Thesis, IKV, Technischen Hochschule, Aachen, Germany, 1970.
4. R. E. Gaskell, “The Calendering of Plastic Materials,” *J. Appl. Mech.*, **17**, 334–336 (1950).
5. J. M. McKelvey, *Polymer Processing*, Wiley, New York, 1962, Chapter 9.
6. J. T. Bergen and G. W. Scott, “Pressure Distribution in Calendering of Plastic Materials,” *J. Appl. Mech.*, **18**, 101–106 (1951).
7. I. Brazinsky, H. F. Cosway, C. F. Valle, Jr., R. Jones, R. Clark, and V. Story, “A Theoretical Study of Liquid-film Spread Heights in the Calendering of Newtonian and Power Law Fluids,” *J. Appl. Polym. Sci.*, **14**, 2771 (1970).
8. W. W. Alston and K. N. Astill, “An Analysis of the Calendering of Non-Newtonian Fluids,” *J. Appl. Polym. Sci.*, **17**, 3157 (1973).
9. P. R. Paslay, “Calendering of Viscoelastic Materials,” *J. Appl. Mech.*, **24**, 602 (1957).
10. N. Tokita and J. L. White, “Milling Behavior of Gum Elastomers,” *J. Appl. Polym. Sci.*, **10**, 1011 (1966).
11. J. S. Chong, “Calendering Thermoplastic Materials,” *J. Appl. Polym. Sci.*, **12**, 191–212 (1968).
12. J. F. Agassant and P. Avenas, “Calendering of PVC—Forecast of Stresses and Torques,” paper presented at the 2nd Int. Symp. on PVC, Lyon, France, 1976; also, J. L. Bourgeois and J. F. Agassant, “Calendering of PVC—Defects in Calendered PVC Films and Sheets,” paper presented at the 2nd Int. Symp. on PVC, Lyon, France, 1976.
13. J. L. White, “Elastomer Rheology and Processing,” *Rubber Chem. Technol.*, **42**, 257–338 (1969).
14. M. Finston, “Thermal Effects in Calendering of Plastic Materials,” *J. Appl. Mech.*, **18**, 12 (1951).
15. R. Takserman-Krozer, G. Schenkel, and G. Ehrmann, “Fluid Flow between Rotating Cylinders,” *Rheol. Acta*, **14**, 1066–1076 (1975).
16. N. G. Bekin, V. V. Litvinov, and V. Yu. Petrusanskii, “Method of Calculation of the Energy and Hydrodynamic Characteristics of the Calendering of Polymeric Materials,” *Kauch. Rezina*, **8**, 32 (1975); [English transl., *Int. Polym. Sci. Technol.*, **3**, T 55–T 58 (1976)].
17. C. Kiparissides and J. Vlachopoulos, “Finite Element Analysis of Calendering,” *Polym. Eng. Sci.*, **16**, 712 (1976).

18. R. V. Torner, "Grundprozesse der Verarbeitung von Polymerer," VEB Deutscher Verlag für Grundstoffindustrie, Leipzig, 1974 (translated from Russian).
19. V. Yu. Petrusanskii and A. I. Stachaev, *Uch. Zap. Jaroslavsk. Technol. Inst.*, t. 23 (1971).
20. R. I. Tanner, "Some Experiences Using Finite Element Methods in Polymer Processing and Rheology," *Proc. Seventh Int. Congr. on Rheology*, Gothenburg, Sweden, 1976, pp. 140–145.
21. J. Vlachopoulos and C. Kiparissides, "An Analysis of Thermoplastics in Calendering," paper presented at the 26th Canadian Chemical Engineering Conf., Toronto, Canada, 1976.
22. C. Kiparissides and J. Vlachopoulos, "A Study of Viscous Dissipation of Calendering of Power Law Fluids," *Polym. Eng. Sci.*, **18**, 210–213 (1978).
23. O. C. Zienkiewicz, *The Finite Element Method in Engineering Science*, McGraw-Hill, London, 1971.
24. J. N. Reddy and D. K. Gartling, *The Finite Element Method in Heat Transfer and Fluid Dynamics*, CRC Press, London, 2001.
25. K. H. Huebner, H. Dewhirst, D. L. Smith, and D. E. Byron, *Finite Element Method*, Wiley, New York, 2001.
26. J. Donea and A. Huerta, *Finite Element Methods for Flow Problems*, Wiley, Chichester, UK, 2002.
27. O. C. Zienkiewicz and C. Taylor, "Weighted Residual Processes in Finite Elements with Particular Reference to Some Transient and Coupled Problems," in *Lectures on Finite Element Methods in Continuum Mechanics*, J. T. Oden and E. R. A. Oliveria, Eds., U. A. H. Press, Huntsville, AL, 1973.
28. J. T. Oden, O. C. Zienkiewicz, R. H. Gallagher, and C. Taylor, Eds., *Finite Elements in Flow Problems*, U. A. H. Press, Huntsville, AL, 1974, p. 4.
29. G. E. Myers, "Finite Elements," in *Analytical Methods in Conduction Heat Transfer*, McGraw-Hill, New York, 1971, Chapter 9.
30. Z. Tadmor, E. Broyer, and C. Gutfinger, "Flow Analysis Network (FAN), A Method for Solving Flow Problems in Polymer Processing," *Polym. Eng. Sci.*, **14**, 660–665 (1974).
31. C. S. Desai and J. F. Abel, *Introduction to the Finite Element Method—A Numerical Method for Engineering Analysis*, Van Nostrand Reinhold, New York, 1972, p. 68.
32. E. Broyer, C. Gutfinger, and Z. Tadmor, "Evaluating Flows of a Non-Newtonian Fluid by the Method of Equivalent Newtonian Viscosity," *AIChE J.*, **21**, 198–200 (1975).
33. C. Gutfinger, E. Broyer, and Z. Tadmor, "Analysis of a Cross Head Film Blowing Die with the Flow Analysis Network (FAN) Method," *Polym. Eng. Sci.*, **15**, 381–385 (1975).
34. E. Broyer, C. Gutfinger, and Z. Tadmor, "A Theoretical Model for the Cavity Filling Process in Injection Molding," *Trans. Soc. Rheol.*, **19**, 423–444 (1975).
35. B. David, T. Sapir, A. Nir, and Z. Tadmor, "Twin Rotor Mixers and Extruders, The Extended Cartesian Flow Analysis Network Method," *Int. Polym. Process.*, **5**, 155 (1990).
36. J. L. White, *Twin Screw Extrusion-Technology and Principles*, Hanser, Munich, 1990.
37. E. Mitsoulis, J. Vlachopoulos, and F. A. Mirza, "Finite Element Analysis of Two-dimensional Polymer Melt Flows," *Polym. Process. Eng.*, **1**, 283–308 (1983).
38. J. Vlachopoulos and A. N. Hrymak, "Calendering of PVC: Theory and Experiments," *Polym. Eng. Sci.*, **20**, 725–731 (1980).
39. H. J. Park, D. Kim, K.-J. Lee, and E. Mitsoulis, "Numerical Simulation in Converging Channel Flow of the Fluid M1 Using an Integral Constitutive Equation," *J. Non-Newt. Fluid Mech.*, **52**, 69–89 (1994).
40. X. L. Luo, "A Control Volume Approach for Integral Viscoelastic Models and Its Application to Contraction Flow of Polymer Melts," *J. Non-Newt. Fluid Mech.*, **64**, 173–189 (1996).

41. D. Mewes, S. Luther, and K. Riest, "Simultaneous Calculation of Roll Deformation and Polymer Flow in the Calendering Process," *Int. Polym. Process.*, **17**, 339–346 (2002).
42. A. C. Papanastasiou, L. E. Scriven, and C. W. Macosco, "An Integral Constitutive Equation for Mixed Flows: Viscoelastic Characterization," *J. Rheol.*, **27**, 387–410 (1983).
43. D. Gross, W. Hauger, W. Schnell, and P. Wriggers, *Technische mechanik, Band 4*. Springer-Verlag, Berlin, 1999.
44. L. R. G. Treloar, *The Physics of Rubber Elasticity*, Clarendon Press, Oxford, 1975.

PROBLEMS

- 15.1 *Calendering of Polymers: The Newtonian Gaskell Model*** A 0.2-m-diameter, 1-m-wide, equal-sized-roll calender operates at a speed of 50 cm/s. At a gap separation of 0.02 cm, it produces a 0.022-cm-thick film. Assuming a Newtonian viscosity of 10^4 poise, calculate in the last nip (a) the maximum pressure; (b) the separating force; and (c) estimate the mean temperature rise.
- 15.2 *Separating Force between Rolls in an Experimental Calender*** A cellulose acetate-based polymeric compound is calendered on a laboratory inverted, L-shaped calender with 16-in-wide rolls of 8 in diameter. The minimum gap between the rolls is 15 mil. The sheet width is 15 in. Calculate the separation force and the maximum pressure between a pair of rolls as a function of exiting film thickness, assuming that film thickness equals the gap separation at the point of detachment. Both rolls turn at 10 rpm. The polymer at the calendered temperature of 90°C follows a Power Law model with $m = 3 \times 10^6$ dyne.s^{*n*}/cm² and $n = 0.5$. [Data based partly on J. S. Chong, "Calendering Thermoplastic Materials," *J. Appl. Polym. Sci.*, **12**, 191–212 (1968).]
- 15.3 *Design Considerations of a Calender*** We would like to manufacture a 2 m wide, 0.1 mm thick PVC film at a rate of 1200 kg/h with an inverted-L calender. Suggest a design procedure to select roll sizes, gap separations, and operating conditions.
- 15.4 *Dissipated Work in Calendering*** Calculate the dissipated mechanical work during the forming of the sheet by calendering, as described in Problem 15.1. How much work would be dissipated if the sheet were extruded at the same rate through a sheet die with a 0.02-cm opening and 10-cm-long die lip.
- 15.5 *FEM versus Analytical Solution of Flow in a Tapered Gap*** Consider isothermal pressure flow of a constant viscosity Newtonian fluid, between infinite plates, 10 cm long with a linearly decreasing gap size of 1.5 cm at the entrance and 1 cm at the exit. The distance between the entrance and the exit is 10 cm. The pressure at the inlet and outlet are 2 atmospheres and zero, respectively. (a) Calculate the pressure distribution invoking the lubrication approximation. (b) Calculate the pressure profile using the FEM formulation with six equal-sized elements, and compare the results to (a).

APPENDIX A

Rheological and Thermophysical Properties of Polymers

VICTOR TAN

The Polymer Processing Institute, New Jersey Institute of Technology Newark, NJ

The characterization of polymer in terms of their thermal, rheological, and physical properties is vital for designing polymer processing equipment, for utilizing computer-aided design (CAD) and computer-aided manufacturing (CAM) software, for optimizing their operation, and for understanding and troubleshooting problems occurring during processing.

The thermophysical properties, such as glass transition, specific heat, melting point, and the crystallization temperature of virgin polymers are by-and-large available in the literature. However, the thermal conductivity or diffusivity, especially in the molten state, is not readily available, and values reported may differ due to experimental difficulties. The density of the polymer, or more generally, the pressure–volume–temperature (PVT) diagram, is also not readily available and the data are not easily convertible to simple analytical form. Thus, simplification or approximations have to be made to obtain a solution to the problem at hand.

The typical CAD software for injection molding may need the following properties to carry out a simulation:

- Rheological properties at three processing temperatures;
- Melting points and the heat of fusion;
- Crystallization temperature and the heat of crystallization at various cooling rates (or the ejection temperature of the molded part);
- Specific heat of the solid and melt (single value);
- Thermal conductivity and/or thermal diffusivity of the solid and melt (single value);
- Density of the solid and melt (single value) or the complete PVT diagram.

For the CAD software of the extrusion processes, in addition to these properties, the following are required:

- Bulk density as a function of pressure and temperature;
- Friction coefficient at the polymer/metallic equipment surface interfaces.

The rheological properties of the polymers reported in Table A.1 were measured with a capillary die with diameter of 0.030 in or 0.050 in, and with L/D from 33 to 40. At processing temperatures, the effect of the entrance pressure could be neglected. The shear-rate dependence of viscosity is obtained by applying the Rabinowitsch correction.

The thermal properties of the polymers reported in Table A.2 and Table A.3 were obtained by using a Perkin-Elmer Differential Scanning Calorimeter Model DSC-7 using a heating rate of 20°C/min. The specific heat was obtained using a heating rate of 10°C/min. For semicrystalline material, the heat of fusion was obtained from the measured specific heat curves. The crystallization temperature was obtained at 20°C/min cooling rate.

The density of the polymer at 25°C was obtained by using a molded disk, 0.125 in thick and 2 in in diameter. The melt density at processing temperature was obtained with an Instron Capillary Rheometer with plugged exit. The isothermal compaction at melt-processing temperature was conducted at a plunger speed of 0.05 in/min with attainable pressures up to 25,000 psi.

The thermal conductivity was obtained with a miniaturized hot plate device,¹ using symmetrical heat flow. The apparatus can be heated to above the melt-processing temperature.

ACKNOWLEDGMENTS

We acknowledge Dr. Dongyun Ren, who, with the help of Mr. B. J. Jeong and Drs. J. Guo and Linjie Zhu, evaluated, via mathematical regression, the Power Law model, Carreau model, and Cross model parameters.

1. M. R. Kamal, V. Tan, and F. Kashani, "The Thermal Conductivity and Diffusivity of Polyethylene Solids and Melts," *Adv. Polym. Technol.*, **3**, pp. 89–98 (1983).

TABLE A.1 Parameters of the Power Law, Carreau, and Cross Rheological Models^a for Commercial Polymers

Polymer, Commercial Designation, Manufacturer	Temperature (K)	Power Law Model			Carreau Model			Cross Model				
		Shear rate range (s ⁻¹)	m ($\frac{N \cdot s^m}{m^2}$)	n	Shear rate range (s ⁻¹)	n	λ (s)	η_0 ($\frac{N \cdot s}{m^2}$)	Shear rate range (s ⁻¹)	n	τ^* ($\frac{N}{m}$)	η_0 ($\frac{N \cdot s}{m^2}$)
Acrylonitrile	443	100–5500	1.2×10^5	0.25	100–2000	0.29	0.82	8.0×10^4	–	–	–	–
butadiene styrene	463	100–6000	6.3×10^4	0.25	100–3000	0.26	0.73	4.4×10^4	–	–	–	–
(ABS), AM-1000, Borg-Warner/GE Plastics [®]	483	100–7000	3.9×10^4	0.25	40–4000	0.25	0.57	2.6×10^4	–	–	–	–
ABS, Cycolac KJW, GE Plastics	493	300–14000	4.2×10^4	0.25	10–700	0.44	0.092	3.4×10^3	10–14000	1.77	1.2×10^5	3.6×10^3
	513	300–14000	2.3×10^4	0.30	10–700	0.45	0.1349	2.8×10^3	10–14000	1.73	6.6×10^4	2.9×10^3
	533	300–14000	1.4×10^4	0.32	10–700	0.44	0.1252	2.0×10^3	10–14000	1.70	4.3×10^4	2.3×10^3
Ethylene ethyl acrylate, DPDA-6169, Union Carbide/DOW [®]	443	100–6000	1.2×10^4	0.38	80–6000	0.42	0.40	5.4×10^3	–	–	–	–
	463	100–4000	6.9×10^3	0.43	10–3000	0.58	1.08	3.5×10^3	–	–	–	–
	483	100–6000	3.8×10^3	0.48	40–1000	0.50	0.51	2.3×10^3	–	–	–	–
Nylon, Capron 8200, Allied Chemical/ Honeywell [®]	498	100–2500	2.6×10^3	0.63	100–2000	0.63	0.27	1.6×10^3	–	–	–	–
	503	100–2000	2.0×10^3	0.66	100–2000	0.65	0.32	1.3×10^3	–	–	–	–
	508	100–2300	1.8×10^3	0.66	100–2000	0.68	0.36	1.1×10^3	–	–	–	–
Nylon 6, Nylon 8202, BASF	508	700–3000	1.2×10^4	0.46	3–3000	0.49	0.0049	6.2×10^2	3–3000	1.86	5.0×10^5	6.5×10^2
	518	700–3000	7.1×10^3	0.50	3–3000	0.59	0.0093	5.4×10^2	3–3000	1.73	3.3×10^5	5.8×10^2
	528	700–3000	7.5×10^3	0.48	3–3000	0.55	0.0053	4.3×10^2	3–3000	1.82	3.9×10^5	4.5×10^2
Nylon 6 (Amorphous), Zytel 330, DuPont	503	300–750	8.2×10^4	0.33	3–750	0.46	0.026	5.1×10^3	–	–	–	–
	518	300–1500	4.2×10^4	0.39	3–1500	0.44	0.013	2.7×10^3	–	–	–	–
	533	300–3000	2.9×10^4	0.40	3–3000	0.41	0.0085	1.7×10^3	–	–	–	–

TABLE A.1 (Continued)

Polymer, Commercial Designation, Manufacturer	Temperature (K)	Power Law Model			Carreau Model			Cross Model			
		Shear rate range (s ⁻¹)	m ($\frac{Ns^m}{m^2}$)	n	Shear rate range (s ⁻¹)	λ (s)	η_0 ($\frac{Ns}{m^2}$)	Shear rate range (s ⁻¹)	n	τ^* ($\frac{N}{m^2}$)	η_0 ($\frac{Ns}{m^2}$)
Nylon 6 (Amorphous), Trogamid T-5000 Degussa	553 573 593	100-300 300-1500 300-3000	9.6×10^4 6.3×10^4 7.7×10^3	0.36 0.34 0.54	3-300 3-1500 3-3000	0.42 0.36 0.48	0.054 0.020 0.0071	1.3×10^4 4.5×10^3 9.2×10^2	- - -	- - -	- - -
Nylon 66 + 33% Glass fiber, N 1503-2	553 563 573	71-14164 71-14164 71-14164	3.5×10^3 2.8×10^3 2.3×10^3	0.53 0.53 0.52	- - -	- - -	- - -	- - -	- - -	- - -	- - -
Polybutene-1 (PB-1), DP0800, Shell	423 443 463	200-3000 200-3000 200-3000	2.4×10^3 1.1×10^3 3.4×10^2	0.46 0.53 0.63	3-3000 3-3000 3-3000	0.50 0.58 0.67	0.0446 0.0584 0.0961	3.9×10^2 2.3×10^2 1.2×10^2	3-3000 3-3000 3-3000	2.0×10^4 1.1×10^4 3.6×10^3	5.0×10^2 3.0×10^2 1.8×10^2
Polybutylene terephthalate (PBT), 2000, Ticona	513 598 608	700-14000 700-14000 700-14000	1.0×10^3 7.9×10^2 4.3×10^2	0.69 0.68 0.71	30-14000 30-14000 30-14000	0.71 0.70 0.73	0.0091 0.0084 0.0152	2.2×10^2 1.6×10^2 1.2×10^2	30-14000 30-14000 30-14000	1.3×10^5 1.0×10^5 2.5×10^4	3.0×10^2 2.1×10^2 1.8×10^2
PBT with 30% GF, Vandar 4662 Z, Ticona	523 538 553	10-14000 10-14000 10-14000	2.2×10^4 1.2×10^4 6.5×10^3	0.43 0.42 0.40	- - -	- - -	- - -	- - -	- - -	- - -	- - -
Polycarbonate (PC), Allied Chemical/ Honeywell®	553 573 593	100-1000 100-1000 100-1000	8.4×10^3 4.3×10^3 1.1×10^3	0.64 0.67 0.80	0.01-3000 0.01-2000 0.01-2500	0.26 0.26 0.53	0.002 0.002 0.002	1.5×10^3 8.0×10^2 4.2×10^2	- - -	- - -	- - -

PC, Lexan 141, GE Plastics	573	1000-3000	2.3×10^4	0.43	3-3000	0.26	0.0009	5.1×10^2	3-3000	2.40	1.4×10^6	5.2×10^2
	593	1000-3000	5.6×10^3	0.56	3-3000	-	0.0002	2.6×10^2	3-3000	3.08	1.1×10^6	2.6×10^2
	613	1000-3000	9.2×10^2	0.74	3-3000	0.63	0.0007	1.6×10^2	3-3000	2.35	9.9×10^5	1.6×10^2
High density polyethylene (HDPE), Alathon 7040, DuPont	453	100-1000	6.2×10^3	0.56	100-1200	0.54	0.07	2.1×10^3	-	-	-	-
	473	100-1000	4.7×10^3	0.59	100-1200	0.50	0.08	1.5×10^3	-	-	-	-
	493	100-1000	3.7×10^3	0.61	180-1400	0.58	0.05	1.2×10^3	-	-	-	-
HDPE (MI = 0.7), Marlex, Philips/Chevron	472	300-14000	4.1×10^4	0.27	10-14000	0.30	0.0259	2.4×10^3	10-14000	1.76	1.3×10^5	3.5×10^3
	550	300-14000	2.6×10^4	0.32	10-14000	0.34	0.0292	2.0×10^3	10-14000	1.72	9.7×10^4	3.1×10^3
	525	300-14000	1.8×10^4	0.35	10-14000	0.38	0.0361	1.8×10^3	10-14000	1.68	6.7×10^4	2.9×10^3
HDPE (MI = 10), Marlex, Philips/Chevron	453	100-1500	7.2×10^3	0.51	2-1500	0.54	0.0688	1.7×10^3	-	-	-	-
	463	100-1500	3.3×10^3	0.60	2-1500	0.62	0.0437	8.9×10^2	-	-	-	-
	473	100-1500	2.5×10^3	0.63	2-1500	0.63	0.0311	7.0×10^2	2-1500	1.63	1.3×10^5	7.8×10^2
HDPE (MI > 10), Alathon H-5618, DuPont	473	700-14000	8.0×10^3	0.41	10-14000	0.44	0.0061	3.6×10^2	10-14000	1.70	1.4×10^5	4.4×10^2
	507	700-14000	3.4×10^3	0.49	10-14000	0.52	0.0086	2.7×10^2	10-14000	1.61	8.0×10^4	3.5×10^2
	533	700-14000	2.3×10^3	0.53	10-14000	0.56	0.0078	2.0×10^2	10-14000	1.59	7.7×10^4	2.5×10^2
Low density polyethylene (LDPE), Alathon 1540, DuPont®	433	100-4000	9.4×10^3	0.41	80-1000	0.42	0.59	6.3×10^3	-	-	-	-
	453	100-6500	5.2×10^3	0.46	100-7000	0.47	0.47	3.2×10^3	-	-	-	-
	473	100-6000	4.3×10^3	0.47	100-1000	0.48	0.21	1.7×10^3	-	-	-	-
LDPE (MI = 0.2), 132, DOW	453	3-3000	2.6×10^4	0.34	-	-	-	-	-	-	-	-
	473	3-3000	1.9×10^4	0.37	-	-	-	-	-	-	-	-
	493	3-3000	1.5×10^4	0.37	-	-	-	-	-	-	-	-
LDPE (MI = 2.0), 640, DOW	453	300-3000	2.1×10^4	0.35	3-3000	0.39	0.1822	5.9×10^3	-	-	-	-
	473	300-3000	1.6×10^4	0.37	3-3000	0.42	0.1222	3.3×10^3	-	-	-	-
	493	300-3000	9.9×10^3	0.42	3-3000	0.45	0.1026	2.2×10^3	-	-	-	-

(Continued)

TABLE A.1 (Continued)

Polymer, Commercial Designation, Manufacturer	Temperature (K)	Power Law Model			Carreau Model			Cross Model				
		Shear rate range (s ⁻¹)	m ($\frac{Ns}{m^2}$)	n	Shear rate range (s ⁻¹)	λ (s)	η_0 ($\frac{Ns}{m^2}$)	Shear rate range (s ⁻¹)	n	τ^* ($\frac{N}{m^2}$)	η_0 ($\frac{Ns}{m^2}$)	
LDPE (MI = 50), 1409, Chevron/Philips	423	300-3000	4.4×10^3	0.48	3-3000	0.51	0.0253	5.6×10^2	3-3000	1.64	6.3×10^4	6.8×10^2
	448	300-3000	1.9×10^3	0.55	3-3000	0.57	0.0143	2.6×10^2	3-3000	1.68	8.2×10^4	2.9×10^2
	473	300-3000	1.0×10^3	0.59	3-3000	0.61	0.0108	1.5×10^2	3-3000	1.67	8.2×10^4	1.7×10^2
Linear low density polyethylene (LLDPE) (MI = 6), Dowlex 2035, DOW	453	400-1500	1.3×10^4	0.44	2-1500	0.53	0.0316	1.3×10^3	-	-	-	-
	463	400-1500	6.7×10^4	0.20	-	-	-	-	-	-	-	-
	473	400-1500	8.4×10^3	0.48	2-1500	0.57	0.0372	1.1×10^3	-	-	-	-
LLDPE (MI = 50), Dowlex 2500, DOW	423	300-3000	2.7×10^3	0.57	3-3000	0.55	0.0062	3.1×10^2	-	-	-	-
	448	300-3000	1.1×10^3	0.65	3-3000	0.61	0.0045	1.8×10^2	-	-	-	-
	473	300-3000	5.7×10^2	0.70	3-3000	0.67	0.0047	1.2×10^2	-	-	-	-
Polymethyl methacrylate (PMMA), Lucite 147, DuPont [®] , PMMA, V811-100, Rohm & Haas	493	100-6000	8.8×10^4	0.19	100-4000	0.19	0.09	1.3×10^4	-	-	-	-
	513	100-6000	4.3×10^4	0.25	100-4000	0.25	0.07	6.0×10^3	-	-	-	-
	533	100-7000	2.6×10^4	0.27	100-4000	0.36	0.11	2.9×10^3	-	-	-	-
	473	100-1500	1.7×10^5	0.25	3-1500	0.30	0.199	3.9×10^4	-	-	-	-
	493	100-3000	5.8×10^4	0.31	3-3000	0.43	0.4313	1.0×10^4	-	-	-	-
Polyoxymethylene (POM) (Acetal), Delrin 507, DuPont	513	100-3000	2.3×10^4	0.37	3-3000	0.42	0.4170	4.8×10^3	-	-	-	-
	473	1000-14000	1.5×10^4	0.37	30-14000	0.38	0.002	2.9×10^2	30-14000	1.84	3.6×10^5	3.2×10^2
	483	1000-14000	9.7×10^3	0.40	30-14000	0.40	0.002	2.3×10^2	-	-	-	-
	493	1000-14000	7.5×10^3	0.42	30-14000	0.40	0.0016	1.9×10^2	30-14000	1.85	3.3×10^5	2.1×10^2

POM (Copolymer), Celcon U10-01, Ticona	453 468 483	3-3000 3-3000 75-3000	6.7×10^3 1.1×10^4 1.8×10^4	0.57 0.49 0.42	- - 3-3000	- - 0.45	- - 0.1403	- - 4.9 $\times 10^3$	- - 4.9 $\times 10^3$	- - 1.62	- - 1.8×10^5	- - 5.4×10^2
POM (Copolymer), Celcon MM3.5H, Ticona	453 468 483	300-1500 300-1500 300-1500	4.4×10^3 2.8×10^3 1.3×10^3	0.57 0.60 0.69	3-1500 3-1500 3-1500	0.66 0.68 0.72	0.0318 0.021 0.0197	7.3×10^2 4.9×10^2 3.5×10^2	7.3×10^2 4.9×10^2 3.5×10^2	1.56 1.67 1.61	1.7×10^5 4.6×10^5 4.3×10^5	4.0×10^2 2.1×10^2 1.5×10^2
Polyphenylene Sulfide (PPS), Fortron 0214B1, Ticona	598 603	1000-14000 1000-14000	1.1×10^3 5.4×10^2	0.66 0.72	140-14000 140-14000	0.66 0.66	0.0017 0.0007	1.3×10^2 8.0×10^1	1.3×10^2 8.0×10^1	1.76	8.1×10^5	8.5×10^1
Polypropylene (PP), CD 460, Exxon Mobil Chemical®	453 463 473	100-4000 100-3500 100-4000	6.8×10^3 4.9×10^3 4.4×10^3	0.37 0.41 0.41	70-4000 70-4000 50-3000	0.38 0.41 0.41	0.49 0.51 0.40	4.2×10^3 3.2×10^3 2.5×10^3	4.2×10^3 3.2×10^3 2.5×10^3	- - -	- - -	- - -
PP, E612 ExxonMobil Chemical®	483 513	100-3000 50-3000	3.2×10^4 2.2×10^4	0.25 0.28	100-3500 50-3500	0.24 0.27	1.05 0.81	3.5×10^4 2.0×10^4	3.5×10^4 2.0×10^4	- -	- -	- -
PP (MFI = 1.4), -, Shell	463 483	3-3000 3-3000	2.1×10^4 1.7×10^4	0.32 0.32	- -	- -	- -	- -	- -	- -	- -	- -
PP (MFI = 7.8) Shell	503 463 483	3-3000 3-3000 3-3000	1.4×10^4 6.9×10^3 4.9×10^3	0.35 0.41 0.44	- - -	- - -	- - -	- - -	- - -	- - -	- - -	- - -
PP (MFI = 53) Shell	503 463 483	3-3000 300-3000 300-3000	3.6×10^3 1.2×10^3 6.7×10^2	0.47 0.61 0.67	3-3000 3-3000 3-3000	0.45 0.49 0.50	0.0305 0.0222 0.0115	5.0×10^2 3.0×10^2 1.8×10^2	5.0×10^2 3.0×10^2 1.8×10^2	1.69 1.68 1.75	3.7×10^4 3.9×10^4 5.7×10^4	6.2×10^2 3.6×10^2 2.0×10^2
PP-PE copolymer, 7523, Basell	463 483 503	10-1400 10-14000 10-14000	1.9×10^4 2.1×10^4 1.8×10^4	0.35 0.31 0.31	- - -	- - -	- - -	- - -	- - -	- - -	- - -	- - -
Polystyrene (PS), Dylene 8, ARCO/BP®	463 483 498	100-4500 100-4000 100-5000	4.5×10^4 2.4×10^4 1.6×10^4	0.22 0.25 0.28	30-6000 30-4000 30-4000	0.24 0.27 0.30	0.27 0.32 0.35	1.4×10^5 9.2×10^3 6.6×10^3	1.4×10^5 9.2×10^3 6.6×10^3	- - -	- - -	- - -

(Continued)

TABLE A.1 (Continued)

Polymer, Commercial Designation, Manufacturer	Temperature (K)	Power Law Model			Carreau Model			Cross Model				
		Shear rate range (s ⁻¹)	m ($\frac{Ns^m}{m^2}$)	n	Shear rate range (s ⁻¹)	λ (s)	η_0 ($\frac{Ns}{m^2}$)	Shear rate range (s ⁻¹)	n	τ^* ($\frac{N}{m^2}$)	η_0 ($\frac{Ns}{m^2}$)	
PS, Styron 615, DOW	453	100–3000	2.9×10^4	0.33	3–3000	0.35	0.2678	1.1×10^4	–	–	–	
	473	100–3000	1.7×10^4	0.33	3–3000	0.35	0.1074	3.5×10^3	–	–	–	
	493	100–3000	7.9×10^3	0.38	3–3000	0.40	0.0614	1.3×10^3	3–3000	1.69	3.6×10^4	1.8×10^3
PS, Styron 685, DOW	453	3–3000	4.8×10^4	0.30	–	–	–	–	–	–	–	
	473	3–3000	3.1×10^4	0.28	–	–	–	–	–	–	–	
	493	3–3000	1.5×10^4	0.34	–	–	–	–	–	–	–	
High-impact polystyrene (HIPS), MC6800,	473	10–16000	1.7×10^4	0.32	–	–	–	–	–	–	–	
	498	10–16000	9.6×10^3	0.34	–	–	–	–	–	–	–	
	523	10–16000	5.5×10^3	0.38	–	–	–	–	–	–	–	
Chevron/Philips HIPS, LX2400, Solutia®	443	100–7000	7.6×10^4	0.20	50–1000	0.26	6.77	2.1×10^5	–	–	–	
	463	100–7000	4.6×10^4	0.21	50–1000	0.22	5.31	1.5×10^5	–	–	–	
	483	100–7000	3.6×10^4	0.19	100–3000	0.16	2.57	1.1×10^5	–	–	–	
Polyurethane (PU), TTFG80A	416	100–1400	1.9×10^5	0.21	10–1400	0.21	0.028	1.1×10^4	–	–	–	
	438	300–7000	1.0×10^5	0.26	10–7000	0.28	0.0148	4.2×10^3	–	–	–	
	466	1000–14000	1.3×10^4	0.41	10–14000	0.40	0.0031	4.6×10^2	10–14000	1.78	3.6×10^5	5.2×10^2
Polyvinyl chloride (PVC), Polyvin 9774	438	400–14000	3.5×10^4	0.23	10–14000	0.25	0.0393	2.6×10^3	10–14000	1.79	7.5×10^4	4.4×10^3
	453	400–14000	1.2×10^4	0.33	10–14000	0.36	0.0377	1.1×10^3	10–14000	1.69	3.7×10^4	1.8×10^3
	473	400–14000	3.5×10^3	0.44	10–14000	0.45	0.0149	3.1×10^2	10–14000	1.64	3.8×10^4	4.4×10^2
Styrene acrylonitrile (SAN), Lustran® 31–1000, Solutia®	463	100–9000	9.0×10^4	0.21	100–8000	0.21	0.17	2.2×10^4	–	–	–	
	493	100–8000	3.2×10^4	0.27	80–8000	0.28	0.18	9.0×10^3	–	–	–	
	523	100–8000	1.1×10^4	0.35	100–5000	0.36	0.25	4.2×10^3	–	–	–	

Styrene-butadiene-styrene (SBS), 787, Shell [®]	463	400–16000	1.3×10^4	0.29	20–16000	0.30	0.0216	7.8×10^2	20–16000	1.74	4.3×10^4	1.3×10^3
	508	400–16000	7.9×10^3	0.32	20–16000	0.32	0.0102	3.3×10^2	20–16000	1.75	4.7×10^4	4.5×10^2
	553	400–16000	3.7×10^3	0.38	20–16000	0.36	0.0061	1.6×10^2	20–16000	1.75	4.7×10^4	2.0×10^2
Polyethylene terephthalate (PET), 7352, Amoco/BP, 573	553	1400–14000	7.4×10^3	0.48	70–14000	0.51	0.0028	3.2×10^2	70–14000	1.69	3.5×10^5	3.9×10^2
	563	1400–14000	4.9×10^3	0.51	70–14000	0.51	0.0018	2.3×10^2	70–14000	1.75	4.4×10^5	2.6×10^2
	573	3500–14000	4.1×10^3	0.51	70–14000	0.59	0.0021	1.6×10^2	70–14000	1.66	3.6×10^5	1.9×10^2
Thermoplastic elastomer (TPE), Riteflex, Ticona	463	300–14000	1.2×10^4	0.41	10–14000	0.44	0.0185	9.7×10^2	10–14000	1.65	8.9×10^4	1.4×10^3
	473	300–14000	8.7×10^3	0.43	10–14000	0.45	0.0159	7.6×10^2	10–14000	1.65	8.9×10^4	1.0×10^3
	483	300–14000	5.2×10^3	0.48	10–14000	0.51	0.0237	6.6×10^2	10–14000	1.59	5.3×10^4	9.4×10^2
Thermoplastic olefin (TPO), Vistaflex905 B, ExxonMobil Chemical [®]	473	100–5000	2.8×10^4	0.27	40–5000	0.28	1.62	3.6×10^4	–	–	–	–
	493	100–4000	1.8×10^4	0.30	70–2000	0.31	1.42	2.2×10^4	–	–	–	–
	513	100–3000	2.0×10^4	0.28	70–2000	0.31	0.72	1.4×10^4	–	–	–	–
Polyether sulphone (PES), Uitem 1010, GE Plastics	608	1400–7000	5.6×10^4	0.37	14–7000	0.48	0.0116	2.3×10^3	14–7000	1.66	4.8×10^5	2.9×10^3
	623	1400–14000	4.2×10^4	0.37	14–14000	0.45	0.0062	1.2×10^3	14–14000	1.70	4.9×10^5	1.4×10^3
	643	1400–14000	1.5×10^4	0.45	14–14000	0.51	0.0054	6.7×10^2	14–14000	1.65	3.7×10^5	8.0×10^2
PES, 3600G, ICI	603	7–750	1.5×10^3	0.88	7–750	0.85	0.050	1.1×10^3	–	–	–	–
	623	15–3000	1.2×10^3	0.80	15–3000	0.75	0.0218	6.3×10^2	15–3000	1.50	3.6×10^5	7.4×10^2
	643	15–3000	7.0×10^2	0.80	15–3000	0.79	0.0793	4.3×10^2	15–3000	1.29	9.5×10^3	8.0×10^2

[®]Data appeared in Appendix A of First Edition.

Power Law model:

$$\eta(\dot{\gamma}) = m\dot{\gamma}^{n-1}$$

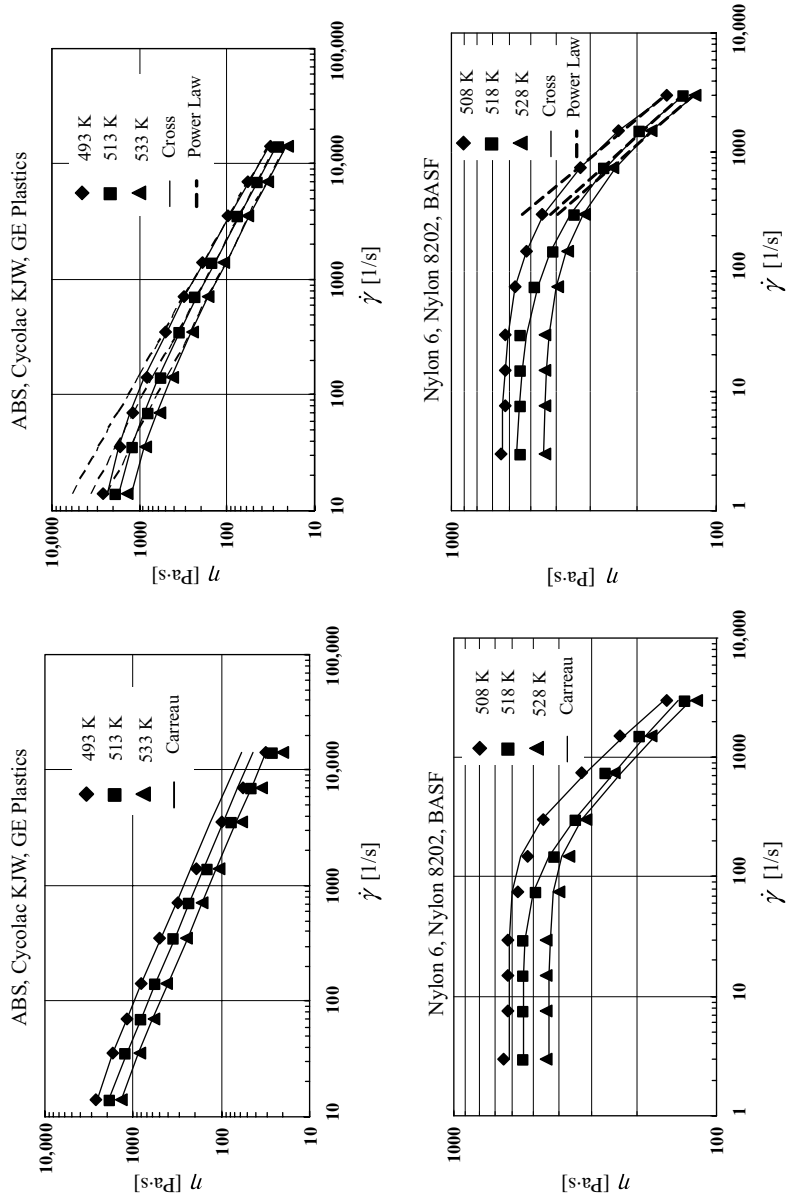
$$\frac{\eta(\dot{\gamma}) - \eta_{\infty}}{\eta_0 - \eta_{\infty}} = \frac{1}{[1 + (\lambda\dot{\gamma})^2]^{(1-n)/2}}$$

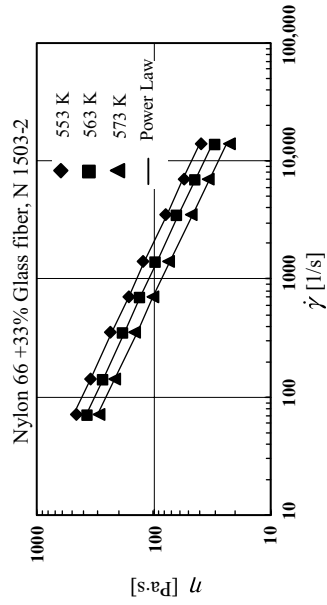
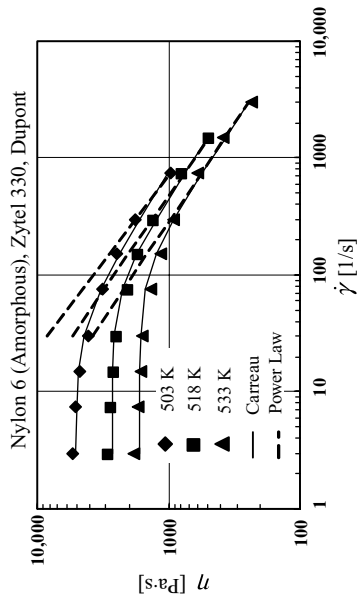
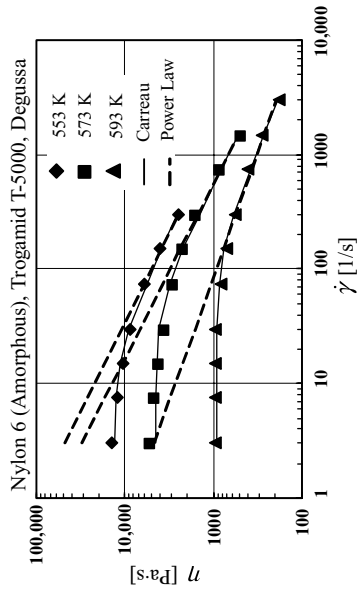
Parameters given with η_{∞} set to zero

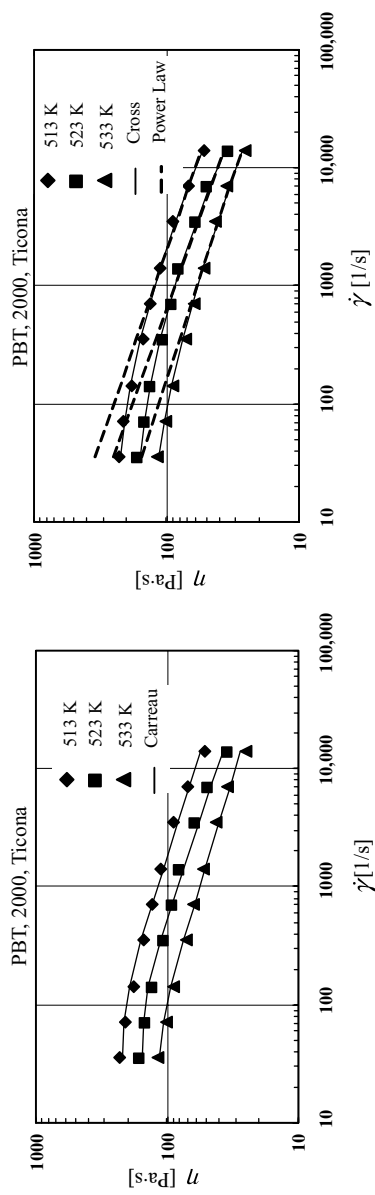
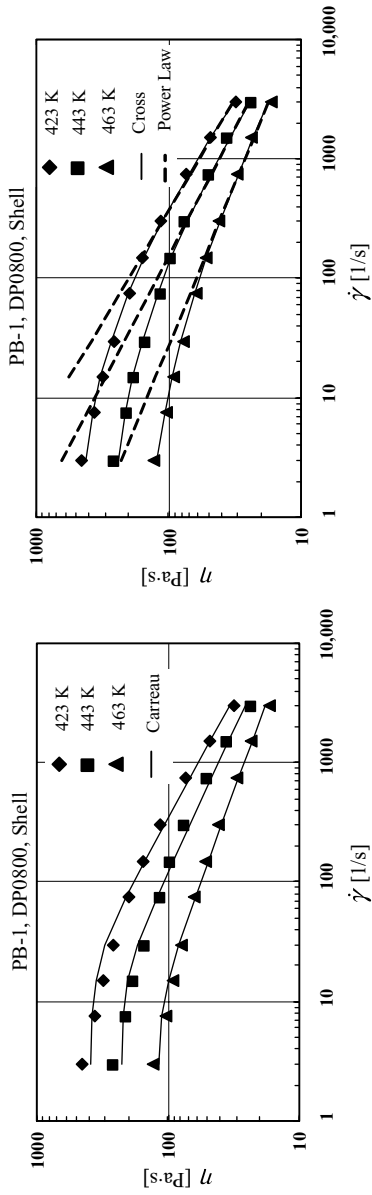
Cross model:

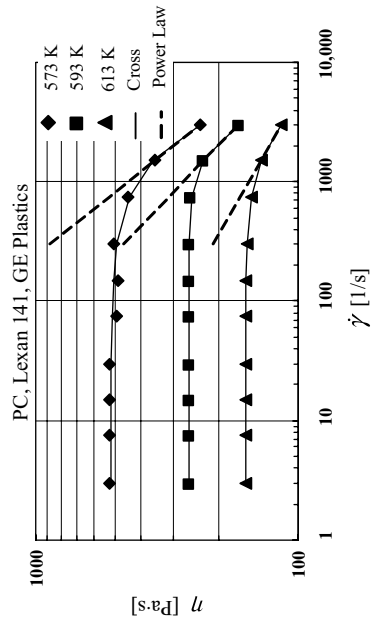
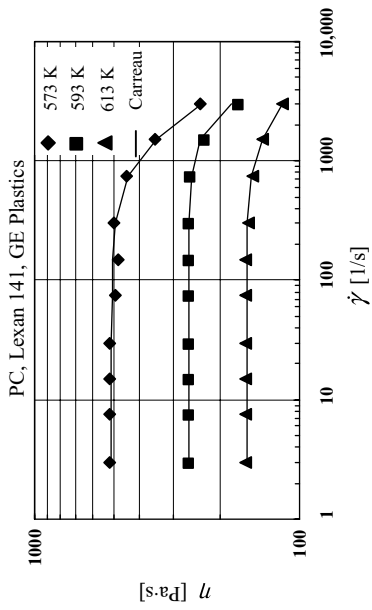
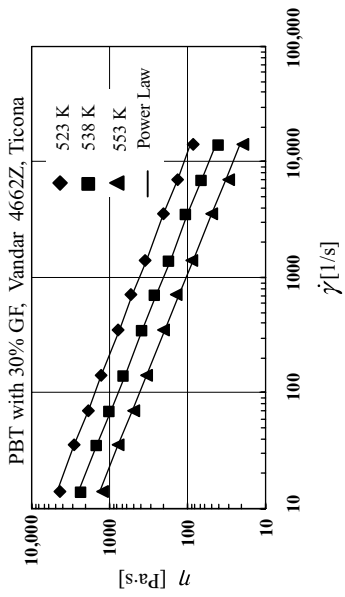
$$\eta(\dot{\gamma}, T, P) = \frac{\eta_0(T_1)}{1 + \left[\frac{\eta_0(T_1)}{r\dot{\gamma}}\right]^{n-1}}$$

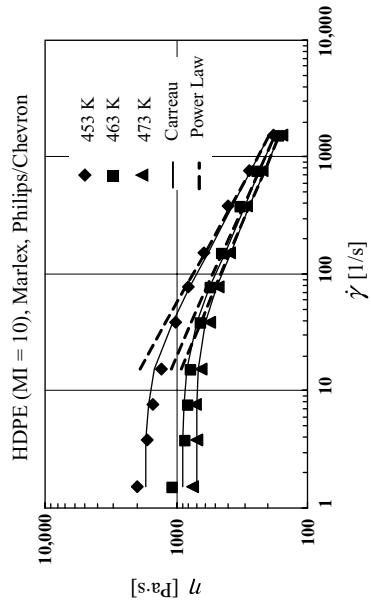
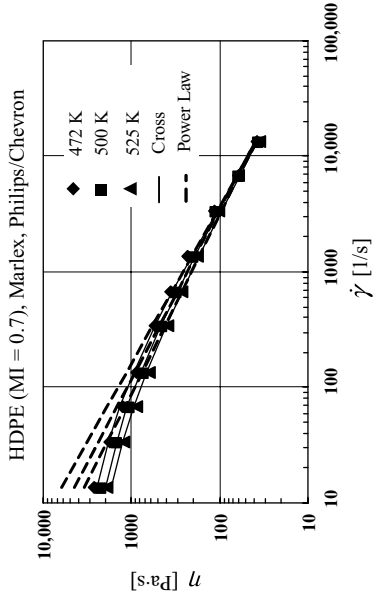
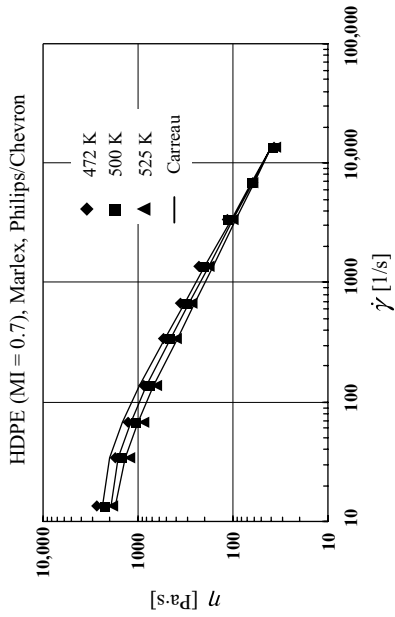
**EXPERIMENTAL RESULTS AND POWER LAW, CARREAU,
AND CROSS MODELS CURVE FITS**

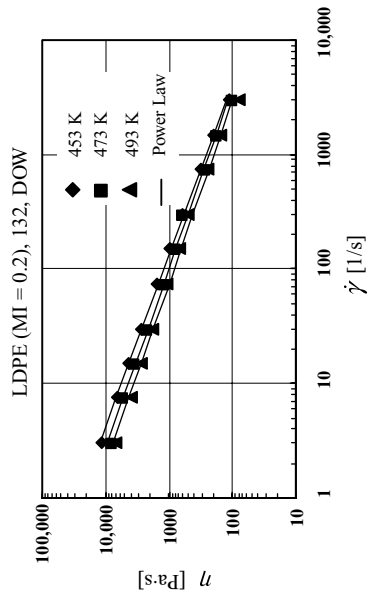
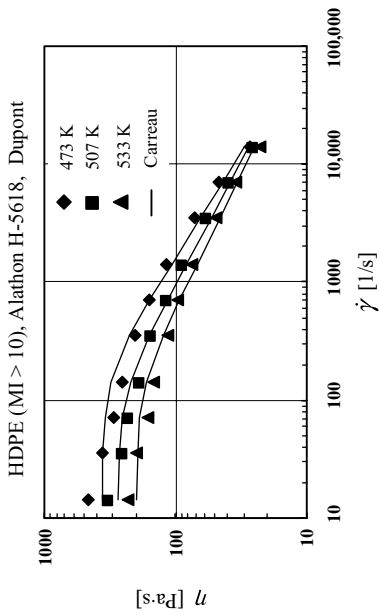
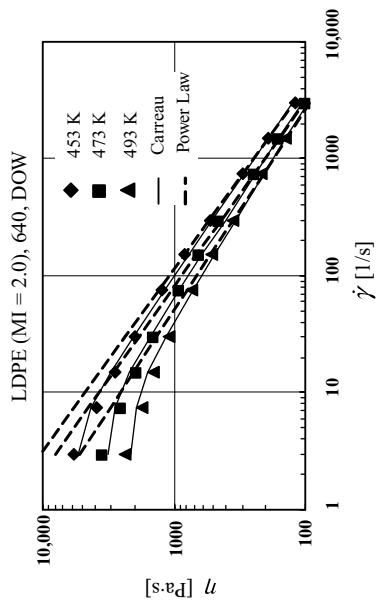
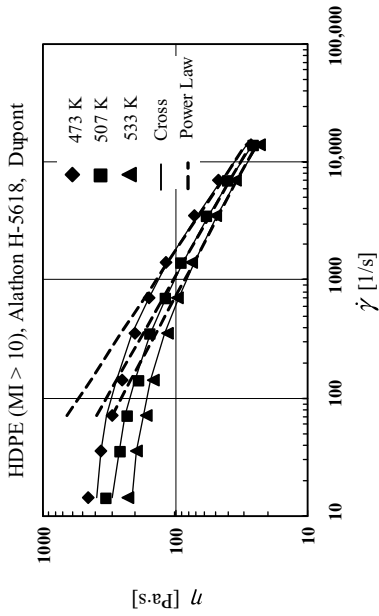


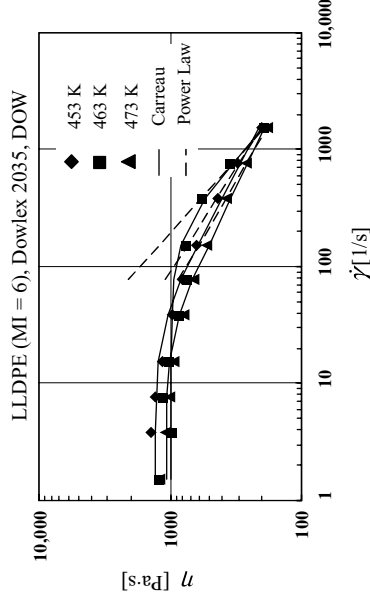
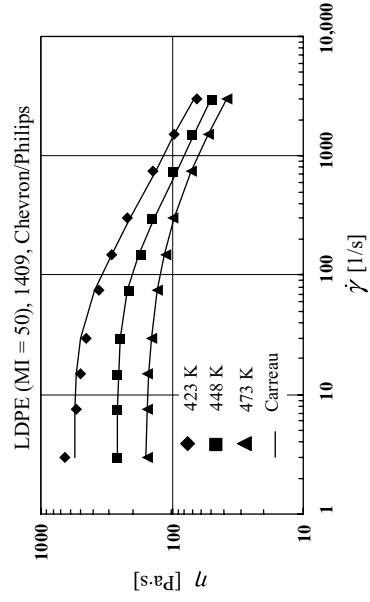
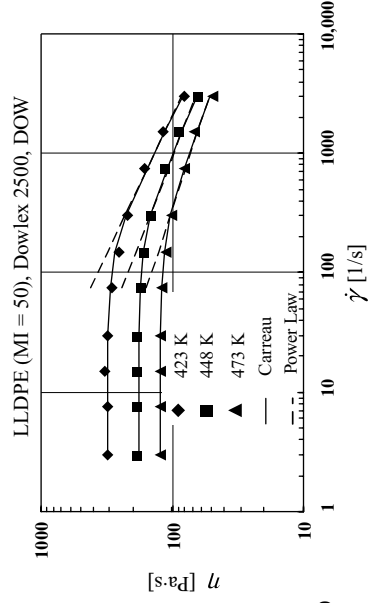
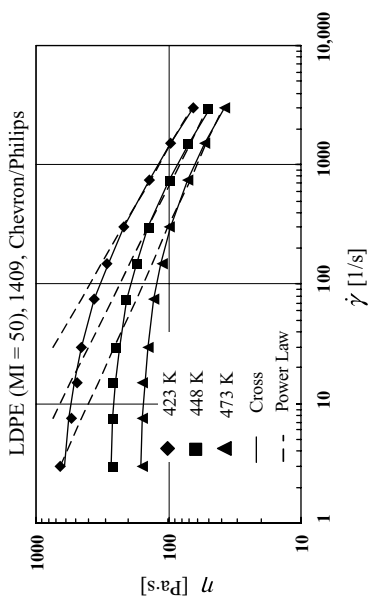


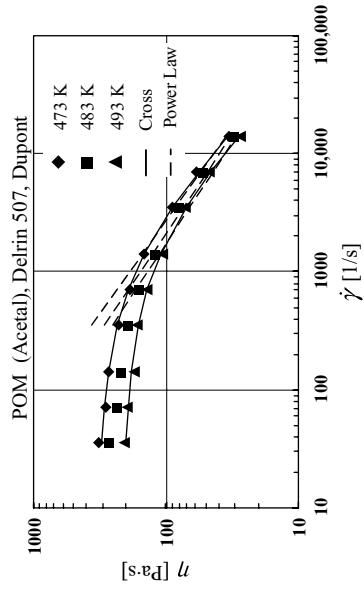
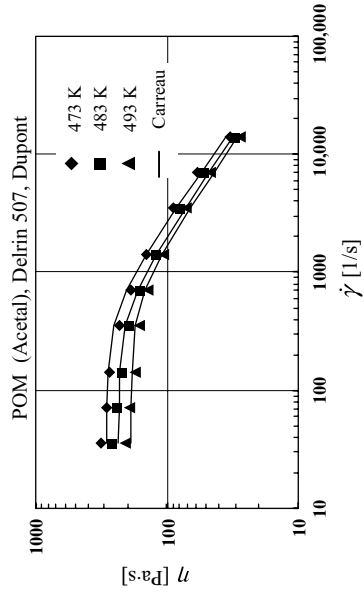
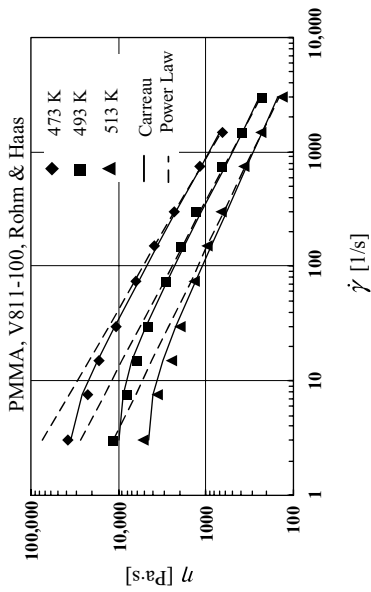


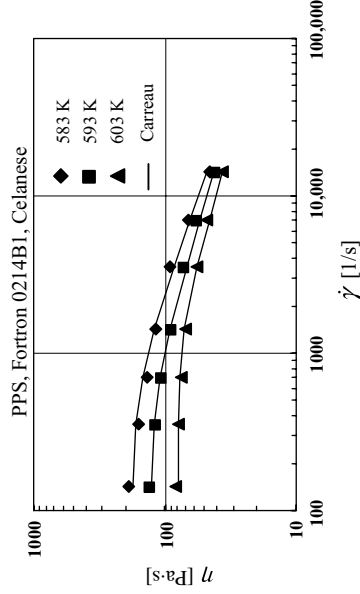
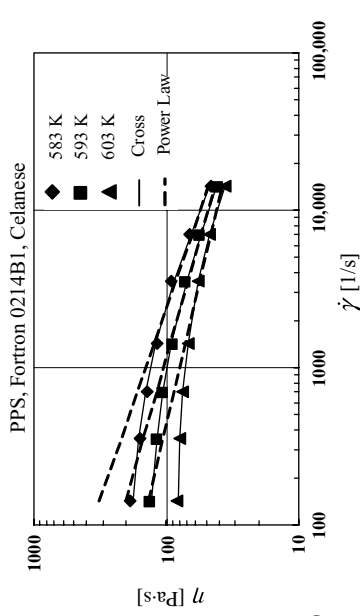
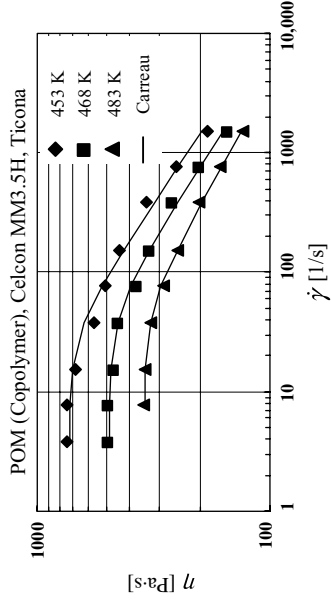
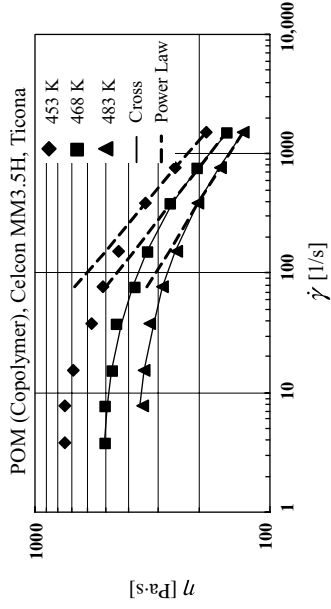


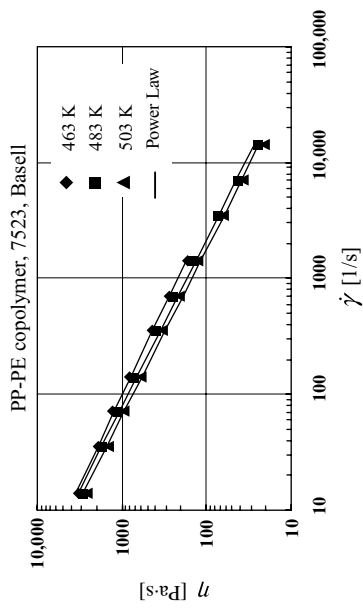
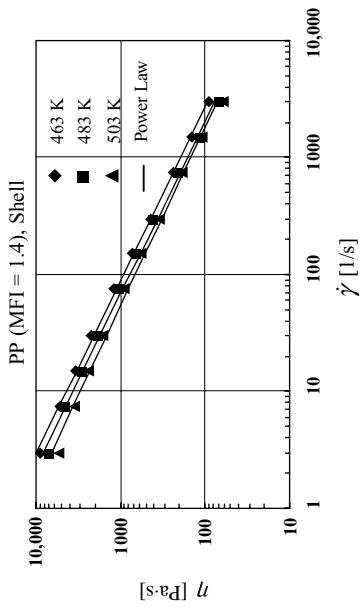
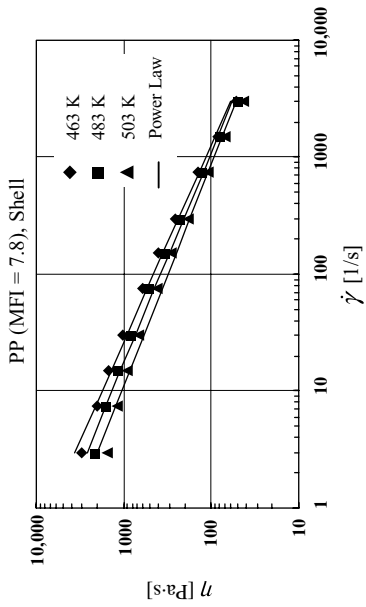


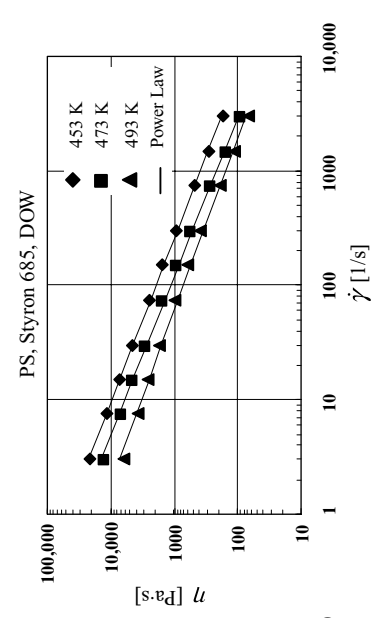
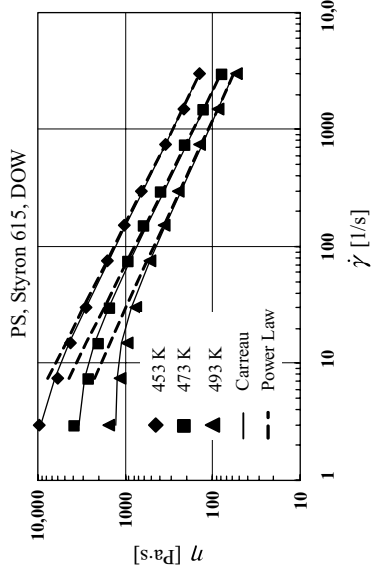
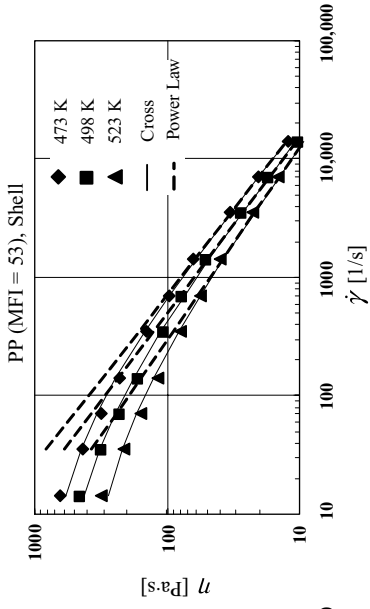
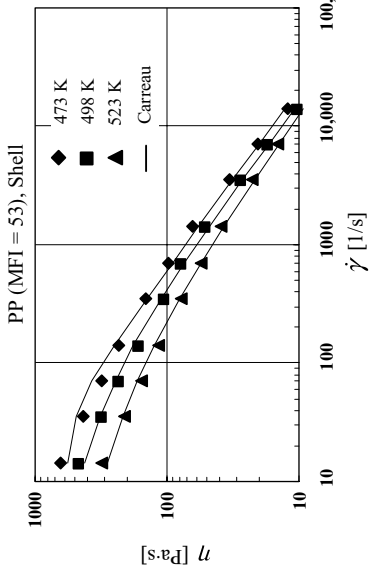


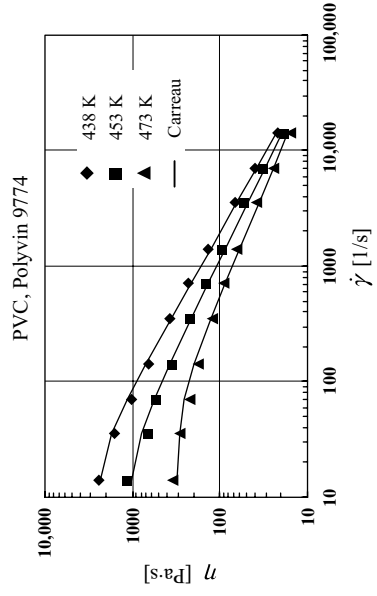
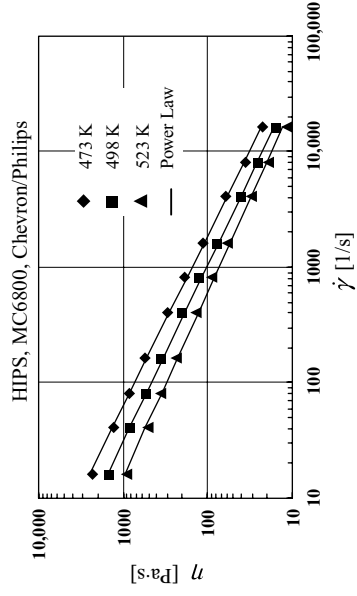
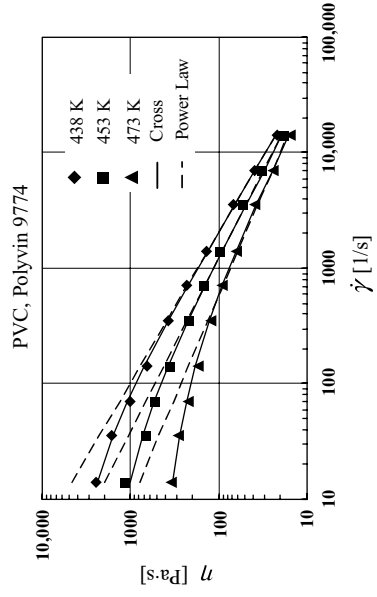
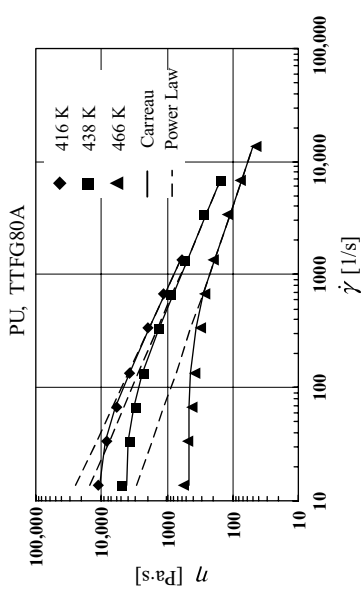


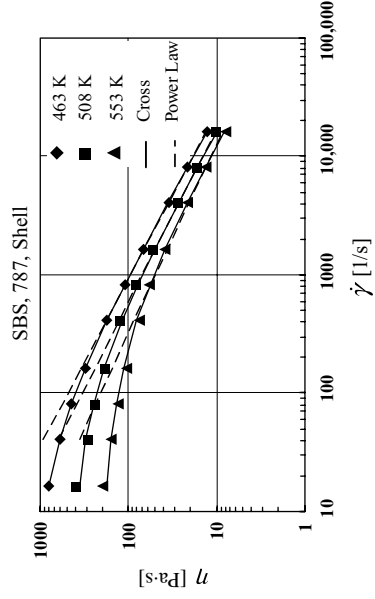
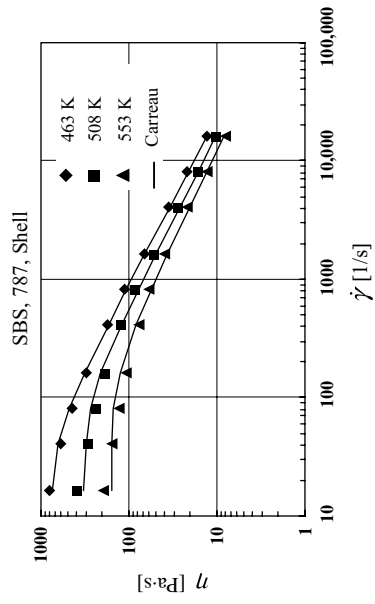
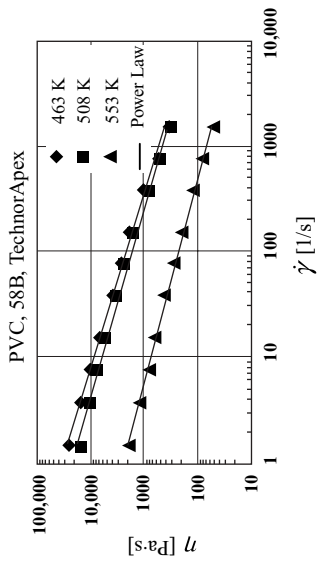


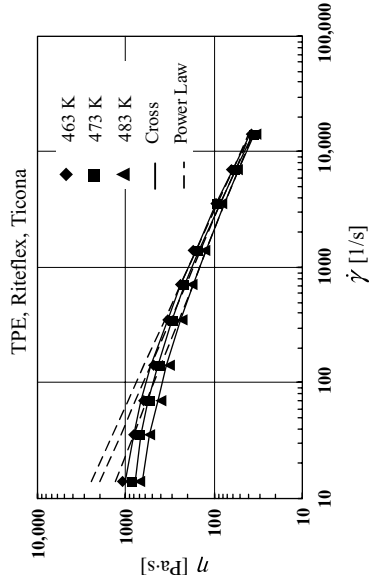
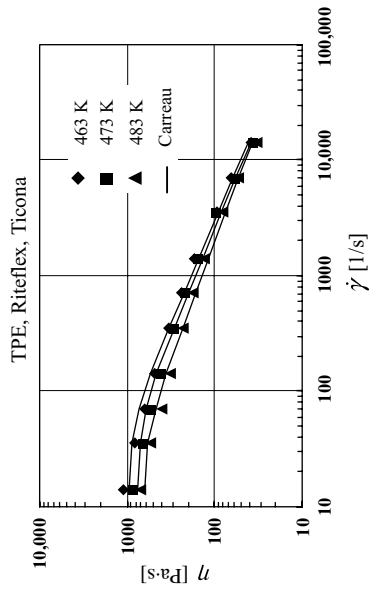
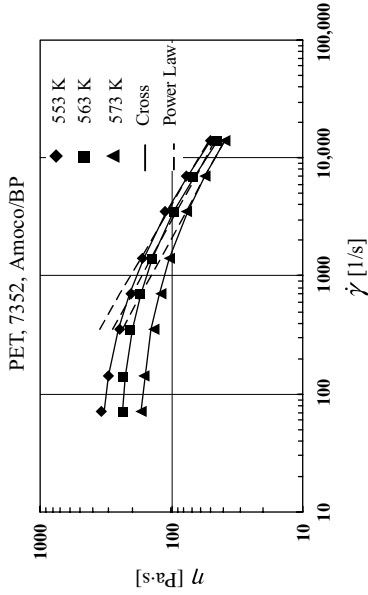
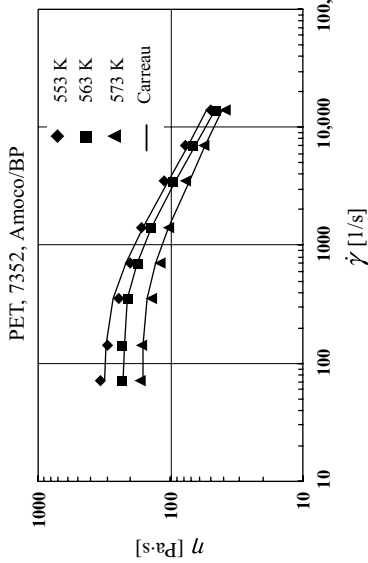


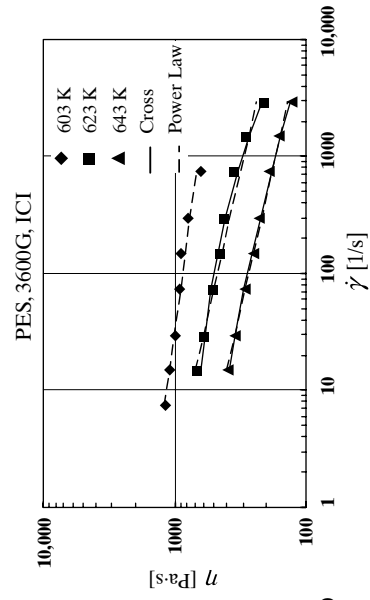
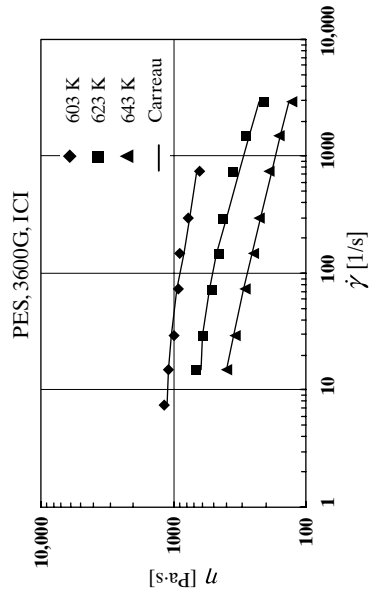
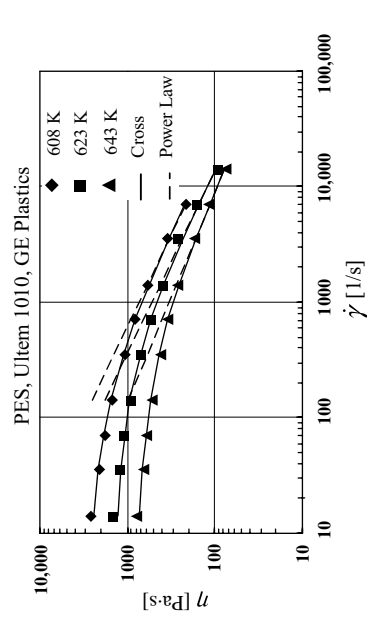
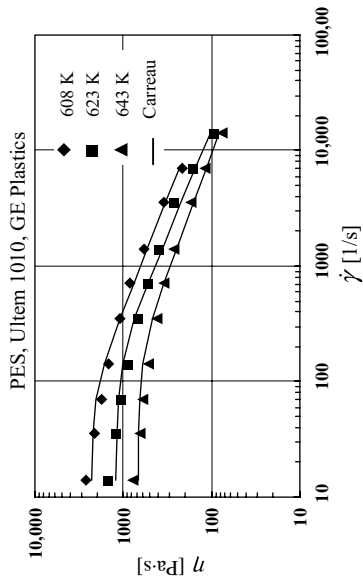












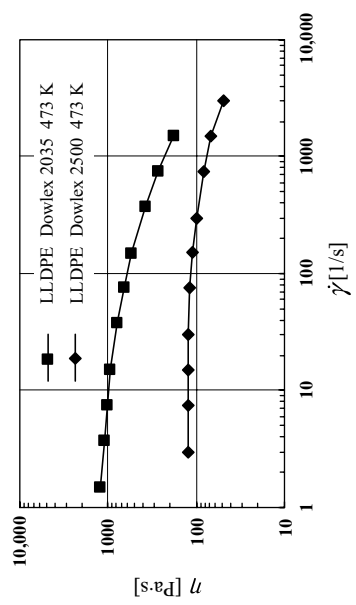
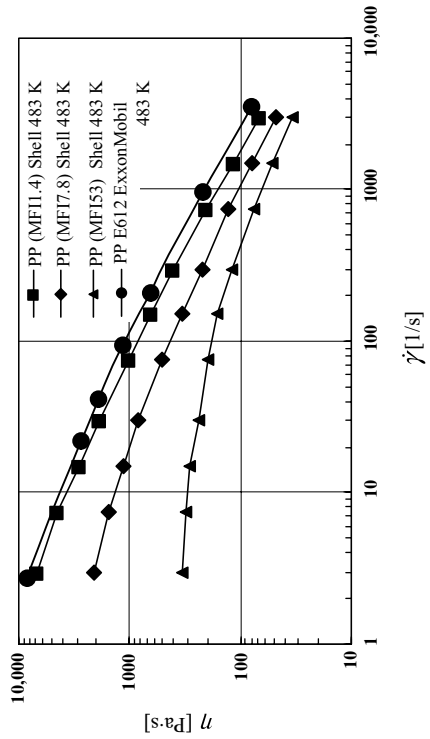
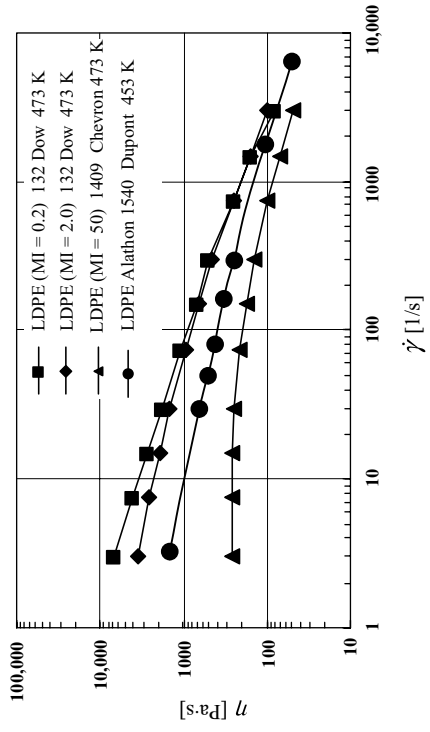


TABLE A.2 Thermophysical Properties of Semi-crystalline Thermoplastic Polymers

	Specific Heat [cal/g°C]		Heat of Fusion [J/g]	Glass Transition [°C]	Melting Point [°C]	Crystalli- zation Temp. [°C]	Solid Density at 25°C [g/cm ³]	Melt Density Temp [°C]	Melt Density [g/cm ³]		Thermal Conductivity [W/m/ K]		Thermal Diffusivity 10 ⁻⁴ [cm ² /s]	
	Solid at 25°C	Melt (average)							at 0	at 10 ⁴	Solid	Melt	Solid	Melt
LCP (Xydar)	0.221	0.405	0.39		421-432	357-330	1.68	340	1.590	1.680	0.167	0.233	10.8	8.7
LCP (Vectra)	0.252	0.446	0.48	110	276-286	236	1.408	288	1.320	1.378	0.190	0.260	12.8	10.6
Nylon 6	0.649	0.919	11.6	70	220	182	1.130	240	0.958	1.010	0.317	0.341	10.3	9.3
Nylon 66	0.339	0.638	10.6	48	265	231	1.192	280	1.023	1.090	0.215	0.268	12.7	9.8
PBT	0.286	0.489	10	50	224-236	175	1.292	260	1.147	1.218	0.196	0.240	12.7	10.2
PB-1	0.398	0.628	7.5		118-128	79-58	0.915	160	0.813	0.877				
HDPE	0.453	0.631	39	-120	135	115	0.941-0.968	200	0.767	0.816	0.373	0.324	20.7	16.0
LDPE	0.540	0.600	18.7-23.7	-25	112-114	90-88	0.91-0.92	200	0.763	0.830	0.272	0.220	13.1	11.5
LLDPE	0.450	0.479	23.7		135	86	0.922-0.94	150	0.792	0.866	0.368	0.243	20.8	15.3
PEEK	0.241	0.503	8.5	150	350	310	1.453	370	1.228	1.389	0.251	0.197	17.1	7.6
PET	0.284	0.492	13.7	70	243-248	159	1.308	270	1.211	1.298	0.146	0.289	9.4	11.6
PMP	0.432	0.731	11.8	29	240	164	0.835	285	0.710	0.823	0.285	0.310	18.8	14.2
POM	0.337	0.526	32.6	-80	168	142	1.385	180	1.195	1.277	0.308	0.291	15.7	11.0
copolymer														
PP	0.421	0.669	21.6	-10	167	101	0.910	210	0.764	0.833	0.298	0.234	18.6	10.9
PPS (40% Filled)	0.227	0.420	10.8	91	285	232	1.653	300	1.550	1.627	0.215	0.289	13.7	10.6

TABLE A.3 Thermophysical Properties of Amorphous Thermoplastic Polymers

	Specific Heat [cal/g/°C]		Glass Transition [°C]	Solid Density at 25°C [g/cm ³]	Melt Density Temp [°C]	Melt Density [g/cm ³]		Thermal Conductivity [W/m/ K]		Thermal Diffusivity 10 ⁻⁴ [cm ² /s]	
	Solid at 25°C	Melt (average)				at 0	at 10 ⁴	Solid	Melt	Solid	Melt
					psi	psi					
ABS	0.284	0.445	100	1.226	200	1.154	1.216	0.155	0.205	10.6	9.5
Polyamide-imide	0.247	0.505	272	1.36	360	1.260	1.320	0.218	0.243	15.5	9.1
Polyamide, amorphous	0.314	0.538	155	1.19	260	1.052	1.112				
Polyarylsulfone	0.261	0.480	220	1.29	360	1.192	1.277	0.195	0.238	13.9	10.0
Polyarylester	0.260	0.412	185					0.233	0.243		
Polyetherimide	0.261	0.481	218	1.275	280	1.220	1.287	0.162	0.218	11.6	8.9
Polycarbonate	0.258	0.432	145	1.2	230	1.132	1.207	0.175	0.255	13.5	12.5
Polymethyl- methacrylate	0.307	0.508	105	1.183	200	1.130	1.179	0.172	0.202	11.3	8.4
Polystyrene	0.296	0.499	100	1.067	200	0.970	1.040	0.153	0.185	11.6	9.1
Polyurethane	0.659	0.776		1.26	165	1.073	1.130	0.230	0.247	6.6	7.1
Polyvinylchloride	0.317	0.400	65	1.353	165	1.241	1.307	0.169	0.185	9.4	8.9

Note: For engineering estimates of the dependence of polymer melt density on pressure and temperature use:
 Compressibility $\sim 10^{-9}$ (N/m²)⁻¹ $\sim 7 \times 10^{-6}$ (psi)⁻¹ and Thermal Expansion Coefficient $\sim 5 \times 10^{-4}$ (K)⁻¹

APPENDIX B

Conversion Tables to the International System of Units (SI)

*The International System of Units (SI) and Conversion Tables**

Quantity	Unit	SI Symbol	
Basic units			
Length	meter	m	
Mass	kilogram	kg	
Time	second	s	
Electric current	ampere	A	
Thermodynamic temperature	kelvin	K	
Luminous intensity	candela	cd	
<i>Supplementary units</i>			
Plane angle	radian	rad	
Solid angle	steradian	sr	
Derived units			
Acceleration	meter per second squared	—	m/s^2
Activity (of a radioactive source)	disintegration per second	—	(disintegration/s)
Angular acceleration	radian per second squared	—	rad/s^2
Angular velocity	radian per second	—	rad/s
Area	square meter	—	m^2
Density	kilogram per cubic meter	—	kg/m^3
Electric capacitance	farad	F	$\text{A} \cdot \text{s}/\text{V}$
Electric field strength	volt per meter	—	V/m
Electric inductance	henry	H	$\text{V} \cdot \text{s}/\text{A}$
Electric potential difference	volt	V	W/A
Electric resistance	ohm	Ω	V/A
Electromotive force	volt	V	W/A
Energy	joule	J	$\text{N} \cdot \text{m}$
Entropy	joule per kelvin	—	J/K
Force	newton	N	$\text{kg} \cdot \text{m}/\text{s}^2$
Frequency	hertz	Hz	—
Magnetomotive force	ampere	A	—
Power	watt	W	J/s

*E. A. Mechtly "The International System of Units," NASA SP-7012, Washington, D.C. 1969; also, *AIChE J.*, **17**, 511 (1971).

Quantity	Unit	SI Symbol	
Pressure	newton per square meter	—	N/m ²
Quantity of electricity	coulomb	C	A · s
Quantity of heat	joule	J	N · m
Radiant intensity	watt per steradian	—	W/sr
Specific heat	joule per kilogram-kelvin	—	J/kg · K
Stress	newton per square meter	—	N/m ²
Thermal conductivity	watt per meter-kelvin	—	W/m · K
Velocity	meter per second	—	m/s
Viscosity, dynamic	Newton-second per square meter	—	N · s/m ²
Viscosity, kinematic	square meter per second	—	m ² /s
Voltage	volt	V	W/A
Volume	cubic meter	—	m ³
Wavenumber	reciprocal meter	—	(wave)/m
Work	joule	J	N · m

SI Prefixes

Factor	Prefix	Symbol	Factor	Prefix	Symbol
10 ¹²	tera	T	10 ⁻¹	deci	d
10 ⁹	giga	G	10 ⁻²	centi	c
10 ⁶	mega	M	10 ⁻³	milli	m
10 ³	kilo	k	10 ⁻⁶	micro	μ
10 ²	hecto	h	10 ⁻⁹	nano	n
10 ¹	deka	da	10 ⁻¹²	pico	p

Physical Constants

	Unit	Value	
Avogadro constant	k mole ⁻¹	6.0222	E + 26*
Gas law constant	J/kmole · K	8.3143	E + 3
Boltzmann constant	J/K	1.3806	E - 23
Stefan-Boltzmann constant	W/m ² K ⁴	5.66916	E - 8
Planck constant	J · s	6.6262	E - 34
Gravitational acceleration	m/s ²	9.80665	E + 00

*E + 26 denotes 10²⁶.*Conversion Table to SI Units*

To Convert from	To	Multiply by
angstrom	meter (m)	1.000 000* E - 10
atmosphere (normal)	newton/meter ² (N/m ²)	1.013 250* E + 05
barrel (for petroleum, 42 gal)	meter ³ (m ³)	1.589 873 E - 01
Bar	newton/meter ² (N/m ²)	1.000 000* E + 05
British thermal unit (International Table)	joule (J)	1.055 04 E + 03
Btu/lbm-°F (heat capacity)	joule/kilogram-kelvin (J/kg · K)	4.186 800* E + 03
Btu/second	watt (W)	1.054 350 E + 03

Conversion Table to SI Units—(Continued)

To Convert from	To	Multiply by
Btu/ft ² -hr-°F (heat transfer coefficient)	joule/meter ² -second-kelvin (J/m ² · s · K)	5.678 264 E + 00
Btu/ft ² -hr (heat flux)	joule/meter ² -second (J/m ² · s)	3.154 591 E + 00
Btu/ft-hr-deg F (thermal conductivity)	joule/meter-second-kelvin (J/m · s · K)	1.730 735 E + 00
Calorie (International Table)	joule (J)	4.186 800* E + 00
cal/g-°C	joule/kilogram · kelvin (J/kg · K)	4.186 800* E + 03
cal/sec-cm-K	joule/meter-second-kelvin (J/m · s · K)	4.186 800* E + 02
centimeter	meter(m)	1.000 000* E - 02
centimeter ² /second	meter ² /second (m ² /s)	1.000 000* E - 04
centimeter of mercury (0°C)	newton/meter ² (N/m ²)	1.333 22 E + 03
centimeter of water (4°C)	newton/meter ² (N/m ²)	9.806 38 E + 01
centipoise	newton-second/meter ² (N · s/m ²)	1.000 000* E - 03
centistokes	meter ² /second (m ² /s)	1.000 000* E - 06
degree Celsius	kelvin (K)	t _K = t _C + 273.15
degree Fahrenheit	kelvin (K)	t _K = (t _F + 459.67)/1.8
degree Rankine	kelvin (K)	t _K = t _R /1.8
dyne	newton (N)	1.000 000* E - 05
dynes/centimeter ²	newton/meter ² (N/m ²)	1.000 000* E - 01
erg	joule (J)	1.000 000* E - 07
fluid ounce (U.S.)	meter ³ (m ³)	2.957 353 E - 05
foot	meter (m)	3.048 000* E - 01
foot (U.S. survey)	meter (m)	3.048 006 E - 01
foot of water (39.2°F)	newton/meter ² (N/m ²)	2.988 98 E + 03
foot ²	meter ² (m ²)	9.290 304* E - 02
foot/second ²	meter/second ² (m/s ²)	3.048 000* E - 01
foot ² /hour	meter ² /second (m ² /s)	2.580 640* E - 05
foot-pound-force	joule (J)	1.355 818 E + 00
foot ² /second	meter ² /second (m ² /s)	9.290 304* E - 02
foot ³	meter ³ (m ³)	2.831 685 E - 02
gallon (U.S. liquid)	meter ³ (m ³)	3.785 412 E - 03
gram	kilogram (kg)	1.000 000* E - 03
gram/centimeter ³	kilogram/meter ³ (kg/m ³)	1.000 000* E + 03
horsepower (550 ft · lb _f /s)	watt (W)	7.456 999 E + 02
horsepower-hour	joule (J)	2.6845 E + 06
hour (mean solar)	second (s)	3.600 000 E + 03
inch	meter (m)	2.540 000* E - 02
inch of mercury (60°F)	newton/meter ² (N/m ²)	3.376 85 E + 03
inch of water (60°F)	newton/meter ² (N/m ²)	2.488 4 E + 02
inch ²	meter ² (m ²)	6.451 600* E - 04
inch ³	meter ³ (m ³)	1.638 706* E - 05
kilocalorie	joule (J)	4.186 800* E + 03
kilogram-force (kgf)	newton (N)	9.806 650* E + 00
kilowatt-hour	joules (J)	3.600 000 E + 06
liter	meter ³ (m ³)	1.000 000* E - 03
micron	meter (m)	1.000 000* E - 06
mil	meter(m)	2.540 000* E - 05
mile (U.S. statute)	meter (m)	1.609 344* E + 03

Conversion Table to SI Units—(Continued)

To Convert from	To	Multiply by
mile/hour	meter/second (m/s)	4.470 400* E - 01
millimeter mercury (0°C) (torr)	newton/meter ² (N/m ²)	1.333 224 E + 02
minute (angle)	radian (rad)	2.908 882 E - 04
minute (mean solar)	second (s)	6.000 000* E + 01
ohm (international of 1948)	ohm (Ω)	1.000 495 E + 00
ounce-mass (avoirdupois)	kilogram (kg)	2.834 952 E - 02
ounce (U.S. fluid)	meter ³ (m ³)	2.957 353 E - 05
pint (U.S. liquid)	meter ³ (m ³)	4.731 765 E - 04
poise (absolute viscosity)	newton-second/meter ² (N · s/m ²)	1.000 000* E - 01
poundal	newton (N)	1.382 550 E - 01
pound-force (lbf avoirdupois)	newton (N)	4.448 222 E + 00
pound-force-second/foot ²	newton-second/meter ² (N · s/m ²)	4.788 025 E - 01
pound-force-second/inch ²	newton-second/meter ² (N · s/m ²)	6.894 757 E + 03
pound-mass (lbm avoirdupois)	kilogram (kg)	4.535 924 E - 01
pound-mass/foot ³	kilogram/meter ³ (kg/m ³)	1.601 846 E + 01
pound-mass/foot-second	newton-second/meter ² (N · s/m ²)	1.488 164 E + 00
pound-mass/foot ² -second (mass transfer coefficient)	kilogram/meter ² -second (kg/m ² · s)	4.88243 E + 00
psi (pounds per inch ²)	newton/meter ² (N/m ²)	6.894 757 E + 03
quart (U.S. liquid)	meter ³ (m ³)	9.463 529 E - 04
second (angle)	radian (rad)	4.848 137 E - 06
slug	kilogram (kg)	1.459 390 E - 01
stoke (kinematic viscosity)	meter ² /second (m ² /s)	1.000 000* E - 04
ton (long, 2240 lbm)	kilogram (kg)	1.016 047 E + 03
ton (short, 2000 lbm)	kilogram (kg)	9.071 847 E + 02
torr (mm Hg, 0°C)	newton/meter ² (N/m ²)	1.333 22 E + 02
volt (international of 1948)	volt (absolute) (V)	1.000 330 E + 00
watt (international of 1948)	watt (W)	1.000 165 E + 00
watt-hour	joule (J)	3.600 000* E + 03
watt/centimeter ² -°K	joule/meter ² -second-K (J/m ² · s · K)	1.000 000* E + 04

*An asterisk after the sixth decimal place indicates the conversion factor is exact and all subsequent digits are zero.

APPENDIX C

Notation

Only symbols used repeatedly in the text are included here. Reference is made to the equation, section, or example where the symbol is first used.

a	Temperature dependence coefficient of viscosity parameter m of a Power Law model fluid (3.3-25)
a_T	Time-temperature superposition shift factor (3.3-30)
A	Interfacial area element (E7.1-14)
A	$= dH/dz$ taper of a screw channel in the down channel direction (9.3-31)
A_f	Free area between screws and barrel in an intermeshing twin screw extruder(6.8-6)
A^*	Dimensionless surface area of a deformed bubble (8.10-2)
b	$= a(T_1 - T_0)$ (5.7-25)
b'	$= b/n$ (5.7-43)
Br	Brinkman number Newtonian (E2.7-3); Power Law model (5.7-28)
c_i	Molar concentration of species i . (2.10-1)
c_e	Equilibrium molar concentration (9.4-8)
C_v	Specific heat at constant volume (2.9-16)
C_p	Specific heat at constant pressure (2.9-16)
C_s, C_m	Specific heat of solid and molten polymer (Section 5.1)
C_L	Centerline distance between intermeshing screws (6.8-1)
Ca	Capillary number (Section 7.1; 8.7-2)
d	Diameter
D	Diameter
D	Deformation of a droplet (7.1-14)
D_b	Inside diameter of an extruder barrel (6.3-4)
D_s	$= D_b - 2H$ diameter of the root of the screw
D_f	$= D_b - 2\delta_f$ diameter of the screw at the tip of the flight
De	Deborah number (3.1-23)
D_N	Dispersion index of molecular weight distribution (7.3-9)
Da	Damkohler number (11.2-26)
\mathcal{D}	Diffusion coefficient of solvent in molten polymer (8.5-2)
\mathcal{D}_{AB}	Binary mass diffusion coefficient in Fick's law (Example 2.4)

e	Total specific energy of a system (2.9-9)
e	Flight width (6.3-2)
e_v	Rate of viscous heating per unit volume (12.1-7)
E	Total energy of a system (2.9-1)
E	Activation energy
\hat{E}	Dimensionless activation energy (11.2-11)
E_n	Separation efficiency of n stages (9.4-9)
E_v	Rate of conversion of mechanical energy into heat (E9.1-2)
\hat{E}_v	Rate of conversion of mechanical energy into heat per unit mass flow rate (E9.1-7)
erf(z)	error function (E5.2-8)
f	Kinematic coefficient of friction (4.1-7)
f'	Static coefficient of friction (4.1-1)
f_L	Leakage flow correction factor for the pressure flow rate in screw extruders (6.3-28)
$f(t)dt$	External residence time distribution function (Section 7.3)
f_k	Exit passage distribution function (Section 7.3)
$f(\gamma)d\gamma$	Exit strain distribution function (Section 7.3)
$f(\gamma)d\gamma$	external strain distribution function (Section 7.3)
F	Force
$F(t)$	Cumulative exit residence time distribution function (7.3-12)
$F(\gamma)$	Cumulative exit strain distribution function (7.3-21)
F_c	Cohesive force of the agglomerate (7.1-21)
F_d	Drag flow shape factor in a screw extruder (6.3-20)
F_d^*	Drag-flow shape factor for co-rotating disk processor (Example 6.12)
F_D	Air drag-force on fiber in fiber-spinning (E14.1-2)
F_h	Hydrodynamic forces acting on a particle in a sheared liquid (7.1-22)
F_k	Cumulative exit passage distribution function (Section 7.3; 7.3-29)
F_N	Normal force (E3.2-12)
F_p	Pressure-flow shape factor in a screw extruder (6.3-21)
F_p^*	Pressure-flow shape factor for co-rotating disk processor (Example 6.12)
F_{DTW}	Volumetric drag-flow correction factor for nonintermeshing twin-screw extruder (6.8-45)
F_{PTW}	Volumetric pressure-flow correction factor for nonintermeshing twin-screw extruder (6.8-46)
F_0	Fourier number (13.1-16)
g	Gravitational acceleration (2.5-7)
g_N	Skewness measure of a molecular weight distribution (7.3-10)
$g(t)dt$	Internal residence time distribution function (Section 7.3)
$g(\gamma)d\gamma$	Internal strain distribution function (Section 7.3)
$g_k(t)$	Passage distribution function in batch systems (Section 7.3)
$g(Z)$	Generating function (7.3-27)
G	Mass flow rate (9.2-1)
G	Dimensionless pressure gradient (E3.6-4)
$G(t)$	Cumulative internal residence time distribution function (7.3-11)
$G(\gamma)$	Cumulative internal strain distribution function (7.3-19)

$G_k(t)$	Cumulative passage distribution function (7.3-23)
$G'(\omega)$	In-phase dynamic modulus (3.1-22)
$G''(\omega)$	Out-of-phase dynamic modulus (3.1-22)
G_z	Graetz number (12.1-17)
h	Heat transfer coefficient (5.2-1)
h	Enthalpy (Section 2.9)
\hat{h}	Enthalpy per unit mass (E9.1-4)
h	Half-separation between two rolls (Section 6.4)
H	separation between parallel plates (Example 2.5); channel depth of a screw
H_0	Half-minimum gap between rolls (Section 6.4 and Fig.6.22)
H_1	Half thickness of sheet leaving the roll; also half separation between rolls at point of detachment at axial location X_1 (Section 6.4 and Fig.6.22)
H_2	Half-separation between the rolls at axial location X_2 (Section 6.4 and Fig.6.22)
i_k	Internal-passage distribution function (Section 7.3; 7.3-29)
I	Intensity of segregation (7.4-10)
$I_{en}(\beta)$	Shanon's relative entropy (7.4-18)
I_k	Cumulative internal passage distribution function (Section 7.3)
I_τ	First scalar invariant of the stress tensor (2.6-2)
II_τ	Second scalar invariant of the stress tensor (2.6-3)
III_τ	Third scalar invariant of the stress tensor (2.6-4)
J	Rate of homogeneous nucleation (8.6-1)
J_{Ai}	Mass flux of component A in the i direction relative to the mass average velocity (Example 2.4)
J_n	n^{th} -order Bessel function (Example 2.9)
J_R	Steady state shear compliance (12.2-3a)
k	Boltzmann constant
k	Thermal conductivity in Fourier's law (Example 2.4)
\bar{k}	Mean number of passages (7.3-24)
k_c	Mean packing coordination number (7.1-18)
k_s, k_m	Thermal conductivity of solid and molten polymer
K	Ratio of compressive stress in the horizontal direction to compressive stress in the vertical direction in bins and hoppers (4.3-2)
l	Axial direction in single screw extruders (9.2-25)
L	Characteristic length of flow channels
L_s	Lead of a screw (6.3-1)
L^*	Effective capillary length to account for end effect (Section 12.1)
m	Power Law model parameter (3.1-9)
m_0	$m(T_0)$ (3.3-24)
M	Mass
M_x	Concentration of molecules of x-mers (Section 7.3)
\bar{M}_n	Number average molecular weight

\overline{M}_w	Mean weight average molecular weight
\overline{M}_z	Mean z -average molecular weight
n	Unit outward normal vector
n	Power Law model parameter (3.1-9)
n_f	Number of fully filled chambers in counterrotating intermeshing twin screw extruders (10.2-1)
N	Screw speed (frequency of screw rotation) (6.3-4)
N_C	Number of compressions during transit time in co-rotating twin screw extruders (10.3-5)
N_R	Number of screw rotations during transit time in co-rotating twin screw extruders (10.3-4)
Nu	Nusselt number (11.2-19)
p_w	Power input per unit area in parallel plate flow (E2.5-21)
p_w	Power generated by interparticle friction (5.9-1)
P	Pressure (2.5-8)
P_a	Atmospheric pressure
P_w	Total power input; in parallel plate flow (E2.5-22)
\hat{P}_w	Power per unit mass flow rate (E9.1-4)
P_1	Vapor pressure of the solute over an ideal solution (8.4-1)
P_1^0	Vapor pressure of the pure solute (8.4-1)
q	Heat flux (2.9-5)
q	Volumetric flow rate in parallel plate flow per unit width (E2.5-9)
q_d	Volumetric drag flow rate in parallel plate flow per unit width (E2.5-10)
q_p	Volumetric pressure flow rate in parallel plate flow per unit width (E2.5-11)
\hat{q}_h	Heat added to per unit mass flow rate (E9.1-4)
Q	Volumetric flow rate
Q_d	Volumetric drag flow rate in a screw extruder (6.3-22)
Q_l	Leakage flow rate in a counter rotating intermeshing twin screw extruder (10.2-3)
Q_p	Volumetric pressure-flow rate in a screw extruder (6.3-22)
Q_{ch}	Volumetric flow rate per channel in a co-rotating intermeshing twin screw extruder (6.8-12)
Q_{th}	Theoretical volumetric flow rate in a counterrotating intermeshing twin screw extruder (10.2-2)
Q_D	Volumetric flow rate through an extruder die (9.2-6)
r	Radial coordinate in cylindrical and spherical coordinates
r	Striation thickness (E7.1-21; 7.4-11)
r_e	Critical radius of a bubble (8.7-1)
R	Radius
$R(r)$	Coefficient of correlation (7.4-7)
R_C, R_L	Circumferential and longitudinal radii of curvature (14.2-19)
R_{cr}	Equilibrium critical radius of a bubble (8.9-13)
s	$= 1/n$; n is the Power Law model parameter
S	Surface area

S	Entropy of a system (7.4-12)
\mathbf{S}_{ED}^{IA}	Doi-Edwards chain orientation tensor (3.4-7)
\mathbf{S}_{MSF}	Molecular Stress Function theory orientation tensor (3.4-10)
S_R	Recoverable strain (12.2-2)
S^2	Variance of samples taken from mixture (7.4-6)
σ	Scale of segregation (7.4-9)
sign	function with either plus or minus values
t	Time
t_0	Minimum residence time
$t_{1/2}$	Half life time (Section 11.1)
$t_f(\xi)$	Fraction of time a fluid particle spends in the upper part of a screw channel (9.2-24)
t_D	diffusion characteristic time (11.3-2)
t_G	Characteristic time for heat release in batch reactor (11.2-5)
t_R	Characteristic time for heat removal in batch reactors (11-2-6)
t_{transit}	Transit time of a charge through one lobe of a co-rotating intermeshing twin-screw extruder (10.3-1)
\bar{t}	Mean residence time
\mathbf{T}'	Traction vector (Section 2.6)
T	Temperature
\hat{T}	Dimensionless temperature (11.2-3)
T_g	Glass transition temperature
T_m	Melting point
T_s	Temperature of the solid polymer
T_m	Temperature of the molten polymer
\mathcal{T}	Torque (E2.9-12)
u	Internal energy (2.9-9)
\mathbf{u}'	Chain deformation vector (3.4-7)
u_i	Dimensionless velocity component
U	Tangential velocity of calender rolls (Section 6.4)
U_1	Viscous-dissipation dimensionless term in polymer melting (5.7-53)
U_2	Dimensionless factor for temperature dependence of drag flow (5.7-51)
\mathbf{v}	Velocity vector
v_i	Velocity components
v_l	Velocity component in a screw extruder in axial direction (6.3-24)
V	Volume
V_0	Plate velocity in parallel plate flow (Example 2.5)
V_b	Velocity of the extruder barrel relative to screw (6.3-4)
V_f	Free volume between screws and barrel in an intermeshing twin-screw extruder (6.8-7)
\mathbf{V}_j	Relative velocity vector between barrel surface and solid bed (9.3-1)
V_{pl}	Axial velocity of the solids in the solids conveying zone of a single-screw extruder (9.3-2)
V_{sz}	Down-channel velocity of the solid bed in a screw extruder (9.3-27)
w_a	Rate of melting per unit area (E5.4-14)

w_L	Rate of melting per unit length in drag-removal melting (5.7-38); in single screw extruders (9.3-14)
w_T	Total rate of melting in pressure-induced melting (5.8-1)
W	Width of flow channel; screw channel width (6.3-2)
W_x	Weight fraction of x-mers (7.3-2)
x, y, z	Cartesian coordinates
\bar{x}_N	Number-average molecular chain length (7.3-4)
\bar{x}_W	Weight-average molecular chain length (7.3-5)
\bar{x}_z, \bar{x}_{z+1}	z-average molecular chain lengths (7.3-6)
X	Width of the solid bed (Sections 5.7 and 9.3)
Y_x	Mole fraction of x-mers (7.3-1)
z	Helical length of a screw channel (6.3-3)
Z	Ratio of hydrodynamic to cohesive forces (7.1-27)
Z_T	Down-channel length of melting in single screw extruders (9.3-30)

Greek Letters

α	Thermal diffusivity (E5.2-1)
α	Parameter in the Ellis model (3.3-26)
α	Angle defining the width of the flight tip in intermeshing twin screws (6.8-2 and Fig. 6.43)
α	Angle formed by polymer melts in the entrance region or capillary flow (12.2-5)
β	Parameter for the pressure dependence of viscosity (12.1-5)
γ	Total shear strain (E7.1-9)
$\bar{\gamma}$	Mean shear strain (7.3-20 and 7.3-22)
$\dot{\boldsymbol{\gamma}}$	Rate of deformation tensor (2.7-7)
$\dot{\gamma}$	Shear rate (2.7-11); magnitude of $\dot{\boldsymbol{\gamma}}$ (3.3-21)
$\bar{\dot{\gamma}}$	Mean shear rate (Example 9.2)
$\dot{\gamma}_w$	Shear rate at the wall (E3.1-9)
$\dot{\gamma}_w^*$	Corrected shear at the wall of a capillary (12.1-3)
$\dot{\gamma}_{xy}$	Components of the shear stress tensor (2.7-2)
Γ	Surface tension (2.11-1)
Γ_w	Newtonian shear rate at the wall in capillary flow (E3.1-11)
δ	Thermal penetration depth (E5.3-8)
δ	Melt film thickness (Section 5.7; in singles screw extruders 9.3-34)
δ	Solubility parameter (8.4-3)
δ_f	Radial flight clearance between flight tip and barrel (6.3-27)
δ	Unit tensor (2.5-9)
δ_i	Unit vectors
ΔH_r	Heat released by chemical reaction in a batch reactor ($-\Delta H_r$) (11.2-1)
ΔE	Flow activation energy (3.3-24)
ΔP	Pressure difference over a finite channel length or flow region

ΔP_D	Pressure drop through a die (9.2-6)
ΔT_a	Adiabatic temperature rise in PED (5.9-3)
ε	Porosity of particulate solids (4.5-2)
ε	Separation efficiency of one stage (9.4-8)
$\dot{\varepsilon}$	Uniaxial elongational strain rate (3.1-1)
$\dot{\varepsilon}_{pl}$	Planar elongational strain rate (3.1-6)
ε_{bi}	Biaxial elongational strain rate (3.1-7)
ζ	$= H/H_1$ dimensionless height between nonparallel plates (Example 2.8)
η	Non-Newtonian shear rate-dependent viscosity (3.1-8)
η_0	Zero shear viscosity; Ellis Model (3.3-26); Cross model (3.3-29); Carreau model (3.3-33)
η_∞	Infinite shear rate viscosity; parameter in the Carreau model (3.3-33)
η', η''	Components of complex viscosity $\eta^* = \eta' - i\eta''$ (3.1-21)
$\bar{\eta}$	Elongational viscosity (3.1-26)
$\bar{\eta}^+$	Elongational stress-growth viscosity (3.1-27)
θ	Angle in cylindrical and spherical coordinates
θ	Helix angle of an extruder screw (6.3-1)
θ	Spherical and cylindrical coordinate
θ_b, θ_s	Helix angle of an extruder screw at the barrel surface ($D = D_b$) and root of the screw ($D = D_s$) (6.3-1)
Θ	Dimensionless temperature (E5.3-1)
λ	Relaxation time (3.1-23)
λ	Heat of fusion (5.7-10)
λ^*	Modified heat of fusion (5.7-15)
λ^{***}	Modified heat of fusion (5.7-39)
μ	Viscosity of a Newtonian fluid (2.8-1)
μ_f	Viscosity in the flight clearance of a screw extruder (6.3-28)
μ_r	r^{th} moment of a molecular-weight distribution (7.3-3); moment generating function (7.3-28)
ξ	Dimensionless coordinate
π	$= P\delta + \tau$ the total stress tensor (2.5-8)
π'	$= -\pi^\dagger$
π_{ij}	Stress tensor components (2.5-10)
ρ	Density
ρ_s, ρ_m	Density of solid and molten polymer (Section 5.1)
ρ_i	Position vector (E7.1-1)
σ	Normal stress in particulate solids (4.1-1)
σ	Tensile strength of an agglomerate (7.1-17)
σ	Stefan-Boltzmann radiation constant (5.2-2)
σ_y	Yield stress (4.1-2)

σ^2	Variance of binomial distribution (7.4-2)
σ_N^2	Molecular weight distribution variance (7.3-8)
τ	Shear stress; magnitude of the stress tensor (2.6-5)
τ_w	Shear stress at wall (E3.1-4)
τ_y	Yield stress (3.3-34)
τ_{ij}	Dynamic stress tensor components (2.5-10)
τ^*	Parameter in the Cross model (3.3-29)
τ_w^*	Corrected shear stress at the wall of a capillary (12.1-1)
τ	Dynamic or deviatoric stress tensor (2.5-8)
ϕ	Spherical coordinate
ϕ	Solids conveying angle (4.9-1; 9.3-2)
Φ_r	Newtonian rate of viscous heating per unit volume
χ_{12}	Flory-Huggins interaction parameter (8.4-3)
Ψ	Half the angle bounding the interpenetrating region between intermeshing screws (6.8-1 and Fig. 6.43)
Ψ	Dimensionless number measuring melting rate in singles-screw extruders (9.3-23)
Ψ_1	Primary normal stress coefficient (3.1-10)
Ψ_2	Secondary normal stress coefficient (3.1-11)
ω	Vorticity tensor (2.7-8)
Ω	Angular velocity
Ω	Number of microstates (7.4-12)

Mathematical symbols

D/Dt	Substantial derivative (2.3-2)
$\mathcal{D}/\mathcal{D}t$	Corotational or Jauman derivative (3.3-3)
∇	Vector operator “del” or “nabla” (Footnote 6, Chapter 2)

Abbreviations

ASA	acrylonitrile styrene acrylate
BR	butyl rubber
CAD	computer aided design
CFM	computerized fluid mechanics
CM	continuous mixer
COC	cyclic olefin copolymers
Co-TSE	co-rotating twin screw extruders
CPFR	continuous plug flow reactor
CR-PP	controlled rheology polypropylene
CSTR	continuous stirred tank reactor
CV	control volume
DMF	dimethyl formamide

DMM	dissipative mix-melting
EPDM	ethylene-propylene-diene
EPM	ethylene-propylene monomer
EPOM	engineering polymers oil modified
FAN	flow analysis network
FED	frictional energy dissipation
FEM	finite element method
GMA	glycidyl methacrylate
GRP	glass reinforced polymers
HBR	helical barrel rheometer
HFIP	hexafluoroisopropanol
LCFR	linear continuous flow reactor
LCP	liquid crystal polymers
L/D	length-to-diameter ratio
LDPE	low density polyethylene
LLDPE	linear low density polyethylene
MAH	maleic anhydride
MFR	melt flow rate
MOS	magnesium oxysulfate
MW	molecular weight
MWD	molecular weight distribution
NPD	number of passage distribution
OD/ID	outer-to-inner diameter ratio
PA	polyamide
PBT	polybutylene terephthalate
PC	polycarbonate
PDMS	polydimethylsiloxane
PED	plastic energy dissipation
PEEK	polyetherether ketone
PEI	polyetherimide
PEO	polyethylene oxide
PES	polyethersulfone
PET	polyethylene terephthalate
PETG	glassy PET modified with cyclohexanemethanol
PFR	plug flow reactor
PI	polyimide
PMMA	polymethyl methacrylate
PMP	polymethylpentene
POM	polyoximethylene
POX	peroxide
PP	polypropylene
PPA	polymer processing additive
PPO	polyphenylene oxide
PPS	polyphenylene sulfide
PTFE	polytetrafluorethylene
PS	polystyrene
PUR	polyurethane
PVC	polyvinyl chloride

RIM	reaction injection molding
RMS	rheometrics mechanical spectrometer
RTD	residence time distribution
SDF	strain distribution function
SIS	styrene-isoprene-styrene block copolymer
SMA	styrene maleic anhydride
SME	screw mixing elements
SSE	single screw extruder
SSMEE	single screw mixing element evaluator
TIM	thermoplastic injection molding
TFR	tubular flow reactor
TGIC	triglycidyl isocyanurate
TSE	twin screw extruder
TSMEE	twin screw mixing element evaluator
VED	viscous energy dissipation

AUTHOR INDEX

- Abbott, L. E., 857
Abdel-Khalik, S. I., 133, 743
Abel, J. F., 885
Acierno, D., 858
Acrivios, A., 350, 351, 397, 431, 441, 640, 671
Agassant, J. F., 130, 131, 132, 135, 298, 299,
303, 316, 695, 855, 859, 870, 884
Agur, E. E., 517
Ahlefeld, E. H., 24, 357, 397, 526, 594
Ainsler, A., 229, 581, 583, 595, 598
Ajdari, A., 400
Albalak, R. J., 409, 428, 433, 434, 435, 436,
437, 438, 440, 441, 442
Alemanskin, K., 391, 399
Alfrey, T., 629, 670, 745
Allemaskin, K., 171
Allen, V. R., 820
Allersma, H. G. B., 165, 166, 172
Alston, W. W., 870, 884
Altobelli, S. A., 166, 171, 172
Amaiwa, T., 569, 570, 571, 572, 597
Amano, T., 599, 856
Amontons, G., 147
Anastasiades, S. H., 670
Andersen, J. G., 669
Andersen, P. G., 572, 574, 575, 576, 594, 597,
602, 655, 673
Anderson, D. M., 595
Anderson, P. D., 393, 394, 395, 399, 595
Andrews, K. Z., 171
Angell, R. G., Jr., 820
Aoba, T., 762, 817
Appeldoorn, J. K., 685, 743
Aral, B., 672
Archimedes, 319
Aref, H., 334, 335, 336, 396
Aris, R., 61, 72
Armstrong, R. C., 68, 106, 115, 116, 133, 140,
232, 316, 597, 776, 818, 856, 870
Arnold, E., 147
Arruda, W., 864
Asai, T., 397
Ashuror, N., 671
Asimov, I., 315
Ast, W., 837, 857
Astill, K. N., 870, 884
Astruc, M., 353
Atochem Corporation, 669
Atwood, J. L., 22, 24
Avenas, P., 298, 299, 303, 316, 855, 884
Avgeropoulos, G. N., 673
Baaijens, F. P. T., 24, 135, 779, 780, 818, 819
Beaijens, H. P. W., 131
Babic, M., 172
Baer, E., 227
Bagley, E. B., 683, 743, 744
Bagyi, I., 171
Baird, D. G., 132, 860, 862
Balanchandar, S., 336, 396
Balch, G., 315
Baldwin, A. J., 24, 397, 594
Balke, S. T., 669
Ballenger, T. F., 695, 744
Ballman, R. L., 752, 761, 816
Banbury, F., 528
Bang, D. S., 555, 556, 557, 596
Bankoff, S. G., 227
Barlow, J. W., 673
Barnes, D. K., 441
Barrie, I. T., 770, 817, 823
Barthez, J. M., 818
Bastian, H., 93, 131, 134, 135
Baumann, D. K., 644, 672
Baumberger, T., 171
Bawiskar, S., 226, 229, 580, 595, 598
Beall, G. N., 858
Beauxis, J., 669

- Beavers, G. S., 86
 Becker, O., 790, 819
 Beek, W. J., 216, 219, 228, 519
 Bekin, N. G., 872, 873, 884
 Bell, P. W., 830, 831, 855
 Bellet, M., 859
 Berezhnaya, G. V., 744
 Bergem, N., 697, 698, 744
 Bergen, J. T., 270, 271, 316, 366, 368, 378, 395, 561, 596, 869, 884
 Berger, J. L., 817
 Bergmann, J., 596
 Beris, A. N., 830, 856
 Berlis, A., 320
 Bernhardt, E. C., 23, 24, 254, 316
 Bernnat, A., 135
 Bernstein, B., 104, 133, 143, 850, 858
 Beyer, C. E., 761, 816, 850, 858
 Bhattacharji, S., 291, 316
 Biddisow, P. H., 673
 Biesenberger, J. A., 358, 362, 409, 415, 424, 425, 426, 440, 441, 442, 546, 547, 595, 604, 616, 620, 668, 670, 674
 Bigg, D. M., 227, 340, 341, 396, 518, 639, 640, 671
 Biggs, R. D., 232
 Binning, G., 171
 Bird, R. B., 25, 28, 30, 35, 38, 44, 46, 57, 58, 59, 68, 72, 99, 101, 105, 106, 115, 116, 123, 124, 133, 134, 139, 140, 141, 232, 291, 293, 316, 597, 685, 691, 692, 724, 725, 743, 744, 745, 775, 814, 817, 820, 870
 Birks, R. M., 698, 744
 Bischoff, K. B., 73
 Blake, J. W., 818
 Blander, M., 422, 441
 Blyler, L. L., Jr., 137, 744
 Bogaerds, A. C. B., 135, 778, 779, 780, 818
 Bogue, D. C., 98, 105, 106, 133, 696, 744, 857
 Böhm, G. G. A., 673
 Bolen, W. R., 397, 561, 596
 Bomal, Y., 641, 671
 Bonner, R. M., 679
 Booy, M. L., 259, 300, 301, 302, 315, 317, 450, 517
 Borisenkova, E. K., 744
 Bourgeois, J. L., 884
 Bourne, J. R., 385, 398
 Boussinesq, M. J., 253, 742
 Bowden, F. P., 147, 149, 171
 Bradley, N. L., 745
 Brandrup, J., 396, 440, 671
 Braudo, C., 135
 Bravo, V. L., 585, 586, 587, 588, 599, 673
 Brazinsky, I., 870, 884
 Bregsse, L., 317
 Brekelmans, W. A. M., 24
 Brennen, C. E., 172, 426, 441
 Brenner, H., 742
 Brinkman, H. C., 685, 743
 Briskoe, B. J., 171
 Brizzolara, J., 655, 672
 Brodkey, R. S., 395
 Brothman, G., 327, 395
 Brouwer, T., 623
 Brown, H. R., 668
 Brown, R. L., 171, 856
 Brown, S. B., 674
 Broyer, E., 138, 196, 320, 486, 518, 727, 745, 790, 814, 815, 819, 820, 823, 885
 Bruker, I., 259, 315
 Brydon, A., 400
 Brzowski, R., 673
 Bucknall, C. B., 670
 Bullman, S. D., 746
 Bulters, M., 780, 818
 Burdick, I. W., 171
 Burggaf, O. R., 464
 Burkhardt, U., 317, 594
 Burrell, H., 396
 Busby, F., 228
 Butterfield, R., 154, 171
 Byron, D. E., 885
 Cahn, R. W., 343, 396, 656
 Cain, J. J., 837, 841, 858
 Campbell, G. A., 837, 858
 Canedo, E. L., 431, 432, 441, 529, 558, 559, 563, 565, 566, 567, 594, 596, 597, 653, 672
 Canevari, G. P., 440
 Cao, B., 858
 Capaccio, G., 829, 855
 Capel, J. E., 595
 Caprihan, A., 171
 Caras, F. C., 816
 Carey, G. F., 399
 Carley, J. F., 706, 745, 863
 Carneiro, O. S., 735, 746
 Caroli, B., 171
 Caroli, C., 171
 Carreau, P. J., 105, 106, 110, 111, 133, 134, 598
 Carrier, G. W., 395
 Carslaw, H. S., 195, 196, 227

- Cesar de Sa, J. M. A., 859
 Chabot, J. F., 2, 23
 Chabra, R. P., 598
 Chaiken, J., 336, 337, 396
 Chan, H. T., 228, 594
 Chan, T. W., 706, 745
 Chang, C. S., 166, 172
 Chang, J. C., 857
 Chang, M. C. O., 818
 Chang, R. Y., 517
 Charalambopoulos, D. N., 242, 673
 Charles, M., 743
 Charneau, J. Y., 818
 Charrier, J. M., 854, 859
 Chen, I., 98
 Chen, I. J., 857
 Chen, J., 98, 105
 Chen, L., 490, 518
 Chen, Z., 855
 Cheng, C. Y., 172, 297
 Cheng, J. J., 561, 585, 597, 598
 Cheng, Y. F., 170, 172
 Cheung, Y. K., 819
 Chevray, R., 336, 337, 396
 Chibber, C., 337, 396
 Chien, W. L., 337, 396
 Cho, J. W., 595
 Chong, J. S., 870, 884, 886
 Choo, K. P., 259, 315, 517
 Christiano, J. P., 585, 599
 Christiansen, R. L., 817
 Christiansen, E. B., 100, 132, 775
 Chu, C. K., 396
 Chu, E., 818
 Chu, S., 134
 Chung, C. I., 518
 Chung, D. H., 776, 777, 818
 Churchill, S. W., 192, 227
 Clapeyron, B. P., 190
 Clark, E. S., 793, 817, 819
 Clark, R., 884
 Clausing, A. M., 227
 Cleereman, K. J., 794, 795, 819
 Clere, T., 744
 Clift, R., 170
 Clmett, W. R., 669
 Clump, W., 398
 Coates, P., 855
 Cogswell, F. N., 133, 694, 697, 700, 704, 744, 748
 Cohen, C., 671
 Cohen, D., 199
 Cole, R., 441
 Coleman, B. D., 101, 133
 Collias, D. I., 132, 860, 862
 Collin, V., 352, 353, 397, 672
 Collins, E. A., 181, 743
 Colwell, R. E., 259, 315, 397, 459, 460, 517, 561, 596
 Cooper, K. W., 441
 Coperion Werner and Pfeleiderer Corporation, 524, 530
 Coran, A. Y., 316, 395
 Cosway, H. F., 884
 Couette, M. M., 85, 132
 Coughlin, R. W., 440
 Coulomb, C.-A., 147
 Coupez, T., 135
 Cowin, S. C., 153, 171
 Cox, B. G., 787, 819
 Cox, D. R., 376, 398
 Cox, H. W., 686, 687, 688, 725, 743
 Cox, R. G., 351, 397
 Cox, W. P., 132
 Coyle, D. J., 818, 819
 Crank, J., 193, 227, 768, 817
 Crawley, R. L., 690, 743
 Criminale, W. O., Jr., 102, 133
 Crosby, E. J., 376, 398
 Cross, M. M., 110, 134
 Cruz-Saenz, G. F., 856
 Cundall, P. A., 165, 166, 167, 169, 170, 172
 Curry, J. E., 228, 229, 669, 673
 Dahl, R. B., 816
 Daily, J. W., 441
 Danckwerts, P. V., 360, 385, 397, 398
 Danescu, R. I., 337, 396
 Darnell, W. H., 474, 482, 485, 518
 Datta, S., 668
 Dave, R. N., 172
 David, B., 315, 514, 519, 673, 885
 Davies, J. E. D., 24
 Davis, G. deV., 227
 Deacour, M. L., 581, 583, 598
 Dealy, J. M., 132, 745, 858, 850, 858
 Debbaut, B., 135, 854, 859
 Dee, H. B., 762, 817
 Dees, J. R., 827, 855
 deGennes, P. G., 125, 127, 128, 134
 de Josselin de Jong, A. G., 165, 170, 172
 DeKee, D. C. R., 598
 Delacour, M. L., 229, 595
 Della Valle, G. J., 317

- DeLorenzi, H. G., 854, 859
 Demay, Y., 135
 Demejo, L. P., 172
 Denelsbek, D. A., 228, 597, 598
 Denn, M. M., 62, 73, 696, 744, 818, 830, 835, 837, 841, 855, 856, 857, 858
 den Otter, J. L., 698, 744
 Denson, C. D., 317, 853, 859
 Dertinger, S. K. W., 400
 Desai, C. S., 885
 de Waele, A., 108, 133
 Dewhirst, H., 885
 Dey, S. K., 242, 546, 547, 595, 670
 Dhavalkikar, R., 625, 669
 Dietz, W., 775, 817
 Dillon, R. D., 696, 744
 DiMatia, D. P., 858
 Dinh, S. M., 776, 818
 DiRaddo, R. W., 849, 858, 859
 Doboczky, Z., 307, 317
 Dodson, A. G., 746
 Doi, M., 127, 128, 129, 134
 Domine, J. D., 804, 805, 807, 808, 809, 820
 Donea, J., 885
 Donnelly, G. J., 856
 Donoian, G. S., 519
 Donovan, R. C., 519, 755, 816
 Dorn, M., 608, 669
 Doufas, A. K., 830, 856
 Dougherty, T. J., 598
 Dowson, D., 171
 Drake, R. M., Jr., 227
 Dreiblatt, A., 594, 669
 Druin, M. L., 858, 845, 858
 Dubois, J. H., 23
 Duda, J. L., 420, 421, 441
 DuFresne, D. A., 228
 Durand, V., 818
 Durrill, P. L., 820
 Dusinberre, G. M., 227
 Duvdevani, I. J., 228, 518, 743
- Eckert, E. R. G., 227, 742
 Edelist, I., 284, 285, 315, 316, 519.
 Edie, D. D., 830, 831, 855
 Edmundson, I. R., 519
 Edwards, M. F., 859, 860
 Edwards, S. F., 127, 128, 129, 134
 Ehrecke, P., 93, 135
 Ehrmann, G., 267, 269, 884
 Eighmy, G. W., Jr., 884
 Eirich, F. R., 826
- Eise, K., 594
 Eisenberg, J., 227
 Elbe, W., 182, 226
 Elbirli, B., 460, 517
 El Kissi, N., 102, 133
 Ellis, S. B., 110, 134
 Engels, T. A. P., 24
 Epstein, B. N., 668, 669
 Erdmenger, R., 529, 594
 Ericksen, J. L., 102, 133
 Erk, S., 196
 Erwin, L., 183, 227, 395, 653, 654, 672, 676
 Eshelby, J. D., 200, 227
 Essegheir, M., 221, 228, 229, 242, 673
 Evans, L. B., 192, 227
 Everage, A. E., Jr., 752
 Eyring, H., 743
- Fairbrother, F., 785, 787, 819
 Fan, L. T., 385, 398
 Farrel Corporation, 508, 509, 510, 522, 527
 Favelukis, M., 428, 432, 433, 441, 442
 Favis, B. D., 673
 Feke, D. L., 352, 397
 Feldman, S. M., 395
 Feller, W., 398
 Fenner, R. T., 460, 517, 519
 Ferry, J. D., 104, 132, 133, 661, 673, 743
 Feters, L. J., 670, 671
 Feynman, R., 25
 Fiber-world Classroom Website, 825
 Filbey, G. L., Jr., 102, 133
 Finlayson, D., 253, 315
 Finston, M., 316, 872, 873, 884
 Fisher, R. J., 835, 855, 856
 Fletcher, D., 670
 Flory, P. J., 134, 343, 396, 416, 417, 418, 440, 669
 Flynn, K., 744
 Fortin, A., 135
 Fortin, M., 856
 Fox, T. G., 820
 Frank-Kamenetskii, D. A., 615, 670
 Frankel, N. A., 640, 671
 Frankland, J. D., 848
 Fredrickson, A. G., 104, 133, 724, 725, 745, 814, 820
 Frenkel, J., 200, 201, 227
 Fricke, A. L., 228
 Friedrichs, B., 776, 818
 Fritz, H. G., 12, 669
 Fujita, H., 420, 441

- Fukui, T., 397
 Fukushima, E., 171, 172
 Fuller, L. J., 596
 Fuller, T. R., 228
 Funatsu, K., 532, 538, 539, 540, 541, 542, 543, 544, 545, 569, 570, 571, 572, 589, 590, 591, 592, 593, 594, 595, 597, 599, 858

 Gadzenveld, K. J., 547, 548, 551, 595, 596
 Galaktionov, O. S., 393, 394, 395, 399, 595
 Galili, N., 689, 743
 Gallagher, R. H., 885
 Gallot, Y., 670
 Ganattz, I., 670
 Garcia, A. C., 818
 Gardner, G. C., 153, 171
 Gartling, D. K., 885
 Gaskell, R. E., 263, 270, 271, 316, 321, 869, 884
 Gauri, V., 787, 788, 789, 790, 819
 Gaurus, A. L., 135
 Gaylord, N. G., 668, 669
 Gazonnet, J. P., 818
 Geil, P. H., 227
 Geng, X., 228, 229, 580, 598
 Georghiades, S., 860
 Gerber, Ch., 171
 Gerrard, J. E., 685, 686, 743
 Gerson, P. M., 228
 Gessler, A. M., 349, 397
 Geyer, P., 397
 Geyling, F. T., 857
 Giesekus, H., 693, 744, 746, 788, 789, 819, 830, 850, 856
 Gilmore, G. D., 172, 761, 792, 816
 Gilver, R. C., 172
 Glasscock, S. D., 690, 743
 Goddard, J. D., 99, 101, 102, 133
 Goddard, P., 641, 671
 Goffart, D., 317
 Gogos, C. G., 24, 151, 171, 172, 184, 221, 222, 226, 228, 229, 242, 576, 578, 579, 580, 582, 584, 594, 597, 611, 626, 647, 653, 655, 666, 668, 669, 670, 672, 673, 685, 687, 704, 705, 743, 745, 769, 770, 771, 776, 804, 805, 808, 809, 817, 820, 822, 855
 Goldacker, E., 156
 Goldblatt, P. H., 743
 Good, P. A., 276, 277, 316
 Goodman, T. R., 188, 227, 231
 Goodyear, C., 1, 23
 Gotsis, A. D., 584, 598

 Gottlieb, M., 744
 Goublomme, A., 135
 Gounelle, M., 171
 Govaert, L. E., 24
 Goyal, S. K., 818
 Grace, H. P., 347, 348, 397
 Gracia-Rejon, A., 849, 850, 858
 Graessley, W. W., 88, 126, 134, 690, 691, 692, 693, 743
 Graham, L., 400
 Graham, R. S., 818
 Grail, T. J., 669
 Gray, J. B., 342
 Gray, M., 2, 4, 23, 242
 Green, A. E., 101, 133, 746
 Green, M. S., 124, 128, 134, 143
 Greener, Y., 321
 Greenspan, M., 426, 441
 Greci, J., 620, 670
 Grest, G. S., 127, 134
 Griffith, R. M., 259, 315, 459, 460, 517
 Griskey, R. G., 820
 Gröber, H., 196
 Gross, D., 886
 Groves, D. J., 128, 129, 134, 819
 Gügeri, S. I., 776, 818
 Guégan, P., 673
 Guennete, R., 856
 Guenther, R. P., 232
 Gueram, P., 670
 Guo, S. J., 170, 172
 Gupta, M., 711, 745
 Gupta, R. K., 837, 841, 857
 Gutfinger, H., 72, 138, 196, 727, 745, 819, 823, 885
 Guth, E., 134

 Haagh, G. A. A. V., 818
 Haasen, P., 343, 396, 656
 Hachmann, P., 93, 134, 135
 Haff, P. K., 166, 172
 Hagler, G. E., 857
 Hähner, G., 64
 Halmos, A. L., 519
 Hamada, H., 778, 818
 Hamaker, H. C., 350, 397
 Hami, M. L., 259, 315, 517
 Hamielec, A. E., 549, 596, 608, 669
 Hammitt, F. G., 441
 Han, C. D., 641, 671, 694, 712, 713, 715, 716, 743, 744, 745, 747, 749, 750, 829, 835, 837, 841, 857, 858

- Han, L. S., 742
 Happel, J., 742
 Harkness, R. M., 171
 Harlen, O. G., 128, 129, 134, 818, 819
 Harlow, F. H., 340, 396
 Harry, D. H., 817
 Hart, A. C., Jr., 137, 744
 Hartnett, J. P., 227
 Harvey, E. N., 425, 426, 441
 Hashimoto, N., 228, 545, 546, 595
 Hashizume, S., 397
 Hassager, O., 68, 106, 115, 116, 133, 140, 232, 316, 597, 743, 787, 819, 870
 Hasson, A., 315
 Hatzikiriakos, S. G., 703, 704, 744, 745, 856
 Haudin, J. M., 818
 Hauger, W., 886
 Haupt, F., 742
 Haw, J. R., 671
 Haward, R. N., 23, 24
 Heidemeyer, P., 573, 597, 598
 Helfand, E., 634, 671
 Herrmann, H., 2, 23, 317, 525, 594, 669
 Hertlein, T., 669
 Heslot, F., 171
 Hess, W. M., 349, 397
 Higashi, H., 599
 Hildebrand, J. H., 396
 Hilton, B. T., 585, 586, 598
 Himelblau, D. M., 73
 Hinch, E. J., 431, 441
 Hinrich, R., 518
 Hinton, E., 746
 Hirai, N., 743
 Hirshberger, M., 118, 134, 517
 Hobbs, S. Y., 779, 794, 818, 819
 Hocq, B., 859
 Hold, P., 3, 5, 24, 315, 316, 397, 519, 594
 Holle, H., 596
 Homer, 645
 Hong, K. M., 671
 Hong, M. H., 556, 557, 596
 Hoogstraten, H. W., 317
 Horie, M., 745
 Hostettler, J., 670
 Houghton, W. T., 744
 Hovey, V. M., 23
 Hovis, G., 526, 594
 Howell, H. G., 149, 171
 Hrymak, A. N., 586, 587, 588, 599, 673, 773, 776, 817, 885
 Hsu, C. W., 517
 Hsu, D. C., 517
 Hu, W., 670
 Huang, C. F., 759, 769, 770, 771, 776, 793, 816, 817, 818, 822
 Hubka, V., 237, 314
 Huebner, K. H., 885
 Huerta, A., 885
 Huggins, M. L., 343, 396, 416, 417, 418, 440
 Hugues, K. R., 228
 Hunt, M. L., 172
 Hurt, C. V., 399
 Hutchings, I. M., 147
 Hutchinson, B. C., 399
 Hutton, J. F., 133
 Huzyak, P. C., 787, 788, 819
 Hwang, B. K., 317
 Hyatt, J. W., 2, 4, 23
 Hyman, J. M., 399
 Hyman, M. A., 817
 Hyun, J. C., 833, 836, 837, 841, 858, 857, 856
 Hyun, K. S., 172, 174, 175, 855
 Ide, Y., 856, 857
 Immergut, B., 396
 Immergut, E. H., 396, 440, 671
 Inkson, N. J., 128, 129, 134, 819
 Inoue, K., 357, 397, 673
 Irvine, T. F., 742
 Irving, H. F., 341, 395
 Ishibashi, A., 316
 Ishikawa, T., 568, 569, 570, 571, 572, 588, 589, 590, 593, 597, 599
 Iso, Y., 671
 Ito, K., 854, 859, 710, 745
 Jackson, G. B., 817
 Jackson, S., 669
 Jaeger, J. C., 195, 196, 227
 Jaffer, S. A., 585, 599
 Jakopin, S., 317, 594
 James, H. M., 134
 Jana, S. C., 401
 Janeschitz-Kriegl, H., 135
 Janssen, H. A., 150, 151, 171
 Janssen, J. M. H., 345, 346, 348, 396, 656, 673
 Janssen, L. P. B. M., 304, 307, 317, 533, 534, 535, 536, 547, 595, 596, 670
 Jayaraman, G. S., 227
 Jeffrey, H., 103, 133
 Jenike, A. W., 146, 153, 166, 171
 Jeong, B., 626, 670

- Jeong, E. K., 171
 Jepson, E. H., 395
 Ji, Z., 598
 Johanson, J. R., 153, 171
 Jones, R., 884
 Jongbloed, H. A., 596
 Joo, Y. L., 830, 832, 856
 Joseph, D. D., 86
 Ju, S. T., 421
 Julesz, B., 380, 381, 398
 Jung, H. W., 226, 229, 582, 598, 833, 837, 841, 856, 857
- Kabanemi, K. K., 858, 859
 Kacir, L., 518
 Kajiwara, T., 537, 538, 539, 540, 541, 542, 543, 544, 545, 555, 591, 592, 594, 595, 599, 858
 Kakizaki, J., 228
 Kalyon, D. M., 584, 598, 672, 850, 851, 858, 860
 Kamal, M. R., 672, 762, 792, 817, 818, 819, 850, 855, 858, 860, 888
 Kamimori, K., 397
 Kaminski, R., 790, 819
 Kanai, T., 837, 857
 Kantz, M. R., 793, 819
 Kaplan, A., 310, 314, 317, 554, 596
 Kaplan, S., 817
 Kase, S., 830, 855, 856
 Kashani, F., 888
 Kassahun, B., 517
 Katayama, K., 856
 Katsuki, S., 591, 592, 594, 599
 Katz, D. L., 708, 867
 Katz, J. L., 422, 441
 Katz, S., 398
 Kaufman, A. A., 248
 Kaufman, M., 23, 171, 252, 253, 315, 392, 398, 399
 Kawaguchi, T., 172
 Kaye, A., 143, 850
 Kearsley, E. A., 104, 133, 143, 850, 858
 Keller, A. P., 441
 Keller, J. P., 669
 Kelley, M., 172
 Kenig, S., 762, 817
 Kenny, M.J., 669
 Kessidis, G., 415, 440, 442
 Kessler, H. B., 679
 Keuerleber, R., 803, 819
 Khan, S. A., 92, 133
- Khandpur, A. K., 670, 673
 Kher-adi, F., 553, 554, 596
 Kiani, A., 585, 598, 655, 673
 Kihara, S. I., 569, 570, 571, 572, 589, 590, 591, 592, 593, 594, 597, 599.
 Killeffer, D. H., 24, 355
 Kim, B. M., 856, 857
 Kim, D., 885
 Kim, G., 670
 Kim, H., 858
 Kim, H. T., 743
 Kim, M., 647, 672
 Kim, M.-H., 24, 184, 220, 222, 223, 224, 225, 226, 229, 561, 576, 578, 579, 582, 584, 597
 Kiparissides, C., 271, 316, 872, 873, 884, 885
 Kirk, R. O., 228
 Kjeldsen, M., 441
 Klein, I., 210, 228, 247, 315, 447, 450, 461, 462, 463, 475, 480, 481, 490, 496, 497, 498, 503, 506, 517, 518, 519, 520, 743, 670
 Kleinberger, R., 199
 Klenk, K. P., 307, 317
 Klenk, P., 518
 Klomp, E. M., 317
 Klompen, E. T. J., 24
 Knapp, R. T., 441
 Knudsen, J. G., 708
 Kobayashi, N., 595
 Koberstein, J. T., 670
 Kocherov, V. L., 316
 Koehring Company, 754
 Koelling, K. W., 787, 788, 789, 790, 819
 Kondo, A., 696, 744
 Koo, J. Y., 669
 Koopmans, R. J., 135
 Kouba, K., 854, 859
 Kowalski, R. C., 594, 604, 606, 607, 668, 669
 Kramer, E. J., 343, 396, 656
 Kremer, K., 127, 134
 Krieger, I. M., 598
 Krueger, W. L., 760, 763, 764, 765, 790, 816, 822
 Krujit, P. G. M., 399
 Krumbansh, J. A., 395
 Kuch, D. L., 671
 Kuczynski, G. C., 200, 227
 Kuhn, W., 345
 Kulkarni, J. A., 830, 856
 Kumazawa, T., 673
 Kuo, Y., 792, 819

- Kurtzbeck, S., 134
 Kwon, T. H., 776, 777, 818

 LaBombard, D., 397
 Lagally, P., 596
 Lahti, G. P., 742
 La Mantia, F. P., 858
 Lamb, P., 694, 697, 744
 Lamé, G., 190
 Landel, R. F., 661, 673
 Landes, D., 6, 24
 Lane, J., 440
 Langlois, W. E., 77
 Langouche, F., 134
 LaNieve, H. L., III, 696, 744
 Lapidus, L., 61, 73
 Laroche, D., 850, 854, 855, 858, 859
 Larson, R. G., 92, 124, 126, 128, 133, 134, 642, 672
 Lastochkin, D., 442
 Latimer, S. L., 597, 598
 Latinen, G. A., 414, 415, 440, 442-443
 Lau, K. H., 170, 172
 Laun, H. M., 90, 117, 132, 133, 135, 642, 643, 672
 Laurencena, B. R., 817
 Lavie, R., 816
 Lavrenteva, O. M., 441
 Lawal, A., 584, 598
 Leal, L. G., 671
 Lee, J., 153, 154, 171
 Lee, J. C., 858
 Lee, K., 135
 Lee, K.-J., 885
 Lee, L. J., 802, 820
 Lee, S., 856
 Lee, S. J., 857
 Lee, S. T., 424, 425, 426, 441
 Lehn, J.-M., 24
 Leider, P. J., 291, 293, 294, 316
 Leong, C. W., 338, 339, 670
 Leonov, A. I., 717, 745, 837, 858
 Leppard, W. R., 100, 132
 Leversen, L. D., 816
 Levine, M. C., 831, 833, 834, 856
 Levinson, M., 154, 171
 Lewis, T. B., 639, 640, 671
 Li, H. Y., 170, 172
 Li, T., 537, 538, 555, 556, 595
 Liang, R. Y., 172
 Libera, M., 670
 Lidor, G., 372, 398, 470, 504, 518
 Lidorikis, S., 745
 Lifshitz, S. D., 815, 820
 Lightfoot, E. N., 25, 28, 30, 35, 38, 44, 46, 57, 58, 59, 72, 124, 134
 Lilleleht, L. U., 518
 Lim, S., 535, 595
 Lindenfelzer, M., 585, 599
 Lindt, J. T., 460, 517, 518, 555, 596
 Ling, F. H., 670
 Lingelser, J. P., 670
 Lipshitz, S. D., 816
 List, H., 397
 List Corporation, 413
 Litvinov, V. V., 884
 Liu, H. T., 421
 Liu, L., 599
 Liu, T., 228
 Lo, J. R., 203, 227
 Lobe, V. M., 638, 671
 Lodge, A. S., 104, 106, 125, 126, 133, 143, 149, 171, 402, 691, 743
 Lohse, D. J., 668, 671
 Long, M., 155, 156, 172
 Lonz, J. F., 227
 Lord, H. A., 817, 823
 Lovegrove, J. G. A., 487, 518
 Lu, Y., 620, 621, 622, 623, 670
 Lukach, Yu. L., 316
 Luo, X. -L., 837, 858, 880, 881, 885
 Luther, S., 881, 882, 883, 886
 Luwa Corporation, 413

 Maack, H., 745
 Mack, M., 572, 597
 Mackley, M. R., 133, 135
 Macosko, C. W., 132, 277, 316, 594, 598, 628, 630, 631, 633, 634, 635, 659, 670, 671, 673, 686, 687, 688, 725, 743, 801, 802, 803, 814, 815, 816, 818, 820, 855, 886
 Maddock, B. H., 474, 506, 518
 Madock, B., 490
 Maillefer, C., 505
 Maire, V., 742
 Makinouchi, A., 859
 Malguarnera, S. C., 802, 820
 Malkin, Ya., 744
 Malloy, R. A., 2, 23
 Manas-Zloczower, I., 171, 345, 348, 349, 352, 372, 391, 392, 395, 396, 397, 398, 399, 518, 537, 538, 555, 556, 561, 566, 568, 585, 595, 597, 598, 637, 648, 649, 651, 654, 672, 676

- Mann, U., 376, 398
 Marchal, J. M., 859
 Marchessault, R. N., 785, 819
 Marckmann, G., 854, 859
 Marco, S. M., 742
 Marechal, P., 670, 673
 Marič, M., 634, 671
 Mark, H. F., 826, 855
 Marrucci, G., 858
 Marschall, H. B., 426, 441
 Marshall, C. M., 397
 Marshall, D. E., 743
 Marshall, D. I., 316, 447, 868, 884
 Marten, F. L., 549, 596
 Martin, B., 232
 Martin, C., 557, 558, 596
 Mascia, L., 636, 671
 Mason, S. G., 347, 351, 397, 785, 819
 Mathieu, L., 818
 Matovich, M. A., 830, 855
 Matsuhisa, S., 746
 Matsuo, T., 830, 855
 Matthews, G., 395
 Mavridis, H., 317, 595, 712, 716, 718, 719, 720,
 745, 771, 773, 775, 776, 817
 Maxwell, B., 3, 5, 24, 272, 316, 607
 Mayer, P., 819
 McCabe, W. L., 14, 152
 McCullough, T. W., 228, 585, 586, 598
 McElroy, W. D., 441
 McFadden, G. B., 595
 McHugh, A. J., 856
 McKelvey, J. M., 23, 256, 263, 266, 270, 316,
 323, 395, 710, 742, 745, 869, 870, 884
 McLeish, T. C. B., 128, 129, 130, 134, 818,
 819
 McLuckie, C., 743
 Mechtly, E. A., 914
 Medalia, A. I., 349, 397
 Mehta, P. S., 288, 289, 315, 316, 321, 411, 415,
 440, 516, 519, 669
 Meijer, H. E. H., 23, 24, 135, 343, 345, 346, 348,
 393, 394, 395, 396, 399, 595, 656, 673, 778,
 781, 782, 783, 784, 818, 819, 855
 Meissner, J., 93, 134, 135, 670, 859
 Meissner, K., 561, 596
 Mekkaui, A. M., 519
 Melish, U., 226, 229, 580, 598
 Menges, G., 182, 226, 518, 771, 772, 802, 817,
 819
 Mertz, E. H., 132
 Metcalfe, G., 400
 Metzner, A. B., 744
 Mewes, D., 881, 882, 883, 886
 Mewis, J., 598
 Mezghani, A., 102, 133
 Marič, I., 400
 Mhaskar, R. D., 856
 Miaw, C., 315
 Michaeli, W., 855
 Middleman, S., 321, 340, 341, 396, 517, 518,
 860
 Mighton, J. W., 816
 Migler, K. B., 699, 700, 701, 702, 744, 856
 Miller, C., 99, 102, 133, 856
 Miller, D. R., 816, 820
 Mirza, F. A., 880, 885
 Misra, A., 172
 Mitsoulis, E., 776, 818, 880, 885
 Miyazaki, M., 591, 592, 594, 599
 Modern Plastics Encyclopedia, 842, 843, 844
 Moet, A., 316, 395
 Mohr, W. D., 395
 Mol, E. A. J., 474, 482, 485, 518
 Monasse, B., 818, 859
 Mørch, K. A., 441
 Morgan, C., 526, 594
 Morrette, R. A., 685, 687, 743
 Mount, E. M., III, 203, 228
 Mulder, R. K. S., 596
 Mulders, L. P. H. R. M., 317
 Muliawan, E. G., 700, 703, 704, 744
 Mund, C., 320
 Münstedt, H., 134
 Mussatti, F. G., 815, 820
 Mutel, A. T., 642, 671, 672
 Myers, G. E., 227, 876, 885
 Nadav, N., 382, 388, 398
 Nagashima, Y., 538, 539, 540, 541, 542, 543,
 544, 545, 595, 599
 Nahme, R., 685, 743
 Nahr, K. A., 580, 598
 Nakagawa, M., 171
 Nakagawa, T., 859
 Nakamura, K., 830, 856
 Nakano, Y., 538, 539, 540, 541, 542, 543, 544,
 545, 595, 599
 Nakayama, A., 673, 670
 Naor, P., 398
 Narh, A., 229
 Narkis, M., 199
 Navier, C. L., 45
 Nebrensky, J., 259, 315

- Nedler, J. A., 135
 Nettelbrecker, H. J., 594, 669
 Neumann, F., 190
 Neuville, B., 227
 Newman, H. H., Jr., 793, 819
 Newman, R. E., 414, 440
 Ng, T. T., 166, 171, 172
 Nguyen, K., 555, 596
 Nicholls, K. R., 259, 315, 459, 460, 517
 Nichols, B. D., 399
 Nichols, R. J., 553, 554, 555, 596
 Nicol, D. D., 24
 Nicolson, P., 193, 227, 768, 817
 Nied, H. F., 859
 Nielsen, L. E., 639, 640, 671
 Nir, A., 171, 349, 350, 351, 397, 398, 441, 648, 672, 885
 Nóbrega, J. M., 734, 735, 746
 Noll, W., 101, 133
 Noolandi, J., 671
 Nouatin, O.H., 135

 Obot, N. T., 858
 O'Brien, G. G., 768, 817
 Oda, K., 817
 Odaira, H., 762, 817
 Oden, J. T., 853, 859, 876, 885
 Odian, G., 669, 820
 Oehler, P. R., 819
 Oertel, G., 803, 819
 Ogawa, K., 397
 Oh, J. S., 857
 Okada, T., 357, 397
 Oldroyd, J. G., 104, 133, 746
 Oliveira, P. J., 735, 746
 Orbey, N., 850, 858
 Orr, C., Jr., 171
 Orr, F. M., 776, 818
 Osswald, T. A., 399
 Ostwald, W., 108, 133
 Otsuki, Y., 850, 858
 Ottino, J. M., 337, 338, 339, 396, 399, 401, 670, 820
 Oyanagi, Y., 698, 744

 Pabedinskas, A., 669
 Pagilagan, R. U., 669
 Pahl, F. W., 803, 819
 Pallas, R., 598
 Papanastasiou, T. C., 830, 855
 Papanastasiou, A. C., 881, 886
 Park, H. J., 880, 885
 Park, J. Y., 837, 841, 857
 Parnaby, J., 726, 727, 745
 Parrott, R. G., 817
 Paslay, P. R., 870, 884
 Pasquetti, C., 2, 24
 Paul, D. R., 670, 673, 745
 Peaceman, D. W., 820
 Pearson, J. R. A., 203, 206, 208, 228, 259, 315, 459, 517, 519, 706, 710, 726, 745, 817, 830, 833, 837, 855, 856, 857, 862
 Pease, D. C., 441
 Pecora, L., 858, 859
 Pelgrom, J. J., 317
 Pennwalt Corporation, 669
 Perkins, T. T., 126, 134
 Peseux, B., 859
 Peters, G. W. M., 24, 135, 393, 394, 395, 399, 595, 778, 779, 780, 781, 782, 783, 784, 807, 818, 819
 Petrie, C. J. S., 696, 744, 837, 854, 855, 856, 857, 859
 Petrusanskii, V. Yu., 873, 884, 885
 Peuvrel-Disdier, E., 352, 397, 672
 Pfeffer, R., 171
 Philippoff, W., 743
 Piau, J. M., 102, 133
 Pinho, F. T., 735, 746
 Pinto, G., 517
 Pittman, J. F. T., 259, 315, 517, 746
 Plamedia Research Corporation, 850, 852
 Pnueli, D., 72
 Pohl, T. C., 154, 171, 177
 Polsterdorf, B., 596
 Polymer Processing Institute, 657, 658, 660, 661, 662, 663, 664, 665, 667, 668
 Pooley, C. M., 171
 Poorter, O., 536, 595
 Porter, R. S., 743
 Poslinski, A. J., 787, 819
 Potente, H., 154, 171, 177, 226, 229, 580, 598
 Potluri, R., 597
 Price, W. L., 779, 818
 Proctor, B., 751
 Prud'homme, R. K., 92, 133, 744
 Put, J., 22, 24

 Qian, B., 24, 229, 576, 579, 580, 594, 597, 666, 673, 705, 745
 Qian, G. H., 171
 Qiao, F., 744
 Quate, C. F., 171
 Quensel, D. J., 172

- Rachford, H. H., Jr., 820
 Raible, T., 859
 Rakos, R., 746
 Ranz, W. E., 820
 Rao, D. A., 750
 Rao, M. A., 227, 230
 Rapetski, W. A., 24, 397, 594
 Rashid, K., 259, 315, 517
 Rauwendaal, C., 655, 672
 Rayleigh, Lord, 344, 396
 Read, R., 135
 Reddy, J. N., 885
 Redhefer, R. M., 133
 Reher, E. O., 596
 Rehner, J., 134
 Reiner, M., 90, 272
 Rekers, G., 135
 Renyi, A., 391, 398
 Resnick, W., 171
 Reuleaux, P., 237, 314
 Reynolds, O., 64, 146
 Richards, J. C., 171
 Richmond, O., 153, 171
 Richter, D., 671
 Rielly, F. J., 778, 818
 Riest, K., 881, 882, 883, 886
 Rimai, D. S., 172
 Rios, A. C., 399
 Rising, H., 337, 338, 339, 396, 670
 Rivlin, R. S., 101, 133, 746
 Roberts, G. W., 440
 Robinson Plastic Corporation, 756
 Rodriguez-Villa, A., 854, 859
 Rogers, M., 743
 Rohrer, H., 171
 Rolando, R. J., 594
 Roman, J. F., 692, 743
 Rosato, A. D., 172
 Rosato, A. V., 858
 Rosato, D. V., 858
 Roscoe, R., 598
 Rose, W., 290, 316, 765, 817
 Rosenhow, W. M., 227
 Rosenthal, D., 193, 227
 Ross, R. A., 856
 Ross, T. K., 178, 226
 Röthemeyer, F., 732, 733
 Rouse, P. E., Jr., 123, 134
 Roux, D., 818
 Roux, S., 171
 Rowell, R. S., 253, 315
 Roylance, D., 517
 Rubin, I. I., 757, 816
 Rubinovitch, M., 398
 Rubinstein, L. I., 227
 Rubio, P., 93, 135
 Rudman, M., 399, 400
 Rumpf, H., 170, 349, 397
 Rumscheidt, F. D., 347, 397
 Rutgers, I. L., 639, 671
 Rutgers, R. P. G., 133
 Rutledge, G. C., 833, 834, 856
 Ryan, M. E., 849, 858
 Ryu, S. H., 610, 611, 669
 Sabia, R., 717, 745
 Sailor, R. A., 744
 Saito, T., 628, 630, 631, 670
 Sakai, T., 228, 545, 546, 572, 595, 597, 602
 Sakiades, B. C., 683, 743
 Salame, M., 847
 Samann, H. J., 598, 655, 673
 Sampson, J., 172
 Santa Clara University School of Engineering
 Design Center, 785
 Sapir, T., 885
 Sarkar, D., 711, 745
 Satija, S., 554, 596
 Sato, T., 853, 859
 Savic, P., 291, 316
 Saxton, R. L., 341, 395
 Scalora, A. J., 3, 5, 24, 272, 316
 Scargo, P. G., 519
 Schaeffer, J., 134
 Scharer, H. R., 24, 397, 594
 Schaul, J. S., 846
 Schechter, R. S., 746
 Schenkel, G., 23, 307, 314, 317, 884
 Schepens, A., 780, 818
 Schmidt, F. M., 845, 855, 859
 Schmidt, L. R., 762, 776, 793, 817, 863
 Schneider, K., 156, 171, 172, 485, 518
 Schnell, W., 886
 Schonhorn, H., 233
 Schoone, P., 778, 784, 818
 Schott, N. R., 356, 397
 Schreiber, H. R., 743
 Schrenk, W. J., 629, 670, 745
 Schultz, J. M., 828, 829
 Schwanz, K., 819
 Schwartz, A. J., 316
 Scott, C. E., 633, 670, 671
 Scott, G. W. Jr., 270, 271, 316, 869, 884
 Scott, J. R., 291, 293, 316

- Scott, R. L., 396
 Scriven, L. E., 428, 441, 776, 818, 855, 886
 Scurati, A., 397
 Sebastian, D. H., 604, 613, 614, 615, 618, 619, 668, 673, 674, 746, 855
 Seinfeld, J. H., 61, 73
 Selen, S. H. A., 135
 Semenov, W. N., 613, 669
 Sentmanat, M. L., 702, 703, 704, 744, 745
 Sergeant, J.-Ph., 298, 299, 303, 316
 Seth, M., 744
 Seville, J. P. K., 170
 Seymour, N., 745
 Shannon, C. E., 390, 398
 Shapiro, J., 519
 Shaw, H., 171
 Shaw, Y. T., 856
 Shen, Y., 399
 Sheptak, N., 850, 858
 Shete, P., 671
 Shih, C. K., 221, 228, 597, 598
 Shinnar, R., 376, 398
 Shrivastava, S., 855, 859
 Shroff, R. N., 712, 716, 718, 719, 720, 745
 Shusman, T., 816
 Sidiropoulos, V., 837, 857, 858
 Sienz, J., 734, 746
 Simon, H., 412
 Simon, H. A., 237, 314
 Simon, R. H. M., 418, 440
 Simon, R. H. S., 414, 440
 Skidmore, R. H., 596
 Smith, D., 526, 594
 Smith, D. E., 134
 Smith, D. L., 885
 Smith, J. C., 14, 152
 Smith, J. M., 315, 317, 595
 Smith, M. D., 856
 Smutter, B., 171
 Society of Plastics Industries (SPI), 7, 24
 Sokolnikoff, I. S., 95, 133
 Son, Y., 744
 Song, H.-S., 857, 858
 Souveton, G., 229, 581, 583, 595, 598
 Spalding, M. A., 172, 174, 175
 Spencer, N., 64
 Spencer, R., 392, 399
 Spencer, R. D., 158, 172
 Spencer, R. S., 323, 327, 329, 395, 696, 744, 761, 792, 816
 Speur, J. A., 317, 537, 548, 595, 596
 Sporyagin, E. A., 316
 Spruiell, J. E., 827, 855
 Squires, P. H., 679
 Stachaeu, A. I., 873, 885
 Stammers, E., 216, 219, 228
 Starrison, J. W., 669
 Staton, J. C., 669
 Stefan, J., 190
 Steidler, R. E., 685, 743
 Steinkamp, R. A., 669
 Stern, D. M., 104
 Stern, D. M., 133
 Stevens, J., 171
 Stewart, W. E., 25, 28, 30, 35, 38, 44, 46, 57, 58, 59, 72, 124, 134
 Stigale, F. H., 793, 819
 Stokes, G. G., 45
 Stokes, V. R., 819
 Stone, H. A., 400
 Story, V., 884
 Stoughton, P., 526, 594
 Strack, O. D. L., 165, 167, 169, 170, 172
 Street, J. R., 439, 442
 Street, L. F., 596
 Stroehrer, B., 669
 Stroock, A. D., 400
 Stubbs, A. E., 785, 787, 819
 Stuber, N. P., 549, 596
 Suetzugu, Y., 648, 654, 672
 Suh, N. P., 183, 227, 802, 820
 Sun, Y., 711
 Sundararaj, U., 594
 Sundstrom, D. W., 203, 206, 213, 215, 227, 228
 Suvanaphen, P. K., 859, 860
 Swanson, P. D., 338, 339, 670
 Swartz, A. J., 277
 Syrjälä, S., 461, 517
 Szarvasy, I., 746
 Szydowski, W., 317, 598
 Tabor, D., 147, 149, 171
 Tabor, M., 336, 337, 396
 Tadmor, Z., 5, 24, 133, 136, 138, 139, 141, 151, 171, 184, 196, 203, 210, 226, 228, 247, 284, 285, 288, 289, 310, 314, 315, 316, 317, 320, 321, 345, 348, 349, 358, 372, 382, 388, 395, 396, 397, 398, 427, 433, 434, 435, 436, 437, 438, 440, 440, 441, 442, 450, 461, 462, 463, 470, 474, 475, 480, 481, 486, 490, 496, 497, 498, 503, 504, 506, 507, 514, 516, 517, 518, 519, 520, 522, 554, 566, 594, 596, 597, 637, 648, 651, 653, 654, 672, 727, 745, 760, 763, 764, 765, 770, 773, 774, 775,

- 790, 816, 817, 819, 822, 823, 855, 879,
880, 885
- Tagami, Y., 671
- Takayama, T., 599
- Takserman-Krozer, R., 689, 743, 872, 884
- Talmon, Y., 427, 433, 434, 435, 436, 437, 438,
440, 441, 442
- Tan, Q. M., 336, 337, 396
- Tan, V., 96, 795, 858, 888
- Tanaka, T., 172
- Tang, J., 855, 859
- Tanguy, A., 171
- Taniguchi, K., 397
- Tanner, R. I., 132, 691, 743, 837, 858, 885
- Tanue, S., 850, 858
- Tayeb, J., 317
- Taylor, C., 885
- Taylor, C. A., 859
- Taylor, G. I., 346, 347, 397, 431, 432, 786, 787,
819
- Templeton, J. S., 153, 171
- Tendulkar, M., 790, 819
- Terada, K., 858
- Tervoort, T. A., 24
- Thackray, G., 23, 24
- Thamm, R. C., 793, 794, 819
- Thayer, G. B., 816
- Thiele, W. C., 527, 557, 594
- Thomas, D. E., 816
- Thomas, D. G., 639, 671
- Thompson, E., 818
- Throne, J. L., 227, 230, 820, 858
- Timmermans, P. H. M., 24
- Titomanlio, G., 858
- Tjahjadi, M., 401
- Tobolsky, A. V., 124, 128, 134, 143
- Todd, D. B., 221, 228, 229, 242, 411, 440, 525,
527, 599, 530, 531, 572, 574, 575, 580, 584,
594, 597, 598, 599, 603, 620, 644, 666, 668,
670, 672, 673, 705, 745
- Tokita, N., 673, 870, 884
- Tomotika, S., 344, 396
- Toner, H. P., 227
- Toor, H. L., 816
- Tordella, J. P., 696, 744
- Torner, R. V., 873, 885
- “Touchstones of Modern Polymer
Processing—From Classic Polymer
Processing to Macromolecular
Process Science” Report, 23
- Toussaint, F., 102, 133
- Townsend, P., 746
- Train, D., 156, 171
- Treloar, L. R. G., 128, 134, 886
- Trolez, Y., 317
- Trommsdorff, E., 549, 596
- Trouton, F. T., 91, 133
- Truesdell, C., 598
- Tschiegg, C. E., 426, 441
- Tsuji, Y., 172
- Tsunasawa, H., 778, 818
- Tucker, C. L., III, 802, 820
- Tucker, C. S., 554, 596
- Tukachinsky, A., 415, 427, 438, 440, 441
- Tupin, R. A., 598
- Turian, R. M., 685, 743
- Turkovich, R., 654
- Tüzün, U., 170
- Tyggvason, G., 399
- Tynan, D. G., 228
- Tzoganakis, C., 608, 669
- Uhl, R. H., 743
- Uhl, V. W., 342
- Unkrüer, W., 268, 271, 316, 868, 869, 884
- Unverdi, S. O., 399
- Utracki, L. A., 668, 673
- Valle, C. F., Jr., 884
- Valsamis, L. N., 288, 289, 315, 316, 321, 440,
516, 519, 529, 558, 559, 563, 565, 566, 567,
594, 596, 597, 653, 672
- Van-den Weghe, T., 671
- van der Goot, A. J., 536, 595
- VanderVeen, A., 669
- van der Velden, P. J. L., 778, 784, 818
- van der Wal, D. J., 317, 595
- Van de Vosse, F. N., 399, 595, 818
- Vanel, L., 172
- van Gurp, M., 135
- Van Leeuwen, J., 743
- Van Straelen, S., 441
- Vantal, M. H., 854, 859
- Veariel, T. R., 705, 745
- Venet, C., 133
- Verbeeten, W. M. H., 135, 819
- Vergnes, B., 133, 135, 226, 229, 298, 299,
303, 316, 317, 580, 581, 582, 583,
595, 598
- Vermeulen, J. R., 203, 228, 519
- Verrijt, A., 165, 172
- Verron, E., 859
- Vincent, M., 298, 299, 303, 316, 818
- Vinogradov, G. V., 316, 697, 744

- Viriyayuthakorn, M., 517
 Vlachopoulos, J., 267, 269, 271, 316, 317, 517,
 526, 595, 608, 669, 706, 745, 773, 776,
 817, 818, 837, 854, 855, 857, 858, 859, 872,
 873, 880, 884, 885
 Vogte, F., 24
 Vomkarman, T., 670
 von Turkovich, R., 653, 672, 676
 Vos, E., 780, 781, 782, 783, 819
 Vrentas, J. S., 420, 421, 441
- Wagenknecht, U., 561, 596
 Wagner, A. H., 850, 851, 858, 859
 Wagner, J. R., Jr., 526
 Wagner, M. H., 93, 129, 134, 135
 Waheed, N., 833, 834, 856
 Walker, M., 171
 Wall, F. T., 134
 Wallace, J. F., 227
 Walters, C., 746
 Walters, K., 104, 132, 133
 Wan, C., 242
 Wang, C., 171
 Wang, R. H., 385, 398
 Wang, S., 854, 859
 Wang, W., 390, 392, 398
 Wang, Y., 584, 598
 Ward, I. M., 829, 855
 Warner, H. R., Jr., 775, 817
 Wassgren, C. R., 172
 Wassner, E., 135
 Weber, C., 344, 396
 Weibel, E., 171
 Weinberger, C. B., 856
 Weinghart, K., 171
 Weinstein, B., 397
 Weissberg, H. L., 694, 744
 Weissenberg, K., 85, 96, 132, 133
 Weissert, F. C., 673
 Welch, J. E., 340, 396
 Werner, H., 582, 594, 598
 Westborg, H., 787, 819
 Westover, R. F., 3, 5, 24, 261, 262, 290, 316
 Wetzel, M. D., 597, 598
 Wheeler, A. A., 595
 Wheeler, J. A., 746
 Whipple, B., 744
 White, D. H., 467, 517
 White, J. L., 395
 White, J. L., 2, 23, 226, 229, 304, 316, 317,
 525, 534, 535, 556, 557, 561, 580, 582, 594,
 595, 596, 597, 598, 638, 671, 673, 683, 692,
 694, 695, 696, 698, 743, 744, 762, 817, 827,
 835, 837, 855, 856, 857, 870, 872, 880,
 884, 885
 Whitely, A. H., 441
 Whitesides, G. M., 400
 Whorlow, R. W., 134
 Widagdo, S., 670
 Wiggins, S., 337, 396, 399, 401
 Wilczynski, K., 595
 Wiley, R., 392, 399
 Wiley, R. M., 172
 Wiley, R. N., 323, 327, 329, 395
 Wilkinson, W. L., 441, 859
 Willert, W. H., 3, 5, 24
 Williams, G., 817, 823
 Williams, I., 291
 Williams, J. G., 487, 518
 Williams, M. C., 817
 Williams, M. L., 104, 133, 661, 673
 Windmoeller & Hoelscher, 836
 Wissbrun, K. F., 132, 745
 Wissler, E. H., 746
 Witten, T. A., 671
 Woldan, N., 395
 Wolf, C. F., 679
 Wolf, D., 467, 517
 Wollaston, W. H., 154, 171
 Wong, A. C. Y., 228
 Wong, T. W., 561, 597
 Wood, P. E., 599
 Wookey, N., 397
 Worth, R. A., 726, 727, 745
 Wriggers, P., 886
 Wright, J. D., 586, 587, 588, 599, 673
 Wu, P. C., 767, 769, 770, 771, 817, 822
 Wu, R., 859
 Wübken, G., 771, 772, 817
 Wyman, C. E., 304, 317
 Wypych, G., 671, 672
- Xanthos, M., 606, 608, 610, 611, 625, 636, 637,
 669, 671, 674, 855
 Xu, Y., 170, 172
- Yamabe, M., 858
 Yamaura, M., 599
 Yandoff, O., 745
 Yang, H. H., 585, 598
 Yang, J., 288, 289, 316
 Yang, J. C., 321
 Yang, W. H., 517
 Yang, W. L., 517

- Yang, Y. C., 315
Yano, K., 569, 570, 571, 572, 597
Yanovskii, Yu. G., 744
Yao, C. H., 597
Yaras, P., 672
Yarin, A. L., 440, 442
Yarlykov, B. V., 744
Yates, B., 459, 460, 517
Yee, A. F., 673
Yilmazer, U., 672
Yoon, C. K., 655, 672
Yoshinaga, M., 599
Young, C.-C., 203, 206, 213, 215, 228
Yu, D. W., 221, 228, 229, 242, 610, 669, 673
Yu, T. C., 713, 715, 745
Yung, K. L., 170, 172
Zamodits, H., 259, 315, 459, 517
Zappas, L. J., 104, 133, 143, 850, 858
Zhu, F., 228, 490, 518
Zhu, L., 226, 228, 229, 580, 598
Zia, I. Y. Z., 351, 397
Ziabicki, A., 831, 856
Zielinski, J. M., 421, 441
Zienkiewicz, O. C., 790, 819, 885
Zirkel, A., 671
Zoetelief, W. F., 135
Zumbrunnen, D. A., 337, 396

SUBJECT INDEX

- ABS
 melting in single screw extruder, 478
 surface temperature in capillary flow, 687
- Advection, 323
 chaotic, 334
- Agglomerates,
 breakup in dispersive mixing, 348–354
 criterion for breakup, 352
 hydrodynamic forces in shear flow on,
 350–352
 strength of, 350
 structure and cohesiveness, 349–350
- Agglomeration of powders, 150
 in compaction, 154–156
- Amonton's law, 146–147
- Angle of internal friction, 151
- Angle of repose, 145
- Annular axial flow,
 combined pressure and drag flow, 729–731
 Ellis model, pressure flow, 739
 Newtonian, pressure flow, 738
 Power law model, pressure flow, 738
 eccentric, Newtonian, pressure flow, 739
 eccentric CEF model, drag flow, 139–140
- Annular tangential flow
 concentric, 365–366
- Apparent viscosity, *see* Non-Newtonian
 viscosity
- Arching, *see* Hoppers
- Asperites, 147–148
- Batch mixers, 354–355
 invention of, 2, 3
 power and temperature considerations in,
 452–453
 two-zone model for dispersive mixing in,
 649–651
- Back-mixed continuous flow reactor, *see*
 Reactors, back-mixed
- Bagley end correction, *see* Capillary flow
- Bakelite, 2, 4
- Bakers' transformation, 324
- Balance equations, *see* Equation of continuity;
 Equation of energy; *and* Equation of motion
- Banbury mixers, *see* Mixers, 2, 355
- Barrier screws, 505–506
- Batch reactors, *see* Reactors
- Bernoulli equation, 56
- Biaxial extensional flow, 83, 93
 kinematics of, 81–83 *see also* Planar
 extensional flow
 in film blowing, 837–841
 in parison inflation, 853–855
- Bins, *see* Hoppers
- Bingham model, 111
- Binomial distribution, 383
- Bipolar coordinates, 139–140
 equations of continuity and motion in, 141
- Bird-Carreau model, 105, 106
- Birefringence, 130
 application in mold filling, 772
 measurement of, 130–132
- Bipolar coordinates, 140
- BKZ model, 104–105, 106
- Blade coating, 320
- Blenders, *see* Mixers
- Blending operations, 11 *see also* Mixing
- Blends, *see* Compounding
- Blow molding, 15, 824, 841–855
 description of, 841–847
 dies, 847–849
 extrusion blow molding, 842
 injection blow molding, 843
 parison formation, 847–855
 stretch blow molding, 843–847
- Bogue-Chen model, 100, 105, 106
- Boiling in devolatilization, *see*
 Devolatilization

- Boiling phenomena *see also* Devolatilization, mechanisms
 bubble deformation in shear flow, 430–433
 bubble growth, 416, 428–430
 bubble rupture, 416
 in polymeric melts, 424–427
 nucleation, 416, 422–423
- Boundary conditions:
 for heat transfer problems, 184–186
 at liquid-liquid interface, 63
 at liquid-solid interface, 62–63
 in polymer processing, common, 62–66
- Bubble dynamics
 in shear flow, 430
 of dissolution, 432–433
- Building blocks for machine synthesis, *see* Machine synthesis
- Brinkman number, 492
- Bulk convective mixing, *see* Distributive mixing
- Caking, *see* Agglomeration of powders
- Calendering, 865–884
 analysis by FEM, 873–884
 Newtonian isothermal model, 263–270
 Non-Newtonian isothermal model, 270–272
 normal stresses in, 870–872
 power input, 268–269
 pressurization in, 259–260
 process of, 865–867
 product nonuniformity and defects, 870
 rolls separating force, 269
 shaping method classification of, 15
 temperature distribution in, 873
- Calenders:
 invention of, 1
 inverted “L” type, 866
 pressurization in, 259–260, 263–272
 roll crossing, bending, and crown, 866–867
 “Z” type, 866
- Capillary flow, 680–705, 737 *see also* Tubular flow
 Bagley correction, 96, 682–683
 rheometry, 86–88, 94–96
 elastic effects, 689–693
 entrance and exit effect, 681–684
 entrance flow patterns and pressure losses, 693–696
 extrudate swelling, 689–691
 melt fracture, 696–706
 recoverable strain, 691–693
 rheometry, 86–88
 slip at the wall, 62–63
 viscous heat generation in, 684–689
- Capillary number, 326, 426,
 criterion for droplet breakup, 344, 346–347
 effect on rate of nucleation, 426–427
- Carbon black,
 strength of agglomerate, 350, 352–254
- Carreau model, 111
 parameters of commercial polymers, Appendix A
- Carboxylation of unsaturated polymers, *see* Reactive processing, chain functionalization
- Cavitation, *see* Boiling phenomena
- Cauchy’s equation, *see* Equation of motion
- CEF equation, 102, 106, 113–117
- Celluloid, 2, 4
- Centripetal pumping, *see* Normal stress extrusion
- Chaotic mixing, 326, 332–339
 elliptic points in, 337
 in cavity flow, 337–339
 two point vortex flow, 334–335
 eccentric cylinder flow, 336–337
 hyperbolic points in, 337
 Poincaré section in, 335
- Characterization of mixing,
 striation thickness, 331, 389
- Characterization of mixtures, 378–391
 entropic, 389–391
 gross uniformity, 380, 383–385
 intensity of segregation, 389
 local structure of, 382
 scale of examination, 380
 scale of segregation, 385–387
 scale of segregation profile, 387–389
 striation thickness, 389
 testing samples of, 380
 texture, 380–383, 385
- Circular section channel flow, 740
- Coat hanger die, *see* Dies
- Coating: knife and roll, 259–260, 262–263
- Codeformational constitutive equations, 101, 103–105
See also Constitutive equations
- Codeformational reference frame, 102
- Coefficient of correlation, 385
- Coefficient of friction, 146–150
 definition, 146
 static, 146, 148
 kinematic, 148
 interparticle, 146

- Cohesive energy density, 343
- Compatibility of polymers, *see* Miscibility of polymers
- Complex viscosity, 89
- Compounding, 10, 11, 635–668
 - additives and modifiers used in, 636–638
 - dispersive mixing in, 646–653
 - distributive mixing in, 653–655
 - handling of solids in, 644–645
 - melting in, 645–646
 - of blends, 655–668
 - of particulate filled systems, 643–655
 - rheology of particulate filled polymer matrices, 638–643
- Compressive melting, 182. *See also* Melting
- Compression molding, 811–816
 - description of, 811
 - reactive, 814–816
 - squeezing flow in, 291–294
- Computer aided design (CAD)
 - blow molding, 850–852
 - calendaring, 881–884
 - molding, 796–800
 - single screw extruders, 503
- Compression melting, 182
- Compression ratio, of extruder screws, 495
- Computational analysis of mixing, *see* Mixing, computational analysis
- Concentric annular pressure flow, 738
- Conduction melting with forced melt removal, 181–182, 183–184, 201–219
 - drag induced, 202–216
 - Newtonian fluids, 208–210
 - power-law model fluids, 202–208
 - pressure induced, 216–218
- Conduction melting (heating) without melt removal, 180, 186–193
 - boundary conditions in, 184–185
 - by sintering, 199–201
 - constant thermophysical properties, 186–188
 - finite differences, 193
 - moving heat sources, 193–199
 - phase transition (Stefan-Neumann problem), 190–193
 - semi-infinite solid, 186–193
 - variable physical properties, 188–190
- Cone-and-plate viscometer, 96–100
- Configurational emissivity factor, 185
- Consistency index of power law model, 109
 - temperature dependence, 109
- Constitutive equations,
 - Based on continuum mechanics, 100–111
 - Based on molecular theories, 122–132
 - Bingham model, 111
 - BKZ model, 104–105, 106
 - Bogue, Chen-Boge, Bird-Carreau, 105, 106
 - Carreau model, 111
 - comparison, 106
 - CEF, 102, 106, 113–117, 139
 - Cross model, 110
 - definition of, 40
 - Ellis model, 110
 - generalized Newtonian fluid (GNF), 100, 106
 - Goddard-Miller model, 102–103, 106
 - Lodge rubberlike liquid, 104, 106
 - LVE model, 100
 - Molecular models, 122–132
 - Doi-Edwards model, 127, 129
 - entanglement network theories, 124–132
 - McLeash-Larson pom-pom models, 128–129
 - reptation models, 125–129
 - single-molecule theories, 123–124
 - Maxwell model, 103
 - Newtonian model, 43
 - Oldroyd-Walters-Fredrickson, 104
 - Power-Law model, 108–109
 - Second order fluid, 102, 106
 - White-Metzner model, 104, 106
 - ZFD model, 103, 106
- Contact melting, *see* Conduction melting
- Continuity, equation of, *see* Equation of continuity
- Continuous mixers, 558–572, *see also* Twin screw machines
 - Buss Ko-Kneader, 357
 - FCM, 3, 357, 526–529
 - invention of, 3, 4
 - melting in, 559–561
 - Newtonian wedge flow analysis in, 561–567
 - non-Newtonian wedge flow analysis in, 567–571
 - power and temperature considerations in, 453–454
 - Transfermix, 357
- Continuous stirred tank
 - in twin non-intermeshing screw extruders, 547
 - NPD in, 372–378
 - RTD in, 362
- Control volume, 26
- Convected coordinates, 29

- Convective mixing *see* Distributive mixing;
Laminar mixing; and Mixing
- Coordinate transformation, 73
- Corotational constitutive equations, 102–103.
See also Constitutive equations
- Corotational reference frame, 102
- Co-rotating disk processor, 506–516
design of, 508–510
devolatilization in, 415, 515–516
invention of, 3, 5
mixing in, 513–515
plasticating model, 510–513
non Newtonian isothermal pumping model,
278–289
synthesis of, *see* Synthesis of pumping
machines
- Correlograms, 386
- Couette flow, 76
for power law fluid, 365–368
strain distribution function in, 365–368
- Crank-Nicolson method, 768
- Creeping flows, definition of, 45
- Criminale-Ericksen-Filbey (CEF) equation,
102, 106, 113–117
eccentric, annular axial drag flow,
139–140
torsional flow between parallel disks,
272–278
tube flow, 113–117
- Critical stress for melt fracture, 696
- Cross head die, 722
- Cross model, 110 *see* Constitutive equations
parameters of commercial polymers *see*
Appendix A
- Crystallization temperature, of generic
commercial polymers, *see* Appendix A
- Curl, 29. *see also* Del operations
- Curvilinear coordinates, *see* Bipolar
coordinates; Cylindrical coordinates
- Cylindrical coordinates:
del operations in, table, 115
equation of continuity, table, 30
equation of energy, table, 58,59
equation of motion, table, 35, 46
stress components, table, 44
unit vectors, 73
vorticity tensor, table, 116
- Damkohler number, 619
- Deborah number, 90
- Del operation,
definition of, 29
- Deformation melting, 182–183, 219–226
- Delay zone, in single screw extrusion,
489–490
- Density of generic commercial polymers, *see*
Appendix A
of particulate solids, effect of pressure,
156
- Devolatilization, 409–446
boiling and foaming mechanism of,
414, 422–430, *see also* Boiling
phenomena
coefficient of diffusion, 420–421
degree of superheat in, 418–419
diffusion controlled, 414–415
elementary step of, definition, 11
equipment, 411–413
in co-rotating disk processor, 515–516
in single screw extruders, 415–416
in counterrotating twin screw extruders,
545–546
mechanisms, 413–416
scanning electron microscopy in, 433–440
superheat in, 418–419
ultrasonically enhanced, 427
vacuum staging in, 419–420
- Die characteristics curves, 451
- Die forming, 15, 677–746 *see also* Capillary
flow
definition of, 15, 16
design equation, 680, 706–720
extrudate melt fracture, *see* capillary flow
fiber spinning, 825–836
multilayer sheet forming, 711–719
non-uniformities in, 677–680
parisons, 722
profiles, 731–735
tubes, pipes, and tubular (blown) films,
720–727
sheets and film casting, 705–720
weld lines, 720–721
wire coating, 727–731
- Dielectric heating, 179 *See also* Melting of
polymers
- Die swell, *see* Extrudate swell
- Dies, 677–680, *see also* Blow molding dies
blown film, 722
coat hanger, 706–711
cross head, 722
parison forming, 731–735
profile, 731–735
spiral mandrel, 723
wire coating, 727–728

- Diffusion in mixing, bulk, "eddy", molecular, 323
- Diffusivity,
in polymeric systems, 420–421
- Dilatancy of powders, *see* Particulate solids
- Dilatational viscosity, 43
- Discrete element method, (DEM)
in particulate solids, 152, 165–170
- Disk processor, *see* Synthesis of pumping machines
- Diskpack 3, 5 *see* co-rotating disk processor
- Dispersive mixing,
definition, 324
of solid agglomerates, 348–354
in compounding 646–653
two-zone model in batch mixers, 649–651
- Dispersion of agglomerates, *see* Dispersive mixing, Agglomerates
- Dissipative-mix-melting, 18, 183
- Distribution functions, 357–378 *see* Molecular weight distribution; Passage distribution functions, Residence time distribution, and Strain distribution functions
- Distributive mixing, 323 *see also* mixing
in motionless mixers, 324, 356–357, 393–395
ordered, 323
random, 323
striation thickness in, 331, 389
- Drag flow rate, 49
between parallel plate flow, 49
in rectangular channel, 255
in screw extruders, 255, 450
- Drag induced flow 236
between concentric cylinders, 52–54
of particulate solids, 159–165
of viscous liquids, 239–247
- Drag-induced melt-removal, *see* Conduction melting with drag removal
- Droplet and filament breakup, 342–348
deformation in shear flow, 346–347
Rayleigh instability, 344–346
- Dynamic pressurization: *See* pressurization and pumping
- Eccentric annular flow, *see* Annular flow
- Elastic liquid, *see* Non-Newtonian fluids
- Elementary steps:
analysis of polymer processing in terms of, 14–19
analysis of single screw extrusion in terms of, 448–506
definition of, 16
devolatilization, 409–446
handling of particulate solids, 144–177
in non-intermeshing counterrotating screw extruders, 553–557
melting, 178–234
mixing, 322–408
modeling processing machines with, 447
pressurization and pumping, 235–321
- Ellis model, 110
circular tube flow, 737
concentric annular flow, 738–739
parallel plate flow, 736
- Elliptical channel flow, 740
- Elongational flows, 90–93
breakup of agglomerates in, 352
in advancing melt fronts, 771–777
in blow molding, 853–855
in fiber spinning, 829–830
film blowing, 838–841
in mixing, 324, 332, 344–348, 352
kinematics of, 80–84
- Elongational strain, 80–84
- Elongational stress growth, 90–93
- Elongational viscosity, 83, 90–93
in capillary entrance flow, 694–695
in melt spinning, 835–836
- End effects, in capillary (tube) flow, 681–684
- Enthalpy, balance in continuous systems, 453
of mixing, 342
- Entrance pressure loss, *see* Capillary flow
- Entropy,
of mixing, 342
- Equation of continuity,
derivation of, 28–30
for binary mixtures, 60
in bipolar coordinates, table, 141
in various coordinate systems, table, 30
incompressible fluids, 30
- Equation of energy,
derivation of, 54–57
in several coordinate systems, tables, 58, 59
macroscopic, 54–55
with a homogeneous energy source, 179
- Equation of motion, derivation of, 32–35
in bipolar coordinates, 141
Navier-Stokes equation, table, 46
in various coordinate systems, table, 35

- Equations of change *see* Equation of continuity;
Equation of energy; *and* Equation of motion
- Equivalent Newtonian viscosity, 138–139
- Error function, 187
- Euler equation, 45
- Extensional flows, *see* Elongational flows
- Extensional viscosity, *see* Elongational viscosity
- Extensive mixing, *see* Distributive mixing;
Laminar mixing
- Extrudate roughness, *see* Capillary flow,
Melt fracture
- Extrudate swell, *see also* Capillary flow
macroscopic momentum balance for, 36
in profile extrusion, 733–735
- Extruders, *see* Ram extruders; Single
screw extruders; *and* Twin screw
extruders
- Extrusion: *see* Single screw extrusion;
Twin screw extrusion, *and* Die
forming;
- Extrusion blow molding, *see* Stretch forming
- FAN, *see* Flow analysis network
- FCM, *see* Continuous mixers
- FEM, *see* Finite elements
- Fiber spinning, 824–836, *See also* Die
forming
critical draw ratio, 833
draw resonance, 831–836
dry spinning, 825
melt spinning, 825–836
simulation of, 829–836
spinnability, 831
structuring in, 825–836
wet spinning, 825
- Fibers, 824–825
tenacity of, 825
- Fick's law for diffusion, 40
- Fillers, *see* Compounding additives *and*
modifiers
- Film blowing, 824, 836–841, *See also* Die
forming
simulation of, 837–841
- Film forming, *see* Film blowing; Sheet *and* flat
film forming
- Filmtruder (Luwa) *see* Devolatilization,
equipment
- Finishing operations *see* postreactor finishing
operations
- Finite Differences 193
- Finite elements, 873–879
analysis of calendering with, 873–884
flow in narrow gap with variable thickness,
876–879
- First normal stress difference, *see* Primary
normal stress difference
- First order statistics, 381, *see also* Gross
uniformity; Texture of mixtures
- Flory-Huggins interaction parameter, 343,
416–417, 634
- Flow analysis network, 879–880
in injection molding, 790–791
relationship to FEM, 879–880
- Flow curve, *see* Non-Newtonian viscosity
- Foaming devolatilization, *see* Devolatilization
- Foam injection molding, *see* Reaction injection
molding
- Fountain flow, 765
in mold filling, 765–766
in reaction injection molding, 807
- Fourier's law for heat conduction, 188
- Free energy of mixing, 342
- Free volume in polymers, 420
- Friction, 147–150
- Frictional energy dissipation (FED), 182–183,
219–226
- Friction coefficient, *see* Coefficient of friction
- Gate, in injection molds, 755–757
- Gauss divergence theorem, 29
- Gear pumps, 2, 289, 296–298, 526
- Generalized linear viscoelastic, fluid (GNF), *see*
Constitutive equations
- Generalized Newtonian fluid, definition of,
100. *See also* Constitutive
equations;
- Generating functions, 375
- Glass transition temperature: definition of,
185
for generic commercial polymers, *see*
Appendix A
- Goddard expansion, *see* Corotational reference
frame
- Goddard-Miller model, *see* Constitutive
equations
- Goodness of mixing, *see* Characterization of
mixing
- Graetz number, 688
- Gradient, 29. *See also* Del operations
- Grid melters, 182, 216–219
- Gross (composition) uniformity, *see*
Characterization of mixtures

- Hagen-Poiseuille law, 113
- Handling and transporting of polymer
 particulate solids: 144–177 *see also*
 Solids conveying
 definition, elementary step of, 16
- Heat conduction,
 boundary conditions in, 184–185
 approximate solutions, 188–190
 in slabs, spheres and cylinders,
 194–196
 moving heat sources, 193–199
 semi-infinite solid, 186–193
 sintering, 199–201
 with phase transition (Stefan-Neumann),
 190–193
 with uniform heat source, 231
- Heat of fusion, of generic commercial polymers
see Appendix A
- Heat transfer, *see* Heat conduction
- Heating of polymers, *see* Heat conduction;
- Helix angle, 249
- Henry's law, 418
- Hollow cylinder pump, *see* Synthesis of
 pumping machines
- Homogenization, 324
- Hoppers:
 arching or doming in, 153
 flow instabilities in, 152–154
 funnel flow in, 152
 gravitational flow in, 152–154
 mass flow in, 152
 piping in, 153
 pressure distribution in, 150–152
- Hot runners, in injection molds, 756
- Hydroxilation of saturated polymers, *see*
 Reactive processing, chain
 functionalization
- Identity tensor, 33
- Impact molding, 237
- Incompressible fluid, assumption of, 30
 definition of pressure in, 33
- Infinite shear rate viscosity, *see* Constitutive
 equation Carreau model
- Information entropy, *see* Characterization of
 mixtures, entropic.
- Injection blow' molding, *see* a Blow
 molding
- Injection molding, 2, 15, 753–800 *see also*
 Mold filling
 computer simulation, 796–800
 cooling of molded parts in, 791–793
 cycle, 755
 flow in runner system, 758–759
 fountain flow in, 765–766
 gas assisted, 784–790
 jetting in, 766
 molecular orientation in, 770–778
 mold filling, 761–766
 moldability, 761–762
 of reacting systems, 800–811
 packing in, 759
 pressure profiles in, 760–761
 reactive (RIM), *see* Reactive injection
 molding
 short shots, 756, 770, 780, 790
 simulation of mold filling, 766–800
 sink marks, 761
 skin formation, 761, 767, 810
 structuring in, 754, 793–796
 weld lines in, 763, 764, 794, 796, 800
- Injection molding cycle, 755
- Injection molding machines:
 description of, 753–755
 invention of, 2, 4, 5
 reciprocating, 2
 reciprocating screw, invention of, 3
- Injection molds, 755–757
 gate, 755–757
 runner, 755–757
 sprue, 755–757
- Intensity of segregation, *see* Characterization of
 mixtures
- Intensive mixing, *see* Dispersive mixing
- Interfacial area in mixing, 326–331
 distribution in shear flow, 402
 for homogeneous flows, 331
 orientation of, 331–332
 of randomly distributed elements, 330–331
 relation to strain in simple shear flow,
 326–330
 in motionless mixers, 357
 with random initial orientation of,
 330–333
- Internal energy, 56
- Internal mixers, *see* Batch mixers
- Invariants, of rate of strain tensor, 42
- Invention of machines, *see* Synthesis of
 pumping machines
- Inverse screw extruder, *see* Synthesis of
 pumping machines
- Janssen equation, 150
- Jaumann derivative, 102

- Jet swell, *see* Extrudate swell
- Journal-bearing problem, 68–72
- Kenics static mixer, *see* Motionless mixers
- Kinematics, of viscometric shear flows, 80–81
of elongational flows, 80–84
- Kinetics of polymerization in reaction injector molding, 606–607, 626
- Knetwolf, 3
- Knife coating, *see* Coating
- Ko-Kneader, 3
- Lagrange-Euler equation, 876
- Lagrangian frame, 30
- Lagrangian turbulence, *see* Chaotic mixing
- Laminar mixing, 323, 326–332
chaotic, *see* Chaotic mixing
characterization of, *see* Characterization of mixing, Striation thickness
effect of viscosity ratio, 339–341
interfacial area, as a criterion for 327–332
mean strain in, 365, 368
in Couette flow, 365–368
in homogeneous liquids, 326–332
in motionless (static) mixers, 393–395
in non-homogeneous liquids, 339–341
role of shearing strain in, 326–332
in single screw extruders, 463–470
strain distribution functions in, 364–372
strain in, 324
- Laplacian, 45, *See also* Del operations
- Leakage flow, in screw extruders, 257–258
- Leibnitz formula for differentiating an integral, 95
- Linear viscoelastic flow:
elongational, 91–93
relaxation time, 89
small amplitude oscillatory, 105–107
- Linear viscoelasticity, 100
Boltzman superposition principle, 142
time-temperature superposition in, 111
WLF equation, 111
- Lodge rubber like liquids, 104, 106
- Lubrication, 64
- Lubrication approximation, 25, 64–66
in journal-bearing, 68–72
in melting with drag removal, 204
in non-parallel plate flow, 66–68
- Lubricants, 637
- Macromolecular engineering, 18–23
- Macromolecules, *see* Polymers
- Macroscopic balances
energy, 54–57
linear momentum, 32–35
mass, 28–30
- Maddock fluted screw section, 506
- Molecular and supramolecular engineering, 22
- Magnitude:
of rate of strain tensor, 42
of stress tensor, 39
- Maillefer screw, 505
- Manifold in sheeting dies, *see* Dies, coat hanger
- Mathematical modeling,
principles of, 60–62
of processing machines with elementary steps, 447
- Mathematical operators,
del or nabla, definition, 29
Laplacian, 45
- Maxwell model, *see* constitutive equations
- Mean strain, 365
in batch mixers, 365
in concentric cylinder mixer, 367
in continuous mixers, 368
in parallel plate drag flow, 370, 373
in parallel plate pressure flow, 405
relationship to mean shear rate, 403–404
in single screw extruders, 471
in tubular flow, 373
- Melt conveying,
in single screw extruders, 450–461, 502–504
in co- and counterrotating intermeshing twin screw extruders, 533–545
in counterrotating non-intermeshing twin screw extruders, 554–558
in twin screw extruders, 304–310
in the wedge of a CM, 561–567
- Melt extrusion, *see* Die forming; Single screw extrusion; *and* Twin screw extrusion
- Melt fracture, 696–706
gross distortion, 698
sharkskin, 697
of HDPE, 697–698
of LDPE, 697
of LLDPE, 698–705
- Melt pool, in screw extrusion, 475
- Melting, 178–234
classification of methods of, 179, 183–184
conduction with forced melt removal, 181–182, 201–219

- Melting (*continued*)
- conduction without melt removal, 180
 - compression, 182
 - deformation, 182–183, 219–226
 - dielectric heating, 179
 - dissipative-mix-melting (DMM) 18, 183, 219–226
 - elementary step of, 16, 178–234
 - in co-rotating disk processor, 510–513
 - in co-rotating tintermeshing twin screw extruders, 576–584
 - in co- and counterrotating intermeshing twin screw extruders, 533–545
 - in non-intermeshing counterrotating twin screw extruders, 553–554
 - in single screw extruders, 473–482, 489–502
 - of particulate filled systems in compounding, 645–646
 - mechanism in screw extruders, 477
 - sintering, 199–201
 - thermal energy requirements of, 178–179
 - with moving heat source, 193–199
- Melting point,
of generic commercial polymers, *see*
Appendix A
- Melting zone, in single screw extruders, 481, 489–502
- Metering screw, 504
- Milling, *see* Roll-mills
- Miscibility of polymers, 342–344
- Mixers:
- Banbury, 2, 355, 526–528
 - batch, *see* Batch mixers
 - SDF in, 364–372
 - classification of, 354–355
 - concentric cylinder, 365–368
 - continuous, *see* Continuous mixers
 - internal, high intensity, 2, 355
 - motionless, *see* Motionless mixers
 - power and temperature consideration in
batch and continuous systems,
452–454
 - single screw extruders as, *see* Single screw
extruders
 - static *see* Motionless mixers
- Mixing, 322–408
- advection in, 323
 - basic concepts and mixing mechanisms, 322
 - bulk convective, 323
 - chaotic, *see* Chaotic Mixing
 - characterization of *see* Characterization of
mixing
 - computational analysis, 391–395
 - convection and convective flow in, 323
 - definition of, 322
 - dispersive, *see* Dispersive Mixing
 - distributive, 323, 653–655
 - eddy motion in, 323
 - effect of the viscosity ratio on, 339–342
 - elementary step of, definition, 16
 - homogeneous liquids, *see* Laminar mixing
 - kneading paddles, 529–532
 - immiscible liquids, *see* Droplet and filament
breakup
 - in reactive processing, 623–632
 - intensive, *see* Dispersive mixing
 - interfacial area in, 323
 - laminar, *see* Laminar mixing
 - mechanisms of, 322–326
 - molecular diffusion in, 323
 - protocol of, 324
 - residence time distribution (RTD), 360–364
 - static, *see* Motionless mixing
 - in co-rotating disk processor, 513–515
 - in intermeshing twin screw extruders,
533–545
 - in non-intermeshing twin screw extruders, 555
 - in single screw extruders, 463–473
 - scraped surface heat exchanger, 522
 - strain distribution functions (SDF), 364–372
 - thermodynamics of, 342–344
 - temperature effects and power considerations
in, 452–455
- Mixing indices, 384–385
- Mixtures,
characterization *see* Characterization of
mixtures
definition of, 322
- Modeling, *see* Mathematical modeling
- Mold coating, 15
- Mold filling, 761–800
- computer simulation, 796–800
 - cooling of molded parts in, 791–793
 - chemical reaction in, 800–810
 - cycle, 755
 - flow in runner system, 758–759
 - front instabilities, 778–780
 - front region, 770–778
 - fully developed region, 766–770
 - fountain flow, 765–766
 - gas assisted, 784–790
 - jetting in, 766
 - molecular orientation in, 770–778
 - multicomponent systems, 780–783

- overall flow pattern, 790–791
- packing in, 759
- pressure profiles in, 760–761
- short shots, 756, 766, 770, 780, 790
- skin formation in, 761, 767, 810
- simulation of, 766–800
- sink marks, 761
- structuring in, 754, 793–796
- weld lines, 763, 764, 794, 796, 800
- Molding, *see* Injection molding; coinjection, 783–784
- Molds, injection, 755–757
- Molecular orientation:
 - in injection molding, 770–775, 790
 - in spun fibers, 827–829
 - of parisons, 843
- Molecular weight distribution (MWD), 357–359
 - averages, 359
 - control by viscracking of PP, 607–611
 - controlled long chain branching, 611
 - dispersion index, 359
 - effect on die swell, 690
 - mole fraction and weight fraction distribution, 358
 - moments of, 359
 - skewness, 359
 - standard deviation, 359
- Molecular weight averages, 359
- Molecular weight distribution, 357–359
 - by viscracking, 607–611
 - dispersion index for, 359
- Motion, equation of, *see* Equation of motion
- Motionless mixers, 324, 356–357
 - Kenics static, 324, 356, 393–395
 - Ross ISG, 324, 356–357
 - Sultz, 324
- Navier-Stokes equation, 45
 - in various coordinate systems, table, 46
 - see also* Equation of motion
- Newton's law of viscosity, *see* Constitutive equations; Newtonian fluids
- Newtonian flow problems:
 - axial annular flow, 738
 - axial annular drag flow, 52–54
 - axial annular combined pressure and drag flow, 729–731
 - calenders and roll-mill, 263–272
 - circular section channel, 740
 - circular tube, 113, 737
 - conical channel, 741
 - elliptical channel, 740
 - eccentric annular, 739
 - film blowing, 837–841
 - journal-bearing flow, 68–72
 - non-parallel plate flow, 66–68, 561–565
 - non-parallel plate flow with variable gap, 876–879
 - parallel plate flow, 47–52
 - non-isothermal, 57–60
 - positive displacement flow, plunger-cylinder, 290–291
 - rectangular channel pressure flow, 250–259, 741
 - rectangular channel combined drag and pressure flow, 250–259
 - semi circular channel, 740
 - single screw pump, extruder, 250–259, 450–457
 - triangular channel, 742
 - twin screw extruder, intermeshing counterrotating, 304–310
 - wire and cable coating die, 729–731
- Newtonian fluids: of commercial polymers
 - see* Appendix A
 - constitutive equation for, 43
 - in various coordinate systems, table, 44
 - viscosity of, 43, 48,
- Non-Newtonian flow problems in:
 - axial annular flow, 738–739
 - blow molding, 847–855
 - calenders and roll-mills, 270–272, 870–873
 - circular tube flow, Power Law model, 111–113,
 - CEF fluid, 113–117
 - cone and plate viscometer, 96–100
 - Couette flow, 365–368
 - fiber spinning, 829–830
 - non-parallel plate wedge flow of Carreau model, 566–568
 - parallel disks, torsional flow of CEF fluid, 272–278
 - parallel plate flow Power law model, 117–122
 - single screw extruders, 457–461
 - squeezing flow in, 291–294
 - Wire coating die, 139–140
- Non-Newtonian fluids *see also* Constitutive equations

- Non-Newtonian flow (*continued*)
 definition of, 79
 empirical models for, *see* Constitutive equations
 normal stresses in shear flow of, 85–86
 shear rate dependence of, 84
 stress overshoot 106
 stress relaxation, 125, 141
 stress overshoot of, 106
- Non-Newtonian viscosity, 84–86
 empirical models for, 108–111
 flow curves of commercial polymers, *see* Appendix A
 measurement of, 84–85, 94–99
- Non-parallel plate flow, 66–68, 260–262
- Normal stress differences,
 convention for indices, 85
 measurement of,
 in calendaring, 870–872
 in cone-and-plate, 96–100
 in shear flow, 85–86
see also Primary normal stress coefficient;
 Secondary normal stress coefficient
- Normal stress extruder (pump),
 272–278
 invention of, 3, 5
- Numerical methods:
 finite differences, 193
 finite elements (FEM), 873–879
 flow analysis network (FAN), 879–880
- Number of passage distribution (NPD), *see* Passage distribution functions
- Nylon:
 melting in screw extruders, 477
 pre-processing drying, 145
 temperature distribution in spun fibers, 832
- Oldroyd-Walters-Fredrickson model, *see* constitutive equations
- Operating point of screw extruders, 451
- Orientation, *see* Molecular orientation
- Oswald-de Waele model, *see* Power law model
- Packing, in injection molding, 759
- Parallel disks, radial flow, 767–770
 squeezing flow, 291–294
 torsional flow, 272–278
- Parallel disk plastometer, 291
- Parallel plate flow:
 both plates moving, 278–279
 dynamic viscous pressurization by, 236–247
 Ellis model, 736
 multilayer, 711–720
 Newtonian fluids, isothermal, 47–52, 736
 nonisothermal, 57–60
 optimum plate separation, 50
 of particulate solids, 159–162
 Power Law model, isothermal, 117–122, 736
 nonisothermal, 57–60
 strain distribution functions in, 369–372, 373
- Parison formation, *see* Blow molding
 cooling, 844, 855
 die design for, 847–849
 inflation, 853–855
 programming, 843
 sagging, 848
 simulation, 850–855
- Particulate solids:
 agglomeration of, 150
 angle of internal friction, 151
 coefficient of cohesion at the wall, 151
 compaction of, 154–156
 conveying of, in screw extruders, 482–489
 dilatancy of, 146
 discrete element method in, 152, 165–170
 effect on melting in compounding, 645–646
 handling of, 144–173, in compounding,
 644–645
 flow in closed conduits, 157–165, in straight
 channel, 162–165
 gravitational flow in bins and hoppers,
 152–154
 mechanical displacement flow, 157–159,
 aided by drag, 159–165
 pelleting, tableting 154
 porosity of, 156
 pressure distribution in bins and hoppers,
 150–152
 properties of, 145–146
 size distribution in batch dispersive mixer,
 649–651
- Passage distribution function (NPD),
 372–378
 batch mixer, 375, 377–378
 continuous mixers, 375
 generating function, 375
 in single screw extruders, 470–473
 moments of, 375
 relationship between internal and external
 functions, 376
 theory of recirculation systems, 376–377
 Z-transform, 375
- Pathlines, 334
- Pelleting, *see* Particulate solids, compaction of

- Pelletizing,
 melt fracture in, 705
- Pickle, 1
- Pipe extrusion, *see* Die forming, tubes
- Pipe flow, *see* Tubular flow
- Planar elongational flow:
 kinematics of, 81–83
- Plastic energy dissipation (PED), 16, 182–183, 219–226
- Plasticating single screw extrusion, 473–506
 delay zone, 489–490
 melt conveying, 502–504
 melting, 489
 polymer journey in, 474–482
 solids conveying, 482–489
- Plasticizers, *see* Compounding additives and modifiers
 Plug convective mixing, *see* Distributive mixing
- Plug flow reactor, *see* Reactors, linear
 continuous flow reactors
- Plunger-cylinder flow, 290–291
- Poiseuille flow, *see* Tube, flow
- Poisson ratio, in particulate solids, 156
- Polyethylene,
 cohesive failure at capillary exit, 700
 entrance and exit pressure losses in capillaries, 694
 entrance flow in capillaries, 693–694
 fiber spinning of HDPE, 827
 extrudate melt fracture (HDPE, LDPE, LLDPE) 697–705
 extrudate swell of (HDPE), 692
 fiber spinning of, (HDPE), 827
 melt fracture of, 697–705
 in screw extruders (LDPE), 479, 480
 mixing in Banbury of (LDPE), 342
 rheological properties *see* Appendix A
 thermophysical properties of, *see* Appendix A
 swelling, 692
- Polymer melts: constitutive equations for, *see* Constitutive equations
- Polymer,
 additives and modifiers in compounding, *see* Compounding additives and modifiers
- Polymer processing:
 analysis in terms of elementary steps, 9, 14–18
 as part of the industrial revolution, 3
 current practices, 7–14
 definition of, 1
 historical notes on, 1–5
 in-line, 13–14
 post-reactor, 9–10, 144
 reactive, 10–11
 structural breakdown, 17–18
- Polymer manufacturing in USA, 7
- Polymerization reactors
 particulate products of, 144
- Polymers:
 additives for, *see* Compounding additives and modifiers
 chronology of discovery, 12
 compatibility of, 342–344
 miscibility *see* Polymers compatibility of structuring, 13
 viscracking, 11
- Polypropylene (PP)
 entrance flow in capillaries, 697
 entrance and exit pressure losses in capillaries, 694
 fiber spinning, 826
 melt fracture, 697
 melting in screw extruders, 476
- Polystyrene (PS),
 coefficient of diffusion in, 421
 devolatilization in vented extruder, 415–416
 entrance and exit pressure losses in capillaries, 694
 entrance flow in capillaries, 695
 extrudate swell, 690
 injection molding of, 760–761
 melt fracture, 697
 orientation in injection molding, 771–775
 recoverable strain, 693
 swelling, 690
- Polyvinyl chloride,
 melting in single screw extruders, 475, 481
 calendaring of, 868
 flow in capillary, 687
 thermal degradation of, 181
 viscosity, temperature dependence, 180–181
- Poincaré section, *see* Chaotic mixing
- Positive displacement flow
 in gear pumps, 296–298
 of particulate solids, 157–159
 plunger-cylinder, 290–291
 pressurization (pumping) by, 236
 squeezing, 291–294
 in twin screw extruders, 298–314
- Postreactor polymer processing operations, 9–10
- Powders, *see* Particulate solids
- Power
 in batch and continuous systems, 452–454
 in single screw extrusion, 454, 485–486

- Power law model, 108–109 *see also* Constitutive equations
- axial annular flow, 738–739
 - calenders and roll mills, 270–272
 - circular tube, 111–114
 - coat hanger die, 706–710
 - concentric annular flow, 738
 - conical channel, 741
 - Couette flow (SDF), 365–368
 - error in pressure flows, 136
 - parallel disk flow, radial, 767–770
 - parameters, 109
 - parameters of commercial polymers *see* Appendix A
 - parallel plate flow, 117–122, 736 single screw melt extrusion, 457–461
 - squeezing flow in, 291–294
 - temperature dependence of parameters, 109
 - tubular dies, 724–726
- Pressure, 33
- in incompressible fluid, 33
- Pressured-induced melt removals *see* Conduction melting with forced melt removal
- Pressure flow rate in screw extruders, 255
- Pressurization and pumping, 235–321
- classification of methods of, 236–237
 - drag-induced, 236
 - dynamic normal stress, 272–278
 - dynamic viscous, 236
 - elementary step of, 16
 - of particulate solids, 157–165
 - positive displacement, 285–298
 - static mechanical, 236
- Primary normal stress coefficient:
- definition of, 85
 - described by CEF equation, 106, 113–117, 139
 - from viscosity data, 99
 - measurement of, 96–100
 - prediction by various constitutive equations, 98–99
 - shear rate dependence of, 85
- Primary normal stress difference
- as pressurization source, 272–277
 - in capillary flow, 696
 - definition of, 85–86
 - in torsional flow, 272–277
 - in tubular flow, 113–117
 - measurement of, 96–100
 - see also* Normal stress difference; Primary normal stress coefficient
- Principal elongational ratios, 331
- Product fabrication, 13
- Profile extrusion, 731–735, *see also* Die forming
- Pseudoplastic fluids, *see* non-Newtonian fluids, shear thinning
- Pseudo-steady state approximation, 63
- Pumping *see* Pressurization and pumping
- Pure shear flow, *see* Planar elongational flow
- Purging:
- purging of a tubular die, 404
 - role of RTD in, 360
- Rabinowitsch equation, 96
- with slip at the wall, 137
- Radial flow between parallel disks, 767–769
- Radiation boundary condition, 185
- Radius of curvature, 840
- Ram extruders, 1
- flow in front of ram in, 290–291
 - force requirements for solids, 158–159
- Raoult's law, 416
- Rate-of-deformation tensor, *see* Rate-of-strain tensor
- Rate of strain tensor, 40–43
- invariants of, 104, 108
 - magnitude of, 42, 43, 108,
- Reactive injection molding (RIM), 753, 800–810
- description of, 800–804
 - mold filling in, 804–810
 - thermoplastic (foam) injection molding (TIM), 801, 810
- Reactive processing, 546–550, 603–673
- batch reactors, 612–616
 - chain functionalization, 604–607
 - chain modification, 607–611
 - chain modification reactions, 603–611, 625–628
 - compression molding, 814–816
 - controlled long chain branching, 611
 - interfacial cross-linking in, 628–631
 - mixing consideration in, 623–632
 - modeling in counterrotating twin screw extruders, 546–550
 - multicomponent immiscible and compatibilized systems, 632–635
 - viscracking of PP with peroxides, 607–611
- Reactors,
- back-mixed continuous flow reactors, 620–623
 - batch reactor analysis, 612–616
 - linear continuous flow reactors, 619

- post reactor processing, 144
- classification of, 611–623
- Reciprocating screw injection molding
 - machines, *see* Injection molding
- Recirculating systems, *see* Passage distribution functions
- Rectangular channel flow, 250–259
 - see also* Single screw extrusion
- Reinforcing agents, *see* additives and modifiers used in, 636–638
- Relaxation modulus, 103
- Repetitive mixing, *see* Distributive mixing
- Residence time distribution (RTD) functions, 360–364
 - cumulative, 360
 - in single melt extruders, 463–467
 - external, 360
 - in continuous stirred tank, 362–363
 - in single screw extruders, 463–467
 - internal, 360
 - mean residence time, 360
 - relationship among RTD functions, 360–362
 - in pipe flow, 363–364
- Reynolds equation, *see* Lubrication approximation
- Reynolds Transport Theorem, 26
- Rheological equations of state, *see* Constitutive equations
- Rheological flows,
 - capillary, 94–96
 - cone-and-plate, 96–100
 - dynamic sinusoidally varying, 80
 - elongational, extensional, 80–84, 90–93
 - simple shear flow, 80
 - viscometric, 81
- Rheological Material Functions, *see* Constitutive equations
- Rheological properties of commercial polymers
 - see* Appendix A
- Rheometry, *see also* viscometry, 86
 - capillary flow, 86–88
 - cone-and-plate flow, 96–100
 - Sinusoidally varying shear flow, 86–90
- RIM, *see* Reaction injection molding
- Roll-mills, *see* Calendaring
- invention of, 1, 4
- Roll pump, *see* Synthesis of pumping machines
- Ross mixer *see* Motionless mixers
- Rotating flight extruder, *see* Synthesis of pumping machines
- Rubber and plastics century, 7
- Runners, *see* Injection molds
 - flow in, *see* Injection molding
- Scale of examination, 380
 - profile of, 387–389
 - Scale of segregation, *see* Characterization of mixtures
- Scale-up by mathematical modeling, 60–62
- Scott equation, 294, 813
- Screw characteristics, 258–259
- Screw
 - barrier type, 505–506
 - geometry of, 248–249
 - channel width, 249
 - helix angle, 249
 - designs, 504–506
 - metering, 504
 - mixing sections, 505
- Screw pumps *see also* Single screw extruders; Single screw extrusion
 - flow path in, 255–257
 - flow rate of, 253–254
 - geometry of, 248–249
 - leakage flow in, 257–258
 - modeling of, 250–259
 - Newtonian isothermal model in, 250–259
 - Non-Newtonina models, 259
 - optimum channel depth, 50
 - power input in, 453–454
 - shape factors in, 254–255
 - synthesis of, 242–244
 - velocity profiles, 250–253
- Screwless extruder, 262
- Second normal stress difference, *see* Secondary normal stress difference
- Secondary normal stress coefficient:
 - in CEF equation, 102, 113–117
 - definition of, 85–86
 - measurement of, 96–100
 - prediction by various constitutive equations, 106
 - shear rate dependence, 86
- Secondary normal stress difference:
 - definition of, 85–86
 - measurement of, 96–100
 - in tubular flow, 113–117
 - in wire coating, 139
 - see also* Normal stress difference; Secondary normal stress coefficient
- Second-order statistics, 381–382. *See also* Scale of segregation; Texture of mixtures

- Semicircular channel flow, 740
- Shape factors (in screw extrusion), 254–255
- Shaping methods (steps), 15, 16
- calendering, 1, 865–884
 - compression molding, 811–816
 - definition of, 15–16
 - die forming, 677–746
 - molding, 753–816
 - stretch shaping, 824–855, *see also* Fiber spinning and Blow molding
- Sharkskin *see* Melt fracture
- Shear free flow, *see* Elongational flows
- Shear rate, definition of, 42, *See also* Rate of strain tensor, magnitude of
- Shear strain:
- recoverable, 691
 - role in mixing, 327–332
 - in simple shear flow, 43
 - in single screw extruders, 468–470
- Shear thinning, 84. *See also* Non-Newtonian fluids; Pseudoplastic fluids
- Sheet (free) blowing, 863
- Sheet and flat film forming, 15, 705–720, *see also* Die forming
- coextrusion of, 711–720
- Short shots in injection molding, 763–765
- Shrinkage:
- measurement of orientation in injection molding by, 771–772
- Similarity transformation, 186
- Simple elongational flow, 90
- breakup of agglomerates in, 352
 - response of nonlinear constitutive equations in, 91–93
- Simple fluid, *See* constitutive equations
- Simple mixing, *see* Distributive mixing
- Simple shear flow, 43, 80
- breakup of agglomerates in, 350–354
 - dynamic sinusoidal varying, 80
 - invariants in,
 - normal stresses in, 85, 90
 - rheological response in, 84
- Simplifying assumptions:
- common in polymer processing, 62–64
 - constant thermophysical properties, 63–64
 - incompressibility, 63–64
 - lubrication approximation, 64–66
 - no-slip at the wall, 62–63
 - steady state approximation, 63
- Simulation, mathematical modeling, 60–62
- Single rotor machines, 447–522
- Single screw extruders: *see also* Screw pumps; Single screw melt-extrusion and Single screw plasticating extrusion
- development from parallel plate geometry, 247–259
 - design of HDPE pelletizing extruder, 455–457
 - geometry of, 248–249
 - invention of, 2, 4
 - mixing element evaluator, (SSMEE), 657
 - surging in, 476
 - vented two stage, 17
 - synthesis of, 242–244
- Single screw melt extrusion, 448–473
- characteristic curves of, 258
 - devolatilization in, 415–416
 - dispersive mixing in, 470–473, 651–653
 - flow path in, 255–257
 - leakage flow in, 257–258
 - lumped-parameter model, 461–463
 - melt conveying (pumping), 250–259
 - isothermal Newtonian model of, 250–259, 450–457
 - isothermal non-Newtonian model, 259
 - mixing in, 463–473, 653–655
 - non Newtonian non-isothermal model, 457–461
 - optimum channel depth, 50, 451
 - power consumption, 453–454
 - residence time distribution in, 463–467
 - screw characteristic curves, 450–451
 - shape factors, 254–255
 - strain distribution in, 468–470
 - velocity profiles, 250–253
- Single screw plasticating extrusion, 473–506
- cooling experiments, 474–482
 - delay zone in, 480, 489–490
 - journey of polymer particle, 474–482
 - melt conveying zone, 482, 502–504
 - melt pool, 475
 - melting, 489–502
 - melting zone, 481
 - modeling, 482–498
 - pushing flight and trailing flight, 474
 - solid bed, 475
 - solids conveying zone, 479, 482–489
 - screw designs, 504–506
 - surging in, 476
- Sintering, 199–201
- Slider pad extruder, 261–262
- invention of, 3, 5
- Slip agents, *see* Compounding additives and modifiers

- Slip at the wall, *see* Simplifying assumptions,
common in polymer processing
- Slip-stick, 62–63
role in flow instabilities, 698–699
- Solid bed, in single screw extrusion, 478
profile, 482, 495–502
- Solids conveying, *see also* Particulate solids;
Single screw plasticating extrusion
in co-rotating twin screw extruders, 575–576
in rectangular channels, 162–165
in screw extruders, 482–489
- Solubility parameter, 342–343
- Specific heat,
of generic commercial polymers *see*
Appendix A
- Spinnability, 831
- Spinnerette, 825
- Spiral pump, 319
- Spiral mandrel die, 723
- Sprue, 755, 756
- Square pitched screw, 249
- Squeezing flow:
in compression molding, 811–813
between parallel disks, 291–294
- Stabilizers, *see* Compounding additives and
modifiers
- Static mechanical pressurization, 236
- Static mixers, *see* Motionless mixers
- Stefan-Boltzman radiation constant, 185
- Stefan condition, 191
- Stefan-Neumann problem, 190–193
- Strain in laminar mixing *see* Laminar mixing
- Strain distribution function (SDF), 364–372
in batch mixers, 365
in concentric cylinder mixer, 365–368
in continuous mixers, 368–372
in single screw melt extruders, 468–470
mean strain, 365, 368
in parallel plate mixer, 369–372
relation to RTD in continuous mixers, 373
in single screw extruders, 468–470
- Strain recovery,
In capillary flow, 691–693
- Strain tensor
principal axes of, 331
- Streaklines, 334
- Streamlines, 334
- Streamline mixing, *see* Laminar mixing
- Stream function, 334
- Stress growth:
in elongational flow, 90–91
- Stress optical coefficient, 130
- Stress overshoot, 106
In co-rotating disk pumps, 285
in squeezing flow, 293
- Stress relaxation, 125
- Stress tensor, 33, 37–39
deviatoric, dynamic, 33
invariants of, 39
magnitude of, 39
sign convention, 38
total, 33
- Stretch blow molding, *see* Blow molding
- Stretch shaping, 824–855
blow molding, 841–855
fiber spinning, 824–836
film blowing, 836–841
- Striation thickness, 331, 389
definition, 331
in concentric cylinder mixer, 366
in laminar mixing, 331
in parallel plate mixer, 370
relation to total strain, 331
- Stripping, *see* Devolatilization
- Structuring,
definition of, 13
in fiber spinning, 825–836
in injection molding, 793–796
- Substantial derivative, 29
- Superconcentrate, 342
- Superheat, *see* devolatilization
- Superposition of drag and pressure flows, 255,
520
error for non-Newtonian fluids, 520
- Sultzler mixer, *see* Motionless mixers
- Surface renewal, *see* Devolatilization,
mechanisms
- Surface tension,
boundary condition between two liquids,
63
role in mixing, 326, 344–345, 347
- Surging in screw extruders, 476
- Synthesis of pumping machines, 237–247
building blocks for, 237–238
co-rotating disc processor, 246–247
disk processors, 244–245
hollow cylinder, 242
inverse screw pump, 241–242
machine elements for, 238
roll pumps, 239–241
rotating cup, 245
rotating flight, 246
screw extruder, 242–244
systematic invention, 239–247

- T die, 706
- Tapered channel flow, 66–68, 260–263 *see also*
Lubrication approximation
- Testing samples for mixtures, 380
- Texture of mixtures, *see* Characterization of mixtures
granularity of, 381
recognition by visual perception, 380
- Thermal conductivity: of generic commercial polymers, *see* Appendix A
- Thermal degradation,
rate as function of temperature, 180–181
role of residence time distribution in, 360
- Thermal diffusivity, of generic commercial polymers, *see* Appendix A
- Thermal energy equation, 57
with homogeneous energy source, 179, 183
with PED and FED, 182
- Thermal penetration depth, 189, 231
- Thermodynamics,
in devolatilization, 416–418
of mixing, 342–344
- Thermodynamic system, 26
- Thermoforming, 824
- Thermophysical properties of commercial polymers, *See* Appendix A
- Thin film evaporator, *see* Devolatilization equipment
- Torsional flow between parallel disks, 372–376
- Total strain in mixing, *see* Laminar mixing
- Transfermix,
invention of, 5
- Transport phenomena, 25
- Triangular channel pressure flow, 740, 742
- Tribology, 147
- Trouton viscosity, 91
- Tube and pipe forming, 720–727
- Tubular flow, *see also* Capillary flow
CEF equation, 113–117
Ellis model, 737
Newtonian, 113, 737
reactors, *see* Reactors, linear continuous flow reactors
RTD in, 363–364
SDF in, 373
power law model, 11–113, 684–689, 737
- Twin rotor machines
continuous mixers (CM), 526–529
internal Banbury type mixer, 526–528
types of, 525–532
- Twin shaft machines, *see* Twin rotor machines
- Twin screw extruders, 523–594, 572–594
co-rotating fully intermeshing, 572–594
co-rotating twin screw mixing elements (TSMEE), 657
flow in co- and counterrotating, 533–545
kneading paddles, 529–532
intermeshing co-rotating, 300–304, 525–533
intermeshing counterrotating, 295–296, 304–310, 525–533
invention of, 2, 4, 5
kneading blocks in, 2
melting in co-rotating, 576–584
mixing in co- and counterrotating, 533–545
pumps, 298–314
reactive processing in, 546–550
self-wiping, 525
tangential non-intermeshing, 550–558
tangential non-intermeshing as back-mixed flow reactors, 620–623
types of, 525–532
ZSK in, 572–575
- Twin screw extrusion,
devolatilization in counterrotating, 545–546
feeding and transport of particulates in co-rotating, 575–576
flow in intermeshing co- and counterrotating, 533–545
intermeshing co-rotating, 300–304, 584–594
flow and pressurization in co-rotating intermeshing, 584–594
geometry in, 300–303
intermeshing counterrotating, 295–296
mixing in co- and counterrotating, 533–545, 653–655
Newtonian isothermal model, 304–310
non-intermeshing tangential, 310–314, 550–558
Newtonian isothermal plate-and-frame model for, 311–314
of blends, 655–668
reactive, 546–550
- Ultimate particle in mixing, 382
- Ultrasonic heating, 183, *see also* Melting
- Unit tensor, identity tensor, 33
- Unit vectors, 29
- Units, SI, 914–915
conversion table, 915–917

- Vacuum forming, *see* Thermoforming
- Vacuum staging in devolatilization, *see* Devolatilization
- Variance of,
 binomial distribution, 384
 molecular weight distributions, 359
 completely segregated mixtures, 385
- Variational method:
 in FEM, 876–879
 Lagrange-Euler equation, 876
- Vectors:
 unit, 29
 unit normal, 26, 27
- Velocity gradient tensor, 42
- Viscoelasticity, *see* Linear viscoelasticity
- Viscometry
 capillary, 86–88, 94–96
 cone-and-plate, 96–100
 parallel disks, torsional flow, 372–376
 squeezing flow, 291–294
- Viscometric flow,
 configurations, 81
 definition of, 79
- Viscosity:
 elongational, 91–94
 measurement of, 94–99
 non-Newtonian, 84–86
 pressure dependence of, 683
 temperature dependence of, 109
 of various polymers, Appendix A
- Viscous dynamic seal, 508, 520
- Viscous energy dissipation (VED) 16, 182–183, 219–226
 in capillary flow, 684–689
- Vorticity tensor, 42
 in various coordinate systems, table, 116
- Wear, 147
- Weld lines, 763–764, 793, 800
- Weight average molecular weight, 359
- Weissenberg
 effect, 85–86
 rheogoniometer, 98
- Weissenberg-Rabinowitsch equation, *see* Rabinowitsch equation
- White-Metzner model, 104, 106
- Williams-Landel-Ferry (WLF) equation, 111
- Wine glass effect, 694. *See also* Capillary viscometer entrance region
- Wire coating, 727–731
 coating thickness in, 52–54
 melt fracture in, 729–731
 secondary normal stress difference in, 139–140
 stabilizing forces in, 139–140
- Yield stress, in Bingham fluid, 111
- Z-transform, 375
- Zero shear rate viscosity, 110
- ZFD model, 103, 106
- ZSK, *see also* Twin screw extruders
 invention of, 2, 5
 geometrical classification, 573–575

